POLISH
ACADEMY
OF SCIENCES

COMMITTEE OF
THERMODYNAMICS
AND COMBUSTION

INSTITUTE OF
FLUID FLOW
MACHINERY

# archives of thermodynamics

QUARTERLY

ISSN 1231-0956

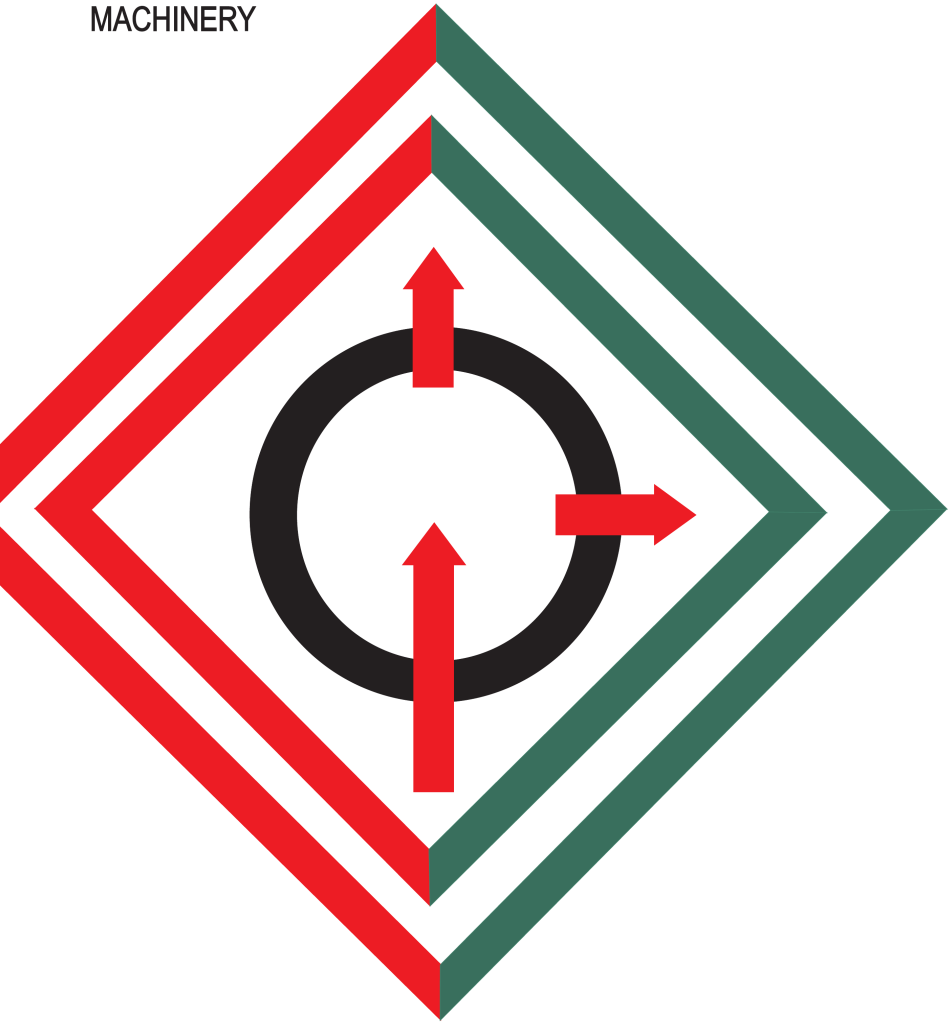

Vol. 44
2023
No. 4

archives of thermodynamics *Appears since 1980*

## Aims and Scope

The aim of the quarterly journal Archives of Thermodynamics (AoT) is to disseminate knowledge between scientists and engineers worldwide and to provide a forum for original research conducted in the field of thermodynamics, heat transfer, fluid flow, combustion and energy conversion in various aspects of thermal sciences, mechanical and power engineering. Besides original research papers, review articles are also welcome.

The journal scope of interest encompasses in particular, but is not limited to:

- Classical and extended non-equilibrium thermodynamics,
- Thermodynamic analysis including exergy,
- Thermodynamics of heating and cooling,
- Thermodynamics of nuclear power generation,
- Thermodynamics in defense engineering,
- Advances in thermodynamics,
- Experimental, theoretical and numerical heat transfer,
- Thermal and energy system analysis,
- Renewable energy sources including solar energy,
- Secondary fuels and fuel conversion,
- Heat and momentum transfer in multiphase flows and nanofluids,
- Energy transition,
- Advanced energy carriers,
- Energy storage and efficiency,
- Energy in buildings,
- Hydrogen energy,
- Combustion and emissions,
- Turbomachinery,
- Thermal energy conversion,
- Integrated energy systems,
- Distributed energy generation,
- Thermal incineration of wastes and waste heat recovery.

**Supervisory Editors**

T. Bohdal, *Koszalin University of Technology, Koszalin, Poland*
M. Lackowski, *The Szewalski Institute of Fluid Flow Machinery, Gdańsk, Poland*

**Honorary Editor**

J. Mikielewicz, *The Szewalski Institute of Fluid Flow Machinery, Gdańsk, Poland*

**Editor-in-Chief**

P. Ocłoń, *Cracow University of Technology, Cracow, Poland*

**Section Editors**

P. Lampart, *The Szewalski Institute of Fluid Flow Machinery, Gdańsk, Poland*
S. Polesek-Karczewska, *The Szewalski Institute of Fluid Flow Machinery, Gdańsk, Poland*
I. Szczygieł, *Silesian University of Technology, Gliwice, Poland*
A. Szlęk, *Silesian University of Technology, Gliwice, Poland*

**Managing Editor**

J. Frączak, *The Szewalski Institute of Fluid Flow Machinery, Gdańsk, Poland*

**Members of Programme Committee**

P. Furmański, *Warsaw Univ. Tech., Poland*
J. Badur, *Inst. Fluid Flow Mach., Gdańsk, Poland*
T. Chmielniak, *Silesian Univ. Tech., Gliwice, Poland*
D. Kardaś, *Inst. Fluid Flow Mach., Gdańsk, Poland*
S. Pietrowicz, *Wrocław Univ. Sci. Tech., Poland*
R. Kobyłecki, *Częstochowa Univ. Tech., Poland*
J. Wajs, *Gdańsk Univ. Tech., Poland*

**International Advisory Board**

J. Bataille, Ecole Centr. Lyon, France
A. Bejan, Duke Univ., Durham, USA
W. Blasiak, Royal Inst. Tech., Stockholm, Sweden
G.P. Celata, ENEA, Rome, Italy
L.M. Cheng, Zhejiang Univ., Hangzhou, China
M. Colaco, Federal Univ. Rio de Janeiro, Brazil
J.M. Delhaye, CEA, Grenoble, France
M. Giot, Univ. Catholique Louvain, Belgium
K. Hooman, Univ. Queensland, Australia
D. Jackson, Univ. Manchester, UK
D.F. Li, Kunming Univ. Sci. Tech., China
K. Kuwagi, Okayama Univ. Science, Japan
J.P. Meyer, Univ. Pretoria, South Africa
S. Michaelides, Texas Christian Univ., USA
M. Moran, Ohio State Univ., USA
W. Muschik, Tech. Univ., Berlin, Germany
I. Müller, Tech. Univ., Berlin, Germany
H. Nakayama, JAEA, Japan
S. Nizetic, Univ. Split, Croatia
H. Orlande, Federal Univ. Rio de Janeiro, Brazil
M. Podowski, Rensselaer Polyt. Inst., USA
R.V. Rao, Sardar Vallabhbhai Nat. Inst. Techn., India
A. Rusanov, Inst. Mech. Eng. Prob., Kharkiv, Ukraine
A. Vallati, Sapienza Univ. Rome, Italy
M.R. von Spakovsky, Virginia Polyt. Inst., USA
H.R. Yang, Tsinghua Univ., Beijing, China

POLISH ACADEMY OF SCIENCES
COMMITTEE OF THERMODYNAMICS AND COMBUSTION
INSTITUTE OF FLUID FLOW MACHINERY

# archives of thermodynamics

QUARTERLY
Vol. 44
2023
No. 4

## Editorial Office

IMP PAN Publishers
The Szewalski Institute of Fluid Flow Machinery, Fiszera 14, 80-231 Gdańsk, Poland,
Phone: (+48) 58-341-12-71 int. 141, E-mail: redakcja@imp.gda.pl
https://www.imp.gda.pl/archives-of-thermodynamics/

Copyright © by the Polish Academy of Sciences, 2023

Copyright © by the Szewalski Institute of Fluid Flow Machinery, 2023

Publication funding of this journal is provided by resources of the Polish Academy of Sciences and the Szewalski Institute of Fluid Flow Machinery

**Terms of subscription outside Poland**
Annual subscription rate outside Poland (2023) is 152 EUR. Price of single issue is 38 EUR. Previously published volumes are available on request. Subscription orders should be sent directly to **IMP PAN Publishers, The Szewalski Institute of Fluid Flow Machinery PASci, ul. Fiszera 14, 80-231 Gdansk, Poland**; dr Jarosław Frączak, phone: (+48) 58-52-25-230; e-mail: jfrk@imp.gda.pl. Payments should be transferred to the bank account of IMP PAN: IBAN 28 1130 1121 0006 5498 9520 0011 at Bank Gospodarstwa Krajowego; Code SWIFT: GOSKPLPW

**Warunki prenumeraty w Polsce**
Roczna prenumerata (2023 r.) wynosi 260.00 PLN. Cena pojedynczego numeru wynosi 65.00 PLN. Osiągalne są również wydania archiwalne. Zamówienia z określeniem okresu prenumeraty, nazwiskiem i adresem odbiorcy należy kierować bezpośrednio do Wydawcy (Instytut Maszyn Przepływowych im. R. Szewalskiego PAN, ul. Fiszera 14, 80-231 Gdańsk, dr Jarosław Frączak, e-mail: jfrk@imp.gda.pl). Wpłaty prosimy kierować na konto Instytutu Maszyn Przepływowych PAN nr 28 1130 1121 0006 5498 9520 0011 w Banku Gospodarstwa Krajowego

**Articles in *Archives of Thermodynamics* are abstracted and indexed within:**

Applied Mechanics Reviews • Arianta • Baidu Scholar • BazTech • Cabell's Directory • Celdes • Chemical Abstracts Service (CAS) – CAplus • CNKI Scholar (China National Knowledge Infrastucture) • CNPIEC • EBSCO (relevant databases) • EBSCO Discovery Service • Elsevier – SCOPUS • ESCI (Emerging Sources Citation Index) • Genamics JournalSeek • Google Scholar • Inspec • Index Copernicus • J-Gate • Journal TOCs • Naviga (Softweco) • Paperbase • Pirabase • POL-index • Polymer Library • Primo Central (ExLibris) • ProQuest (relevant databases) • ReadCube • Referativnyi Zhurnal (VINITI) • SCImago (SJR) • Summon (Serials Solutions/ProQuest) • TDOne (TDNet) • TEMA Technik und Management • Ulrich's Periodicals Directory/ulrichsweb • WorldCat (OCLC)

ISSN 1231-0956
ISSN 2083-6023 (Online)
Journals PAS – Electronic Library Polish Academy of Sciences
https://journals.pan.pl/ather

Typeset in LaTeX by
Drukarnia Braci Grodzickich Sp.j. 05-500 Piaseczno, ul. Geodetów 47a

Printed and bound by
Gimpo, 02-858 Warszawa, ul. Transportowców 11

**archives**
**of thermodynamics**
Vol. **44**(2023), No. 4

# Contents

J. Shi, Y. Zhang, D. Kong, L. Liu, Y. Lu, and K. Hooman: A review on research and application of multi-energy complementary system containing high proportion of renewable energy based on different attributes ..... 3

S. Polesek-Karczewska, D. Kardaś, and I. Wardach-Święcicka: An in-house numerical code to assist in designing a small-scale red-hot air furnace ..... 43

S. Grądziel, W. Zima, A. Cebula, M. Rerak, E. Kazak-Jagieła, A. Pawłowski, R. Blom, L.O. Nord, V.T. Skjervold, and G. Mondino: $CO_2$ capture from flue gases in a temperature swing moving bed ..... 63

M. Majdak, S. Grądziel, W. Zima, A. Cebula, M. Rerak, and E. Kozak-Jagieła: Numerical and experimental analysis of thermal and flow operating conditions of waterwall tubes connected by fins ..... 81

P. Rolka and M. Lackowski: The effect of graphene nanoparticles on the thermal conductivity enhancement of organic phase change material and its energy storage properties ..... 103

J.T. Cieśliński, M. Fabrykiewicz, T.S. Wiśniewski, M. Kubiś, S. Smoleń, A. Eicke, K. Dutkowski, and M. Głuszek-Czarnecka: New empirical correlations for the viscosity of selected organic phase change materials ... 123

J. Kobylarczyk, D. Kuśnierz-Krupa, and M. Nowak-Ocłoń: Impac of paving surface material on thermal conditions within a residential building 141

T.K. Suchocki, P. Kazimierski, K. Januszewicz, P. Lampart, D. Zaniewski, P Klimaszewski and Ł Witanowski: Pyrolysis-derived waste polypropylene oils in gas turbine engines: a comprehensive performance and emission study ..... 157

Ł. Brodzik: Gas temperature distribution in the evaporator of GTM400 turbojet engine ..... 185

M. Banaszkiewicz and M. Skwarło: Numerica investigations of transient thermal loading of steam turbines for SMR plants ..... 197

M. Laskowski, K. Krajewski, P. Chaja, P. Zawadzki, and S. Bykuć: The impact of electrification of heating on the power grid for a selected area microgrids ..... 221

M.J. Kowalczyk, A. Romaniak, M. Łęcki, A. Gutkowski, and G. Górecki: Experimental investigation of the energy efficiency of a linear compressor and comparison with a reciprocating compressor in a small refrigeration system ..... 243

D. Joachimiak, T. Borowczyk, and M. Joachimiak: A model of the steam compression process in a piston reactor ..... 261

T. Ochrymiuk, W. Dudda, and J. Badur: On a Carnot working continuum with non-equilibrium state parameters ..... 285

R. Matysko: Steady state and transient analysis of solid oxide fuel cell within the framework of thermodynamic energy cycles ..... 317

M. Kolodziejski: Review of hydrogen-based propulsion systems in the maritime sector ..... 335

M. Witek and F. Uilhoorn: An approach to coupling the gas flow dynamics and thermodynamics of hydrogen solubility in L485ME steel grade for estimation of fracture toughness ..... 381

T. Bury and M. Hanuszkiewicz-Drapała: Experimental and numerical analysis of the impact of a liquid flow rate on the operational performance of a cross-flow tube-and-fin heat exchanger ..... 405

S. Grosicki and J. Wilk: Mass/heat transfer analogy method in the research of convective fluid flow through channels with a specific geometry ..... 427

T. Hałon, D. Kaczmarek, W. Lada, and B. Zajączkowski: Subatmospheric pool boiling of water at very low liquid levels ..... 447

I. Nazarova and A. Gutkowski: Experimental investigation of limit parameters of direct contact condensation in the heat exchanger for waste heat recovery ..... 463

H. Koshlak: Assessment of heat and mass transfer processes in vapor bubbles under conditions of metastable equilibrium of liquids ..... 483

P. Mirek, M. Panowski, K. Słomczyńska, M. Stanek, and T. Bąkowski: Resources and potential for utilization of low-exergy heat from mung bean sprouts cultivation – case study ..... 507

A. Ryfa, M. Tokarski, W. Adamczyk, A. Klimanek, P. Bargiel, R Białecki, M. Kocot, M. Niesler, H. Kania, J. Stecko, and M. Czaplicka: Determination of an axial gas cyclone separator cut-off point by CFD numerical modeling ..... 535

M. Ciałkowski, M. Joachimiak, M. Mierzwiczak, A. Frąckowiak, A. Olejnik, and A. Kozakiewicz: The analysis of the stability of the Cauchy problem in the cylindrical double-layer area ..... 563

O.A. Al-Munaf Ibrahim, S.A. Kadhim, and M.K.S. Al-Ghezi: Photovoltaic panels cooling technologies: Comprehensive review ..... 581

W. Kuczyński and A. Borowska: The effect of photovoltaic system operating parameters on exergy efficiency ..... 619

K. Rup and T. Sobota: Adiabatic gas transport in the long flow channels ..... 635

R. Matysko and T. Ochrymiuk: Computational analysis of electric field effects on electrodialysis for enhanced desalination processes ..... 653

W. Kuczyński, I. Michalska-Pożoga, M. Szczepanek, and K. Chmiel: Overview of application options for vertical axis wind turbines ..... 665

O.E. Nyong, D.I. Igbong, C.E. Ebieto, B.E. Ene, B. Oluwadare, and A.A. Eso: Numerical simulation of two-phase gas-liquid flow through horizontal annulus pipe ..... 705

**archives**
**of thermodynamics**
Vol. **44**(2023), No. 4, 3–41
DOI: 10.24425/ather.2023.149726

# A review on research and application of multi-energy complementary system containing high proportion of renewable energy based on different attributes

**JIE SHI**[a, b]
**YANNI ZHANG**[a]
**DEQIANG KONG**[a]
**LIAN LIU**[a]
**YUANSHEN LU**[c]
**KAMEL HOOMAN**[d*]

[a] School of Physical Science and Technology, University of Jinan, West Nanxin Zhuang Road 336, 250000 Shizhong District, Jinan City, Shandong Province, China

[b] School of Engineering, Cardiff University, UK

[c] School of Mechanical and Mining Engineering, The University of Queensland, Australia

[d] Delft University of Technology, Delft, Netherlands

**Abstract** To better understand the latest development of renewable energy systems, recent studies on multi-energy complementary power systems with a high proportion of renewable energy are reviewed in this paper. The connection modes of power grids and economic system analysis are summarized and discussed respectively, putting forward some suggestions on the system design and operation optimization. Firstly, the characteristics and differences between an integrated system and an off-grid system are reviewed, concluding that an integrated system is more reliable and cost-effective based on a few case studies. Secondly, the commonly used economic parameters and cost evaluation methods of the hybrid power system are reviewed. Those methods offer crucial tools to optimize the system, and they

*Corresponding Author. Email: k.hooman@tudelft.nl

are able to analyze the system feasibility, enabling the most economical configuration. The results of several cases prove that the hybrid multi-energy system is more economical than the single-energy system. Finally, there are few articles focusing on technical details assessments and environmental impacts, which leaves room for future study.

**Keywords:** Off-grid system; Integrated system; Renewable energy; Multiple complementary systems; Economic analysis

**Acronyms**

| | | |
|---|---|---|
| ASC | – | annual systematic cost |
| ABC | – | artificial bee colony |
| BG | – | biomass generator |
| COE | – | cost of energy |
| CRF | – | capacity recovery factor |
| GA | – | genetic algorithm |
| HOMER | – | renewable energy from hybrid optimization model |
| NDR | – | nominal discount rate |
| NPC | – | net present cost |
| LCOE | – | levelized cost of electricity |
| LPSP | – | loss of power supply probability |
| PSO | – | particle swarm optimization |
| REF | – | Renewable Energy Foundation |

# 1 Introduction

Global energy demand is gradually increasing, even in rural and remote areas scattered in developing countries [1]. These areas are far from the city centers which are normally covered by national grid, though the population and electric power demand is large [2]. At present, fossil fuel is the main energy source of power plants, among which coal accounts for the largest proportion. However, coal combustion is considered as one of the major carbon emission sources, which brings much challenge to global environment.

As a substitute for traditional energy, renewable energy has attracted the attention of scientists and decision-makers [3]. In fact, both solar and wind energy are sufficiently competitive now compared with other existing forms of energy. However, each of them has apparent economic and technical defects. For example, it is the fact that power demands follow peak-trough curves, whereas the productions of solar power are subject to the diurnal cycle and uncontrollable weather factors. While the latter could

be alleviated by optimal engineering designs like oversizing, which leads to a requirement for energy storage to reduce the system cost. Based on the energy conservation principle, mismatch which is between the solar generation curve and grid demand, defines the minimum size of storage units. For instance, the average daily total demand in Australia's eastern power grid follows a typical duck-shaped curve with the biggest peak between 18:00–19:00 (local time) of a day. If the grid supplies electricity solely by PV, it would require battery capacity of around 300 GWh at least, which is simply depicted as the area of enclosure (1) on the chart (Fig. 1), or the sum of enclosures (2) and (3). The area of the enclosures embodies the amount of battery required.

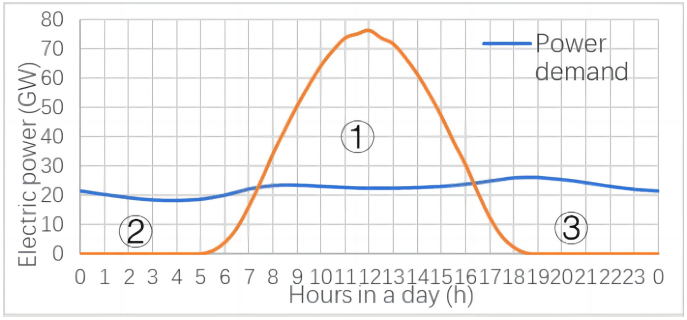


Figure 1: Averaged daily grid demand curve and solar power generation curve in Australia.

In addition, wind energy exhibits much more irregularity due to frequent variations of wind intensity and direction, which makes prediction more difficult. The outputs of wind farms vary in different regions and periods. Apart from wind energy, Biomass fuel is often considered an important energy source because it has the same dispatch ability as traditional fossil fuel-based power generation. However, its renewability is often questioned because a majority of crop waste is mainly produced in the harvest process of 2–3 months per year [4].

To solve those problems, a concept of hybrid renewable energy systems is established so that each type of defect can be made up and the problem of high storage cost is solved. Combined utilization of solar energy and biomass energy can complement each other; likewise, wind and solar energy are complementary in time and intensity [5–8]. Biomass system plays an important role in solar intermission periods [9]. The introduction of biomass energy reduces the negative impacts of only using the combination of so-

lar energy and wind energy [10]. Research also proves that hybrid systems are more efficient and economical than any single renewable energy system. This kind of hybridization helps to overcome the problems of single systems [11]. At the same time, integrating renewable energy systems can significantly reduce operating costs [12].

In recent years, hybrid renewable energy systems have been widely deployed. Multi-energy complementary systems have adjustable resources and flexible operation modes, such as integrated or off-grid systems [13]. This review discusses the similarities and differences between the two kinds of system via some specific cases. In addition, this paper summarizes the optimization and economic feasibility analysis of each energy system to realize the cost reduction.

In addition, in order to improve the grid-connected safety and stability of renewable energy systems, it is also crucial to configure the corresponding energy storage devices. The performance of different batteries is also different, for example, the charge and discharge response speed of electrochemical energy storage system is fast, the technology is mature, but the charge and discharge life is limited. Lithium-ion batteries are widely used by electric vehicles because of their high energy density and long cycle life [14, 15].

In this paper, the existing energy systems in areas based on different situations including climates, economic, and environment are listed respectively, which provide reference for economic optimization or feasibility analysis of multi-energy complementary hybrid energy storage system. In addition, the actual situation in various places and optimization methods are able to attract scholars' interest in multi-energy complementary hybrid energy storage systems.

In conclusion, this review article provides a comprehensive overview of the research and application of multi-energy complementary systems with a high proportion of renewable energy. The review emphasizes the advantages of hybrid renewable energy systems over single systems in terms of problem-solving and cost-reducing. Through a few case studies, the similarities and differences between the integrated and off-grid systems are analyzed. Furthermore, this article summarizes optimization along with economic feasibility analysis approaches to achieve cost saving. As renewable energy plays an increasingly important role in energy transition and environmental protection, the hybrid system optimizations, which combine various renewable energy sources together, become a vital research topic. By addressing the challenges and opportunities in this field, this review

article contributes to the advancement of renewable energy technology and sustainable energy utilization, which can promote global energy transition.

The rest of this article is shown as follows: Section 2 mainly examines the characteristics of the integrated and off-grid systems, investigating the differences between them. Section 3 summarizes the parameters of economic analysis and the methods used in the analyses. In addition, the system optimizations in various regions with different power load situations are studied and compared, followed by conclusions in Section 4.

# 2 The characteristics and differences between the integrated and off-grid multi-energy complementary systems

## 2.1 Characteristics

Integrated system is referred to a local power system in which home power grid and national power grid are linked. Take solar system for example: Photovoltaic panel converts solar irradiation into the voltage required by the national grid through invertors. It is typically seen in roof-top installations of residential buildings. When the electricity generated by solar energy exceeds the electricity requested by domestic appliances, the excess electricity is sent to the public grid. When solar energy cannot meet domestic demands, the integrated system is automatically supplemented by the national power grid [14].

Off-grid system is an independent solar power generation system, which is a system that operates without power grid. It mainly comprises solar panels, energy storage (e.g. batteries), charge and discharge controllers, inverters and other components. The electricity generated by the solar panels is directly either applied for costumers or being stored in the batteries. When it comes to supply for electrical appliances, the direct current in the batteries is converted into the requested voltage by national grid through inverters [15].

Distinguishing the integrated system from the off-grid system depends on the connection way with national grid. Besides, there are other differences between them. For example, the off-grid system must be equipped with batteries, while the integrated system rarely does. The off-grid system is not limited by geographic locations, and it can be applied as long as there is sunlight. So it is very suitable for remote areas without a power grid, such

as isolated islands, fishing boats, outdoor breeding bases, etc. It can also be used as emergency power generation equipment in areas with frequent power outages. The integrated grid system not necessarily have to include batteries, so the cost is greatly reduced. In villages or communities, where the energy demand requirements meet, the integrated grid system which uses hybrid renewable energy sources can be applied via sending electricity to the power grid, which further reduce the system cost.

## 2.2 Study cases of the integrated complementary system

In recent years, studies on selecting and allocating renewable energy technologies into combined hybrid systems have achieved remarkable achievements. These efforts focus on improving the performance of the hybrid renewable energy system, making accurate prediction, ensuring reliability and reducing cost. A typical layout of integrated systems is shown in the following figure [16]. The purposes and effort of designing and applying hybrid combined system basically include two aspects: renewable energy output stability and system cost. The following two parts review the above two aspects, respectively.

### 2.2.1 From view-sights of stability

Solar energy and wind energy are stochastic sometimes. Technical and economic feasibility analysis of solar-biomass systems in the Ludhiana area of Punjab is studied, using the hybrid system to provide electricity in different areas. This case can overcome the shortcomings from applying only a single renewable energy source [4].

Similarly, by comparing the reliability of the solar-biomass hybrid energy system with that of the photovoltaic system, it is found that the reliability of the former is 75.01%, far superior to that of the latter's 28.37%. At the same time, it also reduces the cost, mainly due to the large number of cattle in Cole Hapoel. Animal waste can be used as the feedstock of biogas power plants, with a biomass potential energy of 44.8 MWe, and the biomass potential obtained from forests and wasteland is 46.3 MWe. The system's reliability can be increased by adding an energy source or keeping an energy storage battery [5]. Here, the reliability is usually evaluated by loss of power supply probability (LPSP) [17–19].

Hydropower is added when the cascade reservoirs is taken part in the multi-energy complementary system. A hydropower plant is an engineering

facility that converts gravitational potential energy of water into electric energy through the joint operation of the water turbine and the generator. Its capacity is constrained by factors such as atmospheric precipitation, river runoff, reservoir capacity and turbine characteristics. In a short time (such as one day or several hours), the atmospheric precipitation and water flow change little, so the hydropower station is relatively stable [20].

From the above cases, the hybrid energy system is able to overcome the shortcomings caused by a single energy source, making the energy system more continuous and more stable [21].

### 2.2.2 From view-sights of cost

Firstly the local solar irradiation and wind speed data of the interested place should be obtained, followed by the climatic and geographical characteristics. Secondly, the actual energy consumption and load distribution of the case building should be determined through the water and electricity bills along with dynamic energy simulation [21]. In addition, the ratio of solar and wind energy is also a key issue. In order to evaluate the ability of the wind/solar hybrid power to afford the load of Brazil's northeast grid, 11 wind/solar scenarios have been evaluated by minimizing the need for energy storage systems. The result is shown in Fig. 2. The combination scenario which is 40% of wind and 60% of solar energy is the optimal result to meet the load in Northeast Brazil [22].

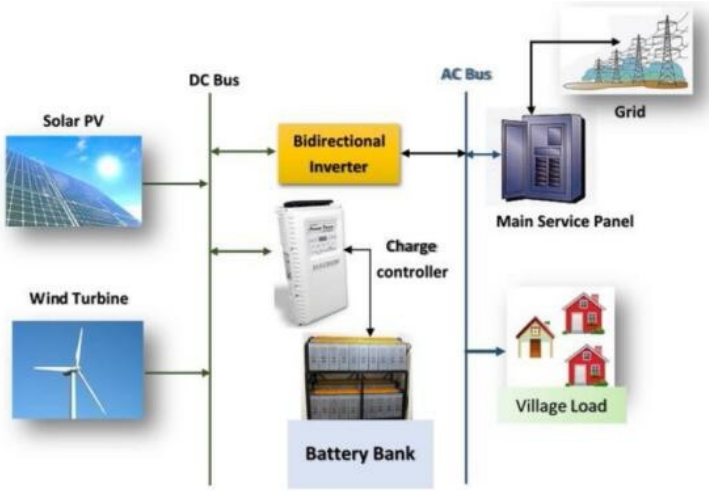


Figure 2: A schematic diagram of the integrated grid system.

The resource evaluation of wind power, biomass energy and solar energy in Pakistan is studied to optimize the integrated system, and HOMER (renewable energy from hybrid optimization model) is used for simulation and optimization so that a total load of wind energy, photovoltaic and biomass resources can be well utilized to the maximum extent. When the local energy demand is low, the extra power will be sent to the grid. The energy cost is calculated under different peak loads, energy demand curves and grid availability. Under the peak load of 73.6 MW, the energy cost of the integrated grid hybrid system is 180 million USD, and the horizontal cost of energy (COE) is 0.0574 USD/kWh [23–26]. In order to minimize the operation cost, a hybrid energy system consisting of wind energy, photovoltaic, gas turbine and energy storage are established via an operation optimization model. A moth flame optimization algorithm is applied for unit scheduling [27–33]. Finally, a micro-grid project is taken as case study for optimization in three configurations, which includes wind power, photovoltaic and energy storage. The case study shows that the operation optimization model can effectively reduce the system's operating cost and obtain the optimal output mode of each unit. It proves that the model has a certain guiding role in the economic dispatch of hybrid energy systems [38]. In the rice mill in Tripura, northeast India, about 24 tons of rice hulls are produced annually. The photovoltaic-biomass hybrid power grid model can save more than 90% of power grid electricity and significantly reduce the system operation cost [39]. Taking slaughterhouses in southern Nigeria as an example, an integrated distributed hybrid power system of solar energy and biomass is proposed in South Australia. The feasibility study shows that the integrated grid hybrid power system is an economical and environment-friendly solution for the annually changing power load [40]. All the above cases show the advantages of hybrid energy system in terms of cost against single energy system.

### 2.3 Study cases of the off-grid complementary system

Electricity demand is a key bottleneck for the development of remote areas. Due to the complex terrain and massive investment, the installation and application of power grid cable to the remote areas have been limited. Even in electrified villages in remote areas, the quality and availability of electricity are sometimes poor and unstable. In remote areas, traditional power supply methods include grid extension and diesel generators. The extension of the power grid faces much challenge, such as a long distance from the

power grid, complex terrain, and huge investment. To solve the above problems, a more efficient distributed off-grid hybrid renewable energy system is established, improving the reliability of power supply in remote rural areas.

The off-grid model alleviates a lot of financial and procedural deficiency, such as huge investment cost and the need of obtaining government permission. High degree of dispersion, low population density and little energy demand usually characterize rural communities. Electricity demand is generally concentrated at night. In many countries, some villages are still far from the power grid center, which brings much challenge to system economic [41, 42].

Due to the intermittency of renewable energy, using single renewable energy system usually leads to defects such as system instability and excessive cost. It can be solved by integrating two or more renewable energy sources. In designing process, it is necessary to consider the type of local renewable energy sources. The schematic diagram of a typical hybrid energy system is shown in Fig. 3.

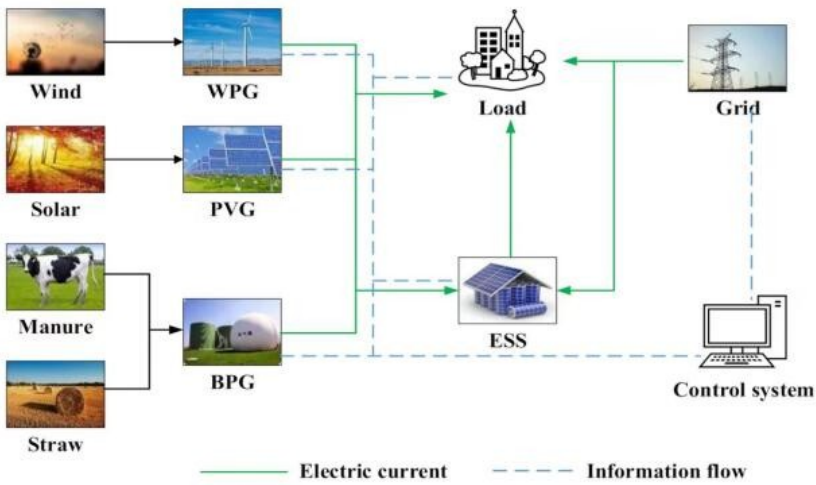


Figure 3: Wind-solar-biomass hybrid energy system: WPG – wind power generator, PVG – photovoltaic generators, BPG – biomass generator, ESS – energy storage system.

In addition, an energy storage unit helps to improve the system stability, reliability and flexibility by adjusting the charging and discharging time and rate. After comparing each battery's cycle efficiency and cost, the lithium battery energy storage method is adopted [43–46].

The battery unit and diesel generator maintain the operation of the hybrid power system, eliminating reliability and power supply problems. The dispatch strategy is used to control the process of battery and diesel generator sets. It depends on factors such as the nature of renewable energy, fuel costs, the capacity of batteries and generators, along with renewable energy amount. A hybrid power system design mainly adopts two scheduling strategies: cyclic charging and load-following [47–51].

### 2.3.1 Wind-photovoltaic combined system

Solar power and wind power are combined to form a hybrid system. The peak of photovoltaic power is usually around noon, when solar irradiance is the highest, while the peak of wind power is usually at a different time. Regions with large power loads often have poor wind energy density, while situations in other regions are just the opposite, which brings difficulties to the economic development of wind power [52,53]. In some cases, using solar and wind energy alone may lead to unreliable energy sources and much cost [54, 55]. However, their combination is technically and economically conductive to generating electricity for remote areas [56–62].

Solar energy and wind energy have higher requirements in the geographical environment. Scholars have analyzed the electrification cost of small wind power system in rural Africa. The result shows that photovoltaic and diesel systems are the most economical and feasible methods for rural electrification in Africa, while wind power system has economic advantages only in the Horn of Africa and a few scattered areas [63].

The application of photovoltaic/wind/diesel hybrid power generation system in rural electrification in three isolated villages with different climatic characteristics in Colombia is analyzed. According to observations, hybrid energy options in remote rural areas usually consider a limited set of renewable energy technologies, such as photovoltaic arrays and wind turbines, with batteries or diesel generators as backup facilities [64, 65].

The system performances of solar-wind energy, solar-pumped storage and wind energy-pumped storage are compared under loss probability with the range of 0–5%. Because the cost of the wind-driven generator is exceptionally high, and they have to withstand typhoons on the island, only one wind-driven generator is considered in the hybrid system. Therefore, the combination of wind and solar energy should be considered when design the optimal power supply system. Energy balance analysis shows that the overall efficiency of the pumped storage system is 52.5%. Sensitivity analy-

sis shows that load demand is a key factor affecting system cost. Compared with battery energy storage, the life cycle cost of pumped storage is significantly reduced, especially when some variables are controlled, such as storage capacity [66].

### 2.3.2 Photovoltaic-biomass combined system

Wind power generation has many advantages however it is challenged by integrating restricts and equipment utilization ratio. Instead, biomass power generation capacity is higher than its nominal installed capacity, indicating that biomass power generation has a higher capacity factor than other power generation [29]. Compared with solar and wind energy, storage and transportation of biomasses are also more convenient. Biomass materials can be converted into organic fertilizers through natural fermentation, such as composting and returning to the fields. Therefore, the proper use of biomass resources is necessary and feasible [67].

Rural areas are often taken as the preferred options in terms of site selections for biomass power plants [68]. In some areas, abundant biomass resources can be easily obtained from agricultural, industrial, and factory wastes, such as 1) burning wood; 2) anaerobic degradation of high organic moderate waste; 3) gasification of wood chips, agricultural waste and particles; 4) high-temperature decomposition [69]. Besides, the biogas system is better than diesel generators as a backup system [70, 71].

If heat, electricity and gas are required for remote areas, a distributed solar-biomass residential integrated energy system can be adopted [72–77]. This kind of system is a solar-biogas industrial combination scheme, making use of solar energy and biomass energy, reducing the dependence level on battery energy storage systems, along with satisfying diverse energy demand in rural areas [78].

### 2.3.3 Wind-photovoltaic-biomass complementary system

Take the remote area of Bhawani India as an example. Based on the annual hourly average resource data, the optimization results of the genetic algorithm (GA) and the particle swarm optimization (PSO) algorithm are compared. In addition, the power loss probability technology is used for system reliability analysis. The optimal configurations of the hybrid renewable energy system are ranked based on the minimizing COE of the system. Compared with GA, PSO is able to effectively optimize the annual

PV (photovoltaic) output power, wind energy output power, diesel generator output power and dump load which is based on load tracking strategy. The above results indicates that with PSO optimization, the PV output power can be increased, and the load-following strategy of PSO is able to obtain more appropriate parameters. Therefore, in the optimization planning, compared with the load tracking strategy, the cyclic charging strategy is more effective [79].

Another case comes from a rural area in western China. The daily and seasonal characteristics of energy supply, the area scale and energy demand mode in remote rural areas are considered. In the Hybrid Optimization Model of Renewable Energy (HOMER), different combination scenarios including photovoltaic panels, wind turbines and biogas generators are modeled and optimized. The most cost-competitive configuration is determined. At the same time, the reliable power supply is obtained to ensure the village's residential, community, commercial and agricultural needs. The input data includes meteorological data, availability of renewable resources, load distribution and technical data. According to the solar radiation data, ambient temperature and monthly mean wind resources obtained, the hourly power generation of solar modules and the output power of wind turbines are calculated in. Biomass can be used as a backup to ensure a stable power supply to a certain extent. The storage battery serves as a supplementary backup facility. The results are shown in Table 1: 104 kW photovoltaic module, three 10 kW wind turbines, 50 kW biogas fueled diesel generator, 331 kWh battery and 99 kW converter are the most economical and reliable configuration schemes for off-grid hybrid power system [23].

Besides, a solar-wind-biomass hybrid system is proposed in Egypt's Monshaet Taher village at Beni-Suef Governorate to solve the problem of unreliable electricity in the village. According to the daily energy availability and load demand data, six energy scenarios are simulated in HOMER to design an optimal renewable energy system to minimize energy costs. Considering the solar and wind energy available in the area, most of the electricity in the optimal solution comes from biomass generators, which provide a cheap source of electricity for the local area [36]. In addition, hybrid energy systems including the traditional energy along with photovoltaic, wind, biomass and battery are analyzed and compared under different climatic conditions in seven selected locations in Australia. The result showes that compared with traditional energy, hybrid energy system has the advantages of lower cost and emission reduction [37]. It can be seen that the hybrid multi-energy system is superior to the traditional energy system to some

Table 1: The different characteristics of the integrated and off-grid systems.

| Ref. | Publication date | Study area | Network mode | Energy composition | Average daily (kW) | Features |
|---|---|---|---|---|---|---|
| [31] | 2019 | A remote rural village in Ethiopia | Off-grid | PV, WT, battery, diesel generator | 19.6 | Determine the optimal system configuration through sensitivity analysis |
| [21] | 2016 | Shivaji University, Kolhapur | Off-grid | Wind-solar, PV-biomass | 17.591 | Modelling without energy storage based on data that has been tested in the field for a year |
| [4] | 2020 | India | Grid | Solar, biomass | – | Study the advantages of the combined use of solar energy and biomass energy |
| [38] | 2015 | Nijhum Dwip of Bangladesh | Off-grid | PV, WT, BG | – | Compare the economic and environmental aspects of hybrid renewable energy systems with traditional systems |
| [33] | 2020 | An institutional building | Off-grid | Biomass, PV, WT, batteries | 87.6 | Sensitivity analysis of hybrid renewable energy systems |
| [39] | 2014 | Tripura | Grid | PV, biomass | – | Analyze the impact of the system on the power grid |
| [28] | 2020 | A rural community in Ismailia Governorate, Egypt | Grid | PV, WT | 463 | Three scenarios are proposed to study the relationship between the grid and the hybrid renewable energy system |
| [40] | 2021 | Morocco | Off-grid | PV, biomass | – | Sensitivity analysis on the amount of biomass resources |
| [26] | 2016 | – | Off-grid | PV, wind, biomass, battery | – | Artificial bee colony algorithm has good convergence and the ability to provide high-quality results |

BG – biomass generation, WT – wind turbine, PV – photovoltaic.

extent, not only technically overcoming the shortcomings of conventional energy, but also significantly reducing the cost [80].

## 2.4 Summary

The use of renewable energy is increasing. Due to the instability of these resources at different times and locations, using only a single resource may

lead to the unreliability of power output. The integrated system can be directly supplied by the grid to ensure reliability when renewable energy can't satisfy the load requirements. At the same time, it can also sell excessed electricity to the grid when there is a surplus, further reducing energy cost. In isolated islands or rural areas which are far away from the power grid, the off-grid mode can be adopted due to the high cost of installing the power grid. According to the local natural and geographical environments considering sunlight, wind speed, and biomass, suitable renewable energy types is selected. For example, wind power generation is more ideal for areas with high wind speeds, such as the seaside. In addition, an energy source or energy storage battery can be added to improve reliability.

# 3 Economic analysis of multi-energy complementary system

## 3.1 The parameters of economic analysis

It is essential to know the parameters in the economic analysis of a multi-energy complementary system. Firstly, it is necessary to understand that the economic parameters used in the analysis mainly include cost parameters (COE, NPC, LCOE, etc.), benefit parameters (NPC, etc.). Secondly, there are closed relations among economic parameters, so it is necessary to further analyze how economic parameters interact with each other and what are the influence. Finally, environment and economy are inseparable, so it is essential to analyze the system environment. Therefore, the environmental parameters are briefly introduced in this article.

### 3.1.1 Economic parameters of system cost

Net present cost (NPC): The total net present cost of a system is the present value of all the costs in which the system incurs over its lifetime minus the present value of all the revenue which it earns over its lifetime. Costs include capital costs, replacement costs, operational and management costs and fuel costs [81,82]:

$$C_{\mathrm{NPC}} = \sum_{t=0}^{T} C_{\mathrm{Cap},t} + C_{\mathrm{O\ \&\ M},t} + C_{\mathrm{Replace},t} + C_{\mathrm{Fuel},t} - R_{\mathrm{Salvage},t}\,, \quad (1)$$

where, $C_{\mathrm{Cap},t}$ is the capital cost at time moment $t$, $C_{O\ \&\ M,t}$ is the operational management cost at time $t$, $C_{\mathrm{Replace},t}$ is the replacement cost at

time $t$, $C_{\mathrm{Fuel},t}$ is the fuel cost at time $t$, $R_{\mathrm{Salvage},t}$ is the present value of all the revenue which it earns over its lifetime at time $t$.

Cost of energy (COE): COE divides the annualized cost of the system by the electrical load [42]:

$$C_{\mathrm{COE}} = \frac{C_{\mathrm{AT}}}{\mathrm{Load}}, \tag{2}$$

where, $C_{\mathrm{AT}}$ is the annualized cost of the system and Load is the electrical load.

Levelized Cost of Energy (LCOE): It is the power generation cost calculated after leveling the cost and power generation in the life cycle of the project. LCOE is the ratio of the present cost value to the present value of the power generation in the life cycle [83]:

$$\mathrm{LOCE} = \frac{\text{Total life cycle cost}}{\text{Total lifetime energy production}}. \tag{3}$$

For an energy system, total NPC refers to the difference between the present value of all costs generated in the life cycle and the present value of all revenues obtained. HOMER is used to indicate the life cycle cost of the system. This value may be positive or negative [84]. NPC plays a very important role in the optimization analysis of a multi-energy storage system. It should be reduced as much as possible in the optimization process. In addition to the optimization process, NPC is also considered in the economic analysis of the energy system. COE is another parameter that is equally important, and it is usually taken into account with NPC. The most economical system with the fewest NPC and COE, is obtained through optimization. An index called AT (annual total cost) should be introduced in the calculation of NPC and COE, both NPC and COE of the system will be affected by it with positive influence results [85]. Now, the LCOE can be calculated by leveling the cost and power generation in the life cycle of the project, which is defined by HOMER software as the average cost of useful power generated by the system per kilowatt hour [86].

### 3.1.2 Economic parameters of benefit

Nominal discount rate (NDR): It mainly reflects some changes in discount rate under the influence of inflation because money suppliers must require an increase in the interest rate to compensate for the loss of their purchasing

power in the case of inflation, which leads to changes in the cost of capital and the rate of return on investment.

Inflation rate (IR): It refers to the rate of increase in the general price level within a certain period ( usually one year).

In economic analysis the parameters of the cost are more intuitive, and the parameters of benefit will lead to some impact on the cost parameters to a certain extent. In a long-life cycle, the cost of operation will inevitably increase, which affects NPC of the whole system. According to NDR calculation formula , the value of NDR will increase as the rate of inflation rising, and the impact of NDR on these two cost economic parameters is opposite to the life cycle. A higher NDR will lead to higher COE and lower NPC, so the inflation rate will indirectly affect the COE of the system through NDR.

In addition, the solar energy and wind speed of each region also leads to some influence on the cost of a multi-energy complementary system. If solar and wind resources are abundant in an area, the cost may be low. Take wind energy as an example, the wind resource reduces the COE and NPC of the system according to different values of Weibull shape parameter $k$. In this case, the cost of the system will be greatly reduced in areas with abundant easy-access biomass resources [87]. However, if the biomass price is too high, the cost will increase accordingly [50]. Similarly, the renewable energy (REN) factor for wind is also one of the inevitable influencing factors of cost. The sensitivity analysis shows that the higher the value of REN factor is, the lower the value of LCOE will be [88].

Based on keeping similar charge and discharge efficiency, as round-trip efficiency increasing, LCOE decreases sharply. Battery efficiency is also a factor which is affecting LCOE. To make the study more simple, charge and discharge efficiency is set as the same value. Different round-trip efficiency values are compared to find that LCOE would decline sharply as round-trip efficiency increases [89].

As is shown in Table 2, the corresponding relationship between cost parameters and multiple indicators are listed. where , '+' indicates positive influence, and '–' indicates negative influence. For NPC case, 'life cycle' and 'biomass price' lead to positive effects. For NDR, "inflation rate", 'solar radiation' and 'wind speed' lead to negative effects. For COE, NDR and 'biomass prices' lead to positive effects, while 'inflation rate', 'life cycle', 'solar radiation' and 'wind speed' lead to negative effects. For LCOE, the effects of 'REN factor' and 'battery efficiency' are both negative.

Table 2: Influence factors of cost economic parameters ('+' – positive influence, '–' – negative influence).

| | NDR | Inflation rate | Life cycle | Solar radiation | Wind speed | Biomass price | REN factor | Battery efficiency |
|---|---|---|---|---|---|---|---|---|
| NPC | – | – | – | – | – | + | | |
| COE | + | – | – | – | – | + | | |
| LCOE | | | | | | | – | – |

### 3.1.3 Environment parameter

Modified combustion efficiency (MCE): It is defined as the excess mole fraction of $CO_2$ divided by the sum of the excess mole fractions of $CO_2$ and CO [52]:

$$\mathrm{MCE} = \frac{\Delta \mathrm{CO}_2}{\Delta \mathrm{CO}_2 + \Delta \mathrm{CO}}\,, \tag{4}$$

where, $\triangle CO_2$ is the excess mole fraction of $CO_2$, $\triangle CO$ is the excess mole fraction of CO.Power generation carbon intensity is defined as the amount of carbon generated by each degree of power generation in a given region and time [54]. Equivalent carbon emission of power generation side within the region is defined as

$$e = e_{\mathrm{up},k} + e_{\mathrm{constr},k} + e_{\mathrm{comb},k}\,, \tag{5}$$

where $e_{co2eq,k}$ is the equivalent carbon emissions of power generation side in region $k$, $e_{\mathrm{up},k}$ is the equivalent carbon emission generated in the upstream production process of fuel in region $k$, $e_{\mathrm{constr},k}$ is the equivalent carbon emissions generated by the construction of power plant in region $k$, $e_{\mathrm{comb},k}$ is the equivalent carbon emission generated by combustion for power generation in regional $k$.

The equivalent carbon emission of the power side within the region is defined as

$$e_{\mathrm{use},k} = e_{\mathrm{CO_{2eq},k}} - e_{\mathrm{pump},k} + e_{k,i} - e_{k,e} - e_{\mathrm{loss},k}\,, \tag{6}$$

where $e_{\mathrm{use},k}$ is the equivalent carbon emission generated by electricity consumption in region $k$; $e_{\mathrm{pump},k}$ is the equivalent carbon emission generated by the pumping load used in region $k$; $e_{k,i}$ and $e_{k,e}$ are the equivalent carbon emissions generated by imported power obtained from station $i$ and

exported to station $e$ in region $k$, $e_{\text{loss},k}$ is the equivalent carbon emission generated from the loss of transmission and distribution network in regional $k$.

The center of low-carbon development is technological innovation, institutional innovation and the change of development concept, which will involve the readjustment of production mode, lifestyle and view of value. As the most important energy sector in China, the power industry should strive to achieve low-carbon electricity and shoulder the responsibility of leading the low-carbon development of the whole society.

In addition to the above economic parameters, the analysis of multi-energy systems is often inseparable from the environment. The relationship between the environment and the economy is always inseparable, and protecting the environment is our obligatory responsibility. Emissions is regarded as an important index of environmental analysis [52, 53]. In the process of optimization, emissions, especially carbon dioxide emissions, will be reduced as much as possible against environmental pollution [90].

## 3.2 Research methods or platforms

When using software for optimization or economic analysis of multi-energy storage systems, different software and algorithms will perform different economic results. In addition to platforms and algorithms, the optimization of the system and economic analysis are inseparable from economic research methods. The parameters which are taken into consideration and the economic research methods which are used also vary according to different systems and platforms. The above issues will be introduced and analyzed briefly in this section.

### 3.2.1 Life cycle cost analysis

By comparing life cycle costs (LCC), the optimal system can be selected when studying multiple energy storage systems. The life cycle cost analysis method mainly focuses on the cost occurring in the life cycle of the system. It considers the upgrade and discount rate based on the net present value method. When the inflation rate and discount rate are equal, LCC can be calculated as the current value. LCC is the sum of installation cost, maintenance cost and insurance cost [91, 92]. The calculation formula is as follows

$$\text{LCC} = C_I + C_O + C_M + C_D\,, \tag{7}$$

where $C_I$ is the purchase cost, $C_O$ is the operating cost, $C_M$ is maintenance cost, $C_D$ is the processing cost.

### 3.2.2 Exergy economic algorithm

Exergy is also known as effective energy when the system changes reversibly from an arbitrary state to a state in equilibrium in the given environment, which can be transformed indefinitely into other forms of energy [93]. Different forms of energy have different abilities to convert into 'higher energy'. If this conversion capacity is used as a scale, the merits and demerits of various forms of energy can be evaluated.

Exergy can be considered as the maximum useful work that can be made or the minimum useful work consumed in theory in a reversible process under given environmental conditions. Correspondingly, all energy that cannot be converted into exergy is called 'anergy'. Exergy ($E_x$) and anergy ($A_n$) combine to any energy $E$ [94, 95]:

$$E = E_x + A_n \,. \tag{8}$$

Thermal economic analysis is often used in the economic analysis of solar biomass systems. Exergy destruction is the main problem of low thermal efficiency in all power systems, which is directly related to equipment cost. Exergy economic analysis is designed to minimize those inefficiencies and associated costs. Appropriate modelling systems are characterized by obtaining optimal values for selected criteria leading to efficient systems [96–98]. Conventional exergy analysis results only reveal the exergy damage value of each component without providing more information. Similar to advanced exergy analysis, advanced exergy economic analysis divides exergy destruction cost and investment cost of components into endogenous, exogenous, avoidable and inevitable parts. Exergy economic analysis is a key method to model and optimize cost-benefit systems [99].

### 3.2.3 Platform for economic analysis

In the analysis of multi-energy storage systems, there are many analysis platforms. HOMER is one of the important software in economic analysis. The hybrid optimization model of electric renewable energy (HOMER) is a tool developed by NREL (National Renewable Energy Laboratory) for the pre-feasibility of any project based on analyzing system cost and optimization. HOMER is a computer model that simplifies the task of evaluating

options for remote, independent, and distributed generation systems, both in off-grid and integrated cases. A few studies show that HOMER is very feasible in application [70]. HOMER optimization and sensitivity analysis algorithms can be used to evaluate the economics of the system and the feasibility of technology choices, as well as considering the changes in technology cost and the availability of energy resources. HOMER software has been widely used in modelling, simulation and optimization, and the economic results are extraordinary ideal [71–76]. HOMER can handle all kinds of emerging technologies, such as photovoltaic, wind energy, fuel cell, hydro power and so on.

In addition, PSASP is a comprehensive program for power system analysis developed by China Electric Power Research Institute. Based on the support of basic database in power grid, fixed model library and user-defined model library, PSASP can perform various calculations and analysis of power system (transmission, power supply and distribution system). PSASP has designed as a powerful user-defined modeling method. The model of any component can be freely established as a model base for various calculations. There are intuitive and convenient editing methods of text and graphics, which are simple to call and fast to calculate, but the calculation mode has certain limitations. Besides, PAS (power system application software) power application software is a kind of power grid operation analysis software, which is helpful for automation personnel to monitor and maintain the weak links of automation system according to the state estimation results. Power flow calculation software has the advantages of fast calculation speed, high calculation accuracy and intuitive analysis results. PAS advanced application software will play a greater role in the safe, stable and economic operation of power grid.

### 3.2.4 System for economic analysis

Optimizing is an important topic when studying the energy system. Taking the integrated solar/wind/biomass hybrid system in Egypt as an example, to solve the problem of unreliable power in this village, it is necessary to design and optimize a renewable energy system. That system has to minimize the energy cost according to the daily data of energy availability and load demand. From the view-sights of system cost, reliability and greenhouse gas emissions, the Arual community in Ilia, Egypt was studied [26]. Under different weather conditions, taking the maximization of the renewable energy foundation (REF) of the system as the objective function and

considering the minimization of two objective functions power supply probability (LPSP) and cost of energy (COE), a mathematical model of hybrid system output power estimation is established. The results show the good portion of each component in the total energy to satisfy the power demand. Based on the power selling situation or power purchasing ability of the hybrid system, the relationship between the power grid and the hybrid system is studied. Three scenarios are selected along with this relationship. The results of the multiple objective particle swarm optimization (MOPSO) are divided into three parts: the economically optimal solution (lowest COE), the renewable energy application angle (highest REF) and the environmentally optimal solution (lowest greenhouse gas emission) [27].

## 3.3 The analysis of economic optimization

### 3.3.1 Optimization algorithm

There are many optimization algorithms for a multi-energy storage system, such as the artificial bee colony (ABC) algorithm, the genetic algorithm (GA), the particle swarm optimization (PSO) and so on.

Artificial bee colony algorithm is an algorithm inspired by bee colony behavior. It was proposed by the Karaboga group in 2005 to optimize algebra problems. The artificial bee colony algorithm is an optimization method that imitates the behavior of bees, and it is a specific application of the idea of swarm intelligence. It does not need to know the special information of the problem but only needs to compare the advantages and disadvantages of the problem and finally make the global optimal value pop out in the colony through the local optimization behavior of each worker bee. It has a fast convergence rate [77–81].

Genetic algorithm was firstly proposed by John Holland in the 1970s. The Algorithm is designed and proposed according to the laws of biological evolution in nature. It is a computational model of biological evolution that simulates the natural selection and genetic mechanism of Darwin's biological evolution and a method to search for the optimal solution by simulating the natural evolution process [100].

Particle swarm optimization is a random search algorithm based on group cooperation, which was invented by Eberhart and Kennedy. It was developed by simulating the foraging behavior of birds. It's generally considered a type of swarm intelligence (SI), and it can be incorporated into multiagent optimization system (MAOS) [84–86].

Table 3: Optimization algorithm feature table.

| Arithmetic | Advantage | Deficiency |
|---|---|---|
| ABC | Solve multi-variable function optimization problem | The calculation speed is slow in the later stages of optimization |
| GA | When solving complex combinatorial optimization problems, compared with some conventional optimization algorithms, better optimization results can be obtained faster | (1) Non-standard coding and inaccurate representation of coding<br>(2) A single genetic algorithm coding cannot fully express the constraints of the optimization problem. One way to consider constraints is to use thresholds for infeasible solutions, which inevitably increase the computation time<br>(3) The efficiency of the genetic algorithm is usually lower than that of other traditional optimization methods<br>(4) Genetic algorithm is prone to premature convergence<br>(5) There is no effective quantitative analysis method for the accuracy, feasibility and computational complexity of the genetic algorithm |
| PSO | The advantage of evolutionary computing is that it can deal with some things those traditional methods cannot.<br>The calculated LCOE is the minimum [101] | (1) The performance is not particularly good on some problems<br>(2) Coding of network weights and selection of genetic operators are sometimes troublesome |

The above optimization algorithms have slightly different economic effects. When scholars like Shakti Singh predicted the minimum LCOE value in the optimization of island micro-grid such as rural multi-energy storage systems, they compared the complete optimization results of the ABC algorithm, HOMER and PSO in case studies. The results show that the ABC algorithm can predict the minimum ASC (annual system cost) of the system with the minimum LCOE. In addition, the ABC algorithm has better performance in calculation time and results compared with particle swarm optimization. Moreover, the performance of the two algorithms is better than the HOMER algorithm.

### 3.3.2 Objective function

NPC represents the life cycle cost of the system. The calculation method of total NPC is to sum up the total discounted cash flow of each year within the project life cycle. Based on HOMER software, the minimum NPC is

taken as the main objective function, which is a very common economic research method in multi-energy energy storage systems. After completing the system optimization, another economic parameter COE is introduced on the basis of the lowest NPC, and the value of COE can be calculated by dividing the total annual cost by the power. The COE of the whole system is minimized to analyze the economic feasibility of the system according to real cases. The options for multi-energy systems are being optimized. The intention of the objective function is to reduce the COE. In the equation, the design process of the hybrid system is put forward, and the partial group optimization method is used to solve it:

$$M_{\text{Toal annual}} = M_{\text{AIC}} + M_{\text{O \& M}}\,. \tag{9}$$

Energy cost is measured by unit electricity cost or constant price of unit energy. Minimize the calculation formula [88]:

$$\text{COE} = \frac{\text{IR} + \text{C}_{\text{O \& M}}}{\text{P}_{\text{AE}}}, \tag{10}$$

where $I$ is the initial project investment cost, $R$ is the coefficient of recovery of equal amount of funds, $\text{C}_{o\,\&\,M}$ is the operation and maintenance cost, and $\text{P}_{\text{AE}}$ is the annual generating capacity of unit.

The concept of annualized system cost (ASC) is introduced [89]. When all constraints and parameters are satisfied, the minimum ASC, that is, the minimum sum of the total annualized costs of each component is considered to obtain the best result. The total ASC of each component can be expressed as the annual cost of any component, which can be calculated by a factor called the capacity recovery factor (CRF). The objective function is to impose a minimum value on several constraint sets.

By minimizing the net present cost (NPC) of the system, the optimal size of the components used in the system is deduced with the minimum LCOE, and the optimal configuration is selected according to LCOE and reliability [101]. LCOE is the average price of energy (useful) generated by the system per kilowatt hour, and the minimum ASC of the system can be predicted by minimizing LCOE:

$$\text{LOCE} = \frac{\text{ASC(USD/year)}}{\text{Toal useful energy served (kWh/year)}}\,. \tag{11}$$

### 3.3.3 Optimization performance

A typical village near Pongalur and Manit is cited here as the examples. By comparing the life cycle costs of different hybrid systems and single

independent systems, it is determined that the most economical hybrid combination with the lowest life cycle cost is solar energy/(wind energy + biomass) = 1/(0.25 + 0.75) [91]. The economy of solar-biomass hybrid power generation system in northern Cameroon is analyzed [102, 103]. The concentrated solar energy (CSP) technology of parabolic trough collector (PTC), linear Fresnel reflector (LFR) and solar tower (ST) is studied. They are hybridised with biomass-fired (BF) technology. The exergy damage of solar field (PTC-BF accounts for 86.3%, ST-BF accounts for 92.2%, and LFR-BF accounts for 85.4%) is the main cause of the whole damage [93]. The hybrid system with LFR-BF accounting for 85.4% is the most cost-effective system. The hybrid system with ST-BF accounting for 92.2% is the least cost-effective. The lower the proportion is, the more cost-effective of the system will be [94]. The details are shown in Figs. 4 and 5.

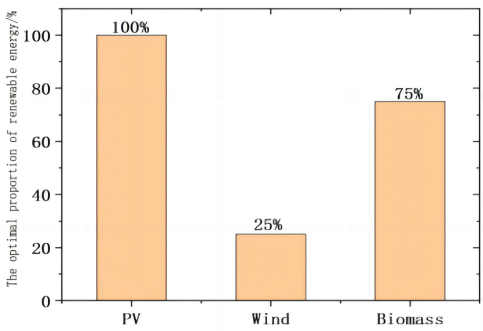


Figure 4: Optimal ratio of solar energy, wind energy and biomass energy [91, 92].

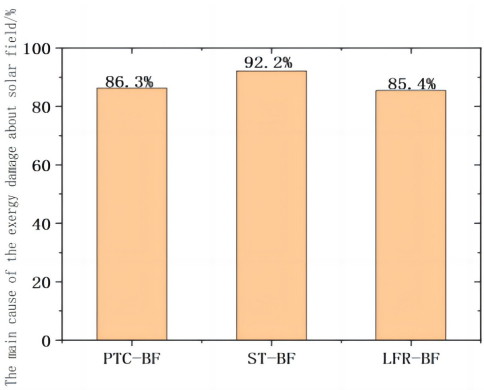


Figure 5: The main cause of the exergy damage about solar field [93].

### 3.4 Economic feasibility study of multi-energy complementary energy storage system

With the decrease in solar thermal cost and the continuous increase of raw materials, fossil fuels and land prices, hybrid power plants have become an increasingly attractive choice [104]. The decrease in solar energy supply means an increase of system operation cost (an increase of biomass consumption). The use of solar energy is very important, and wind energy is a pioneer industry in the field of RES [105]. The hybrid system is introduced as a reliable alternative to improve the traditional wind power plant, and a reliable wind power plant is designed by mixing with biomass energy [106]. In a hybrid system with insufficient solar energy, biomass energy is an effective component. The NPC and COE of each system through economic analysis of multi-energy systems in various places are shown in Table 4.

For a small village in Egypt, a solar photovoltaic/wind/biomass hybrid system can significantly reduce NPC. In rural India, wind-biomass gasifier systems have very low energy costs and operating costs compared to wind-diesel systems. The energy system supplying power to the northern islands near the Bay of Bengal in Bangladesh has also improved economically. Moreover, the hybrid energy system in Bangladesh will also be applicable to other countries with similar environments and other conditions, such as Malaysia, Australia, Singapore and other regions with great potential. In addition, there are energy systems in Pakistan, Australia and other places that are used to supply local electricity, all of which have cost advantages [102].

Take a solar-biomass hybrid system in India as a case. Compared with the single biomass system, the hybrid system can save 29% of biomass and land, which indicated that the hybrid power station is an attractive and beneficial choice. In addition, compared with single energy system, the annual average energy efficiency and primary energy-saving rate of the solar-biomass hybrid system are 25.18% and 94.98%, respectively, reducing carbon emission by about 2961.85 tons per year. Besides, for a multi-generation system using solar energy and biomass, the energy efficiency and exergy efficiency of the whole system are 91.0% and 34.9% respectively. In China, the biomass-solar hybrid power system is especially suitable for the northwest rural areas where the economic development is relatively slow, yet the solar energy and biomass resources are quite abundant.

Table 4: Regional energy system economic index table.

| Ref. (year) | Research area | System energy | Optimization objective | Optimization algorithms or platforms | Installed capacity | NPC (USD) | COE (USD/ kWh) | Economic feasibility | |
|---|---|---|---|---|---|---|---|---|---|
| [49] (2020) | A village in western China | Solar – wind – biomass | Minimize the NPC | HOMER | P V 104 kW<br>WT 30 kW<br>BG 50 kW<br>Battery 331 kWh<br>Converter 99 kW | 587013 | 0.201 | PV/wind/BG/ battery more economically viable than grid expansion | yes |
| [48] (2020) | A village in Fars Province, Iran | Solar – wind – biomass | Minimize the NPC | HOMER | BG 150 kW<br>PV 80.7 kW | 904513 | 0.128 | The development of the project will save up to 8444 USD. | yes |
| [36] (2016) | Egyptian village | Solar – wind – biomass | Minimization of cost | HOMER | PV 150 kW<br>WT 20 kW<br>BG 100 kW | 5772 | | It provides a cheap source of electricity for the area | yes |
| [5] (2014) | In rural India | Wind-biomass gasifier system | Minimum net present value | HOMER | BG 150 kW<br>WT 100 kW<br>Converter 100 kW | | 0.078 | Compared to the wind-diesel system, the energy cost and operating costs are very low | yes |
| [23] (2017) | The remote area of Bwani | Solar – wind – biomass | Minimize the COE | GA, PSO | | | 0.2393 | | yes |
| [24] (2018) | Kallar Kahar, near Chakwal, Punjab province, Pakistan | Solar – wind – biomass | | HOMER | | $180.2 \cdot 10^6$ | | Energy costs are lower | yes |
| [1] (2017) | The northern island of Bangladesh of the Bay of Bengal | Photovoltaic – wind – biomass – diesel | | HOMER | | 160626 | 0.431 | Can reduce the NPC | yes |

Table 4 [cont.]

| Ref. (year) | Research area | System energy | Optimization objective | Optimization algorithms or platforms | Installed capacity | NPC (USD) | COE (USD/ kWh) | Economic feasibility | |
|---|---|---|---|---|---|---|---|---|---|
| [95] (2018) | The remote area of Punjab (Multan) in southern Pakistan | Photovoltaic – wind – biomass – diesel | | HOMER | | | 0.06 | Pakistan has abundant renewable energy resources that could be used to reduce dependence on fossil fuels | yes |
| [49] (2020) | A village in western China | Solar – wind – biomass | Minimize the NPC | HOMER | PV 104 kW<br>WT 30 kW<br>BG 50 kW<br>Battery 331 kWh<br>Converter 99 kW | 587013 | 0.201 | PV/wind /BG/battery more economically viable than grid expansion | yes |
| [48] (2020) | A village in Fars Province, Iran | Solar – wind – biomass | Minimize the NPC | HOMER | BG 150 kW<br>PV 80.7 kW | 904513 | 0.128 | The development of the project will save up to 8444 USD | yes |
| [36] (2016) | Egyptian village | Solar – wind – biomass | minimization of cost | HOMER | PV 150 kW<br>WT 20 kW<br>BG 100 kW | 5772 | | It provides a cheap source of electricity for the area | yes |
| [5] (2014) | In rural India | Wind – biomass gasifier system | Minimum net present value | HOMER | BG 150 kW<br>WT 100 kW<br>Converter 100 kW | | 0.078 | Compared to the wind-diesel system, the energy cost and operating costs are very low | yes |
| [23] (2017) | The remote area of Bwani | Solar – wind – biomass | Minimize the COE | GA, PSO | | | 0.2393 | | yes |

BG – biomass generation, WT – wind turbine, PV – photovoltaic.

### 3.5 Summary

Some cost economic parameters, analysis platforms, economic research methods and various algorithms are taked the references such as NPC and COE. Firstly, they optimize the multi-energy complementary energy storage system economically to make the cost as low as possible. Secondly, the feasibility of different energy systems in various regions are analyzed. By comparing the economic parameters, it can be known that the multi-energy complementary energy storage system is feasible to supply power to various regions. Such as Australia, small villages in Egypt, rural India, northern islands near the Bay of Bengal in Bangladesh, etc. Therefore, the renewable hybrid energy system is more efficient and cost-effective than the single renewable energy system and it also helps to overcome the defects of the single system. Renewable hybrid energy storage systems will be applied in more places and will present a greater potential.

Renewable energy mainly includes wind energy, solar energy and biomass energy. The resources, climates and economic conditions are different in all regions, so the hybrid systems are different. For example, in China, the northwest rural areas are rich in solar energy and biomass resources, so the hybrid system of solar energy and biomass is suitable. However some areas, which are rich in wind energy and solar energy resources, are also suitable to another system. According to a large number of researches, the cost of energy system will be reduced substantially by using the hybrid renewable energy complementary system, and at the same time, the power output is more stable.

## 4 The direction of future research

### 4.1 Optimization system

The need for wind energy and biomass or anything else on top of current PV is only based on the discrepancy between the solar generation curve and grid demand curve. The discrepancy results from the diurnal cycle and weather factors. To solve this problem, we need to find a more appropriate optimization algorithm.

Biomass is essentially similar as fossil-fueled generation in terms of electricity dispatchability characteristics. The only difference, though, is its renewability. But the carbon issue needs to be considered as a dominating factor. For example, In-situ burning of straw not only wastes a lot of resources and energy but also pollutes the environment.

The research of straw utilization technology and the development of energy products have become the urgent problems in the fields of agriculture, energy and environment, which are great significant to ensure national energy security, sustainable development of national economy and environmental protection.

The hybrid wind-PV complementary system is indeed a trend, but there are better ideas than simply adding them together. The essential question lies in 'complementarity'. Therefore, it is particularly important to analyze the types of wind energy resources that significantly complement solar PV in future studies.

In addition, wind resource characterization is the key work of economic analysis and optimization.

In this paper, the analysis of multi-energy complementary hybrid energy storage system comes from many aspects. On the basis of ensuring the stability of the power system, the system is made to be more economic. However, consideration of environmental factors is also essential.

With the further development of remote rural areas in China, the pattern and scale of power demand of various users will also change accordingly, which is worthy of further analysis. In addition, it is necessary to find new alternative and renewable biofuels and explore a better energy combination. In order to increase the penetration of renewable energy in the energy structure and reduce the power generation cost of renewable energy system, it is important to explore detailed sensitivity analysis to consider the changes of technology cost and energy supply. The influence of biomass price on system cost and the way for better usage of renewable energy are also the fields we need to study in the future.

## 4.2 Cost model

There should be more comprehensive and realistic cost models for economic optimization. The labor costs related to solar photovoltaic, wind turbines and biomass plants vary according to cases and countries, and the operation and maintenance costs vary. Economic analysis often ignores spillover costs, such as land value. The land use of a multi-energy complementary system is an essential practical factor to consider the potential investment. Suppose the photovoltaic project covers a large area, once the 'land use tax' and 'farmland occupation tax' are levied, the benefit of the project will be significantly reduced or even fail to meet the expectations. Therefore, the attribute of project land is becoming an important factor that affects an investment decision.

### 4.3 Complementary effect

Identical to any fossil fuel-based generations, biomass electricity has essentially no dispatchability limitation apart from the ones in its renewability. The remaining questions thus are purely on techno-economics which must include the add-on costs associated with its carbon emissions. Wind energy, on the other hand, has its dispatchability issues due to the intermittency. Therefore, optimizations in any practical multi-energy complementary systems ultimately rely on how complementary it is between solar and wind power generations within such systems.

Wind resource distributes more sensitively to geographic conditions and locations than solar irradiation. This brings a substantial challenge in seeking a general conclusion in optimizations of the solar-wind-biomass integration concepts. Nearly all the work reviewed in this paper is case-specific and sometimes seems contradictory to each other. However, a generalized guideline of complementary systems may be 'peak-offset' sought by looking into temporal distributions of the two renewable forms about that of the power demand, provided that wind speeds also exhibit sensible statistical patterns with time.

Almost all of the work reviewed in this paper is case-specific, and they sometimes seem to contradict each other. However, a generalized guideline of complementary systems may be 'peak-offset'. It is sought by looking into temporal distributions of the two renewable forms about that of the power demand.

Taking Australia as an example, a common statistical trend is seen in wind speed variations with the time in a day in different coastal regions. A preliminary study of 1-minute wind data is done by the University of Queensland. The date is measured by multiple weather stations of the Australian Bureau of Meteorology for over ten years. It is revealed that the peaks of wind speed generally occur between 15:00 and 17:00 (local time) of a day, which is 3–5 hours lagging the solar peak at noon. These stations are all located in densely populated urban areas along the coastal lines and have their wind sensors installed on 10–12 m-tall weather masts.The measured data represents a micro-scale observation of the wind speeds at lower altitudes, and mainly focus on the range of 5–20 km/h.

A solar-wind integration concept was thus proposed to incorporate solar PV with small-scale low-altitude vertical axis wind turbines as an isolated grid system. Increasing the proportion of wind turbines in this type of grid system reduces the required battery capacity because the peak of the wind

generation curve is much closer to that of the demand. The trade-off to this is the rise in capital costs as small-scale wind turbines are generally more expensive than PV in terms of dollars per watt actual capacity. The optimal point sits somewhere between the two ends (100% PV and 100% wind). For instance, the study analyzed the LCOEs for a 2.5 MW-equivalent isolated complementary micro community grid in Canterbury and NSW (New South Wales) with different solar-to-wind ratios, shown in Table 5.

Table 5: LCOE (USD/MWh) of the off-grid power system with solar or wind energy.

| The proportion of wind energy (in MW) | LCOE (10 years) | LCOE (20 years) |
|---|---|---|
| 0% (pure solar PV) | 331 | 270 |
| 20% | 330 | 255 |
| 40% | 334 | 244 |
| 60% | 346 | 240 |
| 80% | 368 | 245 |
| 100% (pure wind turbines) | 402 | 261 |

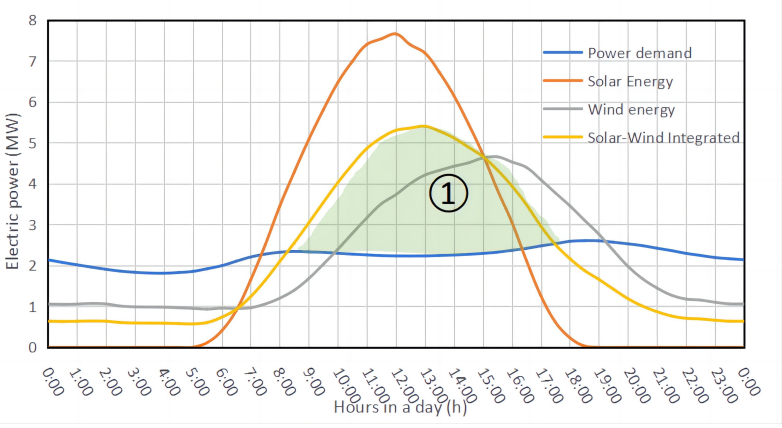


Figure 6: Power supply by pure solar PV, pure wind turbines, and integrated solar-wind (60% wind) in comparison with the grid demand over the 24 hours of a day. The area of enclosure (1) indicates the minimum amount of energy storage required for the integrated solar-wind grid system.

The example demonstrates how to offset the peaks of solar and wind. And the temporal demand curves influenced decision makings in planning, de-

signs, and optimizations are also demonstrated. Of course, these all require true dynamics of the three components to suggest the importance of reliable data collection.

## 5 Conclusions

Hybrid energy system can increase the grid's reliability while reducing the dependence on energy storage. The result shows that the hybrid multi-energy system has more obvious economic advantages than the single energy system. Regarding energy ratio, the energy storage system with complementary hybrid energy has an economic advantage. Based on optimization, NPC or COE of energy systems in various regions are obtained through financial analysis. Through comparison, it can be known that applying hybrid renewable energy systems in these regions is feasible. It can be seen that the renewable energy system has excellent development potential, which is worthy of further research.

*Received 17 July 2023*

## References

[1] Mohaghegh M.R., Heidari M., Tasnim S., Dutta A., Mahmud S.: *Latest advances on hybrid solar–biomass power plants.* Energ. Source. Part A **135**(2021), 1–24.

[2] Shezan S.K.A., Ping H.W.: *Techno-economic and feasibility analysis of a hybrid PV-wind-biomass-diesel energy system for sustainable development at offshore areas in Bangladesh.* Curr. Alternative Energ. **1**(2017), 1, 20–32.

[3] Balali M.H., Nouri N., Omrani E., Nasiri A., Otieno W.: *An overview of the environmental, economic, and material developments of the solar and wind sources coupled with the energy storage systems.* Int. J. Energ. Res. **41**(2017), 14, 1948–1962.

[4] Lakshmi G.S., Harivardhagni S., Divya G., Lavanya V.: *Solar and bio-mass based hybrid power system for rural areas.* In: Proc. 2020 IEEE-HYDCON, Hyderabad, 11 Sept. 2020, 1–5.

[5] Balamurugan P., Ashok S., Jose T.L.: *An optimal hybrid wind-biomass gasifier system for rural areas.* Energ. Source. Part A **33**(2011), 9, 823–832.

[6] Bet Sarkis R., Zare V.: *Proposal and analysis of two novel integrated configurations for hybrid solar-biomass power generation systems: Thermodynamic and economic evaluation.* Energ. Convers. Manage. **160**(2018), 411–425.

[7] Sahoo U., Kumar R., Pant P.C., Chandhary R.: *Resource assessment for hybrid solar-biomass power plant and its thermodynamic evaluation in India.* Sol. Energy **139**(2016), 47–57.

[8] Zhang D., Liu J., Jiao S., Tian H., Lou C., Zhou Z. Zhang J., Wang C., Zuo J.: *Research on the configuration and operation effect of the hybrid solar-wind-battery power generation system based on NSGA-II.* Energy **189**(2019), 116–121.

[9] Suresh N.S., Thirumalai N. C., Dasappa S.: *Modeling and analysis of solar thermal and biomass hybrid power plants.* App. Therm. Eng. **160**(2019), 114–121.

[10] Baredar P., Sethi V.K., Pandey M.: *Correlation analysis of small wind–solar–biomass hybrid energy system installed at RGTU Bhopal, MP (India).* Clean Technol. Envir. Policy **12**(2009), 3, 265–271.

[11] Khalid F., Dincer I., Rosen M.A.: *Thermoeconomic analysis of a solar-biomass integrated multigeneration system for a community.* Appl. Therm. Eng. **120**(2017), 645–653.

[12] Elkazaz M., Sumner M., Thomas D.: *Energy management system for hybrid PV-wind-battery microgrid using convex programming, model predictive and rolling horizon predictive control with experimental validation.* Int. J. Elec. Power **115** (2020), 105–483.

[13] Yang Z., Hu J., Ai X., Wu J., Yang G.: *Transactive energy supported economic operation for multi-energy complementary microgrids.* IEEE T. Smart Grid (2021), 1, 4–17.

[14] Moosavi A., Ljung A.L., Lundström T.S.: *Design considerations to prevent thermal hazards in cylindrical lithium-ion batteries: An analytical study.* Huagong Xuebao/CIESC J. **68**(2017), 8, 3232–3241.

[15] Kumar H.G., Kumar P.S.: *A comprehensive review on energy and exergy analysis of solar air heaters.* Arch. Thermodyn. **41**(2020), 3, 183–222.

[16] Singh A., Baredar P.: *Techno-economic assessment of a solar PV, fuel cell, and biomass gasifier hybrid energy system.* Energy **2**(2016), 254–260.

[17] Chennaif M., Zahboune H., Elhafyani M., Zouggar S.: *Electric system cascade extended analysis for optimal sizing of an autonomous hybrid CSP/PV/wind system with battery energy storage system and thermal energy storage.* Energy **227**(2021), 120444.

[18] Giallanza A., Porretto M., Puma G.L., Marannano G.A.: *sizing approach for stand-alone hybrid photovoltaic-wind-battery systems: A Sicilian case study.* J. Clean. Prod. **199**(2018), 817–830.

[19] Belmili H., Haddadi M., Bacha S., Almi N.F., Bendib B.: *Sizing stand-alone photovoltaic–wind hybrid system: Techno-economic analysis and optimization.* Renew. Sust. Ener. Rev. **30**(2014), 821–832.

[20] Kaur H., Gupta S., Dhingra A.: *Analysis of hybrid solar biomass power plant for generation of electric power.* Mater. Today-Proc. **48**(2022), 1134–1140.

[21] Jagtap K.K.; Patil G.; Katti P.K.; Kulkarni S.B.: *Techno-economic modeling of Wind-Solar PV and Wind-Solar PV-Biomass hybrid energy system.* In: Proc. IEEE Int. Conf. on Power Electronics, Drives and Energy Systems (PEDES), Trivandrum, 14-17 Dec. 2016.

[22] Abo-Elyousr F.K., Elnozahy A.: *Bi-objective economic feasibility of hybrid microgrid systems with multiple fuel options for islanded areas in Egypt.* Renew. Energ. **128**(2018), 37–56.

[23] Sawle Y., Gupta S.C., Bohre A.K.: *Optimal sizing of standalone PV/Wind/Biomass hybrid energy system using GA and PSO optimization technique.* Energy Proced. **117**(2017), 690–698.

[24] Ahmad J., Imran M., Khalid A., Iqbal W., Ashraf S.R., Adnan M., Farooq Ali S., Khokhar K.S.: *Techno economic analysis of a wind-photovoltaic-biomass hybrid renewable energy system for rural electrification: A case study of Kallar Kahar.* Energy **148**(2018), 208–234.

[25] Tajeddin A., Roohi E.: *Designing a reliable wind farm through hybridization with biomass energy.* Appl. Therm. Eng. **154**(2019), 171–179.

[26] Singh S., Singh M., Kaushik S.C.: *Feasibility study of an islanded microgrid in rural area consisting of PV, wind, biomass and battery energy storage system.* Energ. Convers. Manage. **128**(2016) 178–190.

[27] Barakat S., Ibrahim H., Elbaset A.: *Multi-objective optimization of grid-connected PV-wind hybrid system considering reliability, cost, and environmental aspects.* Sustain. Cities Soc. **60**(2020), 102–178.

[28] Jahangir M.H., Shahsavari A,.Rad M.A.V.: *Feasibility study of a zero emission PV/Wind turbine/Wave energy converter hybrid system for stand-alone power supply: A case study.* J. Clean. Prod. **262**(2020), 121–250.

[29] Xingang Z., Jieyu W., Xiaomeng L., Pingkuo L.: *China's wind, biomass and solar power generation: What the situation tells us.* Renew. Sust. Ener. Rev. **168**(2012), 8, 6173–6182.

[30] Gabra S., Miles J., Scott S. A.: *Techno-economic analysis of stand-alone wind micro-grids, compared with PV and diesel in Africa.* Renew. Energ. **143**(2019), 928–1938.

[31] Gebrehiwot K., Mondal M.A.H., Ringler C., Gebremeskel A.G.: *Optimization and cost-benefit assessment of hybrid power systems for off-grid rural electrification in Ethiopia.* Energy **177**(2019), 234–246.

[32] Ma T., Yang H., Lu L., Peng J.: *Optimal design of an autonomous solar-wind-pumped storage power supply system.* Appl. Energ. **160**(2015), 728–736.

[33] Malik P., Awasthi M., Sinha S.: *Analysis of sensitive parameters influencing a SPV/WT/Biomass/Battery based hybrid system.* In: Proc. 8th Int. Conf. on Power Systems (ICPS), Jaipur, 20-22 Dec. 2019.

[34] Li C., Yang H., Shahidehpour M., Xu Z., Zhou B., Cao Y.: *Optimal planning of islanded integrated energy system with solar-biogas energy supply.* IEEE T. Sustain. Energ. **11**(2019), 4, 2437–2448.

[35] Morais P.H., Lodi A., Aoki A.C., Modesto M.: *Energy, exergetic and economic analyses of a combined solar-biomass-ORC cooling cogeneration systems for a Brazilian small plant.* Renew. Energ. **157**(2020), 1131–1147.

[36] Barakat S., Samy M.M., Eteiba M.B., Wahba W.I.: *Viability study of grid connected PV/Wind/Biomass hybrid energy system for a small village in Egypt.* In: Proc. 18th Int. Middle East Power Systems Conf. (MEPCON), Cairo, 27-29 Dec. 2016.

[37] Liu G., Rasul M.G., Amanullah M.T.O., Khan M.M.K.: *Feasibility study of stand-alone PV-wind-biomass hybrid energy system in Australia.* In: Proc. Asia-Pacific Power and Energy Engineering Conf., Wuhan, 25-28 Mar. 2011.

[38] Hossain M.M, Barua S, Matin M.A.A.: *Pre-feasibility study for electrification in Nijhum Dwip using hybrid renewable technology.* In: Proc. ICEEE-2015, Rajshahi, 04-06 Nov. 2015.

[39] Bhattacharjee S., Dey A.: *Techno-economic performance evaluation of grid integrated PV-biomass hybrid power generation for rice mill.* Sustain. Energ. Technol. Assess. **7**(2014), 6–16.

[40] Allouhi A., Rehman S., Krarti M.: *Role of energy efficiency measures and hybrid PV/biomass power generation in designing 100% electric rural houses: A case study in Morocco.* Energ. Buildings **136**(2021), 110770.

[41] Vendoti S., Muralidhar M., Kiranmayi R.: *Techno-economic analysis of off-grid solar/wind/biogas/biomass/fuel cell/battery system for electrification in a cluster of villages by HOMER software.* Environ. Dev. Sustain. **23**(2021), 351–372.

[42] Wesly J., Brasil Jr A.C.P., Frate C.A., Badibanga R.K.: *Techno-economic analysis of a PV-wind-battery for a remote community in Haiti.* Case Stud. Chem. Environ. Eng. **2**(2020), 100044.

[43] Boussetta M., EI Bachtiri R., Khanfara M., EI Hammoumi K.: *Assessing the potential of hybrid PV–Wind systems to cover public facilities loads under different Moroccan climate conditions.* Sustain. Energ. Technol. Assess. **22**(2017), 74–82.

[44] Shahzad M.K., Zahid A., Rashid T., Rehan M.A., Ali M., Ahmad M.: *Techno-economic feasibility analysis of a solar-biomass off grid system for the electrification of remote rural areas in Pakistan using HOMER software.* Renew. Energ. **106**(2017), 264–273.

[45] Acevedo-Arenas C.Y., Correcher A., Sánchez-Díaz C., Ariza E., Alfonso-Solar D., Vargas-Salgado C.: *MPC for optimal dispatch of an AC-linked hybrid PV/wind/biomass/H2 system incorporating demand response.* Energ. Convers. Manage. **186**(2019), 241–257.

[46] Ma T., Javed M.S.: *Integrated sizing of hybrid PV-wind-battery system for remote island considering the saturation of each renewable energy resource.* Energ. Convers. Manage. **182**(2019), 178–190.

[47] Perkins G.: *Techno-economic comparison of the levelised cost of electricity generation from solar PV and battery storage with solar PV and combustion of bio-crude using fast pyrolysis of biomass.* Energ. Convers. Manage. **171**(2018), 1573–1588.

[48] Jahangir M.H., Cheraghi R.: *Economic and environmental assessment of solar-wind-biomass hybrid renewable energy system supplying rural settlement load.* Sustain. Energ. Technol. Assess. **42**(2020), 100895.

[49] Li J., Liu P., Li Z.: *Optimal design and techno-economic analysis of a solar-wind-biomass off-grid hybrid power system for remote rural electrification: A case study of west China.* Energy **208**(2020), 118387.

[50] Pina E.A., Lozano M.A., Serra L.M., Hernández A., Lázaro A.: *Design and thermoeconomic analysis of a solar parabolic trough-ORC-Biomass cooling plant for a commercial center.* Sol. Energy **215**(2021), 92–107.

[51] Erwin E., Soemardi T.P., Surjosatyo A., Nugroho J., Nugraha K., Wiyono S.: *Design optimization of hybrid biomass and wind turbine for minapolitan cluster in Domas, Serang, Banten, Indonesia.* IOP Conf. Ser. Earth Env. Sci. **105**, Gothenburg, 8-12 Oct. 2018.

[52] Al-Ghussain L., Ahmad A.D., Abubaker A.M., Mohamed M.A.: *An integrated photovoltaic/wind/biomass and hybrid energy storage systems towards 100% renewable energy microgrids in university campuses.* Sustain. Energ. Technol. Assess. **46**(2021), 101273.

[53] Pérez-Navarro A.: *Hybrid biomass-wind power plant for reliable energy generation.* Renew. Energ. **35**(2010), 7, 1436–1443.

[54] Liu Q., Bai Z., Wang X., Lei J., Jin H.: *Investigation of thermodynamic performances for two solar-biomass hybrid combined cycle power generation systems.* Energ. Convers. Manage. **122**(2016), 252–262.

[55] Blanchet C.A.C., Pantaleo A.M., van Dam K.H.: *A process systems engineering approach to designing a solar/biomass hybrid energy system for dairy farms in Argentina.* Comput. Aided Process Eng. **46**(2019), 1609–1614.

[56] Li C., Zheng Y., Li Z., Zhang L., Zhang L., Shan Y.: *Techno-economic and environmental evaluation of grid-connected and off-grid hybrid intermittent power generation systems: A case study of a mild humid subtropical climate zone in China.* Energy **203**(2021), 120728.

[57] Malik P., Awasthi M., Sinha S.: *Techno-economic and environmental analysis of biomass-based hybrid energy systems: A case study of a Western Himalayan state in India.* Sustain. Energ. Technol. Assess. **45**(2021), 101189.

[58] Dhass A.D., Harikrishnan S.: *Cost effective hybrid energy system employing solar-wind-biomass resources for rural electrification.* Int. J. Renew. Energ. Res. IJRER **3**(2013), 1, 222-229.

[59] Suresh P.V., Sudhakar K.: *Life cycle cost assessment of solar-wind-biomass hybrid energy system for energy centre, MANIT, Bhopal.* In: Proc. Int. Conf. on Green Computing, Communication and Conservation of Energy ICGCE-2013, Chennai, 12-14 Dec. 2013.

[60] Chong W.T., Naghavi M.S., Poh S.C., Mahlia T.M.I., Pan K.C.: *Techno-economic analysis of a wind–solar hybrid renewable energy system with rainwater collection feature for urban high-rise application.* Appl. Energ. **88**(2011), 11, 4067–4077.

[61] Ullah Z., Elkadeem M.R., Kotb K.M., Taha I.B., Wang S.: *Multi-criteria decision-making model for optimal planning of on/off grid hybrid solar, wind, hydro, biomass clean electricity supply.* Renew. Energ. **179**(2021), 885–910.

[62] Gonzalez A., Riba J.R., Esteban B., Rius A.: *Environmental and cost optimal design of a biomass–wind–PV electricity generation system.* Renew. Energ. **126**(2018), 420–430.

[63] Bamisile O., Huang Q., Dagbasi M., Adebayo V., Adun H., Hu W.: *Steady-state and process modeling of a novel wind-biomass comprehensive energy system: An energy conservation, exergy and performance analysis.* Energ. Convers. Manage. **220**(2020), 113139.

[64] Zhang X., Yang J., Fan Y., Zhao X., Yan R., Zhao J.: *Experimental and analytic study of a hybrid solar/biomass rural heating system.* Energy **190**(2020), 116392.

[65] Sahoo U., Kumar R., Singh S.K., Tripathi A.K.: *Energy, exergy, economic analysis and optimization of polygeneration hybrid solar-biomass system.* Appl. Therm. Eng. **145**(2018), 685–692.

[66] Calise F., Figaj R.D., Vanoli L.: *A novel polygeneration system integrating photovoltaic/thermal collectors, solar assisted heat pump, adsorption chiller and electrical energy storage: Dynamic and energy-economic analysis.* Energ. Convers. Manage. **149**(2017), 798–814.

[67] Giglio A., Lanzini A., Leone P., Garcia M.M.R., Moya E.Z.: *Direct steam generation in parabolic-trough collectors: A review about the technology and a thermo-economic analysis of a hybrid system.* Renew. Sust. Ener. Rev. **74**(2017), 453–473.

[68] Pantaleo A.M., Camporeale S.M., Miliozzi A., Russo V., Shah N., Markides C.N.: *Novel hybrid CSP-biomass CHP for flexible generation: Thermo-economic analysis and profitability assessment.* Appl. Energ. **204**(2017), 994–1006.

[69] Biboum A.C., Yilanci A.: *Advanced exergoeconomic analysis of solar-biomass hybrid systems for multi-energy generation.* Int. J. Exergy **33**(2020), 1, 1–27.

[70] Malik P., Awasthi M., Sinha S.: *Study on an existing PV/wind hybrid system using biomass gasifier for energy generation.* Pollution **6**(2020), 2, 325–336.

[71] Hossain M.S., Rahman M.F.: *Hybrid solar PV/Biomass powered energy efficient remote cellular base stations.* Int. J. Renew. Energ. Res. IJRER **10**(2020), 1, 329–342.

[72] Li M., Lenzen M., Yousefzadeh M., Ximenes F.A.: *The roles of biomass and CSP in a 100 % renewable electricity supply in Australia.* Biomass Bioenerg. **143**(2020), 105802.

[73] Sarkar T., Bhattacharjee A., Samanta H., Bhattacharya K., Saha H.: *Optimal design and implementation of solar PV-wind-biogas-VRFB storage integrated smart hybrid microgrid for ensuring zero loss of power supply probability.* Energ. Convers. Manage. **191**(2019), 102–118.

[74] Ma T., Yang H., Lu L.: *A feasibility study of a stand-alone hybrid solar–wind–battery system for a remote island.* Appl. Energ. **121**(2014), 149–158.

[75] Olatomiwa L., Mekhilef S., Huda A.S.N., Ohunakin O.S.: *Economic evaluation of hybrid energy systems for rural electrification in six geo-political zones of Nigeria.* Renew. Energ. **83**(2015), 435–446.

[76] Kalamaras E., Belekoukia M., Lin Z., Xu B., Wang H., Xuan J.: *Techno-economic assessment of a hybrid off-grid DC system for combined heat and power generation in remote islands.* Energy Proced. **158**(2019), 6315–6320.

[77] Pavankumar Y., Kollu R., Debnath S.: *Multi-objective optimization of photovoltaic/wind/biomass/battery-based grid-integrated hybrid renewable energy system.* IET Rene. Power Gen. **15**(2021), 7, 1528–1541.

[78] Eteiba M.B., Barakat S., Samy M.M., Wahba W.I.: *Optimization of an off-grid PV/biomass hybrid system with different battery technologies.* Sustain. Cities Soc. **40**(2018), 713–727.

[79] Singh S., Kaushik S.C.: *Optimal sizing of grid integrated hybrid PV-biomass energy system using artificial bee colony algorithm.* IET Renew. Power Gen. **10**(2016), 5, 642–650.

[80] Maleki A., Pourfayaz F.: *Optimal sizing of autonomous hybrid photovoltaic/wind/battery power system with LPSP technology by using evolutionary algorithms.* Sol. Energy **115**(2015), 471–483.

[81] Singh A., Basak P.: *Conceptualization and techno-economic evaluation of microgrid based on PV/Biomass in Indian scenario.* J. Clean. Prod. **317**(2021), 128378.

[82] Hatata A.Y., Osman G., Aladl M.M.: *An optimization method for sizing a solar/wind/battery hybrid power system based on the artificial immune system.* Sustain. Energ. Technol. Assess. **27**(2018), 83–93.

[83] Javed M.S, Song A, Ma T.: *Techno-economic assessment of a stand-alone hybrid solar-wind-battery system for a remote island using genetic algorithm.* Energy **176**(2019), 704–717.

[84] Karsh R.K., Debnath R., Soren N., Roy A.K., Pandey A.D.: *Optimal economical analysis and performance assessment of wind-biomass hybrid energy system.* In: Proc. Int. Conf. on Automation, Computational and Technology Management (ICACTM), London, 24-26 Apr. 2019.

[85] Bukar A.L., Tan C.W., Lau K.Y.: *Optimal sizing of an autonomous photovoltaic/wind/battery/diesel generator microgrid using grasshopper optimization algorithm.* Sol. Energy **188**(2019), 685–696.

[86] Yuan A., Zhao Z., Wang S., Huang Q., Xie X.: *Optimized scheduling of multiple energy complementary power stations with hydro/wind/photovoltaic/battery storage based on cascade hydropower stations.* CSEE J. Power Energ. Sys. JPES (2019).

[87] Xu X., Hu W., Cao D., Huang Q., Chen C., Chen Z.: *Optimized sizing of a standalone PV-wind-hydropower station with pumped-storage installation hybrid energy system.* Renew. Energ. **147**(2020), 1418–1431.

[88] Aykut E., Terzi U.K.: *Techno-economic and environmental analysis of grid connected hybrid wind/photovoltaic/biomass system for Marmara University Goztepe campus.* Int. J. Green Energ. **17**(2020), 15, 1036–1043.

[89] Bilal O., Sambou V., Ndiaye P.A., Kébé C.M..F., Ndongo M.: *Optimal design of a hybrid solar–wind-battery system using the minimization of the annualized cost system and the minimization of the loss of power supply probability (LPSP).* Renew. Energ. **35**(2010), 10, 2388–2390.

[90] Pantaleo A.M., Camporeale S.M., Sorrentino A., Miliozzi A., Shah N., Markides C.N.: *Concentrating solar/biomass hybrid plants with Brayton and organic Rankine cycles: Techno-economic feasibility in selected Mediterranean areas.* Renew. Energ. 147(2018), 3, 2913–2931.

[91] Hussain C.M.I., Norton B., Duffy A.: *Technological assessment of different solar-biomass systems for hybrid power generation in Europe.* Renew. Sust. Ener. Rev. **68**(2017), 1115–1129.

[92] Pantaleo A.M., Camporeale S.M., Sorrentino A., Miliozzi A., Shah N., Markides C.N.: *Solar/biomass hybrid cycles with thermal storage and bottoming ORC: System integration and economic analysis.* Energy Proced. **129**(2017), 724–731.

[93] Oyekale J., Petrollese M., Cau G.: *Modified auxiliary exergy costing in advanced exergoeconomic analysis applied to a hybrid solar-biomass organic Rankine cycle plant.* Appl. Energ. **268**(2020), 114888.

[94] Shukla P., Dhar S., Fujino J.: *Renewable energy and low carbon economy transition in India.* J. Renew. Sustain. Ener. **2**(2010), 3, 031005.

[95] Paul A.W., Philipp S., Tobias P.: *Uncommon turbine architectures for distributed power generation – development of a small velocity compounded radial re-entry turbine.* Arch. Thermodyn. **41**(2020), 4, 235–253.

[96] Raheem A, Hassan M.Y, Shakoor R, Rasheed N.: *Economic feasibility of stand-alone wind energy hybrid with bioenergy from anaerobic digestion for electrification of remote area of Pakistan.* Int. J. Integr. Eng. **6**(2014) 3, 1–7.

[97] Nagel J.: *Determination of an economic energy supply structure based on biomass using a mixed-integer linear optimization model.* Ecol. Eng. **16**(2000), 91–102.

[98] Wang C., Liu Y., Li X.: *Energy management system for stand-alone diesel-wind-biomass microgrid with energy storage system.* Energy **97**(2016), 90–104.

[99] Zhou Z., Ge L.: *Operation of stand-alone microgrids considering the load following of biomass power plants and the power curtailment control optimization of wind turbines.* IEEE Access **7**(2019), 186115–186125.

[100] Ghenai C., Janajreh I.: *Design of solar-biomass hybrid microgrid system in Sharjah.* Energy Proced. **103**(2016), 357–362.

[101] Bai Z., Liu Q., Lei J.: *Thermodynamic evaluation of a novel solar-biomass hybrid power generation system.* Energ. Convers. Manage. **142**(2017), 296–306.

[102] Baredar P., Sethi V.K., Pandey M.: *Correlation analysis of small wind–solar–biomass hybrid energy system installed at RGTU Bhopal, MP (India).* Clean Technol. Envir. Pol. **12**(2010), 3, 265–271.

[103] Anoune K., Bouya M., Astito A., Abdellah A.B.: *Sizing methods and optimization techniques for PV-wind based hybrid renewable energy system: A review.* Renew. Sust. Ener. Rev. **93**(2018), 652–673.

[104] Nykamp S., Molderink A., Hurink J.L., Smit G.J.: *Statistics for PV, wind and biomass generators and their impact on distribution grid planning.* Energy **45**(2012), 1, 924–932.

[105] Wang Y., Li F., Yu H., Wang Y., Qi C., Yang J.: *Optimal operation of microgrid with multi-energy complementary based on moth flame optimization algorithm. Energy Sources, Part A: Recovery.* Util. Environ. Eff. **42**(2020), 7, 785–806.

[106] Sanni S.O., Oricha J.Y., Oyewole T.O., Bawonda F.I.: *Analysis of backup power supply for unreliable grid using hybrid solar PV/diesel/biogas system.* Energy **227**(2021), 120506.

**archives**
**of thermodynamics**
Vol. **44**(2023), No. 4, 43–61
DOI: 10.24425/ather.2023.149708

# An in-house numerical code to assist in designing a small-scale red-hot air furnace

**SYLWIA POLESEK-KARCZEWSKA***
**DARIUSZ KARDAŚ**
**IZABELA WARDACH-ŚWIĘCICKA**

Institute of Fluid Flow Machinery, Polish Academy of Sciences,
Fiszera 14, 80-231 Gdańsk, Poland

**Abstract** The implementation of a sustainable development concept that involves an improvement of resource use efficiency, whilst maximizing the utilization of locally available biomass resources, has contributed to an increased interest in the combined heat and power systems based on externally fired gas turbines. Since the high-temperature gas/gas heat exchangers intended to heat the turbine inlet air are the key components of such systems, intensified research on exchangers of this type has been observed over the last decade. This work presents the in-house calculation code developed to analyze the heat transfer between the hot-side and cold-side streams in the small-scale red-hot air furnace of a unique design. The performed calculations, based on the assumed thermal and flow operation parameters and technical specifications, allowed to determine the required heat exchange surface area of the furnace to achieve the target outlet conditions. The calculation code allows for determining the geometry of a furnace, including its overall dimensions, number of tubes, and their bent sections in the heat exchange parts. The study of the laboratory-scale furnace performance has demonstrated its good agreement with the simulation results, thereby proving the code a reliable tool in designing.

**Keywords:** Red-hot air furnace; Design; Calculation methodology; Parametric characteristics; Heat exchange surface area

*Corresponding Author. Email: sylwia.polesek-karczewska@imp.gda.pl

## Nomenclature

| | | |
|---|---|---|
| $A$ | – | heat exchange surface area, cross-sectional area, $m^2$ |
| $\bar{c}_p$ | – | average specific heat, J/(kgK) |
| $d$ | – | diameter, m |
| $dT$ | – | temperature increment, K |
| $dz$ | – | tube diameter, m |
| HTC | – | heat transfer coefficient |
| $\dot{H}$ | – | mass flow enthalpy, W |
| $k$ | – | overall heat transfer coefficient, W/($m^2$K) |
| $L$ | – | gas layer thickness, characteristic dimension, length of section, m |
| $m$ | – | flame-to-chamber volume ratio |
| $\dot{m}$ | – | mass flowrate, kg/s |
| $N_p$ | – | number of tubes |
| Nu | – | Nusselt number |
| $p$ | – | pressure, kPa |
| $p_n$ | – | partial pressure, kPa |
| Pr | – | Prandtl number |
| $\dot{q}$ | – | heat flux, W/$m^2$ |
| $\dot{Q}$ | – | thermal output, W |
| $\dot{Q}_{\mathrm{LHV}}$ | – | chemical energy, W |
| Re | – | Reynolds number |
| $R_g$ | – | tube bending radius, m |
| $T$ | – | temperature, K |
| $X$ | – | mole fraction, mol/mol |

### Greek symbols

| | | |
|---|---|---|
| $\alpha$ | – | heat transfer coefficient, W/($m^2$K) |
| $\delta$ | – | wall thickness, m |
| $\varepsilon$ | – | emissivity |
| $\lambda_w$ | – | thermal conductivity of tube material, W/(m K) |
| $\lambda$ | – | excess air ratio |
| $\rho$ | – | density, kg/$m^3$ |
| $\sigma$ | – | Stefan-Boltzmann constant, $= 5.678 \cdot 10^{-8}$ W/($m^2K^4$) |
| $\theta$ | – | logarithmic mean temperature difference, K |
| $\psi$ | – | degree of wall screening |
| $\xi$ | – | slagging factor |

### Subscripts and superscripts

| | | |
|---|---|---|
| 0 | – | initial value |
| $a$ | – | air |
| ad | – | adiabatic |
| com | – | combustion |
| conv | – | convection |
| corr | – | correction |
| err | – | limitation value/error value |
| $dh$ | – | hydraulic diameter |

| | | |
|---|---|---|
| $f$ | – | fuel, fluid |
| $fg$ | – | flue gas |
| $fl$ | – | flame |
| $g$ | – | gas, gaseous non-luminous part of the flame |
| $i$ | – | iteration procedure index |
| in | – | inlet |
| inn | – | inner |
| $j$ | – | iteration procedure index |
| $k$ | – | iteration procedure index |
| $l$ | – | luminous part of the flame |
| loss | – | loss to the surroundings |
| mid | – | between high- and medium-temperature sections |
| new | – | next step value |
| old | – | previous step value |
| out | – | outlet |
| $ox$ | – | oxidizer (combustion air) |
| rad | – | radiation |
| $s$ | – | surface |
| tot | – | total |
| $w$ | – | combustion chamber wall |
| $x$, $y$, $z$ | – | $x$-, $y$-, $z$-direction |
| $xy$ | – | cross-section |

**Acronyms**

| | | |
|---|---|---|
| CHP | – | combined heat and power |
| EFGT | – | externally-fired gas turbine |
| HT | – | high-temperature |
| THE | – | high-temperature heat exchanger |
| MT | – | medium-temperature |
| ORC | – | organic Rankine cycle |
| RHAF | – | red-hot air furnace |

# 1 Introduction

Small-scale energy systems have gained increasing interest over the past decades owing to the emerging concept of the sustainable use of locally available renewable energy resources. Along with this, efforts have been intensified toward the development of conversion technologies that would meet the growing demands of distributed energy generation. Aiming at minimizing $CO_2$ emissions, while maximizing the system's efficiency, the focus has been put on the combined heat and power (CHP) technologies based on biomass of different kinds [1]. Besides the thermochemical methods, such as pyrolysis and gasification, combustion remains the basic route of biomass

conversion for energy purposes, due to the maturity of the technology of furnaces [2]. However, the combustion of biomass entails operational problems that are mainly caused by more intensive fouling and increased corrosion rates due to the presence of alkali compounds in the fuel. These problems may be reduced through adjustment of the operation parameters for the specific boiler design to provide efficient combustion [3]. The large diversity of biomass properties to be potentially utilized in small-scale CHP units is challenging in terms of technical and economic feasibility and, therefore, the research in the area of distributed energy systems requires further advances. Within the small power range of CHP systems (below 1 MWel), apart from the technologies involving Stirling and steam engines, or turbine organic Rankine cycle (ORC), these are the externally-fired gas turbine (EFGT) systems that are considered the promising solution [4,5], especially due to fuel flexibility [6]. The biomass furnace and the high-temperature heat exchangers (HTHEs), typically air-cooled, are the key components of the EFGT system, critical in terms of performance reliability, and the system's total cost. For this reason, efforts are undertaken to provide possibly highly efficient devices to preserve reduced energy consumption and investment costs that contribute to increased energy generation efficiency and lower emission levels. The constraint to be encountered in developing gas/gas HTHE technology is due to lower heat transfer coefficients of gas compared to those for liquid coolants, which is said to result in the air-side resistance exceeding 85% of the total thermal resistance [7]. One of the options is the furnace-integrated HTHEs. Such designs allow additionally to take advantage of thermal radiation, and simultaneously, to obtain smaller and more compact constructions which result in reducing manufacturing costs. In this context, one of the key issues is the reliable evaluation of the furnace exit gas temperature needed to define the basic design feature in terms of dividing the heat exchange surfaces into the irradiated and convection sections [8], thereby optimizing the furnace's dimensions and weight.

Commonly, computational fluid dynamics (CFD) has been involved in the designing and optimization of thermal devices. Owing to the possibility of reproducing the full geometry of a device and complex three-dimensional flow structures [9], this approach may provide more accurate predictions of thermal performance. But this will always be done at the expense of larger computing power demand. The computations become even more time-consuming when the radiation heat transfer has to be accounted for, which is the case with the heat exchangers operated under high-temperature

regimes and emitting/absorbing media such as a flue gas [10]. Precisely due to increased computational cost, radiation is often neglected [11], though it is important to the accurate predictions of the high-temperature units' performance. Żukowski *et al.* [12] used CFD tools for simulating heat transfer in a cross-current plate heat exchanger designed to heat the combustion air from the exhaust gas flow to burn waste organics in a fluidized bed furnace. The authors studied different geometries of the inter-plate space focusing on identifying the dead zones in the airflow. Thek *et al.* [13] performed CFD analysis in designing a biomass furnace and cylindrical tube bundle HTHE for a small-scale micro-CHP system of $\sim$ 100 kW nominal electric power based on a gas turbine. Through simulations, they obtained the optimized designs with reduced peaks in flue gas temperature and velocity in the furnace, and possibly evenly distributed flue gas inflow to HTHE. The latter has been designed as a two-duct heat exchanger to use different materials for each section. The higher quality and more expensive stainless steel (type 1.4876) was used only in the duct exposed to high temperatures. There are also other approaches proposed offering a reduction of CPU time. Recently, Wajs *et al.* [14] have developed a numerical model of a high-temperature mini-channel heat exchanger for a gas micro-CHP system and carried out the analysis of its thermo-hydraulic performance using OpenFOAM environment.

The relatively simple and reliable calculation tools, which may bring benefit to the efficiency of designing the HTHEs, are not numerous. The widely used lumped methods, such as logarithmic mean temperature difference (LMTD) and the number of transfer units (NTU) method, are applicable thereto. Both methods, in general, require inlet and outlet temperatures of the fluids, though they may involve the iteration procedure when the outlet temperatures are to be determined [15]. Schulte-Fischedick *et al.* [16] made use of the LMTD method in designing a prototype ceramic HTHE for an externally fired combined cycle of 6 MWel output fueled with woody biomass. The plate-fin flue gas/air heat exchanger was designed as a counter-flow type. Baina *et al.* [17] utilized the NTU method to model two types of exhaust gas/air HTHEs, the corrugated plate one and of shell-and-tube type, for the EFGT system fueled with biomass producer gas. The reported discrepancies between the experimental data and predictions for a plate heat exchanger in terms of outlet temperatures of working air and flue gas did not exceed 1.5% and 2.1%, respectively. The same calculation method was applied by Al-attab and Zainal [18] to determine the heat exchange surface area of a stainless steel HTHE designed for a small-scale EFGT system fired

with waste wood blocks (of $\sim$ 57 kWth and $\sim$ 5.6 kWel). A more advanced approach was applied by Jolly *et al.* [19], who developed a numerical code to determine the heat transfer and pressure drop characteristics and optimize the initial design concept of a bayonet tube gas-gas HTHE. The program utilized the semi-explicit method, wherein the problem was reduced to one-dimensional (1D) calculations solving basic equations for a modular unit of a designed heat exchanger. The model also involved the radiation between the flue gas and the tube surface. Cordiner and Mulone [2] proposed a 1D thermal balance approach with a two-zone combustion model to account for the heat release and radiation contribution and simulated the performance of biomass furnace-integrated HTHE in the micro-EFGT system of $\sim$ 70 kW electric power output.

As the literature review shows, the relatively simple and computationally efficient approaches for developing the HTHEs designs for micro-scale CHP units are rather limited. The objective of the present work is to demonstrate the in-house numerical approach that served as a support in designing a red-hot air furnace for a small-scale EFGT system, whilst taking account of the specific technological and technical limits. Despite the unique design concept of the furnace under consideration, to evaluate the heat transfer between the hot side stream (flue gas) and tube side stream (working air), the basic governing equations, including the correlations for conduction, convection and radiation, were utilized in the computational solution method. Focusing on the design simplicity, computer code flexibility, and optimization usability, the calculation procedure makes use of iteration methods and multiplication of predefined tubing sub-elements (tube segments) of the heat exchange sections. The developed simulation tool was used for multivariant analysis to find the optimum, in terms of heat transfer rate and manufacturing costs, furnace design for the defined inlet thermal and flow parameters. This eventually allowed to determine the required heat exchange surface area of the furnace. The computation results were then validated through the experimental study of a designed laboratory-scale air furnace.

## 2 The furnace design assumptions

The general aim that lies behind the development of the calculation methodology presented herein was to draw up the basic design guidelines for the small-scale red-hot air furnace (RHAF) of 20 kW capacity, performing the

role of a heat source in a CHP unit using an externally-fired gas turbine. The RHAF is intended to heat the working air to the designed temperature exceeding 800°C under low-pressure flow conditions [1]. Given the techno-economical limits, resulting from the high-temperature operational regimes of a device to be involved and, on the other hand, from the thermal and mechanical properties of materials available on the market, a two-module design of a furnace was assumed.

The furnace is considered to be composed of high-temperature (HT) and medium-temperature (MT) sections. The HT part (the red-hot section) is modeled as a two-zone section, wherein the first is a firebox and the other is the remaining part of a combustion chamber with the wall tubes. The MT part is limited to the heat exchange section separated from the direct fire zone and involves convection as the dominating heat transfer mechanism. This concept is intended to reduce the use of costly heat-resistant materials. Thus, the austenitic heat-resistant steel (AISI 304) was taken into consideration only for the HT section, and the first zone of the MT part. The maximum permissible long-term operation temperature for this type of steel is approximately 1150°C. The convection part of the heat exchanger is made of P265GH boiler steel. The screening tubes in the HT section were assumed to consist of bent parallel tubes for each wall of the combustion chamber (Fig. 1a). The MT heat exchange part constitutes the flue gas channel with the bundle of parallel tubes, bent in the horizontal plane as demonstrated in Fig. 1b. The furnace is assumed to be fired by propane ($C_3H_8$).

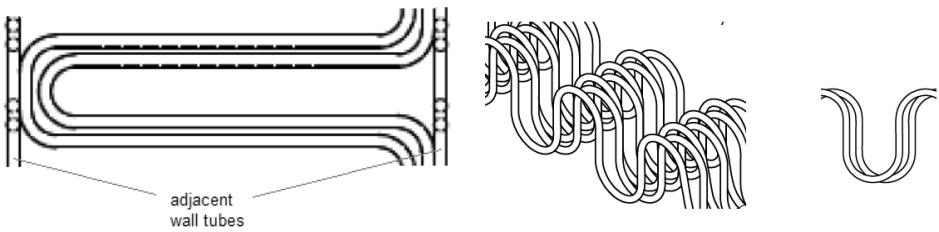


Figure 1: The geometry of furnace tubing sub-elements: (a) wall tubing segment in the high-temperature section; (b) tube bundle in the medium-temperature section, the spatial view (left) and the side view on the tube bundle segment (right).

## 3 Calculation details

The calculation code was developed to determine the required heat exchange surface for the target outlet temperature of the working air, based on the set input thermal and flow parameters on the hot and cold sides, which included:

- the amount and temperature of combustion air;
- the temperature of working air at the furnace inlet and outlet, and the outlet from the MT section; the latter is assumed at the level of the maximum temperature permissible for the boiler steel.

For simplicity, the counter-current flow of media, i.e. the working fluid (air) and flue gas, is considered.

The required heat exchange surface is expressed as

$$A = \frac{\dot{Q}}{k\theta}\,, \tag{1}$$

where $\dot{Q}$ is the thermal output, $k$ represents the overall heat transfer coefficient given as

$$k = \frac{1}{\alpha_{fg}} + \frac{\delta}{\lambda_w} + \frac{1}{\alpha_a} \tag{2}$$

with $\alpha_{fg}$ and $\alpha_a$ denoting the heat transfer coefficient on the hot and cool sides, respectively. The parameters $\delta$ and $\lambda_w$ stand for the thickness and thermal conductivity of a tube wall, respectively. The heat transfer coefficient for the hot side (flue gas) takes into account both, the convection and radiation heat transfer coefficients, and is given as

$$\alpha_{fg} = \alpha_{fg}^{\mathrm{conv}} + \alpha_{fg}^{\mathrm{rad}}\,. \tag{3}$$

The parameter $\theta$ is the mean logarithmic temperature difference, defined as follows:

$$\theta = \frac{\Delta T_1 - \Delta T_2}{\ln \dfrac{\Delta T_1}{\Delta T_2}}\,, \tag{4}$$

where

$$\Delta T_1 = T_{fg}^{\mathrm{in}} - T_a^{\mathrm{out}} \quad \text{and} \quad \Delta T_2 = T_{fg}^{\mathrm{out}} - T_a^{\mathrm{in}}\,.$$

In the above, $T$ denotes temperature, and superscripts in and out refer to the inlet and outlet parameters of the hot and cold fluids, flue gas (subscript $fg$) and working air (subscript $a$), respectively.

### 3.1 Radiation on the flue-gas side

The triatomic components of flue gas, i.e. water and carbon dioxide ($H_2O$ and $CO_2$), are accounted for in the calculation of radiation heat transfer. Since the burning of gaseous fuel (propane) was considered, no additional thermal radiation from the particulate matter was included in the analysis. The radiation heat transfer coefficient between the flowing gas ($g$) and the surface ($s$) is expressed by the formula [20]

$$\alpha_{\mathrm{rad}} = \frac{\dot{q}}{T_s - T_g} = \frac{\varepsilon_s + 1}{2}\sigma\varepsilon T_g^3 \frac{1 - \left(\frac{T_s}{T_g}\right)^4}{1 - \left(\frac{T_s}{T_g}\right)}, \tag{5}$$

where $\dot{q}$ represents the density of heat flux, $\sigma$ is a Stefan-Boltzmann constant, and $\varepsilon$ is the thermal emissivity, whereby the latter without index refers to the radiating medium in the combustion chamber (including luminous and non-luminous part), and the other with superscript $s$ refers to the irradiated surface.

As regards the HT heat exchange section, its emissivity may be calculated from

$$\varepsilon = \frac{\varepsilon_{fl}}{\varepsilon_{fl} + (1 - \varepsilon_{fl})\,\psi\xi}, \tag{6}$$

where $\psi$ is the degree of wall screening, and $\xi$ is the slagging factor. The latter, for gaseous fuels, amounts to 0.8 [20]. Parameter $\varepsilon_{fl}$ refers to the flame emissivity that depends on the emissivity of the luminous part of the flame ($\varepsilon_l$) related to the glowing particulates (ash and soot), and that of the gaseous non-luminous part ($\varepsilon_g$)

$$\varepsilon_{fl} = m\varepsilon_l + (1 - m)\varepsilon_g, \tag{7}$$

where $m$ represents the flame-to-chamber volume ratio, which for the case of gaseous fuel burning is assumed at 0.2 [20]. Emissivity $\varepsilon_l$ is given as

$$\varepsilon_l = 0.9\,[1 - \exp\,(-k_p p L)], \tag{8}$$

where $p$ denotes pressure in the firebox, and $k_p$ is a temperature-dependent absorption coefficient described by

$$k_p = 1.6\frac{T}{1000} - 0.5. \tag{9}$$

Parameter $L = 3.6\dfrac{V}{F}$ stands for the thickness of the radiating gas layer as the ratio of the volume of a combustion chamber ($V$) and the total irradiated surface ($F$).

In the case studied the surface $F$ is the sum of the chamber walls and the screening tubes' outer surface. The emissivity of the non-luminous part, i.e. the flue gas, is expressed by

$$\varepsilon_g = 1 - \exp\left(-k_g L\right), \tag{10}$$

where $k_g$ is the absorption coefficient given as [20]

$$k_g = \frac{0.8 + 1.6 X_{\mathrm{H_2O}}}{\sqrt{p_n L}} \left(1 - 0.38 \frac{T}{1000}\right) \left(X_{\mathrm{H_2O}} + X_{\mathrm{CO_2}}\right). \tag{11}$$

In the above, $X_{\mathrm{H_2O}}$ and $X_{\mathrm{CO_2}}$ represent the mole fractions of water and carbon dioxide, respectively, and $p_n$ denotes the partial pressure of these components.

Further, to describe the degree of wall screening ($\psi$), the ratio of the tubes' surface ($A_s$) to the chamber wall surface ($A_w$), i.e. $\psi = A_s/A_w$ was adopted [20]. In the MT heat exchange section, the non-luminous gas layer is considered. In this case, parameter $m$ (Eq. (7)) amounts to 0, which implies $\varepsilon = \varepsilon_g$ in Eq. (5).

### 3.2 Convection heat transfer

Knowing the Nusselt number (Nu), the heat transfer coefficient may be calculated as

$$\alpha = \frac{\mathrm{Nu}\,\lambda_f}{L}, \tag{12}$$

where $\lambda_f$ represents the thermal conductivity of the fluid and is determined using the correlation [21, 22]

$$\mathrm{Nu} = C\mathrm{Re}^n \mathrm{Pr}^m, \tag{13}$$

where the constants $C$, $n$, and $m$ depend on the character of the flow (laminar, transition, turbulent) [21, 22]. For the cold side, the characteristic dimension $L$ is the inner diameter, $L = d_{\mathrm{inn}}$, and for the hot side (flue gas flow), this dimension is represented by the hydraulic diameter.

### 3.3 Fuel combustion

Following the assumed limit for the tube wall temperature in the firebox ($< 1150°C$), the combustion with an excess of air was considered. Taking into account the heat loss to the surroundings ($\dot{Q}_{\text{loss}}$), the energy balance for the combustion chamber takes the form

$$\dot{H}_{ox}^{\text{in}} + \dot{H}_{f}^{\text{in}} + \dot{Q}_{\text{LHV}} = \dot{H}_{fg} + \dot{Q}_{\text{loss}}\,, \tag{14}$$

where $\dot{H}$ represents the mass flow enthalpy and $\dot{Q}_{\text{LHV}}$ stands for the fuel chemical energy.

For a set flue gas temperature at the outlet from the furnace to the chimney ($T_{fg}^{\text{out}}$), the heat given off by the hot medium is expressed as

$$\dot{Q}_{fg} = \dot{m}_{fg}\bar{c}_{p,fg}\left(T_{\text{com}} - T_{fg}^{\text{out}}\right) \tag{15}$$

and the heat absorbed by the working air is determined from

$$\dot{Q}_{a} = \dot{m}_{a}\bar{c}_{p,a}\left(T_{a}^{\text{out}} - T_{a}^{\text{in}}\right). \tag{16}$$

Parameter $T_{\text{com}}$ in Eq. (15) represents theoretically calculated combustion temperature, whereas $\bar{c}_p$ refers to the specific heat of respective fluids for arithmetically averaged temperature between the inlet and outlet values. The details for the physicochemical properties of fuel and fluids are provided elsewhere [1].

### 3.4 Numerical procedure

The calculations for each heat exchange section of a furnace, i.e. the HT and MT sections, are carried out in separate loops, starting from determining the parameters in the firebox. The flow diagram of a numerical algorithm is shown in Figs. 2 and 3. The calculation procedure involves the following steps:

i. Given the temperatures and mass flow rates of combustion air and fuel, the combustion temperature is determined (using Eq. (14)). Owing to the dependence of the flue gas heat capacity on temperature, the iterative method is utilized. The initial temperature, which is the calculated adiabatic combustion temperature of $C_3H_8$ ($T_{\text{ad}}$), is decreased by $dT = 0.1$ K in each step until the convergence between

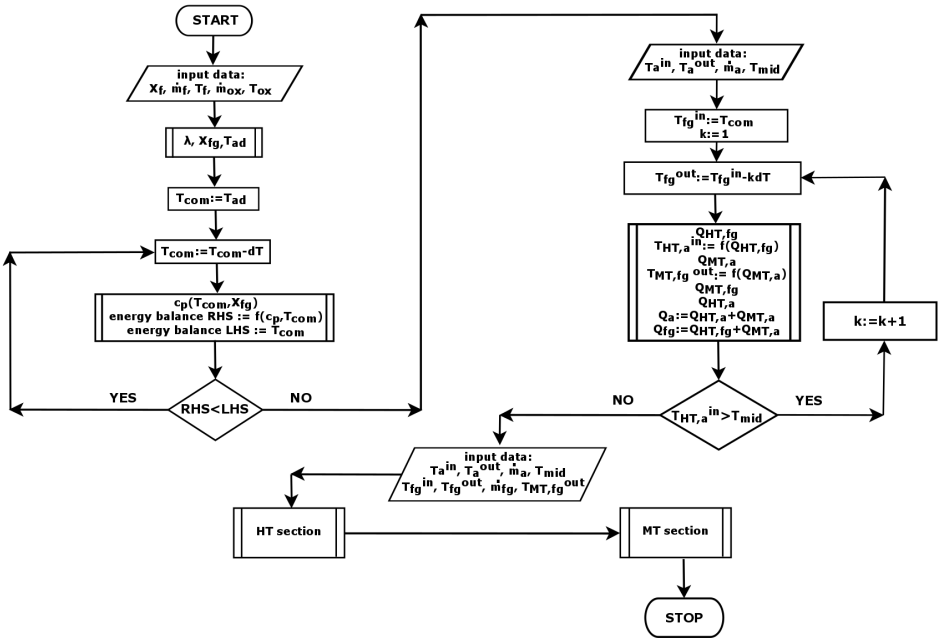


Figure 2: The general flow diagram of the developed numerical algorithm for designing the furnace.

the left-hand (LHS) and right-hand sides (RHS) of the equation is reached. The resulting temperature value ($T_{\mathrm{com}}$) is the inlet temperature of the HT heat exchange section of a furnace.

ii. For the input parameters of working air (i.e. flow rate ($\dot{m}_a$), temperatures at the inlet to ($T_a^{\mathrm{in}}$), and the outlet from the furnace ($T_a^{\mathrm{out}}$), and additionally in between the MT and HT sections), and given $T_{\mathrm{com}}$, the flue gas outlet temperature ($T_{fg}^{\mathrm{out}}$) is calculated based on the flue gas/working air energy balance. This is done by iteratively decreasing the flue gas temperature leaving the HT section until the assumed air temperature between the MT and HT sections ($T_{\mathrm{mid}}$) is achieved for a set convergence criterion. The energy balance for the HT section is calculated for the determined inlet and outlet temperatures of the fluids in the section.

iii. The results of the iterative temperature calculations are the input data to the design loops of the HT and MT sections.

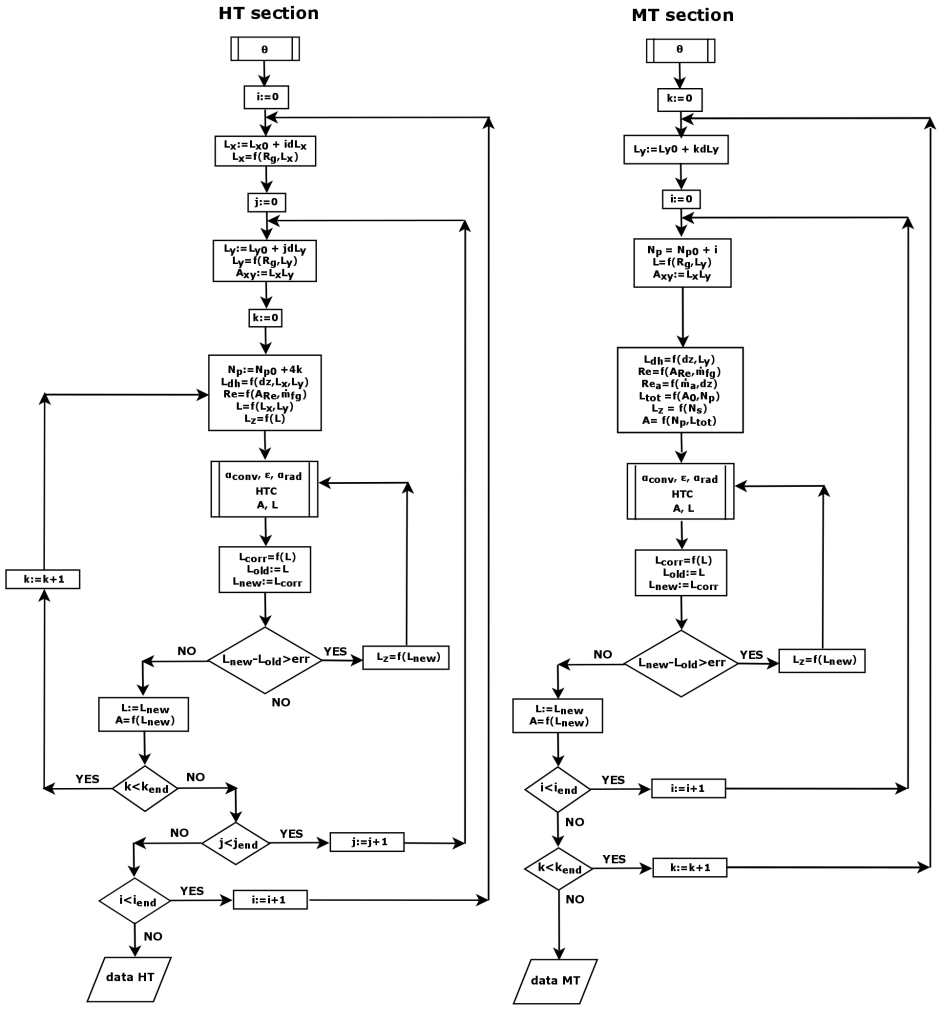


Figure 3: Detailed schemes of numerical algorithms for calculations in HT and LT sections of a furnace.

iv. The mean logarithmic temperature difference $\theta$ (Eq. (4)) in the HT section is calculated.

v. Starting from the initial geometry $(L_{x0}, L_{y0})$ of the section and based on the technical parameters related to tube bending ($L$ – the length of the flue channel, $R_g$ – bending diameter, and wall tubing configuration), the geometry of the firebox with the integrated HT heat exchange section is presumed by multiplying the tubing segments.

vi. For the set geometry, the flow characteristics (Re and Nu numbers, heat transfer coefficients) are determined to calculate the total heat transfer coefficient ($k$) in the HTC procedure and, eventually, the required heat exchange surface area ($A$) using Eq. (1).

vii. Steps (iv)–(vi) are then executed for the MT section while accounting for the assumed shape and arrangement of bent tubes in the flue gas channel.

## 4 Model predictions and experimental validation

The developed methodology allowed for the parametric analysis of the thermal characteristics of the design to aid the choice of an optimum solution in terms of required outlet temperatures and construction cost. The key variable geometrical parameters involved the dimensions of the combustion chamber and flue gas channel, and the number of tubes. The convection part of the furnace (MT) can be analyzed separately from the HT part, however, due to technical reasons the geometry of the screening tubes implies the number of tubes in the bundle in the MT section. Also, due to practical reasons, of importance was the total length of a single tube in each section, either in the HT or the MT section, which is related to the standard tube lengths available on the market. The results of a numerical parametric analysis are shown in Figs. 4 and 5. The input data were chosen as the main assumptions for designing the whole system, which were: the

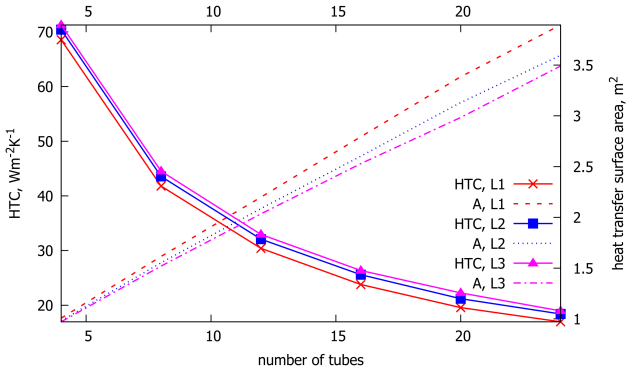


Figure 4: Heat transfer coefficient (HTC) and heat transfer area ($A$) in the HT heat exchanger section *vs.* the number of tubes for different cross-sections of a combustion chamber: $L1 = 0.5 \times 0.5$ m$^2$, $L2 = 0.75 \times 0.75$ m$^2$, $L3 = 1 \times 1$ m$^2$.

mass flow rates for the flue gas and the working air, the input fluid temperatures, the required output temperature for working air and its temperature between the HT and MT sections ($T_{\text{mid}} = 624°\text{C}$). Due to the available sizes of the steel and heat-resistant boiler tubes and the need to connect them between the MT and HT sections, only one diameter size (outer diameter of $21.3 \cdot 10^{-3}$ m) was taken into consideration. Additionally, because of the technical limit on the tube bending radius, the minimum values of the radius for the HT and MT sections were accounted for, i.e. $93.15 \cdot 10^{-3}$ m and $77.5 \cdot 10^{-3}$ m, respectively. The input data for the fuel flow rate results from the required thermal power output of the furnace. In addition, heat losses to the surroundings at 15% of the total chemical fuel energy were assumed.

The correlation between the overall heat transfer coefficient (HTC) and the number of tubes in the radiative (HT) section is presented in Fig. 4. As it can be seen, the HTC value is higher for a lower number of tubes, which then results from higher Re values for the flow of working air. In other words, the more tubes the slower the airflow and the lower HTC. Correspondingly, for a smaller number of tubes, as expected, the total heat transfer surface area needed to achieve the set operation parameters is smaller. Moreover, the smaller size (cross-sectional area) of a combustion chamber translates into a higher value of overall HTC, which is due to higher Re for flue gas flow in a smaller cross-section area.

A similar trend may be observed in the case of a correlation between the overall HTC and the number of tubes in the convective (MT) section. As it can be seen from Fig. 5, the HTC value is higher for a lower number

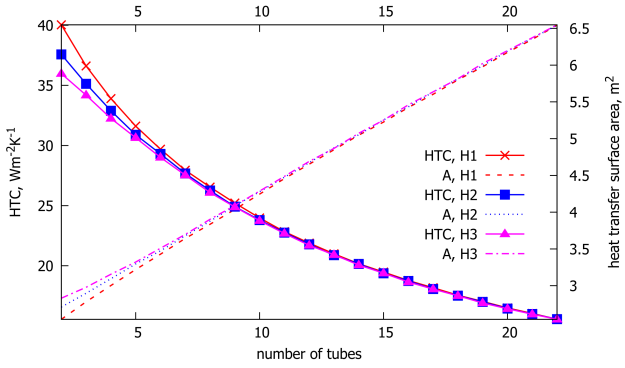


Figure 5: Heat transfer coefficient (HTC) and heat transfer area ($A$) in the MT heat exchanger section *vs.* the number of tubes for different heights of the flue gas channel: $H1 = 0.35$ m, $H2 = 0.5$ m, $H3 = 0.65$ m.

of tubes (again, it results from increased Re of the airflow for a decreasing number of tubes). Consequently, the predicted heat transfer area is smaller for a lower number of tubes. Moreover, an increase in the height of a flue gas channel results in lowering overall HTC, which comes from the lower Re value for flue gases in the greater cross-section area. It should be noted that in the proposed calculation methodology, the width of the flue gas channel is defined by the number of tubes. The influence of the channel height on the HTC and heat transfer area is visible only for the number of tubes lower than 10, which stems from the flow laminarisation effect in the case of a greater number of tubes.

Comparing Figs. 4 and 5 one may see that the maximum value of overall HTC for the HT section is nearly twice as high as that for the MT section (e.g. 70 W/m$^2$K *vs.* 40 W/m$^2$K), which is due to additional radiative effects in a combustion chamber. The heat transfer surface area predicted for this section is thus almost twice as small as that for the MT section (4 m$^2$ *vs.* 6.5 m$^2$).

The calculation results of the selected design variant, including basic thermal and flow parameters, and main dimensions of both furnace heat exchange sections, are presented in Table 1. As aforementioned, greater

Table 1: Parametric characteristics of a furnace – sample calculation results.

| MT heat exchange section | | | | | | | |
|---|---|---|---|---|---|---|---|
| Number of tubes | Channel width (m) | $\mathrm{Re}_{fg}$ | $\mathrm{Re}_a$ | $k$ (W/(m$^2$K)) | $A$ (m$^2$) | $\dot{Q}$ (kW) | Section length* (m) |
| 6 | 0.28 | 1069 | 8093 | 29.7 | 3.4 | 15.0 | 0.7 |
| 8 | 0.36 | 832 | 6070 | 26.5 | 3.8 | | 0.6 |
| 10 | 0.45 | 680 | 4856 | 24.0 | 4.3 | | 0.5 |
| 16 | 0.70 | 440 | 3035 | 18.8 | 5.4 | | 0.4 |
| HT heat exchange section | | | | | | | |
| Number of wall tubes | Section cross-area (m$^2$) | $\mathrm{Re}_{fg}$ | $\mathrm{Re}_a$ | $k$ (W/(m$^2$K)) | $A$ (m$^2$) | $\dot{Q}$ (kW) | Section height (m) |
| 8 | 0.4 × 0.4 | 939 | 4374 | 40.5 | 1.7 | 8.7 | 2.5 |
| 16 | 0.4 × 0.4 | 751 | 2187 | 22.7 | 2.9 | | 2.5 |
| 8 | 0.5 × 0.5 | 791 | 4374 | 41.8 | 1.6 | | 2.1 |
| 16 | 0.5 × 0.5 | 653 | 2187 | 23.8 | 2.8 | | 2.1 |

*) For three-pass flue gas channel flow assumed

tube number in both sections contributes to lowering cold and hot fluid flow parameters, which leads to a decrease in the overall HTC and thereby to increased needed heat transfer area. Considering the technical limitations and possible pressure drop increase, eight tubes were taken for the design. The designed air furnace has undergone the experimental test series to validate the calculation outcomes [1]. The measurement results and predicted parameters are in satisfactory agreement, as shown in Table 2 (in the table, input values for calculation are marked in bold). As can be seen, the relative difference between the experimentally obtained and calculated outlet temperature of heated working air is only 2.7%, whereas in the case of outlet parameters on the hot side (flue gas) these differences do not exceed 5%.

Table 2: Comparison of simulation/predicted and measured parameters.

| Parameter | Calculation | Measurements [1] | Relative difference, % |
|---|---|---|---|
| Fuel mass flowrate ($\dot{m}_f$), kg/h | **3.07** | 3.14 | 2.2 |
| Combustion air flowrate ($\dot{m}_{ox}$), kg/h | **80.0** | 87.0 | 8.0 |
| Flue gas flowrate ($\dot{m}_{fg}$), kg/h | 83.07 | 90.14 | 7.8 |
| Working air flowrate ($\dot{m}_a$), kg/h | **89.0** | 83.3 | 6.8 |
| Fuel temperature ($T_f$), °C | **20** | 20 | – |
| Combustion air temperature ($T_{ox}$), °C | **20** | 35 | – |
| Outlet flue gas temperature ($T_{fg}^{\text{out}}$), °C | 206 | 215 | 4.2 |
| Inlet working air temperature ($T_a^{\text{in}}$), °C | **46** | 52 | – |
| Outlet working air temperature ($T_a^{\text{out}}$), °C | 926 | 951 | 2.6 |

# 5 Summary

In this paper, the approach developed to design the red-hot air furnace for the small-scale combined heat and power systems based on the externally-fired gas turbines was presented. The calculation procedure implemented in the in-house numerical code to predict the furnace performance, based on the required output thermal parameters, as well as on the material-related and manufacturing technical limitations, was demonstrated. The developed computational program has served to determine the heat exchange surface area of an optimized, in terms of heat transfer rate and manufacturing costs, design of the furnace.

The proposed algorithm enables the determination of the main geometrical parameters of both, high- and medium-temperature sections of the furnace. It was shown that using more tubes in both sections leads to lower cold and hot fluid flow parameters, and in consequence, to lower overall heat transfer coefficients and larger required heat transfer area. The latter affects the device size and its manufacturing cost. Taking into account the economic aspect, the obtained data enables choosing the optimal geometrical parameters for the construction of the red-hot air furnace while minimizing its cost at the same time.

The developed code allows for a multivariant analysis of the furnace designs and has resulted in the construction of the device that achieved the target operational parameters. Thereby, the approach used proved itself to be reliable in designing and optimizing effective high-temperature air furnaces and showed its usefulness in the future development of such devices.

## Acknowledgements

The study was financially supported by the National Centre for Research and Development within the framework of the project VoltAeris (Project No. POIR.04.01.04-00-014/17).

*Received 30 November 2023*

# References

[1] Kardaś D., Polesek-Karczewska S., Turzyński T., Wardach-Święcicka, Hercel P., Szymborski J., Heda Ł.: *Thermal performance enhancement of a red-hot air furnace for a micro-scale externally fired gas turbine system.* Energy **282**(2023), 128591.

[2] Cordiner S., Mulone S.: *Experimental-numerical analysis of a biomass fueled micro-generation power-plant based on microturbine.* Appl. Therm. Eng. **71**(2014), 905–912.

[3] Kobyłecki R., Zarzycki R., Bis Z., Panowski M., Wiński M.: *Numerical analysis of the combustion of straw and wood in a stoker boiler with vibrating grate.* Energy **222**(2021), 119948.

[4] Al-Attab K.A., Zainal Z.A.: *Externally fired gas turbine technology: a review.* Appl. Energ. **138**(2015), 474–487.

[5] Pantaleo A.M., Camporeale S.M., Shah N.: *Thermo-economic assessment of externally fired micro-gas turbine fired by natural gas and biomass: applications in Italy.* Energ. Convers. Manage. **75**(2013), 202–213.

[6] Bdour M., Al-Addous M., Michael Nelles M., Ortwein A.: *Determination of optimized parameters for the flexible operation of a biomass-fueled, microscale externally fired gas turbine (EFGT).* Energies **9**(2016), 856.

[7] Chai L., Tassou S.A.: *A review of airside heat transfer augmentation with vortex generators on heat transfer surface.* Energies **11**(2018), 2737.

[8] Rutkowski Ł., Szczygieł I.: *Calculation of the furnace exit gas temperature of stoker fired boilers.* Arch. Thermodyn. **42**(2021), 3, 3–24.

[9] Aziz A., Rehman S.: *Analysis of non-equidistant baffle spacing in a small shell and tube heat exchanger.* Arch. Thermodyn. **41**(2020), 2, 201–221.

[10] Hanuszkiewicz-Drapała M., Bury T., Widziewicz K.: *Analysis of radiative heat transfer impact in cross-flow tube and fin heat exchangers.* Arch. Thermodyn. **37**(2016), 1, 99–112.

[11] Kontogeorgos D.A., Keramida E.P., Founti M.A.: *Assessment of simplified thermal radiation models for engineering calculations in natural gas-fired furnace.* Int. J. Heat Mass Transf. **50**(2007), 5260–5268.

[12] Żukowski W., Migas P., Gwadera M., Larwa B., Kandafer S.: *A numerical analysis of heat transfer in a cross-current heat exchanger with controlled and newly designed air flows.* Open Chem. **16**(2018), 627–636.

[13] Thek G., Brunner T., Oberberger I.: *Externally with biomass and internally with natural gas fired micro gas-turbine-system, furnace and high temperature heat exchanger design as well as performance data from first test runs.* In: Proc. 18th Eur. Biomass Conf. Exhib., Lyon 2010, 1891–1899.

[14] Wajs J., Kura T., Mikielewicz D., Fornalik-Wajs E., Mikielewicz J.: *Numerical analysis of high temperature minichannel heat exchanger for recuperative microturbine system.* Energy **238**(2022), 121683.

[15] Kardaś D., Wardach-Święcicka I., Grajewski A.: *Partially transient one-dimensional thermal-flow model of a heat exchanger, upwind numerical solution method and experimental verification.* Arch. Thermodyn. **43**(2022), 4, 63–83.

[16] Schulte-Fischedick J., Dreißigacker V., Tamme R.: *An innovative ceramic high temperature plate-fin heat exchanger for efcc processes.* Appl. Therm. Eng. **27**(2007), 1285–1294.

[17] Baina F., Malmquist A., Alejo L., Palm B., Fransson T.H.: *Analysis of a high-temperature heat exchanger for an externally-fired micro gas turbine.* Appl. Therm. Eng. **75**(2015), 410–420.

[18] Al-Attab K.A., Zainal Z.A.: *Performance of high-temperature heat exchangers in biomass fuel powered externally fired gas turbine systems.* Renew. Energy **35**(2010), 913–920.

[19] Jolly A.J., O'Doherty T., Bates C.J.: *COHEX: A computer model for solving the thermal energy exchange in an ultra high temperature heat exchanger. Part A: Computational theory.* Appl. Therm. Eng. **18**(1998), 1263–1276.

[20] Orłowski P.: *Steam boilers – design and calculation.* WNT 1972, Warszawa (in Polish).

[21] Hobler T.: *Heat transfer and heat exchangerS.* WNT 1986, Warszawa (in Polish).

[22] Serth R.W., Lestina T.G.: *Process heat transfer. Principles, applications and rules of thumb* (2nd Edn.). Academic Press, 2014.

**archives**
**of thermodynamics**
Vol. **44**(2023), No. 4, 63–80
DOI: 10.24425/ather.2023.149718

# $CO_2$ capture from flue gases in a temperature swing moving bed

**SŁAWOMIR GRĄDZIEL**[a*]
**WIESŁAW ZIMA**[a]
**ARTUR CEBULA**[a]
**MONIKA RERAK**[a]
**EWA KAZAK-JAGIEŁA**[a]
**ADAM PAWŁOWSKI**[a]
**RICHARD BLOM**[b]
**LARS OLOF NORD**[c]
**VIDAR TORARIN SKJERVOLD**[c]
**GIORGIA MONDINO**[b]

[a] Cracow University of Technology, Faculty of Environmental Engineering and Energy, Warszawska 24, 31-155 Kraków, Poland

[b] SINTEF Industry, P.O. Box 124 Blindern, N0314 Oslo, Norway

[c] Norwegian University of Science and Technology, Department of Energy and Process Engineering, P.O. Box 8900, NO-7491 Trondheim, Norway

**Abstract** This paper presents a test stand for the capture of $CO_2$ from flue gases arising due to firing pulverised hard coal. The stand, financed from the 2014–2021 Norway Grants, is installed at a Polish power plant. The innovation of the proposed $CO_2$ capture method, developed by the Norwegian partner in the project (SINTEF Industry), lies in the use of activated carbon in the process of temperature swing adsorption in a moving bed. The paper also presents preliminary results of numerical simulations performed using the General PROcess Modelling System (gPROMS) software. The simulations concerned the operation of a supercritical power unit combined with a system for capturing $CO_2$ from flue gases. Transient operation of the system was analysed, assuming rapid changes in the power unit load. Special attention was paid to the $CO_2$ capture process energy consumption at an

*Corresponding Author. Email: slawomir.gradziel@pk.edu.pl

increase in load by 5% of the power unit nominal capacity in 30 s. It is found that the proposed $CO_2$ capture method "keeps up" with such rapid load changes at the method energy consumption smaller than 2 MJ/kg $CO_2$.

**Keywords:** Innovative $CO_2$ capture method; Activated carbon; Test stand; Numerical simulations; Energy consumption; Energy consumption of the method

# 1 Introduction

According to an International Energy Agency report, as much as 36.8 billion tons of $CO_2$ were produced in 2022, which is the highest amount ever [1]. Meanwhile, the Intergovernmental Panel on Climate Change predicts that if greenhouse gas emissions continue at the current rate, we are likely to reach a warming of 1.5°C in the years 2030–2052 [2]. In order to limit the warming to 1.5°C (as per the Paris Agreement), $CO_2$ emissions would have to fall by 45% by 2030 compared to 2010, and finally reach zero in 2050 [2]. The $CO_2$ capture and storage technologies have thus become some of the most promising solutions for combating climate change. Carbon capture technologies include three main methods, i.e. oxy-combustion, pre-combustion capture and post-combustion capture [3].

This paper is devoted to the last of the above-mentioned methods, which is most often realised using absorption, adsorption, cryogenic separation or membrane processes [4–6]. The main advantage of post-combustion capture methods is that they do not require extensive modifications to the power plant [7]. Moreover, the ease of regeneration of adsorbent materials is also important. Carbon dioxide removal from flue gases is considered the most advanced $CO_2$ separation technique among the available carbon capture and storage (CCS) technologies [8].

Three kinds of $CO_2$ adsorption are distinguished: pressure/vacuum swing adsorption (PSA/VSA), temperature swing adsorption (TSA) and electric swing adsorption (ESA). This paper puts forward the use of temperature swing adsorption based on the moving bed temperature swing adsorption (MBTSA) technology.

The operation of $CO_2$ adsorption in the TSA process is analysed in [9–12]. In these processes, the adsorbent is usually in the shape of balls or granules packed in a series of columns that are located cyclically, alternating between adsorption and regeneration stages. One of the main downsides of fixed bed processes is the requirement to ensure high flue gas flow rates and

the high pressure drop occurring in the packed bed. This can be overcome by using appropriate shapes of the adsorbent granules. Another important factor hindering the commercialisation of TSA systems for post-combustion $CO_2$ capture is that a large temperature change is often needed to achieve the required $CO_2$ purity and the process adequate efficiency [13, 14].

In [15], the TSA performance indices are shown in terms of $CO_2$ purity, $CO_2$ capture efficiency and energy consumption in the process. Respectively, they total 96.22%, 86.5% and 663.8 kWh per ton of captured $CO_2$ (2.39 MJ/kg $CO_2$). It should be mentioned that the testing was performed using the Mg-MOF-74 adsorbent.

The authors of [16] consider the use of the moving bed temperature swing adsorption (MBTSA) process for $CO_2$ capture as an alternative to commercial absorption-based technologies in the context of a natural gas combined cycle (NGCC) power plant. The power plant operation was simulated using the gPROMS software. Two cases with different regeneration temperatures were analysed. In both of them, the $CO_2$ capture purity was achieved in the range of 95.1%–95.8%, while the $CO_2$ capture efficiency was included in the range of 96.0%–98.2%.

In [17], simulations are performed of $CO_2$ capture from a waste treatment plant based on the MBTSA technology. The heat transfer coefficients of the heating section of an MBTSA demonstration unit using activated carbon balls were investigated. The obtained results were used as input data for the process simulation. The outcome was satisfactory: the $CO_2$ capture efficiency of about 90% and the $CO_2$ purity above 95%. However, the $CO_2$ capture energy consumption was rather high, totalling about 5.7 MJ/kg $CO_2$. The MBTSA technology offers the opportunity to internally recover part of the heat needed for the sorbent regeneration and thus reduce the demand for external energy [13, 18].

Many works focus on the development of general models of entire power plants and on the use of computer programs, both for steady-state and transient conditions [19, 20]. However, most of them fail to achieve the desired accuracy. Mesarovic [21] presented a case for the power plant emergency states using mass, momentum and energy balance equations.

Many works are also devoted to modelling the thermal and flow phenomena occurring in the boiler heating surfaces. A method for modelling the boiler evaporator dynamics is proposed in [22]. The proposed distributed parameter model, based on solving balance equations describing the principles of mass, momentum and energy conservation, enables an analysis of transient-state processes.

In the literature to date, much attention has been given to modelling transient operation of steam superheaters in large power boilers. The first mathematical models were very simple, with lumped thermal parameters [19, 20]. It should be noted that simple lumped parameter models are still used to simulate water heaters (economisers), boiler evaporators and steam superheaters/reheaters with a complex structure [23–25], mainly for the needs of automatic control systems in boilers.

A distributed parameter mathematical model of the steam superheater and the feed water heater is proposed in [26–29]. The model was built using mass, momentum and energy balance equations.

A mathematical model is developed in [30] to enable thermal and flow analysis of the phenomena occurring in the waterwalls of furnace chambers of supercritical boilers. The aim of the numerical calculations was to determine the temperature distributions of the medium and of the metal of the waterwall tubes. The model results were compared with the results obtained from computational fluid dynamics (CFD) testing.

The authors of [31] present a mathematical model of a natural circulation boiler which makes it possible to simulate the thermal and flow phenomena occurring in power boilers in conditions of rapid changes in thermal loads. The analysis of the results obtained from the proposed model shows very good agreement between the calculated and the measured values. The mathematical models presented in the paper can be used to develop comprehensive models of other boilers, including supercritical ones. In addition, they can prove helpful in the development of power unit simulators.

A mathematical model simulating the dynamics of a supercritical boiler is presented in [32]. Distributed parameter models of the boiler heating surfaces (the evaporator, steam superheaters and reheaters, the feed water heater, the selective catalytic reduction (SCR) reactor, the air heater) were developed. The performed numerical testing results allow the statement that the developed model is suitable for the simulation of rapid changes in the boiler thermal load.

Analysing the above literature, it can be seen that all the $CO_2$ capture models are simulated using computer programs, but there are no experimental tests carried out on real facilities operating in power plants.

This paper presents a test stand for the capture of $CO_2$ from flue gases arising due to firing pulverised hard coal. The test stand is installed at a Polish power plant on a natural circulation boiler.

The paper also presents a numerical simulation of the operation of a supercritical power unit combined with a system for capturing $CO_2$ from

flue gases. Transient operation of the system is analysed, assuming rapid changes in the power unit load. Special attention is paid to the energy consumption of the $CO_2$ capture process at a rise in the power unit load. The simulation is performed using the gPROMS software [33].

## 2 Test stand

A test stand for $CO_2$ capture from flue gases (based on MBTSA) was installed at a Polish power plant (at a subcritical boiler with a steam output of 210 Mg/h). The stand is shown schematically in Fig. 1a, with an example photo in Fig. 1b. It consists of three basic components: a reactor (adsorption section), a heating section (desorption section) and a cooling section. The reactor is made in the form of a polycarbonate column with the height of 1.5 m and the inner diameter of 0.5 m, filled with Mellapak structured packing [34] ensuring a uniform distribution of the sorbent flow.

The adsorbent is fed by a rotary-valve feeder into the reactor from above. Rotary-valve feeders are also installed downstream of the reactor, the heating section and the cooling section. The BKRV150 feeder is intended for collection and proportioning of bulk materials and materials with small-sized particles. The feeder consists of the following components: a gear-motor, the rotor assembly, a steel body (Fig. 2). The rotor is driven by a shaft passing through the side lids and supported by two bearing units. This feeder type is characterised by good tightness and infinitely variable adjustment of the amount of fed adsorbent. The basic data of the BKRV150 feeder are listed in Table 1.

Table 1: Basic data of the BKRV150 feeder type.

| | | |
|---|---|---|
| Output | kg/h | 1000 |
| Working temperature | °C | –20–+60 |
| Gear-motor power | kW | 0.18 |
| Output speed | 1/min | 13 |
| Weight | kg | 19 |
| Motor rotational speed | 1/min | 1385 |

Activated carbon was chosen as the adsorbent due to, among other things, high values of the heat transfer coefficient on its side, totalling 69–117 W/(m$^2$K) [17]. Activated carbon appears to perform satisfactorily

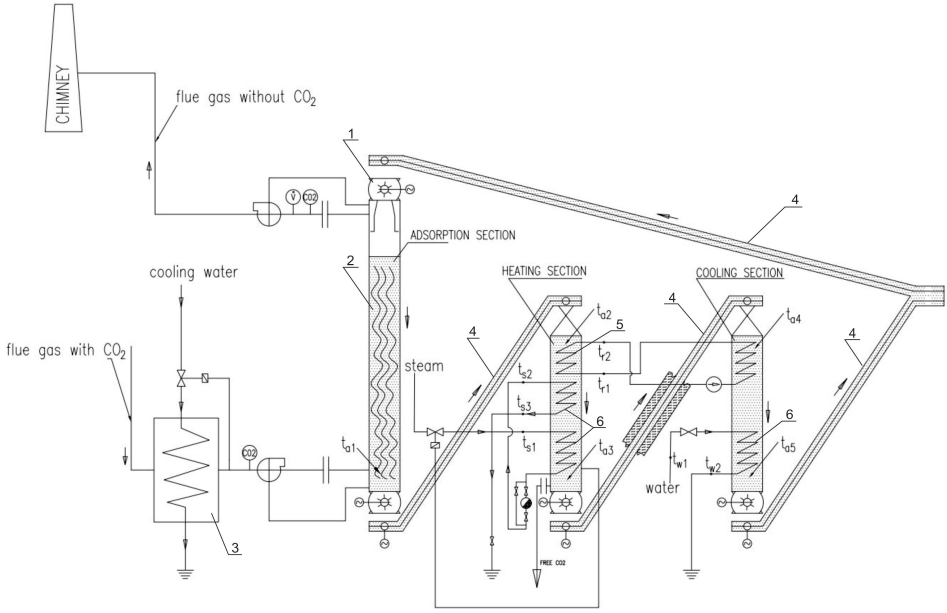


(a)

(b)

Figure 1: The test stand scheme (a) and photo (b): 1 – feeder, 2 – reactor, 3 – flue gas cooler, 4 – conveyor belts, 5 – heat exchanger intended for heat recovery, 6 – heat exchangers.

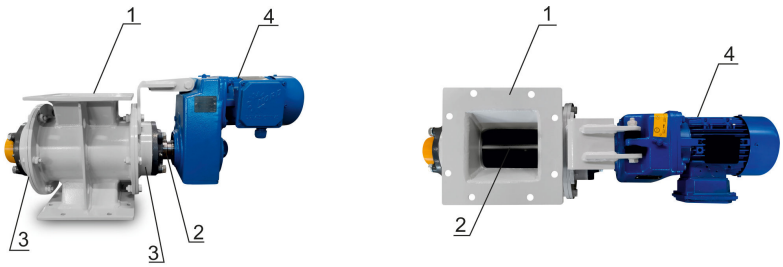


Figure 2: Diagram of the BKRV150 feeder: 1 – body, 2 – rotor assembly, 3 – side lids, 4 – gear-motor.

as an adsorbent also in the presence of water vapour, when regeneration takes place at temperatures of 150°C and higher [35]. Keeping the regeneration temperature possibly low is necessary to minimise the energy consumption of the method. The basic properties of activated carbon are listed in Table 2.

Table 2: Activated carbon basic parameters [36].

| | | |
|---|---|---|
| Mean size of particles | mm | $\sim 0.7$ |
| Coal dust content | ppm | $> 600$ |
| Specific heat | J/(kgK) | 880 |
| Specific surface | $m^2/g$ | 1100–1300 |
| Bulk density | g/ml | $\sim 0.6$ |

After passing through the adsorption section, activated carbon is supplied to the rotary-valve feeder driven by a gear-motor connected to the power supply using a frequency converter (inverter). In this way, by adjusting the motor rotational speed, it is possible to control the amount of the fed activated carbon.

The feeder carries the sorbent to a belt conveyor which transports activated carbon to the heating section. Such conveyors are also used between individual sections. Due to internal heat recovery, the heating section and the cooling section are thermally insulated. Basic information on the conveyors used on the stand is given in Table 3.

The heating section consists of a series of (shell-and-tube) heat exchangers in which the sorbent is heated indirectly by steam drawn from the turbine bleed. For the adsorbent regeneration, the temperature of the bed in the heating section should be between 180°C and 200°C.

Table 3: Basic data of the BKBC400L belt conveyor.

| | | |
|---|---|---|
| Output | kg/h | 1000 |
| Total length | mm | 6100–6650 |
| Lift height | mm | 4400–4800 |
| Lift angle | deg | 64–67 |
| Belt width | mm | 400 |
| Total weight | kg | 1165–1310 |
| Belt speed | m/s | 0.8 |

The adsorbent temperature is measured using five thermocouples placed at different locations in the reactor, in the heating and cooling sections ($t_{a1}$–$t_{a5}$ in Fig. 1). In addition, three thermocouples to measure the steam temperature at the inlet and outlet of the heat exchangers ($t_{s1}$–$t_{s3}$ in Fig. 1), two thermocouples at the inlet and outlet of the heat exchanger cooling the sorbent in the cooling section ($t_{w1}$ and $t_{w2}$ in Fig. 1) and two thermocouples at the inlet and outlet of the heat exchanger intended for heat recovery ($t_{r1}$ and $t_{r2}$ in Fig. 1) are installed. The mass flow rates of water and steam in the cooling section and in the heating section are also measured.

The cooling section is similar to the heating section. Municipal water is used as the cooling agent. Having passed the cooling section, the sorbent is transported by belt conveyors to the upper feeder located above the reactor.

The flue gases collected from the boiler and containing $CO_2$ flow through a heat exchanger where they are cooled to the temperature of about 30°C and then directed to the reactor lower part. The content of $CO_2$ in flue gases is measured at the reactor inlet and outlet by the Vaisala CARBOCAP GMP251 carbon dioxide probe. The probe is based on the patented second-generation CARBO-CAP technology and enables full temperature compensation of the measurement results, according to the temperature of the surroundings. The probe basic characteristic data are listed in Table 4.

All measurements collected from the stand are recorded using a data acquisition system, stored on a computer and visualised in a SCADA system. A diagram of the test stand is shown in Fig. 3.

The test stand was designed and the sorbent characteristics were selected so that the MBTSA process should meet the requirements for the $CO_2$ purity level of at least 95% and a capture rate higher than 90%. These are the parameters typically required for CCS applications [37, 38].

Table 4: Characteristic data of the Vaisala CARBOCAP GMP251 probe.

| | | |
|---|---|---|
| Measurement range | % $CO_2$ | 5–10 |
| Operating temperature | °C | –40–+60 |
| Calibration uncertainty | % | ±0.05% $CO_2$ (at 5% $CO_2$) |
| | | ±0.19% $CO_2$ (at 20% $CO_2$) |
| Accuracy (at 25°C, 1013 hPa) | % | ±0.2% $CO_2$ (at 0–8% $CO_2$) |
| | | ±0.4% $CO_2$ (at 8–20% $CO_2$) |

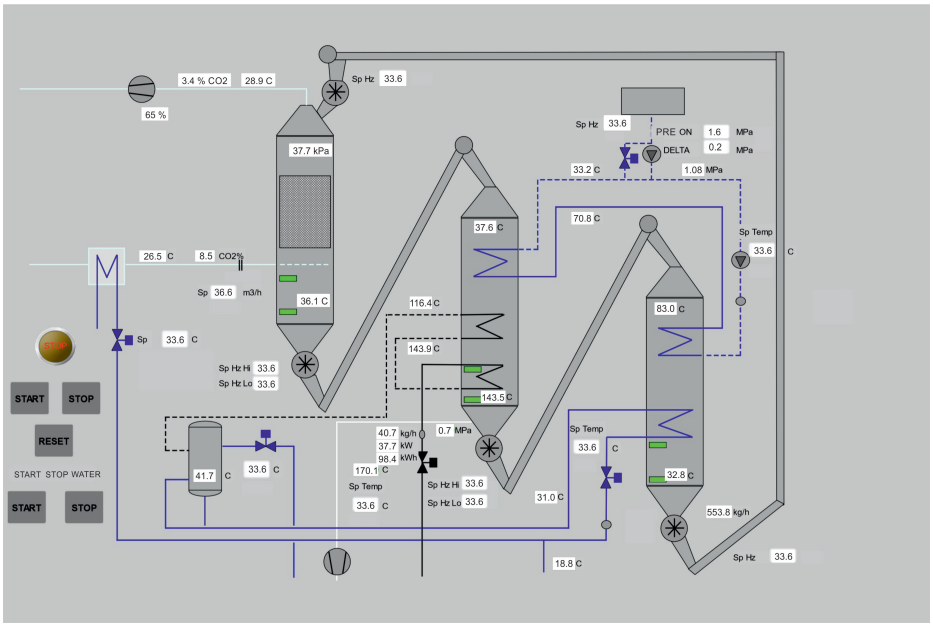


Figure 3: Visualisation of the test stand with preliminary measurement results.

## 3 Selected simulation results

A simulation was performed of the process of $CO_2$ capture from flue gases arising due to firing pulverised hard coal in a supercritical boiler (CCS-ready power unit) operating in a power plant in Poland. The simulation was carried out using the gPROMS software [33], which makes it possible to model both the boiler system and the $CO_2$ capture process.

The basic part of the designed dynamic computational model of $CO_2$ capture from flue gases is the model of the boiler section (Fig. 4).

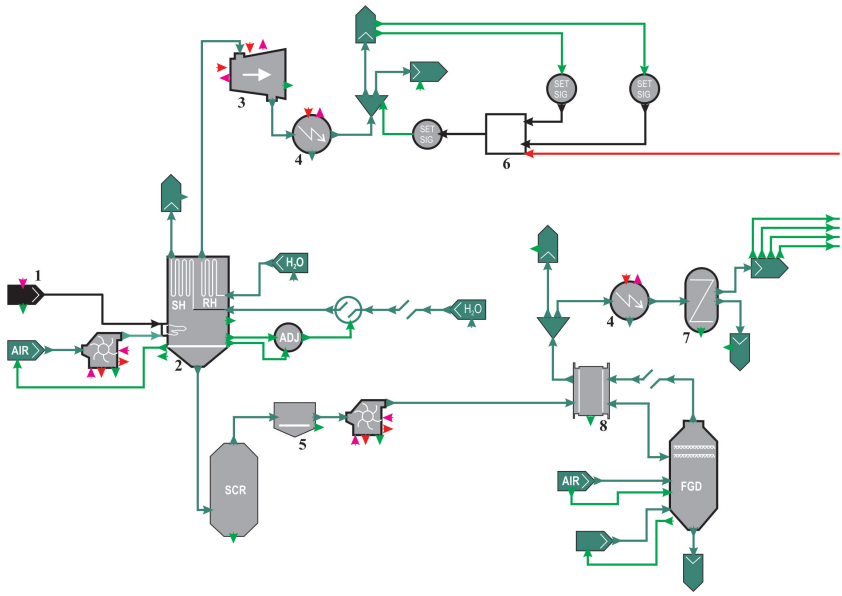


Figure 4: Boiler section of the computational model of $CO_2$ capture from flue gases created in the gPROMS Process environment: 1 – coal supply, 2 – pulverised coal boiler, 3 – turbine, 4 – cooler, 5 – electrostatic precipitator, 6 – calculation block, 7 – component splitter, 8 – gas-gas heater, SH – superheater, RH – reheater, SCR – selective catalytic reduction, GET SIG – change of signal type, SET SIG – change of signal type, FGD – flue gas desulphurisation, ADJ – adjust.

This is the part where flue gases are produced. Depending on the boiler load, the molar content of individual chemical compounds and elements, including $CO_2$, changes. Carbon dioxide is then captured in the next section. The designed model takes detailed account of the fuel feeding method, the fuel composition, the air heating and supply to the boiler, the boiler operating parameters and the flue gas purification system before flue gases are entered into the $CO_2$ capture section. The steam and the boiler feed water circulation systems were designed using some simplifications. The next stage was to introduce a "block" calculating the amount of steam that should be drawn from the turbine bleed to the $CO_2$ capture section to regenerate the adsorber in the heating (regeneration) column. The steam mass flow is calculated in the block called "Calc_steam_flow", which was additionally created in the program to meet the project needs. The block is fed on-line with the steam enthalpy and pressure values, as well as the demand for heat from the $CO_2$ capture station (red line in Fig. 4).

The $CO_2$ capture section was also created using the gPROMS software, not in the "Process" environment, however, but in "ModelBuilder" due to the chemical capabilities of this part of the program (Fig. 5). Using the available tools, a model was made of the system removing carbon dioxide from flue gases. The diagram shows the flue gases flowing through the system (turquoise line), while the flue gases still to enter the capture section are marked with a black line. The purple colour indicates the closed loop of the adsorbent purifying the flue gases. The grey lines mark the information transfer between the system various components and PID (proportional–integral–derivative) controllers. The transfer of information on the heat demand for the adsorbent regeneration from the heating column to the model calculating the demand for steam from the turbine bleed is marked in red.

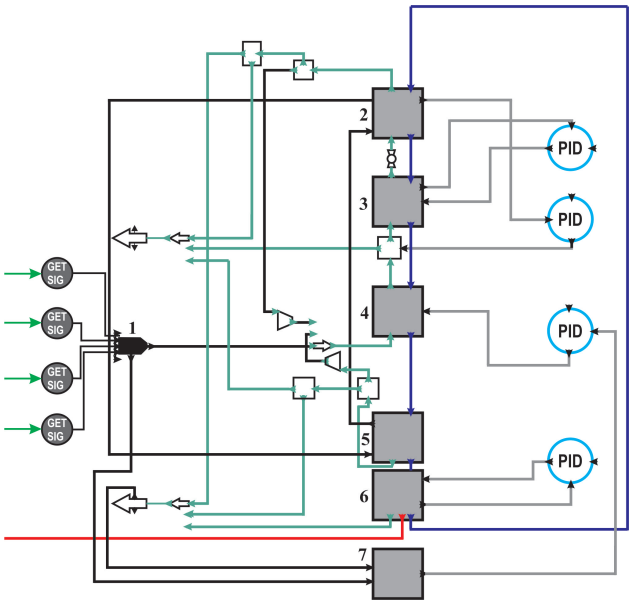


Figure 5: Diagram of the MBTSA stand created in the gPROMS ModelBuilder environment: 1 – flue gas feed, 2 – precooling section, 3 – cooling section, 4 – adsorption section, 5 – preheating section, 6 – desorption section, 7 – signal ratio, PID – proportional-integral-derivative controller, GET SIG – change of signal type.

In the central part of the model there is a block that represents the reactor column of the real system (Point 3, Fig. 5). The injected flue gases come into contact with the adsorbent, giving up a significant amount of $CO_2$ and a small amount of $N_2$ (the ratio between these two quantities determines the

capture purity). Below the column, two more blocks can be seen (Points 5 and 6, Fig. 5). Together they form a heating column consisting of a part for the sorbent preheating and a desorption (regeneration) part. In this part, the turbine bleed steam is used to preheat the adsorbent to a temperature of about 180°C, at which the bed is regenerated. On the adsorbent further path, a cooling column was also modelled. It consists of precooling and proper cooling parts (Fig. 5, Point 2 and Point 3, respectively). Owing to the water circulating in the heat exchangers, the adsorbent temperature drops to 30°C. In this temperature the adsorbent demonstrates sufficient purity of the $CO_2$ captured from flue gases.

Performing a dynamic simulation in the gPROMS program after the two sections are combined makes it possible to analyse the results accurately. The results of the simulation calculations can be checked for all necessary parameters in each component of the system.

The following parameters of the boiler were adopted for the simulation: the boiler nominal thermal power – 1838 MW (the power unit gross capacity: 910 MW), which corresponds to the live steam mass flow of $2368 \times 10^3$ kg/h (at the steam pressure of 28.5 MPa and temperature of 603°C).

The boiler transient operation was analysed, assuming changes in the boiler load at the rate of 5% of the nominal load in 30 s (Fig. 6).

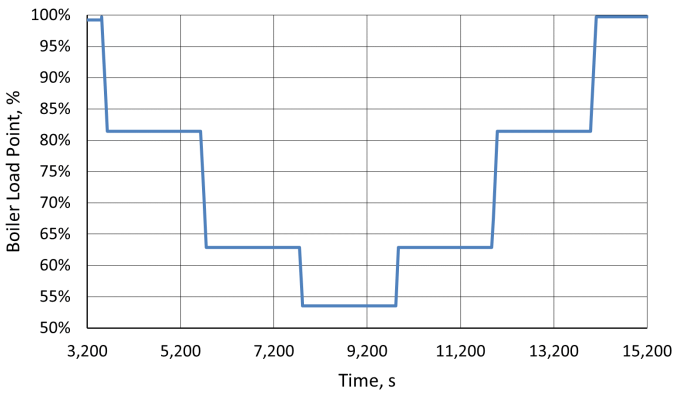


Figure 6: Changes in the power boiler load.

The calculated history of changes in the flue gas mass flow at the reactor inlet is shown in Fig. 7, whereas Fig. 8 illustrates changes in the $CO_2$ molar concentration in flue gases. These histories were treated as input data for the $CO_2$ capture section (MBTSA) in the gPROMS ModelBuilder program.

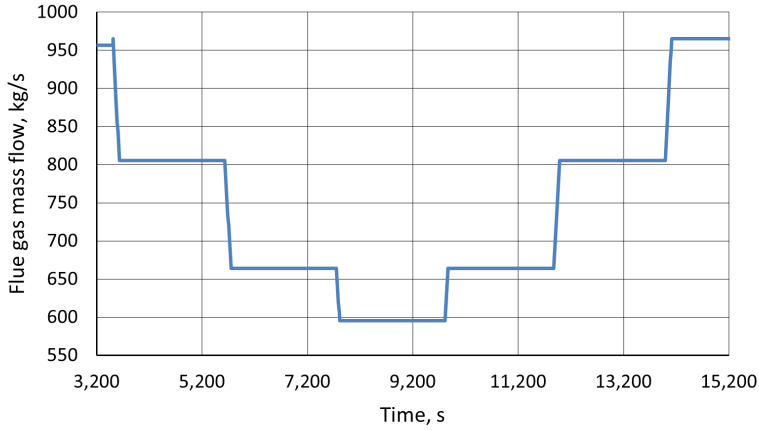


Figure 7: History of changes in the flue gas mass flow.

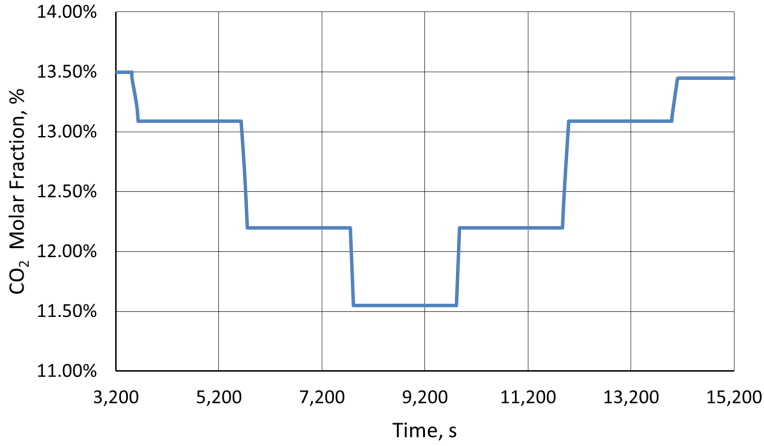


Figure 8: History of changes in the $CO_2$ molar concentration.

In order to calculate the steam demand for the heating section, the steam parameters available from the turbine bleed were analysed, assuming 100% load of the power unit. Figure 9 shows the history of changes in the demand for heating power for the heating section, whereas Fig. 10 illustrates the changes in the steam mass flow needed to heat the adsorbent. In the case of the analysed bleed, the heating power demand totals $\sim$ 265 MW. This results from the need to heat approx. 2700 kg/s of the adsorbent from the temperature of about 30°C to the temperature of about 180°C.

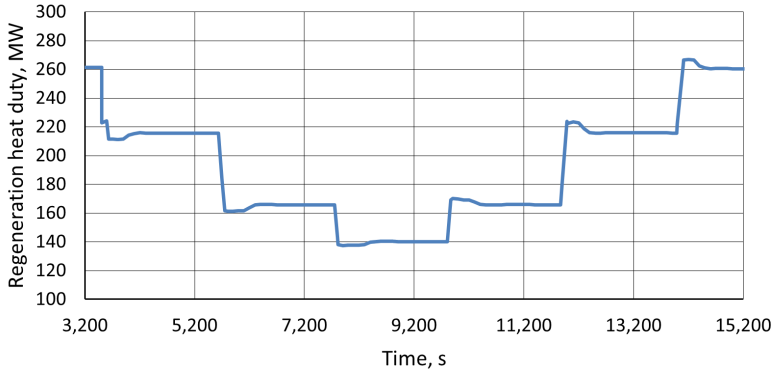


Figure 9: Heating section demand for heating power.

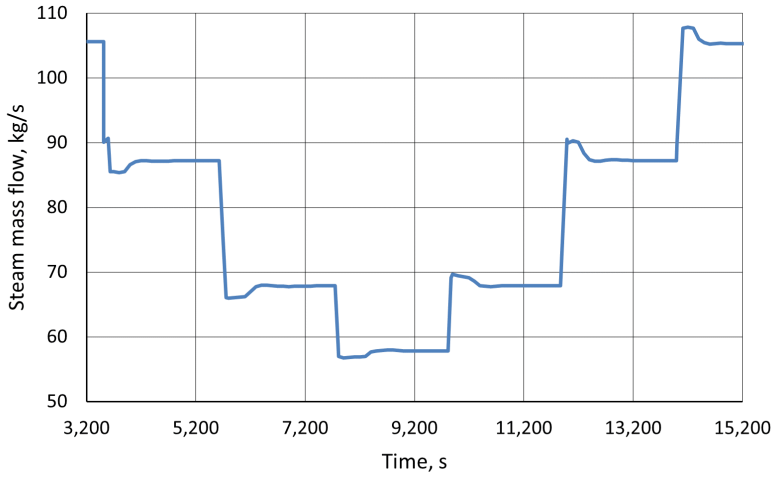


Figure 10: Heating section demand for the steam mass flow.

Figure 11 presents the history of the calculated demand for energy needed to capture 1 kilogram of $CO_2$ (the method energy consumption). From this figure it can be seen that the method energy consumption varies between $\sim 1.4$ MJ/(kg $CO_2$) and $\sim 1.7$ MJ/(kg $CO_2$), which is very promising compared to the energy consumption of other methods of $CO_2$ capture [39]. The figure also shows the time needed for the $CO_2$ capture section stabilisation (after a change in the boiler load).

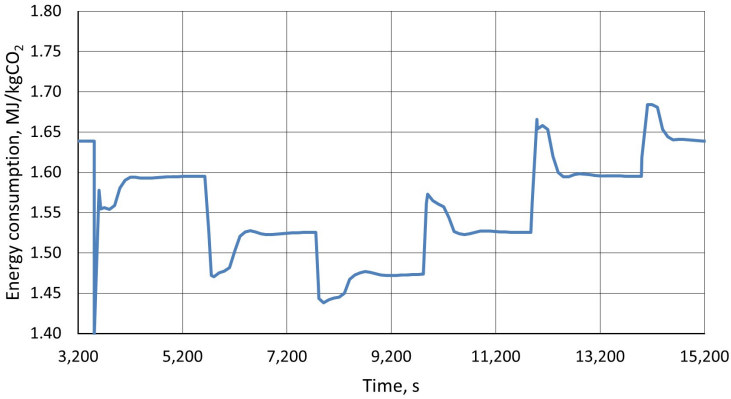


Figure 11: Energy consumption of the method.

# 4 Summary and conclusions

The paper presents a stand intended for $CO_2$ capture from flue gases based on the moving bed temperature swing adsorption (MBTSA) process using activated carbon as the adsorber. The stand, built in a Polish power plant, is a research station which enables $CO_2$ adsorption only from a part of the flue gases produced in the boiler. The main advantages of the MBTSA method are low pressure drops in the adsorption zone and the possibility of a faster rate of the adsorbent heating compared to standard adsorption technologies.

In order to estimate the method energy consumption, simulation calculations were performed of the $CO_2$ capture from flue gases arising due to firing pulverised hard coal in a supercritical boiler (the boiler is a part of a CCS-ready power unit). The simulations were carried out using the gPROMS software, which makes it possible to combine the boiler section with the $CO_2$ capture section. The simulation results indicate that the proposed method is characterised by lower energy consumption (about 1.7 MJ/kg $CO_2$) compared to other methods described in the literature.

## Acknowledgements

The research leading to the presented results was financed from the 2014-2021 Norway Grants via the National Centre for Research and Development (Grant NOR/POLNORCCS/0015/2019-00).

*Received 20 December 2023*

# References

[1] International Energy Agency: *Global Energy Review: $CO_2$ Emissions in 2022*. https://www.iea.org/t&c/ (accessed: 26 June 2023).

[2] Intergovernmental Panel on Climate Change (IPCC): *Global Warming of 1.5° C*. Cambridge Univ. Press, 2022. doi: 10.1017/9781009157940.001

[3] Jiang L., Wang R.Q., Gonzalez-Diaz A., Smallbone A., Lamidi R.O., Roskilly A.P.: *Comparative analysis on temperature swing adsorption cycle for carbon capture by using internal heat/mass recovery*. Appl. Therm. Eng. **169**(2020), 114973.

[4] Mondal M.K., Balsora H.K., Varshney P.: *Progress and trends in $CO_2$ capture/separation technologies: a review*. Energy **46**(2012), 431–441.

[5] Zhao R., Deng S., Liu Y., Zhao Q., He J., Zhao L.: *Carbon pump: Fundamental theory and applications*. Energy **119**(2017), 1131–1143.

[6] Olegovich V., Kindra V.O., Milukov I.A., Shevchenko I.V., Shabalova S.I., Kovalev D.S.: *Thermodynamic analysis of cycle arrangements of the coal-fired thermal power plants with carbon capture*. Arch. Thermodyn. **42**(2021), 4, 103–121. doi: 10.24425/ather.2021.139653

[7] Lian Y., Deng S., Li S., Guo Z., Zhao L., Yuan X.: *Numerical analysis on $CO_2$ capture process of temperature swing adsorption (TSA): Optimization of reactor geometry*. Int. J. Greenh. Gas Control **85**(2019), 187–198.

[8] Niegodajew P., Asendrych D., Drobniak S.: *Numerical analysis of $CO_2$ capture efficiency in post-combustion CCS technology in terms of varying flow conditions*. Arch. Thermodyn. **34**(2013), 4, 123–136. doi: 10.2478/aoter-2013-0033

[9] Akhtar F., Andersson L., Ogunwumi S., Hedin N., Bergström L.: *Structuring adsorbents and catalysts by processing of porous powders*. J. Eur. Ceram. Soc. **34**(2014), 7, 1643–1666.

[10] Farmahini A.H., Krishnamurthy S., Friedrich D., Brandani S., Sarkisov L.: *Performance-based screening of porous materials for carbon capture*. Chem. Rev. **121**(2021), 17, 10666–10741.

[11] Masala A., Vitillo J.G., Mondino G., Martra G., Blom R., Grande C.A., Bordiga S.: *Conductive ZSM-5-based adsorbent for $CO_2$ capture: active phase vs monolith*. Ind. Eng. Chem. Res. **56**(2017), 30, 8485–8498.

[12] Rezaei F., Webley P.: *Structured adsorbents in gas separation processes*. Sep. Purif. Technol. **70**(2010), 3, 243–256.

[13] Morales-Ospino R., Santos V.N., Lima Jr A.R.A., Torres A.E.B., Vilarrasa-García E., Bastos-Neto M., Cavalcante Jr C.L., Azevedo D.C.S., Marques C.R.M., de Aquino T.F., Vasconcelos L.B., Knaebel K.S.: *Parametric analysis of a moving bed temperature swing adsorption (MBTSA) process for post-combustion $CO_2$ capture*. Ind. Eng. Chem. Res. **60**(2021), 29, 10736–10752. 10.1021/acs.iecr.0c05067

[14] Zanco S.E., Mazzotti M., Gazzani M., Romano M.C., Martínez I.: *Modelling of circulating fluidized beds systems for post-combustion $CO_2$ capture via temperature swing adsorption*. AlChE J. **64**(2018), 5, 1744–1759.

[15] Ben-Mansour R., Qasem N.A.A.: *An efficient temperature swing adsorption (TSA) process for separating $CO_2$ from $CO_2/N_2$ mixture using Mg-MOF-74*. Energy Conv. Manag. **156**(2018), 10–24.

[16] Mondino G., Grande C.A., Blom R., Nord L.O.: *Moving bed temperature swing adsorption for $CO_2$ capture from a natural gas combined cycle power plant*. Int. J. Greenh. Gas Control **85**(2019), 58–70.

[17] Mondino G., Grande C.A., Blom R., Nord L.O.: *Evaluation of MBTSA technology for $CO_2$ capture from waste-to-energy plants*. Int. J. Greenh. Gas Control **118**(2022), 103685.

[18] Kim, K., Son, Y., Lee, W.B., Lee, K.S.: *Moving bed adsorption process with internal heat integration for carbon dioxide capture*. Int. J. Greenh. Gas Control **17**(2013), 13–24.

[19] Åström K.J., Eklund K.: *A simplified non-linear model of a drum boiler-turbine unit*. Int. J. Control **16**(1972), 1, 145–169.

[20] Chien K.L., Ergin E.I., Ling C., Lee A., Calif A.: *Dynamic analysis of a boiler*. ASME Trans. **80**(1958), 1809–1819.

[21] Mesarovic M.M.: *A mathematical simulation method for the evaluation of operational and accidental transients in thermal power systems. Mathematical modelling and computer simulation of processes in energy systems*. Proc. Int. Ctr Heat Mass Transf. Hemisphere, 1990.

[22] Grądziel S.: *Analysis of thermal and flow phenomena in natural circulation boiler evaporator*. Energy **172**(2019), 881–891.

[23] Chaibakhsh A., Ghaffari A., Moosavian S.A.A.: *A simulated model for a once-through boiler by parameter adjustment based on genetic algorithms*. Simul. Model. Pract. Theory **15**(2007), 1029–1051.

[24] Li H., Huang X., Zhang L.: *A lumped parameter dynamic model of the helical coiled once-through steam generator with movable boundaries*. Nucl. Eng. Des. **238**(2008), 1657–1663.

[25] Li X.: *Dynamic behaviour of superheated steam and ways of control, Front*. Energy Power Eng. China **22**(2008), 1, 25–30.

[26] Zima W.: *Simulation of dynamics of a boiler steam superheater with an attemperator*. Proc. Inst. Mech. Eng. A: J. Power Energy **220**(2006), 793–801. doi: 10.1243/09576509JPE268

[27] Zima W.: *Mathematical modelling of transient processes in convective heated surfaces of boilers*. Forschung im Ingenieurwesen **71**(2007), 113–123.

[28] Zima W.: *Modelling of the dynamics of the convective heating surfaces of boilers*. Arch. Thermodyn. **20**(1999), 1-2, 71–92.

[29] Zima W.: *Numerical modelling of dynamics of steam superheaters*. Energy, **26**(2001), 1175–1184.

[30] Zima W., Grądziel S., Cebula A.: *Modelling of heat and flow phenomena occurring in waterwall tubes of boiler for supercritical steam parameters*. Arch. Thermodyn. **31**(2010), 3, 19–36. doi: 10.2478/v10173-010-0012-y

[31] Zima W., Grądziel S., Cebula A., Rerak M., Kozak-Jagieła E., Pilarczyk M.: *Mathematical model of a power boiler operation under rapid thermal load changes*. Energy **263**(2023). doi: 10.1016/j.energy.2022.125836

[32] Taler J., Zima W., Ocłoń P., Grądziel S., Taler D., Cebula A., Jaremkiewicz M., Korzeń A., Cisek P., Kaczmarski K., Majewski K.: *Mathematical model of a supercritical power boiler for simulating rapid changes in boiler thermal loading*, Energy **175**(2019), 580–592.

[33] gPROMS Model Builder Version 6.0. Process System Enterprise (PSE). UK 2019.

[34] Mellapack 500Y, Sulzer, Switzerland. https://www.sulzer.com/-/media/files/products/separation-technology/distillation-and-absorption/brochures/structured_packings.pdf (accessed 26 June 2023).

[35] Mondino G., Grande C.A., Blom R.: *Effect of gas recycling on the performance of a moving bed temperature-swing (MBTSA) process for $CO_2$ capture in a coal fired power plant context*. Energies **10**(2017), 745. doi: 10.3390/en10060745

[36] https://kureha.de/bac-activated-carbon/ (accessed 26 June 2023).

[37] Joss L., Gazzani M., Mazzotti M.: *Rational design of temperature swing adsorption cycles for post-combustion $CO_2$ capture*. Chem. Eng. Sci. **158**(2017), 381–394.

[38] Nord L.O., Bolland O.: *Carbon Dioxide Emission Management in Power Generation*. Wiley, 2020.

[39] Feron P.H.M., Cousins A., Jiang K., Zhai R., Garcia M.: *An update of the benchmark post-combustion $CO_2$ capture technology*. Fuel **273**(2020), 117776.

**archives**
**of thermodynamics**
Vol. **44**(2023), No. 4, 81–102
DOI: 10.24425/ather.2023.149719

# Numerical and experimental analysis of thermal and flow operating conditions of waterwall tubes connected by fins

**MAREK MAJDAK***
**SŁAWOMIR GRĄDZIEL**
**WIESŁAW ZIMA**
**ARTUR CEBULA**
**MONIKA RERAK**
**EWA KOZAK-JAGIEŁA**

Cracow University of Technology, Faculty of Environmental Engineering and Energy, Warszawska 24, 31-155 Kraków, Poland

**Abstract** This paper presents a method for determining the temperature distribution in the cross-section of waterwall tubes connected by fins using an in-house numerical algorithm prepared in the MATLAB environment, based on differential equations with separable variables. In order to verify the correctness of the algorithm operation, the temperature values obtained from it, determined for the frontal area of the tubes, are compared with the temperatures found in the Ansys Fluent environment and those measured on the test stand. A system corresponding to a fragment of the combustion chamber wall of a supercritical steam boiler was selected to perform the analysis. The system consists of three tubes connected by fins. The temperature distributions in the cross-sections of the tubes were compared for the case when each of the tubes was heated on one side with the same heat flux and when the heat flux falling on the central tube was by 50% higher than the heat flux incident on the neighbouring tubes. Experimental verification was carried out on a stand equipped with three vertical tubes connected by fins, heated on one side by infrared radiators.

**Keywords:** Heat transfer; Supercritical boiler; Waterwall tube

*Corresponding Author. Email: marek.majdak@pk.edu.pl

# 1 Introduction

The occurrence of thermal stresses exceeding allowable values is one of the most serious problems encountered in power boilers. In subcritical steam boilers, the temperature of the medium flowing in the tubes reaches values corresponding to the steam saturation state (Fig. 1).

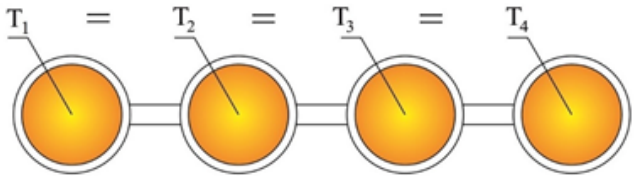


Figure 1: Temperature of the medium in waterwall tubes of subcritical steam boilers.

In supercritical steam boilers, on the other hand, the medium temperature can vary considerably in individual tubes (Fig. 2). This creates additional thermal stresses on the width of the combustion chamber wall. Therefore, it is necessary to monitor the condition of individual fragments of the waterwalls, since exceeding the allowable value of thermal stresses can lead to damage to the waterwall tubes and the fins connecting them, which necessitates the boiler repairs.

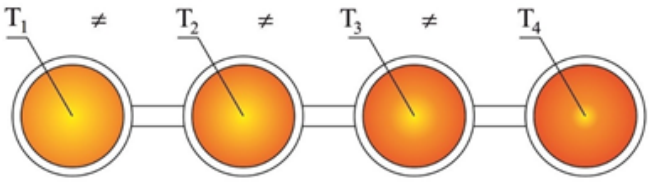


Figure 2: Temperature of the medium in waterwall tubes of supercritical steam boilers.

The literature offers numerous simplified studies taking account of averaged parameters of the medium flowing through the tubes [1], average parameters of the walls of waterwall tubes or a uniform distribution of the thermal load. Many publications analyse the issue of the heat transfer inside waterwall tubes – either by determining more precise relations that make it possible to determine the value of the heat transfer coefficient [2–4], or based on a series of experimental tests [5]. Another method of determination of temperature distribution in thick-walled element of steam pipeline based on inverse heat conduction was presented in [6]. Cases are considered where the occurrence

of the boiling crisis [7] during two-phase flows and the problems arising therefrom, with a correct description of the convective heat transfer, are taken into account; they also cover problems related to the operation of boilers at reduced thermal loads [8, 9]. Issues related to the operation of combined-cycle power plants, such as steam-gas plants, are also considered. The authors of [10] investigate the effect of individual operating parameters on the efficiency of the system, determining the conditions under which the system can achieve the highest efficiency values.

Authors of [11] presented the mathematical model for analysis of the distribution of fluid enthalpy and waterwall temperature in supercritical boiler. Proposed method is based on calculations in which were used thermophysical parameters of fluid and parameters of material of waterwall tubes computed in real-time. Moreover, many publications point to the variation in the heat flux along the combustion chamber wall width occurring in supercritical boilers. Analyses of the temperature distribution conducted for waterwalls at uniform and non-uniform heating of neighbouring tubes are presented in [12, 13]. The authors of [3, 14] discuss the heat transfer occurring in spiral waterwall tubes installed in ultra-supercritical boilers.

An analysis of the thermal conditions of a stoker boiler is presented in [15]. The authors analysed the hydrodynamic conditions occurring in the boiler combustion chamber during biomass combustion using a vibrating grate that makes it possible to change the air flow supplied from the bottom of the combustion chamber. They also investigated the effect of the distribution of the fuel mass flow and secondary air on the boiler operating parameters.

In [16], a simulation was carried out of the boiler operation under conditions of increased production of thermal energy. Cases were analysed in which the increased amount of bleed steam was directed to the heat exchanger, and the use of solutions based on an absorption heat pump, i.e. waste heat utilization, was investigated. The impact of each solution on the parameters of the boiler working medium and on the operating parameters was presented, and an economic analysis was performed of the profitability of the implementation of the solutions.

The problem of determining the technical condition of steam power plants and turbines was discussed in [17]. A method based on the Monte-Carlo simulation was proposed to analyse the results of investigations of damage to power plant components. The method takes account of the course of technological processes, their duration, as well as the failure rate and the metal remnant life. The presented model can be used to create

predictive models, making it possible to extend the life of the components of power plants.

This paper presents the results obtained using an in-house numerical algorithm, created in the MATLAB environment [18] based on differential equations with separable variables. In order to verify the proposed model, the numerical calculation results were compared with the results obtained from the CFD (computational fluid dynamics) model created in the Ansys Fluent environment [19]. The results from the numerical algorithm were then compared with the measured data collected on a test stand intended for the simulation of the conditions occurring in waterwall tubes of subcritical boilers. Such experimental analyses, performed for a few tubes connected by fins, have not been discussed in the literature yet. This is also the first time that verification has been presented of the temperature distribution established using an in-house numerical algorithm by means of two methods: by comparing the obtained results with the CFD model results and with the temperatures determined on the dedicated test stand.

## 2 Proposed numerical algorithm

The temperature distribution in the analysed fragment of the waterwall was determined by solving mass, momentum and energy conservation equations according to the methodology described in [20]. The flowing medium analysis was performed for a control volume determined inside a single tube with a constant cross-section, as presented in Fig. 3 [21]:

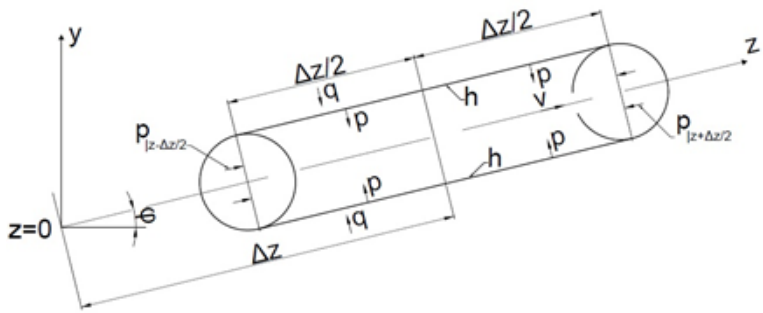


Figure 3: Analysed control volume: $h$ – heat transfer coefficient, $\varphi$ – tube inclination angle, $p$ – pressure, $q$ – heat flux, $\Delta z$ – analysed control volume length in the fluid flow direction.

## 2.1 Initial balance equations for the medium

The mass balance equation for the control volume presented in Fig. 3 has the following form:

$$\frac{\partial(\Delta V\rho)}{\partial\tau} = (A\rho v)\Big|_{z-\frac{\Delta z}{2}} - (A\rho v)\Big|_{z+\frac{\Delta z}{2}}, \tag{1}$$

where: $V$ – volume, m$^3$; $\varphi$ – tube inclination angle, deg; $\rho$ – fluid density, m$^3$/kg; $\tau$ – time, s; $A$ – surface area, m$^2$; $v$ – fluid velocity, m/s; $\Delta z$ – analysed control volume length in the fluid flow direction, m.

Considering a constant cross-section of the analysed tube and assuming that the fluid density in the entire volume is equal to the fluid density at the control volume centre, and assuming further that the control volume is infinitely small, Eq. (1) can be expressed as

$$\frac{\partial\rho}{\partial\tau} = -\frac{\partial(\rho v)}{\partial z}, \tag{2}$$

or

$$\frac{\partial\rho}{\partial\tau} = -\frac{1}{A}\frac{\partial\dot{m}}{\partial z}, \tag{3}$$

where: $\dot{m}$ – fluid mass flow rate, kg/s.

The fluid mass flow rate is defined by the following relation:

$$\dot{m} = Av\rho. \tag{4}$$

The next balance equation is the momentum conservation equation, which has to take account of the rate of changes in the momentum accumulated in the control volume, the momentum fluxes flowing into and out of the control volume, and all the forces acting on the control volume. The following forces have to be taken into consideration: the forces exerted by the fluid on the tube wall, the forces opposite to vectors normal to the inlet and the outlet cross-section of the analysed control volume and the friction force between the fluid and the tube wall. The momentum conservation equation for the control volume under analysis can be written as

$$\begin{aligned}\frac{\partial}{\partial\tau}(Av\rho\Delta z) = {} & (\dot{m}v)|_{z-\frac{\Delta z}{2}} - (\dot{m}v)|_{z+\frac{\Delta z}{2}} + A\left(p|_{z-\frac{\Delta z}{2}} - p|_{z+\frac{\Delta z}{2}}\right) \\ & - \sigma_\tau U\Delta z - \rho g\Delta V\sin\varphi,\end{aligned} \tag{5}$$

where: $g$ – gravitational acceleration, m/s$^2$; $p$ – pressure, Pa; $U$ – tube perimeter, m; $\sigma_\tau$ – tangential stresses, N/m$^2$.

Considering that the control volume length is infinitely small and determining the pressure related to the friction force and the fluid velocity, Eq. (5) can be rearranged to

$$\frac{\partial \dot{m}}{\partial \tau} = -\frac{1}{A}\frac{\partial}{\partial z}\left(\frac{\dot{m}^2}{\rho}\right) - A\left(\frac{\partial p}{\partial z} + \frac{\partial p_\tau}{\partial z} + \rho g \sin\varphi\right), \tag{6}$$

where: $p_\tau$ – pressure related to the friction force, Pa.

The internal energy balance of the fluid, related to a unit of its mass, must take account of kinetic energy, both potential and internal. It can be expressed using formula

$$e = \frac{v^2}{2} + gz\sin\varphi + u\,, \tag{7}$$

where: $e$ – energy per mass, J/kg; $u$ – unit internal energy, J/kg.

In order to simplify the formula for the purposes of the case under analysis, it is assumed that the work done by volume and surface forces is negligibly small. The relations describing individual forms of energy are presented in detail in [22]. After appropriate simplifications and rearrangements, Eq. (7) can be written in the form of a differential equation with separable variables, i.e.:

$$\frac{\partial i}{\partial \tau} = \left(1 - \frac{1}{\rho}\frac{\partial p}{\partial i}\right)^{-1}\left[\frac{\dot{m}}{A\rho}\left(\frac{1}{\rho}\frac{\partial p}{\partial z} - \frac{\partial i}{\partial z} + \frac{1}{\rho}\frac{\partial p_\tau}{\partial z}\right) + \frac{4h(\theta - t)}{d_{\text{in}}\rho} - \frac{1}{A\rho}\frac{\partial p}{\partial \rho}\frac{\partial \dot{m}}{\partial z}\right], \tag{8}$$

where: $d_{\text{in}}$ – tube inner diameter, m; $i$ – enthalpy, J/kg; $t$ – fluid temperature, °C; $h$ – heat transfer coefficient, W/(m$^2$·K); $\theta$ – tube wall temperature, °C.

## 2.2 Solving balance equations for the fluid

Properly modified, the relations expressed in Eqs. (1)–(8) will enable determination of the distributions of the fluid mass flow rate, pressure and enthalpy. Reduced to the form of differential equations with separable variables, they will become the basis for a mathematical model enabling the analysis of the thermal and flow phenomena occurring in the boiler water-wall tubes. In their final version, the balance equations are written in a form

with time derivatives on one side of the equation and space derivatives on the other [23].

The derivatives are then replaced with difference quotients:

- energy balance equation:

$$\frac{\partial i}{\partial z} = \frac{A\rho}{\dot{m}} \left[ -\frac{\partial i}{\partial \tau} + \frac{4h(\theta - t)}{d_{in}\rho} \right], \tag{9}$$

applying the method of lines, the following is obtained:

$$\frac{di_j^{\tau}}{dz} = \frac{A\rho_j^{\tau-\Delta\tau}}{\dot{m}_j^{\tau-\Delta\tau}} \left[ -\frac{h_j^{\tau} - h_j^{\tau-\Delta\tau}}{\Delta\tau} + \frac{4h_j^{\tau-\Delta\tau}\left(\theta_j^{\tau-\Delta\tau} - t_j^{\tau-\Delta\tau}\right)}{d_{in}\rho_j^{\tau-\Delta\tau}} \right], \tag{10}$$

- mass balance equation:

$$\frac{\partial \dot{m}}{\partial z} = -A\frac{\partial \rho}{\partial \tau}, \tag{11}$$

applying the method of lines, the equation is expressed as

$$\frac{d\dot{m}_j^{\tau}}{dz} = -A\frac{\rho_j^{\tau} - \rho_j^{\tau-\Delta\tau}}{\Delta\tau}, \tag{12}$$

- momentum balance equation:

$$\frac{\partial}{\partial z}\left(\frac{\dot{m}^2}{A^2\rho} + p\right) = -\frac{1}{A}\frac{\partial \dot{m}}{\partial \tau} - \frac{\partial p_{\tau}}{\partial z} - \rho g \sin\varphi, \tag{13}$$

applying the method of lines, the equation is expressed as

$$\frac{d}{dz}\left[\frac{(\dot{m}^2)_j^{\tau}}{A^2\rho_j^{\tau}} + p_j^{\tau}\right] = -\frac{1}{A}\frac{(\dot{m}^2)_j^{\tau} - (\dot{m}^2)_j^{\tau-\Delta\tau}}{\Delta\tau} - \frac{dp_{\tau}}{dz} - \rho_j^{\tau} g \sin\varphi. \tag{14}$$

The relations prepared in this way were used in the numerical program to determine the temperature distribution of the fluid flowing through the waterwall tubes. The numerical model assumes that the water temperature will be the same throughout the entire cross-section of the tube. It is determined in each cross-section at each time step on the basis of differential equations describing the principles of conservation of mass, momentum and energy.

### 2.3 Energy balance equations for waterwall tube walls

The time- and space-dependent distribution of the temperature of waterwall tubes was determined using the transient heat conduction equation. For the purposes of the model, it is assumed that the entire pitch of spacing of a single tube in the cross-section under analysis is heated with an identical heat flux. The numerical model ensures determination of thermodynamic parameters at each of the set characteristic points of the walls of the tubes and of the fins connecting them, in each time step, which makes it possible to achieve high accuracy of the results. The temperature distribution inside the walls of the waterwall tubes was established using the division proposed in [24, 25] and presented in Fig. 4.

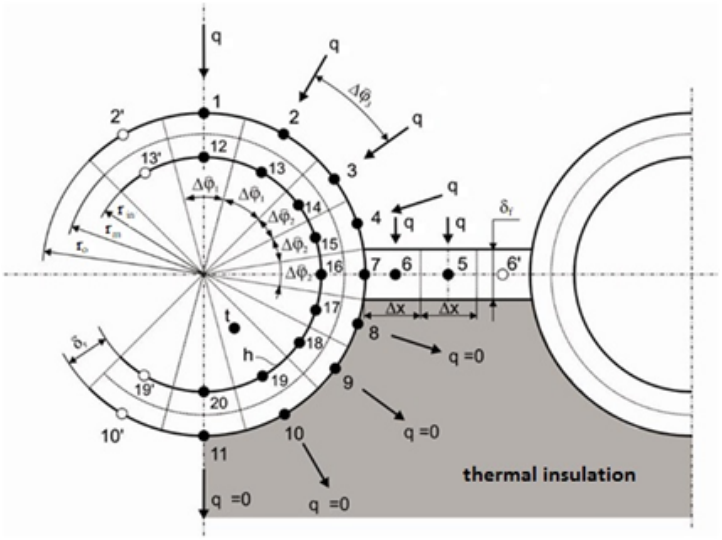


Figure 4: Division of the cross-section of a tube with a fin into control volumes.

The cross-section of the tube-fin connection was divided into control volumes (Fig. 4). Energy balance equations were written for each node. An example equation, for Point 1, is presented below:

$$
\begin{aligned}
c_1\rho_{1,j}\frac{\Delta\hat{\varphi}_1}{2}\left(r_o^2-r_m^2\right)\Delta z\frac{d\theta_{1,j}}{d\tau} &= k_{1,j}\frac{\theta_{2,j}-\theta_{1,j}}{\Delta\hat{\varphi}_1 r_o}\delta_t\Delta z \\
&+ \; k_{1,j}\frac{\theta_{12,j}-\theta_{1,j}}{\delta_t}\Delta\hat{\varphi}_1 r_m\Delta z + k_{1,j}\frac{\Delta\hat{\varphi}_1}{2}\left(r_o^2-r_m^2\right)\frac{\theta_{1,j-1}-\theta_{1,j}}{\Delta z} \\
&+ \; k_{1,j}\frac{\Delta\hat{\varphi}_1}{2}\left(r_o^2-r_m^2\right)\frac{\theta_{1,j+1}-\theta_{1,j}}{\Delta z} + q_j\Delta\hat{\varphi}_1 r_o\Delta z\,, \qquad (15)
\end{aligned}
$$

where: $c$ – specific heat, J/(kg·K); $\delta_t$ – tube wall thickness, m; $\Delta z$ – assumed length of the tube section, m; $r_m$ – mean radius of the tube, m; $r_o$ – tube outer radius, m; $k$ – heat conductivity coefficient, W/(m·K).

After rearrangements, a relation is obtained that makes it possible to determine temperature at Point 1 (see Fig. 4):

$$\theta_{1,j}^{\tau+\Delta\tau} = \theta_{1,j}^{\tau} + \frac{\Delta\tau}{c_{1,j}^{\tau}\rho_{1,j}^{\tau}\frac{\Delta\hat{\varphi}_1}{2}\left(r_o^2 - r_m^2\right)\Delta z}\left[k_{1,j}^{\tau}\frac{\theta_{2,j}^{\tau} - \theta_{1,j}^{\tau}}{\Delta\hat{\varphi}_1 r_o}\delta_t\Delta z\right.$$
$$+ \; k_{1,j}^{\tau}\frac{\theta_{12,j}^{\tau} - \theta_{1,j}^{\tau}}{\delta_t}\Delta\hat{\varphi}_1 r_m\Delta z + k_{1,j}^{\tau}\frac{\Delta\hat{\varphi}_1}{2}\left(r_o^2 - r_m^2\right)\frac{\theta_{1,j-1}^{\tau} - \theta_{1,j}^{\tau}}{\Delta z}$$
$$\left. + \; k_{1,j}^{\tau}\frac{\Delta\hat{\varphi}_1}{2}\left(r_o^2 - r_m^2\right)\frac{\theta_{1,j+1}^{\tau} - \theta_{1,j}^{\tau}}{\Delta z} + q_j^{\tau}\Delta\hat{\varphi}_1 r_o\Delta z\right]. \tag{16}$$

Writing down the equations, developed in the same manner as for Eqs. (15)–(16), for all 20 elements, makes it possible to create a matrix of coefficients describing the temperature distribution in a half of the cross-section of a single waterwall tube connected to a fin. Further expansion of the model, for a system of several connected tubes, is carried out in the same way.

## 3 Numerical verification of the proposed method

In order to verify the correctness of the results obtained from the numerical algorithm, calculations and a comparative simulation were carried out based on the operating parameters of an 858 MW supercritical power boiler installed in a power plant in Poland. A system consisting of three tubes connected by fins was adopted for the analysis. Water with mass flow of an 0.77 kg/s and pressure 29.96 MPa flows into each tube with outer diameter 33.7 mm and wall thickness 6.1 mm. The length of the tube element is assumed to be 0.5 m and the time step is determined in each iteration using the Courant-Friedrichs-Lewy condition. The system characteristic points were determined as presented in Fig. 5.

The results are presented using the temperature distributions obtained 45 m from the inlet. Two cases were analysed: the heat flux falling on the tubes has an identical value (case 1) and the central tube is heated with a heat flux by 50% higher compared to the heat flux incident on the pitches of spacing of the neighbouring tubes (case 2). The temperature values obtained from the numerical model and the values from the simulation carried

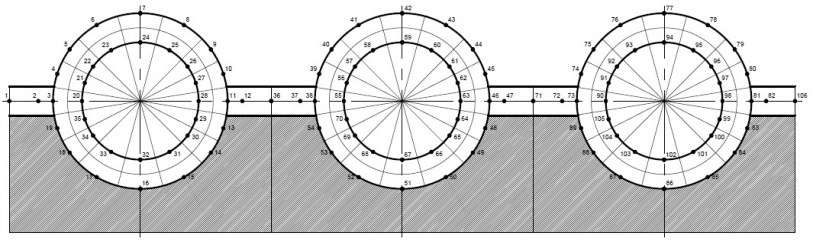

Figure 5: Division of the cross-section of three tubes with fins into control volumes.

out in the Ansys Fluent environment are presented. In Ansys Fluent analysed system was divided to 15 m parts due to problems with calculations. There was used the quadrilateral mesh with a size of 1 mm × 1 mm for the cross-sections of the analysed model and with an element length of 5 cm in the direction of the tube length. In order to define the correctness of the results obtained from the numerical model and the CFD model, the relative error was calculated from the following relation:

$$e_{\mathrm{CFD}} = \frac{|\theta_{\mathrm{CFD}} - \theta_{\mathrm{MOD}}|}{\theta_{\mathrm{CFD}}} \times 100\%, \tag{17}$$

where: $e_{\mathrm{CFD}}$ – relative error in the wall temperature determination, %; $\theta_{\mathrm{MOD}}$ – wall temperature determined using the numerical algorithm, K; $\theta_{\mathrm{CFD}}$ – wall temperature obtained from the Ansys Fluent program, K.

Figures 6 and 7 illustrate the analysis for uniformly heated tubes. Figure 6 presents the temperature distribution in the tubes and fins found using the proposed algorithm, whereas Fig. 7 shows the temperature distribution produced by the CFD model. Table 1 presents a comparison between the results produced by the proposed model and the CFD simulation. It also shows the calculated relative error.

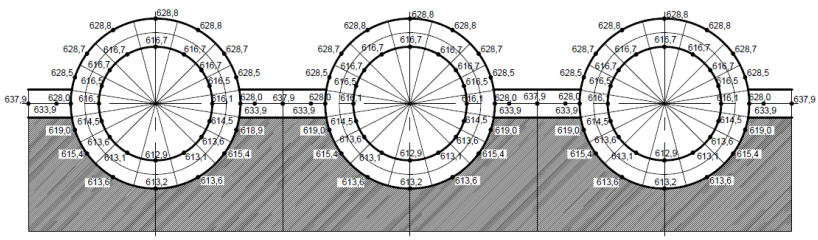

Figure 6: Temperature values (given in Kelvin scale) obtained in selected characteristic points at uniform heating of the system.

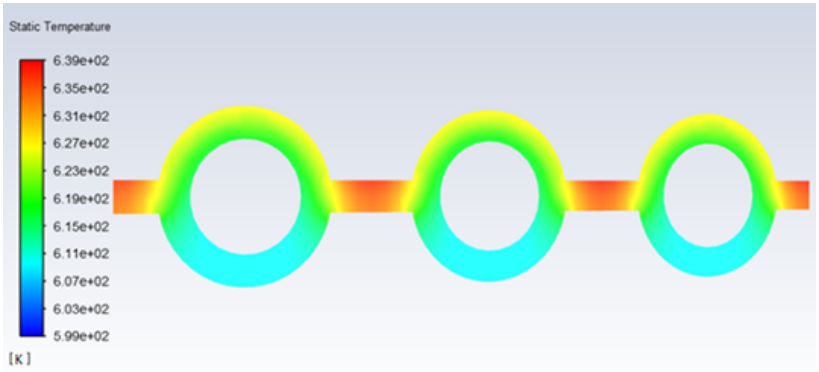


Figure 7: Temperature distribution (given in Kelvin scale) obtained from the CFD model at uniform heating of the tubes.

Table 1: Comparison of temperature values at selected points – uniform heating of the system.

| Characteristic point number | Temperature from the CFD model, $\theta_{\mathrm{CFD}}$, K | Temperature from the numerical model, $\theta_{\mathrm{MOD}}$, K | Temperature difference, K | Relative error $e_{\mathrm{CFD}}$, % |
|---|---|---|---|---|
| 7 | 627.7 | 628.8 | 1.1 | 0.18 |
| 16 | 611.8 | 613.2 | 1.4 | 0.22 |
| 42 | 627.7 | 628.8 | 1.1 | 0.18 |
| 51 | 611.8 | 613.2 | 1.4 | 0.22 |
| 77 | 627.7 | 628.8 | 1.1 | 0.18 |
| 86 | 611.8 | 613.2 | 1.4 | 0.22 |

Figures 8 and 9 illustrate the analysis for non-uniformly heated tubes. Figure 8 presents the temperature distribution in the tubes and fins found using the proposed algorithm, whereas Fig. 9 shows the temperature distribution produced by the CFD model at non-uniform heating of the tubes. Table 2 presents a comparison between the results produced by the proposed model and the CFD simulation. It also shows the calculated relative error.

Analysing Figs. 6–9 and Tables 1–2, it can be seen that the obtained temperature distributions demonstrate high convergence. The differences between the results obtained from the numerical model and the simulation are quite small. The maximum relative error in the presented comparisons is $e_{\mathrm{CFDmax}} = 0.31\%$. The largest discrepancies in the temperature distribution

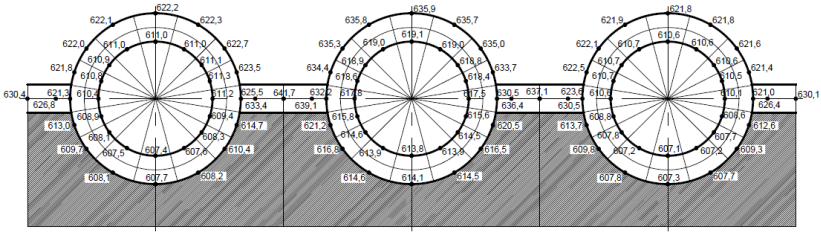

Figure 8: Temperature values (given in Kelvin scale) obtained in selected characteristic points at non-uniform heating of the system.

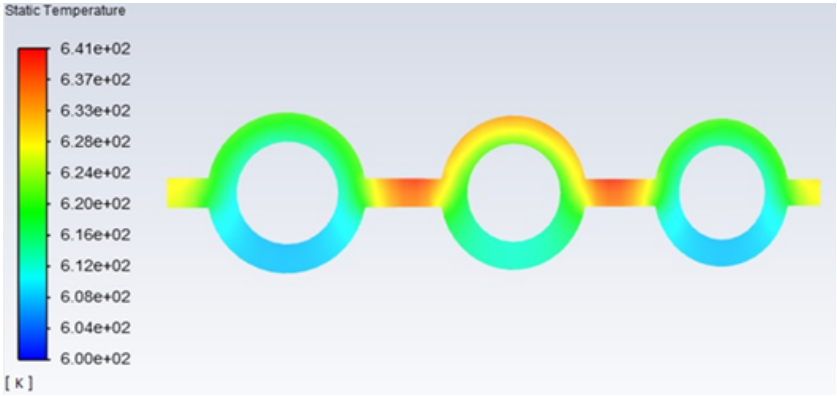


Figure 9: Temperature distribution (given in Kelvin scale) obtained in the Ansys Fluent environment at non-uniform heating of the system.

Table 2: Comparison of temperature values at selected points – non-uniform heating of the system.

| Characteristic point number | Temperature from the CFD model, $\theta_{CFD}$, K | Temperature from the numerical model, $\theta_{MOD}$, K | Temperature difference, K | Relative error $e_{CFD}$, % |
|---|---|---|---|---|
| 7 | 622.9 | 622.2 | 0.7 | 0.11 |
| 16 | 609.4 | 607.7 | 1.7 | 0.28 |
| 42 | 634.3 | 635.9 | 1.6 | 0.25 |
| 51 | 614.3 | 614.1 | 0.2 | 0.03 |
| 77 | 621.8 | 621.8 | 0.0 | 0.00 |
| 86 | 609.3 | 607.3 | 1.9 | 0.31 |

can be seen at the centre of the fins connecting the tubes. They are due to the way, adopted in the numerical model, of dividing the cross-section of the analysed tubes into control volumes.

The results presented above indicate that the proposed algorithm can successfully be applied to determine the temperature distribution in several adjacent waterwall tubes heated uniformly. The simulation results can be used as input data while determining the stress distribution in the analysed model section.

## 4 Experimental verification of the proposed method

In order to confirm the correctness of the results obtained using the numerical model, a test stand was designed and built. A detailed description of the stand structure can be found in [26].

The main elements of the stand are three tubes connected to each other by fins imitating a fragment of the combustion chamber wall. The tubes and the fins are made of P265GH steel with known thermophysical properties. According to the assumptions made earlier, the tubes were thermally insulated on one side and connected to a cooling water tank. Systems of heat radiators connected to power controllers were installed in front of the tubes, which made it possible to simulate the operation of a system heated on one side non-uniformly or uniformly. Figure 10 shows a diagram of the test stand, along with the location of the thermocouples installed in specific measuring sections. A Wilo Stratos GIGA 40/1-45/3,8 pump was used to ensure a stabilized flow of water; the pump main parameters are listed in Table 3 [27].

Table 3: Circulation pump technical data.

| Parameter and unit | Value |
|---|---|
| Elevation head, m | 1–45 |
| Power supply, V | $3 \times 400$ |
| Pump motor power, kW | 3.8 |
| Allowable range of rotational speed, rpm | 500–4000 |
| Pumped fluid temperature, °C | $-20 + 140$ |
| Maximum working pressure, bar | 16 |

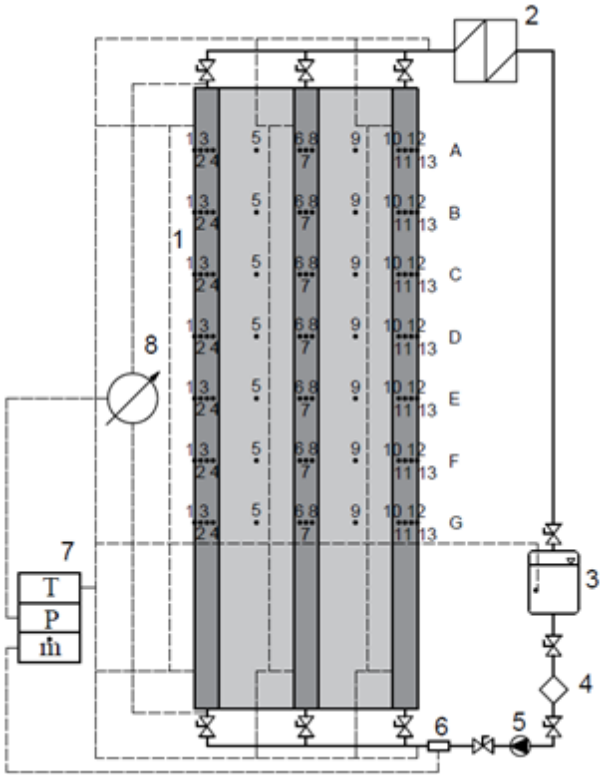


Figure 10: Diagram of the test stand: 1 – system of tubes connected by fins, 2 – cooler, 3 – circulating water tank, 4 – contamination filter, 5 – circulation pump, 6 – flowmeter, 7 – data acquisition system, 8 – power control system for the heating elements.

The pump installed on the test stand makes it possible to pump high-temperature water over a wide range of output and rotational speed. The operating parameters can be changed using an inverter. The pump circulates water through the test stand and the system of tubes connecting it to the tank. Due to that, the rise in the temperature of the medium flowing in the circulation loop occurs quite quickly.

In order to ensure one-side uniform heating of the tubes installed on the test stand, a system of radiant heaters was applied. The radiant heaters were connected in rows on a frame placed parallel to the tubes along the length of the selected test section. In each of the three rows, eight 1000W Victory/Philips HeLeN radiant heaters were installed. The radiant heaters were mounted in IRZ1000 housings, making it possible to properly direct

the radiation beams. The deviation of the side walls of the housings was wide enough to enable heating of the fins connecting the tubes with a heat flux similar to that incident on the tubes. The radiant heaters were placed on a supporting structure locating them at a distance of about 10 cm from the heated elements. According to the manufacturer's data, this location makes it possible to obtain the highest heat flux value. By connecting each of the radiant systems to a power controller, it was possible to set the value of the heat flux falling on each pitch of spacing of the waterwall tubes according to current needs. Three BTE-435 power controllers were used to regulate the power of the rows of the infrared radiators. Their basic parameters are listed in Table 4 [28].

Table 4: Parameters of the BTE-435 power controller module.

| Parameter and unit | Value |
|---|---|
| Operating range, kW | 0–10 |
| Accuracy, % of power | 1.0 |
| AC voltage, V | 230 |
| Maximum output current, A | 80 |

The water flow in the system was measured using an MPP 600 flowmeter made by ENKO-POMIAR Sp. z o.o. The main advantages of the flowmeter include the lack of moving parts and a flow diameter close to the diameter of the pipe supplying water to the vertical tubes. Owing to that, no additional losses arise in the system. The flowmeter most important parameters are presented in Table 5 [29].

Table 5: Parameters of the ENKO-POMIAR Sp. o.o. MPP 600 flowmeter.

| Parameter | Value |
|---|---|
| Measuring range, m/s | 0–10 |
| Accuracy, % of the flow rate | 0.2–1.0 |
| Allowable working medium | Water; current-carrying, inert or chemically aggressive liquids |
| Current output signal, mA | 4–20 |

NiCr-NiAl jacket thermocouples manufactured by ALF-SENSOR Sp. j. [30] were used to measure the temperature of water flowing into the measuring section and for selected points on the face of the tubes and the connecting fins. The thermocouples were attached to the stand using thermal paste and

neodymium magnets with increased resistance to high temperatures. The permissible temperature range for this type of sensors is −40°C–1000°C, the permissible deviation of sensor readings in the range of −40°C–375°C is ±1.5°C, in the range of 375°C–1000°C the permissible deviation is ±0.004 of the temperature value expressed in degrees Celsius.

The data indicated by the described measuring devices were recorded using an Ahlborn ALMEMO MA 5690-2 data acquisition system [31]. The acquisition system cooperates with the AMR Win Control software [32], intended for analysing data from Ahlborn devices and enabling the export of results to a spreadsheet.

Numerical calculations and measurements were made for cases in which the tubes were heated uniformly and for cases in which the heat flux falling on the central tube was different compared to the outermost tubes. In each measuring series, at each tube inlet, water reached the pressure of $p = 1.4$ MPa and the temperature of $t = 313$ K, and the average mass flow rate of water was $\dot{m} = 0.278$ kg/s. The following data were adopted in the numerical model: spatial step $\Delta z = 5$ cm, time step $\tau = 0.1$ s. Eight radiators were installed along each tube (24 in total). The surface area of irradiation with eight radiators is $A = 0.84$ m$^2$. The highest achievable heat flux is $q = 9\,500$ W/m$^2$. The test stand at the time of the measurements is shown in Fig. 11.

In order to define the correctness of the results obtained from the numerical model and of the measuring data, the relative error was calculated from the following formula:

$$e_{\mathrm{MES}} = \frac{|\theta_{\mathrm{MES}} - \theta_{\mathrm{MOD}}|}{\theta_{\mathrm{MES}}} \times 100\%\,, \tag{18}$$

where: $e_{\mathrm{MES}}$ – relative error in the wall temperature determination, %; $\theta_{\mathrm{MOD}}$ – temperature determined using the numerical algorithm, K; $\theta_{\mathrm{MES}}$ – temperature measured on the test stand, K.

Table 6 presents the results for selected points located on the outer frontal surface of individual tubes (marked in the system diagram (Fig. 10) as 3 (it corresponds Point 7 in Fig. 5), 7 (it corresponds Point 42 in Fig. 5) and 11 (it corresponds Point 77 in Fig. 5)). The tubes were heated using radiators operating at 80% of their maximum power. The mean heat flux falling on the pitch of spacing of the waterwall tubes is $q = 7.600$ W/m$^2$. Considering that, according to the characteristics of the applied radiators, the heat flux reaching the analysed fragment is strongly dependent on the distance from the radiator, the results obtained for the points closest to

Figure 11: Tests stand at the time of the measurements.

the radiators are burdened with the smallest errors. The maximum relative error in the presented comparisons totals $e_{\mathrm{MESmax}} = 0.71\%$.

Table 7 presents the results for selected points located at the centres of individual tubes in the case of non-uniform heating. It presents the results for the same points as in the case of uniform heating of the tubes (Points: 3, 7, and 11). The central tube was heated using radiators operating at 80% of maximum power. The heat flux falling on the pitch of spacing of the central tube is $q = 7.600\ \mathrm{W/m^2}$. The outermost tubes were heated using radiators operating at 60% of their maximum power. The heat flux falling on the pitch of their spacing was $q = 5.700\ \mathrm{W/m^2}$. The maximum relative error in the presented comparisons totals $e_{\mathrm{MESmax}} = 1.0\%$.

To summarize, it can be noted that there are differences in tube temperature values obtained using the numerical algorithm and measured on the test stand methods do not exceed 2.5 K for uniform heating of the analysed system (maximum relative error is 0.71%) and do not exceed 3.5 K for non-

Table 6: Temperature distribution obtained at uniform heating of the analysed system for different measuring levels.

| Measuring point | Measured temperature $\theta_{MES}$, K | Calculated temperature $\theta_{MOD}$, K | Temperature difference, K | Relative error $e_{MES}$, % |
|---|---|---|---|---|
| B3 | 324.5 | 324.9 | 0.4 | 0.12 |
| B7 | 324.7 | 324.9 | 0.2 | 0.06 |
| B11 | 324.1 | 324.9 | 0.8 | 0.25 |
| D3 | 324.3 | 323.2 | 1.1 | 0.34 |
| D7 | 325.5 | 323.2 | 2.3 | 0.71 |
| D11 | 324.1 | 323.2 | 0.9 | 0.28 |
| F3 | 318.5 | 318.4 | 0.1 | 0.03 |
| F7 | 320.1 | 318.4 | 1.7 | 0.53 |
| F11 | 317.3 | 318.4 | 1.1 | 0.35 |

Table 7: Temperature distribution obtained at non-uniform heating of the analysed system for different measuring levels.

| Measuring point | Measured temperature $\theta_{MES}$, K | Calculated temperature $\theta_{MOD}$, K | Temperature difference, K | Relative error $e_{MES}$, % |
|---|---|---|---|---|
| B3 | 320.9 | 323.6 | 2.7 | 0.84 |
| B7 | 322.0 | 325.0 | 3.0 | 0.93 |
| B11 | 320.4 | 323.6 | 3.2 | 1.00 |
| D3 | 320.0 | 321.4 | 1.4 | 0.44 |
| D7 | 320.3 | 323.0 | 2.7 | 0.84 |
| D11 | 319.7 | 321.4 | 1.7 | 0.53 |
| F3 | 316.4 | 317.2 | 0.8 | 0.25 |
| F7 | 318.7 | 318.3 | 0.4 | 0.13 |
| F11 | 316.6 | 317.2 | 0.6 | 0.19 |

uniform heating of the analysed system (maximum relative error is 1.00%). One of the main reasons for the occurrence of temperature differences between the results obtained from the numerical model and the measurements were the problems related to the correct attachment of thermocouples to the surface of the system under consideration. Analysing the errors for the obtained experimental results and those produced by the numerical calcu-

lations, it can be concluded that the proposed numerical algorithm provides satisfactory computing accuracy. Owing to that, the results obtained from it can be used, for example, to determine the stress distribution for the analysed area.

# 5 Conclusions

The paper presents a numerical model for the analysis of thermal and flow phenomena occurring in smooth tubes connected by fins. The model basic assumptions are presented, along with the way in which the cross-section of the analysed system is divided into control volumes. Unlike the solutions presented in most to-date studies, the proposed model makes it possible to determine the temperature distribution in a few waterwall tubes connected by fins. This in turn enables correct simulation of the operation of the combustion chamber walls of sub- and supercritical boilers. By determining the parameters of the fluid and the tube walls in each time step, and using a variable time step, the accuracy of the results was improved. The temperature distribution determined for selected characteristic points, after approximation for the remaining part of the cross-section, can be used to establish the distribution of thermal stresses, for example to identify fragments with the highest hazard of the occurrence of stresses exceeding allowable values.

The numerical algorithm results were verified by comparison with the temperature distribution obtained from CFD calculations. The temperature for points on the centre of front wall of analysed tubes obtained from CFD model is 627.7 K and 628.8 K for results from the numerical model – for the case in which tubes are heated with the same heat flux. For the non-uniform heated tubes the temperature for point on the centre of front wall of centre tube obtained from CFD model is 634.3 K and 635.9 K for results from the numerical model, and for the side tubes accordingly 622.9 K/621.8 K for results from CFD calculations and 622.2 K/621.8 K for numerical algorithm results.

The numerical algorithm results were also verified by comparison with the measurements on the prepared test stand. Considering that the stand had to simulate possibly uniform heating of the entire pitch of spacing of the tubes connected by the fins, a system was used of infrared radiators placed in parallel to three heated tubes. Comparing the simulation results and the experimentally measured temperatures with the results produced

by the numerical algorithm, high convergence was found between them. The highest temperatures for points on the centre of front wall of analysed tubes obtained from measurements are within the range 324.1–324.7 K and the highest temperature for results from the numerical model is equal to 324.9 K – for the case in which tubes are heated with uniform heat flux. For the non-uniform heated tubes the highest temperature for point on the centre of front wall of centre tube obtained from measurements is 322.0 K and 325.0 K for results from the numerical model, and for the side tubes accordingly 320.9 K/320.4 K for results from measurements and 323.6 K/323.6 K for numerical algorithm results.

It is therefore concluded that the proposed numerical model enables correct determination of the temperature distribution in the waterwall tubes and in the fins connecting them, both at uniform and non-uniform heating of individual pitches of spacing of the tubes making up the analysed system. The solutions applied on the test stand enabled satisfactory simulation of the conditions occurring in the combustion chamber. The determined temperature distribution can be used to establish the distribution of thermal stresses for the cross-section of the analysed model.

## Acknowledgements

The research leading to the presented results was financed from the 2014–2021 Norwegian Funds through the National Centre for Research and Development (Grant NOR/POLNORCCS/0015/2019-00).

*Received 24 October 2023*

# References

[1] Jackson J.D.: *Fluid flow and convective heat transfer to fluids at supercritical pressure*. Nucl. Eng. Des. **264**(2013), 24–40.

[2] Taler D.: *A new heat transfer correlation for transition and turbulent fluid flow in tubes*. Int. J. Therm. Sci. **108**(2016), 108–122.

[3] Grądziel S., Majewski K., Majdak M., Mika Ł., Sztekler K., Kobyłecki R., Zarzycki R., Pilawska M.: *Testing of heat transfer coefficients and frictional losses in internally ribbed tubes and verification of results through CFD modelling*. Energies **15**(2022), 207.

[4] Granda M., Trojan M., Taler D.: *CFD analysis of steam superheater operation in steady and transient state*. Energy **199**(2020), 117423.

[5] Węglowski B.: *Identification of Thermal Operating Conditions of Boiler Furnace Tube*. Zeszyty Naukowe Politechniki Krakowskiej **2**(1995). Wydaw. PK, Kraków 1995 (in Polish).

[6] Grądziel S.: *Determination of temperature and thermal stresses distribution in power boiler elements with use inverse heat conduction method*. Arch. Thermodyn. **32**(2011), 3, 191–200.

[7] Huang C.N., Kharangate C.R.: *A new mechanistic model for predicting flow boiling critical heat flux based on hydrodynamic instabilities*. Int. J. Heat Mass Tran. **138**(2019), 1295–1309.

[8] Zima W., Taler J., Grądziel S., Trojan M., Cebula A., Ocłoń P., Dzierwa P., Taler D., Rerak M., Majdak M., Korzeń A., Skrzyniowska D.: *Thermal calculations of a natural circulation power boiler operating under a wide range of loads*. Energy **261**(2022), 125357.

[9] Taler J., Trojan M., Dzierwa P., Kaczmarski K., Węglowski B., Taler D., Zima W., Grądziel S., Ocłoń P., Sobota T., Rerak M., Jaremkiewicz M.: *The flexible boiler operation in a wide range of load changes with considering the strength and environmental restrictions*. Energy **263**(2023), 125745.

[10] Khan M.: *Performance of a combined cycle power plant due to auxiliary heating from the combustion chamber of the gas turbine topping cycle*. Arch. Thermodyn. **42**(2021), 1, 147–162.

[11] Zima W., Grądziel S., Cebula A.: *Modelling of heat and flow phenomena occuring in waterwall tubes of boilers for supercritical steam parameters*. Arch. Thermodyn. **31**(2010), 3, 19–36.

[12] Qu M., Yang D., Liang Z., Wan L., Liu D.: *Experimental and numerical investigation on heat transfer of ultra-supercritical water in vertical upward tube under uniform and non-uniform heating*. Int. J. Heat Mass Tran. **127**(2018), 769–783.

[13] Kong X., Li H., Zhang Q., Guo K., Luo Q. Lei X.: *A new criterion for the onset of heat transfer deterioration to supercritical water in vertically-upward smooth tubes*. Appl. Therm. Eng. **151**(2019), 66–76.

[14] Wang S., Yang D., Zhao Y., Qu M.: *Heat transfer characteristics of spiral water wall tube in a 1000 MW ultra-supercritical boiler with wide operating load mode*. Appl. Therm. Eng. **130**(2018), 501–514.

[15] Kobyłecki R., Zarzycki R., Bis Z., Panowski M., Wiłski M.: *Numerical analysis of the combustion of straw and wood in a stoker boiler with vibrating grate*. Energy **222**(2021), 119948.

[16] Panowski M., Zarzycki R., Kobyłecki R.: *Conversion of steam power plant into cogeneration unit – case study*. Energy **231**(2021), 120872.

[17] Sultanov M.M, Griga S.A., Ivanitckii M.S., Konstantinov A.A.: *Monte-Carlo method for assessing and predicting the reliability of thermal power plant equipment*. Arch. Thermodyn. **42**(2021), 4, 87–102.

[18] MATLAB R2019b Update 5 (9.7.0 1319299). The MathWorks Inc. 2020.

[19] Ansys Workbench 2019 R3 19. 5.0. 2019072818. ANSYS Inc. 2019.

[20] Majdak M., Grądziel S.: *Influence of thermal and flow conditions on the thermal stresses distribution in the evaporator tubes*. Energy **209**(2020), 118416.

[21] Zima W., Grądziel S.: *Simulation of transient processes in heating surfaces of power boilers: Mathematical modelling and experimental verification*. LAP Lambert Academic Publishing 2013.

[22] Grądziel S., Majewski K.: *Simulation of heat transfer in combustion chamber waterwall tubes of supercritical steam boilers*. Chem. Process Eng. **3**(2016), 2, 199–213.

[23] Grądziel S.: *Selected Issues of Power Boiler Operation*. Wydaw. PK, Kraków 2023 (in Polish)

[24] Zima W., Nowak-Ocłoń M.: *A new 1D/2D model of the conjugate heat transfer in waterwall tubes of the supercritical steam boiler combustion chamber*. Heat Transf. Eng. **39**(2018), 13–14, 1272–1282.

[25] Majdak M., Grądziel S.: *Analysis of thermal flow in waterwall tubes of the combustion chamber depending on the fluid parameters*. Therm. Sci. **23**(2019), 1333–1344.

[26] Majdak M.: *Thermal flow and strength analysis of combustion chamber waterwall tubes operation*. PhD thesis, Cracow University of Technology, Kraków 2021 (in Polish).

[27] Wilo SE: *Wilo Stratos GIGA 40/1-45/3,8*. https://wilo.com/id/en/Products-and-expertise/en/products-expertise/wilo-stratos-giga/stratos-giga-40-1-45-3-8 (accessed 20 Oct. 2023).

[28] GOTRONIK PPHU: *Power regulator parameters (BTE-435)*. https://www.gotronik.pl/modul-regulatora-mocy-10000w-p-4278.html (accessed 20 Oct. 2023).

[29] ENKO-POMIAR Sp. z o.o.: *Electromagnetic flow meters*. https://www.enko-pomiar.pl/52,81,0 (accessed 20 Oct. 2023).

[30] ALF-SENSOR Sp. J.: *Thermocouples*. https://alf-sensor.com/catalogue-of-our-products/thermocouples.html (accessed 20 Oct. 2023).

[31] *Ahlborn ALMEMO MA 5690-2 Manual*. https://www.ahlborn.com/download/anleitung/eng/56902e.pdf (accessed 20 Oct. 2023).

[32] *AMR Win Control software*. https://www.ahlborn.com/download/pdfs/kap05/eng/WinControle.pdf (accessed 20 Oct. 2023).

**archives**
**of thermodynamics**
Vol. **44**(2023), No. 4, 103–121
DOI: 10.24425/ather.2023.149710

# The effect of graphene nanoparticles on the thermal conductivity enhancement of organic phase change material and its energy storage properties

**PAULINA ROLKA***
**MARCIN LACKOWSKI**

Institute of Fluid Flow Machinery, Polish Academy of Sciences, Fiszera 14, 80-231 Gdańsk, Poland

**Abstract** Organic phase change materials (PCMs), which are typically used as the accumulating material in latent heat thermal energy storage, provide chemical and thermal stability, but have low thermal conductivity. This limits heat transfer rates and prolongs storage charging/discharging time. A method to improve the thermal conductivity of organic PCMs is to add nanomaterials with high thermal conductivity. The paper presents the research on the effect of the addition of graphene nanoparticles (GNPs) on the thermal conductivity of organic PCM (RT28 HC), and its energy storage properties. The transient hot wire and the pipe Poensgen apparatus methods were used to measure thermal conductivity, and the differential scanning calorimetry method was used to determine the heat capacity and phase change temperature. The achieved characteristics of thermal conductivity depending on the amount of added graphene nanoparticles (and stabilizer) indicate that GNPs allow to increase the thermal conductivity on average by 26–87% in the solid state and by 7–28% in the liquid, but this reduces the PCM heat capacity. Therefore, the paper indicates what mass fraction of dopants is optimal to achieve the greatest improvement in thermal conductivity of RT28 HC and its smallest reduction in heat capacity, to use this nano-enhanced PCM in practice.

**Keywords:** Phase change materials (PCMs); Nano-enhanced phase change materials (NEPCMs); Thermal conductivity; Heat capacity; Latent heat thermal energy storage (LHTES)

*Corresponding Author. Email: prolka@imp.gda.pl

### Nomenclature

| | | |
|---|---|---|
| $C$ | – | heat storage capacity (combination of latent and sensible heat in a specific temperature range), J/g |
| $d$ | – | diameter, m |
| $I$ | – | current, A |
| $L$ | – | pipe length, m |
| $T$ | – | temperature, K |
| $T_m$ | – | melting temperature of PCM, K |
| $T_s$ | – | solidification temperature of PCM, K |
| $U$ | – | voltage, V |

#### Greek symbols

| | | |
|---|---|---|
| $\lambda$ | – | thermal conductivity, W/m·K |

#### Subscripts

| | | |
|---|---|---|
| $l$ | – | liquid |
| $p$ | – | pipe |
| $s$ | – | solid |

#### Acronyms

| | | |
|---|---|---|
| DSC | – | differential scanning calorimetry |
| GNP | – | graphene nanoparticles |
| MTPS | – | modified transient plane source |
| MWCNT | – | multi-walled carbon nanotubes |
| NEPCM | – | nano-enhanced phase change material |
| LHTES | – | latent heat thermal energy storage |
| PCM | – | phase change material |
| PPA | – | pipe Poensgen apparatus |
| SDBS | – | sodium dodecylbenzenesulfonate |
| THM | – | T-history method |
| THW | – | transient hot wire |
| 3LC | – | three-layer calorimeter |

## 1 Introduction

The growing demand for energy and human activities harmful to the environment make it necessary to carry out an energy transformation towards renewable energy sources. Due to the periodic and time-varying availability of renewable energy sources, depending on weather conditions, the use of energy storage facilities is required. Thermal energy generated in renewable energy systems can be stored using the following types of thermal energy storage (TES): sensible heat thermal energy storage (e.g. water

tanks), latent heat thermal energy storage (LHTES) or thermochemical storage. Among them, latent heat thermal energy storage units are increasingly used, which, compared to "cheaper" water tanks, are characterized by a higher energy storage density and ensure the optimal size of the energy storage tank [1], and compared to thermochemical energy storage units, they do not require high temperatures of the processes that determine energy storage and have moderate operational problems [2].

The accumulating material in LHTES units are phase change materials (PCMs) which have the ability to absorb and release energy during a phase transition, usually occurring from a solid to a liquid state (and *vice versa*), in a specific temperature range. LHTES can store heat from solar collector systems [3, 4], waste heat [5], cold from night ventilation systems [6], or energy generated from wind power and photovoltaic installations [4], and next allows to use it to support building's heating/cooling systems like e.g. HVAC (heating, ventilation, air conditioning), heat pumps or district heating networks [7–10]. Moreover, PCMs can be used separately – encapsulated PCM (usually macrocapsulated PCM) can be incorporated into building elements (e.g. walls, floors, suspended ceilings) and passively improve thermal comfort in rooms [11, 12], or can allow for cooling of photovoltaic panels [13] or electronics [14, 15].

In practice, organic phase change materials are most often used because, compared to inorganic materials, there is no phase separation and they exhibit little or no undercooling, which makes them chemically and thermally stable during many phase change cycles. They also have high latent heat and compatibility with most materials. However, the problem with organic PCMs is their low thermal conductivity that increases the thermal resistance during the phase change process, limits heat transfer and prolongs the time of PCMs melting and solidification, and thus impacts charging/discharging time of the thermal storage. This can result in ineffective use of accumulation materials in the case of sources with a relatively short lifespan (e.g. waste heat from technological processes, solar energy), and a reduction of effectiveness and cost-effectiveness of the LHTES application.

To avoid too long charging/discharging times of storages with PCMs, the heat transfer surface in LHTES is increased or methods are proposed to increase the thermal conductivity of storage materials. Increasing the area of heat exchange in LHTES can be achieved by using special fins in the construction of storages (e.g. longitudinal, radial, ring, round), using fin-and-tube heat exchangers, or using capillary tube bundles as heat exchangers,

also using encapsulated PCM (macro- or micro-encapsulated) [7, 16, 17]. One of the methods aimed at improving thermal conductivity in LHTES is the use of porous materials (in the form of foams or matrixes) filled with PCM [17, 18]. Although the use of special heat exchangers increasing the heat exchange surface or the use of porous materials improving the intensification of heat transfer shortens the melting/solidification times of PCM, it leads to a significant reduction in the amount of PCM in the tank. As indicated in the analysis [17], the volume of PCM in the total volume of the tank is 30–50% in the case of storage with macro-encapsulated PCM (depending on the type of capsules and packaging), 35–90% in the case of storage with fins and a fin-tube exchanger, 60–90% in the case of storage with a porous structure, over 90% in the case of storage with a capillary bundle as a heat exchanger. Therefore, these solutions may lead to a reduction in heat capacity or an increase in the mass and volume of the storage tank, and thus generate a higher cost per unit of stored energy.

Another way to reduce the charging and discharging times of LHTES is to directly improve the thermal conductivity of organic phase change materials by adding admixtures in the form of nanomaterials with high thermal conductivity [19, 20]. Nanomaterials added to organic PCMs may be metal nanoparticles, metal oxide nanoparticles or carbon-based nanoparticles [19–21]. Wu *et al.* [21] indicate that after adding copper nanoparticles to paraffin (at a content of 2% wt. Cu) achieved a maximum increase in thermal conductivity up to 14.2% in the solid state and 18.1% in the liquid. Temel *et al.* [22] investigated the effect of various nanoparticles (metal oxide nanoparticles and carbon nanoparticles) on improving the thermal conductivity of organic PCM – a commercially available material called A82. The results of their research indicate that the improvement in thermal conductivity of A82 composites doped with a 5% mass fraction of metal oxide nanoparticles: ZnO, $TiO_2$, $Al_2O_3$ and MgO was 2.6%, 3.6%, 6.5% and 8.4%, respectively. A higher improvement in thermal conductivity was achieved using carbon nanoparticles – multi-walled carbon nanotubes (MWCNT) and graphene nanoparticles (GNP), obtaining an increase of 26.7% and 154.9%, respectively. Moreover, their research indicates that by adding admixtures, the latent heat of the base PCM is reduced by up to 18%, depending on the type of nanoparticles and their mass fraction. Only when zinc oxide nanoparticles were used, the latent heat increased, which the authors of [22] explain as the effect of intermolecular attraction between the nanoparticles and the organic PCM.

A higher thermal conductivity of base organic PCMs as a result of doping them with carbon-based nanoparticles rather than with metal oxide nanoparticles was reported in the works [15,19,20,23]. The research of Radhakrishnan *et al.* [23] indicates that after adding nanomaterials with a mass content of 0.1% and 1%, an increase in thermal conductivity was achieved by approx. 7% and 17% for $Al_2O_3$ nanoparticles, 7% and 18% for $SiO_2$ nanoparticles, 12% and 30% for graphene nanoparticles. They also noted a decrease in latent heat of approx. 7% and 27% for $Al_2O_3$ nanoparticles, 7% and 14% for $SiO_2$ nanoparticles, 7% and 21% for graphene nanoparticles. Moreover, this investigation showed that after some time, nanoparticles and PCM may separate in the liquid – sedimentation of nanomaterials occurs. The sedimentation of nanoparticles in nano-enhanced PCMs (NEPCMs) is noted in the works [19, 20, 24]. To improve the stability of NEPCMs, the use of surfactants is proposed [15, 19, 20, 24]. Choi *et al.* [24] conducted tests, in which they showed that adding a surfactant in the form of polyvinylpyrrolidone (PVP) stabilizes NEPCM in the liquid state even for several days. Studies have shown that the thermal conductivity of NEPCM (stearic acid with graphene nanoparticles, or graphite nanoparticles or MWCNT nanoparticles) without added surfactant has a lower value than for NEPCM with a stabilizer (polyvinylpyrrolidone). Moreover, the highest improvement in thermal conductivity was achieved when graphene nanoparticles were added to organic PCM (stearic acid).

The paper presents research on improving the thermal conductivity of the organic phase change material, namely RT28 HC (with a melting point in the range of 27–29°C), which could be used in LHTES integrated with heating and cooling installations of buildings, as well as for cooling photovoltaic panels or microelectronics. Based on the literature analysis, it was decided to improve the thermal conductivity of the RT28 HC material by adding graphene nanoparticles with a mass fraction in the range of 1–5% and a surfactant to ensure stability. Although tests on improving the thermal conductivity of RT28 HC as a result of adding graphene, MWCNT, $Al_2O_3$, or CuO nanoparticles to it were already carried out in [15], they were only carried out for a 1% mass fraction of nanoparticles. Therefore, the aim of the research presented in the article is to present the characteristics of the influence of graphene nanoparticles on the thermal conductivity and latent heat of the base RT28 HC (organic PCM) depending on the weight fraction of the nanoparticles, which has not been carried out so far. The experimental results of thermal conductivity tests presented in the manuscript were carried out using two different measurement methods

other than that used in [15]. The first one is the transient hot wire method (usually used in the measurement of NEPCMs) and the second is the pipe Poensgen apparatus method, which has not been used so far to measure the thermal conductivity of NEPCMs. The comparison of thermal conductivity values achieved by different thermal conductivity measurement methods aims to clearly determine the increase in thermal conductivity as a result of the use of nanoadditives – graphene nanoparticles and surfactant (nanoparticle stabilizer). Moreover, the work also considers the influence of different weight contents of nanoparticles on other thermophysical properties of the base PCM, e.g. the temperature range of the phase change of the tested material. Additionally, the presented results of experimental work provide valuable knowledge about what mass fraction of graphene nanoparticles is the optimum, between achieving the greatest improvement of the thermal conductivity of the organic PCM and the lowest possible reduction in its heat capacity, which has a significant impact on the application of NEPCM in practice.

## 2 Materials and methods

### 2.1 Materials used and preparation of nano-enhanced phase change material

The organic phase change material, that was the subject of the research on increasing its thermal conductivity in the presented article, was a commercially available material, namely RT28 HC (Rubitherm GmbH). The RT28 HC material was selected for testing due to the wide range of possible applications of stored energy in practice (e.g. refrigeration installations, heating installations, passive cooling in suspended ceilings, cooling of photovoltaic (PV) modules and microelectronics), as well as due to its well-known thermophysical properties, which are presented in Table 1.

Graphene nanoparticles (GNP), were chosen as the material to help increase the thermal conductivity of the base PCM (RT28 HC) because they are characterized by high thermal conductivity (from 3000 W/m·K to 5000 W/m·K) [25], and compared to other used nanomaterials in previous studies [15, 22–24] showed the greatest improvement in thermal conductivity of phase change materials. In this research, commercially available GNPs are used with the following properties: particle size up to $2 \cdot 10^{-6}$ m, thickness $(1–4) \cdot 10^{-9}$ m, specific surface area 700–800 $m^2/g$ and purity 91%, specified by the manufacturer (PlasmaChem GmbH [26]). In the litera-

Table 1: Thermophysical properties of base organic PCM – RT28 HC (a summary of data from the literature [6, 15, 28–30]).

| Properties | Method | | | | | | | |
|---|---|---|---|---|---|---|---|---|
| | 3LC | THM | THM | DSC | | | PPA | MTPS |
| | | | | Heating rate | | | | |
| | | | | 1 K/min | 1 K/min | 2 K/min | | |
| $T_m$ (K) | 301.15 | 300.46 | – | 302.04 | 307.00 | 302.03 | – | – |
| $T_s$ (K) | 300.15 | 300.79 | – | 299.95 | 300.65 | 300.18 | – | – |
| $C$ (J/g)* | 250 | $268^h$<br>$220^c$<br>$244^{av}$ | 246 | $255^h$<br>$258^c$<br>$256.5^{av}$ | $258^h$<br>$252^c$<br>$255^{av}$ | 250 | – | – |
| $\lambda_s$ (W/m·K) | – | – | – | – | – | – | 0.33 | 0.22 |
| $\lambda_l$ (W/m·K) | – | – | – | – | – | – | 0.20 | 0.15 |
| Reference | [28] | [6] | [30] | [15] | [29] | [30] | [6] | [15] |

$^h$ heating process, $^c$ cooling process, $^{av}$ average, * combination (sum) of latent heat and sensible heat at temperature range (294.15–309.15 K).

ture [15,19,20,24], a surfactant – a sodium dodecylbenzenesulfonate (SDBS, manufacturer Sigma-Aldrich [27]) was used to ensure the stability of suspension, after the addition of GNP to the base organic PCM (RT28 HC).

Samples with nano-enhanced PCM (NEPCM) were prepared using a two-step method, in which "ready-made" admixtures (nanomaterials) are added to the base PCM in the liquid, and then the mixture is mixed appropriately [15, 19, 20]. Therefore, the preparation of NEPCM samples started by melting RT28 HC. The RT28 HC material was heated to above 305.15 K and then maintained at approximately 305.15–308.15 K by placing the beaker with liquid PCM on the heating platform of a magnetic stirrer (magnetic stirrer SBS-MR-1600/1T Pro Steinberg). Then, a stabilizer – sodium dodecylbenzenesulfonate was added to the melted PCM in a ratio of 4:1 of graphene nanoparticles (as in [15]) and mixed using a magnetic stirrer at a stirring rate of 450 rpm for 30 min. After that, GNPs with a mass fraction of 1%, 3% and 5% were added to the mixture, respectively, and were stirred by a magnetic stirrer (at 450 rpm) for 2.5 hours. Each obtained solution was poured from the beaker into a special vessel and then mixed using an ultrasonic mixer (Sonoplus HD 2070.2 Bandelin) for 1 hour to achieve uniform and intense sonication (dispersion of nanoparticles in NEPCM). As a result, samples with three NEPCMs differing in the mass fraction of nanomaterials (nanoparticles of GNP and SDBS) were obtained.

## 2.2 Methods of measuring the thermal conductivity of base phase change material and nano-enhanced phase change material

Two different methods were used to measure the thermal conductivity of the base PCM (RT28 HC) and NEPCM: the transient hot wire (THW) method and the pipe Poensgen apparatus (PPA) method.

The transient hot wire method is based on placing a linear heat source (heating wire) in the tested material and measuring the temperature increase over time at a specific distance from the heat source. It is assumed that the heat source is powered by electricity and the heat flux released over time is constant and uniform over the entire length of the tested material. The THW method was used in this investigation because this method was the most frequently used in other research of NEPCM [19, 20]. Measurements using the THW method were carried out using a commercial device – a thermal properties analyzer TEMPOS (METER Group) along with two measurement sensors: KS-3 and SH-3 (see Fig. 1). The SH-3 measurement probe was used to measure the thermal conductivity of base PCM and NEPCM in the solid state, and the KS-3 sensor in the liquid.

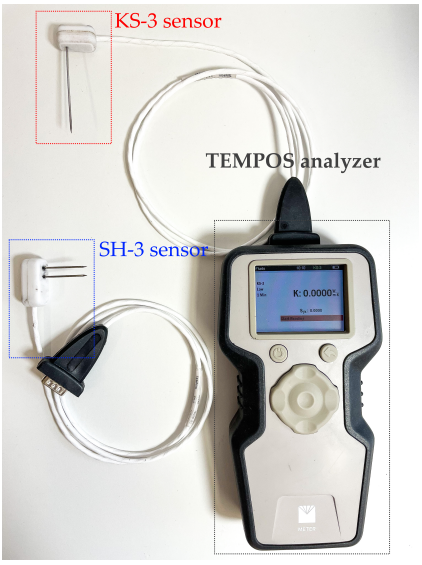


Figure 1: A commercial device used in the research to measure the thermal conductivity of base PCM and NEPCM using the transient hot wire method.

In the research presented in this paper, the pipe Poensgen apparatus method was used as a second method for measuring the thermal conductivity of the base PCM and NEPCM due to its simple measurement and the ability to perform measurements using a "low cost" device compared to commercial devices typically used in the literature [15, 19–22, 24].

The pipe Poensgen apparatus method is based on the measurement of a 'steady-state' temperature difference on walls of two pipes placed concentrically (the outer wall of the inner pipe and the inner wall of the outer pipe), during a constant heat flow from the heat source – an electric heater. During the measurement, the tested material (in this case base PCM or NEPCM) is between the two pipes placed concentrically (see Fig. 2a). Knowing the set heat flux (through the voltage and current setting of the electric heater), and the geometric parameters of the device, the thermal conductivity is determined according to the following relationship

$$\lambda = \frac{UI \ln \dfrac{d_{p,\text{out}}}{d_{p,\text{in}}}}{2\pi L \left(T_{p,\text{in}} - T_{p,\text{out}}\right)},$$

where $d_{p,\text{in}}$, $d_{p,\text{out}}$ denote the diameters of the inner and outer pipes, $T_{p,\text{in}}$, $T_{p,\text{out}}$ – the temperature of the outer wall of the inner pipe and the inner wall of the outer pipe, respectively.

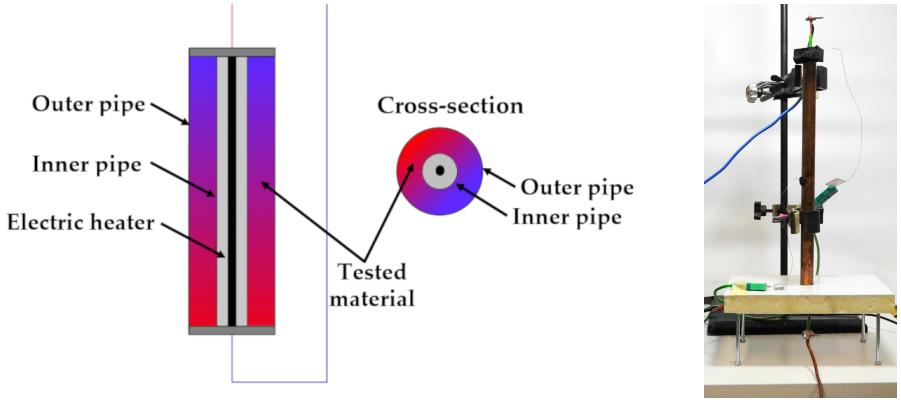


Figure 2: An in-house device for measuring the thermal conductivity of base PCM and NEPCM using the pipe Poensgen apparatus method: (a) simplified conceptual diagram (scheme) of the device's construction; (b) ready-made device.

The device used in this research, based on the pipe Poensgen apparatus method, for measuring the thermal conductivity of the base PCM and NEPCM, is shown in Fig. 2b, and the technical details regarding to the construction of this device are presented in [4].

### 2.3 Methods of measuring heat capacity and temperature range of phase change of base phase change material and nano-enhanced phase change material

To investigate the heat capacity and temperature range of phase transition of the base PCM and NEPCM, it was decided to use the differential scanning calorimetry (DSC) method. For this purpose, a commercial measuring device was used, DSC Q2000 (TA Instrument). DSC measurements for samples with base PCM and NEPCM were performed at a constant heating/cooling rate of 1 K/min due to ensuring an optimal measurement time and achieving good agreement of the measurement results compared with the results from other methods (3LC and T-history) in the case of measuring base PCM [6]. Sample tests were carried out in the temperature range 291.15–311.15 K. The samples of the tested materials had masses ranging from approx. $(18–30)\cdot10^{-3}$ kg. Samples of the tested NEPCM materials immediately after preparation in the liquid state, were placed in aluminium crucibles with a lid and hermetically closed.

## 3 Results

Each sample of the tested material, immediately after preparation, in the liquid state was poured into the pipe Poensgen apparatus in an amount of $46 \cdot 10^{-3}$ l. First, measurements were made in the liquid by supplying a heat flow and heating the material to 308.15–310.15 K until a constant temperature gradient of walls in the pipe Poensgen apparatus was achieved. The measurement of the temperature difference at the walls of the device while the tested material was in the liquid lasted several minutes, and on its basis, the thermal conductivity was determined, for which the average value was estimated and marked in grey in Fig. 3a (depending on the mass fraction of GNP in NEPCM). After performing measurements in the liquid, the tested material was left in the pipe Poensgen apparatus to solidify at an ambient temperature of approx. 289.15–290.15 K. The laboratory room was air-conditioned, which allowed the ambient temperature to be set at

approx. 289.15–290.15 K. After complete solidification of the tested material, measurements were made in the solid state. The electric heater (inside the pipe Poensgen apparatus) was set to heat the solidified tested material to the temperature of approx. 294.15 K. After achieving a constant temperature gradient at the walls of the pipe Poensgen apparatus, measurements of the tested material in the solid state began. The obtained averaged thermal conductivity results are shown in grey in Fig. 3b (depending on the mass content of GNP in NEPCM).

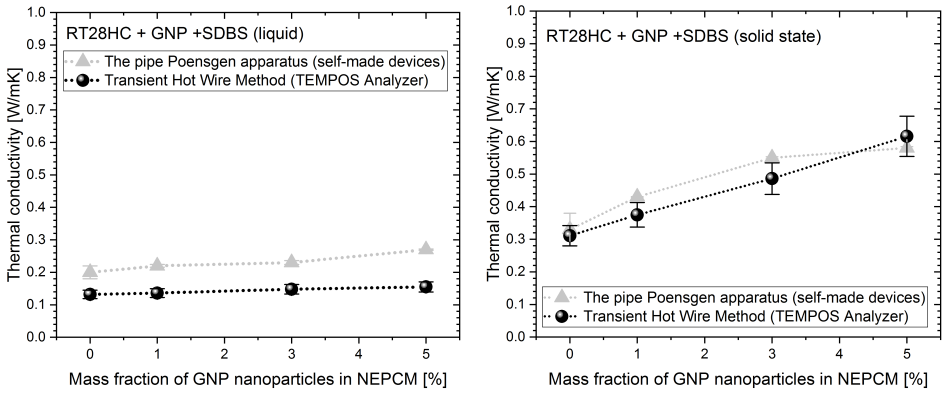


(a) (b)

Figure 3: Results of thermal conductivity of NEPCM – RT28 HC with GNP and SDBS admixtures (depending on the content of GNP nanoparticles in the mixture): (a) in the liquid; (b) in the solid state. The thermal conductivity of base RT28 HC (without nanomaterials) was marked by a point of 0% mass fraction.

Right after preparation, material samples (prepared with the same mass fraction of GNP and SDBS nanoparticles as the samples tested in the pipe Poensgen apparatus) were poured into special containers or test tubes with a flat bottom before measurement using the Tempos analyzer. Material samples poured into screw-on test tubes with a flat bottom (after inserting the KS-3 sensor through the hole in the test tube cap) were placed in a thermal chamber filled with air at a temperature of approx. 305.15–306.15 K to perform the measurement in the liquid. The measurement in the liquid was started after the sample temperature stabilized. The measurement in the liquid using the Tempos analyzer was performed 5 times, and the average of the measurements is marked in black in Fig. 3a. These material samples poured into special containers were placed in the refrigerator to "quickly"

solidify, and after solidification, two holes were made in them to place the SH-3 sensor. Thermal conductivity tests in the solid state were carried out at room temperature (approx. 296.15–297.15 K). The solid-state measurement using the Tempos analyzer was performed 5 times, and the results of the average thermal conductivity are marked in black in Fig. 3b.

The results of thermal conductivity measured with the pipe Poensgen apparatus and Tempos analyzer indicate that as the mass fraction of graphene and SDBS in NEPCM increases, the thermal conductivity of organic PCM – RT28 HC increases too (see Fig. 3).

The analysis of measurements of the thermal conductivity of the RT28 HC material in the solid state indicates that depending on the mass content of graphene nanoparticles in the range of 1–5%, the thermal conductivity increases by 0.1–0.25 W/m·K when measured using the pipe Poensgen apparatus, and by 0.06–0.30 W/m·K when measured with the Tempos analyzer (see Fig. 3b), compared to the thermal conductivity of "pure" RT28 HC. The highest thermal conductivity in the solid state was obtained by RT28 HC with SDBS and 5% GNP mass fraction, the value of which when measured with the pipe Poensgen apparatus was $0.58 \pm 0.03$ W/m·K, and measured with a Tempos analyzer was $0.62 \pm 0.06$ W/m·K. On the other hand, the thermal conductivity of RT28 HC with SDBS and 1% GNP mass fraction reached $0.43 \pm 0.001$ W/m·K with the pipe Poesngen apparatus, and $0.38 \pm 0.04$ W/m·K with the Tempos analyzer.

The results of thermal conductivity in the liquid indicate an increase in the thermal conductivity of RT28 HC as a result of doping it with GNP and SDBS (depending on the mass fraction of GNP in the range of 1–5%) by 0.02–0.07 W/m·K in measurements with the pipe Poensgen apparatus, and by 0.004–0.023 W/m·K in measurements with the Tempos analyzer (see Fig. 3a). The highest thermal conductivity in the liquid was achieved for RT28 HC with SDBS and 5% mass fraction of GNP ($0.27 \pm 0.002$ W/m·K with PPA and approx. $0.16 \pm 0.02$ W/m·K with the Tempos analyzer), and the lowest for RT28 HC with SDBS and 1% mass fraction of GNP ($0.22 \pm 0.004$ W/m·K with PPA and approx. $0.14 \pm 0.01$ W/m·K with the Tempos analyzer).

The results of thermal conductivity measurements of the base PCM and prepared NEPCMs obtained using two different measurement methods (PPA and THW methods) reach slightly different values. Slightly higher values are observed for measurements obtained using the pipe Poensgen apparatus method, but it shows very good agreement with the results achieved using the THW method in both states (liquid and solid state).

In order to determine the effect of admixtures (GNP and SDBS nanoparticles) on the properties determining the ability to store energy by organic RT28 HC, such as the heat capacity and the phase change temperature range, NEPCMs with different mass fractions of nanoadditives were tested using the DSC method. A summary of the obtained values of heat capacity and solidification and melting temperatures in DSC measurements is presented in Table 2. However, to clearly show the impact of admixtures on the change in the heat capacity of the base organic PCM, Fig. 4 presents the results of the heat capacity values, determined for the temperature range of 294.15–308.15 K, depending on the mass fraction of GNPs.

Table 2: Thermophysical properties of the base RT28 HC and RT28HC doped with GNP and SDBS obtained in DSC measurement.

| Test material | $T_{m,\text{onset}}$ (K) | $T_{m,\text{peak}}$ (K) | $C^h$ (J/g) | $T_{s,\text{onset}}$ (K) | $T_{s,\text{peak}}$ (K) | $C^c$ (J/g) |
|---|---|---|---|---|---|---|
| RT28 HC | 299.53 | 302.1 | 255 | 299.17 | 298.15 | 210 |
| RT28 HC with 1% GNP + SDBS | 299.45 | 302.7 | 212 | 299.15 | 297.44 | 195 |
| RT28 HC with 3% GNP + SDBS | 299.38 | 301.48 | 200 | 299.15 | 298.29 | 174 |
| RT28 HC with 5% GNP + SDBS | 299.55 | 301.1 | 169 | 299.15 | 298.93 | 147 |

$^h$ heating process, $^c$ cooling process.

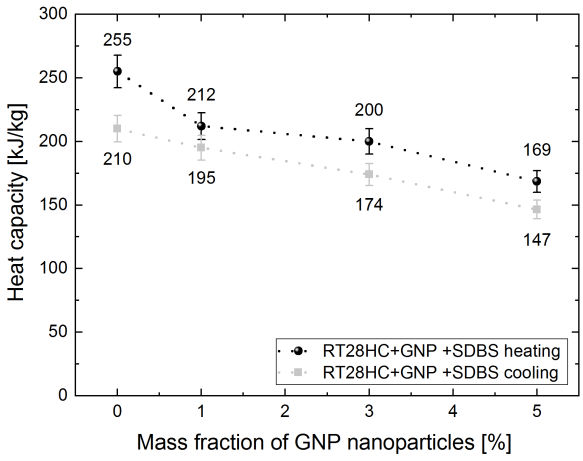


Figure 4: Heat storage capacity results of NEPCM – RT28 HC with GNP and SDBS admixtures (depending on the mass fraction of GNP nanoparticles in the mixture). The heat capacity of base RT28 HC (without nanomaterials) was marked by a point of 0% mass fraction.

The heat capacity results presented in Fig. 4 and Table 2 indicate that as the mass content of admixtures increases, the heat capacity of the base RT28 HC decreases. The decrease in heat capacity in the heating process is 17–34%, and in the cooling process 7–30%. The smallest decrease in heat capacity was obtained for RT28 HC with SDBS and 1% wt. graphene nanoparticles. Based on the DSC measurement results, it was not found that the selected admixtures had an impact on the phase transition temperature range of RT28 HC.

## 4 Discussion

The thermal conductivity experiment results clearly show that after adding graphene nanoparticles and stabilizer (SDBS) to organic RT28 HC, its thermal conductivity is improved. To determine the effect of graphene nanoparticles and their mass fraction on the improvement of the thermal conductivity of RT28 HC, the thermal conductivity enhancement factor was calculated as the ratio of the thermal conductivity of RT28 HC with the specific mass fraction of GNP to the thermal conductivity of the base RT28 HC (see Fig. 5).

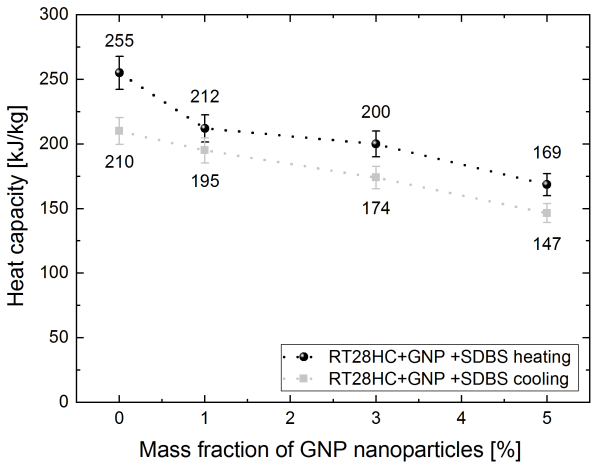


Figure 5: Thermal conductivity enhancement factor of RT28HC with SDBS and GNP nanoparticles (depending on the mass fraction of GNP nanoparticles in NEPCM). The thermal conductivity enhancement factor of base RT28 HC (without nanomaterials) was marked by a point of 0% mass fraction (point 0 – abscissa, and point 1 ordinate).

Based on the thermal conductivity enhancement factor, it can be assumed that the addition of graphene nanoparticles with a weight fraction of 1–5% allowed for an improvement in the thermal conductivity of organic PCM (RT28 HC) by an average of 26–87% in the solid state, and by 7–28% in the liquid. Moreover, a better improvement in thermal conductivity was achieved in the solid state than in the liquid, which was also noticed in the works [15, 20]. Because NEPCM has an ordered microstructure in the solid state but not in the liquid, heat is transferred more efficiently in the solid state. On the other hand, adding admixtures to RT28 HC causes a reduction in the heat capacity of "pure" PCM. This happens because the PCM content in the mixture decreases.

Figure 6 shows a comparison of thermal conductivity (average of the results of experimental measurements obtained by the PPA and THW methods) and heat capacity (average of the results of the heating and cooling process obtained by the DSC method) of base organic PCM (RT28 HC) and NEPCM (RT28 HC with GNP and SDBS). Based on Fig. 6, it can be concluded that as the mass fraction of graphene nanoparticles in RT28 HC increases, its thermal conductivity increases and the ability to accumulate energy decreases. In the case of a heating (or cooling) system, where it

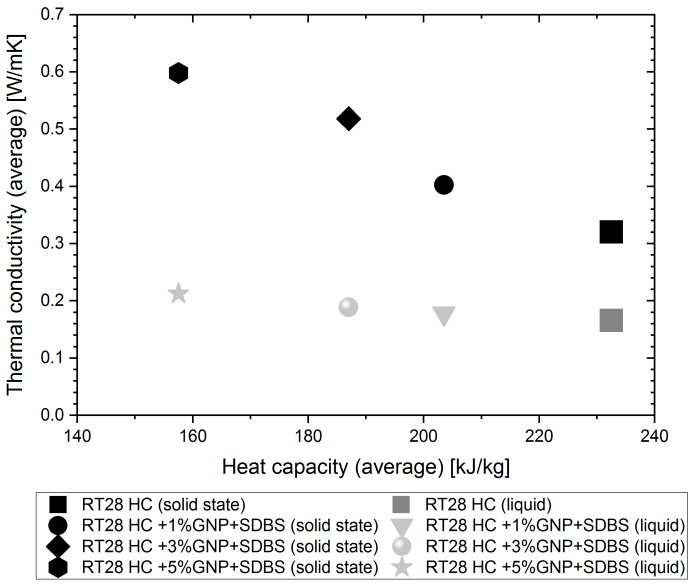


Figure 6: Comparison of thermal conductivity and latent heat obtained in tests of base RT28 HC and RT28 HC with graphene and SDBS nanoparticles.

is required to quickly absorb and release energy by the storage (LHTES), a better choice is to use a phase change material with the highest possible thermal conductivity coefficient, i.e. in this case the highest mass fraction of graphene nanoparticles – RT28 HC with SDBS and 5% weight fraction of graphene nanoparticles. However, in most cases, the decisive factor in choosing the accumulation material for LHTES is its high heat capacity. Therefore, it is important for NEPCM – in this case, RT28 HC with GNP and SDBS, to find the optimum between the increased thermal conductivity and the smallest reduction in the heat capacity of the material. Figure 6 shows that such optimal values are obtained by adding graphene nanoparticles with a mass fraction of 1% to RT28 HC.

## 5 Conclusions

In this research, the effect of addition of graphene nanoparticles on the thermal conductivity of organic PCM (RT28 HC) and its energy storage properties was investigated. Two independent methods were used to test the thermal conductivity: the transient hot wire method (commonly used in NEPCM measurements) and the pipe Poensgen apparatus method (which has not been used so far to measure the thermal conductivity of NEPCM). Additionally, the DSC method was used to determine the heat capacity and phase change temperature. The results of this research are summarized and the main conclusions are presented as follows:

- thermal conductivity results obtained using the pipe Poensgen apparatus are in good agreement with the measurement results performed using the transient hot wire method (Tempos analyzer);
- the addition of graphene nanoparticles to organic PCM (RT28 HC) increases its thermal conductivity in solids and liquids, and with the increase in the mass fraction of graphene nanoparticles, the enhancement of the thermal conductivity of RT28 HC is greater;
- characteristics of the thermal conductivity enhancement factor show that the addition of graphene nanoparticles (with a weight fraction of 1–5%) allowed for an improvement in the thermal conductivity of RT28 HC by an average of 26–87% in the solid state and by 7–28% in the liquid;

- the addition of graphene nanoparticles and stabilizer (SDBS) does not affect the temperature range of phase change, but reduces the heat capacity of RT28 HC by 17–34% in the heating process and by 7–30% in the cooling process;
- the heat capacity is one of the most important criteria for selecting the storage material in LHTES, so it is important to find the optimum between the increased thermal conductivity coefficient and the smallest reduction in the heat capacity of the material caused by the addition of GNP and SDBS nano-particles to organic PCM;
- characteristic of thermal conductivity versus heat capacity present that the optimal point between the increased thermal conductivity and the reduction in heat capacity is reached for 1% mass fraction of GNP added together with SDBS to RT28 HC.

The research results presented in the article, clearly indicate that the use of graphene nanoparticles has a significant impact on the direct improvement of the thermal conductivity of organic PCM and thus can improve the thermal response of the LHTES storage. Therefore, in the future, it is proposed to carry out comparative tests of the loading and unloading time of LHTES, where the accumulation material will be "pure" RT28 HC and RT28 HC with the addition of SDBS and GNP (with a mass fraction 1%).

*Received 12 December 2023*

## References

[1] Rolka P., Przybylinski T., Kwidzinski R., Lackowski M.: *The heat capacity of low-temperature phase change materials (PCM) applied in thermal energy storage systems*. Renew. Energ. **172**(2021), 541–550. doi: 10.1016/j.renene.2021.03.038

[2] Lizana J., Chacartegui R., Barrios-Padura A., Ortiz C.: *Advanced low-carbon energy measures based on thermal energy storage in buildings: A review*. Renew. Sust. Energ. Rev. **82**(2018), 3, 3705–3749. doi: 10.1016/j.rser.2017.10.093

[3] Mahfuz M.H., Anisur M.R., Kibria M.A., Saidur R., Metselaar I.H.S.C: *Performance investigation of thermal energy storage system with phase change material (PCM) for solar water heating application*. Int. Commun. Heat Mass Transf. **57**(2014), 132–139. doi: 10.1016/j.icheatmasstransfer.2014.07.022

[4] Rolka P., Kwidzinski R., Przybylinski T., Tomaszewski A.: *Thermal characterization of medium-temperature phase change materials (PCMs) for thermal energy storage using the t-history method*. Materials **14**(2021), 7371. doi: 10.3390/ma14237371

[5] Kuta M.: *Mobilized thermal energy storage for waste heat recovery and utilization-discussion on crucial technology aspects*. Energies **15**(2022), 8713. doi: 10.3390/en15228713

[6] Rolka P., Przybylinski T., Kwidzinski R., Lackowski M.: *Thermal properties of RT22 HC and RT28 HC phase change materials proposed to reduce energy consumption in heating and cooling systems*. Renew. Energ. **197**(2022), 462–471. doi: 10.1016/j.renene.2022.07.080

[7] Karwacki J.: *Cooling system with PCM storage for an office building: Experimental investigation aided by a model of the office thermal dynamics*. Materials **14**(2021), 1356. doi: 10.3390/ma14061356

[8] Karwacki J., Kwidzinski R., Leputa P.: *Performance analysis and PCM selection for adsorption chiller aided by energy storage supplied from the district heating system*. Arch. Thermodyn. **43**(2022), 4, 135–169. doi: 10.24425/ather.2022.144409

[9] Vérez D., Borri E., Crespo A., Mselle B., de Gracia Á., Zsembinszki G., Cabeza L.: *Experimental study on two PCM macro-encapsulation designs in a thermal energy storage tank*. Appl. Sci. **11**(2021), 6171. doi: 10.3390/app11136171

[10] Szczesniak A., Bujalski W., Grzebielec A., Futyma K., Karwacki J., Rolka P.: *A hybrid district heating substation with an adsorption chiller and PCM storage units: a concept and preliminary study*. E3S Web Conf. **321**(2021), 02009. doi: 10.1051/e3sconf/202132102009

[11] Berardi U., Soudian S.: *Experimental investigation of latent heat thermal energy storage using PCMs with different melting temperatures for building retrofit*. Energ. Buildings **185**(2019), 180–195. doi: 10.1016/j.enbuild.2018.12.016

[12] Liu Z., Yu Z., Yang T., Qin D., Li S., Zhang G., Haghighat F., Joybari M.: *A review on macro-encapsulated phase change material for building envelope applications*. Build. Environ. **144**(2018), 281–294. doi: 10.1016/j.buildenv.2018.08.030

[13] Stropnik R., Stritih U.: *Increasing the efficiency of PV panel with the use of PCM*, Renew. Energ. **97**(2016), 671–679. doi: 10.1016/j.renene.2016.06.011

[14] Jaworski M.: *Thermal performance of heat spreader for electronics cooling with incorporated phase change material*, Appl. Therm. Eng. **35**(20212), 212–219. doi: 10.1016/j.applthermaleng.2011.10.036

[15] Arshad A., Jabbal M., Yan Y.: *Preparation and characteristics evaluation of mono and hybrid nano-enhanced phase change materials (NePCMs) for thermal management of microelectronics*. Energ. Convers. Manage. **205**(2020), 112444. doi: 10.1016/j.enconman.2019.112444

[16] Sheikholeslami M., Nematpour Keshteli A., Babazadeh H.: *Nanoparticles favorable effects on performance of thermal storage units*. J. Mol. Liq. **300**(20200, 112329. doi: 10.1016/j.molliq.2019.112329

[17] Delgado-Diaz W., Stamatiou A., Maranda S., Waser R., Worlitschek J.: *Comparison of heat transfer enhancement techniques in latent heat storage*. Appl. Sci. **10**(2020), 16, 5519. doi: 10.3390/app10165519

[18] Mesalhy O., Lafdi K., Elgafy A., Bowman K.: *Numerical study for enhancing the thermal conductivity of phase change material (PCM) storage using high thermal conductivity porous matrix*. Energ. Convers. Manage. **46**(2005), 6, 847–867. doi: 10.1016/j.enconman.2004.06.010

[19] Williams J., Peterson G.: *A review of thermal property enhancements of low-temperature nano-enhanced phase change materials*. Nanomaterials **11**(2021), 2578. doi: 10.3390/nano11102578

[20] Jebasingh E., Arasu V.: *A comprehensive review on latent heat and thermal conductivity of nanoparticle dispersed phase change material for low-temperature applications*. Energ. Stor. Mater. **24**(2020), 52–74. doi: 10.1016/j.ensm.2019.07.031

[21] Wu S.Y., Wang H., Xiao S.: *An investigation of melting/freezing characteristics of nanoparticle-enhanced phase change materials*. J. Therm. Anal. Calorim. **110**(2012), 1127. doi: 10.1007/s10973-011-2080-x

[22] Temel Ü.N., Çiftçi B.Y.: *Determination of thermal properties of A82 organic phase change material embedded with different type nanoparticles*. IsıBilimi ve Tekniği Dergisi **38**(2018), 2, 75–85.

[23] Radhakrishnan N., Thomas S., Sobhan C.B.: *Characterization of thermophysical properties of nano-enhanced organic phase change materials using T-history method*. J. Therm. Anal. Calorim. **140**(2020), 2471–2484. doi: 10.1007/s10973-019-08976-1

[24] Choi D.H., Lee J., Hong H., Kang Y.T.: *Thermal conductivity and heat transfer performance enhancement of phase change materials (PCM) containing carbon additives for heat storage application*. Int. J. Refrig. **42**(2012), 12–120. doi: 10.1016/j.ijrefrig.2014.02.004

[25] Mehrali M., Sadeghinezhad E., Latibari S.T., Kazi S.N., Mehrali M., Zubir M.N., Metselaar H.S.C.: *Investigation of thermal conductivity and rheological properties of nanofluids containing graphene nanoplatelets*. Nanoscale Res Lett. **9**(2014), 15. doi: 10.1186/1556-276X-9-15

[26] Manufacturer's data of graphene nanoparticles. PlasmaChem. https://www.plasmachem.com (accessed 9 Oct. 2023).

[27] Manufacturer's data of sodium dodecylbenzenesulfonate. Sigma-Aldrich. https://www.sigmaaldrich.com/PL/pl/product/aldrich/289957 (accessed 9 Oct. 2023).

[28] Manufacturer's data of RT28 HC Rubitherm. https://www.rubitherm.eu/en/productcategory/organische-pcm-rt (accessed 9 Oct. 2023).

[29] Soares N.: *Thermal energy storage with phase change materials (PCMs) for the improvement of the energy performance of buildings*. PhD thesis, University of Coimbra, Coimbra 2015.

[30] Lovelyn T., Velraj R.: *Thermophysical characterization and comparison of PCMs using DSC and T-History experimental setup*. Mater. Res. Express **6**(2019), 12, 125527. doi: 10.1088/2053-1591/ab5aae

**archives**
**of thermodynamics**
Vol. **44**(2023), No. 4, 123–139
DOI: 10.24425/ather.2023.149732

# New empirical correlations for the viscosity of selected organic phase change materials

**JANUSZ TADEUSZ CIEŚLIŃSKI**[a*]
**MACIEJ FABRYKIEWICZ**[a]
**TOMASZ STEFAN WIŚNIEWSKI**[b]
**MICHAŁ KUBIŚ**[b]
**SŁAWOMIR SMOLEŃ**[c]
**ALBRECHT EICKE**[c]
**KRZYSZTOF DUTKOWSKI**[d]
**MAŁGORZATA GŁUSZEK-CZARNECKA**[e]

[a] Gdansk University of Technology, Narutowicza 11/12, 80-233 Gdańsk, Poland

[b] Warsaw University of Technology, Nowowiejska 21/25, 00-665 Warsaw, Poland

[c] Hochschule Bremen, JR Mayer-Institut für Energietechnik, Neustadswall 30, 28199 Bremen, Germany

[d] Koszalin University of Technology, Racławicka 15-17, 75-620 Koszalin, Poland

[e] Smart Fluid Inc., Rydygiera 8/20A, 01-793 Warsaw, Poland

**Abstract** Although there are many methods and instruments for measuring viscosity, it is still difficult to determine a reliable value of the dynamic viscosity of complex chemicals such as paraffins and fatty acids. This is due to the complex and heterogeneous structure of these compounds in the case of commercial products. On the other hand, the measuring instrument should be selected very carefully, including its measuring principle and measuring range. This paper presents results of viscosity measurements of three organic PCMs (phase change materials) obtained in four different research institutions. Commercial products: paraffin, myristic acid (97%) and mixture of palmitic acid (55%) and stearic acid (45%) were selected

*Corresponding Author. Email: jcieslin@pg.edu.pl

as PCMs. Four different viscometers, namely Fungilab V-Pad, Rheotest LK 2.2, Rheometer Anton Paar MCR 102, and Brookfield DV-II + Pro have been used to determine temperature dependent dynamic viscosity of the tested PCMs. Using a large database of present measurement results, correlations were developed to calculate the dynamic viscosity of fatty acids and paraffins, which predict the experimental data within a band of ±20%.

**Keywords**: PCM; Viscosity; Viscometers; Temperature; Shear rate

## Nomenclature

| | | |
|---|---|---|
| $c$ | – | specific heat, J/(kgK) |
| $D$ | – | diameter, mm |
| $L$ | – | length, mm |
| $n$ | – | speed of rotation, 1/min |
| $r$ | – | heat of phase transition, J/g |
| $t$ | – | temperature, °C |

### Greek symbols

| | | |
|---|---|---|
| $\mu$ | – | dynamic viscosity, mPa·s |

### Subscripts and superscripts

| | | |
|---|---|---|
| $c$ | – | cooling |
| $h$ | – | heating |
| $l$ | – | liquid |
| $m$ | – | mean |
| max | – | maximum |
| min | – | minimum |
| $p$ | – | constant pressure |
| $s$ | – | solid |
| $'$ | – | initial |
| $''$ | – | final |

### Acronyms

| | | |
|---|---|---|
| DSC | – | differential scanning calorimetry |
| PCM | – | phase change material |

# 1 Introduction

Thermal energy storage with phase change materials (PCMs) is of key importance in many areas, such as building [1], heating and air conditioning [2], cooling of portable electronic devices [3], preventing overheating of batteries [4], refrigeration [5], thermoregulated textiles [6] or improving the efficiency of cogeneration systems [7]. Such common use of PCMs requires

knowledge of their thermophysical properties, including viscosity. Although there are many methods and instruments for measuring viscosity, it is still difficult to determine a reliable dynamic viscosity of complex chemicals such as paraffins and fatty acids. This is due to the complex and heterogeneous structure of these compounds in the case of commercial products. Data regarding viscosity of organic PCMs are very sparse. Noureddini *et al.* [8] measured the viscosity of a few vegetable oils and fatty acids. Correlations for viscosity in the temperature scope from 24°C to 110°C have been proposed. Valeri and Meirelles [9] determined a kinematic viscosity of a number of fatty acids and triglycerides. The measurement results for pure components were generalized in the form of correlations as a function of temperature. Correlations for calculating the kinematic viscosity of mixtures of fatty acids and triglycerides have also been developed. González *et al.* [10] measured viscosity of several fatty acids in a wide temperature range: from melting point up to 100°C. Correlations for calculating a dynamic viscosity have been proposed. Rabelo *et al.* [11] determined viscosity of selected pure fatty acids and their mixtures. Measurements were realized in the temperature scope from 20°C to 90°C. A complex correlation for calculating the dynamic viscosity was developed, taking into account the atomic structure of the tested compounds. Ayranci and Akgul [12] measured viscosity of several fatty acids in 2-butanol as a function of concentration in the temperature range from 20°C to 60°C. It was established that for given temperature and concentration viscosity of all tested mixtures increased with the carbon number of the fatty acid. Ferrer and Barreneche *et al.* [13] determined viscosity of a number of fatty acids within the temperature range from 40°C to 100°C. Among the several types of equations tested, it turned out that polynomials give the best results in correlating the obtained experimental data. Ferrer *et al.* [14] and Barreneche *et al.* [15] measured viscosity for a few paraffins. A complex correlation has been developed to calculate the viscosity of a large group of paraffins, taking into account the melting point. Delgado *et al.* [16] proposed an approach for measurement viscosity of almost pure octadecane. Moreover Delgado *et al.* [17,18] presented results of viscosity measurements of the Parafol 18–97 and paraffin conducted by independent institutions. The measurements were realized within temperature scope 25–80°C and large shear rate range 1.65–1000 $s^{-1}$. The highest deviations were observed when uniform temperature throughout the sample was not preserved. Outside of design goals, reliably measured viscosity may serve as benchmark for new categories of thermal fluids, as nanocomposites [19,20], microencapsulated slurries [21,22], shear

thickening fluids [23,24], re-melted suspensions [25,26], non-Newtonian fluids [27], or nanofluids [28–30].

In present study, the viscosity of three organic PCMs has been measured in five different organizations. Commercial products: paraffin, myristic acid (97%) and mixture of palmitic acid (55%) and stearic acid (45%) were selected as PCMs. Four different viscometers, namely Fungilab V-Pad, Rheotest LK 2.2, Rheometer Anton Paar MCR 102, and Brookfield DV-II + Pro have been used to determine temperature dependent dynamic viscosity of the tested PCMs. The prime aim of the present study is to develop a reliable correlations for dynamic viscosity of fatty acids and paraffins.

## 2 Materials

Three commercial organic materials have been tested: paraffin LTP 56 supplied by Polwax S.A. Jaslo, Poland, fatty acid RT54HC supplied by Rubitherm Technologies GmbH Berlin, Germany, and fatty acid P1801 supplied by Konimpex Chemicals Konin, Poland. Table 1 shows the description of the used materials.

Table 1: Materials characteristics.

| Product | Substance | Formula | Share | |
|---|---|---|---|---|
| LTP 56 | Paraffin | $C_{19}H_{38}$–$C_{32}H_{65}$ | 100% | |
| RT54HC | Fatty acid | $C_{14}H_{28}O_2$ | 97% | |
| P1801 | Fatty acid | $C_{16}H_{32}O_2$ Palmitic acid | 58% | 96% |
| | | $C_{17}H_{35}O_2$ Stearic acid | 38% | |

The detailed chemical composition of the tested materials was determined on the basis of chromatographic tests using the GC-MS-QP2010 PLUS Shimadzu gas chromatograph (Fig. 1).

The range of phase transition temperatures, heat of phase transition, and specific heat of the tested materials were estimated by differential scanning calorimetry (DSC) method using the TA Q1000 DSC. The results of the analysis are presented in Fig. 2. As shown in Fig. 2, each tested material exhibits different ranges of the melting and solidification phase transition temperatures. During the melting cycle of LTP56 (Fig. 2a), two peaks are visible, which indicates a different chemical composition. In the case of the solidification cycle, one of the peaks was not recorded due to the limitations

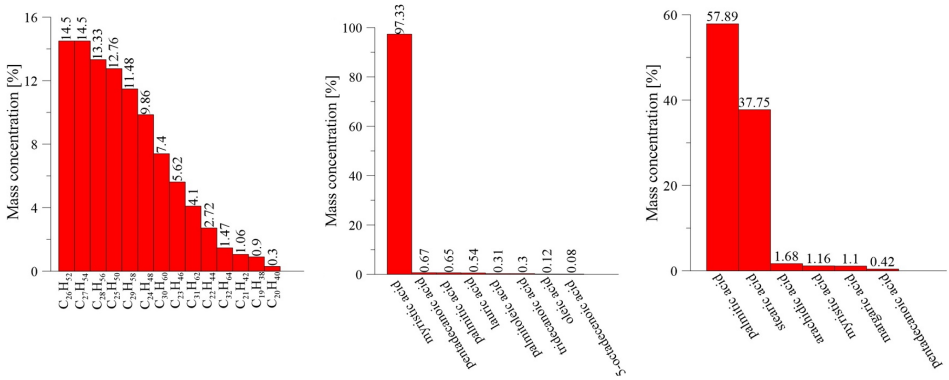


Figure 1: Results of the chromatographic analysis: (a) LTP56, (b) RT54HC, (c) P1801.

of the apparatus used. RT54HC and P1801 show single peaks for both the melting and solidification cycles, which means that the individual chemical compounds of a given material have a similar phase transition temperature. The highest heat of phase transition is shown by RT54HC, which additionally has a higher heat of phase transition during the melting cycle compared to the solidification cycle.

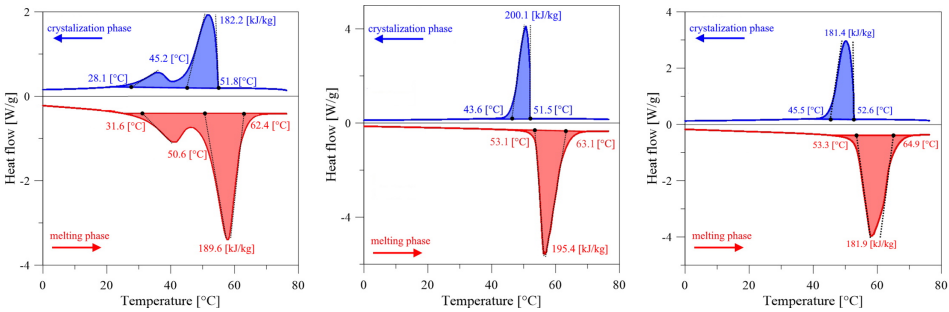


Figure 2: Results of the DSC analysis: (a) LTP56, (b) RT54HC, (c) P1801.

Table 2 shows the results of the DSC measurements of the tested materials, where $t'_h$, $t''_h$, $t'_c$, and $t''_c$ represent initial and final temperature of phase transition during heating and cooling processes (Fig. 2), respectively. Specific heat at constant pressure ($c_p$) for solid and liquid phases and heat of phase transition for heating ($r_h$) and cooling ($r_c$) processes are presented, too.

Table 2: DSC characteristics of the tested materials.

| Parameter | Unit | LTP56 | RT54HC | P1801 |
|---|---|---|---|---|
| $t'_c$ | °C | 51.8 | 43.6 | 52.6 |
| $t''_c$ | °C | 28.1 | 51.5 | 45.5 |
| $t'_h$ | °C | 31.6 | 53.1 | 53.3 |
| $t''_h$ | °C | 62.4 | 63.1 | 64.9 |
| $c_{p_{h,s}}$ | J/(gK) | 2.27 | 1.73 | 1.99 |
| $c_{p_{h,s}}$ | J/(gK) | 2.49 | 2.09 | 2.26 |
| $c_{p_{c,s}}$ | J/(gK) | 2.70 | 1.93 | 2.03 |
| $c_{p_{c,l}}$ | J/(gK) | 2.20 | 2.04 | 1.97 |
| $r_h$ | J/g | 185.9 | 195.4 | 181.9 |
| $r_c$ | J/g | 182.2 | 200.1 | 181.4 |

# 3 Methods

The devices used in each laboratory taking part in the intercomparative tests are specified in Table 3. A large dispersion of the sample volumes used in individual devices as well as the minimum ($n_{\min}$) and maximum ($n_{\max}$) rotation speeds of the spindle or the plate are noticeable.

Table 3: Technical specification of the used instruments.

| Organization | Instrument | Sample (ml) | Speed of rotation (1/min) | |
|---|---|---|---|---|
| | | | $n_{\min}$ | $n_{\max}$ |
| Gdańsk University of Technology | Fungilab V-Pad Spindle L1 | 600 | 0.3 | 250 |
| Warsaw University of Technology | Brookfield DV-II + Pro Spindle SCR-21 | 7.5 | 0.1 | 200 |
| Hochschule Bremen | Rheotest LK 2.2 Capillary 1/2: $D = 1$ mm, $L = 80$ mm | 25 | – | – |
| Koszalin University of Technology | Brookfield DV-II + Pro Spindle SC4-18 | 6.7 | 0.1 | 200 |
| Smart Fluid Inc. | Anton Paar MCR 102 Plate $D = 40$ mm | 0.38 | 0.1 | 1000 |

Table 4 shows measurement range and measurement uncertainty according to the producers of the viscometers, where $\mu_{\max}$ and $\mu^P_{\min}$ represent maximum measurable viscosity and minimum measurable viscosity for given spindle (plate) and speed of rotation, respectively.

Table 4: Measurement range and uncertainty.

| Instrument | $n$ (1/min) | $\mu_{\max}$ (mPa·s) | $\mu^P_{\min}$ par (mPa·s) | Relative error (%) |
|---|---|---|---|---|
| Fungilab V-Pad Spindle L1 | 0.3 | $2 \cdot 10^4$ | 3200 | ±1 |
| | 250 | 24 | 3.84 | |
| Brookfield DV-II + Pro Spindle SCR-21 | 0.1 | $1 \cdot 10^6$ | 32000 | ±1 |
| | 200 | 50 | 5.0 | |
| Rheotest LK 2.2 Capillary 1/2: $D = 1$ mm, $L = 80$ mm | – | 16 | 1 | $\leq 2$ |
| Brookfield DV-II + Pro Spindle SC4-18 | 0.1 | $32 \cdot 10^4$ | 32000 | ±1 |
| | 200 | 1.6 | 1.6 | |
| Anton Paar MCR 102 Plate $D$ =40 mm | 0.1 | $250 \cdot 10^6$ | – | ±3 |
| | 1000 | $250 \cdot 10^6$ | – | |

## 4 Results and discussion

In Figs. 3 to 5 dynamic viscosity against shear rate for temperature 60°C of three tested PCMs is shown. The results obtained with Fungilab V-Pad viscometer are omitted because the device is not equipped with a sample adapter, therefore it was impossible to estimate shear rate. Shear rates for capillary viscometer Rheotest LK 2.2 were not assigned, too.

From Figs. 3 to 5 it can be seen that the viscosity of LTP56 at 60°C is between 6 mPa·s and 8.5 mPa·s, while the viscosity of P1801 is between 10 mPa·s and 13 mPa·s. This means that the viscosity of P1801 is twice that of LTP56. The viscosity of RT54HC lies between LTP56 and P1801. Under the same conditions, regardless of the substance tested, the Brookfield DV-II + Pro (Spindle SCR-21) gave the lowest viscosity and the Anton Paar MCR 102 gave the highest. The measuring points for LTP56 (Fig. 3) and RT54HC (Fig. 4) at minimum shear rate obtained with Brookfield DV-II + Pro and SCR-21 spindle deviate significantly from the trend line. This may indicate that the measurements were taken performed close near to the instrument's limit, at its lower range. It is characteristic that, regard-

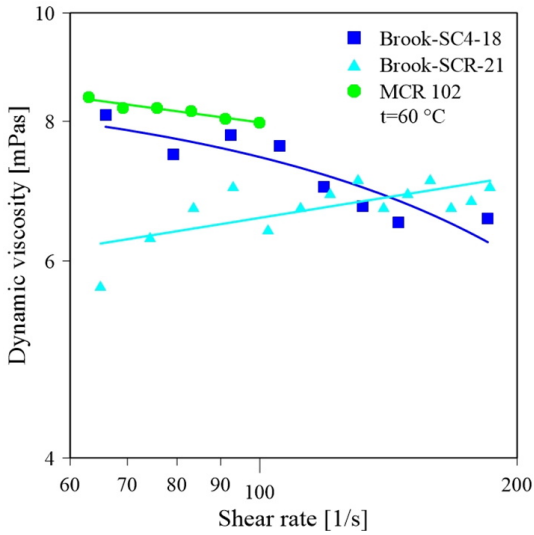


Figure 3: Dynamic viscosity of LTP56 versus shear rate.

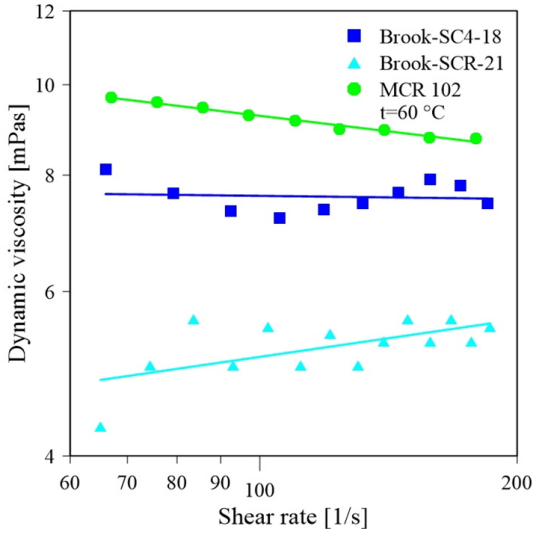


Figure 4: Dynamic viscosity of RT54HC versus shear rate.

less of the substance tested, the viscosity measured using the Anton Paar MCR 102 and Brookfield DV-II + Pro (Spindle SC4-18) decreases slightly with increasing shear rate, whereas the results obtained using the Brookfield DV-II + Pro (Spindle SCR-21) show the opposite tendency. Changes in the

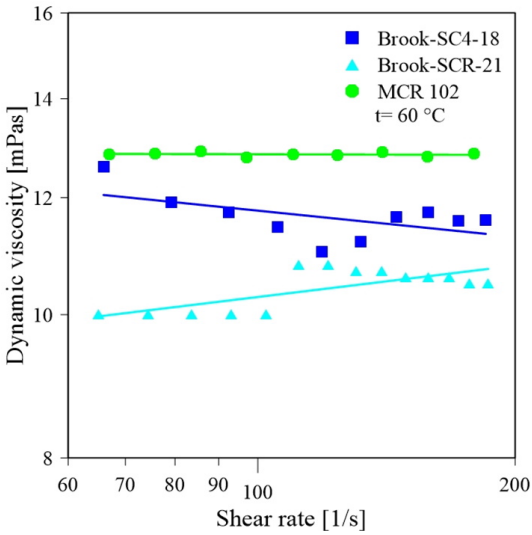


Figure 5: Dynamic viscosity of P1801 versus shear rate.

dynamic viscosity of the three PCMs tested are within the measurement error limits, so the viscosity can be considered as constant regardless of the measuring devices used. It was, therefore, assumed that LTP56, P1801 and RT54HC at a temperature of 60°C have the rheological properties of Newtonian fluids where viscosity is independent on the shear rate. Consequently, Brookfield DV-II + Pro (Spindle SCR-21) showed an average viscosity of 6.71 mPa·s (LTP56), 5.24 mPa·s (RT54HC), and 10.41 mPa·s (P1801). The average viscosity determined by using the Brookfield DV-II + Pro (Spindle SC4-18) compared to the results obtained using the Brookfield DV-II + Pro (Spindle SCR-21) was approximately 7% (LTP56), 40% (RT54HC), and 11% (P1801) higher and in comparison to the data obtained using the Anton Paar MCR 102, the average viscosity was approximately 28%, 75%, and 23% higher for LTP56, RT54HC, and P1808, respectively. It is worth emphasizing that the measurement results presented in Figs. 3 to 5 were obtained at a temperature of 60°C, i.e. a temperature close to the melting point of the tested PCMs. Thereforer, the temperature inside the tested samples could not be uniform, which in turn could affect the measurement results obtained.

In Figs. 6 to 8 dynamic viscosity against temperature of three tested PCMs is shown. First of all, there is a large variation in the results obtained with Fungilab V-Pad depending on the spindle speed. The device used was

not equipped with a commercially available sample adapter. Following the manufacturer's recommendations the measurements were performed with sample volume 600 ml, that is very large in comparison with other devices (Table 3).

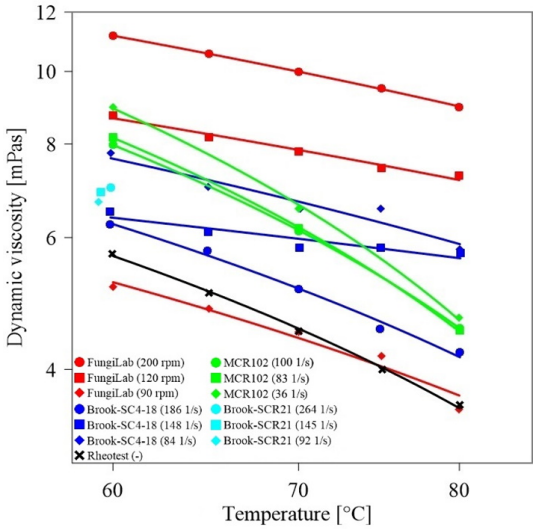


Figure 6: Dynamic viscosity of LTP56 versus temperature.

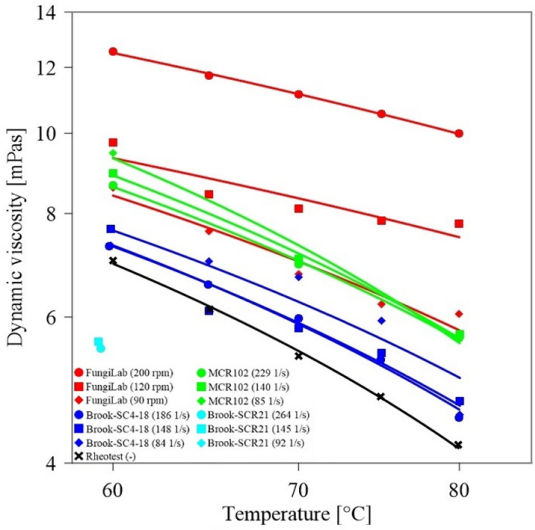


Figure 7: Dynamic viscosity of RT54HC versus temperature.

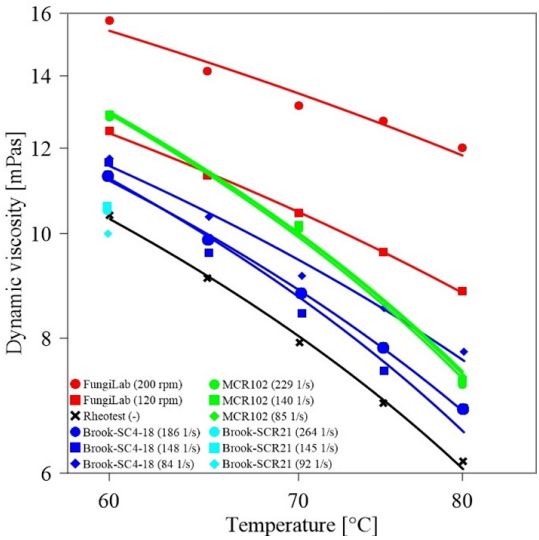


Figure 8: Dynamic viscosity of P1801 versus temperature.

As can be seen in Figs. 6 to 8 for Fungilab V-Pad measurements dynamic viscosity increases with speed of spindle rotation. Irrespective of the PCMs tested the highest dynamic viscosity was observed for the highest speed of spindle rotation used (200 rpm). According to the manufacturer the measurement uncertainty is ±1% of the full scale range and depends on the spindle type and speed of rotation (Table 4). The Brookfield DV-II + Pro equipped with the SCR-21 spindle allowed the measurement of dynamic viscosity only for $t = 60°C$. At higher temperature the viscosity of the PCMs examined was too low. In order to check the behavior of liquid PCMs under the influence of increasing shear stress the tests were carried out for the spindle rotational speeds in the range of 40–200 rpm. As can be seen in Figs. 6 and 7 the dynamic viscosity increases slightly with spindle rotational speed for LTP 56 and P1801, respectively. For RT54HC (Fig. 8) no effect of spindle rotational speed on dynamic viscosity was observed. The use of the Brookfield DV-II + Pro equipped with the SC4-18 spindle allowed the measurement of dynamic viscosity within the temperature range 60–80°C and for spindle rotational speeds between 50 and 200 rpm. However, the measurements were made close to the minimum torque, i.e. 10%. This means that the results may be biased by a large error. This fact probably explains the contradictory influence of spindle rotational viscosity measured using the Fungilab V-Pad and Brookfield DV-II + Pro equipped with the

SC4-18 spindle. As can be seen in Fig. 6 the dynamic viscosity of P1801 measured using the Anton Paar MCR 102 is independent of rotational speed. Rheotest LK 2.2 capillary viscometer – gave the lowest dynamic viscosity values regardless of PCM type and temperature.

Using data obtained with 4 instruments, i.e. Brookfield DV-II + Pro O with spindle SCR-21, Brookfield DV-II + Pro with spindle SC4-18, Anton Paar MCR 102 and Rheotest LK 2.2, least squares regression analysis was used to establish correlation equations for predicting the dynamic viscosity of the tested PCMs at different temperatures. These correlations for LTP 56, RT54HC, and P1801 respectively have the form:

$$\mu = 24.3e^{-2.05\cdot 10^{-2}t}, \tag{1}$$

$$\mu = 21.1e^{-1.77\cdot 10^{-2}t}, \tag{2}$$

$$\mu = 47.8e^{-2.39\cdot 10^{-2}t}, \tag{3}$$

where $\mu$ is the dynamic viscosity in mPa·s and $t$ is the temperature in °C.

In Fig. 9 a comparison of predicted data against the experimentally obtained is displayed for LTP56. For 66% of the experimental points the discrepancy between the experimental data and the values calculated from the proposed correlation is less than ±20%. In addition, Fig. 9 shows the correlation developed by Ferrer *et al.* [17] for paraffin RT55, for which the melting temperature is close to LTP56:

$$\mu = \left(0.02584 - 0.0007849t + 9.801\cdot 10^{-6}t^2 - 4.388\cdot 10^{-8}t^3\right). \tag{4}$$

As can be seen in Fig. 9, the correlation of Ferrer *et al.* [17] underestimates the dynamic viscosity of LTP56 by about 49% compared to the present correlation.

In Fig. 10 a comparison of the predicted data with the experimentally obtained is displayed for RT54HC. For 81% of the experimental points the discrepancy between the experimental data and the values calculated from the proposed correlation is less than ±5%. In addition, Fig. 10 shows the correlation developed by Ferrer *et al.* [16] for fatty acids:

$$\mu = \left(2.95\cdot 10^{-2} - 7.80\cdot 10^{-4}t + 8.37\cdot 10^{-6}t^2 - 3.42\cdot 10^{-8}t^3\right)c, \tag{5}$$

where $c$ is a correction factor on PCM melting temperature

$$c = 15.38 - 0.3t_m + 1.1\cdot 10^{-3}t_m^2. \tag{6}$$

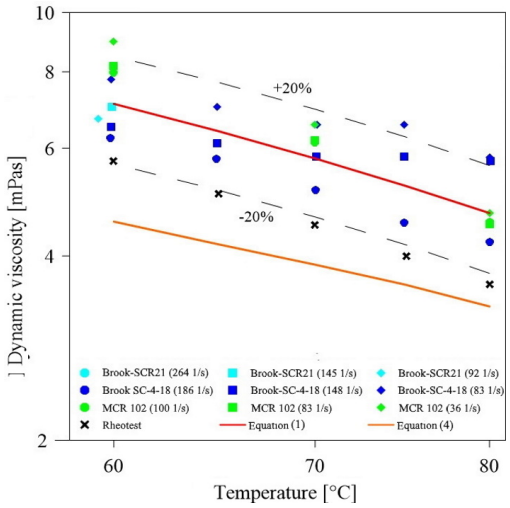


Figure 9: Comparison of measured and calculated dynamic viscosity of LTP56.

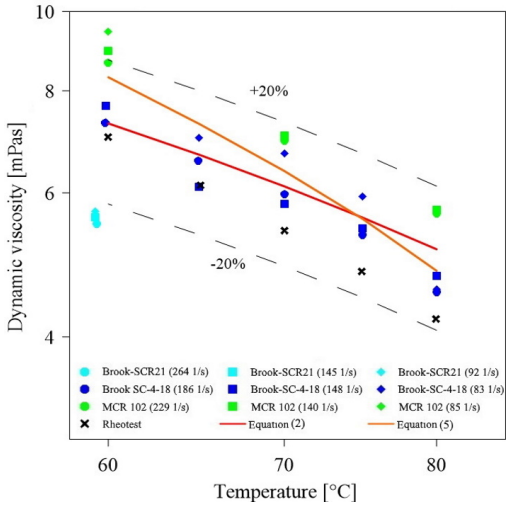


Figure 10: Comparison of measured and calculated dynamic viscosity of RT54HC.

Here the temperature $t_m$ was assumed as the arithmetic mean of the initial melting point ($t'_{c,m}$) during the cooling process, and the final melting point ($t''_{h,m}$) during the melting process:

$$t_m = \frac{t'_{c,m} + t''_{h,m}}{2}\,. \tag{7}$$

Using the results of the DSC tests (Fig. 2b), $t_m = 58.9°C$ was assumed for the calculations.

As can be seen in Fig. 10, the correlation of Ferrer *et al.*, Eq. (5), overestimates the dynamic viscosity of RT54C by about 11% at lower temperatures and underestimates it by about 4% at higher temperature, compared to the present correlation.

In Fig. 11 a comparison of the predicted data with the experimentally obtained is displayed for P1801. For 100% of the experimental points the discrepancy between the experimental data and the values calculated from the proposed correlation is less than ±15%. In addition, Fig. 11 shows the correlation developed by Ferrer *et al.*, Eq. (5), for fatty acids, A correction factor, Eq. (6), was calculated for $t_m = 59.7°C$ using the results of the DSC tests (Fig. 2c). As can be seen, the correlation of Ferrer *et al.* [16], underestimates the dynamic viscosity of P1801 by approximately 54% compared to the present correlation.

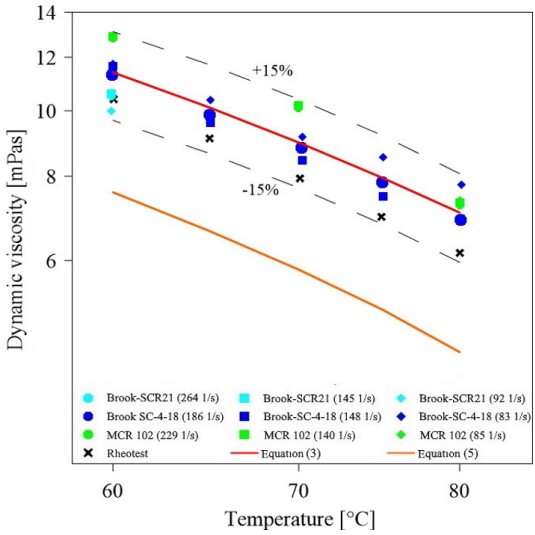


Figure 11: Comparison of measured and calculated dynamic viscosity of P1801.

## 5 Conclusions

The dynamic viscosity-temperature relationships of three phase change materials (PCMs) have been determined using of three spindle rotational viscometers, one plate rotational viscometer, and one capillary viscometer.

A large scatter of results was observed, even when the same type of viscometer (Brookfield DV-II + Pro) was using, which indicates the need for very careful selection of the sample adapter. The results also indicate the need to respect the limitations imposed by the torque limit. The results obtained using the Fungilab V-Pad viscometer are characterised by the greatest uncertainty, due to the lack of precise determination of the geometry of the spindle-sample chamber system. Regardless of the type of PCM, the lowest values of dynamic viscosity were obtained with the capillary viscometer. The discrepancy between the experimental data and the values of dynamic viscosity calculated from the proposed correlation equations does not exceed ±20% for most measurement points. Taking into account the difference in chemical composition, developed correlations reproduce the present results with reasonable agreement.

*Received 28 September 2023*

# References

[1] Kenisarin M., Mahkamov K.: *Passive thermal control in residential buildings using phase change materials.* Renew. Sust. Energ. Rev. **55**(2016), 371–398.

[2] Andrzejczyk R., Kowalczyk T., Kozak P., Muszyński T.: *Experimental and theoretical study of a vertical tube in shell storage unit with biodegradable PCM for low temperature thermal energy storage applications.* Appl. Therm. Eng. **183**(2021), 116216.

[3] Tan F.L., Tso C.P.: *Cooling of mobile electronic devices using phase change materials.* Appl. Therm. Eng. **24**(2004), 159–169.

[4] Liu C., Xu D., Weng J., Zhou S., Li W., Wan Y., Jiang S., Zhou D., Wang J., Huang Q.: *Phase change materials application in battery thermal management system: A Review.* Materials **13**(2020), 4622.

[5] Selvnes H., Allouche Y., Manescu R., Hafner A.: *Review on cold thermal energy storage applied to refrigeration systems using phase change materials.* Therm. Sci. Eng. Prog. **22**(2021), 100807.

[6] Ying B.A., Kwok Y.L., Li Y., Zhu Q.Y., Yeung C.Y.: *Assessing the performance of textiles incorporating phase change materials.* Polym. Test. **23**(2004), 541–549.

[7] Nuytten T., Moreno P., Vanhoudt D., Jespers L., Solé A., Cabeza L.F.: *Comparative analysis of latent thermal energy storage tanks for micro-CHP systems.* Appl. Therm. Eng. **59**(2013), 542–549.

[8] Noureddini H., Teoh B.C., Clements L.D.: *Viscosities of vegetable oils and fatty acids.* J. Am. Oil Chem. Soc. **69**(1992), 1189–1191.

[9] Valeri D., Meirelles A.J.A.: *Viscosities of fatty acids, triglycerides, and their binary mixtures.* J. Am. Oil Chem. Soc. **74**(1997), 1221–1226.

[10] González F.O.C., González M.M.P., Gancedo J.C.B., Suárez R.A.: *Estudio de la densidad y de la viscosidad de algunos ácidos grasos puros*. Grasas y Aceites **50**(1999), 359–368.

[11] Rabelo J., Batista E., Cavaleri F.W., Meirelles A.J.A.: *Viscosity prediction for fatty systems*. J. Am. Oil Chem. Soc. **12**(2000), 1255–1261.

[12] Ayranci E., Akgul G.: *Apparent molar volumes and viscosities of lauric, palmitic, and stearic acids in 2-butanol at (20, 30, 40, and 60)° C*. J. Chem. Eng. Data **48**(2003), 56–60.

[13] Ferrer G., Barreneche C., Palacios A., Solé A., Fernández A.I., Cabeza L.F.: *Empirical equations for viscosity and specific heat capacity determination of fatty acids*. J. Energy Storage **10**(2017), 20–27.

[14] Ferrer G., Gschwander S., Solé A., Barreneche C., Fernández A.I., Schossig P., Cabeza L.F.: *Empirical equation to estimate viscosity of paraffin*. J. Energy Storage **11**(2017), 154–161.

[15] Barreneche C., Ferrer G., Palacios A., Solé A., Fernández A.I., Cabeza L.F.: *Empirical equations for viscosity and specific heat capacity determination of paraffin PCM and fatty acid PCM*. IOP Conf. Ser.: Mater. Sci. Eng. **251**(2017), 012114.

[16] Delgado M., Gschwander S., Lázaro A., Peñalosa C., Zalba B.: *Determining the rheological behavior of octadecane as phase change material: First approach*. Thermochim. Acta **548**(2012), 81–87.

[17] Delgado M., Lázaro A., Biedenbach M., Gamisch S., Gschwander S., Höhlein S., König-Haagen A., Brüggemann D.: *Intercomparative tests on viscosity measurements of phase change materials*. Thermochim. Acta **668**(2018), 159–168.

[18] Delgado M.: *First conclusions of PCM viscosity measurements in the frame of Task 42-Annex 29-IEA*. 1st PCM Rheometry Workshop, Freiburg, 7th March 2018.

[19] Kango S., Kalia S., Celli A., Njuguna J., Habibi Y., Kumar R.: *Surface modification of inorganic nanoparticles for development of organic–inorganic nanocomposites – A review*. Prog. Polymer Sci. **38**(2013), 1232–1261.

[20] Li T.X., Lee J.H., Wang R.Z., Kang Y.K.: *Heat transfer characteristics of phase change nanocomposite materials for thermal energy storage application*. Int. J. Heat Mass Transf. **75**(2014), 1–11.

[21] Giro-Paloma J., Oncins G., Barreneche C., Martínez M., Fernández A.I., Cabeza L.F.: *Physico-chemical and mechanical properties of microencapsulated phase change material*. Appl. Energy **109**(2013), 441–448.

[22] Dutkowski K., Fiuk J.J.: *Experimental investigation of the effects of mass fraction and temperature on the viscosity of microencapsulated PCM slurry*. Int. J. Heat Mass Transf. **126**(2018), 390–399.

[23] Brown E., Jaeger H.M.: *Shear thickening in concentrated suspensions: phenomenology, mechanisms and relations to jamming*. Rep Prog Phys. **77**(2014), 1–23.

[24] Głuszek M., Kubiś M., Zurowski R., Wiśniewski T., Szafran M.: *Enhancement of thermo-rheological properties of smart materials based on $SiO_2$ and PPG modificated with expanded graphite*. J. Appl. Ceram. Technol. **15**(2018), 538–545.

[25] Chan T. Y., Lin S. T.: *Effects of stearic acid on the injection moulding of alumina.* J. Am. Ceram. Soc. **78**(1995), 2746–2752.

[26] Dakskobler A., Kosmač T.: *Rheological properties of re-melted paraffin-wax suspensions used for LPIM.* J. Eur. Ceram. **29**(2009), 1831–1836.

[27] Moorthy M.B.K., Senthilvadivu K.: *Effect of variable viscosity on free flow of non-Newtonian power-law fluids along a vertical surface with thermal stratification.* Arch. Thermodyn. **33**(2012), 4, 109–121.

[28] Cieśliński J.T., Krygier K., Smoleń S.: *Measurement of temperature-dependent viscosity and thermal conductivity of alumina and titania thermal oil nanofluids.* Arch. Thermodyn. **36**(2015), 4, 35–47.

[29] Saeed F.R., Al-Dulaimi M.A.: *Numerical investigation for convective heat transfer of nanofluid laminar flow inside a circular pipe by applying various models.* Arch. Thermodyn. **42**(2021), 1, 71–95.

[30] Zhang X., Liu X., Wang X., Band S.S., Bagherzadehd S.A., Taherifare S., Abdollahi A., Bahramid M., Karimipourd A., Chau K.W., Mosavi A.: *Energetic thermophysical analysis of MLP-RBF feed-forward neural network compared with RLS Fuzzy to predict CuO/liquid paraffin mixture properties.* Eng. Appl. Comput. Fluid Mech. **16**(2022), 764–779.

**archives**
**of thermodynamics**
Vol. **44**(2023), No. 4, 141–155
DOI: 10.24425/ather.2023.149709

# Impact of paving surface material on thermal conditions within a residential building

**JUSTYNA KOBYLARCZYK**[a*]
**DOMINIKA KUŚNIERZ-KRUPA**[a]
**MARZENA NOWAK-OCŁOŃ**[b]

[a] Cracow University of Technology, Faculty of Architecture, Warszawska 24, 31-155 Kraków, Poland

[b] Cracow University of Technology, Faculty of Environmental Engineering and Energy, Warszawska 24, 31-155 Kraków, Poland

**Abstract** This paper presents the impact of paving surface material on thermal comfort in a residential building. The aim of the study was to demonstrate differences in temperature, measured near a building's walls, depending on their location (relative to the cardinal directions) and the type of paving surface material outside the building (in its immediate vicinity, considering the cardinal directions). The study found differences in temperature values recorded near walls located on the south-west side, which faced a garden and a grassy surface, compared to the temperature of the walls that faced a street with asphalt and concrete paving blocks. It should be noted that the study was carried out in the summer, when the interior of the building was not heated. The facade of the building had not been additionally insulated and retained its original historical form (facade render). The method used in the study consisted of temperature measurements taken near the building's walls using a Steinberg System weather station's sensors. The measurement results supported the hypothesis that wall temperature varies depending on a space's placement relative to the cardinal directions and the surface paving material in the space adjoining the building. The results of the study are presented using line graphs. The study is of scientific value and the results may also be useful in site development planning practice. The thermal conditions are a major factor that affecting the comfort of various types of buildings, including housing.

*Corresponding Author. Email: justyna.kobylarczyk@pk.edu.pl

**Keywords:** Thermal comfort; Location; Environmental conditions; Heritage building

**Acronyms**

PET – physiologically equivalent temperature

# 1 Introduction

Contemporary trends in architectural and urban design consider the importance of environmental conditions that directly affect the quality of urban areas. Environmental factors that remain in a relationship with architecture and urban solutions directly impact a space's comfort of use. A space's arrangement, the rational placement of objects with well-defined geometries, and the use of construction materials with specific properties, affects the space's microclimate by influencing external temperature, the hygiene of its cross-ventilation, and air humidity. Proving these relationships became the subject of this study, whose objective was to demonstrate that a space's arrangement, namely the use of specific paving materials, can affect the thermal comfort of buildings located adjacent to such a space. Here, it is key to define thermal comfort and its significance. Kowalewski, Kostecka, and Jezierski, citing Klemm [1] defined thermal comfort as a state of the environment in which the human body maintains thermal balance [2].

A spatial planning policy aimed at producing optimal conditions within urban spaces of different character and use should also consider the geometric parameters of external spaces and development density [3]. These phenomena, as noted by Galal, Mahmoud, and Sailor, among others, impact the thermal comfort of urban interiors. They also demonstrated that the way in which a space is arranged, including the use of specific paving surfaces, affects nearby buildings.

Mechanisms for reducing high temperature and its negative impact on the environment were discussed by Lai *et al.* [4]. They noted that changes in urban geometry, increasing the amount of vegetation, the use of cooling surfaces and the introduction of water features into the urban landscape can produce a more temperate urban microclimate. Importantly, the use of specific surfaces is not without significance here. Reflective surfaces lead to higher physiologically equivalent temperature (PET) values in summer. PET is a thermal index derived from the human energy balance. It is well suited to the evaluation of the thermal component of different climate [5].

The results of these observations are significant from the standpoint of spatial planning, and the arrangement of urban spaces and housing areas. This is due to the fact that greenery not only contributes to a place's aesthetic value, but also its microclimate conditions, including thermal determinants. Planners and designers who wish to create thermally comfortable urban spaces can take advantage of this [6].

This study showed that there are differences in temperature depending on the location of buildings next to paved or biologically vital surfaces. Thermal comfort is particularly important in residential buildings intended for permanent occupancy, as well as in street spaces (outside buildings) intended for pedestrians.

Although this research focused on determining temperature changes in a building, in the future it can be extended to analyses of urban interiors. This subject is discussed by Elnabawi *et al.* [7], who studied the temperature perception of users of city street spaces in the hot and dry climate of Cairo, Egypt. Preferences in terms of perceived temperature were rated using a survey from respondents. The analytical results showed that the temperature fluctuations ranged from 23°C to 32°C PET, while the preferred temperatures were 29°C PET in summer and 24.5°C PET in winter. These values are higher than those preferred in a temperate climate zone. It is important to note that how we experience temperature depends on many factors, including, but not limited to, our age, habits, and living conditions [8]. These feelings can therefore vary.

Although this issue is not the main subject that the authors explore in this study, it is directly connected to it. The choice of finishing materials, including paving surfaces, significantly affects thermal comfort. With regard to urban interiors, the degree of compactness of development and street canyon parameters are also undeniably important, as demonstrated by Chatzidimitriou and Yannas [9]. Proximity to natural elements also has an effect, as they affect an area's microclimate. The need to design and organise parks in urban spaces was explored by Lili Zhang *et al.* [10]. They pointed out that a park's outdoor thermal comfort is an important factor that can attract people to it and encourage them to stay. Using field meteorological monitoring and surveys, they investigated the outdoor thermal comfort of different types of landscape spaces in urban parks in Chengdu, China, in winter and summer.

The effects of rapid urbanisation, which resulted in a number of environmental problems in cities, were addressed by Ruirui Zhu *et al.* [11]. They stated that such problems include the disruption of thermal comfort and human health. City parks can improve this situation due to the cool-

ing island effect that they produce. Urban parks were also investigated in the context of thermal and acoustic comfort by Negar Mohammadzadeh *et al.* [12]. They noted that the external thermal and acoustic environment are the main factors that influence the overall comfort of an urban space. In the study, they used measurements and surveys to investigate the influence of outdoor thermal comfort on acoustic comfort, with a focus on a plant community located in El Goli Park in Tabriz, Iran.

Although this study did not cover park spaces, it should be highlighted that the immediate vicinity of the building under study features a river and riverside green areas, in addition to an allotment garden complex and park-like cemetery vegetation.

Improving the thermal comfort of urban spaces was also the subject of a study by Mutani *et al.* [13], who saw it as one of the most important challenges that cities must address in the coming years. The aim of their study was to assess the impact of urban variables and to quantify the effect of vegetation on outdoor thermal comfort. Mutani *et al.* compared six neighbourhoods in Turin, Italy, that were characterised by different urban forms, contexts and green spaces. Their findings showed how external thermal comfort varies depending on urban form and greenery.

Zhang and Liu [14], on the other hand, used digital tools to analyse the external thermal comfort of buildings to improve the environment of urban residents. They developed a digital simulation system to facilitate the analysis for assessing the outdoor thermal comfort of buildings in urban neighbourhoods. They also explored whether digital simulation techniques can provide a modelling system for assessing the external thermal comfort of buildings in a continuous and efficient manner. Their findings showed that digital simulation techniques and tools can support the analysis of outdoor thermal comfort by providing 3D models, algorithm-based analysis and visual simulation.

Researchers whose scientific interests revolve around thermal comfort in cities often carry out their research in the centres and public spaces of cities located in hot climate zones, where any increase in temperature is highly perceptible. Such studies were conducted by Kurniati *et al.* [15] in Semarang, Indonesia, by Hirashima *et al.* [16] for Belo Horizonte, Brazil, by Huang *et al.* [17] for Taipei in Taiwan, and by Balogun and Daramola in Akure, Nigeria [18]. Among other things, these research teams identified the need to further develop public spaces to potentially accommodate environmental change.

A research gap between urban climatology and urban design in coastal temperate cities in developing countries was filled by Lamarca *et al.* [19],

who studied thermal comfort in urban canyons located in the city of Concepción, Chile, using a multidisciplinary approach that combines morphological, climatic and perceptual factors.

A study of thermal comfort in open urban areas was, in turn, conducted by Vučković *et al.* [20]. They found that thermal comfort in open urban areas can influence medical, sociological, environmental and economic parameters. Therefore, there is a need to establish good thermal comfort in such areas to keep these parameters at an acceptable level.

An interesting aspect of thermal comfort was studied by Urban *et al.* [21], who noted that the external thermal comfort of urban residents is negatively affected by heat waves, which are becoming more frequent and more severe with the ongoing climate crisis. Consequently, assessing outdoor thermal perception and thermal comfort during heat waves has become an important component of successful urban adaptation strategies. The researchers considered an approach to assessing long-term thermal perception that combines features of current approaches (i.e., the use of thermal perception rating scales, the use of questionnaires and the use of photographs that depict sites) and presented a preliminary validation of this approach.

Another aspect of the outdoor comfort of urban residents was studied by Ma *et al.* [22], who analysed the temporal effect of urban morphological features on the thermal comfort of pedestrians in the street using the ENVI-met model. Their results showed that the presence of surrounding buildings could cause average PET values on pavements to fall by up to 6.7°C. Hourly PET values also varied significantly with the compactness of a neighbourhood, the height configuration of the surrounding buildings, their forms and architectural composition.

When discussing the state of research concerning the issue investigated, one cannot ignore the work of Lai *et al.* [23], who provided a comprehensive review of current (at the time of writing of this paper) research on outdoor thermal comfort, including benchmarks, data collection methods and models.

On the basis of the literature survey, it should be noted that there is a research gap regarding the influence that paving surfaces (in the urban spaces that constitute the immediate area of a building) may have on the thermal conditions in the direct proximity of a building's walls or inside it building. The hypothesis tested in this study was that the type of paving around a building can affect temperature. The research conducted by the authors was to not only test this hypothesis, but also to demonstrate the following:

- What are the differences in temperature values depending on the type of paving material used?
- What is the impact of biologically vital areas on thermal conditions?

The scope of the study area was therefore clearly delineated; it was not broad. The answers to the research questions listed add to the existing scope of knowledge, which demonstrates their relevance.

To date, research on thermal conditions has mainly been carried out in the public spaces of cities, located in specific climate zones. The literature cited in this study does not reference Polish conditions. In this regard, it is supplemented by a study by Lewińska [24], which is key from the standpoint of the subject under discussion.

This study considered the solutions in the building's vicinity – the use of different paving surfaces outside the building under study, in its immediate surroundings. The surroundings were an important context for the measurements. They consisted of residential development that formed a series of compact buildings and openings located westward of the building investigated. To the north of the building there was an open area. The main research problem was the necessity to take measurements at different times of day, including in the same timeframe. This required systematic analysis as well as constant observation. The problem was minimised by having the research tools continuously powered.

Before commencing with the analysis, it was realised that greenery had a significant impact on the microclimate of the surrounding area. However, the magnitude of the temperature difference near the walls was unknown due to the variety of the paving surfaces used near the building. The aim of the study was to demonstrate that a building's walls display temperature differences depending on their location (relative to the cardinal directions) and the type of paving surface material outside the building (grass lawn, concrete paving blocks and asphalt).

## 2 Research method

The adopted research objectives – to demonstrate the qualitative influence of the site surface next to a residential building on the temperature in the immediate vicinity of these walls (0.10 m distance), taking into account their exposure relative to the cardinal directions, and to demonstrate the influence of different weather conditions (sunny, cloudy sky, rainy) on temperature changes – required the use of temperature measurements as

a research method. Steinberg System weather stations with indoor temperature monitoring screens [25] were used for this purpose. This ensured a high degree of accuracy in the measurements, although it should be noted that this was not required. The main objective was a qualitative rather than a quantitative analysis and to record trends in temperature changes and differences rather than specific temperature values.

The measurements were taken during the day and at night. Therefore, an additional parameter was recorded – brightness (dark, night). This was done as it was recognised that temperature in the immediate vicinity of a building affects a residential space's microclimate. The procedure was carried out in the year 2020 and involved measuring temperatures during the months between and including June and September. The intention behind the study was to conduct measurements during periods with different temperatures.

Measurements were taken throughout the entire day and night at three-hour intervals, using weather stations located outside the building, placed directly at windows on the south-east and north-west sides. The data from the weather stations was collected using a wireless Wi-Fi network with an accuracy of 0.5°C. The measurement sites were placed 0.10 m from the building wall (outside) and were at a height of 6 m from the ground.

The measurements were therefore taken at locations with different insolation conditions (Figs. 1a and 1b). In the vicinity of the building, the

(a)

(b)

Figure 1: For caption see next page.

(c)

Figure 1: Study location: (a) garden-facing measurement site, (b) street-facing measurement site, (c) top view of the measurement site location (area: 558 $m^2$; building footprint: 125 $m^2$).

surfaces were formed by – on the south-eastern side (sunnier) – low (grass) and medium-height vegetation (conifers), and on the north-western side by a street with an asphalt surface and concrete paving blocks (Fig. 1c). The height of the measurement points above the ground surface was (6 m) due to the nature of the development (this was about 50% of the building's height).

## 3 Results and discussion

The results of the tests carried out in this study, which consisted of measuring the temperature at the walls of a residential building, were illustrated in graphical form after careful analysis. Series 1, as shown in the charts, includes measurements taken from the south-east, while Series 2 refers to measurements taken from the north-west. The results are shown in Figs. 2 through 8. They include distinct weather periods. One such period lasted four days. This meant 32 pairs of results in this specific measurement period. The remaining periods (6 in total) lasted a week Longer periods offered the opportunity to record greater variation in the weather and thus its impact on the measurements. One measurement period was then represented by 56 result pairs.

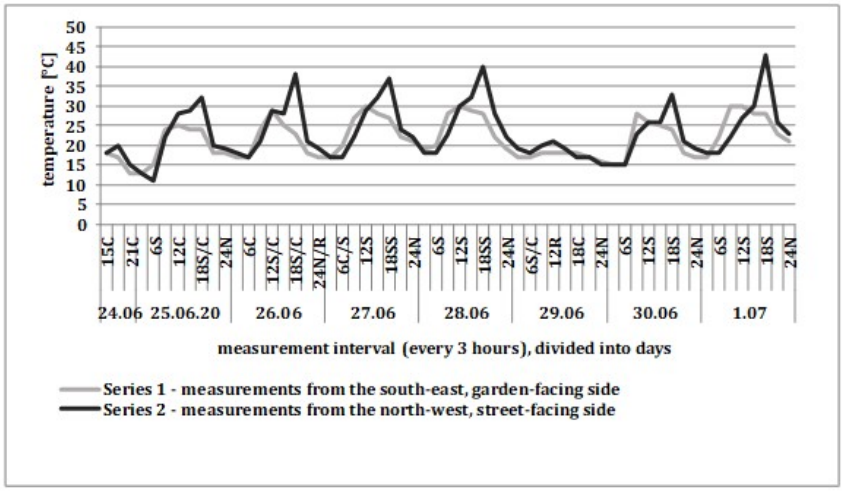


Figure 2: Measurement results for the period between 24 June and 1 July 2020.

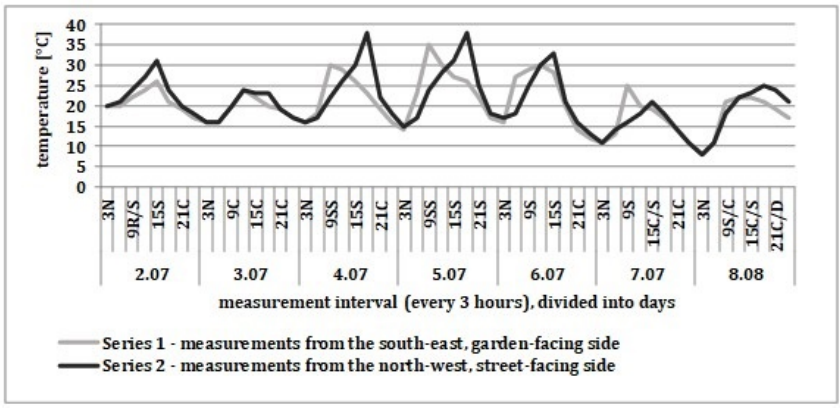


Figure 3: Measurement results for the period between 2 July and 8 July 2020.

The results of the measurements were singular, point readings in terms of duration. They have been presented – for better readability – in the form of jagged lines. The results of the measurements taken on the garden side are shown by the blue line and of those taken on the street side by the red line. The vertices of the lines indicate specific readings, taken every three hours, also during the night, which is indicated by the letter (N). Weather conditions were noted each time. Due to the scale of the drawings, this could not be suitably presented. S (sunny), C (cloudy), D (dusk) and

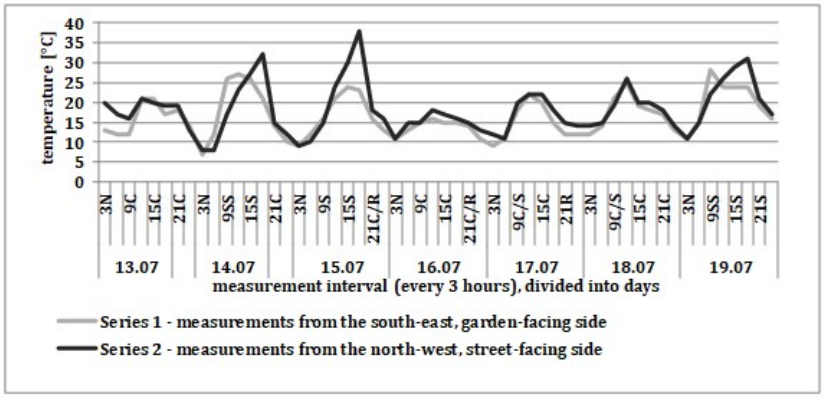


Figure 4: Measurement results for the period between 13 July and 19 July 2020.

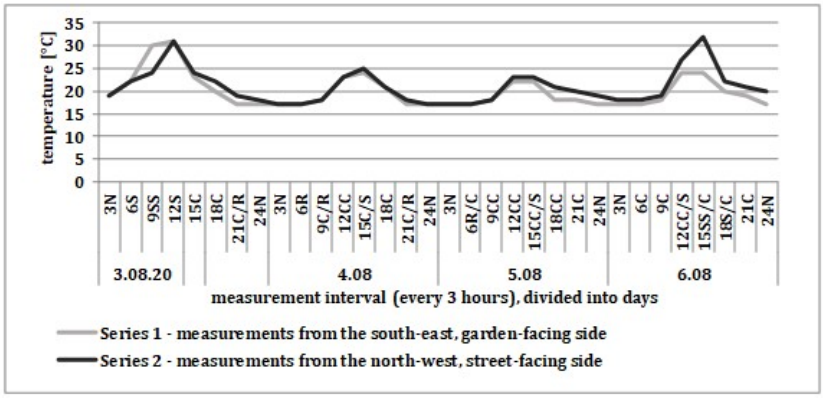


Figure 5: Measurement results for the period between 3 Aug. and 6 Aug. 2020.

N (night), and R (rainy) periods were included. The letters were doubled to indicate severe weather conditions. For example, a designation of (SS) was used for very intense insolation and (CC) was used for very cloudy periods. Three hours is not a long period, but enough for changes in weather to be observed. When the weather did change, a double weather condition marking was used. For example, if there was cloudy and sunny period, a C/S designation was used, with the letter indicating the weather condition that lasted longer being first. For example, the record 6R indicates that it began to rain during the sixth hour of measurement.

The tenement house in which the research was carried out is positioned so that exposure time throughout the day would be similar for both the

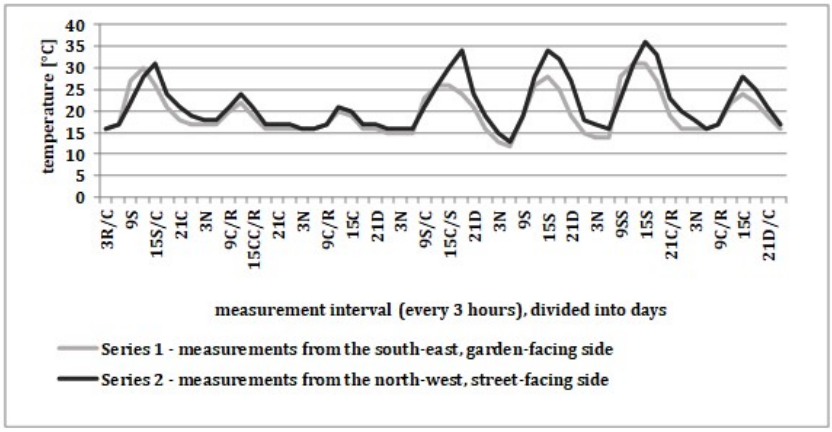


Figure 6: Measurement results for the period between 17 Aug. and 23 Aug. 2020.

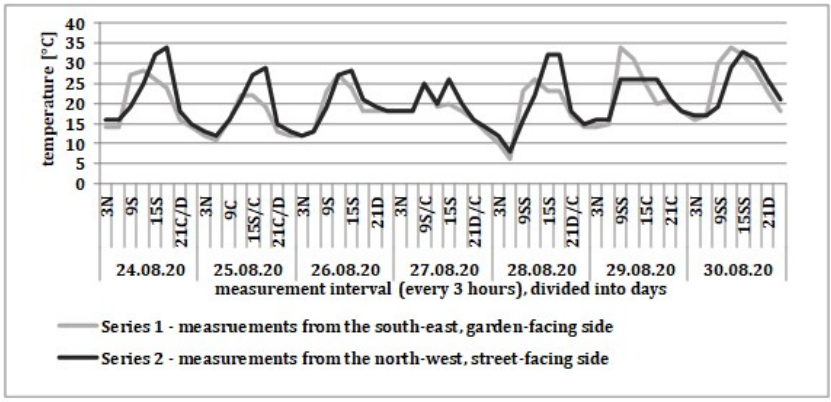


Figure 7: Measurement results for the period between 24 Aug. and 30 Sept. 2020.

garden-facing and street-facing side. Hence, the total heating and cooling times (from evening to morning) of the two walls were also similar. However, these effects, in the form of recorded temperature changes, were different.

The temperature at the wall from the garden-facing side (a lawn) decreased faster than that of the wall from the street-facing side (asphalt and concrete pavement). This is due to the higher proportion of heat emitted from the pavement on the street-facing side. The reported increase was mainly observed on sunny and bright days, with a clear predominance of sunny hours. On rainy and overcast days, the phenomenon was less pronounced.

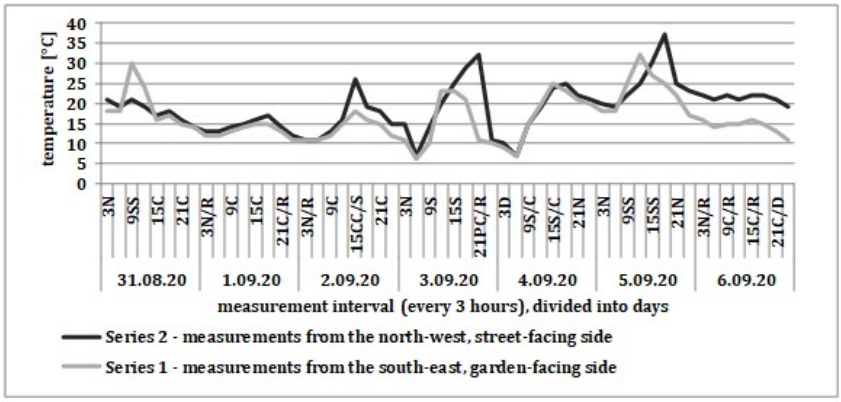


Figure 8: Measurement results for the period between 31 Aug. and 6 Sept. 2020.

Based on the detailed test results, the average temperature measured was higher at the garden-facing wall. Similarly, the average of the lowest daily temperature values and the average of the highest temperature values was also lower at the garden-facing wall. This further demonstrates the effect of the heat emitted from the asphalt and concrete pavement on the temperature at the wall on the street-facing side.

## 4 Final conclusions

This study demonstrates the significant impact of paving surface materials in the vicinity of a heritage building on the temperature of its external walls that were heated by sunlight. This is particularly important in the case of buildings with historical value, given the constraints on altering their structural systems and also in the choice of building materials, including insulation.

Based on an analysis of the measurements taken using Steinberg System weather stations, which were also equipped with indoor temperature monitoring screens, it can be concluded that the heat emission of the heated asphalt and concrete pavement – relative to the grassy surface – results in temperatures near the wall remaining higher for a longer period, as well as slower cooling. This regularity (property) is more pronounced the more sunny the weather (sunny or slightly cloudy days). It should be noted in this regard that the measurements were taken at a height of 6 m above the ground and not directly at ground surface level. Had they been taken

at ground level, the regularities observed would have become even more pronounced.

Naturally, the temperature at the free-standing wall (masonry) on the garden-facing side was higher before midday, due to its south-east orientation, as well as the ground surface – a biologically vital area. In contrast, the temperature at the street-facing facade wall was higher in the afternoon (south-west orientation). What is important is that there was a greater temperature rise at the wall on the street-facing side and that the temperature remained high for longer. This was due to the accumulation of heat by asphalt. There was little difference between the garden-facing wall (gassy surface) and the street-facing wall (asphalt) on rainy and very cloudy days. The street and pavement surface would then heat up much less and thus emit much less heat. It was the cardinal directions that affected temperature changes the most during this time.

The analysis of the measured data made it possible to draw mainly qualitative conclusions and to identify trends regarding the influence of the paving on the temperature of the façade of a historic building (without thermal insulation) and its thermal comfort inside.

*Received 17 August 2023*

## References

[1] Klemm P.: *General Construction*. Arkady, Warszawa 2005 (in Polish).

[2] Kowalewski G., Kostecki I., Jezierski W.: *Assessment of thermal comfort in the single-family residential building after its thermal-modernisation*. Civ. Environ. Eng. **8**(2017), 2, 67–73 (in Polish).

[3] Galai O.M., Mahmoud H., Sailor D.: *Impact of evolving building morphology on microclimate in a hot arid climate*. Sustain. Cities Soc. **54**(2020), 102011. doi: 10.1016/j.scs.2019.102011

[4] Lai D., Liu W., Gan T., Liu K., Chen O.: *A review of mitigating strategies to improve the thermal environment and thermal comfort in urban outdoor spaces*. Sci. Total Environ. **661**(2019), 337–353. doi: 10.1016/j.scitotenv.2019.01.062

[5] Matzarakis A., Mayer H., Iziomon M.G.: *Applications of a universal thermal index: physiological equivalent temperature*. Int. J. Biometeorol. **43**(1999), 76–84.

[6] Huang T., Li J., Xie Y., Niu J., Ming Mak Ch.: *Simultaneous environmental parameter monitoring and human subject survey regarding outdoor thermal comfort and its modelling*. Build. Environ. **125**(2017), 502–514. doi: 10.1016/j.buildenv.2017.09.015

[7] Elnabawi M.H., Hamza N., Dudek S.: *Thermal perception of outdoor urban spaces in the hot arid region of Cairo, Egypt*. Sustain. Cities Soc. **22**(2016), 136–145. doi: 10.1016/j.scs.2016.02.005

[8] Amindeldar S., Heidari S., Khalili M.: *The effect of personal and microclimatic variables on outdoor thermal comfort: A field study in Tehran in cold season*. Sustain. Cities Soc. **32**(2017), 153–159. doi: 10.1016/j.scs.2017.03.024

[9] Chatzidimitriou A., Yannas S.: *Street canyon design and improvement potential for urban open spaces; the influence of canyon aspect ratio and orientation on microclimate and outdoor comfort*. Build. Environ. **38**(2017), 85–101. doi: 10.1016/j.scs.2017.05.019

[10] Zhang L., Wei D., Hou Y., Du J., Liu Z., Zhang G., Shi L.: *Outdoor thermal comfort of urban park — A case study*. Sustainability **12**(2020), 5, 1961. doi: 10.3390/su12051961

[11] Zhu R., Zhang X., Yang L., Liu Y., Cong Y., Gao W.: *Correlation analysis of thermal comfort and physiological responses under different microclimates of urban park*. Case Stud. Therm. Eng. **34**(2022), 102044. doi: 10.1016/j.csite.2022.102044

[12] Mohammadzadeh N., Karimi A., Brown R.D.: *The influence of outdoor thermal comfort on acoustic comfort of urban parks based on plant communities*. Build. Environ. **228**(2023), 109884. doi: 10.1016/j.buildenv.2022.109884

[13] Mutani G., Todeschi V., Beltramino S.: *Improving outdoor thermal comfort in built environment assessing the impact of urban form and vegetation*. Int. J. Heat Technol. **40**(2022), 1, 23–31. doi: 10.18280/ijht.400104

[14] Zhang Y., Liu Ch., *Digital simulation for buildings' outdoor thermal comfort in urban neighborhoods*. Buildings **11**(2021), 11, 541. doi: 10.3390/buildings11110541

[15] Kurniati R., Kurniawati W., Dewi D.I.K., Astuti M.F.K.: *Measurement of thermal comfort in urban public spaces Semarang, Indonesia*. Pertanika J. Sci. Technol. **29**(2021), 3, 1371–1395. doi: 10.47836/pjst.29.3.01

[16] Hirashima S.Q.D., Ferreira D.G., De Assis E.S.: *Thermal comfort description of urban structure types*. In: PLEA 2018: Smart and Healthy within the Two-Degree Limit (Proc. 34th Int. Conf. on Passive and Low Energy Architecture, Dec. 10–12, 2018) Vol. 3, 1105–1106. The Chinese University of Hong Kong, Hong Kong 2018.

[17] Huang Ch., Tsai H., Chen H.: *Influence of weather factors on thermal comfort in subtropical urban environments*. Sustainability **12**(2020), 5, 2001. doi: 10.3390/su12052001

[18] Balogun I.A., Toluwalase M.: *The outdoor thermal comfort assessment of different urban configurations within Akure City, Nigeria*. Urban Clim. **29**(2019), 100489. doi: 10.1016/j.uclim.2019.100489

[19] Lamarca C., Qüense J., Henríquez C.: *Thermal comfort and urban canyons morphology in coastal temperate climate, Concepción, Chile*. Urban Clim. **23**(2018), 159–172. doi: 10.1016/j.uclim.2016.10.004

[20] Vučković D., Jovic S., Bozovic R., Dżamić V., Kićović D.: *Potential of neuro-fuzzy methodology for forecasting of outdoor thermal comfort index at urban open spaces*. Urban Clim. **28**(2019), 100467. doi: 10.1016/j.uclim.2019.100467

[21] Urban J., Pikl M., Zemek F., Novotny J.: *Using Google Street View photographs to assess long-term outdoor thermal perception and thermal comfort in the urban environment during heatwaves*. Front. Environ. Sci. **10**(2022), 878341. doi: 10.3389/fenvs.2022.878341

[22] Ma X., Leung T.M., Chau C.K., Yung E.H.K.: *Analyzing the influence of urban morphological features on pedestrian thermal comfort.* Urban Clim. **44**(2022), 101192. doi: 10.1016/j.uclim.2022.101192

[23] Lai D., Lian Zh., Liu W., Guo Ch., Liu W., Liu K., Chen Q.: *A comprehensive review of thermal comfort studies in urban open spaces.* Sci. Total Environ. **742**(2020), 140092. doi: 10.1016/j.scitotenv.2020.140092

[24] Lewińska J., *City climate. Threat, Resources, Shaping,* Instytut Gospodarki Przestrzennej i Komunalnej, Oddział w Krakowie, Kraków 2000 (in Polish).

[25] https://manuals.expondo.com/10030583 (accessed 18 June 2020).

**archives**
**of thermodynamics**
Vol. **44**(2023), No. 4, 157–183
DOI: 10.24425/ather.2023.149711

# Pyrolysis-derived waste polypropylene oils in gas turbine engines: a comprehensive performance and emission study

**TOMASZ KACPER SUCHOCKI**[a]*
**PAWEŁ KAZIMIERSKI**[a]
**KATARZYNA JANUSZEWICZ**[b]
**PIOTR LAMPART**[a]
**DAWID ZANIEWSKI**[a]
**PIOTR KLIMASZEWSKI**[a]
**ŁUKASZ WITANOWSKI**[a]

[a] Institute of Fluid Flow Machinery, Polish Academy of Sciences, Fiszera 14, 80-231 Gdańsk, Poland

[b] Gdańsk University of Technology, Narutowicza 11/12, 80-233 Gdańsk, Poland

**Abstract** Addressing the burgeoning issue of polymer waste management and disposal, chemical recycling, specifically the production of high-quality oil, presents an enticing solution. This research paper delves into the process of plastic waste pyrolysis, focusing on polypropylene, and thoroughly examines the physico-chemical properties of the resulting pyrolytic oil. The oils, obtained from waste plastic pyrolysis (referred to as WPPO), are then blended with kerosene and utilized as fuel for a gas turbine engine. The primary objective of this investigation is to ascertain how the blend composition influences the performance and emission parameters of the micro gas turbine. In our findings, it was observed that all tested waste plastic pyrolysis blends displayed a trend towards escalating regulated emissions such as nitrogen oxides ($NO_x$) with an average increase of 26% for polypropylene pyrolysis oil (PPO). The emission index (EI) for carbon monoxide (CO) was found to be relatively consistent across all fuel blends tested in this study. Interestingly, when considering the thrust specific fuel consumption (TSFC) within the EI calculation, blends of aviation kerosene and plastic oil showed

*Corresponding Author. Email: tsuchocki@imp.gda.pl

lower values in comparison to the pure Jet A-1 fuel. Furthermore, an augmentation in the proportion of WPPO in the blends consequently led to an elevation in the exhaust gas temperature (an average increase of 8.7% for PPO). Interestingly, the fuel efficiency of the Jet engine, expressed as TSFC, demonstrated a decrease, with an average reduction of 13.8% observed for PPO.

**Keywords:** Waste plastic pyrolysis oil; Gas turbine engine; Polypropylene; Emissions; Performance

## Nomenclature

| | | |
|---|---|---|
| EGT | – | exhaust gas temperature, °C |
| $EI_i$ | – | gas species ($i$) emission index |
| $EI_{i,\tau}$ | – | gas species ($i$) thrust specific emission index |
| HHV | – | higher heating value, MJ/kg |
| LHV | – | lower heating value, MJ/kg |
| $\dot{m}_f$ | – | fuel mass flow rate, kg/s |
| $\dot{m}_i$ | – | gas species ($i$) mass flow rate, kg/s |
| $MW_f$ | – | fuel molecular weight, kg/mol |
| $MW_i$ | – | gas species ($i$) molecular weight, kg/mol |
| TSFC | – | thrust specific fuel consumption, kg/sN |
| $x$ | – | number of carbon atoms in the fuel molecule |

### Greek symbols

| | | |
|---|---|---|
| $\chi_{CO}$ | – | carbon monoxide mole fraction |
| $\chi_{CO_2}$ | – | carbon dioxide mole fraction |
| $\chi_i$ | – | gas species ($i$) mole fraction |
| $\tau$ | – | static thrust, N |

### Abbreviations

| | | |
|---|---|---|
| CHP | – | combined heat and power |
| CO | – | carbon monoxide |
| $CO_2$ | – | carbon diooxide |
| $NO_x$ | – | nitrogen oxides |
| HDPE | – | high-density polyethylene |
| HEFA | – | hydro-processed esters and fatty acids |
| LPDE | – | low-density polyethylene |
| PE | – | polyethylene |
| PET | – | polyethylene terephthalate |
| PP | – | polypropylene |
| PS | – | polystyrene |
| PPO | – | polypropylene pyrolysis oil |
| PP25, PP50, PP75, PP100 | – | blend of PPO with Jet A with 25%, 50%, 75%, 100% of PPO, respectively |
| PVC | – | polyvinyl chloride |
| TPO | – | tyre pyrolysis oil |
| UHC | – | unburned hydrocarbons |
| WPPO | – | waste plastic pyrolysis oil |

# 1 Introduction

Alternative fuels derived from plastic waste have emerged as a potent solution for waste management, while concurrently serving as a viable substitute for fossil fuels. This burgeoning market of alternative fuels bolsters energy independence, given the local availability, ease of storage, predictable quantities, and versatility of waste in meeting a diverse array of energy needs through various energy conversion technologies [1, 2]. The transition from fossil fuels to biofuels or fuels generated from plastic waste is particularly pertinent for small-scale cogeneration heat and power (CHP) plants [3, 4].

A prevailing trend in waste management is the utilization of waste polymers as alternative fuels [5, 6]. Polymers, notably plastics, constitute a significant group of materials employed across various sectors, including electronics, logistics, automotive, and healthcare. In 2019, global plastic production was approximately 368 million tons, with Europe contributing 57.9 million tons [7]. It is estimated that 38% of this was landfilled, 26% recycled, and 36% processed for energy production [8]. The substantial proportion of waste not recycled presents an economically unfavourable scenario due to its prolonged natural decomposition and a high potential for reuse.

Discarded plastics, rich in hydrocarbons, serve as excellent sources of alternative fuels due to their abundant availability and the environmental implications of their disposal [9]. The conversion of plastic waste into fuel, a promising solution, can be achieved through thermal degradation processes such as pyrolysis, gasification, combustion, hydrocracking, or catalytic cracking [10,11]. Pyrolysis, a thermal degradation process that occurs in an oxygen-free environment, yields oil, gas, and a solid residue – char [12]. The quality of the products derived from the pyrolysis process is contingent on the raw materials, the pyrolysis reactor, and process parameters (temperature, residence time, and catalyst) [13, 14]. The liquid fraction – pyrolytic oil can be utilized in various applications such as furnaces, boilers, turbines, and diesel engines without necessitating upgrading or treatment.

The use of the rapid heating process has a positive effect on the increase in volatile fraction. The long residence time during the process allows for the degradation of long chains, which results in an increase in the content of short-chain hydrocarbons [15]. The process temperature above 800°C affects the degradation of polymer hydrocarbon chains, secondary conversion as well as obtaining an increased amount of carbon (approx. 30%) and gas composed of light hydrocarbons such as methane, ethane and propane [15].

The temperature of about 400–500°C allows us to obtain the oil fraction rich in long-chain hydrocarbons, over 80% [16]. The aim of this work is to obtain a large amount of oil, to use as a potential fuel. The performed works are an attempt to perform experiments on a quarter technical scale.

Various studies have been conducted during recent years on pyrolysis oils used as fuels, specifically for diesel engines. Waste plastic pyrolysis oils (WPPO) offered good performance and high efficiency in compression-ignition engines across a wide range of engine loads. Several useful data available in the literature on the performance of diesel engines supplied by blends of waste plastic pyrolysis oil and diesel, with the emissions of harmful exhaust components are gathered in Table 1. The presented results report a generally increasing tendency in CO, $NO_x$, and unburned hydrocarbons (UHC) emissions with a growing content of plastic oil in diesel fuel [12,17–20]. However, in some cases, emissions of CO and $NO_x$ were also found to decrease [21].

The use of pyrolysis oils in various power generation units, including gas turbines was conceptualized in [24]. Compact dimensions and reduced weight of turbine engines compared to diesel engines encourage was use in stationary power plants. The advantages of gas turbines over piston combustion engines are: fewer moving parts, the absence of friction components, lower maintenance costs, lower vibration and noise levels, low consumption of lubricating oil as well as low maintenance costs [25]. In spite of encouraging research results on the use of pyrolysis oils from used plastics in diesel engines, there are only a few papers published in recent years reporting experimental tests with gas turbines supplied by waste- and biomass-based fuels. Suchocki *et al.* [26] described the process of pyrolysis of waste tyres and the application of the obtained liquid fraction – tyre pyrolysis oil (TPO) for the supply of gas turbines in mixtures with aviation fuel – kerosene (Jet A). TPO was found to have parameters like density, viscosity and higher heating value (HHV) similar to those of Jet A. The authors observed that all tested blends of TPO/Jet A involved somewhat more blended fuel than pure Jet A so as to obtain similar values of static thrust, resulting in a slightly increased thrust specific fuel consumption (TSFC). The emissions of $NO_x$ and CO were found higher for all tested TPO/Jet A blends in comparison to those of Jet A.

Fast pyrolysis bio-oil (FPBO) was studied as fuel in a small scale non-regenerated micro gas turbine by Buffi *et al.* [27]. The presence of pyrolysis oil in fuel blends has a significant influence on CO and $NO_x$ emissions, as compared to pure ethanol or diesel oil. The gas turbine had a higher overall

Table 1: Literature survey on the performance and emissions of diesel engines supplied by blends of WPPO and diesel.

| Reference | Fuel | Engine type | Impact on | |
|---|---|---|---|---|
| | | | Combustion/Performance | Emissions |
| Januszewicz *et al.* [22] (2023) | Polypropylene oil (PPO) and polystyrene oil (PSO) | AVL 5402 four-stroke, single-cylinder, DI Diesel engine | Higher WPPO fraction led to: heat release rate ↑↓ in-cylinder pressure ↓ | CO ↑ $NO_x$ ↑↓ HC ↑ |
| Singh *et al.* [21] (2021) | LDPE (low density polyethylene) WPPO20 / D80 | Single cylinder, 4 S, diesel engine Kirlosker, model: TV1 5.2 | Cylinder pressure ↑ Brake thermal efficiency ↑ | $NO_x$ ↓ smoke ↓ |
| Das *et al.* [20] (2020) | Shredded medical plastic wastes 10/20/30% with diesel fuel | Kirloskar, TV1 4 stroke single cylinder water cooled, CI engine | Higher WPPO fraction led to: brake thermal efficiency ↓↑ break specific fuel consumption ↓ break power ↓ | CO ↑ $NO_x$ ↑ UHC ↑ $CO_2$ ↑ |
| Singh *et al.* [19] (2020) | 58.6% PE (HDPE and LDPE), 26.9% PP, 8.8% PS, 5.6% PET; 10-50% WPPO in diesel blends | Single cylinder, 4 S, Diesel engine Kirlosker, model: TV1 5.2 | Higher WPPO fraction led to: brake thermal efficiency ↓ EGT ↑ specific fuel consumption – volumetric efficiency ↓ in-cylinder pressure ↑↓ heat release rate ↑↓ | CO ↑ $NO_x$ ↑ UHC ↑ $CO_2$ ↑ |
| Mani *et al.* [18] (2011) | Assorted WPPO 10/30/50/70% with diesel fuel | Kirloskar TAF1 Four stroke, CI, air cooled, single cylinder, DI engine | Higher WPPO fraction led to: brake thermal efficiency ↓↑ EGT ↑ in-cylinder pressure ↑ ignition delay ↑ heat release rate ↑↓ cylinder pressure ↑ | CO ↓ $NO_x$ ↑ HC ↑ smoke ↑ |
| Kumar *et al.* [12] (2013) | HDPE 10/20/30/40% with diesel fuel | CometVCT-10 four-stroke, CI, water cooled twin cylinder, constant speed engine | Higher WPPO fraction led to: brake thermal efficiency ↓ EGT ↑ break specific energy consumption ↑ mechanical efficiency ↑ | CO ↑ $NO_x$ ↑ UHC ↑ $CO_2$ ↓ |
| Kalargaris *et al.* [17] (2017) | Feedstock: styrene butadiene 47% polyester 26% clay 26% ethylene-vinyl acetate 12% rosin 6% polyethylene 1% polypropylene 1% PPO 25/50/75/90% with Diesel fuel. | AKSA A4CRX46TI four-stroke, CI, DI engine | Higher WPPO fraction led to: cylinder peak pressure ↑↓ cylinder pressure ↓ heat release rate ↑↓ break specific fuel consumption ↑ brake thermal efficiency ↑ EGT ↑ | CO ↑ $NO_x$ ↑ UHC ↑ $CO_2$ ↑ |
| Devaraj *et al.* [23] (2015) | WPO 100% | Kirlosker AV1 four-stroke, CI, DI engine | Brake Thermal Efficiency ↓ Break Specific fuel Consumption ↑ | CO ↑↓ $NO_x$ ↑↓ HC ↑ smoke ↑↓ |

electric efficiency than that recorded for commercial diesel due to the higher HHV of FPBO blends.

The paper [28] studied the combustion and performance characteristics of a small gas turbine fed with commercial Jet A and a 48%/52% mixture of aviation kerosene with synthetic paraffinic kerosene derived from hydro-processed esters and fatty acids (SPK-HEFA). Emission indexes for CO, $CO_2$, and $NO_x$ in exhaust gases for HEFA/Jet A blends decreased in comparison to those of the pure Jet A. Lower fuel consumption was accomplished for the same thrust value, with the discrepancy decreasing with the increasing rotating speed. Two synthetic components of blends were tested, derived from two different materials: HEFA from camelina oil and HEFA from used cooking oil, with the addition of hydro-processed fatty acid sand esters, showing a tendency to mass flow rate and CO emissions decreases [29]. An opposite tendency was observed for $NO_x$ emissions.

Chmielewski *et al.* [30] presented results of application of a fuel-water emulsion (FWE) as an alternative fuel for a micro gas turbine. The addition of water emulsion to the fuel blend was found to decrease the Jet A consumption, specific fuel consumption and turbine outlet temperature (TOT) for the wide range of engine thrust. Up to 35% reduction of $NO_X$ emission was reported at the maximum thrust. Manigandan *et al.* [31] conducted the combustion, emission and exergy analysis of a miniature gas turbine supplied by blends of Jet A with various additives, including biofuels such as rapeseed and canola-sunflower oil blended with ethanol or pentanol. The following blends were considered: R20E (70% Jet A fuel, 20% Rapeseed and 10% ethanol), CS20E (70% Jet A fuel, 20% canola-sunflower and 10% ethanol), R20P (70% Jet A, 20% Rapeseed and 10% pentanol), and CS20P (70% Jet A, 20% canola-sunflower and 10% pentanol). The fuel blends R20E, CS20E, R20P, and CS20P showed a 35%, 15%, 18%, and 10% increase in thermal efficiency of the micro-gas turbine engine, respectively. All examined fuel blends showed lower rates of emission due to the higher level of oxygen present in the samples. The blends R20E, CS20E, R20P and CS20P were recorded with a 16%, 9%, 17% and 1% decrease in average emission of $NO_x$ due to the impact of additives. Badami *et al.* [32] tested a small gas turbine supplied by three various fuels – Jet A kerosene, synthetic gas-to-liquid (GTL) fuel as well as a blend of 30% Jatropha methyl ester (JME) with 70% Jet A. The emissions index for CO was comparable for three combustibles, while the emission of unburned hydrocarbons (UHC) showed decreased trends for all biofuels. Aviation fuel combustion is characterized by lower $NO_x$ emission index values for lower rotating speeds

and higher emissions for higher speeds. Bhele *et al.* [33] studied the performance and emission characteristics of a small gas turbine fed by blends of Jatropha methyl ester (JME) with diesel. With increasing proportions of JME in blends with commercial fuel, emissions of primary air pollutants such as CO, $CO_2$ and UHC would decrease. Gürbüz *et al.* [34] showed the effect of dual-fuel diesel-hydrogen combustion on the performance as well as environmental and economic indicators of a small unmanned aerial vehicle (UAV) turbojet engine. In general, with an increase of hydrogen energy fractions (HEFs) in the entire range of engine speed, the emissions of CO and $CO_2$ were found to decrease, whereas HC and $NO_x$ emissions increased. Performance and emissions characteristics of a 30 kW gas turbine engine burning Jet A, canola methyl ester (CME), soy methyl ester (SME), recycled rapeseed methyl ester (RRME), hog-fat biofuel, and their 50% (volume) blends in Jet A were studied by Habib *et al.* [35]. With the increasing concentration of biofuel in fuel blends, the emission indexes of $NO_x$ and CO were decreased.

While reviewing the literature, it was found that there are no research papers on the combustion of fuels containing (WPPO) in a gas turbine. In this study, the performance and emission characteristics of a GTM-140 miniature gas turbine engine fueled with blends of kerosene Jet A and WPPO derived from polypropylene are investigated. From 25% to 100% of WPPO is used in WPPO/Jet A blends. Turbine exhaust temperatures, static thrust, fuel consumption and thrust specific fuel consumption, as well as thrust specific emissions of $NO_x$ and CO are measured over a broad range of turbine load and compared within the assumed range of fuel composition. The significance of this paper is to provide a better understanding of the effects of Jet A/WPPO mixtures on engine performance characteristics and exhaust emissions, as well as to assess the potential for these fuels for gas turbine applications.

## 2 Pyrolysis of waste plastics

The pyrolytic oil used as fuel in the experimental work was obtained in a semi-technical scale installation for the pyrolysis process. Taking into account the previous experience [36,37], the pyrolytic installation was modified especially for the pyrolysis of waste plastics. The installation includes the fixed bed reactor with electric heating, a panel control with a thermocouple and a system for the collection of the liquid fraction. The cylindrical

reactor has a diameter $D = 350$ mm, height $H = 500$ mm and is made of 3 mm thickness stainless steel. The reactor was closed using the flange connection, screwed and sealed so that the process takes place in an oxygen-free atmosphere. Before the experiment, the stainless steel reactor was placed axially in a cylindrical ceramic heating element of diameter $D = 380$ mm with khantal heaters deployed in the reactor walls. The heat was supplied to the reactor evenly over the entire wall surface. The vermiculite insulation was placed underneath the reactor, over the entire exterior of the heating element, the reactor cover and the pipe for discharging the volatile fraction into the condenser. A scheme of the pyrolytic installation that was used in the present study is illustrated in Fig. 1.

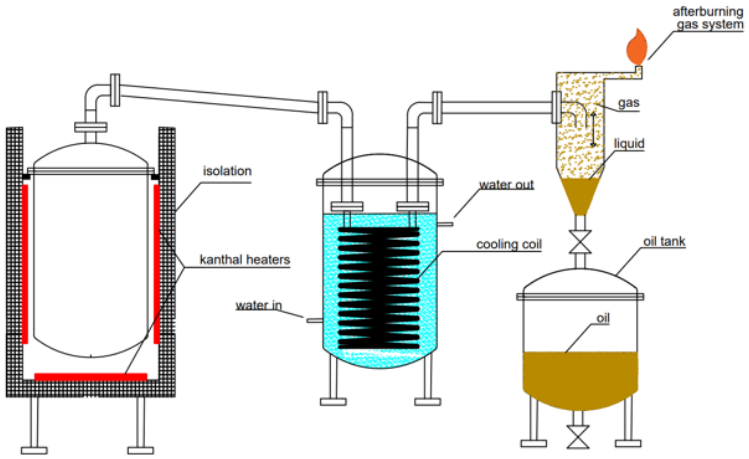


Figure 1: Scheme of the pyrolysis installation.

During the pyrolysis process, the volatile fraction was delivered from the bottom of the spiral, and after condensation, the liquid products were collected in the upper part of the spiral. The two-phase condensate mixture was directed to the tee separator and the liquid products were collected in the tank, while the gaseous fraction was burned and escaped into the atmosphere.

The plastic material was purchased from a company dealing with the recycling of plastic waste. The material was selectively separated and regranulated. In the experiment, polypropylene (PP) was subject to pyrolysis. One cycle of the pyrolysis process was conducted for 20 kg of raw material with a heating rate of 10°C/min and final temperature of 500°C. The final temperature of the process was selected on the basis of thermogravimetric

analysis, analysis of literature data and experimental work in a laboratory scale. Thermogravimetric analysis proved that below 400°C the conversion was not complete, which was also confirmed by preliminary experimental tests. The literature says that the highest liquid fraction yield can be obtained during fast pyrolysis in temperatures up to 500°C [15, 38]. The choice of the final temperature of the process is also dictated by economic considerations taking into account high energy consumption as the tests require long-term heating of the reactor. The catalyst was not used in the experiments due to extra costs involved and insignificant expected increase of the process efficiency. The reactor was thermostated at the final temperature to let the volatile fraction escape from the separator, which took approximately 6 hours. After that time, the reactor was left to cool down and the pyrolysis solid residue was removed. The liquid fraction was collected in an oil condenser with the air and water cooler. The obtained oil was clarified during a two-step process. The first stage was filtration from the suspended solid residue, like char using a peristaltic pump and a filter system containing a mesh dedicated to motor fuels. In the second stage, the oil was clarified by means of vacuum filtration using a Buchner funnel with a filter of pore size 0.13 mm. Solid particles, char and dye residue were removed from the pyrolytic oil during the filtration. The liquid fraction yield was 92% wt. for polypropylene.

## 3 Waste plastic pyrolysis oil properties

The crude PPO were investigated using gas chromatography-mass spectrometry (GC-MS) so as to identify organic compounds of the fuels. The hydrocarbons were divided according to the chain length number varying between $C_6$–$C_9$, $C_{10}$–$C_{24}$ and $C_{25}$–$C_{41}$ carbon atoms (Table 2). In the chromatographic analysis of PPO the majority of the fuel – 62.87% wt. are polycyclic and aromatic hydrocarbons (PAH) with atomic numbers $C_{10}$–$C_{24}$. Distillation curves of three fuels – PPO and the reference fuel Jet A,

Table 2: Carbon number division for PPO via GC-MS.

| Carbon number division | Mass Percentage (wt. %) |
|---|---|
| $C_6$–$C_9$ | 27.7 |
| $C_{10}$–$C_{24}$ | 62.9 |
| $C_{25}$–$C_{41}$ | 9.4 |

and diesel are illustrated in Fig. 2. The GC-MS analysis of the liquid fuel sample obtained by pyrolysis of polypropylene was carried out to know the compounds present in the fuel (Fig. 3) and is summarized in Table 3. While comparing three fuel samples, different shapes of distillation curves can be observed. The Jet A fuel distillates evenly with an increasing temperature, which is related to the diversified composition of the sample containing various chain-length hydrocarbons. A quite different broken line can be observed in the distillation curve for the PPO sample, with PAH and long-chain hydrocarbons responsible for a steep rise of the distillation curve at higher temperatures above 220°C.

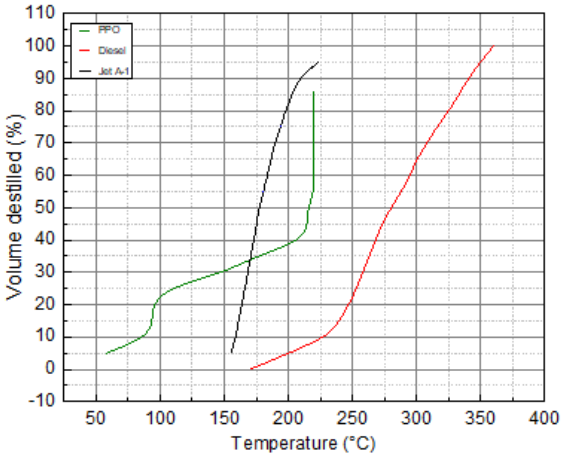


Figure 2: Distillation curves for the considered fuels.

Figure 3 presents the composition of pyrolytic oil derived from polypropylene, encompassing a variety of organic compounds such as alkanes, alco-

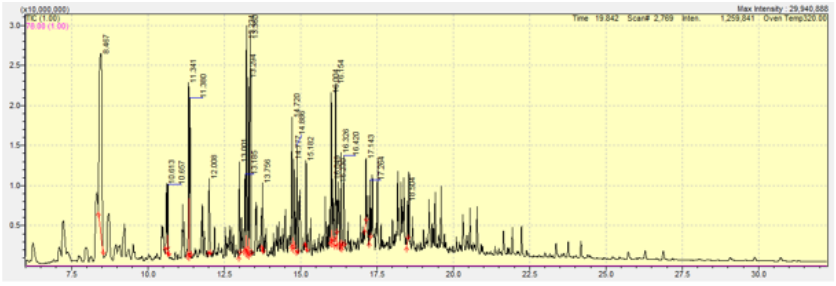

Figure 3: GC-MS spectrum of oil sample obtained at 300°C by pyrolysis of waste polypropylene.

Table 3: Compounds of PPO identified via GC-MS analysis at 300°C.

| Compounds | Chemical formula | Mass percentage (%) | Molecular weight (g/mol) |
|---|---|---|---|
| 2,4-Dimethyl-1-heptene | $C_9H_{18}$ | 20.5 | 126.24 |
| Dodecane, 4,6-dimethyl- | $C_{14}H_{30}$ | 1.29 | 198.39 |
| Heptane, 2,5,5-trimethyl- | $C_{10}H_{22}$ | 1.39 | 142.29 |
| 1-Heptanol, 2,4-diethyl- | $C_{11}H_{24}O$ | 3.6 | 172.31 |
| 2-Isopropyl-5-methyl-1-heptanol | $C_{11}H_{24}O$ | 3.1 | 172.31 |
| (2,4,6- Trimethylcyclohexyl) methanol | $C_{10}H_{20}O$ | 1.8 | 156.27 |
| Oxalic acid, cyclohexyl tetradecyl ester | $C_{22}H_{42}O_4$ | 1.7 | 370.57 |
| Cyclohexane, tetradecyl- | $C_{20}H_{40}$ | 1.3 | 280.53 |
| 1-Heptanol, 2,4-diethyl- | $C_{11}H_{24}$ | 4.9 | 172.30 |
| 2-Isopropyl-5-methyl-1- heptanol | $C_{11}H_{24}O$ | 3.6 | 172.31 |
| 1-Decanol, 2-octyl- | $C_{18}H_{38}O$ | 4.9 | 270.49 |
| Cyclododecanemethanol | $C_{13}H_{26}O$ | 1.0 | 198.34 |
| 1-Dodecanol, 2-hexyl- | $C_{18}H_{38}O$ | 2.3 | 270.49 |
| 1-Dodecanol, 2-octyl- | $C_{20}H_{42}O$ | 1.8 | 298.55 |
| 1-Hexadecanesulfonyl chloride | $C_{16}H_{33}ClO_2S$ | 1.9 | 322.95 |
| (2,4,6-Trimethylcyclohexyl)methanol | $C_{10}H_{20}O$ | 0.15 | 156.26 |
| Dotriacontyl pentafluoropropionate | $C_{35}H_{65}F_5O_2$ | 2.7 | 612.90 |
| Nonadecyl pentafluoropropionate | $C_{22}H_{39}F_5O_2$ | 1.1 | 430.50 |
| 1-Decanol, 2-hexyl- | $C_{16}H_{34}O$ | 3.1 | 242.44 |
| Oxalic acid, butyl 1-menthyl ester | $C_{16}H_{28}O_4$ | 2.4 | 284.39 |
| Tetratriacontyl heptafluorobutyrate | $C_{38}H_{69}F_7O_2$ | 1.5 | 690.90 |
| Cyclooctane, 1-methyl- 3-propyl | $C_{11}H_{22}$ | 1.6 | 154.29 |
| Octatriacontyl pentafluoropropionate | $C_{41}H_{77}F_5O_2$ | 1.1 | 697.00 |
| Octatriacontyl trifluoroacetate | $C_{40}H_{77}F_3O_2$ | 0.9 | 647.00 |
| Hexatriacontyl trifluoroacetate | $C_{38}H_{73}F_3O_2$ | 0.8 | 619.00 |

hols, esters, and fluoroorganic compounds. Alkanes, such as 2,4-dimethyl-1-heptene, 4,6-dimethyldodecane, and 2,5,5-trimethylheptane are main constituents of many fossil fuels, offering high calorific value and chemical stability. Alcohols, including 1-heptanol, 2,4-diethyl-, 1-heptanol, 2-isopropyl-5-methyl-, and (2,4,6-trimethylcyclohexyl)methanol can enhance the octane rating and anti-knock properties of the fuel, but may also increase its hygroscopicity. Esters, such as oxalic acid, cyclohexyl tetradecyl ester,

dotriacontyl pentafluoropropionate, and nonadecyl pentafluoropropionate, can improve the fuel's octane rating and lubricity, but may also increase its hygroscopicity. Fluoroorganic compounds, such as tetratriacontyl heptafluorobutyrate, octatriacontyl pentafluoropropionate, octatriacontyl trifluoroacetate, and hexatriacontyl trifluoroacetate can enhance the fuel's resistance to oxidation and improve its thermal stability. This composition suggests that the pyrolytic oil has potential for fuel application, due to the presence of many compounds typical for fossil fuels. However, the physicochemical properties of such a fuel, such as calorific value, octane rating, hygroscopicity, lubricity, and thermal stability, will depend on the specific proportions of these compounds.

The basic physico-chemical properties of the considered oil were investigated using the standards and methods as defined in Table 4. Specific fuel properties as compared with those of Jet A and diesel are collected in Table 5.

Table 4: ASTM standards and methods of determination of fuel properties.

| ASTM standard | Unit | Property | Method |
|---|---|---|---|
| D1298 | $kg/m^3$ | density | density meters with U-tube oscillators (U-tube) |
| D445 | $m^2/s$ | kinematic viscosity | rheometer |
| D4809-95 | MJ/kg | calorific value | calorimeter |
| D92 | °C | flash point | Persky-Martens flash point test |

The obtained PPO is characterized by a lower density in comparison to the reference oils – Jet A1 and commercial diesel. The difference is equal to 6.5% with respect to kerosene. The higher heating value (HHV) increases with the increasing hydrogen-to-carbon ratio in oil samples as the heat of combustion of pure substances amounts to 120 MJ/kg for elemental hydrogen and 40 MJ/kg for elemental carbon. HHV of PPO equal to 44.7 MJ/kg is by approximately 3% higher than that of Jet A. The above properties have the effect of higher heat release rate and $NO_x$ emissions [17]. The WPPO flash points are below that of aviation fuel and neat diesel, and are 34°C for PPO.

Three uniform and stable blends of each considered pyrolytic oil with kerosene (Jet A) were prepared with 25%, 50%, and 75% wt. of PPO in the blends. The samples were named describing the volume of waste plastic pyrolysis oil in the Jet A blend, eg. PP25, PP50, PP75, and also PP100 as

Table 5: Physical characterization of PP oil comparison with aviation fuel and pure diesel fuel.

| Property | Jet A | PPO | Diesel [17] |
|---|---|---|---|
| Molecular weight (kg/kmol) | 142 | 236.8 | – |
| Chemical formula | $C_{10}H_{22}$ | $C_{10,17}H_{39,55}$ | |
| Density (kg/m$^3$) | 821 (at 15°C) | 767.7 | 840 |
| Viscosity (cP) | 1.5–2.6 (at 20°C) | 1.702 | 2.62 (at 40°C) |
| HHV (MJ/kg) | 43.28 | 44.7 | 42.9 |
| Flash point (°C) | 42 | 34 | 59.5 |
| Sulfur (wt. %) | 0.3 | – | 0.00135 |
| C (wt. %) | 86.15 | 89.3 | 86.57 |
| $H_2$ (wt.%) | 13.85 | 7.4 | 13.38 |
| $O_2$ (wt.%) | 0.10 | 5.5 | 0.05 |
| Aromatic content (wt.%) | 26 | 0 | 29.6 |

pure PPO. The blends were chemically stable when stored in a refrigerator and also at a room temperature. The oil samples were homogeneous and transparent, their colour did not undergo visible changes even after several weeks of room-temperature exposure.

## 4 Experimental facility of the miniature gas turbine and research methodology

Given the high costs associated with experimental studies of gas turbines, several research groups have opted to explore miniature gas turbine engines [39, 40]. Research on small aircraft engines compared to stationary gas turbines is characterized by limitations such as differences in scale, operating regimes, and construction, which can affect the direct applicability of results to larger systems. However, they also offer significant advantages, including greater flexibility in testing various configurations and fuels, easier accessibility for scientific and educational research, and faster adaptation to new technologies. These aspects make research on small aircraft engines a valuable tool in the development of engine technologies, despite their limited direct comparability to large, stationary gas turbines [41, 42].

The research presented in this paper was conducted using a JETPOL GTM-140 gas turbine engine at the Institute of Fluid-Flow Machinery –

Turbine Department, Polish Academy of Sciences in Gdansk. Figure 4 illustrates a schematic diagram of the gas turbine, complete with designated measurement points.

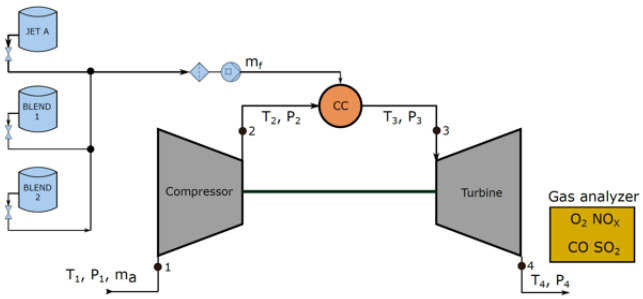


Figure 4: Gas turbine schematic diagram with measurement points [43]; T – temperature, P – pressure, 1 – before compressor, 2 – before combustion chamber, 3 – before turbine, 4 – after turbine; $m_a$ – air mass flow, $m_f$ – fuel mass flow.

The technical performance data for the GTM-140 miniature gas turbine engine under consideration can be found in [26]. The GTM-140 is composed of a single-stage centrifugal compressor, a single-stage axial turbine, and a reverse flow annular combustion chamber with six fuel injectors, all located on the same shaft. The experimental setup was outfitted with measurement instruments designed to capture flow and performance parameters of the gas turbine, as well as emission levels. Table 6 compiles the details of these measurements, providing the range of variation for the main parameters and emission indices, inclusive of the measurement process.

The errors associated with recalculations of certain gas turbine parameters and emission indexes from the measured values were estimated with the help of a method suggested by Moffat [44]. Errors were estimated on the basis of minimum input values and accuracy of the measuring instruments. For $S$ – a function of independent variables $(x_1, x_2, x_3, \ldots, x_n)$, the error of determination of the $S$ function values can be found from equation

$$\frac{\partial S}{S} = \left[ \left( \frac{\partial x_1}{x_1} \right)^2 + \left( \frac{\partial x_2}{x_2} \right)^2 + \cdots + \left( \frac{\partial x_n}{x_n} \right)^2 \right]^{0.5} . \tag{1}$$

For example, in the case of thrust specific fuel consumption (TSFC), being a ratio of the mass flow rate of fuel and thrust:

$$\mathrm{TSFC} = \frac{\dot{m}_f}{\tau} , \tag{2}$$

Table 6: Gas turbine performance and emission measurements.

| Measured parameter | Range | Unit | Device/Sensor type | Resolution | Uncertainty |
|---|---|---|---|---|---|
| Temperatures of inlet/exit compressor/turbine sector (T1–T4) | 0–1100 | °C | Thermocouple K-Type | 1°C | ±1°C |
| Pressure of inlet/exit compressor and turbine sector (P1-P4) | P1 0–0.98 P2–P4 0–9.8 | bar | Digital pressure transducers | 0.01 bar | ±1.0% |
| Static Thrust | 0–200 | N | Strain gauges | 1 N | 1 mV/V |
| Fuel volumetric flow | 0.5–100 | LPH | Oval-gear flowmeter | 0.01 LPH | ±0.5% |
| Rotational speed | 0–200 000 | rpm | Rotational speed sensor – magnetic pick-up | 1 rpm | ±0.5% |

| Gas emissions | Range | Unit | Device/Sensor type | Resolution | Uncertainty |
|---|---|---|---|---|---|
| Oxygen | 0–20.95 | % | Electrochemical | 0.01% | ±0.2% abs. or 5% rel. |
| Carbon monoxide | 0–5000 | ppm | Electrochemical | 1 ppm | ±5 ppm abs. or 5% rel. |
| Nitric oxide | 0–500 | ppm | Electrochemical | 0.1 ppm | ±5 ppm abs. or 5% rel. |
| Sulphur dioxide | 0–2000 | ppm | Electrochemical | 0.1 ppm | ±5 ppm abs. or 5% rel. |

the maximum uncertainty can be found from the formula taking into account percentage uncertainties of measurement devices as presented in Table 6:

$$\frac{\partial \mathrm{TSFC}}{\mathrm{TSFC}} = \left[ \left( \frac{\partial \dot{m}_f}{\dot{m}_f} \right)^2 + \left( \frac{\partial \tau}{\tau} \right)^2 \right]^{0.5} . \tag{3}$$

From Eq. (2), the maximum error in the calculation of TSFC is equal to 0.35%. The errors connected with measured emission indexes for $NO_x$ and CO were found to be 1.08% and 0.28%, thrust specific emission indexes for $NO_x$ and CO – 1.43% and 0.64%, respectively.

Experimental data were recorded in stationary conditions, within the range of 50 000 rpm to 100 000 rpm for pure aviation kerosene. Process values for each rotational speed were registered upon the balancing of temperature and flow in the engine. Initially, the engine was supplied with base fuel, i.e. Jet A, then switched to alternative fuel without changing the throttle settings. The experimental results are presented as line diagrams in

a wide range of microturbine rotational speed, and also as stacked column charts for selected rotational speeds. Within the applied rpm range, the following operational data and indexes were analyzed: static thrust, fuel consumption, TSFC and emission index values for CO, $CO_2$, and $NO_x$.

## 5 Gas turbine performance characteristics

Figure 5 presents the static thrust and fuel mass flow rate in the gas turbine for all evaluated fuel compositions. These tests were conducted under the same throttle settings as those used for Jet A-1. Given the lower density and higher calorific value of pyrolysis plastic oil (PPO), the mass flow rate of PPO blends exhibits a decrease when compared to aviation kerosene.

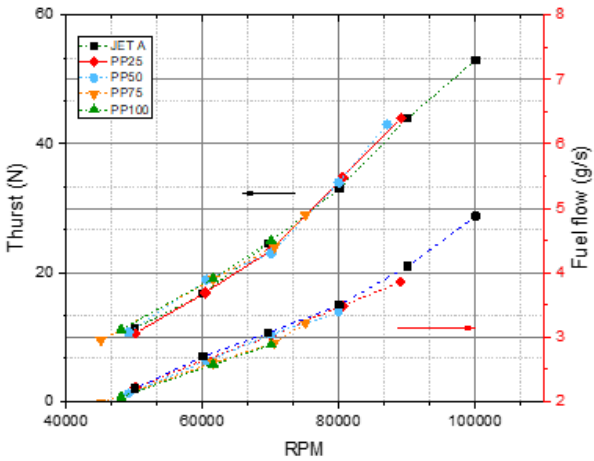


Figure 5: Static thrust and mass flow rate of fuel *vs.* turbine rotational speed for the investigated PPO/JET A blends.

The static thrust for PPO/Jet A-1 blends exhibits a slight increase with the volume share of PPO in the mixture across most of the turbine load. However, conducting tests across the full speed range proved challenging for PPO/Jet A-1 mixtures with a volume concentration of pyrolytic oil exceeding 75%. As the concentration of PPO increased, engine instability and shutdowns became more frequent. This instability accounts for the absence of characteristic data for PP75 and PP100 at rotational speeds exceeding approximately 80 000 rpm. Similar trends were noted in [28]. The thrust obtained in the test is similar, and the amount of fuel depends mainly on the calorific value of the fuel used.

Figure 6 illustrates the variation in thrust specific fuel consumption as a function of the GTM-140 engine speed. The TSFC characteristic curves for PPO/Jet A-1 blends fall below those determined for Jet A-1 across most of the turbine performance characteristics. The most significant difference between pure PPO and aviation kerosene (a TSFC reduction for pure PPO) is observed at approximately 60 000 rpm, reaching 19%. The average TSFC value for PP100 is 13.8% lower than the base fuel, a direct consequence of the higher heating value of PPO fuel. A higher LHV of WPPO results in a high heat release rate and improved combustion conditions, which has a positive effect on TSFC of the engine. Similar findings were reported in [26].

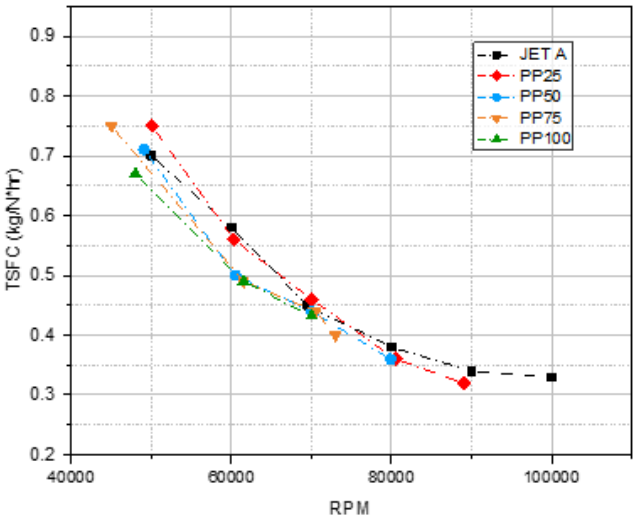


Figure 6: Thrust specific fuel consumption *vs.* turbine rotational speed for the investigated PPO/Jet A blends.

Figure 7 presents a graph depicting the exhaust gas temperature (EGT) as a function of speed. Across the entire speed range considered, EGT fluctuates between 525°C and 630°C. For all tested mixtures, this temperature decreases almost linearly with engine load, typically by 10–15°C for every approximately 10 000 rpm. This identified trend is characteristic of this type of gas turbines [28,29]. The engine outlet temperatures for the PPO/Jet A-1 blends are only marginally higher. From an operational perspective, these differences are negligible, but they could potentially influence $NO_x$ emissions.

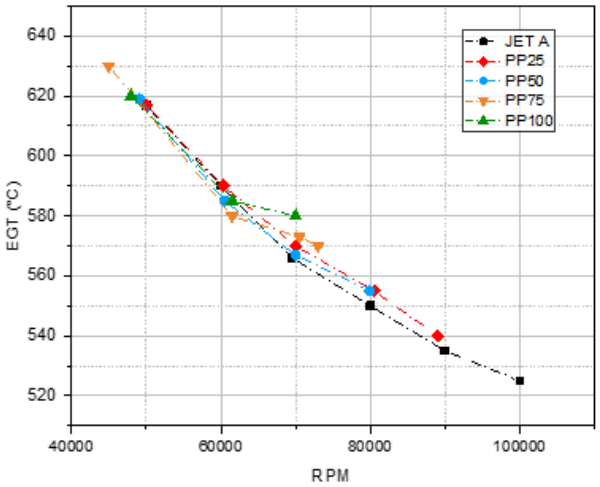


Figure 7: EGT *vs.* turbine rotational speed for the investigated PPO/Jet A blends.

## 6 Emission indexes

Upon obtaining emission concentrations in the gas exhaust, emission indexes were determined for every harmful compound of exhaust gas. The emission index for component $(i)$ is the mass of that component related to the mass of combusted fuel [45]:

$$\mathrm{EI}_i = \frac{m_{i,\,emitted}}{m_{f,\,burned}}\,. \tag{4}$$

The emission index is regarded to assess the combustion process efficiency. For the process of hydrocarbon fuel combustion with air, the emission index can be determined for the concentrations of specific emission components (molar fraction) together with all the components containing an atom of carbon (C). Assuming that all carbon derived from the fuel was transformed into compounds of $CO_2$ and CO contained in exhaust fumes (soot was disregarded), the emission index can be defined as [45]

$$\mathrm{EI}_i = \left(\frac{\chi_i}{\chi_{\mathrm{CO}} + \chi_{\mathrm{CO_2}}}\right)\left(\frac{x\mathrm{MW}_i}{\mathrm{MW}_f}\right). \tag{5}$$

The first part of the equation is represented by moles of component $(i)$ and carbon from the fuel, whereas the part in the second bracket serves the purpose of the necessary conversion of C moles and fuel moles into

mass units. The presented emission indexes are independent of possible dilution of exhaust samples because the measured concentrations of exhaust components appear as a ratio, so the measuring error is eliminated [45]. Another way of illustrating emissions is by means of thrust specific emission indexes. The thrust specific emission indexes for $NO_x$ and CO represent the amount of respective pollutants produced per unit turbine engine thrust [35, 46].

The emission index representing the volume of pollutants per unit of static thrust generated by the engine is expressed as

$$\mathrm{EI}_{i,\tau} = \left(\frac{\chi_i}{\chi_{\mathrm{CO}} + \chi_{\mathrm{CO_2}}}\right)\left(\frac{x\mathrm{MW}_i}{\mathrm{MW}_f}\right)\frac{\dot{m}_f}{\tau}\,. \tag{6}$$

The emission index for nitrogen oxides in the function of turbine rotational speed for the investigated PPO/Jet A blends, calculated based on molar concentration in Eq. (5) is illustrated in Figure 8. The primary mechanism for the formation of nitrogen oxides in this context is the Zeldovich mechanism, also known as the thermal oxidation mechanism of neutral atmospheric nitrogen in high-temperature gas regions. This process, predominantly endothermic, escalates in efficiency at temperatures exceeding 1577°C, leading to a significant formation of $NO_x$.

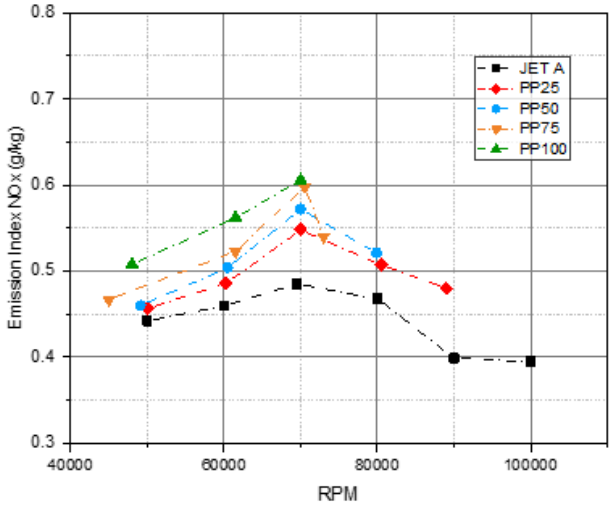


Figure 8: $NO_x$ emission index *vs.* turbine rotational speed for the investigated PPO/Jet A blends.

In the case of PPO/Jet A fuel blends, an observed increase in $NO_x$ emissions is notable. This increase is attributed to the elevated temperatures facilitating the Zeldovich mechanism, where nitrogen and oxygen atoms react more readily to form nitrogen oxides. On average, across the entire range of tested speeds, there is an increase in $NO_x$ emissions ranging from 24% for the PP25 blend to 30% for the PP100 blend. This data underscores the impact of fuel composition on $NO_x$ emission levels, influenced by the intricate interplay of temperature, fuel composition, and combustion dynamics. Other mechanisms of formation of nitrogen oxides are fuel (nitrogen in fuel), and prompt (in fuel-rich conditions), but thermal formation is the main source of $NO_x$ emission in gas turbines.

The thrust specific $NO_{x,\tau}$ emission index for the investigated micro gas turbine fuelled by WPPO and Jet A blends found from Eq. (5) is depicted in Figure 9. Comparable values of the TSFC for polypropylene pyrolysis oil do not strongly affect the thrust specific $NO_{x,\tau}$ emission of investigated blends for almost the whole range of the tested turbine load. Averaging the determined curves, the specific emission index for PP100 is greater than that for Jet A only by 5.2%.

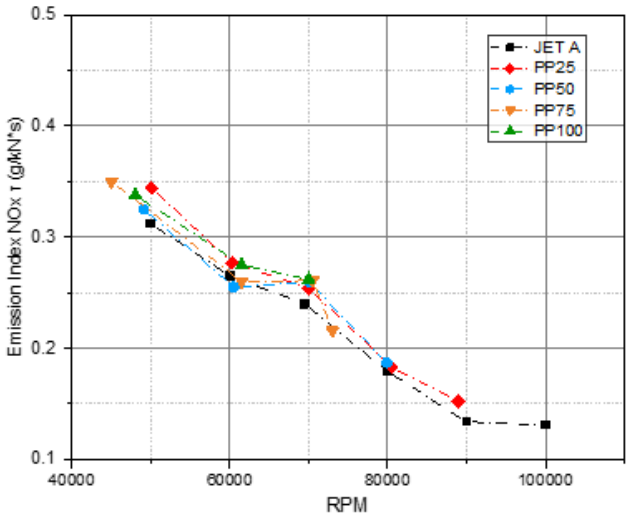


Figure 9: $NO_{x,\tau}$ emission index *vs.* turbine rotational speed for the investigated PPO/Jet A blends.

The CO emission index of the micro gas turbine in the function of turbine rotational speed for the investigated PPO/Jett A blends is depicted

in Figure 10. For the PPO/Jet A blends, the characteristics decrease with the increasing rotational speed. The trend is not exactly clear with respect to the share of PPO in the blend. It can be assumed that the CO emission index does not considerably vary with the share of PPO. Considering definitely higher values of the molecular weight, density and viscosity for PPO with respect to Jet A, similar emission values from those fuels can be considered a satisfying result in the environmental context.

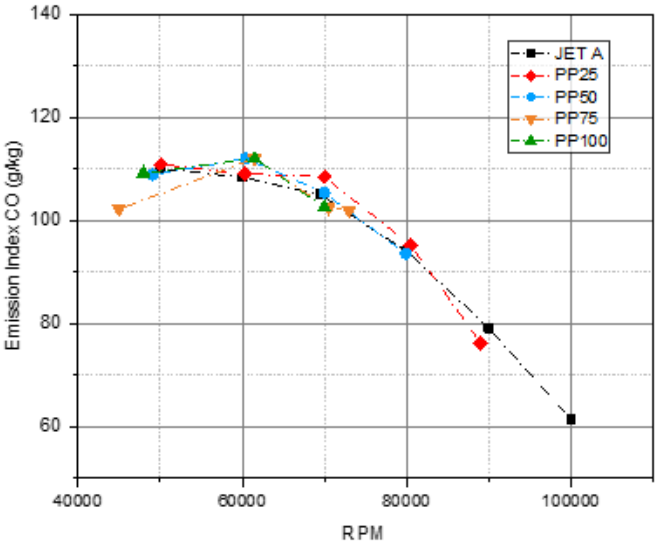


Figure 10: CO emission index *vs.* turbine rotational speed for the investigated PPO/Jet A blends.

The $CO_\tau$ emission index taking into account the fuel efficiency for the investigated PPO/Jet A blends is illustrated in Fig. 11. The thrust specific $CO_\tau$ emission index characteristics for PPO/Jet A blends seem to be located slightly below those for Jet A kerosene by up to 5–10%, although a few exceptions can also be noted. The research conducted suggests that the emission rates of nitrogen oxides and carbon oxides are usually higher (with an exception of $CO_\tau$ emissions for PPO) when using plastic pyrolysis oils. The increase in emissions can be accepted as a method of utilization of waste plastics and turning them into energy, since a large part of plastics is not viable for recycling.

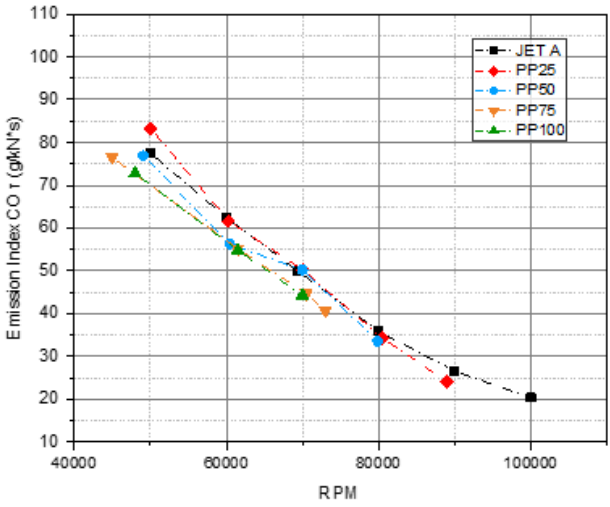


Figure 11: $CO_\tau$ emission index *vs.* turbine rotational speed for the investigated PPO/Jet A blends.

# 7 Conclusions

This study explores the potential of managing plastic waste through its thermal conversion *via* pyrolysis, leading to the production of waste plastic pyrolysis oil (WPPO). This approach focuses on utilizing the resultant liquid fuel in powering gas turbine engines, in conjunction with aviation kerosene. WPPO represents a readily available fuel source, its abundance underpinned by the prevalence of non-recyclable waste.

Building on this, the research extends to examining pyrolytic oil derived specifically from polypropylene. Despite the general challenge of higher emissions associated with this type of pyrolytic oil, its use in micro gas turbines is considered acceptable, primarily due to its origin as a recycling by-product of polypropylene waste, which is otherwise difficult to process. This aspect of the study highlights the environmental benefits of converting challenging waste materials into valuable energy resources.

The combined approach of this research provides valuable insights into sustainable energy solutions, particularly in the management of non-recyclable plastic waste. The properties of WPPO, along with its viability as an alternative fuel, offer a promising avenue for reducing harmful emissions and pollutants. To further align with the future fuel requirements of commercial combined heat and power (CHP) systems, additional testing with

modern recuperative gas turbines can be envisioned. This holistic approach to waste management and energy utilization underscores the importance of innovative and sustainable practices in addressing environmental concerns.

The molecular weight of the derived polypropylene oil (PPO) was determined to be 236.8 g/mol, in contrast to the molecular weight of kerosene at 142 g/mol. The heating value of PPO surpasses that of Jet A by 3.3%, while its flash point is lower at 34°C. The density of the tested fuels was measured at 767.7 kg/m$^3$ for polypropylene oil.

Several fuel blends of polypropylene oil with aviation kerosene Jet A were prepared, incorporating 25%, 50%, 75%, and 100% PPO. The impact of the proportion of pyrolytic oil in PPO/Jet A fuel blends on the performance and emission characteristics of a miniature gas turbine GTM-140 was examined experimentally. The findings are presented as graphs of exhaust turbine temperature, fuel flow, static thrust, thrust specific fuel consumption (TSFC), and thrust specific emissions of $NO_x$,$_\tau$, $CO_\tau$, measured across a broad range of micro gas turbine loads.

Drawing from the experimental results obtained from the micro gas turbine engine facility, the following conclusions can be made:

- Overall, the micro gas turbine engine when powered by polypropylene oil demonstrated superior thermal efficiency (expressed via thrust specific fuel consumption), attributable to its higher calorific value. TSFC for PPO/Jet A blends generally decreased relative to pure Jet A across most characteristics, with the greatest difference between pure PPO and aviation kerosene (a decrease in TSFC for pure PPO) observed at 60 000 rpm, reaching 19%. The average increase in thermal efficiency for pure PPO relative to Jet A was determined to be 13.8%.

- The gas turbine engine outlet temperatures for PPO/Jet A blends were marginally higher compared to pure Jet A.

- The incorporation of propylene oil (PPO) led to an increase in $NO_x$ emissions, although the largest average increase of the thrust specific $NO_x$ index observed for pure PPO relative to pure Jet A did not exceed a modest 5%.

- For PPO/Jet A blends, the thrust specific $CO_\tau$ emission index was typically slightly lower by up to 5–10% in comparison to Jet A kerosene, although a few deviations from this trend were also noted.

- Polypropylene oil emerges as an attractive option, considering its superior thermal efficiency (by 13.8%), marginally lower thrust specific $CO_\tau$ emission, and a mere 5% increase in thrust specific $NO_{x,\tau}$ emission relative to those of Jet A.

A critical element connecting all research on turbine and combustion engines utilizing these types of fuels is the intricate and essential fuel preparation process. This process typically necessitates sophisticated techniques, such as advanced filtration, distillation, or refining systems, to ensure the fuel meets the necessary quality standards for efficient and clean combustion. The complexity and efficacy of these preparation methods play a pivotal role in determining the overall performance and environmental impact of using these fuels in gas turbines. As such, ongoing and future research should also focus on optimizing these preparation techniques to enhance the viability and sustainability of plastic-derived and other alternative fuels in energy production.

*Received 30 November 2023*

## References

[1] Barsali S., De Marco A., Giglioli R., Ludovici G., Possenti A.: *Dynamic modelling of biomass power plant using micro gas turbine*. Renew. Energy **80**(2015), 806–18. doi: 10.1016/J.RENENE.2015.02.064

[2] Chiaramonti D., Goumas T.: *Impacts on industrial-scale market deployment of advanced biofuels and recycled carbon fuels from the EU Renewable Energy Directive II*. Appl. Energy **251**(2019), 113351. doi: 10.1016/J.APENERGY.2019.113351

[3] Daraei M., Avelin A., Dotzauer E., Thorin E.: *Evaluation of biofuel production integrated with existing CHP plants and the impacts on production planning of the system – A case study*. Appl. Energy **252**(2019), doi: 10.1016/J.APENERGY.2019.113461

[4] Gonzalez-Salazar M.A., Venturini M., Poganietz W.R., Finkenrath M., Kirsten T., Acevedo H., *et al.*: *Development of a technology roadmap for bioenergy exploitation including biofuels, waste-to-energy and power generation & CHP*. Appl. Energy **180**(2016), 338–352. doi: 10.1016/J.APENERGY.2016.07.120

[5] Januszewicz K., Kazimierski P., Suchocki T., Kardaś D., Lewandowski W., Klugmann-Radziemska E., *et al.*: *Waste rubber pyrolysis: Product yields and limonene concentration*. Materials (Basel) **13**(2020). doi: 10.3390/ma13194435

[6] Kazimierski P., Januszewicz K., Godlewski W., Fijuk A., Suchocki T., Chaja P., *et al.*: *The course and the effects of agricultural biomass pyrolysis in the production of high-calorific biochar*. Materials (Basel) **15**(2022), 3, 1038. doi: 10.3390/ma15031038

[7] GmbH PMRG (PEMRG) and CM&S.: *Final Report*, 2019.

[8] European Association of Plastics Recycling and Recovery Organisations.: *An analysis of European plastics production, demand and waste data.* Belgium, 2015.

[9] Anuar Sharuddin S.D., Abnisa F., Van Daud W.M.A., Aroua M.K.: A *review on pyrolysis of plastic wastes.* Energy Convers. Manag. **115**(2016), 308–326. doi: 10.1016/j.enconman.2016.02.037

[10] Ziółkowski P., Stasiak K., Amiri M., Mikielewicz D.: *Negative carbon dioxide gas power plant integrated with gasification of sewage sludge.* Energy **262**(2023), 125496. doi: 10.1016/j.energy.2022.125496

[11] Kaszuba M., Ziółkowski P., Mikielewicz D.: *Performance of cryogenic oxygen production unit with exhaust gas bleed for sewage sludge gasification and different oxygen purities.* Arch. Thermodyn. **44**(2023), 3, 63–81. doi: 10.24425/ather.2023.147537

[12] Kumar S., Prakash R., Murugan S., Singh R.K.: *Performance and emission analysis of blends of waste plastic oil obtained by catalytic pyrolysis of waste HDPE with diesel in a CI engine.* Energy Convers. Manag. **74**(2013), 323–331. doi: 10.1016/J.ENCONMAN.2013.05.028

[13] Kazimierski P., Hercel P., Suchocki T., Smoliński J., Pladzyk A., Kardaś D., *et al.*: *Pyrolysis of pruning residues from various types of orchards and pretreatment for energetic use of biochar.* Materials (Basel) **14**(2021), 11, 2969. doi: 10.3390/ma14112969

[14] Kantorek M., Jesionek K., Polesek-Karczewska S., Ziółkowski P., Stajnke M., Badur J.: *Thermal utilization of meat-and-bone meal using the rotary kiln pyrolyzer and the fluidized bed boiler – The performance of pilot-scale installation.* Renew. Energy **146**(2021), 1447–1456. doi: 10.1016/j.renene.2020.10.124

[15] Cai N., Xia S., Xiao H., Chen Y., Chen W., Yang H., *et al.*: *Distinguishing the impact of temperature on iron catalyst during the catalytic-pyrolysis of waste polypropylene.* Proc. Combust. Inst. **39**(2023), 1, 835-845. doi: 10.1016/j.proci.2022.06.008

[16] Aisien E.T., Otuya I.C., Aisien F.A.: *Thermal and catalytic pyrolysis of waste polypropylene plastic using spent FCC catalyst.* Environ. Technol. Innov. **22**(2021), 101455. doi: 10.1016/j.eti.2021.101455

[17] Kalargaris I., Tian G., Gu S.: *Combustion, performance and emission analysis of a DI diesel engine using plastic pyrolysis oil.* Fuel Process. Technol. **157**(2017), 108–115. doi: 10.1016/J.FUPROC.2016.11.016

[18] Mani M., Nagarajan G., Sampath S:. *Characterisation and effect of using waste plastic oil and diesel fuel blends in compression ignition engine.* Energy **36**(2011), 212–219. doi: 10.1016/j.energy.2010.10.049

[19] Singh R.K., Ruj B., Sadhukhan A.K., Gupta P., Tigga V.P.: *Waste plastic to pyrolytic oil and its utilization in CI engine: Performance analysis and combustion characteristics.* Fuel **262**(2020), 116539. doi: 10.1016/J.FUEL.2019.116539

[20] Das A.K., Hansdah D., Mohapatra A.K., Panda A.K.: *Energy, exergy and emission analysis on a DI single cylinder diesel engine using pyrolytic waste plastic oil diesel blend.* J. Energy Inst. **93**(2020), 1624–1633. doi: 10.1016/j.joei.2020.01.024

[21] Singh T.S., Rajak U., Dasore A., Muthukumar M., Verma T.N.: P*erformance and ecological parameters of a diesel engine fueled with diesel and plastic pyrolyzed oil (PPO) at variable working parameters.* Environ. Technol. Innov. **22**(2021). doi: 10.1016/j.eti.2021.101491

[22] Januszewicz K., Hunicz J., Rybak A.: *An experimental assessment on a diesel engine powered by blends of waste-plastic-derived pyrolysis oil with diesel.* Energy **281**(2023). doi: 10.1016/j.energy.2023.128330

[23] Devaraj J., Robinson Y., Ganapathi P.: *Experimental investigation of performance, emission and combustion characteristics of waste plastic pyrolysis oil blended with diethyl ether used as fuel for diesel engine.* Energy **85**(2015), 304–309. doi: 10.1016/j.energy.2015.03.075

[24] Chiaramonti D., Oasmaa A., Solantausta Y.: *Power generation using fast pyrolysis liquids from biomass.* Renew. Sustain. Energy Rev. **11**(2007), 1056–1086. doi: 10.1016/J.RSER.2005.07.008

[25] Pilavachi P.A.: *Mini- and micro-gas turbines for combined heat and power.* Appl. Therm. Eng. **22**(2002), 2003–2014. doi: 10.1016/S1359-4311(02)00132-1

[26] Suchocki T., Witanowski Ł., Lampart P., Kazimierski P., Januszewicz K., Gawron B.: *Experimental investigation of performance and emission characteristics of a miniature gas turbine supplied by blends of kerosene and waste tyre pyrolysis oil.* Energy **215**(2021), 119125. doi: 10.1016/j.energy.2020.119125

[27] Buffi M., Cappelletti A., Rizzo A.M., Martelli F., Chiaramonti D.: *Combustion of fast pyrolysis bio-oil and blends in a micro gas turbine.* Biomass Bioenerg. **115**(2018), 74–85. doi: 10.1016/J.BIOMBIOE.2018.04.020

[28] Gawron B., Białecki T.: *Impact of a Jet A-1/HEFA blend on the performance and emission characteristics of a miniature turboJet engine.* Int. J. Environ. Sci. Technol. **15**(2018), 1501–1508. doi: 10.1007/s13762-017-1528-3

[29] Gawron B., Białecki T., Janicka A., Suchocki T.: *Combustion and emissions characteristics of the turbine engine fueled with HeFA blends from different feedstocks.* Energies **13**(2020), 1–12. doi: 10.3390/en13051277

[30] Chmielewski M, Niszczota P, Gieras M. *Combustion efficiency of fuel-water emulsion in a small gas turbine.* Energy **211**(2020), 118961. doi: 10.1016/j.energy.2020.118961

[31] Manigandan S., Atabani A.E., Ponnusamy V.K., Gunasekar P.: *Impact of additives in Jet-A fuel blends on combustion, emission and exergetic analysis using a micro-gas turbine engine.* Fuel **276**(2020), 118104. doi: 10.1016/j.fuel.2020.118104

[32] Badami M., Nuccio P., Pastrone D., Signoretto A.: *Performance of a small-scale turboJet engine fed with traditional and alternative fuels.* Energy Convers. Manag. **82**(2014), 19–28. doi: 10.1016/j.enconman.2014.03.026

[33] Bhele S.K., Deshpande N.V., Thombre S.B.: *Experimental investigation of combustion characteristics of Jatropha biodiesel (JME) and its diesel blends for gas turbine combustor.* Mater. Today Proc. **5**(2018), 11, 23404-23412. doi: 10.1016/J.MATPR.2018.11.080

[34] Gürbüz H., Akçay H., Aldemir M., Akçay İ.H., Topalcı Ü.: *The effect of euro diesel-hydrogen dual fuel combustion on performance and environmental-economic indicators in a small UAV turbojet engine.* Fuel **306**(2021), 121735. doi: 10.1016/J.FUEL.2021.121735

[35] Habib Z., Parthasarathy R., Gollahalli S.: *Performance and emission characteristics of biofuel in a small-scale gas turbine engine.* Appl. Energy **87**(2010), 1701–1709. doi: 10.1016/j.apenergy.2009.10.024

[36] Lewandowski W.M., Januszewicz K., Kosakowski W.: *Efficiency and proportions of waste tyre pyrolysis products depending on the reactor type — A review.* J. Anal. Appl. Pyrolysis **140**(2019), 25–53. doi: 10.1016/J.JAAP.2019.03.018

[37] Januszewicz K., Kazimierski P., Kosakowski W., Lewandowski W.M.: *Waste tyres pyrolysis for obtaining limonene.* Materials (Basel) **13**(2020), 1–30. doi: 10.3390/ma13061359

[38] Kalargaris I., Tian G., Gu S.: *Experimental characterisation of a diesel engine running on polypropylene oils produced at different pyrolysis temperatures.* Fuel **211**(2018), 797–803. doi: 10.1016/j.fuel.2017.09.101

[39] Krakos (Podwin) A., Janicka A., Molska J., Zawiślak M., Lizanets D., Białecki T., *et al.*: *Microfluidic-assisted toxicity studies of Jet fuels on environmental microorganisms – Towards new lab-on-a-chip sensing applications.* J. Int. Meas. Confed. **204**(2022), 112037. doi: 10.1016/j.measurement.2022.112037

[40] Główka M., Wójcik J., Boberski P., Białecki T., Gawron B., Skolniak M., *et al.*: *Sustainable aviation fuel – Comprehensive study on highly selective isomerization route towards HEFA based bioadditives.* Renew. Energy **220**(2024), 119696. doi: 10.1016/j.renene.2023.119696

[41] Białecki T., Dzięgielewski W., Kowalski M., Kulczycki A.: *Reactivity model as a tool to compare the combustion process in aviation turbine engines powered by synthetic fuels.* Energies **14**(2021), 6302. doi: 10.3390/en14196302

[42] Kotowicz J., Job M., Brzęczek M., Nawrat K., Mędrych J.: *The methodology of the gas turbine efficiency calculation.* Arch. Thermodyn. **37**(2016), 4, 19–35. doi: 10.1515/aoter-2016-0025

[43] Suchocki T., Kazimierski P., Lampart P., Januszewicz K., Białecki T., Gawron B., *et al.*: *A comparative study of pentanol (C5 alcohol) and kerosene blends in terms of gas turbine engine performance and exhaust gas emission.* Fuel **334**(2023), 126741. doi: 10.1016/j.fuel.2022.126741

[44] Moffat R.J.: *Using Uncertainty Analysis in the Planning of an Experiment.* J. Fluids Eng. **107**(1985), 173–178. doi: 10.1115/1.3242452

[45] Turns S.R.: *An Introduction to Combustion – Concepts and Applications.* McGraw-Hill, New York 2012.

[46] Mendez C., Parthasarathy R., Gollahalli S.: *Performance and emission characteristics of a small-scale gas turbine engine fueled with ethanol/Jet A blends.* In: Proc. 50th AIAA Aerosp. Sci. Meet. Incl. New Horizons Forum Aerosp. Expo., Neshvile, 9-12 Jan. 2012, AIAA, 2012–0522, 7654–7666. doi: 10.2514/6.2012-522

**archives**
**of thermodynamics**
Vol. **44**(2023), No. 4, 185–196
DOI: 10.24425/ather.2023.149731

# Gas temperature distribution in the evaporator of GTM400 turbojet engine

**ŁUKASZ BRODZIK***

Poznan University of Technology, Faculty of Environmental Engineering and Energy, Piotrowo 3, 61-138 Poznań, Poland

**Abstract** The paper presents the results of measurements carried out in the GTM400 turbojet engine with a changed combustion chamber geometry. The available publications lack more detailed information on the temperature distribution in evaporators, which are part of the combustion chamber of small turbojet engines. As the results of the analysis showed, this is not simple, because the research takes place in very small spaces. The reason for the work carried out is to check whether the temperatures in the evaporators are high enough. This allows to determine whether the fuel is evaporating properly. Therefore, an analysis was carried out to determine the temperature distribution in the area of the inlet to the evaporator. Thanks to the modification of the combustion chamber, it was possible to measure temperatures, which in the engine literature are simulated using numerical analysis. The analysis described in the paper is one of the stages of preparing the engine for operation with hydrogen. It is modified as part of a project to build a hybrid engine burning traditional JET-A1 fuel and alternative fuel, i.e. hydrogen.

**Keywords:** Turbojet engine; Combustion chamber; Evaporators

## 1 Introduction

Miniature turbojet engines are a source of increasing interest among designers of unmanned aerial vehicles [1–3]. This is primarily due to the continuous increase in the production of these aircraft and their increasing use in

*Corresponding Author. Email: lukasz.brodzik@put.poznan.pl

the military industry [4–8]. The tasks they perform include, among others: imaging the battlefield for commanders at various levels at sea and on land, searching, detecting and pointing out objects using a laser pointer, directing fire, e.g., artillery, anti-aircraft defense, destroying ground, surface and air objects. Most aircraft are powered by electric motors or internal combustion piston engines [9–11]. Despite the relatively high fuel consumption, turbine jet engines have a large reserve of thrust, which makes them attractive wherever this parameter is important [12–16]. The miniaturization of these engines allows to think about their serious use in small unmanned aerial vehicles, which, as mentioned above, have a very wide range of applications.

The paper includes temperature tests in evaporators that occur in small turbojet engines. Placing thermocouples in these places forced a change in the engine geometry due to its incorrect operation. The test allows to indicate areas with lower and higher temperatures, which may indicate whether the fuel evaporation process is correct or which area of the engine is warmer. Evaporators are the part of the engine into which fuel is injected. It is transported together with part of the air into the combustion chamber [17, 18]. The special role of evaporators is that they evaporate the fuel, resulting in a homogeneous gaseous air-fuel mixture at the outlet. This is the reason why the engine is required to warm up well in the first phase of operation before it starts working properly [19]. The warm-up phase is necessary because in small engines the compressor pressure is not high. This involves the use of centrifugal compressors. The consequence of this is a relatively low temperature at the inlet to the combustion chamber, approximately 152°C. Due to its small dimensions, the process of evaporation and atomization of fuel must be quick and simple. Advanced technological solutions would increase the already high price of this type of engines.

Proper work of evaporators is important because it is one of the factors directly influencing the achieved combustion efficiency as well as the amount of NOx emission reduction. In turn, the improvement of operation is influenced by the larger length and diameter of the evaporator, as well as the reduction of the average diameters of fuel drops when a larger amount of air is supplied to the combustion chamber [20].

## 2 Test stand

The most important components of the test stand are: GTM400 engine with automatic start using JET-A1 fuel, gear fuel pump, fuel start solenoid valve, main fuel solenoid valve, Fig. 1 [21]. During operation, the engine

is placed under a polycarbonate cover. The station also has equipment for measuring static thrust, i.e. a strain gauge sensor, an amplifier for the MD11 measuring bridge systems, and a strain gauge beam. The whole thing is mounted on a steel base, to which control and measurement equipment with data acquisition, a fuel tank and a battery are attached.

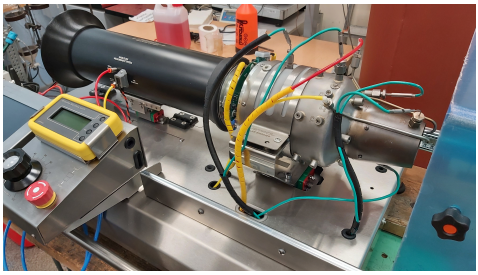

Figure 1: Test stand of GTM400 engine.

The JETPOL engine has measuring ports in various sections, e.g., the combustion chamber. The basic version is characterized by the following parameters:

thrust: 15–400 N,
rotational speed: 30000–88000 rpm,
mass air flow 0.47 kg/s,
fuel consumption 0.98 kg/min.

After engine modification, its parameters changed as follows:

thrust: 15–300 N,
rotational speed: 30000–81000 rpm,
mass air flow 0.59 kg/s,
fuel consumption 0.82 kg/min.

The dimensions of the engine are as follows: diameter 0.15 m, length 0.39 m, and weight is 2.9 kg.

There are twelve evaporators in the engine, and it is possible to perform measurements in half of them. An example of the location of a thermocouple is presented in Fig. 2. Evaporators have the shape of tubes whose axis of symmetry is not parallel to the axis of symmetry of the combustion chamber. In the case of shorter combustion chambers, evaporators bent in the circumferential direction or with a shape similar to the letter S are used [22].

K-type thermocouples (outer diameter of 0.0015 m) were used to measure the temperature inside the evaporators, which can operate in the temperature range $-40°C$ to $1000°C$ [23]. In the first stage of the research, the

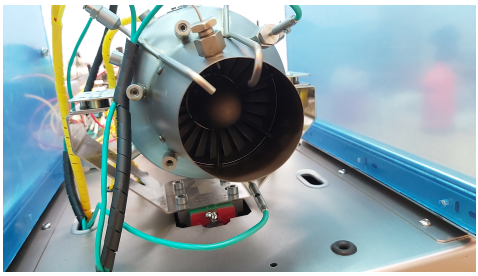

Figure 2: Temperature tappings.

sensors were inserted into the evaporators to the maximum distance, i.e., 0.07 m. In the next three stages, this distance was reduced by 0.01 m each time.

The given distance takes into account the length of the sleeve, nut and screw. The nut is screwed onto a threaded sleeve permanently located in the engine casing. A screw with a hollow hole for the sensor locks it. The sleeve, nut and screw together form the sensor mount, and their total length is 0.0365 m. This is well illustrated in Fig. 2, where the thermocouple is also inserted into the outlet nozzle (the mounting in the evaporator is the same, only smaller elements are present).

The indicated distances also include the reversal channel, the length of which (measured along the axis of symmetry) is 0.02 m. The evaporators (Fig. 3) are 0.08 m long. Therefore, when the sensor was fully inserted, a junction of the thermocouple in the evaporator was at a depth of 0.0135 m.

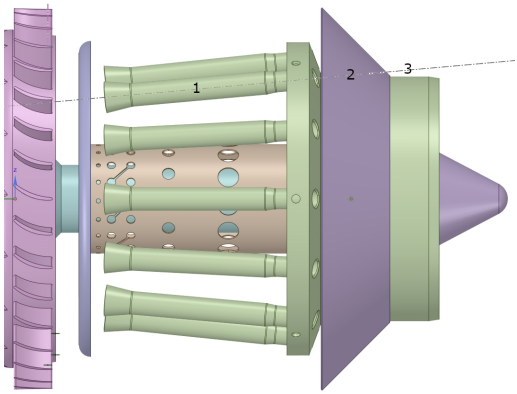


Figure 3: Part of the engine, where the test places are shown on the example of one of the evaporators (the glow tube and part of the engine casing are not visible): 1 – evaporator, 2 – reversing duct, 3 – sensor mounting on the engine casing.

## 3 Measurement analysis

During the measurements, the ambient temperature ranged from 21°C to 24°C. Measurements were made in evaporators according to the numbering (entries to the evaporators placed circumferentially every 60°), as in Fig. 4.

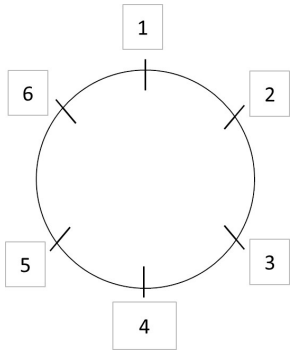


Figure 4: Numbering of evaporators.

The results of the first stage of the research are presented in Fig. 5. The temperatures in individual evaporators differ significantly. They range from approximately 170°C to 330°C.

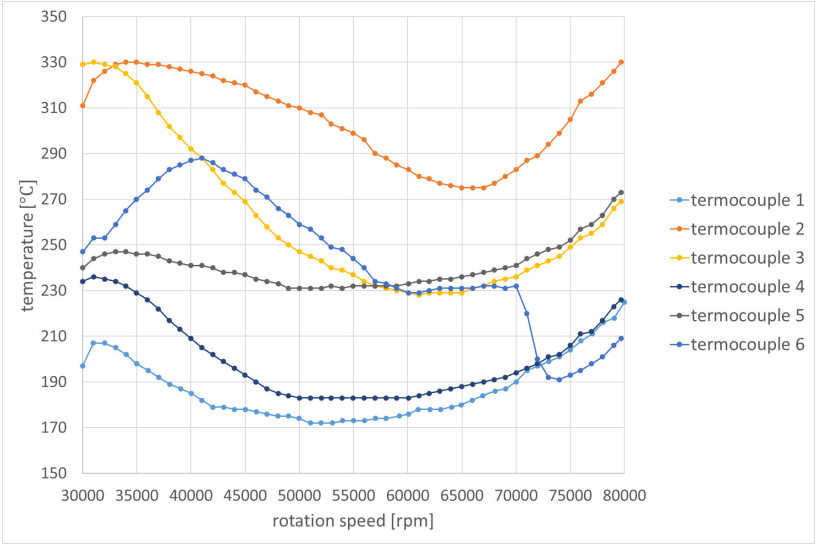


Figure 5: Temperature distribution in evaporators – measurement at a distance of 0.07 m.

The curves shown provide some basic information. The most important ones include:

- the direction of temperature change, i.e., whether it increases throughout its course or not;
- temperature values, as well as the differences observed between individual thermocouples.

With the exception of evaporator 2 and 6, in each function the values first decrease and then increase. The measurement in evaporator 3 showed that the highest temperature appeared there for the lowest rotational speed range. This is related to the gravitational falling of fuel condensate onto the lower areas of the combustion chamber. In this way, the area of the most intense combustion is concentrated there. As the temperature increases, this effect disappears because all the fuel evaporates in the evaporators.

In the second stage of the research, the sensors were inserted to a distance of 0.06 m. Shortening the distance by 0.01 m is associated with the appearance of significantly lower temperatures, which reach just over 200°C, Fig. 6. In contrast to the first stage of the research, the results show much greater consistency in the course of the values. This is especially noticeable after exceeding 65 000 rpm.

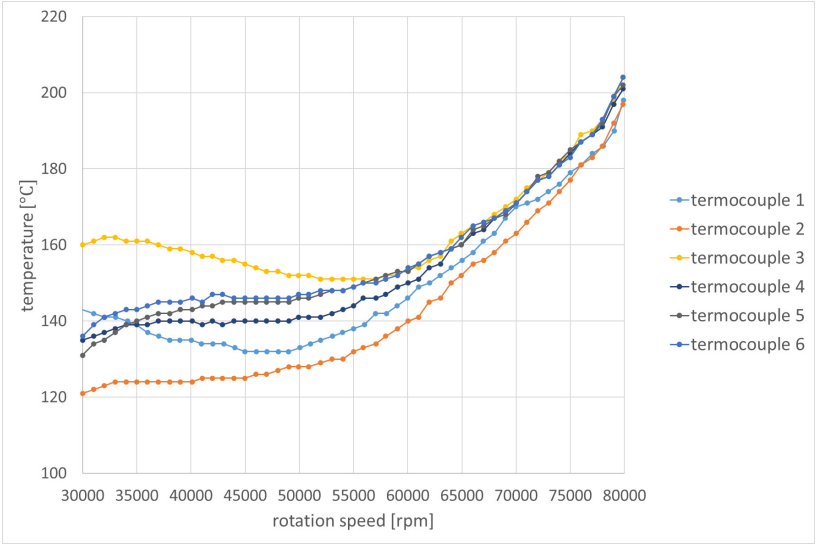


Figure 6: Temperature distribution in evaporators – measurement at a distance of 0.06 m.

Changing the location of the measurement point by another 1 cm did not bring any significant changes in temperature patterns. They are in similar ranges, i.e. 120–210°C, Fig. 7. The maximum temperatures are higher, as in the previous stage of research, but the obtained functions are characterized by even greater consistency in the nature of their course.

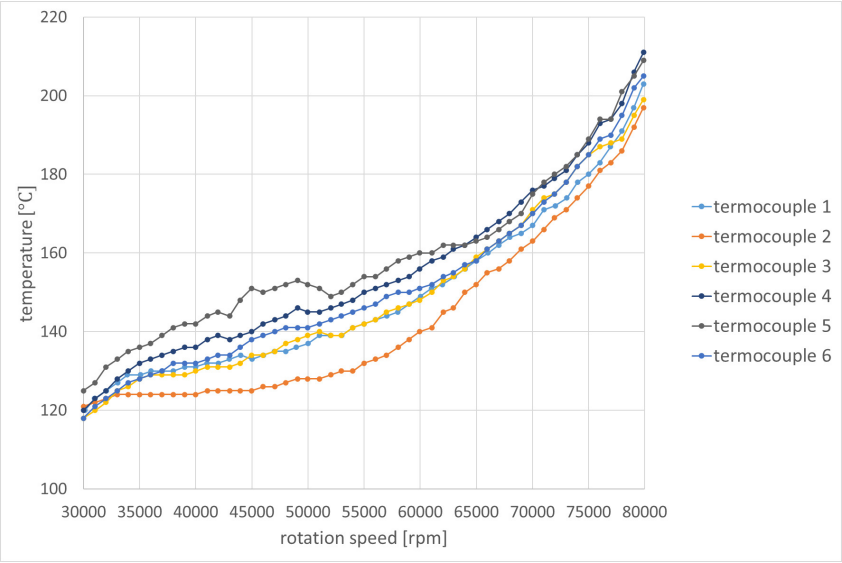


Figure 7: Temperature distribution in evaporators – measurement at a distance of 0.05 m.

In the last stage of the research, measurements in evaporators were made at a distance of 0.04 m, Fig. 8. Compared to measurements made at a distance of 0.05 m, the obtained temperatures are lower, especially in the range of lower rotational speeds. However, they do not represent such consistent courses, which is due to significant differences in the recorded temperatures.

During the measurements, it turned out that there is a serious risk of obtaining incorrect measurements in evaporators using thermoelectric sensor. The purpose of the measurements was to obtain the temperature values recorded in the gas-filled space inside the evaporators. Due to the small dimensions of the turbojet engine, the diameter of the evaporators is 0.008 m. This increases the risk of a situation where the sensor inserted into the evaporator will touch the inside of its wall. This is well illustrated in Figs. 9 and 10, which present an example of the repeatability of measurement values in two selected evaporators. The resulting error is large

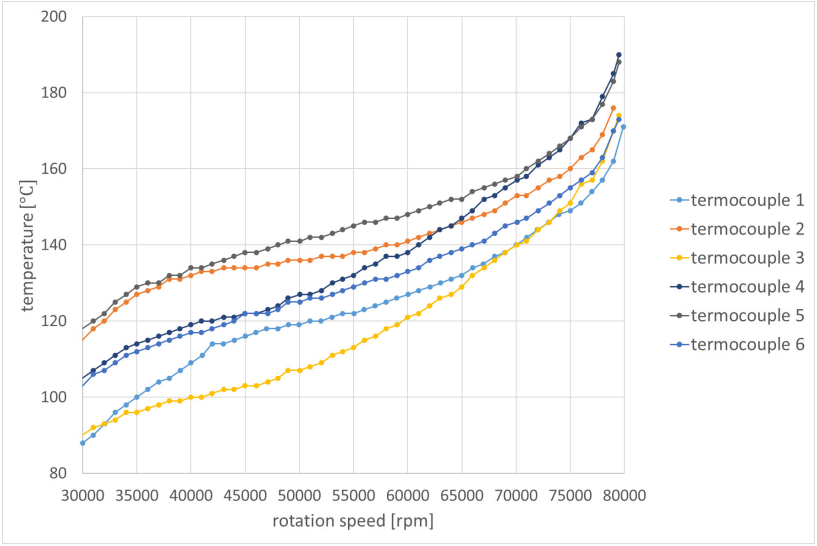


Figure 8: Temperature distribution in evaporators – measurement at a distance of 0.04 m.

because the evaporators are immersed in the hot combustion area, which causes an increase in temperature on the surface of their walls.

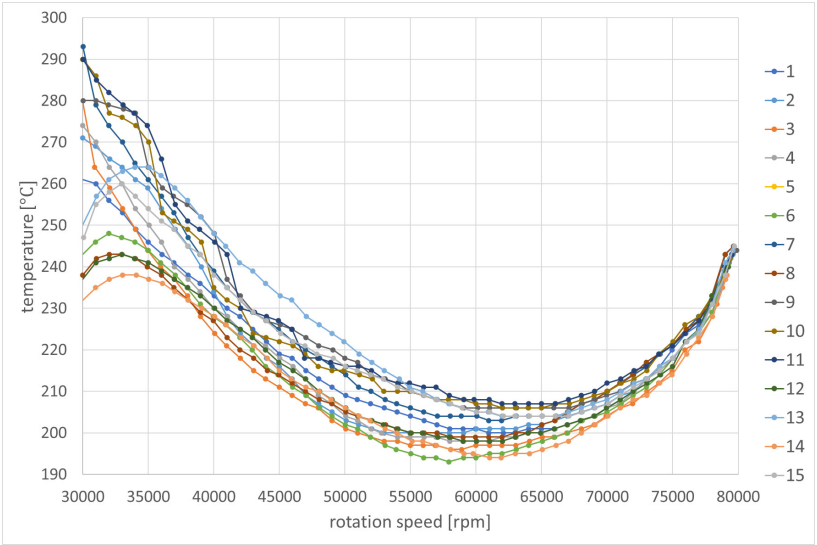


Figure 9: Temperature comparison in evaporators 1 (15 measurements) – measurement at a distance of 0.07 m.

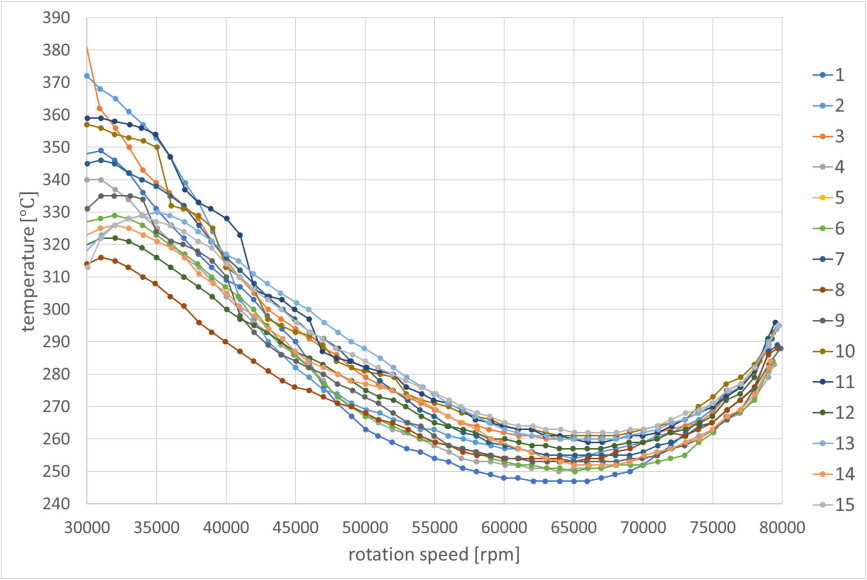


Figure 10: Temperature comparison in evaporators 3 (15 measurements) – measurement at a distance of 0.07 m.

# 4 Conclusions

The study made possible to obtain information regarding the temperature range as a function of rotational speed in two flow areas. The first one was the reversing duct, where the probe was inserted to a length of 0.05 m and 0.04 m. The second were evaporators, where a junction of the thermocouple, after inserting a distance of 0.06 m, was located at the entrance to the evaporator and a distance of 0.07 m, where it was slightly deeper. The last two measurements were crucial from the point of view of the conducted analysis.

The range of observed temperatures corresponds to boiling points, which for this fuel are 90–320°C. From this point of view, it can be seen that the temperature in the return channel is appropriate to initiate the process of evaporation of the fuel that is introduced into the evaporator. The indicated temperatures measured at a depth of 0.0135 m of the evaporator are clearly higher and correspond to the full range of the mentioned boiling points. This indicates that the process of fuel evaporation begins early, already at the inlet to the evaporator.

The temperature range at which fuel auto-ignition occurs is between 220°C and 250°C. However, it should be remembered that this phenomenon is unlikely to occur due to the fuel and air mixture being too lean.

Difficulties in building miniature flow engines result from their scale. The fluid movement as well as the combustion process take place in a very small space. In such a case, the influence of the measurement sensors increases and may cause local speed changes in the reversing channels, which further results in temperature changes in the combustion area. This also makes it difficult to take measurements. An example is the research carried out which confirmed the risk of incorrect readings of the measured parameter. They may be affected by probe deflection due to dynamic gas flow. This may happen even if (before the measurement) it is checked whether the probe is not bent. In some places it is difficult to be sure that the measurement is correct. This is because at the end and the beginning of the evaporator (i.e., in the return channel) the flow is more disturbed and it is difficult to assess whether the temperature differences result from the nature of the flow or as a result of the sensor touching the evaporator wall. It can be assumed that the deeper the probe is inserted, the greater the risk of incorrect reading, because it is easier to touch the wall of the evaporator.

The test results preliminary indicate that from the point of view of temperature distribution, the process of fuel evaporation in the evaporator is carried out correctly. It would certainly be interesting to study temperatures over a longer distance. From the point of view of the above-described problem regarding inserting thermocouples into evaporators and their possible contact with the evaporator wall, temperature measurement will be burdened with a greater risk of error. However, this would be supplementary knowledge about how much the temperature increases in the lower areas of the evaporator. After several inspections by the engine manufacturer, it turned out that the colour of the evaporators had not changed, which may indicate that no combustion process was taking place deep inside them. The analysis also showed, that the variation in the temperature field in a miniature turbojet engine can be significant.

Indirect tests, such as measurements in evaporators, are not a sufficiently accurate way to obtain the temperature distribution in the combustion chamber of a turbojet engine. However, they can additionally indicate the directions of impact of hotter areas, as well as illustrate what is happening in further parts of the combustion chamber. In the next stage of testing, the analysis of checking the correct operation of the engine should be expanded with thermovision, as well as testing with an S-type sensor of sample points in the central part of the chamber where the flame appears.

## Acknowledgements

This research was funded by the Polish Ministry of Science and Higher Education.

*Received 12 September 2023*

# References

[1] Gieras M.: *Miniature Turbojet Engines*. Oficyna Wyd. PW, Warszawa 2016 (in Polish).

[2] Nelson R.J., Dix M.D.: *Development of engines for unmanned air vehicles: some factors to be considered*. Institute for Defense Analyses, Alexandria 2003.

[3] Goraj Z., Frydrychewicz A., Świtkiewicz R., Hernik B., Gadomski J., Goetzendorf-Grabowski T., Figat M., Suchodolski S., Chajec W.: *High altitude long endurance unmanned aerial vehicle of a new generation – a design challenge for a low cost, reliable and high performance aircraft*. Bull. Pol. Acad. Sci. Tech. Sci. **52(**2004), 3, 173–194.

[4] Barnhart R.K., Hottman S.B., Marshall D.M., Shappee E.: *Introduction to Unmanned Aircraft Systems*. Taylor & Francis, 2012.

[5] Dinc A.: *$NO_x$ emissions of turbofan powered unmanned aerial vehicle for complete flight cycle*. Chin. J. Aeronaut. **33**(2020), 6, 1683–1691.

[6] Technical Report, Ver. 0.1: *Unmanned Aircraft System (UAS) Service Demand 2015 – 2035*. United States Air Force 2014.

[7] Turkay M., Gürgen S., Keskin G., Durmus S.: *Research on applications of miniturbojet and turbojet engined military UAVS*. In: Proc. 21st Int. Conf. AFASES, Scientific Research and Education in the Air Force, Braşov 2019.

[8] Kelly C., McCain C., Bertels J., Weekley S., Moody K., Utley L., Copher G., Totty C., Booth T., Spaulding L., Jdiobe M., Rouser K.: *Design of a geared turbofan module for small unmanned aircraft applications*. AIAA Scitech Forum 2021. doi: 10.2514/6.2021-0262

[9] Kreps S.E.: *Drones. Introduction. Technologies. Usage*. PWN, Warszawa 2019 (in Polish).

[10] Becmer D., Skorupka D., Duchaczek A.: *Development trends in unmanned aerial systems*. Wojskowy Instytut Techniczny Uzbrojenia **136**(2015), 4, 19–40 (in Polish).

[11] Becmer D.: *Class I-II unmanned aerial systems in the future combat system*. Zeszyty Naukowe Wyższej Szkoły Oficerskiej Wojsk Lądowych **143**(2007), 1, 34–44 (in Polish).

[12] Łapucha R.: *Combustion Chambers of Turbine-jet Engines: Processes, Calculations, Research*. Wydawn. Naukowe Instytutu Lotnictwa, Warszawa 2004 (in Polish).

[13] Sieniawski J.: *Criteria and Methods of Assessment of Aircraft Turbine Engine Components*. Oficyna Wydawnicza Politechniki Rzeszowskiej, Rzeszów 1995 (in Polish).

[14] Pawlak W.I.: *Turbine Jet Engine: Simulation, Control and Monitoring Elements*. Wydawnictwo Naukowe Instytutu Lotnictwa, Warszawa 2011 (in Polish).

[15] Benets D.J., Mockler T., Maldonado J., Harp J.L., King J.F., Schmitz P.C.: *Propulsion systems for very high altitude subsonic unmanned aircraft*. NASA, Aerospace Power Systems'98, Williamsburg, 21-23, Apr. 1998 (NASA TM-1998-20663).

[16] Zhang B., Song Z., Zhao F., Liu C.: *Overview of propulsion systems for unmanned aerial vehicles*. Energies **15**(2022), 2, 455, 1–25.

[17] Gawron B., Białecki T.: *The laboratory test rig with miniature jet engine to research aviation fuels combustion process*. J. KONBiN **36**(2014), 4, 79–90.

[18] Levy Y., Sherbaum V., Nadvany V., Nekhamkin Y.: *Modified vaporizer for improved ignition in small jet engine*. J. Propuls. Power **22**(2006), 4, 828–834.

[19] Montazeri-Gh M., Fashandi S.A.M., Jafari S.: *Theoretical and experimental study of a micro jet engine start-up behaviour*. Technicki vjesnik–Technical Gazette **25**(2018), 3, 839–845.

[20] Levy Y.: *Environmental protection: EASA noise and emissions certification*. In: Proc. COSCAP-GS Conf., Dubai, 2014.

[21] JETPOL Tomasz Kiciński. https://jetpol.tech/ (accessed 17 May 2023).

[22] Czarnecki M., Orkisz M.: *Preliminary design of micro scale turbojet*. J. KONES Powertrain Transport **15**(2008), 3, 83–87.

[23] Krawczyk P., Badyda K., Szczygieł J., Młynarz S.: *Investigation of exhaust gas temperature distribution within a furnace of a stoker fired boiler as a function of its operating parameters*. Arch. Thermodyn. **36**(2015), 3, 3–14.

**archives**
**of thermodynamics**
Vol. **44**(2023), No. 4, 197–220
DOI: 10.24425/ather.2023.149715

# Numerical investigations of transient thermal loading of steam turbines for SMR plants

**MARIUSZ BANASZKIEWICZ***
**MICHAŁ SKWARŁO**

Institute of Fluid Flow Machinery, Polish Academy of Sciences,
Fiszera 14, 80-231 Gdańsk, Poland

**Abstract** One of the well-known technologies that fit well into the goal of reduction of greenhouse gas emissions is nuclear energy. In particular, the change in approach to the design and construction of nuclear power plants led to the development of small modular reactors (SMRs), which are characterized by a broader range of possible applications than large nuclear reactors and the ability to flexibly operate as per load demand. This paper presents an analysis of the thermal loads of a steam turbine rotor operating in a power plant with SMR. Steam-water cycle and turbine train of a 300 MW unit are presented. High-pressure steam turbine rotor and its thermal loading due to varying steam conditions are investigated for a cold start-up designed with consideration of the thermal characteristics of nuclear reactors. It was shown by numerical simulations that steam condensation on rotor surfaces plays a crucial role in determining its thermal behaviour. Comparison with conventional rotors has shown that the thermal loading of nuclear turbine rotors is lower and more stable than that of conventional turbines.

**Keywords:** Nuclear turbine; Small modular reactor; Heat transfer; Steam condensation

## Nomenclature

| | | |
|---|---|---|
| Bi | – | Biot number |
| $c_p$ | – | specific heat, J/(kg K) |
| $d$ | – | characteristic diameter, m |

*Corresponding Author. Email: mbanaszkiewicz@imp.gda.pl

| | | |
|---|---|---|
| $g$ | – | heat source, W/m$^3$ |
| $h$ | – | specific enthalpy, J/kg |
| $k$ | – | thermal conductivity, W/(m K) |
| Nu | – | Nusselt number |
| $p$ | – | pressure, Pa |
| Pr | – | Prandtl number |
| $r$ | – | radial coordinate, m |
| Re | – | Reynolds number |
| $s$ | – | specific entropy, J/(kg K) |
| $T$ | – | temperature, K |
| $t$ | – | time, s |
| $z$ | – | axial coordinate, m |

**Greek symbols**

| | | |
|---|---|---|
| $\alpha$ | – | heat transfer coefficient, W/(m$^2$K) |
| $\rho$ | – | density, kg/m$^3$ |
| $\omega$ | – | rotational velocity, rpm |

**Subscripts**

| | | |
|---|---|---|
| cond | – | condensation |
| conv | – | convection |
| $f$ | – | fluid |
| $s$ | – | surface |
| sat | – | saturation |
| st | – | steam |

**Abbreviations**

| | | |
|---|---|---|
| BWR | – | boiling water reactor |
| GHG | – | greenhouse gases |
| HP | – | high pressure |
| IAEA | – | International Atomic Energy Agency |
| LP | – | low pressure |
| LWGR | – | light water-cooled graphite moderated reactor |
| PHWR | – | pressurized heavy water reactor |
| PWR | – | pressurized water reactor |
| SMR | – | small modular reactor |
| STG | – | steam turbine and generator |

# 1 Introduction

The power sector, similarly to other branches of industry, has a different structure in different countries. However, in the global view, it is common for most countries that the power sector is one of the largest contributors

of harmful wastes and greenhouse gas (GHG) emissions to nature [1]. According to the International Atomic Energy Agency (IAEA) projection it is expected that electricity demands will double by 2050 [2]. This forecast makes governments, industrial companies, and people around the world even more aware of the need for an energy transformation whose main goal is to achieve net-zero GHG emissions.

The key point is an optimal energy mix (various in different countries), in which the power sector is co-created by renewable energy sources and traditional power plants. One type of traditional power plant is a nuclear plant. The nuclear power units are based on a well-known design and proven technology. They are used to generate electricity as well as for district heating purposes in cogeneration systems [3,4]. The main advantages of nuclear power are as follows: a reliable and secure power that in many countries is fully competitive, moreover, a technology that in normal operation is environmentally benign with zero carbon emissions (the electricity generation process is free of combustion) [5,6]. In comparison to the other conventional power units, nuclear energy has an advantageous position for two main reasons: a longer lifetime of nuclear resources and very small GHG emissions for the nuclear chain (whole cycle of resources management) [7,8].

According to the IAEA, more than 400 nuclear power plants are in service (in thirty countries) and generate approximately 10% of global electricity (data until 2022) [2]. The vast majority of these units are large power plants and over 90% of them are equipped with light water pressurized reactors and boiling water reactors (PWR and BWR, respectively) [5,9]. Nevertheless, regardless of reactor technology, large nuclear units are characterized by a long time of the design and construction phase, a high share of work needed to be performed on-site, and large capital investment. All these factors make this type of power plant lose its attractiveness, in particular to private companies and investors.

The mentioned disadvantages of large nuclear power plants could be eliminated by small modular reactors (SMR). SMRs are defined as advanced nuclear reactors that have a power capacity of up to 300 MW(e) per unit [10]. However, there are also SMRs with greater power output – up to $\sim$ 500 MW(e). SMRs, which can produce a large amount of low-carbon electricity are: i) small (physically a fraction of the size of a conventional nuclear power reactor), ii) modular (making it possible for systems and components to be factory-assembled and transported as a unit to a location for installation), iii) reactors (harnessing nuclear fission to generate heat to produce energy) [10]. In addition to reduced time of design and con-

struction phase [11], usage of prefabricated modules, and saving on cost, the advantage of SMRs is also a wider field of possible applications. Similarly to large nuclear units, the SMRs can be used for electricity generation and district heat (cogeneration systems), but also for various industrial applications (due to their modularity and ability to flexible operation as per load demand).

The nuclear reactors, and especially SMRs, are also considered in the context of a process known as 'retrofit decarbonization' of existing coal power plants. This term, retrofit decarbonization, includes the use of carbon capture, fuel conversion, and the replacement of coal boilers with new low-carbon energy sources [9]. One of the main goals is also re-using the existing equipment of coal power plants to the extent that is economically justified [12]. This process is of particular importance for the Polish energy sector due to the extensive fleet of coal units. The possibility of using SMRs for retrofit decarbonization has been described and analyzed in several recently published papers. The common conclusion of these works is that the high-temperature reactors (which constitute a significant part of the SMRs being developed [13]) seem to be suited best for this purpose because of their ability to provide high parameters of steam [9, 14]. Application of SMRs based on light water reactor technology for repowering a coal power plant is also possible, but due to lower steam parameters it is more difficult (extensive modernization of steam turbine unit is required) and less economically attractive [11].

In terms of power capacity, the idea of small or medium-sized reactors is nothing new. Table 1 shows some examples of small reactors for different steam turbine and generator (STG) power outputs, that are in operation [15]. The table includes pressurized water reactors (PWRs), light water-cooled graphite moderated reactor (LWGR) and pressurized heavy water reactor (PHWR).

Table 1: Small nuclear reactors in operation.

| Name | STG power output | Type | Country |
|---|---|---|---|
| EGP-6 | 11 MW(e) | LWGR | Russia |
| KLT-40S | 35 MW(e) | PWR | Russia |
| RITM-200 | 50 MW(e) | Integral PWR | Russia |
| PHWR-220 | 220 MW(e) | PHWR | India |
| CNP-300 | 300 MW(e) | PWR | China, Pakistan |

These types of reactors are based on the same technologies as large reactors (mainly PWR and BWR). In the case of SMRs, the change primarily concerns the approach to the design and construction phases (modular design) in order to save time and cost. As the SMR units are currently mostly in the design and development phase, there is also a change in the use of different reactor technologies. The IAEA advance reactor database [13] provides a list of approximately eighty SMRs (some of them already under construction). The list includes examples of well-known light water reactors, as well as new-generation reactors (high-temperature reactors).

Table 2 presents some examples of SMRs developed using conventional nuclear fuel and cooling technology (PWR and BWR reactors) with a high probability of deployment in the first half of the next decade [1,15].

Table 2: Small modular reactors in an advanced stage of development.

| Name | STG power output | Type | Developer, country |
|---|---|---|---|
| NuScale Power Module | 77 MW(e) | Integral PWR | NuScale, USA |
| Nuward | 180 MW(e) | PWR | EDF + TechnicAtome, France |
| SMR-160 | 160 MW(e) | PWR | Holtec, USA + SNC-Lavalin, Canada |
| BWRX-300 | 300 MW(e) | BWR | GE Hitachi, USA |
| Candu SMR | 300 MW(e) | PHWR | SNC-Lavalin, Canada |
| Rolls-Royce SMR | 500 MW(e) | PWR | Rolls-Royce, UK |

In terms of steam parameters (pressure, temperature) at the steam generator outlet, they do not differ from parameters achieved in large units [16,17]. However, the main difference is noticeable regarding the steam mass flow rate. A comparison of a few large PWR and BWR reactors with SMR reactor BWRX-300 is presented in Table 3.

Lower mass flow of steam also results in lower volumetric flow at low-pressure (LP) turbine exhaust. Additionally, considering the main design assumptions of SMR – modular and compact components as far as possible factory assembled, steam turbine for SMR units will be full speed machine with 3000 rpm or 3600 rpm operation speed. This is a significant difference compared to half-speed steam turbines in large nuclear units, which causes operation in wet steam conditions to become even more of a challenge and needs additional attention in the case of SMR units based on PWR or BWR technology [22].

Table 3: Steam parameters at steam generator outlet in large nuclear reactors and SMR.

| | | Power plant with nuclear reactor | | | | |
|---|---|---|---|---|---|---|
| | | APR-1400 [18] | EPR-1600 [18] | ABWR [19] | ESBWR [20] | BWRX-300 [21] |
| | Reactor type | PWR | PWR | BWR | BWR | SMR BWR |
| Steam generator outlet: | Pressure (MPa) | 6.84 | 7.80 | 7.07 | 7.17 | 7.20 |
| | Temperature (°C) | 284.3 | 293.0 | 287.8 | 287.7 | 288.0 |
| | Mass flow rate (kg/s) | 2261 | 2443 | 2122 | 2432 | 470 |

Calculations for nuclear power plants are carried out mainly for the design point. It is very difficult to find papers concerning off-design conditions of nuclear power plants, except papers discussing the effect of cooling water temperature on the performance of a nuclear power plant [23, 24]. This problem concerns both large nuclear units and SMR units, but it is particularly important concerning the latter due to the wider range of possible applications and greater requirements for operational flexibility.

The main objective of this paper is to investigate the thermal loads of a high-pressure steam turbine rotor operating in an SMR power plant with a BWR reactor. The choice of this type of nuclear reactor is driven by the fact that, currently, the SMR developed by GE Hitachi Nuclear Energy, BWRX-300, seems to be one of the closest to being implemented into the Polish energy system in the near future [25]. Calculations concerning off-design conditions and, especially, transient conditions are crucial in terms of fatigue assessment of steam turbine components [26]. Calculations presented in this paper include analysis of thermal loads of the HP rotor during operation at transient conditions – steam turbine start-up. Understanding the thermal behaviour of such rotors is critical for determining the operational flexibility of SMR units, which is one of the most demanded features for future applications.

# 2 Steam turbine for SMR unit

## 2.1 Thermal cycle and steam turbine modules

This paper presents the results of analyses carried out for a steam turbine operating in a steam-water cycle with SMR based on BWR technology. This kind of cycle contains the same main components as a cycle with a large

BWR, including a nuclear reactor (steam generator), steam turbine and generator, moisture separator and reheater, condenser, feedwater heaters and pump [16, 17]. A simplified steam-water cycle with SMR BWRX-300 is presented in Fig. 1. In addition, exemplary steam/water parameters are shown in the diagram.

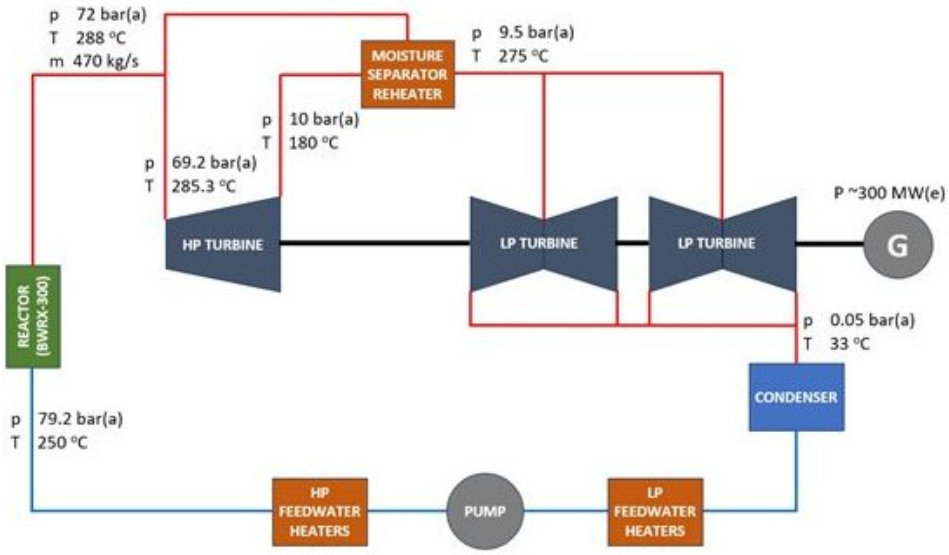


Figure 1: Simplified steam-water cycle with SMR based on BWR technology.

As stated in the definition of SMR, the power capacity of one unit is up to 300 MW(e) (although units with higher power output are also planned). Depending on steam parameters and nominal power output, the steam turbine for the SMR unit may have different configurations. It could be a single casing turbine (combined high pressure (HP) and low pressure (LP) parts) or a multi-casing machine (HP module and one or more LP modules). Possible configurations of a steam turbine for SMR unit based on PWR/BWR technology are presented in Fig. 2.

Referring to Table 3, in BWR/PWR SMR units the steam turbine (HP module) will receive saturated steam at the inlet. This situation occurs for the nominal operating conditions, as well as for partial loads. In these conditions, when analyzing the thermal loads of the HP turbine rotor, a condensation phenomenon (condensation heat transfer model) should be taken into account.

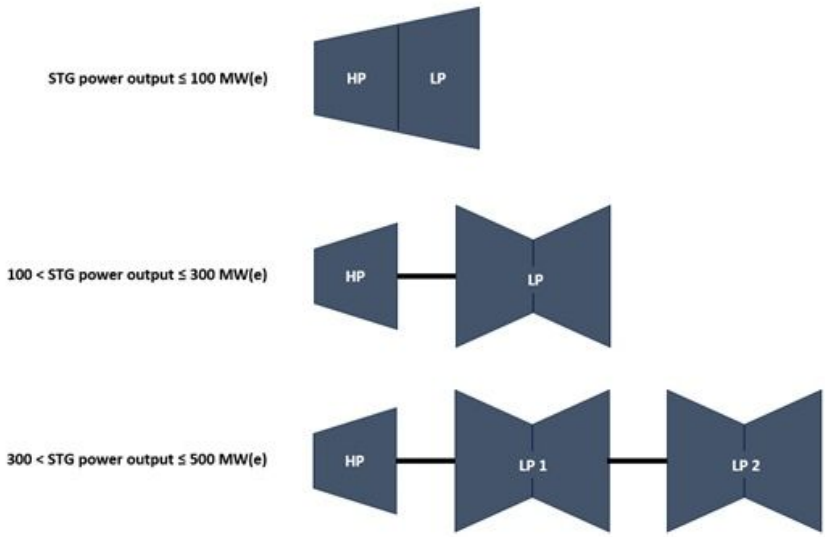


Figure 2: Possible configurations of steam turbine for SMR PWR/BWR power plant.

## 2.2 High-pressure turbine rotor

For the analyzed 300 MW SMR unit, a turbine train with one HP module and two double flow LP modules is adopted. The HP module is single flow and has drum-type rotor with reaction blading as shown in Fig. 3. In the proposed design, the rotor has 10 stages with reaction blades fixed to the rotor by means of a T-root. Two-stage balance piston (high and low) is

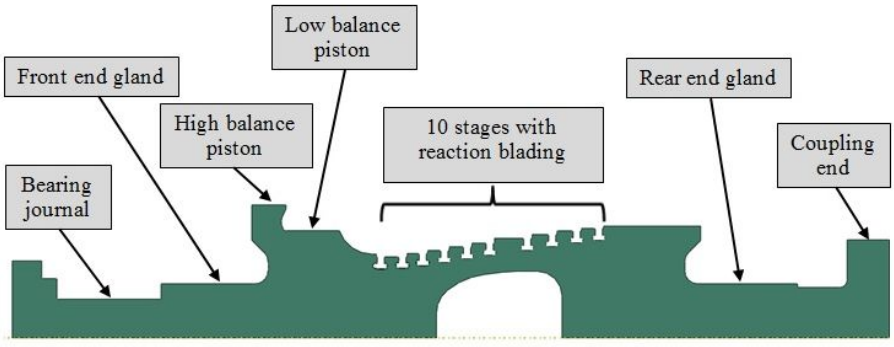


Figure 3: High-pressure turbine rotor.

designed to compensate the axial force generated by pressure drop across the blading. End glands (front and rear) are located on both sides of the rotor. The bearing journal is located at the left end of the rotor while the right end has a coupling end connecting the rotor with the LP module.

Performed calculations indicate that during a transient event – cold start-up of the steam turbine, there is saturated steam at the turbine inlet for most of the time of the turbine loading phase. Only at the beginning of this phase (at very low load, less than 15% of nominal load) the steam at the turbine inlet is slightly superheated. Expansion lines for nominal conditions and transient events (beginning of turbine start-up) are presented in Fig. 4.

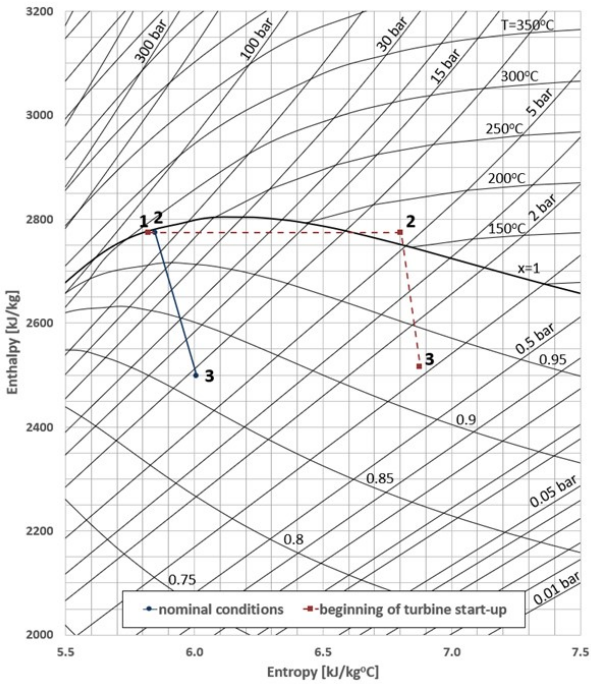


Figure 4: Enthalpy-entropy ($h - s$) diagram, expansion lines for nominal and transient conditions (beginning of turbine start-up) of SMR BWR unit: 1-2 – pressure drop at HP turbine valves, 2-3 – expansion line of HP turbine.

Steam temperatures in the HP turbine at different load conditions are presented in Fig. 5. As stated in the preceding section, the live steam is at the saturation line and its thermodynamic state is maintained during the whole start-up. Steam throttling in the control valves results in little steam

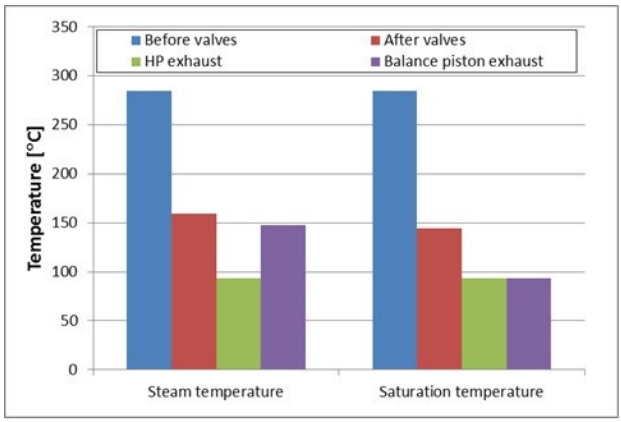


(a)

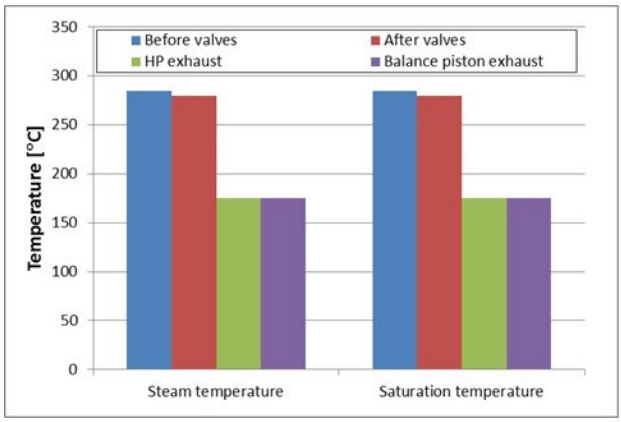


(b)

Figure 5: Steam temperature and saturation temperature in HP turbine at (a) 3000 rpm and no load, (b) 3000 rpm and 300 MW.

superheating at the turbine inlet at the beginning of start-up which diminishes with time and saturated steam conditions are reached at a certain load. Even larger superheating exceeding 50°C occurs at the exhaust of the rotor balance piston and also decreases during loading-up but is still around 1°C at full load. Steam superheating decreases with time along the steam path and at the HP turbine exhaust the saturated steam conditions are present during the whole start-up (similar to the live steam condition). This varying thermodynamic state of steam in the HP turbine is taken into account in further thermal analyses and shown to have a significant impact

on the thermal load of the HP rotor under consideration. In particular, steam condensation on rotor surfaces plays a crucial role in determining its thermal behaviour.

In the case of conventional turbines, steam superheating during start-up and loading increases, and condensation may occur at an early phase of start-up. It is thus an inverse situation as compared to nuclear turbines.

## 3 Problem formulation

The problem under consideration is the transient heating-up of a nuclear steam turbine rotor taking place during start-up and loading. Rotor heating is caused by steam flow through the turbine with varying temperature, pressure and velocity. Non-stationary heat transfer takes place via forced convection and the thermal load is the primary load of the rotor. The rotor rotates with a constant rotational speed $\omega$ in steady-state operation.

The rotor material is assumed isotropic and its physical properties are temperature dependent. The heating process is described by the linear theory of heat conduction and non-linear convective boundary conditions. Due to the geometrical and loading symmetry of the rotor about its axis, the computational region is assumed axisymmetric.

Based on the above assumptions a boundary problem of heat conduction is formulated [27, 28] and solved using a finite element method [29].

### 3.1 Heat conduction problem

Heat conduction in a homogeneous isotropic solid is described by the Fourier-Kirchhoff differential equation [30]:

$$\operatorname{div}\left[k\operatorname{grad}T(x,t)\right] + g(x,t) = \rho c_p \frac{\partial T(x,t)}{\partial t}\,, \tag{1}$$

where $T$ is the metal temperature, $k$ is the thermal conductivity, $g$ is the heat source, $\rho$ is the density, and $c_p$ is the specific heat.

Neglecting the heat source $g$ and assuming heat conduction in the radial and axial direction only, Eq. (1) is re-written in a cylindrical coordinate system as follows:

$$\rho c_p \frac{\partial T}{\partial t} = \frac{1}{r}\frac{\partial}{\partial r}\left(kr\frac{\partial T}{\partial r}\right) + \frac{\partial}{\partial z}\left(k\frac{\partial T}{\partial z}\right), \tag{2}$$

where $r$ represents the radial coordinate, and $z$ is the axial direction. A non-uniform temperature distribution $T(r, z)$ is assumed as the initial condition at $t = 0$. For rotor-free surfaces, the boundary conditions are:

$$\left.\frac{\partial T}{\partial r}\right|_{r=0} = 0 \qquad \text{for} \quad t \geq 0, \tag{3}$$

$$k(z,t)\left.\frac{\partial T}{\partial r}\right|_{r=r_{\text{out}}(z)} = -\alpha(z,t)\left(T_s - T_f(z,t)\right) \qquad \text{for} \quad t \geq 0, \tag{4}$$

where $\alpha(z, t)$ is the heat transfer coefficient varying with time and axial coordinate, $T_s$ is the surface temperature, and $T_f(z, t)$ is the fluid temperature depending on time and axial coordinate. The outer radius of the rotor $r(z)$ varies with the axial coordinate $z$ defining its outer contour.

The material physical properties are temperature-dependent and their variation is described by polynomial functions.

The variation of heat transfer coefficient in time and space $\alpha(z, t)$ is considered by the Nusselt number (Nu), changing in time as a function of the Reynolds number (Re) and Prandtl number (Pr):

$$\text{Nu} = f(\text{Re}, \text{Pr}). \tag{5}$$

The Nusselt number is defined as follows:

$$\text{Nu} = \frac{\alpha d}{k}, \tag{6}$$

where $d$ denotes a characteristic diameter. A detailed form of Eq. (6) depends on the surface type and flow character [31]. The heat transfer model adopted in this study is based on the well-proven formula for heat transfer coefficients in steam turbine rotors [32].

The geometrical model of the rotor is shown in Fig. 6.

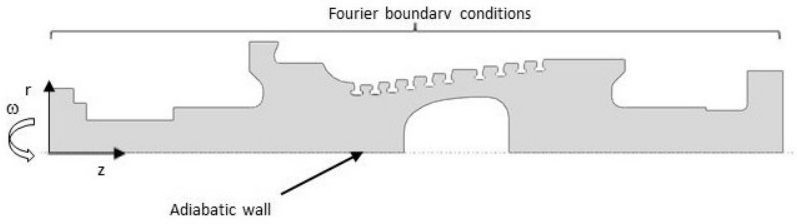


Figure 6: Rotor model with thermal boundary conditions.

### 3.2 Condensation model

Steam condensation on rotor surfaces can occur when steam is superheated or saturated. In this study, a film condensation mechanism is assumed. A schematic illustration of the condensation model adopted in this work is shown in Fig. 7. If the surface temperature is lower than the saturated steam temperature at the corresponding steam pressure, then steam condenses on the surface. The heat transfer to the surface is intensified as a result of the water film appearing on the surface at the saturated steam temperature, and the heat released due to condensation.

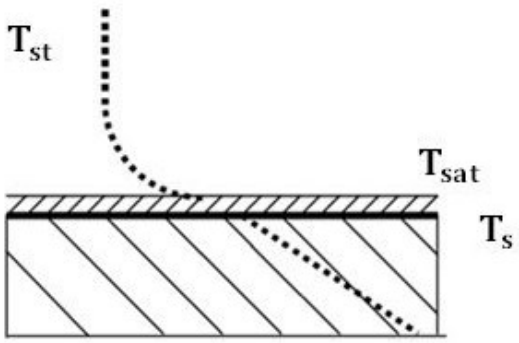


Figure 7: Schematic illustration of film condensation model.

Condensation occurs if the following conditions are satisfied [33–35]:

- the metal surface temperature is below the saturation temperature ($T_{\text{sat}}$) at the local pressure $p$

$$T_{\text{sat}} > T_s\,, \tag{7}$$

- the heat flux from water film to metal is greater than the heat flux from steam to the water film

$$\alpha_{\text{cond}}\,(T_{\text{sat}} - T_s) > \alpha_{\text{conv}}\,(T_{\text{st}} - T_{\text{sat}})\,, \tag{8}$$

where $T_{\text{st}}$ denotes steam temperature.

As concluded in [31], available correlations for Nusselt number for simple geometries, like a flat wall or pipe, can be used for estimating condensation heat transfer coefficient usually with a large error. However, it is known that heat transfer coefficients during steam condensation assume large values

reaching 120 000 W/(m$^2$K) in extreme cases during nucleate condensation of steam [36, 37] and, consequently, the errors of their estimation will only slightly affect the variations of temperature and thermal stress fields in turbine components. It was shown that for Biot number Bi > 20, the variation of the heat transfer coefficient has little influence on the variation of temperature distribution [31]. Due to the lack of proper correlations for real turbine geometries (e.g. labyrinth seals, rotating cylinders) and taking into account the above conclusions, the analyses of condensation heat transfer were performed with constant heat transfer coefficient $\alpha = 11\,000$ W/(m$^2$K). This value is within the range of heat transfer coefficients predicted by Shah [38] for film condensation of water inside pipes.

# 4 Numerical simulations

## 4.1 Cold start-up parameters

Nuclear steam turbines, similar to conventional turbines, undergo start-ups from various initial thermal conditions. The initial thermal state depends on the cool-down time. The main difference between nuclear and conventional units is in live steam temperature and the resulting metal temperature at the hottest sections of the turbine at the beginning of natural cooling. The live steam temperature for BWR reactors is around 290°C and it determines the hot state of the turbine and initial thermal conditions prior to shut-down. This temperature level corresponds to a typical warm state of conventional turbines which is reached after approximately 30 hours of natural cooling. However, the very cold state of both turbines is defined by the same temperature level with a minimum value of 20°C. This start-up type is assumed in this work for detailed investigations.

Figure 8 presents the proposed cold start-up diagram for a 300 MW steam turbine with the BWRX-300 reactor. This diagram describes variations in time of the rotational speed, power output and live steam temperature and pressure. In large nuclear units, steam turbine start-up is conducted with nominal live steam temperature and pressure, and similar conditions are proposed for the SMR turbines. The rotational speed and power output curves are derived based on the start-up diagrams of 360 MW turbines operating at power plants in Poland [39–41].

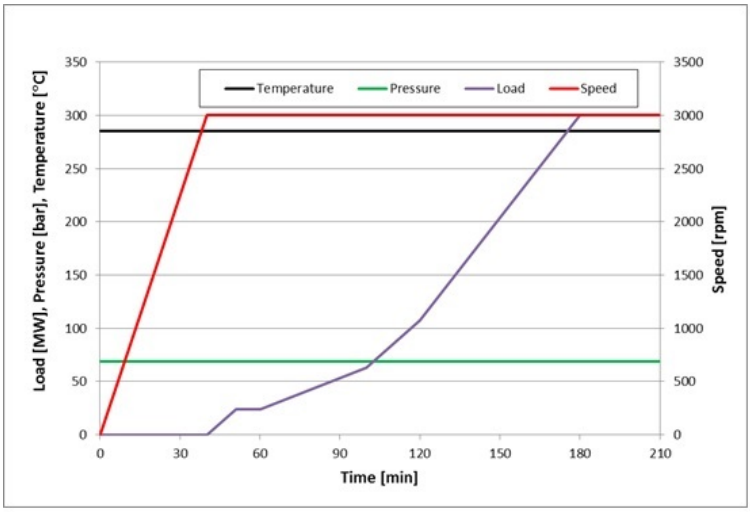


Figure 8: Cold start-up diagram.

## 4.2 Results and discussion

Numerical calculations have been performed using Abaqus finite element code [42]. Live steam temperature and pressure during start-up were kept constant as shown in Fig. 8, while steam parameters at the rotor inlet were changing during start-up due to steam throttling in the control valves. Temperature distributions in the rotor during start-up from a cold state are shown in Fig. 9. Each plot presents temperature distribution corresponding to one of the characteristic time points of the start-up diagram in Fig. 8. Uniform rotor temperature of 20°C was assumed as an initial condition ($t = 0$ min). After reaching 3000 rpm, the temperature distribution becomes non-uniform and rotor temperature exceeds 100°C at steam inlet sections ($t = 40$ min). For the following 20 minutes ($t = 50$ min and $t = 60$ min), the temperature field remains nearly unchanged as there is little change in steam temperature and mass flow during initial loading. Up to this time, predominantly radial temperature gradients are observed in the rotor body. Further turbine loading, accompanied by steam temperature and mass flow rate increase, brings about a rotor temperature increase up to approximately 200°C at steam inlet sections ($t = 100$ min). Further loading up to 100 MW ($t = 120$ min) does not cause a significant increase in temperature and its distribution in the inlet sections becomes more uniform with diminishing radial temperature gradients. The last 60 minutes of

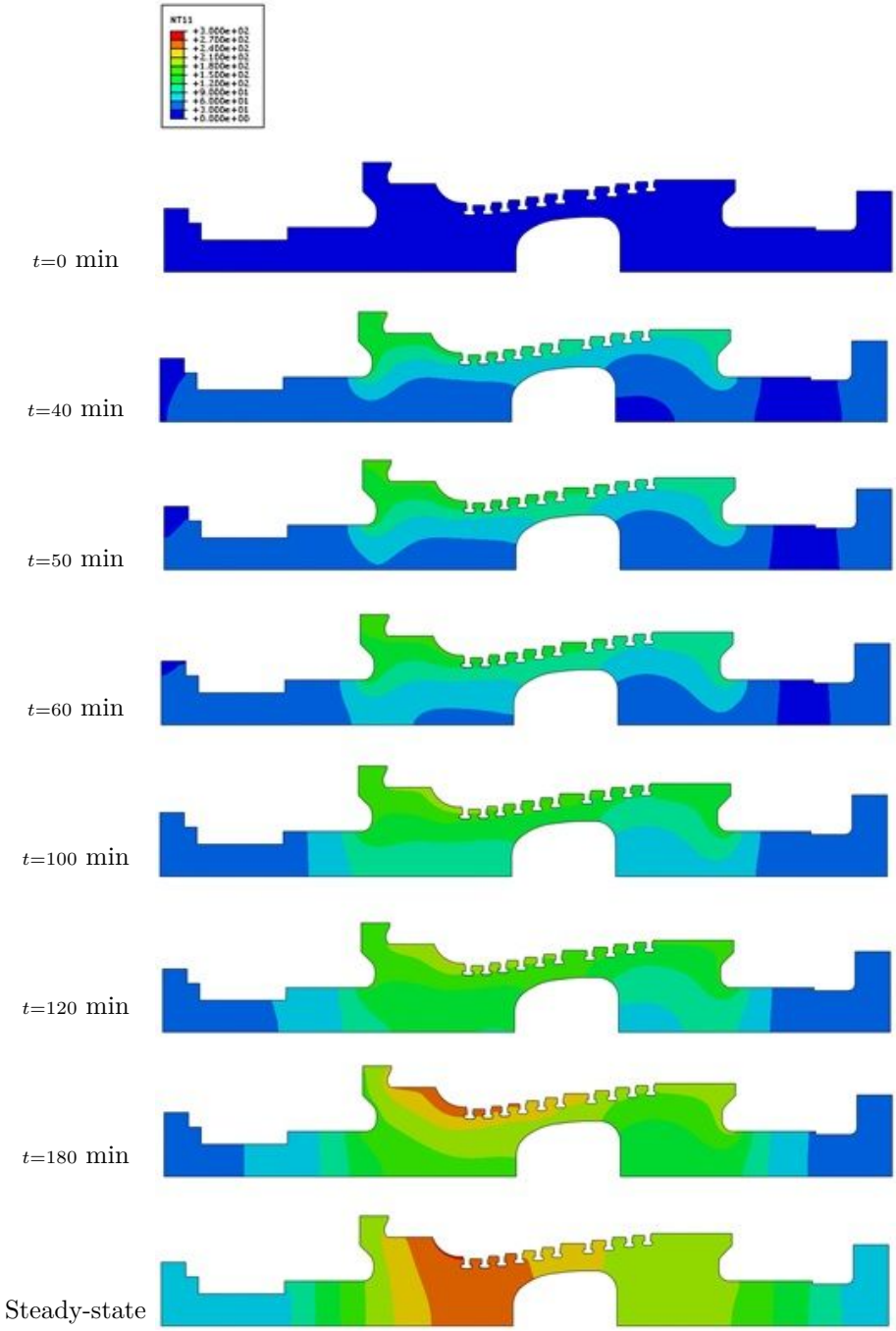


Figure 9: Rotor temperature distributions during cold start-up.

turbine start-up proceeds at an increased loading rate and at reaching nominal load, radial temperature gradients re-occur and rotor inlet surface temperature exceeds 270°C. The temperature distribution is still non-uniform in the steam inlet sections, while the exhaust regions downstream of the cavity are at nearly constant temperature. At time $t = 180$ min, nominal steam mass flow, temperature and pressure upstream of the HP blading are reached and subsequent temperature variations and rotor thermal stabilization take place at constant boundary conditions. At a steady state, a non-uniform temperature field persists in the rotor but radial temperature gradients practically disappear and only axial gradients generated by steam expansion in the HP blading exist.

The presented rotor temperature distributions during turbine start-up show that the highest metal temperatures, their rates of change and gradients occur at the rotor inlet sections, i.e. inlet channel, first blade grooves and balance pistons. These are the most thermally loaded regions of the rotor where the largest heat fluxes from steam to the rotor surfaces are transferred. Consequently, the highest thermal stresses which may lead to fatigue cracking are expected in these regions.

The thermal behaviour of the rotor was investigated in detail for the region of the first rotor gland (between 1st and 2nd blade groove). Steam and metal temperature variations during the cold-start are plotted in Fig. 10. Live steam temperature is kept constant according to the start-up diagram in Fig. 8 and throttling in the control valves at the beginning of run-up results in a steam temperature drop at the turbine inlet (downstream control valves) from nominal value to approximately 150°C. As presented in Section 2, at the early phases of start-up the steam is superheated and its superheating drops with time and vanishes after approximately 50 minutes. Steam condensation occurs immediately after opening the control valves, rotor surface temperature rises above the saturation temperature and further heating takes place due to heat convection from superheated steam to metal. After 40 minutes condensation re-occurs as the steam superheating significantly decreases with a simultaneous decrease of the temperature difference between the rotor surface and saturation temperature. From this time on, rotor surface temperature follows the saturation temperature increasing with steam pressure rise. This is the effect of a large heat transfer coefficient at steam condensation.

The effect of condensation on rotor temperature variations is shown in Fig. 11. The rotor surface temperature from Fig. 10 is plotted together with the mid-wall temperature (at half rotor radius at the first gland) and

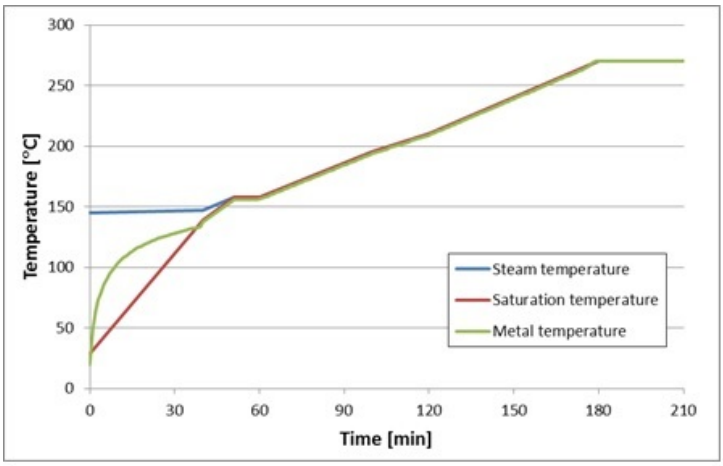


Figure 10: Steam and metal temperature variations at the first rotor gland.

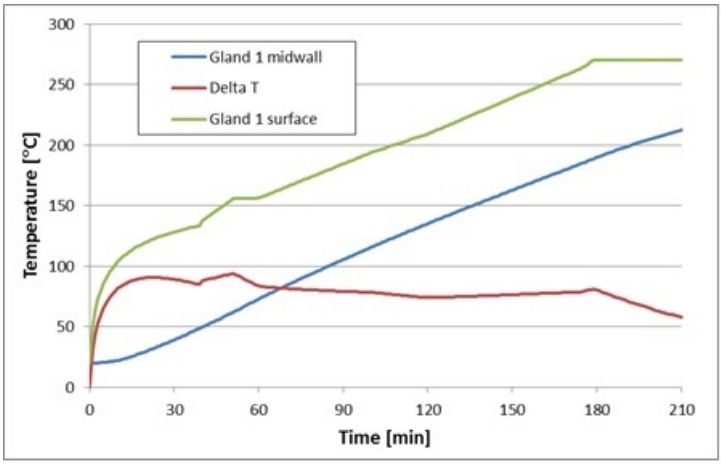


Figure 11: Metal temperature variations at first rotor gland.

their difference. The rotor surface temperature rapidly rises at the beginning of start-up while the mid-wall temperature response is delayed due to rotor thermal inertia and heat resistance. Non-linear transient effects diminish with time and after approximately 20 minutes (10% of start-up time) quasi-steady state conditions prevail. Nearly linear temperature variations are observed and, consequently, the temperature difference remains almost constant. At such conditions, thermal stresses are expected to be

constant and dependent on temperature rate. These conditions prevail simultaneously with steam condensation, and thus the temperature rate linearly depends on the steam pressure rate.

Qualitative and quantitative differences between nuclear and conventional rotor thermal behaviour are observed when considering surface heat fluxes. A comparison of surface heat flux densities in different regions of the nuclear and conventional rotor is presented in Fig. 12. The results for the conventional rotor were obtained assuming a cold start-up diagram for an intermediate pressure turbine with a rotor of similar design which was a basis for designing the high-pressure nuclear rotor investigated in this

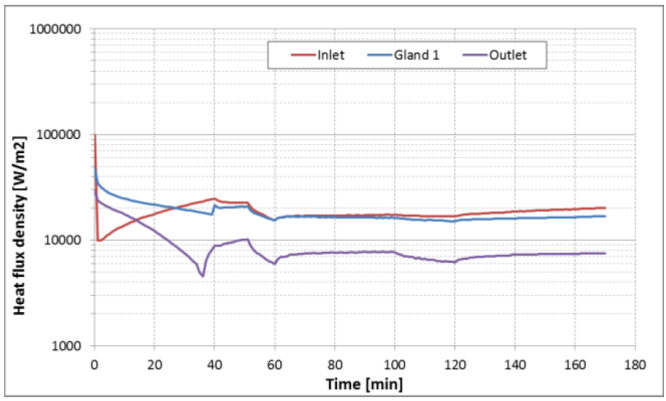


(a)

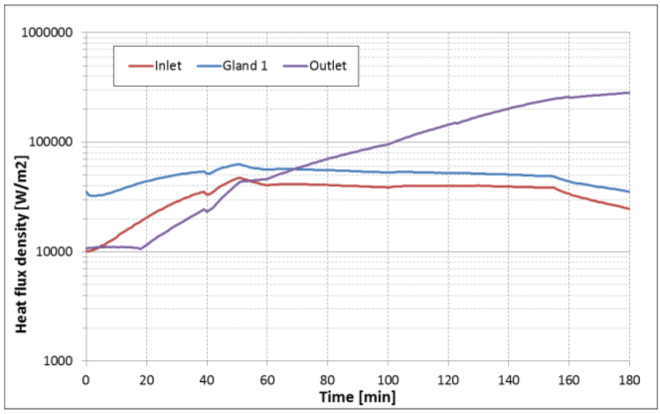


(b)

Figure 12: Variations of surface heat flux densities in rotor different regions (inlet, gland 1 and outlet) for (a) nuclear and (b) conventional steam turbine rotor.

paper. As it is seen from the figures, the heat fluxes in the nuclear rotor initially decrease and after approximately 60 minutes remain constant in the range of 9000–20 000 W/m$^2$. Only at the beginning of start-up, very high heat flux densities reaching 100 000 W/m$^2$ are calculated due to the large condensation heat transfer. A different picture is seen for the conventional rotor where the initial values of heat fluxes are relatively low in the range of 9000–20 000 W/m$^2$ and subsequently increase to approximately 50000 W/m$^2$ after 60 minutes. They remain almost constant in some regions (gland, inlet) or even increase to 300 000 W/m$^2$ at the end of start-up. The above analysis proves that the thermal loading of nuclear turbine rotors is lower and more stable than that of conventional rotors.

Additional differences between these two types of turbines in terms of thermal characteristics can be shown with the help of Biot numbers summarized in Table 4. It is clearly seen that, as a result of the higher heat transfer coefficient, heat conduction inside the conventional rotor body offers much higher thermal resistance than the heat convection at the surface. Thermal resistance for the heat conduction of the nuclear rotor is less variable for the majority of start-up time as compared with the conventional rotor.

Table 4: Comparison of Biot numbers for nuclear and conventional turbines.

| Turbine type | Biot number | | |
|---|---|---|---|
| | 0 rpm | 50% load | 100% load |
| Nuclear | 302.5 | 292.3 | 290.3 |
| Conventional | 3.3 | 53.1 | 96.6 |

It is worth noting that Biot numbers obtained for the nuclear rotor are an order of magnitude larger than that considered as the threshold above which the variation of heat transfer coefficient has little influence on the variation of temperature distribution [31]. This fact justifies the use of a large and constant condensation heat transfer coefficient.

## 5 Summary

Small modular reactors are characterized by a wider range of possible applications than large nuclear reactors and the ability to flexible operation as per load demand. However, this greater flexibility results in more stringent design requirements for most components of the power plant equipped with this type of nuclear reactor.

This paper presented the numerical analysis of the thermal loads of a steam turbine rotor operating in a power plant with an SMR. The calculations performed included transient operation and a detailed analysis of cold start-up was conducted. The cold-start diagram was developed based on start-up diagrams of conventional units and accounting for the thermal characteristics of nuclear reactors.

A thermal cycle was proposed for a 300 MW SMR unit together with a steam turbine train consisting of the single flow HP module and two double flow LP modules. The HP module employs a drum-type rotor and 10 stages with reaction blading. The preliminary design rotor served as an object of detailed thermal investigations at transient operation.

Thermodynamic analysis has shown that steam throttling in the control valves results in steam superheating at the turbine inlet at the beginning of start-up which diminishes with time and saturated steam conditions are reached at a certain load. Even larger superheating exceeding 50°C occurs at the exhaust of the rotor balance piston and decreases during loading-up but is still around 1°C at full load. Steam superheating decreases with time along the steam path and at the HP turbine exhaust saturated steam conditions are present during the whole start-up (similar to the live steam condition).

These varying thermodynamic state of steam in the HP turbine is taken into account in thermal analyses and is shown to have a significant impact on the thermal load of the HP rotor under consideration. In particular, steam condensation on rotor surfaces plays a crucial role in determining its thermal behaviour.

The rotor temperature distributions obtained from turbine start-up simulations show that the highest metal temperatures, their rates of change and gradients occur at the rotor inlet sections, i.e. inlet channel, first blade grooves and the balance pistons. These are the most thermally loaded regions of the rotor where the largest heat fluxes from steam to the rotor surfaces are transferred.

It was also shown that the thermal loading of nuclear turbine rotors is lower and more stable than that of conventional rotors. Biot numbers calculated for nuclear rotors with high and constant condensation heat transfer coefficients are larger and more stable than those for conventional rotors.

*Received 31 October 2023*

# References


[1] Qvist S., Gładysz P., Bartela Ł., Sowiżdżał A.: *Retrofit decarbonization of coal power plants – a case study for Poland.* Energies **14**(2021), 1, 120.

[2] International Atomic Energy Agency: *Energy, Electricity and Nuclear Power Estimates for the Period up to 2050, IAEA Reference Data Series No. 1.* IAEA-RDS-1/4, Vienna 2022.

[3] Kubowski J.: *Nuclear Power Plants.* WNT, Warszawa 2017 (in Polish).

[4] Chmielniak T.: *Power Generation Technologies.* PWN, Warszawa 2021 (in Polish).

[5] Dudek M., Jaszczur M., Kolenda Z.: *Thermodynamic analysis of modular high-temperature nuclear reactor coupled with the steam cycle for power generation.* Arch. Thermodyn. **40**(2019), 4, 49–66.

[6] Fic A., Składzień J., Gabriel M.: *Thermal analysis of heat and power plant with high temperature reactor and intermediate steam cycle.* Arch. Thermodyn. **36**(2015), 1, 3–18.

[7] Stanek W., Szargut J., Kolenda Z., Czarnowska L.: *Influence of nuclear power unit on decreasing emissions of greenhouse gases.* Arch. Thermodyn. **36**(2015), 1, 55–65.

[8] Rusanov A., Subotin V., Shvetsov V., Rusanov R., Palkov S., Palkov I., Chugay M.: *Application of innovative solutions to improve the efficiency of the LPC flow part of the 220 MW NPP steam turbine.* Arch. Thermodyn. **43**(2022), 1, 63–87.

[9] Bartela Ł., Gładysz P., Andreades C., Qvist S., Zdeb J.: *Techno-economic assessment of coal-fired power unit decarbonization retrofit with KP-FHR small modular reactors.* Energies **14**(2021), 9, 2557.

[10] Liou J.: *What are Small Modular Reactors (SMRs)?.* IAEA. https://www.iaea.org/newscenter/news/what-are-small-modular-reactors-smrs (accessed 14 Aug. 2023).

[11] Łukowicz H., Bartela Ł., Gładysz P., Qvist S.: *Repowering a coal power plant steam cycle using modular light-water reactor technology.* Energies **16**(2023), 7, 3083.

[12] Homa D., Kosman W., Bartela Ł.: *Cooperation of turbine island with $4^{th}$ generation nuclear reactor.* In: Proc. XXV Jubilee Cong. of Thermodynamicists, Gdańsk, 11-14 Sept. 2023, Book of papers (J. Cieśliński, D. Mikielewicz, J. Wajs, Eds.), 104–107. (in Polish).

[13] Irnational Atomic Energy Agency: *Advances in Small Modular Reactor Technology Developments. A Supplement to: IAEA Advanced Reactors Information System (ARIS).* IAEA,Vienna 2022.

[14] Bartela Ł., Gładysz P., Ochmann J., Qvist S., Sancho L.M.: *Repowering a coal power unit with small modular reactors and thermal energy storage.* Energies **15**(2022), 16, 5830.

[15] Domański R.: *Modular nuclear reactors – state of knowledge and prospects.* In: Proc. XXV Jubilee Cong. of Thermodynamicists, Gdańsk, 11-14 Sept. 2023, Book of papers (J. Cieśliński, D. Mikielewicz, J. Wajs, Eds.), 72–75. (in Polish).

[16] Chmielniak T.: *Thermodynamic Cycles of Thermal Turbines.* Fluid-Flow Machinery Vol. 2. Ossolineum – Wydawn. PAN, Wrocław 1988 (in Polish).

[17] Perycz S.: *Steam and Gas Turbines*. Fluid-Flow Machinery Vol. 10. Ossolineum – Wydawn. PAN, Wrocław 1992 (in Polish).

[18] Ochmann J., Łukowicz H., Bartela Ł.: *Analysis of the influence of operating conditions of the steam turbine determined by location conditions on its operating characteristics*. In: Proc. XXV Jubilee Cong. of Thermodynamicists, Gdańsk, 11-14 Sept. 2023, Book of papers (J. Cieśliński, D. Mikielewicz, J. Wajs, Eds.), 239–242. (in Polish).

[19] International Atomic Energy Agency: *Status report 97 – Advanced Boiling Water Reactor (ABWR). IAEA Advanced Reactors Information System (ARIS)*, Jul 2011.

[20] *Status report 100 – Economic Simplified Boiling Water Reactor (ESBWR)*. IAEA Advanced Reactors Information System (ARIS). IAEA,Vienna 2021.

[21] GE Hitachi Nuclear Energy: *BWRX-300 General Description. Revision E*. 005N9751, 2023.

[22] Jun G., Kolovratnik M., Hoznedl M.: *Wet steam flow in 1100 MW turbine*. Arch. Thermodyn. **42**(2021), 3, 63–85.

[23] Laskowski R., Smyk A., Jurkowski R., Ance J., Wołowicz M., Uzunow N.: *Selected aspects of the choice of live steam pressure in PWR nuclear power plant*. Arch. Thermodyn. **43**(2022), 3, 85–109.

[24] Laskowski R., Smyk A., Ruciński A., Szymczyk J.: *Determining steam condensation pressure in a power plant condenser in off-design conditions*. Arch. Thermodyn. **42**(2021), 3, 45–62.

[25] Orlen: *Development program of BWRX-300 in Poland*, 2023. https://www.orlen.pl/pl/zrownowazony-rozwoj/projekty-transformacyjne/smr (accessed 10 Sept. 2023)

[26] Wacławiak K., Okrajni J.: *Transient heat transfer as a leading factor in fatigue of thick-walled elements at power plants*. Arch. Thermodyn. **40**(2019), 3, 43–55.

[27] Adamowicz A.: *Axisymmetric FE model to analysis of thermal stresses in a brake disc*. JTAM **53**(2015), 2, 357–370.

[28] Adamowicz A.: *Finite element anlysis of the 3D thermal stress state in a brake disc*. JTAM **54**(2016), 1, 205–218.

[29] Zienkiewicz O.C., Taylor R.L., Zhu J.Z.: *The Finite Element Method: It's Basis and Fundamentals*. Elsevier Butterworth-Heinemann, Burlington 2005.

[30] Hetnarski R.B., Eslami M.R.: *Thermal Stresses – Advanced Theory and Applications*. Springer, 2009.

[31] Chmielniak T., Kosman G.: *Thermal Loads of Steam Turbines*. WNT, Warszawa 1990 (in Polish).

[32] Banaszkiewicz M.: *Numerical investigation of crack initiation in the impulse steam turbine rotors subjected to thermo-mechanical fatigue*. Appl. Therm. Eng. **138**(2018), 761–773.

[33] Banaszkiewicz M.: *On-line determination of transient thermal stresses in critical steam turbine components using a two-step algorithm*. J. Therm. Stresses **40**(2017), 6, 690–703.

[34] Marinescu G., Ehrsam A., Sell M., Brunner P.: *Experimental investigation into thermal behaviour of steam turbine components. Part 3 – startup and the impact on LCF life*. In: Proc. ASME Turbo Expo 2013, San Antonio, June 3-7, 2013.

[35] Banaszkiewicz M., Badur J.: *Practical methods for online calculation of thermoelastic stresses in steam turbine components*. In: Selected Problems of Contemporary Thermomechanics (J. Winczek, Ed.), IntechOpen, 2018, 45–63.

[36] Taler J., Duda P.: *Solving Direct and Inverse Heat Conduction Problems*. Springer, Berlin Heidelberg 2006.

[37] Pilarczyk M., Weglowski B, Nord L.O.: *A comprehensive thermal and structural transient analysis of a boiler's steam outlet header by means of a dedicated algorithm and FEM simulation*. Energies **13**(2020), 1, 111.

[38] Shah M.M.: *A general correlation for heat transfer during film condensation inside pipes*. Int. J. Heat Mass Transf. **22**(1979), 547–556.

[39] Banaszkiewicz M.: *Steam turbines start-ups*. Trans. Inst. Fluid-Flow Mach. **126** (2014), 169–198.

[40] Rusin A., Banaszkiewicz M.: *Control and optimisation of 18K360 turbine start-up*. In: Proc. VI Sci.-Tech. Conf. Thermal Plants – Operation, Modernizations, Overhauls, Słok n/Bełchatow, 4-6 June, 2003 (in Polish).

[41] Banaszkiewicz M.: *Turbine thermal stress controller for retrofits of 370 MW units*. In: Proc. VIII Sci.-Tech. Conf. Thermal Plants – Operation, Modernizations, Overhauls, Słok n/Bełchatow, 21-23 May, 2007 (in Polish).

[42] Abaqus 6.13 user manual.

**archives**
**of thermodynamics**
Vol. **44**(2023), No. 4, 221–241
DOI: 10.24425/ather.2023.149716

# The impact of electrification of heating on the power grid for a selected area microgrids

**MICHAŁ LASKOWSKI***
**KRZYSZTOF KRAJEWSKI**
**PATRYK CHAJA**
**PAWEŁ ZAWADZKI**
**SEBASTIAN BYKUĆ**

Institute of Fluid Flow Machinery, Polish Academy of Sciences,
Fiszera 14, 80-231 Gdańsk, Poland

**Abstract** In an era of changes in the electricity market, where the share of renewable energy sources is increasing and moving away from conventional coal-based energy, the electricity used for heating is gaining importance, for example to power heat pumps. They currently are one of the most common ways for heating buildings as an alternative to fossil fuels and biomass. In this article, the authors present an analysis aimed at answering the question whether using the concept of microgrids in Polish realities provides a feasible solution. Within the framework of this article, analyses were carried out by assuming the electrification of the heating installation of users in a local microgrid located in a selected location of the Polish low-voltage distribution network. The increase in electricity demand needed to generate the corresponding amount of heat was then estimated, and subsequently the impact of this demand on the microgrid was determined. In addition, in the article, the authors estimate the production of a prosumer PV installation at the selected location and analyze the level of autoconsumption of the generated electricity in the PV installation by the heat pump.

**Keywords:** Energy demand; Electrification of heating; Heat pumps; Power grid load; PV self-consumption; Smart metering; Smart grid

*Corresponding Author. Email: laskowski.michal@hotmail.com

# 1 Introduction

National and EU goals for the development of the energy sector focus on renewable energy, reducing harmful emissions, increasing energy efficiency and ensuring energy security. This leads to a gradual shift away from conventional fossil-based energy and the creation of new rules for the sector.

Distribution network operators are already facing a number of challenges, such as the increase in power from distributed high-power RES (renewable energy sources) installations connected to MV (medium voltage) and 110 kV networks, and the significant popularization of RES microinstallations connected to LV (low voltage) networks, leading to an effect of the popularization of RES micro installations power lines and a change in the direction of energy flows in the national electricity system. The solution to the increasing overload of power lines may be the concept of creating microgrids and electrification of heating in their area.

The conversion of surplus electricity production from RES to heat, referred to as 'power to heat' (P2H), increases the balancing capacity of microgrids and increases their flexibility. It also reduces the costs of modernization and development of the power infrastructure, increases the possibility of RES development and can contribute to reducing heating costs.

The most popular P2H technologies today are [1]:

- electric resistance boilers,
- electrode electric boilers,
- resistance heaters,
- heat pumps.

The topics addressed in this article are also reflected in other research papers [2–7] on the issues of the impact of electric heating on the power grid. The problem we are facing today in the context of the sharp reduction of fossil fuels supplied from the East makes the topic of energy transition in Poland gain a lot of momentum. In the presented work, the authors try to find an answer regarding the possibility of replacing fossil fuel heat sources with other types of heat sources powered by electricity, such as heat pumps, and what is their impact on the stability of electricity grids.

# 2 Description of research methodology

In this article, the technical feasibility of electrifying heating in the area of a dedicated microgrid by replacing conventional heating sources with heat

pumps was investigated. This change is dictated by the significantly higher energy efficiency compared to traditional solutions used in Polish households, i.e. coal or pellet fuel boilers. Heat pumps have an energy efficiency factor of more than 3 compared to other technologies, whose efficiency factor is around 1. The energy efficiency factor informs us about the ratio of the heating energy obtained to the energy input in fuel and, in the case of heat pumps, in electricity. The higher the value of the coefficient, the more efficient the source. In the case of heat pumps, this coefficient depends on the design of the pump and the temperature of the heat source. The efficiency of heating with a heat pump, defined as the COP (coefficient of performance) [16], is greater the smaller the temperature difference between the upper source (e.g. water in the heating system) and the lower source (e.g. ground or groundwater).

As part of the study, the electricity consumption of consumers throughout the calendar year was analyzed. In the next step, based on the averaged volume and energy intensity, the heat demand of residential and commercial buildings in the selected area was calculated. For municipal buildings in this area, the calculation was based on the consumption of fuel oil. For the purpose of conducting the study, the demand for domestic hot water in households and commercial buildings was also calculated, based on the methodology in the Prime Minister's Decree. The study then examined what the electricity consumption profiles of the different types of heat pumps are. The demand for electricity and domestic hot water of consumers as well as heat pumps over the entire calendar year was summed to determine the days on which the so-called peak and valley loads occur. Then, for the day with the highest demand (summer and winter) for electricity, it was analyzed what the load on the power grids at the designated location of the microgrid equipped with heat pumps looks like for all consumers.

In addition, due to the growing popularity of prosumer RES installations, an analysis of the heat pumps' ability to autoconsume electricity produced by prosumer PV (photovoltaics) installations was made. For this purpose, the average instalation in the microgrid area as well as the energy production of the PV installations were determined for specific hours of the year, and compared with the energy demand of the heat pumps.

The simulations and analysis below will answer the question of how the replacement of traditional boilers with heat pumps will affect loads on the electricity grid.

# 3 Descripion of the microgrid

As part of the analysis, a village located in the northeastern region of Poland was selected as the location of the microgrid study area. It is a municipality which has a total population of more than 1 800. The municipality houses 52 MV/LV (medium voltage/low voltage) substations. Based on the analysis of electricity demand in the entire municipality, it was decided that the study would analyze the area with the highest consumption, concentrated in the area of 8 MV/LV substations in the central part of the municipality and covering 261 consumers, including: residential and commercial consumers, the City Hall, an elementary school and the Fire Department. Type of municipality: rural. Location: Northeastern part of Poland. The breakdown by tariff group is shown in Table 1. Data on electricity consumption by consumers in the area of the microgrid under study is actual data and comes from PGE (Polish Energy Group) internal materials.

Table 1: Number of electricity customers by tariff and electricity consumption.

| Tariff | Number of electrical energy consumers | Power contracted (kW) | Energy consumed in 2021 (kWh) | (%) |
|---|---|---|---|---|
| B23 | 1 | ~ 800 | 1 439 725 | 56.3 |
| C11 | 13 | ~ 170 | 110 155 | 4.3 |
| C12b | 4 | ~ 20 | 82 730 | 3.2 |
| C12a | 19 | ~ 315 | 301 986 | 11.8 |
| G11 | 176 | ~ 1900 | 416 737 | 16.3 |
| G12 | 12 | ~ 100 | 32 919 | 1.3 |
| G12w | 36 | ~ 550 | 174 647 | 6.8 |
| SUM | 261 | ~ 3855 | 2 558 898 | 100.0 |

## 3.1 Electricity demand analysis

A yearly average hourly demand profile was created for the tariff customers shown in the table above, which is based on energy consumption data from MV/LV substations, see Fig. 1.

The distribution of energy demand by month of the year was also examined, see Fig. 2. The highest average hourly energy demand in the area of the studied microgrid was 747.6 kWh and the highest average monthly consumption in the month of March was 641.41 kWh. The lowest average

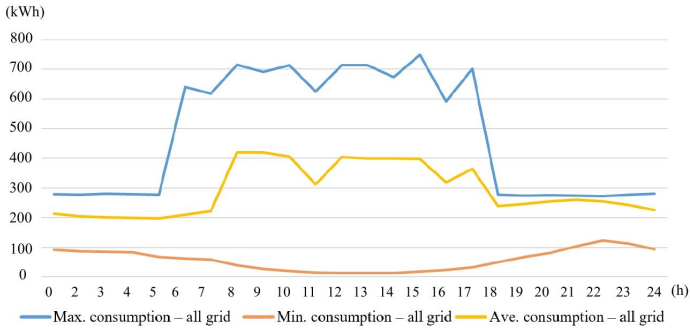


Figure 1: Average annual net energy consumption profile.

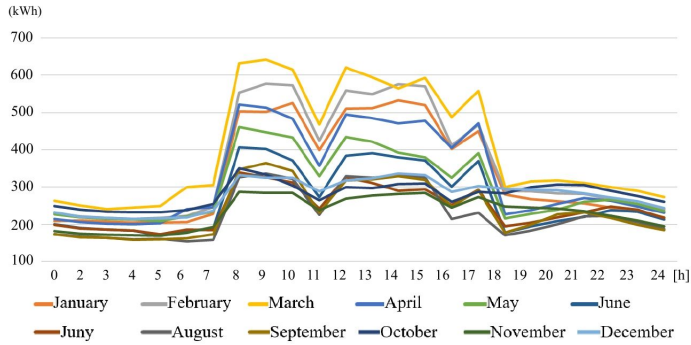


Figure 2: Averaged hourly profile of energy demand.

monthly energy consumption of 173.98 kWh was recorded in the month of August.

## 3.2 Analysis of heat and hot water demand

The distribution of average hourly temperature was obtained from archive data for building energy calculations for the 1972–1992 from the Ministry of Development and Investment, for a station in Ostrołęka, located not far from the microgrid. This hourly profile is shown in Fig. 3.

Based on the average hourly temperatures for Ostroleka, the occurrence frequency of several temperatures as well as other characteristic values were examined, as shown in Tables 2–3. (Own study based on data for energy calculations of buildings, Energy performance of buildings, Ministry of Investment and Development in Poland.)

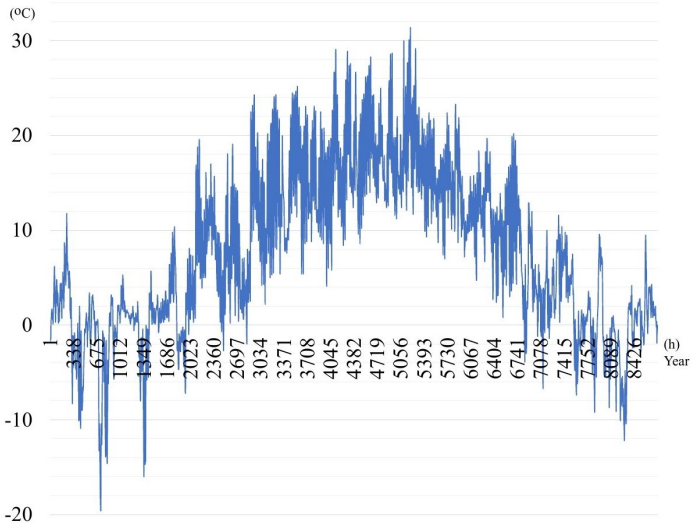


Figure 3: Hourly average temperature for the period 1972–1992 [8].

Table 2: Determination of the number of hours and days by temperature range.

| Temperature | Hours | Days |
|---|---|---|
| below 0°C | 1537 | 64 |
| below –5°C | 405 | 16 |
| below –10°C | 116 | 4 |
| below –15°C | 16 | 0 |

Table 3: Characteristic temperature values.

| Type | Temperature |
|---|---|
| Lowest hourly-average outside temperature | –19.6°C |
| Annual average temperature | 7.8°C |

The analysis of heat demand in the microgrid area will apply to 260 customers including: 224 households (G tariff for electricity), 33 business customers, and 3 public utility customers (a school, the Municipal Cultural Centre and Library and the Municipal Office). The B tariff customer, which has its own biomass heat source, has been excluded from the analysis. Based on the report *Development Strategy of the Municipality of Miastkowo for*

*2017–2024* [9], it was estimated that in 2015, the average floor area of apartments in the vicinity of the studied microgrid was 93.6 $m^2$, while the average number of persons per apartment was 3.82. The average number of persons for the rural municipality is in line with the study *Rural households compared to other types of households* [10], in which the average number of persons per farmer household in 2014 was determined to be 3.93 persons. For the purposes of further analysis, it was assumed that the total of 856 people live in the analyzed households, while commercial buildings are used by 66 people (2 people per facility).

The averaged area of a single-family house in first quarter 2022, according to [11], is 134.5 $m^2$. Averaging the Central Statistical Office (GUS) 2022 index with the average for Miastkowo, we get an average floor area of 114.05 $m^2$. However, as the average area for business facilities is estimated as 2 times the usable area for an individual consumer, this translated into an average area of 228.1 $m^2$ for business.

Heat demand can be divided by purpose into: central heating (CH) and domestic hot water (DHW).

### 3.3 Heat for central heating

For the purpose of estimating the heat demand of buildings, the energy classification of buildings according to the Association for Sustainable Development, shown in Table 4 was used.

Table 4: Energy classification of buildings [12].

| Energy class | Energy rating | Indicator EA kWh/m2/year | Construction period |
|---|---|---|---|
| A+ | Passive | <20 | |
| A | Low energy | 20-45 | |
| B | Energy efficient | 45-80 | |
| C | Medium energy efficient | 80-100 | |
| D | Moderately energy-intensive | 100-150 | From 1999 |
| E | Energy intensive | 150-250 | From 1998 |
| F | highly energy-intensive | >250 | From 1982 |

Assuming that most of the facilities in the microgrid area are 20th century buildings with varying levels of thermal insulation, for the purpose of estimating the demand for central heating, it was assumed that all buildings (households and business customers) are in Class D and the EA index

(indicating the energy intensity class of the building) was assumed to be 110 kWh/m$^2$ per year.

The following formula was used to calculate the annual heat demand for central heating of all the analyzed buildings, except for the municipal ones for which the guide *How to Plan the Heat Demand of a Municipality* was used [25].

For residences (buildings):

$$Q_{W,co} = V_{CO,i}\, L_i\, P_{pu}\,,$$

where: $V_{CO}$ – unit annual heat demand for CH (kWh/m$^2$/year); $L_i$ – number of reference units, number of objects; $P_{pu}$ – usable floor space (m$^2$).

For business (33 buildings):

$$Q_{W,co} = 110 \cdot 33 \cdot 228.1 = 828.0 \text{ MWh/year}.$$

The total annual heat demand for this group of buildings, estimated in this way, was 3638.2 MWh.

On the other hand, the heat demand for heating public facilities was calculated on the basis of the annual consumption of fuel oil used to heat municipal buildings. The municipality consumed 46 119 liters of oil with a calorific value of 38.8 MJ/litre in the year under review. The efficiency of oil boilers was assumed at 90%. The total annual demand of the analyzed municipal buildings was estimated at 447.4 MWh.

The total annual central heating demand of the buildings in the microgrid area was thus estimated at 4 0855 MWh.

### 3.4 Domestic hot water

Estimating the demand for domestic hot water (DHW) is not a straightforward task due, among others, to the following factors: water temperature, uneven intake throughout the days of the week and seasons of the year, changing population, and the quality and quantity of fixtures at the consumption points.

In order to estimate the demand for hot water, the Ordinance of the Minister of Infrastructure of November 6, 2008 was used, in which, in Appendix No. 5, a methodology for calculating the energy performance of a building, dwelling or part of a building constituting an independent technical and utility whole, not equipped with cooling systems, was specified.

In this methodology, a formula for determining the annual useful heat demand and hot water correction factors *kt* and daily hot water consumption for residential buildings of different types *Vcw* [13] is specified.

## 4 Compressor heat pumps

The simplest heat pump or cooling device is an energy device with the reverse action of a heat engine. This device takes in low-temperature heat and using, additional energy, gives off high-temperature heat. Analogous to a liquid pump where there is a 'liquid lift', in a heat pump there is a 'temperature lift'. Under the right conditions, the energy delivered to the system is several times less than the heat received at low temperature. This quotient depends mainly on the temperature difference. The heat delivered at high temperature is the sum of the above two.

Heat pumps and refrigeration equipment accomplish the above by subjecting the refrigerant through a series of thermodynamic transformations according to the Linde dry cycle, during which the refrigerant changes its state of aggregation between liquid and gas. To evaporate the refrigerant in the evaporator, the supplied low-temperature heat is used, while to condense the refrigerant in the condenser, high-temperature heat must be received. These units are also equipped with a compressor and a throttling valve to ensure the appropriate refrigerant pressure differential needed to achieve different evaporation and condensation temperatures.

We distinguish between these devices according to the desired effect, i.e. if the desired effect is the removal of heat through the device then it is a cooling device (e.g. air conditioner, refrigerator), while if the desired effect is the supply of heat through the device then it is a heat pump (e.g. space heating, DHW heating). If the device is able to operate in both modes, then we are talking about the possibility of operation of the device in reverse mode. This requires the use of an appropriate design and special components, such as a four-way valve, or heat exchangers that can operate as a condenser or evaporator.

Heat pumps are classified by their lower and upper heat source, e.g. the simplest air-to-water heat pump extracts heat from the ambient air, and gives the heat back to the water in the central heating system. The upper heat source is also used to heat domestic hot water or air directly, for example, in air ducts. In the case of standard heat pumps, the temperature of the upper source medium does not exceed 65°C, but there are heat pumps

operating in the transcritical circuit, where the medium is $CO_2$, which can supply water at temperatures as high as 90°C. As the temperature of the upper source medium increases, the coefficient of performance of heat pumps decreases, so it is most efficient to use heat pumps with underfloor heating systems, where a temperature of 30°C to 35°C is sufficient.

Atmospheric air is most often used as a lower heat source, due to its simplicity, availability and by far the lowest cost. Such systems achieve a lower efficiency than systems using heat from the ground or groundwater. To extract heat from the ground, ground heat exchangers are most often used, among which several types can be distinguished according to the depth of application. However, the use of waste heat, e.g. in industry, allows you to achieve the most efficient and economical type of heat pump. An inverse relationship can be observed between the availability and cost of the bottom source and the efficiency of heat pump operation.

### 4.1 Analysis of electricity demand for heating and domestic hot water by heat pumps

According to the Low Carbon Management Plan for the Municipality of Miastkowo for 2016–2020, the main fuel used for residential purposes was wood, which accounted for more than 87% of the fuel used. Electricity came next with a share of 12.15% [14]. The public buildings in the microgrid area are equipped with heating sources fired by fuel oil.

In order to ensure the greatest possible security in heat supply while reducing emissions, it was assumed that there will be a significant electrification of heating in the microgrid area, i.e. replacement of 100% of boilers with heat pumps powered by energy from local RES sources. The heat sources at municipal facilities are planned to be replaced with high-temperature heat pumps, while household heating systems would be replaced with low-temperature heat pumps connected to other heating devices in a water loop, which can be compared to a heating microgrid. Such a solution will optimize heating costs while reducing emissions and, at the same time, avoid the significant costs of developing a district heating network in a rural municipality, which makes the economic justification for their development in rural areas unviable.

Analyzing the volume of central heating demand for a standard house in the microgrid area with an area of 114.05 $m^2$ and an estimated central heating demand of 110 $kW/m^2$/year was derived from the performance characteristics of an air source heat pump with a compressor capacity of

2500 W in a typical single-family house [18]. Electricity demand over 12 months for the given type of heat pump is shown in Fig. 4. Atmospheric air temperature from the Meteonorm 7.2 database for Ostroleka was used. The demand for heat and hot water was 18.014 kWh, and electricity consumption was 4.733 kWh.

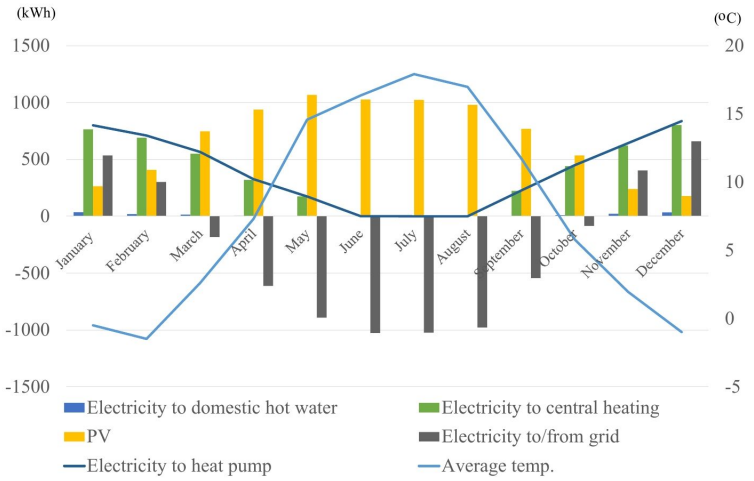


Figure 4: The average monthly electricity demand for an air source heat pump of 2.5 kW.

The air source heat pump operated with a dependent efficiency described by the equation

$$\mathrm{COP} = 0.0013T_a^2 + 0.0671T_a + 2.8787 - 0.0565\,(T_g - 45)\,,$$

where $T_a$ is the ambient air temperature, $T_g$ is the temperature of the upper heat pump exchanger.

However, for the characteristics of a ground-source heat pump with a compressor power of 1.875 W in the model house, the demand for heat and domestic hot water was 18.485 kWh, and the electricity consumption was 3.401 kWh. In Fig. 5, you can observe the electricity demand of the ground source heat pump.

The ground source heat pump operated at the dependent efficiency described by the equation [17]:

$$\mathrm{COP} = -0.125T_g + 9.575,$$

where $T_g$ is the temperature of the upper heat pump exchanger.

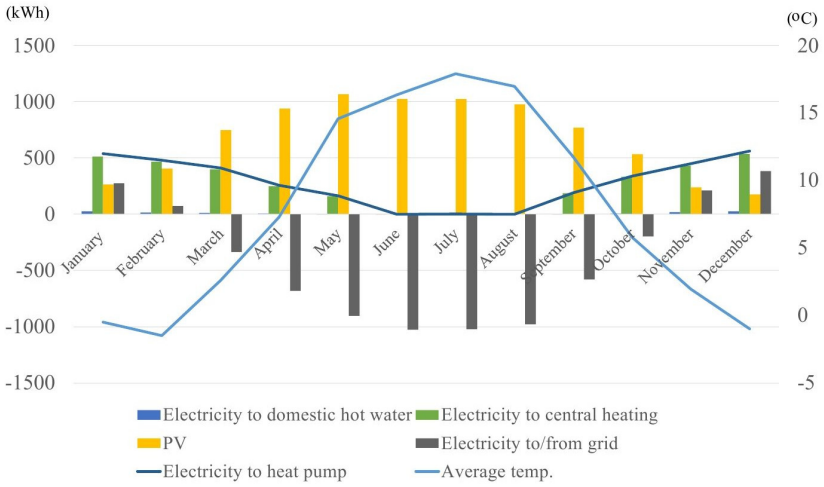


Figure 5: The average monthly electricity demand for a ground source heat pump with a capacity of 1875 W.

For both heat pumps, the COP relationship was assumed by averaging data from product data sheets of Viessman [19], Vaillant [20] and Daikin [21], the Port PC market report [15] and laboratory tests conducted by the Fraunhofer Institute [21]. A bottom heat source temperature of 10°C was assumed for the ground source heat pump.

In addition, the analysis was enriched by characterizing the production from an 8 kW prosumer installation according to Global Solar Atlas parameters [23] where the average annual production for a 1 kWp panel in the microgrid area is 1.022 MWh. The average production from 1 kWp for individual hours and months is shown in Fig. 6. As can be seen in Figure 6, the most energy produced by PV will be between April and August, between 9 am and 2 pm.

The electricity consumption waveforms for the compressor pump for two characteristic days of the year:

- the day with the highest electricity consumption throughout a day in winter;
- the day with the highest electricity consumption throughout a day in summer;
- are presented below in Figs. 7–8. From the point of view of grid operation and the simulations performed, the days with the highest

| | Jan | Feb | Mar | Apr | May | Jun | Jul | Aug | Sep | Oct | Nov | Dec |
|---|---|---|---|---|---|---|---|---|---|---|---|---|
| 0 - 1 | | | | | | | | | | | | |
| 1 - 2 | | | | | | | | | | | | |
| 2 - 3 | | | | | | | | | | | | |
| 3 - 4 | | | | | | | | | | | | |
| 4 - 5 | | | | | 9 | 21 | 12 | | | | | |
| 5 - 6 | | | | 18 | 54 | 60 | 50 | 28 | 1 | | | |
| 6 - 7 | | | 27 | 115 | 160 | 161 | 141 | 116 | 76 | 12 | | |
| 7 - 8 | | 32 | 152 | 254 | 297 | 289 | 267 | 247 | 204 | 126 | 7 | |
| 8 - 9 | 60 | 156 | 274 | 385 | 420 | 404 | 386 | 377 | 329 | 224 | 103 | 45 |
| 9 - 10 | 158 | 237 | 366 | 476 | 505 | 480 | 468 | 467 | 415 | 298 | 155 | 114 |
| 10 - 11 | 189 | 274 | 409 | 508 | 537 | 518 | 506 | 502 | 439 | 320 | 170 | 134 |
| 11 - 12 | 196 | 288 | 428 | 508 | 528 | 507 | 494 | 499 | 439 | 334 | 185 | 147 |
| 12 - 13 | 194 | 288 | 422 | 478 | 497 | 482 | 476 | 478 | 417 | 324 | 174 | 139 |
| 13 - 14 | 165 | 265 | 385 | 427 | 440 | 431 | 425 | 426 | 358 | 265 | 135 | 105 |
| 14 - 15 | 102 | 186 | 291 | 340 | 361 | 359 | 356 | 349 | 276 | 177 | 70 | 31 |
| 15 - 16 | 3 | 94 | 184 | 239 | 264 | 279 | 274 | 255 | 176 | 75 | 0 | |
| 16 - 17 | | 2 | 76 | 130 | 157 | 178 | 174 | 151 | 72 | 1 | | |
| 17 - 18 | | | 2 | 33 | 59 | 76 | 75 | 49 | 5 | | | |
| 18 - 19 | | | | 1 | 14 | 29 | 25 | 4 | | | | |
| 19 - 20 | | | | | | 3 | 1 | | | | | |
| 20 - 21 | | | | | | | | | | | | |
| 21 - 22 | | | | | | | | | | | | |
| 22 - 23 | | | | | | | | | | | | |
| 23 - 24 | | | | | | | | | | | | |
| Sum | 1,066 | 1,820 | 3,016 | 3,912 | 4,302 | 4,279 | 4,128 | 3,949 | 3,208 | 2,157 | 1,000 | 714 |

Figure 6: Average production from 1kWp of installed PV capacity in the microgrid area (Wh) [26].

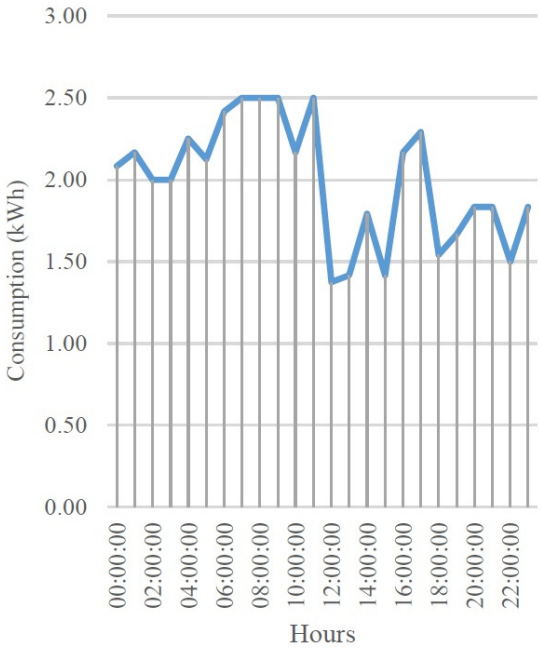


Figure 7: Hourly usage profile of the day with highest usage in winter – 31 Jan. 2021.

electricity consumption put the most strain on the power lines at the selected location. According to the diagram shown in Fig. 7, the selected microgrid location has a single-sided power supply.

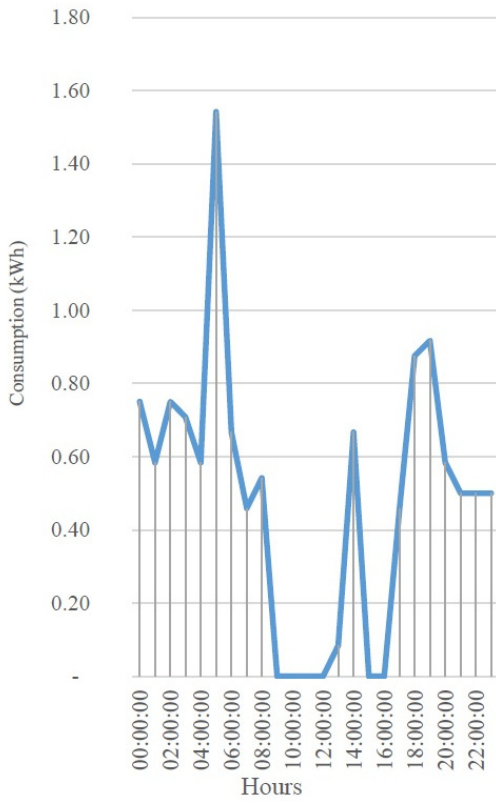


Figure 8: Hourly usage profile of the day with highest usage in summer – 21 Sept. 2022.

## 5 Impact of heating electrification on the microgrid area

The operation of the grid infrastructure was simulated using the NEPLAN tool [26]. In line with the purpose of this article, it was investigated what the network load looks like before and after the implementation of heat pumps at all customers. Simulations were carried out on a selected location with 8 medium-voltage to low-voltage (MV/LV) transformer stations,

from which electricity is supplied to 261 consumers. Figure 9 shows the network diagram at the selected microgrid location. Information such as the length of individual power lines or the number of consumers comes from

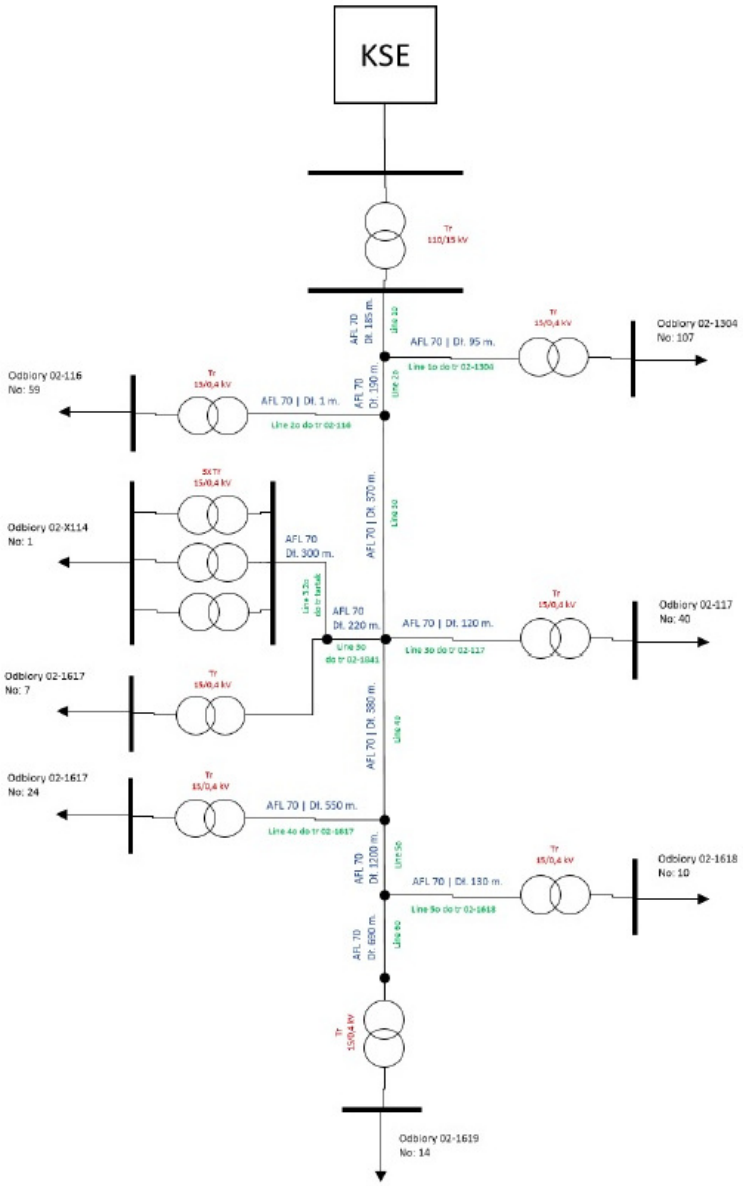


Figure 9: Diagram of the network in the selected location of the microgrid.

map readings found in geoportal360.pl. Other data such as cross-sections of power lines and parameters of transformers, were selected on the basis of available information from the electricity distributor in the indicated area – PGE Dystrybucja S.A. According to information on the electricity supplier's website, AL70 $mm^2$ type lines, or those with larger cross-sections, are used for the main medium-voltage overhead lines. For the purposes of our study, it was assumed that the main lines from the 110 kV/15 kV substation and the individual lines running to the 15 kV/0.4 kV substation are made of AL70$mm^2$ type overhead lines. The characteristics of the transformers adopted for the simulation can be found in Table 5.

Table 5: Parameters of oil transformers adopted for simulation [27].

| Indicator | Unit | Value |
|---|---|---|
| Sn | MVA | 0.16–0.63 |
| Ug (Ur) | kV | 15.75 |
| Ud1 (Ur2) | kV | 0.42 |
| Ud2 | kV | – |
| uzwgd1 (ukr1) | % | 4.22 |
| ΔPcu (uRr1) | kW | 2.343 |
| ΔPFe | kW | 0.28 |
| io | % | 0.6 |
| Connection group | – | Yzn5 |
| Adjustment range | % or kV | $15.75 \pm 3x2.5\%$ |

The MV line supplying 8 transformer stations has a single-sided supply. The demand for electricity at each substation is presented in Table 6. The performed network simulation, allowed us to verify the loads on the lines in the designated microgrid location. The network parameters for the selected days in the winter and summer peaks are presented below. As can be observed, there is no overloading on any of the line sections in the microgrid. The total energy consumption in the winter peak was almost 930 kWh, while in the summer peak it was more than 675 kWh.

In accordance with the purpose of the study, it was assumed that all consumers (261 households) will be equipped with a heat pump with the parameters given in Section 4.1. It is therefore necessary to check whether the network infrastructure in the microgrid will manage to operate in the

Table 6: Summary of electricity consumption for peak and valley demand.

| Station number | Maximum consumption for peak winter 08.03 hours 15 (kWh) | Maximum consumption for peak summer 20.07 hours 9 (kWh) | Maximum consumption for peak winter 08.03 hours 15 (with pumps) (kWh) | Maximum consumption for peak summer 20.07 hours 9 (with pumps) (kWh) |
|---|---|---|---|---|
| 02-116 | 46.32 | 8.43 | 193.2 | 98.9 |
| 02-117 | 17.52 | 4.68 | 118.3 | 66.7 |
| 02-1304 | 81.51 | 19.89 | 348.7 | 184.5 |
| 02-1617 | 15.20 | 1.40 | 75.2 | 38.3 |
| 02-1618 | 6.05 | 0.25 | 29.8 | 14.9 |
| 02-1619 | 9.05 | 4.00 | 44.2 | 25.7 |
| 02-1841 | 6.00 | 14.16 | 22.3 | 24.2 |
| 02-X114 | 747.60 | 622.50 | 750.1 | 624.0 |
| Total | 929.25 | 675.31 | 1581.8 | 1077.3 |

summer peak and winter peak without failure. For this purpose, the maximum electricity consumption was read from the heat pump's annual energy demand waveforms and these values were added to the selected summer peak – 20 July 9:00 am – 675.31 kWh and for the winter peak – 08 March 3:00 pm – 929.25 kWh. The results are presented in Table 6.

The results presented in Table 6, which are the maximum electricity consumption of consumers in the summer and winter peaks, were assigned to individual substations as load, subsequently it was then checked how the change in demand caused by the implementation of heat pumps affects the operation of power lines.

A comparison of the obtained results of the network load in the microgrid with primary electricity consumption and equipped with heat pumps at all customers, can be found in Figs. 10 and 11.

In light of the results presented, it can be seen that the largest load changes occur in Line 10, where the load increases from about 12% to more than 20% in the winter peak and from about 9% to about 14% in the summer peak. The smallest changes occur in the line with the highest consumption feeding the sawmill where the impact of switching the few electricity consumers fed by this line to heat pumps has a small impact on the line's load of less than 0.5 p.p. (percentage point) in both the summer and winter peaks.

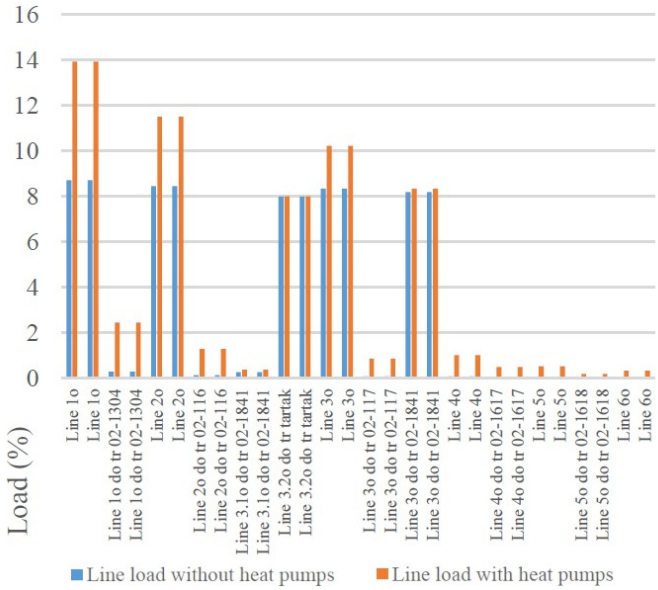


Figure 10: Load results of individual power lines for the summer peak.

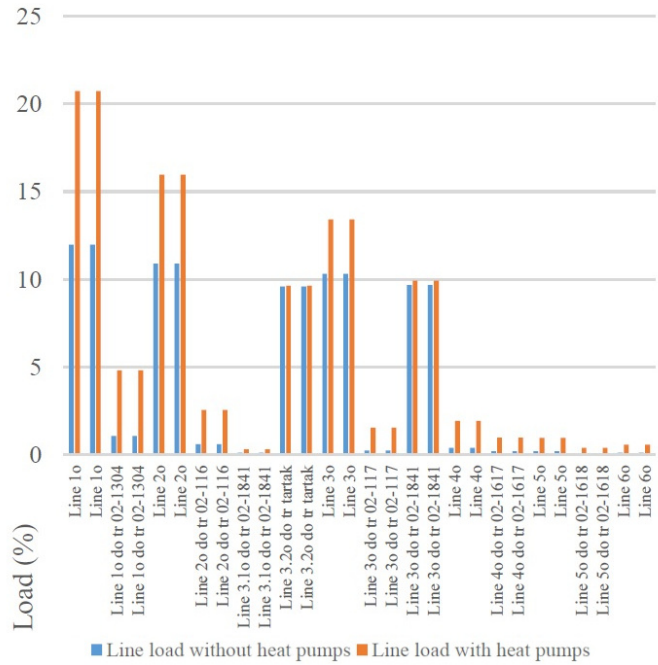


Figure 11: Power line load results for the winter peak.

# 6 Conclusions

The analysis of the impact of switching the heating source of electricity consumers from traditional sources to heat pumps on the power grid section shows that this action does not affect the energy security of the residents of the analyzed power grid section.

Additional analysis of the electricity demand profile of the heat pumps and the electricity generation profile of the PV source showed a 100% consumption level of PV energy during the winter peak in the months of November-February, i.e. the period of highest electricity demand by the heat pumps, and a near-zero autoconsumption level during the summer peak in the months of June-August, i.e. the period of highest electricity generation by the PV system.

In the paper, the authors tried to demonstrate that, in the case of using heat pumps as alternative sources to heating with traditional fuels (coal, biomass, gas), the application of the above approach for the analyzed microgrid system allows full electrification of heating without loss of network parameters and its stable operation.

## Acknowledgements

This article was developed as part of the implementation PhDs carried out at IMP PAN and PGE Polska Grupa Energetyczna S.A.

*Received 16 May 2023*

# References

[1] Institute for Renewable Energy: *Renewable energy sources in the heating industry Technologies that will change reality.* Energy Forum, IEO rep., May 2020 (in Polish).

[2] Lowes R., Woodman B., Speirs J.: *Heating in Great Britain: An incumbent discourse coalition resists an electrifying future*, Environ. Innov. Soc. T. **37**(2020), 1–17.

[3] Marszal-Pomianowska A., Widé J., Le Dréa J., Heiselber P., Bak-Jense B., de Cerio Mendaz I.D.: *Operation of power distribution networks with new and flexible loads: A case of existing residential low voltage network.* Energy **202**(2020), 117715.

[4] Askeland K., Rygg B.J., Sperling K., *The role of 4th generation district heating (4GDH) in a highly electrified hydropower dominated energy system – the case of Norway.* Int. J. Sust. Energ. Plann. Manage. **27** (2020), Spec. Iss., 17–34.

[5] Bolkesjo T.F., Kirkerud J.G., Tromborg E.: *Power market impacts of increased use of electricity in the heating sector.*) Int. Conf. on the European Energy Market, EEM, 2017, 7981955.

[6] Protopapadaki C., Saelens D.: *Heat pump and PV impact on residential low-voltage distribution grids as a function of building and district properties*. Appl. Energ. **192**(2017), 268–281.

[7] Radziszewska W., Bugaj M., Łuniewski M., Hoogsteen G., Chaja P., Bykuć S.: *Testing of a price-based system for power balancing on real-life HVAC installation in real life*. Bull. Pol. Acad. Sci. Tech. Sci. **70**(2022), 2, e140690.

[8] Ministry of Investment and Development in Poland: *Data for energy calculations of buildings* (in Polish). https://www.gov.pl/web/archiwum-inwestycje-rozwoj/dane-do-obliczen-energetycznych-budynkow (accessed 20 July 2023).

[9] Municipality of Miastkowo: *Development Strategy of Miastkowo 2017-2024*. Miastkowo 2017 (in Polish).

[10] Urban S.: *Farm households in comparison with the other type of household*. Probl. Small Agr. Holdings **4**(2016), 93–107 (in Polish). doi: 10.15576/PDGR/2016.4.93

[11] Central Statistical Office: *Construction in Q1 2022*. 10 June 2022. GUS, Warszawa 2022 (in Polish).

[12] http://www.drevohaus.pl/?drev=energooszczednosc (accessed 24 Sept. 2022.).

[13] Minister of Infrastructure: "The methodology of calculating the energy performance of a building and a dwelling or a part of a building constituting a separate technical and utilitarian unit, as well as the method of drawing up and models of their energy performance certificates". DzU Nr 201/2008, poz. 1240 (in Polish).

[14] Municipality of Miastkowo: *Low-carbon management plan for the municipality of Miastkowo for 2016-2020*, Miastkowo 2015 (in Polish).

[15] Lachman P., Rączka J., Schnell C., Wróbel P.: *Scenarios for electrification of heating in single-family buildings in Poland until 2030*, Port PC, 2020 (in Polish).

[16] Magni M., Venturi E., Ochs F., Dermentzis G.: *Impact of the European building energy requirements on the heat pump market*. In: Proc. 4th IEA Heat Pump Conf.15-18 May 2023, Chicago, 2023, 778.

[17] Klein K., Huchtemann K.: *Numerical study on hybrid heat pump systems in existing buildings*. Energ. Buildings **70**(2014), 441–454.

[18] Ghoubali R., Byrne P.: *Simulation study of a heat pump for simultaneous heating and cooling coupled to buildings*. Energ. Buildings **72**(2014), 141–149.

[19] https://www.viessmann.pl/pl/budynki-mieszkalne/pompy-ciepla.html (accessed 22 Jan. 2023).

[20] https://www.vaillant.pl/klienci-indywidualni/produkty-i-systemy/grupy-produktowe/pompy-ciepla/ (accessed 15 Jan. 2023).

[21] https://www.daikin.pl/pl_pl/product-group.html (accessed 22 Jan. 2023).

[22] https://wp-monitoring.ise.fraunhofer.de/wp-effizienz//download/final_report_wp_effizienz_en.pdf (accessed 14 Jan. 2023).

[23] https://globalsolaratlas.info/detail?c=53.078971,21.711731,11&s=53.132354,21.735764&m=site&pv=small,180,38,1 (accessed 19.04.2023).

[24] https://pgedystrybucja.pl/strefa-klienta/przydatne-dokumenty/akordeon-przydatne-dokumenty/zestawienie-wytycznych-do-budowy-systemow-elektroenergetycznych (accessed 25.02.2023).

[25] Upper Silesian Regional Energy Conservation Agency (GRAPE), Foundation for the Efficient Use of Energy (FEWE), Krakow Development Office (BRK) under the direction of Dr. Jan Uruski: *Guidebook on how to plan heat supply in the Municipality*, Katowice – Kraków 1998 (in Polish).

[26] NEPLAN: *Load Flow and Short Circuit*, https://www.neplan.ch/ (accessed 18 Apr. 2023).

[27] https://www.prosper.com.pl/katalogi/Nowa-plus/transformatory.pdf (accessed 10 Apr. 2023).

**archives**
**of thermodynamics**
Vol. **44**(2023), No. 4, 243–260
DOI: 10.24425/ather.2023.149723

# Experimental investigation of the energy efficiency of a linear compressor and comparison with a reciprocating compressor in a small refrigeration system

**MICHAŁ JAN KOWALCZYK***
**ARTUR ROMANIAK**
**MARCIN ŁĘCKI**
**ARTUR GUTKOWSKI**
**GRZEGORZ GÓRECKI**

Lodz University of Technology, Institute of Turbomachinery, Division of Heat Technology and Refrigeration, Wolczanska 217/221, 93-005 Lodz, Poland

**Abstract** The conducted experimental studies of the linear compressor concerned the cooling capacity, efficiency, and Energy Efficiency Ratio (EER). Linear compressor performance tests were carried out for the supply voltage of 190–265 V and the supply frequency in the range of 45–65 Hz, which allowed the compressor to be tested outside its typical operating range. Modulation of the performance was achieved using an inverter. The full range of performance characteristics of a linear compressor was presented. The results were compared with a reciprocating compressor for similar displacement volume, which achieved lower EER values by an average of 38% for a pressure ratio above 1.7. The power consumption of a linear compressor is on average two times lower than that of a reciprocating compressor.

**Keywords:** Power Consumption; Linear compressor; Reciprocating compressor; Energy efficiency ratio; Energy saving compressor

*Corresponding Author. Email: michal.kowalczyk.1@dokt.p.lodz.pl

### Nomenclature

| | | |
|---|---|---|
| CFD | – | computational fluid dynamics |
| EER | – | energy efficiency ratio |
| $h_1$ | – | discharge enthalpy, kJ·kg$^{-1}$ |
| $h_4$ | – | suction enthalpy, kJ·kg$^{-1}$ |
| $h_3$ | – | inlet calorimeter enthalpy, kJ·kg$^{-1}$ |
| $h_7$ | – | outlet calorimeter enthalpy, kJ·kg$^{-1}$ |
| $\dot{m}_{\mathrm{ref}}$ | – | mass flow of refrigerant, g·s$^{-1}$ |
| $N$ | – | number of elements on a sample |
| PR | – | pressure ratio |
| $P_{\mathrm{suc}}$ | – | suction pressure, kPa |
| $p_1$ | – | discharge pressure, kPa |
| $p_4$ | – | suction pressure, kPa |
| $R$ | – | result of a calculation based on one or more measurements |
| $\dot{Q}_{\mathrm{evap}}$ | – | cooling capacity, W |
| $W_{\mathrm{in}}$ | – | electric power consumption, W |
| $X_i$ | – | $i$th variable |

#### Greek symbols

| | | |
|---|---|---|
| $\delta R$ | – | uncertainty in the result |
| $\eta$ | – | compressor efficiency |

## 1 Introduction

In recent years, there has been a growing interest in energy-saving appliances in the heating and cooling energy sector, which accounts for a significant share of energy consumption. Today, in most types of small refrigeration system compressors (up to a cooling capacity of 1 kW), the market is dominated by different varieties of reciprocating compressors. Currently, there is an increasing interest in research into the use of energy-saving linear compressors in small refrigeration systems. The power consumed in the global dimension by small refrigeration systems occupies a significant part of it and increases year by year, Hovgaard [1].

Park *et al.* [2] conducted research on a linear compressor by dividing it into several control volumes. They analyzed the heat transfer for each volume. In the experiment, a calorimeter was used to determine the cooling capacity of a compressor. The energy efficiency ratio (EER) was estimated depending on the changes in the thermal properties of the compressor. The obtained experimental results coincided with the simulation within 5%. Liang [3] dealt with the issues related to the use of an oil-free linear com-

pressor in small refrigeration systems. The oil-free operation will allow the use of mini/micro channel heat exchangers and increase the efficiency of the entire system. With a typical high-pressure ratio in domestic refrigeration, the key challenges are the development of large clearance losses, large piston displacement, and non-linear spring operation. The author made a thorough analysis of the above key issues, which will contribute to the implementation of an oil-free linear compressor for domestic refrigeration. The nonlinear spring model has been validated by experiments for lower pressures. The researcher observed that the gas leakage increases 2.5 times when the piston is fully eccentric in the cylinder. The gas leakage loss can be 27% of the power consumption at a pressure ratio of 13.6 when using R600a refrigerant. Two commercially available designs of linear compressors from LG [4] and Embraco Wisemotion [5] have been developed. Bezrodny *et al.* [6] tested the efficiency of the heat pump with the removal of excessive moisture, which can also contribute to energy efficiency.

An analysis of the possibility of controlling the efficiency of linear compressors and the impact of changes in efficiency on their operation was undertaken. Kim and Jeong [7] with Kim and Kim [8] determined the performance characteristics of a linear compressor for two ways of changing its efficiency (inherent capacity modulated and electronic resonance system). The experimental test conditions were selected to ensure the modulation of the compressor for the efficiency range from 50% to 100% at an evaporating temperature of –26°C and a condensing temperature of 36°C. The difference in the capacity of the refrigeration system for ICM (inherent capacity modulated) control and the electronic resonance system is within 1%. The results for conventional linear compressor control did not consider the power consumed by the electronic drive, so the ICM linear compressor had a potential improvement in energy savings. In another part of the research, they developed the characteristics of the linear compressor parameter change in response to the fluctuating evaporation and condensation temperature occurring in low-power refrigeration equipment. Based on the conducted experimental research, a numerical model and a compressor prototype were developed. The compressor prototype was tested for an evaporating temperature of –35°C to 15°C. For increasing the condensing temperature from 20°C to 50°C, the cooling capacity increased by 241 W and 50 W respectively.

Based on experimental research one-dimensional CFD model was created by Hwang and Lee [9]. The model simulated a temperature distribution inside the compressor and the resulting transitional flows. To shorten

the calculation time, the temperature of the compressor solids was used as the boundary conditions of the wall. The obtained results for the simulation settings allowed us to obtain results with an accuracy of 5%, which improved the accuracy of the model compared to the previous one by 10%. An and Lee [10] developed a three-dimensional numerical CFD model that allowed the prediction of the cooling capacity of a linear compressor. To analyze the operating cycle of a linear compressor, experimental tests were carried out on two linear compressors, and the obtained results were consistent with the results of the numerical simulations. The accuracy of the simulation was increased by considering the detailed behavior of the valves.

This paper attempts to describe the influence of a linear compressor on the work of a refrigeration system also in extreme power supply cases and to compare it to a reciprocating compressor with a similar design displacement volume. The thermodynamic values of each of the elements of the refrigeration system were measured for various compressor power supply parameters. Experimental tests were carried out on a stand with a calorimeter. The article presents and discusses the characteristics of the impact of linear and reciprocating compressors on the refrigeration system. The motivation to undertake the research was the desire to extend the available experimental results in extreme cases of the operation of a linear compressor and to compare it with a reciprocating compressor in terms of energy efficiency. These experimental data will find application in industry and numerical research. The main purpose of the work, which is a novelty, is to determine and compare the energy efficiency of the linear and reciprocating compressors in a wide range of power supply parameters.

## 2 Materials and methods

### 2.1 Objects of study

The research object is a linear compressor (LG FLA 150NBMA), used in small refrigeration devices. It is one of the few linear compressors available commercially. The reciprocating compressor (Secop NLX15KK.3) used for the comparison has a similar volume compression to the linear one. The most important parameters of the tested compressors are presented in Table 1.

Table 1: Parameters of tested refrigeration compressors.

| Compressor type | Linear compressor (LG FLA150NBMA) | Reciprocating compressor (Secop NLX15KK.3) |
|---|---|---|
| Voltage Range (V) | 220–240 | 198–254 |
| Frequency Range (Hz) | 50–60 | 50–60 |
| Resistance, main (Ω) | 9 | 14.6 |
| Displacement ($cm^3$) | 15 | 14.65 |
| Refrigerant | R600a | R600a |

## 2.2 Experimental stand

The refrigeration system has been designed with a calorimeter to determine the cooling capacity of the compressor and EER of the refrigeration system in accordance with ANSI/ASHRAE 23.1 [11]. The test rig is equipped with an analyzer of electric network parameters (DMG 200, LOVATO ELECTRIC), which measures the electric power consumed by the heater in the calorimeter and the power consumed by the compressor. The temperature measurement was conducted with the aid of T-type thermocouples (OMEGA type T thermocouples). The pressure was measured by Danfoss transducers dedicated to refrigeration systems (Danfoss AKS 33). An electronic expansion valve was used for the control of the refrigerant mass flow (Carel E2V09) and a Coriolis-type mass flow meter (Endres + Hauser promass 83) for its measurement. A plate condenser (SWEP B5THx10) and flow meter (Kobold DUK 11G4HL443L) were utilized in the water cooling cycle. During the tests, the compressor performance was changed using an inverter (Sanyu SXE0015T2B). A multimeter (Fluke 8808A) was used to measure the compressor supply voltage. A calorimeter with an intermediate medium was used as the evaporator. In the steady state of heat transfer, the power supplied to the intermediate medium by the electric heater was equal to the power of the evaporator mounted in the top cover of the calorimeter. This power can be taken as the cooling capacity of the compressor. During the construction of the test stand, the experience gained during the stand for testing heat exchangers was used [12].

A diagram of the experimental rig of a refrigeration system is shown in Fig. 1. The pressure and temperature measurement points (P and T) have been marked on it. There are also detailed locations of the components of the refrigeration system. The high-pressure side is marked in a red line,

and the low-pressure side in a blue line. Measurement uncertainties of power consumption, cooling capacity, and EER of the refrigeration system depend on the measured value of the electric power of the compressor and electric heater.

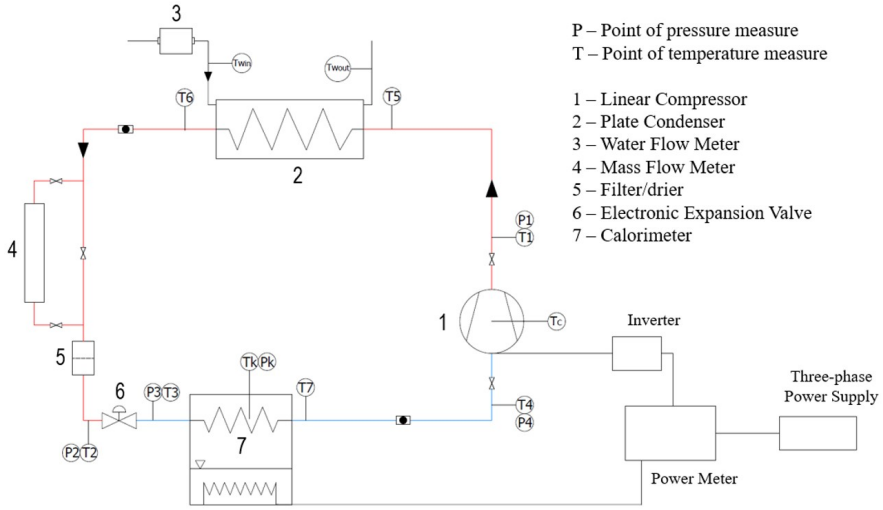


Figure 1: Scheme 2D of the experimental stand.

Compressors are dedicated by the manufacturers to the R600a (Isobutane) refrigerant that was used during the tests. The motivation to choose this refrigerant, despite a small pressure ratio, for the use of small compressors, was the mapping of working conditions in households (small refrigerators). They are powered by an inverter that allows changing the compressor power parameters and performance.

In the first stage of the research, the linear compressor was thoroughly tested in terms of determining its performance characteristics depending on the voltage and frequency of the power supply. The tests were carried out for supply voltage in the range of 190–265 V and current frequency in the range of 45–65 Hz. The temperature in the calorimeter was set to be equal to the ambient temperature, which eliminates heat losses to the environment. Under such conditions, the heater power in the calorimeter is equal to the cooling capacity of the tested compressor. The superheat of the refrigerant was kept at around 5 K.

In the second stage, a reciprocating compressor (Secop NLX15KK_3) with a similar volume displacement (declared by the manufacturer) to the

tested linear compressor. The tests were carried out for a supply voltage of 200–250 V and a supply frequency of 45-55 Hz. The condition for comparison was the same pressure ratio. The adopted test conditions resulted in different parameters of evaporation and condensation temperatures and pressures (Fig. 2 and 3). As can be seen, these parameters are greater for the linear compressor than for a reciprocating one – evaporation parameters (temperature and pressure) by 9 K and 73 kPa on average, while condensation parameters by about 10 K and 140 kPa. This is a result of different mass flow rates generated in the tested devices.

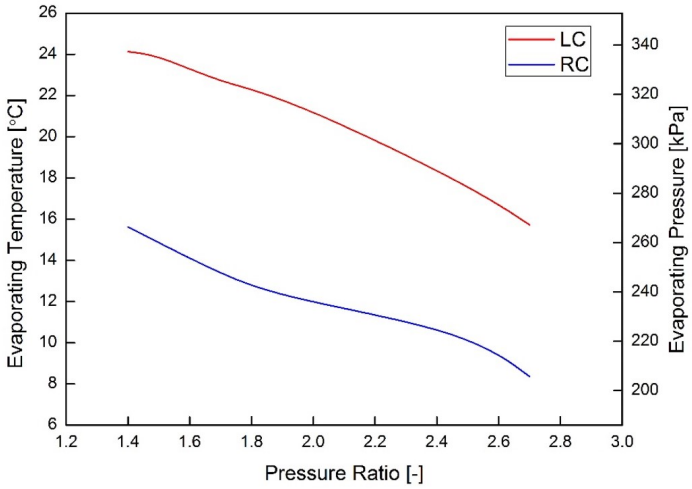


Figure 2: Compressors evaporation temperatures and pressures during the second stage of research.

The $\log p{-}h$ chart of the cycle created from the characteristic points obtained during the tests of the linear compressor, for a selected measurement run (Voltage 230 V and frequency 60 Hz of supply current) is shown in Fig. 4. The achieved evaporation and condensation temperatures, as well as the level of refrigerant subcooling and superheating, are marked on it.

In Table 2, there is a list of devices utilized in the experimental rig along with their respective measurement errors. The error analysis of the individual calculated parameters was carried out in accordance with Moffat [13]. Uncertainties were calculated using the formula

$$\delta R = \left\{ \sum_{i}^{N} \left( \frac{\partial R}{\partial x_i} \delta X_i \right)^2 \right\}^{\frac{1}{2}}. \tag{1}$$

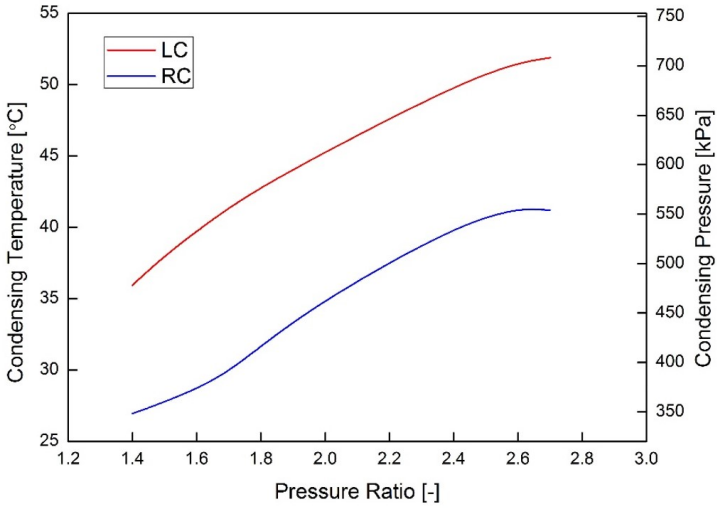


Figure 3: Compressors condensing temperatures and pressures during the second stage of research.

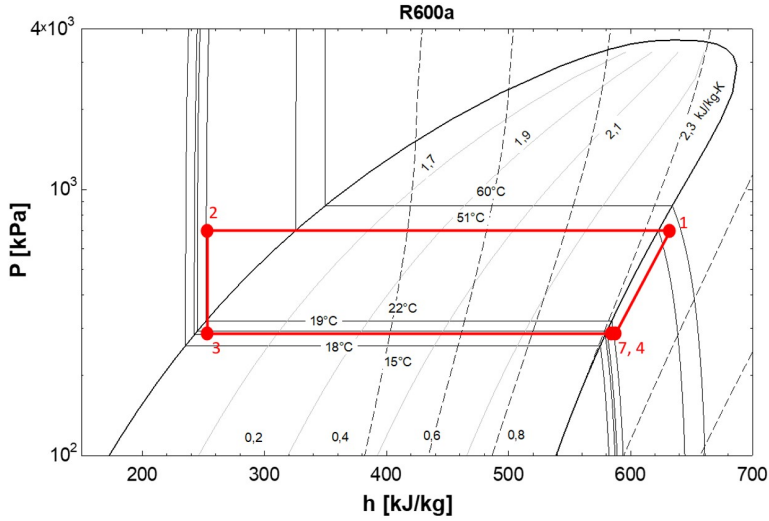


Figure 4: Refrigeration cycle of the tested system in the $p-h$ coordinate system.

The analysis was conducted for the parameters used in further elaboration of the results. The ranges of the uncertainties obtained from calculations are presented in Table 3.

Table 2: List of elements used on the experimental rig with measuring accuracy.

| Element Name | Type | Operating rate | Measurement uncertainty |
|---|---|---|---|
| T – Thermocouple | OMEGA type T | 73.15–623.15 K | ±0.2 K |
| P – Pressure Transducer | Danfoss AKS 33 | –100–3400 kPa | ±0.8% of the measured value |
| Power Meter | Lovato Electric, DMG 200 | 1.5–1380 W | ±1% of the measured value |
| Inverter | Sanyu SXE0015T2B | 10–400 Hz | – |
| Mass Flow Meter | Endres+Hauser promass 83A | 0–0.125 $\mathrm{kg\,s^{-1}}$ | ±1% of the measured value |
| Water Flow Meter | Kobold DUK 11G4HL443L | 0.08–20 $\mathrm{l\,min^{-1}}$ | ±0.7% of the measured value |
| Electronic Expansion Valve | Carel E2V09 | – | – |
| Plate Condenser | SWEP B5THx10 | 0–2000 W | – |
| Multimeter | FLUKE 8808A | 0–300 V | ±0.015% of the measured value |
| Calori Tank | – | 0–1000 W | ±1% of the measured value |
| Filter/drier | Danfoss Eliminator 023Z450191 | – | – |
| Sight glass | Carel | – | – |

Table 3: Uncertainties of the parameters.

| Parameter | Uncertainty |
|---|---|
| Cooling capacity, $\dot{Q}_{\mathrm{evap}}$ | 1.0–2.1% |
| Overall efficiency, $\eta$ | 1.2–3.9% |
| Pressure ratio, PR | 1.7–1.8% |
| Energy efficiency ratio, EER | 0.7–2.0% |

# 3 Results and discussion

Several parameters were chosen for the reduction of the experimental data and their respective characteristics were presented. The parameters originate from the refrigeration system energy balance and can be used for comparison of refrigeration compressors. The values shown in the follow-

ing characteristics (Figs. 5–12) were calculated according to the following formulas:

1. Cooling capacity (validation of calorimeter measurement) – the amount of heat that the evaporator can extract from the refrigerated space:

$$\dot{Q}_{\text{evap}} = \dot{m}_{\text{ref}}(h_7 - h_3). \tag{2}$$

2. Overall efficiency of a compressor – power corresponding to the shaft work of the refrigeration cycle to the electric power consumed by the refrigeration system:

$$\eta = \frac{\dot{m}_{\text{ref}}(h_1 - h_4)}{W_{\text{in}}}\,. \tag{3}$$

3. Pressure Ratio – discharge to suction pressure:

$$\text{PR} = \frac{p_1}{p_4}\,. \tag{4}$$

4. Energy efficiency ratio – the amount of heat absorbed by the evaporator to the electric power consumed by the refrigeration system:

$$\text{EER} = \frac{\dot{Q}_{\text{evap}}}{W_{\text{in}}}\,. \tag{5}$$

### 3.1 Linear compressor performance characteristics

The first characteristic (Fig. 5) shows the change in mass flow rate of the linear compressor (LG FLA150NBMA) as a function of the supply frequency. The mass flow rate for the linear compressor is in the range of 0.14–1.56 $\text{gs}^{-1}$. The trend of the characteristics for each tested voltage increases with the frequency of the supply current. An analogous increase is seen in relation to the rising voltage. This is expected as the voltage is proportional to the length of the piston stroke in a linear compressor.

Compressor regulation carried out by means of a linear motor ensures high precision of mass flow rate setting depending on the needs. This gives a definite advantage over a piston compressor, where the crank system is a limitation.

The characteristic shown in Fig. 6 relates to the cooling capacity of the linear compressor depending on the frequency and the supply voltage. Analyzing the cooling capacity of the tested linear compressor (Fig. 6), one

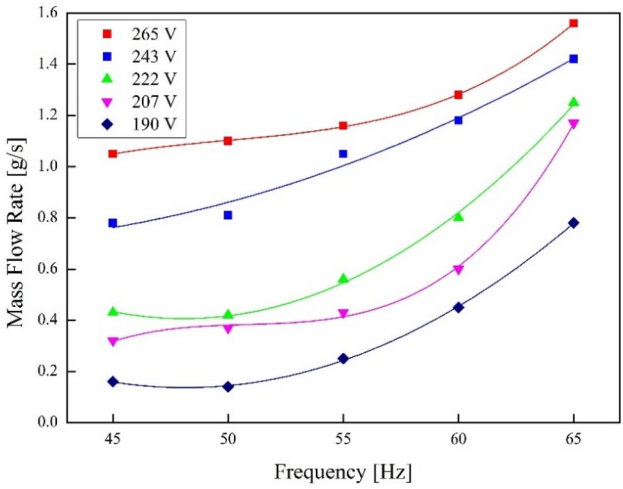


Figure 5: The mass flow rate of a linear compressor against the frequency of the supply current.

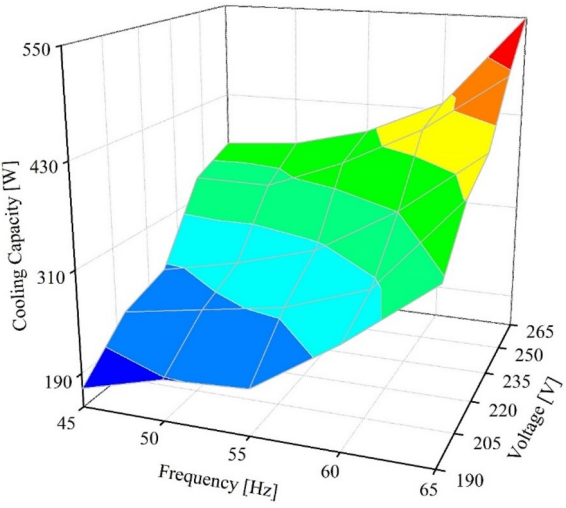


Figure 6: The cooling capacity of a linear compressor against the frequency and voltage of the supply current.

can observe the achieved values of cooling capacity, which is in the range of 172–551 W. The maximum values are achieved for the highest voltages and power supply frequencies. The cooling capacity in the entire range is growing moderately, with a sharp increase which occurs after exceeding the

operating conditions declared by the manufacturer (220–240 V, 50–60 Hz). It is an indication that the operating conditions are close to the inherent frequency of the piston spring system in the linear compressor. This allows modulation of compressor power supply conditions for sudden demands on the refrigeration system during e.g. extra load increases.

The overall efficiency of the linear compressor depending on the change of frequency and the supply voltage is shown in Fig. 7. The trend of changes and the compressor operating points for which it achieves the greatest efficiency are visible.

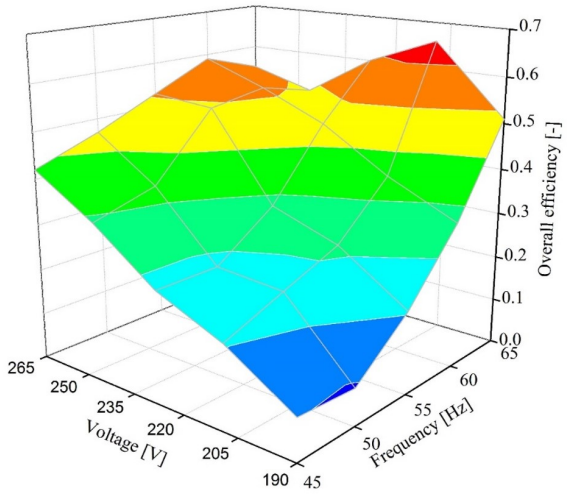


Figure 7: The overall efficiency of a linear compressor against the supply frequency and voltage.

The achieved overall efficiency is in the range of 0.08–0.66. Similar efficiency values were noted by Zhang *et al.* [14]. Local minima in the data at the highest values of the input parameters are probably due to the overlapping of several phenomena occurring in the linear compressor, where the achievement of the maximum operating parameters of the compressor is dominant (large clearance losses – a phenomenon resulting from leakage between the cylinder and the piston, which increases with the pressure ratio, piston drift – a phenomenon occurring during a significant pressure difference between the compressor body and the compression chamber. As a result of the pressure difference, an axial force is created, which is counteracted only by the springs. During large pressure differences, this force affects the position of the piston, which can then hit the head of the cylinder, and cause non-linear

work of the spring – a phenomenon related to piston drift, which results in a change of the piston position). At the highest voltages and frequencies, the compressor may have reached its top dead centre as well (loud compressor operation with high vibration). For lower supply voltage and current values, there is a sharp drop in compressors efficiency.

The last characteristic (Fig. 8) relating to the linear compressor shows the obtained values of the energy efficiency coefficient of the refrigeration system. The energy efficiency ratio of the refrigeration system (Fig. 8) is in the range of 2.2–6.6. In terms of energy efficiency (EER value above 4), the most favorable operating range of the compressor is within the range of power supply parameters of 220–265 V and 50–65 Hz. For the highest values of independent parameters, there is a decrease due to the possible reaching of the top dead center of the compressor. Despite the limitations, the linear compressor is definitely more energy efficient than the commonly used reciprocating compressor, which is described later in the discussion.

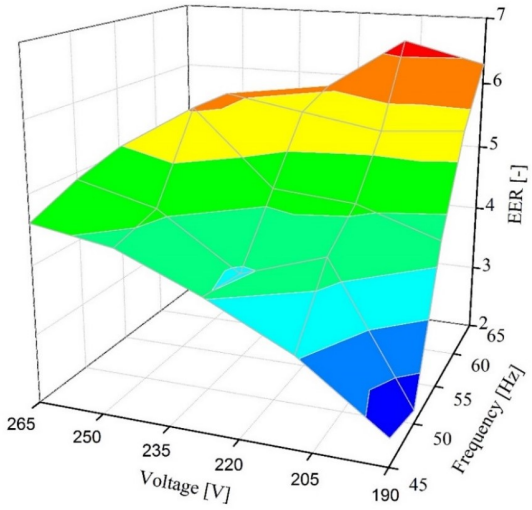


Figure 8: EER of the refrigeration system against the supply frequency and voltage of the linear compressor.

## 3.2 Comparison with the reciprocating compressor

The first comparative characteristic (Fig. 9) shows the mass flow rate of a given compressor as a function of the pressure ratio. Comparison of compressors was carried out for the pressure ratios in the range of 1.4–2.5. As

one can see, the mass flow rates achieved by the reciprocating compressor are much higher than by the linear one. For a linear compressor, it is in the range of 0.15–1.32 $gs^{-1}$, while for a reciprocating compressor, it is in the range of 1.53–2.62 $gs^{-1}$. These differences result from the construction of the linear compressor, which, due to the lack of a crank system, and thus a free piston, achieves a smaller stroke than a reciprocating compressor. For maximum power supply parameters (265 V, 60 Hz), the linear compressor achieves a mass flow value similar to that achieved by a reciprocating compressor for minimum power conditions (230 V, 18 Hz).

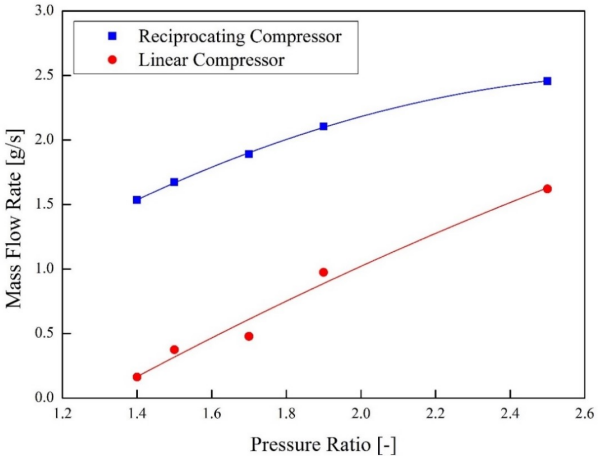


Figure 9: The mass flow rate of a linear compressor and reciprocating compressor against the pressure ratio.

Figure 10 shows the electrical power consumption of a given compressor as a function of the pressure ratio. The electric power consumption (which has a large impact on the energy efficiency ratio) of the linear compressor achieves much lower values of 23–96 W, while the reciprocating compressor for the same pressure ratio reaches values of 95–226 W. This shows, on average, two times lower power consumption to achieve the same pressure ratio. This is mainly due to the lack of flexibility when modulating the reciprocating compressor with a crank system. In addition, the reciprocating compressor has four points of friction compared to the linear compressor and a less energy-efficient motor. This makes the electricity consumption much higher for it.

The third comparative characteristic (Fig. 11) shows the overall efficiency of a given compressor as a function of the pressure ratio. The overall

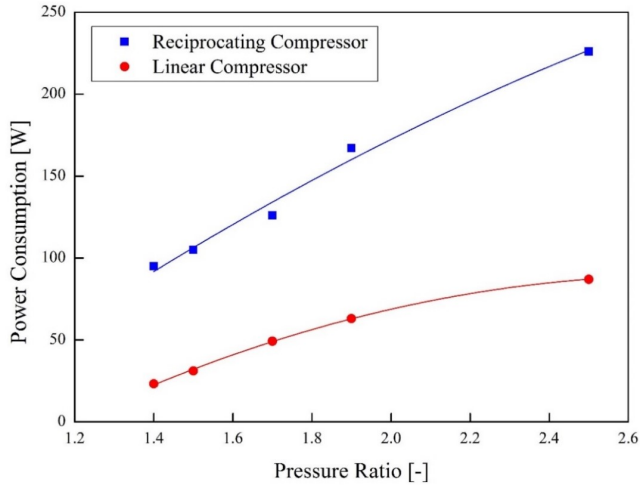


Figure 10: Electric power consumption of the compressor against the pressure ratio.

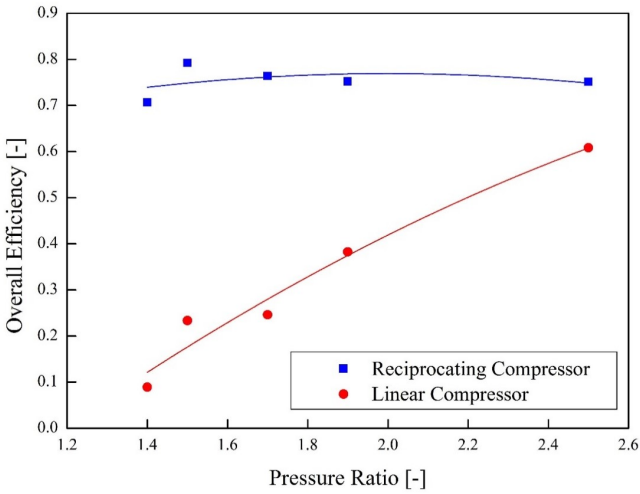


Figure 11: Compressor efficiency against the pressure ratio.

efficiency characteristics show a slight growth for the reciprocating compressor with increasing discharge-suction pressure difference, in the range of 0.71–0.79. The linear compressor, due to its construction, achieves lower efficiency values in the initial phase, to reach its maximum value for the highest value of the pressure ratio. The linear compressor overall efficiency ranges from 0.09–0.61. The achieved values are mainly a result of the construction

of both compressors, where the reciprocating compressor has a constant piston stroke. The results show the possibility of increasing the efficiency of linear compressors. Future research should focus on leak sealing, piston drift prevention, new flow geometry and valves.

The last characteristic (Fig. 12) shows the obtained energy efficiency of the refrigeration system depending on the tested compressor. Regarding EER, a decreasing trend can be seen for the reciprocating compressor with the increasing pressure ratio, where the values fall in the range of 5.6–3.7. This is due to the increasing power consumption, with a disproportionate lower increase in cooling capacity. The linear compressor is characterized by a different trend, where for the low pressure ratios it reaches low values, then as the pressure ratio increases, the EER values grow sharply. The obtained EER is in the range of 2.2–5.6. This proves a proportionally greater increase in cooling capacity in relation to power consumption. For pressure ratios greater than 1.7, a linear compressor is approximately 35% more energy efficient than a reciprocating compressor.

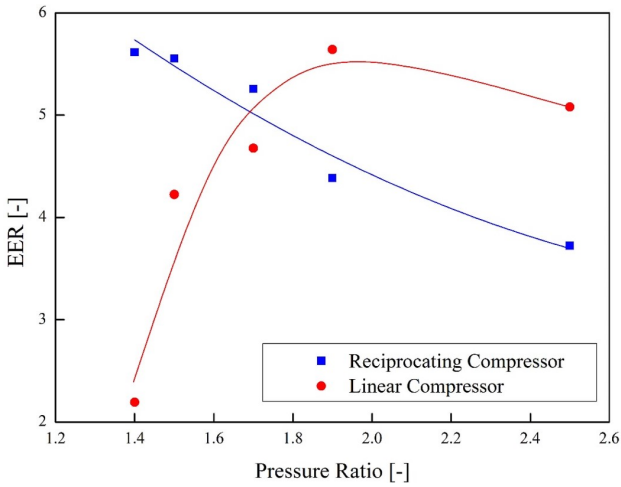


Figure 12: EER of the refrigeration system against the pressure ratio.

## 4 Conclusions

The tests carried out on a linear compressor, going beyond the scope of its typical operation declared by the manufacturer, allowed us to determine the possible, full range of performance characteristics. Subsequent comparative

studies with a reciprocating compressor allowed us to determine its greater energy efficiency and the legitimacy of its use in small refrigeration systems.

- Experimental tests were carried out on a test rig designed in accordance with the ANSI/ASHRAE 23.1-2010 standard.
- A series of characteristics related to a linear compressor have been determined, showing its performance, efficiency and achieved EER values. They have been designated beyond the scope of the operation range declared by the manufacturer.
- Research on a reciprocating compressor was carried out, comparing it with a linear compressor for the same pressure ratio. As a result of the tests, the linear compressor is more energy efficient by an average of 38% compared to the tested piston compressor for a pressure ratio above 1.7. The power consumption of an electric linear compressor is on average two times lower than that of a reciprocating compressor.
- The results can be used for further research on its design and be a guideline for the industry.

## Acknowledgements

This article has been completed while the first and second authors were Doctoral Candidates in the Interdisciplinary Doctoral School at the Lodz University of Technology, Poland.

*Received 16 February 2023*

# References

[1] Hovgaard T.G., Larsen L.F., Skovrup M.J., Jørgensen J.B.: *Power consumption in refrigeration systems – modeling for optimization.* IEEE ADCONIP **4**(2011), 234–239.

[2] Park M., Lee J., Kim H., Ahn Y.: *Experimental and numerical study of heat transfer characteristics using the heat balance in a linear compressor.* Int. J. Refrig. **74**(2017), 548–557. doi: 10.1016/j.ijrefrig.2016.11.010

[3] Liang K.: *Analysis of oil-free linear compressor operated at high pressure ratios for household refrigeration.* Energy **151**(2018), 324–331. doi: 10.1016/j.energy.2018.03.068

[4] Lee H., Ki S., Jung S., Rhee W.: *The innovative green technology for refrigerators – development of innovative linear compressor.* ICEC **19**(2008), 1–6.

[5] *Embraco Wisemotion* (2018). https://www.ctc-n.org/products/embraco-wisemotion (accessed 11 Sept. 2022).

[6] Bezrodny M., Prytula N., Tsvietkova M.: *Efficiency of heat pump systems of air conditioning for removing excessive moisture.* Arch. Thermodyn. **40**(2019), 2, 151–165. doi: 10.24425/ather.2019.129546

[7] Kim J.K., Jeong J.H.: *Performance characteristics of a capacity-modulated linear compressor for home refrigerators.* Int. J. Refrig. **36**(2013), 3, 776–785. doi: 10.1016/j.ijrefrig.2012.12.002

[8] Kim J.K., Kim J.B.: *Modulation characteristics of a linear compressor for evaporating and condensing temperature variations for household refrigerators.* Int. J. Refrig. **40**(2014), 370–379. doi: 10.1016/j.ijrefrig.2013.12.006

[9] Hwang I.S., Lee Y.L.: *CFD analysis of transient flows in a linear compressor using a 1D-CFD coupled model.* Int. J. Refrig. **91**(2018), 20–27. doi: 10.1016/j.ijrefrig.2018.04.015

[10] An I.Y., Lee Y.L.: *Cycle analysis of linear compressors using three-dimensional CFD.* ARPN J. Eng. Appl. Sci. **9**(2014), 6, 874–880.

[11] ANSI/ASHRAE 23.1-2010 (2010). https://ashrae.iwrapper.com/ASHRAE_PREVIEW_ONLY_STANDARDS/STD_23.1_2010 (accessed 30 Sept. 2022).

[12] Kowalczyk M.J., Łęcki M., Romaniak A., Warwas B., Gutkowski A.: *Investigations of thermal-flow characteristics of minichannel evaporator of air heat pump.* Arch. Thermodyn. **42**(2021), 4, 261–279. doi: 10.24425/ather.2021.139662

[13] Moffat R.J.: *Describing the uncertainties in experimental results.* Exp. Therm. Fluid Sci. **1**(1988), 1, 3–17. doi: 10.1016/0894-1777(88)90043-X

[14] Zhang X., Ziviani D., Braun J., Groll E., Zhang O.: *Experimental validation and analysis of a dynamic model for linear compressors.* ICEC **24**(2018), 1–11.

**archives**
**of thermodynamics**
Vol. **44**(2023), No. 4, 261–284
DOI: 10.24425/ather.2023.149725

# A model of the steam compression process in a piston reactor

**DAMIAN JOACHIMIAK**[a*]
**TOMASZ BOROWCZYK**[b]
**MAGDA JOACHIMIAK**[a]

[a] Poznan University of Technology, Institute of Thermal Engineering, Piotrowo 3a, 60-965, Poznań, Poland

[b] Grupa inżynieryjna Konstrubowski Sp. z o.o., Święty Wojciech 7/13, 61-749 Poznań, Poland

**Abstract** The paper discusses the possible determination of steam parameters in a new type of piston machine for steam compression to generate supercritical water parameters. It presents a calculation model that allows one to simulate the process of steam compression in a cylinder with volume regulated by the piston position. In each calculation step, the steam parameters were determined on the basis of fast adiabatic changes which were corrected by the effect of leakage and heat transfer occurrence. The seal of the reactor was assumed to be a compression ring. Depending on the pressure drop on the seal, subcritical and supercritical flow was taken into account. The leak was corrected by the coefficient of flow contraction. Heat transfer was determined by equations for the Nusselt number for water and steam from the homogenous area. The programmed model allows one to simulate changes in the thermodynamic parameters of steam during the process of steam compression with any calculation step. The results presented in this paper show that the application of one compression ring allows us to obtain supercritical steam parameters. Various degrees of sealing leak tightness and their impact on the changeability of steam parameters were analyzed. Heat transfer was shown to have an impact not only on changes in steam temperature, but also on pressure. This paper analyzes the impact of the temperature of the walls of the compression chamber on the value and direction of heat transfer.

*Corresponding Author. Email: damian.joachimiak@put.poznan.pl

**Keywords:** Steam; Critical water parameters; Piston-cylinder system; Compression rings; Thermodynamic parameters; Piston reactor; Heat transfer

## Nomenclature

| | | |
|---|---|---|
| $A$ | – | area, $m^2$ |
| $a$ | – | speed of sound, m/s |
| $c_{\text{pis}}$ | – | speed of piston, m/s |
| $c_p$ | – | specific heat capacity at constant pressure, J/(kgK) |
| $c_v$ | – | specific heat capacity at constant volume, J/(kgK) |
| $D$ | – | cylinder diameter, m |
| $F$ | – | force, N |
| $H$ | – | height, m |
| HT | – | parameter including heat transfer |
| $h$ | – | specific enthalpy, J/kg |
| $i$ | – | iteration, calculation step |
| $m$ | – | mass, kg |
| $\dot{m}$ | – | mass flux, kg/s |
| $p$ | – | pressure, Pa |
| $R$ | – | individual gas constant, J/(kgK) |
| Re | – | Reynolds number |
| $s$ | – | entropy, J/(kgK) |
| $T$ | – | temperature, K |
| $t$ | – | time, s |
| $V$ | – | volume, $m^3$ |
| $v$ | – | specific volume, $m^3/kg$ |
| $x$ | – | steam dryness |
| $z$ | – | piston displacement, m |

### Symbols for calculation variants

| | | |
|---|---|---|
| HT0 | – | exclusion of heat transfer from steam to wall |
| HT1 | – | inclusion of heat transfer from steam to wall |
| L0 | – | exclusion of leakage |
| L$i$ | – | inclusion of leakage by $i$-times of the reference flow area in the piston ring gap $A_{\text{RG}}$ |

### Greek symbols

| | | |
|---|---|---|
| $\alpha$ | – | heat transfer coefficient, $W/(m^2K)$ |
| $\Delta$ | – | elementary growth |
| $\delta$ | – | relative value |
| $\kappa$ | – | isentropic exponent |
| $\lambda$ | – | heat conductivity coefficient, W/(mK) |
| $\mu$ | – | dynamic viscosity, kg/(ms) |
| $\nu$ | – | kinematic viscosity, $m^2/s$ |
| $\rho$ | – | density, $kg/m^3$ |

**Subscripts**

| | | |
|---|---|---|
| cyl | – | cylinder parameter |
| g-w | – | parameter expressing heat transfer between steam and cylinder walls |
| l | – | leakage |
| pis | – | piston |
| RG | – | ring gap |
| sum | – | sum |
| w | – | wall |

# 1 Introduction

Water, in its subcritical and supercritical state, can be used in chemical synthesis reactions, nanoparticles production, hydrothermal liquefaction and gasification [1, 2]. High pressure (more than 22 MPa) and temperature (more than 375°C) of steam constitute technological and economic barriers to its common use [3]. An advantage of a piston reactor is that it can be used to obtain high steam parameters with relatively simple constructional solutions and small investment expenditures [4]. Moreover, it can minimize the time of the chemical reaction, thus providing higher process performance. The impact of a flow nature, described by the Reynolds number, in a continuous supercritical water gasification reactor was investigated in the paper [5]. An increase in the Re number from the laminar flow to the turbulent flow allows a reduction of the gasification time of ethanol and butanol. In the paper [6] a piston engine is treated as a chemical reactor. The impact of the preliminary move of substrates on the process of combustion in a diesel engine was examined. In paper [7] a concept of using the piston-cylinder assembly of a single-stroke rapid compression machine and the piston engine as a chemical reactor was presented.

Depending on the type of machine, operating medium and working conditions, different types of seal are used in piston-cylinder assemblies. In piston compressors with relatively low values of the compression ratio obtained in a single degree non-contact labyrinth groove seals are used [8]. Application of relatively large radial clearance in a non-contact piston-cylinder seal may cause gas expansion not to occur in the constrictions. And this will result in excessive leakage [9]. To minimize leakage in non-contact labyrinth seals in the piston-cylinder assembly, the radial clearances of less than 0.1 mm are used. A seal of this type requires a system to guide

the piston in the cylinder liner. In the paper [10], research on leakage and pressure distribution of the labyrinth seal geometry in a piston compressor with a low pressure drop of 3.2 bar. The results of numerical research on air flow in the piston-cylinder seal are included in the paper [11]. The impact of the seal geometry, that is, of tooth thickness, chamber size, and of the clearance in a labyrinth seal, on the leakage rate is analyzed there. The application of the labyrinth seal to a conceptual engine with a free piston is described in [12]. The results presented there indicate a lower engine efficiency caused by greater leakage compared to the conventional seal with lubricated piston rings. The use of non-contact seals allows oil to be eliminated from the surface of the cylinder liner. Another type of seal, which can be used in piston-cylinder systems, are slot seals. This type of seal can be applied in the case of a very small radial clearance. In slot seals, leakage is reduced by tangential tensions between the fluid and the seal walls [13]. The method to determine the leakage in the radial slot seal is presented in the paper [14]. This method is based on experimentally determined flow coefficients that are a function of the height of clearance. The paper [15] includes the description of the method for calculating the leakage in this type of seal, taking into account the geometry of the channel of the inlet section. The paper [16] includes the description of a generalized model based on the Stodola equation. This model enables determining the leakage for liquids and gases and for compressible and incompressible flows in the groove seal channels. The calculation model that allows for the determination of gas leakage and the distribution of thermodynamic parameters in a slot seal is presented in [17]. In this model, an irreversible adiabatic transition is assumed with dissipation of kinetic energy to frictional heat. The friction coefficient was determined using the corrected Blasius equation. Labyrinth seals in the piston-cylinder assembly are widely used. The paper [18] presents an optimally designed labyrinth seal on the 10 K G-M refrigerator displacer. Various clearance values were experimentally analyzed. Analysis of the impact of cavity width and depth, tooth thickness, and seal clearance on leakage in a piston compressor seal is discussed in [11]. The problem of optimizing labyrinth seals, which can be used in piston-cylinder seals, was described in the paper [19]. It comprises the analysis of the impact of a chamber geometry on the value of liquid leakage. Furthermore, a semi-theoretical model with two new parameters, which are the virtual cavity velocity and the vortex loss coefficient, was presented in it. The paper [20] comprises the analysis of gas flow in the labyrinth seal with an increasingly smaller pitch until the geometry of a slot seal is obtained. The

impact of pitch on leakage and pressure distribution in the seal was investigated there. A numerical analysis of leakage and discharge coefficients in staggered labyrinth seals was presented in [21]. The effect of changing the seal geometry on a decrease in the discharge coefficient was studied. The paper [22] includes a new approach to the design of labyrinth seals that consists of matching the geometry of the seal with the flow conditions. A novelty is adjusting the number and arrangement of teeth and chambers geometry to distribution of the gas kinetic energy in the clearances to obtain as great a degree of energy dissipation in the chambers as possible. The paper [23] presents a numerical study of supercritical carbon dioxide flow in a labyrinth seal consisting of a varying number of teeth. The impact of the number of teeth on the leakage rate was analyzed.

Contact seals with compression rings are commonly used in piston-cylinder assemblies. In the literature, there are some descriptions of computational models for such seals. In the paper [24] a one-dimensional calculation model of the sealing system of a Stirling engine with a free piston is presented. The working medium was helium. A seal consisting of a sealing ring was analyzed. The flow through the sealing ring was assumed to be an incompressible flow. The calculations were discretized every 10 degrees of the crankshaft rotation angle. In the paper [25] a two-dimensional CFD model of the transport of a mass through the crevices of the piston liner in a diesel engine was presented. The leak through the annular gaps is determined analytically and included in the CFD model. In the paper [26] a gas leakage model was discussed, as well as the model of displacing and lubricating rings in a piston-ring-cylinder assembly. In these models, steam was not used as a working medium.

This paper presents a calculation model for the steam compression process in a piston reactor. The main aim of developing this model is to analyze the obtainable thermodynamic parameters, such as steam pressure and temperature, for various variants of the calculations. Results from the calculations will enable verification of obtained peri-critical parameters of steam, and thus they will show if it is possible to create conditions enabling the reaction of hydrothermal gasification to occur. The leakage of the operating medium in the piston-cylinder seal has a direct impact on the obtainable steam parameters. As the subject of this study is the concept of a new-type machine, various types of sealing will be considered during the machine construction. At the stage of a machine design, application of non-contact labyrinth seals should be considered, because they do not need an oil film on the surface of the cylinder liner.

In this paper, the process of steam compression in the piston-liner assembly has been analyzed. The seal system has been assumed to consist of one piston ring (1, Fig. 1a). In such a system, there is an oil control ring below the compression ring (3, Fig. 1a). The first compression ring is primarily responsible for limiting leakage (Fig. 1b).

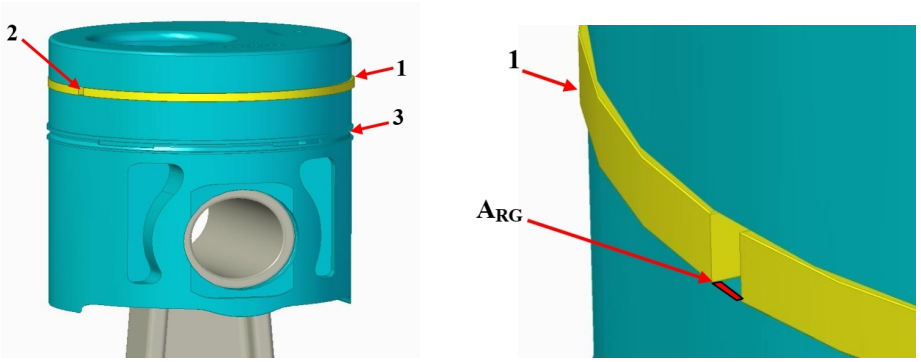


(a) (b)

Figure 1: Piston seal system: (a) general view, (b) $A_{RG}$ – flow reference area in the compression ring gap. 1 – compression ring, 2 – ring gap, 3 – oil control ring.

This type of seal allows a high compression ratio to be obtained; however, it requires the presence of an oil film on the surface of the cylinder liner. The tightness of the seal made up of compression rings is affected by the shape of the sliding layer, the number of rings, and the geometry of the ring gap [27].

Temperature and pressure changes of the operating medium are generally significant in piston-cylinder seals. Changes in these parameters can cause changes in viscosity, and thus changes in flow nature in the seal. The impact of the change of the viscosity parameter after the change in gas temperature in the spiral groove seal was described in the paper [28].

It is mandatory to develop a model of the steam compression process in order to design a piston reactor. In the literature, there is no calculation model that would include leakage and heat transfer for steam in the piston-cylinder assembly. This model will include steam parameters on the basis of the IAPWS-IF97 steam tables [29]. Piston position, pressure, temperature, and leakage values of the operating medium experience rapid changes over time during steam compression in a piston reactor. These parameters affect the intensity of the heat transfer from the operating medium (steam) to

the walls of the reactor compression chamber (these surfaces include the cylinder liner, head, and piston tops). The developed compression model considers the impact of heat transfer, leak tightness, and piston velocity on the thermodynamic parameters of steam in the cylinder of a piston reactor.

## 2 The main calculation model

The concept of a piston reactor shown in Fig. 2 consists of a cylinder liner (1), a piston (2), a compression chamber (3), and a valve system (4). Steam compression occurs during the movement of the piston inside the cylinder liner. The calculation model allows the compressed steam parameters to be determined with 1 mm step of the piston movement (Fig. 3). The model has been programmed in such a way as to perform theoretical calculations of the compression process:

- excluding leakage and heat transfer,
- including leakage,
- including heat transfer,
- including leakage and heat transfer.

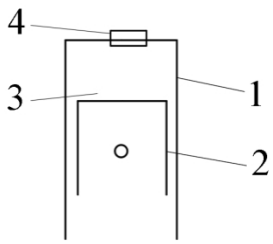


Figure 2: Piston reactor model: 1 – cylinder liner, 2 – piston, 3 – reactor chamber, 4 – valve system.

The authors' own program, ST_IF97, was used in the calculations to determine the steam parameters. The program was written using Fortran with the inclusion of the *ASME International Steam Tables for Industrial Use* [27]. At the beginning of the calculations, the authors assumed the initial pressure of 200 kPa of the dry steam supply to the cylinder (1, Fig. 2) through the valve.

Based on the initial pressure $p(1)$ and with the use of the ST_IF97 program, the parameters (temperature, density, enthalpy, speed of sound, specific heat at constant pressure, specific heat at constant volume, entropy, dynamic viscosity, kinematic viscosity, heat transfer coefficient) were determined for saturated dry steam ($x = 1$) at the initial position of the piston

$$p(1) \xrightarrow{\text{ST_IF97}} T(1), \varrho(1), h(1), a(1), c_p(1), c_v(1), s(1), \mu(1), \upsilon(1), \lambda(1). \quad (1)$$

The gas mass inside the cylinder was calculated according to the formula:

$$m_{\text{cyl}}(i) = V_{\text{cyl}}(i)\varrho(i). \quad (2)$$

The isentropic exponent is changeable for steam. It was expressed by the dependency:

$$\kappa(i) = \frac{a(i)^2}{p(i)\nu(i)}. \quad (3)$$

With the calculation model, it is possible to determine the theoretical distribution of steam parameters during compression in a piston reactor at every $i$th calculation step.

The gas pressure for the subsequent $i$th calculation step (piston positions according to Fig. 3) was determined assuming a rapidly occurring isentropic transformation

$$p(i) = p(i-1)\left(\frac{V_{\text{cyl}}(i-1)}{V_{\text{cyl}}(i)}\right)^{\kappa(i-1)}. \quad (4)$$

The gas temperature for the subsequent $i$th calculation step (piston positions) is also determined on the basis of an isentropic transformation

$$T(i) = T(i-1)\left(\frac{p(i)}{p(i-1)}\right)^{\frac{\kappa(i-1)-1}{\kappa(i-1)}}. \quad (5)$$

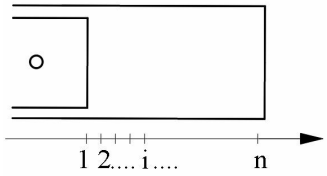


Figure 3: Calculation step.

The remaining part of the paper first describes the main part of the model with the assumed ideally sealed cylinder and without heat transfer between the steam and the cylinder walls. By controlling the model operation, it is possible to include heat transfer between the steam and the compression chamber walls, as well as steam leakage in the piston-cylinder seal. The calculation model to determine leakage values (leakage calculation model, LCM) is described in detail in Section 2.1. Data about the type and geometry of the seal were entered into the program. The flow area through the ring is crucial in the analyzed seal consisting of a compression ring. The area has been defined in the following part of the paper as the flow reference area around the ring gap and marked as $A_{\mathrm{RG}}$ (Fig. 1). The steam mass leaking through the seal over time of the $i$th calculation step $m_{\mathrm{l}}(i)$ is calculated at each calculation step, based on the current pressure, temperature, steam density and isentropic exponent, as conceptually shown below:

$$\text{sealing type},\ A_{\mathrm{RG}},\ D_{\mathrm{cyl}},\ H_{\mathrm{pis}}p(i),\ T(i)\varrho(i),\ \kappa(i) \xrightarrow{\mathrm{LCM}} \dot{m}_{\mathrm{l}}(i). \tag{6}$$

The amount of gas that has leaked out of the cylinder through the seal over time $\Delta t$, was expressed as the following dependency

$$m_{\mathrm{l}}(i) = \dot{m}_{\mathrm{l}}(i)\Delta t(i). \tag{7}$$

If the velocity of the piston changes, then the value of $\Delta t$ and $m_{\mathrm{l}}$ for each $i$th calculation step is different. The amount of gas in the cylinder for the $i$th calculation step corrected by the leakage value was expressed as the following dependency:

$$m_{\mathrm{cyl,l}}(i) = m_{\mathrm{cyl}}(i) - m_{\mathrm{l}}(i). \tag{8}$$

Correction of the gas pressure inside the cylinder, resulting from the leakage, was determined with the assumed fast adiabatic change

$$p(i) = p(i)\left[\frac{m_{\mathrm{cyl,l}}(i)}{m_{\mathrm{cyl}}(i)}\right]^{\kappa(i)}, \tag{9}$$

whereas the correction of the gas temperature inside the cylinder resulting from the change of mass inside the cylinder was expressed with the following formula:

$$T(i) = T(i)\left[\frac{m_{\mathrm{cyl,l}}(i)}{m_{\mathrm{cyl}}(i)}\right]^{\kappa(i)-1}. \tag{10}$$

The next iteration assumed the steam mass value in the cylinder corrected by the leakage value

$$m_{\mathrm{cyl}}(i) = m_{\mathrm{cyl},l}(i). \tag{11}$$

The subsequent stage of the calculations can include the impact of the heat transfer between compressed steam and the cylinder walls on the steam parameters at each calculation step. For this purpose, parameters such as density, dynamic and kinematic viscosity, heat transfer coefficient, and the Prandtl number for steam $(\varrho(i), \mu(i), \upsilon(i), \lambda(i), \mathrm{Pr}(i))$ were obtained from the ST_IF97 program. The Reynolds number at the $i$th calculation step was determined on the basis of the momentary piston velocity:

$$\mathrm{Re}(i) = \frac{c_{\mathrm{pis}}(i) D_{\mathrm{cyl}}}{\nu(i)}\,. \tag{12}$$

Heat is transferred between the compressed steam and the cylinder walls (including the top of the piston). A subprogram, described in Section 2.2 of the paper (heat transfer calculation model, HTCM), was used to determine the amount of heat transferred. The heat transfer coefficient for the steam and the cylinder walls was determined based on the geometry, momentary piston velocity, and steam parameters listed on the left side of formula (13):

$$D_{\mathrm{cyl}},\ h_{\mathrm{cyl}}(i),\ c_p(i),\ \mu(i),\ \lambda(i),\ \mathrm{Re}(i),\ \mathrm{Pr}(i) \xrightarrow{\mathrm{HTCM}} \alpha(i). \tag{13}$$

The height of the cylinder over the piston top $H_{\mathrm{cyl}}(i)$ was different for each calculation step. The surface area of the heat transfer was the side surface of the cylinder and the surface of the top and head of the piston, defined by the dependency

$$A_{\mathrm{g-w}}(i) = 0.5\pi D_{\mathrm{cyl}}^2 + \pi D_{\mathrm{cyl}} H_{\mathrm{cyl}}(i). \tag{14}$$

The heat contained in the gas was expressed using the formula

$$Q_{\mathrm{cyl}}(i) = m_{\mathrm{cyl}}(i) h(i). \tag{15}$$

The amount of heat transferred between the steam and the cylinder walls at temperature $T_{\mathrm{w}}(i)$ was calculated on the basis of the dependency:

$$Q_{\mathrm{g-w}}(i) = \alpha(i) A_{\mathrm{g-w}}(i)\,[T(i) - T_{\mathrm{w}}(i)]\,\Delta t(i). \tag{16}$$

The decrease in gas temperature inside the cylinder was determined based on the known amount of heat transferred between the gas and the walls of

the compression chamber at the $i$th step $\Delta t(i)$

$$\Delta T(i) = \frac{Q_{\mathrm{g-w}}(i)}{m_{\mathrm{cyl}}(i) c_p(i)} \,. \tag{17}$$

The gas pressure was corrected as a consequence of the change in temperature

$$p(i) = p(i) \left[ \frac{T(i) - \Delta T(i)}{T(i)} \right]^{\frac{\kappa(i)}{\kappa(i)-1}} \tag{18}$$

and then the steam temperature in the cylinder was corrected:

$$T(i) = T(i) - \Delta T(i). \tag{19}$$

Based on the data obtained, it is possible to determine the force required to move the piston (and the required power)

$$F(i) = A_{\mathrm{pis}} p(i). \tag{20}$$

The steam parameters for the next calculation steps $i = 2, 3, \ldots, n$ were calculated in the ST_IF97 program based on the current pressure and temperature

$$p(i)T(i) \xrightarrow{\text{ST_IF97}} \varrho(i), h(i), a(i), c_p(i), c_v(i), s(i), \mu(i), \upsilon(i), \lambda(i). \tag{21}$$

Subsequently, the calculations were performed according to formulas (2)–(18). The model, along with subprograms, was written in the Fortran language.

## 2.1 Leakage calculation model

The model assumed that the seal of the piston-cylinder system consisted of a compression ring. Furthemore, leakage has been assumed to occur around the ring gap, as shown in Fig. 1.

The pressure ratio downstream and upstream of the ring was expressed as

$$\beta(i) = \frac{p_{\mathrm{out}}}{p_0(i)} \,. \tag{22}$$

The model was based on the Saint-Venant equation [28], which was used to determine the leakage value around the compression ring gap

$$\dot{m}(i) = A_{\mathrm{RG}} \Psi(i) \sqrt{p_0(i) \rho_0(i)} \,, \tag{23}$$

where $A_{\mathrm{RG}}$ was the flow reference area in the compression ring gap (Fig. 1), and $\Psi$ was the flow number. For the subcritical flow $\beta(i) > 0.5457$, number $\Psi$ was described by the dependency

$$\Psi(i) = \sqrt{2\frac{\kappa(i)}{\kappa(i)-1}\left[\beta(i)^{\frac{2}{\kappa(i)}} - \beta(i)^{\frac{(\kappa(i)+1t)}{\kappa(i)}}\right]} \tag{24}$$

and for the supercritical flow $\beta(i) < 0.5457$

$$\Psi(i) = \sqrt{\kappa(i)\left(\frac{2}{\kappa(i)+1}\right)^{\frac{(\kappa(i)+1)}{(\kappa(i)-1)}}}. \tag{25}$$

The value of leakage through the ring at $i$th time step was determined based on the corrected Saint-Venant equation

$$\dot{m}_l(i) = \mu(i)\dot{m}(i), \tag{26}$$

where the flow contraction coefficient related to the flow through the ring gap was described by the dependency [23]

$$\mu(i) = 0.85 - 0.25\left(\frac{p_{\mathrm{out}}}{p_0(i)}\right)^2. \tag{27}$$

The result value of the mass flux is exported to the main model.

## 2.2 Heat transfer calculation model

Heat transfer between steam and the walls of the cylinder is a significant phenomenon during the stem compression process. The intensity of heat transfer depends on the parameters of steam inside the cylinder and its swirl. The swirl of steam inside the cylinder is described by the Reynolds number (12). The Re number depends on the velocity of the piston, which varies over the time of compression stroke. The model assumed the diameter of the cylinder $D_{\mathrm{cyl}}$ as the characteristic dimension. It included equations that define the Nusselt number for steam in a homogenous area.

For the laminar motion of the steam in the cylinder $\mathrm{Re} < 2000$, the following equation was used [30]:

$$\mathrm{Nu}(i) = 1.615\left(\mathrm{Re}(i)\mathrm{Pr}(i)\frac{D_{\mathrm{cyl}}}{H_{\mathrm{cyl}}(i)}\right)^{\frac{1}{3}}. \tag{28}$$

In the case of turbulent motion of the steam in the cylinder, for $\mathrm{Re} \in [10^4, 10^6]$ and $\mathrm{Pr} \in [0.6, 10^3]$, the Gnielinski equation was used in the model [30]:

$$\mathrm{Nu}(i) = \frac{\left(\frac{\xi(i)}{8}\right)\mathrm{Re}(i)\mathrm{Pr}(i)}{1 + 12.7\sqrt{\frac{\xi(i)}{8}}\left(\mathrm{Pr}(i)^{\frac{2}{3}} - 1\right)}\left[1 + \left(\frac{D_{\mathrm{cyl}}}{H_{\mathrm{cyl}}(i)}\right)^{\frac{2}{3}}\right], \tag{29}$$

where

$$\xi(i) = \left[1.8 \log \mathrm{Re}(i) - 1.5\right]^{-2}. \tag{30}$$

The Nu number of the intermittent flow for $\mathrm{Re} \in [2300, 10^4]$ and $\mathrm{Pr} \in [0.6, 10^3]$ was defined in the following way [30]:

$$\mathrm{Nu}(i) = (1 - \gamma)\mathrm{Nu}_{\mathrm{lam},2300}(i) + \gamma \mathrm{Nu}_{\mathrm{turb},10^4}(i), \tag{31}$$

where

$$\gamma(i) = \frac{\mathrm{Re}(i) - 2300}{10^4 - 2300}(i). \tag{32}$$

The $\mathrm{Nu}_{\mathrm{lam},2300}$ value was determined using Eq. (28) for $\mathrm{Re} = 2300$ and the $\gamma \mathrm{Nu}_{\mathrm{turb},10^4}(i)$ value was determined using the Gnielinski equation (29)–(30) for $\mathrm{Re} = 10^4$.

The heat transfer coefficient was determined on the basis of the Nusselt number

$$\alpha(i) = \frac{\mathrm{Nu}(i)\lambda(i)}{D_{\mathrm{cyl}}}. \tag{33}$$

The value of the heat transfer coefficient is returned to the main model.

## 3 Calculation results

In this part of the paper, the distribution of an ideal leak-free compression process (L0) was determined with the assumption that there is no heat transfer between the steam and the walls of the compression chamber (HT0). In the next part of the paper, it is assumed that these processes are the reference processes.

In the subsequent calculation variants, leakage and heat transfer between the steam and the walls of the compression chamber was taken into account. These variants were to approximate the considered compression process with the real one.

The appearance of leakage of various intensity (L1–L4) and the heat transfer HT1 were assumed. In the programmed model, the inclusion of leakage and heat transfer is autonomous.

During the compression process, when the piston moved up, the compression ring aligned itself inside the piston groove in a way that caused the leakage to occur around the ring gap (Fig. 1). Under real operating conditions, the compression ring deforms around the ring gap as a result of wear and the changing distribution of the compressed gas pressure. As a consequence, leakage can occur not only in the ring gap marked in Fig. 1b. Due to the lack of specific knowledge about the real steam flow area through the compression ring, the other part of the paper used a reference flow area around the ring gap equal to $A_{\mathrm{RG}} = 4 \cdot 10^{-8}\ \mathrm{m}^2$ (Fig. 1). The L1 variant included leakage through a one-time flow area in the ring gap $A_{\mathrm{RG}}$. L2, L3, and L4, respectively, mark the inclusion of the leakage through the flow area equal to the multiplicity of $A_{\mathrm{RG}}$ (multiplied by two, three and four, respectively). Table 1 comprises the analyzed calculation variants.

Table 1: Summary of the analyzed calculation variants.

| Denotement | Description | General description |
|---|---|---|
| HT0 | lack of heat transfer | theoretical compression process |
| L0 | lack of leakage | |
| HT1 | including heat transfer | real compression process |
| L1–L4 | including leakage through a multiple of the flow area in the compression ring gap $A_{RG}$ | |

Heat transfer between the steam and the compression chamber walls occurs in the real compression process. This phenomenon was included in the variant of calculations described in the further part of the paper as HT1. The assumed temperature of the compression chamber walls for the first part of the conducted calculations was $T_{\mathrm{w}} = 120°\mathrm{C}$.

The results presented assumed the calculation step of every 1 mm of the piston displacement. The first calculation step focused on determining the parameters of saturated steam. As a consequence of the movement of the piston towards the head, the volume of the cylinder decreased, causing an increase in the steam pressure. The pressure and steam temperature increased for the next positions of the piston.

Figure 4 shows the change of temperature in the pressure function for the variants of the calculations described above. The simulation of the compres-

sion process started with an initial steam pressure of 200 kPa. Depending on pressure, temperature changes had identical distributions for different variants of calculation. The results obtained differ in terms of final pressure. When leakage and heat transfer were excluded, the final pressure exceeded 45 MPa. When only heat transfer (L0_HT1) was included, the final pressure was lower by 4.32 MPa than in case (L0_HT0).

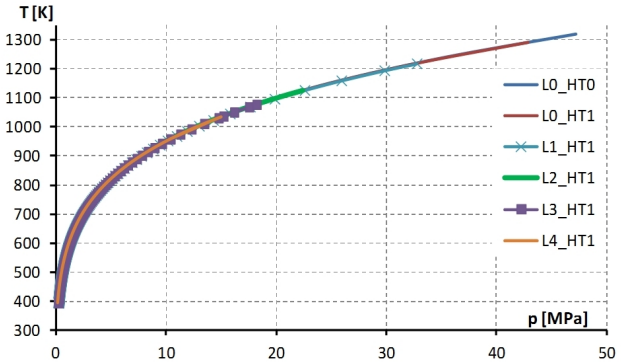


Figure 4: Distribution of the steam temperature in the pressure function for different calculation variants.

Figure 5 shows pressure changes inside the cylinder in the piston position function. Maximum pressure was limited to 30 MPa for better readability of Fig. 5. Differences in the pressure distributions for the considered calculation variants can be seen above 300 mm of the piston stroke. The pressure

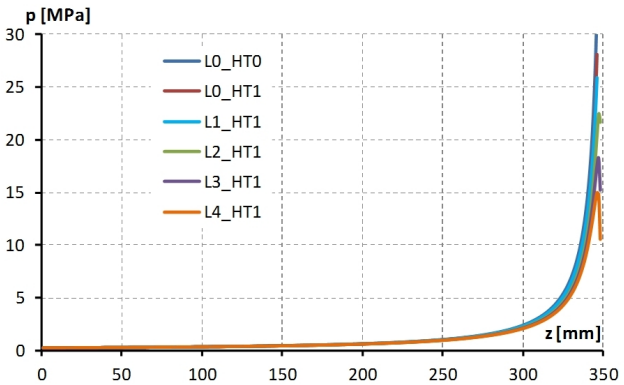


Figure 5: Steam pressure in the piston position function.

of compressed steam began to increase intensively in the last 25 mm of the piston stroke. Then, the steam density increased significantly (Fig. 6). If the steam flux flowing through the seal is too high due to the increase in density, the leakage can cause a sudden decrease in the steam pressure at the end of the compression stroke. A pressure distribution of that type can be observed in the case of variants L2_HT1, L3_HT1, L4_HT1 (Fig. 5).

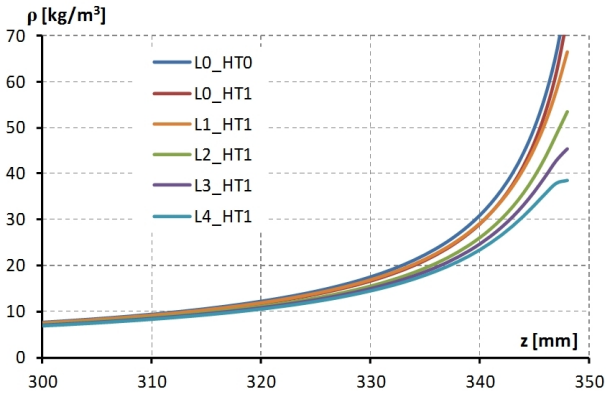


Figure 6: Steam density in the piston position function.

After the inclusion of the heat transfer and leakage (Figs. 4 and 5) the pressure and final temperature values were much lower compared to the ideal compression process (L0_HT0).

Based on Fig. 5 and the comparison of the maximum steam pressure values at the end of the compression stroke, it can be concluded that the heat transfer effect has an impact on the final pressure of the ideal seal of the piston-cylinder assembly (L0-HT0 and L0_HT1). By including the leakage of the value resulting from the flow through the area $A_{RG}$ (L1) to the four times higher value (L4), the authors obtained the respective final pressure values: 32.7, 22.4, 18.2, and 14.9 MPa.

The leakage provides lower pressure and temperature, as well as the resulting lower steam density (Fig. 6). Steam density at the end of the compression stroke increased significantly slower for variants of intense leakage L3_HT1 and L4_HT1.

As a result of the occurrence of leakage and heat transfer to the reactor walls, a lower steam temperature was obtained along with a lower pressure. To clearly define the changes in steam temperature, it was related to the temperature obtained in the ideal compression process (L0_HT0), that is,

adiabatic without leakage, as described by the dependency

$$\delta T = \frac{T}{T_{\mathrm{L0,HT0}}} \,. \tag{34}$$

Figure 7 shows a decrease in the relative steam temperature $\delta T$ in the piston position function. The data included in Fig. 7 shows that the only phenomenon of heat transfer from steam to the walls at temperature $T_{\mathrm{w}} = 120^{\circ}\mathrm{C}$ caused a slight decrease in the relative temperature, equal to 0.0207. Leakage is a crucial factor that causes the decrease in temperature in compressed steam. The inclusion of leakage and the determination of its intensity with the use of the flow reference area decreased the relative temperature by 0.076. On the other hand, by assuming 4 times the reference surface area of the leakage transfer, the temperature decreased significantly by 0.27.

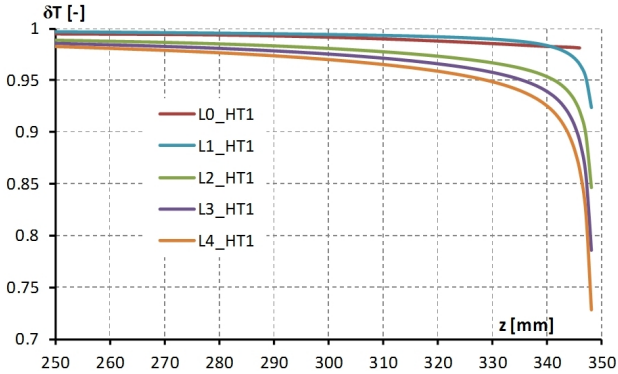


Figure 7: Relative steam temperature decrease in the piston position function.

The relative steam mass within the cylinder related to the ideal conditions (variant L0) was used to precisely define the impact of the leakage on the amount of mass contained in the cylinder (see Fig. 8):

$$\delta m = \frac{m}{m_{\mathrm{L0}}} \,. \tag{35}$$

Figure 8 shows that a significant leak occurred not sooner than in the last 20 mm of the piston stroke. The 0.25 decrease in mass inside the cylinder was obtained for the leakage through the area $A_{\mathrm{RG}}$ (L1). The leakage through double, triple, and quadruplicity of the $A_{\mathrm{RG}}$ flow area (L2–L4) caused the mass to decrease by the respective values of 0.41, 0.56 and 0.67.

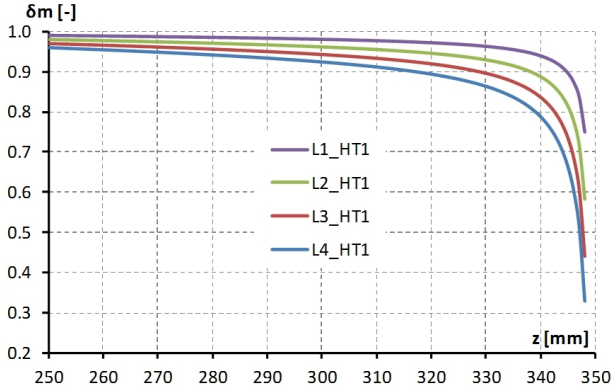


Figure 8: Relative steam mass contained in the cylinder in the piston position function.

The Reynolds number has an impact on the intensity of heat transfer, and is dependent on momentary velocity values of the piston and the steam viscosity, as defined in Eq. (12). The first local maximum of Reynolds number occurred after around 80 mm of the piston stroke and resulted from the momentary, and relatively high, piston velocity. The second maximum occurred around 325 mm of the piston stroke and was caused by the decrease in steam viscosity (Fig. 9).

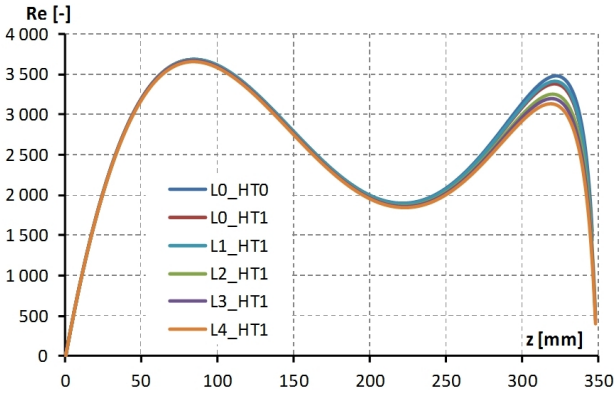


Figure 9: The Reynolds number distribution.

The intensity of gas turbulence within the reactor cylinder defined by the Reynolds number has a direct impact on the heat transfer conditions between the compressed steam and the reactor walls. In addition to the

Reynolds number, the temperature and density of compressed steam affect the heat transfer. The amount of heat transferred to the reactor walls in the first 250 mm of the piston stroke was small due to a low density of steam (Fig. 10). The intensity of the heat transfer reached the local maximum between 330 mm and 340 mm of the piston movement for the analyzed calculation variants under consideration. After 340 mm, a decrease in the intensity of heat transfer could be observed. It was a result of the decrease in the piston velocity and the Reynolds number.

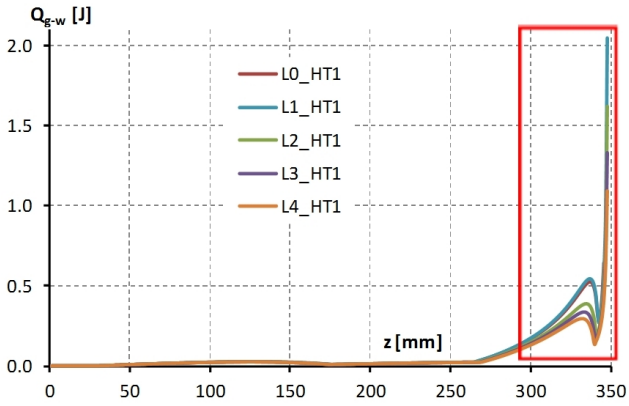


(a)

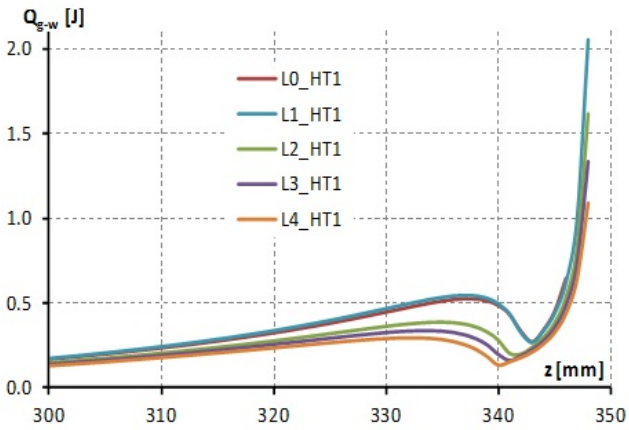


(b)

Figure 10: Heat transferred by steam to the cylinder walls in individual piston positions: (a) for the whole stroke, (b) enlargement of the final part of the stroke.

At the end of the compression stroke, heat transfer resulting from an intense increase in steam density occurred in all calculation variants despite the decreasing piston velocity. Using the following dependency:

$$Q_{\mathrm{g-w,sum}} = \sum_{i=1}^{n} Q_{\mathrm{g-w}}(i), \tag{36}$$

the aggregate amount of heat transferred to the piston reactor walls in a given piston position was calculated (see Fig. 11).

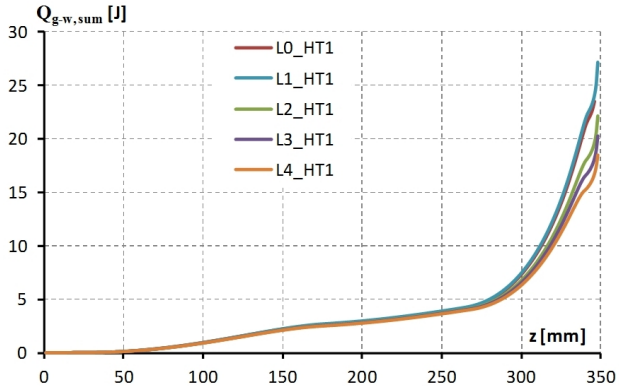


Figure 11: Aggregate amount of the heat transferred from the steam to the cylinder walls of the reactor.

The aggregate amount of heat transferred from the steam to the compression chamber walls (Fig. 11) begins to regularly increase as of 50 mm of the piston stroke. $Q_{\mathrm{g-w,\,sum}}$ values increase more rapidly as of app 280 mm of the piston stroke.

## 3.1 Analysis of the impact of the cylinder wall temperature on the heat transfer intensity

This chapter analyzes the impact of compresson chamber wall temperature on direction and the value of heat transfer between steam and the walls. The calculations include the temperature of the walls ($T_{\mathrm{w}}$) in the range from 100°C to 200°C.

Figure 12 shows the distribution of the aggregate amount of heat transferred from the steam to the walls of the cylinder expressed by the dependency (36). The negative heat value $Q_{\mathrm{g-w,sum}}$ expresses the steam heated

by the cylinder walls. This phenomenon occurs in the calculation variants, in which the initial steam temperature is lower than the assumed temperature of the cylinder walls.

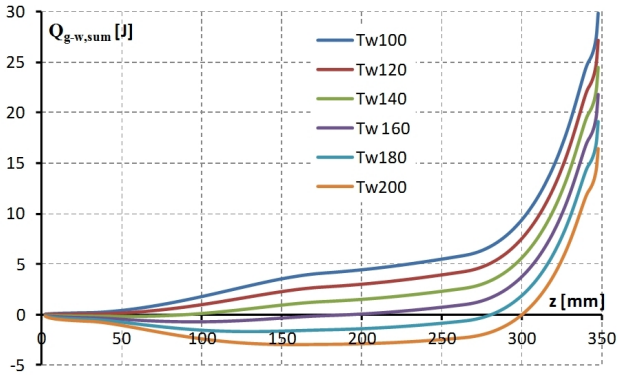


Figure 12: Aggregate amount of heat transferred from the steam to the cylinder walls of the reactor for different pre-set temperatures of the cylinder walls $T_w$.

In the initial stage of the stroke, steam is heated by the cylinder walls in the case where the wall temperature is equal and higher than 140°C (Fig. 12). Heat loss is much lower in the latter stage of the stroke when the steam temperature is higher than the wall temperature. Increasing the temperature of the cylinder walls reduced the amount of heat transferred by compressed steam. In practise, there are temperature limitations, for instance, on the cylinder wall, which result from maintaining the correct oil properties and obtaining the required oil film parameters between the compression ring and the cylinder liner.

## 4 Summary

The calculation results presented in this paper indicate that the concept of a piston reactor allows us to obtain supercritical steam parameters with a seal composed of one compression ring. For the leak tightness cases under consideration (L1–L4), the leak causes a relative drop in compressed steam mass, by a value of 0.25, 0.41, 0.56, and 0.67, consecutively. The seal in variant L1 allows us to obtain steam of pressure of 32.708 MPa and temperature of 944°C, and for variant L2, these parameters are equal to 21.638 MPa and 842°C, respectively. For cases of increased leakage (L2–

L4), at the end of the compression stroke, a pressure drop of 0.79, 3, and 4.44 MPa, respectively, was observed. This drop results from a great increase in leakage caused by a high pressure and density of steam in the last millimeters of piston displacement. The calculations were assumed to include a coefficient of flow contraction in the compression ring for the mixture of air and exhaust. To improve the accuracy of the leakage calculation model, experimental verification is needed.

For a theoretical compression process, the inclusion of heat transfer causes a drop in the final pressure by 4.32 MPa. Depending on the temperature of the walls of the compression chamber, the steam at the beginning of the compression stroke can cool or heat up. For wall temperature $T_w = 100$ and 120°C, steam cools at the beginning of the compression stroke, while $T_w = 140$, 160, 180, and 200°C, steam cools at the piston displacement equal to $z = 90$ mm, 196 mm, 282 mm and 301 mm, respectively. This stage may be crucial because of the behavior of water in a gaseous form in the initial stage of compression. It is possible to pair this model with a two-dimensional model of heat transfer in the wall of the piston reactor. This will enable the accuracy of the calculation results to increase and also allow for a more extensive analysis.

*Received 10 August 2023*

## References

[1] Pińkowska H.: *High-temperature biomass gasification in supercritical water*. Przem. Chem. **86**(2007), 11, 1044–1050 (in Polish).

[2] Pińkowska H.: *Low-temperature biomass gasification in subcritical and supercritical water*. Przem. Chem. **86**(2007), 7, 599–606 (in Polish).

[3] Jitka H.: *Status report on thermal gasification of biomass and waste 2021*. IEA Bioenergy, Task 33, 2022. https://www.ieabioenergy.com/wp-content/uploads/2022/03/Status-Report2021_final.pdf (accessed 13 Apr. 2023).

[4] Ashok A., Katebah M.A., Linke P., Kumar D., Arora D., Fischer K., Jacobs T., Al-Rawashdeh M.: *Review of piston reactors for the production of chemicals*. Rev. Chem. Eng. **39**(2023), 1, 1–30. doi: 10.1515/revce-2020-0116

[5] Hendry D., Miller A., Jacoby W.: *Turbulent operation of a continuous reactor for gasification of alcohols in supercritical water*. Ind. Eng. Chem. Res. **51**(2012), 6, 2578–2585. doi: 10.1021/ie201887e

[6] Borowczyk T.: *Influence of charge movement in inlet manifold on combustion process in compression ignition engines*. PhD thesis, Poznan University of Technology, Poznań 2014 (in Polish).

[7] Atakan B., Kaiser S.A., Herzler J., Porras S., Banke K., Deutschmann O., Kasper T., Fikri M., Schießl R., Schröder D., Rudolph Ch., Kaczmarek D., Gossler H., Drost S., Bykov V., Maas M., Schulz Ch.: *Flexible energy conversion and storage via high-temperature gas-phase reactions: The piston engine as a polygeneration reactor*. Renew. Sustain. Energy Rev. **133**(2020), 110264. doi: 10.1016/j.rser.2020.110264

[8] Vetter H.: *The Sulzer oil-free labyrinth piston compressor*. In: Proc. Int. Compressor Engineering Conf., Purdue 1972, paper 33, 221–228. https://docs.lib.purdue.edu/icec/33 (accessed 14 March 2023).

[9] Joachimiak D., Krzyślak P.: *Comparison of results of experimental research with numerical calculations of a model one-sided seal*. Arch. Thermodyn. **36**(2015), 2, 61–74. doi: 10.1515/aoter-2015-0015

[10] Graunke K.: *Labyrinth leakage flow in a labyrinth-piston compressor*. Sulzer Techn. Rev. **67**(1985), 30–33.

[11] Feng J., Wang L., Yang H., Peng X.: *Numerical investigation on the effects of structural parameters of labyrinth cavity on sealing performance*. Math. Probl. Eng. **2018**(2018), 1–12. doi: 10.1155/2018/5273582

[12] Larjola J., Honkatukia J., Sallinen P., Backman J.: *Fluid dynamic modeling of a free piston engine with labyrinth seals*. J. Ther. Sci. **19**(2010), 2, 141–147. doi: 10.1007/s11630-010-0141-2

[13] Trütnovsky K.: *Noncontacting Seals; Basics and Applications of Slot and Labyrinth Fluid-Flow Seals*. VDI-Verlag bh Dusseldorf, Publishing House of the Association of German Engineers 1964.

[14] Melnik V.A.: *Calculating leaks in rotor-machine radial slot seals. Part 2. A method for integral slot flow rate constants*. Chem. Pet. Eng. **45**(2009), 11–12, 702–706. doi: 10.1007/s10556-010-9265-1

[15] Melnik V.A.: *Calculating leaks in rotary machineradial slot seals. Part 3. Method for calculating leakstaking account of the inlet section*. Chem. Pet. Eng. **46**(2010), 3–4, 146–152. doi: 10.1007/s10556-010-9308-7

[16] Melnik V.A.: *Computed universal dependence for determining leakage of media through groove seals*. Chem. Pet. Eng. **48**(2013), 11–12, 751–759. doi: 10.1007/s10556-013-9691-y

[17] Joachimiak D., Krzyślak P.: *A model of gas flow with friction in a slotted seal*. Arch. Thermodyn. **37**(2016), 3, 95–108. doi: 10.1515/aoter-2016-0022

[18] Hao X.H., Ju Y.L., Lu Y.J.: *Experimental study on the sealing clearance between the labyrinth sealing displacer and cylinder in the 10 K G-M refrigerator*. Cryogenics (Guildf) **51**(2011), 5, 203–208. doi: 10.1016/j.cryogenics.2011.02.002

[19] Asok S.P.: Sankaranarayanasamy K., Sundararajan T., Rajesh K., Sankar Ganeshan G.: *Neural network and CFD-based optimisation of square cavity and curved cavity static labyrinth seals*. Tribol. Int. **40**(2007), 7, 1204–1216. doi: 10.1016/j.triboint.2007.01.003

[20] Joachimiak D., Krzyślak P.: *Analysis of the gas flow in a labyrinth seal of variable pitch*. J. Appl. Fluid Mech. **12**(2019), 3, 921–930. doi: 10.29252/JAFM.12.03.29074

[21] Chun Y.H., Ahn J.: *Effects of geometric parameters of a staggered labyrinth seal on leakage flow*. J. Mech. Sci. Technol. **37**(2023), 6, 2959–2968. doi: 10.1007/s12206-023-0522-6

[22] Joachimiak D.: *Novel Method of the Seal Aerodynamic Design to Reduce Leakage by Matching the Seal Geometry to Flow Conditions*. Energies (Basel) **14**(2021), 23, 7880. doi: 10.3390/en14237880

[23] Yuan H., Pidaparti S., Wolf M., Edlebeck J., Anderson M.: *Numerical modeling of supercritical carbon dioxide flow in see-through labyrinth seals*. Nucl. Eng. Des. **293**(2015), 436–446. doi: 10.1016/j.nucengdes.2015.08.016

[24] Dai Z., Wang C., Zhang D., Tian W., Qiu S., Su G.H.: *Design and analysis of a free-piston stirling engine for space nuclear power reactor*. Nucl. Eng. Tech., **53(**2021), 2, 637–646. doi: 10.1016/j.net.2020.07.011

[25] Lyubarskyy P., Bartel D.: *2D CFD-model of the piston assembly in a diesel engine for the analysis of piston ring dynamics, mass transport and friction*. Tribol. Int. **104**(2016), 352–368. doi: 10.1016/j.triboint.2016.09.017

[26] Wolff A., Koszałka G.: *Influence of engine load on piston ring pack operation of an automotive IC engine*. Combust. Engines **190**(2022), 3, 88–94. doi: 10.19206/CE-141737

[27] Wolff A.: *Modelling of flow phenomena of the system piston-rings-cylinder of an internal combustion engine*. Prace Naukowe Politechniki Warszawskiej. Mechanika **251**. Oficyna Wydawnicza Politechniki Warszawskiej, Warszawa 2013 (in Polish).

[28] Shipeng W., Xuexing D., Junhua D., Jingmo W.: *Steady State Characteristics of Spiral Groove Floating Ring Gas Film Seal Considering Temperature Viscosity Effect*. J. Appl. Fluid Mech. **16(**2023), 4, 891–904. doi: 10.47176/jafm.16.04.1432

[29] Kretzschmar H-J., Wagner W.: *International Steam Tables. Properties of Water and Steam based on the Industrial Formulation IAPWS-IF97*. Springer, Vieweg Berlin, Heidelberg 2019. doi: 10.1007/978-3-662-53219-5

[30] Brunner G.: *Hydrothermal and Supercritical Water Processes*. **5**, Elsevier, 2014.

**archives**
**of thermodynamics**
Vol. **44**(2023), No. 4, 285–316
DOI: 10.24425/ather.2023.149714

# On a Carnot working continuum with non-equilibrium state parameters

**TOMASZ OCHRYMIUK**[a*]
**WALDEMAR DUDDA**[b]
**JANUSZ BADUR**[a]

[a] Institute of Fluid Flow Machinery, Polish Academy of Sciences, Fiszera 14, 80-231 Gdańsk, Poland

[b] University of Warmia and Masury, Faculty of Technical Sciences, Oczapowskiego 11, 10-719 Olsztyn, Poland

**Abstract** We explain that a full description of how the non-equilibrium state of the system evolves in time requires the consideration and solution of its general equation of motion. In the case of the Carnot medium, as a general equation of motion, there must be taken two balances of: non-equilibrium specific volume and non-equilibrium specific entropy. Instead of taking the classical approach where the balance of entropy is postponed to more advanced and theoretical treatments, we focus on the analysis of two, most general, volume and entropy fluxes. These fluxes of motion are universal features of thermodynamics. It has been shown that the Carnot working continuum mathematical model is captured by the two general non-mathematical statements valid for all systems that we call the first law and the second law of thermodynamics.

**Keywords:** Non-equilibrium state parameters; Carnot cycle; Balance of entropy

*Corresponding Author. Email: tomasz.ochrymiuk@imp.gda.pl

# 1 Introduction

In 1823 Sadi Carnot introduced [1] the concep**t** of a four-part thermodynamic cycle, dealing with an ideal gas as a working fluid. The name "working fluid" came from the fact that the Carnot cycle is aimed to convert a "flux of heating energy" into the "flux of working energy". On the level of a whole cycle, by integrating the heating and working fluxes Carnot was able to obtain two basic notions: "cycle heat" and "cycle work" which, helpfully, were known from engineering practice as "heat" and "work".

Sadi Carnot has borrowed the concept of conversion from his father "General Mechanic". Such a situation that the son takes something from his father is normal in our Western civilization. Probably it was in 1818 year in Warsaw, where General Lazar Carnot stayed as a French Revolution emigrant. During the visit of Sadi Carnot, as historians inform us, both – father and son – had an occasion to see the demonstration of a Watt steam engine. Probably then, Lazar Carnot asked: on what principle the steam engines are acting?

It is obvious that Lazar Carnot was a tremendous pattern for young Sadi Carnot. At that time, on the whole European Continent, Lazar Carnot was recognized as: "French Newton". He proposed [2] quite a new concept of mechanics, with the laws of motion that have followed from the Aristotelian principle of least action. Lazar Carnot extending Aristotelian notions of "energea" and "entelehy" was able to introduce the concept of "energy conversion". The main example of energy conversion, developed by Lazar, was the conversion of "potential energy" into "the actual energy" which takes place in mill wheels, with river water as "the working medium". Lazar has introduced the concept of two energy magazines: higher and lower, in the form of water reservoirs. Lazar's working medium possesses two state parameters: "gravitational head" and "flow speed". Unfortunately, the son was a disappointment since in Sadi's concept of working fluid these state parameters are unimportant – the "gravitational head" is constant and "flow speed" is equal to zero. Sadi was impressed to find some analogy.

In the year 1823, Sadi changed the configuration of Lazare's cycle – in his case, both energy magazines were mobile but the working fluid was fixed in a geometrical domain of the engine cylinder. It has led to the case where Lazare's state parameters: "gravitational head" and "flow speed" were nonessential. And it opened the need for a new state parameter of working fluid. Sadi Carnot has decided to introduce two complementary state parameters: "specific volume" and "specific caloric" (nowadays: spe-

cific entropy). In his description of a cycle, Sadi Carnot decided to introduce two yet unknown laws of physics into consideration. These are:

- a law of conservation of specific volume (say $v$) and
- a law of conservation of specific entropy (say $s$).

These laws were expressed in words as: at the cycle end, after four arbitrary transformations of state parameters, working fluid is in the same thermodynamical state as at the beginning, and it is ready to make a new cycle. Let us note that the balance of energy, which can be treated to be the mathematical statement of the First Principle of Thermodynamics does not appear in the Carnot model of working medium. The balance of energy in the Carnot working medium was used in a special place and in a special role (see [1] footnote 9) – only for making calculations of the equality of cycle work and cycle heat: $W_{\text{cycle}} = H_{\text{cycle}}$. It means that in Said Carnot's statement, the first principle of thermodynamics plays a special distinguished role; it is not part of a system of governing equations, since it plays a role in final judgement.

Internal energy located within the whole working fluid is denoted by Sadi Carnot as $U$ (see [1] footnote 5). Expressing the specific internal energy as $\varepsilon = U/m$, where $m$ is a mass of the whole working fluid enclosed within the container volume $\Omega$, taking into account that gravitation energy is constant and kinetic energy is zero, the energy balance of 1 kg of working fluid can be reduced to:

- a law of first principle of thermodynamics:

$$\varepsilon_{(\text{begining of a cycle})} = \varepsilon_{(\text{end of a cycle})}$$

what means that the specific internal energy, being an internal magazine of energy, located within one kilogram of working fluid, after making four conversions, returns to its starting store. In other words, the Carnot mathematical model of working fluid is based only on two balances of state parameters. And in this model, principles of thermodynamics have a passive role and are fulfilled from the very beginning. In this paper, we like to extend this approach to a working fluid within the flow – extending a case of ideal equilibrium thermodynamics to real non-equilibrium thermodynamics.

## 2 Non-equilibrium thermodynamical statements

Every one of us knows that a real engine working fluid cannot be described by permanently stable and reversible behaviour. Unstable phenomena, like temperature and pressure changes, result from inherent fluctuations of the

respective state variables. Near global equilibrium, those fluctuations having a form of peripatetical motions, do not disturb the equilibrium. The natural trend toward equilibrium is distinguished by asymptotically vanishing dissipative contributions. In contrast, non-equilibrium states can amplify the fluctuations, and any local disturbances can even lead the whole system into an unstable or metastable state. This feature is an important indication of the qualitative difference between equilibrium and non-equilibrium states. Equilibrium states are needed for making the constitutive relation between equilibrium state parameters, but non-equilibrium state parameters take parts in every whole balance [4,7,16,28].

Within the Carnot model, there is no irreversibility generated by any flow of fluxes: flux of volume, flux of entropy or flux of momentum. The change of state parameters during four transformations occurs immediately without any fluxes – the change is visualised by virtual volumetric contact of any small part of mass of working fluid with any virtual surface of the heat container (upper and lower) and a mobile surface of the working engine. It is, of course, an ideal thought by Carnot as "equilibrium change". In our approach, we like to go further and to remove this strong condition, by assuming that during any change of state (i.e. heating or working fluxes on the load surfaces), there is a place for appearance of non-equilibrium state fluctuations. Even if, we resign from local action of fluxes, we can obtain some improvement of the Carnot model.

Let us also note that our approach has one important aim – we want to develop and to revalorize the science of the "finite-time thermodynamics" [8] from zero-dimensional and no-time formulation into a three-dimensional statement. There are many models of fluids in the literature, but from the Carnot point of view, those models (like the Navier–Stokes equation [3,21]) are improper for 3D description of the Carnot cycle. It is important for thermodynamics that many different parts of this science have more precise relations and more unique fundamental stones.

Let us recall that in classical thermodynamics, in most of the existing models of working continua, the parameters of state such as: the specific entropy, the specific volume, temperature and pressure are introduced by assuming a kind of local equilibrium [6,7,14,28,33,38], even if this assumption is quite dubious in far-from-equilibrium situations. In fact, it is known that in strict local equilibrium, there is no transport of mass, volume, entropy and momentum ($\mathbf{h}_m = \mathbf{h}_v = \mathbf{h}_s = \mathbf{t} \equiv 0$).

Thus, numerous extensions of thermodynamical ideas to far-from-equilibrium systems, that are summarised in Sieniutycz's monograph [17, chap-

ter 4], from a formal point of view, can be selected into two groups. The first one consists of the models in which the concept of non-equilibrium state is entirely related to notions of non-equilibrium temperature and non-equilibrium pressure. On the contrary, the second one is related to models that are mainly based on the concept of non-equilibrium specific volume and non-equilibrium specific entropy. It must be noticed that there are no more consistent definitions of non-equilibrium state [25, 26]. In the literature [26, 27], one can find a variety of approaches to approximation of non-equilibrium thermodynamics. The one, most frequently used, is "linear irreversible thermodynamics", which has in its basic assumptions, a resignation from a general balances of non-equilibrium entropy and non-equilibrium volume, and replaces these balances with a new type of balance based on a "concept of local non-equilibrium" [29].

Therefore, linear irreversible thermodynamics is advantageous to have a phenomenological approach to describe natural processes. This approach is a rational approximation of non-equilibrium thermodynamics proper to investigate physical, chemical, and biological 3D systems with irreversible processes, but not to describe the Carnot cycles. In the linear irreversible thermodynamics (LIT), the main formalism is coming from the increment of Carnot internal specific energy $\varepsilon$, nowadays known as the Gibbs equation. Nevertheless, it should be remembered that Sadi Carnot has introduced the notion of internal energy only for one need – for connecting together the balance of specific volume and balance of specific entropy, not for the possibility that combines the first and second laws of thermodynamics [7, 28, 29]. The Carnot internal energy increment together with the Gibbs relation have nothing in common with the second law of thermodynamics, as mistakenly assumed in Linear Irreversible Thermodynamics [28].

Yet, another fundamental difference between Carnot and linear irreversible thermodynamics (LIT) lies in the manner how both define and calculate the equilibrium temperature. For Carnot, temperature is a field related through the internal energy with the field of specific entropy; for LIT, temperature is calculated from the field of velocity: $\left\langle \frac{1}{2}\mathbf{v}^2 \right\rangle = \frac{3}{2}k_B T$, which means that molecular rotation and vibration are not accounted for.

In this article, we will analyse the possibility of formulation of a more consistent model of flowing working fluid with non-equilibrium state parameters $s^*$ and $v^*$, respectively. The model under consideration would describe the relaxation $s^* \to s$, and $v^* \to v$ from a non-equilibrium state to the equilibrium state via $n$ additional internal parameters $\xi_\alpha$, $\alpha = 1, 2, 3 \ldots, n$.

We assume that in Carnot fluid continuum, this property is also true when the fluid under consideration is inviscid and non-conductive. To avoid misunderstandings, it is worth mentioning that in the proposed model, the role played by the energy balance is similar to the classical role played by the entropy balance in LIT – it expresses the fact of still growing amount of dissipated energy. Our approach is based on the Beretta-Gyftopulos exposition of thermodynamics in which such classical notions as "heat" and "work" are removed from considerations [6, 9, 38].

## 3 The accompanying state concept

If the framework of LIT is based on a concept of "a local equilibrium", which leads to the correctness of the Gibbs equation and locally well-defined equilibrium internal energy, then in our approach to Carnot fluid continuum we put as a fundamental assumption the fact that every equilibrium state has its "accompanying state". The concept of accompanying state was developed in the XX century by many termodynamicists and finally proved by Josef Kestin [15, 18, 33].

Let us recall that yet in 1901 Władysław Natanson, in his pioneering paper [11], undertook the problem of non-equilibrium measure of specific volume (but in the case of solid body) and its relaxing approaching to the recoverable, equilibrium state. As Natanson showed, in some sense, the model after elimination of relaxing parameters leads to the Maxwell-like model of superposition of elastic and non-elastic components of continuum. This way of reasoning was extended by Mandelstam & Leontonovich [12] into a more thermodynamical framework.

In 1958 Andrzej Szaniawski published a significant paper [13] concerning the non-equilibrium entropy within viscous and conductive fluid. Trying to give an answer to the question "what is to be understood by entropy in a non-equilibrium state", Szaniawski introduced a concept of space non-equilibrium parameters which possess the accompanying equilibrium state and the accompanying reversible process. Following this concept, he considered a state of continuum in which non-equilibrium specific volume $v^*$ and non-equilibrium specific entropy $s^{ast}$ are distinguished from reversible, equilibrium specific entropy $s$ and equilibrium specific volume $v$. Numerous examples of non-equilibrium phenomena were described in the papers by Kestin and Bilicki [18] and Bilicki and Badur [19].

Physically, the phenomenon responsible for differences between $s^* - s$ and $v^* - v$ is explained by the field of internal parameters $\xi_\alpha = \xi_\alpha(\mathbf{x}t)$, $\alpha = 1, 2, 3, \ldots, n$, depending on the position vector $\mathbf{x}$ and time $t$. These parameters take part in the model, no matter whether the fluid under consideration is viscous or not, conductive or not. The dissipate phenomena attributed to $\xi_\alpha = \xi_\alpha(\mathbf{x}t)$ can be explained as the effect of a far-from-equilibrium state, necessary in the places where experimentalists have withdrawn traditionally assumed local-equilibrium state. In the most simple case, the number of parameters is restricted and only two internal (scalar) parameters should be postulated: the first one – to describe the $s^* \to s$ relaxation and the second one to describe the $v^* \to v$ relaxation.

In Fig. 1, the non-equilibrium state is represented by $s^*$, $v^*$, $\xi_\alpha$ whereas a real state of process is described by a point $(P^*)$, and any process by means of a curve $l^*$.

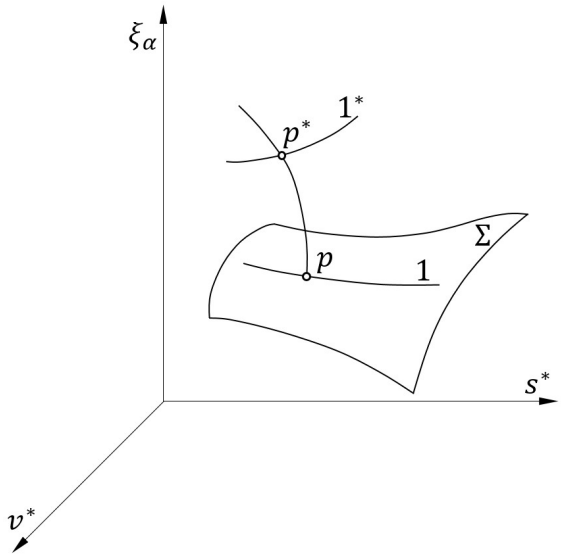


Figure 1: A space of non-equilibrium states with accompanying equilibrium state.

A set of states of equilibrium represents a surface called by Gibbs "*the primitive surface*" $\Sigma(s, v, 0) = 0$. For every state $(P^*)$, one can find on a curve $l$ of the accompanying reversible process, the point $(P)$. It means that if $P^* \to P$, then $s^* \to s$, $v^* \to v$ and parameters $\xi_\alpha \to \bar{\xi}_\alpha(s, v)$ become independent and are functions of the equilibrium state parameters. In particular $\bar{\xi}_\alpha \equiv 0$.

Let us assume that the non-equilibrium state parameters are uniquely split additively into the following series:

$$s^*(v, s, \xi_\alpha) = s + \frac{1}{2} A_{\alpha\beta}(s, v)\xi_\alpha\xi_\beta\,, \tag{1}$$

$$v^*(v, s, \xi_\alpha) = v + \frac{1}{2} B_{\alpha\beta}(s, v)\xi_\alpha\xi_\beta\,, \tag{2}$$

where matrices $A_{\alpha\beta}$, $B_{\alpha\beta}$; $\alpha, \beta = 1, 2, 3 \ldots, n$, should be symmetric and positively defined. Let us also assume that the specific internal energy is only a function of equilibrium state parameters $s$ and $v$; it means that the internal energy stored only elastic part of converted energy transported within working fluid. We omit here important Mandelstam's assumption [12] that a small amount of energy that is liberated during relaxation $P^* \to P$ can be recovered and, therefore, is stored in internal energy (i.e. $\varepsilon = \varepsilon(s, v, \xi_\alpha)$).

## 4 Balances of non-equilibrium entropy and non-equilibrium volume

Our line of reasoning assumes here that in the state of thermal equilibrium, working fluid is completely described by state parameters $s$ and $v$, uniquely determining internal energy $\varepsilon = \varepsilon(s, v, \xi_\alpha)$. During a motion, which in general is not a state of equilibrium, a state of the inviscid non-conductive fluid must be represented by two non-equilibrium state parameters $s^*$ and $v^*$, or according to Eqs. (1)–(2), through two equilibrium parameters $s$, $v$ and $n$ internal parameters $\xi_\alpha$. The balances of changes of non-equilibrium entropy and non-equilibrium volume take the following form [8,30,38]:

$$\frac{d}{dt} \iiint\limits_{\Omega} \rho s^*\, dV \geq \iint\limits_{\partial\Omega_h} \mathbf{h}_s \cdot \mathbf{n}\; dA, \tag{3}$$

$$\frac{d}{dt} \iiint\limits_{\Omega} \rho v^*\, dV \geq \iint\limits_{\partial\Omega_h} \mathbf{h}_v \cdot \mathbf{n}\; dA. \tag{4}$$

In the above, the flux of entropy $\mathbf{h}_s$ and flux of volume $\mathbf{h}_v$ appear on a proper boundary surface oriented by unit normal vector $\mathbf{n}$. But traditionally in the Carnot, Clapeyron, Segiun, and Rankine style of presentation, instead of $\mathbf{h}_v$ and $\mathbf{h}_s$ fluxes, some corresponding energy fluxes are applied and used. Instead of $\mathbf{h}_s$ we have the flux of heating energy $\boldsymbol{\mathcal{F}}_h = T\mathbf{h}_s$ (sometimes

denoted as the vector: $\mathbf{q}$), and instead of $\mathbf{h}_v$ we have the flux of working energy $\boldsymbol{\mathcal{F}}_w = p\mathbf{h}_v$. But in general, the relation between fluxes is complicated especially in the case of continua with heating or working microstructure – then the additional interstitial working flux and interstitial heating flux are needed [20,23,27,35]. The temperature $T$ and pressure $p$ appear in this relation not quite accidentally – they play the role of energy partners.

Rewriting Eqs. (3) and (4) in terms of the appropriate energy fluxes we obtain:

$$\frac{d}{dt}\iiint\limits_{\Omega} \rho s^*\, dV \geq \iint\limits_{\partial\Omega_h} \frac{\boldsymbol{\mathcal{F}}_h \cdot \mathbf{n}}{T}\, dA, \tag{5}$$

$$\frac{d}{dt}\iiint\limits_{\Omega} \rho v^*\, dV \geq \iint\limits_{\partial\Omega_v} \frac{\boldsymbol{\mathcal{F}}_w \cdot \mathbf{n}}{p}\, dA. \tag{6}$$

where $\mathcal{F}_h$ and $\mathcal{F}_w$ are the heating and working fluxes, respectively. If the surface integral in Eq. (5) is replaced and denoted by $\eth Q/T$ and the total entropy in the whole domain is denoted by $S$, then Eq. (5) takes a global form proposed originally by Clausius:

$$dS \geq \frac{\eth Q}{T}\,. \tag{7}$$

It follows from the above that the mathematical expression: $dS = dQ/T$ has no physical sense [see for instance 13, page 4]. The equation similar to Eq. (6) has been proposed by Gyftopoulos and Beretta [6], Beretta [38]. The Said Carnot concept of taking the balance of specific volume has turned an attention of Max Born in 1921 [31], and Peter Bridgeman [32]. The role of Eq. (6) within the framework of ideal fluids turned an attention of Egligt [34] and Badur & Banaszkiewicz [35].

It should be remembered that these fluxes are given on heating and moving surfaces through which working fluid transfers heat and work, respectively. However, $T$ and $p$, in opposite to Clausius' approach, have a cleat physical mining of the thermodynamical temperature and thermodynamical pressure (corresponding to the polish word "prę żność"). For a hyperelastic Carnot material, $T$ and $p$are determined through the following state relation involving internal energy [17]:

$$T = \frac{\partial u}{\partial s}_{\|v=\text{const}}, \qquad p = \frac{\partial u}{\partial v}_{\|s=\text{const}}. \tag{8}$$

It means, according to the Lazar Carnot concept of Aristotelian energy, that internal energy should be a function of "state parameters": multiplicative or additive. Definitely standing against the additive concept of energy, developed early by Biot and Rumfold, Sadi Carnot has proposed a multiplicative form of the internal energy magazine, e.i. $\varepsilon \sim s \cdot v$; $s^2 \cdot v$ or $s \cdot \ln\left(\frac{v}{v_0}\right)$. Then balancing "working" with "heating" energy, he proposed the following state equation written in terms of energy as: $p(v-b) = R(\theta + 273)$, were $b$ is an internal volume of gas molecules, $\theta$ is Celsius temperature and $R = N \cdot k_B$ is the internal contribution of elements of entropy (caloric), with $k_B$ as a quantum of caloric (nowadays: the Boltzmann constant).

Introducing to inequalities (5)–(6) any always positive quantities, the so-called "uncompensated heat and uncompensated work transformations": $\sigma_s$, $\sigma_v$, and with the help of the Reynolds transport theorem and the Gauss-Ostrogradski theorem for surface integral, we are able to change Eqs. (5) and (6) into the following equalities having a customary Cartesian form ($i = x,\ y,\ z$):

$$\iiint\limits_{\Omega} \left[\frac{\partial}{\partial t}\left(\rho s^*\right) + \frac{\partial}{\partial x_i}\left(\rho s^* v_i\right) - \frac{\partial}{\partial x_i}\left(\frac{\mathcal{F}_{(h)i}}{T}\right)\right] dV = \iiint\limits_{\Omega} \rho\sigma_s \, dV, \tag{9}$$

$$\iiint\limits_{\Omega} \left[\frac{\partial}{\partial t}\left(\rho v^*\right) + \frac{\partial}{\partial x_i}\left(\rho v^* v_i\right) - \frac{\partial}{\partial x_i}\left(\frac{\mathcal{F}_{(w)i}}{p}\right)\right] dV = \iiint\limits_{\Omega} \rho\sigma_v \, dV. \tag{10}$$

In the above: $\rho$ – mass density, $\mathbf{v} = v_i \mathbf{e}_i$ is the substantial velocity of working fluid. At this point, we are able to introduce the second law of thermodynamics, in a novel form known also as the requirement that "uncompensated heat and work transformation" should be always positive [8], i.e.:

$$\sigma_s \geq 0, \quad \sigma_v \geq 0. \tag{11}$$

Of course, we agree also with a reader that the form of the second principle of thermodynamics is far from being complete, nevertheless, it is on the line of reasoning started by Aristotle and continued by Thomas of Aqvine, Leonardo da Vinci and Lazare Carnot. Eq. (10) has been proposed by Mieczysław Mieczyński [30].

Then, introducing by usual procedures the substantial time derivatives, one can obtain the field equations resulting from Eqs. (9) and (10). After multiplication of Eq. (9) by $T$ and after multiplication of Eq. (10) by $p$ we

obtain:

$$T\rho\sigma_s = Ts^*\left[\frac{\partial\rho}{\partial t} + \operatorname{div}(\rho\mathbf{v})\right] + T\rho\left(\frac{ds^*}{dt} - \frac{ds}{dt}\right) + T\rho\frac{ds}{dt} - \operatorname{div}(\boldsymbol{\mathcal{F}}_h) + \boldsymbol{\mathcal{F}}_h \cdot \frac{\operatorname{grad} T}{T}, \tag{12}$$

$$p\rho\sigma_v = pv^*\left[\frac{\partial\rho}{\partial t} + \operatorname{div}(\rho\mathbf{v})\right] + p\rho\left(\frac{dv^*}{dt} - \frac{dv}{dt}\right) + p\rho\frac{dv}{dt} - \operatorname{div}(\boldsymbol{\mathcal{F}}_w) + \boldsymbol{\mathcal{F}}_w \cdot \frac{\operatorname{grad} p}{p}. \tag{13}$$

## 5 Balance of linear momentum

The balance of momentum in any continuum is a simple continuation of Newton's approach, which is reducing the whole dynamics to the balance of translational momentum known as: $m\mathbf{a} = \mathbf{f}$. Within a dense continuum of particles, the form of Newton's equation is similar, only two elements are changed. The first one is the definition of acceleration vector, which is now: $= \dfrac{\partial}{\partial t}\mathbf{v} + (\operatorname{grad}\mathbf{v})\mathbf{v}$; this form was established by d'Alembert (in cylindrical coordinates) and by Euler (in arbitrary coordinates). The second one is redefinition of force – in continuum of particles, it is important to add for gravitational part some "particle interaction": $\operatorname{div}\mathbf{t}$, where $\mathbf{t} = t_{ij}\mathbf{e}_i \otimes \mathbf{e}_j$ is the flux of momentum, which has been introduced by Cauchy, and sometimes called the Cauchy stress (tension) tensor. In fluid continuum, there is no reversible shear component, therefore, momentum flux must always be divided into two parts [3, 31]:

$$\mathbf{t} = -\pi\mathbf{I} + \boldsymbol{\tau}, \tag{14}$$

which are identified with elastic and viscous parts, respectively. Sometimes the viscous tensor is traceless $\operatorname{tr}(\boldsymbol{\tau}) = 0$, then splitting of elastic and viscous properties is complete. Thus, introducing the definition of acceleration into account, and turning the form of balance of momentum into "the conservative form", one can obtain

$$\frac{\partial}{\partial t}(\rho\mathbf{v}) + \operatorname{div}(\rho\mathbf{v} \otimes \mathbf{v}) = \operatorname{div}\mathbf{t} + \rho\mathbf{b}, \tag{15}$$

where $\rho\mathbf{b}$ is a body force of general kind. By multiplication of Eq. (15) by velocity vector, we get the partial balance of kinetic energy $\kappa$. Or in

other words: the scalar property of energy will be related to the momentum only if we do scalar multiplication of momentum balance by the specific momentum $\mathbf{v}$:

$$\left[\rho\frac{d}{dt}\mathbf{v} = \operatorname{div}\mathbf{t} + \rho\mathbf{b}\right]\cdot\mathbf{v}. \tag{15a}$$

Assuming, next, that the tensor of momentum flux for this simple (non-gradiental) working fluid is defined as additive contribution of spherical pressure tensor and the viscous (laminar + turbulent) fluid: $\mathbf{t} = -\pi\mathbf{I} + \boldsymbol{\tau}$, we can also split the contribution of energy into the so-called recoverable and dissipative parts:

$$\rho\mathbf{v}\cdot\frac{d}{dt}\mathbf{v} = \rho\frac{d}{dt}\kappa = \rho\mathbf{v}\cdot\mathbf{b} + \rho\pi\frac{d}{dt}\rho^{-1} + \operatorname{tr}(\boldsymbol{\tau}\mathbf{d}) - \operatorname{div}(-\pi\mathbf{v} + \boldsymbol{\tau}\mathbf{v}). \tag{15b}$$

We read the above equation: the rate of change of kinetic energy depends on the gain of production $\rho\mathbf{v}\cdot\mathbf{b}$ taken from diminished gravitational energy, the amount of energy conversion $\rho\pi\dfrac{d}{dt}\rho^{-1}$, part of energy dissipation $\operatorname{tr}(\boldsymbol{\tau}\mathbf{d})$ [where $\mathbf{d} = 0.5(\operatorname{grad}\mathbf{v} + \operatorname{grad}^{\mathrm{T}}\mathbf{v})$ is symmetric part of the velocity gradient], and the exchange of energy by a part of mechanical flux $\boldsymbol{\mathcal{F}}_{\mathrm{work}} = -\pi\mathbf{v} + p\mathbf{h}_v + \boldsymbol{\tau}\mathbf{v}$, where $p$ is thermodynamic pressure and $\pi$ represents co-mechanical pressure due to Gaggioli's concept of internal volume evolution [22]. It means that only in a partial balance of energy we can observe explicitly three manners of energy transformations: expansion, conversion and dissipation[1].

# 6 Equation of the balance of energy

## 6.1 Energy flux concept

Discovery of balance of energy which is consistent with the first principle of thermodynamics is not an easy thing. Every new exposition of thermodynamics needs quite new mathematics and a new flexible system of notations. This statement concerns the Carnot continuum too. The modern

[1] Looking at the mechanical flux of energy in Eq. (15), yet another fundamental question appears – it is somehow strange splitting of energy fluxes into reversible and irreversible parts: $\vec{\mathcal{F}}_{\mathrm{work}} = \vec{\mathcal{F}}^{rev}_{\mathrm{work}} + \vec{\mathcal{F}}^{\mathrm{irr}}_{\mathrm{work}}$; $\vec{\mathcal{F}}_{\mathrm{heat}} = \vec{\mathcal{F}}^{\mathrm{rev}}_{\mathrm{heat}} + \vec{\mathcal{F}}^{\mathrm{irr}}_{\mathrm{heat}}$. From Eq. (15) it follows that in the case of mechanical flux of energy such splitting is possible. However, nothing is known on splitting of thermal energy flux. The only case where $\vec{\mathcal{F}}^{\mathrm{rev}}_{\mathrm{heat}}$ appeared in the literature is the Green-Naghdi theory of heat superconducting [21, 22]. Unfortunately, it means that for the classical Navier-Stokes-Fourier model, the entropy based on the reversible flux of thermal energy cannot be defined.

candidate to an expression of energy balance is the Gyftopoulos-Beretta exposition [6, pp. 38, 103, 108]. They consider some abstract system $A$,which is a system taken in two states $A_1$, $A_2$ – in two times moments. Then the balance of energy is

$$E_2 - E_1 = E^{\leftarrow}. \tag{16}$$

In this balance: $E^{\leftarrow}$ denotes the net energy transferred to system $A$ from all the other interacting systems during the process that changes the state of $A$ from $A_1$ to $A_2$. Precisely interpreting the Gyftopoulos-Beretta exposition, we never express a violating fact that energy gained by the system must be accounted for by the energy transferred across the boundary of the system $E^{\leftarrow}$ – since energy *per se* neither can be created nor destroyed.

Let us continue this idea – then, the energy transition needs to introduce a concept of energy flux, say: $\mathcal{F}_E$ which is transferring energy in time $\Delta\tau_{1-2}$, as follows: $\mathcal{F}_E \Delta\tau_{1-2} = E^{\leftarrow}$. Beretta and Gyftopoulos have underlined that any amount of energy can be transferred to a system, for instance, by doing electrical work on it, but the availability of this energy depends on how the final state is reached. Usually one can define the "adiabatic availability" [6, Chapter 5] to be if the final state is reached without irreversibility – then the available energy is equal to transferred energy. However, if the final state is reached with irreversibility, this capacity will be smaller than the energy transferred, and may even be equal to zero. According to Kestin [15], it should be clarified that the available energy of a system $A$ is derived from the adiabatic availability – it is a case when the system $A$ interacts by reversible in-flow and out-flow with a reservoir. It practically means that the system $A$ is operating at constant thermodynamic conditions and at a permanent stable equilibrium state.

Gyftopoulos and Beretta [6] denote the energy interaction for all possible energy flow by symbols: $E^{\rightarrow}$ or $E^{\leftarrow}$ depending on the in-flow or out-flow of energy. Denoting all interactions by one common letter is a fundamental step for their paradigm of thinking, especially because in everyday language, there exists a single meaningful equivalence for $E^{\leftarrow}$ – it is power: $\mathcal{P}$ [watt = joule per second], which is understood as a rate of energy consumption by any technical devices. We say that devices have more or less power, therefore the balance of energy – being the main manifestation of the first law of thermodynamics – is also interpreted as: the rate of production (or consumption) of energy is governed by power: $\frac{d}{dt}E = \mathcal{P}$. The most convenient and familiar unit of power is watt, which does not mean that this is a rate of making heat or work, since power is a more basic concept

than heat and work. Therefore, heat and work should only be treated as power multiplicated by time (for this line of reasoning unit is kWh, however an established unit for the SI system is joule) – this statement is confirmed by the economy that says: "we buy power, but we pay for energy"[2].

Unfortunately, the word "power" does not indicate a place where the exchange of energy takes place. Therefore, instead of letter $E^{\leftarrow}$ or $\mathcal{P}$, we propose to introduce another letter $\mathcal{F}$, which denotes the flux of net energy supplied to system $A$ from all interacting systems and reservoirs. The energy gained by $A$ must be accounted for as energy transferred across a boundary of the system, because energy neither can be generated *ex nihilo* nor destroyed in $A$:

$$E_2^A - E_1^A = \left( \iint\limits_{\partial A} \boldsymbol{\mathcal{F}}_e \cdot \mathbf{n}\, dS \right) \Delta\tau_{1-2} = \mathcal{F}_E \Delta\tau_{1-2} = E^{\leftarrow}, \tag{17}$$

where: $\boldsymbol{\mathcal{F}}_e$ is the local (3D) form vector of a total flux of energy transferred across the boundary of the system oriented by unit vector $\mathbf{n}$. Only the normal component of energy flux is important – it defines the net flux of energy $\mathcal{F}_E$, which mathematically cannot by differentiated by $\leftarrow$ or $\rightarrow$ arrow. It is worth noting that, independently of phenomena under account [described by quaternions, spinors, tensors, multinions, etc.], the flux of energy is always a vector [9,10,38].

## 6.2 Internal energy concept

Sadi Carnot discovered that if a material continuum underlines the heating flux $\boldsymbol{\mathcal{F}}_h$ acting on a continuum surface $\partial\Omega_h$ then "heat can be stored" in the whole continuum in the form of "internal energy". In means that the operation of storage cannot be direct (one *joule* inflows and one *joule* is stored) and needs some conversion. In the Gyftopoulos-Beretta approach, the energy of a system is a primal property of substance and fields and it is always a sum of internal $\mathcal{U}$, kinetic $\mathcal{K}$ and potential energy $\Phi$:

$$E = a_1\mathcal{U} + a_2\mathcal{K} + a_3\Phi. \tag{18}$$

If we adopt the Aristotelian sense of energy, it means that energy taken as a first invariant of general motion [mathematically expressed as a scalar] is

[2]Truly speaking, we are correct only in converting kilowatt-hours to joules: 1 kWh = 3.6 MJ not *vice versa* – it is a basic amount of energy for payment.

additive, not multiplicative. Additivity means that the mater and the fields are separable primary physical objects. This concept known as Aristotelian *hylomorphism* nowadays is interpreted as a primary assumption that the whole universe is created from three basic components: *matter*, *fields* and *quantum vacuum*. It is worth highlighting that kinetic and potential energies in Eq. (18) are external and account for the system, while internal energy is determined by inter-particle kinetic and potential energies. In the universal system of units, the equivalence coefficients are equal to one: $a_1 = a_2 = a_3 = 1$, what means that pioneering Joule's efforts to measure energy equivalence as $\mathcal{J} = \mathcal{U}/\mathcal{K}$ was baseless.

Another key notion in the Gyftopoulos-Beretta approach is "conversion of energy". If our system $A$ undergoes a process from state 1 to state 2: $A_1 \rightarrow A_2$, then $\mathcal{U}_1$, $\mathcal{K}_1$, $\Phi_1$ change their values to $\mathcal{U}_2$, $\mathcal{K}_2$, $\Phi_2$ and this mysterious process is called energy conversion. Does not exist conversion of heat into work and vice versa – work into heat, since both work and heat are only a comfortable manner of expressing the net amount of energy conversion during a single process, where a net change of $E$ disappears.

Let us mark the finite elementary volume by the sign $dV$, and the whole volume of thermodynamic system $A$ by letter $\Omega$. The system $A$ interacts with the external environment by the processes acting at the system boundary $\partial\Omega$. The internal, kinetic and potential energy can be denoted by $U$, $K$, and $\Phi$, respectively, and besides the integral quantities, there are some quantities related to the unit of mass, such as:

$$\text{Internal energy} \qquad \mathcal{U} = \iiint\limits_{\Omega} \rho\varepsilon \, dV, \tag{19}$$

$$\text{Kinetic energy} \qquad \mathcal{K} = \iiint\limits_{\Omega} \frac{1}{2}\rho \mathbf{v} \cdot \mathbf{v} \, dV = \iiint\limits_{\Omega} \rho\kappa \, dV, \tag{20}$$

$$\text{Potential energy} \qquad \Phi = \iiint\limits_{\Omega} \rho\phi \, dV. \tag{21}$$

The actual volume $\Omega$ is related to the Euler description. Therefore, in arbitrary 3D description, $\rho$ is density, $\phi$ is specific potential energy and $\varepsilon$ represents specific internal energy. Following Gibbs, the specific internal energy [J/kg] related to the unit mass can be denoted by $\varepsilon$. The quantity $\rho\varepsilon$ is volumetric energy density related to actual volume.

Yet, the most restrictive assumption concerning internal energy should be taken into consideration. It must be a function of intensive state parameters. In our case, we have two intensive state parameters: $v$, $s$, thus, the

energy is stored in the Carnot continuum only as: $\varepsilon = \varepsilon(s, v)$. How much energy can be stored in one kilogram of mass? It will be reasonable to assume that there exists some limit value: $\varepsilon^{\text{crit}}$ that can never be exceeded. The first in the literature concise model of "critical energy", known also as "energy hypothesis", was established by Eugenio Beltrami (1885) and rediscovered by Tytus Huber (1904) and Włodzimierz Burzyński (1928) [5].

### 6.3 Splitting of the energy flux

Returning to energy total flux in Eq. (17), we next assume that the energy fluxes are additive. It allows us to formulate the total energy flux as the sum of processes:

$$\mathcal{F}_E = \mathcal{F}_{\text{work}} + \mathcal{F}_{\text{heat}} + \mathcal{F}_{\text{chem}} + \mathcal{F}_{\text{elec}} + \mathcal{F}_{\text{mag}} + \ldots, \tag{22}$$

where, respectively, appear: working, heating, chemical, electric and magnetic energy fluxes. It was R.A. Gaggioli who first proposed to denote various energy fluxes by one common letter [23] – a single letter "$\mathrm{I}_E$", which has a rather weak connotation with 3D formulation, therefore we propose to replace the Gaggioli notation with a more concise denotation by the letter "$\mathcal{F}$". Precisely, Gaggioli has proposed $\mathrm{I}_E = p\mathrm{I}_V$ for volume energy flux and $\mathrm{I}_E = T\mathrm{I}_\theta$ for thermal energy flux (we propose: $\boldsymbol{\mathcal{F}}_h = T\mathbf{h}_s$ and $\boldsymbol{\mathcal{F}}_w = p\mathbf{h}_v$, respectively).

Let us note that Professor Gaggioli introduced the entropy flux density concept (our $\mathbf{h}_s$) in a quite different manner than Eckart (1940) who proposed it in 3D formulation [23]. For Gaggioli, $\mathbf{h}_s$ should be a rate of some "thermal charge" transfer. Up to now, no one is familiar with the notion of "thermal charge" – we are familiar only with an "entropy charge" discovered by Boltzmann as the constant $k_B = 1.38 \cdot 10^{-23}$ J/K. The introduction of $k_B$, called by Boltzmann "the entropy element", is according to Ladislavus Natanson, the absolute beginning of the science of "Quantum Thermodynamics" [27]. Therefore, temperature $T$ in $T\mathbf{h}_s$ plays a role of energy scale multiplayer, quite similar to pressure in $\mathrm{I}_\mathrm{V}$ (our $\mathbf{h}_v$). It should also be added that, for example, $F_{\text{heat}}$ means heat transferred rate, traditionally denoted by: $\dot{Q}$, in watts [W]. This total $F_{\text{heat}}$ relates to heat flux surface density $\boldsymbol{\mathcal{F}}_h$, commonly expressed as vector $\mathbf{q}$ [W/m$^2$], by integrating the flux over the surface of the system. Therefore, overwriting the dot in $\dot{Q}$ is baseless.

The mathematical sum of scalars, presented in Eq. (22) can be treated as universal one – three dots mean that there is a place for new, yet unknown processes. There is a lack of radiative flux, described by the Pointing energy

vector (1899), because it is indirectly related to the system substantial boundary. If the substantial boundary $\partial\Omega$ is oriented outside by the normal unit vector $\mathbf{n}$, that allows us to write the energy flux as a normal component of the total energy vector:

$$\mathcal{F}_E = \iint\limits_{\partial\Omega} (\boldsymbol{\mathcal{F}}_{\text{work}} + \boldsymbol{\mathcal{F}}_{\text{heat}} + \boldsymbol{\mathcal{F}}_{\text{chem}} + \boldsymbol{\mathcal{F}}_{\text{elec}} + \boldsymbol{\mathcal{F}}_{\text{mag}} + \ldots) \cdot \mathbf{n}\, dA. \tag{23}$$

Two first energy fluxes are very well known in literature: $\boldsymbol{\mathcal{F}}_{\text{work}}$ is a mechanical energy flux of Umov (1874) and Volterra (1899), and $\boldsymbol{\mathcal{F}}_{\text{heat}}$ is a heating energy flux of Rankine (1851) and Stokes (1851). Notice that, in practice, the radiation energy flux is localized on a surface, and approximated via the Stefan-Boltzmann radiation flux: $\mathcal{F}_{\text{rad}} = \boldsymbol{\mathcal{F}}_{\text{rad}} \cdot \mathbf{n} = \sigma\,(T_{\text{surf}})^4\ \text{W/m}^2$, where $\sigma = 5.67 \cdot 10^{-8}\ \text{W/m}^2\text{K}^4$ is the Stefan-Boltzmann constant. For instance, the radiation on the earth is: $\mathcal{F}_{\text{rad}} = 1418\ \text{W/m}^2$ (4 January, night) or $\mathcal{F}_{\text{rad}} = 1325\ \text{W/m}^2$ (4 June, day).

## 6.4 Where do energy fluxes come from?

The essence of the proper definition for the various fluxes is to find a correct relationship of the energy flux to the other fluxes, like: momentum, angular momentum, mass, volume, entropy, electricity, etc. If the specific internal energy $\varepsilon$ is expressed by the primary variables of the state, and there are some spatial and time gradients of the variables of state, then fluxes of the mechanical energy and heating energy can be expressed by a relatively simple combination of the momentum flux tensor $\mathbf{t}$ the volume flux vector $\mathbf{h}_v$ and entropy flux vector $\mathbf{h}_s$ to be [21,22,35]:

$$\boldsymbol{\mathcal{F}}_{\text{work}} = \mathbf{t}\mathbf{v} + p\mathbf{h}_v + \boldsymbol{\mathcal{F}}^{\text{int}}_{\text{work}}\,, \qquad \boldsymbol{\mathcal{F}}_{\text{heat}} = T\mathbf{h}_s + \boldsymbol{\mathcal{F}}^{\text{int}}_{\text{heat}}\,, \tag{24}$$

where $\mathbf{v}$ is the velocity vector of the substance, $p$ is the pressure and $T$ is the absolute temperature. Additionally, some energy fluxes: $\boldsymbol{\mathcal{F}}^{\text{int}}_{\text{work}}$, $\boldsymbol{\mathcal{F}}^{\text{int}}_{\text{heat}}$ appear in the above definitions – these are called "the interstitial working" and "the interstitial heating" vectors, and are related to gradient or higher-order models of working continua, presented also in articles [21,23,24]. In the case of electrodynamical field energy, there exists the Pointing radiation energy flux defined as $\boldsymbol{\mathcal{F}}_{\text{em}} = \mathbf{E} \times \mathbf{H}$. The chemical flux of energy is usually defined as [30]: $\boldsymbol{\mathcal{F}}_{\text{chem}} = \mu\mathbf{h}_\mu$, however, the electric energy flux is [17, pp. 70–72]: $\boldsymbol{\mathcal{F}}_{\text{elec}} = z\mathbf{i}$, where $z = c_e z_e$ is a general electric potential and $\mathbf{i} = q\mathbf{E}$ – electric current. To sum up, the energy flux vectors are strictly related to

the model of continua and should rather be postulated as some additional "consistency relations".

In the present paper, we restrict our discussion only to two fluxes: $\boldsymbol{\mathcal{F}}_{\text{heat}} \equiv \boldsymbol{\mathcal{F}}_h = T\mathbf{h}_s$ and $\boldsymbol{\mathcal{F}}_{\text{work}} \equiv \boldsymbol{\mathcal{F}}_m + \boldsymbol{\mathcal{F}}_w \equiv \mathbf{t}\mathbf{v} + p\mathbf{h}_v$.

## 6.5 Conservative and substantial form of balance

We now postulate a balance of total energy for an arbitrary material volume occupying a part $\Omega$ in the present configuration and rewrite it into the so-called *integrated form*:

$$\frac{d}{dt}\iiint\limits_{\Omega} \rho(\varepsilon + \kappa + \phi)\, dV = \iint\limits_{\partial\Omega} \boldsymbol{\mathcal{F}}_e \cdot \mathbf{n}\, dA + \mathcal{S}_e\,. \tag{25}$$

The storages of energy $(\varepsilon + \kappa + \phi)$ are defined above as in Eqs. (19)–(21); the flux of energy is equal to: $\boldsymbol{\mathcal{F}}_e \equiv \boldsymbol{\mathcal{F}}_m + \boldsymbol{\mathcal{F}}_w + \boldsymbol{\mathcal{F}}_h$ and the energy source is

$$\mathcal{S}_e = \iiint\limits_{\Omega} \left(\rho T\sigma_s + \rho p\sigma_v\right)\, dV = \iiint\limits_{\Omega} \rho\mathcal{s}_e\, dV. \tag{26}$$

Then, the local conservative form of Eq. (26) is

$$\frac{\partial}{\partial t}\left[\rho(\varepsilon + \kappa + \phi)\right] + \operatorname{div}\left[\rho(\varepsilon + \kappa + \phi)\mathbf{v}\right] = \operatorname{div}\left(\boldsymbol{\mathcal{F}}_m + \boldsymbol{\mathcal{F}}_w + \boldsymbol{\mathcal{F}}_h\right) + \left(\rho T\sigma_s + \rho p\sigma_v\right). \tag{27}$$

Since the Gibbs equation of evolution of internal energy is described in terms of the "objective" substantial time derivative, we rewrite Eq. (27) into a more consistent form

$$\iiint\limits_{\Omega} \left[(\varepsilon + \kappa + \phi)(\dot{\rho} + \rho\operatorname{div}\mathbf{v})\right] + \rho\left(\dot{\varepsilon} + \dot{\kappa} + \dot{\phi}\right) = \operatorname{div}\left(\boldsymbol{\mathcal{F}}_m + \boldsymbol{\mathcal{F}}_w + \boldsymbol{\mathcal{F}}_h\right) + \rho\mathcal{s}_e\right] dV. \tag{28}$$

Assuming that geometric continuity is always fulfilled: $\dot{\rho} + \rho\operatorname{div}\mathbf{v} = 0$, it must be underlined that this equation is always true, regardless if the set of governing equations (that is, equations for mass, momentum, moment of momentum, volume and entropy balances) is satisfied or not. It will now be shown that, if the fields and variables of state satisfy conditions laid on by governing equations, the equation of energy receives a very important

form allowing for further restrictions to describe fields – it means that even though the solutions may satisfy conservation equations for mass, momentum, volume and entropy, they do not need to satisfy conservation equation for energy, and in consequence lead to generating energy *ex nihilo* [26, 32].

Therefore, we can formulate the strong form of the first principle of thermodynamics, which stands as

$$\text{Energy cannot be created ex nihilo:} \qquad \mathcal{S}_e = 0. \tag{29}$$

### 6.6 An energy justification procedure

Equation (28) represents a local (continuum) form of postulated by Gyftopoulos-Beretta form of energy balance given through Eq. (16). Now we want to present some "energy justification procedure" (EJP) whose aim is to evaluate the correctness of the set of governing equations and to give primary conditions for fulfilment of the first and second law of thermodynamics.

What is the physical meaning of Eq. (28)? To explain the role of energy as a "first invariant of the Aristotelian motion" let us remove from Eq. (28) the substantial objective rates $\dot{\phi}$ and $\dot{\kappa}$. Note that the evolution of potential energy is given as: $\dot{\phi} = \dfrac{d}{dt}\phi = \dfrac{\partial \phi}{\partial \mathbf{x}} \cdot \dfrac{d\mathbf{x}}{dt} = \mathbf{b} \cdot \dot{x} = \mathbf{b} \cdot \mathbf{v}$, and the substantial derivative of kinetic energy $\rho \dfrac{d}{dt}\kappa = \rho\dot{\kappa} = \rho\mathbf{b} \cdot \mathbf{v} + (\operatorname{div} \mathbf{t}) \cdot \mathbf{v} = \rho\mathbf{b} \cdot \mathbf{v} + \operatorname{tr}(\mathbf{t}\,\mathbf{d}) - \operatorname{div}(\mathbf{t}\,\mathbf{v})$ (15b) may be stated in a new form without the substantial derivative of $\phi$ and $\kappa$:

$$\iiint_{\Omega} \left[\rho\dot{\varepsilon} - (\operatorname{div} \mathbf{t} + \rho\mathbf{b} - \rho\dot{\mathbf{v}}) \cdot \mathbf{v} - \operatorname{tr}(\mathbf{t}\,\mathbf{d}) + \operatorname{div}(\boldsymbol{\mathcal{F}}_w + \boldsymbol{\mathcal{F}}_h)\right] dV, \tag{30}$$

where the following identity occurs: $\operatorname{div}(\mathbf{tv}) = (\operatorname{div} \mathbf{t}) \cdot \mathbf{v} + \operatorname{tr}(\mathbf{t}\operatorname{grad} \mathbf{v})$. According to the well-accepted tradition, the velocity gradient, which is $\boldsymbol{l} = \operatorname{grad} \mathbf{v}$, can be decomposed into symmetric and anti-symmetric parts: $\boldsymbol{l} = \mathbf{d} + \mathbf{w}$. Since the moment of momentum of continua is fulfilled and the flux of momentum is symmetric $\mathbf{t} = \mathbf{t}^{\mathrm{T}}$, then $\operatorname{tr}(\mathbf{t}\operatorname{grad}\mathbf{v}) = \operatorname{tr}(\mathbf{td})$.

Taking the following identities: $\operatorname{div}(\mathbf{h}_s T) = T\operatorname{div} \mathbf{h}_s + \mathbf{h}_s \cdot \operatorname{grad} T$ and $\operatorname{div}(\mathbf{h}_v p) = p\operatorname{div} \mathbf{h}_v + \mathbf{h}_v \cdot \operatorname{grad} p$, with $\mathbf{g}_s = \operatorname{grad} T$; $\mathbf{g}_v = \operatorname{grad} p$, and next, through addition and subtraction of $\mp T(\rho\dot{s} - \rho\sigma_s)$ and $\mp p(\rho\dot{v} - \rho\sigma_v)$, the

integral equation (30) becomes:

$$\iiint\limits_{\Omega} \left\{ \begin{array}{c} \rho\dot{\varepsilon} - (\mathrm{div}],\mathbf{t} + \rho\mathbf{b} - \rho\dot{v}) \cdot \mathbf{v} - (\mathrm{div}\,\mathbf{h}_s + \rho\sigma_s - \rho\dot{s})\,T \\ -(\mathrm{div}\,\mathbf{h}_v + \rho\sigma_v - \rho\dot{v})\,p - (\varepsilon + \kappa + \phi)\,(\dot{\rho} + \rho\mathrm{div}\,\mathbf{v}) \\ +T\,(\rho\dot{s} - \rho\sigma_s) + p\,(\rho\dot{v} - \rho\sigma_v) - \mathbf{h}_s \cdot \mathbf{g}_s \\ -\mathbf{h}_v \cdot \mathbf{g}_v - \mathrm{tr}\,(\mathbf{td}) = 0 \end{array} \right\} dV. \tag{31}$$

Now us let introduce some assumption within the concept of volume balance – according to the physical statement that part of gas volume is occupied by the internal volume of molecules. Then, the following splitting of the volume flux is possible and motivated:

$$\mathbf{h}_v = \alpha\mathbf{v} + \mathbf{h}'_v, \tag{32}$$

where $\alpha\mathbf{v}$ can be called the "volume velocity" and

$$\alpha = \frac{p\mathrm{div}(\mathbf{v})}{\|\mathbf{v}^2\|\,\|\mathrm{grad}\,p\|} \tag{33}$$

is the so-called volume-slip coefficient. In Eq. (31), the parts, expressing the balance of mass, momentum, volume and entropy, respectively, are to be fulfilled identically if a set of governing equations is simultaneously solved. By introducing Eq. (32) and $\mathbf{t}' = -(\pi - p)\mathbf{I} + \tau$ into Eq. (31) we are able to reformulate of total momentum flux to be:

$$\iiint\limits_{\Omega} \Big[\rho\dot{\varepsilon} + T\,(\rho\dot{s} - \rho\sigma_s) + p\,(\rho\dot{v} - \rho\sigma_v) - \mathbf{h}_s \cdot \mathbf{g}_s - \mathbf{h}'_v \cdot \mathbf{g}_v - \mathrm{tr}\,(\mathbf{t}'\mathbf{d})\Big] dV = 0. \tag{34}$$

Even if a thermo-elastic Carnot fluid is expressed via scalar state variables $vs$, which is a much simpler situation than in the Carnot solids [20], the mechanism of the internal energy storage is more complex, since one observes the multiplicative, not additive, contribution to $\varepsilon = \varepsilon(s, v)$ The material (objective) time rate of internal energy is: $\dot{\varepsilon} = \dfrac{\partial\varepsilon}{\partial s}\dot{s} + \dfrac{\partial\varepsilon}{\partial v}\dot{v}$. Therefore, by expressing the material derivative of the internal energy, we obtain:

$$\iiint\limits_{\Omega} \Big\{ \Big\{ \rho\left(\frac{\partial\varepsilon}{\partial v} - p\right)\dot{v} + \rho\left(\frac{\partial\varepsilon}{\partial s} - T\right)\dot{s} + \rho T\sigma_s + \rho p\sigma_v - \mathbf{h}_s \cdot \mathbf{g}_s - \mathbf{h}'_v \cdot \mathbf{g}_v - \mathrm{tr}(\mathbf{t}'\mathbf{d}) \Big\} dV = 0. \tag{35}$$

Working fluid will be thermo-elastic in the Carnot sense (completely reversible) if, and only if, thermodynamic pressure and thermodynamic temperature are connected with internal energy by equations of state[3]:

$$p = \frac{\partial \varepsilon}{\partial v}, \qquad T = \frac{\partial \varepsilon}{\partial s}. \tag{36}$$

These two constitutive relations are fundamental for proving that the balance of total energy can be fulfilled in any processes governed by the balance of mass, momentum, moment of momentum, volume and entropy. In the case of ideal gas, the internal energy depends on two constitutive coefficients – $c_v$ and $c_p$ – the specific heat at constant volume and pressure, respectively. From this pair; $c_v$, $c_p$, one can obtain another pair – Carnot's (1824): $R = c_p - c_v$ and Poisson's (1831): $\gamma = \dfrac{c_p}{c_v}$ [34,35]:

Finally, after removing from Eq. (35) the reversible elastic state parameter definitions and after expressing the production of entropy and volume in terms of Eqs. (12)–(13), we obtain the remaining part of the balance of energy as

$$S_e = \iiint_{\Omega} \{\rho T \sigma_s + \rho p \sigma_v - \Phi\} \, dV = 0 \tag{37}$$

and the non-equilibrium sources expressed by Eqs. (12) and (13); few parts in the balance of energy can be excluded and the remaining part of that balance contains this energy that is dissipated. According to Rayleigh, we will call it a dissipated energy and denote it by $\Phi$:

$$\begin{aligned} \Phi = p\rho \left( \frac{dv^*}{dt} - \frac{dv}{dt} \right) + T\rho \left( \frac{ds^*}{dt} - \frac{ds}{dt} \right) + \mathbf{h}'_v \cdot \mathbf{g}_v + \mathbf{h}_s \cdot \mathbf{g}_s \\ + \ \operatorname{tr}(\boldsymbol{\tau}\mathbf{d}) + (\pi - p)\operatorname{div} \mathbf{v}. \end{aligned} \tag{38}$$

Then, the requirement that the energy equation be identically satisfied leads to the inequality relating dissipative "forces" and "fluxes". By setting

$$\frac{d}{dt}v^* = \frac{d}{dt}v + \frac{1}{2}\left( 2B_{\alpha\beta}\xi_a\dot{\xi}_\beta + \frac{\partial B_{\alpha\beta}}{\partial s}\xi_\alpha\xi_\beta\dot{s} + \frac{\partial B_{\alpha\beta}}{\partial v}\xi_\alpha\xi_\beta\dot{v} \right), \tag{39}$$

[3]Additionally, the internal energy cannot be an arbitrary function of intensive variables of state. In accordance with the Principle of Energy Conversion, it has to satisfy a supplementary condition: it is required that the actual state be acquirable with interchangeable cycle combinations; this may be expressed mathematically with the first equation of thermodynamics postulated independently by Carnot (but not explicitly), Clapeyron (1836) and Clausius (1850): $\dfrac{\partial}{\partial v}\left(\dfrac{\partial \varepsilon}{\partial s}\right) = \dfrac{\partial}{\partial s}\left(\dfrac{\partial \varepsilon}{\partial v}\right)$. This equation has been extended by Kirchhoff (1858) to chemical state variables and Gibbs (1878) to electrical state variables. Finally, Maxwell (1871) wrote it to be: $\varepsilon_{,\alpha\beta} = \varepsilon_{,\beta\alpha}$.

$$\frac{d}{dt}s^* = \frac{d}{dt}s + \frac{1}{2}\left(2A_{\alpha\beta}\xi_a\dot{\xi}_\beta + \frac{\partial A_{\alpha\beta}}{\partial s}\xi_\alpha\xi_\beta\dot{s} + \frac{\partial A_{\alpha\beta}}{\partial v}\xi_\alpha\xi_\beta\dot{v}\right), \tag{40}$$

and rejecting the infinitely small quantities of the third order, we finally obtain an expression for the dissipating energy:

$$\begin{aligned}\Phi = \tau_{ij}d_{ij} + (\pi - p)\,(v_{i,i}) + \boldsymbol{\mathcal{F}}_w \cdot \frac{\operatorname{grad} p}{p} + \boldsymbol{\mathcal{F}}_h \cdot \frac{\operatorname{grad} T}{T} \\ + \ (TA_{\alpha\beta} + pB_{\alpha\beta})\,\rho\xi_\alpha\dot{\xi}_\beta \geq 0.\end{aligned} \tag{41}$$

In the above formula for the case of inviscid, non-conductive fluid, the first three parts vanish identically, and dissipative phenomena reduce only to relaxation $s^* \to s$ and $v^* \to v$.

## 7 The neo-classical constitutive relations

Equation (40) resulting from the balance of energy will be regarded as an identity for every choice of the state parameters. It, in our approach, represents one global restriction concerning the form of constitutive equations.

It should be emphasised that so far no mention has been made of restrictions of constitutive equations, which usually in LIT arise from some form of the second law of thermodynamics understood as *entropy inequality* ($dS = d_iS + d_eS$ [28, 29]). In fact, the above inequality can be fulfilled by taking the energy dissipative potential:

$$\begin{aligned}\varpi\left(\mathbf{g}_s, \mathbf{g}_v, \dot{\xi}_\alpha, \mathbf{d}\right) = \frac{1}{2}k_s\mathbf{g}_s\mathbf{g}_s + \frac{1}{2}k_v\mathbf{g}_v\mathbf{g}_v + \mu\mathrm{tr}\,(\mathbf{dd}) \\ + \left(\frac{2}{3}\mu - \lambda'\right)(\mathrm{tr}\mathbf{d})^2 + \frac{1}{2}N_{\alpha\beta}\dot{\xi}_\alpha\dot{\xi}_\beta + L_\alpha\dot{\xi}_\alpha\mathrm{tr}\,(\mathbf{d}),\end{aligned} \tag{42}$$

which leads to linear Onsager-type constitutive relations:

$$\tau = \frac{\partial\varpi}{\partial\mathbf{d}} = 2\mu\mathbf{d} + \frac{2}{3}\mu\,(\mathrm{tr}\mathbf{d})\,\mathbf{I}, \tag{43}$$

$$\pi - p = \frac{\partial\varpi}{\partial\mathbf{d}} = \lambda'\mathrm{tr}\mathbf{d} + L_\alpha\dot{\xi}_\alpha, \tag{44}$$

$$\mathbf{h}_s = \frac{\partial\varpi}{\partial\mathbf{g}_s} = k_s\mathbf{g}_s\,, \qquad \mathbf{h}'_v = \frac{\partial\varpi}{\partial\mathbf{g}_v} = k_v\mathbf{g}_v, \tag{45}$$

$$\xi_\alpha = \frac{\partial\varpi}{\partial\dot{\xi}_\alpha} = N_{\alpha\beta}\dot{\xi}_\beta + L_\alpha(\mathrm{tr}\mathbf{d}), \tag{46}$$

in which, according to the second Onsager postulate $N_{\alpha\beta} = N_{\beta\alpha}$, and the following conditions should be satisfied:

$$N_{\alpha\alpha} > 0, \quad 2\mu + \lambda' \geq 0, \quad (2\mu + \lambda')^2 \geq 0, \quad k_s \geq 0, \quad k_v \geq 0, \tag{47}$$

$$\begin{aligned} &(2\mu + \lambda')\, N_{\alpha\alpha} - L_\alpha^2 \geq 0, \\ &2[(2\mu + \lambda')\, N_{\alpha\alpha}]^{\frac{1}{2}} > 2\,|L_\alpha|\,, \quad \alpha = 1, 2, 3 \ldots, n. \end{aligned} \tag{48}$$

In the above constitutive relations: $k_s$ means an entropy diffusion coefficient connected with the Fourier conductivity coefficient, $k_v$ is the volume diffusion coefficient (say: the Brenner coefficient), $\mu$ and $\lambda'$ are the Stokes shape and volumetric viscosity coefficients and $N_{\alpha\beta}$; $L_\alpha$ are nonequilibrium Maldenstam-Leontonovich diffusion coefficients. Let us note, in addition, that these coefficients must not be constant, but may depend on the parameters of the state of equilibrium.

## 8 The set of governing equations

Having for disposal the postulated balance of non-equilibrium state parameters in Eqs. (9) and (10), and knowing postulated relations between non-equilibrium and equilibrium state parameters (17) and (16), one can establish a final set of governing equations closed by the constitutive relations (43)–(46) and the caloric (recoverable, elastic) state relation (36). Let us note, that in a proposed final set of governing equations, the balance of energy (25) does not appear because it is identically fulfilled by the appropriate and consistent statement of the first and second law of thermodynamics.

The set of governing equations of the Carnot continuum with non-equilibrium state parameters is to be defined as follows:

a) *Balance of working fluid mass*

$$\frac{1}{\rho} = v + \left(1 + \frac{\pi - p}{p}\right) B_{\alpha\beta}\xi_\alpha\xi_\beta\,, \tag{49}$$

b) *Balance of working fluid momentum*

$$\frac{\partial}{\partial t}(\rho v_i) + \frac{\partial}{\partial x_j}(\rho v_i v_j + \pi\delta_{ij}) = \frac{\partial}{\partial x_j}\tau_{ij} + \rho b_i\,, \qquad i, j = x, y, z, \tag{50}$$

c) *Balance of specific non-equilibrium entropy*

$$\frac{\partial}{\partial t}(\rho s^*) + \frac{\partial}{\partial x_j}(\rho s^* v_j) = \frac{\partial}{\partial x_j} h_{(s)j} + \rho \sigma_s \,, \tag{51}$$

d) *Balance of specific non-equilibrium volume*

$$\frac{\partial}{\partial t}(\rho v^*) + \frac{\partial}{\partial x_j}(\rho v^* v_j) = \frac{\partial}{\partial x_j} h_{(v)j} + \rho \sigma_v \,. \tag{52}$$

In the above, it is assumed that the continuity equation is fulfilled from the beginning, and the definition (49) is so exact that one may not use the mass continuity explicitly. Now, the constitutive relations are defined by Eqs. (43)–(46) and (36), respectively. Basic unknown fields are: *velocity* $\mathbf{v}(\mathbf{x}, t)$, *specific equilibrium volume* $\mathrm{v}(\mathbf{x}, t)$, *specific equilibrium entropy* $s(\mathbf{x}, t)$ and the *non-equilibrium parameters* $\xi_\alpha$. The number of governing equations and the number of unknowns is $1 + 3 + 1 + n = 5 + n$, no matter whether we describe viscous or inviscid fluid, conductive or non-conductive fluid. In this approach, temperature appears only as the thermodynamical temperature (36), therefore, putting thermal boundary conditions it must be remembered that a measurable temperature differs from the thermodynamical one.

For the above set of equations, the boundary conditions should be described as follows:

a) *Known velocity vector at the boundary* $C_v$: $\mathbf{v}_{\|C_v} = \mathbf{v}^0$,

b) *Known value of measurable pressure at the boundary* $C_\pi$: $\pi_{\|C_\pi} = \pi^0$,

c) *Known value of thermodynamic temperature at the boundary* $C_T$: $T_{\|C_T} = T^0$ and the thermodynamic pressure $p_{\|C_T} = p^0$,

d) *Known value of volume flux and entropy flux at the boundary* $C_h$: $\mathbf{h}_v \cdot \mathbf{n} = h_v^0$ and $\mathbf{h}_s \cdot \mathbf{n} = h_s^0$,

e) *"Incipient point" for constitutive equation* (46) *for determination of a point and a moment of activation and passivation of this constitutive relation for the internal parameters.*

Boundary conditions a) and b) are related to the linear momentum equation, conditions c) and d) are related to the balance of entropy and balance of volume.

# 9 Further remarks on the concept of "non-equilibrium heat" and "non-equilibrium work"

The approach presented above is not the first solution to the problem. Other concepts, mainly based on the statement of non-equilibrium temperature and non-equilibrium pressure, are presented in the monographs of Kjelstrup and Bedeaux [7], Sieniutycz [17], Lebon *et al.* [28] and Ván [39]. However, within the ideal gas model and the timeless formulation close to the Carnot working continuum model, there are no original formulations that would lead directly to the foundations of finite-time thermodynamics [8].

In other words, within the framework of the approach known in the literature as the timeless approach, there is no clarity which of the models proposed in the literature is an important extension of Carnot's reversible approach to the non-equilibrium case.

In addition to non-equilibrium temperature, non-equilibrium pressure, non-equilibrium entropy, and non-equilibrium temperature, there are also solutions in the literature with "non-equilibrium heat flux" and "non-equilibrium work flux". Let us now discuss this last proposal from a timeless perspective. In this view, the first law of thermodynamics has the classical form of Clausius: $E = \eth Q - A\eth W$, where the Clausius equivalent today has a value of one: $A = 1$, and $dE$ is an increment of internal energy, $\eth Q$ is the heat gain and $\eth W$ is increment of work. This corresponds to our $\dfrac{d}{dt}E = \mathcal{F}_{\text{heat}} + \mathcal{F}_{\text{work}}$.

In 1976, Kestin proposed to divide the heat flux into two parts: a non-equilibrium and an equilibrium one [33]. Using similar arguments, Gujrati in 2011 proposed dividing the work flux into two parts: equilibrium and non-equilibrium [41]. According to this concept, you can write (Fig. 2):

$$\eth Q = d_{\text{irr}}Q + d_{\text{eq}}Q, \qquad \eth W = d_{\text{irr}}W + d_{\text{eq}}W. \tag{53}$$

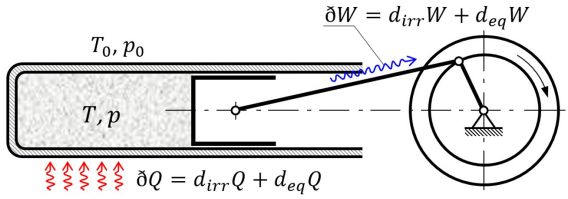


Figure 2: Separation of fluxes into equilibrium and non-equilibrium parts.

Integral values of state parameters are determined by equilibrium quantities: intensive $S$, $V$ and extensive: $T$, $p$. According to Kestin, the reversible part of heating flux defines equilibrium entropy $dS = d_{\mathrm{eq}}Q/T$ and according to Gujrati, the equilibrium part of the working flux defines the equilibrium volume $dV = d_{\mathrm{eq}}W/p$. Using these definitions, we have the first law of thermodynamics in the form

$$\begin{aligned} dE &= \eth Q - A\eth W = d_{\mathrm{irr}}Q + d_{\mathrm{eq}}Q - (d_{\mathrm{irr}}W + d_{\mathrm{eq}}W) \\ &= TdS - pdV + (d_{\mathrm{irr}}Q - d_{\mathrm{irr}}W) = TdS - pdV. \end{aligned} \tag{54}$$

Gujrati notes that the non-equilibrium parts of work and heat fluxes must compensate for each other so that [41, Eq. (4)]

$$(d_{\mathrm{irr}}Q - d_{\mathrm{irr}}W) = 0. \tag{55}$$

This condition strongly limits the magnitude of the fluxes, and it is a reason that the first law of thermodynamics finally becomes equivalent to the Gibbs equation. It is an unacceptable paradoxical result. If we use an uncompensated heat $\mathcal{N}_{\mathrm{heat}} = \oint d_{\mathrm{irr}}S$ and an uncompensated work: $\mathcal{N}_{\mathrm{work}} = \oint d_{\mathrm{irr}}V$, then from Eq. (55) it follows that: $\mathcal{N}_{\mathrm{heat}} = \mathcal{N}_{\mathrm{work}}$.

Therefore, the approach presented in Section 4 is of a different kind; it assumes that uncompensated heat $\sigma_s$ and uncompensated work $\sigma_v$ are to be field sources, not surface ones. Similarly, energy fluxes are conceived, which act as surface quantities that cannot be divided into reversible and irreversible parts. For example, heat energy flux is a function of the temperature gradient $\mathbf{g}_s = \operatorname{grad} T$. It can be divided when the temperature for instance is divisible:$T = T_{\mathrm{eq}} + T_{\mathrm{irr}}$. As you can see from the above, this approach spoils the concept of accompanying state and removes the possibility of developing 3D foundations for finite-time thermodynamics.

## 10 Concept of non-equilibrium energy

The concept of internal energy was finally introduced into thermodynamics by Gibbs in 1873. Internal energy has been defined as an invariant of motion expressed by state parameters. In the case of Carnot's working medium, these parameters were specific volume and specific entropy. Gibbs was the first to find the function $\varepsilon = \varepsilon(v, s)$ and to draw it as a surface in the space of state functions. Delighted by this fact, Maxwell made a plaster model of this surface in a wide range of values of state parameters, i.e.

for water, steam and ice. This surface was learned to be determined by experimentators – first for water and later for other gases and liquids.

It is difficult to imagine anything that would be a "non-equilibrium internal energy". Nevertheless, as of recently, Gian Paolo Beretta, standing in the position of quantum thermodynamics, believes that it is possible to define non-equilibrium internal energy as a function of non-equilibrium, independent, state parameters: $\varepsilon^* = \varepsilon^*(\gamma_1, \gamma_2, \gamma_3, \ldots)$ [38]. To ensure "full flexibility of formulation", Beretta introduces a new law of thermodynamics, which he nominates to the position of the "fourth law of thermodynamics".

In other words, Beretta states that this fourth principle is needed to introduce and motivate the concept of non-equilibrium internal energy. What is characteristic of Beretta's formulation is that he does not consider specific entropy as a basic (non-eliminable) parameter of the state, but expresses it through the experimentally unknown function $s^* = s^*(\gamma_1, \gamma_2, \gamma_3, \ldots)$. Contrary to the fundamental definition of Carnot, Reech, Rankine, Maxwell, the internal energy in Beretta's view is not a direct function of specific entropy.

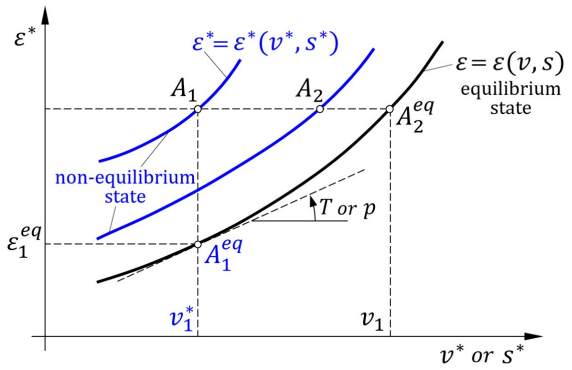


Figure 3: State representation of the non-equilibrium energy.

Note, that proposed by Beretta the evolution equations for non-equilibrium state parameters $\gamma_1$, $\gamma_2$, $\gamma_3$, ... have a form equivalent to our evolutionary equations $v^*$, $s^*$ – see Eqs. (51)–(52). In Beretta's equations, fluxes of non-equilibrium state parameters also appeared. They are marked by him by the letter $\mathbf{J}_\gamma$. They have the same status as our $\mathbf{h}_v$, $\mathbf{h}_s$ vectors, and they have nothing to do with the "thermodynamic fluxes" of LIT. According to Beretta, $\mathbf{J}_\gamma$ fluxes are subjected to various constraints, for example, the fluxes of state parameters should satisfy symmetry conditions similar to

the Onsager symmetry condition supposed on "thermodynamic fluxes". The essence of Beretta's proposal is the introduction of a metric $G_\gamma$ field and an intrinsic dissipation time $\tau_\gamma$, which span over the non-equilibrium space of energy at the point of contact. This metric and time allow the evolution of the non-equilibrium state to the optimal equilibrium state according to the fourth law of thermodynamics (SEA).

In conclusion, Beretta's concept goes further than our assumption about the possible evolution of non-equilibrium state parameters. His concept assumes the existence of a non-equilibrium energy spanning over a tangent space that has its own Riemannian metric and "intrinsic time".

However, in thermodynamical practice, there are no numerous connotations with the notion of "non-equilibrium internal energy" in the literature. Casas-Vázquez and Jou [37] have extensively discussed this problem, and they remark that in practice the internal energy cannot be a function of non-equilibrium state parameter.

## 11 The case of a solid

A solid continuum, like heat resistance steels [5], can be as good a working medium as liquids and gases. For heat engines, alloys that have high hidden heat of phase transition, e.g. austenite-martensite [42], are frequently used and the Carnot cycle has also four transformations.

In a solid body, state parameters and internal energy can also be successfully defined. The intrinsic energy of a solid state was first proposed by de Saint Venant and later by Poisson [42]. It has been called: "storage energy" and was a function of a generalized change in the specific volume of deformation and a generalized change in specific entropy. Both of these state parameters are denoted today by: $\mathbf{v} = v_{ij}\mathbf{e}_i \otimes \mathbf{e}_j$ and $\mathbf{s} = s_{ij}\mathbf{e}_i \otimes \mathbf{e}_j$, respectively. From a mathematical point of view, these are tensors; let us also assume that they are symmetric objects. Specific internal energy is therefore a function of both: $\varepsilon = \varepsilon(\mathbf{v}, \mathbf{s})$. For isotropic materials, the internal energy is a function of the invariants of both tensors [5]. If we accept Kirchhoff's assumption that the entropy tensor is simplified to be a spherical tensor, it is enough to use the entropy scalar $s = \frac{1}{3}\mathrm{tr}(\mathbf{s})$.

The equations of evolution of state parameters have a structure similar to our Eqs. (9)–(10):

$$\rho \overset{\Delta}{\overbrace{\mathbf{v}}} = \mathrm{div}\, \mathbb{h}_v + \rho \mathbf{n}_v\,, \qquad \rho \overset{\Delta}{\overbrace{\mathbf{s}}} = \mathrm{div}\, \mathbb{h}_s + \rho \mathbf{n}_s, \tag{56}$$

where $\mathbb{h}_v = h^v_{ijk}\mathbf{e}_i \otimes \mathbf{e}_j \otimes \mathbf{e}_k$, $\mathbb{h}_s = h^s_{ijk}\mathbf{e}_i \otimes \mathbf{e}_j \otimes \mathbf{e}_k$, are the volume and entropy fluxes, and $\mathbf{n}_v$, $\mathbf{n}_s$ are the uncompensated transformation of work and heat, in analogy to $\sigma_v$ and $\sigma_s$ in Eqs. (9)–(10).

Due to the fact that we deal with tensors, not with scalars, additional elements appear. The $\mathbb{h}_v$, $\mathbb{h}_s$ fluxes are third-order tensors, and their evolution is subjected to the Zaremba principle of relativity and must use an objective time derivative [5, 20]. Additionally, the Gibbs equation now has an objective form:

$$\frac{d}{dt}\varepsilon(\mathbf{vs}) = \frac{\partial \varepsilon}{\partial \mathbf{v}} \cdot \overset{\Delta}{\overbrace{\mathbf{v}}} + \frac{\partial \varepsilon}{\partial \mathbf{s}} \cdot \overset{\Delta}{\overbrace{\mathbf{s}}}. \tag{57}$$

This equation allows us, ultimately, to introduce the equation of evolution of state parameters into the energy balance. Let us note additionally that non-equilibrium parameters $\xi_\alpha$ in solid continuum are also tensors, which in the case of Prandtl-Reuss rate of plasticity can easily be interpreted physically [4, 5].

## 12 Conclusions

In the literature, there are several approaches to modelling of continua in non-equilibrium state (see: [4–6, 36–38]). Evidently, the main difficulty of this physical concept lies in these basic questions: how to define the "internal state", i.e. what are the variables to be chosen for this definition? Which variables can be taken to be: independent or dependent [24, 25]? Which variables can influence the dissipation of energy? Which thermodynamic law is first (more primitive)? Why most of the existing literature on thermodynamics does not admit an entropy balance but postulates an entropy inequality such as the Clausius-Duhem or similar inequalities? [29,30,39,40].

The main purpose of this note was to demonstrate another line of reasoning leading to a more consistent model of continuum with a non-equilibrium state. Two aspects of the present derivation are worth emphasising. First, the inclusion of balances of specific entropy and specific volume in the primitive form of balance of total energy provided a clearer interpretation of Kelvin's principle of desegregated energy. Second, the balance of entropy, which within the framework of inviscid fluid model plays an independent role, in the present development emerges naturally instead of being a separate postulate motivated by Carnot and Clausius.

The paper is based on the Beretta and Gyftopoulos exposition of thermodynamics [10, 38]. It means that "heat", as well as "work", plays no

role in our statement of the first law, also in the definition of internal energy where the intensive state parameters are primary objects. "Heat" and "work" notions are not present in our statement of the second law, and in the definition of entropy and specific volume. Our concept of "the energy flux" is based on collecting particular physical fluxes into one resulting balance. The most important are the momentum, volume and entropy flux exchanges between interacting systems. They are defined using these concepts and laws, after they have been independently and unambiguously introduced. In other words, "heat" and "work" are not the energy exchanged between systems, since we assume them to be more fundamental: heating and working processes. Does not exist "a heat interaction" but only "the flux of entropy".

Finally, let us note that in this paper, we develop and illustrate the general definition of equilibrium and non-equilibrium intensive state parameters within the Carnot working fluid. In view of the importance of non-equilibrium states for a wide range of applications of thermodynamics, we hope our efforts will help to remove obstacles to understating numerous physical phenomena (like the action of laser), yet not described within the framework of thermodynamics.

**Acknowledgements**

Part of the work was supported by NOR/POLNORCCS/NEGATIVE-CO2-PP/0009/2019-00 nCO2PP Negative CO2 emission gas power plant – project co-financed by Programme "Applied research" under the Norwegian Financial Mechanisms 2014–2021. However, another part of this paper has been accomplished within the frame of outgoing fellowship from Warmia and Masuria University at Olsztyn.

*Received 1 September 2023*

# References

[1] Carnot S.: *Réflexions sur la puissance motrice du feu*, Pairs: Bachelier 1824, (critical edition by R. Fox, Vrin, Paris, 1978).

[2] Carnot L.: *Essai sur les machines en général*, Dijon: Defay 1783 (Ital. transl. and critical edition by S.D. Manno and A. Drago, Naples: CUEN 1994).

[3] Ochrymiuk T., Banaszkiewicz M., Lemański M., Kowalczyk T., Ziółkowski P., Ziółkowski P.J., Hyrzyński R., Stajnke M., Bryk M., Kraszewski B., Kruk-Gotzman S., Froissart M., Badur J.: *Fluid solid interactions – a novelty in industrial applications.* Arch. Thermodyn. **43**(2022), 2, 75–96.

[4] Ochrymiuk T., Dudda W., Froissart M., Badur J.: *Principles of stress-strength modelling of the highly loaded materials – the influence of an effect of strength differential on the material effort.* Materials (Basel) **14**(2021), 23, 7449. doi: 10.3390/ma14237449

[5] Dudda W.: *Problems of Thermal Effort of a Heat-Resistant Naterial.* Wyd. UWM, Olsztyn 2021.

[6] Gyftopoulos E.P., Beretta G.P.: *Thermodynamics, Foundations and Applications* (2nd Edn.). Dover, Mineola New York 2005.

[7] Kjelstrup S., Bedeaux D.: *Non-equilibrium Thermodynamics of Heterogeneous Systems*, Word Sci., Singapore 2008.

[8] Feidt M.: *Thermodynamique et optimization énergétique das systems et procédés.* Technique et Documentation, Paris, 1987 (in French).

[9] Zanchini E., Beretta G.P.: *Removing heat and conceptual loops from the definition of entropy.* Int. J. Thermodyn. **13**(2010), 67–76.

[10] Beretta G.P., Gyftopoulos E.P.: *A novel sequence of exposition of engineering thermodynamics.* J. Energ. Res. Technol. **137**(2015), 021009-1. doi: 10.1115/1.4026385

[11] Natanson W.: *On the laws of viscosity.* Phil. Mag. **2**(1901), 342–356.

[12] Maldenstam L., Leontonovich M.: *A theory of sound absorption in liquids.* J. Exp. Theor. Phys. **7**(1937), 438–449.

[13] Szaniawski A.: *Relaxation phenomena in flow problems.* Arch. Mech. **10**(1958), 671–698.

[14] Meixner J.: *TIP has many faces.* In: Irreversible aspects of continuum mechanics (H. Parkus, L. Sedov, Eds.). Springer Verlag 1968, 237–249.

[15] Kestin J.: *Local-equilibrium formalism applied to mechanics of solids.* Int. J. Solids Struct. **29**(1992), 1827–1836.

[16] Brey J.J., Santos A.: *Non-equilibrium entropy of a gas.* Phys. Rev. A, **45**(1992), 8566–8572.

[17] Sieniutycz S.: *Conservation Laws in Variational Thermo-Hydrodynamics.* Kluwer Academic, Dordrecht 1994

[18] Bilicki Z., Kestin J.: *Physical aspects of the relaxation model in two-phase flow.* Proc. Royal. Soc. London A **428**(1990), 379–397.

[19] Bilicki Z., Badur J.: *A thermodynamically consistent relaxation model for turbulent binary mixture undergoing phase transition.* J. Non-Equil. Thermodyn. **28**(2003), 145–172.

[20] Badur J., Nastałek L.: *Thermodynamics of thermo-deformable solids.* In: Encyclopaedia of Thermal Stresses (1st Edn.), (R. Hetnarski, Ed.). Springer Verlag, Dordrecht, 2014.

[21] Badur J., Ochrymiuk, T., Kowalczyk, T., Dudda, W., Ziółkowski P.: *From fluid mechanics backgrounds to modern field theory.* Acta Mech. **233**(2022), 8, 3453–3465.

[22] Gaggioli R.A.: *Principles of thermodynamics.* In: Thermodynamics: Second Law Analysis (R.A. Gaggioli, Ed.); Washington, Washington DC 1980, 1–13.

[23] Fülöp T., Ván P., Csatár A.: *Elasticity, plasticity, rheology and thermal stress – an irreversible thermodynamical theory*. In: Proc. 12th Joint European Thermodynamics Conf., JETC 2013 (M. Pilotelli, G.P. Beretta, Eds.), Brescia, July 1-5, 2013. Snoopy, Brescia 2013, 525–530.

[24] Grmela M., Öttinger H.C.: *Dynamics and thermodynamics of complex fluids. I. Development of a general formalism*. Phys. Rev. **56**(1997), 6620–6632.

[25] von Spakovsky M.R.: *Intrinsic quantum thermodynamic; what it is and what can be done with it*. In: Proc. 12th Joint European Thermodynamics Conf., JETC 2013 (M. Pilotelli, G.P. Beretta, Eds.), Brescia, July 1-5, 2013. Snoopy, Brescia 2013, 359–369.

[26] Palazzo P.: *Proposal for generalized exergy and entropy properties based on stable equilibrium of composed system-reservoir*. J. Mod. Phys. **4**(2013), 52–58.

[27] Ván P.: *Weakly non-local irreversible thermodynamics – The Guyer-Krumhal and the Chan-Hillard equations*. Phys. Lett. A **290**(2001), 88–91.

[28] Lebon G., Jou D., Casas-Vázques J.: *Understanding Non-equilibrium Thermodynamics*. Springer, Berlin 2008.

[29] Bejan A.: *Entropy Generation Through Heat and Fluid Flow*. Wiley, New York 1982.

[30] Mieczyński M.: *The Essence of Symmetry in Classical and Contemporary Thermodynamics*. Oficyna PW, Wrocław 2002 (in Polish).

[31] Born M.: *Kritische Betrachtungen zur traditionellen Darstellung der Thermodynanik*. Phys. Zeitschr. **22**(1921), 210–230.

[32] Bridgeman P.W.: *The Logic of Modern Physics*. Willey, New York 1960.

[33] Kestin J.: *Thermodynamics (An essay)*. In: Fluid-Flow Machinery Problems (Z. Bilicki, *at al.* Ed.), 319–252, Wydawn. IMP PAN, Gdańsk 1993.

[34] Eglit M.E.: *Generalization of the model of an ideal compressible fluid*. PMM **32**(1965), 771–785.

[35] Badur J., Banaszkiewicz M.: *Model of the ideal fluid with scalar microstructure, An application to flashing flow of water*. Trans. Inst. Fluid-Flow Mach. **105**(1999), 115–152.

[36] Lebon G., Casas-Vazquez J., Jou D.: *On the definition of non-equilibrium*. J. Phys. A: Math. Gen. **15**(1982), 565–584.

[37] Casas-Vázquez J., Jou D.: *Temperature in non-equilibrium states: a review of open problems and current proposals*. Rep. Prog. Phys. **66**(2003), 1937–2023.

[38] Beretta G.P.: *Steepest entropy ascent model for far-non-equilibrium thermodynamics. Unified implementation of the maximum entropy production principle*. Phys. Rev. E **90**(2014), 042113.

[39] Ván P. 2020 *Non-equilibrium thermodynamics: emergent and fundamental*. Phil. Trans. R. Soc. A 378, 20200066. doi: 10.1098/rsta.2020.006

[40] Lucia U., Grisolia G.: *Non-equilibrium temperature: An approach from irreversibility*. Materials (Basel) **14**(2021), 8, 2004. doi: 10.3390/ma14082004

[41] Gujrati P.D.: *Generalized non-equilibrium heat and work and the fate of the Clausius inequality*. UATP **1103**(2011), 1–4.

[42] Badur J.: *Evolution of the Energy Notion*. Wydawn. IMP PAN, Gdańsk 2009.

**archives**
**of thermodynamics**
Vol. **44**(2023), No. 4, 317–333
DOI: 10.24425/ather.2023.149712

# Steady state and transient analysis of solid oxide fuel cell within the framework of thermodynamic energy cycles

**ROBERT MATYSKO***

Institute of Fluid Flow Machinery, Polish Academy of Sciences,
Fiszera 14, 80-231 Gdańsk, Poland

**Abstract** The provided article comprehensively explores the modelling and analysis of solid oxide fuel cell (SOFC) systems within the context of thermodynamic energy cycles. The paper provides insight into various applications of these cells, with a specific emphasis on their role as the primary source of electrical energy in systems that work with biogas and heat recovery. The technological structure of these systems is delineated, with a focus on their principal components and the chemical reactions occurring within SOFCs. Moreover, the article incorporates a mathematical model of SOFCs and presents calculation results that illustrate the influence of air and fuel temperature on the cells' efficiency. The research indicates that optimal SOFC efficiency is attained at higher temperatures of supplied air and fuel. The presentation of the results of calculations for the solid oxide fuel cell and its thermodynamic cycle, considering fuel supply and its thermodynamic parameters under both steady-state and transient conditions, is the main aim of the article.

**Keywords:** SOFC; Transient model; Thermal cycle

## Nomenclature

| | | |
|---|---|---|
| $c_p$ | – | specific heat at constant pressure, J/kg/K |
| $E$ | – | reversible potential of each cell, V |
| $h$ | – | molar enthalpy, J/kmol |
| $\Delta H_f^o$ | – | standard enthalpy of formation for the respective chemical species, J/kmol |
| $I$ | – | electric current, A |

*Corresponding Author. Email: matyskor@imp.gda.pl

$K$ – equlibrum reaction constant
$M$ – mass, kg
$\dot{n}$ – molar flow rate, kmol/s
$\dot{Q}$ – heat flow, W
$p$ – pressure, Pa
$P$ – theoretical power, W
$T$ – temperature, K
$t$ – time, s
$U$ – voltage, V
$W$ – ORC turbine power, W

**Subscripts**

act – activation
cat – cathode
$CH_4$ – methane
CO – carbon monoxide
$CO_2$ – carbon dioxide
con – conversion
conc – concentration
cond – ORC condenser
cpo – catalytic partial oxidation of methane
dir – direct internal reforming reaction
evap – ORC evaporator
$fc$ – fuel cell
$H_2$ – hydrogen
$H_2O$ – water
in – inlet
$N_2$ – nitrogen
$O_2$ – oxygen
ohm – Ohmic
out – outlet
prod – production
ref – reforming process
th – theoretically
wgs – water gas shift reaction

**Acronyms**

ORC – organic Rankine cycle
SOFC – solid oxide fuel cell

# 1 Introduction

Thermodynamic cycles that consider the introduction of fuel cells have various accompanying systems in their structure [1]. Below, among many proposed applications, systems are presented where fuel cells constitute the

main source of electric power generation. Figure 1 depicts the technological arrangement of a fuel cell in collaboration with a biogas system and waste heat recovery systems. The arrangement in Fig. 1 is a modification of a gas turbine system described in reference [2]. The configuration in Fig. 2 is a modification of a system presented in reference [3], designed for cooperation with low-temperature systems.

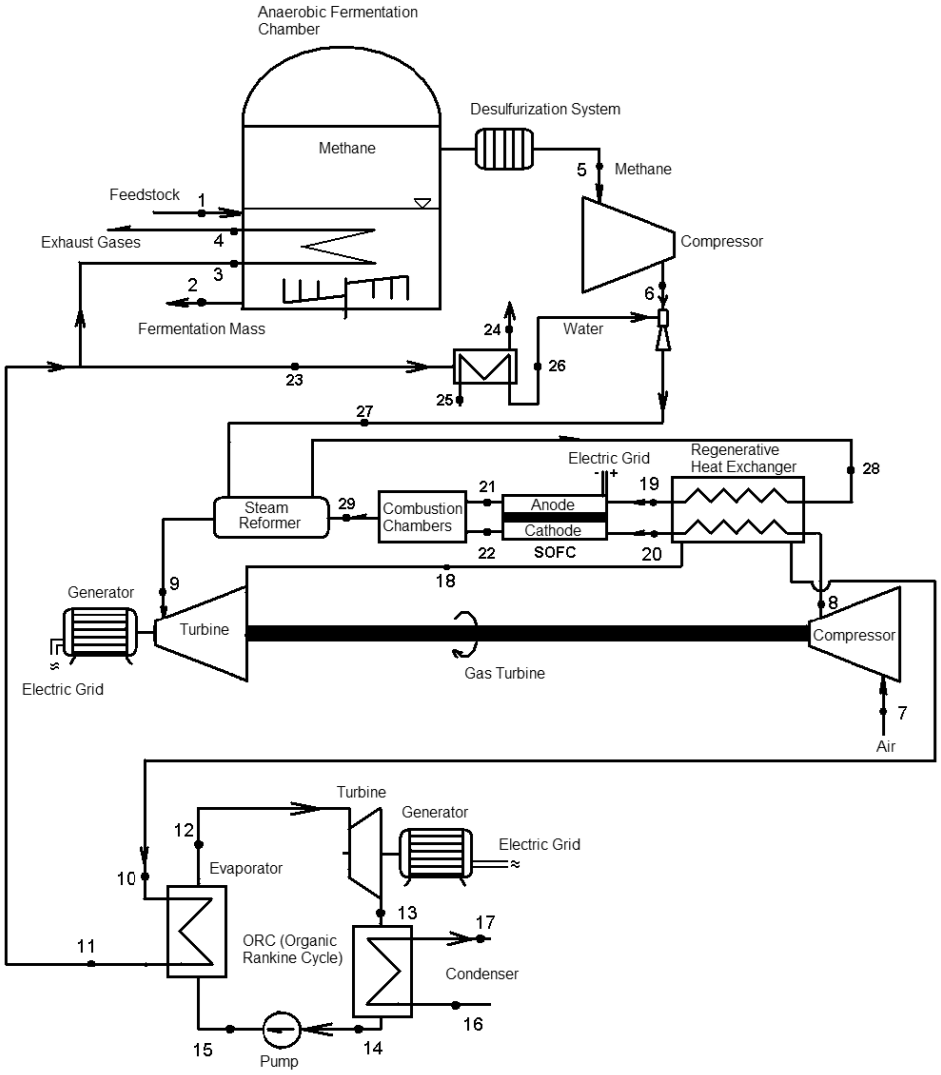


Figure 1: Fuel cell cycle in cooperation with a gas turbine and ORC system.

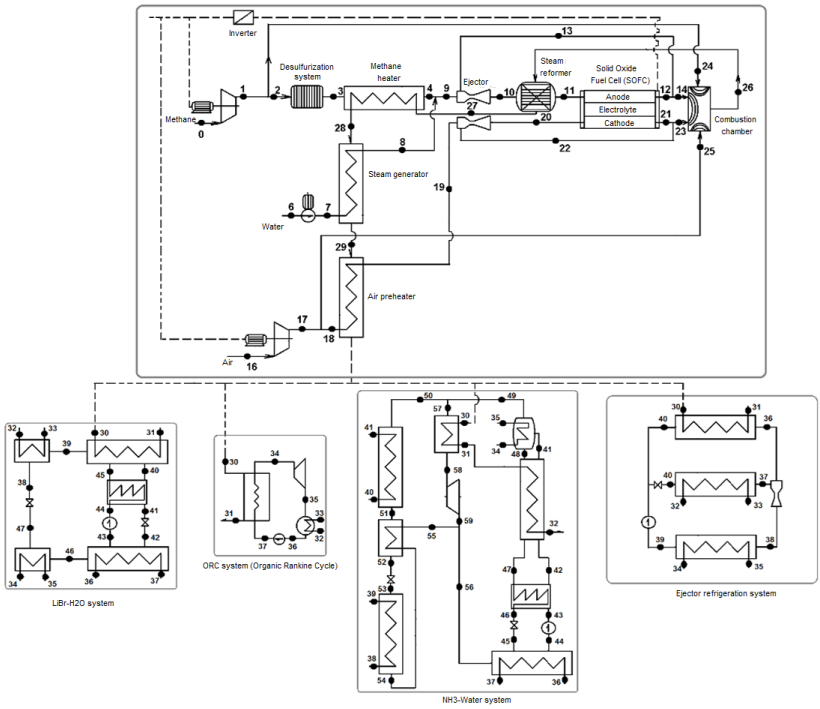


Figure 2: Trigeneration/polygeneration system with a fuel cell and its potential cooperation with absorption systems LiBr-H2O, NH3-H2O, ejector refrigeration cycle, and ORC.

The installation presented in Fig. 2 is constructed with main components such as:

a) fermentation chamber and biogas desulfurization system; this chamber typically comprises a supply system, a heating system, a mixing system, a system for discharging post-fermentation mass, and a biogas disposal system;

b) gas turbine containing an air compressor, combustion chamber, reforming system, fuel cell, and a turbine, where the expansion of the reaction products from the combustion chamber and fuel cell occurs. An additional system in this case is the compression system for biogas to the pressure required in the combustion chamber and fuel cell;

c) ORC (organic Rankine cycle) with a steam generator, condenser, steam turbine with a generator, and circulating pump.

The arrangement in Fig. 2 consists of a fuel cell subsystem [2,4] and/or, alternatively, subsystems for low-temperature heat recovery such as:

- ejector cooling system [3],
- bromide cooling system or heat pumps [5],
- hybrid ammonia cooling system [5],
- ORC system [2].

The fuel cell circuit subsystem comprises a sulfur removal, methane and air preheating, steam generation, steam reforming, solid oxide fuel cell, combustion chamber, and feed pumps and fans.

Additional systems for low-temperature heat recovery significantly enhance the energy efficiency of the entire SOFC-based system. To confirm this, calculations were performed for an SOFC cycle integrated with the ORC system. Below, the mathematical model of the fuel cell and the calculation results for the integrated cycle with the ORC system are presented.

## 2 Modelling of solid oxide fuel cell in steady state

The fuel cell cycle from a thermodynamic perspective is a flow system in which complex chemical reactions occur, leading through catalysis to the breakdown of fuel, generation of electric current, and chemical products of this reaction.

Thermodynamic processes that are essential for the creation of a fuel cell are described in more detail in references [6–9]. These processes include:

- Partial oxidation through catalysis (CPO - catalytic partial oxidation), which is realized according to the reaction [10]:

$$C_nH_m + \frac{n}{2}O_2 \rightarrow nCO + \frac{m}{2}H_2\,. \tag{1}$$

  This reaction occurs within the temperature range of 800 to 900°C. Nickel can serve as a catalyst in this process. In this case, high purity gas without sulfur impurities is required, below 50 ppm.

- Steam reforming (DIR – direct internal reforming), also realized with the presence of a nickel catalyst within the temperature range of

700 to 1100°C. During reforming, an endothermic reaction occurs, consuming heat [11]:

$$CH_4 + H_2O \rightarrow CO + 3H_2\,. \tag{2}$$

- Water gas shift reaction (WGS) – an exothermic reaction, producing heat [11]:

$$CO + H_2O \rightarrow CO_2 + H_2\,. \tag{3}$$

- Reaction in the solid oxide fuel cell (SOFC), which can be divided into local reactions occurring in the anode and cathode, yielding steam as the global product. In contrast to the proton-exchange membrane (PEM) fuel cell [8], in the SOFC, water is produced on the anode side according to the following reactions [7]:

$$\begin{aligned} &H_2 + O^{2-} \rightarrow H_2O + 2e^- \quad \text{– anode reaction,}\\ &\frac{1}{2}O_2 + 2e^- \rightarrow O^{2-} \quad \text{– cathode reaction,}\\ &H_2 + \frac{1}{2}O_2 \rightarrow H_2O \quad \text{– overall reaction.} \end{aligned}$$

In SOFCs, $Y_2O_3$ yttria-stabilized $ZrO_2$ is most commonly used as the electrolyte. The anode material consists of chemical compounds like Co-$ZrO_2$ and $NiZrO_2$. The cathode material utilizes the chemical compound Sr+$LaMnO_3$.

To model the phenomena occurring in the SOFC, the following assumptions were made:

- The model describes a steady-state operation of the SOFC.
- Chemical reactions are modelled using molar mass and energy balances.
- The description of thermodynamic properties of reacting substances relies on Helmholtz equations.
- The processes are described in accordance with the isobaric potential.
- The systems are isolated.
- The reactions occur in an equilibrium manner.
- Issues related to the geometry and material properties of the fuel cell are omitted.

The equations describing the processes occurring in SOFC are presented below (with the symbols explained in the Nomenclature section):

- Molar nitrogen flux on the anode side

$$\dot{n}_{\mathrm{N_2},fc,\mathrm{out}} = \dot{n}_{\mathrm{N_2},\mathrm{cpo},\mathrm{out}} \,. \tag{4}$$

- Molar nitrogen flux on the cathode side

$$\dot{n}_{\mathrm{N_2},\mathrm{cat},\mathrm{out}} = \dot{n}_{\mathrm{N_2},\mathrm{cat},\mathrm{in}} \,. \tag{5}$$

- Molar methane flux during reforming

$$\dot{n}_{\mathrm{CH_4},\mathrm{ref}} = \dot{n}_{\mathrm{CH_4},\mathrm{cpo},\mathrm{out}} K_{fc,\mathrm{CH_4-H_2}} \,. \tag{6}$$

- Equilibrium constant for the reaction $CH_4$-$H_2$

$$K_{fc,\mathrm{CH_4-H_2}} = 0.95. \tag{7}$$

- Molar hydrogen flux during reforming

$$\dot{n}_{\mathrm{H_2},fc,\mathrm{ref}} = 3\dot{n}_{\mathrm{CH_4},\mathrm{ref}} \,. \tag{8}$$

- Molar carbon monoxide flux during reforming

$$\dot{n}_{\mathrm{CO},fc,\mathrm{ref}} = \dot{n}_{\mathrm{CH_4},\mathrm{ref}} \,. \tag{9}$$

- Molar water flux during reforming

$$\dot{n}_{\mathrm{H_2O},fc,\mathrm{ref}} = \dot{n}_{\mathrm{CH_4},\mathrm{ref}} \,. \tag{10}$$

- Molar flow of carbon monoxide during steam conversion

$$\dot{n}_{\mathrm{CO},fc,\mathrm{wgs}} = \left(\dot{n}_{\mathrm{CO},\mathrm{cpo},\mathrm{out}} + \dot{n}_{\mathrm{CO},fc,\mathrm{ref}}\right) K_{fc,\mathrm{CO\text{-}H_2}} \,. \tag{11}$$

- Equilibrium constant for the reaction CO-$H_2$

$$K_{fc,\mathrm{CO\text{-}H_2}} = 0.643. \tag{12}$$

- Molar flow of water vapour during carbon monoxide conversion

$$\dot{n}_{\mathrm{H_2O},fc,\mathrm{wgs}} = \dot{n}_{\mathrm{CO},fc,\mathrm{wgs}} \,. \tag{13}$$

- Molar flow of hydrogen during carbon monoxide conversion with water vapour

$$\dot{n}_{\mathrm{H_2},fc,\mathrm{wgs}} = \dot{n}_{\mathrm{CO},fc,\mathrm{wgs}} \,. \tag{14}$$

- Molar flow of carbon dioxide during carbon monoxide conversion with water vapour

$$\dot{n}_{\mathrm{CO_2},fc,\mathrm{wgs}} = \dot{n}_{\mathrm{CO},fc,\mathrm{wgs}} \,. \tag{15}$$

- Total molar flow of hydrogen resulting from the conducted chemical reactions

$$\dot{n}_{\mathrm{H_2,dir,out}} = \dot{n}_{\mathrm{H_2,cpo,out}} + \dot{n}_{\mathrm{H_2},fc,\mathrm{ref}} + \dot{n}_{\mathrm{H_2},fc,\mathrm{wgs}} \,. \tag{16}$$

- Total molar flow of carbon monoxide resulting from the conducted chemical reactions

$$\dot{n}_{\mathrm{CO,dir,out}} = \dot{n}_{\mathrm{CO},cpo,out} + \dot{n}_{\mathrm{CO},fc,\mathrm{ref}} - \dot{n}_{\mathrm{CO},fc,\mathrm{wgs}} \,. \tag{17}$$

- Total molar flow of water vapour resulting from the conducted chemical reactions

$$\dot{n}_{\mathrm{H_2O,dir,out}} = \dot{n}_{\mathrm{H_2O,cpo,out}} - \dot{n}_{\mathrm{H_2O},fc,\mathrm{ref}} - \dot{n}_{\mathrm{H_2O},fc,\mathrm{wgs}} \,. \tag{18}$$

- Total molar flow of carbon dioxide resulting from the conducted chemical reactions

$$\dot{n}_{\mathrm{CO_2,dir,out}} = \dot{n}_{\mathrm{CO_2,cpo,out}} + \dot{n}_{\mathrm{CO_2},fc,\mathrm{wgs}} \,. \tag{19}$$

- Molar flow of methane resulting from the conducted chemical reactions

$$\dot{n}_{\mathrm{CH_4,dir,out}} = \dot{n}_{\mathrm{CH_4,cpo,out}} \left(1 - K_{fc,\mathrm{CH_4-H_2}}\right) . \tag{20}$$

- Outlet molar flow of methane from SOFC

$$\dot{n}_{\mathrm{CH_4},fc,\mathrm{out}} = \dot{n}_{\mathrm{CH_4,dir,out}} \,. \tag{21}$$

- Outlet molar flow of carbon monoxide from SOFC

$$\dot{n}_{\mathrm{CO},fc,\mathrm{out}} = \dot{n}_{\mathrm{CO,dir,out}} \,. \tag{22}$$

- Outlet molar flow of carbon dioxide from SOFC

$$\dot{n}_{\mathrm{CO_2},fc,\mathrm{out}} = \dot{n}_{\mathrm{CO_2,dir,out}} \,. \tag{23}$$

- Molar flow of hydrogen undergoing conversion in SOFC

$$\dot{n}_{\mathrm{H_2},fc,\mathrm{con}} = \dot{n}_{\mathrm{H_2},\mathrm{dir,out}}\,. \tag{24}$$

- Molar flow of hydrogen at the outlet of SOFC

$$\dot{n}_{\mathrm{H_2},fc,\mathrm{out}} = \dot{n}_{\mathrm{H_2},\mathrm{dir,out}} - \dot{n}_{\mathrm{H_2},fc,\mathrm{con}}\,. \tag{25}$$

- Molar flow of water produced in SOFC

$$\dot{n}_{\mathrm{H_2O},fc,\mathrm{prod}} = \dot{n}_{\mathrm{H_2},fc,\mathrm{con}}\,. \tag{26}$$

- Molar demand for oxygen to facilitate the conversion of hydrogen fuel in SOFC

$$\dot{n}_{\mathrm{O_2},\mathrm{catode,con}} = 0.5\dot{n}_{\mathrm{H_2},fc,\mathrm{con}}\,. \tag{27}$$

- Molar flow at the cathode outlet of SOFC

$$\dot{n}_{\mathrm{O_2,out,catode}} = \dot{n}_{\mathrm{O_2,catode,in}} + \dot{n}_{\mathrm{O_2,catode,con}}\,. \tag{28}$$

- Molar flow of produced water vapour at the anode of SOFC

$$\dot{n}_{\mathrm{H_2O,out}} = \dot{n}_{\mathrm{H_2O,dir,out}} + \dot{n}_{\mathrm{H_2O,prod,out}}\,. \tag{29}$$

- Thermal potential equation describing the substances supplied to SOFC

$$\begin{aligned}
\dot{Q}_{fc,in} = \Big[&\dot{n}_{\mathrm{CH_4,in}}\left(\Delta H^o_{f,\mathrm{CH_4}} + h_{\mathrm{CH_4,in}} - h_{\mathrm{CH_4,amb}}\right)\\
+\ &\dot{n}_{\mathrm{H_2O,in}}\left(\Delta H^o_{f,\mathrm{H_2O}} + h_{\mathrm{H_2O_{in}}} - h_{\mathrm{H_2O_{amb}}}\right)\\
+\ &\dot{n}_{\mathrm{CO,in}}\left(\Delta H^o_{f,\mathrm{CO}} + h_{\mathrm{CO_{in}}} - h_{\mathrm{CO_{amb}}}\right)\\
+\ &\dot{n}_{\mathrm{CO_2,in}}\left(\Delta H^o_{f,\mathrm{CO_2}} + h_{\mathrm{CO_{2,in}}} - h_{\mathrm{CO_{2,amb}}}\right)\\
+\ &\dot{n}_{\mathrm{H_2,in}}\left(\Delta H^o_{f,\mathrm{H_2}} + h_{\mathrm{H_{2,in}}} - h_{\mathrm{H_{2,amb}}}\right)\\
+\ &\dot{n}_{\mathrm{N_2,in}}\left(\Delta H^o_{f,\mathrm{N_2}} + h_{\mathrm{N_{2,in}}} - h_{\mathrm{N_{2,out}}}\right)\Big]_{\mathrm{anode}}\\
+\ &\Big[\dot{n}_{\mathrm{O_2,in}}\left(\Delta H^o_{f,\mathrm{O_2}} + h_{\mathrm{O_{2,in}}} - h_{\mathrm{O_{2,amb}}}\right)\\
+\ &\dot{n}_{\mathrm{N_2,in}}\left(\Delta H^o_{f,\mathrm{N_2}} + h_{\mathrm{N_{2,in}}} - h_{\mathrm{N_{2,out}}}\right)\Big]_{\mathrm{catode}}\,.
\end{aligned} \tag{30}$$

- Equation describing the thermal potential of substances exiting SOFC

$$\begin{aligned}\dot{Q}_{fc,\mathrm{out}} = \Big[&\dot{n}_{\mathrm{CH_4,out}}\left(\Delta H^o_{f,\mathrm{CH_4}} + h_{\mathrm{CH_{4,out}}} - h_{\mathrm{CH_{4,amb}}}\right)\\ &+\ \dot{n}_{\mathrm{H_2O,out}}\left(\Delta H^o_{f,\mathrm{H_2O}} + h_{\mathrm{H_2O_{out}}} - h_{\mathrm{H_2O_{amb}}}\right)\\ &+\ \dot{n}_{\mathrm{CO,out}}\left(\Delta H^o_{f,\mathrm{CO}} + h_{\mathrm{CO_{out}}} - h_{\mathrm{CO_{amb}}}\right)\\ &+\ \dot{n}_{\mathrm{CO_2,out}}\left(\Delta H^o_{f,\mathrm{CO_2}} + h_{\mathrm{CO_{2,out}}} - h_{\mathrm{CO_{2,amb}}}\right)\\ &+\ \dot{n}_{\mathrm{H_2,out}}\left(\Delta H^o_{f,\mathrm{H_2}} + h_{\mathrm{H_{2,out}}} - h_{\mathrm{H_{2,amb}}}\right)\\ &+\ \dot{n}_{\mathrm{N_2,out}}\left(\Delta H^o_{f,\mathrm{N_2}} + h_{\mathrm{N_{2,out}}} - h_{\mathrm{N_{2,amb}}}\right)\Big]_{\mathrm{anode}}\\ &+\ \Big[\dot{n}_{\mathrm{O_2,out}}\left(\Delta H^o_{f,\mathrm{O_2}} + h_{\mathrm{O_{2,out}}} - h_{\mathrm{O_{2,amb}}}\right)\\ &+\ \dot{n}_{\mathrm{N_2,out}}\left(\Delta H^o_{f,\mathrm{N_2}} + h_{\mathrm{N_{2,out}}} - h_{\mathrm{N_{2,amb}}}\right)\Big]_{\mathrm{catode}}. \end{aligned} \tag{31}$$

- Theoretical power generated in the fuel cell

$$P_{fc} = \dot{Q}_{fc,\mathrm{in}} - \dot{Q}_{fc,\mathrm{out}}\,. \tag{32}$$

In Table 1, the input data for the calculations of the fuel cell are presented. The mathematical model of the fuel cell, expressed by Eqs. (4)–(32) was used to compute the fuel cell parameters. When calculating the fuel cell parameters, the inlet temperature of the working fluids to the fuel cell was assumed as the variable parameter.

The results of the calculations based on the model using input data are presented in Fig. 3. As a result of the conducted calculations, it was observed that the power produced in the fuel cell doubles, with an increase in the inlet temperature of the reacting substances by 200°C. This leads to the conclusion that both, the fuel and the oxidant need to be supplied to the SOFC at a high temperature in order to generate electrical power more efficiently. The high thermal parameters impose special requirements on the materials used for pipelines in the installation due to safety concerns and sealing at a pressure of 1.23 MPa.

In Fig. 3, the theoretical power achievable in the fuel cell, resulting from the first law of thermodynamics (specifically from Eqs. (29) to (34)) is presented. the electric current produced in the fuel cell is not directly and strictly related to the theoretical power because it depends on the molar hydrogen flow rate, Faraday's constant, and the material and geometric

Table 1: Input data for fuel cell calculations.

| Molar inflow rates of components at the fuel cell anode for the calculations presented in Fig. 3 | | | |
|---|---|---|---|
| Substance | Symbol | Unit | Value |
| $CH_4$ | $\dot{n}_{CH_4,in}$ | kmol/s | 0.000001110 |
| $H_2O$ | $\dot{n}_{H_2O,in}$ | kmol/s | 0.000007844 |
| CO | $\dot{n}_{CO,in}$ | kmol/s | 0.000002848 |
| $H_2$ | $\dot{n}_{H_2,in}$ | kmol/s | 0.000032700 |
| $N_2$ | $\dot{n}_{N_2,in}$ | kmol/s | 0.000010610 |
| $CO_2$ | $\dot{n}_{CO_2,in}$ | kmol/s | 0.000003474 |
| Molar inflow rates of components at the cathode inlet of the fuel cell during calculations | | | |
| $N_2$ | $\dot{n}_{N_2,in}$ | kmol/s | 0.0002324 |
| $O_2$ | $\dot{n}_{O_2,in}$ | kmol/s | 0.0003850 |

| Thermodynamic parameters of SOFC | | | |
|---|---|---|---|
| Parameter | Symbol | Unit | Value |
| Inlet and outlet pressure on the cathode and anode sides | $p_{in,K}$, $p_{in,A}$, $p_{out,K}$, $p_{out,A}$ | Pa | 1231000 |
| Temperature of the fuel and oxidant at the inlet to the fuel cell | $T_{in,A}$, $T_{in,K}$ | K | 800–1000 |
| Temperature of the substances at the outlet from the fuel cell | $T_{out,K}$, $T_{out,A}$ | K | 1023 |
| Standard molar enthalpy of formation CO | $\Delta H^o_{f,CO}$ | J/kmol | –110 530 000 |
| Standard molar enthalpy of formation $CO_2$ | $\Delta H^o_{f,CO_2}$ | J/kmol | –393 520 000 |
| Standard molar enthalpy of formation $H_2O$ | $\Delta H^o_{f,H_2O}$ | J/kmol | –285 900 000 |
| Standard molar enthalpy of formation $CH_4$ | $\Delta H^o_{f,CH_4}$ | J/kmol | –74 850 000 |

properties of the fuel cell itself. Both material properties and geometric parameters of the fuel cell have an impact on the actual power obtained in the fuel cell. However, a detailed description of these issues significantly exceeds the scope of thermodynamics and falls within the realm of materials engineering and electrochemistry [12–14].

Theoretically, the total electrical current can be determined by the equation

$$\dot{n}_{H_2} 2F = 4\dot{n}_{O_2} F = I\,. \tag{33}$$

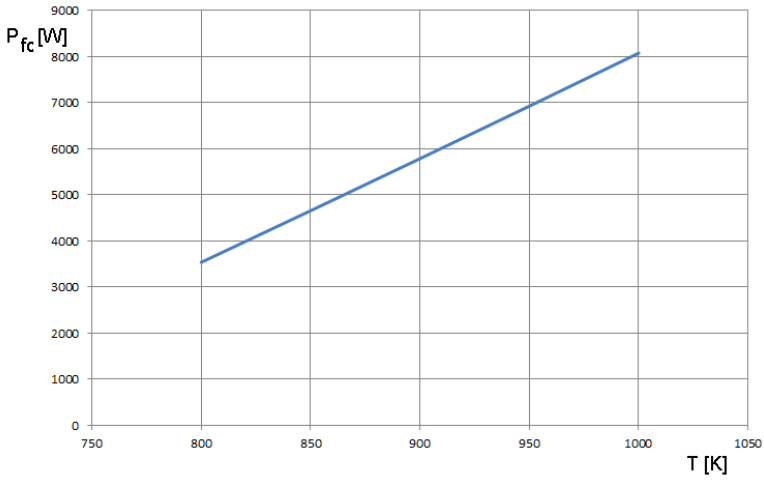


Figure 3: Calculations of the theoretical power obtained in the fuel cell due to the change in the inlet temperature of the working fluids.

The maximum theoretical voltage that can be achieved from the equation

$$UI\eta = P_{fc}\,, \tag{34}$$

where $\eta$ represents the overall efficiency of the SOFC cell, incorporating material properties, electrochemical effects, and more.

In addition to the calculations based on the previously presented mathematical model of the SOFC, the overall system depicted in Fig. 2 was also balanced. In this case, thermal parameters and molar flow rates of reactants at the outlets of the reforming systems and the SOFC were obtained (Fig. 4). As an illustrative solution for heat recovery, an ORC system was employed in this cycle.

The high material requirements for constructing installations with SOFCs contribute to high investment costs. The challenges in designing such installations are not only related to the SOFC system itself but also to its accompanying sub-systems (reformer, heat exchangers, purification and desulfurization systems). These challenges and the associated high costs may arise during the next stages of research, but ultimately, a highly efficient source of electricity production can be achieved. Due to the significant potential for using SOFCs in Europe, implementation-oriented research is already being conducted for SOFC installations with capacities up to 5 kW [15].

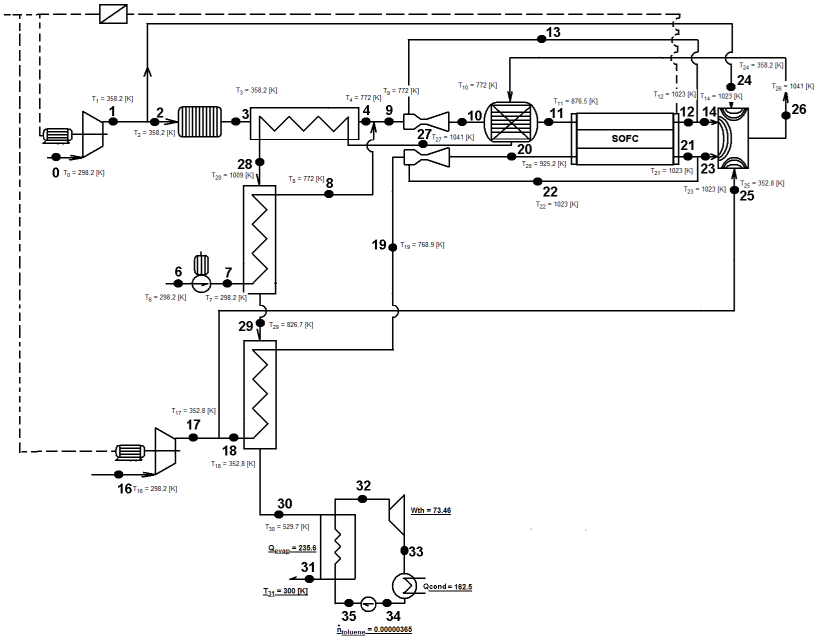


(a)

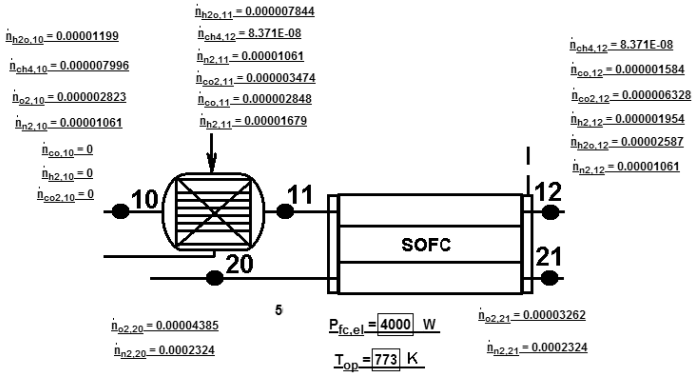


(b)

Figure 4: Exemplary thermal parameters in the fuel cell circuit working with a waste heat recovery system in the form of an ORC system: (a) solid oxide fuel cell (SOFC) circuit; (b) fuel cell parameters: $T_0 = 298.2$ K, $T_1 = 358.2$ K, $T_2 = 358.2$ K, $T_3 = 358.2$ K, $T_4 = 772$ K, $T_6 = 358.2$ K, $T_7 = 298.2$ K, $T_8 = 772$ K, $T_9 = 772$ K, $T_{10} = 772$ K, $T_{11} = 876.5$ K, $T_{12} = 1023$ K, $T_{14} = 1023$ K, $T_{16} = 298.2$ K, $T_{17} = 352.8$ K, $T_{18} = 352.8$ K, $T_{19} = 768.9$ K, $T_{20} = 925.2$ K, $T_{21} = 1023$ K, $T_{22} = 1023$ K, $T_{23} = 1023$ K, $T_{24} = 358.2$ K, $T_{25} = 352.8$ K, $T_{26} = 1041$ K, $T_{27} = 1041$ K, $T_{28} = 1009$ K, $T_{29} = 826.7$ K, $T_{30} = 529.7$ K, $T_{31} = 300$ K, $\dot{Q}_{\mathrm{evap}} = 235.6$ W, $W_{th} = 73.45$ W, $\dot{Q}_{\mathrm{cond}} = 162.5$ W, $\dot{n}_{\mathrm{toluene}} = 0.00000365$ kmol/s.

## 3 Solid oxide fuel cell modelling under transient conditions

In the previous chapter, we discussed the steady-state model of the SOFC. In this chapter, we will describe the mathematical model of the SOFC and its computations for unsteady-state conditions. The mathematical model is similar to the one presented in the previous chapter. However, in contrast to the model described in the first part of this article, we have relaxed the assumption that the model is time-invariant in order to model the phenomena occurring in the SOFC. In the mathematical model presented in this chapter, we assume that SOFC operates under unsteady-state conditions over time.

For the SOFC, the general dynamics equation takes the following form:

$$\frac{d\,(TMc_p)}{dt} = \dot{Q}_{fc,\mathrm{in}} - P_{fc} - \dot{Q}_{fc,\mathrm{out}}\,. \tag{35}$$

If we assume that reacting masses and their specific heats do not change over time, the equation takes the form [7]:

$$Mc_p\frac{dT}{dt} = \dot{Q}_{fc,\mathrm{in}} - P_{fc} - \dot{Q}_{fc,\mathrm{out}}\,. \tag{36}$$

Furthermore, to ascertain the electrical power of the fuel cell at a specific current density ($I = 80$ A), an equation describing the cell voltage has been defined [7]:

$$U_{\mathrm{out}} = E - U_{\mathrm{act}} - U_{\mathrm{ohm}} - U_{\mathrm{conc}}\,. \tag{37}$$

Mathematical relationships describing individual components of Eq. (37) have been presented in [7]. Below, the results of calculations for the fuel cell operating temperature and the assumed temperature of gases supplied to the SOFC are shown (Fig. 5), as well as the values of voltage and current in the fuel cell (Fig. 6), and the power generated in the fuel cell (Fig. 7).

From the presented calculation results in Figs. 5 to 7, it is evident that the variation in the temperature of air supplied to the SOFC system has an impact on the generated power in the SOFC. Altering the temperature of supplied air and fuel affects the electrical current voltage and, consequently, the power generated by the cell. The calculations indicate that a lower air temperature leads to a significant deterioration in the electrical power output of the SOFC. The best operational parameters for the SOFC, as indicated by the theoretical analysis, are achieved when both the temperature of the supplied fuel and air are high and do not deviate significantly from each other.

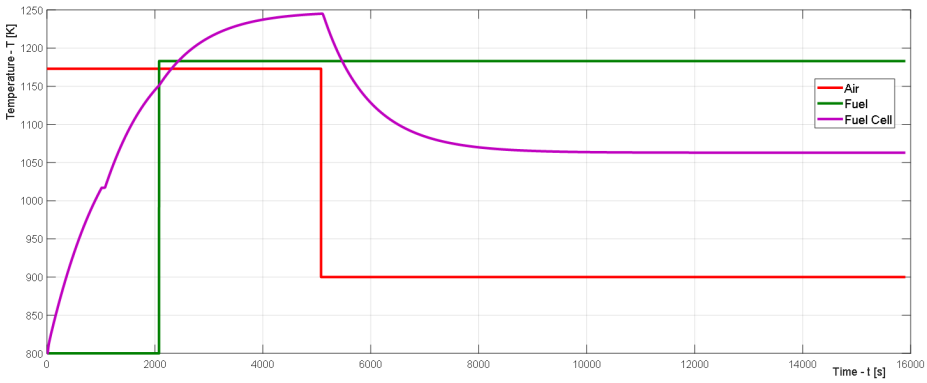


Figure 5: Temperatures of the fuel cell and gases supplied to the SOFC: Air – input air temperature, Fuel – input of fuel temperature, Fuel Cell – the result of the fuel cell temperature calculations.

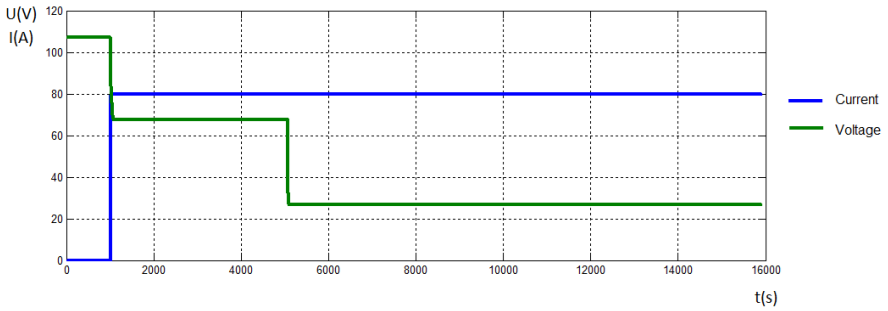


Figure 6: Voltage and current produced in the fuel cell.

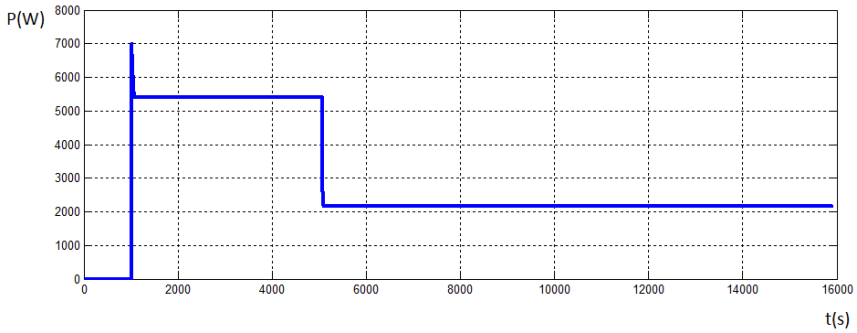


Figure 7: Power produced in the SOFC.

## 4 Summary

The article provides information on the modelling and analysis of a system based on solid oxide fuel cells (SOFCs) in the context of thermodynamic energy cycles. The paper discusses various aspects of systems related to fuel cells, including the use of biogas and heat recovery. It describes system configurations, major components, and chemical reactions occurring in SOFCs.

The paper also presents a mathematical model of SOFCs and provides calculation results regarding the electrical power generated by these cells depending on the temperature of the air and fuel supplied to the system. These results suggest that the optimal performance of SOFCs is achieved at high temperatures for both air and fuel.

It is important to emphasize that investments in SOFC installations can be costly due to high material requirements and the need to consider various subsystems. However, in the long term, they can be an efficient way to produce electrical energy.

The paper presents a comprehensive analysis of SOFCs and their role in thermodynamic energy cycles, taking into account various factors affecting their performance and their potential as a source of electrical energy.

*Received 15 September 2023*

## References

[1] Milewski J., Budzianowski W.: *Recent key technical barriers in solid oxide fuel cell technology.* Arch. Thermodyn. **35**(2014), 1, 17–41. doi: 10.2478/aoter-2014-0002

[2] Mikielewicz J., Matysko R.: *ORC system as a system for improving energy efficiency in a gas turbine installation powered by an anaerobic sludge stabilization system.* Ann Set Environ. Protect. **15**(2013), 2, 1367–1377 (in Polish).

[3] Matysko R.: *Chilled water production in steam circuits.* Chłodnictwo i Klimatyzacja **8**(2012), 54–56 (in Polish).

[4] Matysko R.: *Energetic efficiency of the combined ORC and gas turbine installation powered by the anaerobic sewage sludge stabilization system.* Arch. Thermodyn. **39**(2018), 4, 71–83.

[5] Mikielewicz D., Matysko R.: *Refrigeration absorption systems LiBr-H20 and NH3-H2O*, Chłodnictwo, **51**(2016), 3, 24–32 (in Polish). doi: 10.15199/8.2016.3.3

[6] Sabatier P.: *Catalysis in Organic Chemistry.* Van Nostrand, New York 1922.

[7] Nehrir M., Wang C.: *Modeling and Control of Fuel Cells – Distributed Generation Applications.* IEEE Press, Wiley, Hoboken 2009.

[8] Spiegel C.: *PEM Fuel Cell Modeling and Simulation Using Matlab*. Elsevier, Burlington 2008.

[9] Kupecki J., Badyda K.: *SOFC-based micro-CHP system as an example of efficient power generation unit*. Arch. Thermodyn. **32**(2011), 3, 33–43. doi: 10.2478/v10173-011-0011-7

[10] Nagel F.-P.: *Electricity from wood through the combination of gasification and solid oxide fuel cells – Systems analysis and Proof-of-concept*. PhD thesis, ETH, Zurich 2008.

[11] Liso V.: *Designing and control of a SOFC micro-CHP system*. PhD thesis, Aalborg Univ., 2012.

[12] Asmare M.: *Investigating the effects of reactant gas flow geometrical shape on the performance of solid oxide fuel cell*. Int. J. Sust. Eng. **15**(2022), 1, 323–332. doi: 10.1080/19397038.2022.2150936

[13] Fang X., Zhu J., Lin Z.: *Effects of electrode composition and thickness on the mechanical performance of a solid oxide fuel cell*. Energies **11**(2018), 7, 1735. doi: 10.3390/en11071735

[14] Lee H.L., Han N.G., Kim M.S., Kim Y.S., Kim D.K.: *Studies on the effect of flow configuration on the temperature distribution and performance in a high current density region of solid oxide fuel cell*. Appl. Therm. Eng. **206**(2022), 118120. doi: 10.1016/j.applthermaleng.2022.118120

[15] Design and demonstration of 3 CHP plants using two 5 kW Solid Oxide Fuel Cells (SOFC) working with landfill gas and biogas from anaerobic digestion BIOSOFC Project, Life06 ENV/000054. http://ec.europa.eu/environment/life/project/Projects/index.cfm?fuseaction=home.showFile&rep=file&fil=LIFE06_ENV_E_000054_LAYMAN.pdf (accessed 10 Sept. 2022).

**archives**
**of thermodynamics**
Vol. **44**(2023), No. 4, 335–380
DOI: 10.24425/ather.2023.149728

# Review of hydrogen-based propulsion systems in the maritime sector

**MARCIN KOLODZIEJSKI***

Faculty of Mechanical Engineering, Maritime University of Szczecin, Willowa 2, 701-650 Szczecin, Poland

**Abstract** The maritime industry is undergoing a technology transition that aims to increase the use of low-emission fuels. There is a significant trend visible of new ships being ordered with alternative fuel propulsion. In the future shipping's fuel market will be more diverse and it will rely on multiple energy sources. One of the very promising ways to meet the International Maritime Organisation's decarbonization requirements is to operate ships with sustainable hydrogen propulsion. One of the possible options to limit greenhouse gases emissions is the production of low-carbon 'green' hydrogen by water electrolysis using low-carbon electricity. This hydrogen can then be used directly in fuel cells to produce electricity or in the internal combustion engines, without having a carbon impact and pollutant emissions. Hydrogen can also be converted into its derivatives. This paper presents a review of recent studies of ships' hydrogen propulsion systems, different aspects of production, transportation, storage, and using liquid/gaseous $H_2$ and its derivatives as a fuel in the shipping industry. $H_2$ propulsion in maritime transport is still in the experimental phase. In most cases, these experiments serve as a kind of platform for evaluating the applicability of different technological solutions. This article presents existing ships' hydrogen and its derivates propulsion systems, projects, and existing conceptual studies.

**Keywords:** Fuel cells; Hydrogen; E-ammonia; E-methanol; Hydrogen ship propulsion; Gaseous fuels

*Corresponding Author. Email: m.kolodziejski@pm.szczecin.pl

**Acronyms**

| | | |
|---|---|---|
| AIP | – | air independent propulsion |
| BESS | – | battery energy storage system |
| CTV | – | crew transfer vessel |
| DF | – | dual fuel |
| FC | – | fuel cell |
| GHG | – | greenhouse gases emissions |
| ICE | – | internal combustion engines |
| IMO | – | International Maritime Organisation |
| LH2 | – | liquefied hydrogen |
| LOHC | – | liquid organic hydrogen carrier |
| LNG | – | liquefied natural gas |
| MGO | – | marine gas oil |
| P2X | – | power-to-X |
| PEMFC | – | polymeric electrolytic membrane fuel cell (proton exchange membrane fuel cell) |
| PSV | – | platform support vessels |
| WTIV | – | wind turbine installation vessels |

# 1 Introduction

The 2021 report by Intergovernmental Panel on Climate Change (IPCC) [1] stated that if there are no immediate large-scale reductions in greenhouse gases (GHG) emissions, the global warming of 1.5°C will be exceeded during the 21st century. According to [2], transportation – including marine, road, rail and air contribute to approximately 14% of the global GHG emissions. The shipping industry transports about 80% of global trade and contributes up to 3% of GHG emissions. Ship operators have already experienced increasing pressure to limit the GHG footprint of maritime transport. The Initial International Maritime Organization (IMO) GHG strategy has regulated emissions reduction policy development within international shipping. New regulations (Carbon Intensity Indicator – CII, Energy Efficiency Design Index – EEXI [3], and Ship Energy Efficiency Management Plan – SEEMP – Part III [4] came into force on 1 January 2023. The SEEMP Part III is a part of the IMO's initial strategy aiming to reduce GHG emissions by ships. It includes the ambition to reduce the carbon intensity across international shipping by at least 40% by 2030, pursuing efforts towards 70% by 2050 compared to 2008. Decarbonizing the maritime transport will result in major changes in the ships' fuels production and supply to the shipping market. The shipping industry has heavily re-

lied on carbon-dense bunker fuels and has used virtually no carbon-free fuels. However, due to the IMO regulations, ship operators will be required to apply new technologies and alternative fuels to reduce emissions. The alternative fuels, in particular liquefied natural gas (LNG), battery energy storage systems (BESS) and biofuels along with low-carbon synthetic fuel and hydrogen-based solutions are being investigated.

LNG is recognized as the largest segment of the alternative fuel market however, due to its $CO_2$ footprint, it is only considered the 'bridging fuel' until other alternative fuel options are developed and implemented in the shipping industry.

One of the possible options to limit GHG emissions is the production of low-carbon green hydrogen which can be used directly in fuel cells to produce electricity or in the internal combustion engines (ICE), without having a carbon impact and pollutant emissions like $NO_x$, $SO_x$ and particulate matter. However, most hydrogen is currently produced from natural gas through steam methane reformation and from the gasification of coal but there are several green ways to produce hydrogen:

- from fossil fuels but with $CO_2$ capture systems;
- produced through renewable energy (e.g. wind, solar, wave) or nuclear power electricity by the electrolysis of water.

The use of green hydrogen as a fuel in maritime transport is being developed and it will probably become a primary component of the pathway to decarbonization of the shipping industry. The introduction of green hydrogen as a fuel in the shipping industry is a part of a larger transformation towards cleaner energy sources due the to availability of excess and low cost renewable electricity (wind and solar) and the requirement for storage of the renewable energy. Battery storage systems give great benefits for short term storage however for long term storage the power-to-X-to-power (P2X2P) concept was developed. P2X2P converts low-priced and excess renewable electricity via electrolysis into hydrogen. This hydrogen is stored and converted back to electricity when needed. The first stage of this process is Power-to-X (P2X). Green hydrogen can be processed into its derivatives such as methanol (MeOH), ammonia ($NH_3$), Fischer-Tropsch (FT) diesel/kerosene [5] and methane ($CH_4$). Some of the processes also need $CO_2$, which is provided by $CO_2$ capture. $CO_2$ emission takes into account not only the ship exhaust; the whole value chain needs to be evaluated. If in the production of fuel captured $CO_2$ is used, it will make the overall emissions of such fuels carbon neutral or even negative.

Green hydrogen can be utilized in the P2X2P process to produce ammonia, which can be used as fuel for large deep sea vessel engines. Ammonia can be used as the energy source for fuel cells (FC) but it can also be the fuel source for Dual Fuel (DF) internal combustion engine (ICE). The need for autonomy for long distance shipping is a strong requirement by the shipping transport. On-board storage of hydrogen in large cryogenic tanks is a disadvantage for cargo vessels, where cargo space is very precious. Ammonia density is twice as high (compared with hydrogen). As it is easy to liquefy, it is already transported worldwide in liquid form. Similar to hydrogen, most ammonia is currently produced from natural gas. However, there are a number of projects under development combining wind farm renewable electricity generation with ammonia production process offshore [6]. Green ammonia will offer high emission reduction potential in both 'well-to-wake' and 'tank-to-wake'. In a recent study [7] Det Norske Veritas predicted that ammonia would be one of the most promising emission free fuels, however in order for ammonia to be a viable future fuel, it must be manufactured through green low carbon processes.

An increasing number of orders for methanol-fuelled ships shows that the maritime industry sees e-methanol as another promising alternative fuel. Application of e-methanol as a ship's fuel is only beginning – in November 2020 it was included in the IMO's Interim Guidelines for Low Flash Point Fuels. Methanol as a liquid at ambient temperatures is easier to handle (compared to liquid hydrogen ($LH_2$)) and would be similar to conventional fuel vessels. It has been handled by offshore Platform Support Vessels (PSV) and also transported by chemical carriers. This experience can become a reference point for the wider implementation of methanol as ships' fuel. The capital investment for a retrofit or newbuild e-methanol fuelled vessel is lower, compared to $LH_2$ as there is no need for cryonic tanks and systems. However, due to its lower volumetric energy density, methanol fuel tanks require approximately 2.5 more volume than conventional fuel oil tanks. When methanol is used in dual fuel ICEs it is required to add about five per cent of marine gas oil (MGO) pilot fuel. If a methanol fuel system is retrofitted, the existing fuel tanks or ballast water tanks can be used for storage after the application of a specific internal coating [8].

## 2 Literature review

The requirement for storage of excess energy generated by renewable sources like wind, tide or solar enabled production of hydrogen from water through electrolysis. The 'green' hydrogen production is considered as one

of the sustainable solutions to mitigate climate change. This paves the way for hydrogen as an energy carrier to be further used as a zero-carbon fuel for maritime shipping. However, challenges in hydrogen storage and transportation still create restrictions for its wider implementation as ships fuel. The literature contains a relatively small quantity of papers looking at the use of hydrogen and its derivatives as alternative fuels in maritime transport. Most of the research has been carried out very recently, with the results published in the last 2–3 years. The below review is based on peer reviewed scientific articles. However, in Section 4, describing the latest developments in the hydrogen propulsion, authors used other available sources like manufacturers and Internet publications – some projects presented in the article were implemented very recently (some even this year) and there are no peer reviewed articles available yet. Most of the available scientific publications present theoretical case studies only.

Hydrogen propulsion applications on ships are still in the experimental phase and are limited to smaller ships, which serve as a kind of platform for evaluating the applicability of different technological solutions. This is also reflected in the limited number of available publications – most of the articles presented in this literature review focus on theoretical case studies describing future applications of hydrogen propulsion. Article [9] presents the environmental impacts of alternative shipping fuels for a 12000 GT coastal ferry in Korea. The comparative study was carried out for hydrogen, LNG and MGO. All means of hydrogen production process were considered in the study. Paper [10] explores the possibility of using batteries, ammonia and hydrogen as alternative, low emission fuels. A case study of high speed catamaran ferry operations in Norwegian fiords was presented to carry out the comparison of three propulsion options. Research presented in [11–15] explores life cycle assessment of Hydrogen-Methanol Ship (HyMethShip) propulsion system using the onboard pre-combustion carbon capture concept. The HyMethShip concept combines a dual fuel internal combustion engine, an onboard pre-combustion carbon capture system and electro-methanol energy storage. The system works in a closed $CO_2$ loop with the $CO_2$ capture system onboard. The captured $CO_2$ and green hydrogen are converted ashore into methanol. The pre-combustion process onboard converts methanol to hydrogen and $CO_2$. Hydrogen is used to fuel the ship again. Studies analysed the impact of system design on the overall emission and environmental impact of the novel propulsion unit. Research presented in [16] determines the economic, regulatory and technical feasibility of a coastal general purpose research ship with hydrogen FC propulsion.

Another study [17] presents a comparison of three potential propulsion systems (diesel electric, battery hybrid and hydrogen hybrid) for the new ship required to replace the existing research vessel R/V Robert Gordon Sproul. Levels of zero-emission runtime, emissions and energy efficiency were compared for all three variants of propulsion systems. Reports [18, 19] explore perspectives of a propulsion system for a hydrogen fuelled liquid hydrogen tanker vessel with the boil off hydrogen used as propulsion fuel for a gas turbine and provide economic analysis of such a propulsion. Work [20] focuses on the case of hydrogen and battery-electric ship propulsion solutions for shipping in Norway. This study is limited though to Norwegian coastal shipping; fishing vessels, offshore supply vessels and ferries. Paper [21] presented a case study of small RoRo ferry retrofit of the propulsion system. The study focuses on the feasibility of the installation of hybrid propulsion consisting of proton-exchange membrane fuel cells (PEMFC) fuelled by hydrogen and battery energy storage system. The authors implemented a process simulation to assess the amount of hydrogen that can be stored onboard the ferry including conditions such as shore storage capacity and bunkering time. The results of the study show that introduction of the gaseous hydrogen can be implemented to achieve the zero emission goal. Paper [22] provides the case study for $LH_2$ as a fuel for a new-built vessel utilizing fuel cells. The model used by the authors presented the optimal cost and time for investment compared with the profits of deferring an investment. The impact of a carbon tax on the investment was also assessed in the study.

Chemical energy from hydrogen and its derivatives can be converted into mechanical energy in the ICE or through electrochemical reactions in fuel cells (FCs). FCs are electro-chemical power sources that convert hydrogen chemical energy into electrical energy. The objective of [16] was to develop an environmental impact analysis of both technologies for vessels propulsion; a hydrogen ICE and a hydrogen polymeric electrolytic membrane fuel cell (PEMFC). The study was performed to assess their viability and eligibility compared to traditional ship propulsion. Several types of FCs exist that are characterised by the fuel used, the type of electrolyte and the operating temperature. They can be used in maritime applications depending on the specific operation and available infrastructure; PEMFCs are the most common, followed by molten carbonate FCs (MCFCs) and direct methanol FCs (DMFCs). Among FCs using hydrogen, PEMFCs operate in the lower temperature range (50–85°C). This makes their operation safer. The high temperature FCs, mainly MCFCs and solid oxide

FCs (SOFCs), provide higher efficiency [23]. Fuel cells have been commercially used since the 1960s, and in marine applications since the 1980s and this is reflected in the available literature. According to the results presented in [17] hydrogen FC technology would provide the most effective hybrid supplement to conventional diesel electric propulsion. Report [24] provides prospects and perspectives of hydrogen FCs applications for ship propulsion. Paper [25] explores three different FCs (SOFC, HT-PEMFC and LT-PEMFC) combined with different fuels; LNG, $LH_2$, ammonia and methanol used as a propulsion in expedition cruise ships. The authors evaluated the impact of FC implementation on the operational profile of the cruise vessels. Seven different combinations of the FC with gaseous fuels with three different hybridization models were considered in the study. Paper [26] investigates the possibility of the replacement of a conventional diesel electric propulsion system installed on a hybrid ferry, with hydrogen propulsion based on PEMFC technology. The size of the FC system was determined by the power of the original diesel engine of the ferry. The battery storage system was maintained the same as per the original configuration of the hybrid propulsion. A theoretical case scenario based on a typical operational profile of the ferry is presented in the study. The authors proposed a preliminary redesign of the ship energy management system along with a new power train configuration. Paper [27] investigates the possibilities and applicability of molten carbonate FC technology for medium and large size vessels. The study focuses on the applicability of a combined propulsion system (100 kW fuel cell, 30kW battery storage system and 50kW diesel generator). The case study presented in the article was based on a 5500 TEU container ship. The authors analysed the operational profile of the ship and developed load scenarios applicable to the propulsion system of the vessel. Frequency, voltage and power quality were evaluated during simulated experimental synchronisations and disconnections of all three power sources. Research presented in [28] focuses on a technological review of FC propulsion systems used in the maritime industry in the past two decades, their progress and perspectives. The authors analysed applications of ammonia, green methane and hydrogen as fuel for the FC. Different types of the FCs were presented and their suitability for maritime applications was analysed. The study also reviews various research and projects related to applications of FC in the shipping industry with regard to safety, reliability, cost and operational contexts.

Hydrogen has the highest energy content per mass compared to conventional marine fuels. It exceeds MGO by 2.8 times, and methanol more

than by 5 times. $LH_2$ as a fuel can reduce specific fuel consumption and increase the effective efficiency of a propulsion system. However, due to its low volumetric energy density, $LH_2$ will require four times more storage capacity than MGO and two times more storage space than LNG for a similar amount of energy carried by the ship. $LH_2$ requires temperatures below $-253°C$ to remain in liquid state so the required space to store $LH_2$ will be even higher when considering the necessary insulation materials and vacuum insulation for cryogenic storage. Due to the challenges related to high pressure/low temperature, $LH_2$ can alternatively be carried within other substances such as methanol or ammonia. They require less energy than $LH_2$ to be liquified or compressed. Certain FC's cells can directly utilise methanol, ammonia or other hydrogen carrier fuels using internal reformers to extract hydrogen from fuel. Studies [29, 30] focus on applications of green ammonia and green methanol within maritime shipping. Paper [31] explores options available for $LH_2$ storage. Safety aspects of hydrogen storage are described in the article [32]. A review of hydrogen carriers was carried out in the study [33]. The authors presented issues related to the traditional storage of hydrogen in a liquified or gas state (risk of fire and explosion, low flame point, low volumetric density and transport challenges). The paper investigated 15 different hydrogen carriers and evaluated their characteristics such as gravimetric and volumetric density, safety, handling, logistics and dehydrogenation process.

Low volumetric energy density also creates challenges for hydrogen shipping and transportation (similar to those for storage) – it cannot be economically shipped in a gaseous state. The ideal system for hydrogen transport are existing gas pipeline systems. If they are available, then they can be re-used to transport hydrogen from the production site to its destination; however, in most cases gas pipes are not available and other means of transport are required. There are three methods developed to transport hydrogen but it has to be converted first:

- $NH_3$–$H_2$ can be converted to $NH_3$ (ammonia) by reaction with nitrogen. It has higher energy density than hydrogen, boiling point $-33°C$ and can be transported in conventional LPG tankers;
- $LH_2$ – hydrogen can be cooled down to -253$^o$C and transported in liquid state. It is achievable however expensive and challenging. Shortage of $LH_2$ tankers is an issue;
- LOHCs – liquid organic hydrogen carriers. There are organic chemicals which can reversibly react with hydrogen and form chemicals that can be transported by ships;

- Metal Hydride Storage – hydrogen can be stored within the crystal structure of certain metals at density higher than that of liquified hydrogen however with low storage efficiency (up to 8% by mass).

Research presented in [34,35] explore issues related to hydrogen transportation. Paper [31] provides a review of $LH_2$ transportation in the maritime sector. Study [36] provides a life cycle analysis of different hydrogen production methods along with pipeline and truck transportation in gaseous form. Different scenarios of production and transportation are compared in the work to indicate the best method to minimise the environmental impact of hydrogen production and transportation. Paper [37] presents a comparison of technical and economical characteristics of hydrogen carriers to present better understanding of the ways in which hydrogen could be shipped in an efficient and safe manner. The authors also discussed other factors which will affect the selection of a hydrogen carrier for overseas transport. In another study [38], the authors also investigate the hydrogen carriers in the light of suitability for power generation, shipping, availability, and the energetics. The authors also carried out a safety review of the carriers presented in the study. Paper [21] explores issues of storage and transportation of compressed gases. It presents an innovative solution developed in the European project GASVESSEL. This concept allows storage and transportation of gas fuels with an energy density higher than conventional intermediate pressure systems. The concept is the patented, innovative solution for the manufacturing of pressure vessels that are 70% lighter than current alternatives. Study [39] presents a model developed to assess the cost of shipping of various forms of hydrogen and its derivatives over different routes. It includes transportation in the forms of $LH_2$, methanol, liquid organic carriers and ammonia. A case study of the route from Rotterdam to Australia was presented by the authors. Research presented in [40] explores issues related to the impact of the hydrogen blended natural gas on the energy of the gas that is stored within the pipelines. The article describes limits of the maximum content of hydrogen blended with natural gas in existing offshore piping systems.

Most of the focus in the literature is on the alternative, low emission fuels for ship main propulsion systems. However, paper [28] focuses on the possible reduction of harmful emissions caused by on-board auxiliary systems. The authors analysed if those emissions could be reduced by installing hydrogen FC. The case study was performed based on data developed from an LNG tanker. Simulations presented in the research showed that this solution could have a major contribution in decarbonisation of the shipping

industry, especially if auxiliary loads could be managed without peaks in demand.

In another study [41], the authors presented a niche application of hydrogen in the maritime industry – using excess renewable energy generated on board an experimental ship Energy Observer to produce hydrogen by electrolysis of purified sea water. As an option to store energy, hydrogen produced onboard can supply on demand electricity through FC installed onboard the vessel. The study also focuses on contaminants present in the purified water and their impact on hydrogen quality and subsequently on the performance and lifetime of the FCs.

Study [31] presents a review of $LH_2$ applications in transportation with focus on maritime shipping. The authors aimed to highlight the challenges related to the implementation of $LH_2$ on-board ships. The paper focuses on different aspects of those technologies such as safety, codes, regulations and standards, $LH_2$ bunkering and onboard utilization. It also offers an overview of factors which can hamper the implementation of hydrogen in the maritime shipping. Life assessment of hydrogen as a shipping fuel was performed in a number of publications. Among others, study [42] focuses on life cycle assessment of possible de-carbonization solutions such as e-methanol, e-ammonia, electrolytic hydrogen and green electricity in different ships' propulsions (FC, diesel engines and $CO_2$ capture technologies) in relation to their environmental impact and cost. Article [43] presented a life cycle perspective to ship propulsion systems powered by sustainable hydrogen and the functional/technical requirements of such systems. Paper [44] focuses on the environmental impacts of green alternative shipping fuels, compared to MGO: LNG and hydrogen across each of their life cycles, in the well-to-wake category. Paper [45] focuses on the concept of ESS (energy storage system) using technology called power-to-gas-to-power (P2G2P). It is an innovative system consisting of electrolysers supplied by green electricity and hydrogen powered gas turbines.

## 3 Hydrogen production, storage and transportation

Hydrogen is the most abundant substance in the world and it can be found bonded to a number of substances. The most common production methods are steam reforming and electrolysis. As the majority of the well-to-wake pollutants (carbon foot-print) are composed during hydrogen production, to distinguish different methods and energy sources used for hydrogen produc-

tion, color codes have been introduced [31, 44]. In terms of the production emissions there are five types of hydrogen:

- brown hydrogen derived from coal gasification;
- grey hydrogen derived from processing of natural gas or other fossil fuel;
- blue hydrogen derived from fossil fuels as brown hydrogen however, carbon capture, utilization and storage (CCUS) methods are applied;
- green hydrogen, produced via electrolysis using electricity from renewable energy sources;
- purple hydrogen, the same as green produced via electrolysis, however with electricity from nuclear power stations.

The primary method of hydrogen production is from natural gas (grey hydrogen). The second largest source of $H_2$ production is brown hydrogen. As for 2021 only around 4% of global hydrogen production came from electrolysis. The renewable energy share in the electricity mix is below 30% – it means that only 1% of global hydrogen production was derived from renewable sources. 69% of the global production was grey hydrogen (47% derived from natural gas and 22% derived from oil), 27% was brown hydrogen [47, 48]. However, according to International Energy Agency the number of projects in progress that will produce green hydrogen is rising at an impressive pace. If all the projects under development get realized, the global production of green hydrogen in 2030 will multiply more than twenty times compared to 2021. Another good prognostic is the rapid expansion of electrolyzer capacity. In 2021 alone it increased by 70% compared to the previous year. The global capacity of electrolyzers in 2022 tripled from the 2021 level. The cost of energy derived from renewable sources like wind and solar generation is declining. It means that areas with good renewable energy resources will be able to provide low cost green hydrogen. In certain areas, renewable energy resources are higher than local demand, e.g. Orkney island produces electricity mainly from renewable energy resources (wind, tides and waves). The island connection to the mainland power grid is limited and excess energy cannot be exported. To store the energy hydrogen is used as a storage medium. Excess electrical energy is used for electrolysis of water to produce hydrogen which is compressed and stored under pressure [49].

Green hydrogen can also be used as energy storage media for offshore wind farms. Wind turbines located in the North Sea are an exceptional source of renewable energy however there are challenges with regards to intermittency of the supply and mainland grid connectivity. A new project has been developed to produce green hydrogen offshore through the installation of large electrolyzing system on a converted drilling jack-up rig. The solution will allow storage of the electricity produced during peak times and will allow using the existing offshore infrastructure for storage and transportation of hydrogen [50]. The means of transport of energy generated in this way (*via* ship or pipeline), are flexible. They provide alternatives to the traditional cable lines over the land or in the sea which are already overloaded. Figure 1 [51] presents different means of transporting the energy generated offshore.

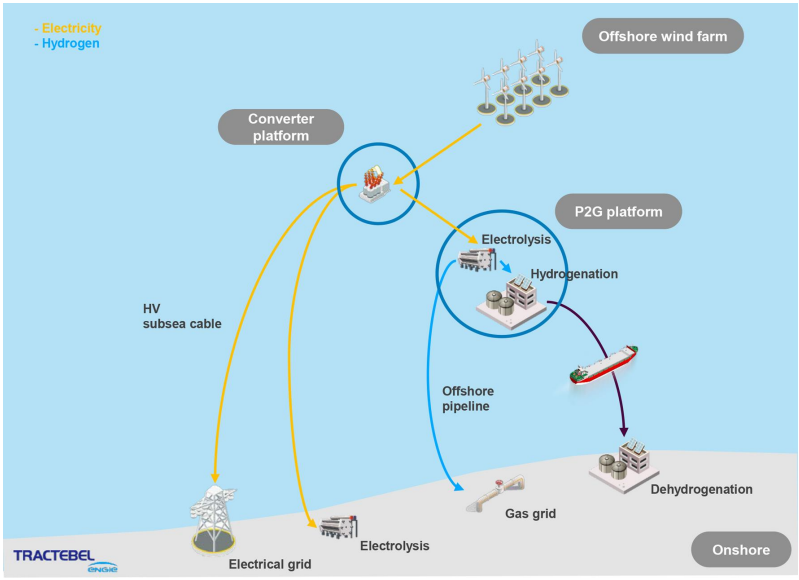


Figure 1: Green energy transport from the offshore wind farms [51].

The real value of hydrogen as an energy carrier is realized when it is further converted to other e-fuels (hydrogen derivatives), especially during P2X conversion (Fig. 2) [52]. P2X includes hydrogen and its derivatives: FT diesel/kerosene [5], ammonia, methane and methanol. Electrolysis of water is used to produce green hydrogen utilizing renewable electricity. Then hydrogen is further processed to its derivatives. Some of them also need $CO_2$ provided by $CO_2$ capture from a biogenic origin. Each step of

conversion adds energy losses to the e-fuel production value chain. However, it is expected that excess renewable electricity will be available and this will decrease the cost of e-fuel and accelerate the production of P2X fuels [52].

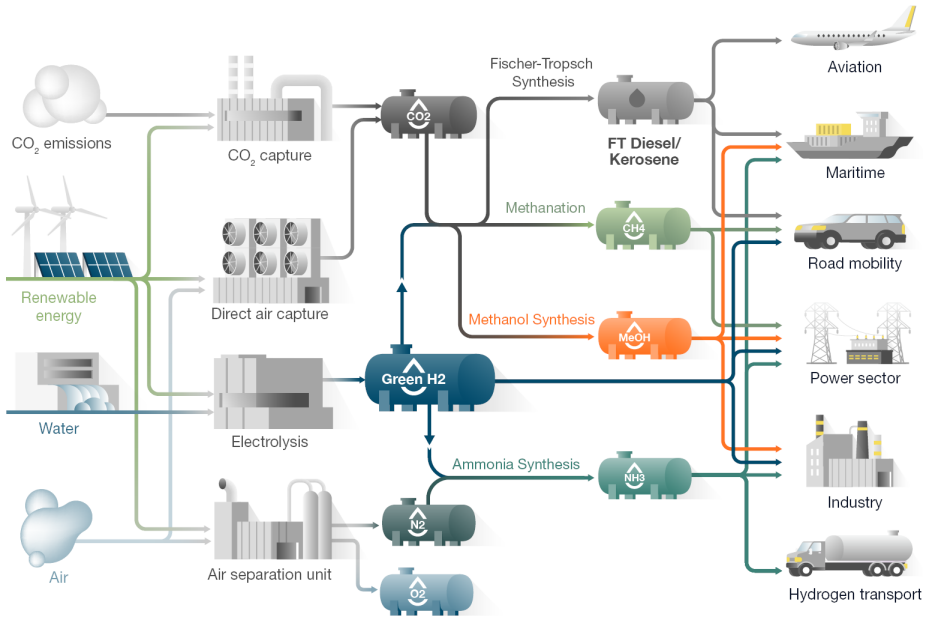


Figure 2: Schematic of P2X Fuels' production and typical application [52].

Apart from the e-fuels produced during P2X conversion, hydrogen can also be chemically bonded into liquid or solid state to increase its volumetric energy density, reduce risk associated with handling hydrogen and solve the hydrogen transport challenges.

Hydrogen storage in the solid state can be carried out by absorption in solids or by adsorption on solid surfaces. The most common process in the marine systems is hydrogen storage in metal hydrides when hydrogen splits into atoms near the metal. The advantage of this method is higher hydrogen density compared to $LH_2$. The disadvantage is storage efficiency which is up to 8% – to store 1 kg of hydrogen 12.5 kg of metal hydride is required. The advantage is reduced risk of fire and explosion [32]. A pilot project of ship using a solid form of sodium borohydride ($NaBH_4$) will be presented in this article.

Hydrogen storage in the liquid state can be performed by LOHCs absorption and release of hydrogen through chemical reactions. During absorption

into the liquid carrier a hydrogeneration catalyst is used. This liquid is then stored and shipped with regular transport at ambient pressure and temperature. It makes it safer and cost efficient. To release hydrogen onboard a ship a dehydrogenation catalyst is used. A ship fuelled with Benzyltoulene oil hydrogen carrier is described in this article.

The cost of hydrogen or its derivatives storage and transport is an important factor of the total, wake-to-well cost of the fuel and is an integral part of the power generation asset. Conventional fuels have high volumetric energy density and require less space for storage. Hydrogen and its gaseous derivative ammonia need to be compressed or liquefied but even then they require more storage space than conventional fuels and it creates storage and transportation challenges. Once hydrogen is converted to either one of the P2X e-fuels or chemically bonded, its volumetric energy density is increased which makes transport and storage more cost-effective. E.g. $NH_3$ volumetric energy density is almost eight times higher than Li-ion batteries used in the marine propulsion applications and its gravimetric density is twenty times higher. Increased energy density of hydrogen derivatives increases the distance that hydrogen can be transported in a cost effective way connecting future shipping hydrogen hubs with high energy demand areas [47]. For a ship hydrogen propulsion system the access to the fuel is crucial. The same applies to the central role of the ports in the transition toward hydrogen propulsion. Today a large proportion of hydrogen production takes place in close vicinity to ports. However, most of $H_2$ is produced from natural gas through steam reforming (grey hydrogen). Large hydrogen hubs existing in ports make it possible for 'green hydrogen' supply chains for shipping to be developed. The decreasing prices of offshore wind and solar electricity will probably make renewable energy technology the cheapest source of green hydrogen. Ports, especially in northern Europe, will become large renewable hydrogen production and distribution centers. With predicted growing demand, production of hydrogen in Europe will not be sufficient. It will be required to import green hydrogen from other continents. The ports and shipping industry are set to benefit from this too. The maritime sector will be a partner in development of the renewable hydrogen supply chain. Hydrogen produced by offshore electrolyzers can be transported by ships to onshore hubs. Offshore vessels involved in wind farms activities can be propelled by hydrogen (crew transfer vessels and commissioning operation service vessels). Those vessels (existing and concept studies) are presented in this article. Offshore platforms can also become $H_2$ hubs at sea, supplying green fuel to the offshore vessels.

# 4 Review of the ships with hydrogen/hydrogen derivatives propulsion systems

Hydrogen propulsion applications in the maritime transport are still in the experimental phase and are limited to smaller ships. In most cases, they serve as a kind of platform for evaluating the applicability of different technological solutions. This section describes existing vessels with hydrogen (and its derivates) propulsion, projects under construction, and completed conceptual studies.

## 4.1 Hydrogen fuel cell submarine

The very first time the marine propulsion fuel cells were used in the German Type 212 submarine which was commissioned in 2005. This type of propulsion allows to submerge the vessel for long periods of time and provides high mobility when submerged. Another advantage of FCs propulsion is low noise to avoid detection and no emissions. Type 212 submarine (Fig. 3) [53] features diesel propulsion (1 × MTU 16V396 2150 kW diesel engine) and Siemens Air Independent Propulsion (AIP) system using hydrogen PEMFCs.

Figure 3: Type 212A Class submarine [53].

The first vessel of this type was equipped with 9 fuel cells, 30 kW each. Subsequent submarines used 2 FCs, 120 kW each. Prime mover for the propulsion is Siemens 1700 kW electric motor which, drives a single propeller. The vessel can operate on diesel power at high speed, or use the AIP system for slow and silent cruising. When the submarine is submerged, AIP can be used to power the propulsion electric motor directly and to top up

the batteries. The FCs have relatively small capacity so the vessel can only cruise slowly when using AIP however, the batteries can be used to provide peak power. The system does not emit vibration – it is very quiet and almost undetectable. Hydrogen propulsion for submarines had been considered for many years, however, the concept was not successful due to risk of explosion and fire. In the 212 Submarine fuel and oxidizer are stored in the tanks outside the crew living quarters, between the outer light hull and the pressure hull. Gases are supplied to the fuel cells through pipes penetrating the pressure hull but there is only small amount of hydrogen and oxygen present in the pipes in the crew accommodation.

## 4.2 FellowSHIP research program

One of the first commercial ships with hybrid battery/FC propulsion was Viking Lady (Fig. 4) already presented by the author in [54].

Figure 4: The offshore supply vessel, Viking Lady [55].

It was purpose built as the research ship for the FellowSHIP research program. The program was established in collaboration between DNV GL, Eidesvik and Wärtsilä. The main purpose of the project was to explore the use of fuel cells, hybrid and battery technology in the shipping industry. It took place from 2003 to 2018, and the initial phase was dedicated to research on fuel cells. The MCFC fuel cell (Fig. 5) [55], which generated an electric output of 330 kW, was installed in 2009 and has successfully run for more than 18,500 hours.

The integration of fuel cells into the Viking Lady propulsion system served to reduce exhaust emissions. According to [57] it is estimated that the annual reduction was a total of 33 t of $SO_2$, 4755 t of $CO_2$ and 180 t of $NO_x$.

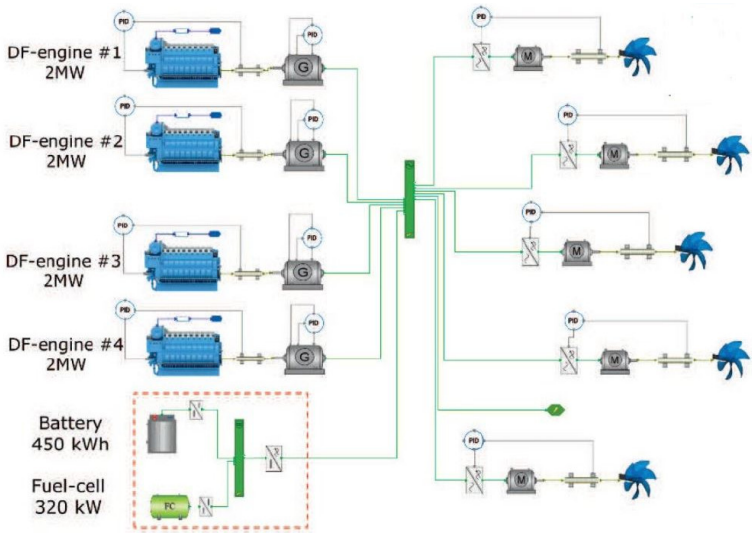


Figure 5: Battery – FC hybrid propulsion system on board the Viking Lady [55].

Following the results of the above project, Eidesvik (participant of the FellowSHIP research program) converted three platform support vessels (Viking Queen, Viking Energy and Viking Princess) into hybrid/battery [55]. Now Eidvik, in cooperation with Wartsila and Norwegian oil major Equinor, are launching a new research project to test a platform support vessel (PSV) propulsion system based on fuel cells running on ammonia derived from green hydrogen. FC modules with a total power of 2 MW will be installed in year 2023 onboard PSV Viking Energy (Fig. 6) [58] allowing her to operate for at least 3000 hours per annum on clean fuel.

Figure 6: PSV Viking Energy [58].

Viking Energy was the first PSV powered by LNG when delivered in 2003. It was also the world's first hybrid supply vessel with 'Battery Power' class notation. Following the installation of ammonia FC's, Viking Energy will become the world's first PSV to sail without $CO_2$ emissions. Testing of the propulsion system will be carried out while the vessel is on contract for Equinor. As part of the testing, the ship will use ammonia in transits between offshore installations and harbour for one year. Additionally, ammonia will be used to supply electricity to the vessel when in harbour. The initial plan for the test period is to supply 60% to 70% of the energy consumption from ammonia. In the later stages it is planned to achieve 90% of the total power demand [59]. After successful completion of the first phase, the project will increase up to 20 MW ammonia FC suitable for oceangoing vessels. Economic and technical knowledge developed in the Viking Energy pilot program will be used in a broader analysis of green ammonia FC propulsion systems in the maritime shipping. The final goal of the Viking Energy project is to demonstrate the feasibility of ammonia FCs for deep sea vessels and long voyages. According to the FC manufacturer, the project will develop into three more vessel types, including an offshore construction vessel, a bulk carrier and a container ship [59].

### 4.3 Hydrogen propulsion with liquid organic hydrogen carrier

In June 2022, offshore wind farms service company Edda Wind took delivery of its first hydrogen-ready commissioning service operation vessel (CSOV), Edda Breeze (Fig. 7) [60]. It is the first ship delivered as part of a nine vessels newbuilding program. Edda Breeze length is 88.3 m, draught 5.5 m and beam of 19.7 m. Ship's propulsion consists of Catepillar 3521E main engine, three Brunvoll transverse thrusters and two Voith Shneider azimuth thrusters. It can accommodate up to 120 persons. This accommodation capacity allows the vessel to work as a walk-to-work ship for personnel involved in the maintenance and construction of the wind farms.

Edda Breeze was prepared for no emission hydrogen fuelled operations with energy carrier in a liquid organic hydrogen carrier (LOHC). LOHC technology was developed and patented by a German based company, Hydrogenious LOHC Technology. The technology is a process of 'loading' hydrogen in oil and releasing it when required. LOHC solves issues related to safety of using hydrogen as a fuel in maritime shipping as it is not explosive or flammable. The technology is an easy, efficient and safe way of

Figure 7: CSOV Edda Breeze [60].

storing hydrogen. LHOC may revolutionize storage and supply of hydrogen for maritime industry, as it can be used to transport large quantities of H2 in ambient temperatures using existing infrastructure. It is possible to 'load' and 'unload' hydrogen into the carrier oil (benzyltoulene) many times – the carrier is recyclable. LOHC energy density is 2–3 times higher, compared to compressed $H_2$ [61, 62].

## 4.4 E-Methanol propulsion

Methanol can be used in the shipping industry, as a fuel for FCs or for ICEs. Leading engine manufacturers offer methanol fuelled DF engines. They have adopted the high pressure diesel combustion process for utilizing methanol as a fuel, the engines are designed to inject high pressure liquid methanol fuel in a similar way to the injection of conventional fuel oils.

The offshore and wind farm vessels can accommodate the use of sustainable fuels such as e-methanol that require more frequent bunkering. One of the first wind turbine installation vessels (WTIV) fuelled by methanol will be dynamic positioning jack-up Boreas, ordered by leading wind turbine installation company Van Oord. It will be equipped with five Wartsila 32 methanol engines (Fig. 8) [63].

The Boreas (Fig. 9) [64] will be able to install (and transport) the next generation of 20 MW wind turbines. It is expected to enter the service in 2025. The ship is the first of its kind to operate on the sustainable e-methanol which will reduce the vessel's $CO_2$ emissions by more than 78%.

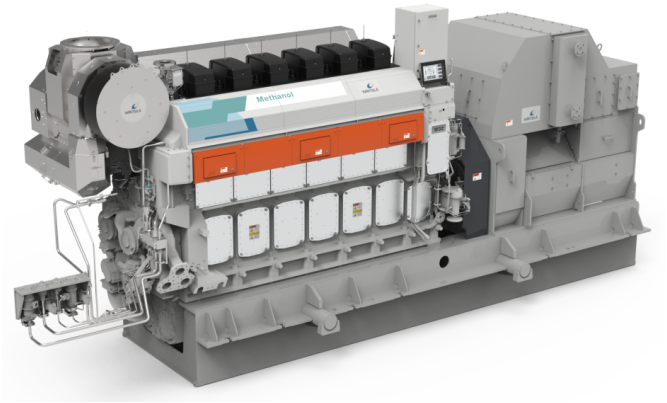


Figure 8: Wärtsilä 32 methanol engine [63].

Figure 9: Boreas – artistic impression [63].

A 5 MWh battery energy storage system (BESS) will accommodate peak loads and allow energy regeneration to reduce fuel consumption and $CO_2$ emissions even more.

Specification of the vessel [64]: length 175.1 m; breadth 63.0 m; depth 13.2 m; draft 8.5 m; tonnage 47017 GT; deadweight 20000 t; speed 12–13 kn; propulsion 4 × 4000 kW azimuth thrusters and 2 × 2700 kW retractable thrusters; bow thrusters 2 × 2700 kW; total power 21750 kW (+5000 kWh battery pack).

Methanol can also be used in the retrofit projects of existing, conventional fuel vessels. The very first vessel converted to the methanol propulsion was Stena Germanica Ro-Pax ferry (Fig. 10) [65]. It is the world's

second biggest Ro-Pax ferry and the largest one in the Nordic region. The vessel is 240 m long, 29 m wide, 6.1 m draft and 3901 lane meters. The vessel can accommodate 1300 passengers and 300 cars.

Figure 10: Stena Germanica – first commercial vessel to run on methanol [65].

The vessel owner commenced the conversion of the ship to test the viability of using fossil methanol as fuel in March 2015. Following the methanol conversion of the propulsion engines, the ship was able to operate on methanol as primary fuel and MGO as backup fuel. The aim of the project was to meet the IMO regulations for special areas like the Baltic Sea known as the Sulphur Emission Control Area (SECA). From January 2015 it was required to use fuel with a maximum sulphur content of 0.1%. Using fossil methanol allowed the vessel to reduce $SO_x$ emissions by 99%. However, if fossil methanol is replaced with hydrogen e-methanol produced during P2X conversion, this project will also allow to reduce $CO_2$ emissions and allow for methanol to become a sustainable shipping fuel.

Stena Germanica is powered by four converted Wartsila Sulzer 8ZAL40S engines with combined propulsion output of 24 000 kW, which enable her to steam with a speed of 25 kn. It was necessary to adopt ballast tanks for methanol storage, high pressure (600 bar) methanol pump room was installed. Cylinder heads were modified – special design of combined methanol/MGO fuel injectors was introduced. Methanol combustion in the cylinder is initiated by pilot injection of MGO [29]. The project also involved the design of a methanol bunkering, storage and distribution systems in both ports (Gothenburg and Kiel).

### 4.5 Energy Observer Project

Another vessel, which has served for many years as a sailing simulation laboratory for energy transition in the maritime transportation is Energy Observer (Fig. 11) [66].

Figure 11: Energy Observer [66].

It is one of the first hydrogen powered, no emission ship, to be self-sufficient in energy, acting as a laboratory for ecological transition. The Energy Observer propulsion system consists of two electric motors, each with 42 kW capacity. Electric motors can also act as hydro-generators (when sailing with wind propulsion). The optimal speed of the vessel is 4.5 knots. Energy Observer has been testing green energy technologies, including hydrogen, solar power and wind in harsh marine conditions. The vessel is powered with three primary green energy sources – wind, solar and hydropower. As the renewable power is intermittent, energy is stored in the BESS and in the hydrogen tanks. The excess of the green energy produced by renewable sources is used to charge the batteries or to produce hydrogen from purified sea water. The hydrogen can be later used to generate electricity in the FCs. The solar panel with 202 $m^2$ surface can generate peak performance of 34 kWp with average daily production 120 kWh. Vessel is also equipped with vertical sail-like OceanWings wind propellers. They can increase the vessel speed, reduce energy consumption for propulsion, and allow surplus energy to be used for production of hydrogen through electrolysis. The most interesting technical aspect of the Energy Observer power system is its hydrogen system. The vessel can store excess energy in the BESS however, most of the surplus energy is used to produce hydrogen. Using hydrogen

as an energy storage medium instead of heavier BESS reduces the weight of the ship. 63 kg of hydrogen stored onboard can provide 1 MWh of electricity or thermal energy. The fuel cell system installed on board Energy Observer was supplied by Toyota – it is similar to that used in the Toyota Mirai FC car [67].

2021 was a record year of the Energy Observer longest crossings. The ship sailed more than 15000 nautical miles which was the vessel's record distance in one year of the operation, duration of the crossings was 2739 hours, average speed was 5 kn. The total electricity consumption was 13950 kW, of which 63% was used for the electric propulsion. Total energy production was 32305 kWh. Solar panels contribution was 38%, energy produced from hydrogen contributed to 17%. 1% of energy was hydro-generated (reversed mode of propulsion electric motors). Estimated aerodynamic contribution of OceanWings sails on the propulsion electric motor consumption was 44% [68].

Following successful tests carried out on 'laboratory vessel' Energy Observer, new project has been launched to design a multipurpose cargo vessel with hydrogen propulsion – Energy Observer 2 (Fig. 12) [69].

Figure 12: Energy Observer 2 concept [69].

The aim of the project was to develop a next generation cargo vessel that would blend zero emission with required transportation capabilities. There is a worldwide requirement to renew the fleet of multipurpose cargo vessels

of approximately 5000 DWT. They are mostly used in coastal shipping and are an alternative to road transport. They constitute almost 37% of the world tonnage and due to their age and old design, are required to be renewed to meet strict IMO regulations for 2050. This vessel type has been identified as a priority segment for the Energy Observer Project and its partners – the specification of Energy Observer 2 concept has been established accordingly. Energy Observer 2 will be the project flagship, It will become the first full scale hydrogen propulsion demonstrator for the shipping industry.

The specification of the vessel [70]: deadweight 5000 t; length 120 m; width 22 m; draft 5 m; RoRo bridge 480 linear meters; containers 240 TEU; electric propulsion 4 MW; fuel cell power (RexH2 EODev) 2.5 MW; liquid hydrogen tanks ($LH_2$) 70 t (1000 $m^3$); range up to 4000 nautical miles; commercial speed 12 kn; the surface of the wings 1450 $m^2$.

Due to low volumetric energy density of hydrogen, one of the limitations that has to be overcome, is high volume of storage tanks. This will be compensated in the vessel design by energy consumption optimization, use of renewable energy mix and propulsion efficiency. To achieve it, Energy Observer 2 will be equipped with four propulsion sails – modern sailing system developed by Ayro for which Energy Observer catamaran was a testbed. Total surface of the sails will be 1450 $m^2$ and it is expected that they will reduce propulsion energy consumption by 15 to 30% [69].

### 4.6 Hydrogen FC ferries

Sea Change (Fig. 13) [71] is the first hydrogen FC ship in the US. The ferry arrived to San Francisco in March 2023 and after testing period it is due to start regular service in California Bay area in Q2 of year 2023. It is a 22 m, 75 passenger catamaran. It is powered by hydrogen FCs and lithium battery.

The ferry is equipped with two 200 kW electric motors for propulsion of fixed pitch propellors, three 120 kW cummins hydrogen fuel cells (Fig. 13) [72] and ten 250 bar gaseous hydrogen storage tanks located on the upper deck, with a total capacity of 246 kg. Two 50 kWh lithium-ion batteries are integrated into the propulsion system. Maximum distance is 300 nautical miles with speed up to 20 kn [72–74].

Sea Change is not the world's first hydrogen fueled ferry however, it is the first to use hydrogen in gaseous state. Hydrogen used by the ferry is produced by an electrolyzer, powered with renewable solar power, so

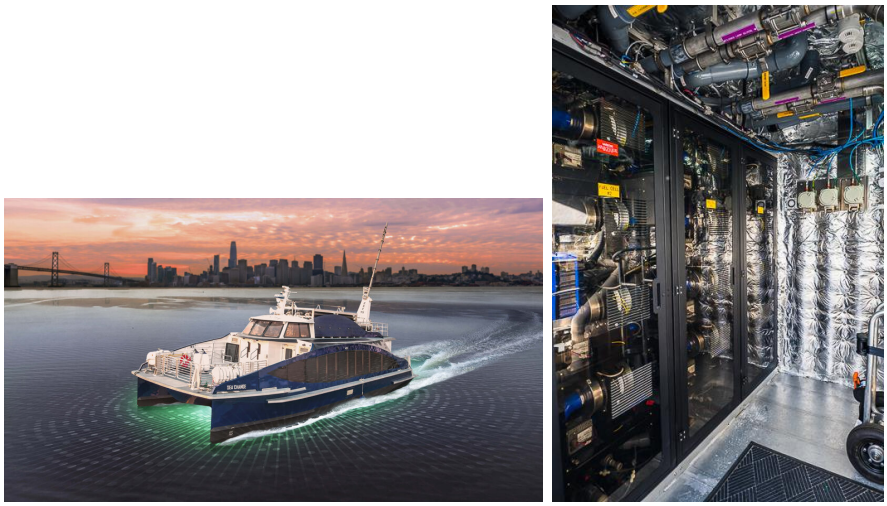

Figure 13: Sea Change [71] Sea Change fuel cells [72].

the ferry propulsion system is zero emission. On 31st March 2023 Norled, Norwegian no emission ferry pioneer put MF Hydra (Fig. 14) [75], the first $LH_2$ fuel cell powered ferry into regular scheduled operation.

Figure 14: Hydrogen Ferry Hydra [75].

The company is known for its innovation in the ferry transportation. In 2015, Norled launched the world's first BESS operated, electric driven ferry presented in [54]. Nowadays Norled has about eighty electric driven ferries

in Norway and made first but fundamental step in the new direction of using liquid hydrogen as propulsion for their ships. The ferry will operate on the route between Hjelmeland, Spikavik and Nesvik with a speed of nine knots.

Specification of the vessel: length overall 82.4 m; draught 2.9 m; depth 4.1 m; beam 17.5 m; gross tonnage 2628 t; capacity 292 passengers, 80 cars, 10 trailers; propulsion 2× Schottel thrusters SRE 340 LFP; auxiliary engines $2 \times 440$ kW (Scania DI16 075M); batteries 1356 kW Corvus Energy Orca; fuel cells $2 \times 200$ kW Ballard; type of fuel: hydrogen; biodiesel; battery power.

The novel propulsion system consists of two L-drive azimuth thrusters powered by vertical frequency controlled permanent magnet type electric motors. Power system uses DC grid and consists of two switchboards, which are fully redundant. Switchboards can be supplied by either hydrogen FCs or the li-ion BESS in addition to diesel generator fueled by biofuel. Batteries can be charged by an automatic plug-in charging system. BEES will also function as a shield to protect FCs during variable loads and rapid load changes [75,76]. Hydrogen fuel will be delivered by Linde's plant in Leipzig, Germany by trucks. Hydrogen will be stored on the top of the vessel in cylindrical tanks of 10.0 m × 3.5 m diameter. 80 $m^3$ volume/4 t capacity, vacuum insulated tank will be sufficient for 12 days of sailings at speed of 9 kn, allowing the vessel to sail for approximately 1000 nautical miles. Linde will use its new 24 MW proton exchange membrane electrolyzer to produce $LH_2$ that will power the ferry [77].

In March 2023, an agreement was signed to deliver hydrogen propulsion systems to two ferries that will operate on Norway's longest connection. The ferries will need to cover long distances of up to four hours sailing. They will have much larger capacity than Hydra with space for up to 120 cars, 599 passengers and 12 trucks. They will be delivered in the Q4 of 2024. PowerCell will supply 13 MW Marine System 200 fuel cell. According to PowerCell, it is the world's largest hydrogen project in the marine industry to date. It is estimated, that application of the hydrogen fuel cell propulsion on this single route will reduce $CO_2$ emissions by 26500 tons per year. There are no details available of the novel propulsion system. The ferries, according to the Norwegian Government requirements, will operate on no more than 15% biofuel and at least 85% of hydrogen. The project is part of the plan to renew similar size conventional propulsion ferries to comply with the Norwegian government's initiative for all ferries cruising on the Vestfjorden crossing to be emission free. The 100 km crossing is between

Bodø and the Lofoten Islands in northern Norway above the Arctic Circle, it is one of the most challenging ferry routes in Norway. The two new hydrogen FC fueled ferries will operate year round, requiring 5×6 t of green hydrogen daily [78].

## 4.7 Windcat Workboats & CMB.TECH concept of hydrogen propulsion

In May 2022, newly built, hydrogen powered crew transfer vessel (CTV) started regular operations to transfer crew to/from the Norther wind farm in the Belgian sector of the North Sea. Hydrocat 48 (Fig. 15) [79] has a length of 25 m, a beam of 7.3 m and draught of 1.9 m. Apart from passengers it can carry 10 t of cargo.

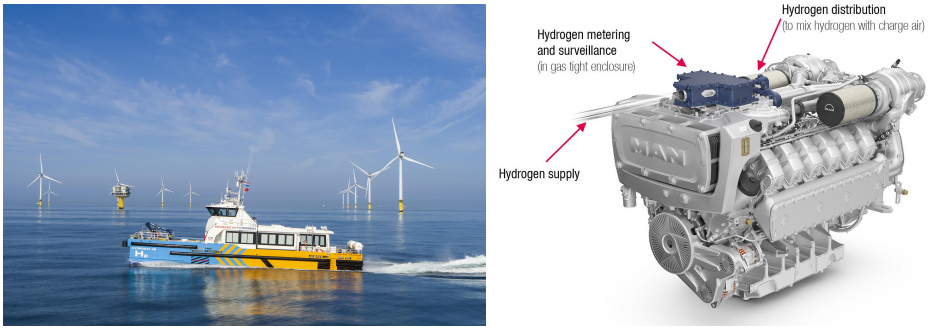


Figure 15: Hydrocat 48 [79] and MAN D2862 LE448 engine fitted to Hydrocat 48 [79].

The CTV is powered by two diesel engines MAN D2862 LE428 (Fig. 15) [79] which underwent modifications to run on hydrogen. The twelve cylinder engines have an output of 749 kW (1019 hp) at 2100 rpm each. MAN used a conventional V12 engine, which did not require major modifications for hydrogen. Hydrogen is introduced into the charge air. The combustion process is according to the diesel principle – it requires pilot injection of approx. 5% of diesel fuel. Injection parameters have been optimized for dual fuel hydrogen-diesel operation. The engines are designed to change over to diesel if hydrogen is unavailable.

The engines drive controllable pitch propellers which can deliver a service speed of 30 kn. The vessel can carry 210 kg of hydrogen [79, 80]. Since the delivery in June 2022 Hydrocat 48 started her maiden operations. Until January 2023 it completed the maintenance program of the 44 8MW Vestas turbines. It is estimated that the ship saved 1.9 ton of $CO_2$ emissions per

day [79]. Following the successful tests the ship operator has ordered six additional hydrogen CTV's [82].

Another sector of the maritime industry, which may benefit from implementation of hydrogen propulsion are harbor tugs. They usually use conventional medium speed diesel engines, which can be converted into a hydrogen – diesel (dual fuel) propulsion. Hydrotug 1 (Fig. 16) [83] is another project developed by Windcat Workboats & CMB.TECH. It will be the world's first hydrogen tug, the boat is due to enter the service in the Port of Ostend in the first half of 2023.

Figure 16: Hydrotug 1 [83].

Ship specification [82]: dimensions length 30 m, breadth 12.5 m, depth: 5 m; hydrogen storage capacity 415 kg of compressed gas; engines $2 \times 2$ MW V12 dual fuel BeHydro and Volvo Penta D8 MG Stage V for auxiliaries; bollard pull 65 t.

The tug is equipped with two V12 BeHydro dual fuel engines that can operate on both hydrogen and diesel. The mix ration is 85% hydrogen and 15% of diesel – diesel is used as a pilot fuel to start the combustion of compressed hydrogen in the cylinder. The tug is the first in the world, to be powered by internal combustion engine that is fuelled by hydrogen and diesel. Storage capacity of Hydrotug is 415 kg of compressed hydrogen in six racks. Testing of the vessel will be carried out in Ostend because the ship can use the existing hydrogen bunkering facilities of Hydrocat 48 which also operates from the same port [85, 86]. The engine manufacturer, BeHydro, developed the technology for medium-speed dual fuel hydrogen-diesel engines. The Hydrotug is the first ship powered by these engines. The combination of dual fuel technology with catalyzer and a particle filter ensure that the tug is ultra-low-emission [87].

In November 2022 Windcat Workboats & CMB.TECH, so far specializing in offshore personnel transfers, announced an order for the construction of a series ('Elevation Series") of wind turbine CSOV with hydrogen propulsion system (Fig. 17) [88].

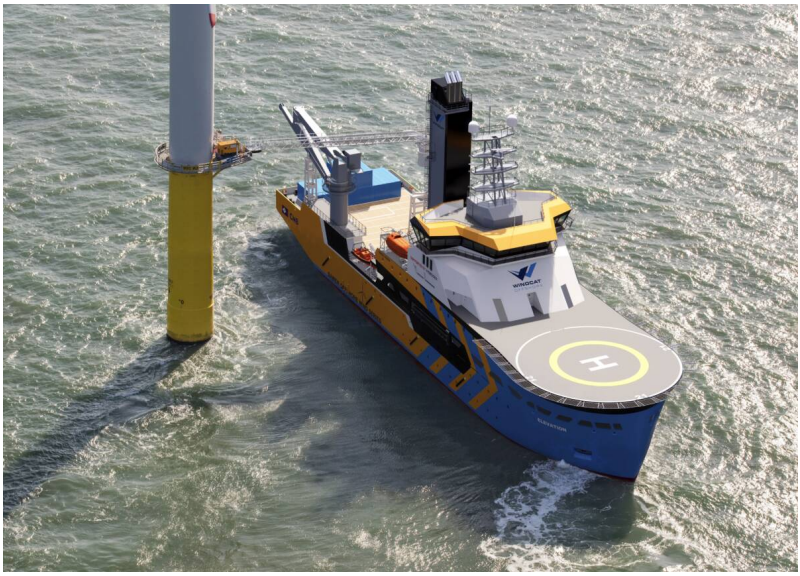

Figure 17: Windcat CSOV visualization [88].

Ships specification [88]: length 89 m; beam 19.7 m; draught 5.3 m; gross tonnage 6700 t; propulsion $3 \times 1800$ kW diesel generators, $1 \times 800$ kW $H_2$/MGO Duel fuel genset, $1 \times 1.7$ MW BESS with capacity 700 kWh for power backup and spinning reserve, $4 \times 1.8$ MW azimuth thrusters.

To reduce the vessels' emissions, Windcat and CMB.TECH will provide the same dual fuel hydrogen/MGO engines (MAN D2862 LE428) as used onboard the CTV Hydrocat 48 [88].

## 4.8 HySeas III Research Program – concept

HySeas III is the final part of a research program looking into the hydrogen propulsion system application for a RoRo ferry. The route of this innovative vessel will be in the Orkney Islands, from Shapinsay to Kirkwall, north of Scotland. Orkney produce electricity from renewable energy resources (wind, tides and waves). As the island connection to the mainland power grid is limited, excess energy cannot currently be exported. To store

the energy hydrogen is used as a storage medium. Excess energy is used for electrolysis of water to produce hydrogen, which is compressed and stored under pressure. However, hydrogen production is still higher than it is consumption on the island thus the project to use it as a fuel for the ferries [47]. HySeas III project aimed to demonstrate that the hydrogen FCs can be integrated with a marine hybrid-electric propulsion system along with bunkering facilities and the hydrogen storage systems. The design of the first hydrogen FCs driven seagoing RoRo ferry has already been completed (Fig. 18) [89]. The double-ended Ro-Pax ferry will be able to carry 120 passengers and 16 cars or 2 trucks.

Figure 18: Hyseas-III Project of R0-Pax ferry design – concept [89].

In 2022, string testing was carried out in Norway to validate the innovative vessel's propulsion system before it is built. To carry out string testing, all of the key system components are assembled and tested as a system. Testing involved assembling all of the key propulsion system components; fuel cell system consisting of 6 100 kW Ballard HD-100 fuel cells, Lithium-ion BESS, two multidrives, transformers, switchboards, load banks required to simulate azimuth and bow thrusters load, hydrogen system, BESS firefighting systems, power management system, safety systems and so on. The test rig is shown in Fig. 19 [90].

The testing program was designed and performed by HySeas III partner Kongsberg Maritime to investigate if the system is suitable for responding to demands which occur during normal Ro-Pax ferry operations. The testing was also intended to test safety and emergency systems [90].

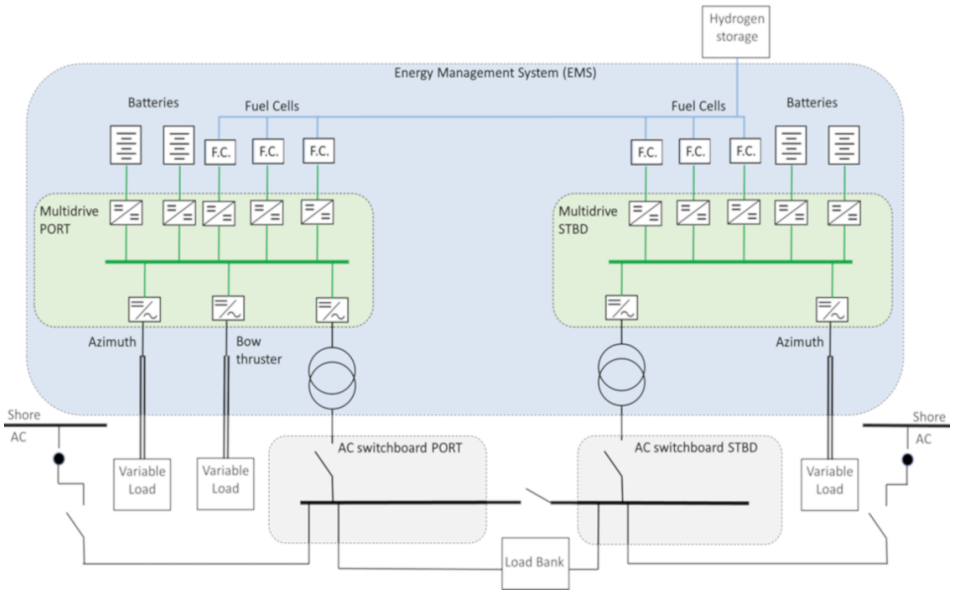


Figure 19: HySeas ferry propulsion system string test schematics [90].

## 4.9 Hyship Project – concept

Fourteen European partners embraced the novel HyShip project of designing and construction of two revolutionary Ro-Ro demonstration ferries fuelled with $LH_2$. The Topeka vessels (Fig. 20) [91] will be no emission through a combination of 3MW proton exchange membrane FC and the BESS of 1 MWh capacity. Project also involves the establishment of hydrogen bunkering platforms and liquid hydrogen supply chain. Both ships will operate on a fixed schedule along the Norwegian coast. They will provide zero emission transportation between offshore supply harbours. Ferries will carry cargo between Bergen, Stavanger and Kristiansund. They will also distribute containerized $LH_2$ to the bunkering hubs. The hubs will supply hydrogen to future $LH_2$-powered ships operating in Norway. The ships are to enter the commercial service in 2024.

The next step of the HyShip Project will be to carry out three replicator studies. The first one will be for 1MW propulsion tanker which will be used in inland waterways. The second study will be for 3 MW fast ferry and the 3rd one for a larger, 20 MW propulsion system for deep sea vessels [91, 92].

Figure 20: Topeka RoRo vessel concept [91].

## 4.10 Ulstein SX190 – concept

The SX190 (Fig. 21) [93] dynamic positioning (DP2), no emission offshore construction support vessel is Ulstein's first hydrogen propulsion offshore vessel, equipped with a Nedstack fuel cell power system. The total power of the vessel is 7.5 MW, of which FC system generates 2.5 MW. Nedstack proton exchange membrane (PEMFC) is located in a separate engine room.

Figure 21: Ulstein SX190 – concept [93].

SX190 specification: length 99 m; beam 23.4 m; draught 6.0 m; accommodation – up to 90 crew members; propulsion thrusters $2 \times 1280$ kW; tunnel thrusters $2 \times 750$ kW.

Due to lack of hydrogen bunkering facilities in ports, designers decided to install a flexible containerized gas storage system on the aft deck of the vessel. $H_2$ gas storage containers can be loaded and unloaded in the

same way as standard containers. This solution provides operational flexibility and eliminates the need for bunkering infrastructure. The containers can be filled at production facilities. With this design, the SX190 is already capable of operating for 4 days with no emissions. For longer trips, Ulstein adopted a dual fuel solution. The vessel can use its conventional diesel-electric propulsion system using MGO. However, with expected developments in FC technologies and $H_2$ storage, designers targeted a future no emission trip duration of up to fourteen days. To extend no emission range, the first step will be to swap the gaseous $H_2$ storage containers with containerized liquid storage tanks. This will triple the volumetric energy density of the fuel. With this solution, the vessel will still use containerised hydrogen storage system. When $LH_2$ bunkering facilities become available in ports, the vessel stores under the main deck will be adopted to install permanent storage tanks for liquid hydrogen. This will extend the duration of the no emission endurance to one month [93].

## 4.11 Wind turbine installation vessel Ulstein J102 Zero Emission – concept

The J102 (Fig. 22) [94] no emission design of WTIV features a hydrogen-hybrid power supply system. The design uses hydrogen technologies, which allow the vessel to operate in no emission mode for 75% of its operational time. The additional cost of $H_2$ installation is less than 5% compared to the conventional vessel. Vessel specification: vessel type – jack-up; length 142 m;

Figure 22: J102 wind turbine installation vessel – concept [94].

beam 87 m; accommodation 120 crew; storage capacity: 4–8 Wind Turbine Generators (size dependant); $CO_2$ reduction per year: 4000 t; $H_2$ FC system – PEMFC; $H_2$ storage system – 7 × 40 ft containers compressed $H_2$.

Most of the latest WTIV designs feature a combination of diesel generator sets and a hybrid BESS. Some already have a future option for adding hydrogen FC's. The disadvantage of BESS is its heavy weight where weight reduction is essential for minimization of elevated weight of the jack-up and for the deck load available for the wind turbine elements. Ulstein designers took a different approach. They analyzed different modes of the operational cycle of WTIVs and power demands of WTIV in those modes. According to the analysis, a WTIV operates 75% of its time in jacked-up position, carrying out crane operations with limited power demand. Using hydrogen FC and a small BESS will be sufficient to meet the power demand in this operational mode. Similar to SX190, due to lack of hydrogen bunker facilities in ports, designers decided to install a flexible containerized gas storage system. However, the hydrogen system has been designed in such a way, that future developments of $H_2$ technology can be implemented to the vessel with no major modifications [94].

### 4.12 'With Orca' Powered by Nature – cargo vessel – concept

Norwegian shipyard Egil Ulvan Rederi was awarded a contract to build' a hydrogen fueled and wind powered bulk carrier. It will be the first zero emission cargo ship in Norway fuel by gaseous hydrogen. 'With Orca' (Fig. 23) [95] will be propelled by hydrogen internal combustion engine, which will be optimized for hydrogen to increase its efficiency. The vessel will be equipped with hydrogen fuel cells too. They will allow energy production in low load condition. The concept of the novel ship has the project name With Orca – Powered by Nature because a large part of the energy required for the propulsion of the ship will be taken from the nature with use of two large rotor sails. It will also be possible to store excessive energy in the BESS.

The 88 meters, 5500 DWT ship's route will be in open waters in the Norwegian coast of the North Sea, where wind assisted propulsion will benefit most from the weather conditions. The self-unloading bulk carrier is expected to enter service in 2024. It will be transporting cement grain from eastern to western Norway and construction aggregates in the opposite direction [96].

Figure 23: With Orca Powered by Nature vessel concept [95].

## 4.13 Neo Orbis vessel pilot concept – application of solid form of hydrogen carrier

Port of Amsterdam commenced the construction of a revolutionary hydrogen propulsion ship Neo Orbis (Fig. 24) [97] – this pilot project may become a breakthrough innovation in marine hydrogen power systems.

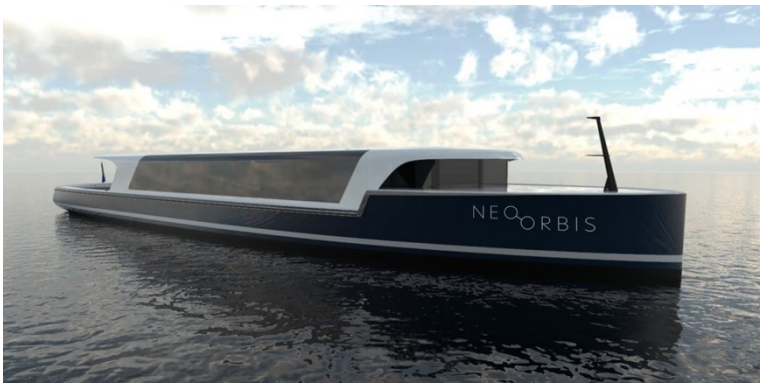


Figure 24: Neo Orbis ship concept [97].

The vessel will use hydrogen in a solid form of sodium borohydride ($NaBH_4$). $NaBH_4$ reacts with water and produces hydrogen. There are a number of benefits in using solid hydrogen carrier compared to gaseous or liquid hydrogen. It is more compact and safer to handle – flash point of sodium

borohydride is higher than for hydrogen and MGO. In the application room (equivalent to the engine room on conventional propulsion vessel) the $NaBH_4$ is 'unpacked' to gaseous hydrogen. Lower explosion limit (LEL) of hydrogen is 4%. The Neo Orbis safety systems will be activated if the hydrogen concentration reaches 0.1%. This will cease all hydrogen operation and the entire application room will be ventilated. The volumetric energy density of sodium borohydride is much higher than for hydrogen, it is actually comparable with MGO. It makes transport and storage of $NaBH_4$ less expensive, compared to $H_2$. However, more space is required onboard the vessel for the additional systems. The conversion result residue, so called 'spent fuel' has to be stored on board. However, this product can be converted on shore to new sodium borohydride with 'green hydrogen'. It makes NaBH4 circular, recyclable and emission free.

## 5 Conclusion

Due to strict IMO requirements regarding emissions, the shipping industry is investigating the alternative fuels, in particular LNG, biofuels, low carbon synthetic fuel and hydrogen-based solutions. Hydrogen has great potential as a fuel in the maritime shipping in terms of sustainability and climate footprint. Production of green hydrogen by water electrolysis using low carbon electricity, either from renewable energy (green hydrogen), or from nuclear power (purple hydrogen) seems to be the best option. Such hydrogen can be used in FCs to produce green electricity and in ICE for ships propulsion, with no $CO_2$, $SO_x$, and $NO_x$ emissions.

Green hydrogen can also be used to produce its derivative e-ammonia, which can be utilized to fuel larger ships. On board storage of $LH_2$ in large and heavy cryonics tanks is not practical for large cargo vessels – size of the tanks will impede on the vessel cargo capacity and impact the range of operations. Ammonia, having volumetric energy density much higher than hydrogen is a very interesting fuel solution – it is easy to liquefy and as it is already transported worldwide, it is believed that $NH_3$ technology is mature enough to be used as a green fuel on large cargo ships.

The inland and short sea vessels are ideal candidates for an adoption of e-methanol. It has strong potential to lower the carbon emissions by shipping. If fossil methanol is used as ship propulsion fuel, it can reduce $CO_2$ emissions by 10% only (compared to conventional fuels). However, it has a great potential to be zero emission fuel if it is produced from green

hydrogen and captured $CO_2$. However, one of its challenges is low energy density – methanol fuel tanks require approximately 2.5 more volume than conventional fuel oil tanks. But, compared with gaseous or liquid hydrogen volumetric energy density, methanol is more efficient at energy storage. Consequently, coastal vessels can easily accommodate the use of sustainable fuels such as e-methanol that require more frequent bunkering.

There are many advantages of hydrogen and its derivatives, however, the storage, transport and production remain a challenge. Those tasks are technologically viable however, still impractical from the economical point of view. The first challenge is that green $H_2$ is not available in the quantities and locations required. Green $H_2$ has to be cost effective to be used as a fuel for the shipping industry, compared with 'bunkered' fuels or LNG. It will only happen if hydrogen is produced on a large scale in the regions where large amounts of clean water and cheap renewable energy are available. Renewable energy must be available in amounts exceeding the electrical feed to the grid. Surplus energy will be converted to hydrogen then at low cost. However today, with an average crude oil price of 75 USD per barrel and USD 4-6/GJ for natural gas, renewable $H_2$ is up to three times more expensive compared to the fossil fuels. Hydrogen storage and transportation is also more expensive compared to the conventional fuels. Another challenge is lack of or limited hydrogen infrastructure. Additional investments in the electrolyzers, liquefaction units, pipelines, storage, and bunkering facilities will be required to allow using hydrogen from remote, renewable sources.

As it was presented in the article, so far quite a few demonstration projects of hydrogen propulsion ships have been launched however, there are no large vessels with hydrogen propulsion yet. It is important now to scale up the existing pilot projects so hydrogen fuel can make an impact on the entire maritime sector. So far hydrogen propulsion has only been used on relatively small vessels and it has a very limited effect on the shipping industry. Existing demonstration projects should also be used to develop new technical and classification standards, as there are no formal worldly accepted regulations for hydrogen propulsion ships' design and operation. There are no hydrogen transportation certification systems for cross border shipping either. Standardisation and compatible regulatory frameworks are required.

The choice of the sustainable shipping industry fuel of the future will be determined by trade-off between the easiness of fuel transportation, storage onboard the ship and the cost. When it comes to the cost of production, pure hydrogen is the cheapest, compared to its derivatives. However, it is

the most challenging fuel with regards to its storage – hydrogen derivatives like e-methanol, e-ammonia, e-diesel or e-LNG have much better volumetric energy density. Low volumetric energy density of $H_2$ and its production cost is still a major barrier for its adoption as a fuel for maritime shipping. Another key barrier is lack of hydrogen bunkering facilities in ports – hydrogen transport infrastructure and supply logistics must be implemented with adequate ship bunkering stations and storage facilities in place in ports.

It is clearly visible that hydrogen and its derivatives are a convenient option for short range ships, inland vessels and offshore support units. National and local regulations and strong public support may drive faster adoption of hydrogen-based ship propulsion systems in specific regions prior to hydrogen becoming a global shipping fuel. It is also the cheapest option if the hydrogen is produced from excess electricity generated by the wind farms. For those types of ships, $H_2$ seems to be the most promising no emission fuel of the future. Hydrogen can also be used as a 'range extender' in short sea and coastal shipping when other propulsion systems like BESS cannot be used all the time due to a lack of local charging facilities. Those vessels have already started the transition of ships propulsion towards sustainable hydrogen. Several pilot vessels fuelled by $H_2$ have already been built. There are a few demonstration projects under development too. All those programs have so far indicated the viability of $H_2$ as a shipping fuel used either to generate electricity in the FC's or to be used in more conventional way in the ICE. It is predicted that necessary technologies will be developed and will make it possible to have more no emission ships in the above categories built within next few years.

There are design projects ongoing to test the suitability of hydrogen based propulsion for larger vessels. Due to issues with energy storage and required propulsion power, there is no optimal strategy for the future no-emission fuel. However, it is anticipated that hydrogen dual fuel engines could be the 'transition bridge' for the implementation of hydrogen as a fuel for larger vessels. If hydrogen is used in FCs, its efficiency is higher compared to ICE. It can reach 60% or even more if fuel cells heat recovery system is installed. Conversion of hydrogen to electricity (Tank-to-Well) is zero emission. Total emissions (Well-to-Wake) depend on the type of hydrogen used. As each energy conversion step represents energy losses, using hydrogen FCs is the greenest way of generating power for the ship and it is a preferred option to implement no-emission fuel. Combustion engines adopted to hydrogen have lower efficiency compared with FCs, blending of conventional fuels with hydrogen in conventional engines will reduce GHG

emissions. A mixture of heavy fuel with 50% of hydrogen will reduce $CO_2$ emissions by up to 43%. Single fuel hydrogen, spark ignited ICE's, are being developed too.

With the current stage of hydrogen ship propulsion system development, more research is required on the safety aspects of bunkering, storage and handling of $H_2$ on board the ships. There are still uncertainties regarding the $LH_2$ behaviour and the explosion thresholds. More experiments are required to test liquid hydrogen behaviour in simulated leakage scenarios during storage and bunkering operations. Those experiments should lead to development of emergency detection, shutdown and ventilation systems which will mitigate the risk of explosion should a leak occur.

*Received 24 July 2023*

## References

[1] The Intergovernmental Panel on Climate Change Report: *Climate Change 2021: The Physical Science Basis*. https://www.ipcc.ch/report/sixth-assessment-report-working-group-i (accessed 22 Apr. 2023).

[2] US Environmental Protection Agency: *Global Emissions*. https://www.epa.gov/ghgemissions/global-greenhouse-gas-emissions-data (accessed 22 Apr. 2023).

[3] International Maritime Organization. Marine Environment Protection Committee (MEPC 76), 10 to 17 June 2021 session. https://www.dnv.com/news/imo-update-marine-environment-protection-committee-mepc-76-203128 (accessed 22 Apr. 2023).

[4] IMO RESOLUTION MEPC.347(78) adopted on 10 June 2022. https://www.ccs.org.cn/ccswzen//articleDetail?id=202212210544869589 (accessed 22 Apr. 2023).

[5] Meurer A., Kern J.: *Fischer–Tropsch synthesis as the key for decentralized sustainable kerosene production*. Energies **14**(2021), 1836. doi: 10.3390/en14071836

[6] Collins L.: *Green hydrogen and ammonia produced offshore*. https://www.hydrogeninsight.com/innovation/plan-unveiled-to-produce-green-hydrogen-and-ammonia-on-a-ship-connected-to-a-1-5gw-wind-farm-in-greenland/2-1-1383080 (accessed 22 Apr. 2023).

[7] DNV Maritime Forecast to 2050. *Energy Transition Outlook 2022*. https://www.dnv.com/maritime/publications/maritime-forecast-2022/index.html (accessed 22 Apr. 2023).

[8] Chryssakis C.: DNV Maritime Impact. *Methanol as fuel heads for the mainstream in shipping*. https://www.dnv.com/expert-story/maritime-impact/Methanol-as-fuel-heads-for-the-mainstream-in-shipping.html (accessed 22 Apr. 2023).

[9] Hwang S.S., Gil S.J., Lee G.N., Lee J.W., Park H., Jung K.H., Suh S.B.: *Life cycle assessment of alternative ship fuels for coastal ferry operating in Republic of Korea*. J. Mar. Sci. Eng. **8**(2020), 660. doi: 10.3390/jmse8090660

[10] Wang H., Trivyza N., Boulougouris E., Foivos M.: *Comparison of decarbonisation solutions for shipping: hydrogen, ammonia and batteries*. In: Proc. SNAME 14th Int. Marine Design Conf. Vancouver, June 2022. doi: 10.5957/IMDC-2022-297

[11] Malmgren E., Brynolf S., Borgh M., Ellis J., Grahn M., Wermuth N.: *The HyMethShip Concept: An investigation of system design choices and vessel operation characteristics influence on life cycle performance*. In: Proc. 8th Transport Research Arena, Helsinki, Apr. 27-30, 2020. doi: 10.3217/ddqpa-7jr80

[12] Malmgren E., Brynolf S., Fridell E., Grahn M., Andersson K.: *The environmental performance of a fossil-free ship propulsion system with onboard carbon capture – a life cycle assessment of the HyMethShip concept.* Sustain. Energy Fuels **5**(2021), 2753–2770. doi: 10.1039/D1SE00105A

[13] Wermuth N., Zelenkaa J., Moeyaertb P., Aulc A., Borgh M.: *The HyMethShip concept: Overview, concept development and obstacles for concept application in ocean-going vessel*. In: Proc. 8th Transport Research Arena, Helsinki, Apr. 27-30, 2020.

[14] Wermuth N., Lackner M., Barnstedt D., Zelenka J., Wimmer A.: *The HyMethShip Project: Innovative emission free propulsion for maritime applications*. In: Proc. 17th FAD-Conf., Dresden, 6-7 Nov. 2019, 150–170. doi: 10.3217/kx18p-txz60

[15] Zelenka J., Wermuth N., Lackner M., Wimmer A., Andersson K., Veelken H., Moeyaert P., Jäger B., Url M., Lang M., Huschenbett M., Devalapalli R., Sahnen D., Grützner J., Mair C., Ellis J.: In: Proc. 19$^{th}$ CIMAC Cong., Vancouver, 10-14 June 2019, 104. https://www.hymethship.com/wp-content/uploads/2021/02/Zelenka-et-al_HyMethShip-CIMAC2019_paper_104.pdf (accessed 22 Apr. 2023).

[16] Fernández-Ríos A., Santos G., Pinedo J., Santos E., Ruiz-Salmón I., Laso J., Lyne A., Ortiz A., Ortiz I., Irabien Á., Aldaco R., Margallo M.: *Environmental sustainability of alternative marine propulsion technologies powered by hydrogen – a life cycle assessment approach*. Sci. Total Environ. **820**(2022), 153189. doi: 10.1016/j.scitotenv.2022.153189

[17] Klebanoff L.E., Caughlan S.A.M., Madsen R.T., Conard C.J., Leach T.S., Appelgate T.B.: *Comparative study of a hybrid research vessel utilizing batteries or hydrogen fuel cells*. Int. J. Hydrogen Energy **46**(2021), 76, 38051–38072. doi: 10.1016/j.ijhydene.2021.09.047

[18] Alkhaledi A., Sampath S., Pilidis P.: *Propulsion of a hydrogen-fuelled LH2 tanker ship*. Int. J. Hydrogen Energy **47**(2022), 39, 17407–17422. doi: 10.1016/j.ijhydene.2022.03.224

[19] Alkhaledi A., Sampath S., Pilidis P.: *Economic analysis of a zero-carbon liquefied hydrogen tanker ship*. Int. J. Hydrogen Energy **47**(2022), 66, 28213–28223. doi: 10.1016/j.ijhydene.2022.06.168

[20] Bach H., Bergek A., Bjørgum Ø., Hansen T., Kenzhegaliyeva A., Steen M.: *Implementing maritime battery-electric and hydrogen solutions: A technological innovation systems analysis*. Transp. Res. D: Transp. Environ. **87**(2020), 102492. doi: 10.1016/j.trd.2020.102492

[21] Taccani R., Malabotti S., Dall'Armi C., Micheli D.: *High energy density storage of gaseous marine fuels: An innovative concept and its application to a hydrogen powered ferry*. Int. Shipbuild. Prog. **67**(2020), 1, 33–56. doi: 10.3233/ISP-190274

[22] Pomaska L., Acciaro M.: *Bridging the Maritime-Hydrogen Cost-Gap: Real options analysis of policy alternatives*. Transp. Res. D: Transp. Environ. **107**(2022), 103283. doi: 10.1016/j.trd.2022.103283

[23] Shakeri N., Zadeh M., Nielsen B.J.: *hydrogen fuel cells for ship electric propulsion: Moving toward greener ships*. IEEE Electrification Mag. **8**(2020), 2, 27–43. doi: 10.1109/MELE.2020.2985484

[24] Peng Y., Xu A.: *Development of hydrogen fuel cell propulsion technology for ships*. Strategic Study CAE **21**(2019), 6, 18–21. doi: 10.15302/J-SSCAE-2019.06.003

[25] van Veldhuizen, B.N., Hekkenberg, R.G., Codiglia, L.: *Fuel cell systems applied in expedition cruise ships: A comparative impact analysis*. In: Proc. 12th Symp. on High-Performance Marine Vehicles, HIPER '20 (V. Bertram, Ed.), 170–188). TU Hamburg-Harburg, 2020.

[26] Minutillo M., Cigolotti V., Di Ilio G., Bionda A., Boonen E.-J., Wannemacher T.: *Hydrogen-based technologies in maritime sector: technical analysis and prospective*. E3S Web Conf. 334 06011 (2022). doi: 10.1051/e3sconf/202233406011

[27] Jeon H., Kim S., Yoon K.: *Fuel cell application for investigating the quality of electricity from ship hybrid power sources*. J. Mar. Sci. Eng. **7**(2019), 241. doi: 10.3390/jmse7080241

[28] Xing H., Stuart C., Spence S., Chen H.: *Fuel cell power systems for maritime applications: Progress and perspectives*. Sustainability **13**(2021), 1213. doi: 10.3390/su13031213

[29] ABS Sustainability Whitepaper. *Methanol as Marine Fuel*. Feb. 2021. https://absinfo.eagle.org/acton/media/16130/sustainability-whitepaper-methanol-as-marine-fuel (accessed 22 Apr. 2023).

[30] ABS Sustainability Whitepaper. *Ammonia as Marine Fuel*. Oct. 2020. https://absinfo.eagle.org/acton/media/16130/sustainability-whitepaper-ammonia-as-marine-fuel (accessed 22 Apr. 2023).

[31] Ustolin F., Campari A., Taccani R.: *An extensive review of liquid hydrogen in transportation with focus on the maritime sector*. J. Mar. Sci. Eng. **10**(2022), 1222. doi: 10.3390/jmse10091222

[32] Panić I., Cuculić A., Ćelić J.: *Color-coded hydrogen: Production and storage in maritime sector*. J. Mar. Sci. Eng. **10**(2022), 1995. doi: 10.3390/jmse10121995

[33] van Rheenen E.S., Paddinga J.T., Slootwegb J.C., Vissera K.: *A review of the potential of hydrogen carriers for zero emission, low signature ship propulsion systems*. In: Proc. 16th Bien. Int. Naval Engineering Conf. and Exhib., Nov. 2022. doi: 10.24868/10649

[34] Matthé J., Jai P., Pierre J.: *Hydrogen in Maritime. Opportunities and Challenges*. June 2022. https://www.wsp.com/en-pl/insights/hydrogen-in-maritime-opportunities-and-challenges (accessed 22 Apr. 2023).

[35] Hyde K., Ellis A.: *Feasibility of hydrogen bunkering*. ITM Power (2019). https://northsearegion.eu/media/9385/feasibility-of-hydrogen-bunkering-final-080419.pdf (accessed 22 Apr. 2023).

[36] Tayarani H., Ramji A.: *Life cycle assessment of hydrogen transportation pathways via pipelines and truck trailers: Implications as a low carbon fuel*. Sustainability **14**(2022), 12510. doi: 10.3390/su141912510

[37] Patonia A., Poudineh R.: *Global trade of hydrogen*. The Oxford Institute for Energy Studies (2022). https://www.oxfordenergy.org/publications/global-trade-of-hydrogen-what-is-the-best-way-to-transfer-hydrogen-over-long-distances/ (accessed 22 Apr. 2023).

[38] Otto M., Chagoya K.L., Blair R.G., Hick M.S., Kapat J.S.: *Optimal hydrogen carrier: Holistic evaluation of hydrogen storage and transportation concepts for power generation, aviation, and transportation*. J. Energ. Stor. **55**(2022), D, 105714. doi: 10.1016/j.est.2022.105714

[39] Johnston C., Khan M.H.A., Amal R., Daiyan R., MacGill I.: *Shipping the sunshine: An open-source model for costing renewable hydrogen transport from Australia*. Int. J. Hydrogen Energy **47**(2022), I47, 20362–20377. doi: 10.1016/j.ijhydene.2022.04.156

[40] Witek M., Uilhoorn F.: *Impact of hydrogen blended natural gas on linepack energy for existing high pressure pipelines*. Arch. Thermodyn. **43**(2022), 2, 111–124. doi: 10.24425/ather.2022.143174

[41] Bacquart T., Moore N., Wilmot R., Bartlett S., Morris A.S.O., Olden J., Becker H., Aarhaug T.A., Germe S., Riot P., Murugan A., Mattelaer V.: *hydrogen for maritime application—quality of hydrogen generated onboard ship by electrolysis of purified seawater*. Processes **9**(2021), 1252. doi: 10.3390/pr9071252

[42] Kanchiralla F.M., Brynolf S., Malmgren E., Hansson J., Grahn M.: *Life-cycle assessment and costing of fuels and propulsion systems in future fossil-free shipping*. Environ. Sci. Technol. **56**(2022), 17, 12517–12531. doi: 10.1021/acs.est.2c03016

[43] Sullivan B.P., Ansaloni G.M.M., Bionda A., Rossi M.: *A life cycle perspective to sustainable hydrogen powered maritime systems – functional and technical requirements*. Int. J. Prod. Lifecycle Manag. **14**(2022), 2-3, 282–301. doi: 10.1504/IJPLM.2022.125822

[44] Lee G.N., Kim J.M., Jung K.H., Park H., Jang H.S., Lee C.S., Lee J.W.: *Environmental life-cycle assessment of eco-friendly alternative ship fuels (MGO, LNG, and hydrogen) for 170 GT nearshore ferry*. J. Mar. Sci. Eng. **10**(2022), 755. doi: 10.3390/jmse10060755

[45] Kotowicz J., Bartela Ł., Dubiel-Jurgaś K.: *Analysis of energy storage system with distributed hydrogen production and gas turbine*. Arch. Thermodyn. **38**(2017), 4, 65–87. doi: 10.1515/aoter-2017-0025

[46] Ajanovic A., Sayer M., Haas R.: *The economics and the environmental benignity of different colors of hydrogen*. Int. J. Hydrogen Energy **47**(2022), 57, 24136–24154. doi: 10.1016/j.ijhydene.2022.02.094

[47] *Hydrogen as Marine Fuel Whitepaper*. https://absinfo.eagle.org/acton/media/16130/hydrogen-as-marine-fuel-whitepaper (accessed 22 Apr. 2023).

[48] *Hydrogen – Energy Transition Technology.* https://www.irena.org/Energy-Transition/Technology/Hydrogen (accessed 22 Apr. 2023).

[49] *HySeas Project.* https://www.hyseas3.eu/the-project/ (accessed 22 Apr. 2023).

[50] *Aquaterra Energy, Lhyfe and Borr Drilling form partnership for pioneering offshore green hydrogen jack-up rig production concept.* https://aquaterraenergy.com/aquaterra-energy-lhyfe-and-borr-drilling-form-partnership-for-pioneering-offshore-green-hydrogen-jack-up-rig-production-concept/ (accessed 22 Apr. 2023).

[51] *Hydrogen production takes system to new levels.* https://tractebel-engie.com/en/news/2019/400-mw-offshore-hydrogen-production-takes-system-to-new-levels (accessed 22 Apr. 2023).

[52] *Hydrogen Power-to-X (P2X) fuels.* https://wartsila.prod.sitefinity.fi/energy/sustainable-fuels/the-many-types-of-sustainable-fuels (accessed 22 Apr. 2023).

[53] *Type 212A class Submarine.* https://www.seaforces.org/marint/German-Navy/Submarine/Type-212A-class.htm (accessed 22 Apr. 2023).

[54] Kolodziejski M., Michalska-Pozoga I.: *Battery energy storage systems in ships' hybrid/electric propulsion systems.* Energies **16**(2023), 1122. doi: 10.3390/en16031122

[55] *Viking Lady.* https://corvusenergy.com/projects/viking-lady/ (accessed 22 Apr. 2023).

[56] European Maritime Safety Agency: *Study on electrical energy storage for ships.* DNV GL. Rep. 2019-0217, Rev. 04. Document No.: 11B59ZDK-1, 2020-05-05, EMSA, Lisbon 2019.

[57] Schuler M.: *First ship with high temperature fuel cell for greener power supply.* gCaptain, 2009. https://gcaptain.com/ship-high-temperature-fuel-cell/ (accessed 22 Apr. 2023).

[58] *Ammonia fuel cells for deep-sea shipping – a key piece in the zero-emission puzzle.* https://shipfc.eu/ammonia-fuel-cells-for-deep-sea-shipping-a-key-piece-in-the-zero-emission-puzzle/ (accessed 22 Apr. 2023).

[59] *Viking Energy with ammonia-driven fuel cell.* https://eidesvik.no/viking-energy-with-ammonia-driven-fuel-cell/ (accessed 22 Apr. 2023).

[60] *CSOV Edda Breeze.* https://eddawind.com/vessels/edda-breeze/ (accessed 22 Apr. 2023).

[61] Vessel review. *Edda Breeze – Edda Wind hydrogen ready, walk-to-work vessel.* https://www.bairdmaritime.com/work-boat-world/offshore-world/offshore-operations-maintenance/offshore-maintenance/vessel-review-edda-breeze-edda-wind-hydrogen-ready-walk-to-work-vessel-that-can-house-120-personnel/ (accessed 22 Apr. 2023).

[62] Burke J.: *Hydrogen-ready vessel delivered.* https://www.dieselgasturbine.com/news/hydrogen-ready-vessel-delivered/8021032.article (accessed 22 Apr. 2023).

[63] *WFIV Boreas.* https://www.vanoord.com/en/updates/van-oord-takes-next-step-implementing-more-sustainable-fuels/ (accessed 22 Apr. 2023).

[64] *Offshore Installation Vessel Boreas*. https://vanoord.de/wp-content/uploads/2022/03/Equipment-leaflet-Offshore-installation-vessel-Boreas-draft.pdf (accessed 22 Apr. 2023).

[65] *Stena Germanica RoPax Ferry*. https://www.ship-technology.com/projects/stena-germanica-ropax-ferry/ (accessed 22 Apr. 2023).

[66] Energy Observer. *From ocean racer to tech wonder*. https://www.yachtingworld.com/extraordinary-boats/energy-observer-from-ocean-racer-to-tech-wonder-132195 (accessed 22 Apr. 2023).

[67] Nagy-McKenna C.: *Meet the Energy Observer, the World's First Hydrogen-powered Boat and Trailblazing Energy Laboratory*. https://www.enerdynamics.com/Energy-Currents_Blog/Meet-the-Energy-Observer-the-Worlds-First-Hydrogen-powered-Boat-and-Trailblazing-Energy-Laboratory.aspx (accessed 22 Apr. 2023).

[68] Energy Observer. *Review of the 15,000 nautical miles of navigation in 2021*. https://www.energy-observer.org/innovations/energy-balance-2021 (accessed 22 Apr. 2023).

[69] Energy Observer. *Energy Observer 2, a demonstrator vessel that runs on liquid H2*. https://www.energy-observer.org/resources/energy-observer-2-liquid-hydrogen (accessed 22 Apr. 2023).

[70] Hakirevic Prevljak N. *Energy Observer unveils zero-emission, LH2-powered cargo ship concept*. https://www.offshore-energy.biz/energy-observer-unveils-lh2-powered-cargo-ship-concept/ (accessed 22 Apr. 2023).

[71] *BAE Systems Provides First Zero-Emission Fuel Cell Propulsion System for U.S. Vessel*. https://seapowermagazine.org/bae-systems-provides-first-zero-emission-fuel-cell-propulsion-system-for-u-s-vessel/ (accessed 22 Apr. 2023).

[72] *Hydrogen Fuel Cell Passenger Ferry for SWITCH Maritime*. https://www.allamericanmarine.com/vessels-gallery/sea-change-hydrogen/ (accessed 22 Apr. 2023).

[73] Ervin H.: *Tour the Sea Change ferry at Marine Log's FERRIES 2022*. https://www.marinelog.com/passenger/ferries/tour-the-sea-change-ferry-at-marine-logs-ferries-2022/ (accessed 22 Apr. 2023).

[74] *Sea Change*. https://www.switchmaritime.com/projects (accessed 22 Apr. 2023).

[75] *Hydrogen Ferry Hydra*. https://corvusenergy.com/projects/mf-hydra/ (accessed 22 Apr. 2023).

[76] Vessel review. *Hydra – Norled takes delivery of ferry designed to run on liquid hydrogen*. https://www.bairdmaritime.com/work-boat-world/passenger-vessel-world/ro-pax/vessel-review-hydra-norled-takes-delivery-of-ferry-designed-to-run-on-liquid-hydrogen/ (accessed 22 Apr. 2023).

[77] *Norled's hydrogen ferry approved for service*. https://www.rivieramm.com/news-content-hub/norleds-liquid-hydrogen-ferry-hydra-to-enter-active-service-75630 (accessed 22 Apr. 2023).

[78] Bahtić F.: *Power Cell to provide hydrogen solutions for two Norwegian state ferries*. https://www.offshore-energy.biz/powercell-to-provide-hydrogen-solutions-for-two-norwegian-state-ferries/ (accessed 22 Apr. 2023).

[79] *MAN Engines: The first dual fuel hydrogen engines in use on a work boat*. MAN Truck & Bus SE Press Newsroom, 01-06-2022. https://press.mantruckandbus.com/ corporate/man-engines-the-first-dual-fuel-hydrogen-engines-in-use-on-a-work-boat/ (accessed 22 Apr. 2023).

[80] Vessel review. *HYDROCAT 48 – Netherlands' Windcat Workboats puts hydrogen-fueled newbuild in operation*. https://www.bairdmaritime.com/work-boat-world/offshore-world/offshore-operations-maintenance/crew-transfer/vessel-review-hydrocat-48-netherlands-windcat-workboats-puts-hydrogen-fuelled-newbuild-in-operation/ (accessed 22 Apr. 2023).

[81] *Windcat Workboats' Hydrogen-Powered Hydrocat 48 Based at Port of Ostend*. https://www.heavyliftnews.com/windcat-workboats-hydrogen-powered-hydrocat-48-based-at-port-of-ostend/ (accessed 22 Apr. 2023).

[82] *Hydrogen-powered Hydrocat 48 completes its first job with Vestas*. https://www.maritimeeconomy.com/post-details.php?post_id=a2lmaQ==&post_name=Hydrogenpowered%20Hydrocat%2048%20completes%20its%20first%20job%20with%20Vestas&segment_name=Operations (accessed 22 Apr. 2023).

[83] *Hydrogen-powered tug is world first for Port of Antwerp*. https://newsroom.portofantwerpbruges.com/hydrogen-powered-tug-is-world-first-for-port-of-antwerp (accessed 22 Apr. 2023).

[84] *Port of Antwerp-Bruges & CMB.TECH prepare Hydrotug, the first hydrogen-powered tugboat*. https://newsroom.portofantwerpbruges.com/port-of-antwerp-bruges–cmb tech-prepare-hydrotug-the-first-hydrogen-powered-tugboat (accessed 22 Apr. 2023).

[85] *World's First Hydrogen-Powered Tug Arrives in Belgium for Final Tests*. https://maritime-executive.com/article/world-s-first-hydrogen-powered-tug-arrives-in-belgium-for-final-tests (accessed 22 Apr. 2023).

[86] *Hydrotug*. https://cmb.tech/hydrotug-project (accessed 22 Apr. 2023).

[87] *BeHydro engine emissions*. https://www.behydro.be/en/home.html (accessed 22 Apr. 2023).

[88] *Windcat Offshore and Damen Shipyards develop future-proof CSOVs*. CMB.TECH. Nov. 29, 2022. https://cmb.tech/news/windcat-offshore-and-damen-shipyards-develop-future-proof-csovs (accessed 22 Apr. 2023).

[89] *First drawings of Scottish led hydrogen-powered ferry project launched*. https://safety4sea.com/first-drawings-of-scottish-led-hydrogen-powered-ferry-project-launched/ (accessed 22 Apr. 2023).

[90] *HySeas Project String Test*. https://www.hyseas3.eu/string-test/ (accessed 22 Apr. 2023).

[91] *Topeka's hydrogen vessels one step closer to reality*. https://www.wilhelmsen.com/media-news-and-events/press-releases/2021/topekas-hydrogen-vessels-one-step-closer-to-reality/ (accessed 22 Apr. 2023).

[92] *HyShip Topeka*. https://hyship.eu/about/ (accessed 22 Apr. 2023).

[93] Ulstein SX190 – concept. https://ulstein.com/vessel-design/sx190 (accessed 22 Apr. 2023).

[94] *J102 Zero Emission*. https://ulstein.com/vessel-design/j102-1 (accessed 22 Apr. 2023).

[95] *Norwegian Ship Design chosen to design the world's first hydrogen powered cargo ship*. https://www.norwegianshipdesign.no/archive/with-orca-powered-by-nature (accessed 22 Apr. 2023).

[96] *Hydrogen-Fueled and Wind-Powered Bulker Receives Design Approval*. https://maritime-executive.com/article/hydrogen-fueled-and-wind-powered-bulker-receives-design-approval (accessed 22 Apr. 2023).

[97] *Neo Orbis ship concept*. https://www.nweurope.eu/media/16834/neo-orbis_en.pdf (accessed 22 Apr. 2023).

**archives**
**of thermodynamics**
Vol. **44**(2023), No. 4, 381–403
DOI: 10.24425/ather.2023.149730

# An approach to coupling the gas flow dynamics and thermodynamics of hydrogen solubility in L485ME steel grade for estimation of fracture toughness

**MACIEJ WITEK***
**FERDINAND UILHOORN**

Warsaw University of Technology, Department of Heating and Gas Systems, Nowowiejska 20, 00-653 Warsaw, Poland

**Abstract** The paper presents the problem of coupling the gas flow dynamics in pipelines with the thermodynamics of hydrogen solubility in steel for the estimation of the fracture toughness. In particular, the influence of hydrogen blended natural gas transmission on hydrogen solubility and, consequently, on fracture toughness is investigated with a focus on the L485ME low-alloy steel grade. Hydraulic simulations are conducted to obtain the pressure and temperature conditions in the pipeline. The hydrogen content is calculated from Sievert's law and, as a consequence, the fracture toughness of the base metal and heat-affected zone is estimated. Experimental data is used to define hydrogen-assisted crack size propagation in steel as well as to a plane strain fracture toughness. The simulations are conducted for a real natural gas transmission system and compared against the threshold stress intensity factor. The results showed that the computed fracture toughness for the heat-affected zone significantly decreases for all natural gas and hydrogen blends. The applied methodology allows for identification of the hydrogen-induced embrittlement susceptibility of pipelines constructed from thermomechanically rolled tubes worldwide most commonly used for gas transmission networks in the last few decades.

**Keywords:** Gas flow dynamics; Hydrogen embrittlement; Fracture toughness; Hydrogen solubility; L485ME steel grade

*Corresponding Author. Email: maciej.witek@pw.edu.pl

# 1 Introduction

## 1.1 Hydrogen induced steel embrittlement

Hydrogen-induced cracking (HIC) [1] occurs as a consequence of hydrogen (H) in atomic form diffusing through the steel surface and accumulating in the interfaces between inclusions and the steel matrix. At temperatures up to 320°C, H atoms combine with each other at the interfaces to form $H_2$ in a gaseous phase and increase the pressure inside the microvoids of the material microstructure. The charging of pressurized hydrogen in such places leads to disbanding of interfaces between inclusions and the steel matrix, and to forming microcracks at either one or both sides of the inclusion tips in an HIC mechanism. Another process of steel degradation associated with H diffusion into the pipe wall is hydrogen environmental assisted cracking (HEC) [1]. In this case, hydrogen atoms are absorbed and adsorbed in the crack tip region and diffuse in the fracture zone which is in front of the crack tip where the stress is highest under local loads and internal pressure [2]. Additionally, H atoms from surrounding regions also diffuses to the fracture zone through the crystal lattice. The crack propagation is caused by HEC of steel below yield strength and results in a subcritical crack growth. During the dynamic hydrogen charging, a strong interaction should exist between hydrogen diffusion and local stress in front of the crack in the notched specimens. The hydrostatic stress is formed at a distance ahead of the crack tip assists hydrogen diffusion [3].

Many hydrogen embrittlement (HE) concepts of steel degradation are presented in literature; however, commonly accepted and mostly used theories are hydrogen enhanced decohesion embrittlement (HEDE) and hydrogen enhanced localized plasticity (HELP). The concept of HEDE [4] suggests degradation due to localized reduction in cohesive strength of the iron lattice, hence the separation of cleavage planes or grain boundaries under a lower stress occurs. The embrittlement is attributed to the weakening of interatomic bonds, resulting in separation of atoms. The HELP mechanisms [5] assume that atomic hydrogen accelerate the dislocation mobility through an elastic shielding effect that causes a local reduction in shear stress. H transportation by dislocation motion could lead to localized high concentrations in front of crack tip. Moreover, local high strains, due to hydrogen clusters around dislocations, might disrupt interfaces and structures. The stresses at these locations increase the risk of failure. When a sufficient hydrogen concentration occurs, the local deformation process leads to brittle fracture of steel.

In study [6], the effect of a low partial hydrogen in a mixture with natural gas (NG) on the tensile, notched tensile properties, and fracture toughness of X70 pipeline steel is investigated. It is confirmed that a mixture of 10 MPa gas and 1% $H_2$ causes a remarkable reduction in the fracture toughness in respect of crack tip opening displacement (CTOD). As per American Petroleum Institute (API) the susceptibility of API X70 weld joints to hydrogen gas is investigated in [7], using slow strain rate tensile tests. The higher susceptibility of the weld and cross-weld specimens was primarily attributed to synergic effects between the microstructural characteristics, stress localization, and microhardness distribution, particularly, microhardness is crucial for nucleation of microcracks and a hydrogen diffusion rate induced in stress and strain localizations. Paper [8] deals with hydrogen HE susceptibility of a weld heat affected zone under thermally simulated conditions of X70 pipe steel in high pressure hydrogen gas at 20°C. Fracture mechanics Single Edge Notched Tension tests at various hydrogen pressures (0.1, 0.6, 10 and 40 MPa $H_2$) have been carried out. The results show that hydrogen causes a strong decrease in the

fracture toughness with increasing hydrogen pressure. The critical hydrogen pressure for the onset of HE was observed to fall between 0.1 MPa and 0.6 MPa. These results were supported by scanning electron microscope (SEM) investigations of the fracture surfaces which showed a clear shift in the fracture mode at 0.6 MPa $H_2$. The sample surface preparation before loading in the autoclave was found to have a significant impact on hydrogen uptake of the steel. The lowest hydrogen uptake in study [9] was found for the induction bend compared to the base material X70M. Against expectations, the hydrogen uptake decreases with increasing exposure time the induction bend as well as L485ME helical welded pipe (SAWH – helically submerged arc welded). For line tube material, similar hydrogen levels were found for different microstructures for normalized and thermomechanically rolled pipes. For tube base material, the different hydrogen uptake may be attributed to a higher alloy content in the pipe. In order to obtain a combination of mechanical properties required for certain steel grades, a precise selection of alloying elements is necessary. However, some alloying components have an adverse influence on the embrittlement susceptibility of pipeline steels through introducing microstructural features that ultimately affect both diffusion and solubility of hydrogen. This effect is highly dependent on the manufacturing process as well as on heat treatment resulting in different microstructures of the base material [10]. The service degradation of Kh70 steel grade is studied in [11] and showed a considerable drop of Charpy energy, decrease in fracture toughness and reduced resistance to fatigue crack growth. The performed analysis of the resistance of the pipeline steels to the corrosion fatigue crack nucleation and growth and the respective recommendations are provided concerning the avoidance of the stress corrosion failure of gas transmission system.

## 1.2 Fracture toughness of low-alloy steel

Fracture toughness is a measure of the material ability to contain defect such as a crack; the higher value, the more resistant is the material to the crack extension. Fracture toughness values are typically presented in the literature in terms of plane strain fracture toughness ($K_{IC}$) for linear elastic materials, elastic-plastic fracture toughness is usually characterized by of J-integral ($J_{IC}$), crack growth resistance curves such as the slope of the fracture resistance curve related to the tearing capability of the material. The elastic-plastic method overall involves generation of J-R (J Resistance) curve for the material which is a plot of the steel resistance to crack extension using the J-integral as a function of stable crack extension. Elastoplastic fracture mechanics is applicable for ductile materials such as low-alloy carbon steel. If non-linear local steel deformation is confirmed to a small region around the crack tip, a plastic zone is small in comparison to the defect dimensions, linear plastic fracture mechanics can be applied.

However, for small scale yielding applicable in a concept of hydrogen embrittlement of steels, a target stress intensity factor is usually called fracture toughness. Linear fracture mechanics applied to an initiated crack as well as hydrogen-assisted propagation under cyclic or quasi-static loading may be used in a structural assessment of the pipeline life [12]. Wang [13] showed that the fracture toughness of L485ME steel grade declines with the rise in $H_2$ concentration achieved under steady-state charging conditions for specimens with the hydrogen. According to publication [3], a decrease in fracture toughness of X70 steel grade depends on several factors such as: (i) hydrogen charging condition and electrochemical charging current, (ii) hydrogen content and distribution in the materials, and (iii) dominant hydrogen embrittlement mechanisms, HELP or HEDE.

The observed fracture toughness degradation is influenced by multiple factors such as: (i) hydrogen concentration, (ii) pH value of the environment, (iii) corrosion rate of low carbon steel and (iv) degree of an activity and predominance of particular HE mechanisms, HELP or HEDE. It is worth mentioning that the decline in fracture toughness and a crack propagation phenomenon was detected and confirmed in different grades of steels, due to multiple active HE mechanisms (HELP + HEDE) [3]. This decrease is independent of activity and predominance of a particular HE mechanism, i.e., it was confirmed both in the case of dominance of HELP and HEDE mechanisms and also due to their synergistic action [3]. Despite numerous studies on possible hydrogen embrittlement mechanisms in steels published and summarized in comprehensive review such as [15], there is still no consensus among researchers on all HE mechanisms and their interactions.

The novelty of this work is the proposed methodology of estimation of the pipeline operating conditions using a dynamic flow model and the material fracture toughness determination. The latter parameter is evaluated against threshold values obtained from experimental data. In particular, the following issues are addressed in the present study:

- calculation of the hydrogen content in the tube wall base material and the heat affected zone using Sievert's law together with a nonisothermal transient gas flow model;
- calculations and experiments are used to compare a fracture toughness parameter, namely, a computed conditional stress intensity factor, with the threshold stress intensity factor for plane strain environmentally-assisted cracking;
- hydrogen-assisted crack size propagation in steel specimens is compared to the subcritical crack growth obtained from constant displacement method measurements and macroscopic/microscopic evaluation;
- estimation of a decrease in fracture toughness as a function of dynamic hydrogen charging in the pipe wall of L485ME steel grade.

## 2 Standardized fracture control qualification test of pipeline steel

A fracture toughness criterion or other method shall be specified to control fracture propagation when a pipeline suitable for transportation of $C_xH_y/H_2$ blends is designed to operate at a hoop stress over 40% of the specified minimum yield strength. When a fracture toughness criterion is applied, control shall be achieved by ensuring that the tube material presents adequate ductility. The tube material tensile requirements shall be specified on the purchasing specification and shall comply with the chemical and tensile requirements of EN-ISO 3183:2019 [16] and API 5L [17].

In this paper, Option B according to ASME B31.12 [18] was applied with the following requirements. The pipe and weld material shall be qualified for adequate resistance to fracture in $H_2$ gas at or above the design pressure and at ambient temperature using the applicable rules provided in Article KD-10 of ASME BPV Code Section VIII, Division 3 [19]. The purpose of this test is to qualify the material of the structure by testing three heats of the steels. The threshold stress intensity factor values ($K_{IH}$) shall be obtained from the thickest section from each heat of the material and a type of the

applied heat treatment. The test specimens shall be in the final heat-treated condition to be used in pipe manufacturing. A set of three specimens shall be tested from each of the following locations: base metal (BM), weld metal (WM) on the tube body, and heat-affected zone (HAZ) of joints, welded with the same qualified welding procedure specification as intended for the piping manufacturing. A change in the welding procedure requires retesting of welded joints in the scope of WM and HAZ. The test specimens shall be in the transverse longitudinal (TL) axis of forcing direction. If TL specimens cannot be obtained from the weld metal and the heat affected zone, then longitudinal transverse (LT) oriented specimens may be used. The values of $K_{IH}$ shall be obtained with the use of the test method described in KD-1040 of ASME BPV Code Section VIII, Division 3 [19]. The lowest measured value of $K_{IH}$ shall be used in the pipeline design analysis.

The values obtained as described above may be used for other tubes manufactured from the same material specification (steel grade) or similar material specification with the same nominal chemical composition, and the same heat treatment condition, providing its tensile and yield strengths do not exceed the values of the material used in the qualification tests by more than 5%. The welded joints shall meet the requirements of the welding procedure specification used for qualifying the construction material. Calculation of the maximum applied stress intensity factor ($K_{IA}$) required at design pressure is for the elliptical surface crack. The critical crack size is developed by applicable fatigue loading. Fatigue design rules specified in Article KD-1010 shall be used, or depth equals $t/4$, length equals $1.5t$, where $t$ is the pipe wall thickness. Determination of threshold stress intensity factor $K_{IH}$ in $H_2$ gaseous atmosphere by applying the test method, as specified in KD-1040.

Additional requirement for the pipe material are as follows:

- phosphorus (P) content of the tube shall not exceed 0.015% by weight;
- sulphur (S) – the maximum content for welded as well as seamless pipes is 0.010% by weight;
- the tube material shall be manufactured with a practical control of inclusions;
- minimum specified yield strength shall not exceed 555 MPa, maximum ultimate tensile strength of the weld metal shall not exceed 760 MPa and tube shall meet all applicable requirements of EN-ISO 3183:2019 [16] and API PSL2 [17];
- brittle and ductile specified in ASME B31.12 [18] shall be met.

## 2.1 Hydrogen embrittlement experiments for L485ME steel grade

The mechanical properties, such as yield and tensile strength, hardness as well as a chemical composition of L485ME steel grade of 10 selected tubes produced by Corinth Pipeworks S.A. [20], are presented in Appendix A. In the case of pipes used for experiments in the present study both hardness criterion set as less than 235 HV10 as well as percentage of selected micro additives determined as $S \leq 0.010\%$, $P \leq 0.0156\%$ are met. The steps applied for experimental evaluation of fracture toughness and crack size extension are defined according to KD-1041 [19]:

- The modified bolt-load specimen configuration as presented in Fig. 1 was utilized in accordance with ASTM E1681-03 international standard [21]. Base metal, weld metal centre line and HAZ testing locations were used as samples. Thirty-six L485

ME steel grade specimens from BM (12 specimens), WM (12), HAZ (12), were prepared from 14.2 mm SAWH pipe for fatigue pre-cracking testing, at ambient temperature, in general compliance with ASTM E1681-03 code.

- A machined notch was further extended through fatigue pre-cracking in ambient temperature conditions. Fatigue pre-cracking testing was performed using Instron Fatigue Propagation Program – Version 8.1 Build 4 following the test control parameters: range – 33 $\text{MPam}^{0.5}$, stress ratio – 0.100, points/cycle – 200, waveform sine frequency – 25 Hz.
- Specimen bolt-loading (crack opening) was performed in an inert atmosphere (pure $N_2$) in which oxygen and moisture were stored, and continuously monitored, below 5 and 50 ppm respectively, as required by the ASME code [18].
- According to the requirements of ASTM E1681 standard [21], the original pre-crack size ($a_o$) was measured after fracture at five locations, as presented in Fig. 1:
  - at the centre of the crack front ($a_o(1/2)$),
  - halfway the centre of the crack front ($a_o(1/4)$ and $a_o(3/4)$),
  - at the ends of the crack front on each side surface ($a_o(L)$ and $a_o(R)$).
- The applied displacement ($V_m$) was measured with the use of a CMOD-type electronic extensometer. Based on ASTM E1681-03 [21] equation in §9.1.3, the applied displacement was calculated for all specimens in order to exceed the minimum required value of applied stress intensity factor $K_{\text{IA}} = 110\ \text{MPam}^{0.5}$, with a typical target of $K_{\text{IA}} = 125\ \text{MPam}^{0.5}$. According to the provisions of standard ASME BPVC Sec. VIII, Division 3, KD-1041 [19], minimum stress intensity factor $K_{\text{IH,min}}$ is equal to 50% of $K_{\text{IA}}$, if the test was applied using the constant displacement method.
- Having completed the loading of specimens, they were placed in the autoclave which was closed tightly.
- Next, before being charged with high purity $H_2$ (grade 6.0), the autoclave was filled with high purity $N_2$ (grade 6.0) and the pressure was elevated to test value. The working pressure for the experiment was set at a minimum of 8 MPa for a duration of 1000 h.

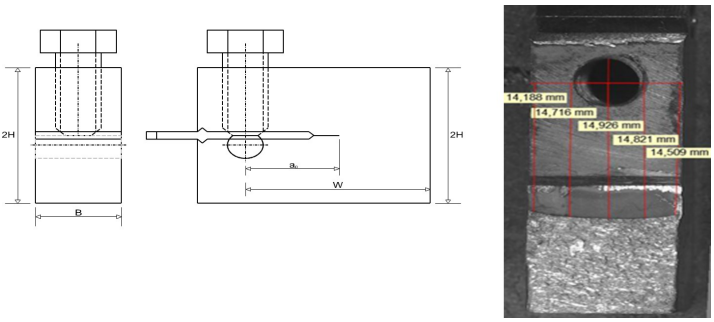


Figure 1: Bolt-load specimen for constant displacement and locations of crack size measurements [20].

- In order to highlight any potential crack propagation, the specimens were heat tinted in the furnace for 1 h and subsequently broken in liquid nitrogen. According to the requirements of ASTM E1681-03 code [21], evaluation of a crack growth caused by hydrogen was conducted perpendicular to the pre-crack at 25% $B$, 50% $B$ and 75% $B$ locations, where $B$ is the specimen thickness. The results of a target and measured crack size ($a_o$), applied displacement ($V_m$), values of target and applied stress intensity factor ($K_{\mathrm{IA}}$) as well as minimum stress intensity factor ($K_{\mathrm{IH,min}}$) are presented for representative specimens in Appendix B [20]. According to the evaluation of the specimens, no subcritical crack growth more than 0.25 mm average on three locations was identified for a minimum of three specimens tested per a position. The table in Appendix B presents in details the measurements of the crack size and fracture toughness values for L485ME steel grade, for thickness of specimens – 12.5 mm, width – 25 mm, and height – 12.1 mm. Transverse longitudinal orientated specimens were taken from BM (12 specimens), WM (12), HAZ (12), from SAWH pipes with the wall thickness of 14.2 mm.
- Post-test macroscopic evaluation of specimens as well as evaluation with Scanning Electron Microscope are presented in the next subchapter.

## 2.2 Macroscopic and microscopic examination of the specimens

All the prepared samples were analysed macroscopically and using the electron microscopy. Macroscopic examination of the sample was performed with the use of Nikon SMZ 1500 stereo-microscope. Observations with a higher magnification microscope were performed with JEOL IT-800 HL SEM under 20 kV accelerating voltage, coupled with EDAX Octane Elect Plus system with the usage of TEAM software. The results of selected macroscopic examinations are presented in Figs. 2(a)–(c), whereas representative electron micrographs are shown in Figs. 3(a)–(c). Similar results were observed in the remaining samples, as listed in Appendix B. Therefore, no HIC was detected in 36 examined samples.

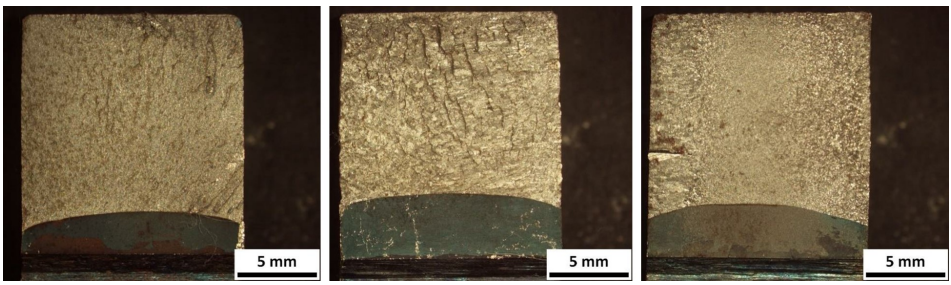


(a) (b) (c)

Figure 2: Macrographs of fracture surfaces of (a) S203A BM1, (b) S203A W4 and (c) S203A HAZ4 [20].

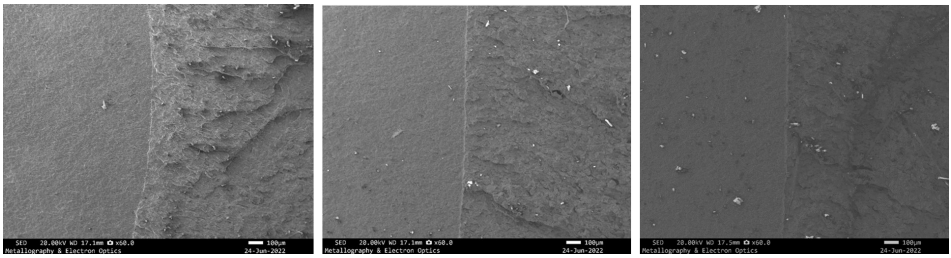

(a) (b) (c)

Figure 3: Electron micrographs (SEM) showing the interface between the fatigue and the crack initiation zone of the fracture surface at (a) 25%, (b) 50%, and (c) 75% of the S203A-BM1 specimen width [20].

# 3 Coupling of flow dynamics, hydrogen solubility and fracture toughness

In this section, the governing equations of the compressible flow model, thermodynamics of hydrogen solubility at equilibrium and empirical correlations for the fracture toughness are presented. The flow model is used to compute the pressure and temperature conditions in the pipeline. The results are used to calculate the hydrogen content in the tube wall using Sievert's law. The fracture toughness can be estimated from the hydrogen content. It is assumed that thermodynamic equilibrium exists between the steel and hydrogen in the gas mixture. This modeling approach allows for identification of the time and location where HE might cause a detrimental failure.

## 3.1 Gas flow model

The flow model constitutes a non-homogeneous hyperbolic system of partial differential equations derived from the conservation principles of mass, momentum, and energy. The governing equations can be written as [22, 23]:

$$\frac{\partial \mathbf{U}}{\partial t} + \mathbf{F}(\mathbf{U})\frac{\partial \mathbf{U}}{\partial x} + \mathbf{S}(\mathbf{U}) = 0, \quad \forall x \in \mathbb{R}, \quad t \in \mathbb{R}^+, \tag{1}$$

with

$$\mathbf{F}(\mathbf{U}) = \begin{bmatrix} -\dfrac{\dot{m}(a_s^2\alpha_2 - RTz)}{Ap} & \dfrac{a_s^2}{A} & \dfrac{a_s^2\dot{m}\alpha_1}{AT} \\ A - \dfrac{a_s^2\alpha_2^2 c_p \dot{m}^2 - R a_s^2 \alpha_1^2 \alpha_2 \dot{m}^2 z}{Ac_p p^2} & \dfrac{\dot{m}(\alpha_2 c_p a_s^2 - Rz a_s^2 \alpha_1^2 + RTc_p z)}{Ac_p p} & \dfrac{a_s^2\alpha_1\dot{m}^2(\alpha_2 c_p - R\alpha_1^2 z)}{ATc_p p} \\ -\dfrac{RTa_s^2\alpha_1\alpha_2\dot{m}z}{Ac_p p^2} & \dfrac{RTa_s^2\alpha_1 z}{Ac_p p} & \dfrac{R\dot{m}z(a_s^2\alpha_1^2 + Tc_p)}{Ac_p p} \end{bmatrix}, \tag{2}$$

and

$$\mathbf{S}(\mathbf{U}) = \begin{bmatrix} -\dfrac{a_s^2\alpha_1\left(\Omega A p + RT\dot{m}f_r z\right)}{A^2 T c_p p} \\ f_r + \dfrac{pAg}{zTR}\sin\theta \\ -\dfrac{a_s^2\alpha_2\left(\Omega A p + RT\dot{m}f_r z\right)}{A^2 c_p p^2} \end{bmatrix}. \tag{3}$$

The parameters $\alpha_1$ and $\alpha_2$ are defined as follows:

$$\alpha_1 = 1 + \frac{T}{z}\left(\frac{\partial z}{\partial T}\right)_p \quad \alpha_2 = 1 - \frac{p}{z}\left(\frac{\partial z}{\partial p}\right)_T. \tag{4}$$

The state vector is defined as $\mathbf{U} = \begin{bmatrix} p & \dot{m} & T \end{bmatrix}$ and the following initial and boundary conditions are as follows:

$$p(x,0) = p_0(x), \qquad T(x,0) = T_0(x), \tag{5}$$

$$p(0,t) = p_0\,, \qquad \dot{m}(L,t) = \phi(t), \qquad T(0,t) = T_0\,, \tag{6}$$

where $\phi(t)$ is the outflow demand. Other variables and parameters are pressure $p$, mass flow rate $\dot{m}$, temperature $T$, cross-sectional area $A$, frictional force $w$, friction factor $f_r$, gravitational acceleration $g$, angle of inclination $\theta$, rate of heat transfer $\Omega$, specific gas constant $R$, compressibility factor $z$, and specific heat at constant pressure $c_p$. The isentropic wave speed $a_s$ is calculated as follows:

$$\left(\frac{\partial p}{\partial \rho}\right)_s = \left[\frac{\rho}{p}\left(1 - \frac{p}{z}\left(\frac{\partial z}{\partial p}\right)_T - \frac{p}{\rho c_p T}\left(1 + \frac{T}{z}\left(\frac{\partial z}{\partial T}\right)_p\right)^2\right)\right]^{-1}. \tag{7}$$

The frictional force $w$per unit length is defined as

$$w = \frac{1}{8} f_r \rho v \left|v\right| \pi d_i\,, \tag{8}$$

with velocity $v$ and internal diameter $d_i$. The friction factor is calculated from [24]:

$$f_r = -0.8685 \ln\left(\frac{1.964\ln(\mathrm{Re}) - 3.8215}{\mathrm{Re}} + \frac{\varepsilon}{3.71 d_i}\right)^{-2}, \tag{9}$$

where $\varepsilon$ denotes the roughness and Re is the Reynolds number.

The steady heat transfer between the fluid and soil per unit length and time is defined as:

$$\Omega = -\pi d U \left(T - T_s\right), \tag{10}$$

where $U$ is the total heat transfer coefficient and consists of the heat transfer between the gas and the inner wall, heat transfer through the pipe wall, and heat transfer between the outer wall and soil with temperature $T_s$. For a pipeline with three different layers, it can be defined as follows:

$$U = \left(\frac{1}{h_i} + r_1\frac{\ln\left(r_2/r_1\right)}{k_1} + r_1\frac{\ln\left(r_3/r_2\right)}{k_2} + r_1\frac{\ln\left(r_4/r_3\right)}{k_3} + \frac{r_1}{r_3 h_o}\right)^{-1}, \tag{11}$$

where $k$ and $r$ refer to the thermal conductivity and a radius of the wall layer, respectively. The heat transfer from the gas to the wall is given by

$$h_i = \mathrm{Nu}\frac{k_{\mathrm{gas}}}{d_i}\,, \tag{12}$$

where $k_{\mathrm{gas}}$ is the thermal conductivity of the fluid. The Nusselt number is obtained from the Dittus-Boelter correlation [25]:

$$\mathrm{Nu} = 0.023\left(\frac{4\dot{m}}{\pi d\mu}\right)^{4/5}\left(\frac{c_p\mu}{k_{\mathrm{gas}}}\right)^{0.3}\,. \tag{13}$$

The heat transfer coefficient between the outer wall and soil is defined as:

$$h_o = \frac{k_{\mathrm{soil}}}{\left(\frac{d_o}{2}\right)\cosh^{-1}\left(\frac{2Z}{d_o}\right)}\,, \tag{14}$$

where $k_{\mathrm{soil}}$ is the thermal conductivity of the soil, and $Z$ is the distance between the top of the soil and the center of the pipe. The equation of state (EOS) GERG-2008 [26], which is explicit in the Helmholtz free energy as a function of density, temperature, and composition, is used to calculate the thermodynamic properties.

For the numerical approximation of Eq. (1), a semidiscretization approach is used, where the flow model is converted into a set of ordinary differential equations (ODEs) by the discretization of the spatial derivatives. The system of ODEs can be written as:

$$\frac{d\mathbf{u}(t)}{dt} = -\mathbf{F}(\mathbf{u})\mathbf{T}\,\mathbf{u}(t) - \mathbf{S}(\mathbf{u}(t)) = f(\mathbf{u}(t)), \tag{15}$$

where $\mathbf{T} = \sum_{j=1}^{n} \mathbf{I}_j \otimes \mathbf{T}^{(j)}$, and $n = 3$ and $\mathbf{T}^{(j)} = \mathbf{T}^{(1)}\ \forall j$, where the coefficients can be found in [27] and refer to a classical five-point, fourth-order finite-difference approximation. For the integration of $f(\mathbf{u}(t))$, the TR-BDF2 scheme [28] is used. The implementation of this scheme can be found in [29,30]. The sparsity of the ODEs is exploited to reduce the computation time.

## 3.2 Hydrogen solubility computations

In thermodynamic equilibrium, the chemical potential of hydrogen in gaseous phase $\mu^{\mathrm{gas}}_{\mathrm{H_2}}$ and hydrogen dissolved in steel $\mu^{\mathrm{M}}_{\mathrm{H}}$ should be equal, i.e., $1/2\mu^{\mathrm{gas}}_{\mathrm{H_2}} = \mu^{\mathrm{M}}_{\mathrm{H}}$ [31]. This condition leads to Sievert's law and is frequently used to describe the hydrogen solubility of metals. The details concerning its derivation can be found, for example, in [32]. Drexler *et al.* [33] extended Sievert's law to low temperatures and high gas pressures, considering microstructural trapping sites, fugacity, and multiaxial stress states in the following manner:

$$c_{\mathrm{H}} = k_0\sqrt{f}\exp\left(-\frac{\Delta H_s - \sigma_H V_H}{RT}\right), \tag{16}$$

where $k_0$ is the solubility coefficient, $f$ is the fugacity of hydrogen, $\Delta H_s$ is the change of the solution enthalpy, $\sigma_H$ is the hydrostatic stress, and $V_H$ is the partial molar volume of hydrogen in solid solution. The solubility coefficient is defined as [34]:

$$k_0 \cong k_0'\left(\frac{N_T}{N_L} + \frac{N_T}{N_{\mathrm{L}}K_T} + 1\right), \tag{17}$$

where $k_0'$ is a constant pre-factor, and $K_T = \exp(-E_b/RT)$ where $N_L$ and $N_T$ are the densities of the lattice and trap sites, respectively, and $E_b$ is the trap binding energy. The hydrostatic stress for thin-wall pipelines ($d/t_w > 20$) is approximated by

$$\sigma_{\mathrm{H}} = \frac{pr_i}{2t_w}, \tag{18}$$

with internal radius $r_i$ and wall thickness $t_w$. It is assumed that the material is linear-elastic, isotropic, and homogeneous, and the stress distributions throughout the wall do not vary. To calculate the hydrogen solubility from Eq. (16), the flow model (1) is used to obtain the gas pressure and temperature. The fugacity of hydrogen in the natural gas mixture is calculated from GERG-2008.

### 3.3 Fracture toughness calculations

Based on experiments, Wang [13] introduced a correlation for the conditional fracture toughness $K_{\mathrm{IQ}}$ according to ASTM E-399-22 [35] as a function of hydrogen concentration under hydrogen pre-charging $K_{\mathrm{IQ},p}$ and dynamic charging $K_{\mathrm{IQ},d}$ at slow strain rate tension for line tube steel API X70. The corresponding correlations are:

$$K_{\mathrm{IQ},p} = 91.29 - 2.15c_{\mathrm{H}} \tag{19}$$

and

$$K_{\mathrm{IQ},d} = 58.31 - 19.84\log c_{\mathrm{H}} \tag{20}$$

respectively. These correlations are used to calculate the fracture toughness of the steel pipeline. However, it is required to perform this estimation carefully for two reasons. Firstly, the chemical composition of the steel, on which the correlations are based, is slightly different (see Table 2). Secondly, it is unknown how well electrochemical hydrogen charging reflects the process of hydrogen diffusion in pipelines under transient flow conditions. Nevertheless, an attempt is made to indicate the fracture toughness for these two scenarios.

## 4 A real case study

For the case study, the Yamal pipeline section on Polish territory between compressor stations CS-1 and CS-2 is considered (see Fig. 4). The pipeline length is 177 km and is made of steel X70M with an internal diameter of 1379.6 mm and roughness of 1.96 μm. The thickness of the pipe wall is 19.22 mm and its thermal conductivity is 45.3 $\mathrm{W\,m^{-1}K^{-1}}$. In Section 2, L485ME steel grade was investigated. The relationship between the case study and Section 2 is that the steel grades can be considered as similar. The Yamal gas transmission pipeline is manufactured from X70M steel grade, according to the European standards from the 1990s. The chemical composition of X70M does not significantly differ from L485ME steel grade used in the experiments, according to EN-ISO 3183 [16] established in 2019. Nevertheless, as pointed out in Section 3.3, care should be taken because of the slight difference in chemical composition.

The soil temperature is 285.15 K and its thermal conductivity is 2.0 $\mathrm{W\,m^{-1}K^{-1}}$. The pipeline depth is 1.5 m. The boundary condition $\dot{m}(Lt) = \phi(t)$ is based on averaged daily values measured in 2020 (see Fig. 5) and the discharge pressure and temperature are set at

$p(0,t) = 8.4$ MPa and $T(0,t) = 290.15$ K, respectively. The service days of the compressors are excluded, and as a result, the simulation period is 351 days. To avoid instability of the compressors, the surge pressure at CS-2 should not drop below 4.9 MPa. The natural gas has the following composition in mol %: 96.803 $CH_4$, 1.773 $C_2H_6$, 0.395 $C_3H_8$, 0.063 $i$-$C_4H_{10}$, 0.057 $n$-$C_4H_{10}$, 0.010 $i$-$C_5H_{12}$, 0.007 $n$-$C_5H_{12}$, 0.009 $C_6$, 0.115 $CO_2$, and 0.768 $N_2$. At node 1, the hydrogen is blended with the natural gas with different volume percentages, namely, 10%, 25%, and 50%.

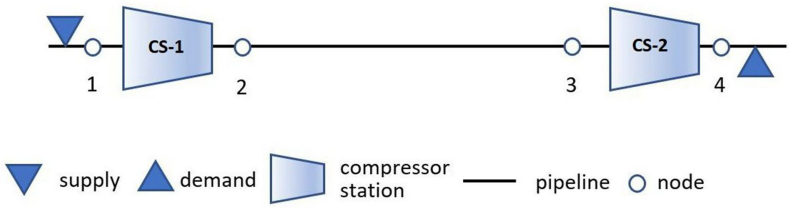


Figure 4: Schematic of the high-pressure pipeline.

The simulations are conducted for BM and HAZ with the parameters given in Table 1. The number of trapping sites per unit volume $N_L$ and binding energy $E_b$ are based on work presented in [14, 36]. These values are estimated from the effective diffusion coefficient for steel with a composition as shown in Table 2. The base metal consisted mainly of a fine-grained ferritic structure, while the HAZ material consisted of a mixture of ferrite and martensite/martensite-austenite due to microstructural alternations taking place during welding.

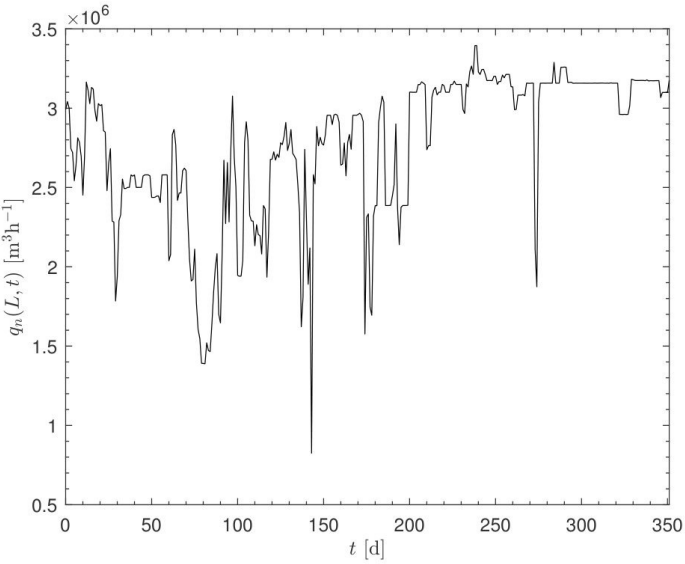


Figure 5: Flow rate boundary condition $\phi(t)$ at $x = L$.

Table 1: Parameters used for estimating the hydrogen content [14, 33, 36].

| Parameters | Values | Units |
|---|---|---|
| Binding energy for BM, $E_{b,\mathrm{BM}}$ | 36 | $\mathrm{kJ\,mol^{-1}}$ |
| Binding energy for HAZ, $E_{b,\mathrm{HAZ}}$ | 41 | $\mathrm{kJ\,mol^{-1}}$ |
| Trap density, $N_T$ | $2.3 \cdot 10^{19}$ | $\mathrm{sites\ cm^{-3}}$ |
| Constant pre-factor, | 33 | $\mathrm{wppm\ bar^{-0.5}}$ |
| Partial molar volume of $H_2$, $V_h$ | $2 \cdot 10^3$ | $\mathrm{mm^3 mol^{-1}}$ |
| Solution enthalpy, $\Delta H_s$ | 27 | $\mathrm{kJ\,mol^{-1}}$ |
| Number of lattice sites, $N_L$ | $5.2 \times 10^{23}$ | $\mathrm{sites\ cm^{-3}}$ |

Table 2: Chemical composition of X70 steels [13, 14].

| | C | Mn | Si | P | S | Cu | Ni | Al | Nb | V | Cr | Mo | Ti | N | Fe |
|---|---|---|---|---|---|---|---|---|---|---|---|---|---|---|---|
| Olden *et al.* [14] | | | | | | | | | | | | | | | |
| BM | 0.09 | 1.71 | 0.3 | 0.012 | 0.001 | 0.04 | 0.05 | 0.05 | 0.05 | 0.01 | 0.07 | 0.02 | 0.02 | 0.005 | |
| HAZ | 0.047 | 1.74 | 0.1 | 0.01 | 0.007 | 0.22 | 0.25 | 0.027 | 0.027 | 0.001 | 0.047 | 0.042 | 0.01 | 0.0025 | |
| Wang [13] | | | | | | | | | | | | | | | |
| – | 0.041 | 1.76 | 0.281 | 0.016 | 0.006 | 0.193 | – | – | 0.067 | – | – | 0.194 | 0.023 | – | balance |

The variations in pressure and temperature at node 3 are shown in Fig. 6. The difference in pressure drop between the mixtures is caused by the lower viscous resistance. The temperature change is caused by the radial convective and conductive heat transfer, accumulation in the soil, and the Joule-Thomson effect [37]. In this work, the simulations are conducted with the same volumetric flow. Blending hydrogen into natural gas decreases the energy density per $\mathrm{m^3}$. To compensate for the latter effect, the gas flow rate should be increased, which will change the flow conditions in the pipeline, and as a result, the hydrogen content in the steel.

The estimated hydrogen content in the steel pipeline for different amounts of hydrogen in natural gas is shown in Fig. 7. The minimum and maximum values are summarized in Table 3 together with the corresponding pressure and temperature. These values are the solutions at each discretization node of the numerical flow model. Compared to BM, the highest hydrogen concentrations are observed for HAZ, with maximum values of 1.91 (10% vol. $H_2$), 2.95 (25% vol. $H_2$), and 4.07 wppm (50% vol. $H_2$). The structure of HAZ is composed of bainite and martensite, while BM is mainly composed of ferrite. During the martensitic transformation, the residual stress and dislocations increase, including the number of trap sites, and as a result, the hydrogen concentration becomes higher. The corresponding maximum values for BM are 0.23, 0.36 and 0.50 wppm. The lowest values, for both BM and HAZ, are noticed at node 2 and $t = 0$, while the maximum values are observed at node 3 and $t = 143$ days.

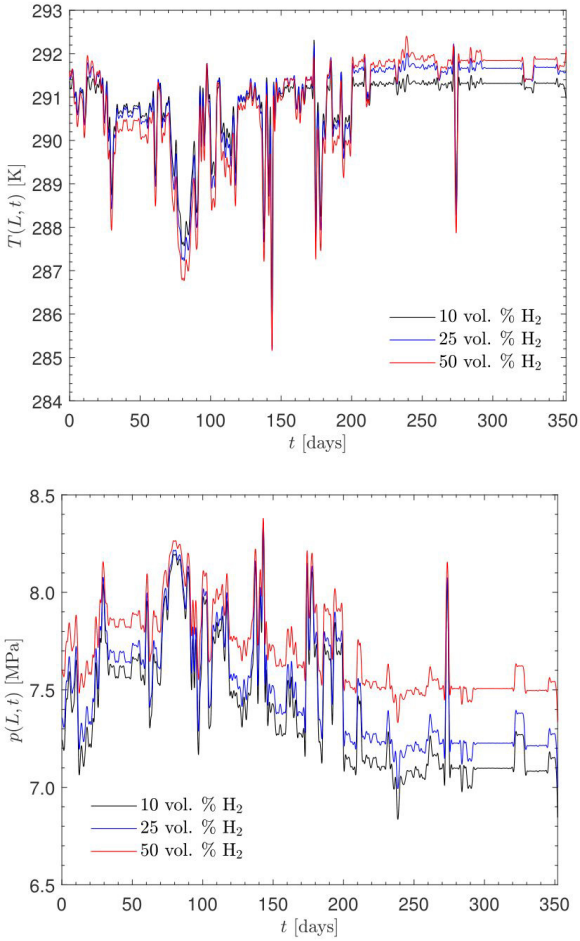


Figure 6: Pressure and temperature evolution for 10%, 25% and 50% vol. $H_2$ in NG.

In [36], an average effective hydrogen diffusion coefficient at room temperature of $7.60 \cdot 10^{-11}$ $m^2s^{-1}$ (BM), $4.01 \cdot 10^{-11}$ $m^2s^{-1}$ for weld metal and $1.26 \cdot 10^{-11}$ $m^2s^{-1}$ for HAZ was found. As it can be observed from the above data, base metal on the pipe body showed a higher effective diffusion coefficient compared to the weld material of L485ME steel grade as well as heat affected zone on tube. An increased alloying level of steel tends to slow down hydrogen diffusion through the tube wall.

To calculate the stress-enhanced hydrogen solubility in pressurized specimens, pipes, and pressure vessels, Drexler *et al.* [38] used the following parameters: $E_b = 30$ kJ mol$^{-1}$, $N_T = 10 \cdot 10^{-7}$ mol mm$^{-3}$, and $N_L = 8.5 \cdot 10^{-4}$ mol mm$^{-3}$. These parameters are considered a rough estimation for ferritic and martensitic steels. The remaining parameters are the same as in Table 1. The results for these parameters are shown in Table 3, and show

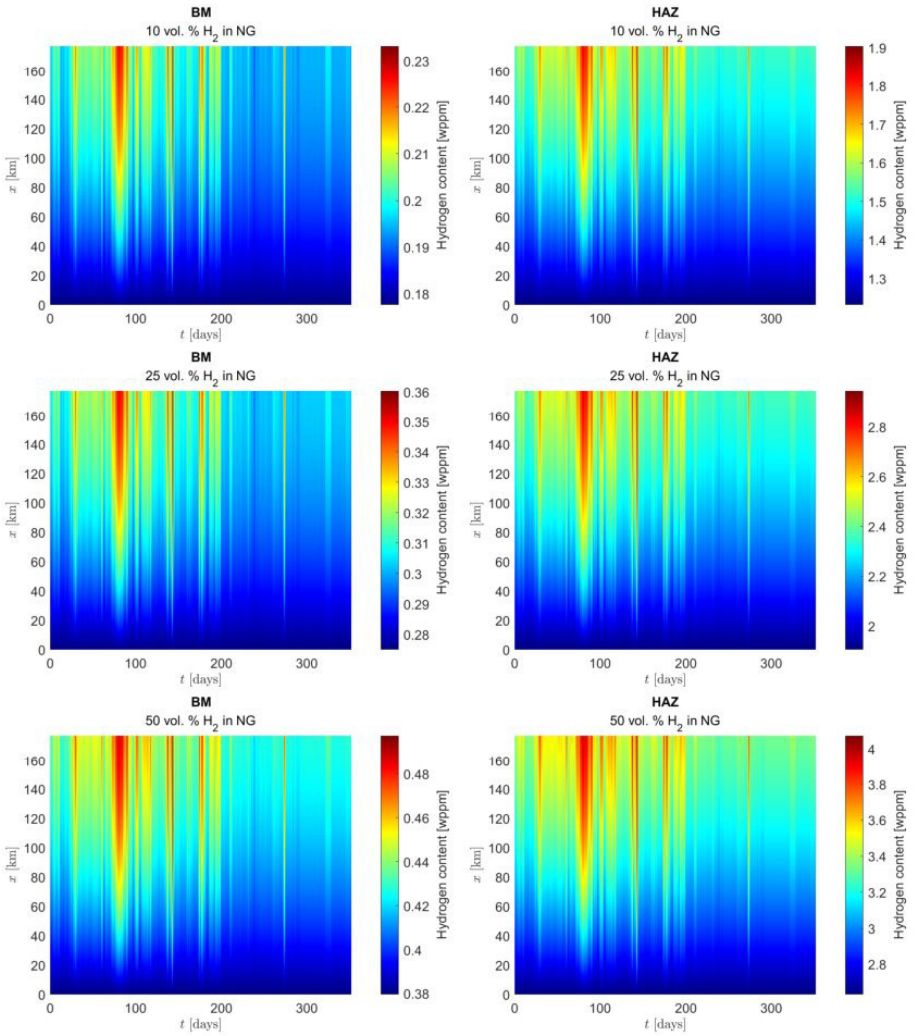


Figure 7: Hydrogen content for BM and HAZ with 10%, 25% and 50% vol. $H_2$ in NG.

significantly lower values for the hydrogen content. It was noticed that the binding energy has a strong influence on the calculated hydrogen content. This parameter depends on the material imperfections, the interatomic forces between hydrogen and iron at the defect sites, and the dilation of the crystal lattice nearby the crystal defects [38].

The results are depicted in Fig. 8 and summarized in Table 3. Compared to BM, the fracture toughness of HAZ significantly decreases for all $C_xH_y/H_2$ blends. The validity of comparison of threshold stress intensity factor $K_{\mathrm{IH}}$ [21] with conditional calculated values $K_{\mathrm{IQ},p}$ and $K_{\mathrm{IQ},d}$ [13] are ensured by size requirements of the specimens [21, 35] meeting criteria for plane strain conditions.

Table 3: Estimated maximum hydrogen content and minimum fracture toughness [14, 36, 38].

| $H_2$ (vol. %) | $c_{H,\min}$ (wppm) | $p$, $T$ (MPa), (K) | $K_{IQ,p}$ (MPa m$^{0.5}$) | $K_{IQ,d}$ (MPa m$^{0.5}$) | $c_{H,\max}$ (wppm) | $p$, $T$ (MPa), (K) | $K_{IQ,p}$ (MPa m$^{0.5}$) | $K_{IQ,d}$ (MPa m$^{0.5}$) |
|---|---|---|---|---|---|---|---|---|
| BM [14, 36] | | | | | | | | |
| 10 | 0.18 | \| | 90.9 | 92.6 | 0.23 | 8.23, 285.8 | 90.8 | 87.2 |
| 25 | 0.28 | 8.45, 308.15 | 90.7 | 83.9 | 0.36 | 8.27, 285.7 | 90.5 | 78.6 |
| 50 | 0.38 | \| | 90.5 | 77.5 | 0.50 | 8.31, 285.4 | 90.2 | 72.1 |
| HAZ [14, 36] | | | | | | | | |
| 10 | 1.23 | \| | 88.6 | 54.2 | 1.91 | 8.17, 285.5 | 87.2 | 45.6 |
| 25 | 1.91 | 8.45, 308.15 | 87.2 | 45.5 | 2.95 | 8.22, 285.4 | 85.0 | 36.9 |
| 50 | 2.63 | \| | 85.6 | 39.1 | 4.07 | 8.23, 285.3 | 82.5 | 30.5 |
| Ferritic and martensitic steels [38] | | | | | | | | |
| 10 | 0.04 | 6.84, 291.3 | 91.2 | 120.5 | 0.05 | 8.32, 286.8 | 91.2 | 117.4 |
| 25 | 0.07 | 7.00, 291.9 | 91.1 | 111.6 | 0.08 | 8.34, 286.5 | 91.1 | 108.8 |
| 50 | 0.10 | 7.33, 292.4 | 91.1 | 104.6 | 0.11 | 8.37, 286.0 | 91.1 | 102.4 |

Information concerning the allowable hydrogen content and fracture toughness enables to demarcate the location and time where HE might appear. Wang [13] found a critical hydrogen concentration of 1 wppm for the X70 pipeline steel, at which the fracture toughness is significantly reduced. The results in Table 3 show that the hydrogen content of HAZ exceeds this critical concentration. From the experimental results reported in Appendix B, a mean $K_{\mathrm{IH,min}}$ of 66.0 and 65.4 MPa m$^{0.5}$ was found for BM and HAZ, respectively. According to KD-1041 [19], if the test was conducted using constant displacement method, $K_{\mathrm{IH,min}}$ is equal to 50% of the applied $K_{\mathrm{IA}}$. Taking into account that $K_{\mathrm{IA}}$ values exceed 110 MPa m$^{0.5}$ for all specimens, the threshold stress intensity factor $K_{\mathrm{IH}}$ value of 55 MPa m$^{0.5}$ can also be qualified as a minimum for all specimens. The latter value is used to evaluate the fracture toughness of L485ME steel that is exposed to hydrogen. The second condition for the material characterization of pipelines and pressure vessels with respect to hydrogen induced cracking is that the defect growth exhibited by the experiments does not exceed 0.25 mm. Simulation results show that only the HAZ material seems to be vulnerable to HE. This would imply that the injection of 10%, 25%, and 50% vol. $H_2$ in the natural gas for the BM material and parameters used for ferritic and martensitic steels may not cause fracture toughness problems for L485ME steel grade. By all means, the results are valid within the assumptions and approximations considered in the case study.

The advantage of the proposed methodology is a possibility to forecast in long time operation that hydrogen environmental cracking may cause a detrimental failure at specific pipeline locations. Moreover, a positive is that the modeling approach can be applied to any low alloyed steel tubes carrying hydrogen blended natural gas. The disadvantage is

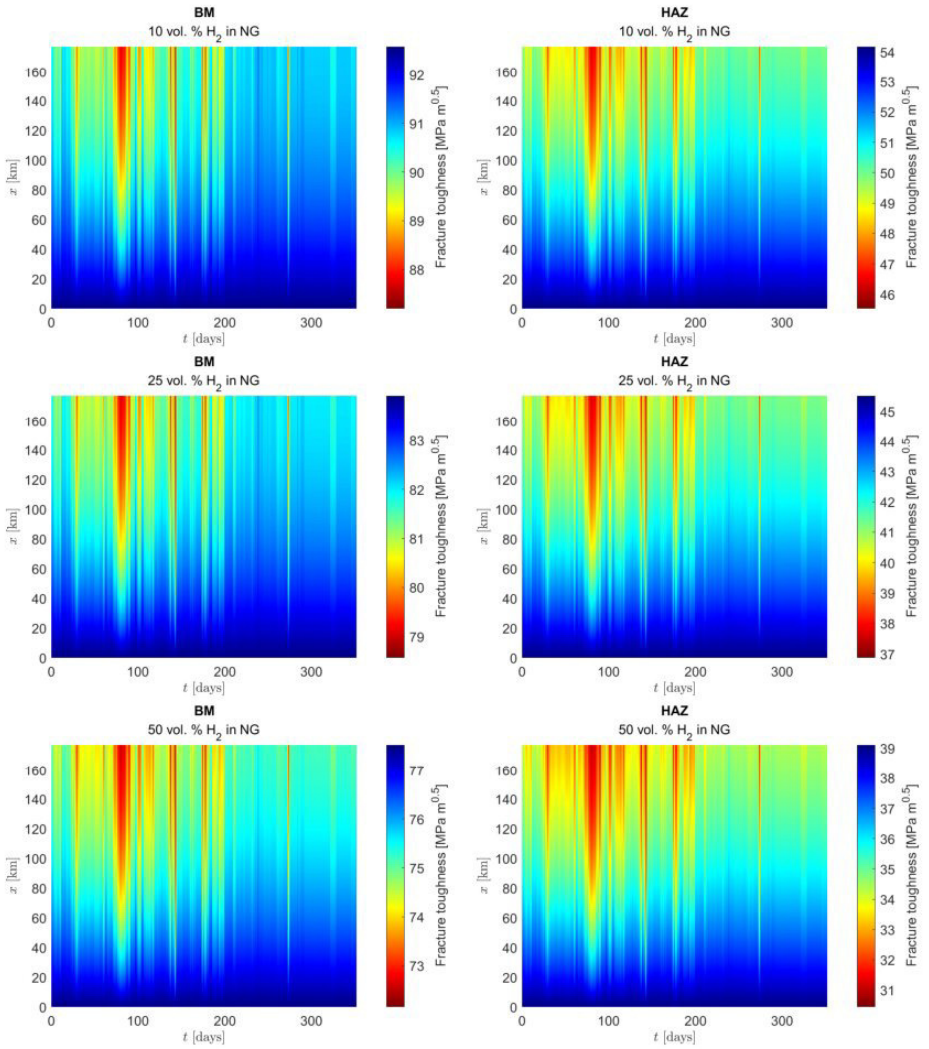


Figure 8: Fracture toughness according Eq. (20) for BM and HAZ with 10%, 25% and 50% vol. $H_2$ in NG.

the uncertainty in acquiring accurate data of the properties required to calculate the hydrogen content (e.g. binding energy, trap density, number of lattice sites) and as a result, the fracture toughness. This also concerns parameters used in the flow model, for example, the soil temperature and properties such as heat capacity and a thermal conductivity change over time, as it alternately wets and dries. These quantities are difficult to determine; however, they can significantly affect a transient flow in the pipeline, particularly the temperature of the gas mixture.

# 5 Conclusions

In this work, the hydrogen content and fracture toughness were calculated for the L485ME low-alloy steel grade that is worldwide used for the construction of gas transmission networks. A transient non-isothermal flow model was used to estimate the pressure and temperature conditions in the pipeline. From Sievert's law, the hydrogen content was calculated, and as a consequence, the fracture toughness of the base metal and heat-affected zone was obtained. The simulation results were compared against the experimental threshold stress intensity factor and showed that the computed fracture toughness for HAZ significantly decreases for all $C_xH_y/H_2$ blends. In the case in which the natural gas is injected with 10%, 25%, and 50% vol. $H_2$, hydrogen embrittlement of base metal of tube body is less likely to occur. This conclusion was provided in respect to a threshold stress intensity factor criterion. The presented methodology is appropriate for evaluation of steels for pipelines carrying hydrogen-blended natural gas.

## Acknowledgements

The authors wish to thank Corinth Pipeworks S.A. for facilitating the experimental data and Reviewers for their valuable comments and suggestions.

*Received 3 August 2023*

# Appendix A.

Tensile, hardness tests and chemical composition of a 14.2 mm wall thickness L485ME steel grade [20].

Tensile and hardness tests results.

| Base material (BM) | | | | Spiral Weld (WM) | | | |
|---|---|---|---|---|---|---|---|
| | | | | | Hardness Max HV10 | | |
| No. | Heat No. | Yield Strength (MPa) | Tensile Strength (MPa) | Tensile Strength (MPa) | HAZ | Base | Weld |
| 1. | 0141335 | 503 | 626 | 635 | 207 | 213 | 227 |
| 2. | 0141948 | 523 | 639 | 627 | 212 | 228 | 229 |
| 3. | 0141261 | 491 | 614 | 660 | 222 | 222 | 233 |
| 4. | 0141950 | 511 | 631 | 645 | 210 | 214 | 229 |
| 5. | 0141149 | 529 | 643 | 638 | 215 | 222 | 231 |
| 6. | 0141341 | 493 | 616 | 610 | 212 | 225 | 226 |
| 7. | 0141427 | 490 | 613 | 659 | 209 | 221 | 228 |
| 8. | 0141256 | 518 | 635 | 645 | 210 | 214 | 229 |
| 9. | 0141950 | 511 | 631 | 662 | 210 | 220 | 227 |
| 10. | 0141151 | 506 | 616 | 647 | 215 | 220 | 229 |

Chemical composition of L485ME steel grade [20].

| No. | Heat No. | C % | Mn % | P % | S % | Si % | Cr % | Ni % | Mo % | Cu % | Ti % | Nb % | V % | Al % | Sn % | Ca % | N % | B % |
|---|---|---|---|---|---|---|---|---|---|---|---|---|---|---|---|---|---|---|
| 1. | 041335 | 0.065 | 1.583 | 0.0087 | 0.0028 | 0.293 | 0.022 | 0.036 | 0.002 | 0.013 | 0.0193 | 0.07 | 0.003 | 0.035 | 0.005 | 0.0017 | 0.0042 | 0.0001 |
| 2. | 040948 | 0.065 | 1.600 | 0.0097 | 0.0035 | 0.280 | 0.04 | 0.036 | 0.003 | 0.015 | 0.0214 | 0.065 | 0.002 | 0.038 | 0.003 | 0.0021 | 0.0041 | 0.0001 |
| 3. | 041261 | 0.067 | 1.565 | 0.0089 | 0.004 | 0.283 | 0.024 | 0.049 | 0.003 | 0.02 | 0.0217 | 0.069 | 0.002 | 0.041 | 0.003 | 0.0033 | 0.0044 | 0.0001 |
| 4. | 041950 | 0.068 | 1.512 | 0.0113 | 0.0032 | 0.277 | 0.028 | 0.041 | 0.003 | 0.014 | 0.0223 | 0.054 | 0.003 | 0.0554 | 0.003 | 0.0026 | 0.0055 | 0.0001 |
| 5. | 041149 | 0.065 | 1.569 | 0.0101 | 0.0032 | 0.285 | 0.034 | 0.041 | 0.008 | 0.014 | 0.0223 | 0.066 | 0.002 | 0.0431 | 0.005 | 0.0021 | 0.0042 | 0.0001 |
| 6. | 041341 | 0.071 | 1.608 | 0.008 | 0.0038 | 0.286 | 0.017 | 0.038 | 0.002 | 0.015 | 0.0208 | 0.064 | 0.002 | 0.0398 | 0.003 | 0.0029 | 0.0045 | 0.0001 |
| 7. | 041427 | 0.068 | 1.547 | 0.0097 | 0.0025 | 0.262 | 0.024 | 0.038 | 0.004 | 0.012 | 0.0217 | 0.058 | 0.001 | 0.0404 | 0.003 | 0.0028 | 0.0044 | 0.0001 |
| 8. | 041256 | 0.065 | 1.531 | 0.0081 | 0.0028 | 0.278 | 0.022 | 0.038 | 0.002 | 0.014 | 0.0213 | 0.058 | 0.002 | 0.0384 | 0.003 | 0.0031 | 0.004 | 0.0001 |
| 9. | 041950 | 0.068 | 1.512 | 0.0103 | 0.0033 | 0.277 | 0.028 | 0.041 | 0.003 | 0.014 | 0.0223 | 0.054 | 0.003 | 0.0554 | 0.003 | 0.0026 | 0.0055 | 0.0001 |
| 10. | 041151 | 0.069 | 1.524 | 0.0095 | 0.0043 | 0.282 | 0.022 | 0.039 | 0.003 | 0.015 | 0.0212 | 0.059 | 0.002 | 0.0318 | 0.003 | 0.0035 | 0.0045 | 0.0001 |

# Appendix B.

The experimental results of target and measured crack size, applied displacement target and applied stress intensity factor as well as stress intensity factor for 14.2 mm wall thickness tubes [20].

| No. | Specimen ID | $a_0$ Target (mm) | $V_m$ Applied (mm) | $K_{IA}$ Target (MPa $m^{0.5}$) | $a_0$ Measured (mm) | $K_{IA}$ Applied (MPa $m^{0.5}$) | $K_{IH,min}$ Minimum (MPa $m^{0.5}$) |
|---|---|---|---|---|---|---|---|
| 1. | S203A-BM1 | 14.290 | 0.606 | 125.0 | 13.993 | 127.5 | 63.7 |
| 2. | S203A-BM2 | 14.690 | 0.621 | 125.0 | 14.956 | 123.1 | 61.5 |
| 3. | S203A-BM3 | 14.730 | 0.625 | 125.0 | 14.772 | 125.1 | 62.6 |
| 4. | S203A-BM4 | 14.570 | 0.619 | 125.0 | 14.206 | 128.3 | 64.1 |
| 5. | S203A-W1 | 14.060 | 0.599 | 125.0 | 14.667 | 120.7 | 60.3 |
| 6. | S203A-W2 | 14.700 | 0.625 | 125.0 | 14.632 | 126.2 | 63.1 |
| 7. | S203A-W3 | 14.470 | 0.614 | 125.0 | 13.473 | 133.2 | 66.6 |
| 8. | S203A-W4 | 14.200 | 0.606 | 125.0 | 14.882 | 120.5 | 60.3 |
| 9. | S203A-HAZ1 | 14.410 | 0.617 | 125.0 | 12.675 | 141.2 | 70.6 |
| 10. | S203A-HAZ2 | 14.530 | 0.619 | 125.0 | 15.132 | 121.4 | 60.7 |
| 11. | S203A-HAZ3 | 14.400 | 0.614 | 125.0 | 14.277 | 126.5 | 63.3 |
| 12. | S203A-HAZ4 | 14.630 | 0.619 | 125.0 | 13.874 | 130.8 | 65.4 |
| 13. | S203B-BM1 | 14.740 | 0.623 | 125.0 | 14.455 | 127.2 | 63.6 |
| 14. | S203B-BM2 | 14.990 | 0.635 | 125.0 | 11.720 | 156.1 | 78.1 |
| 15. | S203B-BM3 | 14.800 | 0.627 | 125.0 | 13.376 | 137.4 | 68.7 |
| 16. | S203B-BM4 | 14.450 | 0.617 | 125.0 | 13.242 | 135.9 | 68.0 |
| 17. | S203B-W1 | 14.260 | 0.606 | 125.0 | 13.657 | 129.8 | 64.9 |
| 18. | S203B-W2 | 14.530 | 0.616 | 125.0 | 14.125 | 128.1 | 64.1 |
| 19. | S203B-W3 | 14.320 | 0.611 | 125.0 | 13.850 | 129.3 | 64.6 |
| 20. | S203B-W4 | 14.460 | 0.647 | 125.0 | 14.725 | 129.8 | 64.9 |
| 21. | S203B-HAZ1 | 14.650 | 0.621 | 125.0 | 13.591 | 133.5 | 66.8 |
| 22. | S203B-HAZ2 | 14.550 | 0.619 | 125.0 | 14.389 | 126.7 | 63.4 |
| 23. | S203B-HAZ3 | 14.170 | 0.613 | 125.0 | 15.656 | 116.7 | 58.4 |
| 24. | S203B-HAZ4 | 14.510 | 0.618 | 125.0 | 14.287 | 127.3 | 63.6 |
| 25. | S203C-BM1 | 14.180 | 0.602 | 125.0 | 13.861 | 127.5 | 63.7 |
| 26. | S203C-BM2 | 15.180 | 0.639 | 125.0 | 13.755 | 136.4 | 68.2 |
| 27. | S203C-BM3 | 14.810 | 0.627 | 125.0 | 14.070 | 131.1 | 65.6 |

| No. | Specimen ID | $a_0$ Target (mm) | $V_m$ Applied (mm) | $K_{IA}$ Target (MPa m$^{0.5}$) | $a_0$ Measured (mm) | $K_{IA}$ Applied (MPa m$^{0.5}$) | $K_{IH,min}$ Minimum (MPa m$^{0.5}$) |
|---|---|---|---|---|---|---|---|
| 28. | S203C-BM4 | 14.880 | 0.630 | 125.0 | 14.601 | 127.6 | 63.8 |
| 29. | S203C-W1 | 14.230 | 0.605 | 125.0 | 14.276 | 124.7 | 62.4 |
| 30. | S203C-W2 | 14.360 | 0.610 | 125.0 | 13.505 | 132.1 | 66.1 |
| 31. | S203C-W3 | 14.420 | 0.612 | 125.0 | 11.916 | 148.4 | 74.2 |
| 32. | S203C-W4 | 14.570 | 0.617 | 125.0 | 13.893 | 130.2 | 65.1 |
| 33. | S203C-HAZ1 | 14.670 | 0.628 | 125.0 | 12.711 | 143.2 | 71.6 |
| 34. | S203C-HAZ2 | 14.570 | 0.617 | 125.0 | 12.105 | 147.1 | 73.5 |
| 35. | S203C-HAZ3 | 14.490 | 0.616 | 125.0 | 14.028 | 128.8 | 64.4 |
| 36. | S203C-HAZ4 | 14.570 | 0.620 | 125.0 | 14.572 | 125.5 | 62.8 |

# References


[1] Cazenave P., Jimenez K., Gao M., Moneta A., Hryciuk P.: *Hydrogen assisted cracking driven by cathodic protection operated at near –1200 mV CSE – an onshore natural gas pipeline failure*. J. Pipeline Sci. Eng. **1**(2021), 1, 100–121.

[2] Abdelghani M., Tewfik G., Witek M., Djahida D.: *Factors of Stress Concentration around Spherical Cavity Embedded in Cylinder Subjected to Internal Pressure*. Materials **14**(11) (2021).

[3] Wasim M., Djukic M.B., Ngo T.D.: *Influence of hydrogen-enhanced plasticity and decohesion mechanisms of hydrogen embrittlement on the fracture resistance of steel*. Eng. Fail. Anal. **123**(2021), 105312.

[4] Troiano A.R.: *The role of hydrogen and other interstitials in the mechanical behavior of metals*. Metallogr. Microstruct. Anal. **5**(2016), 6, 557–569.

[5] Sofronis P., Birnbaum H.K.: *Hydrogen enhanced localized plasticity: A mechanism for hydrogen related fracture*. In: Fatigue and Fracture of Aerospace Structural Materials. American Society of Mechanical Engineers, Aerospace Division (Publication) AD, vol. 36, Publ. by ASME, pp. 15–25, Proc. 1993 ASME Winter Ann. Meet., New Orleans 1993.

[6] Nguyen T.T., Park J., Kim W.S., Nahm S.H., Beak U.B.: *Effect of low partial hydrogen in a mixture with methane on the mechanical properties of X70 pipeline steel*, Int. J. Hydrogen Energy **45**(2020), 3, 2368–2381.

[7] Nguyen T.T., Beak U.B., Park J., Nahm S.H, Tak N.: *Hydrogen environment assisted cracking in X70 welding heat-affected zone under a high-pressure hydrogen gas*. Theor. Appl. Fract. Mech. **109**(2020), 102746.

[8] Alvaro A., Olden V., Macadre A., Akselsen O.M.: *Hydrogen embrittlement susceptibility of a weld simulated X70 heat affected zone under H2 pressure*. Mater. Sci. Eng. A **597**(2014), 29–36.

[9] Golisch G., Genchev G., Wanzenberg E., Mentz J., Brauer H., Muthmann E., Ratke D.: *Application of line pipe and hot induction bends in hydrogen gas*. J. Pipeline Sci. Eng. **2**(2022), 3, 100067.

[10] Ghosh G., Rostron P., Garg R., Panday A.: *Hydrogen induced cracking of pipeline and pressure vessel steels: A review*. Eng. Fract. Mech. **199**(2018), 609–618.

[11] Krasovskii A.Y., Lokhman I.V., Orynyak I.V.: *Stress-corrosion failures of main pipelines*. Strength Mater. **44**(2012), 129–143.

[12] Gangloff R.P., Somerday B.P.: *Gaseous Hydrogen Embrittlement of Materials in Energy Technologies*. In: *Mechanisms, Modelling and Future Developments*. Woodhead Publishing, 2012.

[13] Wang R.: *Effects of hydrogen on the fracture toughness of a X70 pipeline steel*. Corros. Sci. **51**(2009), 12, 2803–2810.

[14] Olden V., Alvaro A., Akselsen O.M.: *Hydrogen diffusion and hydrogen influenced critical stress intensity in an API X70 pipeline steel welded joint – experiments and FE simulations*. Int. J. Hydrogen Energy **37**(2012), 15, 11474–11486.

[15] Zhou D., Li T., Huang D., Wu Y., Huang Z., Xiao W., Wang Q., Wang X.: *The experiment study to assess the impact of hydrogen blended natural gas on the tensile properties and damage mechanism of X80 pipeline steel*. Int. J. Hydrogen Energy **46**(2021), 10, 7402–7414.

[16] EN-ISO 3183:2019. *Petroleum and natural gas industries - Steel pipe for pipeline transportation system*. Tech. rep. Tech. Comm., ISO/TC 67/SC 2 (2019).

[17] API Spec 5L (46th Edn.), April 2018. *Line pipe*. Tech. rep., Washington.

[18] ASME B31.12:2019. *Hydrogen piping and pipelines. ASME code for pressure piping*. Tech. rep., American Society of Mechanical Engineer, 2020.

[19] ASME BPVC Section VIII, Division 3. *Alternative Rules for Construction of High Pressure Vessels. ASME Boiler and Pressure Vessel Code*, Tech. rep., American Society of Mechanical Engineer, 2021.

[20] Corinth Pipeworks S.A: *Hydrogen $K_{IH}$ qualification test report $K_{IH}$ testing of* $40'' \times 14.2mm/L485ME$ *SAWH*. 2022 (*non-published*).

[21] ASTM E1681-03. *Standard Test Method for Determining Threshold Stress Intensity Factor for Environment Assisted Cracking of Metallic Materials*. ASTM Int. Tech. rep., 2020.

[22] Uilhoorn F.E.: *Comparison of Bayesian estimation methods for modeling flow transients in gas pipelines*. J. Nat. Gas Sci. Eng. **38**(2017), 159–170.

[23] Witek M., Uilhoorn F.: *Impact of hydrogen blended natural gas on linepack energy for existing high pressure pipelines*. Arch. Thermodyn. **43**(2022), 3, 111–124.

[24] Techo R., Tickner R.R., James R.E.: *An accurate equation for the computation of the friction factor for smooth pipes from the Reynolds number*. J. Appl. Mech. **32**(1965), 2, 443–443.

[25] Kreith F., Bohn M.S.: *Principles of Heat Transfer* (5th Edn.). West Publ., St Paul 1993.

[26] Kunz O., Wagner W.: *The GERG-2008 Wide-Range equation of state for natural gases and other mixtures: An expansion of GERG-2004*. J. Chem. Eng. Data **57**(2012), 11, 3032–3091.

[27] Schiesser W.E.: *The Numerical Method of Lines: Integration of Partial Differential Equations*. Academic Press, San Diego 1991.

[28] Bank R.E., Coughran W.M., Fichtner W., Grosse E.H., Rose D.J., Smith R.K.: *Transient simulation of silicon devices and circuits*. IEEE Trans. Electron Devices **32**(1985), 10 1992–2007.

[29] Hosea M.E., Shampine L.F.: *Analysis and implementation of TR-BDF2*. Appl. Numer. Math. **20**(1996), 1, 21–37.

[30] Shampine L.F., Reichelt M.W.: *The MATLAB ODE suite*, SIAM J. Sci. Comput. **18**(1997), 1, 1–22.

[31] Fukai Y.: *The Metal-Hydrogen System: Basic Bulk Properties*. Springer Science & Business Media, 2006.

[32] Kirchheim R., Pundt A.: *25 – Hydrogen in Metals*. In: Physical Metallurgy (5th Edn.) (D.E. Laughlin, K. Hono, Eds.), Elsevier, Oxford 2014, 2597–2705.

[33] Drexler A., Konert F., Sobol O., Rhode M., Domitner J., Sommitsch C., Böllinghaus T.: *Enhanced gaseous hydrogen solubility in ferritic and martensitic steels at low temperatures*. Int. J. Hydrogen Energy **47**(2022), 93, 39639–39653.

[34] Kirchheim R.: *Solubility, diffusivity and trapping of hydrogen in dilute alloys. deformed and amorphous metals – II*. Acta Metall. **30**(1982), 6, 1069–1078.

[35] ASTM E399-22. *Standard Test Method for Linear-Elastic Plane-Strain Fracture Toughness $K_{IC}$ of Metallic Materials*. ASTM Int. Tech. rep., 2022.

[36] Skjellerudsveen M., Akselsen O., Olden V., Johnsen R., Smirnova A.: *Effect of microstructure and temperature on hydrogen diffusion and trapping in X70 grade pipeline steel and its weldments*. In: Proc. Eur. Corrosion Conf., Moscow, 13-17 Sept. 2010.

[37] Uilhoorn F.E.: *Dynamic behaviour of non-isothermal compressible natural gases mixed with hydrogen in pipelines*. Int. J. Hydrogen Energy **34**(2009), 16, 6722– 6729.

[38] Drexler A., Depover T., Leitner S., Verbeken K., Ecker W.: *Microstructural based hydrogen diffusion and trapping models applied to Fe–CX alloys*. J. Alloys Compd. **826**(2020), 154057.

**archives**
**of thermodynamics**
Vol. **44**(2023), No. 4, 405–426
DOI: 10.24425/ather.2023.149721

# Experimental and numerical analysis of the impact of a liquid flow rate on the operational performance of a cross-flow tube-and-fin heat exchanger

**TOMASZ BURY***
**MAŁGORZATA HANUSZKIEWICZ-DRAPAŁA**

Silesian University of Technology, Department of Thermal Technology, Konarskiego 22, 44-100 Gliwice, Poland

**Abstract** The paper is dedicated to an issue of the influence of a non-uniform flow of mediums in a cross-flow water-air heat exchanger, the core of which is a bundle of elliptical finned tubes. The main purpose of the work is to determine the impact of non-uniform water inflow for various mass flow rates on the thermal efficiency of the heat exchanger. Multivariate analyses were carried out for various temperatures of water, and for measured non-uniform air distribution at the heat exchanger input. Two variants of water distribution were considered: non-uniform water distribution assumed considering a non-uniform air inflow and water distribution resulting from hydraulic resistances calculated for different locations of water inlet and outlet nozzles. Simulation results were compared with the experimental outcomes obtained in cases of the non-uniform natural inflow of both mediums and to the computation results for a case of the uniform media inflow. The results obtained in this work confirm the significant deterioration of the thermal efficiency of heat exchangers caused by a non-uniform media inflow (by as much as 18.5% compared to the case of a uniform media inflow) which is compliant with other numerous works. The control of the water flow through the individual heat exchanger tubes enables the improvement of thermal efficiency by 4.5% to 18.6% compared to the device with uncontrolled inflow of working fluids, which for some of the analyzed cases is even better than a completely uniform inflow of heat carriers.

*Corresponding Author. Email: tomasz.bury@polsl.pl

**Keywords:** Heat exchanger; Non-uniform inflow of mediums; Controlled inflow of mediums; Heat exchanger capacity; Numerical analysis

## Nomenclature

| | | |
|---|---|---|
| $C_{1\varepsilon}$, $C_{2\varepsilon}$, $C_{3\varepsilon}$ | – | constants |
| $c$ | – | specific heat capacity, J/(kg K) |
| $G_k$ | – | turbulence kinetic energy generation due to the mean velocity gradients, kg/(m s$^3$) |
| $G_b$ | – | turbulence kinetic energy generation due to buoyancy, kg/(m s$^3$) |
| $k$ | – | turbulent kinetic energy, J/kg |
| $\dot{Q}$ | – | heat flux, W |
| $S_k$, $S_\varepsilon$ | – | source terms, kg/(m s$^3$) |
| $t$ | – | temperature, °C |
| $u$ | – | velocity, m/s |
| $\dot{V}$ | – | volumetric flow rate, m$^3$/s |

### Greek symbols

| | | |
|---|---|---|
| $\varepsilon$ | – | dissipation rate, J/(kg s) |
| $\mu$ | – | dynamic viscosity, Pa·s |
| $\rho$ | – | density, m$^3$/kg |
| $\sigma_k$, $\sigma_\varepsilon$ | – | turbulent Prandtl numbers |

### Subscripts

| | | |
|---|---|---|
| $a$ | – | air |
| in | – | at the heat exchanger inlet |
| out | – | at the heat exchanger outlet |
| $t$ | – | turbulent |
| $w$ | – | water |

# 1 Introduction

Experimental and computational studies of heat exchangers show that the flow of working mediums through tube and fin cross-flow heat exchangers can be non-uniform. A non-uniformity (maldistribution) may be, among others, a result of a heat exchanger design, methods of forcing flows of heat carriers, or the shape of inlet channels of mediums. This problem is not new and has been the subject of analyses for many years, but past studies [1,2] have focused on assessing the importance of the form of a maldistributed flow of mediums on the thermal efficiency of heat exchangers. Analyzing available publications, two important aspects have to be highlighted, which actually state a motivation for this work. First, a non-uniform inflow of

working fluids may significantly deteriorate the performance of a heat exchanger compared to a uniform inflow of media. Second, it is possible to improve the performance of a heat exchanger with flow maldistribution by controlling the inflow of mediums.

Minichannel heat exchangers are the subjects of many more recent works. A hydraulic analysis of a minichannel device is presented in [3]. The authors built a computational fluid dynamics model of a minichannel heat sink and carried out a set of simulations to determine the effects of inlet/outlet nozzles' location and flow rate on flow maldistribution. Numerical and experimental investigations on microchannel heat exchangers were realized by Joseph with his co-workers [4]. They found out that the flow maldistribution strongly influenced the thermal performance of the considered heat exchanger. They also indicated the possibility of enhancing the heat exchanger efficiency by changing the flow rate of a working fluid. The problem of medium flow non-uniformity and its meaning to heat exchangers' operational performance was also investigated in [5], in which authors proposed a fast method for evaluating the effect of this phenomenon on the thermal performance of heat exchangers. A proposed method is based on their study findings, which were transformed into a plot. The plot allows the evaluation of flow maldistribution impact on thermal performance for different velocity deviation patterns.

The considered problem of medium flow maldistribution is significant and T'joen *et al.* [6] proposed a numerical tool supporting the design process of heat exchangers taking into account the non-uniform flows of working fluids. The need to take this phenomenon into account for the design of more efficient devices was also stated in the publication of Tereda *et al.* [7]. The research results published so far concern various types of heat exchangers, but the common conclusion is that the non-uniform flow of working fluids can significantly deteriorate the efficiency of a heat exchanger in certain operating modes. Three types of non-uniformities were investigated by De Schampheleire *et al.* [8] with regard to the air-water plate heat exchanger, who found up to 25% increase in heat transfer resistance compared to the uniform case. On the other hand, studies of a cross-current heat exchanger with supercritical pressure carbon dioxide as the working medium carried out under the work of Guo *et al.* [9] showed that maldistribution of the medium inflow and its temperature at the inflow can both worsen and improve the conditions of heat transport in the device. In addition, the authors stated that these positive or negative effects occurring on both sides of the exchanger's partition can be cumulative.

The issue of the non-uniform inflow of mediums to heat exchangers was also investigated by the authors of the present paper. The experimental and computational analyses concerned cross-current tube-and-fin liquid-gas heat exchangers [10,11]. The non-uniformity applies to both fluids (gas and liquid), but due to technical limitations, the range and form of non-uniformity were determined by the gas side measurement only [10,11]. The results of analyses are consistent with the results of other researchers and indicate that the non-uniformity of the mediums inflow may deteriorate the efficiency of the device by up to 20% compared to the heat exchanger operating at uniform inflow of working agents.

The thermal efficiency of any heat exchanger depends on many parameters, such as device dimensions, materials, and operational characteristics. Extending the heat exchange surface is the simplest way to increase the efficiency of the heat exchanger. On the other hand, the size of the device is usually limited because it has to fit in with the rest of the installation. Therefore, other methods of improving the efficiency of such devices without increasing the heat transfer surface are considered. This can be achieved by using active and passive methods, or a combination of both [12]. Passive methods are of particular interest due to relatively low costs and no need for additional energy supply. Such methods often involve modifying the geometry of the heat exchanger or using inserts that increase turbulence in the flow of working fluids. It should be noted, however, that such solutions increase the pressure drop in the flow of factors, which usually also increases the driving power demand of the devices forcing the flow. Coetzee *et al.* [13] performed a series of measurements on a tube-in-tube heat exchanger using a set of spiral inserts. They achieved an increase in the heat exchanger efficiency of 206%, but at the same time, the pressure drop increased by 203%. It should be noted that research on the effectiveness of the passive methods is most often conducted separately from the issue of non-uniform inflow of mediums to heat exchangers.

Bury and Składzień [14] also examined the effectiveness of the use of inserts increasing the degree of turbulence of the gas at the heat exchanger inflow. However, the tests carried out for the cross-current, finned air-water cooler gave negative or inconclusive results. In the subsequent stages of the research, it was assumed that the non-uniform but controlled inflow of media may have a positive effect on the heat exchanger's operation. A similar approach, using the shaping of incoming media streams, was also analyzed by Hajabdollahi *et al.* [15]. They optimized the design of the heat exchanger in terms of the structure of the fins for different inlet

profiles of the two mediums. It was found that it was possible to obtain a thermoeconomic advantage over the exchanger with the uniform inflow of heat carriers. The authors of the present paper conducted analyses of the possibility of increasing the thermal efficiency of a heat exchanger operating with the non-uniform inflow of working fluids as a result of using the passive method [16]. It was assumed that an increase in the heat transfer rate could be obtained as a result of forming a stream of gas flowing to the exchanger using metal inserts mounted in the air supply duct. These inserts directed a larger stream of air into the area of a water inlet manifold, where the temperature difference is greatest. The measurements carried out confirmed the validity of this hypothesis.

The present paper deals with the analysis of the impact of the non-uniform but controlled water inflow to a cross-current, tube-and-fin heat exchanger on the effects of its operation. This issue was already preliminarily recognized as part of the doctoral thesis [17], with an indication of potential positive effects, but the author did not indicate how to control the flow of water. The possibility of improving the thermal efficiency of the considered type of heat exchanger by changing the location of the water inlet and outlet nozzles was analyzed in [18].

A separate problem is the mathematical and numerical modeling of heat exchangers which are usually complex devices. Taler and his co-workers have developed finite volume method-based models in simplified [19, 20], and modernized [21] versions. The models enable simulations of different types of heat exchangers (plate, tube-and-fin, including superheaters). A finite volume is however a repetitive segment of a real device. Another option is the use of CFD (computational fluid dynamics) tools, which are also based on the finite volume method. The computing power of modern computers allows to analyze models of whole heat exchangers with a simple structure, but there are still limitations concerning, for example, finned structures. An intensive application of the CFD approach to heat exchangers has been observed since the beginning of the 2000s. The process of designing the heat exchangers is one possible application of this computational approach [22, 23]. Numerical analyses are sometimes limited and they concern one side of a heat exchanger (one heat carrier) [24, 25]. Other investigators utilize the CFD technique for modeling and simulating the media flow maldistribution impact on the heat exchangers performance, as in works [26, 27].

The subject of this study is a cross-flow water-air heat exchanger, the core of which is a bundle of elliptical finned tubes. The work is dedicated

to analyses of the heat exchanger operating under full control distribution of water. The analyses are an extension and supplement to the preliminary tests carried out for the considered heat exchanger, the results of which were presented in the previous work [28]. The results reported there confirmed the possibility of improving the thermal efficiency of a heat exchanger with a non-uniform, but controlled inflow of liquid, postulated by Widziewicz [17]. Earlier studies [17, 28], however, were carried out for only one value of the liquid mass flow rate. The main purpose of the present work is to determine the impact of water distribution between individual tubes for the assumed various mass flow rates of this medium on the thermal efficiency of a heat exchanger. Multivariate analyses were carried out for various temperatures of water and a non-uniform air distribution at the heat exchanger input. The air distribution is a result of measurements. Two variants of water distributions were considered. One distribution was assumed accounting for a non-uniform air inflow, and the second one was calculated for different locations of water inlet and outlet nozzles using the hydraulic model of the heat exchanger. Multivariate simulations were carried out for uniform and non-uniform air inflow using the previously developed numerical model and calculation methodology presented in [29, 30]. The non-uniform air distribution at the heat exchanger inlet is a result of measurements. The obtained results of multivariate simulations were compared with the results of measurement for a case of the non-uniform inflows of heat carriers and with the results of calculations performed under the assumption of uniform flow of both fluids.

## 2 Measurements

### 2.1 Characteristics of the analyzed heat exchanger

The heat exchanger, which is the subject of research, is a cross-current, tube-and-fin air-water cooler, the core of which is a bundle of 10 tubes with an elliptical cross-section. The tubes are made of steel and finned with flat, rectangular fins. The view and construction details of this heat exchanger are shown in Fig. 1.

The fins are placed with a pitch of 2.8 mm and there are 175 of them on each tube. The thickness of the tube wall is 1 mm. Hot-dip galvanizing was used to ensure good thermal contact between the fins and the tube surface.

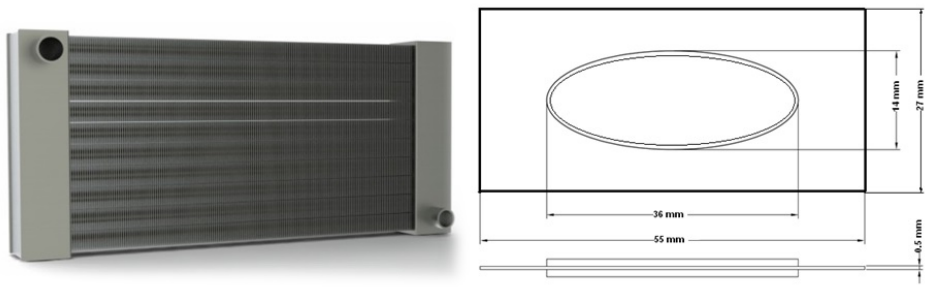


Figure 1: A view and the construction details of the analyzed heat exchanger.

## 2.2 Test station and method of data analysis

The purpose of the experimental research is, among others, to determine the range and form of a non-uniform airflow through the analyzed heat exchanger, as stated in the introduction. The diagram of the test station is shown in Fig. 2. Its most important element is a computer-controlled hot-wire thermoanemometric sensor, which can be used to measure the distribution of air velocity and temperature at the inlet and outlet of the heat exchanger. Distributions of air velocity and temperature at the inlet to the heat exchanger were input data for numerical analyses in the subsequent stages. For this reason, it is important to ensure the stability of these parameters over time. Velocity and temperature field measurements started after reaching a steady state. Measurements carried out as part of previous studies [10, 11, 17] have proven the repeatability of the results obtained at given air and water flow and temperature settings. In addition, data from

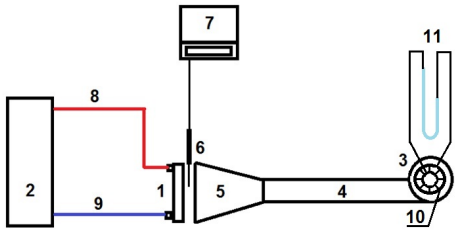


Figure 2: Simplified scheme of the test stand: 1 – heat exchanger, 2 – electric boiler, 3 – fan, 4 – air supply duct, 5 – diffuser, 6 – thermoanemometric sensor, 7 – control computer, 8 – hot water pipeline, 9 – chilled water pipeline, 10 – throttle valve, 11 – manometer.

the hot-wire anemometer sensor are collected at each measurement point in a given time (from a few to several seconds). During this period, sampling takes place with the highest frequency resulting from the data transfer capacity of the measurement card. The results obtained in this way are subjected to statistical processing: outages are eliminated, and the expected value (average) and the standard deviation of this value are determined. The air flow rate is determined by measuring the pressure drop and using the characteristics of the throttle valve, which is used to regulate the gas flow rate.

The station's hot water supply system is equipped with a temperature measurement system (type K thermocouples) and a water flow rate measurement system (a rotameter with a current output). The measurement data allows to calculate the heat flux transferred in the heat exchanger using the equation, expressing a decrease in water enthalpy:

$$\dot{Q}_w = \dot{V}_w \rho_w c_w \left(t_{w,\text{in}} - t_{w,\text{out}}\right), \tag{1}$$

where $\rho_w$ and $c_w$ represent the density and specific heat of water, respectively. The measurements of temperatures of the water at the heat exchanger inlet ($t_{w,\text{in}}$) and outlet ($t_{w,\text{out}}$) and the water volumetric flow rate ($\dot{V}_w$) are considered more accurate than the measurements of air parameters, and thus the thermal performance of heat exchanger was calculated based on presented equation. Uncertainties of the measurements, regarding the heat exchanger output, were calculated using the uncertainty propagation law:

$$u(\dot{Q}_w) = \sqrt{\left(\frac{\partial \dot{Q}_w}{\partial \dot{V}_w}\right)^2 u^2\left(\dot{V}_w\right) + \left(\frac{\partial \dot{Q}_w}{\partial t_{w,\text{in}}}\right)^2 u^2(t_{w,\text{in}}) + \left(\frac{\partial \dot{Q}_w}{\partial t_{w,\text{out}}}\right)^2 u^2(t_{w,\text{out}})}. \tag{2}$$

The standard uncertainties of measured parameters are based on the resolution of the measuring instruments used. The uncertainties of the water volumetric flow rate measurement and the water temperature measurements (at the inlet and outlet) are 0.6 $\text{dm}^3/\text{min}$, 0.06 K, and 0.06 K, respectively.

## 2.3 Measurement results

As part of this work, nine measurement cases were analyzed. All measurements were carried out at maximum air flow rate, three values of the mass flow rate of the water, and three values of temperature of water behind the boiler 50°C, 70°C, and 90°C. The results of the measurements and

their analysis are presented in Fig. 3 and Table 1 (cases from C1 to C9). The distribution of air velocity at the heat exchanger inlet, presented in Fig. 3, shows very clearly that the inflow of this medium is non-uniform. Differences between maximum and minimum velocity are of up to 400%. As mentioned before, non-uniform air distribution is the data for the calculations.

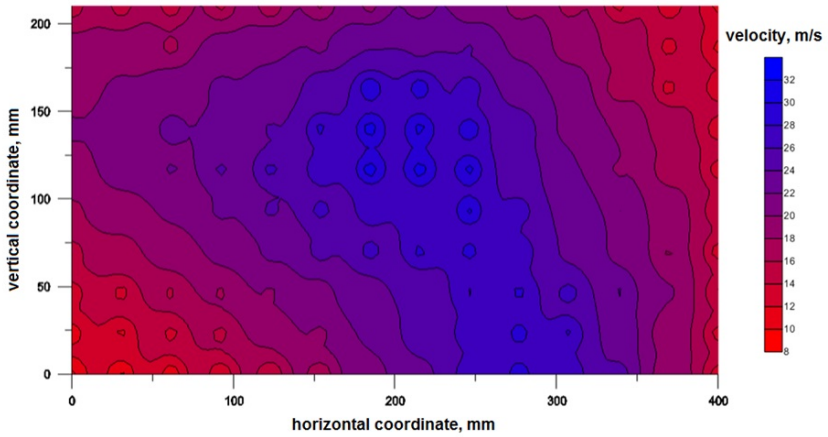


Figure 3: Air inlet velocity distribution measured at the maximum volumetric flow rate (6128 $m^3$/h).

Table 1: Results of the reference measurements.

| Case ID | Air flow rate | Water flow rate | Water temperature | | Heat transfer rate | Uncertainty of measurement |
|---|---|---|---|---|---|---|
| | | | inlet | outlet | | |
| | $m^3$/h | $dm^3$/min | °C | °C | kW | kW |
| C1 | 6128 | 16.7 | 90.1 | 75.8 | 16.66 | 0.48 |
| C2 | 6128 | 16.7 | 70.2 | 61.3 | 10.37 | 0.29 |
| C3 | 6128 | 16.9 | 49.6 | 45.3 | 5.07 | 0.17 |
| C4 | 6128 | 21.8 | 89.9 | 78.1 | 17.95 | 0.48 |
| C5 | 6128 | 21.9 | 70.5 | 63.3 | 11.00 | 0.34 |
| C6 | 6128 | 21.8 | 49.7 | 45.9 | 5.78 | 0.17 |
| C7 | 6128 | 26.5 | 89.9 | 79.3 | 19.60 | 0.57 |
| C8 | 6128 | 26.5 | 70.1 | 63.7 | 11.84 | 0.33 |
| C9 | 6128 | 26.6 | 50.3 | 47.1 | 5.94 | 0.20 |

## 3 Computational models

The computational model of the analyzed heat exchanger was carried out as a part of [17] and was further developed and validated based on the measurement results [16, 29]. The calculation methodology is based on the assumption that the real heat exchanger can be divided into repeatable segments. The heat exchanger operation is simulated by performing sequential calculations for successive repeatable segments.

The division into repeatable segments applied to the analyzed heat exchanger is related to the measurements of the air velocity field at the inlet, during which the air velocity was measured at 140 points. Each exchanger tube was thus divided into 14 sections of equal length, containing 12 fins each. The geometry of the repeatable element is shown in Fig. 4. The element contains the finned tube section, water flowing inside the tube, and a rectangular block of air surrounding the section.

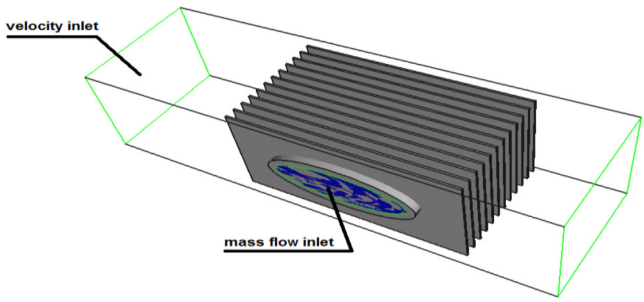


Figure 4: Geometry of the repeatable segment of the analyzed heat exchanger.

The boundary conditions for the first repeatable segment in each tube are the velocity and temperature of air, and mass flow rate and temperature of water at the repeatable element inlet (Fig. 4). It should be stressed here that for the second and remaining repeatable elements of the same tube, the boundary conditions regarding water flow are results of solving the model for previous elements. These conditions are water velocity and temperature fields at the outlet of the element. From the air side, this condition allows taking into account the measurement information about the non-uniform inflow of the fluid, i.e. velocity and temperature of the air inflowing to individual elements. The mass flow rate of water is the result of hydraulic calculations of the heat exchanger in the case of natural, non-uniform water distribution, or it is defined for the case of non-uniform, controlled water

inflow. The remaining planes of the model are considered symmetry planes. The mathematical model consists of a set of equations: flow continuity, energy balance and turbulence model [17, 29, 31]. At the first step, the testing computations aimed at selecting the proper numerical mesh and the turbulence model. The Reynolds stress model of turbulence was selected for basic computations. The developed numerical model was validated based on the measurement results, and the results of this procedure can be found, for example, in works [16, 30].

The geometry of the aforementioned hydraulic model is shown in Fig. 5.

Figure 5: A view of the geometry and boundary conditions of the hydraulic model of the analyzed heat exchanger.

The main boundary conditions are presented in Fig. 5. The mass flow rate of water flowing into the heat exchanger, as well as its temperature, are measured values. The computational domain contains 980 thousand cells which was decided upon the numerical mesh independence test. The test was realized for four discretization schemes: coarse mesh (124 652 cells, mesh number $i = 1$), medium mesh (545 678 cells, $i = 2$), fine mesh (980 128 cells, $i = 3$), and the finest mesh (1 546 258 cells, $i = 4$). The criterion for choice was the relative difference in the water outlet temperature between the subsequent meshes ($i$ and $i + 1$):

$$\Delta = \left| \frac{t_{w,\mathrm{out},i+1} - t_{w,\mathrm{out},i}}{t_{w,\mathrm{out},i}} \right|. \tag{3}$$

The results of the mesh independence test are shown in Fig. 6. It can be seen that making the mesh denser than around 1 million cells does not bring significant changes to the results. Thus, the fine mesh ($i = 3$) was chosen.

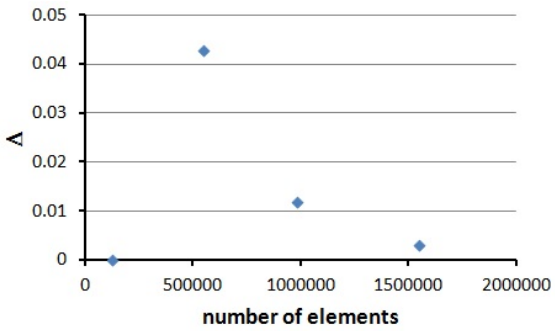


Figure 6: Mesh independence test results.

Testing the turbulence model enabled to choose the $k$-$\varepsilon$ model as giving satisfactory results. First of all, the results given by this model are physically correct. The $k$-$\varepsilon$ model of turbulence is also relatively fast solved. A general form of relationships describing the turbulence kinetic energy $k$, and its rate of dissipation $\varepsilon$ is as follows [31]:

$$\frac{\partial}{\partial t}(\rho k) + \frac{\partial}{\partial x_i}(\rho k u_i) = \frac{\partial}{\partial x_j}\left[\left(\mu + \frac{\mu_t}{\sigma_k}\right)\frac{\partial k}{\partial x_j}\right] + G_k + G_b - \rho\varepsilon - Y_M + S_k\,, \tag{4}$$

$$\frac{\partial}{\partial t}(\rho \varepsilon) + \frac{\partial}{\partial x_i}(\rho \varepsilon u_i) = \frac{\partial}{\partial x_j}\left[\left(\mu + \frac{\mu_t}{\sigma_\varepsilon}\right)\frac{\partial \varepsilon}{\partial x_j}\right] + C_{1\varepsilon}\frac{\varepsilon}{k}(G_k + C_{3\varepsilon}G_b) - C_{2\varepsilon}\rho\frac{\varepsilon^2}{k} + S_\varepsilon\,, \tag{5}$$

where $u_i$ are the components of velocity in $x_i$-direction, $x_i$ are the Cartesian coordinates ($i = 1, 2, 3$), $t$ is the time, $\mu_t$ denotes turbulent viscosity, $G_k$ and $G_b$ represent generation of turbulence kinetic energy due to the mean velocity gradients, and due to buoyancy, respectively. The contribution of the fluctuating dilatation in compressible turbulence to the overall dissipation rate is marked as $Y_M$. Quantities $S_k$ and $S_\varepsilon$ are source terms defined by the user. Turbulent Prandtl numbers for $k$ and $\varepsilon$ are denoted by $\sigma_k$ and $\sigma_\varepsilon$, respectively. Parameters $C_{1\varepsilon}$, $C_{2\varepsilon}$, and $C_{3\varepsilon}$ are the model constants.

The hydraulic model allowed to determine the distribution of water between the tubes of the analyzed heat exchanger.

# 4 Results of computations

The numerical model has been solved using the Ansys Fluent software, version 2023R1 [32]. Water has been treated as a Newtonian fluid, with a temperature-dependent density. The solver has been set to a steady time mode. Pressure-velocity coupling of the coupled scheme was applied. Spatial discretization has been set to second order for pressure, second order upwind for momentum, and the first order upwind for turbulent kinetic energy and turbulent dissipation rate. The main results of hydraulic computations of the heat exchanger are the mass flow rates of water flow through particular tubes. As mentioned before, the natural water distribution is an effect of pressure distribution resulting from hydraulic resistances and depending on the shape of the water flow channel. Figure 7 presents the results of computations realized for various values of total mass flow rate at the heat exchanger inlet: 0.4412 kg/s, 0.3622 kg/s, and 0.2785 kg/s, for the location of water inlet and outlet nozzles presented in Fig. 5. This water flow variant was marked as V1.

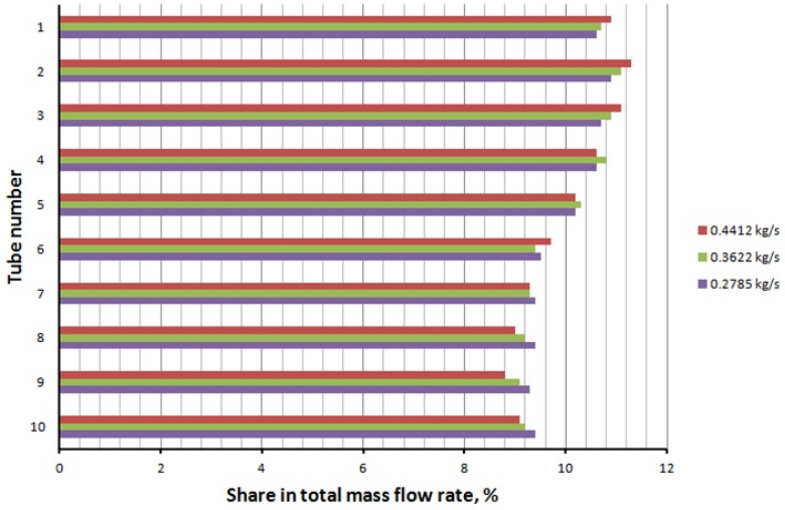


Figure 7: Distribution of water for the non-uniform and uncontrolled flow for three analyzed water flow rates – variant V1.

Assuming the possibility of regulation of water streams flowing through individual heat exchanger tubes, numerical simulations of the heat exchanger operation for two variants were performed. In variant V2, it was assumed that a larger stream of water should flow through the tubes, in the area

in which a larger stream of air also flows. The mass flow of water flowing through a given tube is therefore equal to the proportion of air flowing through the area of the same tube. The input data for this case, presented in Fig. 8, are therefore the result of the assumption made. The distribution of water is independent of the water flow rate as only one air flow rate was considered.

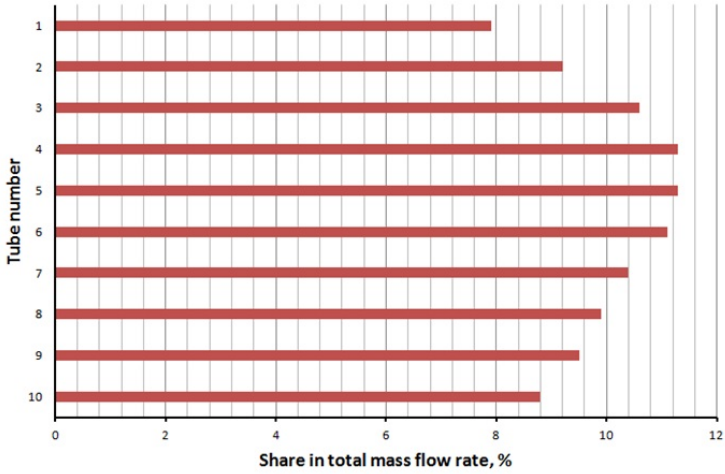


Figure 8: Distribution of water for the non-uniform and controlled flow – variant V2.

The V3 variant assumes that the water inlet and outlet nozzles will be moved towards the center of the height of the water manifolds of the heat exchanger and this would result in symmetrical water distribution relative to the center of the height of the heat exchanger. The location of water nozzles is schematically presented in Fig. 9. This assumption is purely theoretical, however, it refers to the water distribution shown in Fig. 8 to some degree. The values of water mass flow rates for this case are shown in Fig. 10, and they are the result of calculations carried out using the hydraulic model of the heat exchanger. This variant of the water supply cannot be described as controlled, hence it is referred to in the further part of the text by its designation – V3. Some deviation from the symmetric flow of water can be seen there, which may be the result of including gravity in the numerical model.

Analyzing the results of computations done for variants V1 and V3 it may be noted that decreasing the flow rate of water slightly decreases the water distribution non-uniformity. It is more visible for the variant V1.

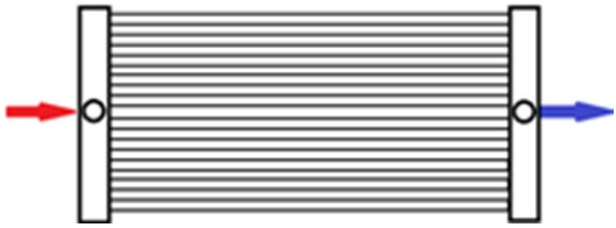

Figure 9: Locations of water inlet and outlet nozzles in variant V3.

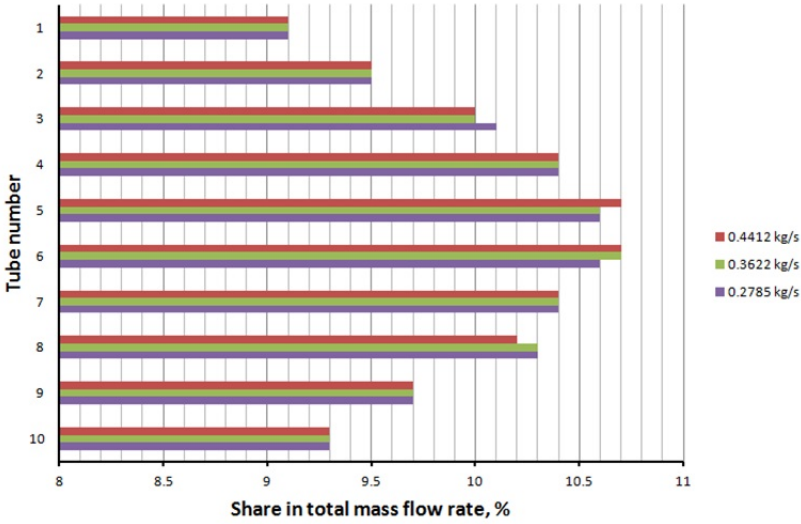


Figure 10: Distribution of water for three analyzed water flow rates for the variant V3.

Obtaining the uniform flow of the mediums on the test stand for the analyzed heat exchangers is impossible. Therefore, to assess the impact of the non-uniform media flow on the device's performance, measurements were carried out in conditions of the non-uniform inflow of both heat carrier – air and water (variant V1, Tables 2–4) and calculations, using the previously presented model, assuming the uniform inflow of air and water (variant VU, Tables 2–4). The calculations were performed for the aforementioned three values of mass flow rate and temperature of water (Table 1, cases C1–C9). The heat fluxes obtained for the conditions of uniform inflow of the air and the water (variant VU) are 5.56 kW for the set water temperature of 50°C at the minimum water mass flow rate (0.2785 kg/s), and 24.05 kW for the temperature of 90°C at the maximum water mass flow rate (0.4412 kg/s).

This means that the uneven flow of mediums (variant V1) causes a decrease in thermal efficiency of up to 18.5% in the considered cases C1–C9 (Tables 2–4). This decrease in the thermal efficiency of the analyzed heat exchanger is greatest at the highest water temperature at the inlet (cases C1, C4, and C7). It can also be seen by comparing the indicated cases that the increasing water flow rate contributes to a greater decrease in thermal efficiency. The same trend is also seen for the lower inlet water temperature. When evaluating these results, it should be noted that with the increasing flow rate of the hot medium, an increase in the thermal efficiency of the heat exchanger is expected. A direct comparison of thermal efficiency allows this regularity to be noticed. However, the work uses relative values when comparing different variants, and hence the observed effect.

Table 2: Comparison of measurements and computational results – minimum water flow rate

| Analyzed case | Flow variant | Heat capacity | Relative heat capacity |
|---|---|---|---|
| | | kW | % |
| C1 | Uniform flow of both mediums, VU | 19.46 | 100.0 |
| | Non-uniform uncontrolled flow, V1 | 16.66 | 85.6 |
| | Non-uniform flow of air, water, V2 | 19.64 | 100.9 |
| | Non-uniform flow of air, water, V3 | 17.34 | 89.1 |
| C2 | Uniform flow of both mediums, VU | 11.54 | 100.0 |
| | Non-uniform uncontrolled flow, V1 | 10.37 | 89.9 |
| | Non-uniform flow of air, water, V2 | 11.86 | 102.8 |
| | Non-uniform flow of air, water, V3 | 10.47 | 90.7 |
| C3 | Uniform flow of both mediums, VU | 5.56 | 100.0 |
| | Non-uniform uncontrolled flow, V1 | 5.07 | 91.2 |
| | Non-uniform flow of air, water, V2 | 5.83 | 104.8 |
| | Non-uniform flow of air, water, V3 | 5.26 | 94.6 |

Using the previously described numerical model of the heat exchanger and performing calculations for both variants (V2, V3) of water distribution of all analyzed cases, a set of results was obtained, which are presented in Tables 2, 3, and 4. It should be noted that the calculations assumed the non-uniform distribution of air velocity at the heat exchanger inlet (no interference with the natural inflow was assumed), which is shown in Fig. 3.

The results of all analyses, experimental and computational, were compared assuming that for the case of the uniform inflow of both heat carriers, the efficiency of the heat exchanger being the subject of the analysis is 100%.

The summary results presented in Tables 2, 3, and 4 show that the controlled distribution of water (variants V2, V3) in each analyzed case causes an increase in the thermal efficiency of the heat exchanger relative to the non-uniform and uncontrolled inflow of mediums (V1). The results indicate that the inflow of water proportional to the amount of air (V2) allows to achieve even better effect than in the case of the uniform inflow of mediums. This is observed for all considered cases, and the greatest differences from the uniform flow case are observed at the water inlet temperature equal to 50°C (cases C3, C6, and C9). The 4.8% difference was recorded for the C3 case (Table 2). This effect was visible for each water mass flow rate considered, with a slight upward trend with decreasing of water flow.

Table 3: Comparison of measurements and computational results – medium water flow rate.

| Analyzed case | Flow variant | Heat capacity | Relative heat capacity |
|---|---|---|---|
| | | kW | % |
| C4 | Uniform flow of both mediums, VU | 21.52 | 100.0 |
| | Non-uniform uncontrolled flow, V1 | 17.95 | 83.4 |
| | Non-uniform flow of air, water, V2 | 21.65 | 100.6 |
| | Non-uniform flow of air, water, V3 | 18.77 | 87.2 |
| C5 | Uniform flow of both mediums, VU | 12.44 | 100.0 |
| | Non-uniform uncontrolled flow, V1 | 11.00 | 88.4 |
| | Non-uniform flow of air, water, V2 | 12.73 | 102.3 |
| | Non-uniform flow of air, water, V3 | 11.02 | 88.6 |
| C6 | Uniform flow of both mediums, VU | 6.44 | 100.0 |
| | Non-uniform uncontrolled flow, V1 | 5.78 | 89.8 |
| | Non-uniform flow of air, water, V2 | 6.70 | 104.1 |
| | Non-uniform flow of air, water, V3 | 5.94 | 92.3 |

Taking into account the measurement uncertainties, the results may be slightly less optimistic, but they definitely exceed the limits of these uncertainties. The obtained efficiency gains, in the range of 0.2% to 18.6% (calculated relative to the case with the non-uniform and uncontrolled in-

Table 4: Comparison of measurements and computational results – maximum water flow rate.

| Analyzed case | Flow variant | Heat capacity | Relative heat capacity |
|---|---|---|---|
| | | kW | % |
| C7 | Uniform flow of both mediums, VU | 24.05 | 100.0 |
| | Non-uniform uncontrolled flow, V1 | 19.60 | 81.5 |
| | Non-uniform flow of air, water, V2 | 24.07 | 100.1 |
| | Non-uniform flow of air, water, V3 | 20.85 | 86.7 |
| C8 | Uniform flow of both mediums, VU | 14.23 | 100.0 |
| | Non-uniform uncontrolled flow, V1 | 11.84 | 83.2 |
| | Non-uniform flow of air, water, V2 | 14.40 | 101.2 |
| | Non-uniform flow of air, water, V3 | 12.58 | 88.4 |
| C9 | Uniform flow of both mediums, VU | 6.92 | 100.0 |
| | Non-uniform uncontrolled flow, V1 | 5.94 | 86.3 |
| | Non-uniform flow of air, water, V2 | 7.08 | 102.5 |
| | Non-uniform flow of air, water, V3 | 6.28 | 90.9 |

flow V1) are similar to the effects obtained for the case of the controlled air supply, which was tested as part of the work [16]. A comparison of the results obtained for the flow variants V2 and V1 indicates an increase of the thermal output at a level of a dozen percent, and this increase is higher for the highest water inlet temperature. Analysis of results for cases C1, C4, C7, and C2, C5, C8, and then C3, C4, C6 allows to state that better thermal output is observed for the highest water flow rate. The assumption stating that moving the inlet and outlet water nozzles to the half-height of the water manifolds (variant V3) would improve the thermal performance of the heat exchanger under consideration has been also proved. However, in this case, an increase in the thermal output is not as significant as in variant V2, and the results of comparison to variant VU are worse for all the considered cases. The greatest differences are around 5% relative to the V1 variant, and they are observed for cases C7, C8, and C9.

Summing up the performed experimental and numerical analyses, it may be stated that controlling the liquid distribution among the tubes of the heat exchanger seems to be an option for improving the thermal performance of the device.

## 5 Final remarks and conclusions

A procedure of controlling the flow of water to individual heat exchanger tubes is much more difficult to implement than controlling the air inflow. However, the intention of the authors of the work is not to indicate the technical possibilities, but to analyze the energy effects of controlling the water in cross-flow tube-and-fin heat exchangers operating with non-uniform inflow of working fluids. The results of analyses show that a controlled inflow of water may have a positive impact on the thermal efficiency of the heat exchanger. The rise in efficiency values ranges from 0.2% to 18.6% and from 0.1% to 4.8% in comparison with the natural non-uniform flow of both heat carriers and with the theoretical uniform flow of both mediums, respectively. This rise depends on mass flow rates of water and water temperature at the heat exchanger inlet.

This work is an extension of the earlier authors' research, in which the effects of shaping the inflow (control) of one of the fluids to the considered heat exchanger were checked. The results of the experimental and computational analyses confirmed the earlier observations. The obtained results also confirm the observations of other researchers about the possible positive impact of a non-uniform but properly shaped media inflow on the thermal efficiency of heat exchangers.

The results obtained in this work indicate the possibility of obtaining higher efficiency of heat exchangers in the case of a non-uniform supply of working fluids than in the case of a uniform supply of these fluids. However, finding such possibilities requires, in principle, an individual analysis on a case-by-case basis. For gas-liquid heat exchangers, it seems technically possible to introduce gas supply control. Controlling the flow of liquid on individual heat exchanger tubes is definitely a more difficult task. It is conceivable that such control could be achieved by the installation of a valve system, which would, however, significantly complicate and increase the cost of the overall construction. Another solution could be a specific solution for liquid inlet and outlet manifolds, which, combined with the tube system, would ensure an appropriate distribution of hydraulic resistance. However, the development of such a liquid flow control system requires knowledge of the distribution of the gas stream flowing to the heat exchanger.

### Acknowledgements

This work was funded by the Ministry of Science and Education: under Statutory Research Funds of the Faculty of Energy and Environmental Engineering, Silesian University of Technology (Poland).

*Received 28 February 2023*

# References

[1] Chiou J.P.: *Thermal performance deterioration in crossflow heat exchanger due to the flow nonuniformity.* J. Heat Transf. **100**(1978), 4, 580–587.

[2] Ranganayakulu Ch., Seetharamu K.N., Sreevatsan K.V.: *The effects of inlet fluid flow nonuniformity on thermal performance and pressure drops in cross-flow plate-fin compact heat exchangers.* Int. J. Heat Mass Trans. **40**(1996), 27–38.

[3] Kumar S., Dwivedi R., Singh P.K.: *Effect of flow maldistribution on thermal performance of water-cooled minichannel heat sink.* In: Advances in Fluid and Thermal Engineering (P. Saha, P.M.V. Subbarao, B.S. Sikarwar, Eds.), 2019, 43–52. doi: 10.1007/978-981-13-6416-7_5

[4] Joseph J.: *Numerical and experimental study of microchannel performance on flow maldistribution.* Micromachines (Basel) **11**(2020), 3, 323, doi: 10.3390/mi11030323

[5] Zhang K., Li M.J., He Y. L.: *A general and rapid method to evaluate the effect of flow maldistribution on the performance of heat exchangers.* Int. J. Therm. Sci. **170**(2021), 107152. doi: 10.1016/j.ijthermalsci.2021.107152

[6] T'joen C., Willockx A., Steeman H.-J., De Paepe M.: *Performance prediction of compact fin-and-tube heat exchangers in maldistributed airflow.* Heat Trans. Eng. **28**(2007), 12, 986–996.

[7] Tereda F.A., Srihari N., Sunden B., Das S.K.: *Experimental investigation on port-to-channel flow maldistribution in plate heat exchangers.* Heat Trans. Eng. **28**(2007), 5, 435–443.

[8] De Schampheleire S., De Kerpel K., Ameel B., Huisseune H., De Paepe, M.: *Thermal analysis of a commercial plate fin heat exchanger with nonuniform inlet flow conditions.* Heat Trans. Eng. **37**(2016), 17, 1466–1477.

[9] Guo J., Huai X., Cheng K., Cui X., Zhang H.: *The effects of nonuniform inlet fluid conditions on crossflow heat exchanger.* Int. J. Heat Mass Trans. **120**(2017), 807–817.

[10] Bury T., Składzień J., Hanuszkiewicz-Drapała M.: *Experimental and numerical analyses of a non-uniform agents flow impact on a finned cross-flow heat exchanger effectiveness.* In: Proc. 22nd Int. Conf. on Efficiency, Cost, Optimization, Simulation and Environmental Impact of Energy Systems – ECOS 2009, Foz do Iguacu, Parana, 31 Aug.–3 Sept. 2009 (on CD).

[11] Bury T., Składzień J., Widziewicz K.: *Experimental and numerical analyses of finned cross flow heat exchangers efficiency under non-uniform gas inlet flow conditions.* Arch. Thermodyn. **31**(2010), 4, 133–144.

[12] Neve R.S., Yan Y.Y.: *Enhancement of heat exchanger performance using combined electrohydrodynamic and passive methods.* Int. J. Heat Fluid Fl. **17**(1996), 4, 403–409.

[13] Coetzee H., Liebenberg L., Meyer J.P.: *Heat transfer and pressure drop characteristics of angled spiraling tape inserts in a heat exchanger annulus.* Heat Trans. Eng. **24**(2003), 6, 29–39.

[14] Bury T., Składzień J.: *Evaluation of selected methods of mitigation of media flow maldistribution impact in finned cross-flow heat exchangers*. Int. J. Thermodyn. **16**(2013), 4, 189-195.

[15] Hajabdollahi Z., Hajabdollahi H., Kim K.C.: *Estimating the non-uniform air velocity distribution for the optimal design of a heat exchanger*. Appl. Therm. Eng. **153**(2019), 704–714.

[16] Bury T., Hanuszkiewicz-Drapała M.: *Numerical and experimental analysis of a tube-and-fin crossflow heat exchanger with controlled non-uniform inflow of media*. E3S Web Conf. **323**(2021), 00005.

[17] Widziewicz K.: *Thermodynamic analysis of a cross-flow heat exchanger considering non-uniformity of working mediums inflow and thermal radiation*. PhD thesis, Institute of Thermal Technology, Silesian University of Technology, Gliwice, 2014 (in Polish).

[18] Bury T., Hanuszkiewicz-Drapała M.: *Analysis of water flow in a cross-current heat exchanger based on a CFD model*. In: Proc. of the 4th Int. Sci. Tech. Conf. on Modern Power Systems and Units, Cracow, 2016, 39–40 (in Polish).

[19] Taler D.: *Mathematical modeling and control of plate fin and tube heat exchangers*. Energ. Conv. Manag. **96**(2015), 452–462.

[20] Węglarz K., Taler D., Taler J.: *New non-iterative method for computation of tubular cross-flow heat exchangers*. Energy **260**(2022), 124955.

[21] Korzeń A., Taler D.: *Numerical modelling of rapid decrease in water flow rate in a plate-and-tube heat exchanger*. Heat Transf. Eng. **44**(2023), 11-12, 1072–1081.

[22] Sunden B.: *Computational fluid dynamic in research and design of heat exchangers*. Heat Trans. Eng. **28**(2007), 11, 898–910.

[23] Bhutta M.M.A., Hayat N., Khan A., Kanwar N.A., Khan S.: *CFD applications in various heat exchangers design: a review*. Appl. Therm. Eng. **32**(2012), 1–12.

[24] Jun S., Puri V.M.: *3D milk-fouling model of plate heat exchangers using computational fluid dynamics*. Int. J. Dairy Tech. **58**(2005), 4, 214–224.

[25] Ozden E., Tari I.: *Shell side CFD analysis of a small shell-and-tube heat exchanger*. Energ. Convers. Manage. **51**(2010), 5, 1004–1014.

[26] Sheik Ismail L., Ranganayakulu C., Shah R.K.: *Numerical study of flow patterns of compact plate-fin heat exchangers and generation of design data for offset and wavy fins*. Int. J. Heat Mass Transf. **52**(2009), 17–18, 3972–3983.

[27] Lee M.S., Li Z., Ling J., Aute V.: *A CFD assisted segmented control volume based heat exchanger model for simulation of air-to-refrigerant heat exchanger with air flow mal-distribution*. Appl. Therm. Eng. **131**(2018), 230–243.

[28] Bury T., Hanuszkiewicz-Drapała M.: *Analysis of a controlled non-uniform liquid inflow impact on cross-flow heat exchanger operation*. In: Advances in the Study of Heat and Mass Transfer (D. Butrymowicz, K. Śmierciew, P. Jakończuk, Eds.), Bialystok Univ. Technol., Białystok 2022, 247–255 (in Polish). doi: 10.24427/978-83-67185-30-1

[29] Hanuszkiewicz-Drapała M., Bury T., Widziewicz K.: *Numerical model of a cross-flow heat exchanger with non-uniform flow of media*. J. Power Technol. **93**(2013), 5, 295–302.

[30] Bury T., Hanuszkiewicz-Drapała M., Widziewicz K.: *The finite difference method and the numerical approach for modeling the maldistribution of the flow of media in tube-and-fin cross-flow heat exchangers*. Heat Trans. Eng. **39**(2018), 13-14, 1179–1191.

[31] ANSYS INC.: *ANSYS Fluent Theory Guide*, Canonsburg, 2021.

[32] ANSYS Fluent Tutorial Guide 2023 R1, http://www.ansys.com (accesed 15 Jan. 2023).

**archives**
**of thermodynamics**
Vol. **44**(2023), No. 4, 427–446
DOI: 10.24425/ather.2023.149722

# Mass/heat transfer analogy method in the research of convective fluid flow through channels with a specific geometry

**SEBASTIAN GROSICKI***
**JOANNA WILK**

Rzeszow University of Technology, Powstańców Warszawy 12, 35-959 Rzeszów, Poland

**Abstract** The present work contains the results of the comparative analysis of the literature data and the own investigations on mass and heat transfer coefficients occurring under conditions of the convective fluid flow through channels characterised by a specific geometry. The authors focused on the available experimental investigations on mass transfer. The considered experiments were carried out using the electrochemical method named limiting current technique. Two channel geometries were discussed: the annular channel of the conventional size and the long minichannel with a square cross-section area. Taking into consideration dimensionless numbers: Schmidt and Nusselt – analogical for mass and heat transfer – the formulas describing the phenomena under consideration were included. In the case of the annular channel the laminar and turbulent range of Reynolds numbers was studied. For the square minichannel – the laminar flow is considered. The analogy between mass and heat transfer introduced by Chilton and Colburn was applied in the analysis. An equivalent boundary condition is included in considerations concerning the mass and heat transfer. It is the Dirichlet boundary condition characterised by constant temperature of the wall which corresponds to the situation of constant ion concentration at the cathode surface in the limiting current technique. The main purpose of the present work was to verify the method for the determination of heat transfer coefficients using the analogy between mass and heat transfer processes in the case of convective fluid flow through the annular and square channels. The problem discussed in the present work is impor-

*Corresponding Author. Email: sebogr@prz.edu.pl

tant and actual due to the possibility of the elimination of temperature measurements in the investigations of heat transfer processes occurring in channels characterised by a specific geometry. It should be noted that sometimes temperature measurement may be difficult or even impossible. This situation also causes high uncertainty of the obtained results. Due to this problem, the presented analysis was performed also with the use of thermal results based on the analytical solution. The verification of the use of mass/heat transfer analogy method in specific cases gives the extended knowledge of correct application of the limiting current technique in heat transfer research. The main objective of the work was achieved by conducting a comparative analysis of the adequate mass and heat transfer results. The existing literature data do not provide an answer to the question about the correctness of using the limiting current technique in the case of discussed annular channels or long square minichannels. The received results make us be critical of applying the mass/heat transfer analogy method in some heat transfer cases.

**Keywords:** Limiting current technique; Analogy method; Annular channel; Square minichannel

## Nomenclature

| | | |
|---|---|---|
| $A$ | – | surface area, $\mathrm{m}^2$ |
| $a$ | – | thermal diffusivity, $\mathrm{m^2 s^{-1}}$ |
| $C$ | – | ion concentration, $\mathrm{kmol \cdot m^{-3}}$ |
| $D$ | – | diffusion coefficient, $\mathrm{m^2 s^{-1}}$ |
| $d$ | – | diameter, m |
| $d_H$ | – | hydraulic diameter, m |
| $F$ | – | Faraday constant, $\mathrm{A \cdot s \cdot kmol^{-1}}$ |
| $f$ | – | friction factor |
| $I$ | – | current, A |
| $L$ | – | channel length, m |
| Nu | – | Nusselt number, $= \alpha \cdot d_H / \lambda$ |
| Pr | – | Prandtl number, $= \nu / a$ |
| Re | – | Reynolds number, $= w \cdot d_H / \nu$ |
| Sc | – | Schmidt number, $= \nu / D$ |
| Sh | – | Sherwood number, $= \beta \cdot d_H / D$ |
| $T$ | – | temperature, °C, K |
| $t$ | – | time, s |
| $w$ | – | mean velocity of the fluid, $\mathrm{m \cdot s^{-1}}$ |

### Greek symbols

| | | |
|---|---|---|
| $\alpha$ | – | heat transfer coefficient, $\mathrm{Wm^{-2} K^{-1}}$ |
| $\beta$ | – | mass transfer coefficient, $\mathrm{m \cdot s^{-1}}$ |
| $\lambda$ | – | thermal conductivity, $\mathrm{Wm^{-1} K^{-1}}$ |
| $\nu$ | – | kinematic viscosity, $\mathrm{m^2 s^{-1}}$ |

# 1 Introduction

Annular channels and square minichannels represent important kinds of channel geometry applied in different thermal systems. These may be: simple heat exchangers, heat sinks, elements of heating systems, minichannel heat exchangers, electronic equipment or even most complicated nuclear reactors. The problem of convective heat transfer during the fluid flow through the annular channel seems to be well recognized, however, there are selected issues that cannot be recognized as fully examined. Recent investigations indicate such problems. These include: ducts with special additional elements for enhancement of heat transfer (spiral wire inserts in cooling processes of high-temperature reactors [1], pin fins arrays manufactured by selective laser melting technology for applications in internal combustion engine components [2]), channels with special fluids transferring heat (molten salts [1,3], new types of refrigerants [4,5]), or channels with two-phase flow (convective boiling [4–6]). For example, the work [1] includes the results of numerical study of the flow and heat transfer of molten salt in an annular channel with a wire coil. The results were compared with those for the smooth annular channel. In turn, the paper [3] presents the results of the investigations of the heat transfer performance of molten salt steam generator used in the solar power tower plant. Various experiments on the heat transfer performance of molten salt with high pressure water/steam in a horizontal tube-in-tube have been carried out. Another topic addressed in contemporary works on heat transfer in annular channels is the problem of rotating internal cylinders. This issue is studied in works [7,8] where the authors investigated the convective heat transfer for an annulus with an inner rotating wall. Additionally, the work [8] presents the results for the finned inner pipe.

In turn, the topic of heat transfer in minichannels has also been widely researched in recent times. The comprehensive review of mathematical and numerical models applied in thermal analysis of minichannels characterized by different cross-sections is included in [9]. In the case of square minichannels the researchers studied the problem of convective nanofluid flow in minichannel heat sinks [10] or cooling performance of heat sinks for heat dissipation from electronic components [11]. Experimental investigation on laminar flow and heat transfer in square minichannels with twisted tapes is presented in [12], while the paper [13] includes the results of the numerical study of heat transfer enhancement in a square minichannel heat sink with butterfly inserts.

Another recently investigated problem related to the presented examples is mass transfer during the fluid flow through channels with an annular cross-section and square minichannels. Similar to the thermal investigations, the results of an experiment on mass transfer in an annular channel with an obstruction were reported in [14]. In turn, the special fluid nanoelectrolyte flowing through the annular channel with the inner surface working as the cathode was studied in [15]. In the case of square minichannels the works [16–18] present the results of investigations of mass transfer coefficients under conditions of the laminar and turbulent flow through the system of long square minichannels.

The main and important topic in heat and mass transfer considerations is the determination and validation of formulas for obtaining mass or heat transfer coefficients, taking into account certain boundary conditions.

In the present study, the comparative analysis of the results of mass/heat transfer coefficients in the case of the fluid flow through channels with annular and mini-square cross sections has been performed. Based on the available literature data and our own research, the comparison of the mass/heat transfer coefficients with the use of the analogy method has been performed. The main goal of the work is to validate the received equations in application to the considered channel geometry. The results obtained from the validation may be important in further mass/heat transfer studies.

## 2 Mass transfer – experimental investigation

This section discusses the results of experimental research on mass transfer during the electrolyte flow through the annular and square channels. The considered data are the results of measurements of mass transfer coefficients. The investigations have been performed using the limiting current technique.

### 2.1 Limiting current technique in the investigation of mass transfer in channels

The electrochemical method named the limiting current technique is a method used to determine mass transfer coefficients. The limiting current technique involves observing the controlled diffusion of ions at the electrode surface. Most often it is the cathode. Once the external voltage is applied to electrodes, which are immersed in the electrolyte, the reduction of anions occurs at the cathode and the oxidation process at the anode, by which the

electric current arises in the external circuit. The current is proportional to the number of reacting ions.

Taking into account Faraday's law the current $I$ is given by

$$I = nFAN, \tag{1}$$

where: $A$ – surface of the cathode, $n$ – valence charge of reacting ions, $N$ – molar flux density, $F$ – Faraday constant.

The process of ion transport occurs by three phenomena: convection, migration and diffusion. However, the convection element is negligibly small. In turn, the migration process can also be neglected when the additional background electrolyte is used. Taking into account only the diffusion process, according to Fick's law about molar flux density and based on the Nernst model of linear dependence of ion concentration vs the distance from the electrode surface in the diffusion layer [19], the following equation is valid

$$I = nFA\beta \left(C_b - C_w\right), \tag{2}$$

where: $\beta$ – mass transfer coefficient, $C_b$, $C_w$ – bulk ion concentration and ion concentration at the electrode surface, respectively.

It is impossible to calculate the mass transfer coefficient from Eq. (2) because $C_w$ is practically non-measurable. In the limiting current technique, an increasing current is caused to flow across the electrodes by increasing the applied voltage.

If the anode surface is much bigger than the cathode surface, a further increase in the applied voltage will not lead to increased current intensity – segment AB in Fig. 1. This segment of the polarization curve is called

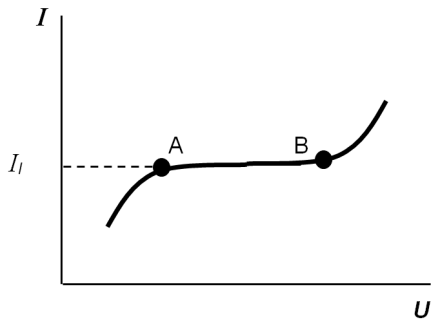


Figure 1: Current *vs* potential curve – voltammogram with the limiting current plateau region.

the limiting current plateau. Under these conditions the ion concentration at the cathode surface $C_w$ approaches zero. Based on the measurement of the limiting current, the mass transfer coefficient can be calculated from the equation

$$\beta = \frac{I_l}{nFAC_b}, \tag{3}$$

where: $I_l$ – limiting current. The experiment performed with the presented method requires measurements of the limiting current and the bulk ion concentration $C_b$.

Different electrochemical systems are used in the limiting current method. The ferri-ferrocyanide system is useful among others due to minimizing the reactions of deposition [20]. In this case, the oxidation-reduction reaction under controlled convective-diffusion is given by

$$[\mathrm{Fe(CN)_6}]^{-4} \underset{\text{reduction}}{\overset{\text{oxidation}}{\longleftrightarrow}} [\mathrm{Fe(CN)_6}]^{-3} + \mathrm{e}. \tag{4}$$

In order to achieve the controlled convective-diffusion process, oxygen must be removed from the electrolyte. The bubbling of the electrolyte with nitrogen satisfies this condition. Electrodes made of nickel are useful in the mentioned system. The value of the ferricyanide ions concentration $C_b$ is measured using iodometric titration. Figure 2 presents the electrochemical system corresponding to Eq. (4).

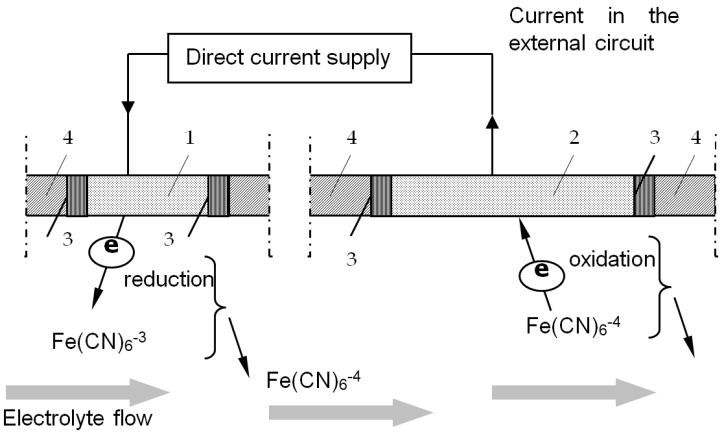


Figure 2: Scheme of the electrochemical system applied in the limiting current method; Electrolyte-aqueous solution of equimolar quantities of $K_3Fe(CN)_6$ and $K_4Fe(CN)_6$ and molar solution of sodium hydroxide NaOH: 1 – nickel cathode, 2 – nickel anode, 3 – electric insulation, 4 – construction element.

Since the ferricyanide reduction at the cathode is a limiting reaction, the cathode surface models the heat transfer surface in mass/heat transfer analogy studies.

In the electrochemical research with the use of the limiting current technique for the determination of mass transfer coefficients, the boundary condition characterised by constant ion concentration at the cathode surface takes place. This is the analogous situation to the Dirichlet condition of constant wall temperature in thermal research.

The discussed method has been applied in some studies of mass transfer in channels with other geometries (in addition to those considered in this paper): short ducts with varied shapes and surface areas along the curved axes [21], short circular minichannels [22,23], long circular and rectangular microchannels [24–26], conventional circular channels [27], or short ducts consisted in cylindrical segments in different configurations [28].

Considering the convective heat transfer during the flow through the concentric annular channel, the most common case, i.e. heat transfer from the outer surface of the inner tube, is discussed. Thus, this surface works as the cathode in mass transfer investigations. In the case of square minichannel the whole inner surface of the channel was the cathode.

## 2.2 Experimental results — annular channel

The results of electrochemical research on mass transfer coefficients during the electrolyte flow through the annular channel were reported in [29]. The tests covered a wide range of Reynolds numbers. Both turbulent and laminar flow were studied. The work [29] includes the results of investigations of Chilton-Colburn coefficients. These results were transformed to the dimensionless mass transfer coefficient that is the Sherwood number:

$$\mathrm{Sh} = \frac{\beta d_H}{D}\,, \tag{5}$$

where: $d_H$ – hydraulic diameter, $d_H = d_o - d_i$, $d_o$ – inner diameter of the outer tube, $d_i$ – outer diameter of the inner tube, $D$ – diffusion coefficient.

The studies reported in [29] concerned two types of annular channels. The first was characterized by $L/d_H = 4.19$, and the second $L/d_H = 6.32$. The obtained Sh *vs* Re relationships in the laminar range are shown in Fig. 3. Figure 3 also includes the classical formula – Leveque correlation for tube [30]. The Leveque equation for mass transfer is given by

$$\mathrm{Sh} = 1.615\mathrm{Sc}^{1/3}\mathrm{Re}^{1/3}\left(\frac{d_H}{L}\right)^{1/3}. \tag{6}$$

Sc number was 1540 in the cited study.

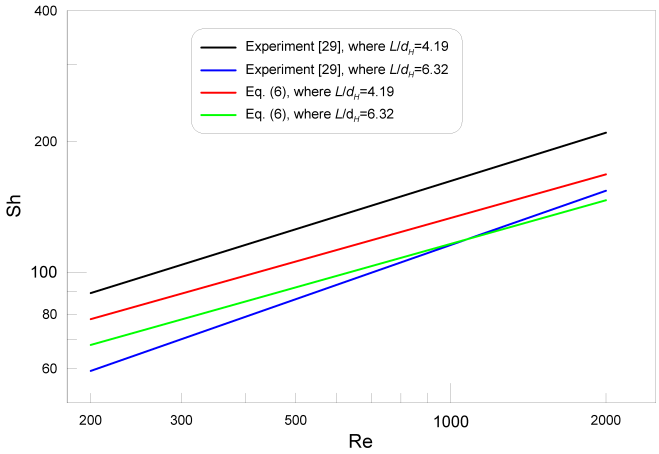


Figure 3: Sh number *vs* Re number for the laminar flow with mass transfer through the annular channel.

As can be seen from the graph in Fig. 3, Eq. (6) differs from the results of mass transfer research. The maximum deviation is about 30% for $L/d_H = 4.19$. At $L/d_H = 6.32$ (the longer channel), the deviation is smaller. It should be noted that the classical Leveque correlation was obtained from studies on the flow through the channel with a circular cross-section.

The results of mass transfer coefficients measurements in turbulent range are included in Fig. 4. The results from [14] concern the electrolyte flow

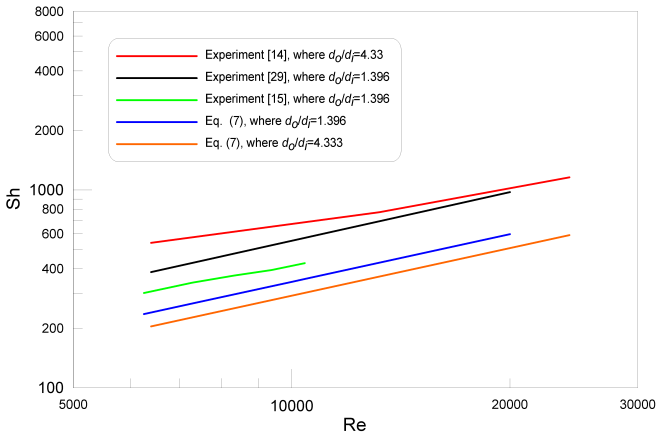


Figure 4: Sh number *vs* Re number for the turbulent flow with mass transfer through the annular channel.

through the annular duct with an obstacle. The corresponding line in Fig. 4 was received for the section of the examined channel behind the obstacle. In this case, the values of the mass transfer coefficient stabilized. In turn, the data from work [29] were averaged for the two investigated surfaces.

Figure 4 also presents the results from work [15] which were received for the same geometry of the annular channel as in [29]: $d_o/d_i = 1.396$ and $L/d_H = 4.19$. Other lines in Fig. 4 present the relationship for mass transfer during the turbulent flow in an annular channel [14]:

$$\mathrm{Sh} = 0.86 \left(\frac{d_i}{d_o}\right)^{-0.16} \mathrm{Sh}^*, \tag{7}$$

where

$$\mathrm{Sh}^* = 0.023 \mathrm{Re}^{0.8} \mathrm{Sc}^{1/3}. \tag{8}$$

As can be seen in Fig. 4 the best agreement of the results from [15] with Eq. (7) for the same geometry is in the range of Re from 6000 to 10 000. The maximum obtained deviation is about 21%. It should be noted that the classical formula (8), valid for mass transfer in turbulent region, was determined using the Chilton-Colburn analogy between mass and heat transfer. Equation (8) is suitable for ducts with different cross sections. However, it was found that the channel cross-section has a significant impact on transfer processes [31]. In addition, measurement uncertainty must be taken into account. In [15] the authors reported the average relative uncertainty of ±2% for determining the mass transfer coefficient and ±8% for the Re number.

### 2.3 Experimental results — square minichannel

The results of investigations of mass transfer coefficients during the laminar flow through the square minichannel using the limiting current technique were reported in [17]. The authors experimentally investigated the system of 100 mm long, 2 mm wide minichannels. The hydraulic diameter characterizing the square channel is equal to its width. The work analysed not fully developed laminar flow region. Due to the long channel with a small hydraulic diameter that was investigated, the change of ion concentration along the channel length has been taken into account. Thus, the average bulk ion concentration in Eq. (3) has been included.

The experiment was carried out on the stand, the diagram of which is shown in Fig. 5.

Similar to the considerations concerning the mass transfer in the annular duct, the results presented in the form of Chilton-Colburn coefficients were

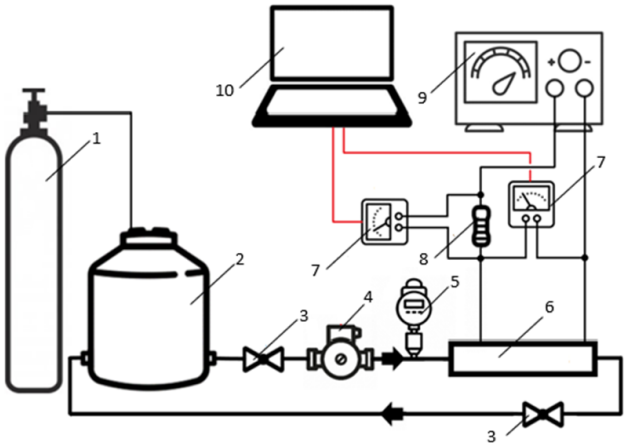


Figure 5: Scheme of the experimental system to measure the mass transfer coefficients in square minichannels [17]: 1 – cylinder with nitrogen, 2 – tank with the electrolyte, 3 – valve; 4 – pump, 5 – flowmeter, 6 – test section with the system of square minichannels, 7 – laboratory digital multimeter, 8 – high precision standard resistor, 9 – DC laboratory power supply, 10 – computer with data logger.

recalculated to the Sherwood number form. The correlation obtained as a fitting of the experimental results is given by

$$\mathrm{Sh} = 0.468\mathrm{Re}^{0.443}\mathrm{Sc}^{1/3}. \tag{9}$$

Figure 6 includes the received Sh results in the considered range of Re numbers. It should be noted that the uncertainty of mass transfer coef-

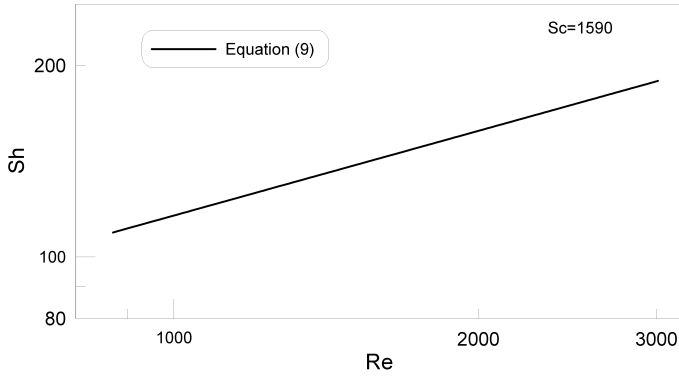


Figure 6: Mass transfer in square minichannel.

ficients determination was reported as equal to 2.5% [17]. In the case of channels characterized by small hydraulic diameters, this factor is of great importance.

# 3 Mass/heat transfer analogy results

## 3.1 Analogy between the heat and mass transfer

In the processes of mass transfer the concentration gradient of the transferred molecules or ions plays a major role. In heat transfer processes, it is a temperature gradient. The analogy between heat and mass transfer processes makes it possible to transform the results of thermal experiment into analogous mass transfer results and vice versa. This is due to the similarity of the differential equations for energy and mass transfer in the boundary conditions when the transport gradients are expressed in terms of dimensionless variables. The non-dimensional transport equations take the form

$$\frac{D\hat{C}}{Dt} = \frac{1}{\mathrm{Re}\,\mathrm{Sc}}\frac{\partial^2 \hat{C}}{\partial \hat{x}^2}\,, \tag{10}$$

for mass transfer, and

$$\frac{D\hat{\Theta}}{Dt} = \frac{1}{\mathrm{Re}\,\mathrm{Pr}}\frac{\partial^2 \hat{\Theta}}{\partial \hat{x}^2}\,, \tag{11}$$

for heat transfer, where: $\hat{C}$, $\hat{\Theta}$, $\hat{x}$ – dimensionless variables representing the concentration, temperature difference and the generalized coordinate. The terms $\frac{D\hat{C}}{Dt}$ and $\frac{D\hat{\Theta}}{Dt}$ are material derivatives.

The existence of the analogy between transfer processes requires that certain conditions have to be fulfilled [32]: there is no mass or energy produced in the system, there is no radiation and no viscous dissipation, the mass or heat transfer processes do not affect the fluid velocity profile, and the fluid physical properties are constant.

Dimensionless concentration and temperature profiles as solutions of Eqs. (10) and (11) are the same when the boundary conditions are equivalent for a given geometrical configuration and dimensionless numbers Sc and Pr are equal.

Under steady-state conditions, the solution to the mass transfer problem has a general form

$$\mathrm{Sh} = f(\mathrm{Re}, \mathrm{Sc}), \tag{12}$$

whereas the heat transfer has a form

$$\mathrm{Nu} = f(\mathrm{Re}, \mathrm{Pr}). \tag{13}$$

Thus, the Sh and Nu numbers are analogous terms which represent the mass transfer intensity by diffusion and the heat transfer intensity by convection.

Based on the analytical description of the transfer processes and the results of experimental research, the simple formula for determining the unknown convective transfer coefficients from the mass/heat transfer analogy takes the form

$$\frac{\mathrm{Nu}}{\mathrm{Sh}} = \left(\frac{\mathrm{Pr}}{\mathrm{Sc}}\right)^{z}, \tag{14}$$

where the exponent $z$ is obtained from experiments.

Chilton and Colburn proposed that $z = 1/3$ [33]. Researchers determined $z$ from a large database which is the result of many experiments performed. These were the experiments with the flow through circular pipes, around cylinders as well as over flat smooth plates. The Chilton-Colburn analogy has been found to be valid mainly for the fully developed turbulent flow. However, the analogy can also be used in the case of laminar flow [34]. It is valid for gases and liquids within the ranges of Sc number from 0.6 to 2500 and Pr number from 0.6 to 100 [32]. In turn, the validation of the Chilton-Colburn mass/heat transfer analogy for processes occurring in minichannels is presented in [35]. The author focused on circular and rectangular channels with a small hydraulic diameter. The conducted analysis did not give a clear answer to confirm the Chilton-Colburn analogy in the considered minichannels because both convergence and divergence of the results were noted.

### 3.2 Comparison of the mass and heat transfer results – the case of annular channel and square minichannel

In order to make a comparative analysis of the results of mass/heat transfer analogy, some correlations for the convective fluid flow through channels were considered.

The first formula based on the theoretical analysis relates to the laminar flow through the circular pipe [36]. It is given by

$$\mathrm{Nu} = \left\{ 3.66^3 + 0.7^3 + \left[ 1.615 \left( \mathrm{RePr} \frac{d}{L} \right)^{\frac{1}{2}} - 0.7 \right]^3 + \left[ \left( \frac{2}{1+22\mathrm{Pr}} \right)^{\frac{1}{6}} \left( \mathrm{RePr} \frac{d}{L} \right)^{\frac{1}{2}} \right]^3 \right\}^{1/3}. \tag{15}$$

Equation (15) is valid for the Dirichlet boundary condition of constant wall temperature. This is the analogous condition to the constant ion concentration at the cathode surface for mass transfer phenomena.

In turbulent region of the flow through the annular channel the comprehensive formula based on the results of many experiments [37, 38] is given by

$$\mathrm{Nu} = \frac{\frac{f_{\mathrm{ann}}}{8} (\mathrm{Re} - 1000)\,\mathrm{Pr}}{1 + 12.7 \left( \frac{f_{\mathrm{ann}}}{8} \right)^{1/2} \left( \mathrm{Pr}^{2/3} - 1 \right)} \left[ 1 + \left( \frac{d_H}{L} \right)^{2/3} \right] 0.75 \left( \frac{d_i}{d_o} \right)^{-0.17} W. \tag{16}$$

The friction factor $f_{\mathrm{ann}}$ in Eq. (16) depends on the diameter ratio $\frac{d_i}{d_{o_i}}$. It is given by [37]

$$f_{\mathrm{ann}} = \left\langle 1.8 \log_{10} \mathrm{Re} \left\{ \frac{\left[ 1 + \left( \frac{d_i}{d_{o_i}} \right)^2 \right] \ln \left( \frac{d_i}{d_{o_i}} \right) + \left[ 1 - \left( \frac{d_i}{d_{o_i}} \right)^2 \right]}{\left[ 1 - \left( \frac{d_i}{d_{o_i}} \right)^2 \right] \ln \left( \frac{d_i}{d_{o_i}} \right)} \right\} - 1.5 \right\rangle^{-2}. \tag{17}$$

Equation (16) is valid when the process of heat transfer occurs from the outer surface of the inner pipe, and the outer pipe is insulated. The parameter $W$ in Eq. (16) characterizes the fluid properties temperature dependence. For gases, $W$ can be written as a ratio of the bulk temperature $T_b$ to the wall temperature $T_w$, raised to the specific power. In the case of liquids, the variations of fluid properties with temperature can be expressed as a ratio of $\mathrm{Pr}_b$ to $\mathrm{Pr}_w$, raised to the specific power. $\mathrm{Pr}_b$ and $\mathrm{Pr}_w$ represent the Prandtl numbers of the fluid at the bulk and wall temperature, respectively.

Heat transfer coefficients received from the investigation on mass transfer [29] and Eq. (15) for the laminar range of Re numbers at different values of Pr number are included in Fig. 7a and 7b. Figure 7a presents the results

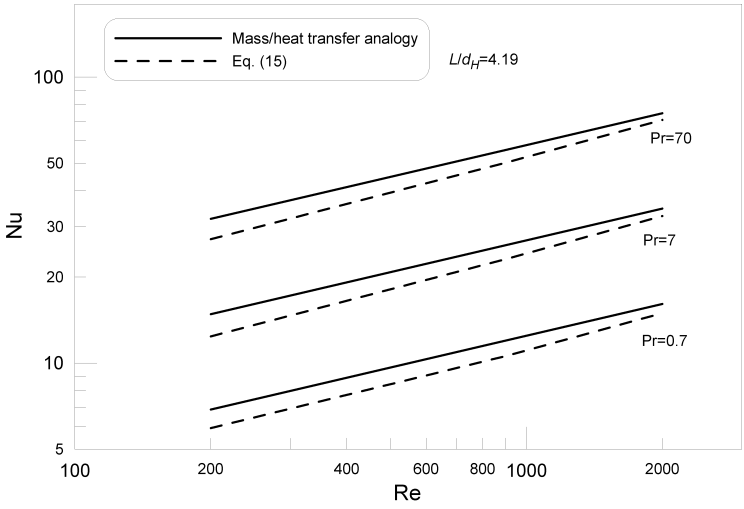


(a)

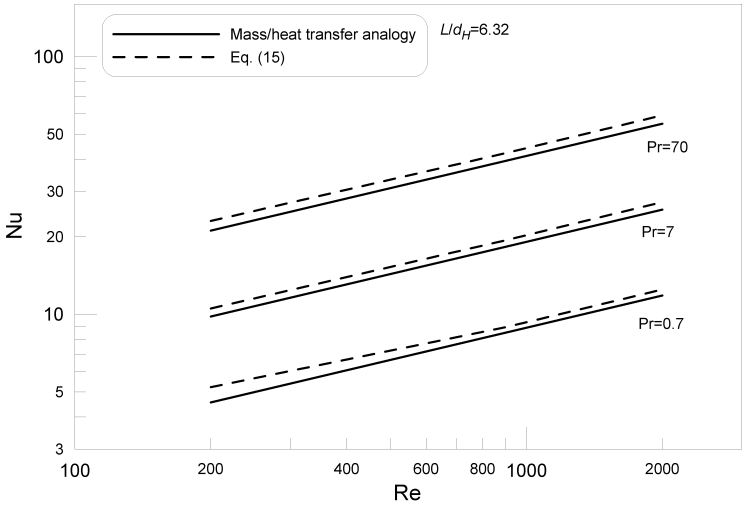


(b)

Figure 7: Chilton-Colburn analogy results for the annular channel in laminar region. Comparison with the theoretical solution for the circular channel: (a) $L/d_H = 4.19$, (b) $L/d_H = 6.32$.

for the shorter channel ($L/d_H = 4.19$). As can be seen, the analogy results lie above the theoretical line representing the boundary condition of constant wall temperature. The maximum deviation between the results is about 15%. For $L/d_H = 6.32$ (Fig. 7b), there is a good agreement of the mass/heat transfer analogy results with the analytical solution for a circular duct. The maximum deviation is about 8%.

The results of comparative analysis for the turbulent region of the fluid flow with mass/heat transfer through the annular channel are shown in Fig. 8. The results of the mass transfer experiment were taken from the authors' investigations [15] due to their better agreement with Eq. (7), (see Fig. 4).

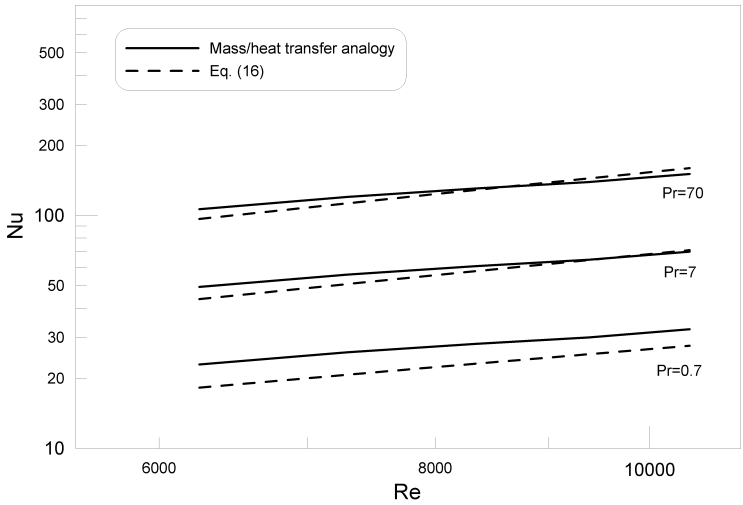


Figure 8: Chilton-Colburn analogy results for the annular channel in turbulent region – comparison with the thermal experimental results.

The analogy results were compared with the Gnielinski formula for the turbulent range of the fluid flow through the annular channel (16). Similar to the laminar region, three representative values of Pr numbers were considered. Parameter $W$ in Eq. (16) was assumed as equal to 1. As can be seen in Fig. 8, a better compliance of the results occurs for the liquid flow at $\mathrm{Pr} = 7$ and 70. The maximum deviation in this case is about 10% while for gases ($\mathrm{Pr} = 0.7$) it is 20%.

In the comparative analysis of the case of convective fluid flow through the square minichannel, Eq. (15) valid for the laminar flow through the circular pipe was taken into account. Additionally, the analytical solution for

a fully developed laminar flow in a straight minichannel with a rectangular cross-section was considered. The approximate formula of this solution has the form [39]:

$$\mathrm{Nu} = 8.235\left(1 - 2.0421K^{-1} + 3.0853K^{-2} - 2.4765K^{-3} + 1.0578K^{-4} - 0.1861K^{-5}\right), \tag{18}$$

where the parameter $K$ is the aspect ratio of the channel cross section (the ratio of the width to the height of the channel). In the case of a square minichannel $K = 1$ and Nu number from Eq. (18) it is equal to 3.61.

Figure 9 presents the results of the comparison. Additionally, the literature data of experimental studies on heat transfer in a square minichannel have been added [10]. These are the results of research of water convective fluid flow (Pr = 7) through the system of 75 mm long, 1 mm wide minichannels.

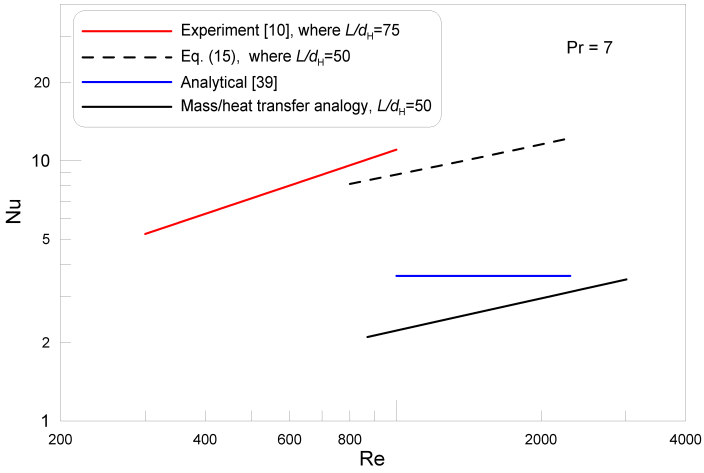


Figure 9: Chilton-Colburn analogy results for the square minichannel. Comparison with the theoretical solution for a circular channel and with heat transfer experimental results.

As can be seen in Fig. 9, the results of analytical study [39] are closest to the mass/heat transfer analogy results. In turn, these are lower than those from the conventional theory (Eq. (15)) and from thermal experimental results. The differences are large – even 75%. The reason for this discrepancy should be considered. The main problem is the channel geometry. A square cross-section with mini dimensions can have a major impact on the intensity of

mass transfer processes. If the diffusion layer thickness is comparable with the channel hydraulic diameter, the obtained mass transfer results may be underestimated [40]. In turn, in thermal investigations, both higher or lower Nu numbers for convective fluid flow through minichannels in comparison to conventional cases can be found [41–43]. It should be noted that in the thermal investigations of the flows in small-sized channels, it is very difficult to measure the temperature, which may result in high uncertainty of the results. Thus, it can be concluded that further research is needed.

## 4 Conclusions

In the present study the authors have tried to carry out a comparative analysis of the Chilton-Colburn analogy results in the case of fluid flow with mass/heat transfer through the annular channel and square minichannel. The data of mass transfer were the results of measurements carried out with the use of the limiting current technique. Based on the received results, some conclusions can be drawn, such as those listed below.

The analogy between mass and heat transfer proposed by Chilton and Colburn is a simple and very useful method in heat transfer research. The analogy method may be applied when the heat experiment may be difficult to carry out. This is important when it is difficult to measure the temperature. Then, the method makes the determination of the unknown convective transfer coefficients become possible.

In the considerations of convective fluid flow through the annular channel, it is advisable to use the analogy method proposed by Chilton and Colburn. The discussed method can be particularly useful for the liquid laminar flow – in this case, the best agreement of the analogy results was obtained. The considerations made in the present study can be a base for applying the analogy method also for the annular ducts characterized by various geometrical configurations.

In the case of convective fluid flow through a long square minichannel, there is a large discrepancy between the mass and thermal experiment results. One of the possible reasons for this could be that the boundary conditions are not compatible. The Dirichlet condition characterizes the limiting current technique while the Newman condition takes place in most thermal experiments - also in the case of the experiment, the results of which were included in the comparative analysis. In the analysis of the case of annular channel, this agreement was maintained.

The second issue that may have an impact on the discrepancy of the results is the geometry of the investigated channel – mini dimensions and the cross-section shape of the channel.

*Received 2 March 2023*

# References

[1] Yang Y., Li M., Zou Y., Chen J.: *Numerical study on heat transfer characteristics of molten salt in annular channel with wire coil*. Appl. Therm. Eng. **199**(2021), 117520.

[2] Lorenzon A., Vaglio E., Casarsa L., Sortino M., Totis G., Sarago G., Lendormy E., Raukola J.: *Heat transfer and pressure loss performances for additively manufactured pin fin in annular channels*. Appl. Therm. Eng. **202**(2022), 117851.

[3] Dong X., Bi Q., Yao F.: *Experimental investigation on the heat transfer performance of molten salt flowing in an annular tube*. Exp. Therm. Fluid Sci. **102**(2019), 113–12.

[4] Zhang J., Wang J., Li W., Liu Z., Kabelac S., Tao Z., Ma L., Tang W., Sherif S.: *R410A flow boiling in horizontal annular channels of enhanced tubes. Part I: Pressure drop*. Int. J. Refrig. **137**(2022), 70–79.

[5] Zhang J., Wang J., He Y., Liu L., Li W., Tang W., Abbas A., Ayub Z.: *R410A boiling coefficient in horizontal annular channels of enhanced tubes. Part II: Heat transfer*. Int. J. Refrig. **137**(2022), 43–50.

[6] Seo J., Lee S., Yang S., Hassan Y.: *Experimental investigation of the annular flow caused by convective boiling in a heated annular channel*. Nucl. Eng. Des. **376**(2021), 111088.

[7] Fenot M., Dorignac E., Giret A., Lalizel G.: *Convective heat transfer in the entry region of an annular channel with slotted rotating inner cylinder*. Appl. Therm. Eng. **54**(2013), 345–358.

[8] Yassin M., Abd El-Hameed H.M., Shedid M.H., Helali A.H.B.: *Heat transfer Enhancement through Annular Flow using Rotating Finned Pipe*. Aerospace Sciences & Aviation Technology, ASAT-17 (2017).

[9] Soudagar M.E.M., Kalam M.A., Sajid M.U., Afzal A., Banapurmath N.R., Akram N., Mane S.D., Saleel C.A.: *Thermal analyses of minichannels and use of mathematical and numerical models*. Numer. Heat Tr. A-Appl. **77**(2020), 5, 497–537.

[10] Arshad W., Ali H.M.: *Experimental investigation of heat transfer and pressure drop in a straight minichannel heat sing using $TiO_2$ nanofluid*. Int. J. Heat Mass Tran. **110**(2017), 248–256.

[11] Ghasemi S.E., Ranjbar A.A., Hosseini S.M.J.: *Cooling performance analysis of water-cooled heat sinks with circular and rectangular minichannels using finite volume method*. Iran. J. Chem. Eng. **37**(2018), 2, 231–239.

[12] Feng Z., Ai X., Wu P., Lin Q., Huang Z.: *Experimental investigation of laminar flow and heat transfer characteristics in square minichannels with twisted tapes*. Int. J. Heat Mass Tran. **158**(2020), 119947.

[13] Sudheer A.P., Madanan U.: *Numerical investigation into heat transfer augmentation in square minichannel heat sink using butterfly inserts*. Therm. Sci. Eng. Prog. **36**(2022), 101522.

[14] Weyns G., Nelissen G., Pembery J., Maciel P., Deconinck J., Deconinck H., Patrick M., Wragg A.: *Turbulent fluid flow and electrochemical mass transfer in an annular duct with an obstruction*. J. Appl. Electrochem. **39**(2009), 2453–2459.

[15] Wilk J., Grosicki S.: *Experimental study of electrochemical mass transfer in an annular duct with the electrolyte nanofluid*. Int. J. Therm. Sci. **129**(2018), 280–289.

[16] Wilk J., Grosicki S., Kiedrzyński K.: *Preliminary research on mass/heat transfer in mini heat exchanger*. E3S Web Conf. **70**(2018), 02016.

[17] Wilk J., Grosicki S., Smusz R.: *Mass/heat transfer analogy method in the research on convective fluid flow through a system of long square mini-channels*. Materials **15**(2022), 4617.

[18] Kumar K.A., Sarma G.V.S., Ramesh K.V.: *Mass transfer at the confining wall of a minichannel*. Mater. Today-Proc. **27**(2020), 534–538.

[19] Bard A.J., Faulkner L.R.: *Electrochemical Methods. Fundamentals and Applications*. Wiley, New York 2005.

[20] Szánto D.A., Cleghorn S., Ponce-de-León C., Walsh F.C.: *The limiting current for reduction of ferricyanide ion at nickel: the importance of experimental conditions*. AIChE J. **54**(2008), 3, 802–810.

[21] Bieniasz B: *Convectional mass/heat transfer in a rotary regenerator rotor consisted of the corrugated sheets*. Int. J. Heat Mass Tran. **53**(2010), 3166–3174.

[22] Wilk J.: *Experimental investigation of convective mass/heat transfer in short minichannel at low Reynolds numbers*. Exp. Therm. Fluid Sci. **33**(2009), 267–272.

[23] Wilk J.: *Convective mass/heat transfer in the entrance region of the short circular minichannel*. Exp. Therm. Fluid Sci. **38**(2012), 107–114.

[24] Sara O.N., Ergu Ő.B., Arzutug M.E., YapıcıS.: *Experimental study of laminar forced convective mass transfer and pressure drop in microtubes*. Int. J. Therm. Sci. **48**(2009), 1894–1900.

[25] Ergu Ő.B., Sara O.N., YapıcıS., Arzutug M.E.: *Pressure drop and point mass transfer in a rectangular microchannel*. Int. Commun. Heat Mass **36**(2009), 618–623.

[26] Acosta R.E., Mulle R.H., Tobiasz C.W.: *Transport processes in narrow (capillary) channels*. AIChE J. **31**(1985), 473-482.

[27] Beiki H., Esfahany M.N., Etesami N.: *Laminar forced convective mass transfer of $\gamma$-$Al_2O_3$/electrolyte nanofluid in a circular tube*. Int. J. Therm. Sci. **64**(2013), 251-256.

[28] Kiedrzyński K.: *Increasing of efficiency of the cooling duct by modification of its geometry*. Arch. Thermodyn. **41**(2020), 3, 103-123.

[29] Bieniasz B.: *The use of electrolysis and the analogy between heat and mass transfer in the design of forced convection heat exchanger elements*. WUPR, Rzeszów 1980 (in Polish).

[30] Martin H.: *The generalized Leveque equation and its practical use for the prediction of heat and mass transfer rates from pressure drop*. Chem. Eng. Sci. **57**(2002), 16, 3217–3223.

[31] Sash R.K.: *Laminar flow friction and forced convection heat transfer in ducts of arbitrary geometry*. Int. J. Heat and Mass Tran. **18**(1975), 849–862.

[32] Welty J., Wicks C., Wilson R., Rorrer G.: *Fundamentals of Momentum. Heat Mass Transfer*. Wiley, Oregon 2007.

[33] Chilton T.H., Colburn A.P.: *Mass transfer (absorption) coefficients prediction from data on heat transfer and fluid friction*. Ind. Eng. Chem. **26**(1934), 11, 1183–1187.

[34] Iwaniszyn M., Jaroszyński M., Ochońska J., Łojewska J., Kołodziej A.: *Heat and mass transfer analogy for the laminar flow: discussion of the problem*. Prace Naukowe IICh PAN **15**(2011), 37–46.

[35] Wilk J.: *Heat/mass transfer analogy in the case of convective fluid flow through minichannels*. Int. J. Therm. Sci. **156**(2020), 106467.

[36] Gnielinski V.: *On heat transfer in tubes*. Int. J. Heat Mass Tran. **63**(2013), 134–140.

[37] Gnielinski V.: *Heat transfer coefficients for turbulent flow in concentric annular ducts*. Heat Transfer Eng. **30**(2009), 6, 431–436.

[38] Gnielinski V.: *Turbulent heat transfer in annular spaces – a new comprehensive correlation*. Heat Transfer Eng. **36**(2015), 9, 787–789.

[39] Rybiński W., Mikielewicz J.: *Analytical solution of heat transfer for laminar flow in rectangular channels*. Arch. Thermodyn. **35**(2014), 4, 29–42.

[40] Wilk J.: *A review of measurement of the mass transfer in minichannels using the limiting current technique*. Exp. Therm. Fluid Sci. **57**(2014), 242–249.

[41] Hetsroni G., Mosyak A., Pogrebnyak E., Yarin L.P.: *Heat transfer in micro-channels: Comparison of experiments with theory and numerical results*. Int. J. Heat Mass Tran. **48**(2005), 25-26, 5580–5601.

[42] Celata G.P., Cumo, M., Marconi V., McPhail S.J., Zummo G.: *Microtube liquid single-phase heat transfer in laminar flow*. Int. J. Heat Mass Tran. **49**(2006), 19-20, 3538–3546.

[43] Kandlikar S.G., Garimella S., Li D., Colin S., King M.R.: *Heat Transfer and Fluid Flow in Minichannels and Microchannels*. Elsevier, Kidlington Oxford 2006.

**archives**
**of thermodynamics**
Vol. **44**(2023), No. 4, 447–461
DOI: 10.24425/ather.2023.149724

# Subatmospheric pool boiling of water at very low liquid levels

**TOMASZ HAŁON***
**DOMINIKA KACZMAREK**
**WIKTORIA LADA**
**BARTOSZ ZAJĄCZKOWSKI**

Wroclaw University of Science and Technology, Department of Thermal Sciences, Wybrzeże Wyspiańskiego 27, 50-370 Wroclaw, Poland

**Abstract** The paper discusses how the vapour bubbles growing during boiling under the near-triple point pressure influence the heat transfer coefficient when the refrigerant level is lower than the bubble departure diameter. The experiments were carried out for liquid levels of 0.57 to 1.89 cm, saturated pressure range between 0.9 and 4 kPa (saturation temperatures between 5.5 and 29°C). Boiling occurred on a plain surface with wall heat flux densities between 0.43 and 5.93 $\mathrm{Wcm}^{-2}$. We determined boiling curves for the low-pressure process and analyzed the changes in wall superheat for different filling levels. The experimentally obtained heat transfer coefficient (HTC) was compared with the theoretical values produced by the most popular mathematical expressions used at higher pressures. We also prepared the boiling map, where we specified two boiling regimes: the regime of convection or small popping bubbles and the regime of isolated bubbles. The results indicate that the level of liquid can be neglected within the heat flux range analyzed in this study. The main mechanism of heat transfer under measured conditions is heat convection and conduction, rather than evaporation. The experimentally determined difference between the heat transfer coefficients for different levels of liquid is under 100 $\mathrm{Wm}^{-2}\mathrm{K}^{-1}$ (for the same heat flux and pressure at the wall).

**Keywords:** Pool boiling; Subatmospheric boiling; Water; Boiling heat transfer

*Corresponding Author. Email: tomasz.halon@pwr.edu.pl

## Nomenclature

| | | |
|---|---|---|
| $A$ | – | area, $m^2$ |
| $c_p$ | – | specific heat, $Jkg^{-1}K^{-1}$ |
| $d$ | – | diameter, m |
| $H$ | – | height, m |
| $h$ | – | heat transfer coefficient, $Wm^{-2}K^{-1}$ |
| Ja | – | Jakob number |
| $Ja^*$ | – | modified Jakob number |
| $k$ | – | heat conductivity, $Wm^{-1}K^{-1}$ |
| $L_c$ | – | characteristic length, m |
| MAD | – | mean absolute deviation |
| $p$ | – | pressure, kPa |
| $Q$ | – | heat, J |
| $\dot{q}$ | – | heat flux, $Wcm^{-2}$ |
| $T$ | – | temperature, K |
| $V$ | – | volume, $m^3$ |

### Greek symbols

| | | |
|---|---|---|
| $\Delta$ | – | increment |
| $\Delta h$ | – | enthalpy difference, $Jkg^{-1}$ |
| $\Delta T$ | – | superheat, K |
| $\lambda$ | – | thermal conductivity, $Wm^{-1}K^{-1}$ |
| $\rho$ | – | density, $kgm^{-3}$ |

### Subscripts and superscripts

| | | |
|---|---|---|
| amb | – | ambient |
| app | – | applied value |
| crit | – | critical |
| $h$ | – | heater |
| $l$ | – | liquid |
| plate | – | heating plate |
| sat | – | saturation |
| $v$ | – | vapour |
| wall | – | wall |

# 1 Introduction

The refrigeration industry is gradually moving towards systems that have a more neutral impact on the environment. This shift is a response to international regulations that govern the maximum allowable global warming potential (GWP) of working fluids. The consequence is the resurgence of natural refrigerants, such as hydrocarbons, carbon dioxide, ammonia, and most importantly water. In terms of safety, water is an outlier in the group.

It is easy to dispose of and does not require additional safety measures during service. The main challenges arise from the fact that as a refrigerant it needs to evaporate at subatmospheric pressures, typically ranging from 1–4 kPa. Sikora and Bohdal highlighted the frequent use of low-pressure refrigerants, such as Novec 649 [1]. Under such conditions, its specific volume increases approximately 70 times, presenting significant difficulties for the design and operation of the evaporator [2]. For this reason, evaporators in chillers are often shell-and-tube or falling-film types [3, 4], which are characterised by a large internal volume and heat transfer surface. However, this also means a large thermal mass that decreases the efficiency of such devices [5].

Another crucial parameter that affects the heat transfer performance is the level of the liquid above the heating surface. Hydrostatic pressure becomes significant at very low operating pressures because it is of a similar magnitude as the saturated pressure. The result is an increase in the temperature of evaporation at the boiling surface and steep temperature and pressure gradients within the liquid volume. Various authors [6, 7] studied how the liquid level affects the nucleation, growth, and departure of the bubble under subatmospheric conditions, highlighting the difference between saturation temperatures at the top and bottom of the bubble. At a few kPa, the liquid level affects the wall temperature due to the cyclic flow of highly subcooled water to the nucleation site (the so-called return flow) [8].

Most studies have concentrated on liquid levels high enough to observe the growth and detachment of bubbles at low pressures (typically $> 10$ cm). This study builds on our previous research, in which we analysed higher liquid levels and superheat values (10 K or more) [9, 10]. In this paper, we examine the thermal effect of extremely low refrigerant levels, ranging from 0.57 to 1.89 cm. This research focuses on reduced heat flux density at lower liquid levels and its impact on producing lower superheats, which correspond to conditions found in both flooded evaporators and the bottom section of falling-film evaporators.

## 2 Setup and procedure

### 2.1 Experimental setup

The experimental test facility is constituted by a 7.7 cm inner diameter stainless-steel cylinder 3 mm thick, filled with distilled water (refrigerant), which is shown in Fig. 1. At the bottom of the cylinder, there is a brass disk

that is connected to an electric heating coil, which is the boiling surface. Its roughness was determined using a contact profilometer at five locations. The mean roughness is 0.0659 cm, mean roughness depth is equal to 4.675 and maximum roughness depth is 8.36. The profilometer length of travel and cut-off length are 0.175 cm and 0.025 cm, respectively.

The electrical power, which is supplied to the coil, is regulated with an autotransformer and measured with an analogue wattmeter (Class I). The evaporation pressure is maintained constant through the effect of the condenser, which is a copper coil. The brass plate that supports the condenser is the top cover of this cylinder. The subatmospheric pressure in the experimental system is obtained by means of a vacuum pump, and the vacuum level is measured with a pressure transducer of 0.1% full scale accuracy. K-type thermocouples connected to a recorder were used to measure temperature. 1 mm below the measured surface, there is a K-type (class I) thermocouple ($\pm 0.5$ K after calibration), which is used for wall temperature measurements. The temperature of the heating surface is calculated from the heat conduction equation assuming 1D heat flow and a constant wall material heat conductivity. Stable boiling conditions are obtained by insulating the cylinder with 2 cm thick polyethylene foam on the walls and 80 mm wool on the top and bottom covers.

## 2.2 Experimental procedure

In this experimental study, two liquid levels were tested, 1.89 and 0.57 cm, which correspond to volumes of 100 and 30 ml, respectively. In the tested experimental stand (shown in Fig. 1), it was easier to measure the volume of water and from it calculate the given height than to measure the height directly. During each series of experiments, the heat transfer surface was rubbed by a microfiber cloth with isopropyl alcohol and after that, the vessel was sealed at the atmospheric pressure. The next test stand was filled with the refrigerant. Low pressure conditions of 2 kPa absolute pressure were obtained by a vacuum pump. The refrigerant started to boil because its temperature was higher than the saturation temperature. After reaching the equilibrium conditions, the vessel was further evacuated to remove any non-condensable gases dissolved in water. Then, it was kept for 24 h for further degassing, after which it was again evacuated by the vacuum pump.

An autotransformer was used to set the heat fluxes (HF). The stabilization process of HF lasted 60 minutes, after which both the pressure inside the vessel and the temperature of the heating wall were recorded.

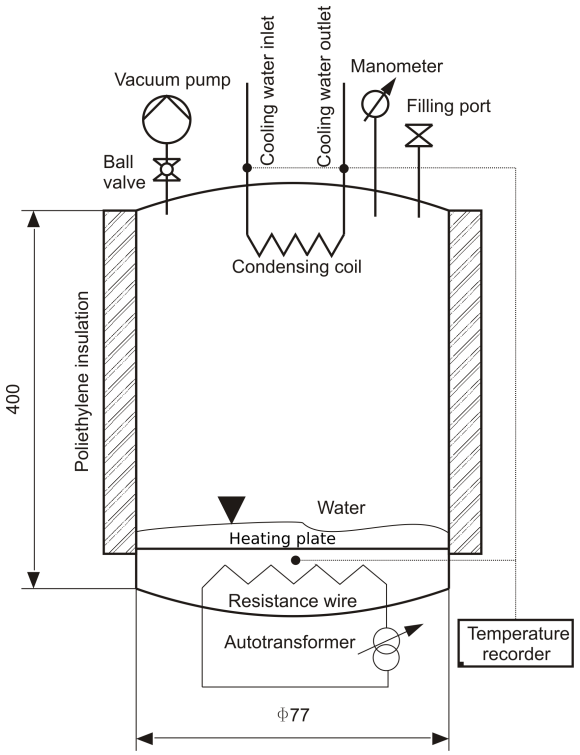


Figure 1: Experimental setup used for the analysis of pool boiling at different levels of refrigerant filling at subatmospheric pressures.

The heat transfer coefficient HTC was calculated using Newton's law of cooling:

$$q = \frac{Q}{A} = \mathrm{HTC}\,(T_{\mathrm{wall}} - T_{\mathrm{sat}})\,. \tag{1}$$

The vessels heat load was calculated from the heat balance – heat conduction through 3 mm stainless steel and 20 mm polyurethane foam. The ambient temperature was 19°C, while the temperature inside the vessel ranged from 6 to 27°C. The heat applied by the heating plate $Q_{\mathrm{plate}}$ was the heat from electric heater $Q_h$ reduced by the heat loss from the heater to the ambient air $Q_{\mathrm{amb}}$:

$$Q_{\mathrm{plate}} = Q_h - Q_{\mathrm{amb}}\,. \tag{2}$$

The CoolProp open-source thermodynamic properties library [11] was used to calculate the saturation temperature $T_{\mathrm{sat}}$ and other thermodynamic

properties of water. The finite differential method was used to calculate the uncertainty of the heat transfer coefficient measurement. The errors were in the range of 12 to 20% of the estimated HTC value. Experiments were conducted for nine different heat fluxes $\dot{q}$ (0.43, 0.64, 1.07, 1.5, 2.14, 2.58, 3.44, 4.3, and 5.93 $\mathrm{Wcm}^{-2}$) and for a pressure range of 0.9 to 4 kPa, which corresponds to saturation temperatures from 5.5°C to 29°C.

## 3 Results and discussion

The analysis is threefold. First, boiling curves ($\dot{q}(\Delta T)$ plots) were determined for water at pressures of 1.3 kPa and 2.55 kPa for two different liquid levels: 0.57 cm and 1.89 cm. Subsequently, the impact of water level on wall superheat was recorded as a function of time to determine its effect on transient behaviour throughout bubble nucleation. Lastly, the impact of filling level on the heat transfer coefficient as a function of pressure was analyzed. For clarity, the presented results always include the hydrostatic head: 56 Pa and 185 Pa for 0.57 cm and 1.89 cm, respectively.

### 3.1 Determination of the boiling curve

Figure 2 shows boiling curves for the analyzed refrigerant pressures and liquid levels compared to the already known Nukiyama curve, which was obtained at 1 bar [12]. Each measurement point in the graphs is an averaged value, which was acquired from 3 to 5 measurements.

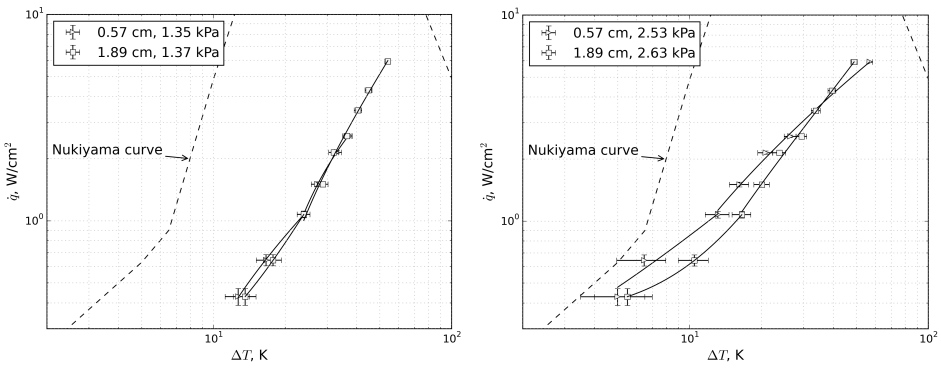


Figure 2: Boiling curves for two liquid levels 0.57 cm and 1.89 cm at two pressure levels: 1.35–1.37 kPa (left) and 2.53–2.63 kPa (right).

The refrigerant level affects boiling curves when the pressure increases from 1.3 to 2.5 kPa. For pressures of 1.3 kPa and with wall heat fluxes in the range of 0.43 $\mathrm{Wcm^{-2}}$ to 5.93 $\mathrm{Wcm^{-2}}$, this effect is negligible as in Fig. 2 (left side), but at higher pressures ($\sim$ 2.5 kPa), the impact of liquid level changes the wall superheat $\Delta T$ of the transition point, as in Fig. 2 (right side).

Particularly in the convective boiling region, where the liquid motion due to the bubble nucleation and departure does not occur, a lower liquid level means lower thermal resistance and, compared to work by Schnabel *et al.* [3], this behaviour is different because, in their work, the difference was observed in the nucleate boiling region. The mentioned authors found that regardless of the degree of superheat, more heat was transferred to the liquid at a higher refrigerant filling level. They also suggested that this behaviour was likely due to their test stand, where the circulation of secondary refrigerant in the spaces between the vessel wall and the heating sample affected the heat transfer. Our test stand was more compact, so the circulation of secondary refrigerant was hindered.

As the pressure decreases, the need for a higher superheat for nucleation increases, as shown in Fig. 2. The same phenomenon was also observed in the literature, [3, 10, 13–15]. For a pressure of 1.3 kPa, the beginning of nucleate boiling occurred at superheat $\Delta T = 20$ K, while for a pressure of 2.5 kPa at $\Delta T = 10.5$ K. For both pressures, the transition took place at the same heat flux of about 1 $\mathrm{Wcm^{-2}}$. It was also observed that the liquid level did not significantly affect superheat, as the peak difference in wall superheat for various refrigerant levels was 7%.

Giraud *et al.* [8] investigated the phenomenon of change in size of vapour bubbles, with decreasing subatmospheric pressure of water. They compared bubble growth before detachment and noted that as the pressure decreases, the bubble diameter increases up to a pressure of 1.8 kPa, below that point the diameter decreases again. Thus, it is possible for the experiments that the detachment bubble diameters for 1.3 kPa and 2.5 kPa are similar. This results in comparable wall superheat values at the highest heat fluxes for both 1.3 and 2.5 kPa pressures.

### 3.2 Wall superheat

The wall superheat is an indicator of the boiling regime. Its fluctuations indicate the presence of unsteady processes near the wall, such as bubble nucleation or fluid motion. Figure 3a. depicts the relation between the wall

superheat and time, which is crucial to estimate the total heat transfer during nucleate boiling. To mathematically model the heat transfer process during boiling, the frequencies of bubble departure and wall superheat were used.

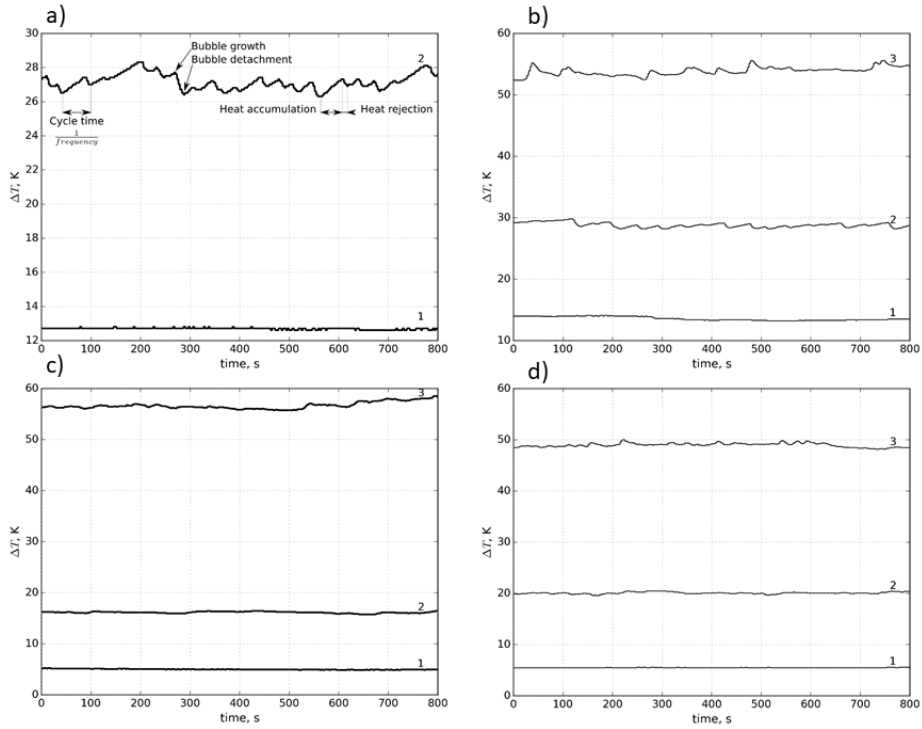


Figure 3: Wall superheat fluctuations for different heat transfer densities: 1 – 0.43 $\mathrm{Wcm^{-2}}$, 2 – 1.5 $\mathrm{Wcm^{-2}}$, 3 – 5.93 $\mathrm{Wcm^{-2;}}$; (a) $p = 1.3$ kPa and 0.57 cm filling, (b) $p = 1.3$ kPa and 1.89 cm filling, (c) $p = 2.5$ kPa and 0.57 cm filling, (d) $p = 2.5$ kPa and 1.89 cm filling.

The heat transfer rate is dependent on a bubble creation rate and departure time. The smaller the bubble creation rate and shorter the departure time (yielding high frequency), the higher the heat transfer rate. For the investigated values of pressures and liquid levels, the amplitude of fluctuations at the lowest heat fluxes remains almost the same, as it varies between 0.1 and 0.2 K, as can be seen in Fig. 3a–d. The reason for this is the low heat flux density, which induces only convective boiling. Higher heat fluxes result in higher amplitudes and frequencies of superheat fluctuations, while higher liquid levels reduce both the amplitude and frequency.

At 1.3 kPa, by increasing the liquid level from 0.57 to 1.89 cm, there was a 24% reduction in nucleation frequency and a 50% reduction in superheat amplitude. At 2.5 kPa superheat fluctuations were suppressed for both analyzed filling levels and all investigated heat flux densities. An increase in liquid level from 0.57 to 1.89 cm resulted in an increase in wall superheat from 16 to 20 K for 1.5 $\mathrm{Wcm^{-2}}$, but a decrease in wall superheat from 56–57 K to 49–50 K for 5.93 $\mathrm{Wcm^{-2}}$.

The small amplitude of wall superheat is due to the fact that the superheat was not sufficient for bubble departure, and thus at both pressures and a heat flux density of 1.5 $\mathrm{Wcm^{-2}}$, the bubbles condensed before reaching the critical diameter. This is analogous to the observations of Tang *et al.* [16] during subcooled boiling at the atmospheric pressure.

The wall superheat for heat fluxes 0.43 $\mathrm{Wcm^{-2}}$ and 1.5 $\mathrm{Wcm^{-2}}$ decreased by 59% and 41%, respectively, for a 0.57 cm refrigerant level, while increasing the pressure from 1.3 kPa to 2.5 kPa, but for a 1.89 cm refrigerant level, the wall superheat decreased by 57% for the heat flux density 0.43 $\mathrm{Wcm^{-2}}$, 33% for 1.5 $\mathrm{Wcm^{-2}}$ and 13% for 5.93 $\mathrm{Wcm^{-2}}$.

In all cases, the application of a heat flux higher than 1.5 $\mathrm{Wcm^{-2}}$ enhanced superheat fluctuations. The amplitudes observed in our work did not exceed 2 K, which is significantly below the 25 K observed by Giraud *et al.* [8] at a heat flux of 9.4 $\mathrm{Wcm^{-2}}$ and liquid level of 20 cm. It means that we did not reach the conditions for fully developed boiling.

### 3.3 Jakob number

To confirm that the main mechanism of heat transfer under the measured conditions is not evaporation but convection and heat conduction, the Jakob number was evaluated. The considered mechanisms coincide with the literature data presented by [8].

The Jakob number is a dimensionless determinant of phase heat transfer. It determines the ratio of the sensible to latent heat [7]:

$$\mathrm{Ja} = \frac{\rho_l}{\rho_v} \frac{c_{p(l)} \Delta T_{\mathrm{wall}}}{\Delta h_{lv}} \,. \tag{3}$$

The Jakob number takes the ratio of liquid density to vapour density into account, but under the tested conditions the density of the gas is so small that the aforementioned density ratio would affect the result too much, so it was decided to use a modified Jakob number. It was further modified by

Eq. (4), so as to easily calculate it with the applied heat flux instead of wall superheat [7]:

$$\Delta T \sim \frac{q_{\text{app}} L_c}{\lambda_l} \,. \tag{4}$$

The outcome is the modified Jakob number Ja*:

$$\text{Ja}^* = \frac{c_{p(l)} L_C q_{\text{app}}}{\Delta h_{lv} \lambda_l} \,. \tag{5}$$

### 3.4 Boiling region map

Figure 4 shows a dimensionless map of boiling regimes, where the values of the modified Jakob number are summarized on the Y axis, and the ratio of vapour pressure to static pressure on the X axis. Dots represent the experimental values we obtained: convection or small popping bubbles and isolated bubble region. As observed by Wojtasik *et al.* [7], by increasing the applied heat flux, first the convection regime and small popping bubbles will appear, and then single non-interacting vapour bubbles can be seen [7].

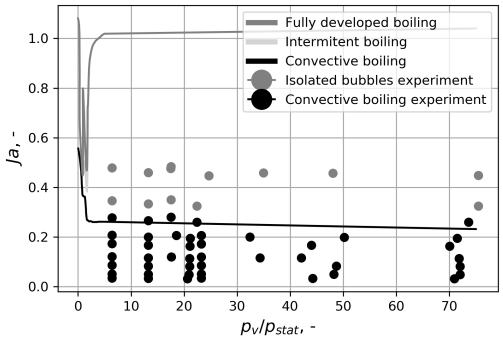


Figure 4: Dimensionless boiling map for subatmospheric pressure (dots) compared with literature data (lines) [7].

The graphs gathered in Fig. 5, showing the dependence of HTC on a given pressure, were used to classify our experimental results. If the data obtained in a given experimental series corresponded to an area of convection (from Fig. 5), they were assigned to the same regime in our dimensionless map (Fig. 4). Received values in our experimental conditions could not be assigned to intermittent boiling or fully developed boiling. Obtaining developed boiling would have occurred at a higher modified Jakob number, i.e. when applying higher heat fluxes.

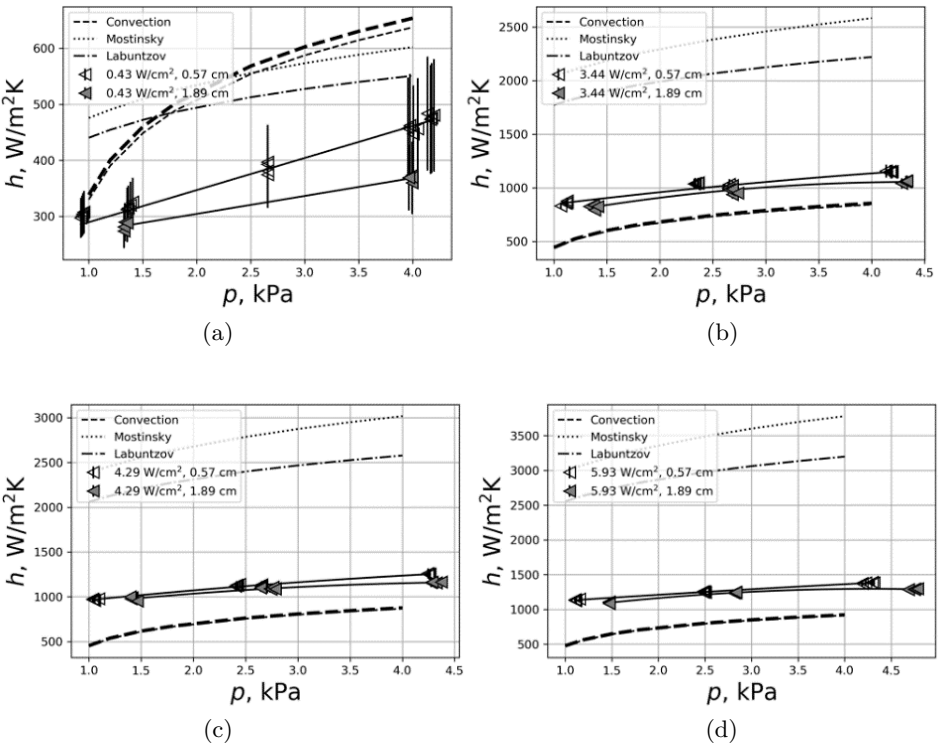


Figure 5: Heat transfer coefficient $h$ as a function of pressure and liquid levels. Heat flux: (a) 0.43 $\mathrm{Wcm}^{-2}$, (b) 3.44 $\mathrm{Wcm}^{-2}$, (c) 4.3 $\mathrm{Wcm}^{-2}$, (d) 5.93 $\mathrm{Wcm}^{-2}$.

The effect of the ratio of vapour pressure to hydrostatic pressure was studied in the $p_v/p_{\mathrm{stat}} > 1$ area. When the vapour pressure is greater than the hydrostatic pressure at low heat fluxes (low modified Jakob number), the occurrence of isolated bubble regimes is achieved more quickly. The higher the hydrostatic pressure (higher liquid level), the greater the subcooling.

The boundary line of interest is the purple line in Fig. 4, corresponding to the modified Jakob number at around 0.3. As the vapour pressure increases, the boundary value of the modified Jakob number, which separates the two regimes observed in the experiment, decreases.

For values around $\mathrm{Ja}^* < 0.3$, the dominance of large regions of convection or small popping bubbles is visible, due to a too small applied heat flux. For $\mathrm{Ja}^* > 0.3$, the isolated bubble regime dominates. The regions can be confirmed by the wall temperature fluctuations from Fig. 3.

### 3.5 Heat transfer coefficient

Figure 5 shows the correlation of the heat transfer coefficient with the pressure and refrigerant level. The pressure presented on the x-axis is the total pressure near the heating wall, which is calculated as a sum of pressure at the vapour-liquid interface and hydrostatic pressure. The difference for liquid levels is less than 100 $\mathrm{Wm^{-2}}$, which translates into an up to 10% increase in favour of lower liquid level.

The analysis considers studies for four heat fluxes with values of 0.43, 3.44, 4.3 and 5.93 $\mathrm{Wcm^{-2}}$. The HTC is increasing with pressure at a rate of about 200 $\mathrm{W{\cdot}m^{-2}K^{-1}}$ per 1 kPa. When the heat flux density increases from 0.43 $\mathrm{Wcm^{-2}}$ to 5.93 $\mathrm{Wcm^{-2}}$ (at about 1 kPa), the heat transfer coefficient also increases from 250 to 1150 $\mathrm{Wm^{-2}K^{-1}}$. A change in pressure to 4 kPa also results in an increase in the heat transfer coefficient to values in the range of 350 to 1400 $\mathrm{Wm^{-2}K^{-1}}$ for heat fluxes of 0.43 $\mathrm{Wcm^{-2}}$ and 5.93 $\mathrm{Wcm^{-2}}$.

Zajączkowski *et al.* [10] in their article compared sixteen correlations for pool boiling, which are available in the literature. For a subatmospheric pressure, the most accurate approximation of the heat transfer coefficient was obtained using the Mostinski correlation with a reduced pressure and the Labunstov correlation. These formulas were also used in this work.

The Mostinski formula and the Labuntsov correlation both consider the heat flux density, as in Eq. (6) and (8), respectively:

$$h = 0.00417 q^{0.7} p_{\mathrm{crit}}^{0.69} F, \tag{6}$$

where

$$F = 1.8 \left(\frac{p}{p_{\mathrm{crit}}}\right)^{0.17} + 4 \left(\frac{p}{p_{\mathrm{crit}}}\right)^{1.2} + 10 \left(\frac{p}{p_{\mathrm{crit}}}\right) \tag{7}$$

and

$$h = 0.75 \left[1 + 10 \left(\frac{\rho_v}{\rho_l - \rho_v}\right)^{0.67}\right] \left[\frac{k_l^2}{v\sigma(T_{\mathrm{sat}})}\right]^{0.33} q^{0.67}. \tag{8}$$

Based on our previous studies of Zajaczkowski *et al.* [10], in dependence of the heat flux, their mean absolute deviation (MAD) ranged from 0.1 to 0.89 for the Labuntsov correlation and from 0.13 to 0.35 for the Mostinsky correlation. For the results examined now, also in dependence of the heat flux, MAD is from 0.36 to 1.38 for the Labuntsov correlation, and from 0.31 to 1.42 for the Mostinsky correlation. Figure 5 presents both the

above-mentioned correlations. The results obtained from our theoretical and experimental investigations have a greater discrepancy. This is most likely because both correlations were designed for fully developed boiling, which we did not obtain in this study. Instead, for the conditions of convective boiling, the heat transfer coefficient $h$ could be calculated from the natural convection formula. For higher heat fluxes, when we reached the isolated region regime, $h$ was between the calculated values of convection and boiling.

Chang *et al.* [17], in their work, experimentally investigated the thermal performance of a two loop thermosyphon in subatmospheric conditions. The working fluid was water in underpressure. This research resulted in three heat transfer correlations by which the heat transfer coefficient over pool boiling, intermittent and vapour regions of the evaporator could be calculated. The pool boiling region was described by Eq. (9):

$$h = \left(1.951 \cdot 10^6 q^{-0.26}\right) P^{(0.508-5.91\cdot 10^{-6} q)}, \tag{9}$$

where $P^*$ means the dimensionless evaporator pressure, which is a ratio of the evaporation pressure to critical pressure.

This correlation did not work for our experimental data and those calculated by other formulas: the heat transfer coefficient values turned out on average 10 times higher than our values. The reason is that the formula was highly empirical and was proposed for a highly confined evaporator with heating at one of the horizontal walls, much like in plate heat exchangers. This type of heat exchanger is more similar to the one investigated by Sène *et al.* [2]. Sène *et al.* proposed a semi-empirical pool boiling model for confined evaporators, but their formula also is not applicable in our experiments, as it uses the confining thickness parameter, which does not occur in non-confined boiling.

## 4 Conclusions

In this study, the effect of the refrigerant filling level (0.57–1.89 cm) on the pool boiling heat transfer coefficient $h$ and wall superheat was experimentally explored. Experiments were performed for pressures ranging from 1 to 4 kPa and for heat flux densities ranging from 0.43 to 5.93 $\mathrm{Wcm}^{-2}$. The results show that under the selected conditions, the impact of liquid level on $h$ is insignificant because an increase of up to 10% for a lower liquid level

was observed, while the measurement error was calculated to be about 12–20%. It was also reported that the difference in the heat transfer coefficient under the same heat flux and pressure conditions near the wall but for different liquid levels is usually less than 100 $\mathrm{Wm^{-2}K^{-1}}$. The heat transfer coefficient increase with pressure is about 200 $\mathrm{Wm^{-2}K^{-1}}$ per 1 kPa.

For the lowest measured heat flux, the superheat is generally greater than 10 K under examined conditions, which is the biggest drawback of flooded evaporators.

The paper also highlights the dependence of wall superheat fluctuations on boiling dynamics. In the conditions we studied, small fluctuations were observed, as they were caused by nucleation and the fluid motion that result from boiling.

The mechanism of boiling at subatmospheric pressure looks different from that at the atmospheric pressure. With different liquid levels, the difference in heat transfer is noticeable only in the region of convective boiling, while its shift to nucleation boiling is moved toward a higher wall superheat. Because as the liquid height increases, the pressure at the wall also increases, lower filling levels are advisable for water under a subatmospheric pressure.

Under the given conditions, the dominant mechanisms of heat transfer are both heat convection and conduction, instead of evaporation. For values of $\mathrm{Ja}^* < 0.3$, the dominance of convection or small popping bubbles is visible, due to low applied heat flux. For $\mathrm{Ja}^* > 0.3$, the isolated bubble regime dominates. We did not reach other boiling regimes in this study.

*Received 13 April 2023*

## References

[1] Sikora M., Bohdal T.: *New environmentally friendly low-pressurere refrigerants mini-channel.* Arch. Thermodyn. **44(**2023), 1, 89–104.

[2] Sène P., Giraud F., Sow M.L., Tréméac B.: *Heat transfer coefficient correlations of water subatmospheric vaporization in a channel of a smooth plate heat exchanger, based on Vaschy-Buckingham theorem.* Appl. Therm. Eng. **213** (2022), 1–17.

[3] Schnabel L., Scherr C., Webe, C.: *Water as refrigerant- experimental evaluation of boiling characteristics at low temperatures and pressures.* In: Proc.VII Minsk Int. Sem. Heat Pipes, Heat Pumps, Refrigerators, Power Sources, Minsk 2008, 322–330.

[4] Schultz K.: *Configured Surface Tubes for Evaporation of Water.* In: Proc. Int. Sorption Heat Pump Conf. Broomfield, 2005, 271–279.

[5] Herold K.E., Radermacher R., Klein S.A.: *Absorption Chillers and Heat Pumps*. CRC, Boca Raton 1996.

[6] Michaie S., Rullière R., Bonjour J.: *Towards a more generalized understanding of pool boiling at low pressure: Bubble dynamics for two fluids in states of thermodynamic similarity*. Exp. Therm. Fluid. Sci. **101**(2019), 217–230.

[7] Wojtasik K., Rullière R., Krolicki Z., Zajaczkowski B., Bonjour J.: *Subcooled boiling regime map for water at low saturation temperature and subatmospheric pressure*. Exp. Therm. Fluid. Sci. **118**(2020), 1–11.

[8] Giraud F., Rullière R., Toublanc C., Clausse M., Bonjour J.: *Experimental evidence of a new regime for boiling of water at subatmospheric pressure*. Exp. Therm. Fluid. Sci. **60**(2015), 45–53.

[9] Hałon T., Zajączkowski B., Królicki Z., Wojtasik K.: *Calculation and experimental verification of heat transfer coefficient for low pressure methanol evaporator*. In: Proc. 24th Int. Cong. of Refrigeration, Yokohama, August 16-22, 2015, 1–8.

[10] Zajaczkowski B., Halon T., Krolicki Z.: *Experimental verification of heat transfer coefficient for nucleate boiling at sub-atmospheric pressure and small heat fluxes*. Heat Mass Transfer **52**(2016), 205215.

[11] Bell I.H., Wronski J., Quoilin S., Lemort V.: *Pure and pseudo-pure fluid thermophysical property evaluation and the open-source thermophysical property library coolprop*. Ind. Eng. Chem. Res. **53**(2014), 6, 2498–2508.

[12] Thome J.R.: *Boiling*. In: Heat Transfer Handbook Handbook (A. Bejan, A.D. Kraus, Eds.), Wiley Hoboken 2003, 635–717.

[13] Giraud F., Rullière R., Toublanc C., Clausse M., Bonjour J.: *Preliminary experimental investigation on water boiling phenomena in a liquid layer at subatmospheric pressure*. In: Proc. 24th Int. Cong. of Refrigeration (ICR 2015), Yokohama, 2015.

[14] Shen B., Mine T., Iwata N., Hidaka S., Takahashi K., Takata Y.: *Deterioration of boiling heat transfer on biphilic surfaces under very low pressure*s. Exp. Therm. Fluid Sci. **113**(2020), 110026.

[15] Zimmermann M., Heinz M., Sielaff A., Gambaryan-Roisman T., Stephan P.: *Influence of system pressure on pool boiling regimes on a microstructured surface compared to a smooth surface*. Exp Heat Transfer **33**(2019), 4, 318–334.

[16] Tang J., Zhu G., Sun L.: *Microbubble emission boiling in subcooled pool boiling and the role of Marangoni convection in its formation*. Exp. Therm. Fluid Sci. **50**(2013), 97–106.

[17] Chang S., Lo D., Chiang K., Lin C.: *Sub-atmospheric boiling heat transfer and thermal performance of two-phase loop thermosyphon*. Exp. Therm. Fluid Sci. **39**(2012), 134–147.

**archives**
**of thermodynamics**
Vol. **44**(2023), No. 4, 463–482
DOI: 10.24425/ather.2023.149729

# Experimental investigation of limit parameters of direct contact condensation in the heat exchanger for waste heat recovery

**IRYNA NAZAROVA***
**ARTUR GUTKOWSKI**

Lodz University of Technology, Institute of Turbomachinery,
Wolczanska 217/221, 93-005 Lodz, Poland

**Abstract** In the present study, a suitable composition of parameters has been obtained to provide an efficient process of cooling flue gas with complete condensation of water vapour from air-water vapour mixture on a water film in co-current upward flow in the tube of the direct contact heat and mass exchanger. The results showed that the value of the irrigation density depends on the velocity of the air-water vapour mixture and the initial vapour content and should be calculated from an empirical equation. The active pipe height depends on the velocity of the air-water vapour mixture and the initial vapour content and should also be calculated from an empirical equation. For example, if the initial vapour content of the air-water vapour mixture is 11%, the velocity of the mixture is 20.8 m/s the height of the channel should not exceed 0.460 m. The value of the water heating limit temperature increases from 46°C to 62°C with a change in the initial vapour content from 11% to 30%. The present experimental results could be helpful in the design of direct contact heat and mass exchangers for waste heat recovery.

**Keywords:** Direct contact heat mass exchanger; Direct contact condensation; Process of cooling flue gas; Air-water vapour mixture

*Corresponding Author. Email: iryna.nazarova@p.lodz.pl

### Nomenclature

| | | |
|---|---|---|
| $c_p$ | – | specific heat, kJ/kg K |
| $d$ | – | diameter, m |
| $D_i$ | – | irrigation density, $m^2/s$ |
| $\dot{m}$ | – | mass flow rate, kg/s |
| $h$ | – | enthalpy, kJ/kg |
| $H$ | – | height of the test section, m |
| $p_{par}$ | – | partial pressure of water vapour, Pa |
| $Q$ | – | heat rate, W |
| Re | – | Reynolds number |
| $T$ | – | temperature, °C |
| $V$ | – | volume flow rate, $m^3/s$ |
| $W$ | – | average velocity, m/s |

#### Greek symbols

| | | |
|---|---|---|
| $\varphi$ | – | initial volume vapour content, % |
| $\omega$ | – | humidity ratio, kg water vapour/kg dry air |

#### Subscripts and superscripts

| | | |
|---|---|---|
| cond | – | condensation |
| dr | – | droplet removal |
| in | – | tube inlet |
| lim | – | limiting value |
| $m$ | – | air-water vapour mixture |
| min | – | minimum value |
| out | – | tube outlet |
| $v$ | – | water vapour |
| $w$ | – | water liquid |

#### Acronyms

| | | |
|---|---|---|
| DCHME | – | direct contact heat mass exchanger |
| AWVM | – | air-water vapour mixture |

## 1 Introduction

The recovery of a portion of the energy in hot stack gases has been practiced for many years. Recently, because of environmental reasons, the use of natural gas in boilers has become more common. As this clean fuel, compared to other fuels, containes more hydrogen than carbon, there is more water vapour in the exhaust flue gas accompanied by latent heat [1].

Natural gas-fired boilers have gradually dominated the process heating sector due to their high thermal efficiency, relatively low emissions, and

convenient fuel delivery system [2]. Nowadays, we are facing a deep natural gas crisis. This year's winter gas season begins with extreme natural gas price levels, with the market tightness expected to continue well into 2026 [3]. When the cost of gas, which is now the most common fuel for industry, reducing heat losses with flue gases can be the most significant energy saving way and the main task. So, the recovery of the latent heat from flue gas to increase the thermal efficiency is very important for natural gas-fired boilers [1, 4]. The products of natural gas combustion contain a sufficiently large amount of water vapour, on the formation of which consumes part of the heat from combustion of fuel. The amount of latent heat loss of the exhaust flue gas from gas-fired boilers is very high. If we recover sensible and latent heats at the same time, the overall energy efficiency can be increased about 10–20% [4, 5].

The thermal efficiency of a gas boiler is mainly influenced by the flue gas temperature. The higher the flue gas temperature, the lower the thermal efficiency. When the flue gas temperature drops from 200°C to 60°C, only sensible heat is recovered and of the thermal efficiency increases slowly. However, if the flue gas is cooled to the dew point, which is around 55°C, the water vapour will start to condense, causing a sharp increase in thermal efficiency. Therefore, cooling the flue gas below the dew point is important for heat recovery [6].

Effective waste heat recovery of flue gases of boilers that uses the heat of condensation of water vapour, can be carried out by direct contact heat exchangers. Boilers can generally lose 20% of the combustion energy in the flue gas, and thanks to flue gas condensers, they can recover 50% of this lost energy depending to the operating conditions.

In direct contact heat exchangers it is possible to cool gases to a temperature below the dew point temperature because cooling the gases by direct contact coolant allows the use of the heat condensation component of the gases.

A direct contact heat exchanger has several advantages over surface heat exchangers such as the elimination of a metallic heat transfer surface between the fluids, which is prone to corrosion and fouling, and the reduction of heat transfer resistance. It can be operated at very low temperature differences or heat transfer driving forces and allows a high heat transfer coefficient (about 20–100 times higher than single-phase or surface type heat exchangers [7]).

In such apparatuses, the heat transfer from the exhausted combustion gases to the heated liquid takes place in direct contact with the coolants,

which significantly improves the conditions for heat and mass transfer and allows nitrogen oxide ($NO_x$) emissions to be reduced. A significant reduction of harmful emissions occurs due to the scrubbing action of the heat exchanger as they are absorbed by the water [8].

These heat exchangers are also called a direct contact heat mass exchangers (DCHME) and it typically have gas and water as the two fluid streams. The transfer processes in such apparatuses occur under the contact between the liquid phase and the gas phase at the interphase surface. Depending on the method of interaction of the contacting phases, the most commonly used designs of heat exchangers are the following types: film, drop, bubble type DCHME [7]. In these types of heat exchangers, the principle of countercurrent movement of heat coolants is applied. The water flows from the top and the gas flows from the bottom. The advantage of the countercurrent flow is that the minimum temperature of the gases at the apparatus outlet is achieved, as the outgoing gases meet the coldest water. The water can be heated to a higher temperature due to a higher average temperature difference. However, the flow rate in DCHME of gas and liquid that moving in countercurrentl is limited by the flooding phenomenon. This phenomenon is characterized by the loss of flow stability and the entrainment of water from the DCHME under the action of a gas flow.

It is necessary to know the parameters that provide an efficient process for cooling gases with complete condensation of water vapour on a liquid film. The process of heat and mass transfer during the contact of gases and water is complex and depends on many factors. In some cases, at certain ratios of the parameters of a two-phase system of wet flue gases and water, the mode of condensation of water vapour can be reversed to the evaporation of water from the surface of the film, leading to a sharp decrease in the efficiency of the DCHME. Unfortunately, it was not possible to find any papers or studies on this issue.

However, the research has been divided into three lines. The first group of papers is devoted to new technologies for waste heat recovery and the efficiency of heat recovery. The technologies involving the use of direct contact heat exchangers for flue gas heat recovery have been extensively studied in the references [4, 9–14]. For example, papers [9–11, 14] present a boiler waste heat recovery technology based on heat pumps and the direct contact total heat exchangers. These technologies can improve the heat capacity of gas boilers by nearly 8–14%. These studies have focused on system performance and not on the heat and mass transfer characteristics during the direct condensation of water vapour from flue gases.

Analytical and experimental solutions of the heat and mass transfer process in different types of direct contact heat exchangers for flue gas heat recovery have been described in the second group [15–22]. In all these studies, however, the principles of countercurrent movement of heat coolants are applied. Men, Liu and Zhang [15] note that when a gas-water spray tower in a waste heat recovery system is optimized, the maximum heat recovery efficiency and the maximum heat transfer rate are achieved. Optimising a heat exchanger means determining the parameters at which the cooling of gases will be the most effective. The optimum spray water flow rate corresponding to the minimum thermal resistance [15], spray nozzle height and type (hollow and full cone), droplet diameter distribution, inlet air velocity and humidity, and water spray velocity are key parameters required to establish a clear understanding of the direct heat exchange performance in spray type heat exchangers [16].

Third group of papers are about heat and mass transfer between gas and liquid two-phase flows in pipes [20, 23–27]. Heat transfer and phase change processes of water droplets in humid airflow were investigated by performing experiments and numerical simulations of heat recovery from biofuel exhaust gas at 40–250°C, which is characteristic for condensing heat exchangers [20]. Dong, Qi and Zhang [24] developed a mechanistic model of flow and heat transfer for upward two-phase slug flow in vertical pipes. The authors found an improvement in heat transfer in two-phase slug flow compared to single-phase flow. This can be attributed to an increase in the turbulence of the liquid due to the injection of air and a reduction in the thickness of the thermal boundary layer due to the frequent alternation between liquid slug and the Taylor bubble. Jia and Dong [25] formulated a mathematical model for flow and heat transfer in two-phase annular flows, which based on the two-fluid concept. The effect of the orientations and flow parameters on the heat transfer was comprehensively investigated. The dependence of the two-phase heat transfer coefficients on the void fractions and pressure multipliers was quantitatively identified and a simple heat transfer correlation was developed. Bhagwat and Ghajar [26] analysed experimental data for void fraction, pressure drop and heat transfer coefficient for their dependence on phase flow rates and pipe inclination. The experiments were carried out in 0.0127 m internal diameter polycarbonate and 0.0125 m stainless steel pipes using air-water as the fluid combination. The results show that increasing the pipe inclination from the horizontal significantly affects the void fraction, total pressure drop and heat transfer coefficient at low values of gas and liq-

uid flow rates. As the gas and liquid flow rates increase, the effect of pipe inclination on the two phase flow variables is observed to diminish. Dong and Hibiki [27] developed a robust correlation of the heat transfer coefficient for two-component two-phase slug flows in vertical pipes. This correlation can predict the heat transfer coefficient under various conditions such as vertical upward and downward flows, developing and fully developed flows, laminar and turbulent flows, and all two-phase flow regimes. In summary, the interaction processes of different flows under different conditions have been studied. However, the question of studying the process of direct contact condensation in co-current upward flow flue gases and water in the DCHME tube has not been investigated and remains open.

It is necessary to know the parameters that provide an efficient process of cooling gases with complete condensation of water vapour on a liquid film, because the process of heat and mass transfer during the contact of gases and water is complex and depends on many factors.

In this paper, measurements of the outlet temperature of the air-vapour mixture and the outlet temperature of the water along the single vertical tube of DCHME were caried out. The experiments were conducted under the conditions of co-current upward flow of air-vapour mixture and water. The effect of flue gas velocity, irrigation density, humidity ratio of the flue gas on limiting temperature of water heating and the active height of the tube were examined. It was also necessary to experimentally determine the value of limit temperature for water heating in direct contact with the upward co-current flow of the air-water vapour mixture (AWVM).

The main aim of the present study was to find an adequate composition of parameters assuring maximum efficiency of cooling flue gas with complete condensation of water vapour on a water film in DCHME with co-current upward flow. The basic design of the DCHME is shown in [28].

Based on an extensive literature review in the field of the already existing studies on direct contact condensation in the heat exchangers for waste heat recovery it was found that there are currently no scientific studies that specifically investigating the process of direct condensation specifically in the ascending co-movement of gases and water. Furthermore, there are no recommendations for the practical application of such a flow configuration in heat exchangers. We assume that the processes of heat and mass transfer in a co-current upward flow of gas and liquid are effective. It will also be easy to regulate the flow rate of gas and heated liquid in a wide range with a constant metal consumption of the DCHME. We expect that this will make

it possible to design more efficient DCHME compared to the countercurrent heat exchangers considered above. The equations proposed in this paper can be used for engineering calculations of such heat exchangers.

## 2 Method

To solve the problems formulated above, experimental methods were used to study the heat and mass exchange processes during the condensation of water vapour from a flue gas with an accompanying upward movement with a water film. During the experiments, the wet flue gas was modelled as an air-water vapour mixture. Under laboratory conditions at the university, it is not always possible to use the combustion products of natural gas directly due to several reasons related to safety. However, in conducting such research, moist air can be used with a sufficient degree of adequacy [28]. Natural gas contains mainly methane. The combustion process is described by the formula: $CH_4 + 2O_2 = CO_2 + 2H_2O$. Oxygen is taken from the blast air, while the remaining nitrogen passes through the combustion chamber without undergoing any reaction. The amount of water vapour is determined by the composition of the fuel burnt, its humidity, and the air excess coefficient. The moisture content of the flue gases is 0.15–0.108 $kg/kg_{d.g}$, depending on the air excess coefficient ($\alpha = 1-1.4$) [29]. Thus, the composition of the combustion products of natural gas differs from that of moistened air by the replacement of oxygen by carbon dioxide, which does not affect the study of the condensation process of water vapour. A multitude of research and experiments in the field of flue gas analysis are conducted using a mixture of air and water vapour, making it a standard and reliable choice for modelling. When switching to flue gases, it is only necessary to recalculate their moisture content, which can be computed according to the ratio derived in [30].

The study was carried out in a specially constructed test facility. Figure 1 shows the diagramt of the installation, which consists of the test section, the systems for supplying liquid water, air and water vapour, and the measuring systems. The test facility was thermally insulated to prevent heat loss to the environment.

Test section (2) is a vertical cylindrical DCHE pipe of made of stainless steel with an internal diameter of 0.017 m and different heights (from 0.2 m to 1.404 m). The object of the research was an upward two-phase flow, consisting of the air-water vapour mixture flow and the water flow.

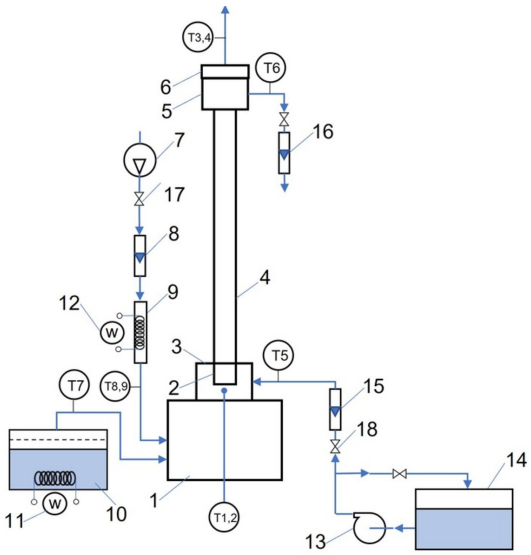


Figure 1: Schematic diagram of experimental installation: 1 – chamber for mixing air and water vapour; 2 – porous insert; 3 – water inlet chamber; 4 – test pipe; 5 – hot water collection chamber; 6 – separator; 7 – compressor; 8, 15, 16 – rotameters; 9 – electric heater; 10 – steam generator; 11, 12 – watt-meters; 13 – pump; 17, 18 – valves; T1–T9 – thermocouples.

The AWVM was produced by mixing air from a compressor (3) with a flow of water vapour produced by a special vapour generator (10) and supplied to the test section through the mixing chamber (1). The required amount of water vapour in the AWVM was provided by regulating the flow of the vapour and air. The upward two-phase flow was created by the flow of an AWVM and water, which was introduced into the working channel through the porous insert (2) and drawn into the upward flow in the form of a film due to the action of the AWVM.

The air was supplied to the unit from the compressor (3) through the rotameter (4). The air flow was regulated by a valve (17). An electric heater (5) was used to heat the air. The power supplied to the electric heater was regulated and controlled by voltage regulators and a wattmeter (12). The heated air was supplied into the mixing chamber (1), the walls of which were thermally insulated. The preheated mixing chamber (1) also received water vapour from the vapour generator (10). In order to prevent carry-over of droplet moisture from the steam generator a separator was installed in its vapour volume. The separator was made in the form of a perforated

sheet with a baffle plate. The vapour flow was regulated by changing the voltage applied to the electric heaters of the steam generator. The heating power was controlled by a wattmeter (11). The air and water vapour were mixed in chamber 1. The formed AWVM entered the test pipe (2).

Cold water was supplied from the water tank by pump (13) through valve (18) into the water inlet camber (3). The water flow was monitored by the rotameter (15). The liquid was injected into the test pipe through the porous insert (2). After passing through the working channel, the water was separated from the air by the separator (6) and fell by gravity into the hot water collection chamber (5), from where it was drained. The water flow rate at the outlet of the unit was measured using the rotameter (16).

The air temperature upstream of the compressor was measured with dry (T8) and wet (T9) thermocouples. The temperature of the AWVM at the inlet to the working channel was measured with dry and wet chromel-copel thermocouples (T1) and (T2), and at the outlet – with dry and wet thermocouples (T3) and (T4). The water temperatures at the inlet and outlet of the working channel were measured with thermocouples (T5) and (T6). The thermocouple readings were recorded using a digital device.

The intensity of the heat and mass transfer processes was calculated from the measured values of the initial and final temperatures and the flow rates of the refrigerants using known methods. The thermodynamic properties of water and humid air were determined using the CoolProp library [31]. In this case $\omega_{m,\text{in}}$, $\omega_{m,\text{out}}$, $p_{\text{par,in}}$, $p_{\text{par,out}}$, $h_{\text{par},w}$ were determined from the values of atmospheric pressure, dry and wet bulb temperatures.

The flow organization and the range of flow parameters of the phases mainly provided film flow regimes with the movement of the water film on the inner walls of the channel.

Before the experiments a series of set-up experiments were carried out. The design of the experimental set-up allowed some parameters to be varied independently while keeping others constant, which is very important when studying heat and mass transfer processes during condensation of water vapour from an AWVM on a liquid film. Table 1 lists the equipment used in the experimental rig along with their respective measurement errors.

The experimental data were processed by drawing up an energy balance shown in Table 2 and in Fig. 2(a).

The condensate mass flow rate was calculated as

$$\dot{m}_{\text{cond}} = (\omega_{m,\text{in}} - \omega_{m,\text{out}})\dot{m}_{m,\text{dry}}$$

Table 1: List of the elements used in the test rig with measurement accuracy.

| Element | Type | Operating rate | Measurement uncertainty |
|---|---|---|---|
| Thermocouple | TCC-1172 | 0–500°C | ±0.2°C |
| Barometer | – | 97.8–100.8 kPa | ±0.05 kPa |
| Water flow rotameter | RS-3 | 0.063 $m^3h^{-1}$ | ±2.5% |
| Air flow rotameter | RS-5 | 16 $m^3h^{-1}$ | ±2.5% |
| Air flow rotameter | RS-7 | 25 $m^3h^{-1}$ | ±2.5% |
| Wattmeter | D50162 | 1.5 kW | ±2% |
| Digital device | A565 | 0–5 mA | ±0.15% |
| Voltage regulator | RNO-250-10 | 0–250 V | – |

and a water mass balance (Fig. 2(b)) is

$$\dot{m}_{w,\mathrm{in}} = \dot{m}_{w,\mathrm{out}} + \dot{m}_{w,\mathrm{dr}} - \dot{m}_{\mathrm{cond}} \,.$$

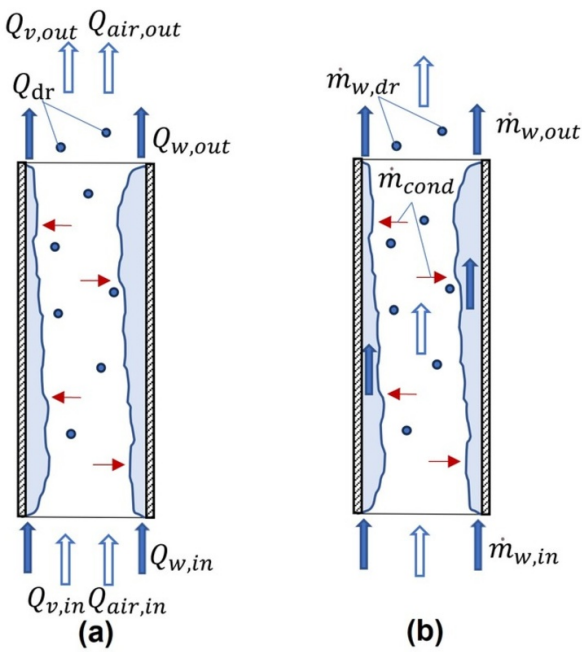


Figure 2: (a) Energy balance. (b) Water mass balance.

Table 2: Energy balance.

| $Q_{\text{air,in}} + Q_{v,\text{in}} + Q_{w,\text{in}} = Q_{\text{air,out}} + Q_{v,\text{out}} + Q_{w,\text{out}} + Q_{\text{dr}}$ | | |
|---|---|---|
| $Q_{\text{air,in}}$ | $\dot{m}_{\text{air,in}}\, h_{\text{air,in}}$ | Inlet air heat rate |
| $Q_{v,\text{in}}$ | $\dot{m}_{w,\text{in}}\, h_{w,\text{in}}$ | Inlet water vapour heat rate |
| $Q_{w,\text{in}}$ | $Q_{w,\text{in}} = \dot{m}_{w,\text{in}}\, c_{pw,\text{in}} T_{w,\text{in}}$ | Inlet water heat rate |
| $Q_{\text{air,out}}$ | $\dot{m}_{\text{air,out}}\, h_{\text{air,out}}$ | Outlet air heat rate |
| $Q_{v,\text{out}}$ | $(\dot{m}_{v,\text{in}} - \dot{m}_{\text{cond}}) h_{v,\text{out}}$ | Outlet water vapour heat rate |
| $Q_{w,\text{out}}$ | $Q_{w,\text{out}} = \dot{m}_{w,\text{out}} c_{pw,\text{out}} T_{w,\text{out}}$ | Outlet water heat rate |
| $Q_{dr}$ | $[\dot{m}_{w,\text{in}} - (\dot{m}_{w,\text{out}} - \dot{m}_{\text{cond}})]\, c_{pw,T_{\text{air,out}}} T_{\text{air,out}}$ | Entrained water droplets |

## 3 Results and discussion

Firstly, the dependence of the temperature and humidity ratio of the AWVM at the outlet of the experimental section on the irrigation density was studied by varying the regime parameters (Fig.3), since one of the main characteristics of contact condensers is the outlet parameters of the air-water vapour flow.

The irrigation density was calculated using the formula

$$D_i = \frac{V_{w,\text{in}}}{\pi d_{\text{in}}}\,. \tag{1}$$

Figures 3(a) and (b) show the dependencie of the mixture outlet temperature $T_{m,\text{out}}$ and humidity ratio $\omega_{m,\text{out}}$ on the irrigation density $D_i$ and the AWVM velocity $W_m$ at the mixture inlet temperature of $T_{m,\text{in}} = 105°\text{C}$ and initial vapour content $\varphi = 11\%$ in the channel height $H = 1.404$ m. It can be seen from the figures that at low irrigation densities the AWVM velocity has almost no effect on both the outlet temperature of the mixture and the outlet humidity ratio of the AWVM flow. At high irrigation densities the effect of air-vapour mixture velocity on the mixture output parameters is more significant.

Secondly, the dependencie of the outlet temperature $T_{m,\text{out}}$ and the humidity ratio $\omega_{m,\text{out}}$ on the irrigation density $D_i$ and the vapour content $\varphi$ at the inlet temperature $T_{m,\text{out}} = 105°\text{C}$ and the velocity $W_m = 20.8$ m/s in the channel height $H = 1.404$ m (Figs. 3(c) and (d)). It can be seen that the outlet temperature $T_{m,out}$ increases as the initial vapour content increases. Also, as the initial water vapour content increases, the output moisture

ratio increases, but this effect is more pronounced at low irrigation densities than at high ones. As can be seen in Figs. 3(e) and (f), the outlet temperature $T_{m,out}$ and the final humidity ratio $\omega_{m,\mathrm{out}}$ are insignificantly dependent on the initial temperature $T_{m,\mathrm{in}}$.

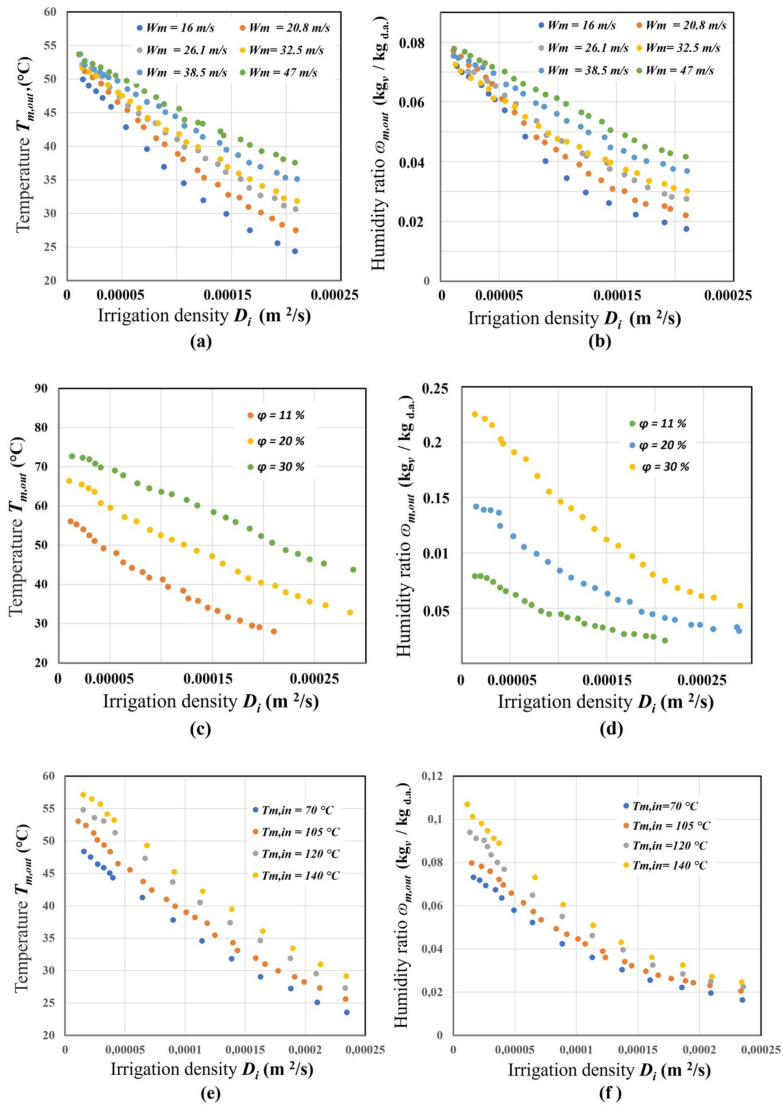


Figure 3: Outlet temperature and humidity ratio of the air-water vapour mixture versus irrigation density for different values: (a), (b) velocity of the AWVM; (c), (d) vapour content of the AWVM; (e), (f) initial temperature of the AWVM.

Figures 3(b), (d) and (f) show the higher humidity ratio at the outlet when the irrigation density is reduced. This can be explained by the fact that when a small amount of cooling water was supplied, it heated up almost immediately to the limit temperature at the entrance of the pipe. With further interaction, the moisture flow moved in the opposite direction, moistening the mixture. When more water was supplied, a greater amount of moisture condensed, and a smaller amount of moisture evaporated.

The experimental data in Fig. 4 are explained by the fact that at irrigation densities below the limit value $D_i < D_i^{\lim 1}$ the water heats up to the limit temperature $T_w^{\lim}$. The water heating limit refers to the reaching of the temperature of a wet bulb thermometer of the AWVM, which is approximately equal to the boiling temperature of water at a partial pressure of water vapour in the AWVM [32]. When a certain limit irrigation density $D_i > D_i^{\lim}$ is reached, the water is not heated to the limit temperature. In this case the water is heated to a certain equilibrium temperature from the cooling conditions of the mixture.

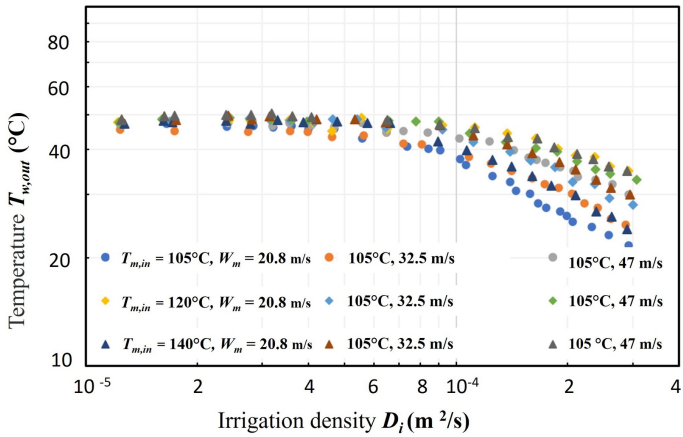


Figure 4: Effect of inlet temperature and velocity of air-vapour mixture on outlet water temperature.

The experiments showed that the value of the limit temperature of water heating increases with increase of the inlet vapour content $\varphi$ (Fig. 5). This can be explained by the fact that, the value of the wet bulb temperature increases as the value of the vapour content increases. When the inlet vapour content is increased from $\varphi = 11\%$ to $\varphi = 30\%$, the limit temperature of the heated water increases from $T_w^{\lim} = 46°\text{C}$ to $T_w^{\lim} = 62°\text{C}$.

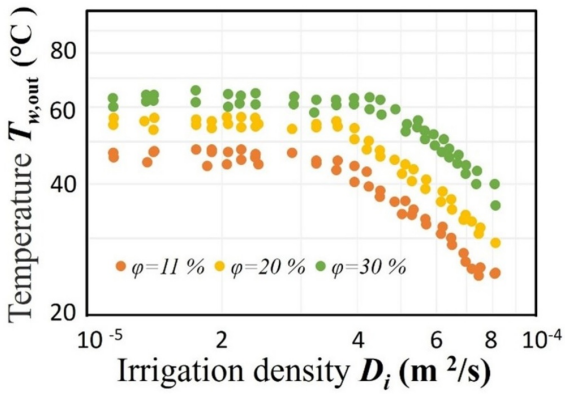


Figure 5: Outlet water temperature versus irrigation density for three different inlet vapour content.

Finally, the water temperature at the outlet of the test section depends on the following parameters:

$$T_{w,\text{out}} = T_w^{\text{lim}}(\varphi) \qquad \text{when} \quad D_i < D_i^{\text{lim}}, \tag{2}$$

$$T_{w,\text{out}}\,(D_i, W_m, \varphi) < T_w^{\text{lim}} \qquad \text{when} \quad D_i > D_i^{\text{lim}}. \tag{3}$$

The following formula is derived to determine the limit temperature of the water to be heated:

$$T_{w,\text{out}} = T_w^{\text{lim}} = 88.94\varphi^{0.3}. \tag{4}$$

Also, it is necessary to note, that the range of variation of the irrigation densities, at which water heats up to the limiting temperature, extends both with increasing of the initial vapour content $\varphi$ (Fig. 5), and with increasing of the velocity $W_m$ (Fig. 4), as one would intuitively expect. That is, the value of the limiting irrigation density depends not only on the velocity of the AWVM, but also on the initial vapour content: $D_i^{\text{lim}} = f(W_m, \varphi)$.

Based on the above, the presence of the evaporation section is associated with the heating of the water to the limit temperature at irrigation densities below a certain limit value $D_i < D_i^{\text{lim}}$, depending on the velocity and initial vapour content of the vapour mixture.

The temperature of the heated water $T_w$ varies along the height of the tube for different values of irrigation density (Fig. 6). The Fig. 5 shows that there is a limit temperature of water heating, which for the given conditions ($T_{m,\text{in}} = 105°\text{C}$, $\varphi = 11\%$, $W_m = 20.8$ m/s) is approximately $T_w^{\text{lim}} = 46°\text{C}$. The water is not heated above this temperature. For each irrigation density

there is a limit value to the working height of the test section, above which the temperature of the heated water does not increase further. For irrigation densities $D_i < D_i^{\lim}$ this is due to reaching the heating water temperature limit, and for $D_i < D_i^{\lim}$ it is due to the maximum cooling of the air-vapour mixture under energy balance conditions.

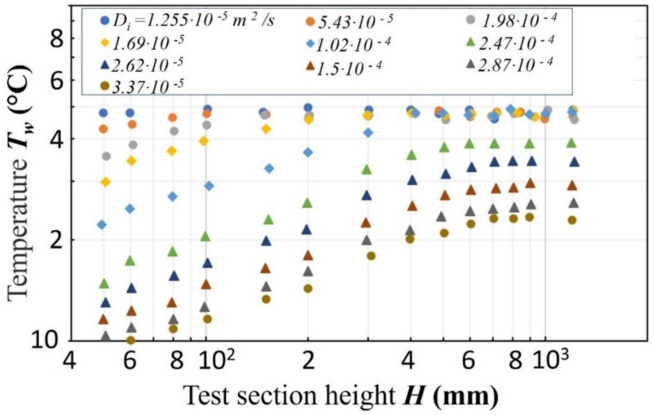


Figure 6: Heating water temperature distribution over the pipe height at initial mixture temperature $T_{m,\text{in}} = 105°\text{C}$, initial vapour content $\varphi = 11\%$ and mixture velocity $W_m = 20.8$ m/s.

Thus, at irrigation densities below a certain limit value $D_i < D_i^{\lim}$ the water is heated to the limit temperature $T_{w,\text{out}} = T_w^{\lim}$ at a certain working height of the test section. For the rest of the pipe section the opposite process takes place – the evaporation.

The experimental data allowed to obtain the dependence of the minimum operating height of the test section of the pipe on the irrigation density (Fig. 7). When $D_i < D_i^{\lim}$ at the working height of the experimental section the water was heated to the limit temperature. When $D_i > D_i^{\lim}$ the water was heated to a certain equilibrium temperature from conditions of energy balance. During the experiments, it was found that with increasing the velocity $W_m$ and the initial vapour content $\varphi$, the minimum operating height of the test section decreases. The equation for determining the minimum operating height of the test section of the pipe is as follows:

a) the water has been heated to $T_w^{\lim}$

$$H_{\min} = 9.2 \cdot 10^8 D_i^{1.38} W_m^{-0.66} \varphi^{-0.4} \qquad \text{for} \quad D_i < D_i^{\lim}, \tag{5}$$

$$H_{\min} = 4.1 \cdot 10^3 D_i^{0.23} W_m^{-0.14} \varphi^{-0.2} \qquad \text{for} \quad D_i > D_i^{\lim}. \tag{6}$$

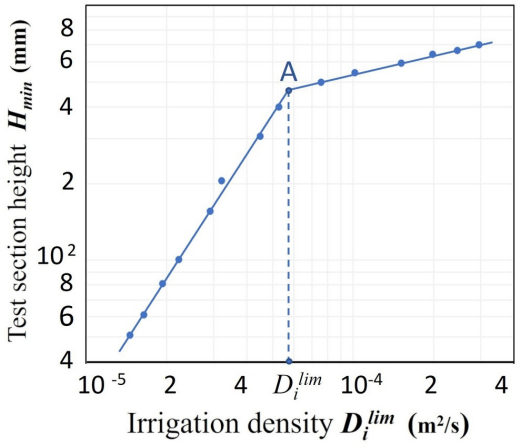


Figure 7: Limiting operating active height of the test section of the pipe versus irrigation density.

The aim of the present work is to find an adequate composition of parameters assuring maximum efficiency, that provide an efficient process of cooling gases with complete condensation of water vapour on a water film. For this purpose, we have obtained the dependency of the limiting operating active height $H_{\min}$ of the test section of the pipe on the irrigation density $D_i$ (Fig. 7). The practical significance in Fig. 6 is point $A$. At the point $A$, the height of the test section ensures two conditions that are important in practice: heating of water to the limit temperature $T_w^{\lim}$ and, at the same time, the maximum irrigation density under this condition, which corresponds to the maximum heating rate of the tube.

The empirical relationships for the irrigation density and the height of the pipe at point A result from the joint solution of the following equations:

$$D_i^{\lim} = 2.22 \cdot 10^{-5} W_m^{0.45} \varphi^{0.17}, \tag{7}$$

$$H_A = 3.48 \cdot 10^{-1} W_m^{-0.04} \varphi^{-0.17} \tag{8}$$

or

$$(H/d)_A = 26.77 \cdot \mathrm{Re}_m^{-0.04} \varphi^{-0.17}. \tag{9}$$

Our study addressed the question of finding an adequate composition of parameters that provide an efficient process of cooling flue gas with complete condensation of water vapour in DCHME with co-current upward flows. Namely, we have obtained an empirical equation for determining the

limiting heating temperature of water heating (4), the limiting irrigation density (7) and the active height of the tube of the DCHME (9).

On the basis of our experimental data, we realized that the processes taking place in the experimental section. At low irrigation densities and a sufficiently long working section, the cooling of the AWVM is first accompanied by condensation processes with a decrease in moisture content, and then by evaporation processes with some increase in humidity ratio of the mixture. As the irrigation density increases, the evaporation section decreases.

At irrigation densities above a certain some limit value, the cooling of the mixture is accompanied only by condensation processes. Since the presence of the evaporation process worsens the performance of the condenser surface due to its irrational use, we have determined the irrigation density, at which the mixture cooling is accompanied only by condensation processes.

According to the experimental results at irrigation densities below the limit value $D_i < D_i^{\lim}$, the water heats up to the limit temperature $T_w^{\lim}$. The limit heating of the water refers to reaching the temperature of a wet bulb thermometer of the mixture, which is approximately equal to the boiling temperature of the water at a partial pressure of water vapour in the AWVM [31]. When a certain limiting irrigation density $D_i > D_i^{\lim}$ is reached, the water has not been heated to the limit temperature. In this case the water is heated to some equilibrium temperature from the energy balance conditions. We have obtained the empirical Eq. (7) to determine the value of the limiting irrigation density that depends on the initial vapour content and the AWVM velocity.

In addition, it should be noted that for the first time the value of the water heating limit temperature has been experimentally determined for the ascending downward movement of the AWVM and the water film. These results converge with previous findings [33] that when comparing the two flow patterns of hot gas and cold water in the heat exchanger, the counterflow allows to get more heated water at the outlet. The results show that the value of the limit temperature of water heating is only 5–7°C lower than the corresponding value of the limit temperature for the countercurrent heating scheme according to Aronov [32].

The results obtained are consistent with the findings presented in [34] that the active height should lead to a complete condensation of the water vapour from the flue gas. Therefore, it directly affects the cost of the heat exchanger by its volume. The active height of the DCHME pipe can be determined by using empirical Eq. (9).

## 4 Conclusions

In the present study, the limit temperature of water heating, the irrigation density limit and the active height of a pipe direct contact heat exchanger were determined experimentally. At the same time, the velocity of the AWVM, the initial vapour content and the initial temperature of the AWVM were varied. From these data, the appropriate composition of parameters to provide an efficient flue gas cooling process with complete condensation of water vapour in DCHME with co-current upward flows was obtained. The results show that, for the first time, the value of the limit temperature of water heating at ascending upward movement of AWVM and water film was experimentally determined The value of the limit temperature of water heating increases from 46°C to 62°C when the initial vapour content changes from 11% to 30%. The dependence (7) for calculating the irrigation density at which there is no evaporation zone in the working channel is obtained. It is found that the effective height of the working channel should not exceed the value determined by Eq. (9), since further increase of the height of the working channel does not change the heat capacity of the working channel. For example, if the initial vapour content of the mixture is 11%, and the velocity of the air-vapour mixture is 20.8 m/s the height of the channel should not exceed 460 mm.

Finally, the experimental data obtained suggest that it is advisable to work with specific values of irrigation density and pipe height. The value of the irrigation density depends on the velocity of the AWVM and the initial vapour content and it should be calculated from empirical Eq. (7). The active pipe height depends on velocity of the AWVM and the initial vapour content and it should be calculated from (9). Under these conditions, the efficiency of the condenser will be high; its capital cost will be minimal. The present experimental results could be helpful in the design of direct contact heat exchangers for waste heat recovery.

*Received 25 July 2023*

## References

[1] Osakabe M., Ishida K., Yagi K., Itoh T., Ohmasa K.: *Condensation heat transfer on tubes in actual flue gas.* Heat Transfer – Asian Research. **30**(2001), 139–151.

[2] Qu M., Abdelaziz O., Yin H.: *New configurations of a heat recovery absorption heat pump integrated with a natural gas boiler for boiler efficiency improvement.* Energ. Convers. Manag. **87**(2014), 175–184.

[3] Gas Market Report, Q4, Paris, 2023. https://www.iea.org/reports/medium-term-gas-report-2023 (accessed 10 June 2023).

[4] Terhan M., Comakli K.: *Design and economic analysis of a flue gas condenser to recover latent heat from exhaust flue gas.* Appl. Therm. Eng. **100**(2016), 1007–1015.

[5] Wang Y., Zhao Q., Zhou Q., Kang Z., Tao W.: *Experimental and numerical studies on actual flue gas condensation heat transfer in a left–right symmetric internally finned tube.* Int. J. Heat Mass Transf. **64** (2013), 10–20.

[6] Maalouf S., Elias B.K., Clodic D.: *Investigation of direct contact condensation for wet flue-gas waste heat recovery using Organic Rankine Cycle.* Energ. Convers. Manag. **107**(2016), 96–102.

[7] Harold R.J., Heimir F.: *Direct contact condensers: a literature survey.* Tech. Rep. IDO-1523-3, Utah Univ., Salt Lake City 1977.

[8] Mahood H.B., Campbell A.N., Sharif A.O., Thorpe R.B.: *Heat transfer measurement in a three-phase direct-contact condenser under flooding conditions.* Appl. Therm. Eng. **95**(2016), 106–114.

[9] Zhu K., Xia J., Xie X., Jiang Y.: *Total heat recovery of gas boiler by absorption heat pump and direct-contact heat exchanger.* Appl. Therm. Eng. **71**(2014), 213–218.

[10] Zajacs A., Bogdanovics R., Borodinecs A.: *Analysis of low temperature lift heat pump application in a district heating system for flue gas condenser efficiency improvement.* Sustain. Cities Soc. **57**(2020), 102–130.

[11] Li F., Duanmu L., Fu L., Zhao X.: *Application of absorption heat pump and direct-contact total heat exchanger to advanced-recovery flue-gas waste heat for gas boiler.* Sci. Technol. Built. Environ. **25**(2019), 149–155.

[12] Wang J., Hua J., Fu L., Zhou D.: *Effect of gas nonlinearity on boilers equipped with vapor-pump (BEVP) system for flue-gas heat and moisture recovery.* Energy **198**(2020), 117375.

[13] Zhang C., Yang Y., Fan L., Huang X.: *Numerical study on operating characteristics of self-driven total heat recovery system for wet-hot flue gas.* Appl .Therm. Eng. **173**(2020), 115223.

[14] Liu H., Zhou X., Fu L.: *Heat transfer performance of direct contact flue-gas condensation heat exchanger.* HVAC. **44**(2014), 97–100.

[15] Men Y., Liu X., Zhang T.: *Analytical solutions of heat and mass transfer process in combined gas-water heat exchanger applied for waste heat recovery.* Energy **206**(2020), 118095.

[16] Kalantari H., Amiri L., Ghoreishi-Madiseh S.A.: *Analysis of the performance of direct contact heat exchange systems for application in mine waste heat recovery.* Int. J. Energ. Res. **46**(2022), 290–307.

[17] Min C., Yang X., He J., Wang K., Xie L., Onwude D. I., Zhang W., Wu H.: *Experimental investigation on heat recovery from flue gas using falling film method.* Therm. Sci. Eng. Prog. **22**(2021), 100839.

[18] Cui Zh., Du Q., Gao J., Bie R., Li D.: *Development of a direct contact heat exchanger for energy and water recovery from humid flue gas.* Appl. Therm. Eng. **173**(2020), 115214.

[19] Wei H., Huang Sh., Zhang X.: *Experimental and simulation study on heat and mass transfer characteristics in direct-contact total heat exchanger for flue gas heat recovery.* Appl. Therm. Eng. **200**(2022), 117657.

[20] Miliauskas G., Podia E., Poškas R., Poškas P., Balčius A., Jouhara H.: *The modelling of transient phase changes of water droplets in flue gas flow in the range of temperatures characteristic of condensing economizer technologies.* Energy **257**(2022), 124719.

[21] Li F., Duanmu L., Fu L., Zhao X.: *Performances of gas-water direct-contact heat transfer.* In: Proc. Cold Climate HVAC 2018 (D. Johansson, H. Bagge, Ĺ. Wahlström, Eds.), SPE, Springer, Lund 2019, 63–67.

[22] Mahood H.B., Thorpe R.B., Campbell A.N., Sharif A.O.: *Experimental measurements and theoretical prediction for the transient characteristic of a two-phase two-component direct contact condenser.* Appl. Therm. Eng. **87**(2015), 161–174.

[23] Phan T.H., Won S.S., Park W.G.: *Numerical simulation of air–steam mixture condensation flows in a vertical tube.* Int. J. Heat Mass. Transf. **127**(2018) 568–578.

[24] Dong Ch., Qi R., Zhang L.: *Mechanistic modelling of flow and heat transfer in vertical upward two-phase slug flows.* Phys. Fluids. **34**(2022), 013309.

[25] Jia Sh., Dong Ch.: *Flow and heat transfer model for turbulent-laminar/turbulent gas-liquid annular flows.* Appl. Therm. Eng. **219** (2023).

[26] Bhagwat S.M., Ghajar A.J.: *Experimental investigation of non-boiling gas-liquid two phase flow in upward inclined pipes.* Exp. Therm. Fluid Sci. **79**(2016), 301–318.

[27] Dong Ch., Hibiki T.: *Correlation of heat transfer coefficient for two-component two-phase slug flow in a vertical pipe.* Int. J. Multiphs. Flow **108**(2018), 124–139.

[28] Varlamov G.B., Romanova K.A., Nazarova I., Daschenko O., Kapustiansky A.: *Improvement of energy efficiency and environmental safety of thermal energy through the implementation of contact energy exchange processes.* Arch Thermodyn. **38**(2017), 4, 127–137.

[29] Bespalov V.V.: *Simulation of natural gas combustion products by humidified air.* In: Modern Technologies, Economy, and Education: Proc. All-Russian Scientific and Methodological Conf., Tomsk, December 27-29, 2019, 34–36.

[30] Galashov N., Tsibulskiy S., Melnikov D., Kiselev A., Gabdullina A.: *Flue gas moisture capacity calculation at the outlet of the condensation heat recovery unit.* MATEC Web of Conf. **110**(2017), 1–4.

[31] Bell I.H., Wronski J., Quoilin S., Lemort V.: *Pure and pseudo-pure fluid thermophysical property evaluation and the open-source thermophysical property library coolprop.* Ind. Eng. Chem. Res. **53**(2014), 2498–2508.

[32] Aronov Y.Z.: *Contact heating of water by natural gas combustion products.* Nedra, Leningrad 1990 (in Russian).

[33] Sideman S., Moalem D.: *Direct contact heat exchangers. Comparison of counter and co-current condensers.* Int. J. Multiphas. Flow **1**(1974), 555–572.

[34] Baqir A.S., Mahood H.B., Hameed M.S., Campbell A.N.: *Heat transfer measurement in a three-phase spray column direct contact heat exchanger for utilisation in energy recovery from low-grade sources.* Energ. Convers. Manag. **126**(2016), 342–351.

**archives**
**of thermodynamics**
Vol. **44**(2023), No. 4, 483–506
DOI: 10.24425/ather.2023.149734

# Assessment of heat and mass transfer processes in vapor bubbles under conditions of metastable equilibrium of liquids

**HANNA KOSHLAK***

Kielce University of Technology, Department of Sanitary Engineering, Aleja Tysiąclecia Państwa Polskiego 7, 25-314, Kielce, Poland

**Abstract** This paper proposes a mathematical model that allows expanding the scope of research into the mechanism of heat transfer during explosive boiling, cavitation and boiling of multicomponent liquids, identifying the most influential factors and optimizing technological processes. The proposed model takes into account the processes of heat accumulation in the high-boiling part of liquid mixtures (for example, emulsions) and the use of this energy in the process of boiling their thermolabile part, as well as for superheating the resulting steam in steam bubbles. This effect can also be used to evaluate the effects of liquid boiling in thermodynamically unstable regions of liquid media.

**Keywords:** Heat and mass transfer; Gas-vapour bubble; Superheated liquids; Mathematical model

## Nomenclature

| | | |
|---|---|---|
| $A$ | – | work |
| $a$ | – | thermal diffusivity coefficient, $\mathrm{m}^2/\mathrm{s}$ |
| $B$ | – | universal gas constant, $\mathrm{J}/(\mathrm{mol\,K})$ |
| $b$ | – | thickness, m |
| $c$ | – | heat capacity, $\mathrm{J}/(\mathrm{kg\,K})$ |
| $L$ | – | heat of vaporization, J/kg |

*Corresponding Author. Email: hkoshlak@tu.kielce.pl

$M$ – molecular mass
$p$ – pressure, Pa
$p_l$ – liquid pressure, Pa
$p_s$ – steam pressure, Pa
$p_1$ – outer pressure, Pa
$Q$ – heat, J
$q$ – specific heat flux, W/m$^2$
$R$ – radius of the bubble, m
$R_1$ – outer radius, m
$r$ – radius, m
$S$ – surface area, m$^2$
$T$ – temperature, °C
$T_l$ – liquid temperature, °C
$T_s$ – steam temperature, °C
$u$ – velocity, m/s
$u_r$ – radial velocity of the liquid at the boundary with the bubble, m/s
$V$ – volume of the bubble, m$^3$

**Greek symbols**

$\alpha$ – heat transfer coefficient, W/(m$^2$K)
$\lambda$ – coefficient of thermal conductivity, W/(m K)
$\mu$ – dynamic viscosity coefficient, Pa·s
$\rho$ – density, kg/m$^3$
$\sigma$ – surface tension, N/m
$\tau$ – time, s

**Subscripts**

0 – initial value
$b$ – buble
$g$ – gas
$i$ – inside
$l$ – liquid phase
$r$ – radial coordinate
$s$ – steam
$\nu$ – vapour

# 1 Introduction

Vapour-gas mixtures are formed in many technological processes, both in the intermediate stage of the implementation of these processes [1–9], for example, evaporation, degassing of water, distillation of petroleum products, surface cleaning, mixing colloidal solutions, foaming, etc., and as the main technological method, for example, homogenization of emulsions, fuel, cavitation, etc. [10–16].

The processes of spontaneous boiling of highly superheated liquids under conditions when the liquid suddenly finds itself in a non-equilibrium metastable state have attracted increased attention from researchers. This interest is determined, on the one hand, by the complexity of the observed phenomena and processes, which are determined by many difficult-to-control factors. On the other hand, understanding the specifics of heat and mass transfer processes in thermodynamically nonequilibrium regions and studying the kinetics of decomposition of a metastable state can contribute to the creation of new high-intensity technologies in various industries [1–5]. In particular, the phenomenon of explosive boiling of superheated liquid was studied theoretically and experimentally in relation to the problem of obtaining finely dispersed water-fuel emulsions [17, 18].

The metastable state occurs in phases of various natures, and the existence of the metastable state is due to the fact that the liquid overheating limit is not reached. Heterogeneous nucleation and the process of nonequilibrium vaporization usually occur during irreversible nonequilibrium interphase mass transfer of metastable liquids through adiabatic channels. Many works are devoted to this class of problems [19–21], the purpose of which was the development of mathematical models or experimental studies of critical flows of a two-phase mixture in channels taking into account irreversible nonequilibrium interphase mass transfer. A change in pressure in a liquid is accompanied by vaporization. We consider a class of problems not related to the critical flow of a mixture, although our model can also be applied to assess such phenomena. The physical processes that are studied in our work are associated with the study of the phenomena of heat and mass transfer between vapor-gas bubbles and liquid at the moment of violation of thermodynamic equilibrium. For example, in the case of a sharp decrease in pressure, as in the above articles, but not in critical flow regimes. In this case, the temperature and pressure of the vapor in the bubbles and the temperature of the boundary layer of the liquid will constantly change. In this case, heat and mass flows can be directed both from liquid to vapor and vice versa, depending on the amount of accumulated energy in these phases [15–17].

The class of problems closest to ours is considered in [22–25]. Unlike flash boiling models, we take into account the influence of bubbles inside the droplet on the heat transfer process. The classical model of a homogeneous nucleon is complemented by a model of bubble growth (Rayleigh). In the cited works, a uniform droplet temperature was assumed, and the droplet energy balance equation was associated with submodels of bubble

formation, growth, and explosion. For single-component fuels, the boiling point can be used to determine whether the liquid fuel reaches the boiling point. However, for multicomponent fuels, evaporation and boiling do not depend only on the boiling point of the components. In general, the process of evaporation of multicomponent droplets is quite complex. Changing the temperature of liquid and vapor or the thermophysical properties of the medium will significantly affect the evaporation regime. Modern models usually focus solely on the evaporation process or the boiling process. The transition between evaporation and boiling is not fully understood. Existing boiling evaporation models used empirical formulas to calculate internal heat transfer and did not adequately consider the effect of the presence of bubbles in the liquid on the evaporation rate. Moreover, most existing boiling evaporation models are designed only for single-component droplets. However, in real environments, such as fuel, many components are present, and their properties vary significantly. In addition, the processes of bubble dynamics at the stage of their development or collapse are interesting from the point of view of the possibility of intensifying heat and mass transfer processes, and in this sense, our task was also to take into account in the model the phenomena of accumulation of thermal energy in a liquid and assess the influence of this phenomenon on the dynamics of vapor bubbles, which also makes it possible to develop technologies for the use of metastable liquids.

The difficulty of directly studying these processes, due to the small size of the droplets and the high intensity of heat and mass transfer, has led to the widespread use of mathematical modelling methods that make it possible to optimize these technological processes.

As a rule, known methods for calculating heat- and mass-transfer processes of this type only approximately take into account the temperature regime of the liquid and phase-transition processes occurring around gas-vapour bubbles. Taking into account transient processes in a liquid will significantly improve the accuracy of the calculations and expand the scope of application of such mathematical models. That is why research in this direction is extremely relevant.

In [17,18], the conditions for the growth of the vapour phase in an emulsion between the surface of a water drop and the continuous phase during heating were considered. A distinctive feature of the boiling of a liquid located in the volume of another is the presence of a continuous phase, which in this case will affect heat exchange processes. In this case, the formation and growth of vapour bubbles will occur at the interface between the com-

ponents of the mixture due to the reduced interfacial tension. The higher boiling phase will accumulate thermal energy, which can be used as an additional heat source when the thermolabile component (water) boils. These features of boiling emulsions were considered in works [26–32].

To increase the accuracy of modelling heat transfer processes in a gas-vapour bubble, it is necessary to take into account the heat transfer to the liquid medium. Several authors assume the liquid temperature to be constant: when calculating the swelling of materials [33–36], when determining the thermodynamic characteristics of steam [37–39] and cavitation bubbles [40, 41].

In [42, 43], the authors consider the heat transfer layer of the liquid to be so thin that the curvature of the bubble surface can be ignored. However, such assumptions are possible only for a very limited group of problems. In the study [44] for cavitation bubbles and in [45] for vapour bubbles, an analytical solution to the problem of unstable thermal conductivity in a layer of liquid surrounding an oscillating bubble is presented. As a result of the boundary conditions introduced by the authors, a solution was obtained in which the heat transfer layer of the liquid is equal to the radius of the bubble and does not depend on the thermophysical characteristics of the liquid. A review of the literature sources shows that phase transition processes in the liquid surrounding a gas bubble have not been sufficiently studied. A change in the phase state of the liquid leads to a significant change in the processes of heat and mass transfer at the boundary. To expand the boundaries of mathematical modelling of a gas-vapour bubble, it is necessary to take into account the phase transition processes of heat transfer in the liquid that surrounds the gas-vapor bubble. The peculiarity of this problem is the movement of the bubble wall, the velocity of which at certain times can reach several tens of metres per second.

Most methods for assessing heat and mass transfer processes in two-phase media were aimed at studying the dynamics of the growth of vapour bubbles that arise either in the bulk of a liquid or on a superheated surface. A feature of the boiling of emulsion media is that the formation of a vapour phase will occur at the interface between liquids if one liquid (for example, oil) is a surfactant or a surfactant is present in the emulsion (in multicomponent emulsions), which is based on the reduction of interfacial tension at the interface between the dispersion medium (water) and the dispersed phase (oil). Experimental data [31, 46–48] indicate that the process of formation of a new phase (steam) is initiated by internal thermal effects on the surface of oil particles. With a sharp release of pressure, the preheated

emulsion will find itself in a state of supersaturation of the thermolabile aqueous phase (water is overheated relative to the saturation temperature at a given pressure), i.e. containing excess heat. This excess heat is spent on the work of forming a vapour layer and further vaporisation.

The purpose of this paper is to create a mathematical model of heat transfer in a liquid that surrounds an oscillating gas-vapour bubble. This mathematical model must take into account the mobility of the bubble wall, phase transitions in the layers of the liquid, and changes in its thermophysical characteristics.

## 2 Research methods

Analysis of literature data shows that today, despite the large number of publications concerning theoretical studies of the dynamics of vapour bubbles, there are no mathematical models that would provide equally accurate prediction of the behaviour of an individual bubble, and, moreover, bubble clusters, in any given interval operating parameters corresponding to real conditions. The imperfection of existing models is primarily due to the fact that such phenomena as acoustic and hydrodynamic cavitation, volumetric condensation, boiling at low superheats, explosive boiling, bubble growth in subcooled liquid traditionally considered and studied as fundamentally different branches of thermophysics. However, from a physical point of view, this is one and the same phenomenon, which represents the process of relaxation of the "bubble-liquid" system tending to a thermodynamic equilibrium state. The behaviour of the bubble in these processes is subject to the same laws and must be described by the same equations, but with different initial conditions. Therefore, a mathematical model of bubble dynamics, taking into account the totality of all the main determining factors, should equally describe any of these phenomena. Such a model cannot contain specific assumptions that are valid only for one of the phenomena, since there are no objective grounds for establishing a clear boundary, and the question of where cavitation ends and boiling begins has no physical meaning.

When studying physical processes in which a dynamically developing bubble plays a decisive role, it is useful to have a physically reliable and, at the same time, not cumbersome mathematical model, which, without additional restrictions and simplifications, would equally well predict the behaviour of a vapour bubble under any initial conditions.

## 2.1 Basic provisions of the model

When developing a model of the dynamics of a single bubble, the following assumptions were made:

- the bubble has a spherical shape,
- the liquid is viscous, but incompressible,
- inside the bubble there is vapour, the amount of which is determined by the mass transfer of the bubble with the surrounding liquid,
- the vapour inside the bubble is considered as a real gas.

The validity of the first of these assumptions is confirmed by an analysis of known experimental data, from which it follows that, in relation to the class of problems considered in this work, the bubble retains a spherical shape at all stages of its development. This assumption is generally accepted in all known models, with the exception of special cases of bubble growth or destruction near solid surfaces, which is beyond the scope of this study.

The second assumption is due to the desire to avoid unnecessary complexity of the problem and an unjustified increase in the cost of computer time when performing calculations. The compressibility factor of a liquid becomes important when describing the shape and propagation of the pressure pulse emitted in a liquid by a bubble at the moment of its explosion.

The fourth assumption significantly increases the reliability of the model, especially when considering dynamic effects in the phenomena of cavitation or explosive boiling.

Let us formulate the problem statement as follows. A bubble with radius $R_0$, which contains, in the general case, in addition to steam, an extraneous noncondensable gas with a partial pressure $p_0$, is in equilibrium with the liquid at temperature $T_0 = \text{const}$. The equilibrium conditions for a bubble in a liquid are determined by the following equation equation that can be obtained by analyzing the equilibrium equations of a vapor bubble presented in [49]:

$$dA = pdV + \sigma dS = \left(p + \sigma \frac{dS}{dV}\right) dV. \tag{1}$$

The general condition for thermodynamic equilibrium in a one-component two-phase disperse system can be written as

$$T_s - T_l = 0\,, \qquad p_s - p_l - \frac{2\sigma}{R} = 0. \tag{2}$$

The $2\sigma/R$ term in the equation can be interpreted as some additional pressure due to the action of surface forces. It follows that in heterogeneous disperse systems, where at least one of the phases is not macroscopic, the condition of mechanical equilibrium between the phases takes the form: $p_s = p_l + 2\sigma/R$.

## 2.2 Equation of motion of the bubble boundary

According to the accepted assumption of spherical symmetry, the fluid flow in the vicinity of the bubble, caused by the movement of its surface, will be irrotational, and the potential of the velocity field potential $\varphi(r,\tau)$, as well as the velocity of the fluid velocity $u(r,\tau)$, depends only on the radial coordinate $r$ and on time $\tau$. Solving the Laplace equation $\Delta\varphi = 0$ in spherical coordinates relative to $\varphi(r,\tau)$ and taking into account that the velocity of the liquid $u(r,\tau)$ at a distance from the centre of the bubble at any time is related to the potential at this point by the relation $u(r,\tau) = \partial(r,\tau)/\partial r$, we obtain the continuity equation of the form $ur^2 = f(\tau)$, where $f(\tau)$ is an arbitrary function of time, the current value of which is the same for the entire volume of liquid. If the radial velocity of the liquid at the boundary with the bubble is known $u_r(\tau) = u(r,\tau)$, we can write that $f(\tau) = u_r(\tau)r^2$ and represent the continuity equation as $ur^2 = u_r r^2$. The values of the fluid velocity and the velocity field potential at an arbitrary point of the fluid at time $\tau$ are determined by the expressions

$$u(r,\tau) = \frac{u_r R^2}{r^2}\,, \qquad \varphi(r,\,\tau) = -\frac{u_r R^2}{r}\,. \tag{3}$$

The movement of a viscous fluid obeys the Navier-Stokes equation, which in vector form has the form:

$$\frac{du}{d\tau} = -\frac{\operatorname{grad} p_l}{\rho_l} + \nu\frac{\operatorname{grad}\operatorname{div} u}{3} + \nu\Delta u. \tag{4}$$

For an inviscid fluid ($\nu = 0$), the last two terms on the right side of (4) disappear and the Navier-Stokes equation is reduced to the Euler equation of motion for an ideal fluid. If the fluid is viscous but incompressible ($\operatorname{div} u = 0$), the second term is excluded from the right side of (4).

The assumption of the irrotational nature of liquid flow in the vicinity of a bubble allows us to use the Euler equation to describe the flow of viscous liquids. Indeed, for any potential flow $\Delta\varphi = 0$ and $u = \operatorname{grad}\varphi$. From the vector analysis, it follows that $\Delta u = \operatorname{grad}\Delta\varphi$. Therefore, the viscosity term

$\nu\Delta u$ can be excluded from the right-hand side of (4), even if $\nu \neq 0$. The result obtained leads to the paradoxical conclusion that the flow of a viscous fluid obeys the equation of motion of an ideal fluid, since both terms in (4), containing viscosity $\nu$, become identically equal to zero. The first term is excluded due to the a priori assumption of the incompressibility of the fluid, and the second term is eliminated due to the assumption of the irrotational nature of the flow.

Since the flow velocity depends only on the coordinate $r$, derivatives of velocity in perpendicular directions are zero. Thus, radial flows do not have any tangential stresses, and there is no internal friction.

Using the rules of vector analysis, Euler's equation [50] in this form

$$\frac{du}{d\tau} + (u\nabla)\, u + \frac{\operatorname{grad} p_l}{\rho_l} = 0 \tag{5}$$

can be reduced to the well-known Lagrange-Cauchy integral [51]:

$$\frac{\partial \varphi}{\partial \tau} + \frac{u^2}{2} + \frac{p}{\rho_l} = f(\tau), \tag{6}$$

which connects the velocity of an unsteady flow at an arbitrary point $r$ with the pressure at this point. The function $\varphi(\tau)$ in (6) represents an arbitrary time function determined from the boundary conditions, and the value of this function is the same throughout the fluid flow.

To transform Eq. (6), we substitute into it the expressions obtained above for potential and velocity:

$$u(r) = \frac{u_r R^2}{r^2}, \quad \varphi(r) = -\frac{u_r R^2}{r}, \quad \frac{\partial \varphi}{\partial \tau} = -\frac{1}{r}\left(\frac{du_r}{d\tau} R^2 + 2R u_r \frac{dr}{d\tau}\right). \tag{7}$$

After transformations, Eq. (6) will take the form

$$-\frac{1}{r}\left(\frac{du_r}{d\tau} R^2 + 2R u_r \frac{dr}{d\tau}\right) + \frac{u_r^2 R^4}{2r^4} + \frac{p_l}{\rho_l} = f(\tau). \tag{8}$$

Due to the fact that the function $f(\tau)$ in (6) does not depend on spatial coordinates, it can be determined using any of two boundary conditions: at an infinite distance from the bubble or at the boundary with the bubble. When $r \to \infty$, the pressure $p_l$ takes on the value $p_\infty$, equal to the external pressure applied to the liquid. Substituting this value $p_l$ into (8), we find the value $f(\tau) = p_\infty/\rho_l$. Obviously, pressure $p_\infty$ can be any given function

of time, including a constant value. Substituting the value $f(\tau) = p_\infty/\rho_l$ into (8), we obtain

$$\frac{p_l(r,\tau) - p_\infty}{\rho_l} + \frac{u_r^2 R^4}{2r^4} - \frac{1}{r}\left(\frac{du_r}{d\tau}R^2 + 2Ru_r\frac{dr}{d\tau}\right) = 0. \tag{9}$$

This equation makes it possible to calculate the pressure field $p_l(r,\tau)$ in the vicinity of the bubble for any moment of time, if the current values of its radius $r(\tau)$ and the fluid velocity $u_r$ at its surface are known.

To determine the velocity of movement of the bubble boundary $u_r(\tau)$ during its expansion or compression, you can use another boundary condition for pressure by substituting in (9) instead of $p_l(r,\tau)$ the value of the liquid pressure at the surface of the bubble $p_l(r,\tau) = p_r(\tau)$, which we agree to consider for now as a known function of time. As a result, we obtain a differential equation, the solution of which makes it possible to find the unknown function $u_r(\tau)$:

$$\frac{du_r}{d\tau} = \frac{p_r - p_\infty - p_l u_r\left(2\dfrac{dr}{d\tau} - \dfrac{u_r}{2}\right)}{\rho_l R}. \tag{10}$$

If we assume that $dr/d\tau = u_r$, Eq. (10) becomes simpler. The assumption $dr/d\tau = u_r$ is strictly justified only in the absence of phase transitions on the surface of the bubble. It will be shown below that even with intense evaporation or condensation on the interphase surface, the difference between these values is small, except in extreme cases.

Also important is the equation of motion for the case when the bubble is not in an infinite volume of liquid but in the center of a limited spherical volume with an outer radius $R_1$, for example, inside a drop of liquid. Then, substituting in (8) the corresponding boundary conditions for pressure: $p_l(R_1) = p_1$ and $p_l(R) = p_1$, we obtain instead of (10) an equation of the form

$$\frac{du_r}{d\tau} = \frac{p_r - p_1 - 1.5\rho_l\left(\dfrac{dr}{d\tau}\right)^2}{\rho_l R} + \frac{u_r^2\left[1 + \dfrac{R}{R_1} + \left(\dfrac{R}{R_1}\right)^2\right]}{2R_1}. \tag{11}$$

Equation (11) can be used to analyse explosive destruction of droplets of highly superheated liquid in a metastable state.

### 2.3 Basic equations of the model

The model contains a system of differential equations with the corresponding initial conditions. The liquid temperature $T_{0l}$ is known. The initial pressure in the liquid is also a known parameter, the subsequent change of which over a given period of time $\Delta\tau$ to a given value $p_l$ determines the further behaviour of the bubble. Under thermodynamic equilibrium conditions, the values of $p_{0l}$ and $T_{0l}$ determine the initial conditions for the temperature, density, and pressure of the vapour and gas inside the bubble. If only vapour is present in the bubble, the initial radius of the bubble $R_0$ is uniquely determined from the condition $p_l = p_{0l} + 2\sigma/R_0$. When analyzing the growth process of the vapor nuclei, the initial gas content has virtually no effect on the subsequent behaviour of the growing bubble.

The following are the basic equations of the bubble model.

Change in the velocity of radial movement of the liquid near the surface of the bubble:

$$\frac{du_r}{d\tau} = \frac{p_r - p_\infty - 1.5\rho_l u_r^2 - \dfrac{2\sigma}{R} - \dfrac{4\mu_l u_r}{R}}{\rho_l R}\,. \tag{12}$$

Changing the radius of the buble [29, 31]:

$$\frac{dr}{d\tau} = u_r + \frac{j}{\rho_l}\,. \tag{13}$$

where $j$ is the transfer of mass through the interfacial surface.

Changing the temperature of the vapour-gas medium in the buble [29, 31]:

$$\frac{dT_b}{d\tau} = \frac{3}{(\rho_g c_g + \rho_l c_l)}\left(q - jc_l T_b - p_g \frac{dr}{d\tau}\right)\frac{1}{R}\,. \tag{14}$$

Change in the amount of heat transferred to the bubble:

$$\frac{dQ_l}{d\tau} = -4\pi R^2\,(jL - g)\,, \tag{15}$$

where $g$ is the rate of heat transfer through the interfacial surface, and $L$ is the heat of vaporization (condensation).

Initial conditions:

$$u_r(0) = u_{R_0}\,, \qquad R(0) = R_0\,, \qquad Q_l(0) = Q_{ol}\,. \tag{16}$$

Additional equations:

- gas pressure in the bubble [18]:

$$p_g = \frac{B\rho_g T_g}{M_g - \rho_g b_g} - \frac{a_g \rho_g^2}{M_g^2}\,. \tag{17}$$

- vapour pressure in the bubble:

$$p_r = \frac{B\rho_\nu T_b}{M_\nu - \rho_\nu b_\nu} - \frac{a_\nu \rho_\nu^2}{M_\nu^2}\,, \tag{18}$$

- pressure of the vapour-gas medium in the buble:

$$p_{\nu g} = p_g + p_r\,, \tag{19}$$

- interfacial mass transfer rate [29,31]:

$$j = 0.25\alpha\left(\rho_l u_s - \rho_r u_\nu\right), \tag{20}$$

- interfacial heat transfer rate [29,31]:

$$g = 025\left(\rho_l u_\nu c_l - \rho_g u_g c_g\right)\left(T_s - T_{\nu g}\right) + j c_l T_s\,, \tag{21}$$

- velocity of molecular kinetic movement of vapour and gas molecules:

$$u_\nu(T_b) = \left(\frac{8BT_{\nu g}}{\pi M_\nu}\right)^{\frac{1}{2}}, \quad u_\nu(T_s) = \left(\frac{8BT_l}{\pi M_\nu}\right)^{\frac{1}{2}}, \quad u_g(T_b) = \left(\frac{8BT_{vg}}{\pi M_g}\right)^{\frac{1}{2}}. \tag{22}$$

Heat balance equation:

$$\left(T_0 - T_s\right)\lambda_l\left(\frac{2}{b} + \frac{1}{R}\right) = -j\left(T_s\right)L\left(T_s\right) - q\left(T_s\right). \tag{23}$$

$$b = 2R\left(\sqrt{1 + \frac{3Q_l}{4\pi R^3 \rho_l c_l\left(T_s - T_l\right)}} - 1\right). \tag{24}$$

# 3 Bubble growth under boiling conditions of highly superheated liquids

## 3.1 Change the radius of the bubble

Figure 1 shows a comparison of experimental [51,52] and calculated dependencies $R = f(\tau)$. The good quantitative agreement between the results of calculations and experiments was unexpected, considering the difference in the thermophysical properties of the objects being studied. The authors' own model adequately describes the kinetics of bubble growth since this model was developed based on this experiment and is intended for its analysis. As noted by the authors themselves [52], "the radius of the bubble is the only variable available for direct measurements."

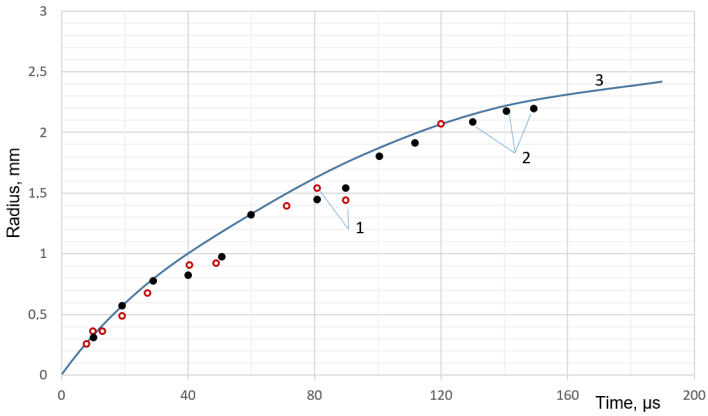


Figure 1: Changes in the radius of a vapour bubble during the explosive boiling of a liquid drop (comparison of experimental results *1* and *2*, according to [51] and [52], respectively, with calculations using our model – curve *3*).

## 3.2 Bubble growth rate

The experimental values of the bubble growth rate (Fig. 2) were determined in [52] by numerical differentiation with respect to the time of the averaged radius change curve, which is presented in Fig. 1. The period of accelerated bubble growth, which, according to the authors, lasts approximately 3 μs, which could not be recorded in the experiment. According to the authors, the difference between the experimental data on $dr/d\tau$ and the calculation

results using their model is 30%. As can be seen in Fig. 2, our model predicts the growth rate with high accuracy.

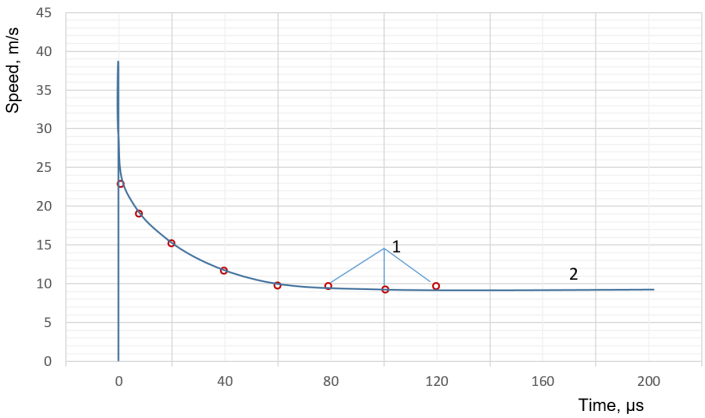


Figure 2: The speed of radial motion of the wall of a bubble growing during explosive boiling of a liquid drop: comparison of experimental results (points *1*) [52] with calculated data using the model (curve *2*).

### 3.3 Transfer of mass of the bubble with the surrounding liquid

Figure 3 shows the experimental data [52] on the change in vapor mass in a droplet during the explosive boiling process, confirming thatwithin the time $\Delta\tau \approx 180$ μs, the entire mass of the droplet transformed into vapor. The experimental data points in this figure were derived from an analysis of the $R = f(\tau)$ dependence in Fig. 1 and subjective assumptions about the mass transfer rate, which are incorporated into their model equation. As can be seen in Fig. 3, calculated curve *2* differs from the experimental data (red points on curve *2*) in that the authors [53] employed the calculated dependence $R = f(\tau)$ from Fig. 1. The $m = f(\tau)$ dependence calculated using our model (Fig. 3, curve *3*) indicates that when the first pressure peak appears (at $\Delta\tau \approx 180$ μs), no more than 8% of the droplet mass has transformed into the vapor phase.

With a sharp drop in pressure, the growth of the vapour bubble occurs in a monotonic regime. In this case, the vapour pressure in the bubble should theoretically decrease. However, because under these conditions the phenomenon of evaporation of water into the bubble also occurs, the pressure in the bubble remains at the same level or can increase and during

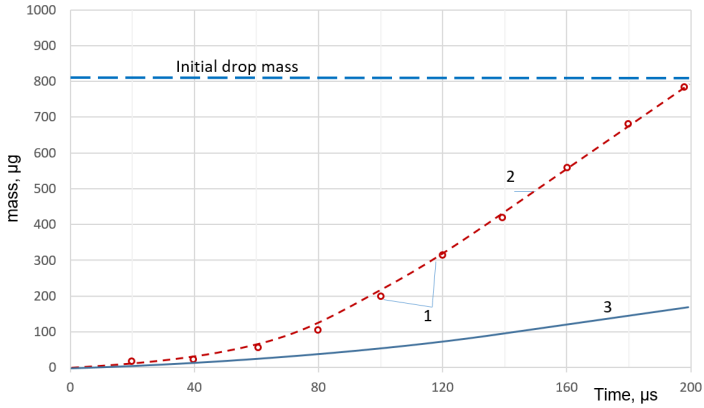


Figure 3: Change in the mass of vapour in a bubble as a result of the evaporation of liquid from a drop into the bubble during the explosive boiling of the drop.

the growth process the condition $p_l > p_{0l}$ is satisfied. This condition is confirmed by all known data on the growth of bubbles under boiling conditions at low and medium superheats.

It is known that in the absence of mass transfer of a bubble with the surrounding liquid, for example, in the case when the bubble contains only noncondensable gas, the release of pressure leads to damped oscillations of such a bubble [18, 52]. Obviously, the experimentally recorded pattern of pressure fluctuations shown in Fig. 4 led the authors [52] to the conclusion

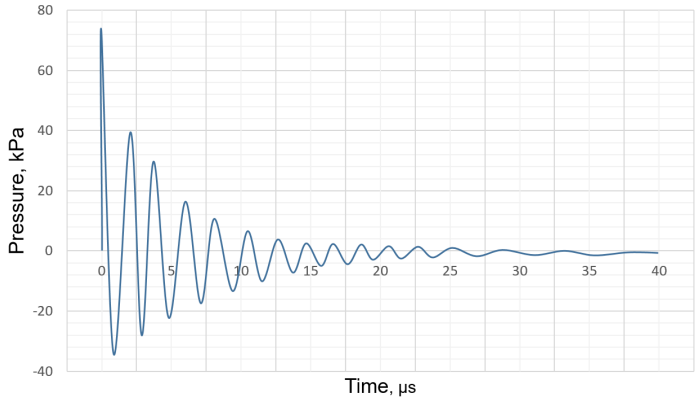


Figure 4: Change in the pressure in the liquid at a distance of 6 mm from the centre of the vapor bubble during the explosive boiling of a drop until its destruction [52].

that at $\tau > 180$ μs the droplet has completely evaporated and the bubble behaves like a 'gas bubble'.

In reality, at very high overheating, which leads to the effect of explosive boiling, the dynamic processes in the inertial stage of growth proceed so intensely that they do not have time to be compensated for by evaporation into the bubble. The thermophysical parameters of the vapour inside the bubble ($T_{ib}$, $p$, $\rho$) and the liquid adjacent to it ($T_l$, $\rho_l$, $\mu_l$, $\sigma$, $L$) change significantly during the process, and in this case the vapour cannot even be approximately considered an ideal gas. All these factors, which, as a rule, are not taken into account in known models, can have a decisive influence on the specific nature of the boiling of highly superheated liquids.

Figure 5 shows the dependences $R = f(\tau)$ and $m = f(\tau)$ calculated using our model in the time interval from 0 to 20 μs. The bubble actually performs damped oscillations, but at the same time mass transfer of the bubble with the surrounding liquid continues. Since no additions were introduced to the model to take into account the specifics of boiling under conditions of severe overheating, this behaviour of the bubble apparently reflects the characteristic features of the phenomenon under study. From Fig. 5 it follows that complete evaporation of a drop in a bubble is completed only 20 μs after the start of the explosion, which is 120 times higher than the value obtained by the authors of [52] when analyzing the experiment.

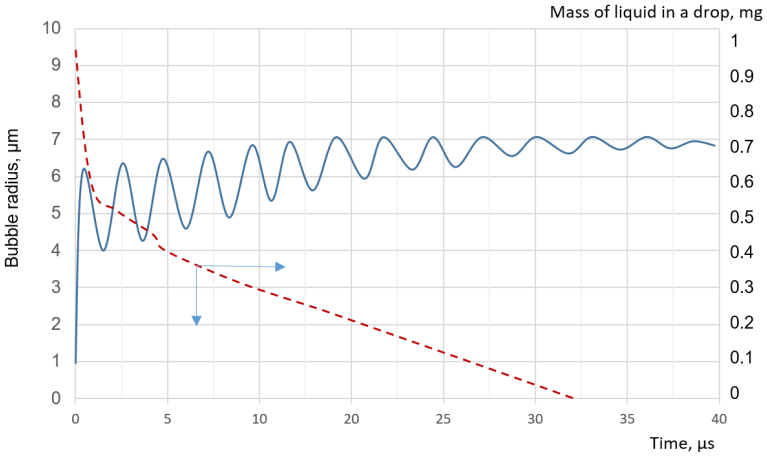


Figure 5: Change in the mass of the droplet $m = f(\tau)$ due to evaporation into the bubble and variation in the size of the vapour bubble $R = f(\tau)$ during the explosive boiling of the droplet: solid line – $m = f(\tau)$; dashed line – $R = f(\tau)$.

The idea of a monotonic distribution of liquid temperature within the thermal layer, adopted in existing models, is quite justified for describing the process of bubble growth, but for oscillating bubbles such a simplification can introduce a significant error, especially when estimating peak temperatures and pressures at the stage of maximum compression of the bubble. Since the period of bubble oscillation is significantly less than the characteristic relaxation time of the temperature field in the liquid, the liquid layers adjacent to the surface do not have time to heat up and cool so quickly and the temperature distribution in the vicinity of the oscillating bubble cannot remain monotonic. Figure 5 shows the change in the radius of the bubble; similar to these changes, the pressure and temperature of the steam also change. The temperature distribution in the vicinity of a spherical particle also changes at different times, after the particle, intensely heating up (due to internal sources) and giving off heat to adjacent layers of liquid, then begins to cool (due to internal heat sinks), while taking away heat from adjacent layers. This temperature distribution also occurs in the vicinity of a pulsating bubble. Taking into account the decisive influence of heat and mass transfer processes on the dynamics of the bubble, the need to correctly take into account the temperature field in the vicinity of the bubble is obvious. If in early works on hydrodynamic and acoustic cavitation the assumption of the adiabatic nature of bubble collapse was used as the main simplifying assumption, then subsequent studies showed that a reliable description of phenomena in cavitation processes is impossible without accurately taking into account interphase heat and mass transfer. Thus, taking into account heat transfer in oscillating and collapsing bubbles leads to a decrease in the thermodynamic parameters of the vapor in the bubble by almost an order of magnitude compared to adiabatic collapse.

An analysis of works on bubble dynamics shows that when modeling the behavior of bubbles, regardless of the applied orientation of the model, the most important thing is an adequate representation of interfacial heat and mass transfer, the thermodynamic state of the vapor phase, as well as the temperature field in the vicinity of the bubble.

In our model, it is assumed that the temperature of the surface of the bubble on the liquid side is different from the temperature of the gas phase, which is equivalent to the assumption that there is a temperature jump on the wall of the bubble on the gas phase side. Due to the temperature difference, vapor and gas molecules, when in contact with the surface of a liquid, completely exchange energy with it, regardless of whether the molecule condenses on the surface or is reflected back. In other words,

the coefficient of thermal accommodation is taken equal to unity, which corresponds to the real mechanism of heat transfer.

With a nonequilibrium nature of phase transitions, the temperature at the interface always undergoes a jump, the magnitude of which determines the intensity of the mass flow from the bubble wall into the gas phase during evaporation or condensation of the vapor.

Analytical solutions to the problem of bubble growth or collapse in the cited works were obtained under the assumption that the bubble size changes monotonically. This assumption is acceptable when analyzing boiling processes, but is not justified when studying bubble oscillation processes. To assess the heat exchange between the liquid and the bubble, it is necessary to know the temperature of the liquid directly at the interface. This temperature is decisive when calculating the rate of mass and heat transfer according to the equations of our model and is included in these equations as an unknown parameter. Therefore, our model is supplemented with an independent equation to determine this temperature.

Table 1 shows the errors in the calculated values of the dynamic characteristics of the bubble with the experimental data proposed in the studies of Shepherd *et al.* and Lesin *et al.* [51, 52].

Table 1: Forecasting errors.

| References | Change in bubble radius over time, % | Velocity of movement of the bubble boundary, % | Duration of the evaporation proces, % | Change in mass over time, % |
|---|---|---|---|---|
| [51] | 17 | 30 | – | – |
| [52] | 8 | 5 | 8 | 12 |

The calculated data are quite difficult to verify if we estimate the velocity of movement of the phase boundary. Previous studies, such as [18, 51–54], have presented high-speed video data of vapor bubble growth that qualitatively align with our calculations. Therefore, we compared our calculated data with the data given in [28, 55–57]. The results of the comparative analysis showed good agreement between our calculated data and the data given in the cited works.

The mathematical model we propose takes into account the temperature jump at the interface between vapor and liquid in a bubble, the oscillation of thermodynamic parameters in the vapor and in the liquid phase, and therefore more accurately describes the transient processes of bubble growth

or collapse. At this stage, we do not take into account the dynamic effects that neighboring bubbles or clusters create. It is obvious that they affect the values of thermodynamic parameters and the processes of heat and mass transfer in bubbles. But the developed model will be the basis for further modeling and is a very convenient tool for performing such an analysis. Thus, we assume that, based on the developed model, we will be able to improve the methodology for predicting the thermodynamic situation not only in single bubbles, but also in clusters.

## 4 Conclusions

Currently, there are no mathematical models capable of predicting with equally high accuracy the behavior of a bubble in boiling processes over a wide range of changes in operating parameters. Well-known models are developed based on the assumption of the quasi-equilibrium nature of the heat and mass transfer process and the monotonic distribution of temperature in the vapor phase and in the liquid. This article shows that currently existing methods for studying the dynamics of bubbles are not able to provide information necessary from a practical point of view regarding the dynamic and kinematic effects accompanying the phenomena of explosive boiling of highly superheated liquids due to the above assumptions.

The presence of a temperature gradient at the phase contact boundary corresponds to real processes of heat and mass transfer between vapor and liquid, and makes it possible to take into account the effects of energy accumulation in the phases and take into account the influence of these effects on the intensity of heat and mass transfer. On the other hand, taking into account the accumulation effect explains the reason for the discrepancies in the data on the duration of water evaporation, which in calculations may be less or more than measured experimentally. The intensification of heat and mass transfer processes depends on the degree of fluid superheating, and in such problems the data discrepancy can reach 180% (for the available analyzed works).The proposed mathematical model of the dynamics of a single bubble describes, with a minimum number of limiting assumptions, the behaviour of bubbles over the entire temperature range of the existence of the liquid phase. The model does not contain empirical coefficients or any fitting parameters and includes into consideration all physical factors that control the behaviour of the bubble, without limiting the degree of influence of a particular factor at various stages of the process.

An example of using the model in relation to the analysis of well-known experiments in the study of the dynamics of the growth of steam and vapour-gas bubbles in superheated liquids showed the ability of this model to predict the quantitative results of experiments with higher accuracy than currently used mathematical models.

Using the model to analyze experimental data allows us to obtain a large amount of additional information and qualitatively new data regarding the laws of boiling processes. The approach we propose can be used in the analysis of various phenomena and effects associated with the behavior of bubbles that are observed in experiments and do not find a clear physical explanation.

*Received 15 October 2023*

## References

[1] Zevnik J., Dular M.: *Cavitation bubble interaction with a rigid spherical particle on a microscale.* Ultrason. Sonochem. **69**(2020), 105252. doi: 10.1016/j.ultsonch.2020.105252

[2] Albanese L., Ciriminna R., Meneguzzo F., Pagliaro M.: *Energy efficient inactivation of Saccharomyces cerevisiae via controlled hydrodynamic cavitation.* Energy Sci. Eng. **3**(2015), 221–238. doi: 10.1002/ese3.62

[3] Podnar A., Dular M., Sirok B., Hocevar M.: *Experimental analysis of cavitation phenomena on Kaplan turbine blades using flow visualization.* J. Fluids Eng. **141**(2019), 7, 071101. doi: 10.1115/1.4041985

[4] Chernin L., Val D.V.: *Probabilistic prediction of cavitation on rotor blades of tidal stream turbines.* Renew. Energy **113**(2017), 688–696. doi: 10.1016/j.renene.2017.06.037

[5] Pham-Thanh N., Van Tho H., Yum Y.J.: *Evaluation of cavitation erosion of a propeller blade surface made of composite materials.* J. Mech. Sci. Technol. **29**(2015), 1629–1636. doi: 10.1007/s12206-015-0334-4

[6] Gasanov B.M., Bulanov N.V.: *Effect of the droplet size of an emulsion dispersion phase in nucleate boiling and emulsion boiling crisis.* Int. J. Heat Mass Transf. **88**(2015), 256–260. doi: 10.1016/j.ijheatmasstransfer.2015.04.018

[7] Roesle M.L., Lunde D.L., Kulacki F.A.: *Boiling heat transfer to dilute emulsions from a vertical heated strip.* J. Heat Transf. **137**(2015), 4, 041503. doi: 10.1115/1.4029456

[8] Rozentsvaig A.K., Strashinskii C.S.: *The growth of vapor bubbles in the volume of superheated drops, dispersed in high-boiling liquid*, Appl. Math. Sci. **8(**2014), 151, 7519–7528. doi: 10.12988/ams.2014.49183

[9] Ganesan B., Martini, S., Solorio J., Walsh M.K.: *Determining the effects of high intensity ultrasound on the reduction of microbes in milk and orange juice using response surface methodology.* Int. J. Food Sci. **2015**(2015), 350719. doi: 10.1155/2015/350719

[10] Chandrapala J., Oliver C., Kentish S., Ashokkumar M.: *Ultrasonics in food processing – Food quality assurance and food safety.* Trends Food Sci. Technol. **26**(2012), 88–98. doi: 10.1016/j.tifs.2012.01.010

[11] Sun X., Chen S., Liu J., Zhao S., Yoon J.Y.: *Hydrodynamic cavitation: A promising technology for industrial-scale synthesis of nanomaterials.* Front. Chem. **8**(2020), 259. doi: 10.3389/fchem.2020.00259

[12] Prajapat A.L., Gogate P.R.: *Depolymerization of carboxymethyl cellulose using hydrodynamic cavitation combined with ultraviolet irradiation and potassium persulfate.* Ultrason. Sonochem. **51**(2019), 258–263. doi: 10.1016/j.ultsonch.2018.10.009

[13] Sun X., Wang Z., Xuan X., Ji L., Li X., Tao Y., Boczkaj G., Zhao S., Yoon J.Y., Chen S.: *Disinfection characteristics of an advanced rotational hydrodynamic cavitation reactor in pilot scale.* Ultrason. Sonochem. **73**(2021), 105543. doi: 10.1016/j.ultsonch.2021.105543

[14] Albanese L., Baronti S., Liguori F., Meneguzzo F., Barbaro P., Vaccari F.P.: *Hydrodynamic cavitation as an energy efficient process to increase biochar surface area and porosity: A case study.* J. Clean. Prod. **210**(2019), 159–169. doi: 10.1016/j.jclepro.2018.10.341

[15] Pavlenko A.M.: *Change of emulsion structure during heating and boiling.* Int. J. Energy Clean Environ. **20**(2019), 291–302. doi: 10.1615/InterJEnerCleanEnv.2019032616

[16] Pavlenko A.M., Basok B.I.: *Regularities of boiling-up of emulsified liquids.* Heat Transf. Res. **36**(2005), 5, 419–424. doi: 10.1615/HeatTransRes.v36.i5.90

[17] Pavlenko A.M., Basok B.I.: *Kinetics of water evaporation from emulsions.* Heat Transf. Res. **36**(2005), 5, 425–430. doi: 10.1615/HeatTransRes.v36.i5.100

[18] Butcher J.C.: *Numerical Methods for Ordinary Differential Equations.* Wiley, New York 2008. doi: 10.1002/9780470753767

[19] Darges S.J., Devahdhanush V.S., Mudawar I., Nahra H.K., Balasubramaniam R., Hasan M.M., Mackey J.R.: *Experimental results and interfacial lift-off model predictions of critical heat flux for flow boiling with subcooled inlet conditions – In preparation for experiments onboard the International Space Station.* Int. J. Heat Mass Tran. **183**(2022), C, 122241. doi: 10.1016/j.ijheatmasstransfer.2021.122241

[20] Yin S., Wang H., Xu Bo, Yang C., Gu H.: *Critical flow leakage of a vapour-liquid mixture from sub-cooled water: Nucleation boiling study.* Int. J. Heat Mass Tran. **146**(2020), 118807. doi: 10.1016/j.ijheatmasstransfer.2019.118807

[21] Xiao J., Zhang J.: *Experimental investigation on flow boiling bubble motion under ultrasonic field in vertical minichannel by using bubble tracking algorithm.* Ultrason. Sonochem. **95**(2023), 106365. doi: 10.1016/j.ultsonch.2023.106365

[22] Xi X., Liu H., Cai Ch., Jia M., Yin H.: *Analytical investigation on homogeneous nucleation of bicomponent fuels.* Int. J. Heat Mass Tran. **132**(2019), 498–507. doi: 10.1016/j.ijheatmasstransfer.2018.12.028

[23] Xi X., Liu H., Cai Ch., Jia M. Zhang W.: *Analytical investigation on the homogeneous nucleation in a mono-component and bi-component droplet.* In: Proc. ASME 2019 6th Int. Conf. on Micro/Nanoscale Heat and Mass Transfer, Dalian, July 8–10, 2019, V001T11A003. doi: 10.1115/MNHMT2019-3968

[24] Xi X., Cai Ch., Liu H., Wen R., Ma X., Song X.: *Analytical and experimental study on binary droplet evaporation: Inhibitory effect of adding mineral oil adjuvant to water.* Int. Commun. Heat Mass Transf. **142**(2023), 106630. doi: 10.1016/j.icheatmasstransfer.2023.106630

[25] Zihe L., Ming J., Xi X., Hong L., Ping Y.: *Simulation of the evaporation/boiling transition for the vaporization of a bi-component droplet under wide-temperature environments.* Int. J. Heat Mass Tran. **193**(2022), 122968. doi: 10.1016/j.ijheatmasstransfer.2022.122968

[26] Roesle M.L., Lunde D.L., Kulacki F.A.: *Boiling heat transfer to dilute emulsions from a vertical heated strip.* Int. J. Heat Mass Tran. **137**(2015), 8. doi: 10.1016/j.ijheatmasstransfer.2011.12.020

[27] Dietzel D., Hitz T., Munz C.D., Kronenburg A.: *Expansion rates of bubble clusters in superheated liquids.* In: Proc. Germany ILASS–Europe 2017, 28th Conf. on Liquid Atomization and Spray Systems, Valencia, 6–8 Sept. 2017. doi: 10.4995/ILASS2017.2017.4714

[28] Pavlenko A.: *Dispersed phase breakup in boiling of emulsion.* Heat Transf. Res. **49(**2018), 633–641. doi: 10.1615/HeatTransRes.2018020630

[29] Pavlenko A.: *Energy conversion in heat and mass transfer processes in boiling emulsions.* Therm. Sci. Eng. Prog. **15**(2019), 1–8. doi: 10.1016/j.tsep.2019.100439

[30] Aktershev S.P., Ovchinnikov V.V.: *Modelling of boiling up of a metastable liquid with appearance of the evaporation fronts.* Mod. Sci. Res. Ideas Results Technol. **1**(2013), 77–82.

[31] Pavlenko A.M., Koshlak H.: *Application of thermal and cavitation effects for heat and mass transfer process intensification in multicomponent liquid media.* Energies **14**(2021), 7996. doi: 10.3390/en14237996

[32] Pavlenko A.M., Szkarowski A., Janta-Lipińska S.: *Research on burning of water black oil emulsions.* Rocz. Ochr. Śr. **16**(2014), 376–385.

[33] Pavlenko A.M.: *Thermodynamic features of the intensive formation of hydrocarbon hydrates.* Energies **13**(2020), 3396. doi: 10.3390/en13133396

[34] Pavlenko A.M., Koshlak H.: *Heat and mass transfer during phase transitions in liquid mixtures.* Rocz. Ochr. Śr. **21**(2019), 234–249.

[35] Koshlak H., Pavlenko A.: *Method of formation of thermophysical properties of porous materials.* Rocz. Ochr. Śr. **21**(2019), 1253–1262.

[36] Mura E., Massoli P., Josset C.; Loubar K.; Bellettre J.: *Study of the micro-explosion temperature of water in oil emulsion droplets during the Leidenfrost effect.* Exp. Therm. Fluid Sci. **43**(2012), 63–70. doi: 10.1016/j.expthermflusci.2012.03.027

[37] Shinjo J., Xia J., Megaritis A., Ganippa L.C., Cracknell R.F.: *Modeling temperature distribution inside an emulsion fuel droplet under convective heating: A key to predicting microexplosion and puffing.* At. Sprays. **26**(2016), 551–583. doi: 10.1615/AtomizSpr.2015013302

[38] Yusof N.S.M., Babgi B., Alghamdi Y., Aksu M., Madhavan J., Ashokkumar M.: *Physical and chemical effects of acoustic cavitation in selected ultrasonic cleaning applications.* Ultrason. Sonochem. **29**(2016), 568–576. doi: 10.1016/j.ultsonch.2015.06.013

[39] Denner F., Schenke S.: *Modeling acoustic emissions and shock formation of cavitation bubbles.* Phys. Fluids **35**(2023). doi: 10.1063/5.0131930

[40] Lee G.L., Law M.C.: *Numerical modelling of single-bubble acoustic cavitation in water at saturation temperature.* Chem. Eng. J.. **430**(2022), 133051. doi: 10.1016/j.cej.2021.133051

[41] Peng K., Qin F.G., Jiang R., Kang S.: *Interpreting the influence of liquid temperature on cavitation collapse intensity through bubble dynamic analysis.* Ultrason. Sonochem. **69**(2020), 105253. doi: 10.1016/j.ultsonch.2020.105253

[42] Phan, T., Kadivar E., Nguyen V.T., Moctar O., Park W.: *Thermodynamic effects on single cavitation bubble dynamics under various ambient temperature conditions.* Phys. Fluids **34(**2022). doi: 10.1063/5.0076913

[43] Dehane A., Merouani S., Hamdaoui O., Alghyamah A.: *A comprehensive numerical analysis of heat and mass transfer phenomenons during cavitation sono-process.* Ultrason. Sonochem. **73**(2021), 105498. doi: 10.1016/j.ultsonch.2021.105498

[44] Feng J., Muradoglu M., Kim H., Ault J.T., Stone H.A.: *Dynamics of a bubble bouncing at a liquid/liquid/gas interface.* J. Fluid Mech. **807(**2016), 324–352. doi: 10.1017/jfm.2016.517

[45] Melikhov V., Yakush S., Le T.: *Evaluation of energy and impulse generated by superheated steam bubble collapse in subcooled water.* Nucl. Eng. Des. **366**(2020), 110753.

[46] Califano V., Calabria R., Massoli P.: *Experimental evaluation of the effect of emulsion stability on micro-explosion phenomena for water-in-oil emulsions.* Fuel **117**(2015), 87–94. doi: 10.1016/j.fuel.2013.08.073

[47] Gilmore F.R.: *The growth or collapse of a spherical bubble in a viscous compressible liquid.* CaliCal. Tecn. Inst. Rep. Los Angeles 1952, 17–29.

[48] Prosperetti A.: *Vapor bubbles.* Annu. Rev. Fluid Mech. **49(**2017), 221–248. doi: 10.1146/annurev-fluid-010816-060221

[49] Bourguignon J.P., Brezis H.: *Remarks on the Euler equation.* J. Funct. Anal. **15**(1974), 341–363, 1974. doi: 10.1016/0022-1236(74)90027-5

[50] Pavlenko A., Koshlak H., Basok B., Hrabova T.: *Thermomechanical homogenization in steam explosion.* Rocz. Ochr. Śr. **25**(2023), 9–15.

[51] Shepherd J.E., Sturtevant B.: *Rapid evaporation at the superheat limit.* J. Fluid Mech. **121**(1982), 379–388. doi: 10.1017/S0022112082001955

[52] Lesin S., Baron A., Branover G., Merchuk I.: *Experimental studies of direct contact boiling at the superheat limit.* High Temp. **31**(1993), 866.

[53] Vogel A., Lauterborn W., Timm R.: *Optical and acoustic investigations of the dynamics of laser-produced cavitation bubbles near a solid boundary.* J. Fluid Mech. **206**(1989), 299–338.

[54] Qin D., Lei S., Chen B., Li Z., Wang W., Ji X.: *Numerical investigation on acoustic cavitation characteristics of an air-vapor bubble: Effect of equation of state for interior gases*. Ultrason. Sonochem. **97**(2023), 106456. doi: 10.1016/j.ultsonch.2023.106456

[55] Nigmatulin R.I., Khabeev N.S., Nagiev F.B.: *Dynamics, heat and mass transfer of vapour-gas bubbles in a liquid*. Int. J. Heat Mass Transf. **24**(1981), 1033–1044. doi: 10.1016/0017-9310(81)90134-4

[56] Merouani S., Hamdaoui O., Rezgui Y., Guemini M.: *Theoretical estimation of the temperature and pressure within collapsing acoustical bubbles*. Ultrason. Sonochem. **21**(2014), 53–59. doi: 10.1016/j.ultsonch.2013.05.008

[57] Fuster D., Dopazo C., Hauke G.: *Liquid compressibility effects during the collapse of a single cavitating bubble*. J. Acoust. Soc. Am. **129(**2011), 122–131. doi: 10.1121/1.3502464

**archives**
**of thermodynamics**
Vol. **44**(2023), No. 4, 507–534
DOI: 10.24425/ather.2023.149727

# Resources and potential for utilization of low-exergy heat from mung bean sprouts cultivation – case study

**PAWEŁ MIREK**[a*]
**MARCIN PANOWSKI**[a]
**KLAUDIA SŁOMCZYŃSKA**[a, b]
**MICHAŁ STANEK**[c]
**TOMASZ BĄKOWSKI**[c]

[a] Czestochowa University of Technology, Faculty of Infrastructure and Environment, Dąbrowskiego 69, 42-201 Częstochowa, Poland

[b] ENERGOPROJEKT-KATOWICE SA, Jesionowa 15, 40-159 Katowice, Poland

[c] Uniflora Sp. z o.o., Lwowska 8, 42-202 Częstochowa, Poland

**Abstract** Poland is a significant producer of vegetable sprouts, which, due to the high content of nutrients, are produced for food purposes. The cultivation cycle of these plants, especially the mung beans (Vigna radiata), is associated with significant exploitation of natural resources (as much as 275 $dm^3$ of water per 1 kg of dry seeds) and requires appropriate temperature conditions. However, since producing of vegetable sprouts is an exothermic process, there are reasons to organize the growth conditions of these plants in a quasi-autonomous manner. Estimated preliminary studies show that during the entire period of sprout growth, as much as 2.86 MJ of heat from 1 kg of dry seeds can be used, which, taking into account the scale of production of these plants, places them among the significant sources of low-temperature waste heat. The paper presents the results of temperature measurements carried out in a growth chamber used for the industrial production of the mung bean vegetable sprouts. Based on the prepared energy balance, the total amount of heat generated (4.9 GJ) and recovered (3.3 GJ) in the seed germination process was determined. The amount of energy lost

*Corresponding Author. Email: pawel.mirek@pcz.pl

in the process of imbibition and the amount of heat needed to ensure optimal plant growth conditions were determined. The study shows that the use of low-temperature heat generated by plants allows for a significant reduction in the energy consumption of the production process.

**Keywords:** Mung beans; Waste heat recovery; Energy balance; Biomass; Sprouts production

## Nomenclature

| | | |
|---|---|---|
| $A$ | – | cross-section, $m^2$ |
| $A_c$ | – | heat exchange surface area, $m^2$ |
| $A_F$ | – | front wall area, $m^2$ |
| $c$ | – | specific heat, J/(kgK) |
| $d$ | – | wall partition thickness, m |
| $E_{a_{\mathrm{con}}}$ | – | energy transferred in the gas phase by convective mixing, J |
| $E_d$, $E_{ds}$ | – | energy contained in the imbibition and irrigation water, respectively, which is discharged through a leak to the drain collector, J |
| $E_{\mathrm{imb}}$ | – | energy supplied to the growth chamber during the imbibition phase, J |
| $E_{\mathrm{in}}$, $E_{\mathrm{out}}$ | – | energy supplied to and removed from the system, J |
| $E_{\mathrm{mass,in}}$, $E_{\mathrm{mass,out}}$ | – | energy transport with mass into and out of the system, respectively, J |
| $E_s$ | – | energy contained in the water flowing through the plant mass in the irrigation process, J |
| $g$ | – | gravitational acceleration, $m/s^2$ |
| $h$ | – | specific enthalpy, J/kg |
| $h_{a_{\mathrm{in}}}$ | – | enthalpy of air supplied to the growth chamber, J/kg |
| $h_{a_{\mathrm{out1}}}$, $h_{a_{\mathrm{out2}}}$ | – | enthalpy of air removed from the growth chamber through pipeline 1 and 2, respectively, J/kg |
| $h_{\mathrm{imb_{in}}}$ | – | enthalpy of water supplied to the growth chamber during the imbibition process, J/kg |
| $h_{\mathrm{imb_{out1}}}$, $h_{\mathrm{imb_{out2}}}$ | – | enthalpy of water discharged from the growth chamber after the imbibition process directly into the drain channel and through the growth cabin, respectively, J/kg |
| $h_{\mathrm{imb_{vap}}}$, $h_{w_{\mathrm{vap}}}$ | – | enthalpy of water evaporated during the imbibition and irrigation phase, respectively, J/kg |
| $h_{\mathrm{in}}$, $h_{\mathrm{out}}$ | – | enthalpy of fluid entering and leaving the control volume, respectively, J/kg |
| $h_{w_{\mathrm{in}}}$ | – | enthalpy of water supplied to the growth chamber during the irrigation phase, J/kg |
| $h_{w_{\mathrm{out1}}}$, $h_{w_{\mathrm{out2}}}$ | – | enthalpy of water discharged from the growth chamber during the irrigation process directly into the outlet channel and through the growth cabin, respectively, J/kg |
| $m$ | – | mass, kg |
| $\dot{m}_{a_{\mathrm{in}}}$, $m_{a_{\mathrm{in}}}$ | – | mass flow rate and mass, respectively, of air supplied to the growth chamber, kg/s, kg |

$\dot{m}_{a_{\text{out}1}}$, $m_{a_{\text{out}1}}$ – mass flow rate and mass, respectively, of air removed from the growth chamber through pipeline 1, kg/s, kg

$\dot{m}_{a_{\text{out}2}}, m_{a_{\text{out}2}}$ – mass flow rate and mass, respectively, of air removed from the growth chamber through pipeline 2, kg/s, kg

$m_{\text{CV}}$ – amount of mass accumulated in the control volume, kg

$\dot{m}_{\text{imb}_{\text{acc}}}$, $m_{\text{imb}_{\text{acc}}}$ – mass flow rate and mass, respectively, of water accumulated in seeds during the imbibition process, kg/s, kg

$\dot{m}_{\text{imb}_{\text{in}}}$, $m_{\text{imb}_{\text{in}}}$ – mass flow rate and mass, respectively, of water supplied to the growth chamber during the imbibition process, kg/s, kg

$\dot{m}_{\text{imb}_{\text{out}}}$, $m_{\text{imb}_{\text{out}}}$ – mass flow rate and mass, respectively, of water discharged from the growth chamber after the imbibition process, kg/s, kg

$\dot{m}_{\text{imb}_{\text{out}1}}$, $m_{\text{imb}_{\text{out}1}}$ – mass flow rate and mass, respectively, of water discharged from the growth chamber during the imbibition process directly into the drain channel, kg/s, kg

$\dot{m}_{\text{imb}_{\text{out}2}}$, $m_{\text{imb}_{\text{out}2}}$ – mass flow rate and mass, respectively, of water discharged from the growth chamber during the imbibition process through the growth cabin, kg/s, kg

$\dot{m}_{\text{imb}_{\text{vap}}}$, $m_{\text{imb}_{\text{vap}}}$ – mass flow rate and mass, respectively, of water evaporated during the imbibition phase, kg/s, kg

$\dot{m}_{\text{in}}$, $m_{\text{in}}$ – mass flow rate and mass, respectively, of fluid entering the control volume, kg/s, kg

$\dot{m}_{\text{out}}$, $m_{\text{out}}$ – mass flow rate and mass, respectively, leaving the control volume, kg/s, kg

$\dot{m}_{w_{\text{acc}}}$, $m_{w_{\text{acc}}}$ – mass flow rate and mass, respectively, of water accumulated in seeds during the irrigation phase, kg/s, kg

$\dot{m}_{w_{\text{in}}}$, $m_{w_{\text{in}}}$ – mass flow rate and mass, respectively, of water supplied to the growth chamber during the irrigation phase, kg/s, kg

$\dot{m}_{w_{\text{out}}}$, $m_{w_{\text{out}}}$ – mass flow rate and mass, respectively, of water discharged from the growth chamber during the irrigation phase, kg/s, kg

$\dot{m}_{w_{\text{out}1}}$, $m_{w_{\text{out}1}}$ – mass flow rate and mass, respectively, of water discharged from the growth chamber during the irrigation process directly into the outlet channel, kg/s, kg

$\dot{m}_{w_{\text{out}2}}$, $m_{w_{\text{out}2}}$ – mass flow rate and mass, respectively, of water discharged from the growth chamber during the irrigation process through the growth cabin, kg/s, kg

$\dot{m}_{w_{\text{vap}}}$, $m_{w_{\text{vap}}}$ – mass flow rate and mass, respectively, of water evaporated during the irrigation phase, kg/s, kg

$m_1$, $m_2$ – amount of mass in the control volume at the time $t_1$, and $t_2$, respectively, kg

$Q$ – heat, J

$Q_c$ – heat coming from the heat storage through the heat transmission, J

$Q_{\text{in}}$, $Q_{\text{out}}$ – heat entering and leaving the control volume, respectively, J

$Q_{\text{vap}}$ – heat needed to evaporate the moisture, J

$Q_{\text{wall}}$ – heat exchanged in the gas phase by heat transmission through the front wall of the chamber, J

$V_a$ – volume of fresh air supplied to the growth chamber, $\text{m}^3$

$v$ – fluid velocity, m/s

$V_d$, $V_s$ – volume of water supplied directly to the drain collector and through the growth cabin, respectively, $m^3$
$V_{imb}$ – volume of water supplied to the growth cabin during imbibition, $m^3$
$t$ – time, s
$T_a$ – inlet air temperature, K
$T_{ex}$ – outside air temperature on the front door side, K
$T_{imb}$ – temperature of the water for soaking the seeds during imbibition, K
$T_{in}$ – average internal temperature in the growth chamber, K
$T_{in1}$, $T_{in2}$ – outlet air temperature in pipeline 1 and 2, respectively, K
$T_{out}$ – used water temperature measured at the drain, K
$T_p$ – temperature of used water discharged directly from the growth cabin, K
$T_{ref}$ – reference air temperature in the growth chamber, K
$T_w$ – irrigation water temperature, K
$T_{0.8}$, $T_{1.1}$, $T_{1.4}$ – temperature of sprouts in the cabin at height 0.8 m, 1.1 m, and 1.4 m, respectively, K
$W_{in}$, $W_{out}$ – work transfer into and out of the system, J
$z$ – leveling height, m

**Greek symbols**

$\alpha_{ex_v}$, $\alpha_{in_v}$ – external and internal convective heat-transfer coefficient for vertical heat transport, respectively, $W/(m^2K)$
$\alpha_{ex_h}$, $\alpha_{in_h}$ – external and internal convective heat-transfer coefficient for horizontal heat transport, respectively, $W/(m^2K)$
$\lambda$ – thermal conductivity coefficient, W/(m K)
$\mu$ – molecular weight, kg
$\rho$ – density, $kg/m^3$
$\Delta E_{CV}$ – change in energy in the control volume due to the change in internal, kinetic and potential energy, J
$\Delta H_{vap}$ – enthalpy of water evaporation, kJ/mol
$\Delta Q$ – heat change in the control volume, J

**Subscripts**

$a$ – air
$w$ – water

**Abbreviations**

ADP – adenosine diphosphate
ATP – adenosine triphosphate
Pi – inorganic phosphate
WHR – waste heat recovery

# 1 Introduction

The European Green Deal clearly identifies achieving zero net greenhouse gas emissions by 2050 as the main task of the European Union's energy policy. This assumption introduces the necessity of economy decarbonization, among others through increasing the share of renewable energy sources (RES) in heat and electricity production technologies, increasing energy efficiency of buildings, wider use of hydrogen technologies and nuclear energy, as well as reduction of energy consumption. The latter goal can be achieved by reusing waste energy. Waste heat accompanies practically all production processes and is often treated as a by-product that is discharged into the environment and irretrievably lost [1,2]. Its reuse (called waste heat recovery – WHR) allows reducing the consumption of conventional fuels, which directly results in a significant reduction in greenhouse gas emissions. The importance of WHR for rational energy policy is emphasized by the huge waste heat resources present in the world. According to the simulations carried out by Firth *et al.* [3] by 2030 they will be at the level of 23% to 53% of global primary energy consumption (depending on the energy scenario adopted for the calculations). Taking into account that about 25% of the total energy consumption falls on the industrial sector [4], it is worth paying attention to the possibility of using waste heat in this very area. In particular, the recovery of heat with low quality parameters, which in production processes constitutes up to 40% of total waste energy, seems to be an important issue [5].

Taking into account the quality parameters, in particular the temperature of the energy carrier, three types of waste heat can be distinguished [6]:

- low-temperature (below 503 K),
- medium-temperature (503–923 K),
- high-temperature (above 923 K).

Despite the widespread use of low-temperature waste heat sources in the industry, its reuse is troublesome and often requires high financial outlays. The difficulties are mainly related to the low-quality parameters of heat carriers, which may be insufficient to directly meet the needs of consumers [7]. Another problem may be the lack of a low exergy heat collection installation. Ensuring effective heat exchange between factors of similar temperature requires reducing their flow velocity. This may result in the necessity of

using very large heat exchangers, which increases investment expenditure and is sometimes impossible to implement [8]. The solution may be the design of hybrid systems using, among others, heat pumps [9,10], cryogenic energy stores [11,12], or the organic Rankine cycle (ORC) [13,14]. Another type of difficulty in utilizing waste heat is the large degree of dispersion in different parts of the production process. Combining the media from all heat sources with similar temperatures into a single stream can help in efficient energy recovery, but often leads to a reduction in the amount of energy recovered compared to recovering directly from each source. On the other hand, such action significantly reduces the cost of the waste heat recovery installation and may be more economically attractive for the company [8].

Despite the many difficulties with low-temperature heat recovery, there are many manufacturing processes where it is implemented. Table 1 shows examples of WHR installations in various industry sectors.

Table 1: Examples of the use of WHR in the manufacturing processes of various industries.

| Industry sector | Waste heat source | Working medium temperature (K) | Nominal heat output | Ref. |
|---|---|---|---|---|
| Food industry | Brewing process – microbrewery (Mexico) | 315–353 | No data available | [15] |
| | Dairy waste water – Arla (Denmark) | 295–298 | 1.5 MW | [16] |
| Petrochemical industry | Catalytic reforming plant – Shijiazhuang Refining & Chemical Company (China) | 371–488 | 3.3 MW | [17] |
| Metallurgical industry | Wastewater from steel production – Angang Lingshan (China) | 303–313 | 9.5 MW | [18] |
| | Ferrosilicon production – Elkem Rana (Norway) | 393 | 22 MW | [19] |
| Textile industry | Yarn Dyeing Process – Dyeing Plant (China) | 353–368 | No data available | [20] |
| | Exhaust fumes – garment factory (Bangladesh) | 459–482 | 3586 MWh/annually | [21] |
| | Textile drying process – Textile factory (Turkey) | 393–453 | No data available | [22] |
| Paper industry | Paper drying process – Skjern Papirfabrik (Denmark) | 316 | No data available | [23] |

One of the examples of sources of low-quality waste energy are biological processes occurring during the production of vegetable sprouts for food purposes. The exothermic nature of these processes accompanies both the germination phase and the further growth of plants, resulting in the formation of a significant stream of low-temperature heat (293–313 K), usually discharged to the environment. The mung bean is one of the most popular plant species produced for food purposes in the form of sprouts. It is a legume plant whose sprouts are grown in the dark, in a hot and humid environment, and is a valuable source of protein and essential amino acids [24]. Bean germination begins inside the seed, causing the embryo to revive and grow. The beginning of germination is the period of water absorption by the plant and the end is the appearance of the embryonic root (i.e. sprout). After the appearance of the root, the growth of the seedling begins [25]. Sprouts produced in the production process for food purposes are defined as 'the product obtained by the germination of seeds and their development in water or another medium, harvested before the development of proper leaves and intended to be eaten whole, including the seed' [26]. A sprouted seed, therefore, includes the sprout, seedling, and shoots [27]. Thus, the production of sprouts for food purposes includes not only the germination process but also the growth of the seedling until the appearance of the first leaves. Figure 1 shows the main phases of the mung bean seed germination.

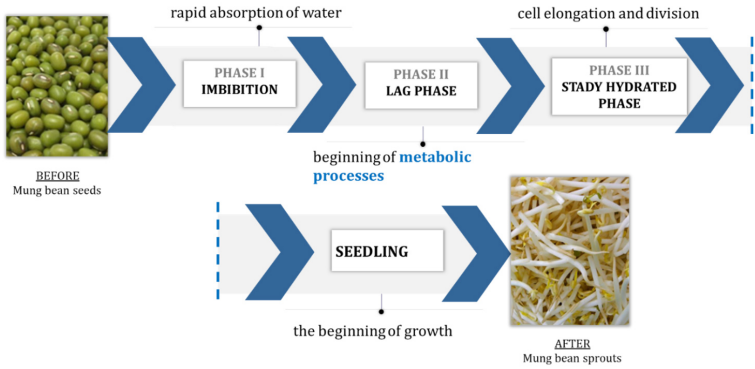


Figure 1: Main stages of the mung bean seed germination process.

Waste heat in the germination process is generated according to two mechanisms [28]. The first one is related to the swelling of seeds, which intensively absorb water in the first stage of germination, called the imbibition stage [29]. The source of heat is then the physicochemical processes related

to mechanical stresses that occur in the seed coat. After the rupture of the seed coat and initiation of metabolic processes, particularly cellular respiration, the main role in heat generation begins to be played by catabolic reactions defined by the equation [28,30]:

$$\text{organic substrate} + O_2 + x\,\text{ADP} + x\,\text{Pi} \rightarrow CO_2 + H_2O + x\,\text{ATP} + Q \quad (1)$$

and anabolic reactions, according to the following equation:

$$\text{organic substrate} + y\,\text{ATP} \rightarrow \text{growth} + y\,\text{ADP} + y\,\text{Pi} + Q. \quad (2)$$

where $x$ and $y$ are stoichiometric coefficients.

During catabolic processes, the spare substances (mainly carbohydrates) found in seeds are oxidized to carbon dioxide and water [25]. The adenosine-5′-triphosphate (ATP) molecule is also produced, which stores and transports the energy obtained from the decomposition of organic matter stored in the spare tissue in seeds. This energy is involved in anabolic reactions, where it is used to create new cells. During these reactions, energy in the form of heat is dissipated to the environment [30, 31]. This heat is a by-product of the cellular respiration process occurring in the seeds [28] and can be reused in the sprout production process. This is extremely important since the cultivation cycle of these plants involves the use of significant amounts of water and requires appropriate temperature conditions. The use of waste heat can help to increase the efficiency of the process and thus reduce the use of conventional energy sources.

Although the mechanism of heat generation by plants is known and research on the determination of heat flux of germinating plants was initiated by Pierce already in 1908 [32], there is still a lack of literature reports on the possibility of its practical application and information on the amount of heat generated by seeds during the production of vegetable sprouts. So far, the energy released by seeds of soybean [33], wheat [31], corn [34] or quinoa [35,36], among others, has been studied under laboratory conditions. These studies were biological analyses and focused only on attempts to determine the course of the germination phase and the influence of various environmental factors on their germination rates [30,31]. Since the object of interest was mainly the germination process itself without seedling growth, the main experiments lasted no longer than 72 hours. From the point of view of the analysis of energy processes occurring under conditions of industrial sprout cultivation, this period is too short. This is because the sprouts' cultivation includes not only the germination process but also the

growth phase (up to the appearance of the first proper leaves) and lasts several days, depending on the plant species cultivated. For this reason, an energy analysis of the growth process must be carried out over the entire production period, from the imbibition phase to the fully formed sprout phase.

The paper presents the results of experimental studies of the growth chamber of the mung bean. Based on temperature measurements carried out during the whole period of the plant growth, the amounts of heat supplied to and removed from the growth chamber were evaluated. The obtained results allowed to determine the amount of energy possible to be reused and the amount of heat generated by the plant mass.

## 2 Mass and energy balance of the growth chamber

Figure 2 shows a block diagram of the installation for the production of the mung bean vegetable sprouts, with the growth chamber being the subject of the analysis. The main component of the installation is the growth chamber, in which the process of plant cultivation is carried out. Providing appropriate conditions for the growth of plants is possible by periodically

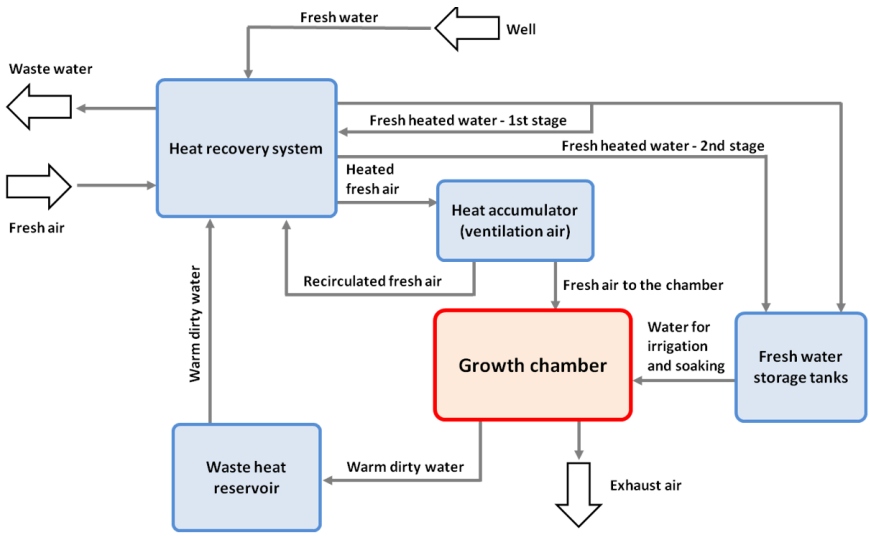


Figure 2: Block diagram of the installation for the production of the mung bean vegetable sprouts with the growth chamber being the subject of the analysis.

ventilating the chamber with the fresh air and supplying the fresh water necessary for the phase of soaking the seeds and irrigation of plant mass. The heat contained in the drainage water from the chamber is recovered in the heat recovery system, whose main task is to heat up the cold water supplied from the deep well.

### 2.1 Mass balance

From the point of view of mass balance, the growth chamber is a control volume in which optimal conditions for plant growth are ensured by supplying both water and air at a certain temperature. Considering a non-steady flow process for a control volume in a time interval from $t_1$ to $t_2$ a balance of mass can be written in general form as [37]

$$\sum m_{\text{in}} - \sum m_{\text{out}} = m_2 - m_1 \,, \tag{3}$$

where $m_2$ and $m_1$ denote the amounts of mass in the control volume at the time $t_2$ and $t_1$ respectively, and $m_{\text{in}}$ and $m_{\text{out}}$ represent amounts of mass that enter and leave the control volume given by the following equations:

$$m_{\text{in}} = \int_{t_1}^{t_2} \rho v A \, dt, \tag{4}$$

$$m_{\text{out}} = \int_{t_1}^{t_2} \rho v A \, dt. \tag{5}$$

The left side of Eq. (3) represents the net amount of mass transferred into the control volume, while the right side represents the amount of mass accumulated within it. The Eq. (3) can be written in the rate form as follows

$$\sum \dot{m}_{\text{in}} - \sum \dot{m}_{\text{out}} = \frac{dm_{\text{CV}}}{dt} \,, \tag{6}$$

where $\dot{m}_{\text{in}}$ and $\dot{m}_{\text{out}}$ denote the rate of mass flow that enters and leaves the control volume.

Figure 3 shows a schematic of the growth chamber with the air and water mass streams.

The mass balance for the air entering and leaving the chamber is defined by the equation

$$\dot{m}_{a_{\text{in}}} = \dot{m}_{a_{\text{out1}}} + \dot{m}_{a_{\text{out2}}} \,. \tag{7}$$

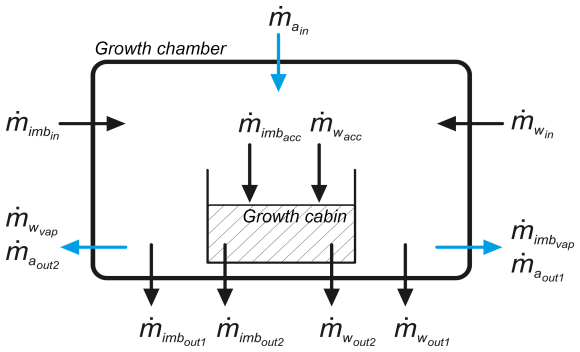


Figure 3: Diagram of the growth chamber with the air and water mass streams entering and leaving the control volume.

The mass balance for water entering and leaving the growth chamber during the imbibition process is given by the equation

$$\dot{m}_{\mathrm{imb_{in}}} = \dot{m}_{\mathrm{imb_{out}}} + \dot{m}_{\mathrm{imb_{acc}}} + \dot{m}_{\mathrm{imb_{vap}}} \,. \tag{8}$$

The mass balance for water entering and leaving the growth chamber during the plant irrigation process is determined by the equation

$$\dot{m}_{w_{\mathrm{in}}} = \dot{m}_{w_{\mathrm{out}}} + \dot{m}_{w_{\mathrm{acc}}} + \dot{m}_{w_{\mathrm{vap}}} \,. \tag{9}$$

As the stream of water supplied from the sprinkler system does not fully reach the growth cabins, part of the water supplied in the process of imbibition and growth is drained directly to the outlet channel. Therefore, it can be written

$$\dot{m}_{\mathrm{imb_{out}}} = \dot{m}_{\mathrm{imb_{out1}}} + \dot{m}_{\mathrm{imb_{out2}}} \,, \tag{10}$$

$$\dot{m}_{w_{\mathrm{out}}} = \dot{m}_{w_{\mathrm{out1}}} + \dot{m}_{w_{\mathrm{out2}}} \,. \tag{11}$$

Finally, the growth chamber mass balance can be expressed by the following equation

$$\begin{aligned} \dot{m}_{a_{\mathrm{in}}} + \dot{m}_{\mathrm{imb_{in}}} + \dot{m}_{w_{\mathrm{in}}} - (\dot{m}_{a_{\mathrm{out1}}} + \dot{m}_{a_{\mathrm{out2}}}) - (\dot{m}_{\mathrm{imb_{out}}} + \dot{m}_{\mathrm{imb_{vap}}}) \\ - (\dot{m}_{w_{\mathrm{out}}} + \dot{m}_{w_{\mathrm{vap}}}) = \dot{m}_{\mathrm{imb_{acc}}} + \dot{m}_{w_{\mathrm{acc}}} \,. \end{aligned} \tag{12}$$

## 2.2 Energy balance

Energy can be transferred to or from a control volume in the forms of heat, work, and mass. Noting that the net transfer of a quantity is equal to the

difference between the amounts transferred in and out, the energy balance can be written in general form as follows

$$E_{\text{in}} - E_{\text{out}} = (Q_{\text{in}} - Q_{\text{out}}) + (W_{\text{in}} - W_{\text{out}}) + (E_{\text{mass,in}} - E_{\text{mass,out}}) = \Delta E_{\text{CV}} \,. \tag{13}$$

The amount of energy transport by mass is given by equation

$$E_{\text{mass}} = m\left(h + \frac{v^2}{2} + gz\right). \tag{14}$$

When the kinetic and potential energies of a fluid stream are negligible and the work done by a system is zero, as is in the case of the growth chamber, the relation (13) simplifies to

$$\Delta E_{\text{CV}} = \Delta Q + \sum m_{\text{out}} h_{\text{out}} - \sum m_{\text{in}} h_{\text{in}} \,, \tag{15}$$

where in

$$\sum m_{\text{in}} = m_{a_{\text{in}}} + m_{\text{imb}_{\text{in}}} + m_{w_{\text{in}}} \,, \tag{16}$$

$$\sum m_{\text{out}} = m_{a_{\text{out1}}} + m_{a_{\text{out2}}} + m_{\text{imb}_{\text{out}}} + m_{\text{imb}_{\text{vap}}} + m_{\text{imb}_{\text{acc}}} + m_{w_{\text{out}}} + m_{w_{\text{vap}}} + m_{w_{\text{acc}}} \,. \tag{17}$$

$\Delta Q$ is the change in heat in the control volume due to heat transmission through the chamber walls, the endothermic process of water evaporation, and the exothermic process of plant cellular respiration. A schematic of the growth chamber is shown in Fig. 4, highlighting the heat and energy transported by air and water to and from the control volume.

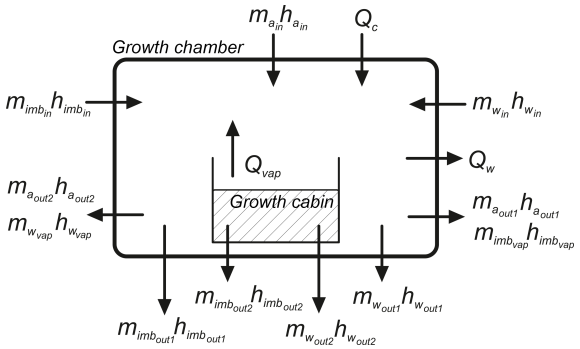


Figure 4: Diagram of the growth chamber with heat and energy transported by air and water to and from the control volume.

The heat supplied to the growth chamber comes from external and internal sources. The transport of heat from the internal source is related to the exothermic process of cellular respiration of germinating plants, while the transport from the external source takes place in the process of heat transmission through a wall. In the same process, heat from the growth chamber is transported to the outside. An additional source of loss is the process of water evaporation during both the imbibition and irrigation phases of the plants. The main mechanism of energy transport to the control volume is the mass flow of air and soaking water. On the other hand, the energy derived from the control volume is associated with the flow of water coming from the sprinkler system, water after the soaking phase, and water absorbing heat from the plant mass contained in the growth cabins. In the further part of the paper, it is assumed that the energy fluxes entering the control volume will be treated as positive and those leaving as negative.

## 3 Research object

The experimental studies were carried out in the growth chamber of the mung bean sprouts shown in Fig. 5. Depending on the cultivation conditions, i.e. the climatic conditions in the growth chamber, the production period of the mung bean vegetable sprouts lasts from 5 to 7 days and begins with seed disinfection. The first phase of production is the imbibition process. The actual growth stage takes place several hours later giving rise to cyclic phases of watering the plants. Their purpose is to provide the necessary water for germinating seeds and to remove the excess heat generated

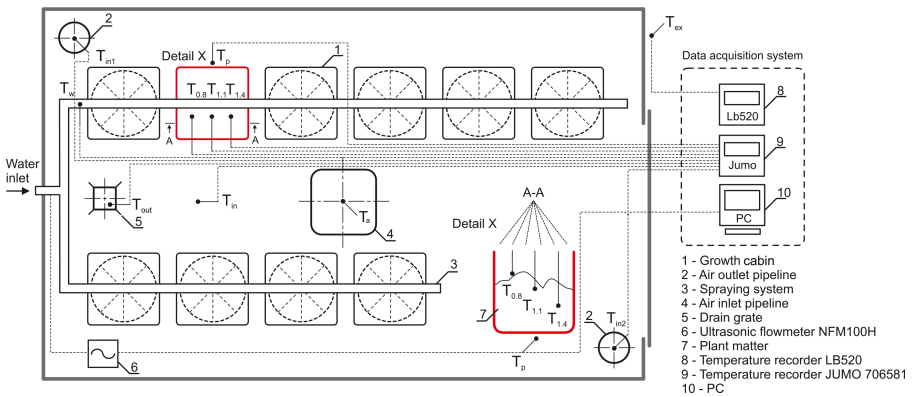


Figure 5: Diagram of the growth chamber of the mung beans.

by the plants in the process of cellular respiration. This heat is a source of low-temperature energy that can be used to increase the efficiency of the production process. In order to avoid excessive heat loss, the chamber is a well-insulated and sealed room equipped with two installations: air and water. The sprouts grow in cabins 1. Gas exchange and oxygen supply are carried out utilizing an inlet 4 and two outlet pipelines 2. The air exchange installation cooperates with two exhaust fans, which are turned on at set intervals and supply air to the chamber. The water installation consists of a sprinkler system 3 supplying water during the soaking and watering phases. This system is integrated with the used water discharge system 5 cooperating with the heat recovery installation. The operation of the soaking and watering installation has been programmed to allow for optimal plant growth conditions.

The aim of the experimental study was to determine the energy streams supplied, withdrawn and generated in the growth chamber during the entire production process. Therefore, during the measurements, the following process parameters were analyzed:

- outlet air temperature in pipelines 1 and 2, respectively – $T_{\text{in1}}$ and $T_{\text{in2}}$,
- inlet air temperature – $T_a$,
- average air temperature in the growth chamber – $T_{\text{in}}$,
- outside air temperature on the front door side – $T_{\text{ex}}$,
- volume flow of water for plant watering and spraying,
- irrigation water temperature – $T_w$,
- temperature of used water discharged directly from the growth cabin – $T_p$,
- used water temperature measured at the drain – $T_{\text{out}}$,
- temperature of sprouts in the cabin $T_{1.4}$, $T_{1.1}$ and $T_{0.8}$ at heights 1.4, 1.1 and 0.8 m, respectively.

The water volume flow was measured on the pipeline supplying water to the sprinkler system using a non-invasive ultrasonic flow meter 6 of the NFM100H type. The signal from the flow meter was recorded with a frequency of 1 Hz. Air temperatures $T_{\text{in1}}$, $T_{\text{in2}}$, $T_a$ and $T_{\text{in}}$ were recorded with the same frequency. For this purpose, resistance sensors type TP-366Pt1000

were used. The signals of the sensors were recorded using the JUMO 706581 recorder, providing a maximum sampling frequency of 8 kHz. The device also recorded the water temperature $T_w$, the temperatures $T_{1.4}$, $T_{1.1}$, and $T_{0.8}$ in the growth cabin, as well as the temperature of used water $T_{\text{out}}$ and $T_p$. Measurement of these parameters was carried out using resistance sensors TP-366Pt100. To eliminate additional resistance of connection cables, all temperature sensors were connected to the JUMO 706581 recorder using four-core silicone compensating cables. The air temperature $T_{\text{ex}}$ in the room on the other side of the front wall of the growth chamber was measured with the use of the LB 520 recorder. The measurement system prepared in this way allowed to determine heat fluxes and energy transported by air and water to the growth chamber, including:

- energy transferred in the gas phase by convection mixing – $E_{a_{\text{con}}}$,
- heat coming from the heat storage through the heat transmission – $Q_c$,
- energy supplied to the growth chamber during the imbibition phase – $E_{\text{imb}}$,

as well as heat and energy flows from the growth chamber, including:

- heat exchanged in the gas phase by heat transmission through the front wall of the chamber – $Q_{\text{wall}}$,
- energy contained in the imbibition water, which is discharged through a leak to the drain collector – $E_d$,
- energy contained in the irrigation water, which is discharged through a leak to the drain collector – $E_{ds}$,
- heat needed to evaporate the moisture – $Q_{\text{vap}}$.

In addition to the above-mentioned heat and energy sources, the energy $E_s$ contained in the water flowing through the plant mass in the irrigation process was also determined.

## 4 Measurement results

The balancing of heat transport in the growth chamber requires the analysis of energy streams exchanged during both soaking and watering phases. These streams occur between the phases air-air, water-air, and water-water and can be determined by measuring the volume flows and the temperature of the air and water supplied to and discharged from the growth chamber.

Proper growth and development of plants depend primarily on ensuring adequate gas exchange. In order to supply the seeds with oxygen and to remove the carbon dioxide produced by the sprouts, it is necessary to ventilate the growth chamber periodically. The source of a fresh air in the process under investigation is the heat store located in the supra chamber space. Figure 6 shows the time courses of air temperatures recorded in the growth chamber, the heat store, and the space on the other side of the front wall. Due to the terms of the agreement on the protection of process data between Czestochowa University of Technology and Uniflora Sp. z o.o., all measurement results have been referred to the maximum values, which are indicated on the diagrams by an apostrophe next to each of the measured values.

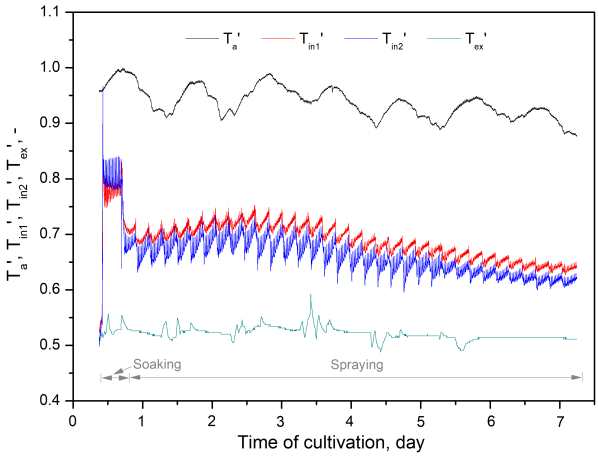


Figure 6: Air temperature time courses recorded in the heat store, the growth chamber, and the space on the other side of the front wall (the designations are taken in accordance with Fig. 5).

Analyzing the course of internal temperature changes in the growth chamber, one can notice their characteristic 'sawtooth' shape. It is an effect of cyclic temperature changes resulting from the periods of plant watering. The maximum temperature values occur at the end of the soaking phase and between the second and third day of the watering phase. As can be seen from the recorded data, to ensure the required conditions for plant growth, the temperature of the supplied air must be 30% to 50% higher than the temperature in the chamber. This difference is needed to cover the losses associated with heat transfer through the walls as well as water evaporation. Figure 7 shows the changes in internal temperature and rel-

ative humidity in the growth chamber for selected three consecutive plant watering cycles.

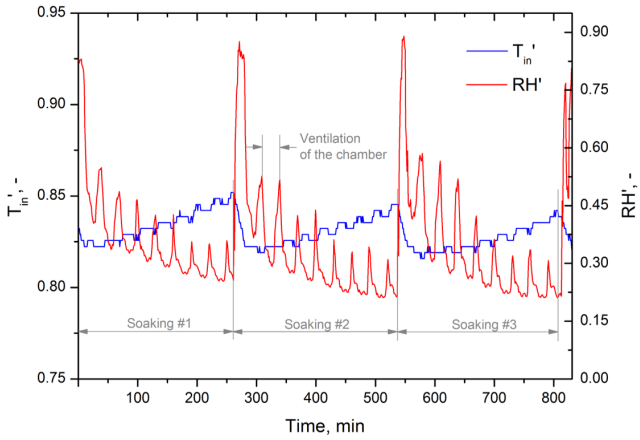


Figure 7: Time series of air temperature ($T'_{\text{in}}$) and humidity recorded (RH′) in the growth chamber for selected three consecutive plant irrigation cycles.

Since the irrigation phase is a cooling process for the plant mass, it is accompanied by a rapid decrease in the air temperature in the chamber. In the period between successive irrigation phases, the air temperature fluctuates periodically with a noticeable upward tendency. Periodic temperature increases are the result of the cyclic supply of air, while decreases are related to the process of intensive evaporation, which is the result of supplying air with a very low relative humidity, not exceeding 10%. As a consequence, in the growth chamber, intensive relative humidity fluctuations within the range from 0.16 to 1 are observed.

The second essential factor for proper plant growth and development is water. Figure 8 shows the time series of soaking, irrigation, and drainage water temperatures recorded in the growth chamber during the imbibition and germination phases. As can be seen, the nature of the changes in this parameter fully coincides with the changes in air temperature. In each of the recorded irrigation cycles the drain water stream $T'_p$ has a temperature higher than the temperature of water for irrigation $T'_w$. This means that the irrigation phase is not only a process that provides the substrate necessary for growth, but also allows for the reception of heat generated by germinating plants.

The maximum amount of heat generated by the plants occurs between the second and third day. During this period, the difference between the ir-

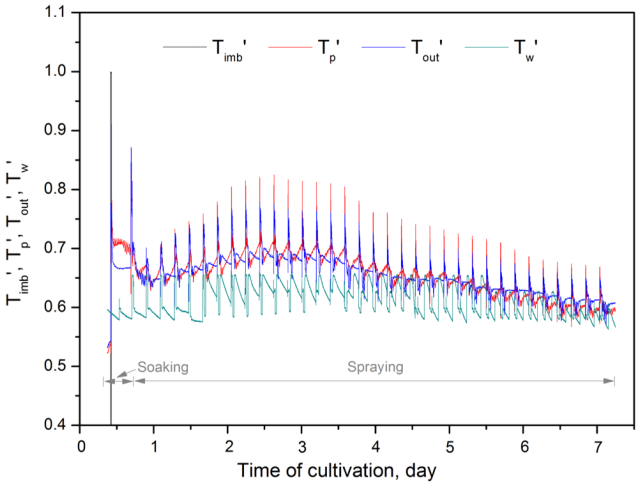


Figure 8: Time series of temperature of soaking, irrigation and drain water recorded in the growth chamber.

rigation and seepage water temperatures exceeds 20%, and at the beginning and the end of the growth cycle, these values are 3% and 9%, respectively.

## 5 Analysis of measurement results

The main goal of thermodynamic analysis of technological processes is usually to carry out a substance, energy or exergy balance calculation, which covers the whole technological process. In the case analyzed here, this objective is defined somewhat differently as determining the amount of heat generated in the plant growth process, i.e., the energy gain from plant mass production. As the result of such an analysis depends on the location of the balance shield of the system, in the case under consideration it was assumed that the plant growth chamber would be covered by this shield.

In the initial phase of plant growth, the dominant energy process is the convective exchange of energy between the air supplied to the chamber from the external heat store and the internal air. This process is periodic and takes place every few tens of minutes from the soaking phase to the full sprout growth phase. The total amount of heat transferred in the gas phase by convective mixing is given by

$$E_{a_{\mathrm{con}}} = V_a \rho_a c_a \big|_{T_{\mathrm{in}}}^{T_a} (T_a - T_{\mathrm{in}}) \,, \tag{18}$$

where $c_a|_{T_{\text{in}}}^{T_a}$ is average specific heat in the given temperature range determined by the relationship

$$c_a|_{T_{\text{in}}}^{T_a} = \frac{c_a|_0^{T_a} T_a - c_a|_0^{T_{\text{in}}} T_{\text{in}}}{T_a - T_{\text{in}}} . \tag{19}$$

Although the energy supplied to the growth chamber with air allows the internal temperature to remain stable, as can be seen from Fig. 6, its value must be large enough to cover the losses associated with the phase change of the water and heat transfer by thermal conduction. The total amount of heat required for the water phase change can be determined from equation

$$Q_{\text{vap}} = V_a \rho_a \frac{\Delta H_{\text{vap}}}{\mu_w} . \tag{20}$$

The heat $Q_{\text{vap}}$ depends not only on the air temperature but primarily on the relative humidity gradient. Therefore, taking into account the dynamic changes of humidity occurring in the growth chamber, the values of this heat are subject to very intensive changes throughout the production cycle.

As the warm air store is located in the direct vicinity of the growth chamber, an additional source of energy is the heat continuously flowing through the wall separating the two rooms. The amount of heat transported along the path of transmission can be determined from the relationship

$$Q_c = \frac{1}{\dfrac{1}{\alpha_{\text{ex_}v}} + \dfrac{d_1}{\lambda_1} + \dfrac{d_2}{\lambda_2} + \dfrac{1}{\alpha_{\text{in_}v}}} A_c t \left(T_a - T_{\text{in}}\right) , \tag{21}$$

where the subscripts 1 and 2 indicate wall partition number.

Apart from the heat stream penetrating the ground, the main source of losses of the growth chamber is the room located on the other side of the front wall. This wall is built of the same partition materials as the wall bordering the heat store. The amount of heat transported outside is determined by the relation

$$Q_w = \frac{1}{\dfrac{1}{\alpha_{\text{ex_}h}} + \dfrac{d_1}{\lambda_1} + \dfrac{d_3}{\lambda_2} + \dfrac{1}{\alpha_{\text{in_}h}}} A_F t \left(T_{\text{ex}} - T_{\text{in}}\right) , \tag{22}$$

where the subscripts 3 indicate wall partition number.

Figure 9 shows a Sankey diagram of the different types of heat entering and leaving the growth chamber with the air.

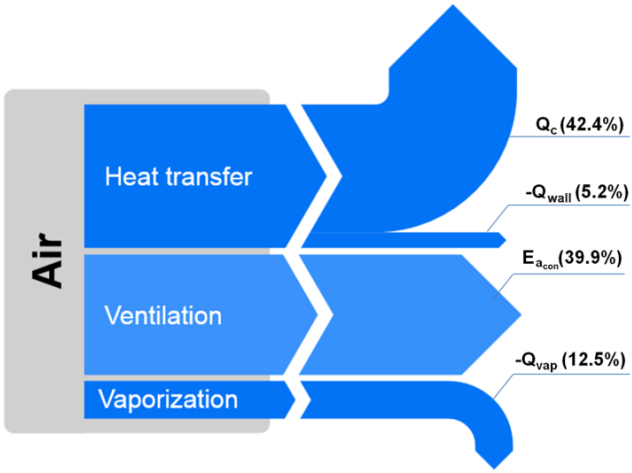


Figure 9: Sankey diagram of the different types of heat entering and leaving the growth chamber with air.

As shown in the figure, the energy sources for the growth chamber are heat transfer (42.4%) and warm air transport (39.9%) from the heat storage. However, the sources of losses are the front wall (5.2%) and the processes associated with moisture evaporation (12.5%). The balance does not take into account the losses due to heat transfer through other walls, which results from a negligibly small value of the temperature gradient. Air-to-air and air-to-water heat exchanges occur during both the soaking and irrigation cycles of the plants. Since the total amount of heat supplied with air and required for optimum plant growth conditions comes from external sources, the overall balance of the chamber will represent an energy gain. However, from the point of view of the whole technological process, this heat must be produced using an external energy source. Figure 10 shows the distribution of the shares of heat exchanged in the gas phase during the entire plant growth cycle in the growth chamber.

The presented results show that ensuring the required conditions for plant growth through an appropriate gas exchange is associated with significant energy expenditure. In the soaking phase, the energy demand is nearly 43 MJ, while in the irrigation phase as much as 1.17 GJ. It should be noted that the amount of heat supplied to the growth chamber along with the air is slightly greater than the amount of heat supplied due to the heat transfer from the heat store. This is because heat is supplied periodically in the air stream for about 17% of the cycle time, while heat is

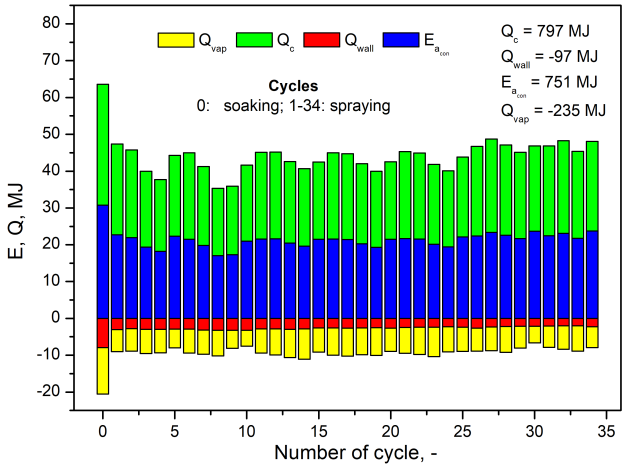


Figure 10: Shares of energy exchanged in the gas phase during the entire plant growth cycle in the growth chamber.

transferred continuously through transmission. The total amount of energy supplied in the gas phase throughout the plant growth cycle is as much as 1.5 GJ.

The second factor that plays a key role in the soaking and irrigation phases of plants is water. It allows seeds to germinate, increase plant mass and collect heat from germinating and growing plants. In the initial soaking phase, the amount of heat supplied to the growth chamber along with the water can be determined by the relationship

$$E_{\text{imb}} = V_{\text{imb}} \rho_w c_w \left(T_{\text{imb}} - T_{\text{ref}}\right). \tag{23}$$

After several hours of imbibition, the heat contained in the water can be determined from the relationship

$$E_d = V_d \rho_w c_w \left(T_p - T_{\text{ref}}\right). \tag{24}$$

Equation (24) determines the heat recovered at the exit of the growth chamber, while the sum of $E_{\text{imb}}$ and $E_d$ determines the energy supplied to the growth chamber during the seed imbibition process. In the entire production cycle of the mung bean sprouts, the only complete exoenergetic process occurs during the watering phase. In this phase the total amount of heat is made up of the heat contained in the water of moderate temperate, which goes directly to the output collector during the irrigation process due

to leakage, and the heat contained in the water flowing through the plant mass. In the first case, the amount of heat output can be determined from the equation

$$E_{ds} = V_d \rho_w c_w \Big|_{T_w}^{T_{\text{out}}} (T_{\text{out}} - T_w)\,, \tag{25}$$

while in the second case the amount of recovered heat is determined by the relation

$$E_s = V_s \rho_w c_p \Big|_{T_w}^{T_{\text{out}}} (T_{\text{out}} - T_w)\,. \tag{26}$$

Figure 11 shows the Sankey diagram for heat supplied and discharged with water from the growth chamber. In the soaking phase, the energy source is warm water supplied from the outside, while in the irrigation phase, the stream of cold water supplied receives energy from the plant mass.

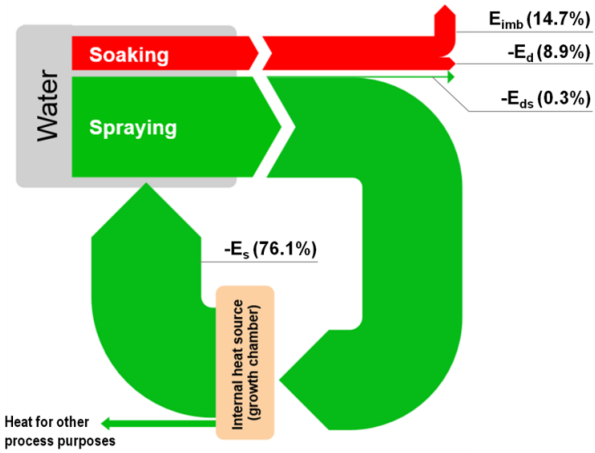


Figure 11: Sankey diagram for heat supplied and discharged with water from the growth chamber.

As plant germination is accompanied by intense heat release, an internal energy source is created in the growth chamber, which allows for effective heating of water that is reused in plant production processes. Figure 12 shows the distribution of the share of heat exchanged in the liquid phase during the entire plant growth cycle in the growth chamber.

This distribution throughout the production cycle is an uneven one due to the nature of the heat generated by the sprouts. This heat in the process of biological mass growth is generated exclusively by nutrients stored in the seeds and reaches a maximum between the eleventh and sixteenth irrigation cycles (245 MJ). From the seventeenth cycle onwards, the amount of heat

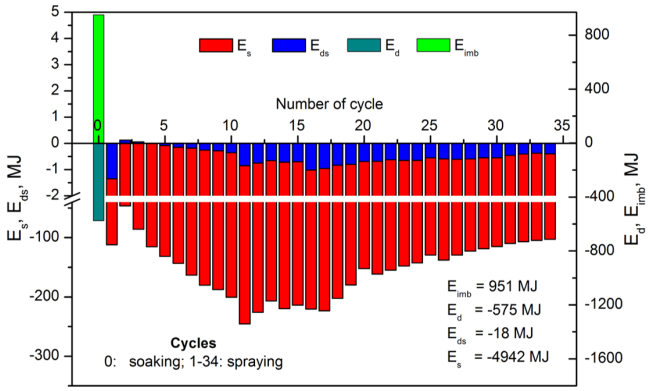


Figure 12: Shares of heat exchanged in the liquid phase during the entire plant growth cycle in the growth chamber.

generated decreases, which means that the energy resources necessary for growth are gradually exhausted. Since the cultivation is carried out in total darkness, the plants cannot carry out photosynthesis, from which they derive the energy needed for further growth in the natural environment. The minimum value of energy determined in the growth process is 46 MJ and occurs during the second cycle of irrigation of the plants. In general, in the soaking phase, when the highest temperature water is supplied, the energy input is as high as 951 MJ. Some of this energy can be recovered, bringing the total heat input to 376 MJ. Overall, the total heat generated by the plants during germination is 4942 MJ.

Figure 13 shows the distribution of the shares of energy input (Fig. 13a) and output (Fig. 13b) from the growth chamber. The presented data show that in both cases, the maximum energy values concern the water phase. In the whole growth cycle, the highest amount of heat input is absorbed in the soaking phase (38%). This is the longest and also the most energy-consuming cycle in the sprout production process. On the other hand, taking into account the dissipated energy, the highest value falls on the irrigation phase, in which almost 85% of the heat is removed from the sprout.

Figure 14 shows a summary of the shares of heat exchanged in the gas and liquid phases during the entire plant growth cycle in the growth chamber. The results show that the heat from germinating plants is mainly transferred to the liquid phase during the irrigation process, which makes this phase of plant production an exothermic one. On the other hand, the

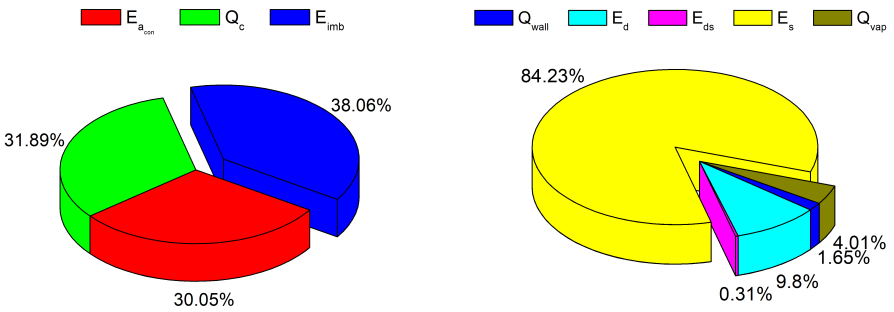


(a) (b)

Figure 13: Distribution of heat shares: (a) supplied to the growth chamber; (b) discharged from the growth chamber.

need to ensure gas exchange in the growth chamber involves the supply of a large amount of heat, making this process an endoenergetic process.

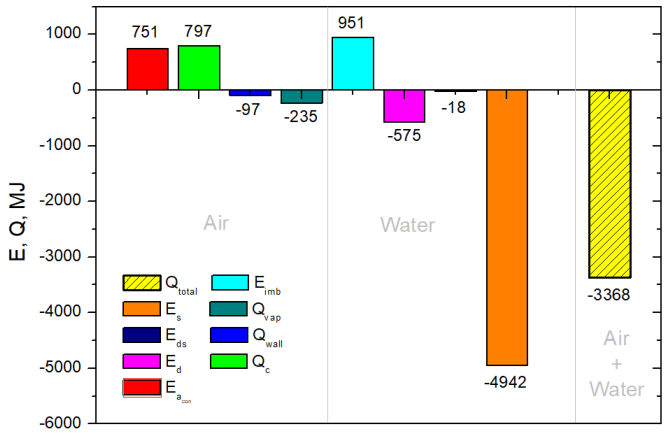


Figure 14: Summary of the heat exchanged in the gas and liquid phase during the entire plant growth cycle in the growth chamber.

The total amount of heat generated by plants in the entire production process is nearly 3.4 GJ. Thus, germinating mung bean seeds provide a significant amount of heat. This energy can be used to prepare the required water and air parameters and contribute to a significant reduction of the energy needs of the production process. Purification and re-use of water used for irrigation can further reduce the over-exploitation of water resources.

## 6 Summary

The conducted experimental research and the analysis of the obtained results allowed the formulation of the following conclusions:

1. The time distribution of the heat generated by plants throughout the production cycle is non-uniform. This heat in the process of biological mass growth reaches its maximum between the eleventh and sixteenth irrigation cycle (245 MJ) and minimum (46 MJ) in the second cycle.

2. The total amount of gross and net heat generated is 4942 MJ and 3368 MJ, respectively.

3. The maximum amount of heat generated by the plants occurs between the second and third day. During this period, the difference between the temperature of the water entering and leaving the growth cabin exceeds 20%.

4. Taking into account the energy transformations occurring in the growth chamber, ensuring the required conditions for plant growth involves supplying air with a temperature between 30% and 50% higher than the temperature in the chamber. In the soaking phase, the demand for energy supplied with air is nearly 43 MJ, while in the irrigation phase as much as 1.17 GJ.

5. Throughout the growth period, the air and water temperatures discharged from the growth chamber reach their maximum values at the end of the soaking phase and between the second and third day of the irrigation phase.

6. In the entire production cycle of the mung beans, the only complete exoenergetic process occurs during the irrigation phase.

7. The main cause of periodic changes of air temperature in the growth chamber are energy processes occurring during the phase of irrigation of plants and the process of water evaporation resulting from the mixing of air streams with a large difference in humidity.

Taking all into account, it should be stated that a significant amount of low exergy heat is generated in the production process of the mung bean sprouts. The use of this heat in a highly efficient installation built based on plate heat exchangers should allow to significantly reduce not only the

energy needs of the production process but also minimize the use of natural water resources.

## Acknowledgements

The research presented in this paper was financially supported by National Center for Research and Development under the projects POIR.01.01.01-00-0759/17 and POIR.01.01.01-00-0058/19, as well as by the statute subvention of the Czestochowa University of Technology, Faculty of Infrastructure and Environmental.

*Received 21 July 2023*

# References

[1] Szargut J., *et al.*: *Industrial Waste Energy: Principles of Utilization, Equipment.* WNT, Warszawa 1993 (in Polish).

[2] Turner W.C., Doty S., Eds.: *Energy Management Handbook* (6th Edn.). Fairmont Press CRC, Taylor & Francis, Lilburn, Boca Raton 2007.

[3] Firth A., Zhang B., Yang A.: *Quantification of global waste heat and its environmental effects.* Appl. Energ. **235**(2019), 1314–1334. doi: 10.1016/j.apenergy.2018.10.102

[4] Eurostat, 2022. *Energy statistics – an overview.* http://ec.europa.eu/eurostat/statistics-explained/index.php?title= Energy_statistics_-_an_overview#Final_-energy_ consumption (accessed 20 Feb. 2022).

[5] Papapetrou M., Kosmadakis G., Cipollina A., La Commare U., Micale G.: *Industrial waste heat: Estimation of the technically available resource in the EU per industrial sector, temperature level and country.* Appl. Therm. Eng. **138**(2018), 207–216. doi: 10.1016/j.applthermaleng.2018.04.043

[6] *Waste Heat Recovery: Technology and Opportunities in U.S. Industry.* BCS Incorporated, 2008. http://www1.eere.energy.gov/manufacturing/intensiveprocesses/pdfs/waste_heat_recovery.pdf (accessed 26 Sept. 2021).

[7] Fitó J., Hodencq S., Ramousse J., Wurtz F., Stutz B., Debray F., Vincent B.: *Energy- and exergy-based optimal designs of a low-temperature industrial waste heat recovery system in district heating.* Energ. Convers. Manage. **211**(2020), 112753. doi: 10.1016/j.enconman.2020.112753

[8] Xu Z.Y., Wang R.Z., Yang C.: *Perspectives for low-temperature waste heat recovery.* Energy **176**(2019), 1037–1043. doi: 10.1016/j.energy.2019.04.001

[9] Adamkiewicz A., Nikończuk P.: *Waste heat recovery from the air preparation room in a paint shop.* Arch. Thermodyn. **40**(2023), 3, 229–241. doi: 10.24425/ather.2019.130003

[10] Deymi-Dashtebayaz M., Valipour-Namanlo S.: *Thermoeconomic and environmental feasibility of waste heat recovery of a data center using air source heat pump.* J. Clean. Prod. **219**(2019), 117–126. doi: 10.1016/j.jclepro.2019.02.061

[11] Morgan R., Nelmes S., Gibson E., Brett G.: *Liquid air energy storage – Analysis and first results from a pilot scale demonstration plant.* Appl. Energ. **137**(2015), 845–853. doi: 10.1016/j.apenergy.2014.07.109

[12] Strahan D. (Ed.): *Liquid air in the energy and transport systems: opportunities for industry and innovation in the UK.* Rep. 021. Centre for Low Carbon Futures, Brighton 2013.

[13] Loni R., Najafi G., Bellos E., Rajaee F., Said Z., Mazlan M.: *A review of industrial waste heat recovery system for power generation with Organic Rankine cycle: Recent challenges and future outlook.* J. Clean. Prod. **287**(2021), 125070. doi: 10.1016/j.jclepro.2020.125070

[14] Uusitalo A., Honkatukia J., Turunen-Saaresti T.: *Evaluation of a small-scale waste heat recovery organic Rankine cycle.* Appl. Energ. **192**(2017), 146–158. doi: 10.1016/j.apenergy.2017.01.088

[15] Carvajal-Mariscal I., De León-Ruíz J.E., Belman-Flores J.M., Salazar-Huerta A.: *Experimental evaluation of a thermosyphon-based waste-heat recovery and reintegration device: A case study on low-temperature process heat from a microbrewery plant.* Sustain. Energy Technol. Assess. **49**(2022), 101760. doi: 10.1016/j.seta.2021.101760

[16] Zühlsdorf B., Jørgensen P.H., Elmegaard B.: *Industrial Heat Pumps, Second Phase IEA Heat Pump Technology (HPT) Programme Annex 48 Task 1: Danish Report.* Danish Technological Institute (2019). https://orbit.dtu.dk/en/publications/industrial-heat-pumps-second-phase-iea-heat-pump-technology-hpt-p (accessed 19 Feb. 2022).

[17] Song J., Li Y., Gu C., Zhang L.: *Thermodynamic analysis and performance optimization of an ORC (Organic Rankine Cycle) system for multi-strand waste heat sources in petroleum refining industry.* Energy **71**(2014), 673–680. doi: 10.1016/j.energy.2014.05.014

[18] Hu B., Liu H., Jiang J., Zhang Z., Li H., Wang R.Z.: *Ten megawatt scale vapor compression heat pump for low temperature waste heat recovery: Onsite application research.* Energy **238**(2022), 121699. doi: 10.1016/j.energy.2021.121699

[19] Knudsen B.R., Rohde D., Kauko H.: *Thermal energy storage sizing for industrial waste-heat utilization in district heating: A model predictive control approach.* Energy **234**(2021), 121200. doi: 10.1016/j.energy.2021.121200

[20] Wu X., Xing Z., He Z., Wang X., Chen W.: *Performance evaluation of a capacity-regulated high temperature heat pump for waste heat recovery in dyeing industry.* Appl. Therm. Eng. **93**(2016), 1193–1201. doi: 10.1016/j.applthermaleng.2015.10.075

[21] Rakib M.I., Saidur R., Mohamad E.N., Afifi A.M.: *Waste-heat utilization – The sustainable technologies to minimize energy consumption in Bangladesh textile sector.* J. Clean. Prod. **142**(2017), 1867–1876. doi: 10.1016/j.jclepro.2016.11.098

[22] Sekkeli M., Kececioglu O.: *SCADA based an energy saving approach to operation of stenter machine in a textile plant using waste heat recovery system.* Tekstil Ve Konfeksiyon **22**(2012), 3, 248–257.

[23] Skjern Papirfabrik: *Sustainability Report 2018.* Skjern 2018. https://www.skjernpaper.com/media/ehypqkge/06_2191827_rapport_2018_uk.pdf (accessed 13 May 2022).

[24] Mubarak A.E.: *Nutritional composition and antinutritional factors of mung bean seeds (Phaseolus aureus) as affected by some home traditional processes*. Food Chem. **89**(2005), 489–495. doi: 10.1016/j.foodchem.2004.01.007

[25] Bewley J.D., Bradford K.J., Hilhorst H.W.M., Nonogaki H.: *Seeds: Physiology of Development, Germination and Dormancy* (3rd Edn.). Springer, New York 2013.

[26] The European Commission: Commission Implementing Regulation (EU) No 208/2013 of 11 March 2013 on traceability requirements for sprouts and seeds intended for the production of sprouts. Official Journal of the European Union, L 68/16, 12.3.2013.

[27] *ESSA hygiene guideline for the production of sprouts and seeds for sprouting*. European Sprouted Seeds Association (2017). https://op.europa.eu/en/publication-detail/-/publication/4d31413a-63a0-11e7-b2f2-01aa75ed71a1 (accessed 6 July 2022).

[28] Criddle R.S., Breidenbach R.W., Hansen L.D.: *Plant calorimetry: how to quantitatively compare apples and oranges*. Thermochim. Acta **193**(1991), 67–90. doi: 10.1016/0040-6031(91)80175-I

[29] Morohashi Y., Sugimoto M.: *ATP Synthesis in cotyledons of cucumber and mung bean seeds during the first hours of imbibition*. Plant Cell Physiol. **29**(1988), 5, 893–896. doi: 10.1093/oxfordjournals.pcp.a077578

[30] Thygerson T., Harris J.M., Smith B.N., Hansen L.D., Pendleton R.L., Booth D.T.: *Metabolic response to temperature for six populations of winterfat (Eurotia lanata)*. Thermochim. Acta **394**(2002), 211–217. doi: 10.1016/S0040-6031(02)00253-8

[31] Skoczowski A., Troć M.: *Isothermal calorimetry and raman spectroscopy to study response of plants to abiotic and biotic stresses*. In: Molecular Stress Physiology of Plants (G.R. Rout, A.B. Das, Eds.), 263–288. Springer, New Delhi 2013. doi: 10.1007/978-81-322-0807-5_11

[32] Pierce G.J.: *A new respiration calorimeter*. Bot. Gaz. **46**(1908), 193–202. doi: 10.1086/329696

[33] Schabes F.I., Sigstad E.E.: *Is it possible to determine physiological quality and best conditions of storage of soybean seeds by isothermal calorimetry?* Thermochim. Acta **579**(2014), 45–49. doi: 10.1016/j.tca.2014.01.014

[34] Stawoska I., Staszak A.M., Ciereszko I., Oliwa J., Skoczowski A.: *Using isothermal calorimetry and FT-Raman spectroscopy for step-by-step monitoring of maize seed germination: case study*. J. Therm. Anal. Calorim. **142**(2020), 755–763. doi: 10.1007/s10973-020-09525-x

[35] Sigstad E.E., Prado F.E.: *A microcalorimetric study of Chenopodium quinoa Willd. seed germination*. Thermochim. Acta **326**(1999), 159–164. doi: 10.1016/S0040-6031(98)00599-1

[36] Sigstad E.E., Schabes F.I., *Isothermal microcalorimetry allows detection of 'aquaporines' in quinoa seeds*. Thermochim. Acta **349**(2000), 95–101. doi: 10.1016/S0040-6031(99)00501-8

[37] Dincer I., Rosen M. A.: *Exergy. Energy, Environment and Sustainable Development* (1st Edn.). Elsevier Sci., 2007.

**archives**
**of thermodynamics**
Vol. **44**(2023), No. 4, 535–562
DOI: 10.24425/ather.2023.149733

# Determination of an axial gas cyclone separator cut-off point by CFD numerical modeling

**ARKADIUSZ RYFA**[a*]
**MIESZKO TOKARSKI**[a, e]
**WOJCIECH ADAMCZYK**[a]
**ADAM KLIMANEK**[a]
**PAWEŁ BARGIEL**[a]
**RYSZARD BIAŁECKI**[a]
**MICHAŁ KOCOT**[b]
**MARIAN NIESLER**[c]
**HARALD KANIA**[c]
**JANUSZ STECKO**[c]
**MARIANNA CZAPLICKA**[d]

[a] Silesian University of Technology, Institute of Thermal Technology, Konarskiego 22, 44-100 Gliwice, Poland

[b] ArcelorMittal Poland, al. Piłsudskiego 92, 41-308 Dąbrowa Górnicza, Poland

[c] Institute for Ferrous Metallurgy, Łukasiewicz Research Network, Karola Miarki 12, 44-100 Gliwice, Poland

[d] Institute of Environmental Engineering, Polish Academy of Sciences, Marii Skłodowskiej-Curie 34, 41-819 Zabrze, Poland

[e] AGH University of Science and Technology, Department of Fuels Technology, Czarnowiejska 30, 30-059, Kraków, Poland

**Abstract** This paper deals with the numerical simulation of a pilot-scale axial cyclone separator. The main purpose of this paper is to develop a numerical model that is able to foresee the cyclone separator cut-off point. This is crucial in blast furnace gas installation to capture large particles containing carbon and iron, while allowing smaller particles such as zinc and lead to pass through. The cut-off point must be designed to give a suf-

*Corresponding Author. Email: arkadiusz.ryfa@polsl.pl

ficiently high zinc and lead content in the sludge created after the second cleaning stage. This allows the sludge to become a commercial product. To design this cut-off point, an investigation of the influence of inlet gas velocity, temperature, and the angle of guiding vanes at the inlet was done. The developed CFD model was validated against experimental data on the fractional efficiency of the cyclone separator. The results were in good agreement with the experimental data for all parameters tested. The behavior of the particles inside the cyclone was also physically correct.

**Keywords:** CFD; Cyclone separator; Dust; Blast furnace; Zinc; Cut-off point

# 1 Introduction

A cyclone separator is a device that uses centrifugal force to separates solid particulates from swirling fluid [1]. Its biggest advantages are simple construction, low maintenance and operational costs, low pressure loss, and usability in difficult operating conditions such as high pressure and temperature. Cyclones can be readily scaled to virtually any mass flow. There are two main types of cyclones, which differ in the method of swirling the gas: axial and tangential. The former has a gas inlet axially located on the top wall and uses guiding vanes to enforce the swirl. A tangential cyclone has an inlet (or inlets) located on the side wall, and the gas is swirled by sliding along the side wall. Both types have to be designed for a specific gas velocity, dust composition, and desired separation efficiency. However, it is possible to alter the separation efficiency of both designs. For the axial construction, the angle of the guiding vanes can be changed, whereas for the tangential one, there are shutters mounted in the inlet channels, which can increase the inlet velocity. For small constructions, this tuning can be done while the cyclone separator is running, but for large constructions, this requires a break in operation.

Cyclones are widely used in industry to separate solid material from a gaseous [2] or liquid phase, in circulating fluidized bed boilers for combustible particle separation [3] and in steel plants for gas cleaning [4] just to name a few applications. The gas flow inside a cyclone separator consists of two vortexes [5]: the outer vortex is located on the side wall of the device, and the gas spirals downward. There, large enough particles slow down and finally slide down to the ash hopper. The second vortex is an ascending one located around the center axis, and it directs the cleaned gas to flow toward the so-called vortex finder, which is an outlet of the cyclone. Such a com-

plex flow may pose a challenge when an attempt is made to build a correct numerical model. Cyclone operation is often analyzed via experiments. Hsu *et al.* [6] tested a variety of geometrical configurations and rated their performance using a quality factor. In this study, a quality index is given as a function of the main geometrical parameters. The particle dynamics and trajectories were experimentally analyzed by Roloff *et al.* [7]. Celis *et al.* [8] investigated the effect of swirl vanes and vortex stabilizers on the flow of a cyclone. The effect of the geometric configuration of the inlet on the collection efficiency and noise of an axial flow cyclone was evaluated by Babaoglu *et al.* [9]. The influence of an apex cone on the flow inside an axial cyclone was investigated by Zhang *et al.* [10], whereas Yoshida [11] investigated the influence of an apex cone on the separation of fine particles. Others, such as Yang *et al.* [12] tested the influence of operating conditions (velocity, temperature) on the performance of a cyclone separator. Such papers have great value because they can provide data for the validation of numerical models. Nowadays, computational fluid dynamics (CFD) is often used to test new cyclone constructions or to test the performance of cyclones under various conditions. Huang *et al.* [13] used CFD to test the performance of a cyclone with a slit on the conical part. Zheng investigated the influence of a shunt device on cyclone performance [14]. Pandey and Brar [15] used numerical modeling to test the behavior of cyclones with different shapes of the conical section. An analysis of the effect of the cross-sectional shape of the inlet on the performance of a multi-inlet gas cyclone was performed by Babaoglu *et al.* [2]. CFD is also used to foresee the influence of geometrical modifications on cyclone operation [16]. When a cyclone separator cut-off point is needed, CFD is a method of a choice [1]. There, the angle of guide vanes at omnidirectional inlet was adjusted to determine its impact on cut-off point. The CFD model can be supplemented with soft computing methods such as neural networks or deep learning to reduce computational time [17]. The effect of inlet duct angle on the performance of a cyclone was simulated by Wasilewski and Brar [18]. Xiang and Lee [19] tested the influence of the diameter of the exit tube on the flow field, whereas Su *et al.* [20] investigated the effect of the inlet configuration on the performance of a cyclone. The influence of the size of a cyclone on the separation efficiency was investigated by Azadi *et al.* [21]. Oh *et al.* [22] simulated the cyclone for varying internal pressure. Tests of the inlet periodic velocity were performed by Chen *et al.* [23]. CFD combined with genetic algorithms or neural networks is also used to find the optimum dimensions and inlet conditions of cyclones [24]. An important aspect when applying CFD to

the simulation of the flow inside a cyclone is the proper selection of the turbulence model. In some papers [25, 26], various turbulence models such as $k$-$\varepsilon$, Reynolds stress model (RSM), and large eddy simulation (LES) were tested. For some time, RSM has been a typical choice for modeling cyclones [24]. The results produced by RSM are in good agreement with the experiments, and yet the model is relatively undemanding in terms of mesh and computational effort. The second choice for modeling cyclones is LES [27]. This option can resolve the flow more accurately than RSM, but it consumes more computational resources. When transient turbulence fluctuations are to be considered LES should be used. This approach was applied to find the characteristic of the turbulence of cyclone separator with vortex stabilizer [28]. Some researchers have analyzed cyclones operating in steady state [29] whereas others used transient models [18]. The approach depends on the goal of the model. Here, both approaches were initially used and compared. Eventually, steady analysis was used. In summary, there are many papers on modeling cyclone separators. Various methods and approaches were used for this purpose. Despite this fact, none of the studies determined the reflection coefficients for the particles.

This work is devoted to the development of a numerical model of a pilot-scale axial cyclone separator. The main aim of the CFD model is to foresee the cut-off point of the cyclone separator for actual blast furnace (BF) gas particles. The main objective of the project under which this work has been carried out is to assess the geometry and flow parameters that will allow the separation of $\approx 85\%$ of the dust from BF gas in a large steel plant. These larger particles contain carbon and iron, which are valuable for the pig iron production process. Thus, the separation of large particles from gas will allow iron- and carbon-rich particles to be recycled into the BF, thus saving natural resources (iron) and energy (coke). In addition, the same large particles contain only a small amount of zinc and lead. These elements are present mainly in fine particles and have a negative impact on the quality of the pig iron produced in the furnace. Hence, the recirculation of these particles is undesirable. The role of the cyclone separator is thus to separate the large particles, while the small particles, containing lead and zinc, should be discharged from the device along with the outlet gas [4]. Those fine particles are then removed from the gas, typically in a wet scrubber (WS). When the zinc and lead content of the sludge is high enough, the sludge can be used further as a commercial product [30]. In the long run, because the gas velocity, geometry of the cyclone separator, and mass of the BF dust particles have a major impact on the separation efficiency, a multi-

parameter analysis needs to be carried out, because only proper fractions of the dust should be recirculated (separated). Due to cost considerations, it was decided to use the same dust in the pilot-scale cyclone separator. The model is validated against experimental data for various operating conditions, such as gas velocity and temperature or guiding vanes angle. The long-term goal is to obtain a robust and fast numerical model that can be used for designing a full-scale industrial cyclone separator for a steel plant's de-dusting installation. For this reason, the dust collected in the steel plant is used in the experimental setup, and the operating conditions of the test cyclone separator are close to the full-scale industrial installation. In this study a 3D steady-state CFD model was developed. The model uses the RSM turbulence model and discrete phase model (DPM) approach to model dust particles. These methods have been selected because they allow one to obtain reliable results within a reasonable computation time. The novelty of the proposed approach is the determination of the reflection coefficient that defines the momentum losses during the particle–wall collisions and the splitting of the model into two parts, which speeds up the calculations and allows for the use of a better-quality mesh. Additionally, each dust fraction was injected separately into the cyclone so that it was easy to calculate the fractional separation efficiency and to use the experimental data. The typical approach found in the literature does not mention the selection of the reflection coefficients or assumes a value of 1.

The paper is divided into 5 sections. First is an introduction. Section 2 describes the test rig and the measurements. Next goes CFD modeling (Section 3) and model validation (Section 4). Last section is devoted to conclusions.

## 2 Experimental rig and measurements

The test rig is shown in Fig. 1 and is presented schematically in Fig. 2. It consists of an air preparation system (including an electrical heater (EH) and a dust dosing device), an axial cyclone separator, a WS, a bag filter system, and a fan. First, ambient air (I) is sucked from the environment and heated by an EH. The heater is controlled by a temperature sensor mounted at the inlet of the cyclone (II) so that the requested operating temperature is maintained. The dust is then dosed with a screw feeder (III). Dust-laden air enters the cyclone separator through the annular tube (diameter 0.196 m), where a portion of the dust is separated and collected at the

bottom of the installation (IV). The part of the cyclone where separation occurs has a height of 0.66 m and a diameter of 0.25 m (cylindrical section). The air containing the remaining dust leaves the cyclone separator through a vortex finder (0.094 m diameter) and flows through the WS and through a baghouse filter. Clean air flows through a fan to the stack (X), while the sludge is removed from underneath the scrubber (VII). Dust separated in the baghouse is collected in (IX).

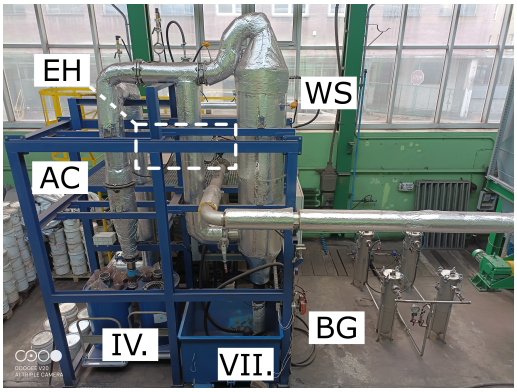


Figure 1: Test rig – general view: EH – electric heater, AC – axial cyclone, WS – wet scrubber, BG – baghouse, VI – collected dust, VII – collected sludge.

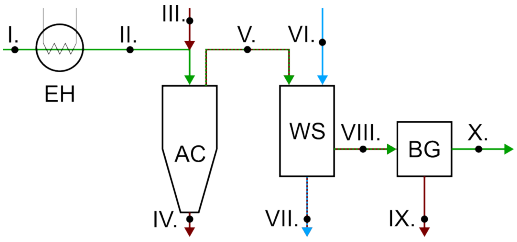


Figure 2: Test rig scheme: EH – electric heater; AC – axial cyclone; WS – wet scrubber; BG – baghouse; measurement points I, II – clean air; III, IV, IX – BF dust; V, VIII – dust laden air, VI – water injection, VII – sludge, X – clean air.

The analysis in this paper is limited to the cyclone separator. The WS is a subject of separate research.

The BF releases gas at a gauge pressure in the range of 0.05 to 0.2 MPa and at a temperature of 373 to 423 K. Although the gas temperature can be easily controlled on a laboratory scale, operation of the test rig at overpressure poses a challenge. First, the amount of air needed in the installation

would require a large compressor and tank to work in a steady state for a longer time. Although this is not essential for the cyclone separator itself, it is essential for the second part of the separation process, which is carried out with a WS. The second issue is that feeding the dust to the compressed gas is problematic, because the dust can escape from the installation, contaminate the environment, and reduce the quality of the determination of the efficiency of the cyclone separator. For these reasons, it was decided to operate the rig at ambient pressure, especially so that the pressure level in the cyclone separator did not affect its operation. The BF gas (present in the real installation) was replaced by ambient air, whose pressure was measured at the inlet to the installation (I) and at the outlet of the cyclone (V) by a piezo-resistance sensor (uncertainty 0.6%). The volumetric flow rate of clean air was measured (I) using an orifice (measurement uncertainty 1%). The temperature of the gas was measured at several locations: at the inlet to the rig (I); at the outlet from the gas heater (II); at the inlet (III); and at outlet (V) of the cyclone by a Pt100 resistance thermometer (maximum uncertainty 0.4 K). Air humidity was measured at the inlet to the rig (I) using an HTDT2500 sensor (uncertainty 2.5%). The dust supplied to the installation was collected from the BF of the steel plant. As seen in Table 1, the mass fraction of the smallest dust ($< 0.028$ mm) is less than 20%. The average fractions (0.028–0.1 mm) contain approximately 60% of the mass, whereas the remaining part is in larger fractions. The demand to separate 85% of the mass means that the cut-off point for cyclone separation must be located at a fraction below 0.02 mm. The cyclone separator used in the experiments was designed with exchangeable guide vanes (denoted as K1, K2, and K3) that allowed for a change in the swirl angle at the inlet of the cyclone separator. In theory, this was supposed to allow control over the separation efficiency, indirectly impacting the separation cut-off point. This point is especially important, because smaller particles contain harmful compounds that cannot be redirected back to the BF. The zinc content in the dust was determined using an ICP-OES Agilent 5100 SVDV spectrometer. As seen in Table 1, zinc was present mainly in the smallest fractions, where its mass fraction was almost 7% for the smallest particles. The zinc content decreased with increasing particle diameter and for the assumed cut-off point was around 2%.

For larger diameters, the zinc mass fraction was gradually reduced to less than 0.5%. The cyclone separation efficiency is computed as

$$\eta = \frac{\dot{m}_c}{\dot{m}_{\text{in}}}\,, \tag{1}$$

Table 1: Dust fractional composition (%) and zinc mass content (%).

| Fraction, mm | ID 4 (8 m/s) | ID 26 (7 m/s) | ID 30 (10 m/s) | Zn content |
|---|---|---|---|---|
| < 0.0019 | 6.4 | 5.2 | 8.9 | 6.7 |
| 0.0019–0.0037 | 2.4 | 2.2 | 3.1 | 6.2 |
| 0.0039–0.0064 | 2.1 | 1.4 | 2.3 | 4.2 |
| 0.0064–0.0088 | 2.5 | 2.3 | 2.7 | 3.6 |
| 0.0088–0.0124 | 1.8 | 1.8 | 2.0 | 2.9 |
| 0.0124–0.0180 | 1.7 | 2.2 | 1.8 | 2.5 |
| 0.0180–0.0232 | 0.9 | 1.0 | 0.9 | 2.2 |
| 0.0232–0.0277 | 0.5 | 0.5 | 0.5 | 2.0 |
| 0.0277–0.056 | 17.2 | 16.0 | 14.0 | 1.9 |
| 0.071–0.056 | 8.1 | 6.8 | 8.8 | 1.2 |
| 0.1–0.071 | 13.8 | 14.6 | 16.0 | 0.8 |
| 0.16–0.1 | 22.5 | 20.8 | 20.8 | 0.8 |
| 0.2–0.16 | 7.0 | 7.6 | 6.1 | 0.6 |
| 0.315–0.2 | 9.3 | 12.6 | 8.3 | 0.6 |
| 0.4–0.315 | 2.2 | 2.8 | 2.0 | 0.5 |
| 0.63–0.4 | 1.6 | 2.0 | 1.8 | 0.5 |
| 0.8–0.63 | 0.2 | 0.3 | 0.2 | 0.5 |
| 1.6–0.8 | 0.0 | 0.1 | 0.0 | 0.4 |
| > 1.6 | 0.0 | 0.0 | 0.0 | 0.0 |

where $m_c$ (kg/s) is the mass of dust collected from the cyclone ash hopper, and $m_{\text{in}}$ (kg/s) is the mass dosed to the installation. All masses are collected for the steady-state operation of a rig for a given measurement. The mass of dust that is fed into the installation can be computed as

$$\dot{m}_{\text{in}} = \frac{m_0 - m_1}{\tau}\,, \tag{2}$$

where $m_0$ (kg) and $m_1$ (kg) are the masses on the ash tray of the screw feeder at the beginning and end of the measurement, respectively, and $\tau$ is the measurement time (s). The fractional efficiency is calculated in the same way:

$$\eta_{c,f} = \frac{\tau \dot{m}_{c,f}}{(m_0 - m_1)\, c_f}\,, \tag{3}$$

where $m_{c,f}$ (kg) is the mass of the dust of a given fraction collected from the ash hopper, and $c_f$ is the mass fraction of a given fraction from Table 1. ID stands for number of measurement taken.

The dust used in the laboratory installation was a mixture of dust and dried sludge collected in the real BF de-dusting installation. Dust and sludge were mixed in the proportion 3:1 and were sampled to verify whether the particle distribution was the same at all sample locations. The dust collected at the bottom of the laboratory installation cyclone separator (IV) was weighted (accuracy 0.1 g) and fractionated using laser diffraction according to the ISO 13320:2009 standard into fractions ranging from less than 0.056 mm to greater than 1.6 mm. The smallest fractions (i.e., below 0.056 mm) were further split with the use of counterflow in a Bahco high-speed centrifuge. In total, there were 19 fractions, with the smallest fraction below 0.0019 mm. The density of each fraction was determined using the pycnometric method. Each analysis was repeated three times to ensure that the dust analysis was correct. The sludge (VII) collected from the WS outlet was analyzed in the same way but was dried beforehand. The results in Table 1 show the average of three analyses of the dust/sludge mixture. Laboratory tests were aimed at determining the parameters that influence the separation efficiency and providing data for the validation of the numerical model. In total, more than 30 measurements were taken. As seen in Table 2, the gas velocity tested at the entrance of the cyclone separator was between 7 m/s and 13 m/s, which corresponds to the expected velocities in the industrial installation. In addition to gas velocity, the gas temperature, dust content, and swirling angle were also varied. Separation efficiency ranged from 90.4 to 95.2%, depending on the conditions. The tests proved that the temperature and dust content, within the tested limits, did not influence the separation efficiency. To test the impact of the swirling angle on the performance of the cyclone separator, three different flow guide vanes were tested. These vanes produced swirl angles of 21° (K1), 30° (K2), and 39° (K3). Measurements showed that the angle of the guide vanes had some, but not an overwhelming, influence on the cyclone separation efficiency. That is, with increasing angle, the separation efficiency also increased, but only by about 1%. One test (ID 201) was conducted without any vanes (no initial gas swirl). For this case, the separation efficiency dropped to about 67%. This indicated that, although the swirl was necessary, the angle was not a crucial parameter, at least not in the tested angle range. Unlike this, the velocity of the gas affected the separation efficiency of the cyclone separator. With increasing velocity, the efficiency also

increased by about 0.5% per 1 m/s increase in velocity. However, this effect was limited. Although the smallest fractions were almost not captured within the investigated velocity interval, for a velocity above 10 m/s, nearly all larger fractions were separated. Therefore, it was difficult to observe any increase in efficiency between 10 and 13 m/s.

Table 2: Performed measurements of the cyclone. Boxed measurements were chosen for numerical model validation: $v_{\mathrm{II}}$ – inlet air mean velocity, $T_{\mathrm{II}}$ – air temperature at the inlet, $\eta$ – separation efficiency of the cyclone.

| ID | $v_{\mathrm{II}}$ | Flow guide | Dust content | $T_{\mathrm{II}}$ | $\eta$ |
|---|---|---|---|---|---|
| – | m/s | – | g/m$^3_n$ | °C | % |
| 3 | 8 | K1 | 15 | 125 | 94.4 |
| 4 | 8 | K1 | 15 | 125 | 91.5 |
| 5 | 8 | K1 | 15 | 125 | 92.6 |
| 6 | 7 | K1 | 15 | 125 | 92.7 |
| 7 | 8 | K1 | 15 | 125 | 92.2 |
| 10 | 8 | K1 | 15 | 100 | 93 |
| 11 | 8 | K1 | 15 | 150 | 91.8 |
| 19 | 7 | K1 | 30 | 125 | 91.3 |
| 23 | 8 | K1 | 15 | 125 | 95.2 |
| 25 | 8 | K1 | 15 | 125 | 91.5 |
| 26 | 7 | K1 | 15 | 125 | 92.4 |
| 27 | 8 | K1 | 15 | 125 | 94.3 |
| 28 | 8 | K2 | 15 | 125 | 94.6 |
| 29 | 8 | K3 | 15 | 125 | 93.3 |
| 30 | 10 | K1 | 15 | 125 | 93.3 |
| 31 | 13.1 | K1 | 15 | 100 | 93.9 |
| 130 | 8 | K1 | 15 | 125 | 93.9 |
| 201 | 8 | – | 15 | 125 | 66.8 |
| 205 | 8 | K1 | 15 | 100 | 92.7 |
| 206 | 10 | K1 | 15 | 100 | 93.8 |
| 208 | 10 | K1 | 15 | 100 | 94.1 |
| 209 | 13.1 | K1 | 15 | 100 | 94.0 |
| 210 | 10 | K1 | 30 | 125 | 93.0 |

For model validation, givens that velocity was the most important parameter that influenced the separation efficiency, three measurement series at different velocities of 7, 8, and 10 m/s were taken. These measurements were denoted as ID 26, ID 4, and ID 30, respectively. Because the performed measurements had very little effect on the swirl angle generated by the flow guides K1, K2, and K3, the measurements (except for two) were executed using the K1 guides.

## 3 CFD model outline and modeling strategy

The calculations were carried out using the commercial CFD package Ansys/Fluent 19.2. The cyclone separator itself consists of three main parts. The first part is an inlet part with a gas supply pipe. Next, there is the main body part of the cyclone, which consists of flow swirling elements, cylindrical and conical tubes, and the vortex finder. There, the flow swirls, and the dust is separated from the gas. The last part is a vertical gas outflow pipe (where the gas containing the non-separated particles is rejected from the device). The main simplifications of the model considered geometry, where small, unimportant features of a cyclone were neglected. In addition, the analysis was finally run in a steady state to save time and computational effort with a negligible impact on solution quality due to the stabilized flow field. Splitting the numerical model into two parts allowed for significant savings in terms of computational time and resources. The inlet zone required a finer mesh and was needed just to generate velocity and particle profiles at the cyclone inlet. The cyclone, on the other hand, with coarse mesh required much longer computational time to stabilize the solution.

A 3D Reynolds-averaged Navier-Stokes formulation of the governing equations was used. The RSM turbulence model was applied based on the scalar dissipation rate ($\varepsilon$) with a linear pressure strain. A standard approach proposed in Fluent was used to model turbulent diffusive transport with scalar turbulent diffusivity. Since all the model constants were default, then in linear pressure strain slow pressure strain term used 1.8 as a constant while rapid pressure strain used 0.6. The wall boundary condition was taken from the kinetic energy equation. The wall reflection term was modelled with $C_1' = 0.5$, $C_2' = 0.3$ and $C_\mu = 0.09$. The dissipation rate constants were 1.44 and 1.92. Scalable wall functions were also used due to the $Y_+$ range of 5.5 to 127. Detailed equations can be found in Section 4.10 of the Ansys Manual [31].

There were three unknown parameters when setting up the mathematical model of the cyclone separator:

- the reflection coefficients, defining the momentum losses during the particle–wall collisions;
- the profile of the inlet velocity;
- the distribution of the particles at the inlet.

The reflection coefficients depend on the properties of the dust and the type and condition of the cyclone separator material. They are extremely difficult to measure, so they were discovered by adjusting the simulation results to those of the experiments. Because the same dust will be used in both the full-scale and laboratory installation, the values obtained in the latter can then be used in the former.

The intersection of the straight outlet and curved inlet pipes produces an unsymmetrical profile of the inlet velocity and a non-uniform distribution of the particles at the inlet of the cyclone separator. Additionally, this distribution differs between fractions of particles. To obtain realistic boundary conditions at the inlet of the cyclone separator, the computational domain was extended by the inlet pipe, as shown in Figs. 3 and 5. To reduce the size of the numerical model of the cyclone separator and the simulation time of parametric studies, the computational domain was divided into two parts separated by a plane (D) (see Fig. 3). An additional advantage of

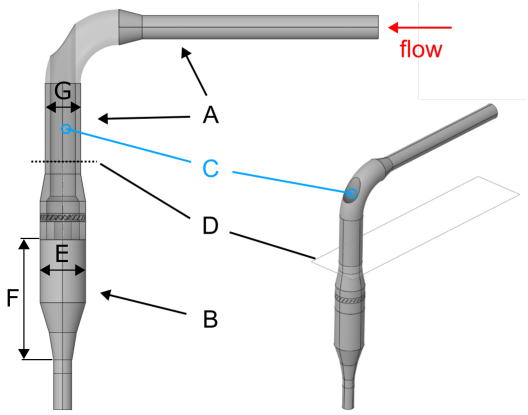


Figure 3: Computational domain: A – inlet zone, B – cyclone, C – outlet pipe, D – split plane, E – diameter of cylindrical part (0.25 m), F – height of the cyclone (0.66 m), G – diameter of inlet pipe (0.196 m).

this approach was the possibility of using a high-quality regular mesh in the cyclone separator. Due to the complex velocity pattern in this device, the choice of an appropriate mesh was of special importance. To verify the correctness of such an approach, one simulation was run iteratively. That is, both the inlet section and the cyclone simulation were run, and velocity and pressure fields were passed between them. The results of such an analysis showed no significant influence of a pressure field generated in the cyclone on the velocity distribution calculated in the inlet section.

The first zone consists of the inlet pipe (A), whereas the second comprises the main body of a cyclone (B), as indicated in Fig. 3. Both zones were solved independently and coupled by a velocity and pressure boundary conditions. The outlet velocity and particulate distribution of zone A were treated as an inlet condition to zone B. The simulations were carried out in steady-state using a pressure-based solver with gravity on. The RSM was used to model turbulence.

Next, steady-state and transient analyses of the flow conditions inside the cyclone separator were performed, and the results were compared with the experimental data (series denoted as ID30). For both models, the setup was the same. In the transient analysis, however, a 0.00013775 s time step was chosen with 10 iterations per time step. Furthermore, the data sampling interval was set to 10 time steps. In our case, however, it was a much shorter period (0.135 s), because this particular study was carried out only to validate the steady-state flow field. It confirmed that, the appropriately stabilized steady-state flow field is identical to the costly time-averaged one. The calculated velocity fields are shown in Fig. 4(b). Both profiles were almost identical (which confirms that steady-state and transient led to essentially the same results), except for slight irregularities (flow oscillations) present in the steady-state. In Fig. 4(a), the fractional separation efficiency is presented and it can be stated that both formulations agreed satisfactorily well with the experimental data. The only noticeable discrepancy concerned the fraction 3.9 µm, where the separation efficiency should be around 82% (experiment), whereas numerical models indicated lower values (i.e., $\approx$ 70% and $\approx$ 48%) according to the steady-state and transient analyses, respectively. Generally, good agreement between the two models indicated that slight flow oscillations in the steady-state analysis did not significantly impact particle behavior. At the same time, steady-state analysis was much less demanding in terms of computational time and resources. Thus, steady-state analysis was chosen for further analysis.

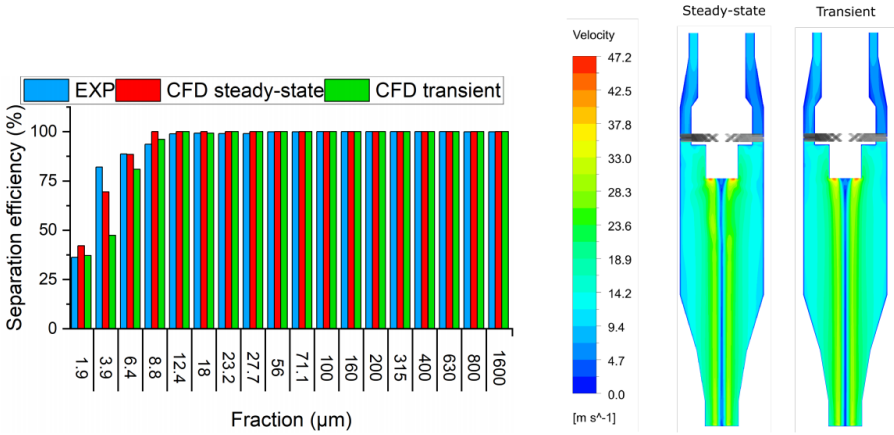


Figure 4: Case ID30 – comparison of the steady-state and transient analysis: a – fractional separation efficiency from experiments (EXP), steady-state (CFD steady-state), and transient (CFD transient) analysis; b – velocity profile provided by the steady-state (left-hand side) and transient (right-hand side) analysis.

## 3.1 Model description

The setup of both models, (A) and (B), was the same and covered the *Coupled* pressure velocity coupling scheme, QUICK spatial discretization of momentum, turbulent kinetic energy, turbulent kinetic dissipation rate, Reynolds stresses, and energy. PRESTO! was used for pressure discretization. The QUICK scheme was used to improve the stability of the solution and the flow field. Second-order schemes are considered sufficient in most cases, but in this particular case, it was decided to go with the QUICK. The reason behind this is that this scheme offers slightly better stability. This was particularly important to avoid costly time-dependent analyses. The higher order scheme also brings disadvantages, such as, for example, more difficult model convergence. The model was considered converged when all residuals stabilised at an appropriate level. This was below $10^{-3}$ for continuity and $10^{-4}$ for velocity and turbulence. Additionally, velocity pressure and mass flux at the outlet were monitored and calculations were terminated when the values at that point did not change.

Because the test rig was located in an enclosed space and the entire piping system with the cyclone separator was insulated, the thermal boundary condition of all model walls was zero heat flux. Particulate matter was

modeled with the discrete phase model (DPM). The particles were tracked with a maximum number of steps of 350 000 and a step length factor of 5. A spherical drag law was enabled for momentum exchange, and a discrete random walk model was enabled with 5 tries and a 0.15-time scale constant. There were 18 separate injections, one for each fraction. With each injection, a constant particle diameter was set equal to the maximal size in the fraction (i.e., for fraction 56 µm, the diameter was 56 µm). The particle type was inert, with a density provided by the measurements. Because the dust content in the gas was low (15 $g/m_n^3$), the interactions between particles were neglected. Moreover, the interaction between the particles and the gas was limited only to the influence of the gas flow on the movement of the particles, whereas the interaction in the opposite direction was disregarded (one-way interaction).

## 3.2 Inlet zone

The inlet zone is a curved pipe consisting of a straight run-up section of length ten internal diameters of the pipe; a curved section that intersects with the outlet pipe (presented in Fig. 5); and a straight annular section up to the plane (D), where the pipe model was separated from the geometry of the cyclone separator.

In the industrial gas cleaning installation, the flow is induced by BF gas, which has a higher pressure than ambient air. For technical reasons, gas flow was kept under pressure at the outlet, which, for the pilot installation,

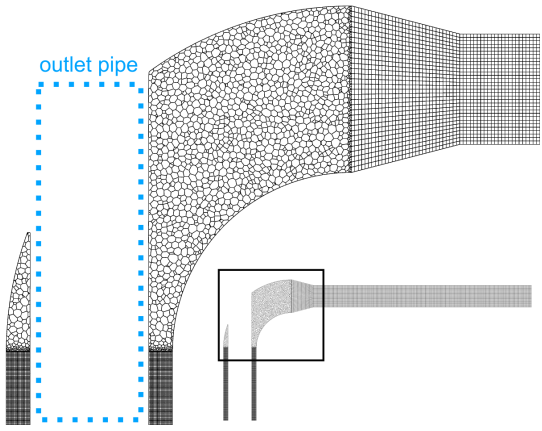


Figure 5: Numerical mesh of the inlet zone at axial cross-section: dotted line – outlet pipe.

was much easier to implement. Because an incompressible model of the gas was employed, the results practically did not depend on the pressure level. The inlet boundary condition (at the entrance of zone A) was set as uniform velocity and temperature with uniformly distributed solid particles.

For the grid independence study, four different grids were tested: 0.25, 0.6, 1.4, and 2.35 mln elements. Dynamic pressure was the parameter observed at the outlet of the zone. The independence study showed that grids with 1.4 and 2.35 mln elements produced very similar results, and the latter was taken for further computations. The final mesh of the inlet zone, being the result of the mesh independence analysis, is presented in Fig. 5 and consists of 2.35 mln elements. Both straight sections were meshed with hexahedral elements, whereas for the curved section, polyhedral elements were used. The minimum orthogonal quality was 0.25, and the maximum aspect ratio was 12.7.

The velocity field in the inlet zone for ID26 is shown in Fig. 6. As shown, a uniform profile was applied at the A.1 inlet. The flow develops throughout the first straight section and then encounters the outlet pipe in the curve region where the profile drastically changes. The velocity profile at the outlet A.2 results from the geometry and is non-uniform.

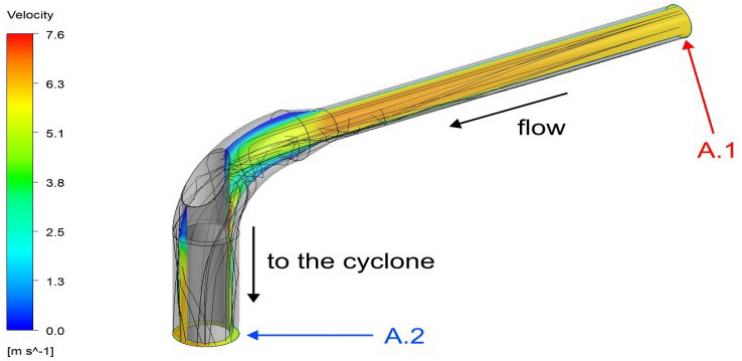


Figure 6: Inlet zone – velocity field and exemplary BF dust trajectories: A.1 – inlet to the inlet zone, A.2 – outlet (inlet to the cyclone).

Several BF dust particle trajectories are also shown as thin black lines. All particle fractions were injected at the A.1 inlet. Some of the heavier particles fell in a straight section and began to bounce off the walls, while the lighter particles remained airborne and continued to move with the airflow. At the A.2 outlet, the intersection coordinates of each particle along with its diam-

eter, density, temperature, flow rate, and velocity components were sorted by diameter and written in text files. This was done automatically using a user-defined function based on the DEFINE_DPM_OUTPUT macro. The files were then read by the cyclone separator model.

The distributions of three BF dust fractions: 3.9, 100, and 800 µm at the A.2 outlet are presented in Fig. 7 for two cases: ID30 and ID26. Case ID30 was characterized by a higher overall mean velocity (higher air flow rate) of approximately 10 m/s, whereas case ID26 corresponded to about 7 m/s. One can see that the gas velocity was always higher at the outer bend of the inlet pipe. The difference between the velocity on the outer and inner sides of the outlet from the inlet zone was about 20%. It became evident that the velocity, combined with the shape of the inlet zone, according to the numerical study, had a serious impact on the distribution of some particles – in this case it was fraction 100 µm, but it also applied to other neighboring fractions. This fraction had a highly non-uniform distribution, where particles tended to aggregate on the inner side of the channel (low-velocity zone), especially visible in the ID26 case. However, smaller dust particles were not affected by the flow and were almost evenly distributed throughout the outlet surface regardless of the gas velocity. The same applied to the largest particles. Wall reflections did not seem to affect the heavy particles' distribution as much as the average one.

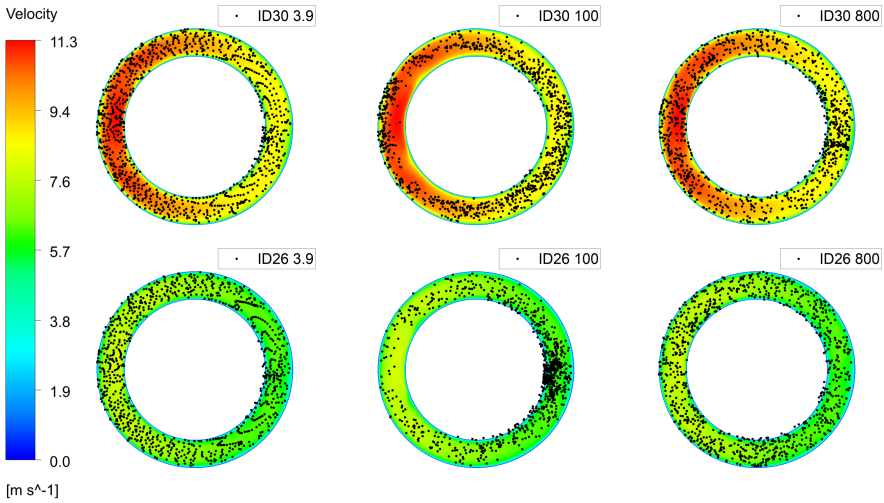


Figure 7: Inlet zone (D-D split plane) – velocity field of cases ID30 and ID26 along with particle distributions of three different fraction: 3.9 µm, 100 µm, and 800 µm.

### 3.3 Cyclone separator

The detailed geometry of the numerical model is shown in Fig. 8. This covers part of the straight inlet pipe starting from the D split plane (for initial development of the flow profile) and the cyclone separator up to the shutoff valve (6) below the conical part. As dust-laden air (a–b) enters the separator, the annular inlet extends slightly. Then, the airflow is swirled by the flow guides (5) and enters the cyclone, where the separation takes place. The dust particles eliminated from the flow (c) are collected in the dust hopper connected to the cyclone separator through the valve (6).

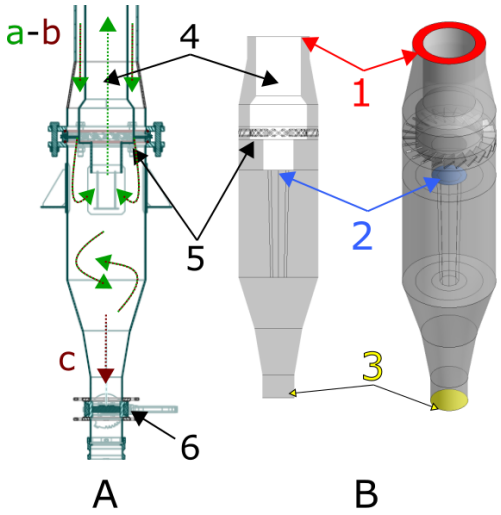


Figure 8: Axial cyclone separator: A – geometry, B – computational domain; a-b – dust laden air, c – captured dust, 1 inlet, 2 – outlet, 3 – particle trap, 4 – outlet pipe, 5 – flow guides, 6 – shut-off valve.

There are three main boundary conditions associated with the computational domain: (1) velocity inlet, (2) pressure outlet, and (3) wall (particle trap). The inlet consists of a velocity profile and a spatial distribution of particles as calculated in zone A. Each dust fraction is applied as a separate injection.

The mesh sensitivity study covered four different mesh sizes ranging from 0.56 to approximately 3 mln elements. These were tested in terms of the predicted velocity profile presented in Fig. 9, where the tangential velocity in the cylindrical zone is shown. The coarsest mesh (0.56 mln el.) appeared to be insufficient, because the maximum velocity near the axis (at 0 m) was

noticeably underestimated when compared with other meshes. Therefore, the second coarsest mesh (0.88 mln el.) was chosen for further simulations, because it produced comparable results to the ones provided by the finer meshes.

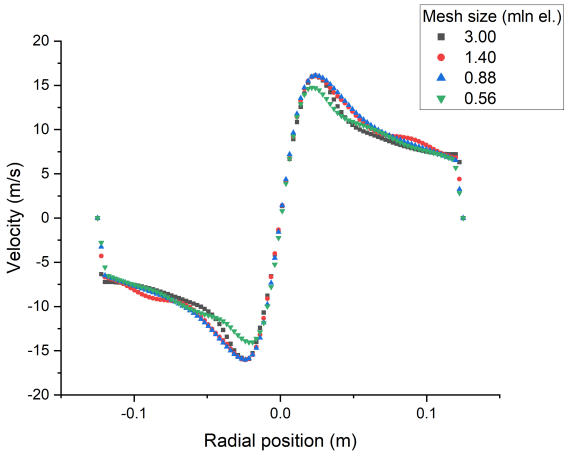


Figure 9: Mesh analysis – comparison of tangential velocity for the tested meshes.

In the next step, courant flow number (CFN) analysis was necessary, because the analyses were performed in a steady state. Such calculations are more robust (which was an important factor during the project) than the transient ones, and the final (averaged) results are the same. However, the computational issues of the steady-state analysis had to be overcome by adjusting the CFN from the default value (200) to 10, which improved the flow stability and convergence. Then, the coarsest mesh providing consistent results was chosen for further calculations, and it was (again) a mesh (0.88 mln) consisting of fully hexahedral elements. The maximum aspect ratio was 4.01. The minimum element quality was 0.45, whereas the maximum skewness was 0.60. The mesh is presented in Fig. 10. On the left-hand side, an axial cross-section is shown throughout the cyclone separator. The normal cross-section A–A is located slightly below the outlet, where an octagonal shape can be observed in the center. This shape improved the quality of the mesh (smoother transition, better structure, similar element size) in the ascending vortex zone. On the right-hand side, a detailed view of the conical part is shown, where the mesh is vertically refined to keep the element's aspect ratio and structure similar.

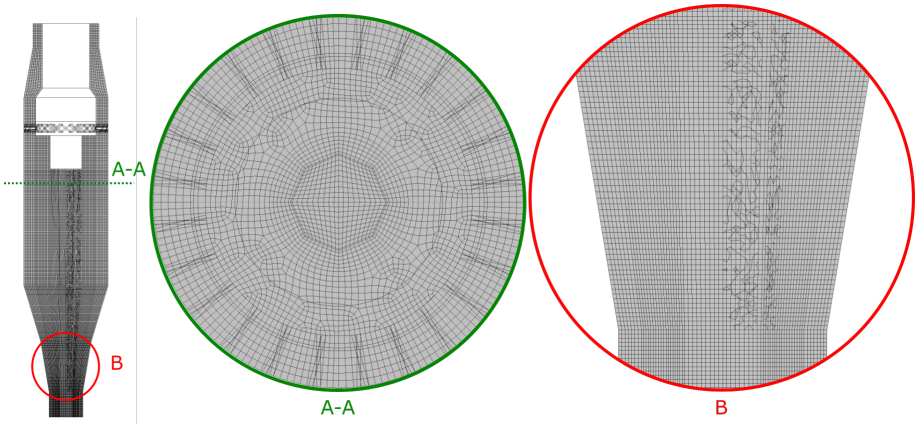


Figure 10: Cyclone separator – final mesh: A – mesh in cross-section, B – detailed mesh in conical part.

Once the mesh was selected, an appropriate value of CFN was required for further stabilization and convergence control of the solution. The impact of four CFN values was investigated: 5, 15, 25, and 35. In all cases, the velocity fields (shown in Fig. 11) and the residuals (not shown) were monitored. At this point, a uniform velocity profile at the inlet was applied; the geometry was axisymmetric, so the velocity field is expected to be symmetric with a low-velocity zone along the axis. As shown, the most symmetrical profile had clearly outlined regions of low velocity (in the axis) below 4.1 m/s, high velocity (in the vicinity of the axis) above 28.7 m/s, and medium velocity (near the wall) between 8.2 and 20.5 m/s with CFN = 15. In the profile for CFN = 5, some minor instabilities were observed, whereas the profiles for CFN = 25 and CFN = 35 were significantly asymmetrical, and the low-velocity region was blurred and even almost completely disappeared. Therefore, CFN = 15 was used in all subsequent calculations.

Once a value of the CFN is established, the reflection coefficients (tangent and normal) need to be determined. The reflection coefficient takes a value between 0 and 1, where 0 stands for no momentum retention and 1 for full momentum retention during the collision of the particle with the wall. The extreme situations, where the particle fully retains or loses momentum, are theoretically possible but not in real application. Therefore, the values 0 and 1 were not considered in the study. Reflection coefficients were chosen according to the separation behavior of the dust measured on the test rig. That is, different pairs of values (tangent and normal) were

tested numerically (from the range 0.1–0.9) using the dust (provided by the experiments). Then, one pair that gave the best fit with the experimental separation, has been chosen and used throughout the model. The coefficients are presented in Table 3, and the chosen pair is given in the box for better clarity. The value of the tangent and normal reflection coefficient was incremented by 0.1 in the range from 0.1 to 0.9. The separation efficiency, calculated as the ratio of trapped (separated) trajectories to all trajectories, was then determined for three different fractions: 3.9, 100, and 800 µm. The chosen fractions covered small, medium, and large particles, because the behavior of particles in the flow depends on mass. The tested reflection coefficients are presented in Table 3, organized in a matrix-like form, and were assumed to be constant. Fractional separation efficiencies are also given (in %). The analysis left two pairs of coefficients that suited the measurements: 0.7–0.8 and 0.8–0.8. The values of the 0.7–0.8 pair are boxed to show that they matched the measurement-based separation efficiencies most closely. Therefore, the reflection coefficients 0.7–0.8 (tangent and normal, respectively) were used in further calculations.

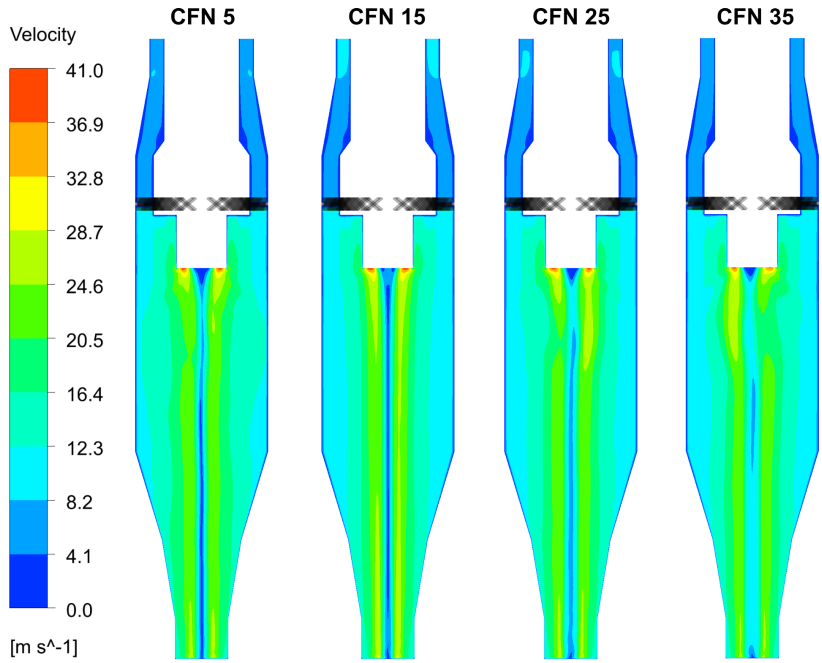


Figure 11: Cyclone – CFN impact on the velocity field (for an axial cross-section).

Table 3: Fractional separation efficiency (%) in terms of different reflection coefficients (values in the box – the best fit with experimental fractional efficiency).

| Fraction, (μm) | | | Reflection Coefficient: Tangent | | | | | |
|---|---|---|---|---|---|---|---|---|
| | | | 0.1 | 0.5 | 0.6 | 0.7 | 0.8 | 0.9 |
| 3.9 | Reflection Coefficient: Normal | 0.1 | 54.74 | | | | | 53.68 |
| | | 0.5 | | 55.79 | | | 55.79 | 52.63 |
| | | 0.6 | | | | | | |
| | | 0.7 | | | | | 56.84 | |
| | | 0.8 | | 55.79 | 57.89 | 61.05 | 57.62 | 56.84 |
| | | 0.9 | 59.29 | | | | | 55.79 |
| 100 | | 0.1 | 100.00 | | | | | 100.00 |
| | | 0.5 | | 100.00 | | | 100.00 | 100.00 |
| | | 0.6 | | | | | | |
| | | 0.7 | | | | | 100.00 | |
| | | 0.8 | | 100.00 | 100.00 | 100.00 | 100.00 | 100.00 |
| | | 0.9 | 100.00 | | | | | 100.00 |
| 800 | | 0.1 | 100.00 | | | | | 100.00 |
| | | 0.5 | | 100.00 | | | 100.00 | 100.00 |
| | | 0.6 | | | | | | |
| | | 0.7 | | | | | 100.00 | |
| | | 0.8 | | 100.00 | 100.00 | 100.00 | 100.00 | 100.00 |
| | | 0.9 | 100.00 | | | | | 100.00 |

# 4 Model validation and discussion

Once the correct CFN value for the model was found, the calculations were performed for three test cases: ID4, ID26, and ID30, which corresponded to three different gas velocities at the input: 8, 7, and 10 m/s, respectively. The numerical model was validated in terms of fractional separation efficiency, but the velocity field needed to be evaluated first. In Fig. 12, the velocity fields of all tested cases are presented. The slightly distorted symmetry of all the profiles was important, yet this was expected since the velocity profile at the inlet is asymmetric. The low velocity region near the axis, as well as the neighboring high-velocity region, is clearly visible. Hence, no anomalies in the velocity field were observed.

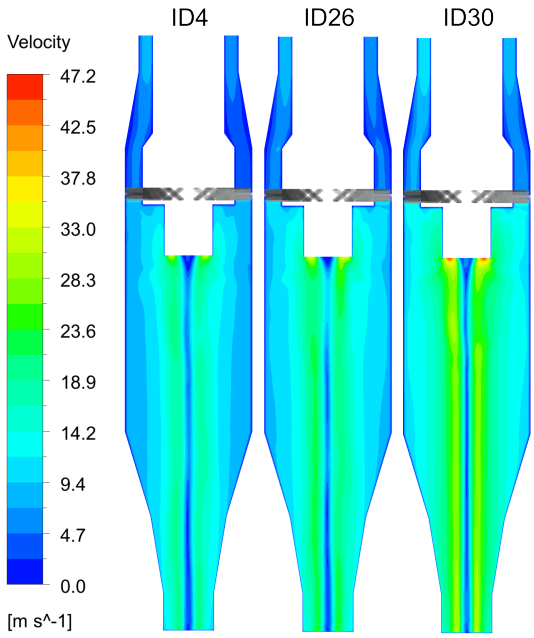


Figure 12: Cyclone separator – velocity field for the validation cases (for CFN = 15).

The predicted behavior of particles with a diameter of 3.9, 100, and 800 µm for a gas velocity of 10 m/s is shown in Fig. 13. For the sake of clarity, only a small number of particles are shown. The 3.9 µm particles moved chaotically, making many laps around the circumference of the cyclone separator. Some of the particles fell into the ash hopper, whereas others reached the internal ascending vortex and left the cyclone separator with the gas. The trajectories of larger particles with a diameter of 100 µm were much more orderly arranged while moving around the cyclone separator. Their trajectories were concentrated near the external walls. Here, all of the particles were separated because they were too heavy for an internal ascending vortex to lift them toward the outlet. The same was observed for the 800 µm particles. However, the trajectories were much steeper in the cylindrical part, while the conical part was crowded (similar to the 100 µm case). It should be noted that, according to the model, the residence time was longer for heavier particles by approximately 2–4 times.

The separation efficiency for each of the measured 18 dust fractions was then compared with the CFD results, which are presented in Fig. 14. Red bars indicate fractional separation efficiencies provided by the CFD model,

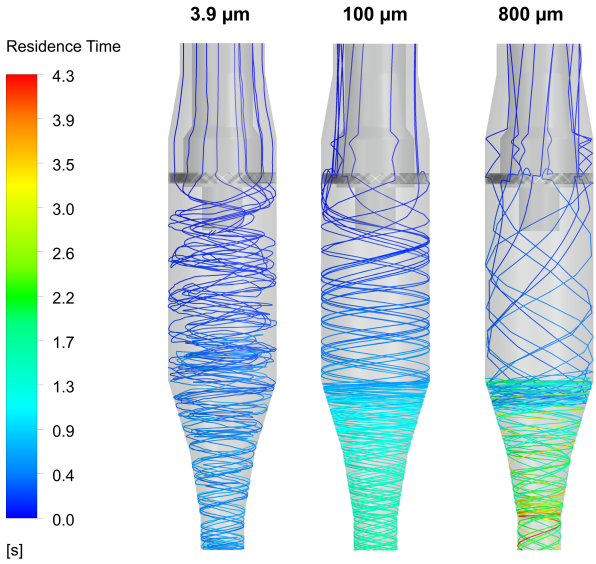


Figure 13: Cyclone separator – predicted particle trajectories and their residence time.

whereas blue bars represent experimental efficiencies. The separation efficiency of the CFD model was calculated as a ratio of the number of trajectories of a given diameter captured at the bottom of a cyclone separator (the particle trap in Fig. 3) to the number of injected trajectories at the inlet of the cyclone separator. For the measurements, the fractional separation efficiency was calculated using Eq. (3). When analyzing the results of the fractional efficiency (see Fig. 14), strange behavior associated with the fraction 56 µm was observed. While the efficiencies changed continuously for other fractions, there was a jump in efficiency for the fraction 56 µm. This can be explained as follows: First, as already mentioned, the sieve analysis was performed on two different devices. The coarse fractions were separated using a laser diffraction device whose smallest sieve was of 71 µm mesh diameter. The mass of the dust leaving this device was transported to a lab located in another city. Here, the counterflow Bahco high-speed centrifuge was used to separate small-diameter fractions. Because the strange and discontinuous behavior of fraction 56 µm was consistent across multiple tests, it is highly likely that most of the dust losses occurred during transportation, lowering the efficiency of this fraction. From a physical point of view, it is impossible that a cyclone separates 100% of the smaller particles and only 80% of the larger particles. Therefore, it was decided to artificially assume

that the efficiency of this fraction was 100%, as it was for fraction 27.7 µm. The fractional separation efficiency for all cases was almost equal to 100% for 8.8 µm. However, measurements show that for this 56 µm fraction, the efficiency was between 94 and 98%. Generally, the CFD model slightly over-predicted the efficiency for the smallest fraction (diameter 1.9 µm) whereas it slightly under-predicts for the following two (i.e., 3.9 µm and 6.4 µm). However, looking at the model, none of the other settings improved these results. Correction of fractional efficiency also increased the total efficiency (see Fig. 14(d)). The differences in global separation efficiency for all three cases showed differences in the range of 0.4–0.7%, which should be considered an acceptable result. The cut-off point for all analyses was located in fraction 8.8 µm and was determined correctly. The differences in results were visible only in the three smallest fractions.

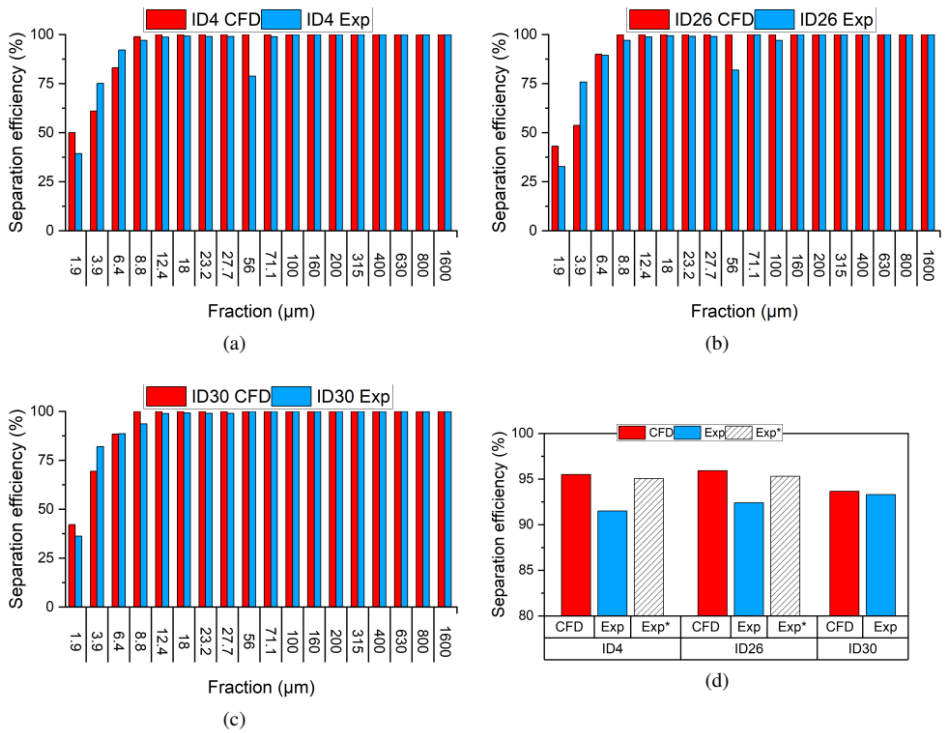


Figure 14: Numerical model validation: a, b, c – fractional separation efficiencies; d – total separation efficiency (CFD – numerical results; Exp – experimental results; Exp* – experimental results assuming 99% separation efficiency of fraction 56 µm in cases ID4 and ID26).

# 5 Conclusions

The main objective of this study was to develop a numerical model of a cyclone separator for the separation of particulate matter that is able to foresee the cyclone separator cut-off point. This allows for designing of the cyclone separator so the most of the zinc and lead pass through while iron and carbon is removed from gas.

The results of numerical simulation showed good agreement between the numerical results and the experiments for all investigated gas velocities and particle fractions. Only for the smallest particles, the numerical model over-predicted the separation efficiency.

Model accuracy was achieved due to proper selection of the normal and tangential reflection coefficients, which have a significant impact on the separation efficiency. These coefficients were adjusted so that no unfeasible results appeared for any of the dust diameters. In addition, the correct CFN was chosen to stabilize the flow and obtain the correct flow field.

These findings of the pilot-scale cyclone separator analysis will next be used to determine the geometry and flow parameters of a full-scale industrial cyclone separator.

## Acknowledgements

This research was supported by the Polish Agency for Enterprise Development within grant no. POIR.01.01.01-00-099/18. Mieszko Tokarski was also supported by the Ministry of Science and Higher Education, Poland, with the grant AGH UST no. 16.16.210.476 and by the NAWA Polish Returns no. 12.12.210.05020 (PPN/PPO/2019/1/00023/U/0001). The publication was supported by statutory research funds of the Faculty of Energy and Environmental Engineering of the Silesian University of Technology.

*Received 20 December 2023*

# References

[1] Lim J.H., Oh S.H., Kang S., Lee K.J., Yook S.J.: *Development of cutoff size adjustable omnidirectional inlet cyclone separator*. Sep. Purif. Technol. **276**(2021), 119397. doi: 10.1016/j.seppur.2021.119397

[2] Babaoglu N.U., Parvaz F., Hosseini S.H., Elsayed K, Ahmadi G.: *Influence of the inlet cross-sectional shape on the performance of a multi-inlet gas cyclone*. Powder Technol. **384**(2021), 82–99. doi: 10.1016/j.powtec.2021.02.008

[3] Wang S., Luo K., Hu C., Fan J.: *CFD-DEM study of the effect of cyclone arrangements on the gas-solid flow dynamics in the full-loop circulating fluidized bed.* Chem. Eng. Sci. **172**(2017), 199–215. doi: 10.1016/j.ces.2017.05.052

[4] Stanek W., Szega M., Blacha L., Niesler M., Gawron M.: *Exergo-ecological assessment of auxiliary fuel injection into blast-furnace.* Arch. Metall. Mater. **60**(2015), 711–719. doi: 10.1515/amm-2015-0196

[5] Li W., Huang Z., Li G., Ye C.: *Effects of different cylinder roof structures on the vortex of cyclone separators.* Sep. Purif. Technol. **296**(2022), 121370. doi: 10.1016/j.seppur.2022.121370

[6] Hsu C.W., Huang S.H., Lin C.W., Hsiao T.C., Lin W.Y., Chen C.C.: *An experimental study on performance improvement of the stairmand cyclone design.* Aerosol Air Qual. Res. **14**(2014), 3, 1003–1016. doi: 10.4209/aaqr.2013.04.0129

[7] Roloff C., Lukas E., Wachem B., Thévenin D.: *Particle dynamics investigation by means of shadow imaging inside an air separator.* Chem. Eng. Sci. **195**(2019), 312–324. doi: 10.1016/j.ces.2018.09.020

[8] Celis G.E.O., Loureiro J.B.R., Lage P.L.C., Silva Freire A.P.: *The effects of swirl vanes and a vortex stabilizer on the dynamic flow field in a cyclonic separator.* Chem. Eng. Sci. **248**(2022), 117099. doi: 10.1016/j.ces.2021.117099

[9] Babaoglu N.U., Hosseini S.H., Ahmadi G., Elsayed K.: *The effect of axial cyclone inlet velocity and geometrical dimensions on the flow pattern, performance, acoustic noise.* Powder Technol. **407**(2022), 117692. doi: 10.1016/j.powtec.2022.117692

[10] Zhang R., Yang J., Han S., Hao X., Guan G.: *Improving advantages and reducing risks in increasing cyclone height via an apex cone to grasp vortex end.* Chin. J. Chem. Eng. **54**(2022), 136–143. doi: 10.1016/j.cjche.2022.04.014

[11] Yoshida H.: *Effect of apex cone shape and local fluid flow control method on fine particle classification of gascyclone.* Chem. Eng. Sci. **85**(2013), 55–61. doi: 10.1016/j.ces.2012.01.060

[12] Yang X., Yang J., Wang S., Zhao Y.: *Effects of operational and geometrical parameters on velocity distribution and micron mineral powders classification in cyclone separators.* Powder Technol. **407**(2022), 117609. doi: 10.1016/j.powtec.2022.117609

[13] Huang A.N., Ito K., Fukasawa T., Yoshida H., Kuo H.P., Fukui K.: *Classification performance analysis of a novel cyclone with a slit on the conical part by CFD simulation.* Sep. Purif. Technol. **190**(2018), 25–32. doi: 10.1016/j.seppur.2017.08.047

[14] Zheng Y., Ni L.: *Numerical study on particles separation using a cyclone enhanced by shunt device: Effects of cylinder-to-cone ratio and vortex finder-to-cylinder ratio.* Powder Technol. **408**(2022), 117767. doi: 10.1016/j.powtec.2022.117767

[15] Pandey S., Brar L.S.: *On the performance of cyclone separators with different shapes of the conical section using CFD.* Powder Technol. **407**(2022), 117629. doi: 10.1016/j.powtec.2022.117629

[16] Martignoni W.P., Bernardo S., Quintani C.L.: *Evaluation of cyclone geometry and its influence on performance parameters by computational fluid dynamics (CFD).* Braz. J. Chem. Eng. **24**(2007), 83–94. doi: 10.1590/S0104-66322007000100008

[17] Le D.K., Guo M., Yoon J.Y.: *A hybrid CFD – deep learning methodology to improve the accuracy of cut-off diameter prediction in coarse-grid simulations for cyclone separators*. J. Aerosol Sci. **170**(2023), 106143. doi: 10.1016/j.jaerosci.2023.106143

[18] Wasilewski M., Brar L.S.: *Effect of the inlet duct angle on the performance of cyclone separators*. Sep. Purif. Technol. **213**(2019), 19–33. doi: 10.1016/j.seppur.2018.12.023

[19] Xiang R.B., Lee K.W.: *Effects of exit tube diameter on the flow field in cyclones*. Part. Sci. Technol. **26**(2008), 467–481. doi: 10.1080/02726350802367829

[20] Su Y., Zheng A., Zhao B.: *Numerical simulation of effect of inlet configuration on square cyclone separator performance*. Powder Technol. **210**(2011), 293–303. doi: 10.1016/j.powtec.2011.03.034

[21] Azadi M., Azadi M., Mohebbi A.: *A CFD study of the effect of cyclone size on its performance parameters*. J. Hazard. Mater. **182**(2010), 835–841. doi: 10.1016/j.jhazmat.2010.06.115

[22] Oh J., Choi S., Kim J.: *Numerical simulation of an internal flow field in a uniflow cyclone separator*. Powder Technol. **274**(2015), 135–145. doi: 10.1016/j.powtec.2015.01.015

[23] Chen L., Ma H., Sun Z., Ma G., Li P., Li C., Cong X.: *Effect of inlet periodic velocity on the performance of standard cyclone separators*. Powder Technol. **402**(2022), 117347. doi: 10.1016/j.powtec.2022.117347

[24] Zhang L., Chen Y., Zhao B., Dang M., Yao Y.: *Numerical simulation on structure optimization of escape-pipe of cyclone separator with downward outlet*. Powder Technol. **411**(2022), 117588. doi: 10.1016/j.powtec.2022.117588

[25] Slack M.D., Prasad R.O., Bakker A., Boysan F.: *Advances in cyclone modelling using unstructured grids*. Chem. Eng. Res. Des. **78**(2000), 1098–1104. doi: 10.1205/026387600528373

[26] Shalaby H., Wozniak K., Wozniak G.: *Particle-laden flow simulation in a cyclone separator*. Proc. Appl. Math. Mech. **6**(2006), 547–548. doi: 10.1002/pamm.200610254

[27] Dong S., Wang C., Zhang Z., Cai Q., Dong K., Cheng T., Wang B.: *Numerical study of short-circuiting flow and particles in a gas cyclone*. Particuology **72**(2023), 81–93. doi: 10.1016/j.partic.2022.02.008

[28] Guo M., Yang L., Son H., Le D.K., Manickam S., Sun X., Yoon J.Y.: *An overview of novel geometrical modifications and optimizations of gas-particle cyclone separators*. Sep. Purif. Technol. **329**(2024), 125136. doi: 10.1016/j.seppur.2023.125136

[29] Huang L., Yuan J., Pan M., Wu J., Qiao J., Jiang H., Duan C.: *CFD simulation and parameter optimization of the internal flow field of a disturbed air cyclone centrifugal classifier*. Sep. Purif. Technol. **307**(2023), 122760. doi: 10.1016/j.seppur.2022.122760

[30] Stecko J., Stachura R., Niesler M., Bernasowski M., Klimczyk A.: *Utilisation of metallurgical sludge by multi-layer sintering*. Ironmak. Steelmak. **45**(2018), 779–786. doi: 10.1080/03019233.2017.1337285

[31] ANSYS. *Ansys Fluent Theory Guide*. Canonsburg 2019.

**archives**
**of thermodynamics**
Vol. **44**(2023), No. 4, 563–579
DOI: 10.24425/ather.2023.149735

# The analysis of the stability of the Cauchy problem in the cylindrical double-layer area

**MICHAŁ CIAŁKOWSKI**[a]
**MAGDA JOACHIMIAK**[a*]
**MAGDALENA MIERZWICZAK**[b]
**ANDRZEJ FRĄCKOWIAK**[b]
**ALEKSANDER OLEJNIK**[c]
**ADAM KOZAKIEWICZ**[c]

[a] Poznan University of Technology, Institute of Thermal Engineering, Piotrowo 3a, 60-965, Poznań, Poland

[b] Poznan University of Technology, Institute of Applied Mechanics, Jana Pawła II 24, 60-965, Poznań, Poland

[c] Military University of Technology, Sylwestra Kaliskiego 2, 00-908 Warszawa, Poland

**Abstract** Ceramic protective coats, for instance, on turbine blades, create a double-layer area with various thermophysical properties and they require metal temperature control. In this paper, it is implemented by formulating a Cauchy problem for the equation of thermal conductivity in the metal cylindrical area with a ceramic layer. Due to the ill posed problem, a regularization method was applied consisting in the notation of thermal balance for the ceramic layer. A spectral radius for the equation matrix was taken as the stability measure of the Cauchy problem. Numerical calculations were performed for a varied thickness of the ceramic layer, with consideration of the non-linear thermophysical properties of steel and a ceramic layer (zirconium dioxide). A polynomial was determined which approximates temperature distribution in time for the protective layer. The stability of solutions was compared for undisturbed and disturbed temperature values, and thermophysical parameters with various ceramic layer thickness. The obtained calculation results confirmed the effectiveness of the proposed regularization method in obtaining stable solutions at random data disturbance.

*Corresponding Author. Email: magda.joachimiak@put.poznan.pl

**Keywords:** Cauchy problem; Quasiregularization method; Protective layer; Cylindrical double-layer area

## Nomenclature

| | | |
|---|---|---|
| $c$ | – | specific heat, J/kgK |
| div | – | divergence |
| $g$ | – | metal layer thickness, m |
| $q$ | – | heat flux, W/m$^2$ |
| $r$ | – | radius, m |
| $T$ | – | temperature, °C |
| $t$ | – | time, s |
| $x$ | – | dimensionless coordinate |

**Greek symbols**

| | | |
|---|---|---|
| $\Gamma$ | – | boundary |
| $\delta_c$ | – | thickness of ceramic, m |
| $\tilde{\delta}$ | – | relative error, % |
| $\lambda$ | – | thermal conductivity, W/mK |
| $\lambda_s$ | – | spectral radius of stability matrix |
| $\rho$ | – | density, kg/m$^3$ |
| $\Omega$ | – | area |
| $\nabla$ | – | gradient |

**Subscripts**

| | | |
|---|---|---|
| $c$ | – | ceramic, the outer surface of the ceramic |
| in | – | inner surface of the metal |
| $m$ | – | metal |
| out | – | outer surface of the metal |
| $s$ | – | specific heat |
| stab | – | stability matrix |

# 1 Introduction

The efficiency of the gas turbine circulation depends, inter alia, on the temperature and pressure of gas flowing out from the combustion chamber [1–5], and their values are limited by the thermal resistance of the washed surface [6]. In order to prevent the blade metal from exceeding a given temperature, cooling channels [7–9] are made in such a blade or a thin ceramic layer is applied on its surface, which is characteristic for high thermal resistance (low value of a thermal conductivity coefficient) [10–12]. Assuming the equality of temperature and heat flux at the metal-ceramic contact point, with an unknown temperature on the outer ceramic surface

leads to the Cauchy problem [10–14]. The problem of inverse thermal conductivity for double-layer areas may also be applied in the analysis of the heat loads of boilers [15–17], heat exchanger pipes with sediment [18], small arms barrels [19] or orbiter skin [20].

Inverse problems are regarded as ill posed in Hadamard sense [21–26], and the solution may be highly sensitive to the input data errors [27–30]. This is particularly important if inverse calculations involve experimental data burdened with a random measurement error [31–35]. Even small data errors may lead to huge errors in solutions which makes inverse problems difficult to solve numerically. Nevertheless, the majority of the existing numerical methods may provide stable solutions for boundary-initial problems by use of regularization techniques [36–38]. Those most popular include: Tikhonov regularization method [39], singular value decomposition method [40], statistical Bayesian inference, gradient-based regularization algorithm, entropy maximum. The regularization methods may need an additional parameter for which the determination of a value poses an additional challenge. One of the optimal parameter selection criteria is a discrepancy principle, L-curve criterion or the generalized cross-validation (GCV) [41, 42].

In this paper, as a regularization method which does not require introducing any additional parameters, a notation of energy balance is used for the ceramic layer covering a metal surface [10]. Whereas, the spectral radius of the equation matrix [43] was used for the stability analysis of the proposed calculation model. The first part of the paper includes the demonstration of the solution model for the Cauchy problem for thermal conductivity in the cylindrical double-layer area. The second part includes the presentation of the numerical calculation results, with particular attention given to solution stability with the various geometry parameters of the tested area.

## 2 Cauchy problem

The calculations were carried out for the double-layer cylindrical area which is presented in Fig. 1. Thermal conductivity takes place in the metal layer for radii $r \in \langle r_{\text{in}}, r_{\text{out}} \rangle$ and in the ceramic layer for radii $r \in \langle r_{\text{out}}, r_c \rangle$. The metal layer thickness is $g = r_{\text{out}} - r_{\text{in}}$ and the ceramic layer thickness is $\delta_c = r_c - r_{\text{out}}$. Thermal conductivity coefficient, density and specific heat for metal are defined as $\lambda_m$, $\rho_m$, $c_m$, respectively, and for the ceramic, these are $\lambda_c$, $\rho_c$, and $c_c$.

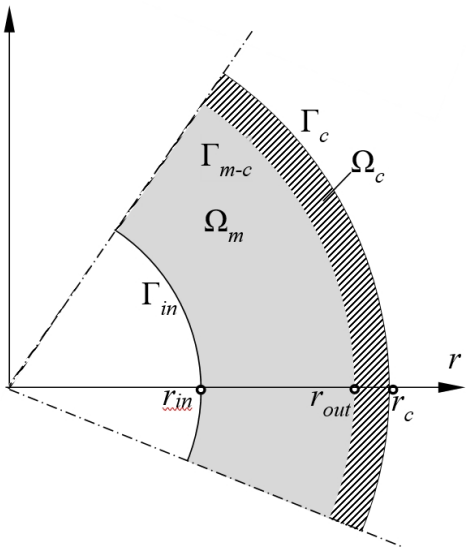


Figure 1: The calculation area consisting of the metal and ceramic layer.

The solution of the Cauchy problem considers an equation for thermal conductivity in the metal layer

$$\rho_m c_m \frac{\partial T_m}{\partial t} = \operatorname{div}\left(\lambda_m \nabla T_m\right), \quad r \in \langle r_{\text{in}}, r_{\text{out}}\rangle, \quad t > 0 \tag{1}$$

and in the ceramic layer

$$\rho_c c_c \frac{\partial T_c}{\partial t} = \operatorname{div}\left(\lambda_c \nabla T_c\right), \quad r \in \langle r_{\text{out}}, r_c\rangle, \quad t > 0. \tag{2}$$

The initial condition was assumed for $t = 0$ for the following the form:

$$T(r, 0) = f(r), \quad r \in \langle r_{\text{in}}, r_c\rangle. \tag{3}$$

On the metal inner surface $\Gamma_{\text{in}}$ (for $r = r_{\text{in}}$) the boundary condition was accepted as

$$T(r_{\text{in}}, t) = T_0(t). \tag{4}$$

On the metal-ceramic contact point $\Gamma_{m_c}$ (for $r = r_{\text{out}}$) the condition of the conformity of temperature and heat fluxes was accepted as

$$T_m(r_{\text{out}}, t) = T_c\left(r_{\text{out}}, t\right) = T_g(t), \tag{5}$$

$$\lambda_m \frac{\partial T_m\left(r_{\text{out}}, t\right)}{\partial r} = \lambda_c \frac{\partial T_c\left(r_{\text{out}}, t\right)}{\partial r}. \tag{6}$$

The solution of the thermal conductivity equation (2) for the ceramic area $\Omega_c$ with initial (3) and boundary (5) and (6) conditions is the Cauchy problem which is an ill posed problem [22]. The problem with the stability of the inverse problems solution necessitates the use of regularization [13, 38, 44, 45]. This paper does not include a classic regularization method [36, 37, 39, 40] but quasiregularization consisting in the consideration of the energy equation in the ceramic area $\Omega_c$. The energy balance equation in the ceramic area $\Omega_c$ was obtained by integrating Eq. (2):

$$\begin{aligned}\int_{r_{\text{out}}}^{r_c} \rho_c(T) c_c(T) \frac{\partial T}{\partial t}\, dr &= \lambda_c\left[T(r,t)\right] \left.\frac{\partial T(r,t)}{\partial r}\right|_{r=r_c} - \lambda_c\left[T(r,t)\right] \left.\frac{\partial T(r,t)}{\partial r}\right|_{r=r_{\text{out}}} \\ &= q_c(t) - q_{\text{out}}(t) = \delta q. \end{aligned} \tag{7}$$

The heat conduction equations for metal (1) and ceramics (2) differ in the values of the thermophysical coefficients ($\lambda$, $\rho$, $c$). In the following analysis, the subscripts denoting metal ($m$) and ceramics ($c$) are omitted. Thus, we consider an equation of the form

$$\rho(T) c(T) \frac{\partial T}{\partial t} = \operatorname{div}\left[\lambda(T) \nabla T\right]. \tag{8}$$

By solving the non-linear Eq. (8) for a given unit of time, iterative calculations were performed to determine the correlated temperature and thermophysical coefficients more accurately, according to the following scheme:

$$\rho\left(T^m\right) c\left(T^m\right) \frac{\partial T^{m+1}}{\partial t} = \operatorname{div}\left[\lambda\left(T^m\right) \nabla T^{m+1}\right], \quad m = 1, 2, \ldots \tag{9}$$

The iterative process was terminated when the inequality was satisfied

$$\left\| T^{m+1} - T^m \right\| < \varepsilon \tag{10}$$

for a given value of $\varepsilon > 0$. The derivative after time $\dfrac{\partial T}{\partial t}$ was approximated by the backward differential quotient for consecutive moments of time $t_{n+1}$ and $t_n$. The differential operation on the right-hand side of Eq. (9) was performed. Thus, the following was obtained:

$$\begin{aligned}\rho\left(T^n\right) c\left(T^n\right) \frac{T^{n+1} - T^n}{\Delta t} &= \lambda\left(T^n\right) \left( \frac{d^2 T^{n+1}}{dr^2} + \frac{1}{r} \frac{dT^{n+1}}{dr} \right) \\ &+ \lambda'\left(T^n\right) \frac{dT^n}{dr} \frac{dT^{n+1}}{dr} \end{aligned} \tag{11}$$

for $r \in \Omega_m$ or $r \in \Omega_c$. Using the central differential quotients at point $r_i$ for the right-hand side of Eq. (11) for time $t_{n+1}$ we obtain the differential form of Eq. (9):

$$\rho\left(T_i^n\right) c\left(T_i^n\right) \frac{T_i^{n+1}-T_i^n}{\Delta t} = \frac{\lambda\left(\frac{T_{i+1}^n+T_i^n}{2}\right)\frac{T_{i+1}^{n+1}-T_i^{n+1}}{r_{i+1}-r_i} - \lambda\left(\frac{T_i^n+T_{i-1}^n}{2}\right)\frac{T_i^{n+1}-T_{i-1}^{n+1}}{r_i-r_{i-1}}}{\frac{r_{i+1}+r_i}{2} - \frac{r_i+r_{i-1}}{2}} + \frac{\lambda\left(T_i^n\right)}{r_i}\cdot\frac{T_{i+1}^{n+1}-T_{i-1}^{n+1}}{r_{i+1}-r_{i-1}} + \lambda'\left(T_i^n\right)\frac{T_{i+1}^n-T_{i-1}^n}{r_{i+1}-r_{i-1}}\cdot\frac{T_{i+1}^{n+1}-T_{i-1}^{n+1}}{r_{i+1}-r_{i-1}}, \quad i=1,2,\ldots \tag{12}$$

Finally, an equation was obtained as follows for each internal point of the area of metal $\Omega_m$ and ceramic $\Omega_c$ we have

$$a_{i,i-1}T_{i-1}^{n+1} + a_{i,i}T_i^{n+1} + a_{i,i+1}T_{i+1}^{n+1} = b_i T_i^n\,. \tag{13}$$

The coefficients $a_{i,i-1}$, $a_{i,i}$, $a_{i,i+1}$, and $b_i$ contain the values of the thermophysical coefficients and temperature at time $t_n$. The nodes adopted in the calculations for the metal and ceramic layers are shown in Fig. 2.

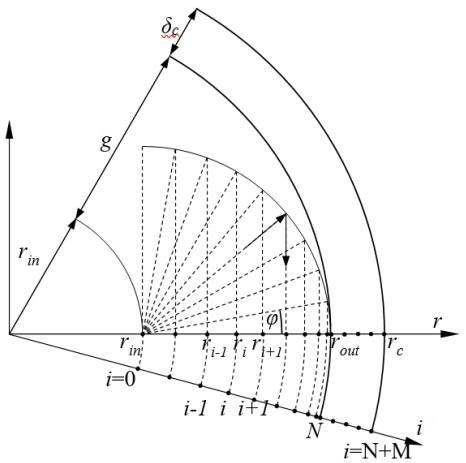


Figure 2: Nodes of a two-layer area.

After using discretization for Eqs. (1) and (2) of the conditions (3)–(6) and the trapezoidal integration of Eq. (7) the problem is reduced to the matrix

equation of the form for time $t_{n+1}$:

$$[\alpha^n]\left\{T^{n+1}\right\} = [\beta^n]\left\{T^n\right\}. \tag{14}$$

The temperature at consecutive nodes $i = 0, 1, 2, \ldots, N+M$ (as shown in Fig. 2) for time $t_n$ and $t_{n+1}$ was described by vectors of the form

$$\left\{T^n\right\} = \left\{T_0^n, T_1^n, \ldots, T_{N+M}^n\right\}^T, \tag{15}$$

$$\left\{T^{n+1}\right\} = \left\{T_0^{n+1}, T_1^{n+1}, \ldots, T_{N+M}^{n+1}\right\}^T. \tag{16}$$

The matrices $[\alpha^n]$ and $[\beta^n]$ written for the metal and ceramic areas supplemented by the initial condition (3), the temperature (5) and heat flux compatibility conditions (6) and the energy balance equation (7) in the ceramic layer at time $t_{n+1}$ after performing the differentiation operation of the non-linear equation according to Eqs. (11)–(12). Hence

$$[\alpha^n] = \begin{bmatrix} A_m^n \\ A_c^n \\ \text{equality of temperature, Eq. (5)} \\ \text{equality of heat flux, Eq. (6)} \\ \text{energy balance, Eq. (7)} \end{bmatrix}. \tag{17}$$

The computational model, together with Eq. (14), is described in detail in [46]. A novelty in the present work is the analysis of the stability of the computational method using the spectral radius, as described later in the paper. Equation (14) can be translated into the form

$$\begin{aligned}[A^n]\left\{T^{n+1}\right\} = [\beta^n]\left\{T^n\right\} &- \left\{\alpha_{00}^n, \alpha_{10}^n, \ldots, \alpha_{N+M,0}^n\right\}^T T_0^{n+1} \\ &- \left\{\alpha_{0N}^n, \alpha_{1N}^n, \ldots, \alpha_{N+M,N}^n\right\}^T T_g^{n+1}.\end{aligned} \tag{18}$$

The matrix $[A^n]$ is formed from the matrix $[\alpha^n]$ by transferring the values obtained from the known temperature $T_0^{n+1}$ and $T_g^{n+1}$ to the right-hand side of the equation. In Eq. (18) $T_0^{n+1}$ is the temperature for radius $r = r_{\text{in}}$, while $T_g^{n+1}$ is the temperature at the metal-ceramic interface for radius $r = r_{\text{out}}$ (according to Eq. (5)) for time $t_{n+1}$. Multiplying Eq. (18) by the

matrix $[A^n]^{-1}$ on both sides, the following was obtained:

$$\begin{aligned}\left\{T^{n+1}\right\} &= [A^n]^{-1}[\beta^n]\{T^n\} - [A^n]^{-1}\left\{\alpha_{00}^n, \alpha_{10}^n, \ldots, \alpha_{N+M,0}^n\right\}^T T_0^{n+1} \\ &\quad - [A^n]^{-1}\left\{\alpha_{0N}^n, \alpha_{1N}^n, \ldots, \alpha_{N+M,N}^n\right\}^T T_g^{n+1} \\ &= [A_{\text{stab}}^n]\{T^n\} + \{c^n\}T_0^{n+1} + \{d^n\}T_g^{n+1} \\ &= [A_{\text{stab}}^n]\{T^n\} + \{e^n\}. \end{aligned} \tag{19}$$

where the matrix $[A_{\text{stab}}^n] = [A^n]^{-1}[\beta^n]$. The subscript "stab" is used to denote the matrix, the spectral radius of which is the measure of the stability of the solution of the inverse problem under consideration.

Thus, for successive moments of time, we have:

$$n = 0: \quad \left\{T^1\right\} = \left[A_{\text{stab}}^0\right]\left\{T^0\right\} + \left\{e^0\right\}, \tag{20}$$

$$\begin{aligned} n = 1: \quad \left\{T^2\right\} &= \left[A_{\text{stab}}^1\right]\left\{T^1\right\} + \left\{e^1\right\} \\ &= \left[A_{\text{stab}}^1\right]\left[A_{\text{stab}}^0\right]\left\{T^0\right\} + \left[A_{\text{stab}}^1\right]\left\{e^0\right\} + \left\{e^1\right\}, \end{aligned} \tag{21}$$

$$\begin{aligned} n = 2: \quad \left\{T^3\right\} &= \left[A_{\text{stab}}^2\right]\left\{T^2\right\} + \left\{e^2\right\} \\ &= \left[A_{\text{stab}}^2\right]\left[A_{\text{stab}}^1\right]\left[A_{\text{stab}}^0\right]\left\{T^0\right\} + \left[A_{\text{stab}}^2\right]\left[A_{\text{stab}}^1\right]\left\{e^0\right\} \\ &\quad + \left[A_{\text{stab}}^2\right]\left\{e^1\right\} + \left\{e^2\right\}, \end{aligned} \tag{22}$$

$$\begin{aligned} n = 3: \quad \left\{T^4\right\} &= \left[A_{\text{stab}}^3\right]\left\{T^3\right\} + \left\{e^3\right\} \\ &= \left[A_{\text{stab}}^3\right]\left[A_{\text{stab}}^2\right]\left[A_{\text{stab}}^1\right]\left[A_{\text{stab}}^0\right]\left\{T^0\right\} \\ &\quad + \left[A_{\text{stab}}^3\right]\left[A_{\text{stab}}^2\right]\left[A_{\text{stab}}^1\right]\left\{e^0\right\} + \left[A_{\text{stab}}^3\right]\left[A_{\text{stab}}^2\right]\left\{e^1\right\} \\ &\quad + \left[A_{\text{stab}}^3\right]\left\{e^2\right\} + \left\{e^3\right\} \end{aligned} \tag{23}$$

and, in general, for a linear issue, $\left[A_{\text{stab}}^k\right] = [B_{\text{stab}}] = \text{const}$. Then, for $n = k$ the equality occurs

$$\left\{T^{k+1}\right\} = [B_{\text{stab}}]^{k+1}\left\{T^0\right\} + \sum_{j=0}^{k}[B_{\text{stab}}]^{k-j}\left\{e^j\right\}. \tag{24}$$

For $k \to \infty$ if the spectral radius of the matrix $[B_{\text{stab}}]$, $\lambda_s([B_{\text{stab}}]) < 1$, then series (24) converges, while the first term tends towards zero (the initial condition at successive moments of time has less and less influence on the solution of the inverse problem). Therefore, for the convergence of the solution of a nonlinear problem at successive moments of time, the inequality must exist

$$\lambda_s\left(\left[A^k_{\text{stab}}\right]\right) < 1. \tag{25}$$

## 3 Numerical calculations

The essence of numerical calculations is demonstrating the impact of the ceramic coat thickness $\delta_c$ on the outer surface of the circular ring with the set geometry (inner radius $r_{\text{in}} = 50$ mm and outer radius $r_{\text{out}} = 100$ mm) on the value of the temperature on the ceramic surface. At the same time, it is assumed that temperature $T_{mc} = 686°\text{C}$ on the metal-ceramic contact point will not be exceeded. When using the ceramic layer with the thickness of $\delta_c = 0.1$ mm the temperature on the outer ceramic surface was 918.6°C after the heating time of 100 s and not exceeding the assumed temperature $T_{mc}$. For the ceramic thickness $\delta_c = 0.2$ mm and $\delta_c = 0.3$ mm, the temperature on the outer ceramic surface was 1177.3°C and 1469.4°C, respectively (Fig. 3). These values indicate that surfaces of e.g. a gas turbine blade with a ceramic layer may operate in the conditions of significantly higher heat loads than without a protective coat.

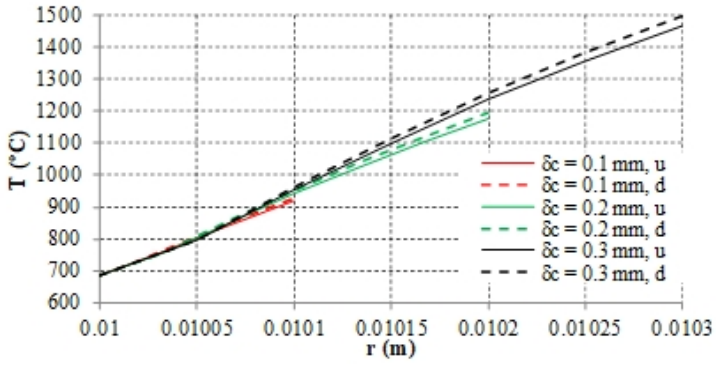


Figure 3: Temperature distribution in the ceramic layer after 100 s for the different thickness of the ceramic layer ($\delta_c = 0.1$ mm, $\delta_c = 0.2$ mm, and $\delta_c = 0.3$ mm) with disturbed (d) and undisturbed (u) input data.

In the subsequent numerical test, the temperature on the metal-ceramic contact point was disturbed randomly to the value of $\tilde{\delta}_T = 0.5\%$. The calculations were conducted with consideration of the non-linear thermophysical properties of metal and ceramic (thermal conductivity coefficient ($\lambda$), density ($\rho$) and specific heat ($s$)). The calculations were performed for the random disturbances of thermophysical parameters with the value of $\tilde{\delta}_{\lambda m} = \tilde{\delta}_{\rho m} = \tilde{\delta}_{sm} = \tilde{\delta}_{\lambda c} = \tilde{\delta}_{\rho c} = \tilde{\delta}_{sc} = 2.5\%$. Temperature courses in the ceramic layer after heating time $t = 100$ s for the disturbed input data differ subtly from the courses for undisturbed data, which is presented in Fig. 3. The temperature course in the ceramic layer may be approximated with the linear function for $\delta_c = 0.1$ mm. Approximation by means of the polynomial of degree 2 and 3 imitates well the temperature course in the ceramic layer for $\delta_c = 0.2$ mm and $\delta_c = 0.3$ mm (Fig. 4), accordingly. In Fig. 4, the approximation functions are shown for the dimensionless ceramic layer thickness coordinate of the form

$$x = \frac{r_i - r_N}{r_{N+M} - r_N} \quad \text{for} \quad r_N \leq r_i \leq r_{N+M}\,. \tag{26}$$

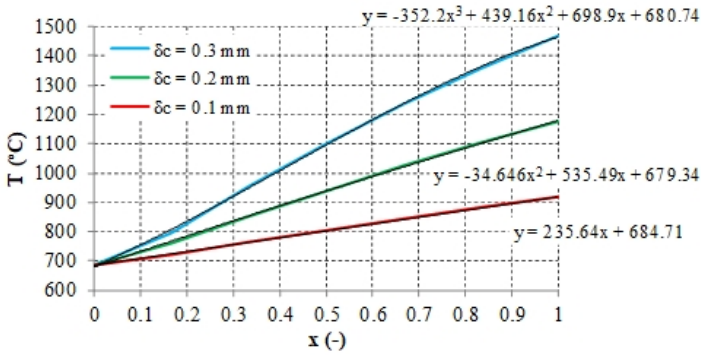


Figure 4: Temperature distribution in the ceramic layer for dimensionless coordinate after 100 s for the different thickness of the ceramic layer ($\delta_c = 0.1$ mm, 0.2 mm, and 0.3 mm) with undisturbed input data.

A basic difficulty in solving of the inverse problem discussed in this paper is its stability considering temperature measurement errors, as well as the disturbance errors of the thermophysical values of steel and zirconium dioxide. A stability measure of the discussed Cauchy problem, which is an ill posed problem [22], is the value of the spectral radius whose values for different numerical tests are presented in Figs. 5–8. The spectral radius

values increase for the subsequent time units from the value of 0.21 to 0.28 for the ceramic layer thickness $\delta_c = 0.1$ mm (Fig. 5). As far as the zirconium dioxide layer $\delta_c = 0.2$ mm is concerned, the spectral radius values increase for the subsequent time units from the value of 0.39 to 0.51, and for $\delta_c = 0.3$ mm, they increase from 0.6 to 0.83 (Fig. 5). The spectral radius values below unities prove a stable solution of the inverse problem. A similar numerical test was carried out also for a high value of inner radius ($r_{\text{in}} = 50$ mm and $r_{\text{in}} = 100$ mm). In such a case, the cylindrical layer approaches the flat layer. Thus, the spectral radii of the stability matrix do not exceed the unity (Fig. 6). For all the cases under consideration, the input data disturbance did not cause significant changes in the spectral radius (Figs. 5–6).

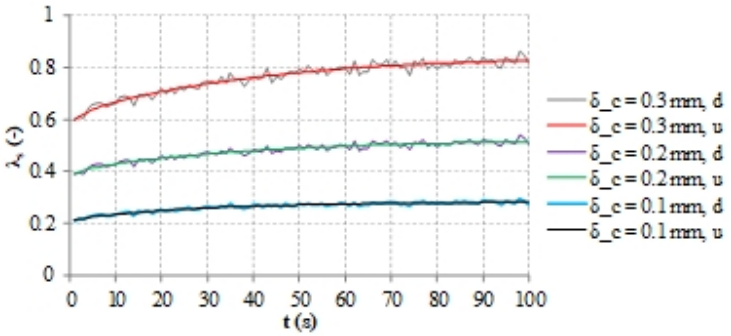


Figure 5: Spectral radius $\lambda_s$ of stability matrix for the different thickness of the ceramic layer ($\delta_c = 0.1$ mm, 0.2 mm, and 0.3 mm) with disturbed (d) and undisturbed (u) input data.

The analysis covered the impact of the ceramic layer thickness $\delta_c$ (from 0.02 to 1 mm) on the spectral radius value with the assumed thickness of the double-layer area $g_{mc} = g + \delta_c$ ($g_{mc}$ amounted to 5.1 mm, 5.2 mm or 5.3 mm) after the warm-up time of $t = 100$ s. The calculations were carried out for the cylindrical area with the radius of $r_{\text{in}} = 5$ mm (Fig. 7) and for the area close to the board with radius $r_{\text{in}} = 100$ mm (Fig. 8). For all the considered cases, the increase in the ceramic layer thickness is connected with the increase in the spectral radius, and the spectral radius courses in the thickness function of the zirconium dioxide layer for disturbed and undisturbed data differ in a negligible degree. The limit value of the spectral radius for which the considered inverse problem is numerically unstable is

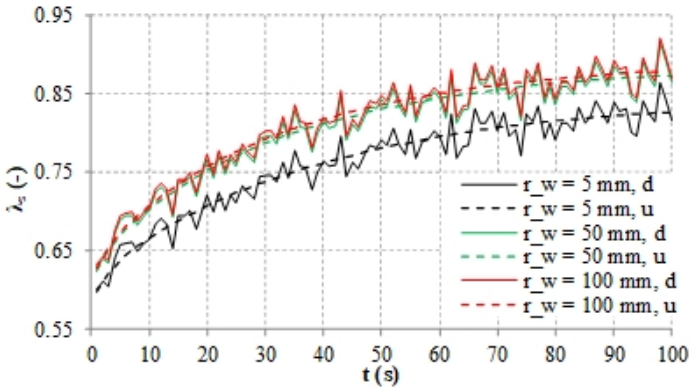


Figure 6: Spectral radius $\lambda_s$ of the stability matrix for different internal radii ($r_{\text{in}}$ = 5 mm, 50 mm, and 100 mm) and the constant thickness of the ring ($g = 5$ mm), the thickness of the ceramic layer $\delta_c = 0.3$ mm with disturbed (d) and undisturbed (u) input data.

$\lambda_s = 1$. The spectral radius was $\lambda_s = 1$ for the ceramic thickness $\delta_c = 0.93$ mm with the double-layer area thickness $g_{mc} = 5.1$ mm; $\delta_c = 0.68$ mm for $g_{mc} = 5.2$ mm and $\delta_c = 0.59$ mm for $g_{mc} = 5.3$ mm (for the inner radius $r_{\text{in}} = 5$ mm, Fig. 7). Similarly, ceramic thickness values for which the spectral radius reached the value of 1 amounted to $\delta_c = 0.86$ mm, $\delta_c = 0.63$ mm, and $\delta_c = 0.55$ mm, subsequently for $g_{mc} = 5.1$ mm, $g_{mc} = 5.2$ mm and $g_{mc} = 5.3$ mm with the inner radius $r_{\text{in}} = 100$ mm (Fig. 8).

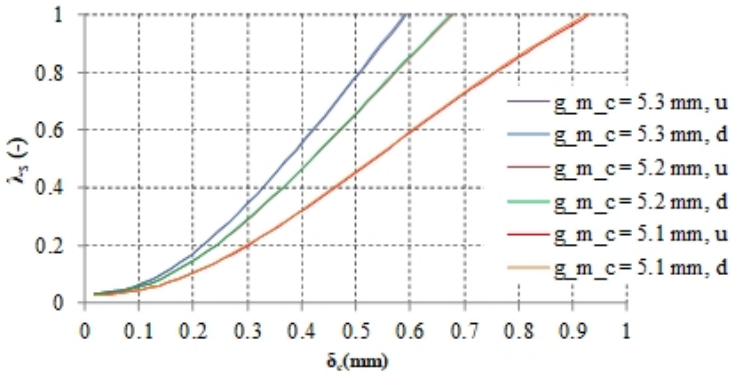


Figure 7: Spectral radius $\lambda_s$ of the stability matrix for $r_{\text{in}} = 5$ mm for variable thickness double-layer area ($g_{mc} = 5.1$ mm, 5.2 mm, and 5.3 mm) and ceramic layer $\delta_c$ from 0.02 mm to 1 mm with disturbed (d) and undisturbed (u) input data.

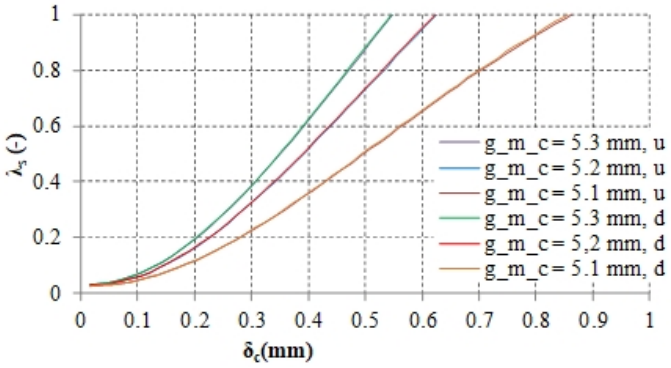


Figure 8: Spectral radius $\lambda_s$ of the stability matrix for $r_{\text{in}} = 100$ mm for variable thickness double-layer area ($g_{mc} = 5.1$ mm, 5.2 mm, and 5.3 mm) and ceramic layer $\delta_c$ from 0.02 mm to 1 mm with disturbed (d) and undisturbed (u) input data.

# 4 Summary

The temperature control difficulty concerning the turbine blade coated with the protective ceramic layer with high heat load was overcome numerically in this paper. The permissible operating temperature was defined for the various thickness of the zircon dioxide layer (0.1, 0.2, and 0.3 mm) for the assumed maximum steel temperature at the level of 686°C. The calculations were carried out for undisturbed data and randomly disturbed data up to the value of 0.5% for the temperature and 2.5% for the thermophysical properties. In both cases stable results were obtained for the temperature distribution, which were subsequently interpolated with the polynomial function. Increasing the ceramic layer thickness ensures the possibility of the turbine blade operation in a higher temperature without a risk of exceeding the permissible thermal resistance of the metal.

The regularization method proposed in this paper based on the notation of the thermal balance for ceramic proved to be effective for the solution of the Cauchy problem. The suggested solution does not introduce a regularization parameter. Thus, we avoid using additional algorithms for determining its optimal value. The spectral radius of the equation matrix proves to be a good measure in the stability assessment of solutions. The change in time of the spectral radii for various geometry was presented in the paper. Notwithstanding the introduction of data disturbance in each of the analysed cases, the results obtained ranged within the solutions for undisturbed data. Furthermore, the value of spectral radii in the function

of ceramic thickness was investigated. Both for undisturbed and disturbed data the results obtained were stable.

The essence of the presented paper was the determination of the temperature on the ceramic surface in the thickness function of the ceramic layer with consideration of the non-linear courses of thermophysical properties and their measurement errors. The thermal conductivity equation is satisfied in each inner point of the ceramic layer; nevertheless, the solution of the inverse problem, defining this temperature, is stable for the ceramic layer thickness $\delta_c < \delta_{c_\max}$. The value of the spectral radius of the stability matrix was investigated in this paper for the subsequent values of the ceramic layer for which the spectral radius $\lambda_s$ of the stability matrix satisfies the inequality $\lambda_s < 1$. The calculations carried out show, Figs. 3 and 4, that the temperature course in the ceramic layer is a linear function in relation to the ceramic thickness for $\delta_c < 0.1$ mm, square function for $\delta_c < 0.2$ mm and cubic function for $\delta_c < 0.3$ mm.

The proposed algorithm is an effective tool for the temperature control of the metal coated with a ceramic protective layer. It may be used for the thermal analysis of the elements exposed to a high thermal load, such as small arms barrels and combustion chambers.

*Received 20 November 2023*

## References

[1] Ciupek B., Gołoś K., Jankowski R., Nadolny Z.: *Effect of hard coal combustion in water steam environment on chemical composition of exhaust gases*. Energies **14**(2021) 20, 6530-1–6530-24. doi: 10.3390/en14206530

[2] Grzymisławski P., Czyżewski P., Ślefarski R.: *Nitrogen dilution effect on swirl stabilized methane burning in gas turbine conditions*. Heat Transfer Eng. **44**(2023), 11-12, 1053–1060. doi: 10.1080/01457632.2022.2113443

[3] Joachimiak D.: *Novel method of the seal aerodynamic design to reduce leakage by matching the seal geometry to flow conditions*. Energies **14**(2021), 23, 7880-1–7880-16. doi: 10.3390/en14237880

[4] Joachimiak D., Frąckowiak A.: *Experimental and numerical analysis of the gas flow in the axisymmetric radial clearance*. Energies **13**(2020), 21, 5794-1–5794-13. doi: 10.3390/en13215794

[5] Joachimiak D., Krzyślak P.: *Experimental research and CFD calculations based investigations into gas flow in a short segment of a heavily worn straight through labyrinth seal*. Pol. Marit. Res. **24**(2017), 2, 83–88. doi: 10.1515/pomr-2017-0053

[6] Joachimiak M., Joachimiak D., Ciałkowski M.: *Investigation on thermal loads in steady-state conditions with the use of the solution to the inverse problem.* Heat Transfer Eng. **44**(2023), 11-12, 963–969. doi: 10.1080/01457632.2022.2113451

[7] Frąckowiak A., Ciałkowski M., Wróblewska A.: *Application of iterative algorithms for gas-turbine blades cooling optimization.* Int. J. Therm. Sci. **118**(2017), 198–206. doi: 10.1016/j.ijthermalsci.2017.04.016

[8] Frąckowiak A., von Wolfersdorf J., Ciałkowski M.: *Optimization of cooling of gas turbine blades with channels filled with porous material.* Int. J. Therm. Sci. **136**(2019), 370–378. doi: 10.1016/j.ijthermalsci.2018.09.005

[9] Frąckowiak A., von Wolfersdorf J., Ciałkowski M.: *Solution of the inverse heat conduction problem described by the Poisson equation for a cooled gas-turbine blade.* Int. J. Heat Mass Tran. **54**(2011), 5-6, 1236–1243. doi: 10.1016/j.ijheatmasstransfer.2010.11.001

[10] Ciałkowski M., Olejnik A., Joachimiak M., Grysa K., Frąckowiak A.: *Cauchy type nonlinear inverse problem in a two-layer area.* Int. J. Numer. Method. H. **32**(2022), 1, 313–331. doi: 10.1108/HFF-09-2020-0584

[11] Ciałkowski M., Olejnik A., Frąckowiak A., Lewandowska N., Mosiężny J.: *Cauchy type inverse problem in a two-layer area in the blades of gasturbine.* Energy **212**(2020), 118751. doi: 10.1016/j.energy.2020.118751

[12] Solekhudin I., Azis M.I.: *A dual reciprocity method for a class of heat conduction problems in two-layered materials.* Int. J. Comput. Sci. **50**(2023), 1, 1–10.

[13] Joachimiak M., Ciałkowski M., Frąckowiak A.: *Stable method for solving the Cauchy problem with the use of Chebyshev polynomials.* Int. J. Numer. Method. H. **30**(2020), 3, 1441–1456. doi: 10.1108/HFF-05-2019-0416

[14] Joachimiak M., Ciałkowski M.: *Influence of the heat source location on the stability of the solution to the Cauchy problem.* E3S Web Conf. **323**(2021), 00016, 1–2. doi: 10.1051/e3sconf/202132300016

[15] Ciupek B., Judt W., Gołoś K., Urbaniak R.: *Analysis of low-power boilers work on real heat loads: A case of Poland.* Energies **14**(2021), 11, 3101-1–3101-13. doi: 10.3390/en14113101

[16] Judt W., Ciupek B., Urbaniak R.: *Numerical study of a heat transfer process in a low power heating boiler equipped with afterburning chamber.* Energy **196**(2020), 117093. doi: 10.1016/j.energy.2020.117093

[17] Taler J., Weglowski B., Pilarczyk M.: *Monitoring of thermal stresses in pressure components using inverse heat conduction methods.* Int. J. Numer. Method. H. **27**(2017), 3, 740–756. doi: 10.1108/HFF-03-2016-0091

[18] Joachimiak M., Ciałkowski M., Bartoszewicz J.: *Analysis of temperature distribution in a pipe with inner mineral deposit.* Arch. Thermodyn. **3**5(2014), 2, 37–49. doi: 10.2478/aoter-2014-0012

[19] Zieliński M., Koniorczyk P., Surma Z., Zmywaczyk J., Preiskorn M.: *Numerical study of heat transfer in a gun barrel made of selected steels.* Energies 15(2022), 1868, 1–24. doi: 10.3390/en15051868

[20] Brodzik Ł., Frąckowiak A.: *Optimization of the heat flow by solving inverse problem in the protective layer of the TPS panel.* Int. J. Numer. Method. H. **30**(2020), 6, 2989–3003. doi: 10.1108/HFF-12-2018-0749

[21] Chung S.Y.: *Uniqueness in the Cauchy problem for the heat equation.* P. Edinburgh Math Soc. **42**(1999), 455–468.

[22] Hadamard J.: *Lectures on Cauchy's Problem in Linear Partial Differential Equations.* Dover Publ., New York 1953.

[23] Joachimiak M., Ciałkowski M.: *Optimal choice of integral parameter in a process of solving the inverse problem for heat equation.* Arch. Thermodyn. **35**(2014), 3, 265–280.

[24] Mierzwiczak M., Kołodziej J.A.: *The determination of heat sources in two dimensional inverse steady heat problems by means of the method of fundamental solutions.* Inverse Probl. Sci. En. **19**(2011), 6, 777–792. doi: 10.1080/17415977.2010.539685

[25] Mierzwiczak M., Kołodziej J.A.: *The determination temperature-dependent thermal conductivity as inverse steady heat conduction problem.* Int. J. Heat Mass Tran. **54**(2011), 4, 790–796. doi: 10.1016/j.ijheatmasstransfer.2010.10.024

[26] Payne L.E., Philippin G.A.: *An ill-posed problem for the heat equation.* Math. Mod. Meth. Appl. S. **19**(2009), 9, 1631–1641.

[27] Belgacem F.B.: *Why is the Cauchy problem severely ill-posed?* Inverse Probl. **23**(2007), 2, 823–836.

[28] Joachimiak M., Ciałkowski M.: *Non-linear unsteady inverse boundary problem for heat conduction equation.* Arch. Thermodyn. **38**(2017), 2, 81–100. doi: 10.1515/aoter-2017-0011

[29] Joachimiak M., Ciałkowski M.: *Stable solution to nonstationary inverse heat conduction equation.* Arch. Thermodyn. **39**(2018), 1, 25–37. doi: 10.1515/aoter-2018-0002

[30] Mierzwiczak M., Chen W., Fu Z.-J.: *The singular boundary method for steady-state nonlinear heat conduction problem with temperature-dependent thermal conductivity.* Int. J. Heat Mass Tran. **91**(2015), 205–217. doi: 10.1016/j.ijheatmasstransfer.2015.07.051

[31] Jaremkiewicz M., Taler J.: *Online determining heat transfer coefficient for monitoring transient thermal stresses.* Energies **13**(2020), 3, 704, 1–13. doi: 10.3390/en13030704

[32] Joachimiak M.: *Analysis of thermodynamic parameter variability in a chamber of a furnace for thermo-chemical treatment.* Energies **14**(2021), 10, 2903, 1–18. doi: 10.3390/en14102903

[33] Joachimiak M., Joachimiak D.: *Analysis of heating time and of temperature distributions for cylindrical geometry with the use of solution to the inverse problem.* E3S Web Conf. **323**(2021), 00013, 1–4. doi: 10.1051/e3sconf/202132300013

[34] Joachimiak M., Joachimiak D.: *Modelling of the cylindrical geometry cooling process based on the solution of the inverse problem.* E3S Web Conf. **321**(2021), 02017, 1–5.

[35] Joachimiak M., Joachimiak D., Ciałkowski M., Małdziński L., Okoniewicz P., Ostrowska K.: *Analysis of the heat transfer for processes of the cylinder heating in the heat-treating furnace on the basis of solving the inverse problem.* Int. J. Therm. Sci. **145**(2019), 105985, 1–11. doi: 10.1016/j.ijthermalsci.2019.105985

[36] Engl H.W., Hanke M., Neubauer A.: *Regularization of Inverse Problems. Mathematics and its Applications*. Kluwer, Dordrecht 1996.

[37] Hansen P.C.: *Regularization tools: a Matlab package for analysis and solution of discrete ill-posed problems*. Numer. Algorithms **6**(1994), 1-2, 1–35.

[38] Joachimiak M.: *Choice of the regularization parameter for the Cauchy problem for the Laplace equation*. Int. J. Numer. Method. H. **30**(2020), 10, 4475–4492. doi: 10.1108/HFF-10-2019-0730

[39] Tikhonov A.N., Arsenin V.Y.: *Solution of Ill-Posed Problems*. Wiley, New York 1977.

[40] Hasanov A., Mukanova B.: *Relationship between representation formulas for unique regularized solutions of inverse source problems with final overdetermination and singular value decomposition of input-output operators*. J. Appl. Math. **80**(2015), 3, 676–696.

[41] Hansen P.C.: *Discrete Inverse Problems: Insight and Algorithms*. SIAM, Philadelphia 2010.

[42] Marin L.: *Numerical solution of the Cauchy problem for steady-state heat transfer in two-dimensional functionally graded materials*. Int. J. Solids Struct. **42**(2005), 4338–4351.

[43] Wang M., Troesch, A.W.: *Numerical stability analysis for free surface flows*. Int. J. Numer. Meth. Fl. **24**(1997), 893–912.

[44] Joachimiak M., Frąckowiak A., Ciałkowski M.: *Solution of inverse heat conduction equation with the use of Chebyshev polynomials*. Arch. Thermodyn. **37**(2016), 4, 73–88. doi: 10.1515/aoter-2016-0028

[45] Joachimiak D., Judt W., Joachimiak M.: *Numerical analysis of the heating of a die for the extrusion of aluminium alloy profiles in terms of thermochemical treatment*. Arch. Thermodyn. **44**(2023), 2, 159–175. doi: 10.24425/ather.2023.146563

[46] Ciałkowski M., Joachimiak M., Mierzwiczak M., Frąckowiak A., Olejnik A., Kozakiewicz A.: *Cauchy type nonlinear inverse problem in a two-layer cylindrical area*. Heat Transfer Eng. (*in print*).

**archives**
**of thermodynamics**
Vol. **44**(2023), No. 4, 581–617
DOI: 10.24425/ather.2023.149720

# Photovoltaic panels cooling technologies: Comprehensive review

**OSAMA ABD AL-MUNAF IBRAHIM**
**SAIF ALI KADHIM***
**MOAFAQ KASEIM SHIEA AL-GHEZI**

Mechanical Engineering Department, University of Technology – Iraq, Baghdad 10066, Iraq

**Abstract** The solar radiation absorbed by photovoltaic panels is not fully utilized in the production of electricity. When the photovoltaic panels are exposed to solar radiation, part of the energy of the incident radiation is transformed into heat accumulated inside these panels. The heat accumulated inside the photovoltaic panels causes two types of losses. The first type of losses is the increase in the operating temperature of the panels and the deterioration of their efficiency and life span. The second type of losses explains that part of the energy of the incident radiation is transformed into heat inside the panels and does not contribute to the production of electrical energy. There are several cooling systems that have been applied to photovoltaic panels for the purpose of regulating their temperature including air, water, and nanofluid cooling systems, which are mostly done by placing a solar collector in the back side of the photovoltaic panels (PV/T). There is also a recently used system that uses phase change material (PCM) in cooling. This paper provides a comprehensive review of several cooling methods and their improvements that researchers have focused on. Through this review, it is clear that the best improvement in the performance of the photovoltaic panel occurs when using PCM because of the high heat transfer coefficient of these materials. Performance improves more when the addition of nanoparticles to the phase change material (PCM-Np) and also when merging (PCM) with (PV/T).

**Keywords:** Solar energy; Photovoltaic panels; Solar collector; Cooling; Phase change materials

*Corresponding Author. Email: 20292@uotechnology.edu.iq

# 1 Introduction

The world is moving towards exploiting and benefiting from renewable energy as clean energy. This energy can be obtained from wind, water, earth and sun. One of those clean energies is solar energy because it does not contain harmful emissions (carbon dioxide, carbon monoxide, etc), and has zero waste generation [1]. Solar energy provides the world's energy requirements such as electricity, hot water, etc. to a limited extent, but it has begun to escalate in recent years [2–6]. Photovoltaic (PV) panels consist of solar cells that use solar energy to generate electrical energy from solar radiation, and their use has spread greatly in recent years because they are considered clean energy that has no side effects on the environment, no fuel costs, and are inexpensive in terms of maintenance. This explains the increase in global demand for solar energy. In addition to the fact that photovoltaic systems can provide electrical energy at night in the absence of sunlight by using batteries and charging them during the day and then using them at night. These features encouraged investors and global energy producers to expand toward the production of electric energy utilizing photovoltaic panels [7]. Photovoltaic cell consists of semiconductors, usually silicon that are compressed into a specially treated wafer to form an electric field positive at one end and negative at the other. When the light energy reaches the cell, electrons are released from the atoms in the semiconductor material. The electrons reach a higher energy state to generate electricity and the electrons are collected in the form of an electric current [8]. Photovoltaic panels have been recognized all over the world due to their inexpensive maintenance and operating costs [9]. The global market of photovoltaic panels in 2019 released a report stating that there was a 12% increase in the installation of photovoltaic panels from 2018 to 2019 [10]. Exactly at the end of 2019, a total of (720 GW) of photovoltaic panels have been installed worldwide, and the capacity of photovoltaic panels will be around (8500 GW) as expected by 2050 [11, 12], as illustrated in Fig. 1.

The disadvantages of the available photovoltaic units are that electricity production is not high because they produce approximately 5% to 25% of the electricity harvested from solar radiation [12], and because solar radiation generates heat in the photovoltaic panels [13]. The generation of heat resulting from solar radiation raises the photovoltaic panel operating temperature, and this has a negative effect on its electrical performance [14] and lifespan [15], and causes an increase in the recovery period [16].

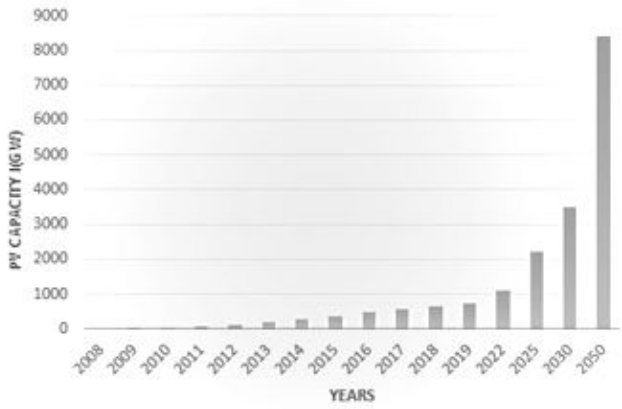


Figure 1: The growth of photovoltaic panel capacity globally [12].

Manufacturers of photovoltaic panels set their test temperature to operate optimally at 25°C. Practically the maximum efficiency of photovoltaic panels is in the operating temperature range from 15°C and 35°C. Any increase in the temperature of the photovoltaic panels leads to a deterioration in their efficiency. It has been reported by the National Renewable Energy Laboratory that the impact of high operating temperatures of photovoltaic panels outside the recommended range leads to a deterioration in efficiency between 0.005–0.008 per year. To ensure that photovoltaic panels operate at maximum efficiency, their temperature must be controlled within 15–35°C, hence the idea of cooling photovoltaic panels [2].

Many researchers suggested multiple cooling solutions, such as taking advantage of the heat absorbed from photovoltaic panels as useful thermal energy, and this is named the hybrid photoelectric/thermal system [17]. The obtained heat from this system is used in heating domestic water [18], drying food [19], ventilation [20], and some other applications. Hybrid systems need less space than photovoltaic panels to obtain the same amount of energy [21]. Therefore, some researchers have placed a solar thermal collector behind the photovoltaic panels to harvest most of the energy that is disposed from the solar panels to avoid its loss and reuse it for productive purposes [22, 23], as illustrated in Fig. 2.

The photovoltaic panels will not operate in standard conditions but close to them, with good productivity, and take advantage of the heat transferred by refrigerants (air, water, and nanofluids) in many other applications [24]. This technique has several options in which more hybrid configurations can

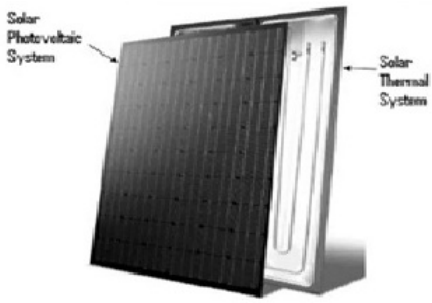


Figure 2: Solar photovoltaic system combined with solar thermal system in a hybrid photovoltaic thermal (PV/T) system [23].

be considered [25] such as using silicon or non-silicon materials in manufacturing photovoltaic cells, or solar thermal collectors [26].

Researchers exploited the hybrid system of photovoltaic panels to develop it using water in cooling with different techniques, whether through copper tubes or spraying water, and others [27–30]. The other researchers used a phase change material (PCM) to store heat such as paraffin wax, sheep fat, etc. It was concluded that when nanoparticles are added to the phase-changing materials (PCM-Np) in the photovoltaic panels cooling systems, the efficiency and the heat capacity of these systems improve. This means that they can absorb larger amounts of heat accumulated inside the photovoltaic panels and reduce their operating temperature, thus increasing the efficiency of those panels [31–36].

This study provides a comprehensive review of the most prominent technologies used in photovoltaic solar panel cooling, such as cooling by water or nanofluid or air through tubes, cooling by water spraying, and cooling by using phase change material (PCM), etc., then, comparing these technologies and highlighting the advantages and disadvantages of each.

## 2 The temperature effect on the performance of photovoltaic panels

When the photovoltaic panel is exposed to sunlight, energy is transmitted to the electron resulting from the fall of photons generated from solar radiation on the atom, and this energy enables the electron to move to the conduction zone and release from the valence zone [37]. Raising an electron to the conduction zone requires the least energy required, and this energy is called

the gap energy. This energy is equal to the energy of a photon and can be expressed by Eq. (1) [38]:

$$E_G = E = h\,f\,, \tag{1}$$

where: $E_G$ – the bandgap energy (J), $E$ – the energy of a photon, $h$ – Planck constant $= 6.63 \cdot 10^{-34}$ Js, $f$ – frequency of solar radiation photons (Hz).

The solar cells operating temperature (photovoltaic panel) increases due to the thermal loss of electrons [13]. An electron releases energy when it crosses the conduction zone when it returns to the same range. Heat is generated in the photovoltaic panel and its operating temperature increases as a result of the energy emitted from the electron while crosses the conduction zone and returns to the same zone again [39]. In the event that the electron does not have enough energy to cross the conduction zone, the electron discharges energy on its way back to the valence zone. This energy will lead to an increase in temperature [40]. A photon hits an electron with energy equal to the band gap energy, this causes the electron to move to the conduction zone from the valence zone. This means that when the photon's energy is greater than the bandgap energy, the excess energy results in the heat for the materials. When the energy of a photon is less than the band gap energy, the electron is excited to the conduction zone from the valence zone and instantly back to the valence zone and electron energy is emitted as heat, that heat called band gap losses [37, 41].

The dependence of the temperature on the efficiency of the photovoltaic panel obtained from the dependence of the open circuit voltage on the temperature is as follows [41, 42]:

$$\eta_e = \frac{V_{oc}\,I}{G_T\,A}\,, \tag{2}$$

$$\frac{d(V_{oc})}{dt} = \frac{1}{T_{pv}}\left(V_{oc} - \frac{E_G}{q}\right), \tag{3}$$

where: $\eta_e$ – electrical efficiency of the photovoltaic panel, $V_{oc}$ – open circuit voltage (V), $I$ – supplied current (A), $G_T$ – incident solar radiation (W/m$^2$), $A$ – panel area (m$^2$), $T_{pv}$ – photovoltaic panel operating temperature (°C), $q$ – heat losses (J).

Because $\frac{E_G}{q}$ will be greater than $V_{oc}$, the change in the open circuit voltage $\left(\frac{d(V_{oc})}{dt}\right)$ will be negative due to the increase in temperature. Therefore, when the operating temperature rises, the open circuit voltage of the

photovoltaic panels decreases [43]. Figure 3 shows the change in voltage and current at different temperatures and Fig. 4 shows the open circuit voltage and the power of the photovoltaic panel ($P_{\max}$) for crystalline silicon solar cell. If the temperature is increased, the short circuit current ($I_{sc}$) is increased by a little [44, 45].

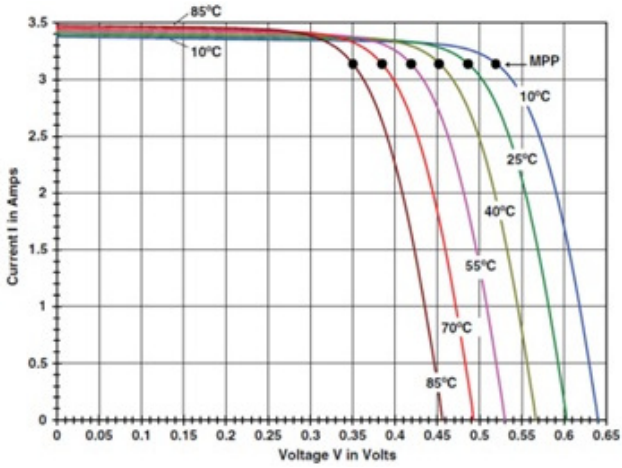


Figure 3: The change in voltage and current with temperatures as a parameter [13].

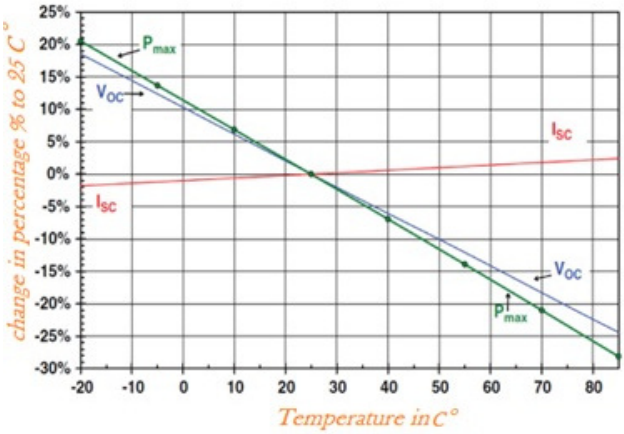


Figure 4: The change of $V_{oc}$, $P_{\max}$, and $I_{sc}$ with temperature [13].

The researchers had an active role in studying the effect of high temperature of photovoltaic panels in different climatic conditions on their electrical performance. Wysocki and colleagues [46] studied how photovoltaic

energy from the sun converts to a semiconductor in the case of a different bandgap from 0.7 to 2.4 V and at temperatures ranging from 0–400°C. In the case of temperature increase, the electrical performance is significant in high bandgap semiconductors. They found that gallium arsenide (GaAs) performs well at temperatures less than 200°C.

Akhmad *et al.* [47] examined two different PV modules for their electrical performance and used (amorphous silicon – polycrystalline silicon) in outdoor conditions in Japan. The efficiencies of crystalline crystals and amorphous silicon decreased by (92% and 89%), over 2 years from the beginning of their installation because of the effect of its temperature increase and ageing of modules.

Radziemska *et al.* [48] changed the temperature from 22°C to 70°C for a monocrystalline PV panel and observed a 0.8% decrease in PV output power. Radziemska *et al.* [49] and Meneses-Rodrıěguez *et al.* [50] tested the effect of increasing the temperature on a silicon crystal panel. The results of the study explain that when the plate temperature was increased by one degree Kelvin, the output power and efficiency reduction rate were about 0.65% and 0.08%, respectively.

Brinkworth *et al.* [51] and Usami *et al.* [52] studied the effect of increasing the temperature on the photovoltaic panels (cadmium telluride) made of stainless steel layer and showed that the OCV (open circuit voltage) decreases linearly in the case of increasing temperature with a slope 2.5 mV/°C.

Huang *et al.* [53] studied how different temperatures affect photovoltaic panels behaviour and found a good result with the relationship as shown in Eq. (4):

$$V_{oc} = A_{oc} - C_T T_J \,, \tag{4}$$

where: $A_{oc}$ – intercept coefficient, $C_T$ – temperature coefficient (V/°C), $T_J$ – solar cell junction temperature (°C). It is clear from Eq. (4) that the open circuit voltage (OCV) in the photovoltaic panel decreases in the case of increasing temperature.

Singh and Ravindra [54] conducted a theoretical study to investigate the effect of temperature on the electrical properties of photovoltaic panels. The study included an analysis of the performance of several types of photovoltaic cells (GaAs, Ge, InP, Si, CdTe, CdS) for operating temperature ranges between (273–523 K), a solar spectrum (0 AM and 1.5 AM) found a direct relationship between the temperature increase and the reverse saturation current, while the relationship between the temperature

and the performance of the photovoltaic panels is inverse. In addition, the bandgap decreased with increasing temperature, which consequently led to increase the current of the short circuit.

Bando *et al.* [55] conducted an investigation to study how the photovoltaic units are degraded after a long period of time up to (28 years) in a desert area. After the detection procedure, the coating material was discoloured and the glass was broken and scratched, discharged, discoloured and hot spots formed; the energy decline rate for the year was 1.2%.

It is clear from the previously mentioned papers that the electrical performance is affected when the operating temperature of photovoltaic panels is changed, meaning that the electrical performance decreases with increasing temperature and vice versa in multiple climatic conditions. High temperatures shorten the life span of photovoltaic panels. Therefore, controlling and managing high temperatures is necessary [56,57]. The researchers made many attempts to improve the performance of the photovoltaic cell by using various techniques in its cooling, which will be discussed in the next sections.

## 3 Cooling of photovoltaic panels by water and nanofluids

The simplest type of photovoltaic panel cooling system consists of a heat exchanger installed on the back surface of the photovoltaic panels [58], as in Fig. 5. The main component of the heat exchanger are tubes usually made of copper through which the heat transfer fluid (water) passes. The heat is absorbed from the photovoltaic panel through the pipes, then transmit-

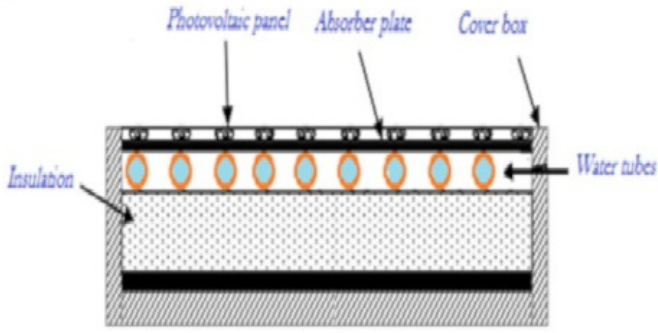


Figure 5: Cross section of photovoltaic panel water cooling [59].

ted to the cooling medium to be removed to the outside or used in other applications such as heating residential homes, for example. These systems can be complicated by changing the composition of the heat exchanger by changing the shape and type of material from which these tubes are made, in addition to changing the heat transfer fluid (cooling medium), such as using oils, phase-changing materials, or adding nanoparticles to these cooling media. There are other techniques for cooling photovoltaic panels with water like spraying and immersion.

Different researchers conducted different studies of water cooling photovoltaic cells using different heat absorber designs, for example, Huang *et al.* [60] used different types of crystal heat absorbers aimed at increasing the efficiency of photovoltaic panels, some of which consist of tubes in the form of channels of tube spacing $W$ and diameter $D$ equal to 6.2 and 10, respectively. The others consist of polycarbonate, this type showed the best results in the thermal performance of the panels. The test was carried out on a daily basis, the average solar radiation ranged according to the hours of the day, starting from 250 W/m$^2$ in the early morning to 850 W/m$^2$ in the middle of the afternoon; the readings were taken for several days. The ambient temperature ranged from 25°C to 34°C, according to the days of the test. The results showed a direct behaviour between the water temperature and the PV panel temperature, and a daily electrical efficiency for conventional PV was found at 9%.

Chow *et al.* [59] used an aluminum heat sink and its flow channels were made in a rectangular shape, the readings were taken on one summer day from 8:00 to 16:00, and recorded every 5 minutes. The absorptivity of the photovoltaic panel was 0.8, the emissivity was 0.8, the intensity of solar radiation was 800 W/m$^2$, the ambient temperature was 20°C, and the wind speed was 2.5 m/s, the daily thermal efficiency ranged from 37.6% to 48.6%, and daily electrical efficiency ranged from 10.3% to 12.3%.

Ji *et al.* [61] studied the pipe size effect and water mass flow rate on thermal and electrical performance. The test was conducted for three days to check the performance of the electrical power and for 3 different flow rates. Increasing the size of the tube led to a high heat loss from the outer tube surface, in addition to an increase in the water mass flow rate to more than 0.03 kg/s. These led to a decrease in the operating temperature of the photovoltaic panel due to the increase in the rate of heat transfer by increasing the conduction between the photovoltaic panels and the outer surfaces of tubes on the one hand, and on the other hand, increasing the heat transfer by convection between the inner surface of the tubes and the cooling

medium that passes inside them. On days 2 and 3, it was observed that the daily electrical energy output improved slightly, despite the increase in the flow rate from 0.1 to 0.9 kg/s. On day 3, however, power output only improved by less than 10 W. The highest solar radiation intensity was 432 W/m$^2$ and the ambient temperature was 25°C.

Ibrahim *et al.* [62] carried out simulations of different heat absorbers and discovered that the so-called spiral type heat absorbers had a high performance in general, this performance attributed to the hollow tubes that are used, and these tubes are rectangular in shape. The tests were at an ambient temperature of 25°C. It was observed in the results that the design of the spiral flow gave the highest total efficiency (thermal and electrical) of 68%, but the serpentine flow design gave the lowest total efficiency of 45%, relative to the flow rate.

Bahaidarah *et al.* [63] made a performance test on a photovoltaic panel cooled by water on the back surface (by canals), from 9 am to 4 pm during one day. The surface temperature of the photovoltaic panel was 45°C, while it decreased when using water to 34°C. The energy production of the PV system with water was approximately four times higher than that of the PV system alone. Also, the results showed a decrease in the operating temperature of the photovoltaic panel and an increase in electrical efficiency that reached 2.7% when using cooling technology.

Matias *et al.* [64] investigated the possibility of increasing the PV output power by reducing the operating temperature, as their production increased after using water at a flow rate of 0.6 l/s at an initial temperature of the photovoltaic panel 25°C equal to the ambient temperature. The photovoltaic panel produced maximum power during test day 63.09 W without cooling and in the case of cooling it produced 78.74 W.

Fakouriyan *et al.* [65] conducted an empirical analysis of the efficiency of photovoltaic panels and they made a comparison in the case of presence or absence of the cooling system. During the test day at the ambient temperature of 37°C, a power improvement of 10 watts was obtained, and the panel surface temperature without and with cooling was 62°C or 44°C, respectively. It was also concluded that the daily electrical efficiency of photovoltaic panels without a cooling system was 10.9%, while the daily electrical efficiency of the same panels with a cooling system improved to 12.3%.

Moharram *et al.* [66] used the technique of spraying with water only once and during a specified period of time to improve the performance of the cell. They discovered through their studies that this method is useful

and can be used in the regions where the weather is characterized by high temperatures or is dusty. The PV panel temperature was 45°C and the ambient temperature was 35°C. The test was conducted in two days, a day in June and a day in July were chosen. They have concluded that the cooling rate of the photovoltaic panels was 2°C/min and this led to an improvement in efficiency and output power for these cells. The maximum electrical efficiency of the PV panel improved from 10.5% to 12%; this means that the electrical efficiency improved by 1.5% in July.

Nižetić *et al.* [67] worked on regulating the temperature of the photovoltaic panel by using the technique of spraying water on PV front and back surface with a flow rate of 225 l/h and a pressure of 4.8 bar, as shown in Fig. 6. The test was conducted on a clear summer day, and the ambient temperature ranged from 27°C to 30°C, and the solar radiation rate ranged between 810 W/m$^2$ and 850 W/m$^2$. It was noticed that cooling from the back surface lowered the temperature more than what happened in the surface frontal, therefore, the maximum electrical efficiency during the test improved from 13.92% to 15.92%, and the maximum output power increased by 4.9 W. It is worth noting that droplet size is a key parameter in cooling effectiveness [68].

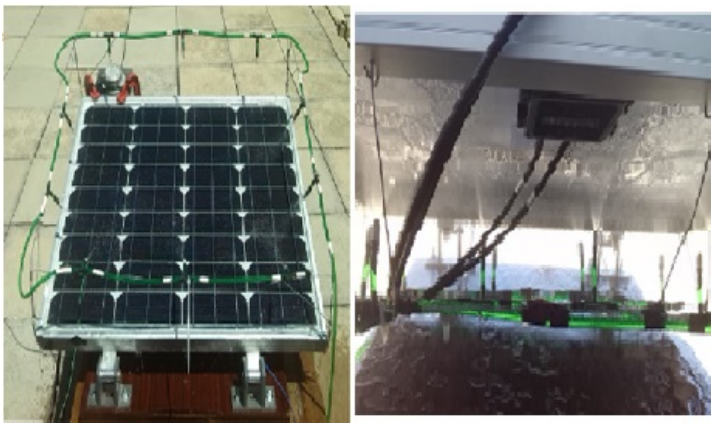

Figure 6: Cooling the front and the backside of the photovoltaic panel [67].

Mehrotra *et al.* [69] used a water immersion cooling technique for photovoltaic panels, as shown in Fig. 7. The test was conducted in April during 6 days, the average intensity of solar radiation ranged between 670 and 1170 W/m$^2$ during the day, and the ambient temperature ranged between 33.5 and 38.4°C. They showed that there is an increase in the daily electri-

cal efficiency of the photovoltaic panel by $\sim 1\%$ when immersed to a depth of 1 cm.

Abdulgafar *et al.* [70] presented the study for the cooling of PV panels through the water immersion technique. The tests are done on a small polycrystalline silicon panel with different depths from 1 to 7 cm. On the test day, conditions were as follows: the average solar radiation value – 700 W/m$^2$, the ambient temperature – 36°C, and the water temperature range was between 28–30°C. Through the results, it was observed that the best power output was at a depth of 1 cm with solar radiation of 444 W/m$^2$, which reached 0.111 W.

Figure 7: Photovoltaic panel immersion technique [69].

The PV cooling system technology has been upgraded by using additives for water such as nanomaterials and alcohols to create liquids with high thermal properties to obtain the best rate of heat transfer between photovoltaic panels and the solar thermal absorber. Several researchers presented studies on the usage of nanofluids to cool photovoltaic panels. Aberoumand *et al.* [71] used Ag/water nanofluid for cooling a PV/T system, by using 4 wt% nanofluids (with the turbulent flow), the test was conducted during 7 consecutive days in June, the average solar radiation ranged from 400–850 W/m$^2$, and the ambient temperature was 25°C. It was observed that the electrical efficiency during daylight hours ranged between $\sim 8.1$–$9.8\%$,

$\sim 9.4-10.9\%$ and $\sim 10.3-12.2\%$ for no cooling, water cooling and nanofluid cooling, respectively.

Al-Ghezi *et al.* [72] used a nanofluid consisting of copper oxide nanoparticles and surfactants dispersed in water with different weight concentrations as cooling fluids. The test was conducted during one day, and the ambient temperature was 25°C, the solar radiation rate ranged from 250–1000 W/m$^2$. The results showed that the daily electrical efficiency of the photovoltaic panel was enhanced by 2.9% approximately when using the prepared nanofluid (2.0% nano-CuO), compared to the use of water only.

Murtadha *et al.* [73] used titanium dioxide nanofluid with different weight concentrations as a cooling fluid in two passes circulation as shown in Fig. 8, to lower the PV panel surface temperature and improve the performance of the photovoltaic/thermal system. Standard test conditions during test day were: ambient temperature equal to 25°C and the solar radiation intensity ranged from 501 to 866 W/m$^2$. It was discovered that the cooling system reduced the surface temperatures by 19.0% at a higher weight concentration, the results showed that the increase in the daily electrical efficiency was 1.26% compared to the use of water during the test day.

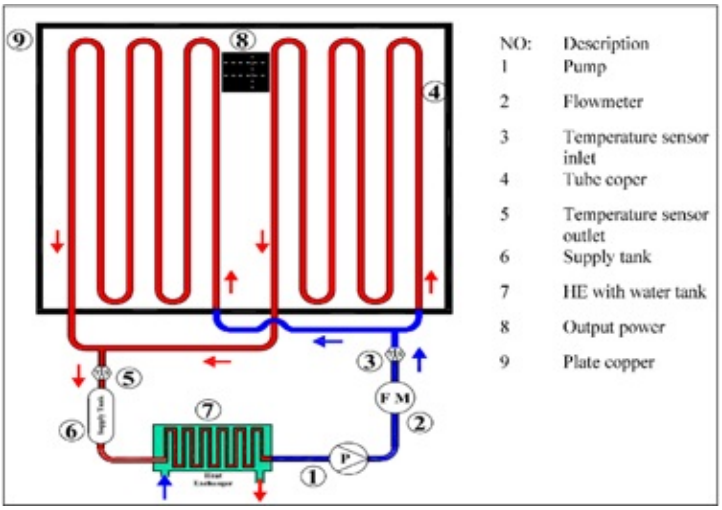


Figure 8: Schematic diagram of two passes fluid circulation in PV/T system [73].

Sathyamurthy *et al.* [74] used a hybrid nanofluid (carbon nanotube & aluminum oxide/water) as a cooling fluid. The tests were conducted at an ambient temperature ranging between 25–35°C. The intensity of solar radiation ranged between 100–1050 W/m$^2$. The maximum temperature of

the photovoltaic panel was 56°C without cooling, and 30°C with cooling during the test day. The electrical efficiency increased during the noon by 4.5% and 2%, compared to those without cooling and with water cooling, respectively.

Ebaid *et al.* [75] used two types of nanofluids, namely $Al_2O_3$ in a water-polyethylene glycol mixture at pH 5.7, and $TiO_2$ in a water-cetyltrimethyl ammonium bromide mixture at pH 9.7 with three concentrations of weight. Results showed on the test day that the nanofluid cooled PV panel in both types caused a higher decrease in the average PV panel temperature compared with the cooled cell with water and without cooling. In addition, electrical analysis of power and efficiency showed that $TiO_2$ nanofluid gives better performance at all volume flow rates. The concentrations studied were compared with water cooling and without cooling. The increase in the daily electrical efficiency of photovoltaic panels in the presence of nanofluid is 0.82% and for water cooling is 0.48% compared to the absence of cooling.

Kazem *et al.* [42] used a fluid consisting of water, copper oxide nanoparticles, and ethylene glycol to cool a photovoltaic panel. The results showed that the daily efficiency of the photovoltaic panel was enhanced by 2.5% for the prepared nanofluid (2.0% nano-CuO) compared to the use of the base fluid only (water).

## 4 Cooling of photovoltaic panels by air

In these cooling systems, the working fluid (cooling medium) is air. Air flows under conditions of forced or natural flow. The fluid flows through openings or channels at the top of the photovoltaic panel and at the bottom of it. The fluid (air) flows up and under the photovoltaic panel, and the air cools it by convection [76]. Adding fins behind the photovoltaic panel increases convective heat losses from the photovoltaic panel [77], as shown in Fig. 9. The heated air which is obtained can be used in several applications.

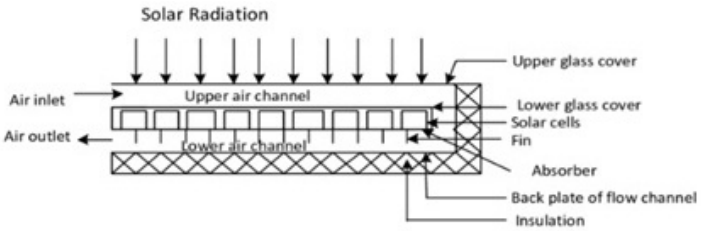


Figure 9: Cross-sectional view of double-pass air photovoltaic panel with fins [77].

The performance of air-cooled photovoltaic panels has been investigated by numerous researchers using different heat sink designs by controlling the flow of different masses of coolant (air). This process was done by Sopian *et al.* [78] who studied the photovoltaic panel cooled by air at 0.046 kg/s where the maximum enhancement in electrical and thermal performance was obtained.

Air-cooled photovoltaic panel experimental analysis was performed by Othman *et al.* [79] who combined a photovoltaic panel with a composite parabolic collector and fins using forced air convection. The effect of increasing the flow rate on the electrical efficiency was small in relation to the amount of air entering where the best increase in electrical efficiency did not exceed 1% at conditions of a flow rate of 2 kg/s in the test day, constant solar radiation of 500 W/m$^2$ and an ambient temperature 31–32°C. The thermal performance increased significantly under these conditions.

Tripanagnostopoulos [80] made a different development in the photovoltaic panel by using a thin metal plate in the centre of the channel and embedded fins behind the channel's back wall. This led to an increase in the daily electrical efficiency to 1.9% at an ambient temperature of 20°C during the test day.

Sopian *et al.* [81] improved the thermal efficiency of an air-cooled photovoltaic system using porous media in the bottom channel of the coupling. The thermal efficiency was very close between the values obtained theoretically and experimentally for solar radiation of less than 570 W/m$^2$, the introduction of porous media into the second channel increases the heat transfer area. At an ambient temperature of 33.5°C, at radiation intensity from 546 W/m$^2$ to 614 W/m$^2$, the thermal efficiency ranged from 70–90%. It can also be seen that the thermal efficiency increases with the increase in solar radiation.

Mohd *et al.* [82] performed a study to investigate PV performance improvement using a grooved absorbent plate by a solar simulator with intensities set at 386 W/m$^2$ and 817 W/m$^2$. The study found an increase in daily electrical efficiency by about 1% and thermal efficiency that may reach 30% when using this type of absorbent plate. They found that the electrical and thermal efficiency increase when the radiation intensity and air velocity increase.

Hussain *et al.* [83] placed an aluminum honeycomb heat exchanger absorbent plate behind the monocrystalline photovoltaic panel and studied the effect of different masses of air from the air. The highest daily thermal efficiency achieved was 87% at an air mass flow rate of 0.11 kg/s and irra-

diance of 828 W/m$^2$. The system of honeycomb photovoltaic panels shows better results for electrical efficiency at the same air flow rate. The daily electrical efficiency improved from 7% to 7.13% compared to the case of absence of the heat exchanger.

Mazón-Hernández *et al.* [84] conducted research on the effect of cooling air freely as well as when it is forcibly passed on photovoltaic panels at different velocities 2 m/s and 4 m/s. Air was projected into a channel of variable height. The tests were conducted in one day under different ambient temperatures ranging between 5–30°C. Forced convection with an air velocity of 4 m/s gave the best performance, as the daily electrical efficiency improved by 0.8 to 1%. The operating temperature of the photovoltaic panel was about 45°C, then decreased by about 15°C when subject to forced air cooling.

Popovici *et al.* [85] used the heat sinks cooling method to improve the efficiency of the photovoltaic panels that contain ribs set at different angles (45°, 90°, and 135°). The average operating temperature of the photovoltaic panel was 41.87°C, while the maximum operating temperature was 56°C during a clear summer day. The highest energy was obtained during the day at an ambient temperature of 25°C where the maximum electrical power of the photovoltaic panels increased from 6.97% to 7.55% relative to the results of the base case for angles 45° and 90°.

## 5 Cooling of photovoltaic panels by using phase change materials

Phase change materials (PCMs) offer an attractive solution because they have a heat capacity several times greater than systems based on cooling by air or water. This is because these materials are capable of absorbing and releasing a large amount of latent thermal energy by changing their state from one phase to another (solid to liquid) or vice versa within a certain temperature range [86]. Because of the low storage capacity of the thermal photovoltaic system based on water and air, researchers were inspired to develop a thermal management system that stores latent heat with phase change materials. These materials have the ability to absorb heat and release it during the melting or solidifying process. Phase change materials keep absorbing heat without an increase in the operating temperature and when these materials solidify, they release latent heat to the environment [87]. When using these materials in the heat storage process,

the temperature of the storage materials is kept constant [88]. Consequently, phase change materials are very convenient for the thermal control of photovoltaic panels [89]. In the 1980s and early 1990s, phase-change materials found their way into solar energy applications [90].

## 5.1 Classifying phase change materials

Phase change materials are used in photovoltaic panels for the purpose of storing thermal energy. These materials have three known states: solidification, solubility, and gaseousness. The states of solidification and fusion are considered among the basic properties [91]. These materials are energy storage materials whose fusion temperature is high [92]. Phase change materials are classified into three types: organic, inorganic and eutectics, each has merits and demerits [88], which can be distinguished on the basis of the latent heat of fusion and temperature of the melt, as shown in Fig. 10.

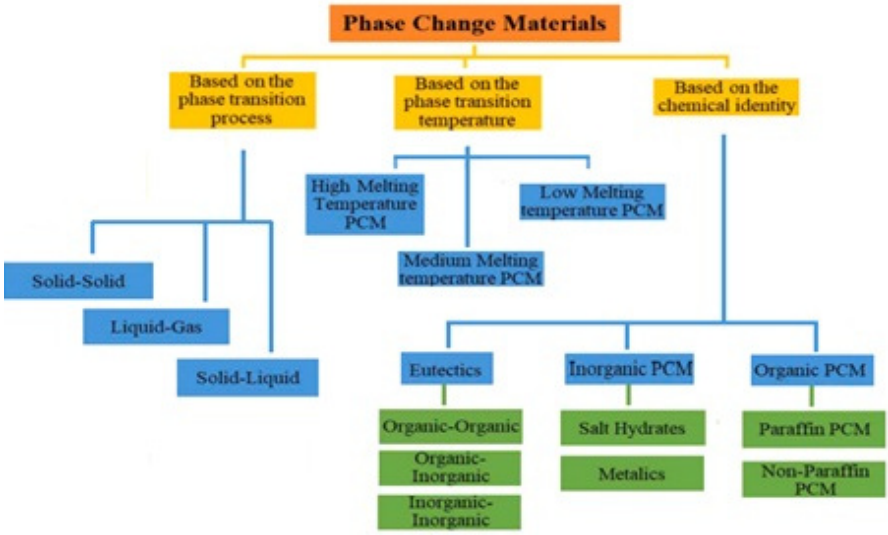


Figure 10: Phase change material description chart [93].

## 5.2 Selection criteria for phase change materials

Several types of phase change materials are available that have been used by many researchers. Therefore, care must be taken in choosing the phase change materials because of their great importance. Sharma *et al.* [94], Abhat [95], Sarbu and Sebarchievici [96] indicate that these materials have

multiple properties that must be taken into consideration such as chemical, thermal, physical and economic properties in order to reach the optimum thermal performance. However, no substance possesses all of these properties [97].

In the case of selecting a phase change material, the temperature of the phase transition is determined, which in turn is dependent on the melting temperature of the phase change material. The phase change materials absorb heat after completing the melting phase without raising its temperature. Moreover, thermal conductivity is a requirement for the selection of phase-change materials as well as a heat storage density to complete the melting phase. On the other hand, the main characteristics of the photovoltaic system based on phase change materials are uniform cooling of the photovoltaic panel [98], high rate of heat absorption, long-term cyclic stability with a greater mass density, absence of super-cooling, immobile parts, significantly lower maintenance cost and ease of use for practical applications [17]. It is assumed that phase change materials that are environmentally friendly are selected. It should be noted that most phase change materials are very expensive materials in the commercial market.

### 5.3 Improving phase change materials

Researchers have been widely using phase change materials in controlling the thermal control of photovoltaic panels. Many researchers recommended that the melting temperature of these materials is 25°C, and this temperature is suitable for the photovoltaic panel in terms of thermal control in summer [99, 100]. Other researchers have chosen a high melting point for phase change materials to suit the conditions of a warm climate [101]. The melting point of these materials is the key factor that improves the thermal performance of photovoltaic panels to obtain high electrical power. To have good thermal control of the PV panel, the temperature of the PV panel should be higher than the melting temperature of the phase change materials [102]. The operating factors of phase change materials, for example, the layer thickness and melting temperature were improved in order to improve the thermal management of the photovoltaic panel; the phase change materials were improved by exposing them to different solar radiation and temperature [103].

PCMs are installed on the back of the photovoltaic panel and placed inside a container as shown in Fig. 11 [104], the container in some cases made of aluminum and isolated from the outside with a wooden box. One of the

advantages of PCMs is that when they absorb heat from the photovoltaic panel, the operating temperature does not increase but is regulated [105]. Some researchers studied the behaviour of heat absorption of phase change materials with its temperature, as shown in Fig. 12. As the temperature of the PCM rises as a result of heating, then heat absorption occurs by the PCM, and at the same time, its temperature remains almost constant [106]. It is useful to control a constant temperature of the PCM to maintain a continuous heat sink and to avoid overheating it to its maximum capacity.

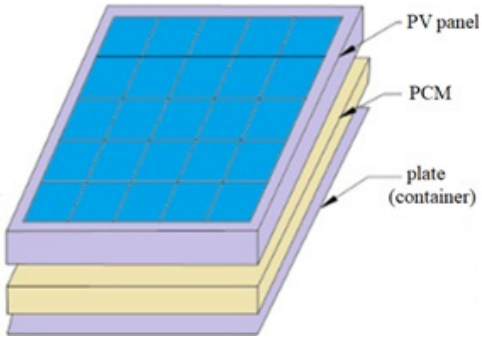


Figure 11: PCM installation in PV panel [104].

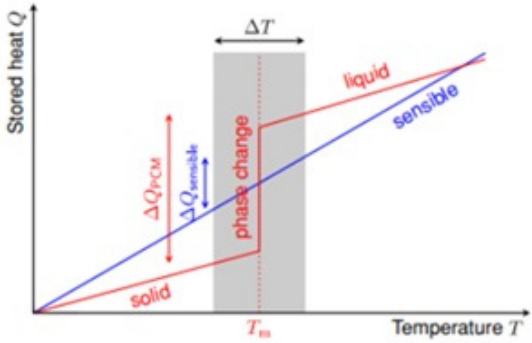


Figure 12: Thermal behaviour of PCM [106].

## 5.4 The most prominent studies to increase the performance of PV panel using PCM

Most researchers in this field (cooling by PCM) have used Rubitherm (RT) which is an organic phase change material. The solid-to-liquid fusion process (and vice versa) is utilized for these materials in order to store and release

heat at a temperature depending on their melting point due to their specific purity and composition. These phase-change materials exhibit a remarkable latent heat capacity in narrow temperature ranges. They are chemically inert and have an indefinite lifetime. It has many types such as RT25–RT20 (paraffin wax), GR40 (Rubitherm GmbH 2000), etc. [107].

Simulations were made for three models of different metals to preserve the phase-changing materials, and fins were added to the metals, as done by Huang *et al.* [108] who found that using this system with fins would well regulate the operating temperature of the photovoltaic panels. The radiation intensity was 1000 W/m$^2$ and the melting point of the paraffin wax (PCM) was 32°C. Aluminum and copper fins were used in it. The average temperature for aluminum was 38.3°C and for copper was 37.6°C for the test time. The time taken in the test was from 0 to 100 minutes. The ambient temperature was 20°C. Simulation and theoretical analysis of paraffin wax and its thermal behaviour were made, showing that it had a significant effect on reducing the temperature of the photovoltaic panel, and storing heat and keeping it in aluminum containers (aluminum is considered a good material for container manufacturing and has a low cost). The photovoltaic panel temperature was controlled under 38°C for 1.5 hours during the day.

Huang *et al.* [109] introduced various shapes of fins such as straight, wire matrix, ribbon matrix, and a container filled with phase change materials RT25 and GR40. The solar radiation was 750 W/m$^2$ and the ambient temperature was 23°C. It was found that the temperature of the photovoltaic panel can be kept below 29°C if the type of fins called wire-array is used for a long time with the RT25. It is proved that RT25 has a better temperature control of the PV panel and thus may provide a potential increase in electricity.

Hasan *et al.* [99] made four systems of phase change photovoltaic materials: system 1 of aluminum, having an internal width of 5 cm; system 2 of perspex, having an internal width of 5 cm; system 3 of aluminum, having an internal width of 3 cm; system 4 of the perspex, with an inner width of 3 cm, using five different phase change materials (RT20, capric palmitate, capric lauric acid, calcium chloride and salt hydrate commercial blend SP22). The melting temperature for PCMs was $25 \pm 4$°C and the radiation intensity was 1000 W/m$^2$. The temperature of the photovoltaic panels was reduced by 10°C as a maximum.

Huang *et al.* [110] studied and evaluated the thermal performance of the photovoltaic phase change system by using three different types of phase

change materials such as WaxsolA, RT27 and RT35. Note that the temperature was reduced by 21°C compared to a regular PV panel when using the RT27 at a radiation intensity of 750 W/m$^2$. Its melting point is 25–28°C, and the ambient temperature is 19°C.

Huang *et al.* [111] manufactured photovoltaic phase change material systems by placing and mixing the phase change materials: RT21, RT24, RT27, RT31 and RT60 in a container. Mixing the two materials RT27 and RT24 contributed to the effect of decreasing the temperature of the photovoltaic panels, and reduced the temperatures to 21°C and 25°C. The largest received electrical energy was 1.9 kWh/day with respect to the reference PV panel in one-day performance in June.

Japs *et al.* [112] mixed an aluminum polymer complex with paraffin-based phase change materials in variable-material bags. These bags are well-wrapped and glued behind the photovoltaic panel. The readings were stable for a period of time at the temperature of the photovoltaic panel compared to the normal panel, and this period was 5.5 hours. During the test day, which was on July 21, the maximum temperature of the ordinary PV panel reached 53–55°C, while the maximum temperature of the photovoltaic module containing phase change materials reached 45–48°C. It can be concluded that the high heat capacity of the PCM storage leads to a higher output of electrical energy, and the higher thermal conductivity of PCM results in a lower operating temperature of the PV panel.

Hasan *et al.* [113] used three types of phase change materials to reduce the temperature of the photovoltaic panel (cool it), and these materials are salt hydrates, fatty acids, paraffin wax, and RT22. It was pointed out that the phase change material used should have a melting temperature close to the operating temperature of the photovoltaic panel. The fusion temperature of the mixtures is high, however, the mixture is easy to melt and has a melting temperature and a solidification temperature between 19°C and 25°C. The mixture has a melting point temperature that is close to the temperature of the photovoltaic panel (25°C). Eventually, this is good for controlling the temperature of the photovoltaic panel.

Hasan *et al.* [114] conducted an empirical study in Ireland and Pakistan, and as it is known that the climate of Ireland is cold and the climate of Pakistan is hot and dry, they used two measuring devices of phase change materials to evaluate the performance of capric palmitate and salt hydrate. The use of salt hydrates in the photovoltaic phase change material system lowered the temperature of the photovoltaic panel by 10°C and 21.5°C in Ireland and Pakistan, respectively. The experiments were conducted in

3 days with solar radiation ranging between 400–950 W/m$^2$. The melting point of PCM with CaCl26H2O was 8.29°C. An improvement in electrical energy by 3% was found when using PCM with $CaCl_{26}H_{2O}$.

Indartono *et al.* [115] used yellow petroleum jelly as a phase change material which was contained in an aluminum rectangular tube and located at the back part of the photovoltaic panel. This study compared the performance of two photovoltaic panels; the first one used PCM, and the second one was without PCM. The result was that the photovoltaic panel surface with PCM has lower temperature compared to PV without PCM, and the daily electrical efficiency of the photovoltaic panel increased by (2–3)% during test day.

Hasan *et al.* [116] enhanced the PV efficiency and avoided heat transfer to the inner spacing by using RT42 in the system based on adding phase changing materials to photovoltaic panels. This contributed to lowering the photovoltaic panel temperature by 12.3°C and 22.6°C from the front and back surfaces of the panel. An increase in the daily electrical efficiency of the photovoltaic panel was observed between 5.5–7.2%.

Hachem *et al.* [117] regulated the temperature of the polycrystalline photovoltaic panel by using pure phase-change materials, petroleum jelly, and impure phase-change materials such as copper and graphite in different amounts. Pure petroleum jelly lowered the temperature by 6.5°C resulting in a 3% increase in electrical performance compared to a conventional PV panel. Copper and graphite lowered the temperature of the PV plate by 6.3°C for a longer period of time compared to petroleum jelly, and the electrical performance increased to 5.8%.

Lim *et al.* [118] carried out a two-dimensional thermal analysis, using a computer program to evaluate the thermal behaviour of two impure phase change materials: petroleum jelly and coconut oil. These materials were placed in a container made of steel of aggregate type in a bag of plastic. The maximum temperature drop was 4°C and a 6% enhancement in electrical efficiency when petroleum jelly was introduced into the disc container.

Karthik *et al.* [119] used $Na_2SO4.10H_2O$ as a phase change material for the thermal management of a photovoltaic panel. The test was conducted on a day in May. The photovoltaic panel peak temperature was 8°C lower compared to no phase-change material, which enhanced its electrical efficiency by 4% at noon.

Ezan *et al.* [120] developed a computer program to study natural convection and its effect on a photovoltaic phase change material system. One of these models was a photoelectric phase change material system whose ther-

mal conductivity is controlled, heat transfer does not occur naturally, and the second is a photoelectric phase change material system whose convection is controlled (natural convection). Increasing the solar radiation from 400 to 800 W/m$^2$ led to an increase in convective heat transfer in the liquid phase change material. The thickness of 10 cm achieved the highest electrical efficiency, increased by 3.11% as compared to the no-phase condition of the materials.

Some researchers developed the technology of a PV cooling system by combining two or more phase change materials (hybrid PCM) for the purpose of using them to cool photovoltaic panels.

Karami *et al.* [31] studied how to increase the electrical efficiency of a photovoltaic unit by using graphite, paraffin, and coconut oil compound as phase change materials. They proved that when adding graphite powders to coconut oil increases the thermal conductivity of the photovoltaic panels, and when using coconut oil and paraffin together by half each, leads to a uniform distribution of temperatures on the surface of the photovoltaic panel compared to pure beef tallow and paraffin. The average temperature was 64.02°C and the resulting power reached 4.875 W.

Zohra *et al.* [121] conducted a numerical study where they combined two types of phase change materials RT42 and RT62. These two materials have different melting points. Through simulations, the authors noticed a significant improvement in the behaviour of thermal systems and a decrease in the production and storage time by about 20 minutes, where the storage time was reduced by 10%.

Other researchers carried out additional experiments on photovoltaic panels by adding nanoparticles to phase change materials (PMC-Np) and learning their effect on the performance of the panels. Nada *et al.* [122] conducted a study to improve the thermal performance and electrical efficiency of photovoltaic units using a phase change material with $Al_2O_3$ nanoparticles. The test conditions on the test day were as follows: the ambient temperature between 30–39°C and the solar radiation was 1100 W/m$^2$. After analyzing the results, it was found that integrating PCM with the PV module reduces and regulates the module temperature, which leads to an improved module power and efficiency. The addition of $Al_2O_3$ nanoparticles to PCM increases the temperature-regulating potential. It reduced the temperature of the units by 8.1°C and 10.6°C, and it increased their efficiency from 15.1% to 15.95% and from 15.1% to 17.1%, respectively. The voltage open circuit (VOC) increased in the case of PCM compared to the normal case by 0.5 V, and the power increased by 5 W.

Siahkamari *et al.* [35] conducted an experimental investigation that focused on using a new phase change material in a photovoltaic panel to increase its cooling. This material absorbs heat from the surface of the photovoltaic unit well and controls its heat capacity and raises the overall efficiency of the system. To delay the dissolution of PCM, they used sheep fat as a phase change material; to increase the efficiency of this material, copper nanoparticles were added to it. The authors found from their research experiments that using lipids and copper nanoparticles (PCM-Np) the maximum temperature of the photovoltaic panel during the examination day reached 87°C in the absence of refrigeration, and when using PCM sheep fat and copper nanoparticles, it is decreased to 60°C. The highest electrical energy obtained during the 1.5 hour test period at a water flow rate of 31 ml/s was 26.2%, compared to 24.6% electrical energy obtained at a flow rate of 6 ml/s. In the case of sheep fat alone, the efficiency improved from 18.2 to 19.5% when the flow rate was changed from 6 to 31 ml/sec, and in the case of paraffin wax, the efficiency improved from 11.8 to 13% at the same flow rates.

Jamil *et al.* [123] conducted an experimental study of cooling PV panels using PCM and three different types of nanoparticles with different concentrations 0.25% wt and 0.5% wt blended with PCM. The test was conducted within one day. The results showed that the use of PCM-Np was better compared to PCM by lowering the temperature and increasing the electrical efficiency, and the high concentration of nanoparticles yielded better results compared to the low concentration in PCM-Np. The maximum electrical efficiency at the highest concentration, for PV-PCM (MWCNTs) was 12.07%. For PV–PCM (GNPs), the max. electrical efficiency was 12.10%, for PV–PCM (MgO) – 11.9%, for PV-PCM – 11.74% and for PV – 10.98%.

Some researchers conducted studies on thermal photovoltaics combined with phase change material (PV/T)/PCM system and others developed this system by adding nanoparticles to the working fluid such as water or others. Malvi *et al.* [124] performed a numerical study and simulation on a thermoelectric system with PCM. The performance was evaluated in relation to the various thermal and physical properties of PCM in addition to the water flow change. Copper tubes were used inside PCM behind the photovoltaic panel. The photovoltaic panel combined with PCM absorbs heat during the day and extracts the heat stored in PCM at night by running water through the copper tubes. The heat storage capacity is better compared to normal PCM. The radiation intensity was 1000 $W/m^2$ and the melting point of PCM was 28°C. The data was recorded within 24 hours.

The operating temperature was 36°C and the water flow rate was more than 5 l/h. The performance of the photovoltaic panel increased by 2.3% from 1.46 to 1.49 kWh/day.

Yin *et al.* [125] used a similar material (phase change material) called functionally graded material for the PV modules. This material is a mixture of aluminum and polyethylene with a high density. Copper tubes are placed behind the photovoltaic panel. The flow rate for water with different masses was 33 ml/min and 66 ml/min. The temperature was 50 and 55°C for the photovoltaic panel without water flow with irradiation of 850 W/m$^2$ and 1100 W/m$^2$. In the case of cooling, the temperature of the photovoltaic panel decreased and stabilized at 32°C and 38°C with a flow of 33 ml/min and 66 ml/min. The daily electrical efficiency of the photovoltaic panel increased to 14.5% from 13.1%.

Browne *et al.* [126] conducted an experimental study on a thermoelectric system in which water is used and a phase change material is added to it. In this pilot study, the water pipe is integrated with the phase change material in the photovoltaic panel back wall. The melting point of the PCM was 22.4°C, and the radiation intensity ranged between 200–1000 W/m$^2$. The test was conducted over a period of 7 days. It was found through the simulation conditions that the improvement was in the first three days of the test, the difference in the temperature of the inlet and outlet was approximately 8°C.

Sardarbadi *et al.* [127] studied the effect of using water and zinc oxide/water with and without a phase change material as coolant mediums for a photovoltaic panel, in terms of increasing their efficiency and decreasing their temperature. The radiation intensity ranges from 600 to 1000 W/m$^2$ during the test day. The temperature absorption in the photovoltaic panel occurs by the phase change material PCM, as a result of which the panel surface temperature is reduced and its temperature is stable. Also, a high-temperature absorption occurs by the ZnO nanofluid/water due to its high thermal conductivity value due to the addition of nanoparticles. This heat absorption also led to an increase in thermal energy. The best increase in average power output is about 13% while using PCM in the PV/T system compared to the normal photovoltaic system.

Al-Waeli *et al.* [32] performed modelling to experimentally verify the thermal system of photovoltaic panels using coolant nanofluid and nanophase change materials. A mathematical model for the energy balance of the nanofluid system and the thermal regime of the photovoltaic panel using nanophase change materials was proposed and tested. The deviation

between the calculated and measured electrical and thermal efficiencies was found 3.72% and 5.05%, respectively. The temperature was measured at different stages to confirm the results. It was shown that the temperature of the liquid increases through heat transfer in different phases with the highest temperature being 60.45°C. Finally, the overall efficiency of the thermal photovoltaic system improved to 85.7%, which is very good for high temperatures.

Al-Waeli *et al.* [36] conducted a performance evaluation of the thermal system of the photovoltaic panel using improved paraffin and nanofluids, which helps in optimizing the heat transfer process. The permeable nanofluid will gain more heat, as shown in Fig. 13. The cooling of the photovoltaic panel led to maintaining its electrical efficiency. While using nanofluids for cooling, the efficiency was about 13.7% compared to the traditional photovoltaic panel about 7.1%.

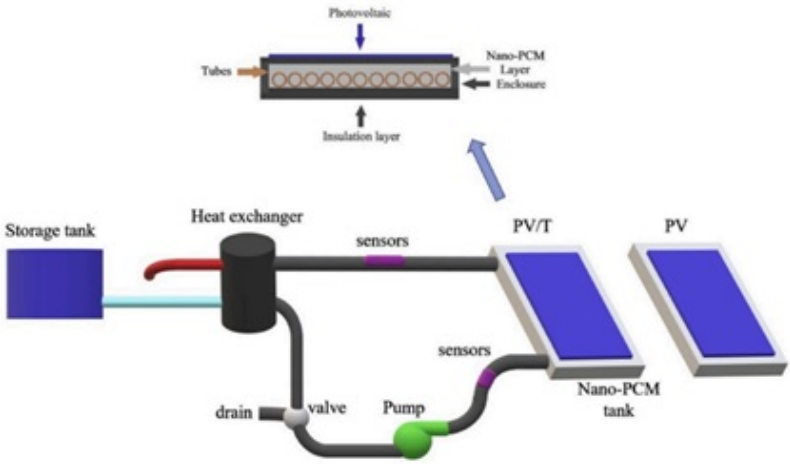


Figure 13: A schematic diagram of the PV/T system and a cross-section of the collector [36].

## 6 Advice for future research

As mentioned in the previous research on the thermal management of photovoltaic panels and methods of cooling them and increasing their electrical efficiency, multiple methods and techniques were used to cool photovoltaic panels, including air cooling (forced convection and free convection), water cooling (pipes, spraying, and immersion), in addition, technical additives to

water, and also using phase change materials (pure and impure). Recently, researchers relied in their studies on the use of phase change materials added to them with nanofluids or nanomaterials to improve the electrical efficiency of photovoltaic panels *via* reducing their temperature.

Here are some tips on how to develop future research.

1. Most of the research and studies conducted on photovoltaic panels based on phase change material showed positive results, but it was for a short time, so it is better to conduct experiments over a longer time for the purpose of evaluating phase change materials and their thermal management with photovoltaic panels.

2. It is recommended to design and develop new types of solar thermal systems and to use new and different materials to study their impact and effectiveness.

3. The nanofluid, when it acts as a medium in the photovoltaic panel system, can improve heat transfer when combined with phase change materials.

4. Consider the solidification process and not just focus on the melting process. Sometimes secondary cooling of phase change materials leads to incomplete solidification that reduces the performance of these materials in a short period.

5. Integrate phase change materials with the thermal system of photovoltaic panels. Such a (photovoltaic thermal) system depends on the phase change material and the addition of nanoparticles to the phase change material or working fluid, to obtain the best results. It is recommended to conduct further research in this aspect.

# 7 Conclusions

The previous literature discussed numerous studies on the thermal control of photovoltaic panels using several cooling methods that are still under research, study and development. The experiments that are being conducted on this topic are still in place so as to reach the best results. Some experiments are sometimes expensive for researchers, and others are not. It has been noted from the presented studies that the best of these methods is the one using phase change materials (PCMs) because they absorb heat

from the photovoltaic panel at a high rate, and this is what makes these materials a great solution in the present time for thermal management. PCMs regulate the temperature of the photovoltaic panel depending on their thermal properties and the addition of nanomaterials enhances these properties. These materials are characterized by their good storage density and thermal conductivity, which enables them to regulate the temperature of photovoltaic panels. These are essential features to achieve better thermal performance. However, the use of these materials is expensive and their storage capacity is limited in case the maximum storage capacity is reached, when the temperature increases and this is a negative trait of the photovoltaic panel. In the second place, the use of nanofluids comes as a great solution for cooling photovoltaic panels, but it is more expensive compared to water, which in turn is considered better than using air in the process of cooling photovoltaic panels. The main focus of researchers is to reach the best results to improve the efficiency of photovoltaic cells, as they generate clean energy, and the topic is still under testing and development, so it is possible that the currently costly technologies will be inexpensive in the future, just as photovoltaic cells were very expensive in the past. Therefore, it is difficult at the present time to determine the best technology for use in terms of both: performance and cost.

*Received 30 January 2023*

## References

[1] Duffie J.A., Beckman W.A., Blair N.: *Solar Engineering of Thermal Processes, Photovoltaics and Wind*. Wiley, 2020.

[2] Krawczyk P., Badyda K.: *Two-dimensional CFD modeling of the heat and mass transfer process during sewage sludge drying in a solar dryer*. Arch. Thermodyn. **32**(2011), 4, 3–16. doi: 10.2478/v10173-011-0028-y

[3] Al-Maliki W.A.K., Mahmoud N.S., Al-Khafaji H.M., Alobaid F., Epple B.: *Design and implementation of the solar field and thermal storage system controllers for a parabolic trough solar power plant*. Appl. Sci. **11**(2021), 13, 6155. doi: 10.3390/app11136155

[4] Kadhim S.A., Ibrahim O.A.A.M.: *Improving the thermal efficiency of flat plate solar collector using nano-fluids as a working fluids: A Review*. Iraqi J. Ind. Res. **8**(2021), 3, 49–60. doi: 10.53523/ijoirVol8I3ID86

[5] Al-Ghezi M.K., Ahmed R.T., Chaichan M.T. *The influence of temperature and irradiance on performance of the photovoltaic panel in the middle of Iraq*. Int. J. Renew. Energ. Dev. **11**(2022), 2, 501–513. doi: 10.14710/ijred.2022.43713

[6] Kadhim S.A., Al-Ghezi M.K., Shehab W.Y.: *Optimum orientation of non-tracking solar applications in Baghdad City*. Int. J. Heat Technol. **41**(2023), 1, 125–134. doi: 10.18280/ijht.410113

[7] Patel M.R., Beik O.: *Wind and Solar Power Systems: Design, Analysis, and Operation*. CRC, 2021.

[8] Armaroli N., Balzani V.: *Towards an electricity-powered world*. Energ. Environ. Sci. **4**(2011), 9, 3193–3222. doi: 10.1039/C1EE01249E

[9] Diwania S., Agrawal S., Siddiqui A.S., Singh S.: *Photovoltaic–thermal (PV/T) technology: a comprehensive review on applications and its advancement*. Int. J. Energ. Environ. Eng. **11**(2020), 1, 33–54. doi: 10.1007/s40095-019-00327-y

[10] IEA: *Status of Power System Transformation 2019*. IEA, Paris 2019.

[11] Gielen D., Gorini R., Wagner N., Leme R., Gutierrez L., Prakash G., Renner M.: *Global Energy Transformation: A Roadmap to 2050*. IRENA, 2019.

[12] Hosenuzzaman M., Rahim N.A., Selvaraj J., Hasanuzzaman M., Malek A.A., Nahar A.: *Global prospects, progress, policies, and environmental impact of solar photovoltaic power generation*. Renew. Sust. Energ. Rev. **41**(2015). 284–297. doi: 10.1016/j.rser.2014.08.046

[13] Häberlin, H.: *Photovoltaics: System Design and Practice*. John Wiley & Sons, 2012

[14] Al Tarabsheh A., Voutetakisb S., Papadopoulosb A.I., Seferlisb P., Etiera I., Saraereha O.: *Investigation of temperature effects in efficiency improvement of non-uniformly cooled photovoltaic cells*. Chem. Eng. T. **35**(2013), 1387–1392. doi: 10.3303/CET1335231

[15] Teo H.G., Lee P.S., Hawlader M.N.A.: *An active cooling system for photovoltaic modules*. Appl. Energ. **90**(2012), 1, 309–315. doi: 10.1016/j.apenergy.2011.01.017

[16] Agrawal B., Tiwari G. N.: *Life cycle cost assessment of building integrated photovoltaic thermal (BIPVT) systems*. Energ. Buildings **42**(2010), 9, 1472–1481. doi: 10.1016/j.enbuild.2010.03.017

[17] Islam M.M., Pandey A.K., Hasanuzzaman M., Rahim N.A.: *Recent progresses and achievements in photovoltaic-phase change material technology: a review with special treatment on photovoltaic thermal-phase change material systems*. Energ. Convers. Manage. **126**(2016), 177–204. doi: 10.1016/j.enconman.2016.07.075

[18] Kalogirou S.A., Tripanagnostopoulos Y.: *Hybrid PV/T solar systems for domestic hot water and electricity production*. Energ. Convers. Manage. **47**(2006), 18-19, 3368–3382. doi: 10.1016/j.enconman.2006.01.012

[19] Mortezapour H., Ghobadian B., Minaei S., Khoshtaghaza M.H.: *Saffron drying with a heat pump–assisted hybrid photovoltaic–thermal solar dryer*. Dry. Technol. **30**(2012), 6, 560–566. doi: 10.1080/07373937.2011.645261

[20] Lin W., Ma Z., Sohel M.I., Cooper P.: *Development and evaluation of a ceiling ventilation system enhanced by solar photovoltaic thermal collectors and phase change materials*. Energ. Convers. Manage. **88**(2014), 218–230. doi: 10.1016/j.enconman.2014.08.019

[21] Sathe T.M., Dhoble A.S.: *A review on recent advancements in photovoltaic thermal techniques*. Renew. Sust. Energ. Rev. **76**(2017), 645–672. doi: 10.1016/j.rser.2017.03.075

[22] Tonui J.K., Tripanagnostopoulos Y.: *Improved PV/T solar collectors with heat extraction by forced or natural air circulation.* Renew. Energ. **32**(2007), 4, 623–637. doi: 10.1016/j.renene.2006.03.006

[23] Sahay A., Sethi V. K., Tiwari A.C., Pandey M.: *A review of solar photovoltaic panel cooling systems with special reference to Ground coupled central panel cooling system (GC-CPCS).* Renew. Sust. Energ. Rev. **42**(2015), 306–312. doi: 10.1016/j.rser.2014.10.009

[24] Al-Waeli A.H., Kazem H.A., Sopian K., Chaichan M.T.: *Techno-economical assessment of grid connected PV/T using nanoparticles and water as base-fluid systems in Malaysia.* Int. J. Sustain. Energ. **37**(2018), 6, 558–575. doi: 10.1080/14786451.2017.1323900

[25] Devendiran D.K., Amirtham V.A.: *A review on preparation, characterization, properties and applications of nanofluids.* Renew. Sust. Energ. Rev. **60**(2016), 21–40. doi: 10.1016/j.rser.2016.01.055

[26] Ebrahimnia-Bajestan E., Moghadam M. C., Niazmand H., Daungthongsuk W., Wongwises S.: *Experimental and numerical investigation of nanofluids heat transfer characteristics for application in solar heat exchangers.* Int. J. Heat Mass Tran. **92**(2016), 1041–1052. doi: 10.1016/j.ijheatmasstransfer.2015.08.107

[27] Raju M., Sarma R.N., Suryan A., Nair P.P., Nižetić S.: *Investigation of optimal water utilization for water spray cooled photovoltaic panel: A three-dimensional computational study.* Sust. Energ. Tech. As. **51**(2022), 101975. doi: 10.1016/j.seta.2022.101975

[28] Yildirim M.A., Cebula A., Sułowicz M.: *A cooling design for photovoltaic panels–Water-based PV/T system.* Energy **256**(2022), 124654. doi: 10.1016/j.energy.2022.124654

[29] Singh K., Singh S., Kandpal D.C., Kumar R.: *Experimental performance study of photovoltaic solar panel with and without water circulation.* Mater. Today-Proc. **46**(2021), 6822–6827. doi: 10.1016/j.matpr.2021.04.393

[30] Mohammed M.F., Daud H.A., Ekaab N.S.: *Numerical study of cooling system for photovoltaic thermal collector.* J. Eng. Sci. Technol. **16**(2021), 6, 4817–4832.

[31] Karami B., Azimi N., Ahmadi S.: *Increasing the electrical efficiency and thermal management of a photovoltaic module using expanded graphite (EG)/paraffin-beef tallow-coconut oil composite as phase change material.* Renew. Energ. **178**(2021), 25–49. doi: 10.1016/j.renene.2021.06.067

[32] Al-Waeli A.H., Chaichan M.T., Sopian K., Kazem H.A., Mahood H.B., Khadom A.A.: *Modeling and experimental validation of a PVT system using nanofluid coolant and nano-PCM.* Sol. Energy **177**(2019), 178–191. doi: 10.1016/j.solener.2018.11.016

[33] Chintakrinda K., Weinstein R.D., Fleischer A.S.: *A direct comparison of three different material enhancement methods on the transient thermal response of paraffin phase change material exposed to high heat fluxes.* Int. J. Therm. Sci. **50**(2011), 1639–1647. doi: 10.1016/j.ijthermalsci.2011.04.005

[34] Al Hariri A., Selimli S., Dumrul H.: *Effectiveness of heat sink fin position on photovoltaic thermal collector cooling supported by paraffin and steel foam: An experimental study*. Appl. Therm. Eng. **213**(2022), 118784. doi: 10.1016/j.applthermaleng.2022.118784

[35] Siahkamari L., Rahimi M., Azimi N., Banibayat M.: *Experimental investigation on using a novel phase change material (PCM) in micro structure photovoltaic cooling system*. Int. Commun. Heat Mass **100**(2019), 60–66. doi: 10.1016/j.icheatmass transfer.2018.12.020

[36] Al-Waeli A.H., Sopian K., Kazem H.A., Chaichan M.T.: *Evaluation of the electrical performance of a photovoltaic thermal system using nano-enhanced paraffin and nanofluids*. Case Stud. Therm. Eng. **21**(2020), 100678. doi: 10.1016/j.csite.2020.100678

[37] Solanki C.S.: *Solar Photovoltaics: Fundamentals, Technologies and Applications* (3rd Edn.). PHI learning Pvt. Ltd., Delhi 2015.

[38] Smets A.H., Jäger K., Isabella O., Swaaij R.A., Zeman M.: *Solar Energy: The Physics and Engineering of Photovoltaic Conversion, Technologies and Systems*. UIT Cambridge, 2015.

[39] Mukerjee A.K., Thakur N.: *Photovoltaic Systems: Analysis and Design*. PHI Learning Pvt. Ltd., Delhi 2011.

[40] Tiwari G.N., Dubey S.: *Fundamentals of Photovoltaic Modules and Their Applications*. RSC, 2009.

[41] Goswami D.Y.: *Principles of Solar Engineering*. CRC Press, 2015

[42] Kazem H.A., Chaichan M.T., Al-Waeli A.H.: *Effect of CuO-water-ethylene glycol nanofluids on the performance of photovoltaic/thermal energy system: an experimental study*. Energ. Source. A **44**(2022), 2, 3673–3691. doi: 10.1080/15567036.2022.2070305

[43] Kaldellis J.K., Kapsali M., Kavadias K.A.: *Temperature and wind speed impact on the efficiency of PV installations. Experience obtained from outdoor measurements in Greece*. Renew. Energ. **66**(2014), 612–624. doi: 10.1016/j.renene.2013.12.041

[44] Fesharaki V.J., Dehghani M., Fesharaki J.J., Tavasoli H.: *The effect of temperature on photovoltaic cell efficiency*. In: Proc. 1st Int. Conf. on Emerging Trends in Energy Conservation ETEC, Tehran, 20-21, Nov. 2011.

[45] Bagienski W., Gupta M.C.: *Temperature dependence of polymer/fullerene organic solar cells*. Sol. Energ. Mat. Sol. C. **95**(2011), 3, 933–941. doi: 10.1016/j.solmat.2010.11.026

[46] Wysocki J.J., Rappaport P.: *Effect of temperature on photovoltaic solar energy conversion*. J. Appl. Phys. **31**(1960), 3, 571–578. doi: 10.1063/1.1735630

[47] Akhmad K., Kitamura A., Yamamoto F., Okamoto H., Takakura H., Hamakawa Y.: *Outdoor performance of amorphous silicon and polycrystalline silicon PV modules*. Sol. Energ. Mat. Sol. C. **46**(1997), 3, 209–218. doi: 10.1016/S0927-0248(97)00003-2

[48] Radziemska E., Klugmann E.: *Thermally affected parameters of the current–voltage characteristics of silicon photocell*. Energ. Convers. Manage. **43**(2002), 14, 1889–1900. doi: 10.1016/S0196-8904(01)00132-7

[49] Radziemska E.: *The effect of temperature on the power drop in crystalline silicon solar cells*. Renew. Energ. **28**(2003), 1, 1–12. doi: 10.1016/S0960-1481(02)00015-0

[50] Meneses-Rodrıěguez D., Horley P.P., Gonzalez-Hernandez J., Vorobiev Y.V., Gorley P.N.: *The effect of temperature on the power drop in crystalline silicon solar cells*. Sol. Energy **78**(2005), 2, 243–250. doi: 10.1016/j.solener.2004.05.016

[51] Brinkworth B.J., Sandberg M.: *Design procedure for cooling ducts to minimise efficiency loss due to temperature rise in PV arrays*. Sol. Energy **80**(2006), 1, 89–103. doi: 10.1016/j.solener.2005.05.020

[52] Usami A., Seki S., Mita Y., Kobayashi H., Miyashiro H., Terada N.: *Temperature dependence of open-circuit voltage in dye-sensitized solar cells*. Sol. Energ. Mat. Sol. C. **83**(2006), 6-7, 840–842. doi: 10.1016/j.solmat.2008.09.040

[53] Huang B.J., Yang P.E., Lin Y.P., Lin B.Y., Chen H.J., Lai R.C., Cheng J.S.: *Solar cell junction temperature measurement of PV module*. Sol. Energy **85**(2011), 2, 388–392. doi: 10.1016/j.solener.2010.11.006

[54] Singh P., Ravindra N.M.: *Temperature dependence of solar cell performance – an analysis*. Sol. Energ. Mat. Sol. C. **101**(2012), 36–45. doi: 10.1016/j.solmat.2012.02.019

[55] Bandou F., Arab A.H., Belkaid M.S., Logerais P.O., Riou O., Charki A.: *Evaluation performance of photovoltaic modules after a long time operation in Saharan environment*. Int. J. Hydrogen Energ. **40**(2015), 39, 13839–13848. doi: 10.1016/j.ijhydene.2015.04.091

[56] Krauter S.: *Increased electrical yield via water flow over the front of photovoltaic panels*. Sol. Energ. Mat. Sol. C. **82**(2004), 1-2, 131–137. doi: 10.1016/j.solmat.2004.01.011

[57] Vokas G., Christandonis N., Skittides F.: *Hybrid photovoltaic–thermal systems for domestic heating and cooling – a theoretical approach*. Sol. Energy **80**(2006), 5, 607–615. doi: 10.1016/j.solener.2005.03.011

[58] Michael J.J., Iniyan S., Goic R.: *Flat plate solar photovoltaic–thermal (PV/T) systems: A reference guide*. Renew. Sust. Energ. Rev. **51**(2015), 62–88. doi: 10.1016/j.rser.2015.06.022

[59] Chow T.T., He W., Ji J.: *Hybrid photovoltaic-thermosyphon water heating system for residential application*. Sol. Energy **80**(2006), 3, 298–306. doi: 10.1016/j.solener.2005.02.003

[60] Huang B.J., Lin T.H., Hung W.C., Sun F.S.: *Performance evaluation of solar photovoltaic/thermal systems*. Sol. Energy **70**(2001), 5, 443–448. doi: 10.1016/S0038-092X(00)00153-5

[61] Ji J., Han J., Chow T.T., Yi H., Lu J., He W., Sun W.: *Effect of fluid flow and packing factor on energy performance of a wall-mounted hybrid photovoltaic/water-heating collector system*. Energ. Buildings **38**(2006), 12, 1380–1387. doi: 10.1016/j.enbuild.2006.02.010

[62] Ibrahim A., Othman M.Y., Ruslan M. H., Alghoul M., Yahya M., Zaharim A., Sopian K.: *Performance of photovoltaic thermal collector (PVT) with different absorbers design*. Wseas Trans. Env. Dev. **5**(2009), 3, 321–330.

[63] Bahaidarah H.M., Rehman S., Gandhidasan P., Tanweer B.: *Experimental evaluation of the performance of a photovoltaic panel with water cooling.* In: Proc. 39st Photovoltaic Specialists Conf. (PVSC), IEEE, 2987-2991, June 2013. doi: 10.1109/PVSC.2013.6745090

[64] Matias C.A., Santos L.M., Alves A.J., Calixto W.P.: *Increasing photovoltaic panel power through water cooling technique.* Trans. Env. Electr. Eng. **2**(2017), 1, 60–66.

[65] Fakouriyan S., Saboohi Y., Fathi A.: *Experimental analysis of a cooling system effect on photovoltaic panels' efficiency and its preheating water production.* Renew. Energ. **134**(2017), 1362–1368. doi: 10.1016/j.renene.2018.09.054

[66] Moharram K.A., Abd-Elhady M.S., Kandil H.A., El-Sherif H.: *Enhancing the performance of photovoltaic panels by water cooling.* Ain Shams Eng. J. **4**(2013), 4, 869–877. doi: 10.1016/j.asej.2013.03.005

[67] Nižetić S., Čoko D., Yadav A., Grubišić-Čabo F.: *Water spray cooling technique applied on a photovoltaic panel: The performance response.* Energ. Convers. Manage. **108**(2016), 4, 287–296. doi: 10.1016/j.enconman.2015.10.079

[68] Mzad H., Otmani A.: *Simulation of photovoltaic panel cooling beneath a single nozzle based on a configurations framework.* Arch. Thermodyn. **42**(2021), 1, 115–128. doi: 10.24425/ather.2021.136950

[69] Mehrotra S., Rawat P., Debbarma M., Sudhakar K.: *Performance of a solar panel with water immersion cooling technique.* Int. J. Sci. Env. Technol. **3**(2014), 3, 1161–1172.

[70] Abdulgafar S.A., Omar O.S., Yousif K.M.: *Improving the efficiency of polycrystalline solar panel via water immersion method.* Int. J. Innov. Res. Sci. Eng. Technol. **3**(2014), 1, 8127–8132.

[71] Aberoumand S., Ghamari S., Shabani B.: *Energy and exergy analysis of a photovoltaic thermal (PV/T) system using nanofluids: An experimental study.* Sol. Energy **165**(2018), 167–177. doi: 10.1016/j.solener.2018.03.028

[72] Al-Ghezi M.K., Abass K.I., Salam A.Q., Jawad R.S., Kazem H.A.: *The possibilities of using nano-CuO as coolants for PVT system: An experimental study.* In: J. Phys.: Conf. Series, IOP Publishing, **1973**, 1, 012123, Aug. 2021. doi: 10.1088/1742-6596/1973/1/012123

[73] Murtadha T.K., dil Hussein A.A., Alalwany A.A., Alrwashdeh S.S., Ala'a M.: *Improving the cooling performance of photovoltaic panels by using two passes circulation of titanium dioxide nanofluid.* Case Stud. Therm. Eng. **36**(2022), 102191. doi: 10.1016/j.csite.2022.102191

[74] Sathyamurthy R., Kabeel A.E., Chamkha A., Karthick A., Muthu Manokar A., Sumithra M.G.: *Experimental investigation on cooling the photovoltaic panel using hybrid nanofluids.* Appl. Nanosci. **11**(2021), 2, 363–374. doi: 10.1007/s13204-020-01598-2

[75] Ebaid M.S., Ghrair A.M., Al-Busoul M.: *Experimental investigation of cooling photovoltaic (PV) panels using ($TiO_2$) nanofluid in water-polyethylene glycol mixture and ($Al_2O_3$) nanofluid in water-cetyltrimethylammonium bromide mixture.* Energ. Convers. Manage. **155**(2018), 324–343. doi: 10.1016/j.enconman.2017.10.074

[76] Hussain F., Othman M.Y H., Sopian K., Yatim B., Ruslan H., Othman H.: *Design development and performance evaluation of photovoltaic/thermal (PV/T) air base solar collector*. Renew. Sust. Energ. Rev. **25**(2013), 431–441. doi: 10.1016/j.rser.2013.04.014

[77] Kumar R., Rosen M.A.: *Performance evaluation of a double pass PV/T solar air heater with and without fins*. Appl. Therm. Eng. **31**(2011), 8-9, 1402–1410. doi: 10.1016/j.applthermaleng.2010.12.037

[78] Sopian K., Liu H.T., Kakac S., Veziroglu T.N.: *Performance of a double pass photovoltaic thermal solar collector suitable for solar drying systems*. Energ. Convers. Manage. **41**(2000), 4, 353–365. doi: 10.1016/S0196-8904(99)00115-6

[79] Othman M.Y.H., Yatim B., Sopian K., Bakar, M.N.A.: *Performance analysis of a double-pass photovoltaic/thermal (PV/T) solar collector with CPC and fins*. Renew. Energ. **30**(2005), 13, 2005–2017. doi: 10.1016/j.renene.2004.10.007

[80] Tripanagnostopoulos Y.: *Aspects and improvements of hybrid photovoltaic/thermal solar energy systems*. Sol. Energy **81**(2007), 9, 1117–1131. doi: 10.1016/j.solener.2007.04.002

[81] Sopian K., Alghoul M.A., Alfegi E.M., Sulaiman M.Y., Musa E.A.: *Evaluation of thermal efficiency of double-pass solar collector with porous–nonporous media*. Renew. Energ. **34**(2009), 3, 640–645. doi: 10.1016/j.renene.2008.05.027

[82] Mohd Y.O., Hafidz R., Kamaruzzaman S., Jin G.L.: *Performance study of photovoltaic-thermal (PV/T) solar collector with grooved absorber plate*. Sains Malaysiana **38**(2009), 4, 537–541.

[83] Hussain F., Othman M.Y., Yatim B., Ruslan H., Sopian K., Anuar Z., Khairuddin S.: *Comparison study of air base photovoltaic/thermal (PV/T) collector with different design of heat exchanger*. In: World Renew. Energ. Forum, WREF **1**(2012), 189–194.

[84] Mazón-Hernández R., García-Cascales J.R., Vera-García F., Káiser A.S., Zamora B.: *Improving the electrical parameters of a photovoltaic panel by means of an induced or forced air stream*. Int. J. Photoenergy **2013**(2013). doi: 10.1155/2013/830968

[85] Popovici C.G., Hudişteanu S.V., Mateescu T.D., Cherecheş N.C.: *Efficiency improvement of photovoltaic panels by using air cooled heat sinks*. Enrgy. Proced. **85**(2016), 425–432. doi: 10.1016/j.egypro.2015.12.223

[86] Senthil R., Patel A., Rao R., Ganeriwal S.: *Melting behavior of phase change material in a solar vertical thermal energy storage with variable length fins added on the heat transfer tube surfaces*. Int. J. Renew. Energ. Dev. **9**(2020), 3, 361–367. doi: 10.14710/ijred.2020.29879

[87] Tatsidjodoung P., Le Pierrès N., Luo L.: *A review of potential materials for thermal energy storage in building applications*. Renew. Sust. Energ. Rev. **18**(2013), 327–349. doi: 10.1016/j.rser.2012.10.025

[88] Zhou D., Zhao C.Y., Tian Y.: *Review on thermal energy storage with phase change materials (PCMs) in building applications*. Appl. Energ. **92**(2012), 593–605. doi: 10.1016/j.apenergy.2011.08.025

[89] Ma T., Yang H., Zhang Y., Lu L., Wang X.: *Using phase change materials in photovoltaic systems for thermal regulation and electrical efficiency improvement: a review and outlook*. Renew. Sust. Energ. Rev. **43**(2015), 1273–1284. doi: 10.1016/j.rser.2014.12.003

[90] Wang F., Maidment G., Missenden J., Tozer R.: *A review of research concerning the use of PCMs in air conditioning and refrigeration engineering*. Adv. Building Technol. **II**(2002), 1273–1280. doi: 10.1016/B978-008044100-9/50158-3

[91] Günther E., Hiebler S., Mehling H., Redlich R.: *Enthalpy of phase change materials as a function of temperature: required accuracy and suitable measurement methods*. Int. J. Thermophys. **30**(2009), 4, 1257–1269. doi: 10.1007/s10765-009-0641-z

[92] Qureshi Z. A., Ali H.M., Khushnood S.: *Recent advances on thermal conductivity enhancement of phase change materials for energy storage system: a review*. Int. J. Heat Mass Tran. **127**(2018), 838–856. doi: 10.1016/j.ijheatmasstransfer.2018.08.049

[93] Kumar R.R., Samykano M., Pandey A.K., Kadirgama K., Tyagi V.V.: *Phase change materials and nano-enhanced phase change materials for thermal energy storage in photovoltaic thermal systems: A futuristic approach and its technical challenges*. Renew. Sust. Energ. Rev. **133**(2020), 110341. doi: 10.1016/j.rser.2020.110341

[94] Sharma A., Tyagi V.V., Chen C.R., Buddhi D.: *Review on thermal energy storage with phase change materials and applications*. Renew. Sust. Energ. Rev. **13**(2009), 2, 318–345. doi: 10.1016/j.rser.2007.10.005

[95] Abhat A.: *Low temperature latent heat thermal energy storage: heat storage materials*. Sol. Energ. **30**(1983), 4, 313–332. doi: 10.1016/0038-092X(83)90186-X

[96] Sarbu I., Sebarchievici C.: *A comprehensive review of thermal energy storage*. Sustain. **10**(2018), 1, 191. doi: 10.3390/su10010191

[97] Ma T., Li Z., Zhao J.: *Photovoltaic panel integrated with phase change materials (PV-PCM): technology overview and materials selection*. Renew. Sust. Energ. Rev. **116**(2019), 109406. doi: 10.1016/j.rser.2019.109406

[98] Bahaidarah H.M., Baloch A.A., Gandhidasan P.: *Uniform cooling of photovoltaic panels: A review*. Renew. Sust. Energ. Rev. **57**(2016), 1520–1544. doi: 10.1016/j.rser.2015.12.064

[99] Hasan A., McCormack S.J., Huang M.J., Norton B.: *Evaluation of phase change materials for thermal regulation enhancement of building integrated photovoltaics*. Sol. Energy **84**(2010), 9, 1601–1612. doi: 10.1016/j.solener.2010.06.010

[100] Waqas A., Jie J., Xu L.: *Thermal behavior of a PV panel integrated with PCM-filled metallic tubes: An experimental study*. J. Renew. Sust. Energ. **9**(2017), 5, 053504. doi: 10.1063/1.4995022

[101] Nada S.A., El-Nagar D.H.: *Possibility of using PCMs in temperature control and performance enhancements of free stand and building integrated PV modules*. Renew. Energ. **127**(2018), 630–641. doi: 10.1016/j.renene.2018.05.010

[102] Kant K., Shukla A., Sharma A.: *Ternary mixture of fatty acids as phase change materials for thermal energy storage applications*. Energ. Rep. **2**(2016), 274–279. doi: 10.1016/j.egyr.2016.10.002

[103] Kazemian A., Khatibi M., Ma T.: *Performance prediction and optimization of a photovoltaic thermal system integrated with phase change material using response surface method*. J. Clean. Prod. **290**(2021), 125748. doi: 10.1016/j.jclepro.2020.125748

[104] Sharaf M., Yousef M.S., Huzayyin A.S.: *Review of cooling techniques used to enhance the efficiency of photovoltaic power systems*. Environ. Sci. Pollut. R. **29**(2022), 18, 26131–26159. doi: 10.1007/s11356-022-18719-9

[105] Stultz J.W., Wren L.C.: *Thermal performance testing and analysis of photovoltaic modules in natural sunlight*. Jet Propulsion Laboratory, Pasadena 1978.

[106] Günther E., Hiebler S., Mehling H., Redlich R.: *Enthalpy of phase change materials as a function of temperature: required accuracy and suitable measurement methods*. Int. J. Thermophys. **30**(2009), 4, 1257–1269. doi: 10.1007/s10765-009-0641-z

[107] https://www.rubitherm.eu/en/productcategory/organische-pcm-rt (accessed 15 Dec. 2022).

[108] Huang M.J., Eames P.C., Norton B.: *The application of computational fluid dynamics to predict the performance of phase change materials for control of photovoltaic cell temperature in buildings*. In: Proc. World Renewable Energy Cong. VI, Pergamon, Jan. 2000, 2123–2126. doi: 10.1016/B978-008043865-8/50454-2

[109] Huang M.J., Eames P.C., Norton B.: *Phase change materials for limiting temperature rise in building integrated photovoltaics*. Sol. Energy **80**(2006), 9, 1121–1130. doi: 10.1016/j.solener.2005.10.006

[110] Huang M.J., Eames P.C., Norton B., Hewitt N.J.: *Natural convection in an internally finned phase change material heat sink for the thermal management of photovoltaics*. Sol. Energ. Mat. Sol. C. **95**(2011), 7, 1598–1603. doi: 10.1016/j.solmat.2011.01.008

[111] Huang M.J.: *The effect of using two PCMs on the thermal regulation performance of BIPV systems*. Sol. Energ. Mat. Sol. C. **95**(2011), 3, 957–963. doi: 10.1016/j.solmat.2010.11.032

[112] Japs E., Sonnenrein G., Steube J., Vrabec J., Kenig E., Krauter S.: *Technical investigation of a photovoltaic module with integrated improved phase change material*. In: Proc. 28st Eur. Photovoltaic Solar Energy Conf. Exhib., Paris, Sep. 2013, 500–502.

[113] Hasan A., McCormack S.J., Huang M.J., Norton B.: *Characterization of phase change materials for thermal control of photovoltaics using differential scanning calorimetry and temperature history method*. Energ. Convers. Manage. **81**(2014), 322–329. doi: 10.1016/j.enconman.2014.02.042

[114] Hasan A., McCormack S.J., Huang M.J., Sarwar J., Norton B.: *Increased photovoltaic performance through temperature regulation by phase change materials: Materials comparison in different climates*. Sol. Energy **115**(2015), 264–276. doi: 10.1016/j.solener.2015.02.003

[115] Indartono Y.S., Suwono A., Pratama F.Y.: *Improving photovoltaics performance by using yellow petroleum jelly as phase change material*. Int. J. Low-Carbon Technol. **11**(2016), 3, 333–337. doi: 10.1093/ijlct/ctu033

[116] Hasan A., Alnoman H., Rashid Y.: *Impact of integrated photovoltaic-phase change material system on building energy efficiency in hot climate*. Energ. Buildings **130**(2016), 495–505. doi: 10.1016/j.enbuild.2016.08.059

[117] Hachem F., Abdulhay B., Ramadan M., El Hage H., El Rab M.G., Khaled M.: *Improving the performance of photovoltaic cells using pure and combined phase change materials – Experiments and transient energy balance*. Renew. Energ. **107**(2017), 567-575. doi: 10.1016/j.renene.2017.02.032

[118] Lim J. H., Lee Y. S., Seong Y. B.: *Diurnal thermal behavior of photovoltaic panel with phase change materials under different weather conditions*. Energies **10**(2017), 12, 1983. doi: 10.3390/en10121983

[119] Karthick A., Murugavel K.K., Ramanan P.: *Performance enhancement of a building-integrated photovoltaic module using phase change material*. Energy **142**(2018), 803–812. doi: 10.1016/j.energy.2017.10.090

[120] Ezan M.A., Yüksel C., Alptekin E., YılancıA.: *Importance of natural convection on numerical modelling of the building integrated PVP/PCM systems*. Sol. Energy **159**(2018), 616–627. doi: 10.1016/j.solener.2017.11.022

[121] Zohra M.B., Riad A., Hassoune H., Alhamany, A., Mansouri M.: *A new system for the production and storage of thermal energy based on two complementary and different types of phase changing materials*. Case Stud. Therm. Eng. **26**(2021), 101072. doi: 10.1016/j.csite.2021.101072

[122] Nada S.A., El-Nagar D.H., Hussein H.M S.: *Improving the thermal regulation and efficiency enhancement of PCM-Integrated PV modules using nano particles*. Energ. Convers. Manage. **166**(2018), 735–743. doi: 10.1016/j.enconman.2018.04.035

[123] Jamil F., Ali H. M., Nasir M.A., Karahan M., Janjua M.M., Naseer A., Pasha R.A.: *Evaluation of photovoltaic panels using different nano phase change material and a concise comparison: An experimental study*. Renew. Energ. **169**(2021), 1265–1279. doi: 10.1016/j.renene.2021.01.089

[124] Malvi C.S., Dixon-Hardy D.W., Crook R.: *Energy balance model of combined photovoltaic solar-thermal system incorporating phase change material*. Sol. Energy **85**(2011), 1440–1446. doi: 10.1016/j.solener.2011.03.027

[125] Yin H.M., Yang D.J., Kelly G., Garant J.: *Design and performance of a novel building integrated PV/thermal system for energy efficiency of buildings*. Sol. Energy **87**(2013), 184–195. doi: 10.1016/j.solener.2012.10.022

[126] Browne M.C., Lawlor K., Kelly A., Norton B., Mc Cormack S.J.: *Indoor characterisation of a photovoltaic/thermal phase change material system*. Energy. Proced. **70**(2015), 163–171. doi: 10.1016/j.egypro.2015.02.112

[127] Sardarabadi M., Passandideh-Fard M., Maghrebi M.J., Ghazikhani M.: *Experimental study of using both ZnO/water nanofluid and phase change material (PCM) in photovoltaic thermal systems*. Sol. Energy **161**(2017), 62–69. doi: 10.1016/j.solmat.2016.11.032

**archives**
**of thermodynamics**
Vol. **44**(2023), No. 4, 619–633
DOI: 10.24425/ather.2023.149736

# The effect of photovoltaic system operating parameters on exergy efficiency

**WALDEMAR KUCZYŃSKI***
**ANNA BOROWSKA**

Technical University of Koszalin, Faculty of Mechanical Engineering and Energy, Department of Energy, Racławicka 15-17, 75-620 Koszalin, Poland

**Abstract** Solar energy is a unique source of renewable energy due to its availability and the unlimited quantity. It has long attracted the attention of scientists who are conducting theoretical and experimental research into its use. Solar energy plays an increasingly important role in the context of energy conservation. With the rising cost of conventional energy sources and limited access to natural resources, interest in the use of renewable energy sources is increasing. In this context, environmental protection is another factor favoring the development of technologies based on renewable energy sources. With economic development, the significance of new environmentally friendly technologies is increasing. One of the most popular ways for the average household to utilize renewable energy sources is by installing photovoltaic panels. Such an installation allows the use of solar energy to generate electricity, which contributes to reducing energy costs and protecting the environment. The article presents the results of an analysis of the exergy efficiency of prosumer photovoltaic systems found in the area of northern Poland. The analysis presented was based on actual operating parameters over a certain time interval. A key aspect is the analysis of exergy, which is not distributed in renewable energy sources (RES) systems.

**Keywords:** Renewable energy sources; Photovoltaic; Exergy; Electric power

*Corresponding Author. Email: waldemar.kuczynski@tu.koszalin.pl

**Nomenclature**

| | | |
|---|---|---|
| $\dot{b}_r$ | – | radiation exergy flux, W |
| $F$ | – | surface area of photovoltaic modules, $m^2$ |
| $\dot{I}_\beta$ | – | radiation energy flux, W |
| $P_{el}$ | – | electric power, W |
| PV | – | photovoltaic |
| RES | – | renewable energy sources |
| $T$ | – | surface temperature emitting radiation, K |
| $T_0$ | – | ambient temperature, K |
| $\eta_{B,\mathrm{PV}}$ | – | exergy efficiency, % |
| $\eta_{E,\mathrm{PV}}$ | – | energy efficiency, % |

# 1 Introduction

The development of renewable energy sources as a substitute for fossil fuels has been taken into account in the last few years of the decade. Solar energy as an accessible, low-cost, ecological and friendly alternative source has been and continues to be the subject of much theoretical and experimental research. Energy from the sun plays an important role in the aspect of energy conservation. The use of solar energy in the desalination process is an opportunity to provide potable water from salt water. Exergy analysis evaluates the effective use of solar energy [1].

Non-conventional energy sources have become a popular alternative to conventional energy. Energy derived from solar radiation, wind or water ripples and tides is free, requires no transportation, is not counted, and most importantly, has no negative impact on the environment. Solar radiation energy and its utilization allows to perform exergy analysis studies. An important indicator of the quality of photovoltaic installations is exergy efficiency. It is defined as the ratio of the amount of electricity produced by the installation to the amount of energy required to produce, install and maintain the installation. It thus seeks to ensure that the installation generates more electricity than it consumes for its maintenance [2].

Climate change and environmental degradation are among the greatest challenges facing humanity today. With the rising cost of traditional energy sources, such as coal and gas, and increasing access to renewable energy technologies, such as solar, wind and geothermal, many countries around the world are seeking to increase their energy production from renewable sources. At the same time, the negative effects of atmospheric emissions,

such as smog and climate change, are becoming increasingly apparent, with negative impacts on human health, economic development and ecosystems. Therefore, more and more people and institutions are paying attention to the need to protect the environment by reducing harmful emissions and increasing the use of energy from renewable sources [3, 4].

The primary reason behind the popularity of photovoltaic systems is the clean and limitless nature of this energy source. In contrast to fossil fuels, which become increasingly challenging to access as reserves deplete, solar radiation offers a constant and readily available energy supply, ensuring power generation round the clock. Furthermore, photovoltaic systems produce no environmentally harmful emissions nor generate noise, thus making them a more eco-friendly choice. Figure 1 shows a generalized schematic of a photovoltaic system.

A number of studies confirm that photovoltaic systems will make a significant contribution in the future, and their development will accelerate due to technological innovations, improvements in the efficiency of photovoltaic panels, and support programs from the government and the private sector [5].

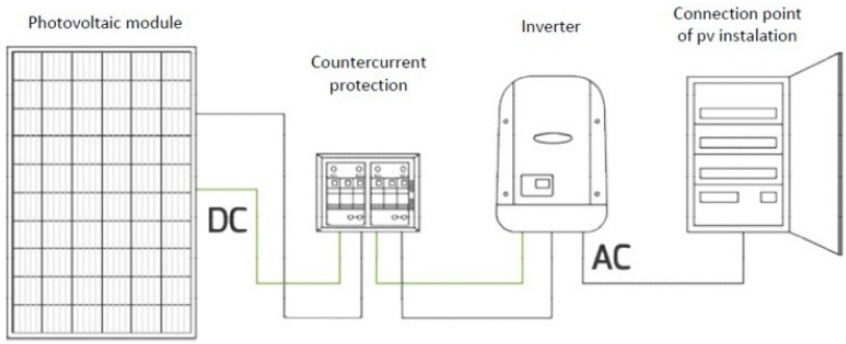


Figure 1: Schematic diagram of the photovoltaic system: DC – direct current, AC – alternating current [6].

## 1.1 Sustainable development and renewable energy sources

An important aspect is the pursuit of a balance between economic and social progress, and environmental protection. This is why the construction and operation of machinery, equipment, installations and systems for renewable energy sources is so important for our future. They allow to use

energy in a sustainable and environmentally safe way. The implementation of modern RES (renewable energy sources) technologies and systems contributes to improving the quality of life of the population by providing clean energy and generating new jobs. At the same time, we reduce emissions of greenhouse gases and air pollutants, thus balancing development and environmental protection. That is why it is so important to develop and use renewable technologies, such as solar panels, wind turbines and heat pumps, and to support the development of electric transportation. In the context of long-term sustainable development, it is crucial to develop and use technologies that strike a balance between economic progress, social progress and environmental protection. In this way, a future can be created that is safe for us and for future generations.

Energy supply is a key element for the socio-economic development of the European Union. Recently, the European Union has placed increasing emphasis on improving energy efficiency and increasing the share of renewable energy sources in total energy production. This is key to creating a secure, clean and competitive energy market that will contribute to stable economic development while minimizing environmental impact [7].

The European Union's energy policy is based on the Europe 2020 Strategy, which sets goals related to improving energy efficiency and increasing the share of renewable energy in total energy production. This way, the European Union aims to reduce emissions of greenhouse gases and other air pollutants. This is crucial for future generations, as by providing a clean and safe environment, we create the conditions for stable economic development.

Improving energy efficiency and increasing the share of renewable energy in total energy production also has a positive impact on the competitiveness of the European Union. Investment in renewable technologies and improved energy efficiency stimulate the development of innovative economic sectors and industries, which contributes to employment and economic growth.

Economic development requires an ever-increasing demand for electricity to ensure the comfort of human life. The exploitation of fossil fuels has a negative impact on the environment, hence the need for a healthy and sustainable energy transition such as harnessing the potential of renewable energy [8].

In summary, the development of energy efficiency and the utilization of renewable energy sources are crucial for creating a stable, clean, and competitive energy market in the European Union. This enables the achievement of goals such as reducing greenhouse gas emissions, protecting the

environment, and enhancing economic stability. The Europe 2020 strategy is a significant tool of the European Union's energy policy and should be consistently implemented to achieve the intended outcomes.

In addition, renewable energy also has beneficial effects on human health. Compared to traditional energy sources such as coal and gas, renewable energy does not generate toxic dusts that negatively affect human health, such as PM2.5 or PM10 particulate matter. Reducing emissions of these particulates can help reduce respiratory and cardiovascular diseases, which can improve people's health and quality of life.

Except environmental and human health benefits, renewable energy also has economic benefits. Renewable energy production generates new jobs in sectors related to the design, manufacture, installation and maintenance of RES-related facilities. At the same time, renewable energy generation can help reduce dependence on fossil fuel imports and reduce their prices, which can contribute to competitiveness and economic stability.

Renewable energy has a positive impact on the environment, human health and the economy. Therefore, more and more countries and institutions are introducing programs and initiatives to increase the share of renewable energy sources in total energy production, which can contribute to long-term sustainable development [9, 10].

## 1.2 Exergy efficiency

As a result of the application of a sustainable and emission-free way of generating electricity from solar radiation, quality indicators are sought, which are used to evaluate the efficiency and performance of photovoltaic installations. With this in mind, a key indicator is the exergy of the equipment used in these installations.

Kinetic energy, potential energy and energies associated with the motion of molecules are considered types of mechanical energy that are readily convertible to other forms of energy, such as electricity or heat. On the other hand, the internal energy of substances and the energy of chemical bonds are forms of internal energy that are more difficult to convert into other types of energy. Internal energy is also responsible for thermodynamic processes, such as thermal conduction and heat flow, which are crucial in many technological processes. Depending on the context, different types of energy can have different significance and uses [11–13].

The term exergy refers to the concept of qualitative energy analysis, which takes into account the ability to convert energy into mechanical work

or other desired effect. Exergy is also referred to as 'real energy' because it takes into account energy losses due to thermodynamic imbalances and process imperfections [14].

In the context of photovoltaic installations, exergy is used to assess the efficiency of converting solar radiation energy into electricity. Exergy analysis makes it possible to determine the maximum amount of electricity that can be produced by a given installation under ideal conditions, which is important information for designers and users of photovoltaic systems [15]. An important feature of exergy is that it can be used as a tool to compare different technologies and processes from the point of view of their energy efficiency. Thus, it can help select the most economical and environmentally friendly technological solutions [16].

## 2 Analysis of operating parameters of photovoltaic installations

Three photovoltaic installations located in the northern Poland, in the West Pomeranian Voivodeship of Koszalin County, were analyzed. The installations in question belong to prosumer RES systems. They were designed and installed on household buildings, according to the electricity needs of the household members living there. In order to juxtapose and compare them, the photovoltaic installations differ in the direction of the location of the photovoltaic modules in relation to the south, i.e., they are installations mounted in the following directions: south-west, south, south-east. The power value of the photovoltaic installation is the same in each case and is 4.94 kWp. At the design stage, a simulation was carried out to determine the amount of electricity generated by each system. Table 1 summarizes of the two most important values: the projected amount of electricity generated and the amount of energy generated from 1 kWp, the so-called characteristic annual yield.

Table 1: Summary of the results obtained in the program for PVsol.

| | Installation facing south | Installation facing south-west | Installation facing south-east |
|---|---|---|---|
| Forecasted amount of electricity generated (kWh/year) | 4 667.6 | 4 317.0 | 4 740.2 |
| Characteristic annual yield (kWh/kWp) | 940.0 | 869.0 | 956.6 |

The designed photovoltaic system constitutes a current-generating unit classified as a micro source of renewable energy utilizing solar power. The primary objective of this system is to generate electricity for the facility's own needs. By being connected in parallel with the internal grid, it enables the excess energy generated to be fed back into the power grid of the operator of the distribution system (OSD) in case the facility's consumption is insufficient. This sustainable energy system not only allows for the utilization of clean solar energy to power the facility but also contributes to the overall energy balance by supplying surplus energy to the distribution grid. With such a solution, the facility can benefit from eco-friendly energy, minimizing its environmental impact while also leveraging the opportunity for energy exchange with the distribution grid.

Each photovoltaic (PV) installation has the ability to remotely read the hourly, daily, monthly and annual amount of electricity generated. With the help of monitoring the operation of the installed equipment, the annual amount of electricity generated is recorded in Table 2. Table 3 shows the actual annual yield values, in order to identify how much each plant will generate electricity from 1 kWp to compare them with each other.

Table 2: Reading the results from the Fronius SolarWeb photovoltaic monitoring application [17].

| Actual amount of electricity produced (kWh/year) | | | |
|---|---|---|---|
| Year | Installation facing south | Installation facing south-west | Installation facing south-east |
| 2018 | 5 357.45 | 5 380.06 | 4 518.07 |
| 2019 | 4 814.38 | 4 815.30 | 3 917.59 |
| 2020 | 4 730.73 | 5 053.60 | 3 758.20 |

The monitoring system for PV installations on the FroniusWeb platform allows users to track the performance and operation of their installation. With this tool, users can monitor the performance of photovoltaic panels in real-time and analyze historical data on energy production. The FroniusWeb platform also provides access to various system parameters such as voltage, current, power, and temperature, allowing for a thorough evaluation of the installation's operation. Additionally, users can receive notifications of any malfunctions or irregularities in the system operation, enabling quick response and issue resolution. Overall, the monitoring sys-

tem for PV installations on the FroniusWeb platform offers a comprehensive tool for monitoring and optimizing the operation of a photovoltaic system.

Table 3: Actual annual yield.

| Characteristic annual yield (kWh/kWp) | | | |
|---|---|---|---|
| Year | Installation facing south | Installation facing south-west | Installation facing south-east |
| 2018 | 1 084.50 | 1 089.08 | 916.44 |
| 2019 | 974.57 | 982.04 | 794.64 |
| 2020 | 957.64 | 1 023.00 | 762.31 |

The explanation for the differences in the magnitude predicted by the program and the actual state is the fact of cyclical weather anomalies. It can be observed that the climate is warming from year to year. The year 2018 was abundant in the number of sunny days as can be seen in Table 4. It can also be seen that the average sunshine from 1998 to 2005 differs from 2018 by about 653.30 hours.

Table 4: Number of hours of sunshine on an annual basis and for individual months [18].

| Month | Year | | |
|---|---|---|---|
| | 2018 | 2019 | 2020 |
| January | 32.5 | 47.8 | 37.7 |
| February | 102.0 | 72.8 | 68.6 |
| March | 149.4 | 92.2 | 184.0 |
| April | 248.7 | 298.2 | 286.2 |
| May | 373.2 | 224.4 | 258.3 |
| June | 307.7 | 354.1 | 260.9 |
| July | 292.3 | 267.8 | 223.0 |
| August | 259.3 | 266.1 | 286.5 |
| September | 205.4 | 145.7 | 208.5 |
| October | 176.9 | 94.2 | 91.0 |
| November | 88.9 | 45.5 | 38.1 |
| December | 6.5 | 41.1 | 37.6 |

Both the forecasted amount of electricity generated and the characteristic annual yield deviate from the actual state. This is because the program in which the simulation of the operation of photovoltaic installations was carried out works on the basis of analyses of the number of hours of sunshine from 1986–2005, and for the selected location takes its average value. Table 4 shows the actual number of solar hours on an annual basis for each month, for those years for which the three selected photovoltaic installations are analyzed.

Figure 2 shows a diagram of the dependence of the sum of hours of sunshine from 1998 to 2020. The characteristics do not show a clear regularity. The parameter of sunshine is a variable quantity, but with each year there is a trend of its increase compared to previous years.

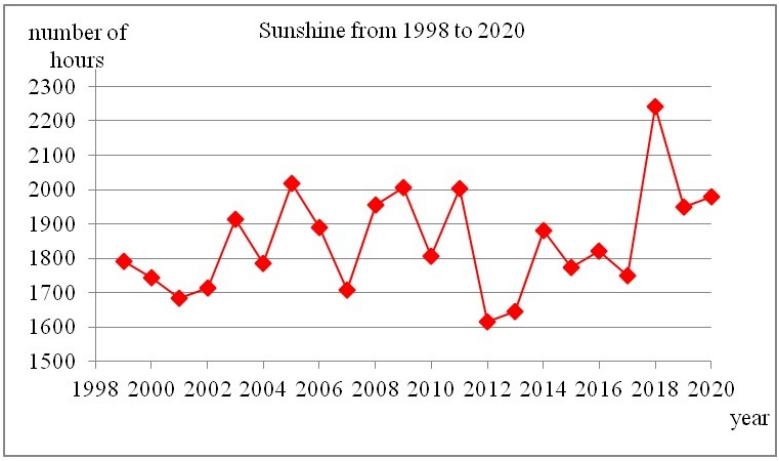


Figure 2: Diagram of sunshine hour totals by year from 1998 to 2020.

Another, deviating from the so-called pure theory, is the fact that an installation facing south has slightly worse performance than an installation facing south-west, while it should be just the opposite. An installation facing south should generate the best electricity production. This is due to the location of these installations. Koszalin is a city located in the northwestern part of Poland. In the summer, a long time of sunset can be observed. The area of northwestern Poland is better insolated than the rest of the country, as shown in Fig. 3.

The characteristics shown in Figs. 4–6 illustrate the amount of electricity generated by a photovoltaic system. In each of them, three main stages of

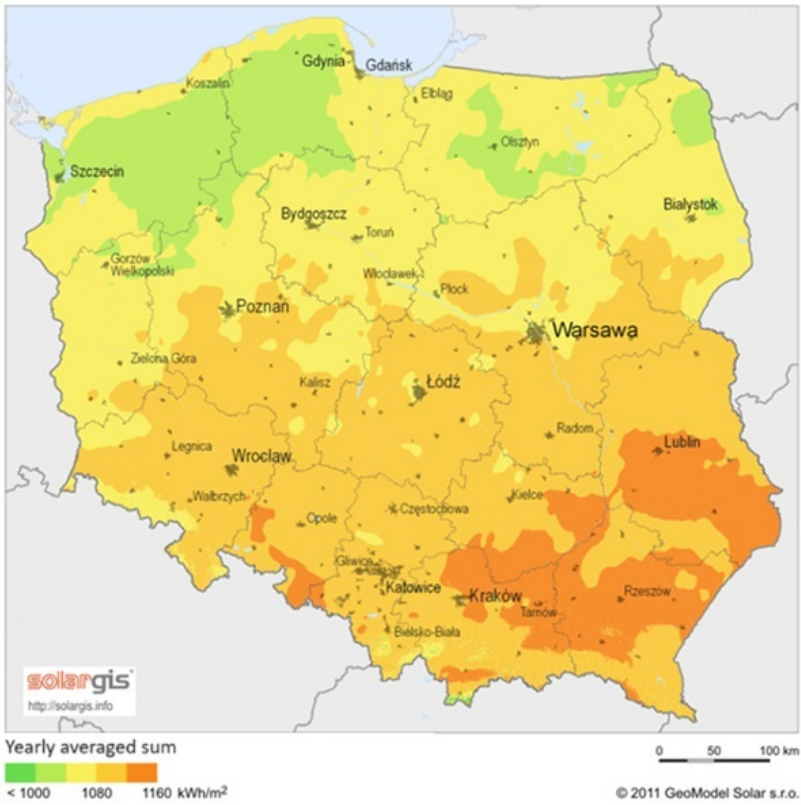


Figure 3: Map of insolation of Poland [19].

operation can be distinguished: start of operation, maximum energy generation and end of operation. The start of operation as well as its endare characterized by a flattening of the graph. At the time of the peak in energy generation, the curve resembles a parabola in its shape. The graphs that show shaky operation of the system (Fig. 5) reflect disturbances caused by weather changes. Table 5 makes a summary of the values for the highest daily energy generation read from the graphs showing the operation of each plant.

Based on the data in Table 5, the regularity of photovoltaic system operation is preserved. Despite the differences in terms of directionality of the location of the installations, each of them begins and ends operation and generates electricity at a similar hour. Small deviations are due to climatic changes (occurrence of cloudy, rainy days) and sunshine.

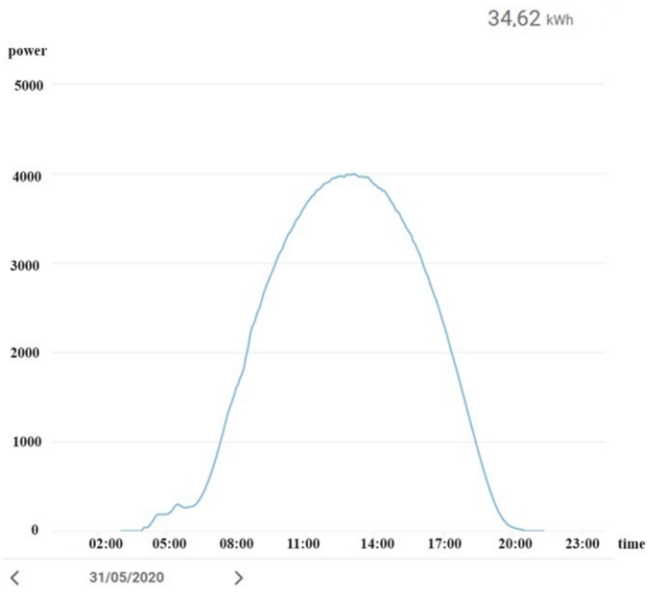


Figure 4: Largest daily electricity generation of installation facing south in 2020 [17].

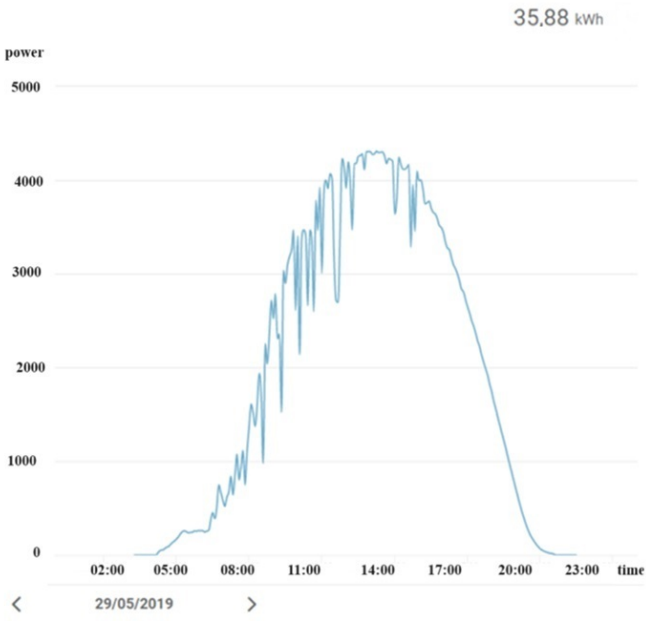


Figure 5: Largest daily electricity generation of installation facing south in 2019 [17].

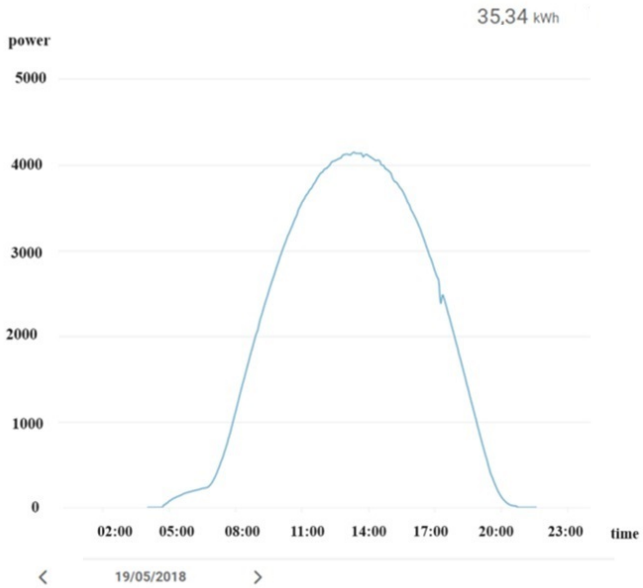


Figure 6: Largest daily electricity generation of installation facing south in 2018 [17].

Table 5: Summary of the various stages of operation of photovoltaic installations.

| | | Year 2018 | Year 2019 | Year 2020 |
|---|---|---|---|---|
| Installation facing south | start of operation | 4:50 (40 W) | 4:20 (20 W) | 4:00 (3 W) |
| | maximum generation of electricity | 13:20 (4 148 W) | 13:00 (4 303 W) | 13:00 (3 995 W) |
| | end of operation | 20:45 (1 W) | 20:35 (6 W) | 20:24 (14 W) |
| Installation facing south-west | start of operation | 5:25 (18 W) | 4:50 (36 W) | 4:45 (50 W) |
| | maximum generation of electricity | 14:30–15:50 (4 302 W) | 13:50–14:25 (4 305 W) | 14:30–15:30 (4 302 W) |
| | end of operation | 21:05 (14 W) | 21:45 (9 W) | 21:00 (25 W) |
| Installation facing south-east | start of operation | 4:50 (14 W) | 4:30 (30 W) | 5:10 (1 W) |
| | maximum generation of electricity | 10:10 (4 274 W) | 10:45 (4 214 W) | 11:15 (4 206 W) |
| | end of operation | 19:45 (6 W) | 19:40 (1 W) | 20:30 (1 W) |

## 3 Exergy efficiency in photovoltaic installations

The technology of electricity generation through photovoltaic installations is characterized by lower efficiency compared to systems powered by non-renewable energy sources. However, it is worth noting that energy efficiency is not the only criterion for selecting an energy source. In addition, renewable energy sources allow energy independence and reduce the costs associated with purchasing electricity from traditional suppliers [20].

The following methods can be used to determine solar exergy and direct exergy efficiency for solar-powered systems: balance, thermodynamic and empirical. In each method, it is necessary to take into account the characteristics of photovoltaic modules (such as efficiency, operating temperature, lighting conditions), the design characteristics of the system (e.g., orientation of modules with respect to the sun, geometry of the system), and the efficiency of conversion of solar energy to electricity [21].

The following equation was used to determine the value of exergy efficiency [21]:

$$\eta_{B,PV} = \frac{P_{el}}{F\dot{b}_r} = \eta_{E,PV}\frac{\dot{I}_\beta}{\dot{b}_r}. \tag{1}$$

The present values were calculated based on energy efficiency, determining the exergy flux of solar radiation according to the formula

$$\frac{\dot{b}_r}{\dot{I}_\beta} = 1 - \frac{4T_0}{3T} + \frac{1}{3}\left(\frac{T_0}{T}\right)^4. \tag{2}$$

The exergy efficiency for an installation facing south-west is 13.95%, for the south-east it is 15%, for the south it is 13.95%.

## 4 Summary and conclusions

The purpose of this paper was to analyze the exergy efficiency of three photovoltaic installations mounted on household facilities operating in northern Poland in the West Pomeranian Voivodeship, Koszalin County. Each installation faces a different direction of the world: south, south-east and south-west. The analysis was based on collected operating parameters in a monitoring system that archives readings with hourly accuracy over 3 years (from 2018 to 2020). Conducting this analysis led to the following conclusions:

1. Both the projected amount of electricity generated and the characteristic annual yield deviate from reality. This is because the design program works on the basis of analysis of the number of hours of sunlight from 1986 to 2005, and for the selected location takes its average value.

2. The designed photovoltaic system is a current-generating unit classified as a micro source using renewable (solar) energy. Its primary purpose is to generate electricity by the system for the facility's own needs. Making it in a system of parallel connection with the internal grid allows giving back the excess of generated energy in case of consumption at this facility – to the power grid of the operator of the distribution system.

3. Analysis of the exergy efficiency of the installations facing south and south-west shows the same value (i.e., 13.95%) while the installation facing south-east shows a value 1.05% higher. This is due to the fact that the installation with the lower exergy efficiency is made of polycrystalline modules, while the installation facing south-east consists of monocrystalline modules. The exergy efficiency of a monocrystalline module is higher than that of polycrystalline modules.

*Received 18 July 2023*

## References

[1] Bigorajski J.: *Photovoltaic development and financial support instruments*. Polska Energetyka Słoneczna (2015), 1-4, 21–26 (in Polish).

[2] Bogdanienko J.: *Renewable Sources of Energy*. PWN, Warszawa 1989 (in Polish).

[3] Klugmann-Radziemska E.: *Photovoltaics in Theory and Practice* (1st Edn.). BTC, Legionowo 2010 (in Polish).

[4] Klugmann E., Klugmann-Radziemska E.: *Alternative Energy Sources. Photovoltaic Energy*. Wydawn. Ekonomia i Środowisko, Bialystok 1999 (in Polish).

[5] Kumar A., Baredar P., Qureshi U.: *Historical and recent development of photovoltaic thermal (PVT) technologies*. Renew. Sustain. Energy Rev. **42**(2015), 1428–1436.

[6] https://oemenergy.pl/oferta/fotowoltaika/ (accessed 01 Oct. 2023).

[7] Góralczyk I., Tytko R.: *Photovoltaics: Devices, Photovoltaic and Electric Installations* (4th Edn. suppl.). Wydawnictwo i Drukarnia Towarzystwa Słowaków w Polsce, Kraków 2016.

[8] Hadjidj H.S., Bibi-Triki N., Didi F.: *Analysis of the reliability of photovoltaic-microwind based hybrid power system with battery storage for optimized electricity generationat Tlemcen, north west Algeria*. Arch. Thermodyn. **40**(2019), 1, 161–185. doi: 10.24425/ather.2019.128296

[9] Tol R.: *Environmental Crises*. Springer-Verlag, Berlin Heidelberg 2008.

[10] Zacher L.W.: *Technology Society and Sustainability. Selected Concepts, Issues and Cases*. Springer Int. Publ., 2017.

[11] Sażyn B.S.: *Warp Dryer Technology*. Khimia. Moscow 1984 (in Russian).

[12] Szargut J.: *Engineering Thermodynamics*. Wydawn. Pol. Śl., Gliwice 2000 (in Polish).

[13] Kozaczka J.: *Thermodynamic Analysis*. Wydawn. AGH, Kraków 1988 (in Polish).

[14] Szargut J., Petela R.: *Exergy*. WNT, Warszawa 1965 (in Polish).

[15] Kramarz J., Wyczesany A.: *Exergetic Evaluation of Coal Processing Towards Liquid Fuels*. Wydawn. PK, Kraków 1991 (in Polish).

[16] Szargut J.: *Exergy: A Guide to Calculation and Application*. Wydawn. Pol. Śl., Gliwice 2007 (in Polish).

[17] https://www.solarweb.com (accessed 01 Oct. 2023).

[18] www.weatheronline.pl/weather/maps/city?WMO=12105&CONT=plpl&LAND weather/maps/city?WMO=12105&CONT=plpl&LAND=PL&ART=SOS& LEVEL=162&MOD=MOA (accessed 01 Oct. 2023).

[19] http://www.gsfotowoltaika.pl/fotowoltaika/mapa-naslonecznienia-polski/ (accessed 01 Oct. 2023).

[20] Saidur R., Boroumand Jazi G., Mekhlif S., Jameel M.: *Energy analysis of solar Energy applications*. Renew. Sustain. Energy Rev. **16**(2012), 1, 350–356.

[21] Stanek W.: *Exergy Analysis in Theory and Practice*. Wydawn. Pol. Śl., Gliwice 2016 (in Polish).

**archives**
**of thermodynamics**
Vol. **44**(2023), No. 4, 635–652
DOI: 10.24425/ather.2023.149717

# Adiabatic gas transport in the long flow channels

**KAZIMIERZ RUP***
**TOMASZ SOBOTA**

Cracow University of Technology, Faculty of Environmental Engineering and Energy, Warszawska 24, 31-155 Kraków, Poland

**Abstract** The paper present the determination of the state parameters of natural gas at the pipeline inlet based on knowledge of the pressure and temperature at the receiving point. Natural gas transport will be carried out through an offshore section of a transmission pipeline. The equations of the Fanno flow model will be used to describe the thermodynamic parameters of the gas in the flow lines. The mathematical equations of the flow mentioned above models have been derived from an analysis of the mass, energy and momentum balance equations. They also take into account the viscous friction forces in the transported gas. Based on the carried out calculations, changes in the Mach number, pressure and velocity of methane transported along the analysed pipeline were determined. In addition, the total entropy gain in the analysed methane flow was determined. The novelty of the calculations presented is the use of the Fanno flow model, which considers a realistic adiabatic gas flow. This is in contrast to the isothermal flow model, which assumes an unchanging temperature of the transported gas. In the case under consideration, the adopting model was possible because of the similar temperature values of the gas flowing in the pipeline and the corresponding temperature values of the surrounding seawater. The fundamental advantage of the Fanno flow model is that it satisfies the mass balance of the flowing gas in each cross-section. Thus, the product of the velocity and density of the gas in a pipeline of constant diameter assumes a constant value.

**Keywords:** Natural gas pipeline; Fanno flow; Adiabatic flow; Mach number; Redlich-Kwong state equation

*Corresponding Author. Email: kazimierz.rup@pk.edu.pl

### Nomenclature

| | | |
|---|---|---|
| $a$ | – | speed of sound, m/s |
| $D$ | – | pipeline inner diameter, m |
| $k$ | – | wall roughness, m |
| $L$ | – | length, m |
| $L_*$ | – | critical pipeline length, m |
| $M$ | – | Mach number |
| $p$ | – | pressure, Pa |
| $p_{01}$, $p_{02}$ | – | stagnation pressure for the pipeline inlet and outlet sections respectively, Pa |
| $\dot{Q}_m$ | – | mass flow rate, kg/s |
| $\dot{Q}_v$ | – | volumetric flow rate, $m^3/s$ |
| $R$ | – | individual gas constant, J/(kgK) |
| $r$ | – | residual |
| Re | – | Reynolds number |
| $S$ | – | constant cross-sectional area, $m^2$ |
| $s$ | – | specific entropy, J/(kgK) |
| $T$ | – | temperature, K |
| $v$ | – | specific volume, $m^3/kg$ |
| $w$ | – | velocity, m/s |

#### Greek symbols

| | | |
|---|---|---|
| $\eta$ | – | dynamic viscosity, $Ns/m^2$ |
| $\kappa$ | – | isentropic exponent |
| $\lambda$ | – | coefficient of friction losses |
| $\rho$ | – | density, $kg/m^3$ |

#### Subscripts

| | | |
|---|---|---|
| 1 | – | inlet parameter |
| 2 | – | outlet parameter |
| $c$ | – | critical |
| $m$ | – | mass |
| $v$ | – | volumetric |
| * | – | denotes that state where $M = 1$ |

#### Superscript

| | | |
|---|---|---|
| r | – | real gas |

# 1 Introduction

Natural gas is one of the fastest-growing energy sources for thermal and chemical plants. The need to reduce carbon dioxide emissions into the atmosphere or stabilise them has created significant demand for this resource.

Natural gas is a mineral resource formed from the anaerobic decomposition of organic substances accumulated deep beneath the Earth's surface. The composition of natural gas is variable and depends primarily on the location from which it is extracted. It comprises hydrocarbon components, the main ($CH_4$) and other so-called heavy hydrocarbons, usually not in significant quantities. In addition, carbon dioxide ($CO_2$), hydrogen ($H_2$), hydrogen sulphide ($H_2S$), nitrogen ($N_2$), and noble gases such as helium (He) and argon (Ar) may be present in natural gas [1, 2].

It should be noted that the content of individual hydrocarbons varies in natural gas from different fields. Gas that consists almost exclusively ($> 90\%$) of methane and ethane is called dry gas. A typical dry gas is a Norwegian gas containing nearly 97% $CH_4$ and $C_2H_6$ in its composition. In contrast, a gas that contains hydrocarbons with a higher molecular weight than methane is called condensate gas or wet gas. This gas is generally found together with oil fields.

It is worth noting that high molecular weight hydrocarbons and non-hydrocarbon components should be removed from natural gas (up to the content specified by the relevant standards) before transport or processing [2].

Natural gas distribution systems are highly complex installations and are not infrequently used to transport other gases like hydrogen. This makes the design and operation of natural gas distribution systems increasingly complex, requiring multi-criteria optimisation. Koo [3] proposed a novel implicit method of characteristics (MOC) that provides efficient and reliable transient flow analyses for natural gas pipelines. Zhang *et al.* [4] proposed the transient pressure simulation method to determine the pressures caused by the movement of the smart isolation device in subsea gas pipeline maintenance technology. The technique was verified experimentally, presenting its good accuracy in simulating the moving process caused in gas pipelines by isolation devices. Glot *et al.* [5] numerically and experimentally investigated processes of propagation of deformation waves in the underground gas pipeline. The numerical simulation of dynamic processes in the underground pipelines allowed the development of deformation wave propagation and decay patterns. Koo [6] analyzed two numerical methods of modelling transient flow in a single natural-gas pipeline – the pressure-based finite-volume method and the conventional implicit method of characteristics depending on the nature of the gas flow. Zhou *et al.* [7] developed a dynamic model to simulate the behaviour of a single pipeline and pipeline network according to the actual geographical topology.

Ensuring flexibility in the operation of the electricity grid with renewable energy sources (RES) and energy storage can be achieved by transporting natural gas supplemented with hydrogen. This hydrogen is usually produced by electrolysis processes realised using excess electricity from RES. Witek and Uilhoorn in [8], particularly determined the permissible hydrogen content that can be blended with natural gas in existing pipeline systems and then investigated the impact on linepack energy for both compressor start-up and shut-down scenarios.

In addition to natural gas, liquefied natural gas (LNG) can be used in power generation systems. Szczygieł and Rutczyk [9] analysed the change in the parameters of LNG during its transportation by ship and the regasification process. It is mainly used for power generation, but some facilities allow the use of LNG cryogenic exergy for other tasks, such as in the food industry for freeze-drying food. Wieczorek [10] proposed using liquefied petroleum gas (LPG) to remove inert gas from the tank. For this purpose, she developed a thermodynamic model of this process, which made it possible to determine the required concentration and amount of LPG gas to accomplish this process. The developed thermodynamic model was tested for various conditions [11].

Trawinski [12] noted the need to identify working fluids when developing the mathematical models used to describe thermodynamic systems. In particular, the paper [12] analysed the semi-ideal gas model as an extension of the ideal gas model for selected gases in extended ranges of thermodynamic parameters. The Redlich-Kwong, Peng-Robinson, Soave-Redlich-Kwong, and Lee-Kesler models were analysed. The Redlich-Kwong and Lee-Kesler equations of state proved to be the most accurate for describing the gases under study: humid atmospheric air, high-methane natural gas and flue gas.

Generally, it can be said that the equations of the isothermal model or the corresponding equations of the Fanno flow model [8,12,13] describe the thermodynamic parameters of the gas in transport pipelines. The mathematical equations of the aforementioned flow models were derived from the analysis of the mass, energy and momentum balance equations, and they also take into account the viscous friction forces in the transported gas [13–15]. Classical methods of calculating the parameters of gas flowing in a pipeline cannot be applied to the case under consideration due to the large parameter variations. These parameter changes are due to the expansion process of the transported gas.

Since the Fanno model equations describe gas flows under realistic adiabatic conditions, they will be used in the further analysis included in this

paper. Theoretical considerations and experimental studies show that the Fanno model equations accurately describe both subsonic and supersonic gas flows [14, 15]. An essential advantage of subsonic flow in the Fanno model under consideration is that there is no restriction on the length of the flow pipe (Fanno tube). It is worth noting that the Fanno model equations in question often assume a constant value for the coefficient of frictional loss $\lambda$. In Fanno flow, the temperature of the gas changes and therefore the value of the Reynolds number also changes. An analysis of the formula describing the Reynolds number $\left(\mathrm{Re} = \dfrac{\rho w D}{\eta}\right)$ shows that in a pipe of constant diameter, its value is only affected by a change in gas viscosity. Given that in the flows under consideration, the gas temperature changes only slightly, the assumption mentioned above of invariability of the friction loss coefficient $\lambda = \lambda\left(\mathrm{Re}, \dfrac{k}{D}\right)$ is justified. When larger gas temperature differences are present, it is recommended that the averaged value of the frictional loss coefficient along the length of the Fanno tube be included in the calculation [13, 15].

## 2 Estimation of gas parameters at the inlet to pipeline

Due to the high methane content (98%) of the transported natural gas in the Baltic Pipe pipeline, the calculations are limited to the case of methane flow. Due to this, the thermophysical properties of the transported gas will be determined as for pure methane. Based on the assumption according to [16] that the transmission capacity of the Baltic Pipe pipeline is $\dot{Q}_v = 8 \cdot 10^9\ \mathrm{nm^3/year}$ with a density of $\rho = 0.7167\ \mathrm{kg/nm^3}$ the corresponding methane mass flow rate in the pipeline under consideration can be calculated:

$$\dot{Q}_m = \dot{Q}_v \rho = 8 \cdot 10^9\ \frac{\mathrm{nm^3}}{\mathrm{year}} \cdot \frac{\mathrm{year}}{365 \cdot 24 \cdot 3600\ \mathrm{s}} \cdot 0.7167\ \frac{\mathrm{kg}}{\mathrm{nm^3}} = 181.711\ \frac{\mathrm{kg}}{\mathrm{s}}. \quad (1)$$

The calculations included for transported methane: $T_n = 273.15$ K, $p_n = 1013.25$ hPa, 1 year $= 365 \cdot 24 \cdot 3600$ s.

Considering the characteristic dimensions of the offshore section of the Baltic Pipe pipeline (from Denmark to Poland): $L = 275$ km, $D = 900$ mm and $k/D = 0.0001$, the parameters of transported methane in the flow region can be determined. The working pressure of the Baltic Pipe pipeline

given by the operator is between 5 MPa and 12 MPa, depending on the volume of gas to be transported [16]. It should be noted that in further calculations, the values of thermodynamic parameters of transported methane in the outlet section of the pipeline were assumed. They are $T_2 = 288$ K, and $p_2 = 170$ kPa. It can be stated that the temperature and pressure values adopted are based on the customer's needs. In addition, the calculations take into account: $R = 518.33\ \mathrm{J/(kg\,K)}$ – the individual gas constant of methane, $\kappa = 1.30$ – the isentropic exponent, $\eta(T = 298\ \mathrm{K}) = 0.01 \cdot 10^{-3}\ \mathrm{N\,s/m^2}$ – dynamic viscosity of methane [17]. The adopted calculation scheme according to the Fanno model for the Baltic Pipe pipeline under consideration is shown in Fig. 1.

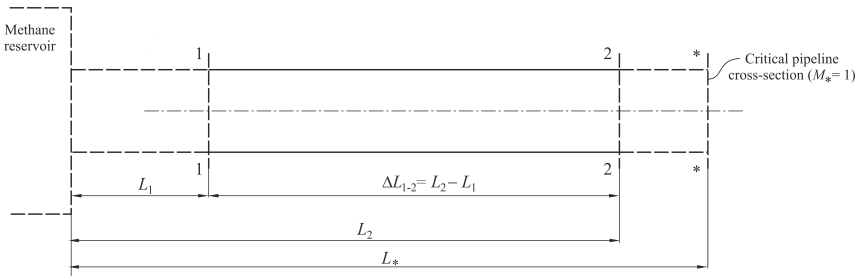


Figure 1: Fanno pipeline diagram with marked sections $L_1$, $L_2$, and $L_*$.

Because the values of the methane parameters in the outlet section of the pipeline section are close to ambient conditions, the density $\rho_2$ in this section is determined from the equation of the state of an ideal gas:

$$\rho_2 = \frac{p_2}{R T_2} = 1.139\ \frac{\mathrm{kg}}{\mathrm{m}^3}\,. \tag{2}$$

The velocity of methane in the outlet section of the pipeline is calculated from the flow continuity equation:

$$\dot{Q}_m = w_2 \rho_2 S_2\,, \tag{3}$$

where: $w_2$ – methane velocity in the outlet cross-section, $\rho_2$ – density of methane in the outlet cross-section, $S_2 = S$ – constant cross-sectional area of the pipeline.

According to the aforementioned values of the transported gas parameters and the pipeline dimensions, the value of the velocity and the Mach

number in the outlet section (2–2) will be determined:

$$S_2 = \frac{\pi D^2}{4} = 0.6362 \text{ m}^2,$$
$$w_2 = \frac{\dot{Q}_m}{\rho_2 S_2} = 250.9 \frac{\text{m}}{\text{s}}.$$

The following relation describes the Mach number at the outflow:

$$M_2 = \frac{w_2}{a_2}, \tag{4}$$

where $a_2 = \sqrt{\kappa R T_2}$ is the speed of sound in methane calculated for the parameters in the outlet section.

Assuming the methane temperature $T_2 = 288$ K in the outlet cross-section, the corresponding speed of sound will take the value $a_2 = 440.53$ m/s. After substituting the corresponding values into Eq. (4), is obtained

$$M_2 = 0.56954.$$

The coefficient of friction loss $\lambda = \lambda\left(\text{Re}, \frac{k}{D}\right)$ for methane flow in the pipeline is determined from the formula

$$\frac{1}{\sqrt{\lambda}} = -1.8 \log\left[\left(\frac{\frac{k}{D}}{3.7}\right)^{1.11} + \frac{6.9}{\text{Re}}\right], \quad 4000 \leq \text{Re} \leq 10^8. \tag{5}$$

Because of the significant value of the Reynolds number,

$$\text{Re} = \frac{\rho w D}{\eta} = \frac{\rho_2 w_2 D_2}{\eta_2} = 2.572 \cdot 10^7, \tag{6}$$

the Haaland formula will be used to determine the value of the friction loss coefficient. After substituting the appropriate values, this yields $\lambda = 0.01237$. The low $\lambda$ value is because the inside of the gas pipeline is coated with a special layer of high-smoothness material to minimise pressure losses caused by viscous friction.

The value of Mach number $M_1$ in the inlet section of the Baltic Pipe pipeline under consideration is calculated from the Fanno formula [13–15]:

$$\frac{1}{\kappa}\frac{(1 - M_1^2)}{M_1^2} + \frac{(\kappa + 1)}{2\kappa} \ln\left[\frac{\left(\frac{\kappa + 1}{2}\right) M_1^2}{1 + \left(\frac{\kappa - 1}{2}\right) M_1^2}\right] = \lambda \frac{(L_* - L_1)}{D}. \tag{7}$$

It is worth mentioning that the value of the Mach number $M_1$ is calculated by knowing the value of the parameter of the right-hand side of Eq. (7). To calculate the parameter $\lambda\dfrac{(L_* - L)}{D}$ the known value of the Mach number $M_2$ will be used. After substituting the value of $M_2$ into the Fanno formula, it will result in the following:

$$\frac{1}{\kappa}\frac{(1-M_2^2)}{M_2^2} + \frac{(\kappa+1)}{2\kappa}\ln\left[\frac{\left(\dfrac{\kappa+1}{2}\right)M_2^2}{1+\left(\dfrac{\kappa-1}{2}\right)M_2^2}\right] = \lambda\frac{(L_* - L_2)}{D}\,. \tag{8}$$

Figure 1 shows the segments $L_1$, $L_2$ and $L_*$ appearing in the formulae (7) and (8). It is seen from Fig. 1 that the difference in length of the pipeline sections $L_2 - L_1 = \Delta L_{1-2} \cong L$, which is equal to the length of the undersea section of the Baltic Pipe. This difference in the length of the pipeline sections will be used in the further calculations. After substituting into Eq. (8) values of Mach number $M_2 = 0.56954$ and isentropic exponent $\kappa = 1.30$, is obtained

$$0.6881 = \lambda\frac{(L_* - L_2)}{D}\,. \tag{9}$$

Assuming a constant value of the friction loss coefficient $\lambda$, with a constant diameter $D$ of the pipeline, the following will be written from Fig. 1:

$$\lambda\frac{\Delta L_{1-2}}{D} = \lambda\frac{(L_* - L_1)}{D} - \lambda\frac{(L_* - L_2)}{D}\,. \tag{10}$$

From Eq. (10) is obtained

$$\lambda\frac{(L_* - L_1)}{D} = \lambda\frac{\Delta L_{1-2}}{D} + \lambda\frac{(L_* - L_2)}{D}\,. \tag{11}$$

After the substitution of the corresponding parameter values in Eq. (11), the parameter of the right-hand side of Eq. (7) takes the value of

$$\lambda\frac{(L_* - L_1)}{D} = 3780.4103.$$

Having calculated the value of the parameter $\lambda\dfrac{(L_* - L_1)}{D}$ in Eq. (7) results in a non-linear algebraic equation from which the value of the Mach number $M_1$ is determined:

$$\frac{1}{1.3}\frac{(1-M_1^2)}{M_1^2} + \frac{(1.3+1)}{2\cdot 1.3}\ln\left[\frac{\left(\dfrac{\kappa+1}{2}\right)M_1^2}{1+\left(\dfrac{\kappa-1}{2}\right)M_1^2}\right] = 3780.4103. \tag{12}$$

The non-linear algebraic Eq. (12) was solved using Newton's method, considering the subsonic flow range in the pipeline section under consideration. The value of the determined Mach number is $M_1 = 0.01425$ ($r = 5 \cdot 10^{-5}$). According to the Fanno flow concept, the ratio of methane pressure in the inlet and outlet sections is determined from the formula [14, 15]

$$\frac{p_1}{p_2} = \frac{M_2}{M_1}\left[\frac{2+(\kappa-1)M_2^2}{2+(\kappa-1)M_1^2}\right]^{0.5}. \tag{13a}$$

After substituting the corresponding values in Eq. (13), the pressure ratio is calculated $\frac{p_1}{p_2} = 40.922$. Taking into account the assumed value of the outlet pressure $p_2 = 170$ kPa, the value of the methane pressure in the pipeline inlet section is calculated, which is $p_1 = 40.922 p_2 = 6956.742$ kPa.

Equation (13a) can also be written in the form

$$\frac{p_1}{p_2} = \frac{M_2}{M_1}\left(\frac{T_1}{T_2}\right)^{0.5}, \tag{13b}$$

from which the temperature of the methane in the inlet section of the pipeline is determined:

$$T_1 = \left(\frac{p_1}{p_2}\right)^2 \left(\frac{M_1}{M_2}\right)^2 T_2\,. \tag{14}$$

After substituting the relevant parameter values into Eq. (14), the value of the methane temperature in the inlet section is obtained and is $T_1 = 302$ K.

Due to the slight temperature difference of methane in the inlet and outlet sections of the pipeline, the value of the friction loss coefficient will remain constant. The methane velocity at the inlet cross-section is determined using a known value of the Mach number $M_1$:

$$M_1 = \frac{w_1}{a_1}\,. \tag{15}$$

where $a_1$ is the speed of sound in methane under thermodynamic conditions of the inlet section.

Speed of sound $a_1$ is determined from the known formula

$$a_1 = \sqrt{\kappa R T_1}\,. \tag{16}$$

By substituting the relevant parameter values into Eq. (16), the following result is obtained: $a_1 = 451.11$ m/s. The calculated speed of sound $a_1$ to

determine the methane velocity in the inlet section (1–1) (Fig. 1), i.e., $w_1 = a_1 M_1 = 6.43$ m/s.

Notably, the general dependence of the variation of gas velocity in individual sections of the Fanno tube is described by the relation [13,15]

$$\frac{w_2}{w_1} = \frac{M_2}{M_1}\left[\frac{2+(\kappa-1)M_1^2}{2+(\kappa-1)M_2^2}\right]^{0.5}. \tag{17}$$

To compare the results obtained with the Fanno model, corresponding calculations were additionally conducted with the isothermal flow model. Taking into account the model of isothermal flow in the pipeline under consideration, the Mach number in the inlet section was determined from the relation [14]

$$\lambda\frac{L}{D} = \frac{1}{\kappa}\frac{(1-M_1^2)}{M_1^2} + \ln\left(\kappa M_1^2\right). \tag{18}$$

Considering the calculated values of the friction loss coefficient $\lambda$ and the dimensions of the pipeline, the value of Mach number was obtained from relation (18) $M_1 = 0.1424847$ ($r = 6.5 \cdot 10^{-4}$).

The corresponding value of the Mach number $M_2$ in the outlet section for the isothermal flow model was determined from the formula

$$\lambda\frac{L}{D} = \lambda\frac{L}{D}\Big|_1 - \lambda\frac{L}{D}\Big|_2 = \frac{1}{\kappa}\frac{(1-M_1^2)}{M_1^2} - \frac{1}{\kappa}\frac{(1-M_2^2)}{M_2^2} + \ln\left(\frac{M_1}{M_2}\right)^2. \tag{19}$$

By substituting the relevant data, the Mach number value of the outlet section was obtained $M_2 = 0.87750$ ($r = 6.5 \cdot 10^{-4}$).

It is easy to see that the calculated values of the Mach number $M_2$ in the pipeline outlet section show a significant difference $\Delta M_2 = 0.87750 - 0.56954 = 0.30796$. It is worth mentioning that the methane flow under consideration in the pipeline is a subsonic flow for both the Fanno and the isothermal models.

The corresponding static pressure and flow velocity changes for the isothermal model were determined from the relationship [14]:

$$p_2 = p_1\frac{M_1}{M_2}, \tag{20}$$

$$w_2 = w_1\frac{M_1}{M_2}. \tag{21}$$

Due to the very similar values of the Mach number $M_1$ in the pipeline inlet cross-section, it was assumed that the static pressure in the inlet

cross-section is identical for both models considered. The calculations also considered that the temperature in the inlet section $T_1$ of the transported methane is similar for both models.

The Mach number, static pressure and velocity distribution along the pipeline determined from Eqs. (19)–(21) are shown as dashed lines in Figs. 2 to 4, respectively. Figures 2–4 have also shown the changes in the Mach number, static pressure and velocity of the flowing methane as a function of the Baltic Pipe pipeline length calculated from Eqs. (12), (13), and (17) – the Fanno model. It should be noted that the beginning of the pipeline is located on Danish territory, while the end is situated respectively on the Polish coast.

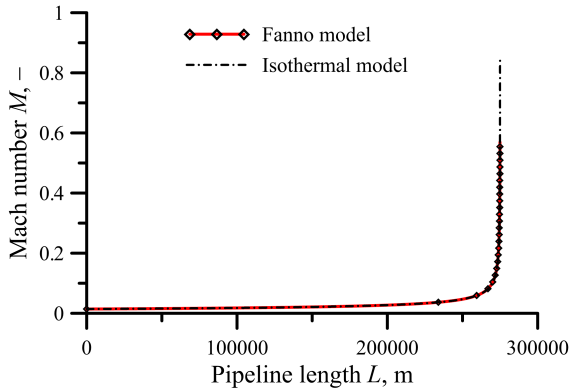


Figure 2: Change in Mach number value along the Baltic Pipe undersea section.

The significant changes in the Mach number values describing the methane flow in the final part of the pipeline, i.e. at the Polish coast, can be seen in Fig. 2. As can be seen, for most of the pipeline length, the methane flow has the features of incompressible flow.

It can be seen from Fig. 3 that the highest static pressure value is assumed in the flowing methane in the pipeline inlet section located in Denmark. At half the length of the pipeline, the pressure is about 30% lower than the corresponding pressure at the mentioned inlet cross-section. The static pressure value in the transported methane ($CH_4$) decreases by 50% at about 70 km from the outlet cross-section. Due to the decreasing value of the discussed pressure of flowing methane, the Baltic Pipe pipeline wall thickness could be considerably reduced over a large part of the pipeline.

Determined form Fanno model the corresponding changes in the flow velocity of the transported gas are shown in Fig. 4. The velocity of flow-

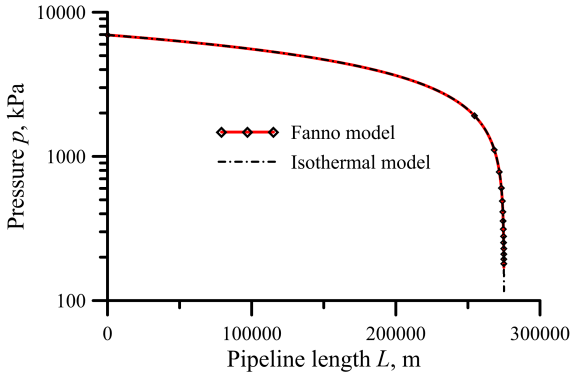


Figure 3: Change in static methane pressure along the Baltic Pipe undersea section.

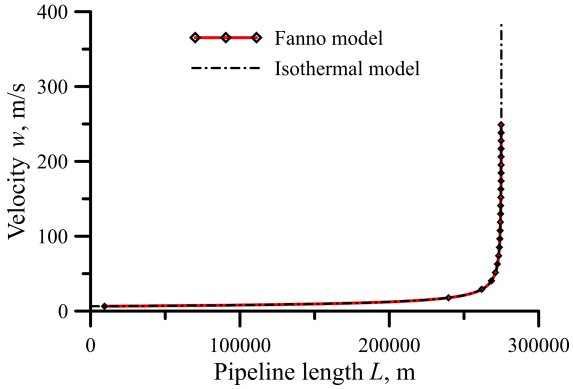


Figure 4: Change in methane velocity along the Baltic Pipe pipeline undersea section.

ing methane in the outlet section of the pipeline reaches the highest values. Approximately one kilometer before the outlet section, the transported methane ($CH_4$) velocity reaches $w = 100$ m/s. Evident compressibility of flowing methane ($M \geq 0.3$) is marked at the end of the pipeline, i.e. approximately 400 m upstream of the outlet cross-section.

Due to the unchanging temperature of the flowing gas in the isothermal model, the obtained values of the methane parameters in the outlet cross-section show significant differences compared to the corresponding results obtained in the adiabatic Fanno model. Because of the very small value of the Mach number calculated for the methane flow in the inlet section ($M_1 = 0.01425$), the considered Fanno flow, as well as isothermal flow features incompressible flow over a large part of the pipeline section.

In particular, it is only at a distance of approximately 400 m upstream of the pipeline outlet cross-section (Fig. 5) that the Mach number reaches a value of $M_3 = 0.3$. In the mentioned final section of the pipeline, there is an intensive expansion of the flowing methane, characterised mainly by the Mach number value in the outlet section $M_2 = 0.56594$.

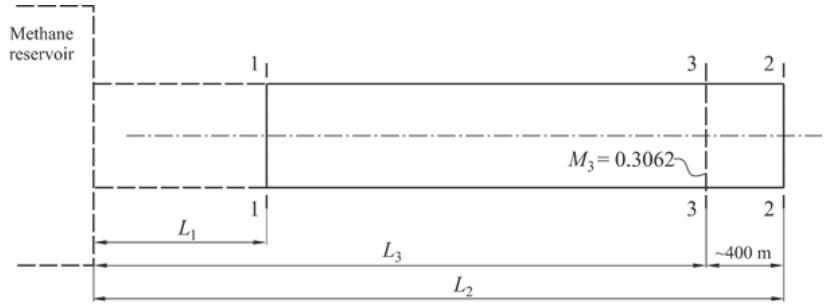


Figure 5: Diagram of section 3–3 location in Fanno flow.

The considered methane flow velocity in the subsea section of the Baltic Pipe increases continuously from a value of $w_1 = 6.43$ m/s in the inlet section to a value of $w_3 = 134.9$ m/s in the cross-section, where the Mach number is $M_3 = 0.3$ (Fig. 5), reaching a value of $w_2 = 250.90$ m/s in the outlet section.

The methane density in the pipeline's inlet section in Fanno model is described by the following formula [13, 15]:

$$\frac{\rho_1}{\rho_2} = \frac{M_2}{M_1}\left[\frac{2+(\kappa-1)M_1^2}{2+(\kappa-1)M_2^2}\right]^{0.5}. \tag{22}$$

Substitution of the Mach number and isentropic exponent values into Eq. (22) gives $\frac{\rho_1}{\rho_2} = 39.0247$ from which $\rho_1 = \rho_2 \cdot 39.0247 = 44.449$ kg/m$^3$.

Based on calculated from Fanno model values of the thermodynamic parameters of methane in the pipeline inlet section, the mass flow rate is determined:

$$\dot{Q}_m = \rho_1 w_1 S. \tag{23}$$

Taking into account the values of the individual quantities in Eq. (23) gives $\dot{Q}_m = 181.83$ kg/s.

By comparing the calculated value of the methane mass flow rate in the inlet section of the pipeline with the corresponding value in the outlet section, it can be said that a high leak tightness characterises the pipeline.

In the considered flow, furthermore, the differential stagnation pressures at the inlet and outlet sections, respectively, will be determined:

$$\Delta p_0 = p_{01} - p_{02}\,. \tag{24}$$

The individual stagnation pressures for the inlet and outlet sections are determined from the following equations [14, 15]:

$$\frac{p_{01}}{p_1} = \left(1 + \frac{\kappa - 1}{2} M_1^2\right)^{\frac{\kappa}{\kappa - 1}}, \tag{25}$$

$$\frac{p_2}{p_{02}} = \frac{1}{\left(1 + \frac{\kappa - 1}{2} M_2^2\right)^{\frac{\kappa}{\kappa - 1}}}. \tag{26}$$

After substitution data into Eqs. (25)–(26) it results in: $p_{01} = 6.598 \cdot 10^6$ Pa, $p_{02} = 208.856 \cdot 10^3$ Pa from which $\Delta p_0 = 6389$ kPa.

Considering that the Fanno flow is non-isentropic, the entropy gain between the outlet and inlet sections will be determined using the equation [15]

$$s_2 - s_1 = R \ln\left(\frac{p_{01}}{p_{02}}\right). \tag{27}$$

After the substitution of the calculated stagnation pressures, the entropy gain in the considered flow is $\Delta s = s_2 - s_1 = 1789.37$ J/(kg K).

The difference in stagnation pressure $\Delta p_0$ determines the approximate value of the excess pressure in the inlet cross-section needed to transport the assumed mass flow of methane in the pipeline under consideration.

## 3 Analysis of the calculation results obtained with the Fanno model

It is worth noting that the Fanno model equations are designed to describe the adiabatic flow of gas, considering internal friction in a flow pipe with a constant cross-sectional area. They are consistent with a flowing gas's mass, momentum and energy balance equations. However, it should be noted that the Fanno model equations include the equation of the state of an ideal gas. Thus, the Fanno model equations can be used without limitations to describe the motion of gases whose thermodynamic parameters ($p$, $T$) differ little from the corresponding ambient parameters.

In the case of the calculation results obtained in this work, especially in the pipeline inlet section, the differences in the mentioned parameters are considerable. It is easy to see that the calculated pressure in the pipeline inlet section is $p_1 = 6.957$ MPa, which is about 40.9 times higher than the corresponding pressure in the outlet section. From the ideal gas equation of state, the density of flowing methane in the inlet section is $\rho_1 = 44.449$ kg/m$^3$.

To validate the obtained calculation results, the equation of state of the real gas written in the form of the Redlich-Kwong equation was used [17,18]:

$$p = \frac{RT}{v-b} - \frac{a}{T^{0.5}v(v+b)}\,, \tag{28}$$

where $a = \dfrac{0.42748R^2T_c^{2.5}}{p_c}$ and $b = \dfrac{0.08664RT_c}{p_c}$ are constants in the Redlich-Kwong real gas state equation, $p_c$ and $T_c$ are the critical pressure and temperature for gas, $v = 1/\rho$ is specific volume.

In the case of methane, the critical pressure and temperature are $p_c = 45.992{\cdot}10^5$ Pa and $T_c = 190.6$ K [17,18]. After substituting into Eq. (28) the values of the relevant parameters, i.e., $R = 518.33$ J/(kgK), $T_1 = 302$ K, $v_1 = 1/\rho_1 = 0.022498$ m$^3$/kg, the corresponding pressure value was calculated $p_1^{(r)} = 6270244$ Pa $\approx 6.27$ MPa. It is easy to see that the relative deviation of the results obtained does not exceed 10%. The Redlich-Kwong equation was tested in this work using tabulated values of methane thermodynamic parameters $p_a = 6$ MPa, $v_a = 0.02343$ m$^3$/kg, and $p_b = 8$ MPa, $v_b = 0.01706$ m$^3$/kg [18]. The respective relative deviations of the results obtained were: for data with subscript $(a)$ $\delta_{R-K} = 0.2\%$ and $(b)$ $\delta_{R-K} = 0.1\%$.

Apart from the aforementioned test of the Redlich-Kwong model, an additional corresponding examination of the Lee-Kesler model was carried out in this study. The general form of the equation describing the Lee-Kesler model is of the form [12]

$$Z = \left(\frac{p_r v_r}{T_r}\right) = 1 + \frac{B}{v_r} + \frac{C}{v_r^2} + \frac{D}{v_r^5} + \frac{c_4}{T_r^3 v_r^2}\left(\beta + \frac{\gamma}{v_r^2}\right)\exp\left(-\frac{\gamma}{v_r^2}\right). \tag{29}$$

Coefficients of Lee-Kesler equation of state are given as

$$B = b_1 - \frac{b_2}{T_r} - \frac{b_3}{T_r^2} - \frac{b_4}{T_r^3}\,, \quad C = c_1 - \frac{c_2}{T_r} - \frac{c_3}{T_r^3}\,, \quad D = d_1 - \frac{d_2}{T_r}\,,$$

$$p_r = \frac{p}{p_c}, \quad T_r = \frac{T}{T_c}, \quad v_r = \frac{vp_c}{RT_c},$$

where constants $b_1$, $b_2$, $b_3$, $b_4$, $c_1$, $c_2$, $c_3$, $c_4$, $d_1$, $d_2$, $\beta$, $\gamma$ are the constants of the Lee-Kesler model, whose numerical values were taken from [12].

The corresponding relative deviations for the Lee-Kesler model were obtained by performing similar calculations as for the Redlich-Kwong model: for data with subscript $(a)$ $\delta_{L-K} = 1.63\%$ and $(b)$ $\delta_{L-K} = 2.74\%$. As the calculated relative deviations of the analysed results for the Redlich-Kwong model are smaller than the corresponding deviations obtained for the Lee-Kesler model, the real gas model described by Eq. (28) was used for further calculations.

The methane flow considered in the Baltic Pipe pipeline is a single-phase flow of a medium exhibiting the characteristics of superheated steam. Therefore, changes in the coefficients describing the specific heat $c_p$ and $c_v$ for methane are negligibly small in the considered flow case. Analysing the change in specific heat at constant pressure $c_p$ for methane in the temperature range 275 K to 310 K and pressure of 8 MPa, the relative difference in values is in the range 7% [17, 18].

Since the velocity of methane in the inlet section $v_1$ was determined using the calculated Mach number $M_1$, the speed of sound in methane, $a_1$ was also determined by the equation

$$a_1 = \sqrt{\kappa \left[ \frac{RT_1}{(1 - b\rho_1)^2} - \frac{a}{T_1^{0.5}} \frac{\rho_1 (2 + b\rho_1)}{(1 + b\rho_1)^2} \right]}. \tag{30}$$

Equation (30) is derived from Eq. (28), in which the inverse of density replaces specific volume ($v_1 = 1/\rho_1$). In particular, Eq. (30) was achieved after determining the partial derivative from pressure after density at a constant temperature [15]. After substituting the values for the quantities appearing in Eq. (30), the $a_1^{(r)} = 409.72$ m/s was obtained.

Using the previously calculated value of the Mach number in the inlet section $M_1 = 0.014251$, the corresponding methane velocity under real gas conditions is $w_1^{(r)} = M_1 a_1^{(r)} = 5.84$ m/s.

Calculated velocity $w_1^{(r)} = 5.84$ m/s is less than the corresponding velocity calculated for the ideal gas model ($w_1 = 6.43$ m/s).

From the analysis of the calculation results obtained with the Fanno model and the related results obtained with the real gas model, it can be concluded that they differ slightly. It also appears that the deviations noted cannot pose a threat to the correct operation of the pipeline.

# 4 Conclusions

According to the calculations, it can be concluded that the isothermal model shows greater simplicity compared to the adiabatic Fanno model. However, the adiabatic Fanno model allows for more precise results describing the transported gas in the pipeline under consideration.

Based on the above, the Fanno flow model equations were used to calculate the thermodynamic parameters of methane in the subsea section of the Baltic Pipe pipeline. It is worth remarking that the Fanno model equations are valid for adiabatic flow involving viscous friction of the gas. It can also be stated that the methane flow in the Baltic Pipe pipeline with a multilayer wall of thickness $g = 87.5{-}137.5$ mm, located on the seabed, meets the conditions for adiabatic flow. The calculations indicate that the temperature of the transported gas varies between $T_1 = 302$ K and $T_2 = 288$ K.

Based on the carried out calculations, the respective values of the pressure ratios in the corresponding pipeline cross-sections were also determined, i.e., ratio of inlet and outlet pressure $p_1/p_2 = 40.925$, and ratio of pressure the inlet and approximately 400 m from the pipeline outlet $p_1/p_3 = 21.192$.

The pressure values in the corresponding pipeline cross-sections can be estimated from the quoted pressure ratios. For the outlet pressure $p_2 = 170$ kPa, the pressure in the inlet section is $p_1 = 6.957$ MPa, and the corresponding pressure in the pipeline section where the Mach number reaches $M_3 = 0.3$ takes the value $p_3 = 328.277$ kPa. It can be found that the value of pressure $p_3$ is only about twice the outlet section pressure $p_2$. A good agreement can be found by comparing the obtained results of calculating the pressure of methane transported in the pipeline inlet section with the corresponding working pressure values given by the Baltic Pipe pipeline operator.

The calculated difference in stagnation pressures determined for the inlet and outlet sections is $\Delta p_0 = 6389$ kPa. The calculated values of the stagnation pressures were also used to calculate the total entropy increase in the methane flow under analysis, and it is $\Delta = 1789.37$ J/(kgK).

*Received 20 October 2023*

# References

[1] Molenda J.: *Natural Gas. Fuel and Feedstock* (3rd Edn.). WNT, Warszawa 1996 (in Polish).

[2] Kidnay A.J., Parrish W.R., McCartney D.G.: *Fundamentals of Natural Gas Processing* (3rd Edn.). CRC, Boca Raton 2020.

[3] Koo B.: *A novel implicit method of characteristics using pressure-referenced correction for transient flow in natural gas pipelines*. J. Nat. Gas Sci. Eng. **104**(2022), 104665. doi: 10.1016/j.jngse.2022.104665

[4] Zhang K., Chen S., Gong Y., Ning D., Zhang Z.: *Method to simulate transient pressure behaviours in subsea natural gas pipelines with a moving smart isolation device*. Eng. Fail. Anal. **144**(2023), 106985. doi: 10.1016/j.engfailanal.2022.106985

[5] Glot I., Shardakov I., Shestakov A., Tsvetkov R.: *Analysis of wave processes in an underground gas pipeline (mathematical model and field experiment)*. Eng. Fail. Anal. **128**(2021), 105571. doi: 10.1016/j.engfailanal.2022.105571

[6] Koo B.: *Comparison of finite-volume method and method of characteristics for simulating transient flow in natural-gas pipeline*. J. Nat. Gas Sci. Eng. **98**(2022), 104374. doi: 10.1016/j.jngse.2021.104374

[7] Zhou D., Jia X., Ma S., Shao T., Huang D., Hao J., Li, T.: *Dynamic simulation of natural gas pipeline network based on interpretable machine learning model*. Energy **253**(2022), 124068. doi: 10.1016/j.energy.2022.124068

[8] Witek M., Uilhoorn F.: *Impact of hydrogen blended natural gas on linepack energy for existing high pressure pipelines*. Arch. Thermodyn. **43**(2022), 3, 111–124. doi: 10.24425/ather.2022.143174

[9] Szczygieł I., Rutczyk B.P.: *Theoretical analysis of LNG regasifier supplementing gas turbine cycle*. Arch. Thermodyn. **42**(2021), 4, 47–67. doi: 10.24425/ather.2021.139650

[10] Wieczorek A.: *Analysis of selected aspects of a tank gassing-up process on board liquefied petroleum gas carrier. Part I*. Arch. Thermodyn. **42**(2021), 2, 43–58. doi: 10.24425/ather.2021.137552

[11] Wieczorek A.: *Analysis of selected aspects of a tank gassing-up process on board liquefied petroleum gas carrier. Part II*. Arch. Thermodyn. **42**(2021), 2, 59–69. doi: 10.24425/ather.2021.137553

[12] Trawiński P.: *Development of real gas model operating in gas turbine system in Python programming environment*. Arch. Thermodyn. **41**(2020), 4, 23–61. doi: 10.24425/ather.2020.135853

[13] Balachanoran P.: *Fundamentals of Compressible Fluid Dynamics*. PHI Leating, New Delhi 2009.

[14] Bar-Meir G.: *Fundamentals of Compressible Fluid Mechanics* (Version 0.4.8.6). Potto Project, 2004. https://www.potto.org/downloads.php. doi: 10.5281/zenodo.5521908 (accessed 23 Dec. 2009).

[15] Rup K.: *Isentropic and Non-Isentropic Gas Flows*. PWN, Warszawa 2013 (in Polish).

[16] Baltic Pipe Project. https://www.baltic-pipe.eu/ (accessed 17 Jan. 2023).

[17] Sonntag R.S., Borngnakke C.: *Fundamentals of Thermodynamics* (10th Edn.). Willey, Hoboken 2019.

[18] Friend D.G., Ely J.F., Ingham H.: *Tables for the Thermophysical Properties of Methane*. NIST Technical Note 1325, National Institute of Standard and Technology, Boulder 1989.

**archives**
**of thermodynamics**
Vol. **44**(2023), No. 4, 653–664
DOI: 10.24425/ather.2023.149713

# Computational analysis of electric field effects on electrodialysis for enhanced desalination processes

**ROBERT MATYSKO***
**TOMASZ OCHRYMIUK**

Institute of Fluid Flow Machinery, Polish Academy of Sciences,
Fiszera 14, 80-231 Gdańsk, Poland

**Abstract** This study elucidates the technologies employed in membrane-based water purification processes. The theoretical underpinnings of semi-permeable membrane functionalities are expounded upon through the lens of Onsager's reciprocal relations in non-equilibrium thermodynamics, delineating the fluxes and the driving forces that instigate them. Utilising a simplified Onsager matrix tailored for the ion-exchange membrane electrodialysis process, computational fluid dynamics (CFD) simulations were conducted. The computations presented herein depict the intricacies of both dialysis and electrodialysis in saline water solutions.

**Keywords:** Membranes; CFD; Electrodialysis; Onsager relations

## 1 Introduction

Desalination constitutes the technologically-mediated extraction of saline and mineral constituents from marine or brackish water sources, rendering the resultant fluid suitable for potable or industrial applications. A myriad of desalination technologies are extant [1]:

1. Reverse Osmosis (RO): Predominantly, this modality stands as the epitome of energy-efficient desalination, particularly when meticu-

*Corresponding Author. Email: matyskor@imp.gda.pl

lously optimised and deployed in locales with constrained freshwater availability.

2. Electrodialysis (ED): This technique excels in the treatment of low-salinity aqueous solutions and may surpass distillation in energy efficiency, albeit falling short in efficiency compared to RO for high-salinity matrices.

3. Heat Pump-Assisted Vacuum Distillation: The incorporation of a heat pump substantially augments the thermodynamic efficiency of the distillation process.

4. Multi-Stage Flash Distillation (MSF).

5. Cryogenic Desalination.

Cutting-edge membrane technologies, distinguished for their energy efficiency, are increasingly prevalent in the domains of fluid filtration and purification [2, 3]. These technologies employ a gamut of physical mechanisms to facilitate the membrane transport of particulates. Inherent and passive transport modalities are governed by osmotic pressure interactions (osmosis) and solute concentration gradients (dialysis). Moreover, externally applied active forces, such as mechanical pressure and electrostatic fields, can also instigate membrane particulate transport.

Osmosis, Reverse Osmosis (RO), Electrodialysis, and Dialysis are distinct membrane-mediated processes, each with unique operational principles and applications, despite their apparent similarities [2]:

- Osmosis is a spontaneous phenomenon where a solvent, predominantly water, traverses a semi-permeable membrane towards a region of higher solute concentration, aiming to achieve osmotic pressure equilibrium. This process is fundamental in various biological systems, including plant water uptake and cellular activities.

- Dialysis facilitates the selective permeation of dissolved substances through a membrane based on molecular size and electrostatic charge. This technique is pivotal in medical applications, notably in renal dialysis, where it substitutes for impaired kidney functions.

- Electrodialysis employs ion-exchange membranes to segregate ions and dissolved substances, leveraging their intrinsic electric charges.

An applied electric current facilitates ion migration across the membrane, making it instrumental in various industrial applications, including water desalination and chemical separation.

- Reverse Osmosis (RO) is an engineered process that employs external pressure to propel a solvent through a semi-permeable membrane, counter to the direction dictated by natural osmotic pressure. RO is extensively utilized in desalination technologies and potable water recovery from lower-salinity sources.

At present, membrane technologies are utilized in thermal energy applications for the preparation of fuels and also in the domain of oxidizer purification and separation [4]. Additionally, membranes are deployed in the purification of combustion by-products and in carbon dioxide capture processes [5].

## 2 Mathematical model of membrane processes in a thermodynamic framework

Membrane processes are described by mass, momentum, and energy balance equations. Additional relationships, such as Maxwell's equations or chemical reactions, may serve as supplements to the fundamental equations used in describing issues related to transport through membranes. Below are the general equations describing transport through a membrane, which can then be further specified depending on the transport process being modelled. In the dialysis process, the governing equations are those of mass, momentum, and energy balance, as presented below [3,6,7].

Mass balance equation:

$$\frac{\partial \rho}{\partial t} + \nabla \cdot (\rho \mathbf{v}) = 0, \tag{1}$$

where: $\rho$ – density, $\mathbf{v}$ – velocity, $t$ – time.

Momentum balance equation:

$$\rho \left( \frac{\partial \mathbf{v}}{\partial t} + (\mathbf{v} \cdot \nabla) \mathbf{v} \right) = -\nabla P + \rho g + \nabla \cdot \mathbf{T} + \rho \mathbf{F}_{\text{elmag}} , \tag{2}$$

where: $P$ – pressure, $g$ – gravity vector, $\mathbf{T}$ – shear stress tensor, $\mathbf{F}_{\text{elmag}}$ – electromagnetic force.

Energy balance equation:

$$\rho c\left(\frac{\partial T}{\partial t}+(\mathbf{v}\cdot\nabla)\,\mathbf{T}\right)=-\mathbf{P}\nabla\cdot\mathbf{v}+\nabla\cdot(k\nabla T)+Q_{\text{heat}}+Q_{\text{elmag}}\,, \tag{3}$$

where: $T$ – fluid temperature, $c$ – heat capacity of the fluid, $k$ – thermal conductivity of the fluid, $Q_{\text{heat}}$ – heat flux originating from chemical reactions or other processes, $Q_{\text{elmag}}$ – heat flux introduced due to electromagnetic field interactions.

To model membrane processes in an electromagnetic field environment, Maxwell's equations are introduced [8].

Gauss's law for electric field:

$$\nabla\cdot E=\frac{\rho_e}{\varepsilon_o}\,, \tag{4}$$

Gauss's law for magnetic field:

$$\nabla\cdot B=0\,, \tag{5}$$

Faraday's law of electromagnetic induction:

$$\nabla\times E=-\frac{\partial E}{dt}\,, \tag{6}$$

Ampère's law with conductance:

$$\nabla\times B=\mu_0 J+\mu_0\varepsilon_o\frac{\partial E}{dt}\,, \tag{7}$$

where: $E$ – electric field, $B$ – magnetic field, $\rho_e$ – electric charge density, $J$ – electric current density, $\varepsilon_o$ – electric permittivity in vacuum, $\mu_0$ – magnetic permeability in vacuum, $t$ – time, $\nabla\cdot$– divergence, $\nabla\times$ – curl.

For the above equations, the general Onsager relations (Fourth Law of Thermodynamics) can be written in matrix form, describing non-equilibrium phenomena occurring in membrane systems interacting with an electromagnetic field [6,7,9,10]:

$$\begin{bmatrix}J_v\\J_m\\J_C\\J_q\\J_e\\J_b\end{bmatrix}=\begin{bmatrix}L_{11}&L_{12}&L_{13}&L_{14}&L_{15}&L_{16}\\L_{21}&L_{22}&L_{23}&L_{24}&L_{25}&L_{26}\\L_{31}&L_{32}&L_{33}&L_{34}&L_{35}&L_{36}\\L_{41}&L_{42}&L_{43}&L_{44}&L_{45}&L_{46}\\L_{51}&L_{52}&L_{53}&L_{54}&L_{55}&L_{56}\\L_{61}&L_{62}&L_{63}&L_{64}&L_{65}&L_{66}\end{bmatrix}\begin{bmatrix}-\nabla P_m\\-\nabla P_o\\-\nabla C\\-\nabla T\\-\nabla E\\-\nabla B\end{bmatrix}, \tag{8}$$

where: $J_v$ – volumetric flux induced by the mechanical pressure gradient $-\nabla P_m$, $J_m$ – volumetric flux induced by the osmotic pressure gradient $-\nabla P_o$, $J_C$ – volumetric flux induced by the concentration gradient $\nabla C$, $J_q$ – heat flux induced by the temperature gradient $\nabla T$, $J_e$ – electric charge flux induced by the electric field gradient $\nabla E$, $J_b$ – magnetic flux induced by the magnetic field gradient $-\nabla B$.

In the electrodialysis process, it is assumed that only the concentration gradient and the electric field are present, serving as stimuli for ion flow through the membrane system. The general Onsager matrix simplifies to a two-dimensional matrix due to these two stimuli:

$$\begin{bmatrix} J_C \\ J_e \end{bmatrix} = \begin{bmatrix} L_{11} & L_{12} \\ L_{21} & L_{22} \end{bmatrix} \begin{bmatrix} -\nabla C \\ -\nabla E \end{bmatrix}. \tag{9}$$

The individual flux equations are represented as:

$$J_C = \frac{dC}{dt} \quad \text{and} \quad J_e = \frac{dq}{dt}\,, \tag{10}$$

$$\begin{cases} \dfrac{dC}{dt} = -L_{11}\nabla C - L_{12}\nabla E\,, \\ \dfrac{dq}{dt} = -L_{21}\nabla C - L_{22}\nabla E\,. \end{cases} \tag{11}$$

For each $i$-th component of the fluid, the equations can be written as:

$$\frac{dC_i}{dt} = D_i \nabla C_i + F C_i z_i u_{m,i} \nabla E, \tag{12}$$

$$\frac{dq}{dt} = I = F \sum_i \left( -F C_i z_i^2 u_{m,i} \right) \nabla E, \tag{13}$$

$$I = -k \nabla E. \tag{14}$$

The Onsager matrix coefficients are (assuming that the cross-effect of concentration on electric current is neglected $L_{21} = 0$)

$$L_{11} = D_i\,, \tag{15}$$

$$L_{12} = F C_i z_i u_{m,i}\,, \tag{16}$$

$$L_{22} = k = F \sum_i \left( -F C_i z_i^2 u_{m,i} \right). \tag{17}$$

## 3 Computational fluid dynamics calculations of the electrodialysis process for saline water

Computational fluid dynamics (CFD) calculations were performed assuming three computational domains, with the fluids bordering a membrane on which electrodes were placed to induce salt ion transport. The assumptions are as follows [2]:

- For the dialysate and permeate in the steady state, the equation includes convective, diffusive, and migration terms influenced by the electric field:

$$\nabla \cdot \left(-D_i \nabla C_i - F C_i z_i^2 u_{m,i} \nabla E\right) + \mathbf{u} \cdot \nabla C_i = 0. \tag{18}$$

- For the membrane in the steady state, the equation includes diffusive and migration terms influenced by the electric field:

$$\nabla \cdot \left(-D_i \nabla C_i - F C_i z_i^2 u_{m,i} \nabla E\right) = 0. \tag{19}$$

The electric field interacts only within the membrane area due to the placement of electrodes at the membrane boundaries. The equation describing the electric field in the steady state is [2]:

$$\nabla \cdot (\varepsilon_0 \varepsilon_r \nabla E) = 0. \tag{20}$$

On both boundary conditions for the electric field, it is assumed that $E = V$, which is consistent with the notations in Fig. 1. The following assumptions were made: $D_i = 10^{-9}\ \mathrm{m}^2/\mathrm{s}$ for both the fluid and membrane regions, relative electrical permittivity for water $\varepsilon_r = 80$, moblility $u_{m,i} = 0.000001\ \mathrm{s\,mol/kg}$, charge number $z_i = 10\ \mathrm{l}$, and $F$ is Faraday's constant.

Discontinuities at the phase boundary between the membrane and the fluid are described by the following relations [2]:

- Between the dialysate and the membrane:

$$\left(-D_d \nabla C_1 - F C_1 z_i^2 u_{m,i} \nabla E + C_1 \mathbf{u}\right) \cdot \mathbf{n} = M\left(C_2 - K C_1\right), \tag{21}$$

$$\left(-D_m \nabla C_2 - F C_2 z_i^2 u_{m,i} \nabla E\right) \cdot \mathbf{n} = M\left(K C_1 - C_2\right). \tag{22}$$

- Between the membrane and the permeate:

$$\left(-D_m \nabla C_2 - F C_2 z_i^2 u_{m,i} \nabla E\right) \cdot \mathbf{n} = M\left(K C_3 - C_2\right), \tag{23}$$

$$\left(-D_p \nabla C_3 - F C_3 z_i^2 u_{m,i} \nabla E + C_3 \mathbf{u}\right) \cdot \mathbf{n} = M\left(C_2 - K C_3\right), \tag{24}$$

where $K = 0.7$ and $M = 1e^4\ \mathrm{m/s}$.

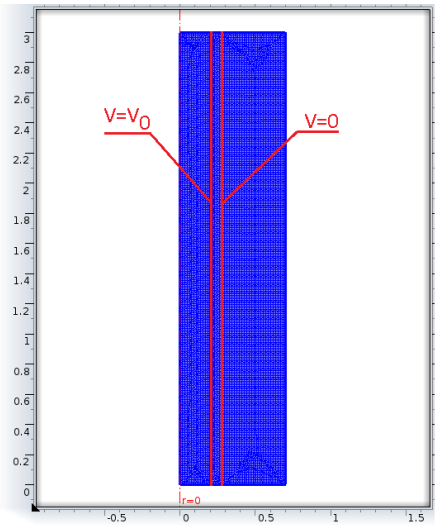


Figure 1: Geometry of the membrane system and boundary conditions for the electric field.

The meshing parameters (Fig. 1) for this process include several key settings. Firstly, the "Maximum Element Growth Rate" is set to 1.3, limiting the allowed increase in mesh element size from one region to another. A higher value would permit more significant size variation. Secondly, the "Resolution of Curvature" is established at 0.3, indicating a finer mesh resolution around curved features for improved accuracy. In contrast, the "Resolution of Narrow Regions" is set to 2, specifying a moderate level of refinement for tight geometry areas. Additionally, a "Minimum Element Size" of 0.0009 is enforced to prevent excessively small elements. Finally, the chosen mesh generation method is the "Free Triangular Delaunay", which employs Delaunay triangulation to create high-quality triangular elements without predefined shapes, ensuring flexibility in mesh generation. These parameters collectively govern the mesh quality and adaptability to meet specific modelling and simulation requirements.

The solver employed for solving the electrostatic equations is MUMPS (Multifrontal Massively Parallel Sparse direct Solver) [11], which is known for its efficiency in handling sparse linear systems in parallel computing environments. In contrast, the PARDISO [11] solver is utilized for solving equations related to diluted species, providing a specialized approach for this type of problem.

For the stationary electrostatic equations, the solver configuration is set to "Automatic linearity", meaning that the solver will automatically determine whether the problem is linear or nonlinear. A relative tolerance of 0.001 is specified, indicating the acceptable level of solution accuracy. The system being solved for the electrostatic equations involves a substantial number of degrees of freedom, with a total of 26,883 deg of freedom considered.

On the other hand, when dealing with diluted species, the solver handles a system with a different scale, involving a more modest number of degrees of freedom. Specifically, for the diluted species problem, there are 7,116 deg of freedom that the solver takes into account. These solver configurations and degree of freedom specifications are tailored to address the distinct characteristics and requirements of the electrostatic and diluted species problems, ensuring effective and accurate solutions for each.

Below are the calculations for concentration distribution obtained from the presented model. The calculations were performed assuming that the dialysate at the inlet has a concentration of $C_{d,\mathrm{in}} = 1$ mol/l. The figure illustrates the concentration equilibration along the dialysis path, resulting from convective movements and ion transport due to concentration differences. The electrodialysis modelling results for a system where the electric field is turned off are presented in Fig. 2.

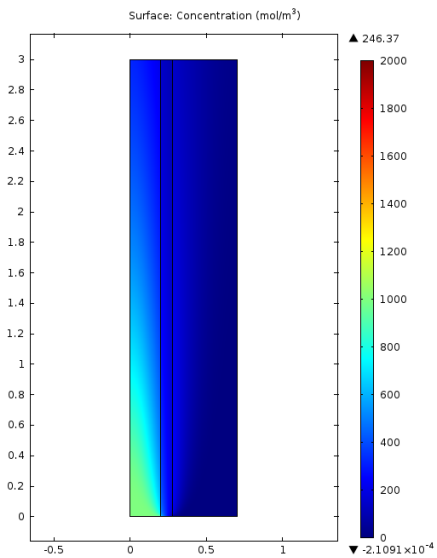


Figure 2: Calculation results for concentrations in the dialysis process.

Figures 3 and 4 present the modelling results of the electrodialysis process when the electric field is activated (Fig. 4). Electrodes generating the

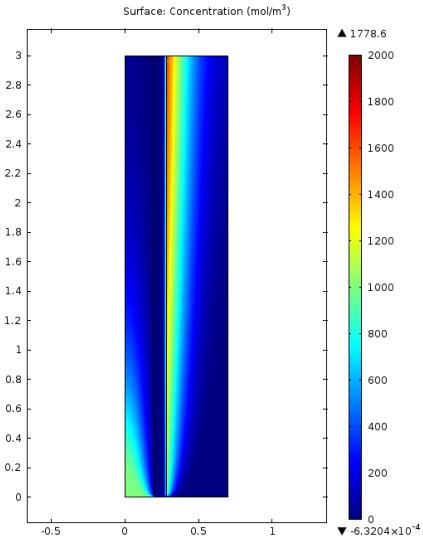


Figure 3: Calculations of transport intensification through the membrane due to the applied electric field.

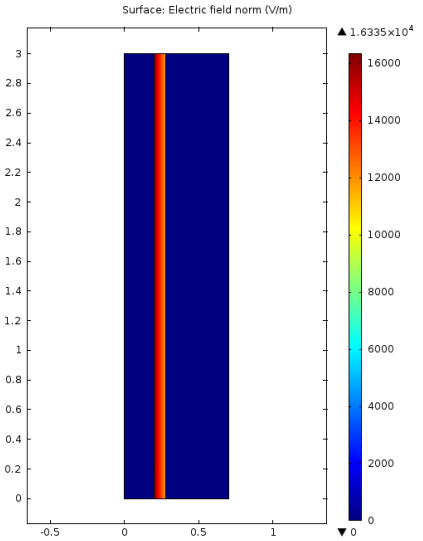


Figure 4: Electric field resulting from the interaction of electrodes placed at the membrane boundaries.

electric field are placed at the membrane boundaries, intensifying the salt ion transport into the permeate space (Fig. 3).

The results presented in Figs. 3 and 4 illustrate the impact of the electric field on the process of salt ion transport through the membrane. The influence of the electric field operating within the membrane region enhances mass exchange. Reduced salt solution concentrations in water are observed at the dialysate-membrane phase boundary. Additionally, an increase in concentration is evident in the solid-liquid phase boundary region at the membrane-permeate interface. Comparing the calculation results (Fig. 5), it is clear that the effluent (purified) liquid exhibits significantly lower salt concentrations in the presence of an electric field.

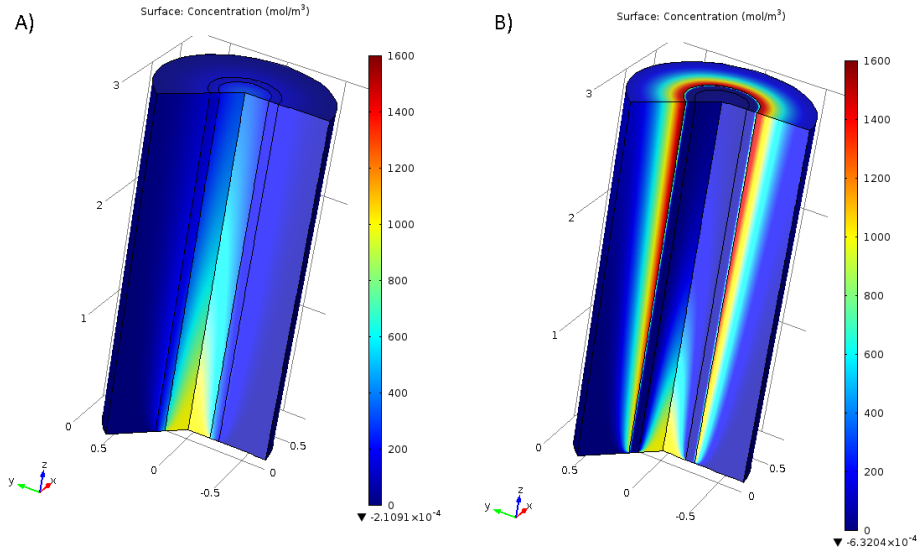


Figure 5: Calculation results in 3D geometry for the dialysis (A) and electrodialysis (B) membrane system.

## 4 Summary

This study focuses on modelling the impact of an electric field in the electrodialysis process, aiming to intensify desalination procedures. The paper presents:

1. Description of membrane technologies: Various desalination technologies such as reverse osmosis, electrodialysis, vacuum distillation with

a heat pump, multi-stage distillation, and cryogenic desalination are discussed. It is pointed out that membrane technologies are currently the most energy-efficient in the field of fluid filtration and purification.

2. Theoretical foundations of membrane operations: Differences between osmosis, dialysis, electrodialysis, and reverse osmosis are presented. Attention is drawn to particle transport mechanisms through the membrane, such as osmotic pressure, concentration differences, and active interactions.

3. Mathematical model of membrane processes: Membrane processes are described in the context of mass, momentum, and energy balance equations. Maxwell's equations, which describe electromagnetic interactions in membrane systems, are introduced. Onsager's relations, describing non-equilibrium issues in membrane systems under the influence of an electromagnetic field, are also presented.

4. CFD calculations of electrodialysis in saline water: Modeling results of electrodialysis in the absence and presence of an electric field are presented. The results show that the electric field intensifies the transport of salt ions through the membrane, leading to more efficient desalination.

The study proves that the electric field can significantly impact the efficiency of the electrodialysis process, which is crucial for the industry of water purification and seawater desalination.

*Received 5 October 2023*

## References

[1] Lewicki P.P.: *Process Engineering and Equipment for the Food Industry.* WNT, Warszawa 2005 (in Polish).

[2] Mulder M.: *Basic Principles of Membrane Technology.* Kluwer, 1996.

[3] Bird R.B., Stewart W.E., Lightfoot E.N.: *Transport Phenomena.* Wiley, 2002.

[4] Berdowska S., Skorek-Osikowska A.: *Technology of oxygen production in the membrane cryogenic air separation system for a 600 MW.* Arch. Thermodyn. **33**(2012), 3, 65–76. doi: 10.2478/v10173-012-0018-8

[5] Kotowicz J., Skorek-Osikowska A., Janusz-Szymanska K.: *Membrane separation of carbon dioxide in the integrated gasification combined cycle systems.* Arch. Thermodyn. **31**(2010), 3, 145–164. doi: 10.2478/v10173-010-0020-y

[6] Ceynowa J.: *An Outline of Non-equilibrium Linear Thermodynamics of Continuous and Membrane Systems*. UMK, Toruń 1997 (in Polish).

[7] Wiśniewski S., Staniszewski B., Szymanik R.: *Thermodynamics of Non-equilibrium Processes*. PWN, Warszawa 1973 (in Polish).

[8] Maxwell J.C.: *A Treatise on Electricity and Magnetism*. Clarendon, Oxford 1873.

[9] Onsager L.: *Reciprocal relations in irreversible processes. I.* Phys. Rev. **37**(1931), 405–426.

[10] Onsager L.: *Reciprocal relations in irreversible processes. II.* Phys. Rev. **38**(1931), 2265–2279.

[11] www.comsol.com

**archives**
**of thermodynamics**
Vol. **44**(2023), No. 4, 665–704
DOI: 10.24425/ather.2023.149737

# Overview of application options for vertical axis wind turbines

**WALDEMAR KUCZYŃSKI**[a*]
**IWONA MICHALSKA-POŻOGA**[b]
**MARCIN SZCZEPANEK**[c]
**KRZYSZTOF CHMIEL**

[a] Technical University of Koszalin, Faculty of Mechanical Engineering and Energy, Department of Energy, Racławicka 15-17, 75-620 Koszalin, Poland

[b] Technical University of Koszalin, Faculty of Mechanical Engineering and Energy, Department of Food Processes and Equipment, Racławicka 15-17, 75-620 Koszalin, Poland

[c] Maritime University of Technology of Szczecin, Faculty of Mechanical Engineering, Willowa 2, 75-500 Szczecin, Poland

**Abstract** The article presents an analysis of the use of Savonius wind turbines with vertical axis of rotation. The first part presents an analysis of the literature with the dentification of the properties of the basic atmospheric parameters related to the air movement referred to as wind. Used mathematical descriptions used in the analysis of air movement and enabling the identification of basic thermodynamic parameters of wind turbines with a vertical axis of rotation were presented. Then, the historical background of the development of wind turbines with a vertical axis of rotation was presented, and constructions of this type currently used were described. Proposals for modification of the configuration and design of Savonius rotors and the impact of these activities on their efficiency were analyzed. These issues were presented in relation to the experimental work carried out in the international research centers. Obvious advantages and disadvantages of using this type of equipment in the field of wind energy were indicated.

**Keywords:** Wind energy; Wind turbines; Savonius' law

*Corresponding Author. Email: waldemar.kuczynski@tu.koszalin.pl

### Nomenclature

| | | |
|---|---|---|
| $C_D$ | – | drag coefficient |
| $c_p$ | – | Betz coefficient |
| $P$ | – | mechanical power, W |
| Re | – | Reynolds number |
| $T$, $t$ | – | temperature, K, °C, respectively |
| VAWT | – | vertical axis wind turbine |
| $\mathbf{v}$ | – | air speed, m/s |

**Greek symbols**

| | | |
|---|---|---|
| $\mu$ | – | dynamic viscosity, Pa·s |
| $\nu$ | – | kinematic viscosity, $m^2/s$ |
| $\rho$ | – | density, $kg/m^3$ |
| $\lambda$ | – | speed factor (ratio) |

# 1 Introduction

The constantly growing demand for energy in recent decades has created global concerns about the consequences of the massive exploitation of non-renewable energy sources such as pollution, global warming and the reduction of the political and economic profitability of using non-renewable energy resources. This forced the search for alternative and renewable energy sources.

Wind energy is a serious competitor among renewable resources and it also complements other energy sources. It is one of the most promising sources of renewable energy: pollution-free, widely available in the Earth's atmosphere, and locally transformable thus it may help reduce dependence on fossil fuels. Many developed and developing countries have realized the importance of wind as an important resource for energy production, and all over the world the necessary measures are being taken to use this energy for its efficient use in energy production.

Electricity storage and distribution is still a serious problem, especially when the amount produced varies considerably over time and place, such as in the case of wind energy. A compact, low-speed vertical axis wind turbine (VAWT) machine such as the Savonius turbine seems to be particularly promising as it can be used for local electricity production in urban, rural and less accessible areas, as well as for collecting climate data. The use of unconventional devices such as the Savonius wind turbine is a low cost solution with a lower environmental impact for decentralized power generation. VAWT concepts are suitable for generating electricity in conditions

where traditional designs, such as high wind speeds and turbulent flows are not applicable. Savonius turbines have been proposed as an alternative to distributed energy and are the focus of the recent research.

## 2 The air in the Earth's atmosphere

Atmospheric air in the ground layer is an approximately homogeneous mixture of gases, including: nitrogen 78.09%, oxygen 20.95%, argon 0.93%, carbon dioxide 0.03% and neon, helium, krypton, xenon, hydrogen and ozone up to 0.003% in total. Moreover, the air consists of water vapor, dust pollutants and gases of volcanic, organic and industrial origin. The content of the air composition does not change up to the height of about 80 km, i.e. Mesopause, as shown in Fig. 1, where the vertical distribution of the mean temperature of the atmosphere is presented [1].

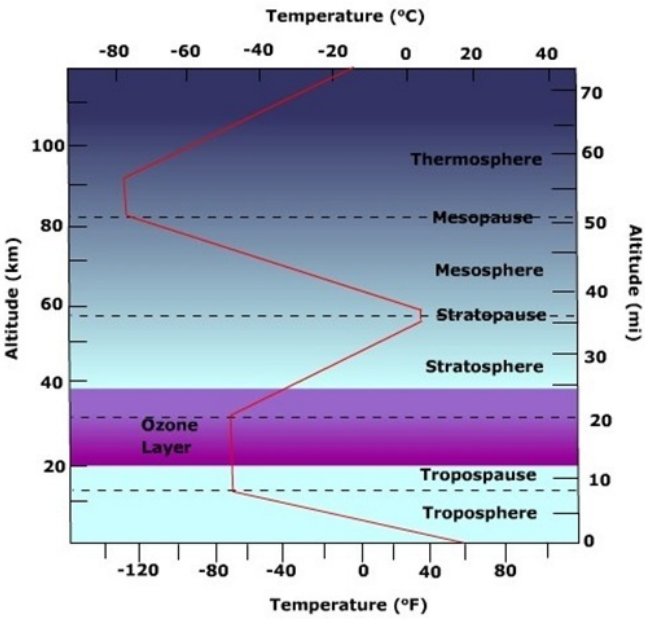


Figure 1: Diagram of the Earth atmosphere into layers [2].

On the other hand, considerations in the field of wind energy concern the troposphere, because it contains about 80% of the total air mass and almost all water vapor in the Earth's atmosphere. It identifies the so-called normal conditions adopted in meteorology and wind energy as average values:

- air temperature $t = 15°\text{C}$ (288 K),
- air pressure $p = 1013$ hPa,
- air volume density $\rho = 1.255$ kg/m$^3$,
- dynamic viscosity $\mu = 1.7894 \cdot 10^{-5}$ Pa·s,
- kinematic viscosity $\nu = \mu/p = 1.4607 \cdot 10^{-5}$ m$^2$/s.

According to an approximate formula, the dynamic viscosity of the air $\mu$ in the low pressure range does not depend on the air density $\rho$ or the atmospheric pressure $p$, but on the temperature $T$:

$$\mu = \mu_0 \left(\frac{T}{T_0}\right)^{0.76}, \tag{1}$$

where $T_0 = 273$ K, $\mu_0 = 1.71 \cdot 10^{-5}$ Pa·s.

As the altitude increases, the air pressure, temperature and density change (Fig. 2, where $H$ is the height and $\tau$ temperature). The dependence of temperature on altitude is not uniform in different latitudes, its value can be identified, for example, from the correlation shown in Fig. 3.

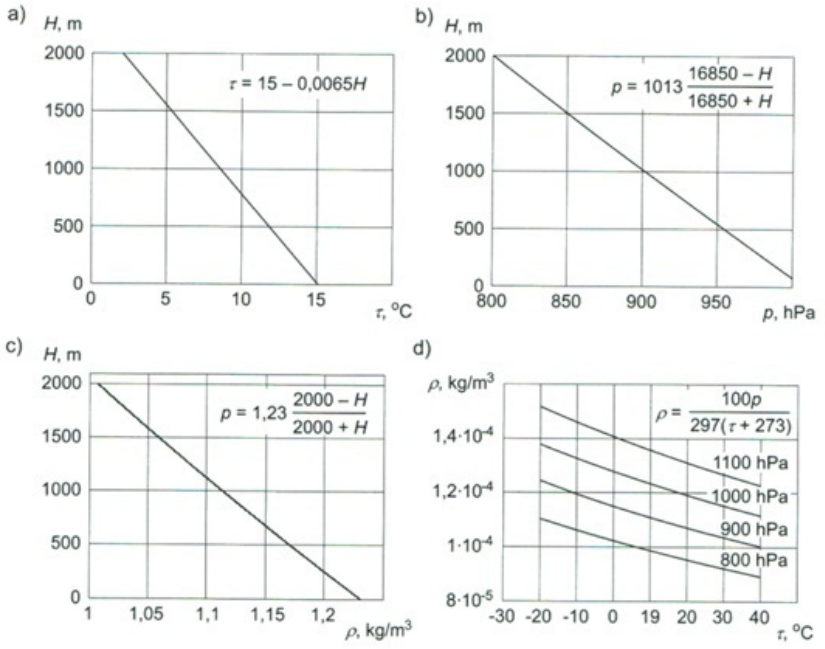


Figure 2: Characteristics of the dry air [1].

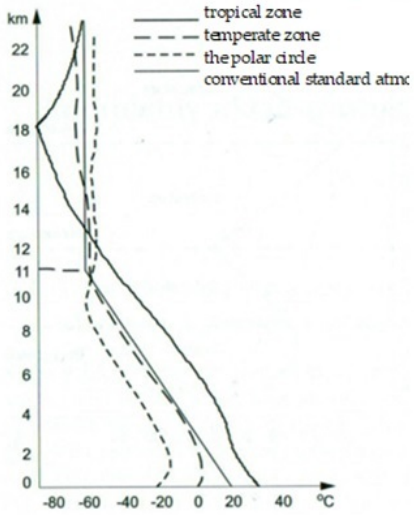


Figure 3: Temperature dependence on altitude in different latitudes [1].

The average values up to a height of 11 km are determined from the following formulas:

$$t = t_0 - 0.0065H\,, \tag{2}$$

$$t = t_{\text{real}} - 0.0065H\,, \tag{3}$$

$$\rho = \rho_0 \frac{20000 - H}{20000 + H}\,, \tag{4}$$

where $t_0$ is 15°C, $t_{\text{real}}$ – actual temperature at the place of measurement, $\rho_0$ – air density.

## 2.1 The movement of air masses

The air in the Earth's atmosphere is in constant motion relative to the Earth's surface. This phenomenon is called wind. The main reason for the formation of wind is the incidence of electromagnetic radiation of the Sun on the Earth's surface, which causes its uneven heating and the formation of a pressure difference. The movement of air masses takes place from high to low pressure and is the more intense the greater the pressure difference and depends on the distance of media with different pressures as well as on the terrain.

The movement of air masses in the Earth's atmosphere is a very complex phenomenon. Heating of air in the equatorial zone causes air masses to move vertically and then splits into two streams in the upper atmosphere towards the north and south poles and in the opposite direction in the ground layer (Fig. 4). The direction of the wind depends on the centrifugal forces caused by the rotation of the Earth and the Coriolis force [1,3].

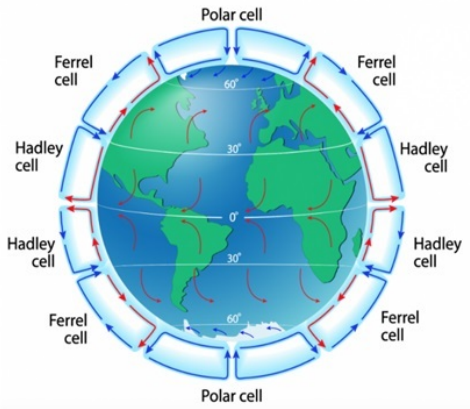


Figure 4: Diagram of the circulation of the Earth's atmosphere [4].

The direction and speed of the wind change throughout the day. This phenomenon results from the faster heating and cooling of the land surface than the surface of water reservoirs. The result is the daytime sea breeze, i.e. the wind blowing from the sea towards the land. The opposite phenomenon occurs at night, when water gives off heat more slowly than land, when the pressure above the surface of the water is lower than the pressure above the surface of the land. The night land breeze takes the opposite direction to the day one and brings dry air with it above the water surface [5]. Another important phenomenon is the faster heating and cooling of mountain slopes from the valleys. The slopes on the southern side heat up intensively, at the same time heating the air in contact with the surface of the slopes, after which it expands and rises upwards on the slopes creating a daily valley slope wind. Sometimes this type of wind causes the formation of clouds on mountain peaks. The opposite occurs at night, when the air adjacent to the slopes cools down more than the air at the same height above the valley. The more cooled air is heavier, so it falls down the slopes, causing mountain slope winds [5]. Wind machines using this phenomenon, i.e. moving in the direction of the air mass flow and using head pressure, are presented below.

## 2.2 Characteristics of wind machines

When the wind acts on solids, it encounters resistance, while the bodies, under the influence of the wind, are subjected to forces called pressure. A necessary condition for keeping the body at rest is the application of a force equal to the pushing force, but directed in the opposite direction. Relative air velocity in relation to the body is important, but it is irrelevant whether the body moves in relation to the stationary air or vice versa, i.e. air in relation to the stationary body. The wind action related to the area of the largest cross-section of the body perpendicular to the wind direction is called the frontal drag coefficient. Thus, the force exerted by the wind on the bodies at rest is the force against the frontal resistance which the body encounters as it moves in still air.

One of the simplest types of wind machines is the one that moves along a straight line under the influence of the wind. The drag device can be considered with a model of a trolley propelled by a collinear wind with velocity $v$ pushing against the transverse surface $A$, and the condition must be $v > u$ [6].

Based on [7], the force driving the engine using the frontal wind pressure of speed $v$ acting on the plane of the rotor blades with surface $A$ in accordance with the lifting speed $u$ is

$$P = \frac{1}{2}\rho C_D A(v-u)^2 = \frac{1}{2}\rho C_D A\left(v^2 - 2uv + u^2\right). \tag{5}$$

The concave side of the rotor blades rotates in line with the thrust force driving the rotor, while the convex side turns in the opposite direction, so the resultant of the forces is the difference of these forces:

$$\begin{aligned} P &= \frac{1}{2}\rho C_{D_1} A(v-u)^2 - \frac{1}{2}\rho C_{D_2} A(v+u)^2 \\ &= \frac{1}{2}\rho A\left[C_{D_1}(v-u)^2 - C_{D_2}(v+u)^2\right]. \end{aligned} \tag{6}$$

Disregarding the frictional forces and in the absence of load on the wind turbine, this force is

$$P = \frac{1}{2}\rho A\left[C_{D_1}(v-u)^2 - C_{D_2}(v+u)^2\right] = 0. \tag{7}$$

The wind speed relative to the carriage is $(vu)$ while $C_D$ is the drag coefficient. An analogy of the turbine speed discriminant is the dimensionless

carriage speed defined as $\lambda$, which is

$$\lambda = \frac{u}{v}\,, \tag{8}$$

then

$$P = \frac{1}{2}\rho C_D A v^2 \left(1 - 2\lambda + \lambda^2\right). \tag{9}$$

The product of the driving force and the speed of the carriage defines the power obtained from the flow:

$$P = Tu = \frac{1}{2}\rho C_D A v^3 \lambda \left(1 - 2\lambda + \lambda^2\right). \tag{10}$$

The $c_p$ power factor is

$$c_p = \frac{P}{\frac{1}{2}\rho v^3 A} = \frac{\frac{1}{2}\rho C_D A v^3 \lambda \left(1 - 2\lambda + \lambda^2\right)}{\frac{1}{2}\rho v^3 A} = \lambda \left(1 - 2\lambda + \lambda^2\right) C_D\,. \tag{11}$$

The power factor $c_p$ reaches its maximum if

$$\frac{dc_p}{d\lambda} = 0, \tag{12}$$

so

$$\lambda|_{c_{p\max}} = \frac{1}{3} \tag{13}$$

and

$$c_{p_{\max}} = \frac{4}{27} C_D = 0.148 C_D\,. \tag{14}$$

The maximum drag coefficient for a concave hemispherical surface subjected to frontal wind pressure (according [7]) is $C_D = 1.33$. The maximum power factor for a turbine using a concave surface perpendicular to the direction of wind flow is

$$c_{p_{\max}} = 0.148 C_D = 0.148 \cdot 1.33 = 0.197. \tag{15}$$

This means that the theoretical maximum use of wind energy in a device using frontal pressure is about 20% of the energy of the raw wind stream.

## 2.3 Savonius turbine mathematical model

The mathematical model based on the pressure drop on both sides of a rotor with a vertical axis of rotation was first proposed by Chauvin and Benghrib [8] to determine the power of a classic Savonius two-bladed turbine (Fig. 5).

If $\vec{\omega} = \dot{\alpha}\vec{k}$ is a vector of instantaneous rotation and due to the symmetry of the Savonius rotor $\dot{\alpha} = \vec{\omega} = \text{const}$ then the torque $Q$ is equal to

$$Q = \sum_i \left(\overrightarrow{OM} \times \vec{F}_i\right) \cdot \vec{k}. \tag{16}$$

The above sum has two components:

$$Q = Q_M + Q_D\,, \tag{17}$$

where: $Q_M$ – pressure component, $Q_D$ – drag component.

Assuming that the pressure difference on the braked blade and the driven blade is $\Delta p_M$ and $\Delta p_D$, respectively, the total driving torque can be written as

$$Q = 2r^2 H \int_0^{\pi/2} (\Delta p_M - \Delta p_D) \sin 2\theta \, d\theta. \tag{18}$$

The mean power $P$ obtained by integrating the torque from 0 to $\pi$:

$$P = \omega Q = \frac{\omega}{\pi} \int_0^{\pi} Q \, d\alpha. \tag{19}$$

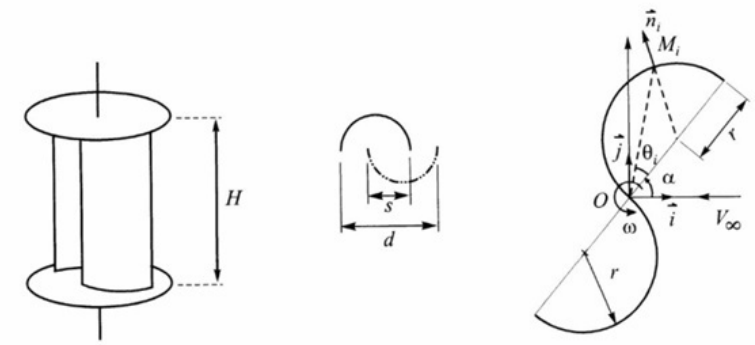


Figure 5: Savonius rotor-calculation diagram [9].

Whereas the power factor $c_p$ is

$$c_p^* = \frac{P}{\frac{1}{2}\rho V^3 (4rH)}, \tag{20}$$

where $r$ is the radius of the Savonius rotor with the aperture ratio $s/d = 0$ ($r$, $s$ and $d$, see Fig. 5). In this case, the face of the turbine is the same as the total area washed by the turbine. After carrying out the experiments, Chauvin [8] proposed the pressure distribution according to the formula

$$\frac{\Delta p_M^{(i)}}{\frac{1}{2}\rho V_e^2} = K, \tag{21}$$

where $K$ is a sinusoidal function $\alpha$ ($\alpha$, see Fig. 5).

The total flow velocity $\vec{V}_e$ is the difference between the undisturbed flow velocity $\vec{V}_\infty$ and the absolute velocity of the point $M_i$ of the rotor blade $\vec{V}_i$:

$$\vec{V}_e = \vec{V}_\infty - \vec{V}_i\,. \tag{22}$$

The component $Q_M$ of the torque is

$$Q_M = \rho r^2 H K \left( V_\infty^2 + 2\dot{\alpha}^2 r^2 - \frac{\pi}{2} V_\infty \dot{\alpha} r \cos\alpha - 2 V_\infty \dot{\alpha} r \sin\alpha \right). \tag{23}$$

The pressure distribution was assumed to calculate the torque $Q_D$ component (Eq. (25)):

$$\frac{\Delta p_D^{(i)}}{\frac{1}{2}\rho V_i^2} = K'\,, \tag{24}$$

so

$$Q_D = 2\rho r^4 H \dot{\alpha}^2 K'. \tag{25}$$

The pressure difference on both sides of the turbine blade at seven points $k$ of the blade is shown in Fig. 6 for both driving and braking half-cycles [9].

The experimental starting torque for a full revolution of the turbine is shown in Fig. 7, which shows that the braking component is negligibly small compared to the driving component.

Using Eqs. (11)–(17) the approximate value of the power factor $c_p^*$ was determined, which is a function of the speed ratio:

$$c_p^* = \frac{K\lambda}{2}\frac{1}{2} - \frac{K\lambda^2}{2\pi} + \frac{K - K'}{K}\frac{\lambda^3}{4}\,. \tag{26}$$

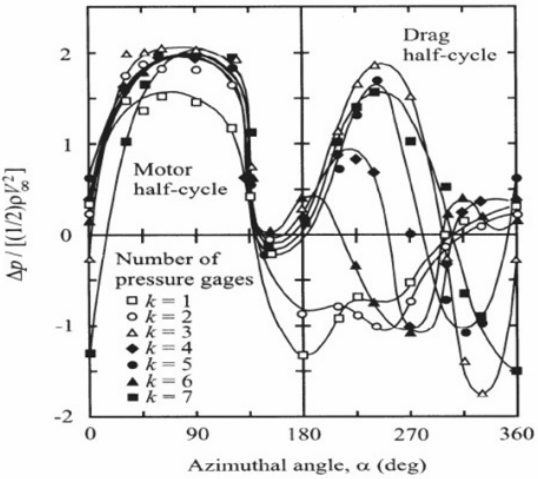


Figure 6: Pressure distribution as a function of the azimuthal angle [9].

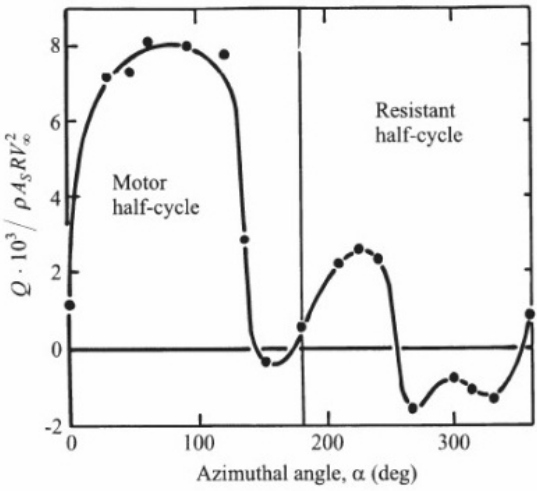


Figure 7: Starting torque when starting the turbine [9].

This equation in graphic form is a family of curves dependent on the parameter $K'$. Physically, a solution exists for $K' \geq 0.73K$. If we take $K' = K$, we can omit the term containing $\lambda^3$ which has no physical dimension. Then

$$c_p^* = K\frac{\lambda}{2}\left[\frac{1}{2} - \frac{\lambda}{\pi}\right] = c_{p_m}^* 16\left(\frac{\lambda}{\pi}\right)\left[\frac{1}{2} - \left(\frac{\lambda}{\pi}\right)\right], \tag{27}$$

where $c_{p_m}^* = 0.17$ for $\lambda_M = 0.78$.

The limiting value of the speed-specific discriminant is $\lambda L = 2\lambda_M = 1.57$. The normalized power factor was compared with the experimental data of other researchers. The differences between the mathematical and experimental model are the result of not taking into account the frictional forces and the fact that the experimental model had a gap with the parameters $s/d = 0.25$. Figure 8 shows the results of tests by Chauvin and other researchers, on the basis of which the maximum value of the power factor was determined to be approximately 0.17 [8].

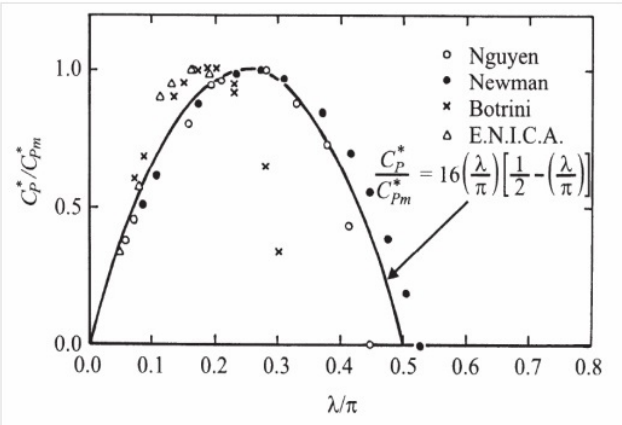


Figure 8: Power factor as a function of the speed index [8].

## 3 Wind turbines – historical background

The first devices using headwind pressure were used more than 3000 years ago. The use of a turbine with a vertical axis of rotation made it possible to connect the drive shaft directly to the rotor to a mechanical load at ground level and was used for grinding grain and pumping water. The earliest records of the use of wind energy come from the East [10–14]. Some concepts of a windmill-like device described in Pneumatica, probably in the first century AD: a Dutch rotor driving a disk with four pins that repeatedly raise the piston in an air pump [15] – Fig. 9a, a device with a rotor water mill [16] – Figs. 9b and 9c, sketch of Heron's drive according to Alexandria and Schmidt [16] – Fig. 9c. According to Drachmann [14], Fig. 9c shows the closest to the original interpretation of the sketch of a primitive Heron drive based on a wind rotor. It was concluded that the device shown in Fig. 9 may have been a toy and not a working use-full machine.

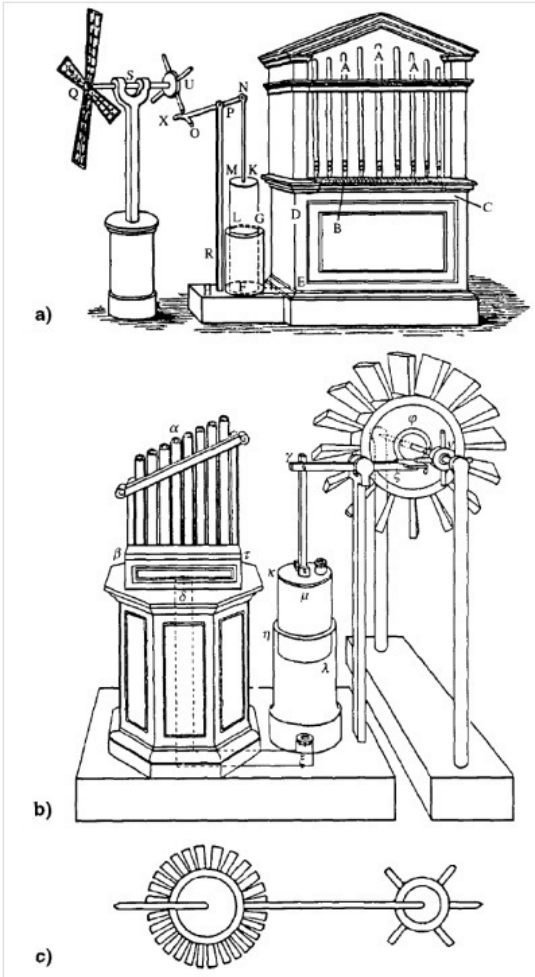


Figure 9: Some concepts of a windmill-like device described by Heron of Alexandria in Pneumatica [16]: a) a Dutch rotor driving a disc with four pins, b) a device with a water-mill rotor, c) sketch of Heron's drive.

The second construction was a Persian windmill with a vertical axis of rotation. Al-most all the notes from the period of 1st−12th century AD come from the Middle East and Central Asia, which is why these regions of the world were considered the cradle of the windmill. The first documented use of a windmill dates back to the 10th century AD from Persia. The records and reliable drawings correspond to the remains of ancient and modern mills, which are still in use today [17, 18].

Around 1300, the Syrian cosmographer al-Dimashqi (1256–1326) provided a detailed description and drawing of a two-story walled structure with millstones on top and a rotor on the bottom consisting of a spoked reel with vertical ribs covered with fabric, forming the sails. The wall surrounding the structure was equipped with slots corresponding to the height of the rotor, and in the upper part of the wall, the circumference towards the center (above the rotor) was reduced to achieve a higher wind speed in the rotor, regardless of the direction.

In 1963, Wulff [19] observed about 50 windmills of still in operation Neh. The structure consisted of a rotor about 5.5 m high and 4.3 m in diameter closed in the side walls about 6.5 m high and a half-wall which leaves a 2.2 m wide opening facing north, the main wind direction. The central wooden shaft was about 0.43 m in diameter. The lower end extending down the mill chamber contained a steel pinch which rested on a wooden pinch block in a chamber lined with a lubricating backing consisting of multiple layers of cloth soaked in tallow. The upper millstone was attached to a steel mandrel, and the lower stone, 2 m in diameter, rested on a brick structure. Eight blades are attached directly to the rotor shaft, while the rotor blades are made of several long bundles of reeds pressed with tie rods, approximately 0.56 m wide and 0.15 m thick. The tie bars are attached with pegs and ropes to several sets of guy ropes that tie together the rotor assembly (Fig. 10).

The joint system was insufficiently stiff to operate stably and the thrust block with a tallow soaked grease pad acting as a bearing was imprecise, which required the system to be adjusted frequently in order for the millstones to function with sufficient clearance.

Wulff [19] gives several figures relating to the performance of these mills. When he visited Neh in 1963, there were 50 more mills, each milling an average of 1 ton of grain in 24 hours, so a total of 6000 tons of flour were produced during the 120-day wind season. Based on a wind speed of about 30 m/s, effective turbine exposure to 1.5 rotor blades, and a mill efficiency of 50%, Wulff estimated the output power to be about 75 hp per mill. The calculations were overestimated as the power calculation with the same assumptions is based on the aerodynamic drag according to the equation

$$c_p = \frac{P}{\frac{1}{2}\rho v^3 A}\,, \tag{28}$$

which would allow to obtain a maximum of 22 hp at a wind speed of 30 m/s.

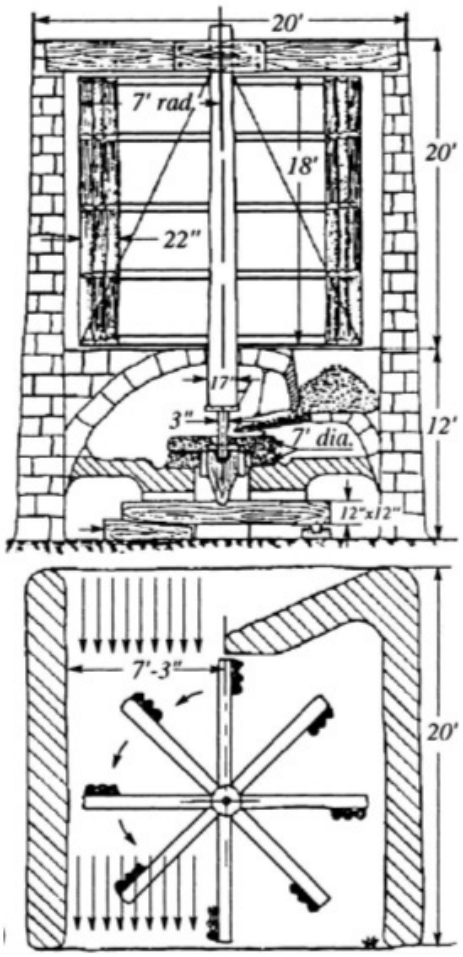


Figure 10: Existing Persian-type windmill in Neh (sketch of the construction and operation of the windmill) [19].

Wulff [19] suggests that the earlier concept was taken from an ancient Norse or Greek water mill, in which the mill itself had to be placed above the water wheel. Relocating the rotor improved efficiency by exposing the rotor to higher wind speeds and certainly made handling much easier. Other noticeable changes are the use of reed instead of cloth as the work surface and the use of a single wind gap instead of the four described by al-Dimashqi, although this may have been limited to the region around the Neh, where the wind blows steadily from the north in summer.

It is commonly claimed that the windmill was invented in China more than 2000 years ago, but Needham [11] states that the earliest record dates from 1219. Chinese mills have a characteristic form with eight sails mounted on masts around a vertical axis, arranged in a way that allows their automatic alignment. Figure 11a shows the arrangement of masts supported on the rotor shaft by radial crossbars. The power is taken off by means of a rectangular drive consisting of toothed wheels with pin teeth. Figure 11b illustrates the operation of the sails during the rotation of the rotor. Each sail was mounted asymmetrically and held against the wind by a rope (positions $G$, $H$, $A$, and $B$) until it reached a pivot point where it pivots, flips and leans outwards ($C$ and $D$), from there entering the wind axis skew, which resulted in the generation of low shaft rotation resistance forces ($E$ and $F$). Thanks to this solution, curtain walls such as in Sistan were not used and wind from any direction was used.

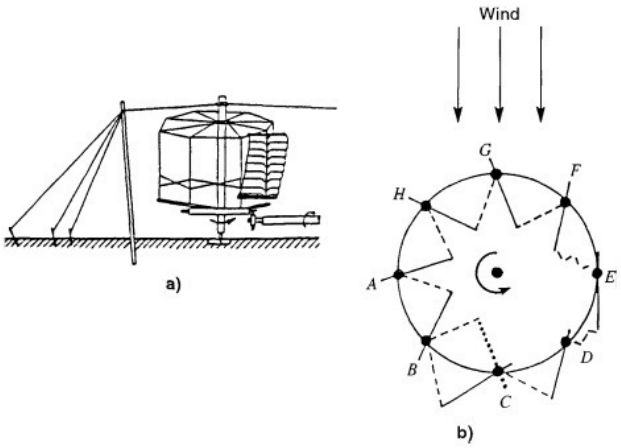


Figure 11: Chinese windmill with a vertical axis of rotation [20]: a) general arrangement of sails, masts, main shaft and power take-off, b) automatic positioning of the sails during rotation; in positions $E$ and $F$ the sails deflect with little resistance.

This type of mill is still used in eastern China. The Chinese vertical windmill construction, unlike the Persian one, was used in north-western Europe. At the end of the 12th century, the concept of windmills with a horizontal axis of rotation was created. Over the next years, windmills of this type were improved and used throughout Europe, but the prototype of this solution was the device described by Heron

# 4 Modern turbines with a vertical axis of rotation

## 4.1 Types of turbines with a vertical axis of rotation and their characteristics

Units with a vertical axis of rotation can be divided into two types: the first, where the working blades move slower than the wind, and the second, where the blades move faster than the wind (Fig. 12).

Figure 12: Various rotor designs with vertical axis of rotation [21].

Units of the first type (Fig. 12), are characterized by a low wind power utilization factor (less than 0.3), low rotational speed (the optimal blade speed is about 0.3–0.7 wind speed), which requires the use of heavy mechanical and electrical equipment to obtain electricity.

The high velocity orthogonal units (Fig. 12, items 8–18) convert the work done by the forces arising from the outflow of the rotor blade profile with aerodynamic profiles with a smoothly shaped leading edge. An important advantage of machines with a vertical spin axis is their independence from the wind direction.

Front wind pressure devices were not improved from the early Middle Ages to the beginning of the 20th century. Concepts similar to modern ones

were built and tested intensively in the years 1920–1930 and found a new application with the invention of a new type of rotor: the Savonius turbine and the Darrieus turbine.

The Savonius turbine was invented by the Finnish engineer S.J. Savonius in 1922. The straight Savonius rotor is S-shaped in cross section, which can be made by cutting the barrel in half, inverting one of the halves and joining them together (Fig. 5).

The original Savonius rotor models were able to achieve a maximum efficiency of less than 20%. The dependencies of the power factor and torque on the speed factor of various designs of wind turbines are shown in Figs. 13 and 14.

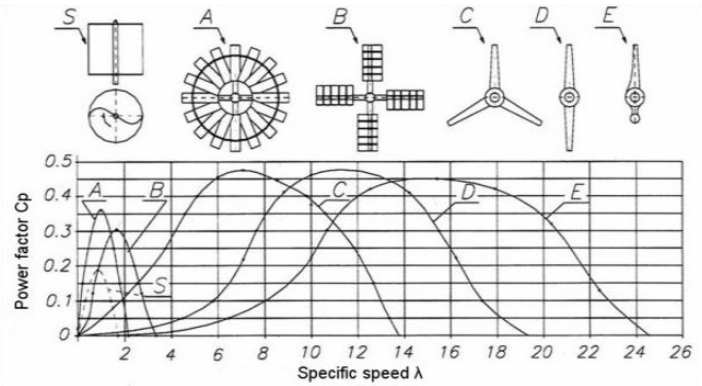


Figure 13: Dependence of the wind energy utilization coefficient $C_p$ on the speed factor $\lambda$ and the number of blades of the rotor and Savonius rotor [22]: $A$ – multi-blade rotor, $B$ – four-blade rotor, $C$ – three-blade rotor, $D$ – two-blade rotor, $E$ – single-blade rotor, $S$ – Savonius rotor.

A Savonius turbine is only useful and economical for low energy requirements such as pumping water, driving a small electric generator, providing ventilation and mixing water to protect fish ponds in winter conditions, or as an ocean current meter. The technology required to design and manufacture a Savonius rotor is very simple and is recommended for applications in developing countries or in isolated areas without a power grid. The current development and popularization of the Savonius turbine is based on the premise of microgeneration of electric current.

Systematic research carried out by Savonius and later repeated by other scientists under experimental conditions allowed to determine the optimal forms of rotors and to increase the efficiency of advanced structures to the level of 30% (Fig. 15).

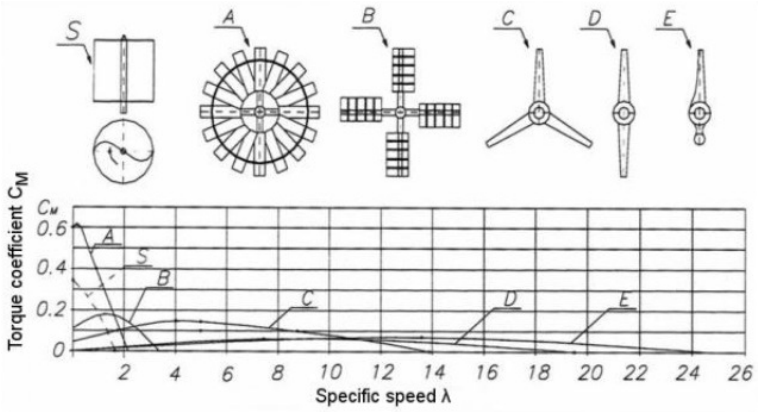


Figure 14: Dependence of the (relative) torque $C_M$ of the function of the high speed discriminant $\lambda$ and the number of blades of the rotor and the Savonius rotor [22]: $A$ – multi-blade rotor, $B$ – four-blade rotor, $C$ – three-blade rotor, $D$ – two-blade rotor, $E$ – single-blade rotor, $S$ – Savonius rotor.

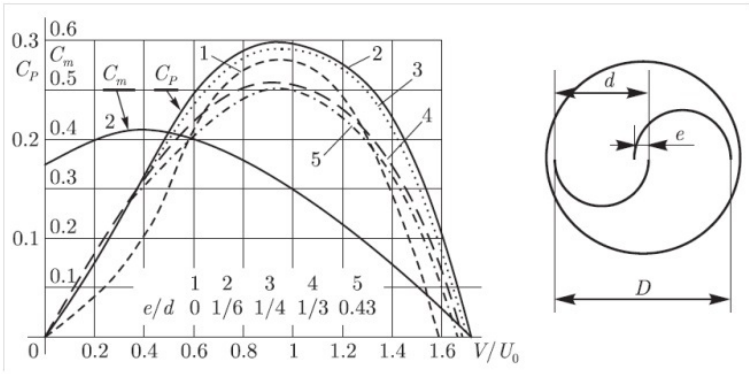


Figure 15: Diagram of dependence of the torque $C_m$ and the power factor $C_P$ of Savonius rotors with different dependencies of the gap between the blades to the diameter of one blade [21].

The efficiency of the system reaches 30% with the thickness of the stream passing from one side of the rotor to the other equal to 1/6 of the diameter of the rotor's working half-cylinder. The efficiency of the rotor increases with the greater relative height and it is not recommended to use a height lower than the rotor diameter.

The Savonius rotor, like many orthogonal machines, has so-called dead zones, i.e. positions in which the rotor will not start to turn on its own,

even though the average torque is quite high (Fig. 15, line $C_m$). When the rotor is at an angle between 300° and 0°, the pressure coefficient is negative and the rotor will not turn in the required direction (Fig. 16).

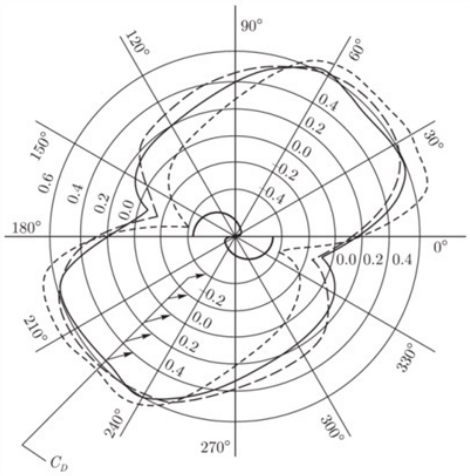


Figure 16: Diagram of the air stream flow through the Savonius turbine with the gap between the blades [21].

This problem was solved by using a multi-level (double) Savonius rotor consisting of two interconnected rotors rotated relative to each other by an angle of 90° (Fig. 17).

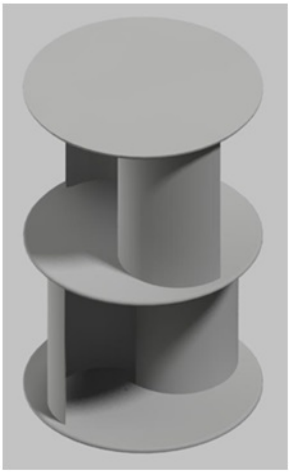

Figure 17: A two-tier Savonius rotor (own elaboration).

## 4.2 Design improvements to vertical axis wind turbines

Numerous improvements have been made to the low-speed orthogonal units to in-crease energy efficiency. This goal was achieved by introducing control devices that fold the 'sail' at the working element moving in the direction of the wind and unfold the 'sail' at the optimal moment with the working element moving in the direction of the wind (in some inventions this is done automatically, e.g. under the influence of wind force). Due to the low rotational speed, the unit consumption of materials (per unit of power) remains high.

For low-speed machines, the highest possible drag coefficient $C_D$ is required in the place where the working element moves along the flow. The resistance to the working element must be the lowest in the next point of rotation of the turbine. This was achieved by a special form of the rotor blades in the form of moving elements changing their position in relation to the air stream, which allowed to increase the efficiency of VAWT turbines to over 30% (Figs. 18 and 19).

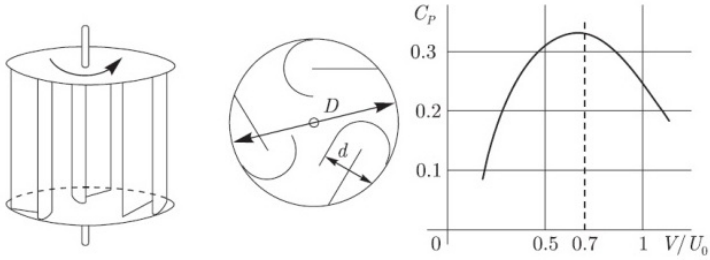


Figure 18: Low-speed rotor with directional fairings [21].

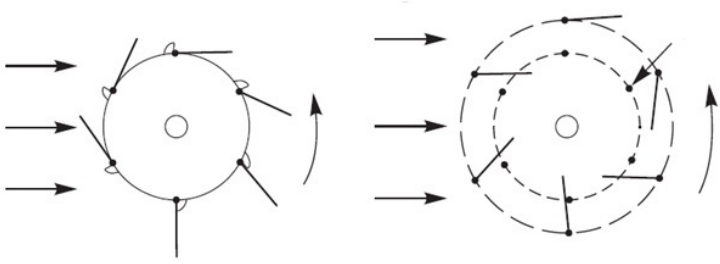

Figure 19: Rotors with rotating plates [21].

Another solution was to equip the blades with an internal flatness on the sides and push them out under the influence of aerodynamic and centrifugal

forces causing the rotor to become almost cylindrical and the blades to move apart in light winds. This solution was implemented in a Lafond turbine with multiple blades (Fig. 20).

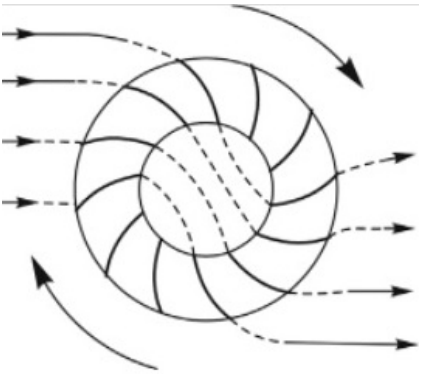

Figure 20: Lafond turbine with many blades [21].

## 4.3 Influence of Savonius rotor configuration on aerodynamic efficiency

Most significant experimental studies of Savonius rotor configurations were conducted in the 4.9×6.1 m Vought Corporation System Division low-speed wind tunnel commissioned by Sandia Laboratories US Energy Research and Development Administration in 1975. The tests included such parameters such as the number of blades, air stream speed, rotor height and slot width (Table 1).

Table 1: The range of values of various parameters of the Savonius turbine.

| Parameters | Unit | Value |
|---|---|---|
| Number of rotor's blades | – | 2 and 3 |
| Nominal speed of the air stream | m/s | 7 and/or 14 |
| Reynolds number per meter | – | $4.32 \cdot 10^5$ and $4.32 \cdot 10^8$ |
| Rotor's height | m | 1 and 1.5 |
| Rotor's diameter | m | 1 |
| Overlay on containment discs | – | 0–0.1 |
| Ratio of the width of the gap between the rotor blades | – | 0.0, 0.1, 0.15, 0.20 |

The measured test variables were torque and rotational speed. The data is presented as power and torque factors as a function of speed (or angular position for static starting torques). It has been determined that increasing the Reynolds number and/or aspect ratio improves efficiency, and the optimal configuration consists of two sets of twin-blade rotors, rotated through 90°, with the slit width being 0.1–0.15 of the width of a single blade.

Representative test models are shown in Figs. 21, 22. The rotor and end disks are made of 6061 T6 aluminum alloy. Each pair of end plates was

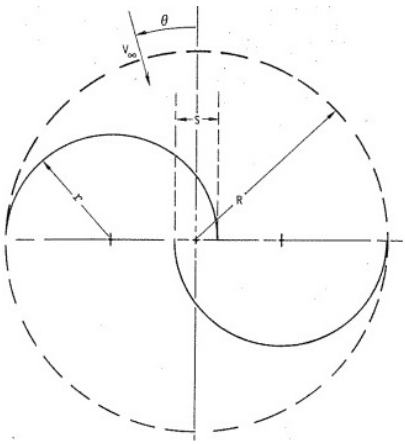


Figure 21: Diagram of a two-blade Savonius rotor shifted by 180° [23].

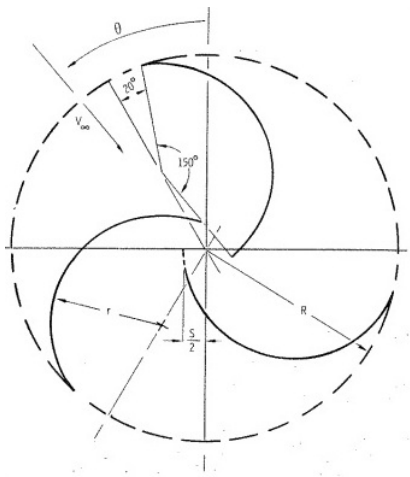


Figure 22: Diagram of a three-blade Savonius rotor with an offset of 150° [23].

adapted to several bucket con-figurations. The rotor was attached to the end plates with machine screws.

The Vought Systems Division Low Speed Wind Tunnel is a closed-circuit facility consisting of 11.9 m rectangular test sections measuring 2.1 m × 3.0 m and 4.6 m × 6.1 m. due to its dimensions and speed range of 3–23 m/s. All instrumentation related to facility handling and wind tunnel flow conditions were provided by Vought. Sandia provided instrumentation related to the measurement of torque and rotational speed of the turbine.

Prior to testing each configuration, the rotor was rotated with an air motor at a very low but constant speed to determine the tare torque due to friction in the bearings. Values of the order of 0.678 J were recorded for each configuration and used to correct the data. A wind tunnel turbulence coefficient of 1.4 was determined, but due to differences between wind speed and rotor speed, the Reynolds number was not corrected.

The object placed in the wind tunnel causes the creation of a tunnel blockade, which causes an increase in the local wind speed on the test section. This increase was taken into account by determining the tunnel congestion coefficient $\xi$ called the speed increase. The total factor is the sum of the speed gain due to excitation lock and permanent lock. It is very difficult to pinpoint these two lock corrections in the case of an unusual shape such as the Savonius rotor. Pope and Barlow [24] suggest that the total correction of tunnel congestion is given by the equation:

$$\xi = \frac{1}{4}\frac{\text{FRONT AREA OF THE MODEL}}{\text{CROSS SECTION AREA OF THE TEST SECTION}}\,. \tag{29}$$

The surface area of the turbine with the stand and the installed accessories was assumed as the face area of the model. The correction factor was set at $\xi = 0.0125$ for a 1 m high rotor and $\xi = 0.0162$ for a 1.5 m high rotor. Later analytical studies showed that the Savonius rotor experiences lateral forces that are of the same order of magnitude as the drag force and equation (29) is imprecise.

Based on the correction of the tunnel congestion, the air velocity $v$ and the dynamic pressure $p$ were corrected:

$$v_{\text{kor}} = (1 + \xi)v, \tag{30}$$

$$p_{\text{kor}} = (1 + \xi)p. \tag{31}$$

The Reynolds number per unit length is defined as

$$\text{Re} = \frac{\rho v}{\mu}\,. \tag{32}$$

Reynolds numbers refer to a length of 1 m and are an approximate Reynolds number based on the diameter of the turbine. The reason why the Reynolds number is presented as a value per meter is because there is no universally accepted length scale with which to calculate the Reynolds number for a Savonius rotor.

The measurement data of the Savonius rotor was used to calculate the efficiency in the form of torque coefficient $C_M$ and power factor $C_P$, and presented speed factor $\lambda$:

$$C_M = \frac{Q + Q_f}{\frac{1}{2}\rho v^3 A}, \tag{33}$$

$$C_P = \frac{\omega(Q + Q_f)}{\frac{1}{2}\rho v^3 A}. \tag{34}$$

The results indicate that the static torque coefficient is positive for all angular positions except for the zero gap configuration. The two-blade Savonius rotor exhibits a large variability of the static torque with the change of angular position. On the other hand, the Savonius rotor in the configuration with three blades shows a significantly lower value of the static torque coefficient than the configuration with two blades.

The test results showed that the two-bladed Savonius rotor is insufficient as a starting system for other VAWT wind turbines (Darrieus), because the minimum starting torque is too low in many cases. This problem was solved by using two sets of Savonius rotors, the first of which is rotated by 90° with respect to the second (Fig. 23).

In the two-blade configuration, the Reynolds number has been shown to have an effect on the static torque coefficients as evidenced by shifts in the $C_Q$ torque curves due to delayed separation around the rotor blades with increased Reynolds number. The power factors for all configurations (two blades) peaked at a speed differential of about 0.9 except for the non-slotted configuration where the power factor peaked at a speed differential of about 0.8. The peak power factor for the twin-blade rotor configuration ranges from 0.22 to 0.26 (Fig. 24). The maximum torque ratio occurs at a lower speed ratio, typically around 0.4 for all two-blade configurations, although there is a noticeable increase in power and torque ratio as the Reynolds number increases.

The test data shows the best aerodynamic performance for a gap width of $s/d = 0.1{-}0.15$. The use of both a larger and a smaller gap causes

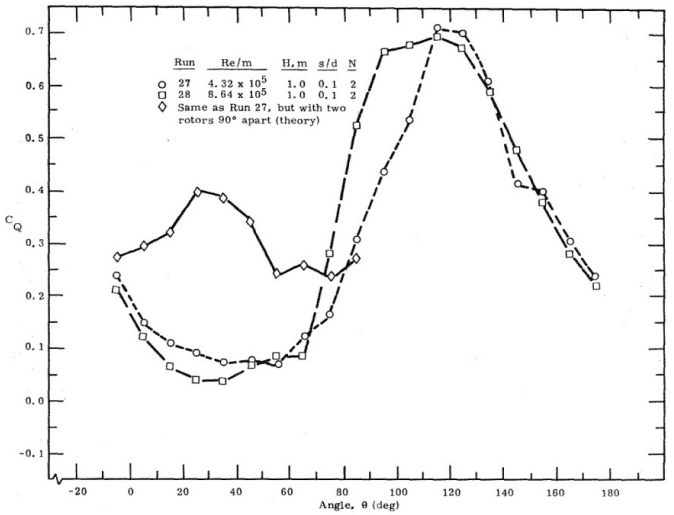


Figure 23: Static coefficient of torque versus angular position for a two-blade Savonius rotor with a slot width ratio of 0.10 for both Re/$m$ values (circle and square) together with the torque curve for a typical hypothetical double-rotated Savonius rotor (rhombus) [24].

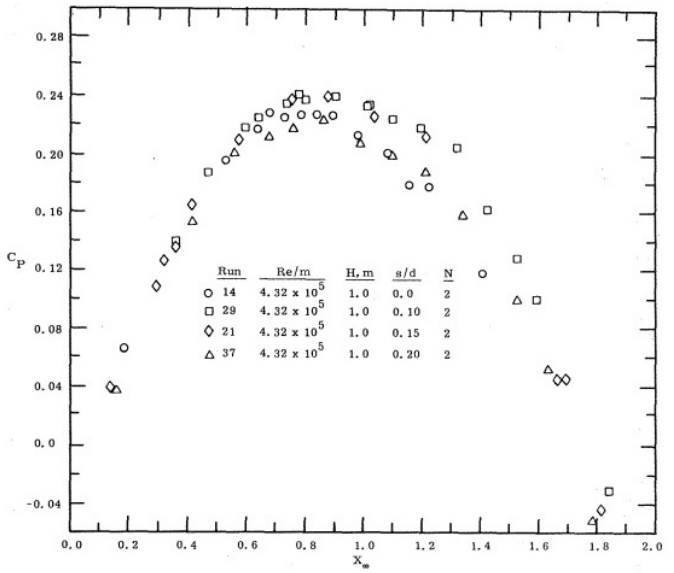


Figure 24: Power factors for 1-metre, two-bladed Savonius rotors with different slot width ratios at Re/m $4.32 \cdot 10^5$ [24].

a decrease in efficiency. The difference in performance is most noticeable with higher gear ratios. A similar trend was achieved for test data with a high Reynolds number. The data clearly indicates that the optimal gap width s/d should be in the range of 0.1 to 0.15 (Fig. 25).

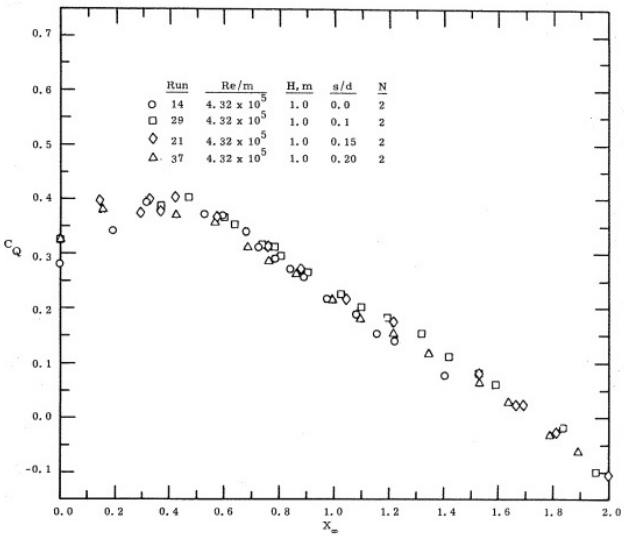


Figure 25: Torque for 1-metre, two-bladed Savonius rotors with different slot width ratios at $\mathrm{Re}/m = 4.32 \cdot 10^5$ [24].

In configurations with three blades, no angular position was observed where the static torque coefficient would be negative. The three-blade configurations showed less variability in the static torque coefficient than the two-blade configurations. The average torque coefficient for one cycle was typically in the range of 0.3 to 0.4 for the three-blade configuration and was analogous to the coefficient for the two-blade configuration. As with the two-blade configuration, the angular position at which the stall occurs was a function of the Reynolds number.

Analysis of the power factor and torque versus turbine speed ratio curves for the three-blade configuration for two Reynolds numbers showed a slight improvement in efficiency with increasing Re. This is not true for all data, and the exact reason for these anomalies where data with a lower Reynolds number has better performance is not known.

From an efficiency point of view, the two-blade configuration is superior in many respects. The maximum power factor in the two-blade configuration is approximately 1.5 times that of the three-blade configura-

tion (Fig. 26). The speed factor at which $C_p$ reaches its maximum value is greater when using a two-blade rotor. The performance advantage of the three-blade configuration over the two-blade configuration is the higher minimum static torque value (Fig. 27), however, this advantage can be eliminated by combining two sets of two-blade rotors into a two-level rotor staggered by 90° from each other.

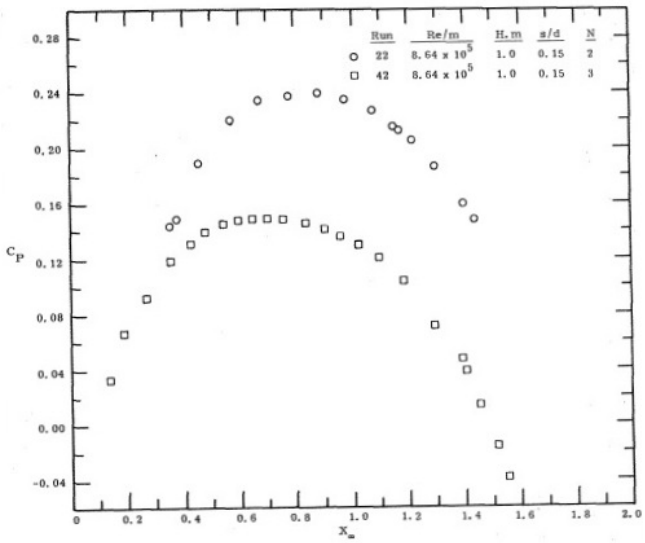


Figure 26: Comparison of the power factors of two- and three-blade Savonius rotors with a slot width ratio 0.15 at Re/$m$ being $8.64 \cdot 10^5$ [24].

The effect of rotor height was tested for the two-blade configuration at $s/d = 0.15$. The fact that the power and torque factors increase slightly with increasing blade height indicates that the endplates provide a reduction in terminal losses. Data for turbines 1.5 m high were comparable to turbines 1 m high (Figs. 28, 29).

Dependencies of the gap width smaller than $s/d = 0.2$ reach approximately the same maximum power and show better parameters than the curve $s/d = 0.2$. At low rotational speeds, the $s/d = 0$ curve seems to be the most favorable, but it shows worse performance at high rotational speeds. Zero gap width exhibits maximum torque, but worse at higher rotational speeds. The configuration with the largest gap width shows the worst performance at low and medium speeds. The general conclusion to be drawn from the data is that the gap is desirable, but should not be large

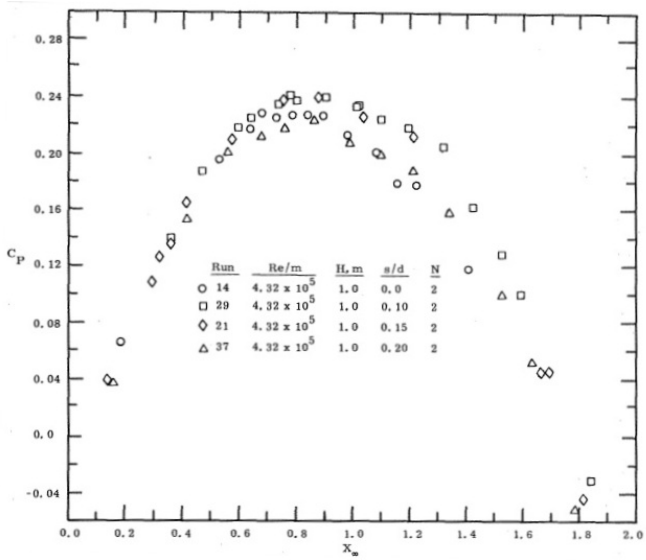


Figure 27: Power coefficients for 1-meter twin-blade Savonius rotors with different gap width ratios at $\mathrm{Re}/m = 4.32 \cdot 10^5$ [24].

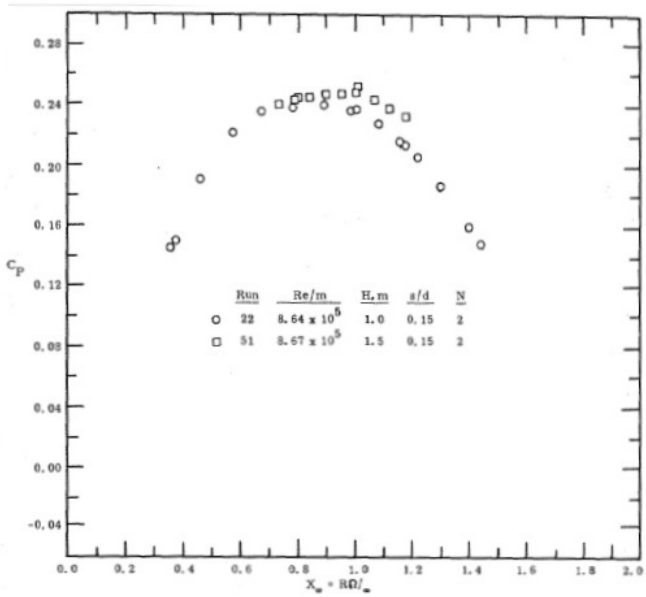


Figure 28: Comparison of power factors for a two-blade configuration with a slot width ratio of 0.15 at $\mathrm{Re}/m$ being $8.6 \cdot 10^5$ for two rotor's heights [24].

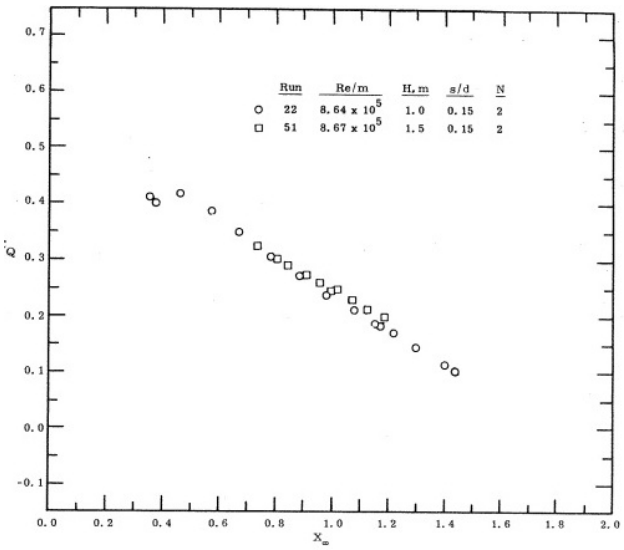


Figure 29: Comparison of torque for a two-blade configuration with slot width ratio 0.15 at Re/$m$ being $8.6 \cdot 10^5$ for two rotor's heights [24].

enough to cause a reduction in the sweep area of the rotor and the radius of rotation.

Summarizing the researches of various configurations of the Savonius rotor, it was found that:

- the static torque coefficient is much more variable with angular position in a two-blade configuration than in a three-blade configuration;
- two-blade configurations have better aerodynamic performance than three-blade configurations, with the exception of starting torque;
- increasing the Reynolds number improves overall aerodynamic performance;
- aerodynamic efficiency slightly increases with increasing height to diameter ratio;
- dimensionless slot width $s/d = 0.1{-}0.15$ for optimal performance;
- for a fixed rotor blade size, the recommended slot width is $s/d = 0.1{-}0.15$;
- the optimal configuration is two sets of two-blade rotors, rotated relative to each other by 90°, each rotor should have a gap of $s/d = 0.1{-}0.15$.

### 4.3.1 Improving the performance of the Savonius rotor by using quarter blades

The solution of using quarter blades and comparing their efficiency with the conventional model were presented in their studies by Indian scientists [25]. The research was based on CFD (computational fluid dynamics) numerical simulation using the Ansys CFX environment. The validation study was performed on a conventional configuration (Fig. 30), comparing numerical simulation results with [26–50] experimental results for seven different inlet velocities to provide a numerical platform for comparative testing. The way to conduct the comparative study was to set a baseline for comparison and keep other parameters unchanged. The rotor geometry remained the same except for the addition of quarter blades (Fig. 31) so that the maximum dimensions of the rotor remained the same so that the aspect ratio and swept area remained constant for both configurations. The blade overlap ratio and spacing were kept constant.

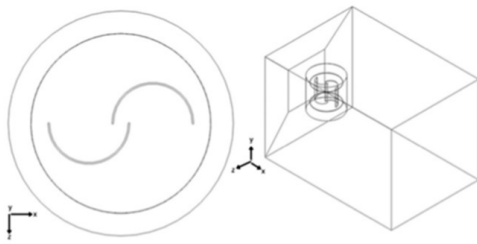

Figure 30: Conventional configuration [25].

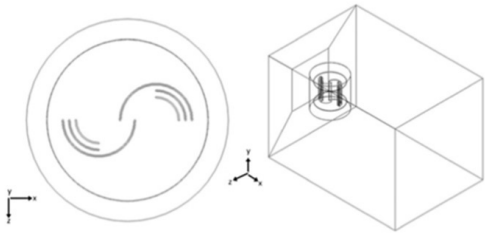

Figure 31: New configuration with quarter blades [25].

A Savonius rotor is a hydrokinetic turbine that uses the kinetic energy of the fluid to generate force on the blade walls. The torque generated on the advancing blade is greater than that on the return blade, providing a net

positive torque. The output torque and $C_P$ of the new and conventional rotor were estimated using a numerical analysis method, with the settings unchanged (Fig. 32).

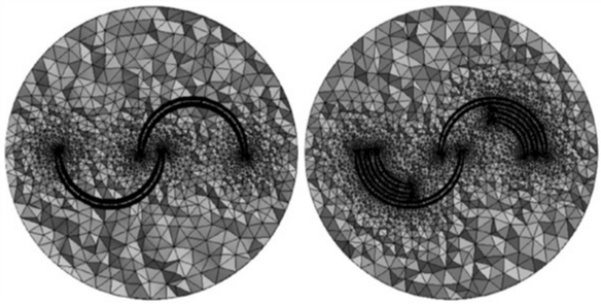

Figure 32: Cross-section view of the mesh generated for the conventional and new configuration [25].

Significant improvements were obtained in efficiency from 8.89% to 13.6%. Under the action of the rotation of the rotor, the fluid surrounding it also begins to rotate. Coverage of the return blade has occurred, but to a limited extent, since the incoming fluid is directed tangentially to the rotational motion of the fluid, but impedes the fluid from impinging on the moving rotor at certain angles. The rotor was placed near the inlet leading to a rapid deflection of the incoming fluid to the periphery of the spinning domain, partially blocking the swirling fluid path (Fig. 33).

The results show a similar trend in torque and power factor for both configurations. The maximum $C_P$ value reached 0.2081 and 0.2266 for an inlet velocity of 8.23 m/s for the conventional and new configurations, respectively, showing an improvement of 8.89%. The maximum improvement in performance was noted for the case of an inlet velocity of 9.21 m/s with an increase in the $C_P$ value of 13.69%. The average rotor torque was evaluated at each time step for all speed reference cases. The distribution of forces on the rotor in the new configuration is shown in Fig. 34.

Each time step corresponds to two degrees of rotation. There was an improvement in the torque performance of the new configuration over the conventional one (Fig. 35). Increasing the exposed area on the pushing side leads to an increase in the effective use of the available kinetic energy from the incoming fluid, also contributing to the increase in positive torque. In order to obtain better accuracy, the torque values generated during the second rotation of the rotor were taken into account for comparison.

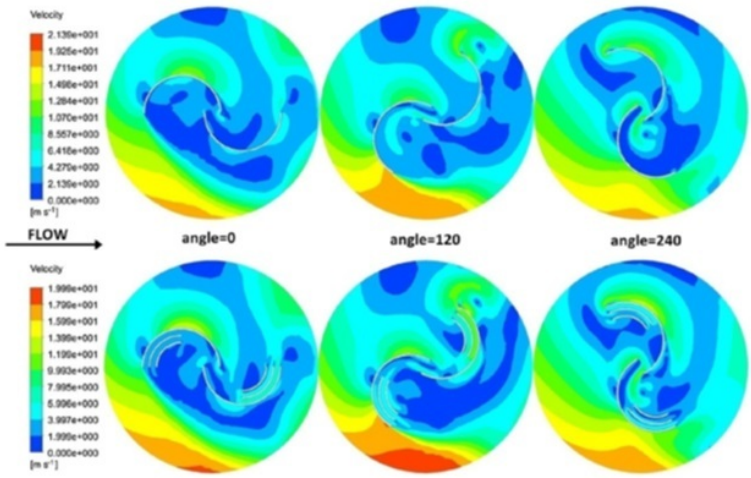


Figure 33: Speed distribution for conventional configuration (above) and new configuration (below) for $v = 8.23$ m/s [25].

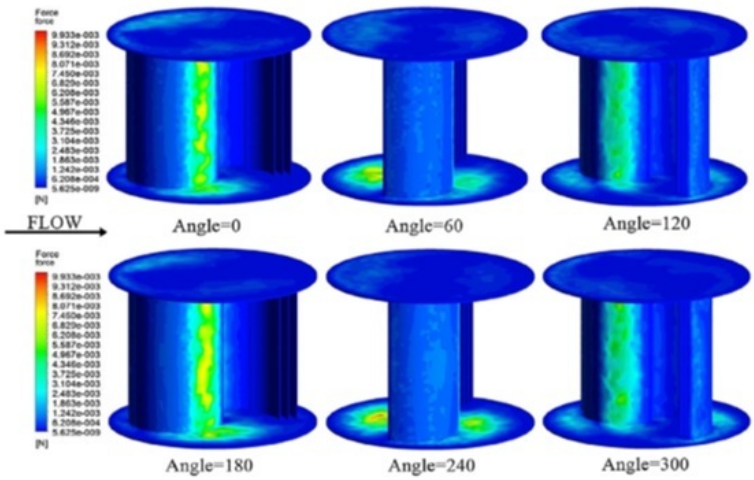


Figure 34: Distribution of forces on the rotor in the new configuration [25].

The numerical validation study was consistent with the experimental data of Saha [26]. In a comparative study, the new configuration was observed to have better performance than the conventional configuration, reaching a maximum $C_P$ value of 0.2266 at $v = 8.23$ m/s with an improvement of 8.89% (Fig. 36).

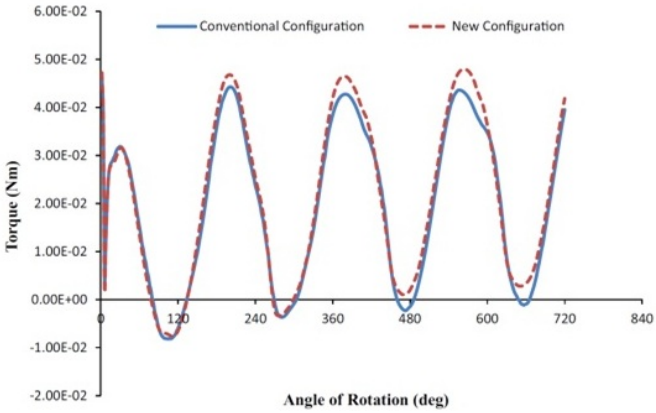


Figure 35: Dependence of the rotor torque on the angle of rotation [25].

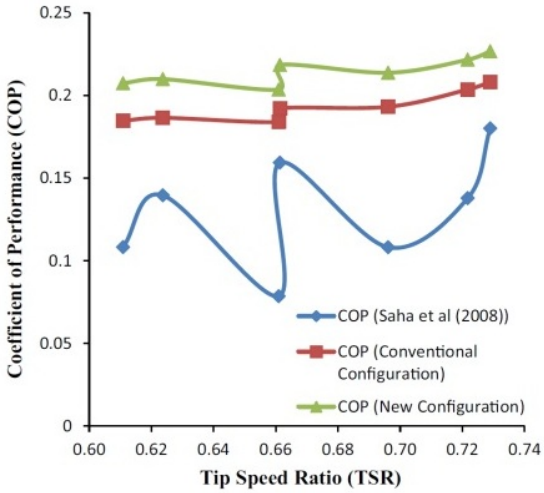


Figure 36: Dependence of the power factor as a function of the speed factor [25].

The tests were carried out keeping the shape factor, external dimensions and flow parameters the same for both configurations in each case. An additional set of quarter blades captures some of the unused kinetic energy of the incoming fluid stream, resulting in in-creased aerodynamic efficiency. The study confirms that the improvement in the performance of the Savonius rotor can be achieved without increasing the spatial parameters and without making complex structural changes to the rotor while maintaining a simple structure.

### 4.3.2 Optimization of a Savonius turbine with an obstacle shielding the returning rotor blade

The main advantages of the Savonius turbine are simplicity, compactness and strength of the structure as well as low cost, therefore modifications introducing high complexity should not be used. Taking into account the results of previous studies [26,51], some simple guide or deflector plates lead to improved performance at the lowest possible cost and complexity. The influence of the obstacle partially shielding the returning blade of the two- and three-blade Savonius turbines was investigated numerically (Fig. 37). The addition of a shielding obstacle should reduce the negative torque and consequently increase the total torque of the turbine. The position and angle of the shielding obstacle were optimized by a suitable mathematical procedure.

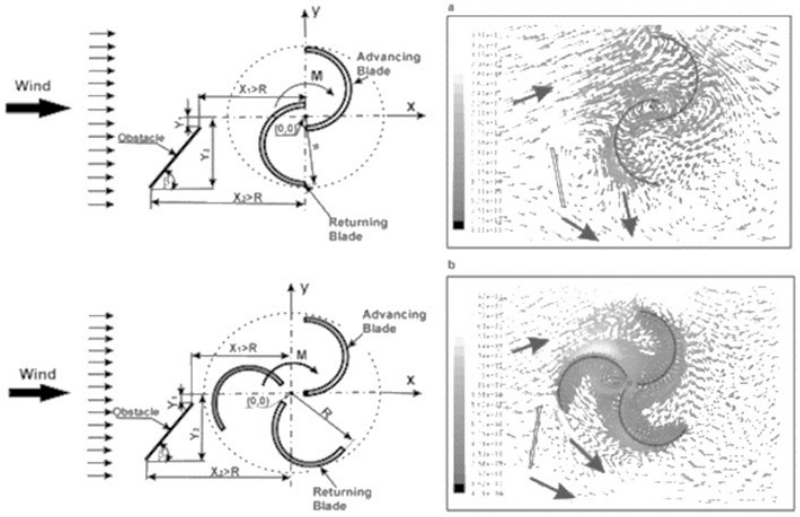


Figure 37: Schematic description and main parameters characterizing the Savonius rotor in configuration with two or three blades, together with a comparison of instantaneous flow structures [52].

By installing an obstacle, the self-starting ability of the turbines was improved. Whereas the conventional two-blade Savonius turbine exhibits negative values for static torque within a certain range, the use of a shielding obstacle resulted in positive static torque at any angle for both designs (Fig. 38). The optimization led to an increase in the output power factor by 27.3%. An increase in the value was observed for the torque factor with

higher values of $\lambda$. Taking into account the output power factor obtained and the cost and complexity of the rotor, the two-blade configuration is clearly more efficient than the three-blade turbine. The optimal configuration has peaked the output power factor $C_P = 0.258$ at $\lambda = 0.8$.

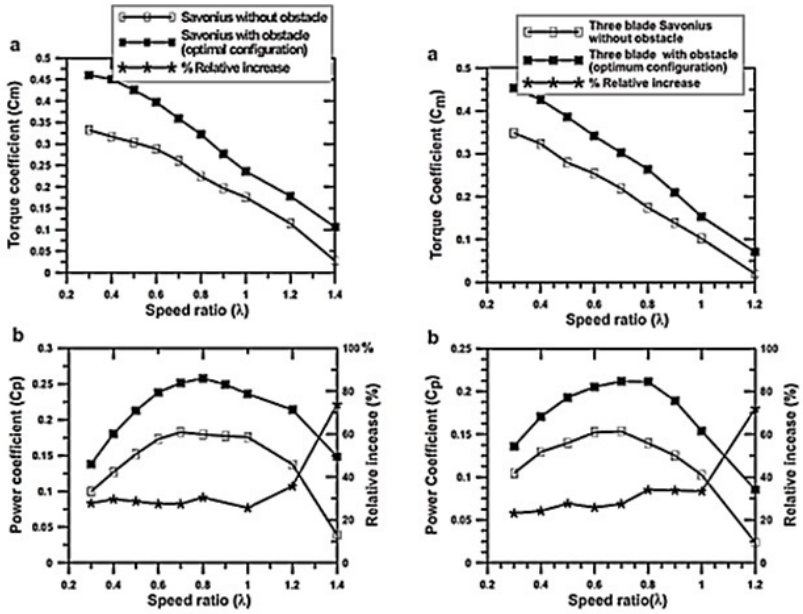


Figure 38: Performance comparison of the conventional configuration without shielding obstacle (white squares), with shielding obstacle (black squares) and relative increments (asterisks) [52].

Using an obstacle shielding the returning blade, an increase in the power and torque coefficients was shown. The optimized configuration is slightly more complex, more expensive and heavier, but guarantees a significant improvement in the aerodynamic parameters of the Savonius turbine with little effort.

## 5 Conclusions

Summarizing the information presented above, it should be stated that the selection of a wind turbine with a vertical axis of rotation used to generate mechanical and electric energy should be made by analyzing the basic parameters depending on the given structure. The most frequently

considered are the cost of installation and service, applicability, durability and efficiency. However, these systems have both obvious disadvantages and advantages that determine the scope of their use. Referring to the imperfections of these devices, the following should be mentioned first of all: low efficiency, susceptibility to turbulence, torque variability depending on the angular position during rotation, power control limitations at high wind speeds, low-speed units require low-speed generators or gearboxes, which additionally reduces low efficiency, the need to use bearings for the upper part of the rotor due to deviations from the axis of rotation in the absence of it.

However, it should be noted that many more advantages are identified, which include: simple and cheap construction, noiseless operation and its performance regardless of the wind direction (no need to use systems for positioning the turbine perpendicular to the wind), mobility due to easy installation and de-installation, the possibility of installation in the infrastructure s, etc., high aesthetics making it fit into the urban infrastructure, resistance to un-favorable of the urban agglomeration, e.g. on the facades and roofs of buildings, street lamps, lamppost weather conditions such as high-speed winds, atmospheric precipitation, low temperatures, low power losses in basic and movable connections, the generator on the shaft does not require bearing connections.

The conducted analysis indicates that the essence of the use of this type of structure is basically the individual preferences of potential users who belong to the group of the so-called low-enthalpy distributed energy.

*Received 19 July 2023*

## References

[1] Flaga A.: *Wind Engineering: Fundamentals and Applications;* Arkady, Warszawa 2008 (in Polish).

[2] *Atmospheric Structure Available.* https://www.thephysicalenvironment.com/Book/atmosphere/atmospheric_structure.html (accessed 14 Nov. 2022).

[3] Shepherd W., Zhang L.: *Electricity Generation Using Wind Power* (2nd Edn.), World Scientific, New Jersey 2017.

[4] *What Is Global Atmospheric Circulation Available.* https://www.internetgeography.net/topics/what-is-global-atmospheric-circulation/ (accessed 14 Nov. 2022).

[5] Wolańczyk F.: *Wind Power Plants* (2nd Edn.). Wydawnictwo i Handel Książkami KaBe, Krosno 2014 (in Polish).

[6] Maroński R.: *Wind Power Plants.* Wyd. PW, Warszawa 2016 (in Polish).

[7] Jagodziński W.: *Wind Engines*. PWT, Warszawa 1959 (in Polish).

[8] Chauvin A., Benghrib D.: *Drag and lift coefficients evolution of a Savonius rotor*. Exp. Fluids **8**(1989), 118–120. doi: 10.1007/BF00203076

[9] Paraschivoiu I.: *Wind Turbine Design: With Emphasis on Darrieus Concept*. Presses Internat. Polytechnique, Montreal 2009.

[10] Boas M. *Hero's Pneumatica: A study of its transmission and influence*. Isis **40**(1949), 1, 38–48. doi: 10.1086/348993

[11] Cullen C.: *Science and Civilisation in China. Vol. 5: Chemistry and Chemical Technology. Part 2: Spagyrical Discovery and Invention: Magisteries of Gold and Immortality*. China Q. **65**(1976), 143–144. doi: 10.1017/S0305741000031908

[12] Vowles H.P.: *An inquiry into origins of the windmill*. Trans. Newcomen Soc. **11**(1930), 1–14. doi: 10.1179/tns.1930.001

[13] White L.: *Medieval Technology and Social Change*. Oxford Univ. Press, London 1980.

[14] Drachman R.J.: *Extension of the variational method for Hard-Sphere Bosons*. Phys. Rev. **121**(1961), 643–647. doi: 10.1103/PhysRev.121.643

[15] Greenwood J.G., Woodcroft B.: *The Pneumatics of Hero of Alexandria, From the Original Greek*. History of science library. London, Taylor, Walton and Maberly, 1851.

[16] Hero of Alexandria, Schmidt W.: *Herons Von Alexandria Druckwerke Und Automatentheater = Pneumatica et Automata*. Legare Street Press, 2022.

[17] Bellew H.W.: *From the Indus to the Tigris*. Creative Media Partners, LLC 2018.

[18] Hedin S.A.: *Overland to India:* Vol. 2. Creative Media Partners, LLC 2018.

[19] Wulff H.E.: *The Traditional Crafts of Persia: Their Development, Technology, and Influence on Eastern and Western Civilizations*. MIT. Press, 1966.

[20] Spera D.A.: *Wind Turbine Technology: Fundamental Concepts of Wind Turbine Engineering*. ASME Press, 2009.

[21] Lyatkher V.M.: *Wind Power: Turbine Design, Selection, and Optimization*. Wiley, 2013.

[22] Wolniewicz K., Kuczyński W., Zagubień A.: *Method for wind turbine selection basing on in-field measurements*. J. Mech. Energy Eng. **3**(2019), 77–84. doi: 10.30464/jmee.2019.3.1.77

[23] Sheldahl R.E., Blackwell B.F., Feltz L.V.: *Wind tunnel performance data for two- and three-bucket Savonius rotors*. J. Energy **2**(1978), 160–164. doi: 10.2514/3.47966

[24] Pope A., Barlow J.R., Rae W.H.: *Low-Speed Wind Tunnel Testing*. Wiley India Pvt, 2010.

[25] Sharma S., Sharma R.K.: *Performance improvement of Savonius rotor using multiple quarter blades – a CFD investigation*. Energy Convers. Manage. **127**(2016), 43–54. doi: 10.1016/j.enconman.2016.08.087

[26] Saha U.K., Rajkumar M.J.: *On the performance analysis of Savonius rotor with twisted blades*. Renew. Energy **31**(2006), 1776–1788. doi: 10.1016/j.renene.2005.08.030

[27] Akwa J.V., Alves da Silva Júnior G., Petry A.P.: *Discussion on the verification of the overlap ratio influence on performance coefficients of a Savonius wind rotor using computational fluid dynamics*. Renew. Energy **38**(2012), 141–149. doi: 10.1016/j.renene.2011.07.013

[28] Akwa J.V., Vielmo H.A., Petry A.P.: *A review on the performance of Savonius wind turbines*. Renew. Sustain. Energy Rev. **16**(2012), 3054–3064. doi: 10.1016/j.rser.2012.02.056

[29] Alexander A.J., Holownia B.P.: *Wind tunnel tests on a Savonius rotor*. J. Wind Eng. Ind. Aerodyn. **3**(1978), 343–351. doi: 10.1016/0167-6105(78)90037-5

[30] Aslam Bhutta M.M., Hayat N., Farooq A.U., Ali Z., Jamil Sh.R., Hussain Z.: *Vertical axis wind turbine – a review of various configurations and design techniques*. Renew. Sustain. Energy Rev. **16**(2012), 1926–1939. doi: 10.1016/j.rser.2011.12.004

[31] Boczar T.: *Use of Wind Energy* (2nd Edn.). Wydawn. PAK, Warszawa 2010 (in Polish).

[32] Fujisawa N.: *On the torque mechanism of Savonius rotors*. J. Wind Eng. Ind. Aerodyn. **40**(1992), 277–292. doi: 10.1016/0167-6105(92)90380-S

[33] Jeon K.S., Jeong J.I., Pan J.K., Ryu K.W.: *Effects of end plates with various shapes and sizes on helical Savonius wind turbines*. Renew. Energy **79**(2015), 167–176. doi: 10.1016/j.renene.2014.11.035

[34] Kumbernuss J., Chen J., Yang H.X., Lu L.: *Investigation into the relationship of the overlap ratio and shift angle of double stage three bladed vertical axis wind turbine (VAWT)*. J. Wind Eng. Ind. Aerodyn. **107-108**(2012), 57–75. doi: 10.1016/j.jweia.2012.03.021

[35] Manwell J.F., MacGowan J.G., McGowan J.G., Rogers A.L.: *Wind Energy Explained: Theory, Design and Application*. Wiley, 2009.

[36] Saha U.K., Thotla S., Maity D.: *Optimum design configuration of Savonius rotor through wind tunnel experiments*. J. Wind Eng. Ind. Aerodyn. **96**(2008), 1359–1375. doi: 10.1016/j.jweia.2008.03.005

[37] Posa A., Parker C.M., Leftwich M.C., Balaras E.: *Wake structure of a single vertical axis wind turbine*. Int. J. Heat Fluid Flow **61**(2016), 75–84. doi: 10.1016/j.ijheatfluidflow.2016.02.002

[38] Shahizare B., Nik-Ghazali N., Chong W.T., Tabatabaeikia S., Izadyar N., Esmaeilzadeh A.: *Novel investigation of the different omni-direction-guide-vane angles effects on the urban vertical axis wind turbine output power via three-dimensional numerical simulation*. Energy Convers. Manage. **117**(2016), 206–217. doi: 10.1016/j.enconman.2016.03.034

[39] Yin C., Zhang Z., Wang Z., Guo H.: *Numerical simulation and experimental validation of ultrasonic De-Icing system for wind turbine blade*. Appl. Acoust. **114**(2016), 19–26. doi: 10.1016/j.apacoust.2016.07.004

[40] Wekesa D.W., Wang C., Wei Y., Zhu W.: *Experimental and numerical study of turbulence effect on aerodynamic performance of a small-scale vertical axis wind turbine*. J. Wind Eng. Ind. Aerodyn. **157**(2016), 1–14. doi: 10.1016/j.jweia.2016.07.018

[41] Nezamolmolki D., Shooshtari A.: *Investigation of nonlinear dynamic behavior of lattice structure wind turbines*. Renew. Energy **97**(2016), 33–46. doi: 10.1016/j.renene.2016.05.070

[42] Wang L., Kolios A., Nishino T., Delafin P.L., Bird T.: *Structural optimisation of vertical-axis wind turbine composite blades based on finite element analysis and genetic algorithm*. Compos. Struct. **153**(2016), 123–138. doi: 10.1016/j.compstruct.2016.06.003

[43] Akbar M.A., Mustafa V.: *A new approach for optimization of vertical axis wind turbines*. J. Wind Eng. Ind. Aerodyn. **153**(2016), 34–45. doi: 10.1016/j.jweia.2016.03.006

[44] Giahi M.H., Dehkordi A.J.: I*nvestigating the influence of dimensional scaling on aerodynamic characteristics of wind turbine using CFD simulation*. Renew. Energy **97**(2016), 162–168. doi: 10.1016/j.renene.2016.05.059

[45] Li Q., Murata J., Endo M., Maeda T., Kamada Y.: *Experimental and numerical investigation of the effect of turbulent inflow on a horizontal axis wind turbine (part II: Wake characteristics)*. Energy **113**(2016), 1304–1315. doi: 10.1016/j.energy.2016.08.018

[46] Campobasso M.S., Drofelnik J., Gigante F.: *Comparative assessment of the harmonic balance Navier–Stokes technology for horizontal and vertical axis wind turbine aerodynamics*. Comput. Fluids **136**(2016), 354–370. doi: 10.1016/j.compfluid.2016.06.023

[47] Chong W.T., Gwani M., Shamshirband S., Muzammil W.K., Tan C.J., Fazlizan A., Poh S.C., Petković D., Wong K.H.: *Application of adaptive neuro-fuzzy methodology for performance investigation of a power-augmented vertical axis wind turbine*. Energy **102**(2016), 630–636. doi: 10.1016/j.energy.2016.02.082

[48] Zuo W., Wang X., Kang S.: *Numerical simulations on the wake effect of H-type vertical axis wind turbines*. Energy **106**(2016), 691–700. doi: 10.1016/j.energy.2016.02.127

[49] Jia X., Jin C., Buzza M., Wang W., Lee J.: *Wind turbine performance degradation assessment based on a novel similarity metric for machine performance curves*. Renew. Energy **99**(2016), 1191–1201. doi: 10.1016/j.renene.2016.08.018

[50] Wang Y, Sun X., Dong X., Zhu B., Huang D., Zheng Z.: *Numerical investigation on aerodynamic performance of a novel vertical axis wind turbine with adaptive blades*. Energy Convers. Manage. **108**(2016), 275–286. doi: 10.1016/j.enconman.2015.11.003

[51] Menet J.L.: *A double-step Savonius rotor for local production of electricity: A design study*. Renew. Energy **29**(2004), 1843–1862. doi: 10.1016/j.renene.2004.02.011

[52] Mohamed M.H., Janiga G., Pap E., Thévenin D.: *Optimization of Savonius turbines using an obstacle shielding the returning blade*. Renew. Energy **35**(2010), 2618–2626. doi: 10.1016/j.renene.2010.04.007

**archives**
**of thermodynamics**
Vol. **44**(2023), No. 4, 705–731
DOI: 10.24425/ather.2023.150105

# Numerical simulation of two-phase gas-liquid flow through horizontal annulus pipe

**OKU EKPENYONG NYONG**[a*]
**DODEYE INA IGBONG**[b]
**CELESTINE EBIETO EBIETO**[c]
**BASSEY EKPO ENE**[a]
**BENJAMIN OLUWADARE**[d]
**ARCHIBONG ARCHIBONG ESO**[e]

[a] Thermo-fluid, Combustion and Energy System Research Group, Department of Mechanical Engineering, University of Cross River State, PMB 1123, Calabar, Nigeria

[b] Department of Mechanical Engineering, University of Port Harcourt, PMB 5323 Choba, Rivers State, Nigeria

[c] Energy and Thermofluid Research Group, Department of Mechanical Engineering, Faculty of Engineering, University of Port Harcourt, PMB 5323 Choba, Rivers State, Nigeria

[d] Department of Mechanical Engineering, Ekiti State University, PMB. 5363 Ado-Ekiti, Ekiti State, Nigeria

[e] Department of Mechanical Engineering, University of Birmingham, Academic City – Dubai – United Arab Emirates, UK

**Abstract** Chemical, petroleum and nuclear systems are only a few of the industrial processes that utilize gas-liquid flow in annular closed channels. However, concentric horizontal annuli flow patterns have received little attention. The ability to precisely characterize two-phase flow patterns using computational techniques is crucial for the production, transportation, and optimization of designs. This current research aims to establish the accuracy of the computational fluid dynamics (CFD) model in predicting the gas-liquid flow pattern in the concentric annulus pipe and validating the flow pattern of liquid holdup with experimental results from the literature.

*Corresponding Author. Email: nyong.oku@uncross.edu.ng

The simulations were done on a test section of a 12.8 m length pipe with a hydraulic diameter of 0.0168 m using air and water as the working fluids. The volume of fluid (VOF) model in Ansys Fluent based on the Eulerian-Eulerian approach in conjunction with the realizable $k$-$\varepsilon$ turbulence model was used to model the gas-liquid flow pattern, i.e. dispersed bubble, elongated bubble, and slug in a horizontal annulus. A comparison of the model with the experimental high-speed video images shows a reasonable agreement for the flow pattern and liquid holdup data.

**Keywords:** Elongated bubble flow; Gas-liquid two-phase flow; Liquid holdup; PDF; Annulus pipe; CFD modelling

## Nomenclature

| | | |
|---|---|---|
| $C_l$ | – | lift coefficient |
| $C_{wl}$ | – | wall lubrication coefficient |
| $D$ | – | pipe diameter, m |
| $F$ | – | external body force, N |
| $\vec{F}_{\text{lift}}$ | – | lift force |
| $\vec{F}_{td}$ | – | turbulence dispersion force |
| $\vec{F}_{wl}$ | – | wall lubrication force |
| $\vec{F}_{vm}$ | – | virtual mass force |
| $f$ | – | drag function |
| $G_b$ | – | generation of turbulence kinetic energy due to buoyancy |
| $G_k$ | – | generation of turbulence kinetic energy due to mean velocity gradients |
| $\vec{g}$ | – | gravitational acceleration, m/s$^2$ |
| $K_{pq} = K_{qp}$ | – | interface exchange coefficient |
| $\dot{m}_{pq}$ | – | mass flow rate from $q$ to $p$ phase, kg/s |
| $\vec{n}_w$ | – | unit normal vector pointing away from the wall |
| $P$ | – | pressure, Pa |
| PDF | – | probability density function |
| $\vec{R}_{pq}$ | – | interactive force term between gas and liquid phase |
| Re | – | Reynolds number |
| $u$, $V$ | – | fluid velocity, m/s |
| $V_{\text{SL}}$ | – | superficial liquid velocity, m/s |
| $V_{\text{SG}}$ | – | superficial gas velocity, m/s |
| $\vec{V}_{pq}$ | – | inter-phase velocity dependent on the mass flow rate |
| $v$ | – | volume, $m^3$ |
| $X$ | – | volume fraction |
| $Y_M$ | – | contribution of the fluctuating dilatation in compressible turbulence to the overall dissipation rate |
| $y^+$ | – | distance of the first grid cell, m |

### Greek symbols

| | | |
|---|---|---|
| $\varepsilon$ | – | turbulent dissipation rate |
| $\mu$ | – | dynamic viscosity, Pa s |
| $k$ | – | turbulent kinetic energy |
| $\rho$ | – | density, kg/m$^3$ |

$\sigma_k$ – turbulent Prandtl number for $k$ equation
$\sigma_\varepsilon$ – turbulent Prandtl number for $\varepsilon$ equation
$\tau$ – stress-strain tensor

**Subscripts**

$i$ – inner
$o$ – outer
$q$ – $q$-th phase
$p$ – $p$-th phase
$L$, $l$ – liquid
$G$, $g$ – gas
SL – superficial liquid
SG – superficial gas

**Acronyms**

CFD – Computational Fluid Dynamics
FSI – Fluid Structure Interaction
LIF – Laser-Induced Fluorescence
PIV – Particle Image Velocimetry
RANS – Reynolds-Average Navier-Stokes
RSM – Reynolds Stress Model
SIMPLE – Semi-Implicit Method for Pressure Linked Equation
VOF – Volume of Fluid
3D – 3 Dimensional

# 1 Introduction

The transportation of two-phase media such as liquid-liquid or gas-liquid flow is common in many industries, including the chemical, nuclear, oil, and gas industries. In oil and gas facilities, flow parameters like flow pattern, liquid holdup, and pressure drop are observed and must be precisely predicted when constructing production systems as well as maintaining and running downstream facilities. These parameters enhance a reliable design for a two-phase flow pipeline and engineers can develop pipeline operation in the best possible way by having a thorough knowledge of the flow characteristic being demonstrated in a domain. Flow patterns or regimes in two-phase flow refer to the different types of fluid behaviour that can occur when two immiscible fluids (e.g., gas-liquid, liquid-liquid, etc.) flow together in a pipeline and disperse into different regions within the conduit. The flow pattern is influenced by a number of factors such as pipe geometry [1,2], fluid parameters [3–5], and the conditions of flow, which influence the flow pattern or regime [6]. The work of Ekberg *et al.* [7] studied the

impact of pipe geometry in a narrow horizontal annulus where the flow pattern was tested on two different annuli. The first pipe geometry has an inner diameter ($D_i$) and outer diameter ($D_o$) of 0.0066 m and 0.00863 m, respectively, while the second pipe geometry has an inner diameter ($D_i$) and outer diameter ($D_o$) of 0.03315 m and 0.0352 m, respectively [7]. Plug, slug, distributed bubble, churn, and other hybrid regimes were among the outcomes they got in their studies.

Numerous studies have been undertaken throughout the years to understand and gain more insight into the flow characteristics in these channels because of the significance of two-phase flow in annuli. Previous studies have shown that the centre pipe's flow obstruction causes the flow structure in the annuli configuration to differ from that of circular pipes [8, 9]. Additionally, compared to vertical flow, the gravitational effect causes the annulus with horizontal geometry to exhibit more complex flow behavior, thus, various flow regimes have distinct characteristics [9]. However, flow characteristics with unrestricted channels have been extensively studied experimentally [10,11] with the vertical [12,13] and inclined pipelines [14–16]. In horizontal annulus settings, the most common flow regimes captured by high-speed camera photography are the dispersed bubble, elongated bubble, slug, wavy slug, churn, wavy annular, and annular [8, 17]. Previous research has demonstrated that annulus eccentricity has an effect on the shape and structure of the wavy annular, elongated bubble, and annular flow regimes [8,18]. The transition from elongated bubble to dispersed bubble may occur at high liquid superficial velocities [8]. In comparison, a fully eccentric annulus, as opposed to a concentric annulus, causes the transitions between various flow regimes to happen at higher liquid and lower gas superficial velocities [8, 19]. According to other researchers, flows in totally eccentric annuli have a more well-defined structure than concentric annuli. However, the concentric annulus results in a greater pressure drop than the fully eccentric annulus [20]. Abdulkadir [2] presented an experimental and numerical investigation of gas-liquid flow in 90-degree curved pipes. The study aims to understand the effects of curvature on flow behaviour, including flow patterns, pressure drop and liquid holdup. The experiments were conducted using air and water as the gas and liquid phases, respectively. Different flow patterns, such as stratified flow, wavy stratified flow, and annular flow were observed in the curved pipes for different gas and liquid flow rates. The pressure drop and liquid holdup are measured and compared with the predicted values found from existing correlations. In addition to the experimental work, numerical simulations using the commer-

cial CFD software Star-CCM+ [20] were performed to gain further insights into the gas-liquid flow behaviour in the curved pipes. The simulations use the Eulerian-Eulerian approach to model the two-phase flow and the $k$-$\varepsilon$ turbulence model to account for turbulence effects. The CFD results show good agreement with the experimental data for the flow patterns and pressure drop. The simulations also provide detailed information on the velocity and turbulence fields, revealing the complex flow behavior near the bend region [2]. Friedemann *et al.* [21] carried out a numerical study on the two-phase flow at 0–40° inclination in an eccentric annulus. They implemented the $k$-$\omega$ turbulence model with VOF in the Open FOAM solver [20]. In their analysis, they discovered that the horizontal case had a slug and wavy flow regime. Sultan *et al.* [22] conducted a CFD study to investigate the pressure losses and deposition velocities in horizontal annuli with different geometries and particle sizes. The study used Ansys Fluent software [23] to simulate the flow of air and particles in two different annulus geometries, namely a concentric annulus and an eccentric annulus. The particle size and the velocity of the air flow were varied to investigate their effects on the pressure losses and deposition velocities. The results of the study showed that the pressure losses in the eccentric annulus were higher than those in the concentric annulus. This was attributed to the presence of a narrow gap between the inner and outer walls of the eccentric annulus, which caused a higher resistance to flow and increased turbulence. The study also found that the pressure losses increased with increasing particle size and air flow velocity. The study also investigated the effects of different annulus geometries on the deposition velocities. The results showed that the eccentric annulus had higher deposition velocities than the concentric annulus due to the increased turbulence and particle-wall interactions in the narrow gap region. Gouidmi *et al.* [24] carried out a study on two-phase flow through an upward vertical concentric annular pipe. They investigated the effect of different flow conditions such as the gas and liquid flow rates, on the flow patterns, void fraction distribution and pressure drop. They implemented the VOF and $k$-$\varepsilon$ turbulence models to simulate the flow, and the numerical results were validated against experimental data. They found out that the flow patterns in the annulus pipe were strongly influenced by the gas and liquid flow rates. The annular flow regime was observed at low gas and high liquid flow rates, while the dispersed bubble flow regime was observed at high gas and low liquid flow rates. The study also found that the void fraction distribution and pressure drop were strongly affected by the flow conditions and the flow regime. The study concluded that the numerical

model was able to predict the flow patterns and pressure drop in the annulus pipe reasonably well and provided useful insights into the behaviour of the two-phase flow in the pipe [24]. Kiran *et al.* [13] investigated two-phase flow in a vertical annulus using both experimental and modelling methods. Their model entails using two turbulence models (realizable $k$-$\varepsilon$ and SST $k$-$\omega$ models) coupled with the VOF model to simulate the pressure drop, void fraction and flow regime. Their model predictions and the experimental result agreed rather well, with a mean error of 20%. Nyong *et al.* [17] numerically studied the CFD analysis of the liquid holdup and flow regime in an annulus section. They implemented the VOF model coupled with the turbulence model (realizable $k$-$\varepsilon$) to predict liquid holdup and dispersed bubble flow patterns. Within the condition studied at $V_{SG} = 0.18$ m/s and $V_{SL} = 1.94$ m/s, they observed the dispersed bubble flow which is composed of tiny gas bubbles dispersed throughout a continuous liquid phase. Segev *et al.* [25] worked on slug regime transitions in a two-phase flow in a horizontal rounded pipe using CFD simulations aimed to investigate the characteristics of flow pattern transitions between slug and wavy regimes in gas-liquid two-phase flows. The study used a commercial CFD code Ansys Fluent to model the two-phase flow in a horizontal round pipe. The volume of fluid (VOF) method was employed to capture the gas-liquid interface, while the $k$-$\varepsilon$ turbulence model was used to simulate the turbulence effects. Their simulation results showed that the flow pattern transition from slug to wavy regime is primarily affected by the gas superficial velocity and liquid viscosity. The slug-to-wavy transition was found to occur at a lower gas velocity when the liquid viscosity was increased. Additionally, the simulations revealed that the transition from wavy to slug regime occurs at a higher gas velocity as compared to the slug-to-wavy transition.

In addition, it is established that flows in the gas phase are difficult to mathematically describe [26]. Yunpeng *et al.* [27] conducted a thorough review of the research on annular two-phase flow in vertical pipes, with a focus on investigation methodologies and advances in understanding the mechanism. Some of the experimental techniques used to measure the flow regime, void fraction and film thickness were such as the optical method [28], Laser-induced fluorescence (LIF) [29, 30], particle image velocimetry (PIV), wire mesh sensor [31], gamma-absorption technique [32], etc.

Model validation on horizontal annulus configurations and flow regime features have received relatively little research. The vast majority of descriptions of flow regimes universally relied on experimental evidence [7,8,19,33], analytical models [34] and mechanistic models [4, 15, 19, 35–37], while the

flow channel unusual shapes obstructed and deformed vision, making the experiment difficult. It is important to note that most research done prior to 2000 had limitations on data and application ranges [38]. However, among the most popular tools used for examining and characterizing flow regimes in complex geometries are CFD tools. The physics of flow, accessibility of computational resources, the level of accuracy required, and the time needed for the solution – all have an impact on the fidelity of the results and the selection of turbulence model for a CFD problem. The usefulness of well-known Reynolds-averaged Navier-Stokes (RANS) turbulence models, that is the $k$-$\varepsilon$ model, $k$-$\omega$ model, and RSM in addition to large eddy simulation (LES) for steady fluid flow *via* pipelines has considerably been investigated in literature [39–42]. This current research aims at establishing the accuracy of the CFD model in predicting the gas-liquid flow pattern in the concentric annulus pipe and validating the flow pattern liquid holdup with experimental results from the literature [8].

## 2 Model

### 2.1 Computational geometry

The model was developed using the Ansys 19.0 commercial package [23]. ANSYS 19.0 Workbench [23] offers a user-friendly and intuitive graphical interface that allows users to access and navigate through different simulation tools and workflows. It seamlessly integrated with CAD software, allowing users to import geometries directly from computer-aided design (CAD) systems and perform simulations on the CAD models. This integration streamlines the simulation setup process and ensures accurate geometry representation. It also supports multiphysics simulations, enabling users to analyse the interactions between different physical phenomena. It allows for coupling between fluid dynamics, thermal analysis, and more to accurately model real-world engineering problems. This model was actualized on an HP Intel Core I7 computer with 12 Gigabytes of RAM and a 4.7 GHz microprocessor. The geometry for the CFD model were prepared in Ansys 19.0 workbench [23]. The model has two sections. The first section is made of a stainless steel of length 2 m and the section proceeding the 2 m section is a test section, which is transparent pipe of length 10.8 m as shown in Fig. 1. The mixtures (gas and liquid) are injected separately into the test section via an inclined pipe at 90° forming a tee section at the beginning of the test section. Figure 1 depicts the geometrical parameters of

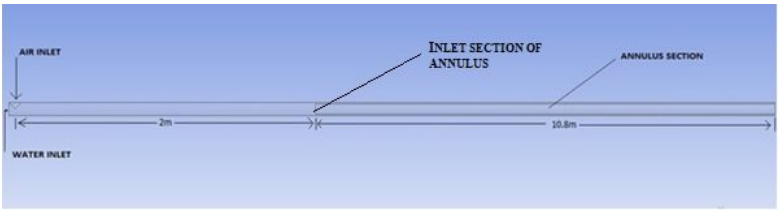


Figure 1: The side view with dimensions of the test section of the facility.

test section of the facility. Details of experimental setup of the test facility and representation of the geometrical can be found in the works of Eyo *et al.* [8]. Gas and liquid enters the 2 m pipe length through the air and water inlet port and mixing of the fluid takes place along the 2 m pipe section before advancing to the inlet section of the annulus. This arrangement is to allow for fully developed flow along the axial direction as earlier detailed in the experimental setup [43, 44]. The annulus section is made of pipe in pipe configuration. This arrangement has two PVC pipes, one with an inner pipe diameter of 0.06 m and the other with an outer pipe diameter of 0.078 m placed concentrically forming hydraulic diameter of 0.0168 m. The geometric parameters for the simulation is found in Table 1. The fluid used at the entrance are gas (air) and liquid (water) phase, which are assigned with velocities called the superficial velocities of gas and liquid respectively. The phases have been clearly defined with the primary phase as air and the secondary phase as water. The volume fraction and the density of each phase were both prescribed at the entrance. The properties of the fluid used for this simulation is found in Table 2. The pipe roughness height was

Table 1: Geometric parameters for the CFD calculation [1].

| Geometrical parameter | Value |
|---|---|
| Outer pipe diameter (m) | 0.0768 |
| Inner pipe diameter (m) | 0.060 |
| Hydraulic diameter (m) | 0.0168 |
| Length of mixing section (m) | 2 |
| Length of annulus section (m) | 10.8 |
| Wall roughness height (m) | 0.000015 |
| Wall roughness constant | 0.5 |

considered to be 0.000015 m for the wall, while the roughness constant was taken as 0.5. The gas-liquid phases were maintained at a room temperature of 15°C and atmospheric pressure of 101 325 Pa. The superficial gas and liquid velocities for the conditions studied ranges from 0.18 to 0.62 m/s and 0.28 to 1.94 m/s respectively. The time-series of area average liquid hold-up were recorded from inlet section of the annulus pipe up to about 6 m.

## 2.2 Mesh distribution and study

The outcome of the simulation relies greatly on the mesh characteristics. The geometry of the annulus section is a circular pipe. The variation in mesh construction is one of the primary causes of deviations in flow characterization. Mesh sensitivity is used to describe the dependence of the numerical results on the mesh size used in the simulation. The grid or mesh of points is used to discretize the domain being simulated such as a fluid domain or a solid domain. In a numerical simulation, the results are typically more accurate as the mesh size is reduced, because a finer mesh captures more details of the flow or behaviour as being simulated. However, using a very fine mesh can be computationally expensive and time-consuming, and may not always be necessary. In this study, a numerical simulation was run with different mesh densities and comparing the results to determine if the solutions are significantly affected by increasing the mesh density. This helps to identify the optimal mesh density to use for this simulation, balancing accuracy and computational efficiency. The current simulation was performed by running with a coarse mesh and gradually refining the mesh until the results converge and are no longer significantly affected by further refinement. As a result of no-slip condition, the shear flow that develops near the wall contributes to the instability of the interface and is therefore essential to the development of the overall flow. Figure 2 shows the top and side view of the annulus section; it is seen that for the present modelling a quadrilateral structured mesh was selected and refined near the inner and outer wall region and reasonably coarser mesh at the central region of the annulus [45]. The simulation was tested at conditions of superficial velocities of $V_{\mathrm{SL}} = 1.94$ m/s and $V_{\mathrm{SG}} = 0.18$ m/s, with fluid density for liquid and gas given as $\rho_L = 998.2\ \mathrm{kg/m^3}$ and $\rho_G = 1.225\ \mathrm{kg/m^3}$, respectively. The pressure was taken after the entrance length of 2 m that is at the inlet of the annulus section.

Figure 3 clearly shows the decline in pressure gradient from 25 kPa to about 14.7 kPa, where a consistency is maintained at a mesh density be-

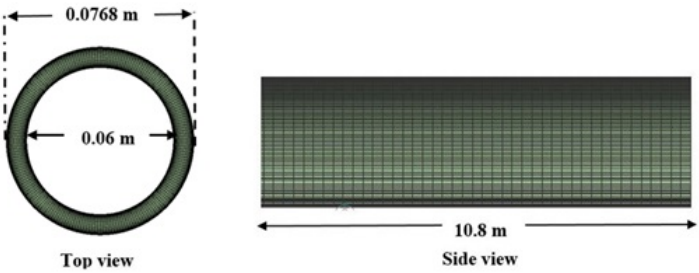


Figure 2: The top and side view of the annulus section.

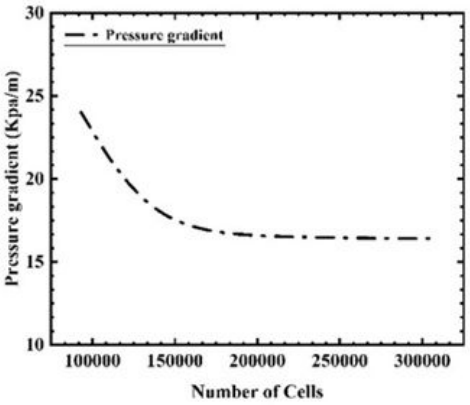


Figure 3: The mesh sensitivity analysis.

tween 205 000 and 306 000 cells. Further increase in the volume of cells resulted in no significant change in the pressure gradient (less than 0.4%). However, the flow solution and the integrated quantities will not be altered even if the number of mesh cells used to model the flow is increased beyond this volume of cells. Therefore, the mesh density of 205 000 cells was used in simulating the flow conditions. The mesh quality recorded an orthogonal quality of 0.998 which signifies a very good mesh. It is important to note that mesh sensitivity is just one aspect of the overall numerical simulation accuracy, and other sources of error such as boundary conditions and numerical scheme were also considered.

The $y^+$ was used as a guide to determine the appropriate wall modelling strategy to use in the simulation. The $y^+$ value in CFD modelling is determined by the distance of the first grid cell from the wall of the simulation domain, typically a solid boundary. The $y^+$ value is a dimensionless param-

eter used to evaluate the adequacy of the resolution of the near-wall region of a CFD simulation. It is defined as

$$y^+ = \frac{(\rho u y)}{\mu}, \tag{1}$$

where $\rho$ is the fluid density, $u$ is the velocity of the fluid, $y$ is the size of the first grid cell. If the $y^+$ value is too high, the first grid cell may not be able to accurately capture the flow behaviour in the near-wall region, leading to incorrect or inconsistent results. On the other hand, if the $y^+$ value is too low, the simulation may become computationally expensive or unstable, as a large number of grid cells would be needed to resolve the boundary layer. Typically, for this study, a $y^+$ value of 1 was used for wall-resolved simulations, where the near-wall region was resolved with the grid. However, a value of $y^+ > 30$ has been the recommended standard for wall-modelled simulations, where the near-wall region is modelled using the $k$-$\varepsilon$ turbulence model [23]. In the current work, a $y^+$ above 50 was adopted. The boundary conditions were specified at the inlet port for water and gas and at the inlet section of the annulus, while the outlet port was denoted as the pressure outlet condition. The turbulence was specified in terms of intensity and hydraulic diameter. The intensity was assumed to be 5%, while the hydraulic diameter was 0.0168 m in this case. The outlet was open to the atmosphere and hence the pressure at the outlet boundary was considered to be 0 Pa (gauge pressure). At the entrance, both the density and volume fraction of each phase were specified. The fluid properties of gas and liquid used in the simulation are given in Table 2.

Table 2: Fluid properties for the CFD simulation study.

| Density of liquid ($\rho_L$), kg/m$^3$ | Density of gas ($\rho_G$), kg/m$^3$ | Dynamic viscosity of liquid ($\mu_L$), kg/ms | Dynamic viscosity of gas ($\mu_G$), kg/ms | Temperature of the fluid, °C | Pressure, Pa | Surface tension ($\sigma$), N/m |
|---|---|---|---|---|---|---|
| 998.2 | 1.225 | 0.000894 | 0.00001821 | 15 | 101325 | 0.07286 |

## 2.3 Computational method

The VOF model is based on the Eulerian–Eulerian approach, which is used in the current CFD simulation. The VOF model works on surface tracking methods implemented for immiscible (two-phase) fluids [46]. It can be

applied for steady or transient tracking of any gas-liquid interface. The VOF model is effectively used in this work because of its relative simplicity and low computational cost. The approach of the Eulerian-Eulerian approach is that it separately solves equations of conservation of mass and momentum for each phase, however allowing interaction between both phases through interfacial terms. However, the conservation equations can be derived by averaging the local instantaneous balance for each phase [47], or the mixture theory method could be applied [48, 49]. If the phase is $q$ then phase volume $v_q$ is given as

$$v_q = \int X_q \, dv, \tag{2}$$

$$\sum_{q=1}^{n} X_q = 1, \tag{3}$$

where $X_q$ – the volume fraction phase and $n$ signifies the number phases. In the modelling, '$q$' and '$p$' represent the primary phase of liquid and '$q$' represents the secondary phase of gas, respectively. Assuming no mass transfer occurs; the gaseous phase is referred to as a dispersed phase, while the liquid phase is represented as a continuum, and the governing equations (continuity and momentum) for the gas phase are given by Eqs. (4)–(5) [50, 51]:

$$\frac{\partial}{\partial t}\left(\rho_q X_q\right) + \nabla \cdot \left(\rho_q X_q \vec{V}_q\right) = 0, \tag{4}$$

$$\begin{aligned}\frac{\partial}{\partial t}\left(\rho_q X_q \vec{V}_q\right) + \nabla \cdot \left(\rho_q X_q \vec{V}_q \vec{V}_q\right) &= -X_q \nabla P + \nabla \cdot \overline{\tau}_q + \rho_q X_q \vec{g} \\ &+ \sum_{p=1}^{n} \left(\vec{R}_{pq} + \dot{m}_{pq}\vec{V}_{pq} - \dot{m}_{qp}\vec{V}_{qp}\right) \\ &+ \left(\vec{F}_q + \vec{F}_{\text{lift},q} + \vec{F}_{td,q} + \vec{F}_{wl,q} + \vec{F}_{\nu m,q}\right),\end{aligned} \tag{5}$$

where $\rho_q$ is the density of the $q$-th phase in the solution domain and $\vec{V}_q$ is the velocity of the $q$-th phase, $P$is the pressure shared by the entire phase, $\overline{\tau}_q$ is the $q$-th phase stress-strain tensor, $\vec{g}$ is the acceleration due to gravity, $\dot{m}_{pq}$ is the mass flow from ($q$ to $p$) phase, $\vec{F}_q$ is the external body force, $\vec{F}_{lift,q}$ is the lift force, $\vec{F}_{td,q}$ is the turbulence dispersion force, $\vec{F}_{wl,q}$ is the wall lubrication force and $\vec{F}_{\nu m,q}$ is the virtual mass force which is applied upon the particle owing to the inertia of the primary mass encountered by the accelerated particle and if there are droplets entrained constantly between the '$q'$(gas) and '$p'$(liquid) phases, $\vec{R}_{pq}$is an interaction force between the

gas and liquid phases, $\vec{V}_{pq}$ is the inter-phase velocity, and it is dependent on the mass flow rate.

The secondary phase (gas phase) of gas-liquid flows is assumed to form bubbles and exchange momentum with the liquid through the drag term as it passes through. The drag term, which dominates all other interfacial terms, is defined in Eq. (6) as

$$\sum_{p=1}^{n} \vec{R}_{pq} = \sum_{p=1}^{n} K_{pq} \left( \vec{V}_p - \vec{V}_q \right), \tag{6}$$

where $K_{pq} = K_{qp}$ is the interface exchange coefficient given as

$$K_{qp} = \frac{X_q X_p \rho_q f}{\tau_q}. \tag{7}$$

Here $f$ is the drag function dependent on the Reynolds number. In contrast to the anisotropic drag law employed in this work, the bulk of drag models are isotropic in nature. This has an advantage over other drag laws in that it permits higher drag in the normal direction to the interface and lower drag in the tangential direction to the interface. When calculating the lift force, consideration is given to the liquid shear field, which acts perpendicular to the main flow direction and is proportional to the gradient of the liquid velocity field. Equation (8) gives the lift force in terms of the slip velocity and the curl of the liquid phase velocity:

$$\vec{F}_{\text{lift},g} = -C_l \rho_g X_g \left( \vec{V}_l + \vec{V}_g \right) \times \left( \nabla \times \vec{V}_l \right). \tag{8}$$

Compared to the drag force, the lift force is negligible, but it is significant for larger bubbles. For the model, the Eötvös number determines the lift force. This model offers some advantages in the prediction of the bubble size cross-over point at which particle distortion results in a change in the lift force sign. The liquid flow rate between the wall and the bubble is less than that between the bubble and the main flow, which results in the wall lubrication force. The wall lubrication force equation is written as

$$\vec{F}_{wl,g} = C_{wl} \rho_l X_l \left( \vec{V}_l + \vec{V}_g \right)_{\parallel} |\vec{n}_w. \tag{9}$$

The realizable ($k$-$\varepsilon$) turbulence model developed by Launder and Spalding [52] with standard wall functions was implemented in the Ansys code [23] to solve the flow problem. The $k$-$\varepsilon$ turbulence model is an isotropic turbulence model that is well suited for modelling the gas phase in two-phase flow

because it takes into account the effects of turbulent eddies on the transport of momentum and energy. It is based on two transport equations, one for the turbulent kinetic energy ($k$) and the other for the rate of dissipation of the turbulent kinetic energy ($\varepsilon$). It is computationally efficient, making it well-suited for modelling large-scale and complex two-phase flow problems. For the current work, the $k$-$\varepsilon$ turbulence model was chosen because of its robustness. It had been used by previous authors to validate flow applications [53]. In that juncture, the model is used to improve the numerical solution of flows. The simultaneous solution of two separate transport equations is made possible by two-equation turbulence models, and thus allows for the measurement of the turbulent time scale and length. The transport equations for the $k$-$\varepsilon$ model are given by the following Eqs. (9) and (10) [23, 52]:

$$\frac{\partial}{\partial t}(\rho k)+\frac{\partial}{\partial x_i}(\rho k u_i)=\frac{\partial}{\partial x_j}\left[\left(\mu+\frac{\mu_t}{\sigma_k}\right)\frac{\partial k}{\partial x_j}\right]+G_k+G_b-\rho\varepsilon-Y_M+S_k \quad (10)$$

and

$$\frac{\partial}{\partial t}(\rho\varepsilon)+\frac{\partial}{\partial x_i}(\rho\varepsilon u_i)=\frac{\partial}{\partial x_j}\left[\left(\mu+\frac{\mu_t}{\sigma_\varepsilon}\right)\frac{\partial \varepsilon}{\partial x_j}\right]+C_{1\varepsilon}\frac{\varepsilon}{k}(G_k+C_{3\varepsilon}G_b) - C_{2\varepsilon\rho}\frac{\varepsilon^2}{k}+S_\varepsilon\,, \quad (11)$$

where $u_i$ are the components of velocity in $x_i$-direction, $x_i$ are the Cartesian coordinates ($i = 1, 2, 3$), $t$ is the time, $G_k$, $G_b$, $Y_M$ are the generation of turbulence kinetic energy as a result of mean velocity gradients, generation of turbulence kinetic energy due to buoyancy, and the contribution of the fluctuating dilatation in compressible turbulence to the overall dissipation rate, respectively. $C_{1\varepsilon}$, $C_{2\varepsilon}$, and $C_{3\varepsilon}$ are constants, $\sigma_k$, and $\sigma_\varepsilon$ are turbulent Prandtl numbers for $k$ and $\varepsilon$, respectively, while the source terms are represented as $S_k$ and $S_\varepsilon$.

In the current simulation, after the mesh has been created, the boundary condition were stated. At the walls, the conditions were assumed to be non-slip at $v = 0$, and the approach of the wall function was used. The implicit body force was enacted in the model to satisfy the equilibrium condition between body force and pressure gradient terms of the momentum equation, which also handles the convergence issues in case of partial equilibrium. A pressure-based solver was used where the governing equations were discretized adopting the finite volume method. Semi-Implicit Method for

Pressure-Linked Equations (SIMPLE) scheme was activated for pressure-velocity coupling calculations [23]. For the spatial discretization, PRESTO (Pressure Staggering Option) was adopted for pressure coupling, the second order upwind for the momentum, turbulence kinetic energy and turbulence dissipation rate. Furthermore, to save computational cost, the first order implicit scheme was adopted for the transient formulation. The inlet flow conditions were initialized using the usual initialization procedure. The liquid phase was patched throughout the entire flow domain after initiation. 100 iterations were permitted for each step, with a time step of 0.001 s, which satisfies the convergence criteria [54]. The standard convergence criterion of 0.0001 was selected for residuals of continuity, velocity ($u$, $v$, $w$), kinetic energy ($k$) and dissipation rate ($\varepsilon$). Flow time was used to track parameters such as volume fraction and pressure gradient. From the Ansys Fluent solver, the time series and probability density function (PDF) plots of liquid holdup were obtained. The area weighted average volume fraction distribution was captured in order to further characterize the flow pattern that was observed in the modelling. The previous studies [13] have made extensive use of PDF to describe the flow structure and calculate the fraction of liquid holdup in the spatial domains employing the kernel density function of MATLAB to plot the pattern of flow. In this present work, the kernel smoothing density function of MATLAB was adopted to describe the PDF for the CFD flow patterns.

## 2.4 Validation

The validation of the model started with checking the mesh quality, which is crucial in getting the right numerical solutions. The convergence behaviour was checked by initiating several runs and varying the density of cells. The pressure drop along the pipe was used as a criterion to check the convergence behaviour. The cell values of the corresponding pressure gradient are shown in Fig. 3. The numerical simulation was validated with the experimental work of Eyo *et al.* [8]. Three conditions of study were initiated with the superficial velocities displayed in Table 2. Case 1 represents the simulated data for superficial velocities for air-water at $V_{SG} = 0.18$ m/s and $V_{SL} = 1.94$ m/s, respectively. Case 2 represents the simulation data for air-water with superficial velocities of $V_{SG} = 0.21$ m/s and $V_{SL} = 0.27$ m/s, and lastly, Case 3 represents the simulation data for air-water with a superficial velocities at $V_{SG} = 0.62$ m/s and $V_{SL} = 0.28$ m/s. The test matrix for the simulation is displayed in Table 2. The study was to establish the

accuracy of the turbulent model in predicting the flow regime in an annulus concentric pipe. The VOF model in Ansys 19.0 [23] was used with the Eulerian-Eulerian approach in conjunction with the turbulence (realizable $k$-$\varepsilon$) model to simulate the gas-liquid flow pattern. The modelling was carried out on an axial length of 12.8 m as shown in Fig. 1. The entire length was calculated for a simulation time of 10 s; the time it takes for the fluid to be fully developed along the 2 m section of the pipe was ignored. The calculated volume fractions of air and water were taken on a distance of 6.01 m from the inlet to the annulus section. Results obtained from the CFD simulation show that the VOF and $k$-$\varepsilon$ model are adequate to mimic the flow pattern for elongated bubble and slug flow. Slight deviations were found in PDF of liquid holdup as compared with the experimental results, which is depicted in Figs. 4–9.

Table 3: Conditions and flow regime.

| Cases | Superficial velocity for liquid ($V_{SL}$), m/s | Superficial velocity for gas ($V_{SG}$), m/s | Flow regime |
|---|---|---|---|
| 1 | 1.94 | 0.18 | Dispersed bubble |
| 2 | 0.27 | 0.21 | Elongated flow |
| 3 | 0.28 | 0.62 | Wavy slug flow |

# 3 Results and discussions

## 3.1 Dispersed bubble flow

Figure 4(a) shows the CFD contours of water volume fraction at the condition of $V_{SG} = 0.18$ m/s and $V_{SL} = 1.94$ m/s, respectively. The CFD image is taken from the point where the fluid mixture enters the annulus section up to 6.01 m along the annulus section of the pipe. In Fig. 4(a), the contour plot shows the dispersed bubble flow in a horizontal concentric annulus pipe that is characterized by the formation of small gas bubbles dispersed throughout the liquid phase. These bubbles are small in size and have a spherical or elongated shape. The bubbles tend to move in a random motion, colliding and coalescing with each other, which could lead to changes in their size and shape. The liquid phase in dispersed bubble flow occupies the majority of the pipe volume, while the gas phase is dispersed as bubbles throughout the liquid phase. This type of flow is predominant with low superficial gas velocity and higher superficial liquid velocity as reported by previous

authors [8, 17]. These bubbles are created by the breaking of the slug and the movement of elongated bubbles along the annulus section. This effect results in significant liquid holdup values along the annulus region. The shape of the bubbles can also influence their dynamics, with non-spherical bubbles experiencing different drag forces than spherical bubbles. The distribution of bubbles in the flow can affect the overall flow behaviour, as the presence of bubbles can induce turbulence and promote mixing between the phases. The dynamics of dispersed bubbles can lead to a variety of complex phenomena such as bubble coalescence, breakup, and interaction with solid surfaces. For example, bubble coalescence can lead to the formation of larger bubbles, which can alter the overall flow characteristics and reduce the mass transfer efficiency. On the other hand, bubble breakup can lead to the formation of smaller bubbles, which can increase the interfacial area and promote mixing between the phases [55–57]. Figure 4(b) depicts the video image captured from the high speed camera, which shows the formation of very small gas bubbles dispersed throughout the liquid phase. The bubbles of the CFD image look slightly larger than those of the experiment; this might be attributed to the runtime of the simulation, which if run further between 12 s and 15 s, it could have captured more details of the breakup of large bubbles.

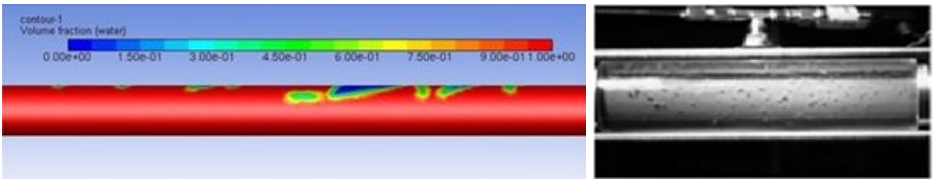


(a) (b)

Figure 4: (a) CFD contour plot of volume fraction of water in the annulus region; (b) visual image of dispersed flow from high speed camera [1]; $V_{SG} = 0.18$ m/s and $V_{SL} = 1.94$ m/s.

The flow pattern is further characterized by using the time series of the liquid holdup for the experimental data and the PDF plots of liquid holdup generated from the CFD data. Figure 5(a) depicts the simulated variation of the liquid holdup. In Fig. 5(b), it is seen that the dispersed bubble flow exhibits a uniform oscillation of the time-varying liquid holdup between the values of 0.917 and 0.93, which is close to 1, indicating the presence of spherical bubbles scattered along a continuous liquid phase as revealed in Fig. 5(a). The liquid holdup of the dispersed gas phase (i.e. the bubbles) is

very small, while the liquid phase occupies almost the entire volume of the flow as rightly observed by other authors [57]. When compared with the time variation of liquid holdup in the experiment, a more steady oscillation was observed for time variation liquid holdup of about 1 signifying the dispersed bubble in a continuous liquid phase. Figure 5(c) shows a comparison between the simulated CFD model and experimental PDF trend; both the simulation and experiment showed their unimodal peak values at liquid holdup values of 0.93 and 0.97, respectively which is eventually close to 1. Then, the error of the CFD simulation is estimated to be 4% when compared with the experimental data. From the plot, it is established that the VOF model coupled with the $k$-$\varepsilon$ turbulence model adequately predicts the probability density function (PDF) trend of liquid holdup for dispersed bubble flow.

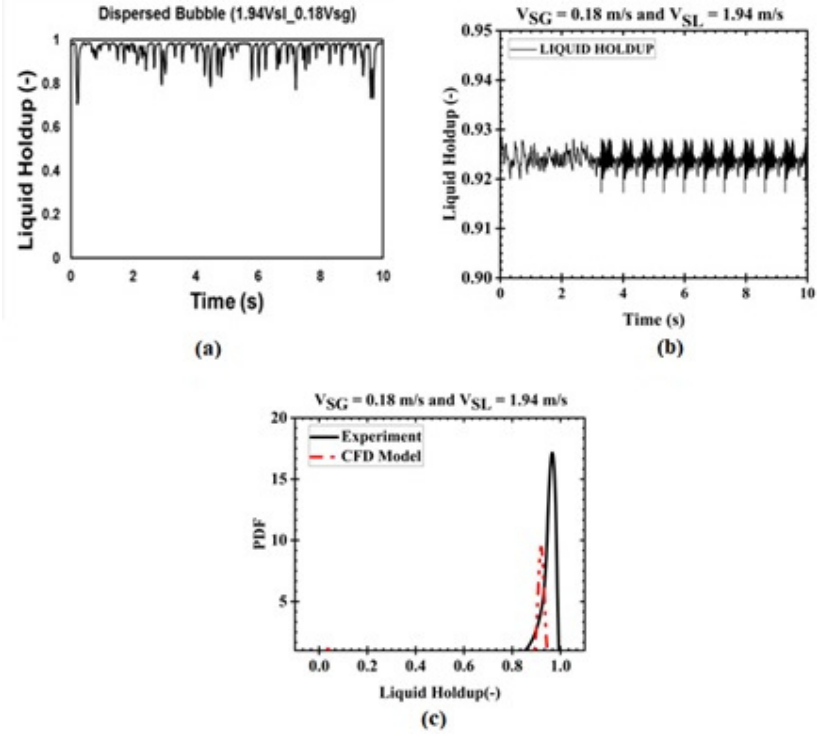


Figure 5: The time variation of liquid holdup and PDF trend at $V_{SG} = 0.18$ m/s and $V_{SL} = 1.94$ m/s: (a) the measured time variation of liquid holdup, (b) PDF trend obtained for dispersed bubble by visual image in literature [1], (c) comparison of PDF of simulated variation of liquid holdup with the experimental trend for dispersed bubble flow.

### 3.2 Elongated bubble flow

Figure 6(a) depicts the calculated contours of liquid volume fraction for the elongated bubble at $V_{SG} = 0.27$ m/s and $V_{SL} = 0.21$ m/s. Within the region, the bubble flow is characterized by a discontinuous liquid body that fills the annulus zone and is limited at its top by gas plugs. As previously reported in the literature [57–59], at lower gas and liquid superficial velocities, this particular flow pattern is significant and is characterized by an alternating liquid body that fills the entire cross section of the annulus and gas plugs confined at the annulus top. The pattern of the formed gas plug is rightly conditioned by the annulus configuration. The elongated bubble flow is formed in a horizontal concentric annulus pipe as a result of continuous gas phase flow through a liquid phase, creating elongated bubbles. The shape of the annulus and the flow rates of the gas and liquid phases can influence the formation of elongated bubbles. At low liquid flow rates, elongated bubbles can form due to the low frequency of liquid slugs. At high gas flow rates, the gas can displace the liquid and create elongated bubbles. Additionally, the presence of obstacles or bends in the annulus can also affect the formation of elongated bubbles.

In comparison with the experimental image captured from the high speed camera in Fig. 6(b), the calculated elongated bubbles are slightly larger in shape; this might be due to the shear force acting on them in the centre of the annulus. It is seen that the VOF and $k$-$\varepsilon$ model adequately predict the flow pattern for elongated bubble as compared with the video image obtained from the experiment.

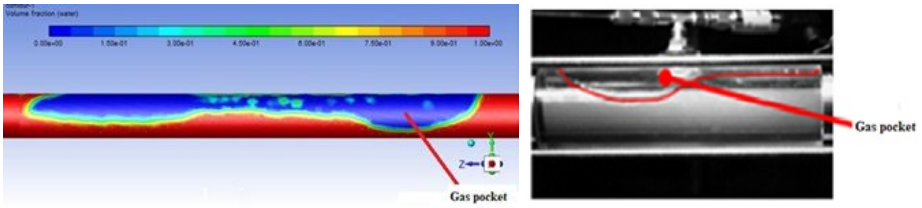


(a) (b)

Figure 6: Comparison between (a) CFD contour plot of volume fraction of water in the annulus section for elongated bubble flow and (b) visual image of elongated bubble flow from a high speed camera [1]; $V_{SG} = 0.27$ m/s and $V_{SL} = 0.21$ m/s.

The time variation of liquid holdup in the experiment and the CFD model is shown in Fig. 7. In Fig. 7(a), the time variation of liquid holdup plot in the experiment fluctuated intermittently from a crest value of 0.8 to

a crest value of 1, which indicates high closeness to liquid holdup value. This means that the annulus section is completely filled with liquid, as indicated by the higher crest value. The crest value for the simulated time-varying liquid holdup plot was observed to fluctuate between 0.1 and 0.6. It can be seen that the CFD model underestimates the time-varying liquid holdup for elongated bubble flow. In contrast to the visual appearance from the experiment, the PDF trend from the simulated data in Fig. 7(c) displays two peak values that are further apart with bimodal peak values of 0.2 and 0.6, while the experimental results demonstrate two peak values of liquid holdup of 0.7 and 1.0.

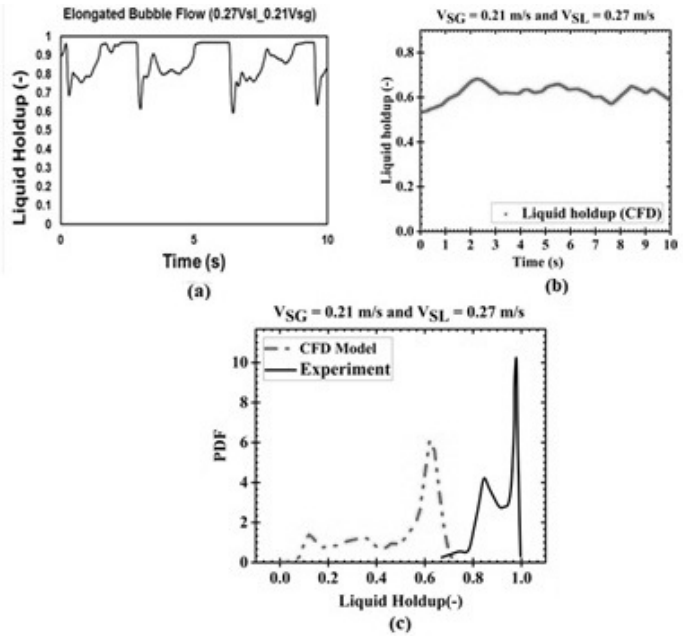


Figure 7: The time variation of liquid holdup and the PDF of liquid holdup at $V_{SG}$ = 0.27 m/s and $V_{SL}$ = 0.21 m/s: (a) the experimentally measured time variation of liquid holdup for elongated bubble from experiment [1]; (b) CFD simulated time variation of liquid holdup obtained for elongated bubble flow; (c) comparison of CFD and experimental PDF of liquid holdup for elongated bubble flow.

### 3.3 Slug flow

Figure 8(a) depicts the simulated contours of volume fraction of air-water at superficial velocities of air and water $V_{SG}$ = 0.62 m/s and $V_{SL}$ = 0.28 m/s, respectively. It is clear that the air phase appears in two different forms:

large and small spherical bubbles dispersed in the water phase. Large bubbles occupy almost the entire cross section of the annulus and move uniformly upwards. The liquid (water) phase appears as liquid plugs that span over the cross section of the annulus pipe, and as falling liquid films that flow downwards between the large bubbles (slug air) and the tube walls. The slugs (water) which separate the main successive bubbles contain small dispersed spherical gas bubbles. As a result of a decrease in flow holdup and increased turbulence, the liquid phase wraps itself around the inner pipe of the annulus and contains some entrained air bubbles flowing close to the top of the annulus [8]. As a result of the high gas superficial velocity, the wavy interface and stratified smooth flow are observed along the annulus section during the flow simulation. The contour phase distribution for this case shows a clear chaotic, unstable and wavy spike image, whose behaviour was reported by Roberto *et al.* [60]. A similar trend was captured from the visual (experimental) image placed in Fig. 8(b) [8]. It can be seen that the VOF and $k$-$\varepsilon$ models conveniently predict the slug flow with the studied condition, showing a good agreement with the video image captured from the experiment.

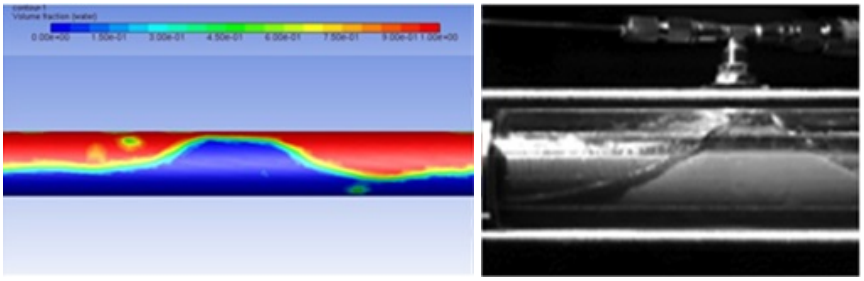

(a) (b)

Figure 8: The comparison between (a) the CFD contour plot of volume fraction of air-water along the annulus section for slug flow and (b) the visual observations from high-speed imaging of slug flow; $V_{SG} = 0.62$ m/s and $V_{SL} = 0.28$ m/s [1].

Figure 9 shows the time variation and the PDF of liquid holdup for both the model and experimental data. In Fig. 9(a), the experimental time-varying liquid holdup for slug flow is illustrated. The experiment shows a pulsating flow between the crest values of 0.3 and 1, which shows how the slug liquid body and Taylor bubble alternate with the annulus section. Figure 9(b) shows the time-varying liquid holdup for the CFD model having pulsating flow between the crest value of 0.3 and 0.5. However, Fig. 9(c) shows the

comparison of the simulated and experimental PDF of liquid holdup for slug flow. From the plot, a bimodal trend is observed for the simulated data, which is in line with the experimental data. It can be seen from the plot in Fig. 9(c) that two distinct peaks are observed from the CFD model. The first peak occurs within the liquid holdup range of 0.3–0.5, while the second peak is within the range of 0.3–0.4. The first peak was adequately predicted, falling in the same range as in the experiment, while the higher peak was underestimated compared with the experiment where it falls in the range of 0.8–0.9.

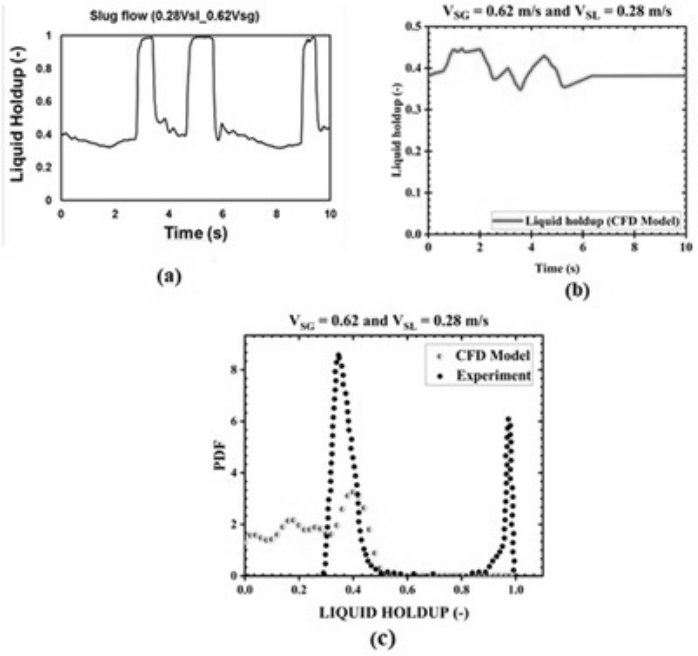


Figure 9: The time variation of liquid holdup and the PDF trend at $V_{SG} = 0.62$ m/s and $V_{SL} = 0.28$ m/s: (a) the measured time variation of liquid holdup from experiment [1]; (b) simulated time variation of liquid holdup for slug flow; (c) comparison between the CFD model and experiment for PDF of liquid holdup for slug flow.

## 4 Conclusions

The current work was carried out to establish the accuracy of the CFD model in predicting the flow pattern and also validate the work of Eyo *et al.* [8] in a horizontal concentric annulus pipe. This was achieved through

the use of the VOF model, which is based on Eulerian-Eulerian approach in conjunction with the turbulence model (realizable $k$-$\varepsilon$) in Ansys Fluent. Simulations were done on a 12.8 m long pipe with a hydraulic diameter of 0.0168 m using air and water as the main operating fluids. The entire length was calculated for a simulation time of 10 seconds; the time it takes for the fluid to be fully developed along the 2 m section of the pipe was ignored. The calculated volume fractions of air and water were taken on a distance of 6.01 m from the inlet to the annulus section. Three basic two-phase flow regimes were predicted for the condition of superficial velocities studied. These flow patterns were obtained by varying the superficial velocity of air and water to obtain regimes such as the elongated bubble, dispersed bubble and slug flow regimes. The validation of the model started with the checking of the mesh quality, which is crucial in getting the right numerical solutions. The convergence behaviour was checked by initiating several runs and varying the density of cells. The pressure drop along the length of the pipe was used as a criterion to check the convergence behaviour. The cell values of the corresponding pressure gradient were recorded. The validation of CFD results of two-phase flow patterns determined as a combination of time series and PDF of the liquid holdup was made with the help of an experiment of visual image capture from a high-speed camera. The PDF model was used to describe the flow structure and calculate the fraction of liquid holdup in the spatial domains employing the kernel density function of MATLAB to plot the pattern of flow. From the PDF trend results, the crest value for the simulated time-varying liquid holdup plot for elongated bubble was observed to fluctuate between 0.1 and 0.6. It can be seen that the CFD model underestimated time-varying liquid holdup for an elongated bubble flow. For slug flow the first peak was adequately predicted which falls in the same range as in the experiment and the higher peak was underestimated compared with the experiment data, where it falls in the range of 0.8–0.9. The numerical results showed a good agreement with the corresponding experimental data over a studied range of flow conditions.

Future works are underway to ensure that the turbulence (realizable $k$-$\varepsilon$) model can be used to simulate other flow regimes of liquid holdup for concentric and fully eccentric pipes at varying superficial velocities conditions and also to predict the pressure gradient of the system.

*Received 5 February 2023*

# References


[1] Crawford N.M., Cunningham G., Spence S.W.T.: *An experimental investigation into the pressure drop for turbulent flow in 90 elbow bends.* Proc. Inst. Mech. Engrs. E: J. Process Mech. Eng. **221**(2007), 77–88. doi: 10.1243/0954408JPME84

[2] Abdulkadir M.: *Experimental and computational fluid dynamics (CFD) studies of gas-liquid flow in bends.* PhD thesis, Univ. Nottingham, 2011.

[3] Sarica C., Pereyra E.J.: Brito R.: *Effect of medium oil viscosity on two phase oil gas flow behavior in horizontal pipes.* In: Proc. Offshore Technology Conf., Houston, May 2013. doi: 10.4043/24048-MS

[4] Tzotzi C., Bontozoglou V., Andritsos N., Vlachogiannis M.: *Effect of fluid properties on flow patterns in two-phase gas – liquid flow in horizontal and downward pipes.* Ind. Eng. Chem. Res. **50**(2011), 2, 645–55. doi: 10.1021/ie100239v

[5] Matsubara H., Naito K.: *Effect of liquid viscosity on flow patterns of gas-liquid two-phase flow in a horizontal pipe.* Int. J. Multiphas. Flow **37**(2011), 10, 1277–1281. doi: 10.1016/j.ijmultiphaseflow.2011.08.001

[6] Waelchli S, von Roh P.R.: *Two-phase flow characteristics in gas–liquid microreactors.* Int. J. Multiphas. Flow **32**(2006), 7, 791–806. doi: 10.1016/j.ijmultiphaseflow.2006.02.014

[7] Ekberg N.P., Ghiaasiaan S.M., Abdel-Khalik S.I., Yoda M., Jeter S.M.: *Gas–liquid two-phase flow in narrow horizontal annuli.* Nucl. Eng. Des. **192**(1999), 1, 59–80. doi: 10.1016/S0029-5493(99)00078-3

[8] Eyo E.N., Lao L.: *Gas-liquid flow regimes in horizontal annulus.* J. Petrol. Sci. Eng. **175**(2019), 573–586. doi: 10.1016/j.petrol.2018.12.056

[9] Barnea D., Luninski Y., Taitel Y.: *Flow pattern in horizontal and vertical two phase flow in small diameter pipes.* Canadian J. Chem. Eng. **61**(1983), 617–20.

[10] Izwan Ismail A.S., Ismail I., Zoveidavianpoor M., Mohsin R., Piroozian A., Misnan M.S., *et al.*: *Experimental investigation of oil–water two-phase flow in horizontal pipes: Pressure losses, liquid holdup and flow patterns.* J. Petrol. Sci. Eng. **127**(2015), 409–420.

[11] Mandhane J.M., Gregory G.A., Aziz K.: *A flow pattern map for gas – liquid flow in horizontal pipes.* Int. J. Multiphas. Flow **1**(1974), 537–553.

[12] Farman Ali S., Yeung H.: *Experimental study of two-phase air–water flow in large-diameter vertical pipes.* Chem. Eng. Commun. **202**(2015), 823–842.

[13] Kiran R., Ahmed R., Salehi S.: *Experiments and cfd modelling for two phase flow in a vertical annulus.* Chem. Eng. Res. Des. **153**(2020), 201–211.

[14] Jagan V., Satheesh A.: *Experimental studies on two phase flow patterns of air–water mixture in a pipe with different orientations.* Flow Meas. Instrum. **52**(2016), 170–179.

[15] Barnea D., Shoham O., Taitel Y., Dukler A.E.: *Flow pattern transition for gas-liquid flow in horizontal and inclined pipes. Comparison of experimental data with theory.* Int. J. Multiphas. Flow **6**(1980), 217–225.

[16] Rodriguez O.M.H., Baldani L.S.: *Prediction of pressure gradient and holdup in wavy stratified liquid–liquid inclined pipe flow.* J. Petrol. Sci. Eng. **96-97**(2012), 140–151.

[17] Nyong O., Fakorede D., Ifere M., Bepaye A., Igbong D., Ebieto C., *et al.*: *CFD modelling of dispersed bubble two-phase flow in a concentric annulus pipe.* Int. Res, J. Innovat. Eng, **5**(2021), 82.

[18] Ibarra R., Nossen J., Tutkun M.: *Two-phase gas-liquid flow in concentric and fully eccentric annuli. Part I: Flow patterns, holdup, slip ratio and pressure gradient.* Chem. Eng. Sci. **203**(2019), 489–500.

[19] Lage A.C., Rommetveit R., Time R.W.: *An experimental and theoretical study of two-phase flow in horizontal or slightly deviated fully eccentric annuli.* In: Proc. IADC/SPE Asia Pacific Drilling Technology, OnePetro; 2000.

[20] Adapco C. Star-CCM+ Theory Guide. CD-adapco. 2021.

[21] Friedemann C., Mortensen M., Nossen J.: *Two-phase flow simulations at 0–4° inclination in an eccentric annulus.* Int. J. Heat Fluid Fl. **83**(2020), 108586.

[22] Sultan R.A., Rahman M.A., Rushd S., Zendehboudi S., Kelessidis V.C.J.: *CFD analysis of pressure losses and deposition velocities in horizontal annuli.* Int. J. Chem. Eng. (2019), 7068989.

[23] Fluent A. *Ansys Fluent theory guide.* Ansys Inc, USA. 2011; 15317:724-46.

[24] Hamza G., Benderradji R., Beghidja A., Tayebi T.: *Numerical study of upward vertical two-phase flow through an annulus concentric pipe.* J. Adv. Res. Fluid Mech. Therm. Sci. **58**(2020), 187–206.

[25] Sergeev V., Vatin N., Kotov E., Nemova D., Khorobrov S.J.: *Slug regime transitions in a two-phase flow in horizontal round pipe.* CFD Simulations **10**(2020), 8739.

[26] Gioia F., Hewitt G.F., Alimonti C.: *Multiphase Flow Metering: Principles and Applications. Multiphase Flow Metering: Principles and Applications.* Elsevier Sci., 2009.

[27] Xue Y., Stewart C., Kelly D., Campbell D., Gormley M.J.W.: *Two-phase annular flow in vertical pipes: A critical review of current research techniques and progress.* Water **14**(2022), 3496.

[28] Lin R., Wang K., Liu L., Zhang Y., Dong S.: *Study on the characteristics of interfacial waves in annular flow by image analysis.* Chem. Eng. Sci. **212**(2020), 115336.

[29] van Eckeveld A.C., Gotfredsen E., Westerweel J., Poelma C.: *Annular two-phase flow in vertical smooth and corrugated pipes.* Int. J. Multiphase Flow **109**(2018), 150–163.

[30] Häber T., Gebretsadik M., Bockhorn H., Zarzalis N.: *The effect of total reflection in plif imaging of annular thin films.* Int. J. Multiphase Flow **76**(2015), 64–72.

[31] Banowski M., Beyer M., Szalinski L., Lucas D., Hampel U.: *Comparative study of ultrafast X-ray tomography and wire-mesh sensors for vertical gas–liquid pipe flows.* Flow Meas. Instrum. **53**(2017), 95–106.

[32] Hanus R., Zych M., Mosorov V., Golijanek-Jędrzejczyk A., Jaszczur M., Andruszkiewicz A.J.M., *et al.*: *Evaluation of liquid-gas flow in pipeline using gamma-ray absorption technique and advanced signal processing.* Metr. Meas. Syst. **28**(2021), 145–159.

[33] Sorgun M., Osgouei R.E., Ozbayoglu M.E., Ozbayoglu A.M.: *An experimental and numerical study of two-phase flow in horizontal eccentric annuli. Energy Sources, Part A: Recovery.* Util. Environ. Eff. **35**(2013), 891–899.

[34] Osgouei R.E., Ozbayoglu E.M., Ozbayoglu M.A., Yuksel E.: *Flow pattern identification of gas-liquid flow through horizontal annular geometries.* In: Proc. SPE Oil and Gas India Conf. Exhibit. 2010.

[35] Abbasi M., Baniamerian Z.: *Analytical simulation of flow and heat transfer of two-phase nanofluid (stratified flow regime).* Int. J. Chem. Eng. (2014), 474865.

[36] Ozbayoglu M.E., Omurlu C.: *Modelling of two-phase flow through concentric annuli.* J. Petrol. Sci. Technol. **25**(2007), 1027–1040.

[37] Omurlu C., Ozbayoglu E.M.: *A new mechanistic model for two-phase flow through eccentric horizontal annulus.* In: Proc. SPE Europec/EAGE Ann. Conf. Exhib. 2006.

[38] Lahiri S., Ghanta K.: *Computational technique to predict the velocity and concentration profile for solid-liquid slurry flow in pipelines.* In: Proc. 17th Int. Conf. on Hydrotransport, Capetown 2007, 149–175.

[39] Vijiapurapu S., Cui J.: *Performance of turbulence models for flows through rough pipes.* Appl. Math. Model. **34**(2010), 1458–1466.

[40] Markatos N.C.: *The mathematical modelling of turbulent flows.* Appl. Math. Model. **10**(1986), 190–220.

[41] Kelessidis V.C., Dalamarinis P., Maglione R.: *Experimental study and predictions of pressure losses of fluids modeled as Herschel–Bulkley in concentric and eccentric annuli in laminar, transitional and turbulent flows.* J. Petrol. Sci. Eng. **77**(2011), 305–312.

[42] Sultan R.A.: *A comprehensive study on multiphase flow through pipeline and annuli using cfd approach.* Memorial University of Newfoundland; 2018.

[43] Laufer J.: *The structure of turbulence in fully developed pipe flow.* NASA, Natl. Bureau Stand., 1953.

[44] Lien K., Monty J., Chong M., Ooi A.: *The entrance length for fully developed turbulent channel flow.* In: Proc. 15th Australian Fluid Mechanics Conf., Univ. of Sydney, Sydney, 2004, 356–363.

[45] Friedemann C., Mortensen M., Nossen J.: *Gas-liquid slug flow in a horizontal concentric annulus, a comparison of numerical simulations and experimental data.* Int. J. Heat Fluid Fl. **78**(2019), 108437.

[46] Brackbill J.U., Kothe D.B., Zemach C.: *A continuum method for modeling surface tension.* J. Comput. Phys. **100**(1992), 335–354.

[47] Anderson T.B., Jackson R.: *Fluid mechanical description of fluidized beds. Equations of motion.* Ind. Eng. Chem. Fund. **6**(1967), 527–539.

[48] Atkin R.J., Craine R.E.: *Continuum theories of mixtures: Applications.* IMA J. Appl. Math. **17**(1976), 153–207.

[49] Bowen R.: *Continuum physics* Vol. 4. 1976.

[50] Dakshinamoorthy D., Dai Y., Agrawal M.: *CFD modeling of bubbly, slugand annular flow regimes in vertical pipelines.* In: Proc. Offshore Technology Conf., Houston, 2013, 6–9.

[51] Manual U.J.T.G. Ansys Fluent 12.0. 2009.

[52] Launder B.E., Spalding D.B.: *The numerical computation of turbulent flows.* In: Numerical Prediction of Flow, Heat Transfer, Turbulence and Combustion (S.V. Patankar, A. Pollard, A.K. Singhal, S.P. Vanka, Eds.), Pergamon, 1983, 96–116.

[53] Fathi Roudsari S., Turcotte G., Dhib R., Ein-Mozaffari F.: *CFD modeling of the mixing of water in oil emulsions.* Comput. Chem. Eng. **45**(2012), 124–136.

[54] Kiran R., Ahmed R., Salehi S.J.: *Experiments and cfd modelling for two phase flow in a vertical annulus.* **153**(2020), 201–211.

[55] Renze P., Buffo A., Marchisio D.L., Vanni M.: *Simulation of coalescence, breakup, and mass transfer in polydisperse multiphase flows.* Chem. Ing. Tech. **86**(2014), 1088–1098.

[56] Luewisutthichat W., Tsutsumi A., Yoshida K.: *Bubble characteristics in multi-phase flow systems: Bubble sizes and size distributions.* J. Chem. Eng. Japan **30**(1997), 461–466.

[57] Deendarlianto A.M., Widyaparaga A., Dinaryanto O., Khasani I.: *CFD studies on the gas-liquid plug two-phase flow in a horizontal pipe.* J. Petrol.Sci. Eng. **147**(2016), 779–787.

[58] Julia J.E., Ozar B., Dixit A., Jeong J.-J., Hibiki T., Ishii M.: *Axial development of flow regime in adiabatic upward two-phase flow in a vertical annulus.* J. Fluids Eng. **131**(2009), 021302.

[59] Caetano E.F., Shoham O., Brill J.P.: *Upward vertical two-phase flow through an annulus — Part II: Modeling bubble, slug, and annular flow.* J. Energ. Res. Technol. **114**(1992), 14–30.

[60] Ibarra R., Nossen J., Tutkun M.: *Two-phase gas-liquid flow in concentric and fully eccentric annuli. Part II: Model development, flow regime transition algorithm and pressure gradient.* Chem. Eng. Sci. **203**(2019), 501–510.

# Notes for Contributors

Archives of Thermodynamics publishes original papers which have not previously appeared in other journals. The journal does not have article processing charges (APCs) nor article submission charges. The language of the papers is English. The paper should not exceed the length of 25 pages. All pages should be numbered. The plan and form of the papers should be as follows:

1. The heading should specify the title (as short as possible), author, his/her complete affiliation, town, zip code, country and e-mail. Please indicate the corresponding author. The heading should be followed by *Abstract* of maximum 15 typewritten lines and *Keywords*.

2. More important symbols used in the paper can be listed in *Nomenclature*, placed below *Abstract* and arranged in a column, e.g.:
   $u$ – velocity, m/s
   $v$ – specific volume, m/kg
   etc.
   The list should begin with Latin symbols in alphabetical order followed by Greek symbols also in alphabetical order and with a separate heading. Subscripts and superscripts should follow Greek symbols and should be identified with separate headings. Physical quantities should be expressed in SI units (*Système International d'Unités*).

3. All abbreviations should be spelled out first time they are introduced in the text.

4. The equations should be each in a separate line. Standard mathematical notation should be used. All symbols used in equations must be clearly defined. The numbers of equations should run consecutively, irrespective of the division of the paper into sections. The numbers should be given in round brackets on the right-hand side of the page.

5. Particular attention should be paid to the differentiation between capital and small letters. If there is a risk of confusion, the symbols should be explained (for example *small c*) in the margins. Indices of more than one level (such as $B_{f_a}$) should be avoided wherever possible.

6. Computer-generated figures should be produced using **bold lines and characters**. No remarks should be written directly on the figures, except numerals or letter symbols only. Figures should be as small as possible while displaying clearly all the information requires, and with all lettering readable. The relevant explanations can be given in the caption.

7. The figures, including photographs, diagrams, etc., should be numbered with Arabic numerals in the same order in which they appear in the text. Each figure should have its own caption explaining the content without reference to the text.

8. Computer files on an enclosed disc or sent by e-mail to the Editorial Office are welcome. The manuscript should be written as a MS Word file – $*.doc$, $*.docx$ or LaTeX file – $*.tex$. For revised manuscripts after peer review process, figures should be submitted as separate graphic files in either vector formats (PostScript (PS),

Encapsulated PostScript (EPS), preferable, CorelDraw (CDR), etc.) or bitmap formats (Tagged Image File Format (TIFF), Joint Photographic Experts Group (JPEG), etc.), with the resolution not lower than 300 dpi, preferably 600 dpi. These resolutions refer to images sized at dimensions comparable to those of figures in the print journal. Therefore, electronic figures should be sized to fit on single printed page and can have maximum 120 mm x 170 mm. Figures created in MS World, Exel, or PowerPoint will not be accepted. The quality of images downloaded from websites and the Internet are also not acceptable, because of their low resolution (usually only 72 dpi), inadequate for print reproduction.

9. The references for the paper should be numbered in the order in which they are called in the text. Calling the references is by giving the appropriate numbers in square brackets. The references should be listed with the following information provided: the author's surname and the initials of his/her names, the complete title of the work (in English translation) and, in addition:

   (a) for books: the publishing house and the place and year of publication, for example:
   [1] Holman J.P.: *Heat Transfer*. McGraw-Hill, New York 1968.

   (b) for journals: the name of the journal, volume (Arabic numerals in bold), year of publication (in round brackets), number and, if appropriate, numbers of relevant pages, for example:
   [2] Rizzo F.I., Shippy D.I.: *A method of solution for certain problems of transient heat conduction*. AIAA J. **8**(1970), No.11, 2004–2009.

   For works originally published in a language other than English, the language should be indicated in parentheses at the end of the reference.

   Authors are responsible for ensuring that the information in each reference is complete and accurate.

10. As the papers are published in English, the authors who are not native speakers of English are obliged to have the paper thoroughly reviewed language-wise before submitting for publication.

**Manuscript submission** Manuscripts to be considered for publication should be electronically submitted to the Editorial Office via the online submission and reviewing system, the Editorial System, at http://www.editorialsystem.com/aot. Submission to the journal proceeds totally on line and you will be guided stepwise throughout the process of the creation and uploading of your files. The body of the text, tables and figures, along with captions for figures and tables should be submitted separately. The system automatically converts source files to a single PDF file article, for subsequent approval by the corresponding Author, which is then used in the peer-review process. All correspondence, including notification confirming the submission of the manuscripts to the Editorial Office, notification of the Editors's decision and requests for revision, takes place by e-mails. Authors should designate the corresponding author, whose responsibility is to represent the Authors in contacts with the Editorial Office. Authors are requested not to submit the manuscripts by post or e-mail.

The illustrations may be submitted in color, however they will be printed in black and white in the journal, so the grayscale contributions are preferable. Therefore, the figure

caption and the entire text of the paper should not make any reference to color in the illustration. Moreover the illustration should effectively convey author's intended meaning when it is printed as a halftone. The illustrations will be reproduced in color in the online publication.

**Further information** All manuscripts will undergo some editorial modification. The paper proofs (as PDF file) will be sent by e-mail to the corresponding author for acceptance, and should be returned within two weeks of receipt. Within the proofs corrections of minor and typographical errors in: author names, affiliations, articles titles, abstracts and keywords, formulas, symbols, grammatical error, details in figures, etc., are only allowed, as well as necessary small additions. The changes within the text will be accepted in case of serious errors, for example with regard to scientific accuracy, or if authors reputation and that of the journal would be affected. Submitted material will not be returned to the author, unless specifically requested.
A PDF file of published paper will be supplied free of charge to the Corresponding Author.

Submission of the manuscript expresses at the same time the authors consent to its publishing in both printed and electronic versions.

**Transfer of Copyright Agreement** Submission of the manuscript means that the authors automatically agree to assign the copyright to the Publisher. Once a paper has been accepted for publication, as a condition of publication, the authors are asked to send by email a scanned copy of the signed original of the Transfer of Copyright Agreement, signed by the Corresponding Author on behalf of all authors to the Managing Editor of the Journal. The copyright form can be downloaded from the journal's website at http://www.imp.gda.pl/archives-of-thermodynamics/ under Notes for Contributors.

*The Editorial Committee*